Transactions of the ASME®

Technical Editor, **LEWIS T. WHEELER (1997)**

Department of Mechanical Engineering,
University of Houston,
Houston, TX 77204-4792

APPLIED MECHANICS DIVISION

Chairman, **C. T. HERAKOVICH**
Secretary, **T. HUGHES**
Associate Technical Editors,
J. R. BARBER (2000)
J. L. BASSANI (1999)
R. C. BECKER (1998)
R. C. BENSON (2000)
M. M. CARROLL (2000)
I. M. DANIEL (1999)
W. J. DRUGAN (2000)
A. A. FERRI (2000)
J. T. JENKINS (1999)
J. W. JU (1998)
V. K. KINRA (1999)
S. KYRIAKIDES (2000)
S. LICHTER (1998)
W. K. LIU (1999)
M. ORTIZ (1998)
N. C. PERKINS (1999)
M.-J. PINDERA (2000)
K. T. RAMESH (2000)
J. N. REDDY (1998)
D. A. SIGINER (2000)
M. TAYA (1999)

BOARD ON COMMUNICATIONS

Chairman and Vice-President
R. MATES

OFFICERS OF THE ASME
President, **K. B. THAYER**
Executive Director, **D. L. BELDEN**
Treasurer, **J. A. MASON**

PUBLISHING STAFF
Managing Director, Engineering
CHARLES W. BEARDSLEY
Director, Technical Publishing
PHILIP DI VIETRO
Managing Editor, Technical Publishing
CYNTHIA B. CLARK
Managing Editor, Transactions
CORNELIA MONAHAN
Production Coordinator
JUDITH SIERANT
Production Assistant
MARISOL ANDINO

Transactions of the ASME, Journal of Applied Mechanics (ISSN 0021-8936) is published quarterly (Mar., June, Sept., Dec.) for $210.00 per year by The American Society of Mechanical Engineers, 345 East 47th Street, New York, NY 10017.

Periodicals postage paid at New York, NY and additional mailing office. POSTMASTER: Send address changes to Transactions of the ASME, Journal of Applied Mechanics, c/o THE AMERICAN SOCIETY OF MECHANICAL ENGINEERS, 22 Law Drive, Box 2300, Fairfield, NJ 07007-2300.

CHANGES OF ADDRESS must be received at Society headquarters seven weeks before they are to be effective. Please send old label and new address. **PRICES:** To members, $40.00; to nonmembers, $230.00; single issue, $92.00. Add $40.00 (airmail $60.00) for postage to countries outside the United States and Canada.

STATEMENT from By-Laws. The Society shall not be responsible for statements or opinions advanced in papers or . . . printed in its publications (B7.1, Para. 3), **COPYRIGHT** © **1997** by The American Society of Mechanical Engineers. Authorization to photocopy material for internal or personal use under circumstances not falling within the fair use provisions of the Copyright Act is granted by ASME to libraries and other users registered with the Copyright Clearance Center (CCC). Transactional Reporting Service provided that the base fee of $3.00 per article is paid directly to CCC, Inc., 222 Rosewood Drive, Danvers, MA 01923. Request for special permission or bulk copying should be addressed to Reprints/Permission Department. **INDEXED** by Applied Mechanics Reviews and Engineering Information, Inc. Canadian Goods & Services Tax Registration #126148048.

Journal of Applied Mechanics

Published Quarterly by The American Society of Mechanical Engineers

VOLUME 64 • NUMBER 4 • DECEMBER 1997

TECHNICAL PAPERS

729 **Self-Similar Crack Expansion Method for Three-Dimensional Crack Analysis**
Yonglin Xu, B. Moran, and T. Belytschko

738 **Stress Concentrations in an Intermingled Hybrid Composite**
H. A. Luo and Q. Wang

743 **Spherical Cavity Expansion in a Drucker-Prager Solid**
D. Durban and N. A. Fleck

751 **Scale Effects in Media With Periodic and Nearly Periodic Microstructures, Part I: Macroscopic Properties**
M. W. Schraad and N. Triantafyllidis

763 **Scale Effects in Media With Periodic and Nearly Periodic Microstructures, Part II: Failure Mechanisms**
M. W. Schraad and N. Triantafyllidis

772 **Enhanced Elastic Buckling Loads of Composite Plates With Tailored Thermal Residual Stresses**
S. F. Müller de Almeida and J. S. Hansen

781 **Micromechanical Modeling of Creep Behavior in Particle-Reinforced Silicone-Rubber Composites**
Chao-Hsun Chen and Chaing-Ho Cheng

787 **Linear Elastic Behavior of a Low-Density Kelvin Foam With Open Cells**
W. E. Warren and A. M. Kraynik

795 **A Multicontinuum Approach to Structural Analysis of Linear Viscoelastic Composite Materials**
M. R. Garnich and A. C. Hansen

804 **Fracture Mechanics of Composites With Residual Thermal Stresses**
J. A. Nairn

811 **Crack Initiation From Homogeneous and Bimaterial Corners**
J. L. Grenestedt and S. Hallstrom

819 **Theoretical Transient Analysis of the Interaction Between a Dynamically Propagating In-Plane Crack and Traction-Free Boundaries**
Chwan-Huei Tsai and Chien-Ching Ma

828 **Flexural Wave Scattering at a Through Crack in a Conducting Plate Under a Uniform Magnetic Field**
Y. Shindo, I. Ohnishi, and S. Tohyama

835 **Viscoelastic Model of Finitely Deforming Rubber and Its Finite Element Analysis**
Seung Jo Kim, Kyeong Su Kim, and Jin Yeon Cho

842 **Post-buckling Analysis of Multiply Delaminated Composite Plates**
Haiying Huang and G. A. Kardomateas

847 **Stability Analysis of Piezoelectric Circular Cylindrical Shells**
Cheng Chang-qing and Shen Ya-peng

853 **Total Deformation, Plane-Strain Contact Analysis of Macroscopically Homogeneous, Compositionally Graded Materials With Constant Power-Law Strain Hardening**
A. E. Giannakopoulos

861 **Enrichment of the Finite Element Method With the Reproducing Kernel Particle Method**
Wing Kam Liu, R. A. Uras, and Y. Chen

871 **Thermal Analysis of a Round Roll**
W. R. Qualls and J. K. Good

877 **Boundary Element Solution for Free Edge Stresses in Composite Laminates**
G. Davì and A. Milazzo

885 **Koiter-Based Solution for the Initial Post-buckling Behavior of Moderately Thick Orthotropic and Shear Deformable Cylindrical Shells Under External Pressure**
G. A. Kardomateas

(Contents continued on outside back cover)

This journal is printed on acid-free paper, which exceeds the ANSI Z39.48-1992 specification for permanence of paper and library materials. ♾™

♻ 85% recycled content, including 10% post-consumer fibers.

Downloaded 04 May 2010 to 171.66.16.52. Redistribution subject to ASME license or copyright; see http://www.asme.org/terms/Terms_Use.cfm

CONTENTS (CONTINUED)

897 **In-Plane Stress and Displacement Distributions in a Spinning Annular Disk Under Stationary Edge Loads**
Jen-San Chen and Jhi-Lu Jhu

905 **Derivation of Plate Theory Accounting Asymptotically Correct Shear Deformation**
V. G. Sutyrin

916 **Air Entrainment During Steady-State Web Winding**
M. B. Keshavan and J. A. Wickert

923 **Different Features of a Stability Problem of Underconstrained Structures**
K. Y. Volokh and O. Vilnay

929 **Approximate and Analytic Solutions for Deformation of Finite Porous Filters**
S. I. Barry, G. N. Mercer, and C. Zoppou

935 **Contact Stresses in Cables due to Tension and Torsion**
K. Kumar, J. E. Cochran, Jr., and J. A. Cutchins

940 **Localized Modes in Periodic Systems With Nonlinear Disorders**
C. W. Cai, H. C. Chan, and Y. K. Cheung

946 **A Quasi-Decoupling Approach for Nonclassical Linear Systems in State Space**
Gexue Ren and Zhaochang Zheng

951 **Three-Dimensional Vibrations of a Beam on an Elastic Half-Space: Resonance Interaction of Vertical-Longitudinal and Lateral Beam Waves**
A. V. Metrikine and H. A. Dieterman

957 **Explicit Vibration Solutions of a Cable Under Complicated Loads**
P. Yu

965 **A Lyapunov Function for Systems Whose Linear Part is Almost Classically Damped**
S. J. Cox and J. Moro

969 **On the Computation of Relative Rotations and Geometric Phases in the Motions of Rigid Bodies**
O. M. O'Reilly

975 **Stochastic Averaging of Quasi-Integrable Hamiltonian Systems**
W. Q. Zhu, Z. L. Huang, and Y. Q. Yang

985 **Time-Integral Variational Principles for Nonlinear Nonholonomic Systems**
J. G. Papastavridis

992 **The Fiber-Matrix Interface Crack**
R. Chao and N. Laws

BRIEF NOTES

On Bonded Circular Inclusions in Plane Thermoelasticity 1000
C. K. Chao and M. H. Shen

Influence of the Interface Periodic Array of Coplanar Cracks on the Free-Surface Oscillations 1004
M. Ciarletta and M. A. Sumbatyan

On the Use of Deflection Components in Timoshenko Beam Theory 1006
K. H. Lee and C. M. Wang

The Occurrence of Painleve's Paradox in the Motion of a Rotating Shaft 1008
E. V. Wilms and H. Cohen

1010 Saddle-Point Principles for General Nonlinear Material Continua
A. Carini

1014 Impact Coefficients and Tangential Impacts
R. M. Brach

1017 On the Transient Response of a Spinning Disk Under a Space-Fixed Load
Jen-San Chen and C.-M. Hsu

1019 Slip With Friction Between a Layer and a Substrate Caused by SH Waves
Yu Guilan, Wang Yuesheng, and Gai Bingzheng

DISCUSSION

1022 **Contact Between Elastic Bodies With an Elliptic Contact Interface in Torsion, by J. F. Cuttino and T. A. Dow—Discussion by J. Jäger**

1024 **Investigation of a New Formulation of the Lagrange Method for Constrained Dynamic Systems, by A. Rosen and E. Edelstein—Discussion by P. Hagedorn**

1027 **Modal Decoupling of Systems Described by Three Linear Operators, by A. A. Renshaw—Discussion by W. Kliem**

(Contents continued on p. 964)

Downloaded 04 May 2010 to 171.66.16.52. Redistribution subject to ASME license or copyright; see http://www.asme.org/terms/Terms_Use.cfm

CONTENTS (CONTINUED)

BOOK REVIEW

1029 **Dislocation Based Fracture Mechanics, by J. Weertman—Reviewed by L. M. Keer**

ANNOUNCEMENTS AND SPECIAL NOTICES

737 Symposium on Rheology and Fluid Mechanics of Nonlinear Materials—Call for Papers

762 Finite Element Books Bibliography on the Internet

794 Periodicals on ASMENET

818 Change of Address Form

999 Symposium on Recent Developments in the Study of Impacts on Composite Materials—Call for Papers

1028 PACAM VI—Call for Papers

1030 Worldwide Mechanics Meetings List

1033 Mechanics of Nonlinear Materials—Call for Papers

1034 Information for Authors

1035 Annual Author Index

Downloaded 04 May 2010 to 171.66.16.52. Redistribution subject to ASME license or copyright; see http://www.asme.org/terms/Terms_Use.cfm

Yonglin Xu
Research Assistant Professor of Civil Engineering.

B. Moran
Associate Professor of Civil Engineering.

T. Belytschko
Walter P. Murphy Professor of Computational Mechanics.

Department of Civil Engineering, Northwestern University, Evanston, IL 60208

Self-Similar Crack Expansion Method for Three-Dimensional Crack Analysis

The self-similar crack expansion method is developed to calculate stress intensity factors for three-dimensional cracks in an infinite medium or semi-infinite medium by the boundary integral element technique. With this method, the stress intensity factors at crack tips are determined by calculating the crack-opening displacements over the crack surface, and the crack expansion rate, which is related to the crack energy release rate, is estimated by using a technique based on self-similar (virtual) crack extension. For elements on the crack surface, regular integrals and singular integrals are evaluated based on closed-form expressions, which improves the accuracy. Examples show that this method yields very accurate results for stress intensity factors of penny-shaped cracks and elliptical cracks in the full space, with errors of less than one percent as compared with exact solutions. The stress intensity factors of subsurface cracks are in good agreement with other numerical solutions.

1 Introduction

The evaluation of stress intensity factors for cracks is of importance in determining the fatigue life of materials, such as castings. From observations, it is known that fatigue failures usually occur from the initiation and propagation of surface or near-surface cracks. Boundary effects on stress intensity factors for a crack near a free surface are also of interest in fracture analysis.

Stress intensity factors of three-dimensional cracks are often determined from the tip displacements. However, such computations of the stress intensity factor limit the accuracy of the calculation. Based on an energy analysis, Cruse and Besunner (1975) and Cruse and Meyers (1977) proposed the crack extension method, where the stress intensity factors are determined from the variation of the strain energy with crack growth. In this paper we develop a method based on self-similar crack expansion method for the determination of stress intensity factors along a three-dimensional crack front. In the method, the derivative of the strain energy is directly calculated in terms of the crack opening volume. Thus, the stress intensity factors can be estimated in terms of crack displacement over the crack surface. The self-similar crack expansion method is related to the weight function method (Rice, 1972; Nikishkov and Piminov, 1991), where stress intensity factors are obtained by integrating a product of the load with a function (weight function) over the crack surface.

In the boundary integral equation method, the accuracy of the results depends greatly on the accuracy of the evaluation of the element integrals, especially the singular integrals. These integrals are carefully analyzed in this paper. Singular integrals on the elements which are not near to a crack edge are directly estimated by a line integral around the element boundary, so that computer time is saved and accuracy is improved. Singular integrals on the elements near the crack edge are evaluated after first transforming the two-dimensional singular integral to a one-dimensional regular integral. This combination of improved integrals and the self-similar crack expansion method significantly increases the accuracy of stress intensity factor calculations. The stress intensity factors for penny-shaped cracks and elliptical cracks are evaluated with errors of less than one percent compared to exact solutions. These techniques are applicable to the analysis of cracks with arbitrary geometry.

Related works in the numerical calculations of stress intensity factors for three-dimensional cracks are Bui (1977), who obtained a singular integral equation by the use of single layer and double layer potential for a three-dimensional crack; Murakami (1985) and Lee and Keer (1986) used the body-force method to reduce the problem of a planar crack to singular integral equations over the crack surface; Weaver (1977) has presented explicit forms of the boundary integral equations for three-dimensional cracks under mixed-mode loading conditions. Some investigators (Cruse, 1974; Polch et al., 1987; Gray et al., 1990) used path integrals with analytical methods to evaluate the integrals on boundary elements in the boundary element methods. Recently, Guo et al. (1995) used a line integral around an element to evaluate integrals on regular elements for three-dimensional crack analysis. In this paper, the line integral technique used by Guo et al. (1995) is extended to evaluate integrals on singular elements.

2 Basic Formulation

For problems consisting of a planar crack in an infinite or semi-infinite domain, the boundary integral equations for crack analysis have been presented in the literature using the reciprocal principle (Cruse, 1988) or by applying body force methods (Murakami and Nemat-Nasser, 1982). The boundary integral equations for three dimensional cracks are

$$\sigma_{ij}(\mathbf{x}) = \int_{\Omega} S_{ijk}(\mathbf{x}, \boldsymbol{\xi})\, \Delta u_k(\boldsymbol{\xi})\, d\Omega(\boldsymbol{\xi}) \qquad (2.1)$$

where the crack surface is denoted by Ω. The difference in crack surface displacements is represented by $\Delta u_k = u_k^+ - u_k^-$, and

$$S_{ijk}(\mathbf{x}, \boldsymbol{\xi}) = -c_{ijpm} G_{pq,mn}(\mathbf{x}, \boldsymbol{\xi})\, c_{klqn} n_l(\boldsymbol{\xi}). \qquad (2.2)$$

For isotropic materials

$$c_{ijkl} = \mu \left\{ \delta_{ik}\delta_{jl} + \delta_{il}\delta_{kj} + \frac{2\nu}{1-2\nu}\, \delta_{ij}\delta_{kl} \right\}$$

Contributed by the Applied Mechanics Division of THE AMERICAN SOCIETY OF MECHANICAL ENGINEERS for publication in the ASME JOURNAL OF APPLIED MECHANICS.

Discussion on this paper should be addressed to the Technical Editor, Professor Lewis T. Wheeler, Department of Mechanical Engineering, University of Houston, Houston, TX 77204-4792, and will be accepted until four months after final publication of the paper itself in the ASME JOURNAL OF APPLIED MECHANICS.

Manuscript received by the ASME Applied Mechanics Division, Jan. 19, 1996; final revision, Sept. 24, 1996. Associate Technical Editor: J. W. Ju.

Copyright © 1997 by ASME

Downloaded 04 May 2010 to 171.66.16.34. Redistribution subject to ASME license or copyright; see http://www.asme.org/terms/Terms_Use.cfm

where μ, ν are material constants (shear modulus and Poisson's ratio, respectively), and δ_{ij} is the Kronecker delta. The Green's function for the displacement is

$$G_{ij}(\mathbf{x}, \boldsymbol{\xi}) = \frac{1}{16\pi\mu(1-\nu)r}\{(3-4\nu)\,\delta_{ij} + r_{,i}r_{,j}\} \quad (2.3)$$

where

$$r = \sqrt{(\xi_1 - x_1)^2 + (\xi_2 - x_2)^2 + (\xi_3 - x_3)^2} \quad (2.4)$$

and the traction T_{ij} associated with the Green's function is

$$T_{ij}(\mathbf{x}, \boldsymbol{\xi}) = \lambda G_{ik,k}n_j + \mu(G_{ij,k} + G_{ik,j})n_k \quad (2.5)$$

or

$$T_{ij}(\mathbf{x}, \boldsymbol{\xi}) = \frac{-1}{8\pi(1-\nu)r^2}\{(1-2\nu)\delta_{ij} + 3r_{,i}r_{,j}]r_{,k}n_k - (1-2\nu)(r_{,i}n_j - r_{,j}n_i)\} \quad (2.6)$$

where differentiations are with respect to $\boldsymbol{\xi}$, and $T_{ij}(\mathbf{x}, \boldsymbol{\xi})$ represents the jth component of the traction on a surface with unit normal vector $n_k(\boldsymbol{\xi})$, caused by a unit point load in the ith direction at the point $\mathbf{x}$. For isotropic materials, the function S_{ijk} defined by (2.2) is given as

$$\begin{aligned} S_{ijk} = \frac{\mu}{4\pi(1-\nu)r^3}\{&3[(1-2\nu)\delta_{ij}r_{,k} \\ &+ \nu(\delta_{ik}r_{,j} + \delta_{jk}r_{,i}) - 5r_{,i}r_{,j}r_{,k}]r_{,l}n_l \\ &+ n_i[(1-2\nu)\delta_{jk} + 3\nu r_{,k}r_{,j}] \\ &+ n_j[(1-2\nu)\delta_{ik} + 3\nu r_{,k}r_{,i}] \\ &+ n_k[3(1-2\nu)r_{,i}r_{,j} - (1-4\nu)\delta_{ij}]\}. \end{aligned} \quad (2.7)$$

For a three-dimensional flat crack in the $x_1 - x_2$ plane as shown in Fig. 1, the integral equations can be written as

$$\sigma_{3j}(\mathbf{x}) = \int_\Omega S_{3jk}(\mathbf{x}, \boldsymbol{\xi})\Delta u_k(\boldsymbol{\xi})d\Omega(\boldsymbol{\xi}) \quad (2.8)$$

where

$$S_{333} = \frac{\mu}{4\pi(1-\nu)r^3} \quad (2.9)$$

and

$$S_{3jk} = \frac{\mu}{4\pi(1-\nu)r^3}[(1-2\nu)\delta_{jk} + 3\nu r_{,j}r_{,k}], \quad (j, k = 1, 2). \quad (2.10)$$

Once Eq. (2.8) has been solved for Δu_k on the crack surface, the stresses at interior points may be calculated by using (2.1). In this paper, calculations are made for three-dimensional cracks under tensile loading and, thus, the kernel of the integral Eq. (2.8) is S_{333}.

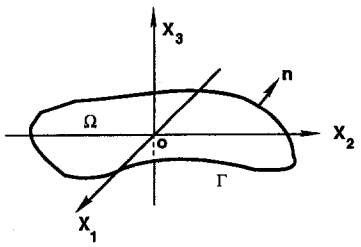


Fig. 1 Three-dimensional crack located in the $x_1 - x_2$ plane

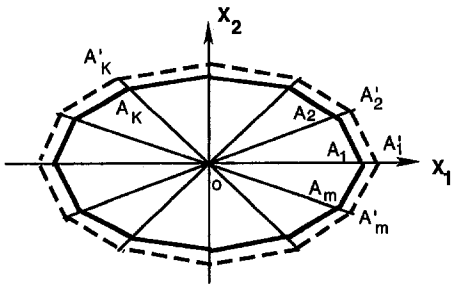


Fig. 2 Self-similar crack expansion in the $x_1 - x_2$ plane

3 Self-Similar Crack Expansion Method for Stress Intensity Factors Calculations

The self-similar crack expansion method stems from a method based on crack extension (crack extension method) which was originally proposed by Cruse and Besunner (1975) and Cruse and Meyers (1977). In the crack extension method, the stress intensity factors are determined from the variation of the strain energy as the crack edge extends a small distance δa, and the energy release rate is obtained indirectly, where the strain energy needs to be calculated twice, and the magnitude of the crack advance δa needs to be determined from experience. In the self-similar crack expansion method, the energy release rate is calculated directly by taking advantage of a self-similar expansion. The strain energy is calculated once, and the relationship between energy release rate and the crack-opening volume is employed.

Stress intensity factors along a crack front can be written in terms of the local crack-opening displacements as

$$K_I = \frac{\mu}{1-\nu}\sqrt{\frac{\pi}{2r}}\,u_3 \quad (3.1)$$

where r is a normal distance to the crack tip. Instead of using the local displacement at the crack tip, the self-similar crack expansion method uses the displacement field over the entire crack surface to estimate the stress intensity factors. For this purpose the relationship between the energy release rate and the displacement on the crack surface (for mode I) is employed. For a crack in the $x_1 - x_2$ plane under a uniform tensile load p, the energy release (or variation) due to a virtual crack extension $\delta a(s)$ is given by Rice (1985),

$$\delta\frac{1}{2}\int_\Omega p\Delta u_3 d\Omega = \int_\Gamma \frac{1-\nu^2}{E}K_I^2\delta a(s)d\Gamma \quad (3.2)$$

where s denotes distance along the crack front, and Γ is the boundary of the crack. If the crack expands self-similarly (Fig. 2), the change in crack size can be written as

$$\delta a(s) = \alpha a(s) \quad (3.3)$$

where α is a parameter, and $a(s)$ is the distance from the crack edge to the similarity center. The similarity center can either be the geometrical center or any other point. Note that $\delta a(s)$ is a virtual crack extension and may be negative. The stress intensity factors around the crack edge can be expressed as

$$K_I(s) = f(s)K_{I0} \quad (3.4)$$

where $f(s)$ is the distribution function of the stress intensity factor, which can be determined from the displacements at the crack tip, and K_{I0} is a reference stress intensity factor calculated at some suitable reference point. The distance between the similarity center and the reference point is denoted by a_0.

For a crack under remote tensile loading p, the left side of (3.2) can be written as $(1/2)\,p\delta V$, where δV is the variation in the crack-opening volume, V, which is the volume generated by the opening of the opposing surfaces of the crack. The crack-

Downloaded 04 May 2010 to 171.66.16.34. Redistribution subject to ASME license or copyright; see http://www.asme.org/terms/Terms_Use.cfm

opening volume can be expressed as $V = \beta a_0^3$, where $\beta = \beta(p)$ is independent of the crack size variation since $\Delta u_3/a_0$ is constant as long as the crack expands self-similarly as described by (3.3). Thus, the variation of the crack volume can be written as

$$\delta V = \frac{3V}{a_0}\,\delta a_0 \quad \text{or} \quad \delta V = 3V\alpha. \tag{3.5}$$

Substituting (3.3) and (3.4) into the right side of (3.2) and using (3.5) on the left side of (3.2) yields

$$\frac{3}{2}pV = \frac{1-\nu^2}{E}K_{I0}^2\int_\Gamma f^2(s)a(s)d\Gamma. \tag{3.6}$$

Hence, a modified reference stress intensity factor can be written as

$$K_{I0}^{*} = \sqrt{\frac{3EpV}{2(1-\nu^2)\displaystyle\int_\Gamma f^2(s)a(s)d\Gamma}}. \tag{3.7}$$

To compute K_{I0}^{*}, it is necessary to know $f(s)$ and $a(s)$, the latter is obtained directly from the geometry of the crack. To obtain $f(s)$, the relative crack-tip displacement Δu_3 is used since it is directly proportional to K_I, see Eq. (3.1). Thus, by evaluating Δu_3 at a given value of r near the crack edge, $f(s)$ can be determined using (3.1). This is used in (3.7) to evaluate K_{I0}^{*}, and $K_I(s)$ is obtained from an expression analogous to (3.4), i.e.,

$$K_I(s) = f(s)K_{I0}^{*}. \tag{3.8}$$

4 Numerical Implementation and Integral Evaluation on Elements

The boundary integral Eqs. (2.8) are rewritten here for completeness

$$\sigma_{3j}(\mathbf{x}) = \int_\Omega S_{3jk}(\mathbf{x}, \boldsymbol{\xi})\Delta u_k(\boldsymbol{\xi})d\Omega(\boldsymbol{\xi}). \tag{4.1}$$

A general method to reduce the singularity of the kernel S_{3jk} in (4.1) is to find a function F_{3jk} which satisfies $\nabla^2 F_{3jk} = -S_{3jk}$. Then the above can be written as

$$\sigma_{3j}(\mathbf{x}) = \int_\Omega F_{3jk,q}(\mathbf{x}, \boldsymbol{\xi})\Delta u_{k,q}(\boldsymbol{\xi})d\Omega(\boldsymbol{\xi}). \tag{4.2}$$

For planar cracks under tensile loading condition, the kernel function in (4.1) is $S_{333}(\mathbf{x}, \boldsymbol{\xi})$ as given in (2.9), and

$$F_{333}(\mathbf{x}, \boldsymbol{\xi}) = \frac{\mu}{4\pi(1-\nu)r} \tag{4.3}$$

where $r = \sqrt{(\xi_1 - x_1)^2 + (\xi_2 - x_2)}$. Thus Eq. (4.2) can be written as (for $j = 3$)

$$\sigma_{33}(\mathbf{x}) = \frac{\mu}{4\pi(1-\nu)}\int_\Omega \frac{1}{r^3}[(\xi_1 - x_1)\Delta u_{3,1} + (\xi_2 - x_2)\,\Delta u_{3,2}]d\Omega(\boldsymbol{\xi}). \tag{4.4}$$

The kernel function in (4.4) has a lower order singularity than that of (4.1). In this paper, the solution for the crack-opening displacement is based on (4.4).

To evaluate the above integral, the crack is discretized into $N = m \times n$ elements, where m is the number of segments in the circumferential direction and n is the number of segments in the radial direction (Fig. 3). In discretizing (4.4), we may take a single source point (x, y) at the center of each element. The crack-opening displacement in the elements is approximated by

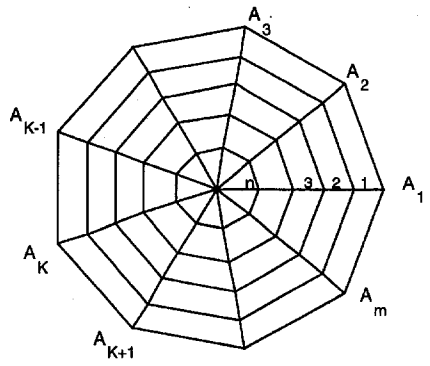


Fig. 3 Boundary elements ($m \times n$) on the crack surface

$$\Delta u_3 \equiv \Delta u_z = \sum_{K=1}^{4} N_K(x, y)\Delta u_{zK} \tag{4.5}$$

where the shape functions N_K can be evaluated using either an isoparametric formulation or a formulation which uses the basis $(1, x, y, xy)$. To simplify the evaluation of the integrals, the basis $(1, x, y, xy)$, $N_K = D_K/D$, is used, where D is a determinant of nodal coordinates given by

$$D = \det\begin{pmatrix} 1 & x_1 & y_1 & x_1y_1 \\ 1 & x_2 & y_2 & x_2y_2 \\ 1 & x_3 & y_3 & x_3y_3 \\ 1 & x_4 & y_4 & x_4y_4 \end{pmatrix} \tag{4.6}$$

and D_K is the matrix where the kth row of D is replaced by $(1\ x\ y\ xy)$. The discrete form of the integral Eq. (4.4) can be written as

$$\sigma_{zz}(\mathbf{x}) = \frac{\mu}{4\pi(1-\nu)}\sum_{n=1}^{N} J_n(\mathbf{x}) \tag{4.7}$$

where (using $\xi = \xi_1$, $\eta = \xi_2$)

$$J_n = \int_{\Omega_n}\frac{1}{r^3}[(\xi - x)N_{K,\xi} + (\eta - y)N_{K,\eta}]\Delta u_{zK}d\Omega \tag{4.8}$$

and where Δu_{zK} $(K = 1, 2, 3, 4)$ represent the crack-opening displacements (z-direction) at the element nodes. The derivatives of the shape functions may be written as

$$N_{K,\xi} = A_K + B_K\eta, \quad N_{K,\eta} = C_K + D_K\xi \tag{4.9}$$

where the constants A_K, B_K, C_K, and D_K can be obtained directly from (4.6) and (4.7). Therefore, Eq. (4.7) becomes

$$\sigma_{zz} = \sum_{n=1}^{N}\frac{\mu}{4\pi(1-\nu)}\int_{\Omega_n}\frac{1}{r^3}[(A_K + B_Ky)(\xi - x) + (C_K + D_Kx)(\eta - y) + (B_K + D_K)(\xi - x)(\eta - y)]\Delta u_{zK}d\Omega. \tag{4.10}$$

In the above, three integrals need to be evaluated for each element, i.e.,

$$I_1 = \int_{\Omega_e}\frac{\xi - x}{r^3}d\Omega, \quad I_2 = \int_{\Omega_e}\frac{\eta - y}{r^3}d\Omega, \quad I_3 = \int_{\Omega_e}\frac{(\xi - x)(\eta - y)}{r^3}d\Omega. \tag{4.11}$$

The evaluation of these integrals will be discussed below for both regular and singular elements.

Downloaded 04 May 2010 to 171.66.16.34. Redistribution subject to ASME license or copyright; see http://www.asme.org/terms/Terms_Use.cfm

4.1 Regular Element Integral Evaluation. Using Green's theorem, the integrals in (4.11) can be evaluated by line integrals as

$$I_k = \int_{\Gamma_e} (A_{k\xi} n_\xi + A_{k\eta} n_\eta) d\Gamma \quad (k = 1, 2, 3) \tag{4.12}$$

where (n_ξ, n_η) are components of the unit normal to the element boundary, and the functions $A_{k\xi}$ and $A_{k\eta}$ are given by

$$A_{1\xi} = \frac{(\xi - x)^2}{r^3} - \frac{1}{r} \quad A_{1\eta} = \frac{(\xi - x)(\eta - y)}{r^3}$$

$$A_{2\xi} = \frac{(\xi - x)(\eta - y)}{r^3} \quad A_{2\eta} = \frac{(\eta - y)^2}{r^3} - \frac{1}{r}$$

$$A_{3\xi} = \frac{1}{3}\left[\frac{(\xi - x)^2(\eta - y)}{r^3} - \frac{\eta - y}{r^3}\right]$$

$$A_{3\eta} = \frac{1}{3}\left[\frac{(\xi - x)(\eta - y)^2}{r^3} - \frac{\xi - x}{r^3}\right]. \tag{4.13}$$

The line integrals in (4.12) are evaluated in a local coordinate system for each side of the element. The relationship between the two coordinate systems is linear and given by

$$\xi = \xi' n_\xi - \eta' n_\eta, \quad \eta = \xi' n_\eta + \eta' n_\xi \tag{4.14}$$

so the corresponding integrals in the local and global coordinate systems are of the same form. The terms in (4.13) which form the integrals if (4.12) can be written in the form

$$f_{qmn} = \frac{(\xi' - x')^m (\eta' - y')^n}{r^q}$$

$$(m, n \geq 0,\ m + n \leq 3,\ q = 1 \text{ or } 3). \tag{4.15}$$

The corresponding integrals for these functions are listed in the Appendix. Thus, the regular element integrals can be analytically evaluated based on the ten line integrals given in the Appendix, which is analogous to the procedure given by Guo et al. (1995).

4.2 Singular Element Integral Evaluation. Many techniques have been developed to evaluate singular element integrals. One common technique for singular integrals (Brebbia et al., 1984) is to use the relation

$$\int_s T_{ij} d\Omega = -\delta_{ij} \tag{4.16}$$

where, for a three-dimensional problem in the crack plane, $T_{13} (\xi - x)/[8\pi(1 - \nu)r^3]$ and $T_{23} = (\eta - y)/[8\pi(1 - \nu)r^3]$.

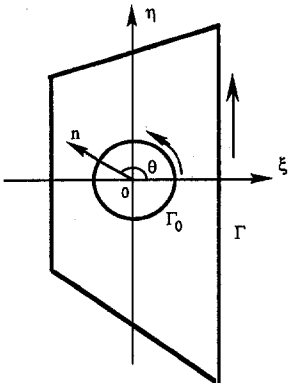


Fig. 4 The singular integral can be expressed as line integrals on Γ and Γ_0

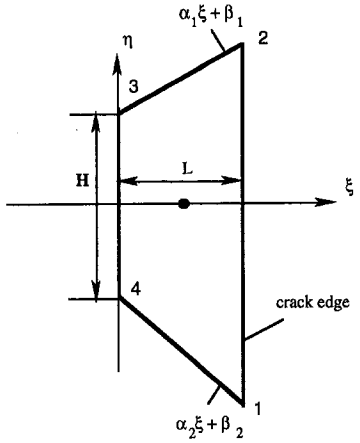


Fig. 5 Singular elements near crack edge

This indirect method for estimating singular integrals has been widely used in the boundary element method. Using Green's Theorem, the Cauchy principal value of the singular integral (4.16) can be represented as a path integral of the form (see Fig. 4)

$$I = \int_\Gamma f(\xi, \eta, x, y) ds - \int_{\Gamma_0} f(\xi, \eta, x, y) ds. \tag{4.17}$$

Fortunately, the line integral on Γ_0 is zero for a three-dimensional planar crack. Thus, the singular integral has the same form as the regular integral. The use of the expressions for the regular integrals in estimating the singular integrals is very effective, and it greatly simplifies the analysis for the singular elements. Calculations show that with this explicit expression of the integral, the accuracy of the calculation is much better than that obtained by using (4.16), where the regular integrals are evaluated using Gaussian quadrature.

4.3 Singular Element Near Crack Tip. The integral for a singular element near the crack edge or crack tip is a special singular integral which contains two singularities. However, it is still possible to transform these two-dimensional singular integrals to one-dimensional regular integrals which are easier to integrate accurately. The procedure is as follows:

For the element as shown in Fig. 5, the crack-opening displacement in the local coordinate system (ξ, η) may be expressed in the form

$$\Delta u_z = \frac{\sqrt{L - \xi}}{\sqrt{L}}\left[\frac{\eta - \eta_4}{\eta_3 - \eta_4} \Delta u_{z3} + \frac{\eta_3 - \eta}{\eta_3 - \eta_4} \Delta u_{z4}\right] \tag{4.18}$$

where $L = \xi_2 - \xi_3$, the nodal displacements Δu_{z1} and Δu_{z2} vanish because of the zero displacement condition at the crack edge. Equation (4.18) indicates that the displacement has a linear variation in the tangential (η) direction and varies with the square root of the distance from the crack edge in the normal (ξ) direction. Thus, the integral J_n in (4.8) for an element near the crack edge can be written as

$$J_n = \frac{1}{H\sqrt{L}}\{(J_1 + J_2 - \eta_4 J_3)\Delta u_{z3} + (-J_1 - J_2 + \eta_3 J_3)\Delta u_{z4}\} \tag{4.19}$$

where $H = \eta_3 - \eta_4$, and the functions J_K $(K = 1, 2, 3)$ on the right side of (4.19) are the following integrals:

$$J_1 = \int_{\Omega_e} \frac{\eta}{r^3}\sqrt{L - \xi}\, d\Omega, \quad J_2 = -\int_{\Omega_e} \frac{\xi - L/2}{r^3} \frac{\eta}{2\sqrt{L - \xi}} d\Omega$$

$$J_3 = -\int_{\Omega_e} \frac{\xi - L/2}{r^3} \frac{1}{2\sqrt{L - \xi}} d\Omega \tag{4.20}$$

Downloaded 04 May 2010 to 171.66.16.34. Redistribution subject to ASME license or copyright; see http://www.asme.org/terms/Terms_Use.cfm

where the source point (x, y) is at the center of the trapezoidal element, i.e., $x = L/2$ and $y = 0$. If the equations for the two sides between nodes 2-3 and nodes 1-4 are $\eta = \alpha_1\xi + \beta_1$ and $\eta = \alpha_2\xi + \beta_2$, respectively, then taking advantage of the trapezoidal geometry and integrating in the η direction, these integrals can be expressed as

$$J_K = F_K(\alpha_1, \beta_1) - F_K(\alpha_2, \beta_2) \tag{4.21}$$

where

$$F_1(\alpha, \beta) = -\int_0^L \frac{\sqrt{L - \xi}}{\sqrt{\left(\xi - \frac{L}{2}\right)^2 + (\alpha\xi + \beta)^2}}\, d\xi \tag{4.22}$$

$$F_2(\alpha, \beta) = \int_0^L \frac{\xi - \frac{L}{2}}{2\sqrt{L - \xi}\sqrt{\left(\xi - \frac{L}{2}\right)^2 + (\alpha\xi + \beta)^2}}\, d\xi \tag{4.23}$$

$$F_3(\alpha, \beta) = -\int_0^L \frac{\alpha\xi + \beta}{2\left(\xi - \frac{L}{2}\right)\sqrt{L - \xi}\sqrt{\left(\xi - \frac{L}{2}\right)^2 + (\alpha\xi + \beta)^2}}\, d\xi. \tag{4.24}$$

The values of these integrals on the finite interval $(0, L)$ are bounded, but there are still singularities in (4.23) and (4.24). The following analysis aims to transform the singular integrals (4.23) and (4.24) into regular integrals for numerical implementation. The function F_1 in (4.22) is a regular integral, and it can be written as (with a change of variables $\xi/L \to \xi$)

$$F_1(\alpha, \beta) = -\sqrt{L}\int_0^1 \frac{\sqrt{1 - \xi}}{\sqrt{\left(\xi - \frac{1}{2}\right)^2 + \left(\alpha\xi + \frac{\beta}{L}\right)^2}}\, d\xi. \tag{4.25}$$

The function F_2, which has a singularity at $\xi = L$, can be regularized through integration by parts,

$$F_2(\alpha, \beta) = \sqrt{L}\left\{\frac{-1}{\sqrt{1 + 4\left(\frac{\beta}{L}\right)^2}} + \left(\frac{\alpha}{2} + \frac{\beta}{L}\right) \times \int_0^1 \frac{\sqrt{1 - \xi}\left(\alpha\xi + \frac{\beta}{L}\right)}{\left[\left(\xi - \frac{1}{2}\right)^2 + \left(\alpha\xi + \frac{\beta}{L}\right)^2\right]^{3/2}}\, d\xi\right\}. \tag{4.26}$$

The integral F_3 has two singularities, one singular point is at $\xi = L/2$ and the other at $\xi = L$. The function F_3 can be written as

$$F_3(\alpha, \beta) = \alpha\int_0^L \frac{d\xi}{2\sqrt{L - \xi}\sqrt{\left(\xi - \frac{L}{2}\right)^2 + (\alpha\xi + \beta)^2}} + \left(\frac{\alpha L}{2} + \beta\right) \times \int_0^L \frac{d\xi}{2\left(\xi - \frac{L}{2}\right)\sqrt{L - \xi}\sqrt{\left(\xi - \frac{L}{2}\right)^2 + (\alpha\xi + \beta)^2}}. \tag{4.27}$$

The first integral in (4.27) can be evaluated through integration by parts. For the second integral, there is a singular point at $\xi = L/2$ where the singular behavior is similar to the integral

$$\Phi = \int_0^L \frac{d\xi}{2\left(\xi - \frac{L}{2}\right)\sqrt{L - \xi}}. \tag{4.28}$$

The Cauchy principal value of the integral Φ can be directly estimated. Using integration by parts, the nonsingular expression for (4.27) is

$$\begin{aligned} F_3(\alpha, \beta) = \frac{1}{\sqrt{L}}\Bigg\{ & \frac{\alpha}{\sqrt{\left(\frac{1}{2}\right)^2 + \left(\frac{\beta}{L}\right)^2}} - \alpha\int_0^1 \frac{\sqrt{1 - \xi}\left[(1 + \alpha^2)\xi + \left(\frac{\alpha\beta}{L} - \frac{1}{2}\right)\right]}{\left[\left(\xi - \frac{1}{2}\right)^2 + \left(\alpha\xi + \frac{\beta}{L}\right)^2\right]^{3/2}}\, d\xi \Bigg\} \\ & + \frac{\operatorname{sgn}\left(\frac{\alpha L}{2} + \beta\right)}{\sqrt{L}}\left\{\frac{\sqrt{2}}{2}\lg(3 + 2\sqrt{2}) + \frac{1 - \alpha^2 - 4\alpha\frac{\beta}{L}}{2r_0\left[r_0 + \left|\frac{\beta}{L} + \frac{\alpha}{2}\right|\right]}\right\} \\ & + \frac{\operatorname{sgn}\left(\frac{\alpha L}{2} + \beta\right)}{\sqrt{L}}\left\{\int_0^1 \frac{\sqrt{1 - \xi}\left(\frac{\alpha}{2} + \frac{\beta}{L}\right)\left[\alpha(2\xi - 1) - (1 - \alpha^2)\left(\alpha\xi + \frac{\beta}{L}\right)\right]}{r^3\left[r + \left|\frac{\alpha}{2} + \frac{\beta}{L}\right|\right]}\, d\xi \right. \\ & \left. - \int_0^1 \frac{\sqrt{1 - \xi}\left[(1 + \alpha^2)\left(\xi - \frac{1}{2}\right) + \alpha\left(\alpha + \frac{2\beta}{L}\right)\right]\left[\left(\xi - \frac{1}{2}\right) + \alpha\left(a\xi + \frac{\beta}{L}\right)\right]}{r^2\left[r + \left|\frac{\alpha}{2} + \frac{\beta}{L}\right|\right]^2}\, d\xi\right\} \end{aligned} \tag{4.29}$$

Downloaded 04 May 2010 to 171.66.16.34. Redistribution subject to ASME license or copyright; see http://www.asme.org/terms/Terms_Use.cfm

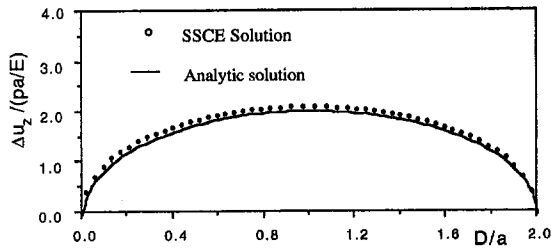


Fig. 6 Normalized crack-opening displacement of a penny-shaped crack under tensile loading

where

$$r = \sqrt{\left(\xi - \frac{1}{2}\right)^2 + \left(\alpha\xi + \frac{\beta}{L}\right)^2}, \quad r_0 = \frac{1}{2} + \frac{\beta}{L} \tag{4.30}$$

and sgn (x), the sign function, is defined as 1 when x is positive and -1 when x is negative. In this way, all the integrals are expressed as regular integrals and can be accurately evaluated.

5 Stress Intensity Factors for Numerical Examples

Numerical calculation based on the above formulation shows good accuracy for three-dimensional crack problems. Consider a penny-shaped crack under tensile loading; the crack surface discretization is shown in Fig. 3. There are $m \times n$ elements (m elements in the circumferential direction and n elements in the radial direction) and $m(n-1)+1$ unknowns. The least-square method is used for determining the $m(n-1)+1$ nodal crack-opening displacement Δu_z on the crack surface in terms of $m \times n$ equations. The crack-opening volume and its variation can be determined as described above.

Figure 6 shows the crack-opening displacement of a penny-shaped crack by the self-similar crack expansion method (35 $\times$ 17 elements) in comparison with the analytical solution. The discretization for a penny-shaped crack problem is shown in Fig. 7. Good results are obtained for all points on the crack edge. Results of stress intensity factors from a coarse discretization (25 $\times$ 15) satisfy engineering requirements (two percent error). For more refined discretizations, such as 81 $\times$ 31 elements, the maximum crack-opening displacement and stress intensity factor around the penny-shaped crack edge ($\nu = 0.3$) are $u_{\max} = 2.3392\ pa/E$ and $K_I = 2.0118\ \sqrt{a/\pi}$ as compared with the analytical solution $2.32\ pa/E$ and $2.0\ \sqrt{a/\pi}$ with error of less than one percent.

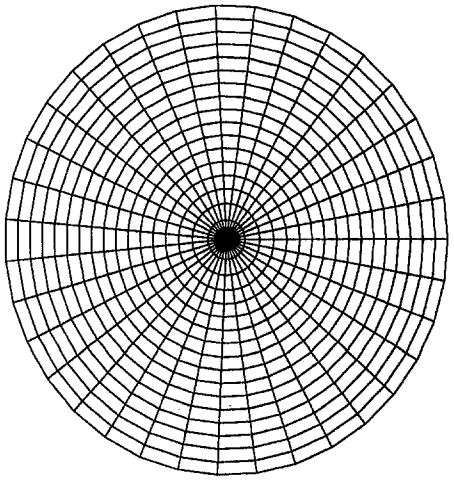


Fig. 7 Boundary elements (35 $\times$ 17) for a penny-shaped crack

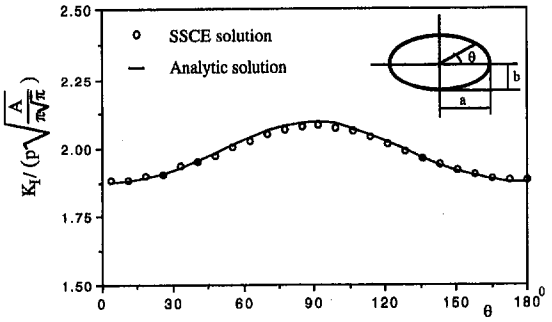


Fig. 8 Normalized stress intensity factors for the elliptical crack with 49 $\times$ 25 elements ($b/a = 0.8$)

Table 1 Normalized stress intensity factors for an elliptical crack ($b/a = 0.8$) with 81 $\times$ 31 elements

θ	$K_I/\left(p\sqrt{\frac{A}{\pi\sqrt{\pi}}}\right)$	Analytic solution	Error
0 deg	1.8896	1.8740	0.83 percent
15 deg	1.9063	1.8914	0.78 percent
30 deg	1.9490	1.9367	0.64 percent
45 deg	2.0046	1.9938	0.54 percent
60 deg	2.0551	2.0464	0.43 percent
75 deg	2.0901	2.0824	0.37 percent
90 deg	2.1019	2.0952	0.32 percent

For elliptical cracks, the displacement and stress intensity factors are calculated for cases of crack aspect ratio length $b/a = 0.8$ and $b/a = 0.5$, where a and b are the semi-major and semi-minor axis, respectively, of the crack. The stress intensity factors around the crack are shown in Fig. 8, where the elliptical crack is divided into 49 $\times$ 25 elements. The stress intensity factors for a more refined discretization (81 $\times$ 31) are listed in Table 1, where A denotes crack area. Errors in stress intensity factors are less than one percent.

For an elliptical crack with aspect ratio $b/a = 0.5$, the stress intensity factors for 49 $\times$ 25 elements (see Fig. 9) are shown in Fig. 10. Table 2 lists the stress intensity factors for the ellip-

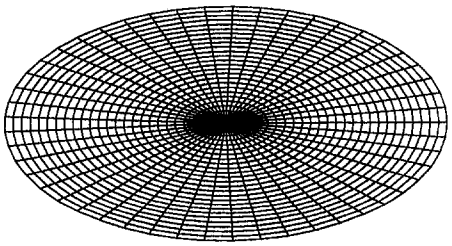


Fig. 9 Boundary elements (49 $\times$ 25) for an elliptical crack ($b/a = 0.5$)

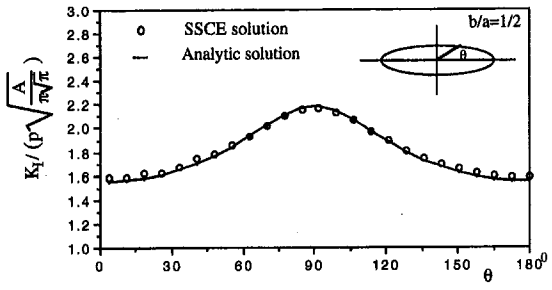


Fig. 10 Normalized stress intensity factors for the elliptical crack with 49 $\times$ 25 elements ($b/a = 0.5$)

Downloaded 04 May 2010 to 171.66.16.34. Redistribution subject to ASME license or copyright; see http://www.asme.org/terms/Terms_Use.cfm

Table 2 Normalized stress intensity factors for an elliptical crack ($b/a = 0.5$) with 85×33 elements

θ	$K_I/\left(p\sqrt{\frac{A}{\pi\sqrt{\pi}}}\right)$	Analytic solution	Error
0 deg	1.5546	1.5425	0.78 percent
15 deg	1.6224	1.6147	0.48 percent
30 deg	1.7795	1.7741	0.30 percent
45 deg	1.9428	1.9395	0.17 percent
60 deg	2.0719	2.0710	0.04 percent
75 deg	2.1513	2.1534	0.10 percent
90 deg	2.1785	2.1814	0.13 percent

tical crack in comparison with the analytical solution. Errors in stress intensity factors are less than one percent.

6 Three-Dimensional Cracks Near a Free Surface

The presence of a free surface can significantly increase the stress intensity factors along a subsurface crack and plays an important role in fatigue crack initiation and subsequent growth. Accurate evaluation of stress intensity factors for near-surface cracks is therefore important for fatigue life prediction especially in castings where cracks may initiate from near-surface defects or pores.

When the crack is located in the plane $x_1 - x_2$ plane (Fig. 11) and under tensile loading, the boundary integral equation corresponding to (4.1) can be written as

$$\sigma_{33}(x) = \int_\Omega [S_{333}(\mathbf{x}, \boldsymbol{\xi}) + \bar{S}_{333}(\mathbf{x}, \boldsymbol{\xi})]\Delta u_3(\boldsymbol{\xi}) d\Omega(\boldsymbol{\xi}) \quad (6.1)$$

where the function S_{333} is the same as that of the full space which was given in (2.9). The second part, due to boundary effects, can be expressed as

$$\bar{S}_{333} = \frac{\mu}{4\pi(1-\nu)}\left\{-\frac{5-20\nu+24\nu^2}{r_2^3} + \frac{12(1-2\nu)(1-\nu)}{r_2(r_2+x_2+\xi_2)^2} - \frac{6[2\nu(1-2\nu)(x_2+\xi_2)^2 - 3x_2\xi_2]}{r_2^5}\right\} \quad (6.2)$$

where

$$r_1 = \sqrt{(\xi_1 - x_1)^2 + (\xi_2 - x_2)^2},$$
$$r_2 = \sqrt{(\xi_1 - x_1)^2 + (\xi_2 + x_2)^2}. \quad (6.3)$$

The function $\bar{S}_{333}$ is related to the half-space Green function which was given by Mindlin (1953). The expressions for the stress and high order derivatives can be found in Isida (1984). The expression (6.2) for three-dimensional planar cracks was given by Isida (1984), and the special case ($\nu = 0$) was discussed by Murakami and Nemat-Nasser (1982).

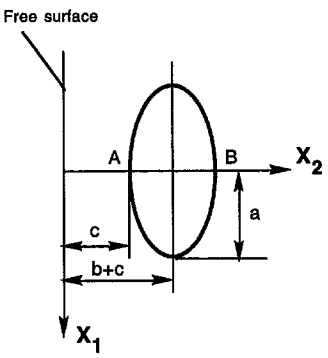


Fig. 11 Geometry of a surface crack

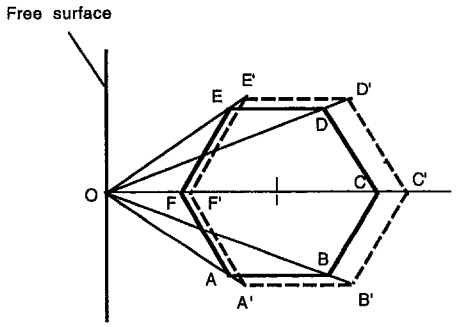


Fig. 12 Self-similar crack expansion near a free surface

In Eq. (6.1), a singular integral only occurs in the kernel S_{333}. Thus, the analysis for the full space can be applied to the half-space problem.

For crack expansion in a full space, it is usual to take the geometrical center of the crack as the similarity center for the self-similar crack expansion method, as shown in Fig. 2 for example. However, crack expansion in a half-space (see Fig. 11), is not a self-similar problem if the similarity center is taken at the crack center, because the distance between crack and the free surface has to be considered also. One way to employ the self-similar expansion technique for the half-space problem is to choose the similarity center at the free surface as shown in Fig. 12. As the crack expands, the crack edge will satisfy

$$\frac{OA'}{OA} = \frac{OB'}{OB} = \frac{OC'}{OC} = (1+\alpha) \quad (6.5)$$

where α is a small parameter. In this way, the energy release rate can be evaluated using

$$U = \int_\Gamma \frac{1-\nu^2}{E} K_I^2 \delta a(s) d\Gamma. \quad (6.6)$$

The reference stress intensity factor can be determined using (3.6) as in the full space problem. It is noted that $\delta a(s) < 0$ over part of the crack edge is possible, which implies that the virtual energy release over this part of the crack edge is negative.

The geometry of a subsurface crack (elliptical crack) near a free surface is shown in Fig. 11, where a and b are the half-length of the elliptical crack, and $b + c$ is the distance between crack center and the free surface. Figure 13 shows the stress intensity factors $K_{I,A}$ and $K_{I,B}$ for a penny-shaped crack at points A and B in comparison with the analytical solution by Isida (1973), where $K_{I,\infty}$ represents the stress intensity factor of the penny-shaped crack in the infinite medium.

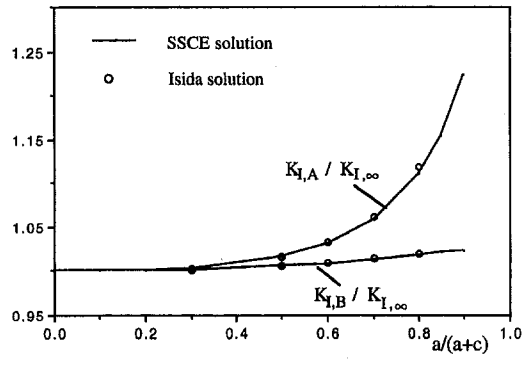


Fig. 13 Boundary effects on stress intensity factors of a penny-shaped crack

Downloaded 04 May 2010 to 171.66.16.34. Redistribution subject to ASME license or copyright; see http://www.asme.org/terms/Terms_Use.cfm

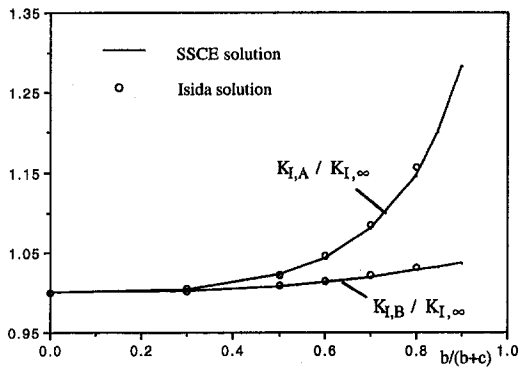


Fig. 14 Boundary effects on stress intensity factors of an elliptical crack (b/a = 0.75)

For an elliptical crack with aspect ratio $b/a = 0.75$ (see Fig. 14), the stress intensity factors at A and B are a function of the distance between the crack center and the free surface, where $K_{I,\infty}$ represents the stress intensity factor of the elliptical crack (point A or B) in the infinite medium. The curves in Fig. 14 show that the numerical results are in good agreement with the analytic solutions.

7 Conclusion

It has been shown that stress intensity factors for three-dimensional cracks can be accurately calculated using the self-similar crack expansion method developed here in conjunction with the boundary integral equation method. The numerical results also show that the accuracy of the stress intensity factors for three-dimensional cracks can be improved by accurate evaluation of the element integrals (both regular and singular). Regular integrals can be accurately evaluated using techniques based on Green's Theorem (see Guo et al., 1995), which can also be used to evaluate singular integrals as described in the present paper. A special technique has been developed for integration of singular integrals near the crack edge. For trapezoidal elements near the crack edge, the singular integrals have been accurately integrated by first transforming the two-dimensional singular integrals to one-dimensional regular integrals. The numerical method shows good accuracy for three-dimensional crack analysis, with errors of less than one percent in stress intensity factors around the crack edge. The self-similar crack expansion method can be further applied to more complicated crack problems including surface breaking cracks (Xu et al., 1997).

Acknowledgment

The support of the National Institute of Standards and Technology and the Army Office of Research are gratefully acknowledged. The authors are grateful for helpful comments by the reviewers.

References

Brebbia, C. A., Telles, J. C. F., and Wrobel, L. C., 1984, *Boundary Element Techniques,* Springer-Verlag, New York.

Bui, D. D., 1977, "An integral equations method for solving the problem of a plane crack of arbitrary shape," *Journal of Mechanics and Physics of Solids,* Vol. 25, pp. 29–39.

Cruse, T. A., 1974, "An improved boundary-integral equation method for three dimensional elastic stress analysis," *Computer and Structures,* Vol. 4, pp. 741–754.

Cruse, T. A., and Besunner, P. M., 1975, "Residual life prediction for surface cracks in complex structural details," *Journal of Aircraft,* Vol. 12, pp. 369–375.

Cruse, T. A., and Meyers, G. J., 1977, "Three-dimensional fracture mechanics analysis," *J. Struct. Divn., ASCE,* Vol. 103, pp. 309–320.

Cruse, T. A., 1988, *Boundary Element Analysis in Computational Fracture Mechanics,* Kluwer, Dordrecht, The Netherlands.

Gray, L. J., Martha, L. F., and Ingraffea, A. R., 1990, "Hypersingular integrals in boundary element fracture analysis," *International Journal for Numerical Methods in Engineering,* Vol. 29, pp. 1135–1158.

Guo, Q., Wang, J. J., Clifton, R. J., and Mertaugh, L. J., 1995, "Elastic analysis of planar cracks of arbitrary shape," ASME JOURNAL OF APPLIED MECHANICS, Vol. 62, pp. 108–115.

Isida, M., and Noguchi, H., 1984, "Tension of a plate containing an embedded elliptical crack," *Engineering Fracture Mechanics,* Vol. 20, No. 3, pp. 387–408.

Lee, J. C., and Keer, L. M., 1986, "Study of a three dimensional crack terminating at an interface," ASME JOURNAL OF APPLIED MECHANICS, Vol. 53, pp. 311–316.

Liebowitz, H., and Moyer, Jr., E. T., 1989, "Finite element methods in fracture mechanics," *Computer and Structures,* Vol. 31, pp. 1–9.

Mindlin, R. D., 1953, "Force at a point in the interior of a semi-infinite solid," *Midwestern Conf. Solid Mech.,* pp. 56–59.

Murakami, Y., 1985, "Analysis of stress intensity factors of modes I, II and III for inclined surface cracks of arbitrary shape," *Engineering Fracture Mechanics,* Vol. 22, pp. 101–114.

Murakami, Y., and Nemat-Nasser, 1982, "Interacting dissimilar semi-elliptical surface flaws under tension and bending," *Engineering Fracture Mechanics,* Vol. 16, No. 3, pp. 373–386.

Nikishkov, G. P., and Piminov, V. A., 1991, "Computation of weight functions for three-dimensional cracks by the boundary element method," *Computational Mechanics,* Vol. 9, pp. 211–220.

Polch, E. Z., Cruse, T. A., and Huang, C.-J., 1987, "Traction BIE solution for flat cracks," *Computational Mechanics,* Vol. 2, pp. 253–267.

Rice, J. R., 1972, "Some remarks on elastic crack-tip stress fields," *International Journal of Solids and Structures,* Vol. 8, pp. 751–758.

Rice, J. R., 1985, "First Order Variation in Elastic Fields due to Variation Location of a Planar Crack Front," ASME JOURNAL OF APPLIED MECHANICS, Vol. 52, pp. 571–579.

Weaver, J., 1977, "Three-dimensional crack analysis," *International Journal of Solids and Structures,* Vol. 13, pp. 321–330.

Xu, Y., Moran, B., and Belytschko, T., 1997, "Self-Similar Crack Expansion Method for Analysis of Surface Cracks and Edge Cracks," to be published.

APPENDIX

Ten Basic Integrals

Line integrals on P_1-P_2,

$$J_{100} = \int_{P_1}^{P_2} \frac{1}{r}\, ds = \frac{1}{2} \lg\left[\frac{\sqrt{h^2+\eta^2}+\eta}{\sqrt{h^2+\eta^2}-\eta}\right]\Bigg|_{y_1}^{y_2}$$

$$J_{110} = \int_{P_1}^{P_2} \frac{\xi - x}{r}\, ds = hJ_{100}$$

$$J_{101} = \int_{P_1}^{P_2} \frac{\eta - y}{r}\, ds = \sqrt{h^2+\eta^2}\,|_{y_1}^{y_2}$$

$$J_{320} = \int_{P_1}^{P_2} \frac{(\xi - x)^2}{r^3}\, ds = \frac{\eta}{\sqrt{h^2+\eta^2}}\Bigg|_{y_1}^{y_2}$$

$$J_{302} = \int_{P_1}^{P_2} \frac{(\eta - y)^2}{r^3}\, ds = J_{100} - J_{320}$$

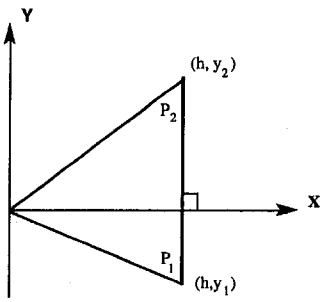


Fig. A1 Line integral from P_1 to P_2

Downloaded 04 May 2010 to 171.66.16.34. Redistribution subject to ASME license or copyright; see http://www.asme.org/terms/Terms_Use.cfm

$$J_{311} = \int_{p_1}^{p_2} \frac{(\xi - x)(\eta - y)}{r^3}\, ds = -\frac{h}{\sqrt{h^2 + \eta^2}}\Bigg|_{y_1}^{y_2}$$

$$J_{330} = \int_{p_1}^{p_2} \frac{(\xi - x)^3}{r^3}\, ds = hJ_{320}$$

$$J_{303} = \int_{p_1}^{p_2} \frac{(\eta - y)^3}{r^3}\, ds = \frac{2h^2 + \eta^2}{\sqrt{h^2 + \eta^2}}\Bigg|_{y_1}^{y_2}$$

$$J_{321} = \int_{p_1}^{p_2} \frac{(\xi - x)^2(\eta - y)}{r^3}\, ds = -hJ_{311}$$

$$J_{312} = \int_{p_1}^{p_2} \frac{(\xi - x)(\eta - y)^2}{r^3}\, ds = h(J_{100} - J_{320}).$$

On integral line p_1–p_2, it holds $r = \sqrt{h^2 + \eta^2}$, and $J_{qmn} = \int_{p_1}^{p_2} ((\xi - x)^m(\eta - y)^n/r^q)\, ds$.

Downloaded 04 May 2010 to 171.66.16.34. Redistribution subject to ASME license or copyright; see http://www.asme.org/terms/Terms_Use.cfm

H. A. Luo
Professor.

Q. Wang
Graduate Student.

Department of Engineering Mechanics,
Shanghai Jiao Tong University,
Shanghai 200030, China

Stress Concentrations in an Intermingled Hybrid Composite

This paper studies the stress redistribution in a tensile hybrid composite sheet due to the breakage of a high modulus fiber. Employing a continuous distribution of dislocations, a set of singular integral equations is established to analyze the fiber crack impinging upon weakly bonded fiber-matrix interfaces. After solving the integral equations numerically, the stress concentration factors of both high modulus and low modulus fibers are evaluated as a function of loading stress and interfacial parameters. The results are compared with those obtained from shear-lag model solution.

1 Introduction

A hybrid composite is an important engineering material. In a common matrix, a hybrid composite usually contains two or more types of fibers which can be arranged in an intermingled or interlaminated manner. To achieve ideal hybrid effects, fibers with different fracture strains are generally adopted in the mixture. In practice, fibers with high elongation and low elongation correspond to fibers with low modulus and high modulus, respectively. Compared with single fiber composites, hybrid composites often have low cost, high fracture toughness and manifold material properties.

In the study of hybrid composites, one crucial problem is how stress redistribution occurs upon some low elongation fibers having been broken. Hedgepeth (1961) first studied this phenomenon for a composite with a single fiber system. Using a shear-lag model, he derived the stress concentration factors in the continuous fibers around the broken ones. Later, Fukuda and Chou (1983) applied a shear-lag model to the hybrid composites and gave the stress concentration factors on both unbroken low elongation and high elongation fibers.

It should be noted that the above formulations are all based on the following assumptions: All axial load is sustained by the fibers alone, the matrix phase can only transfer shear stress, the interface between fibers and matrix is perfectly bonded, and only axial equilibrium is considered in the analysis. Thus, in one-dimensionalizing the problem some microstructural aspects, such as the interfacial toughness, the residual stresses and the axial load carrying capacity of the matrix phase, have been neglected. However, the rationale for these simplifications is still not very clear cut, especially for the hybrid systems with relatively strong matrix and weak interface.

Dollar and Steif (1992) thoroughly investigated a crack impinging upon debondable and frictional interfaces in a homogeneous medium. They found that the energy to debond the interfaces and the residual stress at the interfaces have pronounced effect on the stress concentration near the crack.

This paper will generalize Dollar and Steif 's work to the intermingled hybrid composite so as to gain a comparison between the elastic solution and the elementary solution for this class of composite. In this study, a central high modulus fiber is assumed to be broken, meanwhile some interfacial debonding is developing near the site of fiber breakage. By means of the singular integral equation method, the effect of various microstructural parameters, which may not be included in the elementary model, on the stress redistribution around the defect is explored.

2 Formulation

2.1 Fundamental Solutions. Consider a multilayered elastic medium as shown in Fig. 1. Layers 1 to $n-1$ are isotropic, with Lame's constants (λ_k, μ_k) where $k = 1, 2, \ldots, n-1$. Layer n is orthotropic, its stiffness coefficients are $(b_{\alpha\beta}, \mu_{xy})$:

$$\begin{pmatrix} \sigma_{xx} \\ \sigma_{yy} \\ \sigma_{xy} \end{pmatrix} = \begin{pmatrix} b_{11} & b_{12} & 0 \\ b_{12} & b_{22} & 0 \\ 0 & 0 & \mu_{xy} \end{pmatrix} \begin{pmatrix} \epsilon_{xx} \\ \epsilon_{yy} \\ \gamma_{xy} \end{pmatrix}. \tag{1}$$

Assume that a single edge dislocation b_x is embedded at the origin. To solve this problem, we first consider an infinite bimaterial medium which is simply formed by removing layer 3 to layer n and extending layer 1 and layer 2 to infinity. The bimaterial medium is free of any traction and constraint. Due to embedded dislocation b_x, its stress and displacement fields are as follows (Dundurs, 1969). When $y < 0$,

$$\tilde{\sigma}_{yy}^{(1)} = \frac{Cb_x}{\pi}\left[\frac{y}{r^2} - (1-\beta)\frac{2y^3}{r^4}\right],$$

$$\tilde{\sigma}_{xy}^{(1)} = \frac{Cb_x}{\pi}\left[\frac{x}{r^2} - (1-\beta)\frac{2xy^2}{r^4}\right],$$

$$\tilde{u}^{(1)} = \frac{Cb_x}{2\mu_1\pi}\left\{\left[1 + \frac{1}{2}(1-\beta)(\kappa_1 - 1)\right]\tan^{-1}\frac{y}{x} + (1-\beta)\frac{xy}{r^2}\right\},$$

$$\tilde{v}^{(1)} = \frac{Cb_x}{2\mu_1\pi}\left\{\left[1 - \frac{1}{2}(1-\beta)(\kappa_1 + 1)\right]\ln r + (1-\beta)\frac{y^2}{r^2}\right\}; \tag{2}$$

when $y > 0$,

$$\tilde{\sigma}_{yy}^{(1)} = \frac{Cb_x}{\pi}\left[\frac{y}{r^2} - (1+\beta)\frac{2y^3}{r^4}\right],$$

$$\tilde{\sigma}_{xy}^{(1)} = \frac{Cb_x}{\pi}\left[\frac{x}{r^2} - (1+\beta)\frac{2xy^2}{r^4}\right],$$

Contributed by the Applied Mechanics Division of THE AMERICAN SOCIETY OF MECHANICAL ENGINEERS for publication in the ASME JOURNAL OF APPLIED MECHANICS.

Discussion on the paper should be addressed to the Technical Editor, Professor Lewis T. Wheeler, Department of Mechanical Engineering, University of Houston, Houston, TX 77204-4792, and will be accepted until four months after final publication of the paper itself in the ASME JOURNAL OF APPLIED MECHANICS.

Manuscript received by the ASME Applied Mechanics Division, Mar. 28, 1996; final revision, Mar. 3, 1997. Associate Technical Editor: W. J. Drugan.

Copyright © 1997 by ASME

Downloaded 04 May 2010 to 171.66.16.34. Redistribution subject to ASME license or copyright; see http://www.asme.org/terms/Terms_Use.cfm

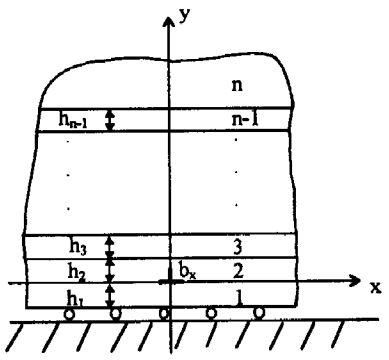


Fig. 1 A single dislocation b_x embedded in a multilayered system

$$\tilde{u}^{(1)} = \frac{Cb_x}{2\mu_2\pi}\left\{\left[1 + \frac{1}{2}(1+\beta)(\kappa_2 - 1)\right]\tan^{-1}\frac{y}{x} + (1+\beta)\frac{xy}{r^2}\right\},$$

$$\tilde{v}^{(1)} = \frac{Cb_x}{2\mu_2\pi}\left\{\left[1 - \frac{1}{2}(1+\beta)(\kappa_2 + 1)\right]\ln r + (1+\beta)\frac{y^2}{r^2}\right\}; \quad (3)$$

and on the interface $y = 0$,

$$\tilde{\sigma}_{yy} = -\beta C b_x \delta(x), \quad \tilde{\sigma}_{xy} = \frac{Cb_x}{\pi}\frac{1}{x}. \quad (4)$$

Here $\delta(x)$ is the Dirac delta function and

$$r = \sqrt{x^2 + y^2},$$

$$C = \frac{2\mu_1(1+\alpha)}{(\kappa_1+1)(1-\beta^2)} = \frac{2\mu_2(1-\alpha)}{(\kappa_2+1)(1-\beta^2)}, \quad (5)$$

α and β are the Dundurs constants:

$$\alpha = \frac{\mu_2(\kappa_1+1) - \mu_1(\kappa_2+1)}{\mu_2(\kappa_1+1) + \mu_1(\kappa_2+1)},$$

$$\beta = \frac{\mu_2(\kappa_1-1) - \mu_1(\kappa_2-1)}{\mu_2(\kappa_1+1) + \mu_1(\kappa_2+1)}, \quad (6)$$

$\kappa_i = 3 - 4\nu_i$ for plane strain and $\kappa_i = (3-\nu_i)/(1+\nu_i)$ for plane stress where ν_i is Poisson's ratio, $i = 1, 2$.

Taking Fourier sine and cosine transforms to the displacement and stress components,

$$\tilde{U}^{(i)} = \int_0^\infty \tilde{u}^{(i)}(x,y)\sin\xi x dx, \quad \tilde{V}^{(i)} = \int_0^\infty \tilde{v}^{(i)}(x,y)\cos\xi x dx,$$

$$\tilde{\Sigma}_{xy}^{(i)} = \int_0^\infty \tilde{\sigma}_{xy}^{(i)}(x,y)\sin\xi x dx,$$

$$\tilde{\Sigma}_{yy}^{(i)} = \int_0^\infty \tilde{\sigma}_{yy}^{(i)}(x,y)\cos\xi x dx, \quad (7)$$

we get

$$\tilde{U}^{(1)}(\xi, -h_1) = \frac{Cb_x}{4\mu_1}\left\{\left[1 + \frac{1}{2}(1-\beta)(\kappa_1 - 1)\right]\frac{1}{\xi} - (1-\beta)h_1\right\}e^{-h_1\xi},$$

$$\tilde{V}^{(1)}(\xi, -h_1) = \frac{Cb_x}{4\mu_1}\left\{\left[1 - \frac{1}{2}(1-\beta)(\kappa_1 + 1)\right]\frac{1}{\xi} + (1-\beta)h_1\right\}e^{-h_1\xi},$$

$$\tilde{\Sigma}_{xy}^{(1)}(\xi, -h_1) = \frac{Cb_x}{2}[1 - (1-\beta)h_1\xi]e^{-h_1\xi},$$

$$\tilde{\Sigma}_{yy}^{(1)}(\xi, -h_1) = -\frac{Cb_x}{2}[\beta - (1-\beta)h_1\xi]e^{-h_1\xi}, \quad (8)$$

and

$$\tilde{U}^{(2)}(\xi, h_2) = \frac{Cb_x}{4\mu_2}\left\{\left[1 + \frac{1}{2}(1+\beta)(\kappa_2 - 1)\right]\left(-\frac{1}{\xi}\right) + (1+\beta)h_2\right\}e^{-h_2\xi},$$

$$\tilde{V}^{(1)}(\xi, h_2) = \frac{Cb_x}{4\mu_2}\left\{\left[1 - \frac{1}{2}(1+\beta)(\kappa_2 + 1)\right]\left(-\frac{1}{\xi}\right) + (1+\beta)h_2\right\}e^{-h_2\xi},$$

$$\tilde{\Sigma}_{xy}^{(2)}(\xi, h_2) = \frac{Cb_x}{2}[1 - (1+\beta)h_2\xi]e^{-h_2\xi},$$

$$\tilde{\Sigma}_{yy}^{(2)}(\xi, h_2) = -\frac{Cb_x}{2}[\beta + (1+\beta)h_2\xi]e^{-h_2\xi}. \quad (9)$$

The solution of the problem shown in Fig. 1 can be expressed as

$$u^{(i)} = \bar{u}^{(i)} + \tilde{u}^{(i)}, \quad v^{(i)} = \bar{v}^{(i)} + \tilde{v}^{(i)},$$

$$\sigma_{xy}^{(i)} = \bar{\sigma}_{xy}^{(i)} + \tilde{\sigma}_{xy}^{(i)}, \quad \sigma_{yy}^{(i)} = \bar{\sigma}_{yy}^{(i)} + \tilde{\sigma}_{yy}^{(i)}, \quad (10)$$

where $\tilde{u}^{(i)} = \tilde{v}^{(i)} = \tilde{\sigma}_{xy}^{(i)} = \tilde{\sigma}_{yy}^{(i)} = 0$, when $i \geq 3$. The Fourier transforms of $\bar{u}^{(i)}$, $\bar{v}^{(i)}$, $\bar{\sigma}_{xy}^{(i)}$ and $\bar{\sigma}_{yy}^{(i)}$ are denoted by $\bar{U}^{(i)}$, $\bar{V}^{(i)}$, $\bar{\Sigma}_{xy}^{(i)}$ and $\bar{\Sigma}_{yy}^{(i)}$, respectively, in the manner similar to (7). Using the field equations of elasticity, it can be shown that for $i = 1, 2, \ldots, n-1$,

$$\bar{U}^{(i)}(\xi, y) = (A_1^{(i)}h_1 + A_2^{(i)}y)e^{-\xi y} + (A_3^{(i)}h_1 + A_4^{(i)}y)e^{\xi y},$$

$$\bar{V}^{(i)}(\xi, y) = \left[A_1^{(i)}h_1 + \left(\frac{\kappa_i}{\xi} + y\right)A_2^{(i)}\right]e^{-\xi y} + \left[-A_3^{(i)}h_1 + \left(\frac{\kappa_i}{\xi} - y\right)A_4^{(i)}\right]e^{\xi y},$$

$$\bar{\Sigma}_{xy}^{(i)}(\xi, y)/2\mu_i = -[\xi(A_1^{(i)}h_1 + A_2^{(i)}y) + (1-2\nu_i)A_2^{(i)}]e^{-\xi y} + [\xi(A_3^{(i)}h_1 + A_4^{(i)}y) - (1-2\nu_i)A_4^{(i)}]e^{\xi y},$$

$$\bar{\Sigma}_{yy}^{(i)}(\xi, y)/2\mu_i = -[\xi(A_1^{(i)}h_1 + A_2^{(i)}y) + 2(1-\nu_i)A_2^{(i)}]e^{-\xi y} + [-\xi(A_3^{(i)}h_1 + A_4^{(i)}y) + 2(1-\nu_i)A_4^{(i)}]e^{\xi y}; \quad (11)$$

for $i = n$,

$$\bar{U}^{(i)}(\xi, y) = \sum_{j=1}^{4} A_j^{(i)}e^{s_j\xi y}, \quad \bar{V}^{(i)}(\xi, y) = \sum_{j=1}^{4} A_j^{(i)}d_j e^{s_j\xi y},$$

$$\bar{\Sigma}_{xy}^{(i)}(\xi, y) = \mu_{xy}[\xi\sum_{j=1}^{4} A_j^{(i)}s_j e^{s_j\xi y} - \xi\sum_{j=1}^{4} A_j^{(i)}d_j e^{s_j\xi y}],$$

$$\bar{\Sigma}_{yy}^{(i)}(\xi, y) = b_{12}\xi\sum_{j=1}^{4} A_j^{(i)}e^{s_j\xi y} + b_{22}\xi\sum_{j=1}^{4} A_j^{(i)}d_j s_j e^{s_j\xi y}, \quad (12)$$

Downloaded 04 May 2010 to 171.66.16.34. Redistribution subject to ASME license or copyright; see http://www.asme.org/terms/Terms_Use.cfm

where $A_j^{(i)}$'s ($i = 1, 2, \ldots, n$) are the unknown functions of ξ,

$$d_j = [\beta_2 s_j^3 - (\beta_1\beta_2 - \beta_3^2)s_j]/\beta_3 \tag{13}$$

and the s_j ($j = 1, 2, \ldots, 4$) are the roots of the equation

$$s^4 + \frac{\beta_3^2 - \beta_1\beta_2 - 1}{\beta_2} s^2 + \frac{\beta_1}{\beta_2} = 0. \tag{14}$$

In (13) and (14),

$$\beta_1 = b_{11}/\mu_{xy}, \quad \beta_2 = b_{22}/\mu_{xy}, \quad \beta_3 = 1 + b_{12}/\mu_{xy}. \tag{15}$$

The elastic field given by (10) should satisfy the continuity conditions on each interface. In the ξ domain, they are

$$\begin{aligned}
\bar{U}^{(k+1)}(\xi, y_k) - \bar{U}^{(k)}(\xi, y_k) &= \tilde{U}^{(k)}(\xi, y_k)\delta_{k2}, \\
\bar{V}^{(k+1)}(\xi, y_k) - \bar{V}^{(k)}(\xi, y_k) &= \tilde{V}^{(k)}(\xi, y_k)\delta_{k2}, \\
\bar{\Sigma}_{xy}^{(k+1)}(\xi, y_k) - \bar{\Sigma}_{xy}^{(k)}(\xi, y_k) &= \tilde{\Sigma}_{xy}^{(k)}(\xi, y_k)\delta_{k2}, \\
\bar{\Sigma}_{yy}^{(k+1)}(\xi, y_k) - \bar{\Sigma}_{yy}^{(k)}(\xi, y_k) &= \tilde{\Sigma}_{yy}^{(k)}(\xi, y_k)\delta_{k2},
\end{aligned} \tag{16}$$

where δ_{k2} is the Kronecker delta, $k = 1, 2, \ldots, n-1$, $y_1 = 0$ and $y_k = \Sigma_{j=2}^{k} h_j$ for $k \geq 2$.

In addition, the boundary conditions require

$$\begin{aligned}
\bar{V}^{(1)}(\xi, -h_1) &= -\tilde{V}^{(1)}(\xi, -h_1), \\
\bar{\Sigma}_{xy}^{(1)}(\xi, -h_1) &= -\tilde{\Sigma}_{xy}^{(1)}(\xi, -h_1), \\
\bar{\Sigma}_{xy}^{(n)}(\xi, \infty) = 0, &\quad \bar{\Sigma}_{yy}^{(n)}(\xi, \infty) = 0,
\end{aligned} \tag{17}$$

where $n > 2$ is implied. Equations (16) and (17) altogether provide $4 \times n$ equations to solve for $4 \times n$ unknowns $A_j^{(i)}(\xi)$ ($i = 1, 2, \ldots, n, j = 1, 2, 3, 4$).

With Fourier inverse transforms we find on the interface $y = 0$,

$$\begin{aligned}
\bar{\sigma}_{yy}(x, 0) &= \frac{2}{\pi}\int_0^\infty [-\xi h_1(A_1^{(1)} + A_3^{(1)}) \\
&\quad + 2(1 - \nu_1)(A_4^{(1)} - A_2^{(1)})] \cos \xi x d\xi \\
&\equiv F_1(x)b_x, \\
\bar{\sigma}_{xy}(x, 0) &= \frac{2}{\pi}\int_0^\infty [\xi h_1(A_3^{(1)} - A_1^{(1)}) \\
&\quad - (1 - 2\nu_1)(A_2^{(1)} + A_4^{(1)})] \sin \xi x d\xi \\
&\equiv G_1(x)b_x
\end{aligned} \tag{18}$$

and in the kth layer

$$\begin{aligned}
\bar{\sigma}_{xx}^{(k)}(x, y) &= \frac{2}{\pi}\int_0^\infty \{[\xi(A_1^{(k)}h_1 + A_2^{(k)}y) - 2\nu_k A_2^{(k)}]e^{-\xi y} \\
&\quad + [\xi(A_3^{(k)}h_1 + A_4^{(k)}y) + 2\nu_k A_4^{(k)}]e^{\xi y}\} \cos \xi x d\xi \\
&\equiv H_1^{(k)}(x, y)b_x.
\end{aligned} \tag{19}$$

In the same manner, we can derive the fundamental solution $\bar{\sigma}_{yy}(x, 0) = F_2(x, \zeta)$, $\bar{\sigma}_{xy}(x, 0) = G_2(x, \zeta)$, and $\bar{\sigma}_{xx}^{(k)}(0, y) = H_2^{(k)}(y, \zeta)$ for a unit dislocation b_x embedded at $(0, \zeta)$ with $-h_1 < \zeta < 0$. The expressions of stresses $\tilde{\sigma}_{yy}$, $\tilde{\sigma}_{xy}$ for this dislocation can be found in the literature (Dundurs, 1969).

Here it should be mentioned that in studying the interfacial flaw of a multilayered medium, Erdogan and Gupta (1971) also derived the Green function of an interfacial dislocation with Fourier transforms. The derivation given in this paper differs from their work in that we separate the singular parts of the field quantities first so as to facilitate the manipulation and introduce an orthotropic outer layer in the multilayered medium for its later use in a general self-consistent model.

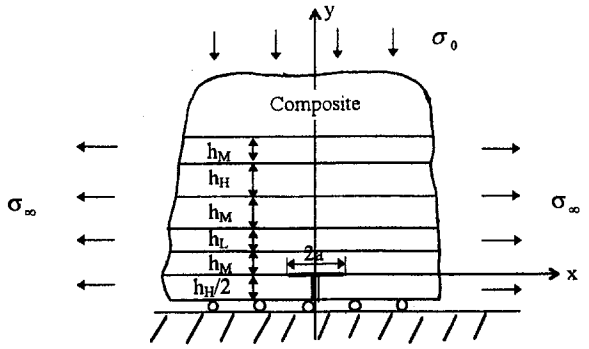


Fig. 2 A stressed hybrid composite with a discontinuous high modulus fiber

2.2 Singular Integral Equations. Consider an intermingled hybrid composite sheet in which there is a discontinuous high modulus fiber. Assume that in the composite the interfaces between fibers and matrix are weak in the sense of the category suggested by He and Hutchinson (1989). As a consequence, under axial load certain interfacial debonds will develop in the vicinities of the tips of the fiber crack. The length of debond depends on the load magnitude and the interfacial bonding strength. Fig. 2 shows one half of the typical H-shaped defect thus formed in a hybrid composite where layers 1, 3, and 5 represent high modulus, low modulus, and high modulus fibers, respectively, layers 2, 4, 6 represent the matrix phase and layer 7 is the effective medium to the hybrid composite. The effective moduli of the hybrid composite can be calculated by using Voigt and Reuss approximations. They are

$$\begin{aligned}
E_x &= (h_H E_H + h_L E_L + h_M E_M)/(h_H + h_L + h_M), \\
E_y = E_z &= (h_H + h_L + h_M)\Big/\left(\frac{h_H}{E_H} + \frac{h_L}{E_L} + \frac{h_M}{E_M}\right), \\
\mu_{xy} &= (h_H + h_L + h_M)\Big/\left(\frac{h_H}{\mu_H} + \frac{h_L}{\mu_L} + \frac{h_M}{\mu_M}\right), \\
\nu_{xy} = \nu_{xz} &= (h_H\nu_H + h_L\nu_L + h_M\nu_M)/(h_H + h_L + h_M),
\end{aligned} \tag{20}$$

where the subscripts H, L, and M denote high modulus layers, low modulus layers, and matrix layers; E, μ, and ν are the Young's modulus, shear modulus, and Poisson's ratio, respectively. The stiffness coefficients of layer 7 ($b_{\alpha\beta}$, μ_{xy}) can be easily derived from (20). The multilayered system is subjected to uniform far-field axial stress σ_∞ and lateral stress σ_0 which is used to simulate the compressive residual stress. Thus, without fiber breakage, the stress on the broken high modulus fiber would be $\sigma_{H0} = \sigma_\infty(E_H/E_x)$. It was found (Dollar and Steif, 1992) that due to the effect of Poisson's ratio and the compressive residual stress the debonded interfaces are closed except in the very beginning stage of debonding. As a result, for a certain length of debond, the boundary conditions are

$$\begin{aligned}
\sigma_{xx}(0, y) &= -\sigma_{H0}, \quad (-h_H/2 < y < 0), \\
\sigma_{xy}(0, y) &= 0, \quad (-h_H/2 < y < 0), \\
\sigma_{xy}(x, 0) &= \mu[\sigma_{yy}(x, 0) - \sigma_0] \operatorname{sgn}(x), \quad (|x| < a), \\
\sigma_{yy}(x, 0) - \sigma_0 &\leq 0, \quad (|x| < a)
\end{aligned} \tag{21}$$

and

$$\begin{aligned}
v(x, -h_H/2) = 0, &\quad \sigma_{xy}(x, -h_H/2) = 0, \quad (-\infty < x < \infty), \\
\sigma_{xy}(x, \infty) = 0, &\quad \sigma_{yy}(x, \infty) = 0, \quad (-\infty < x < \infty),
\end{aligned}$$

Downloaded 04 May 2010 to 171.66.16.34. Redistribution subject to ASME license or copyright; see http://www.asme.org/terms/Terms_Use.cfm

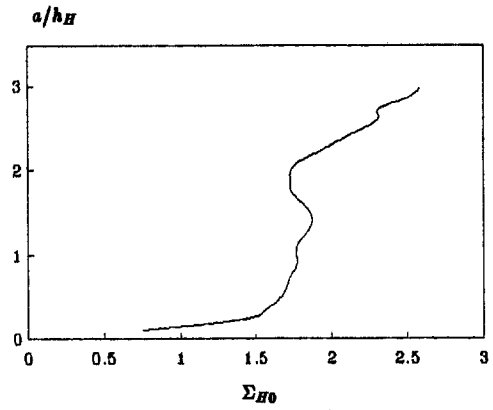


Fig. 3 Debond length a/h_H as a function of applied stress Σ_{H0}

$$\sigma_{xy}(\pm\infty, y) = 0, \quad \sigma_{yy}(\pm\infty, y) = 0, \quad (-h_H/2 < y < \infty), \quad (22)$$

where μ is the friction coefficient of the sliding interface.

The above boundary conditions can be satisfied by distributing "opening" dislocations, of density $B_x^{\text{nch}}(y)$, along the notch $x = 0$, $-h_H/2 < y < 0$ and "sliding" dislocations, of density B_x^{int}, along the debonded interface $y = 0$, $|x| < a$. This leads to the following singular integral equations:

$$\int_{-h_H/2}^{0} \frac{B_x^{\text{nch}}}{y - \zeta}\, d\zeta + \int_{-h_H/2}^{0} K_1(y, \zeta) B_x^{\text{nch}}(\zeta) d\zeta + \int_0^a K_2(y, x_0) B_x^{\text{int}}(x_0) dx_0 = \frac{\pi(1 + \alpha)}{C(1 - \beta^2)} \sigma_{H0}, \quad (-h_H/2 < y < 0)$$

$$\int_0^a \frac{B_x^{\text{int}}(x_0)}{x - x_0}\, dx_0 + \mu\beta\pi B_x^{\text{int}}(x) + \int_0^a [K_3(x, x_0) - \mu K_4(x, x_0)] B_x^{\text{int}}(x_0) dx_0 + \int_{-h_H/2}^{0} [K_5(x, \zeta) - \mu K_6(x, \zeta)] B_x^{\text{nch}}(\zeta) d\zeta = -\frac{\pi}{C} \mu\sigma_0, \quad (0 < x < a) \quad (23)$$

where K_1, K_2, K_3, K_4, K_5, and K_6 are the regular kernels which are given in the Appendix.

3 Results and Discussions

Dollar and Steif have made thorough studies on the behavior of a crack impinging upon a debondable and slipping interfaces (Dollar and Steif, 1989, 1991, 1992). For the present problem the response of the breakage of a high modulus fiber can be summarized as follows. Under the action of σ_{H0}, the induced high stress concentration near the fiber crack tips will cause debonding of the weak interfaces. The length of debond depends on the magnitude of the load, the interfacial toughness and the other microstructural parameters. Provided there is some debonding, the stresses immediately ahead of the broken fiber are finite. Meanwhile, mode II stress singularity is incurred at the tips of sliding interfaces. In the course of debonding growth, the stress intensity factor K_{II} of the interface crack reaches its critical value K_{IIcr}. For convenience of analysis, define the dimensionless loading stress

$$\Sigma_{H0} = \frac{\sigma_{H0}\sqrt{h_H}}{8\mu_H G_{cr}/(\kappa_H + 1)} \quad (24)$$

and the dimensionless residual stress

$$\Sigma_0 = \frac{\sigma_0\sqrt{h_H}}{8\mu_H G_{cr}/(\kappa_H + 1)} \quad (25)$$

where

$$G_{cr} = K_{IIcr}^2/4C \quad (26)$$

is the interfacial toughness and $\kappa_H = (3 - \nu_H)/(1 + \nu_H)$. Combined with the debond condition $K_{II} = K_{IIcr}$ and the crack-tip singularity conditions, singular integral Eqs. (23) can be solved numerically (Lu and Erdogan, 1983; Miller and Keer, 1985). To study the debond growth process, in calculations the value of a/h_H is first assumed, and then the dimensionless loading stress Σ_{H0} and the dislocation densities are solved from these equations (Dollar and Steif, 1992). The numerical computation is stable. When the moduli of both high modulus and low modulus fibers are equal to the moduli of matrix, we recover the data for K_{II} versus a derived by Dollar and Steif (1991).

According to Fukuda and Chou (1983), the stress concentration factor of a continuous fiber in hybrid composite (Fig. 2) is defined as the ratio between the average axial stress of the

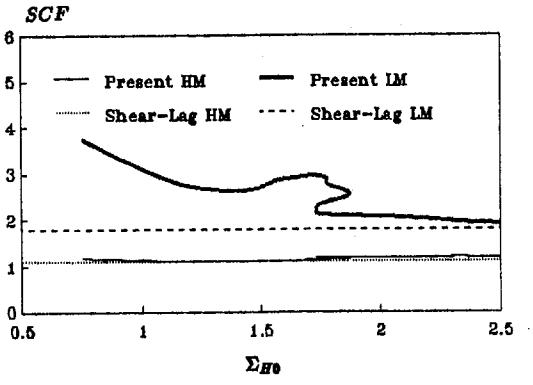


Fig. 4 Stress concentration factors of the nearest high modulus and low modulus fibers induced by the fiber breakage

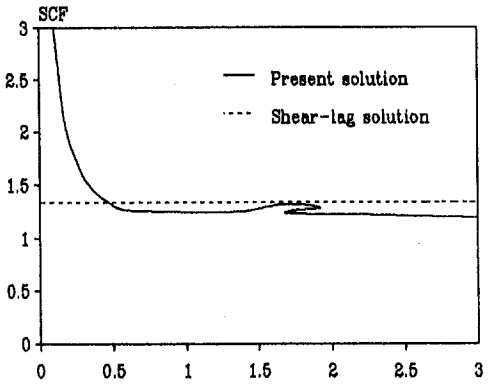


Fig. 5 Stress concentration factor of the nearest fiber to the broken one in all-high modulus fiber composites

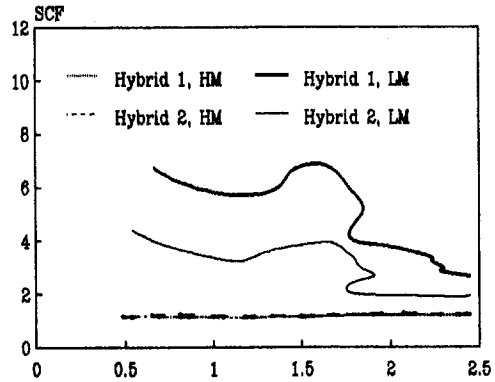


Fig. 6 Dependence of the stress concentration factors on the parameter R

Downloaded 04 May 2010 to 171.66.16.34. Redistribution subject to ASME license or copyright; see http://www.asme.org/terms/Terms_Use.cfm

fiber at the crack plane $x = 0$ and the axial stress of the same fiber at infinity. Thus, for low and high modulus fibers the stress concentration factors SCF_L and SCF_H are

$$(SCF)_L = 1 + \frac{(\sigma_{xx})_L}{\sigma_{H0}} \frac{E_H}{E_L}$$

$$(SCF)_H = 1 + \frac{(\sigma_{xx})_H}{\sigma_{H0}}, \tag{27}$$

respectively, where $(\sigma_{xx})_L$ and $(\sigma_{xx})_H$ are the average stresses induced by the above boundary value problem over low modulus and high modulus fibers at $x = 0$, respectively. This average stress concentration factor can give a good comparison to its one-dimensional counterpart. However, it should be pointed out that in a two-dimensional model the fiber failure criterion is more complicated than in a one-dimensional model and remains to be further investigated.

Figure 3 depicts the relation between the normalized debond length a/h_H and Σ_{H0} for a hybrid composite sheet with $E_L/E_H = \frac{1}{3}$, $h_L/h_H = 1$, $E_M/E_H = \frac{1}{10}$, $h_M/h_H = \frac{1}{5}$ and $\mu = 0$. It is seen that a/h_H increases with the increase of Σ_{H0}. At some values of Σ_{H0}, for example at $\Sigma_{H0} = 1.88$, the interfaces suddenly "unzip" to a large debond length.

Figure 4 plots in terms of Σ_{H0} the average stress concentration factors of the low modulus and high modulus fibers nearest to the broken one. It is shown that the stress concentration factor of the high modulus fiber is lower than that of the low modulus fiber and also lower than that in the all-high modulus fiber composite which is given in Fig. 5. As a result, the high modulus fiber in a hybrid composite can sustain higher load than that in non-hybrid composites. This is the so-called "hybrid effect." From these figures it is also seen that in the present solution the stress concentration factors, especially for the fiber nearest to breakage, are load and interfacial toughness dependent, which is quite different from that in the shear-lag model solution.

In computation we also examine the effect of the dimensionless residual stress Σ_0 on the stress concentration factor of the nearest low modulus fibers. It is found that the application of compressive residual stress tends to increase the magnitude of the stress which causes the interfaces to unzip. After interface unzipping, high compressive residual stress will correspond to high stress concentration factor of the nearest low modulus fibers. The computation also shows, however, that residual stress has only negligible influence on the stress concentration factor of the adjacent high modulus fibers.

Fukuda and Chou (1983) introduced a dimensionless parameter $R = E_L h_L / E_H h_H$. According to shear-lag theory, they found that the stress concentration factors of hybrid composites depend only on R. To examine the accuracy of this relationship, two hybrid composite systems are considered here. They are hybrid system 1 with $E_L/E_H = \frac{1}{6}$, $h_L/h_H = 1$, $E_M/E_H = \frac{1}{10}$, $h_M/h_H = \frac{1}{5}$, $\mu = 0$ and hybrid system 2 with $E_L/E_H = \frac{1}{3}$, $h_L/h_H = \frac{1}{2}$, $E_M/E_H = \frac{1}{10}$, $h_M/h_H = \frac{1}{5}$, $\mu = 0$. Both systems share the same value of $R = \frac{1}{6}$. Figure 6 depicts the stress concentration factors of the nearest low modulus and high modulus fibers versus Σ_{H0} for these two hybrid systems. It is shown that although R can quite precisely characterize the stress concentration factor of the adjacent high modulus fiber, there is considerable error for using the single parameter R to describe the stress concentration of the immediately adjacent low modulus fiber, especially in the early stage of debonding.

4 Conclusions

A refined mathematical model has been presented to analyze the stress distribution in an intermingled hybrid composite sheet. Assuming that one high modulus fiber is broken, the average stress concentration factors of both low modulus and high modulus fibers nearest to the breakage are calculated. They are compared with the corresponding results produced with the shear-lag model. It is found that the "hybrid effect" still exists in the two-dimensional model. In the beginning stage of interface debond the stress concentration factor of the nearest low modulus fiber is sensitively dependent on the interfacial toughness and residual stress, as found by Dollar and Steif (1992) in a homogeneous medium. With the debond developing, the load dependence of the stress concentration factor dies out. The examples of this paper show that as the dimensionless loading stress Σ_{H0} exceeds about 2, the stress concentration factor approaches a value not far from that given by the shear-lag model solution. Thus, for the composite systems with rather weak interfaces and low interfacial residual stress, the load dependence of stress concentration factor can be insignificant.

Acknowledgment

This work has been supported by the National Natural Science Foundation of China and the National Lab of MMC at Shanghai Jiao Tong University, China. Their supports are greatly appreciated.

References

Fukuda, H., and Chou, T. W., 1983, "Stress Concentrations in a Hybrid Composite Sheet," ASME JOURNAL OF APPLIED MECHANICS, Vol. 50, pp. 845–848.

Dollar, A., and Steif, P. S., 1989, "A Tension Crack Impinging Upon Frictional Interfaces," ASME JOURNAL OF APPLIED MECHANICS, Vol. 56, pp. 291–298.

Dollar, A., and Steif, P. S., 1991, "The Branched Crack Problem Revisited," ASME JOURNAL OF APPLIED MECHANICS, Vol. 58, pp. 584–586.

Dollar, A., and Steif, P. S., 1992, "Interface Blunting of Matrix Cracks in Fiber-Reinforced Ceramics," ASME JOURNAL OF APPLIED MECHANICS, Vol. 59, pp. 796–803.

Dundurs, J., 1969, "Elastic Interaction of Dislocations with Inhomogeneities," *Mathematical Theory of Dislocations,* ASME, New York, pp. 70–115.

Erdogan, F., and Gupta, G. D., 1971, "The Stress Analysis of Multilayered Composites with a Flaw," *International Journal of Solids and Structures,* Vol. 7, pp. 39–61.

He, M., and Hutchinson, J. W., 1989, "Crack Deflection at an Interface Between Dissimilar Elastic Materials," *International Journal of Solids and Structures,* Vol. 25, pp. 1053–1067.

Hedgepeth, J. M., 1961, "Stress Concentrations in Filamentary Structures," NASA TN D-882.

Lu, M.-C., and Erdogan, F., 1983, "Stress Intensity Factors in Two Bonded Elastic Layers Containing Cracks Perpendicular to and on the Interface—I. Analysis," *Engineering Fracture Mechanics,* Vol. 18, pp. 491–506.

Miller, G. R., and Keer, L. M., 1985, "A Numerical Technique for the Solution of Singular Integral Equations of the Second Kind," *Quarterly of Applied Mathematics,* Vol. 42, pp. 455–465.

APPENDIX

The regular kernels of singular integral Eqs. (23) are

$$K_1(y, \zeta) = \frac{\alpha + \beta^2}{(1 - \beta^2)(y + \zeta)} + \frac{2(\alpha - \beta)\zeta}{(1 + \beta)(y + \zeta)^2} - \frac{4(\alpha - \beta)\zeta^2}{(1 + \beta)(y + \zeta)^3} - \frac{\pi(1 + \alpha)}{C(1 - \beta^2)} H_2^{(1)}(y, \zeta),$$

$$K_2(y, x_0) = -\frac{4(1 + \alpha)y^3}{(1 + \beta)(x_0^2 + y^2)^2} + \frac{2(1 + \alpha)(3 - 2\beta)y}{(1 - \beta^2)(x_0^2 + y^2)} - \frac{2\pi(1 + \alpha)}{C(1 - \beta^2)} H_1^{(1)}(-x_0, y),$$

$$K_3(x, x_0) = \frac{1}{x + x_0} + \frac{\pi}{C}[G_1(x - x_0) + G_1(x + x_0)],$$

$$K_4(x, x_0) = \frac{\pi}{C}[F_1(x - x_0) + F_1(x + x_0)],$$

$$K_5(x, \zeta) = \frac{x}{x^2 + \zeta^2} - 2(1 - \beta)\frac{x\zeta^2}{(x^2 + \zeta^2)^2} + \frac{\pi}{C} G_2(x, \zeta),$$

$$K_6(x, \zeta) = \frac{\zeta}{x^2 + \zeta^2} - 2(1 - \beta)\frac{x^2\zeta}{(x^2 + \zeta^2)^2} + \frac{\pi}{C} F_2(x, \zeta).$$

Downloaded 04 May 2010 to 171.66.16.34. Redistribution subject to ASME license or copyright; see http://www.asme.org/terms/Terms_Use.cfm

Spherical Cavity Expansion in a Drucker-Prager Solid

D. Durban
Faculty of Aerospace Engineering,
Technion-Israel Institute of Technology,
Haifa 32000, Israel

N. A. Fleck
Engineering Department,
Cambridge University,
Cambridge CB2 1PZ, U.K.

A finite strain analysis is presented for the pressurized spherical cavity embedded in a Drucker-Prager medium. Material behavior is modeled by a nonassociated deformation theory which accounts for arbitrary strain-hardening. The governing equations of spherically symmetric response are reduced to a single differential equation with the effective stress as the independent variable. Some related topics are discussed including the elastic-perfectly plastic solid, the thin-walled shell, and the Mohr-Coulomb material. Spontaneous growth (cavitation limit) of an internally pressurized cavity is treated as a self-similar process and a few numerical examples are presented. These illustrate, for different hardening characteristics, the pressure sensitivity of material response and that deviations from normality always reduce the caviation pressure.

Introduction

It is commonly accepted and indeed frequently observed in experiments that the plastic response of soils is pressure (mean-stress) dependent. Drucker and Prager (1952) have proposed a simple yield function which models pressure sensitivity of perfectly plastic materials by adding a linear pressure term to the von Mises yield stress. In the present paper we study the spherical cavity problem employing a more general version of the Drucker-Prager solid. Material behavior is assumed to be elastoplastic with arbitrary strain-hardening, and the plastic flow potential is not identical with the yield surface. Thus, the flow rule is nonassociated.

The constitutive model, described in the next section, contains a complete three-dimensional derivation of the appropriate incremental stress-strain relations with large deformations. For the pressurized cavity, however, where the stress path is nearly proportional, we introduce a related deformation theory. It is shown, following Durban and Baruch (1976), that the governing equations can then be reduced to a single first-order nonlinear differential equation with the effective stress as the independent variable. For the associated case the flow theory coincides exactly with the deformation theory.

Some special cases are discussed in detail with emphasis on the elastic-perfectly plastic material. We show, in particular, that both flow and deformation theories predict identical stresses and strains, even when the flow rule is nonassociated.

When the internal pressure approaches a certain asymptotic value the cavity will expand spontaneously in a self-similar mode. This cavitation limit is examined here for both flow and deformation theories. The paper concludes with a few numerical examples that illustrate the pressure sensitivity of material response.

Studies of cavity expansion problems are of fundamental importance in the practice of geotechnical engineering; they are particularly helpful in constructing models of installation of driven piles (Randolph et al., 1979), and in the understanding of field tests (Hughes et al., 1977). Finite strain analysis is imperative in understanding the behavior of dilitant soils. Other important fields of applications include the modeling of the opening and closure of tunnels (Wroth, 1984) and interpretation of pressuremeter test results (Wood, 1990; Pye, 1995). While existing studies on cavity expansion problems concentrate on the Mohr-Coulomb perfectly plastic model (e.g., Chadwick, 1959; Bigoni and Laudiero, 1989; Yu and Houlsby, 1991), we show in this paper that there is no difficulty in incorporating strain-hardening into the Drucker-Prager material response of pressure sensitive solids.

Constitutive Model

The Drucker-Prager (1952) theory suggests a modification of the von Mises yield function by accounting for pressure dependence of the yield surface. The Drucker-Prager yield surface is defined by the effective stress

$$\sigma_e = (\tfrac{3}{2}\,\mathbf{S}\cdot\cdot\,\mathbf{S})^{1/2} + \tfrac{1}{3}\,\mu(\boldsymbol{\sigma}\cdot\cdot\,\mathbf{I}) \tag{1}$$

where $\boldsymbol{\sigma}$ is the Cauchy stress tensor; $\mathbf{S} = \boldsymbol{\sigma} - \frac{1}{3}\,\boldsymbol{\sigma}\cdot\cdot\,\mathbf{II}$ is the stress deviator; $\mathbf{I}$, the second-order unit tensor; and μ, a material parameter which reflects the pressure sensitivity of the solid. Notice that the shear term in (1) is exactly the Mises effective stress.

While in their 1952 paper Drucker and Prager assumed perfectly plastic behavior along with an associated flow rule, we shall allow here for strain-hardening and for a plastic potential g which is similar to but does not coincide with the yield surface.

We define g as

$$g = (\tfrac{3}{2}\,\mathbf{S}\cdot\cdot\,\mathbf{S})^{1/2} + \tfrac{1}{3}\,\eta(\boldsymbol{\sigma}\cdot\cdot\,\mathbf{I}) \tag{2}$$

where the dilitation factor $\eta \neq \mu$, and the plastic branch of the strain rate tensor follows from the normality rule

$$\mathbf{D}^P = \Lambda\,\frac{dg}{d\boldsymbol{\sigma}} = \Lambda[(\tfrac{3}{2}\,\mathbf{S}\cdot\cdot\,\mathbf{S})^{-1/2}(\tfrac{3}{2}\,\mathbf{S}) + \tfrac{1}{3}\,\eta\mathbf{I}] \tag{3}$$

with Λ standing for the proportionality factor. Invoking now the principle of plastic power equivalence, namely

$$\boldsymbol{\sigma}\cdot\cdot\,\mathbf{D}^P = \sigma_e\dot{\epsilon}_P, \tag{4}$$

where the total plastic strain ϵ_P is a known function of σ_e, we find with the aid of (3) that

$$\Lambda = \frac{\sigma_e}{g}\,\dot{\epsilon}_P. \tag{5}$$

Contributed by the Applied Mechanics Division of THE AMERICAN SOCIETY OF MECHANICAL ENGINEERS for publication in the ASME JOURNAL OF APPLIED MECHANICS.

Discussion on this paper should be addressed to the Technical Editor, Professor Lewis T. Wheeler, Department of Mechanical Engineering, University of Houston, Houston, TX 77204-4792, and will be accepted until four months after final publication of the paper itself in the ASME JOURNAL OF APPLIED MECHANICS.

Manuscript received by the ASME Applied Mechanics Division, July 21, 1995; final revision, Aug. 8, 1996. Associate Technical Editor: W. J. Drugan.

Copyright © 1997 by ASME

Downloaded 04 May 2010 to 171.66.16.34. Redistribution subject to ASME license or copyright; see http://www.asme.org/terms/Terms_Use.cfm

The plastic strain rate (3) is therefore

$$\mathbf{D}^P = \frac{\sigma_e}{g}\dot{\epsilon}_P[(\tfrac{3}{2}\,\mathbf{S}\cdot\cdot\,\mathbf{S})^{-1/2}(\tfrac{3}{2}\,\mathbf{S}) + \tfrac{1}{3}\,\eta\mathbf{I}]. \tag{6}$$

Assuming a standard Hookean relation for the elastic part of the strain rate, viz.

$$\mathbf{D}^E = \frac{1}{2G}\left(\overset{\triangledown}{\boldsymbol{\sigma}} - \frac{\nu}{1+\nu}\overset{\triangledown}{\boldsymbol{\sigma}}\cdot\cdot\,\mathbf{II}\right) \tag{7}$$

where (G, ν) are the usual elastic constants and $\overset{\triangledown}{\boldsymbol{\sigma}}$ denotes the objective Jaumann stress rate, we write the total strain rate as

$$\mathbf{D} = \mathbf{D}^E + \mathbf{D}^P. \tag{8}$$

This equation, along with (6) and (7), describes the complete elastoplastic constitutive law for the nonassociated Drucker-Prager solid. The time derivative of the effective strain can be expressed in terms of stress and stress rate by

$$\dot{\epsilon}_P = \left(\frac{d\epsilon_P}{d\sigma_e}\right)\frac{d\sigma_e}{d\boldsymbol{\sigma}}\cdot\cdot\,\overset{\triangledown}{\boldsymbol{\sigma}} \tag{9}$$

where from (1)

$$\frac{d\sigma_e}{d\boldsymbol{\sigma}} = (\tfrac{3}{2}\,\mathbf{S}\cdot\cdot\,\mathbf{S})^{-1/2}(\tfrac{3}{2}\,\mathbf{S}) + \tfrac{1}{3}\,\mu\mathbf{I}. \tag{10}$$

It follows that the constitutive relation (8) can be written as

$$\mathbf{D} = \mathbf{M}\cdot\cdot\,\overset{\triangledown}{\boldsymbol{\sigma}} \tag{11a}$$

with the fourth-order compliance tensor $\mathbf{M}$ given by

$$\mathbf{M} = \frac{1}{2G}\left(\mathfrak{I} - \frac{\nu}{1+\nu}\,\mathbf{II}\right) + \left(\frac{\sigma_e}{g}\right)\left(\frac{d\epsilon_p}{d\sigma_e}\right)\frac{dg}{d\boldsymbol{\sigma}}\cdot\frac{d\sigma_e}{d\boldsymbol{\sigma}} \tag{11b}$$

where $\mathfrak{I}$ is the fourth-order unit tensor. The derivative $dg/d\boldsymbol{\sigma}$ is similar to (10) but with μ being replaced by η. Notice that, by (3) and (10), the plastic part of $\mathbf{M}$ admits the Cauchy symmetry only for an associated flow rule where $\eta = \mu$ (or, trivially, in hydrostatic loading). Rudnicki and Rice (1975, Eqs. (10)) have arrived at a constitutive model which is essentially identical with (11) by proceeding along a more intuitive direction without employing a definite plastic potential.

The dependence of ϵ_P on the flow stress can be determined from a simple uniaxial compression experiment. Denoting by σ_1 the compressive stress we have that $\sigma_e = (-1 + (1/3)\mu)\sigma_1$, $g = (-1 + (1/3)\eta)\sigma_1$ and the constitutive relations specialize to

$$\dot{\epsilon}_1 = \frac{\dot{\sigma}_1}{E} - (1 - \tfrac{1}{3}\,\mu)\dot{\epsilon}_P$$

$$\dot{\epsilon}_2 = \dot{\epsilon}_3 = -\frac{\nu\dot{\sigma}_1}{E} + \frac{(1 - \frac{1}{3}\,\mu)(1 + \frac{2}{3}\,\eta)}{2(1 - \frac{1}{3}\,\eta)}\,\dot{\epsilon}_P \tag{12}$$

where both axial (ϵ_1) and transverse ($\epsilon_2 = \epsilon_3$) strains are logarithmic. Integrating the first of (12) over the loading history results in the variation of ϵ_P with σ_e. An interesting observation that follows from (12) is that in the deep plastic range the transverse contraction ratio approaches asymptotically the value of

$$-\frac{\dot{\epsilon}_2}{\dot{\epsilon}_1} = \frac{(1 + \frac{2}{3}\,\eta)}{2(1 - \frac{1}{3}\,\eta)}, \tag{13}$$

which is independent of μ.

Volume changes are given by

$$\mathbf{I}\cdot\cdot\,\mathbf{D} = \frac{1-2\nu}{E}\,\mathbf{I}\cdot\cdot\,\overset{\triangledown}{\boldsymbol{\sigma}} + \eta\,\frac{\sigma_e}{g}\,\dot{\epsilon}_P \tag{14}$$

In pure hydrostatic tension, where $\boldsymbol{\sigma} = t\mathbf{I}$, the plastic dilatation rate becomes equal to $\mu\dot{\epsilon}_P$ with the flow stress $\sigma_e = \mu t$. The variation of the effective plastic strain with the flow stress, in this particular deformation pattern, is independent of η.

Denoting the deviatoric part of the plastic strain-rate tensor (6) by $\hat{\mathbf{D}}^P$, we find that the equivalent plastic shear strain rate is

$$\dot{\gamma}_P = \sqrt{\tfrac{2}{3}\,\hat{D}_P\cdot\cdot\,\hat{D}_P} = \frac{\sigma_e}{g}\,\dot{\epsilon}_P$$

Thus, the plastic dilatation rate in (14) is equal to $\eta\dot{\gamma}_P$ in agreement with the standard interpretation of the dilatation factor (Rudnicki and Rice, 1975). It also follows that the plastic power $\sigma_e\dot{\epsilon}_p$ is equal to $g\,\dot{\gamma}_P$, with $\dot{\epsilon}_P \equiv \dot{\gamma}_P$ for the associated case ($\eta = \mu$).

The Pressurized Cavity

A spherical cavity, with an initially undeformed radius a, is embedded in an infinite medium and subjected to increasing internal pressure p. Locating the origin of a spherical polar Lagrangian system (r, θ, φ) at the center of the cavity, we have, by symmetry, the nonvanishing stresses $(\sigma_r, \sigma_\theta = \sigma_\varphi)$ and strains $(\epsilon_r, \epsilon_\theta = \epsilon_\varphi)$. The effective stress is

$$\sigma_e = \sigma_\theta - \sigma_r + \tfrac{1}{3}\,\mu(\sigma_r + 2\sigma_\theta), \tag{15}$$

since it is expected that under internal pressure $\sigma_\theta > \sigma_r$ at any point within the body.

Similarly, from (2)

$$g = \sigma_\theta - \sigma_r + \tfrac{1}{3}\,\eta(\sigma_r + 2\sigma_\theta)$$

$$= \frac{(1 + \frac{2}{3}\,\eta)\sigma_e + (\eta - \mu)\sigma_r}{(1 + \frac{2}{3}\,\mu)}. \tag{16}$$

Turning to the constitutive relations (8) we have just two scalar equations:

$$\dot{\epsilon}_r = \frac{1}{E}(\dot{\sigma}_r - 2\nu\dot{\sigma}_\theta) + \left(-1 + \frac{1}{3}\,\eta\right)\frac{\sigma_e}{g}\,\dot{\epsilon}_P \tag{17a}$$

$$\dot{\epsilon}_\theta = \frac{1}{E}[-\nu\dot{\sigma}_r + (1-\nu)\dot{\sigma}_\theta] + \left(\frac{1}{2} + \frac{1}{3}\,\eta\right)\frac{\sigma_e}{g}\,\dot{\epsilon}_P. \tag{17b}$$

Expecting, however, a nearly proportional stress path we proceed with the deformation-type theory whereby (17) is replaced by

$$\epsilon_r = \frac{1}{E}(\sigma_r - 2\nu\sigma_\theta) + \left(-1 + \frac{1}{3}\,\eta\right)\frac{\sigma_e}{g}\,\epsilon_P \tag{18a}$$

$$\epsilon_\theta = \frac{1}{E}[-\nu\sigma_r + (1-\nu)\sigma_\theta] + \left(\frac{1}{2} + \frac{1}{3}\,\eta\right)\frac{\sigma_e}{g}\,\epsilon_P. \tag{18b}$$

Equations (18) are the exact integrals of (17) for the cavity problem when the flow rule is associated ($\eta = \mu \Rightarrow g = \sigma_e$). Otherwise there is an error involved in (18) in comparison with the nonholonomic model (17). Deviations from proportionality can be examined a posteriori by evaluating the ratio σ_e/g and checking whether it remains nearly constant along the loading path. This implies that a sufficient condition for (18) to remain valid in nonproportional loading is that the second term in (16) should be much smaller than the effective stress, or

$$\frac{|\eta - \mu|}{1 + \frac{2}{3}\,\eta}\cdot\frac{|\sigma_r|}{\sigma_e} \ll 1. \tag{19}$$

Downloaded 04 May 2010 to 171.66.16.34. Redistribution subject to ASME license or copyright; see http://www.asme.org/terms/Terms_Use.cfm

Equilibrium requirements are here governed by the single equation

$$r\frac{d\sigma_r}{dr} + 2\frac{1+\dfrac{du}{dr}}{1+\dfrac{u}{r}}(\sigma_r - \sigma_\theta) = 0 \tag{20}$$

where $u = u(r)$ is the radial displacement. Recalling, however, that the finite strain components are

$$\epsilon_r = \ln\left(1+\frac{du}{dr}\right) \quad \epsilon_\theta = \ln\left(1+\frac{u}{r}\right), \tag{21}$$

we can rewrite (20) in the differential form

$$d\sigma_r = 2(\sigma_\theta - \sigma_r)\exp(\epsilon_r - \epsilon_\theta)\frac{dr}{r}. \tag{22}$$

Combining this with the strain compatibility relation, from (21),

$$d\epsilon_\theta = [\exp(\epsilon_r - \epsilon_\theta) - 1]\frac{dr}{r} \tag{23}$$

we arrive at the connection

$$d\sigma_r = \frac{2(\sigma_\theta - \sigma_r)d\epsilon_\theta}{1 - \exp(\epsilon_\theta - \epsilon_r)} \tag{24}$$

which will be reduced to an ordinary differential equation for σ_r in terms of the independent variable σ_e. The formulation centers on the effective stress σ_e as the independent variable and is valid for any strain-hardening characteristic.

To this end we rearrange (15) to obtain

$$\sigma_\theta - \sigma_r = \frac{\sigma_e - \mu\sigma_r}{(1+\frac{2}{3}\mu)}. \tag{25}$$

Next, from (18),

$$\epsilon_\theta - \epsilon_r = \frac{1+\nu}{E}(\sigma_\theta - \sigma_r) + \frac{3}{2}\cdot\frac{\sigma_e}{g}\epsilon_P \tag{26}$$

or, with the aid of (25),

$$\epsilon_\theta - \epsilon_r = \frac{1+\nu}{E}\left(\frac{\sigma_e - \mu\sigma_r}{1+\frac{2}{3}\mu}\right) + \frac{3}{2}\cdot\frac{\sigma_e}{g}\epsilon_P. \tag{27}$$

Finally, we use (15) to eliminate σ_θ from (18*b*) resulting in

$$\epsilon_\theta = \frac{1-\nu}{E}\cdot\frac{\sigma_e}{1+\frac{2}{3}\mu} + \left[(1-2\nu) - \frac{(1-\nu)\mu}{1+\frac{2}{3}\mu}\right]\frac{\sigma_r}{E} + \left(\frac{1}{2}+\frac{1}{3}\eta\right)\frac{\sigma_e}{g}\epsilon_P. \tag{28}$$

The differential form of (28) is

$$d\epsilon_\theta = \frac{\partial\epsilon_\theta}{\partial\sigma_e}d\sigma_e + \frac{\partial\epsilon_\theta}{\partial\sigma_r}d\sigma_r \tag{29}$$

where the partial derivatives are determined from (28) without difficulty.

Substituting now (25), (27) and (29) in (24) we obtain the desired differential equation

$$\frac{d\Sigma_r}{d\Sigma} = -\frac{(\Sigma - \mu\Sigma_r)\left(\alpha_1 + \beta_1\dfrac{\Sigma}{G}\epsilon_P' + \beta_2\dfrac{\Sigma_r}{G^2}\epsilon_P\right)}{\exp\left[\alpha_3(\Sigma - \mu\Sigma_r) + \dfrac{3\Sigma}{2G}\epsilon_P\right] - 1 + (\Sigma - \mu\Sigma_r)\left(\alpha_2 - \beta_2\dfrac{\Sigma}{G^2}\epsilon_P\right)} \tag{30}$$

where all stress components have been nondimensionalized with respect to the elastic modulus

$$\Sigma_r = \frac{\sigma_r}{E}, \quad \Sigma_\theta = \frac{\sigma_\theta}{E}, \quad \Sigma = \frac{\sigma_e}{E}, \quad \epsilon_P' = \frac{d\epsilon_P}{d\Sigma} \tag{31}$$

$$G = \frac{g}{E} = \beta_1\Sigma + \frac{\beta_2}{\beta_1}\Sigma_r \tag{32}$$

and

$$\alpha_1 = \frac{2(1-\nu)}{(1+\frac{2}{3}\mu)^2} \quad \alpha_2 = \frac{2[(1-2\nu) - \frac{1}{3}\mu(1+\nu)]}{(1+\frac{2}{3}\mu)^2}$$

$$\alpha_3 = \frac{1+\nu}{1+\frac{2}{3}\mu} \tag{33}$$

$$\beta_1 = \frac{1+\frac{2}{3}\eta}{1+\frac{2}{3}\mu} \quad \beta_2 = \frac{\eta - \mu}{(1+\frac{2}{3}\mu)}\beta_1. \tag{34}$$

The integration of (30) is carried from infinity, where all stress components vanish, to any chosen value of the effective stress at the cavity $\Sigma\,(r = a) = \Sigma_a$. The corresponding value of the radial stress $\Sigma_r\,(r = a) = -p/E = -P$ determines the internal pressure associated with that particular value of Σ_a. Equation (30) is universal in the sense that each pair (Σ_a, P) represents a state of stress at some radius within the medium. At infinity, where the field is fully elastic, it is permissible to replace (30) by its asymptotic form $\Sigma_r = -\frac{2}{3}\Sigma$. That relation provides convenient starting data for the numerical integration of (30). Notice that in our formulation the infinite spatial domain $a \le r < \infty$ is transformed, by a hodograph-like method, into a finite effective stress domain.

Once the variation of Σ_r with Σ has been determined the circumferential stress follows from (15) as

$$\Sigma_\theta = \frac{\Sigma + (1 - \frac{1}{3}\mu)\Sigma_r}{(1+\frac{2}{3}\mu)}. \tag{35}$$

To obtain the spatial distribution of the stresses we combine (30) with (22), using (25) and (27), which gives

Downloaded 04 May 2010 to 171.66.16.34. Redistribution subject to ASME license or copyright; see http://www.asme.org/terms/Terms_Use.cfm

$$\frac{dr}{r\,d\Sigma} = -\frac{1+\frac{2}{3}\mu}{2}\cdot\frac{\left(\alpha_1+\beta_1\frac{\Sigma}{G}\epsilon_P'+\beta_2\frac{\Sigma_r}{G^2}\epsilon_P\right)\exp\left[\alpha_3(\Sigma-\mu\Sigma_r)+\frac{3}{2}\cdot\frac{\Sigma}{G}\epsilon_P\right]}{\exp\left[\alpha_3(\Sigma-\mu\Sigma_r)+\frac{3}{2}\cdot\frac{\Sigma}{G}\epsilon_P\right]-1+(\Sigma-\mu\Sigma_r)\left(\alpha_2-\beta_2\frac{\Sigma}{G^2}\epsilon_P\right)} \quad (36)$$

This equation when integrated from the cavity ($r = a$, $\Sigma = \Sigma_a$, $\Sigma_r = -P$) to any given radius results in the dependence of Σ on r at any value of internal pressure. Transformation to the Eulerian radial coordinate $R = r + u$ is provided by (28) and the second of (21), viz

$$\ln\frac{R}{r} = \frac{1+\frac{2}{3}\mu}{2}\left(\alpha_1\Sigma+\alpha_2\Sigma_r+\beta_1\frac{\Sigma}{G}\epsilon_P\right). \quad (37)$$

To sum up, the solution of the cavity problem is reduced to the numerical integration of (30) and (36). The same pair of equations describes also the behavior of a thick spherical shell under internal pressure with the outer surface being stress free.

Some Special Cases

Associated Flow Rule. When $\eta = \mu$ the plastic potential g coincides with the effective stress σ_e. The flow theory relations (17) then integrate exactly to the deformation theory relations (18) so no approximation is involved in the solution. From (34) we have that $\beta_1 = 1$ $\beta_2 = 0$ and the governing Eq. (30) becomes

$$\frac{d\Sigma_r}{d\Sigma} = -\frac{(\Sigma-\mu\Sigma_r)(\alpha_1+\epsilon_P')}{\exp[\alpha_3(\Sigma-\mu\Sigma_r)+\frac{3}{2}\epsilon_P]-1+\alpha_2(\Sigma-\mu\Sigma_r)} \quad (38)$$

with a similar simplification of (36). For $\mu = 0$ we recover from (38) the von Mises quadrature solution (Durban and Baruch, 1976).

Elastic-Perfectly Plastic Behavior. While no definite yield point has been assumed so far in the analysis there is no difficulty in handling elasto/plastic response with discontinuous derivatives at the elastic/plastic boundary. At sufficiently low pressures the behavior is elastic. When the pressure (termed P_Y) is attained, yielding begins at the cavity wall. At higher pressures the plastic zone spreads into the body. During the initial elastic phase $\epsilon_P \equiv 0$ and (30) is reduced to

$$\frac{d\Sigma_r}{d\Sigma} = -\frac{\alpha_1(\Sigma-\mu\Sigma_r)}{\exp[\alpha_3(\Sigma-\mu\Sigma_r)]-1+\alpha_2(\Sigma-\mu\Sigma_r)}. \quad (39)$$

This equation is of course completely independent of the plastic parameters and in fact can be recast into the quadrature form

$$\Sigma_r = -\int_0^{\cdot}\frac{2(1-\nu)(\Sigma_\theta-\Sigma_r)d(\Sigma_\theta-\Sigma_r)}{\exp[(1+\nu)(\Sigma_\theta-\Sigma_r)]-1+2(1-2\nu)(\Sigma_\theta-\Sigma_r)} \quad (40)$$

where the remote stress-free state provides the lower limit on the integral. Expression (40) together with the elastic version of (36)—which can likewise be reduced to a simple integral—are the cavity expansion solution for the hypoelastic solid (7) as detailed in Durban and Baruch (1974). If the elastic strains are sufficiently small it becomes possible to recover from (40) the linear elastic relation $\Sigma_r + 2\Sigma_\theta = 0$.

The onset of yielding is signalled by the equality $\Sigma = \Sigma_Y$ where $\Sigma_Y = Y/E$ with Y denoting the yield stress along the $\epsilon_P - \sigma_e$ curve. Plastic flow will first occur at the cavity when the nondimensionalized pressure P reaches the value P_Y as determined by the solution of (39). With further increase in pressure a plastic zone will spread radially from the cavity. Within the plastic zone we rewrite Eq. (30) with the effective strain as the independent variable (since $\Sigma \equiv \Sigma_Y$ and $d\Sigma \equiv 0$) as

$$\frac{d\Sigma_r}{d\epsilon_P} = -\frac{(\Sigma_Y-\mu\Sigma_r)\beta_1\frac{\Sigma_Y}{G}}{\exp\left[\alpha_3(\Sigma_Y-\mu\Sigma_r)+\frac{3}{2}\cdot\frac{\Sigma_Y}{G}\epsilon_P\right]-1+(\Sigma_Y-\mu\Sigma_r)\left(\alpha_2-\beta_2\frac{\Sigma_Y}{G^2}\epsilon_P\right)} \quad (41)$$

where now

$$G = \beta_1\Sigma_Y + \frac{\beta_2}{\beta_1}\Sigma_r. \quad (42)$$

The solution procedure starts with integrating (39) from infinity to the elastoplastic interface where $\Sigma = \Sigma_Y$ and $\Sigma_r = -Pi$ (the interface pressure). This value of Σ_r along with $\epsilon_P = 0$ are used as the initial data for integrating (41) from the interface inwards. The solution is again universal since to each cavity plastic strain ϵ_{Pa} there corresponds a specific pressure P and each pair (ϵ_{Pa}, P) corresponds to a radius within the body. The spatial distribution of stresses and strains can be determined in a similar way from (36) with

$$\frac{dr}{r\,d\Sigma} = -\frac{1+\frac{2}{3}\mu}{2}\times\frac{\alpha_1\exp[\alpha_3(\Sigma-\mu\Sigma_r)]}{\exp[\alpha_3(\Sigma-\mu\Sigma_r)]-1+\alpha_2(\Sigma-\mu\Sigma_r)} \quad (43)$$

in the elastic zone, $0 \le \Sigma \le \Sigma_Y$. In the plastic zone $\Sigma = \Sigma_Y$ and

$$\frac{dr}{r\,d\epsilon_P} = -\frac{1+\frac{2}{3}\mu}{2}\cdot\frac{\beta_1\frac{\Sigma_Y}{G}\exp\left[\alpha_3(\Sigma_Y-\mu\Sigma_r)+\frac{3}{2}\cdot\frac{\Sigma_Y}{G}\epsilon_P\right]}{\exp\left[\alpha_3(\Sigma_Y-\mu\Sigma_r)+\frac{3}{2}\cdot\frac{\Sigma_Y}{G}\epsilon_P\right]-1+(\Sigma_Y-\mu\Sigma_r)\left(\alpha_2-\beta_2\frac{\Sigma_Y}{G^2}\epsilon_P\right)} \quad (44)$$

Downloaded 04 May 2010 to 171.66.16.34. Redistribution subject to ASME license or copyright; see http://www.asme.org/terms/Terms_Use.cfm

where G is given by (42). These differential equations are supplemented by (37) when transforming to the Eulerian spatial radial coordinate.

For the associated flow rule the elastic zone is still described by (39) and (43), but in the plastic zone where $\beta_1 = 1$, $\beta_2 = 0$ and $G \equiv \Sigma_Y$, Eqs. (41) and (44) are reduced to

$$\frac{d\Sigma_r}{d\epsilon_P} = -\frac{\Sigma_Y - \mu\Sigma_r}{\exp[\alpha_3(\Sigma_Y - \mu\Sigma_r) + \frac{3}{2}\epsilon_P] - 1 + \alpha_2(\Sigma_Y - \mu\Sigma_r)} \tag{45}$$

$$\frac{\frac{dr}{r}}{d\epsilon_P} = -\frac{1 + \frac{2}{3}\mu}{2} \times \frac{\exp[\alpha_3(\Sigma_Y - \mu\Sigma_r) + \frac{3}{2}\epsilon_P]}{\exp[\alpha_3(\Sigma_Y - \mu\Sigma_r) + \frac{3}{2}\epsilon_P] - 1 + \alpha_2(\Sigma_Y - \mu\Sigma_r)}. \tag{46}$$

The stress field in the inner plastic domain has the same Eulerian spatial distribution for the nonassociated flow and deformation theories by the following argument. Writing the equilibrium Eq. (20) as $d\sigma_r/dR + 2(\sigma_r - \sigma_\theta)/R = 0$ and combining this with (25) when $\sigma_e \equiv Y$ we find the profiles

$$\Sigma_r = \frac{\Sigma_Y}{\mu} - \left(P + \frac{\Sigma_Y}{\mu}\right)\left(\frac{A}{R}\right)^{\alpha_4}$$

$$\Sigma_\theta = \frac{\Sigma_Y}{\mu} - \alpha_5\left(P + \frac{\Sigma_Y}{\mu}\right)\left(\frac{A}{R}\right)^{\alpha_4} \tag{47}$$

where A is the deformed radius of the cavity, and

$$\alpha_4 = \frac{2\mu}{1 + \frac{2}{3}\mu} \quad \alpha_5 = \frac{1 - \frac{1}{3}\mu}{1 + \frac{2}{3}\mu}. \tag{48}$$

Furthermore, the plastic strain rates of the flow theory (17) form the identity

$$\dot{\epsilon}_r^P + 2\beta_3\dot{\epsilon}_\theta^P = 0 \quad \text{with} \quad \beta_3 = \frac{1 - \frac{1}{3}\eta}{1 + \frac{2}{3}\eta} \tag{49}$$

which integrates to the deformation theory (18) relation

$$\epsilon_r^P + 2\beta_3\epsilon_\theta^P = 0. \tag{50}$$

Upon superposing the elastic strains this is equivalent to

$$\epsilon_r + 2\beta_3\epsilon_\theta = (1 - 2\nu\beta_3)\Sigma_r - 2[\nu - (1 - \nu)\beta_3]\Sigma_\theta. \tag{51}$$

Recalling now that $\epsilon_r = \ln(dR/dr)$ and $\epsilon_\theta = \ln(R/r)$ and using the stresses (47) it becomes possible to integrate (51) and express the undeformed radius r as a quadrature of the deformed radius R,

$$r^{2\beta_3+1} - a^{2\beta_3+1} = (2\beta_3 + 1) \times \int_A^R \left\{\exp\left[\beta_5\left(P + \frac{\Sigma_Y}{\mu}\right)\left(\frac{A}{R}\right)^{\alpha_4} - \beta_4\frac{\Sigma_Y}{\mu}\right]\right\} R^{2\beta_3}dR \tag{52}$$

where

$$\beta_4 = \frac{3(1 - 2\nu)}{1 + \frac{2}{3}\eta} \quad \beta_5 = \frac{3(1 - 2\nu) + \frac{2}{3}(1 + \nu)\mu\eta}{(1 + \frac{2}{3}\eta)(1 + \frac{2}{3}\mu)}. \tag{53}$$

The well-known small strain elastic solution for the outer elastic zone gives vanishing hydrostatic stress $\Sigma_r + 2\Sigma_\theta = 0$. Stress continuity at the elasto/plastic interface implies by (47) that

$$P + \frac{\Sigma_Y}{\mu} = \frac{1 + \frac{2}{3}\mu}{\mu}\Sigma_Y\left(\frac{R_i}{A}\right)^{\alpha_4}. \tag{54}$$

Also at the interface we have the circumferential strain

$$\ln\frac{R_i}{r_i} = [-\nu\Sigma_r + (1 - \nu)\Sigma_\theta]_{\Sigma=\Sigma_Y} \approx \frac{1 + \nu}{3}\Sigma_Y \tag{55}$$

for small strain elasticity. Specifying (52) at the interface gives with the aid of (54), and the approximation $R_i \approx r_i$ from (55),

$$1 - \left(\frac{a}{r_i}\right)^{2\beta_3+1} = \left[(2\beta_3 + 1)\exp\left(-\frac{\beta_4}{\mu}\Sigma_Y\right)\right] \times \int_{t_a}^1 \left[\exp\left(\frac{1 + \frac{2}{3}\mu}{\mu}\beta_5\Sigma_Y t^{-\alpha_4}\right)\right] t^{2\beta_3}dt \tag{56}$$

where $t = R/R_i$ and $t_a = A/R_i$.

Equation (56) provides the relation between R_i/A and r_i/a with the associated pressure given by (54). It is then a matter of ease to evaluate from (52) the relation between r and R for any given internal pressure. Thus, the stress and strain profiles (in both Eulerian and Lagrangian radial coordinates) are identical for the flow and deformation theories. The only difference between the two models lies in the radial distribution of the effective plastic strain ϵ_P. This is, of course, a direct outcome of the degeneracy of the elastic-perfectly plastic model since there is no unique effective plastic strain in simple tension after yield.

The Thin-Shell Thought Experiment. We may imagine the medium as being composed of adjacent infinite layers each behaving as a thin-walled spherical shell under net outward pressure ΔP. The differential Eqs. (30) and (36) can be approximated by their finite differences analogues and combined to yield

$$\Delta P = \frac{2\left(\frac{h_0}{r_0}\right)}{1 + \frac{2}{3}\mu}(\Sigma - \mu\Sigma_r) \times \exp\left[-\alpha_3(\Sigma - \mu\Sigma_r) - \frac{3}{2}\cdot\frac{\Sigma}{G}\epsilon_P\right]. \tag{57}$$

Here we have applied the approximation $dr/r \approx h_0/r_0$ where (h_0, r_0) are, respectively, the undeformed thickness and middle-surface radius of the shell, and it is understood that the r.h.s. of (57) represents the average value over the thickness of each layer. Now, for a hardening material, in the deep plastic range we may assume that $\Sigma \gg \Sigma_r$ so that $G \approx \beta_1\Sigma$, and also neglect the elastic term from the exponent in (57). This leaves us with

$$\Delta P = \frac{2\left(\frac{h_0}{r_0}\right)}{1 + \frac{2}{3}\mu}\Sigma\exp\left(-\frac{3\epsilon_P}{2\beta_1}\right) \tag{58}$$

which has a maximum when

$$\Sigma\epsilon_P' = \frac{2}{3}\beta_1. \tag{59}$$

Downloaded 04 May 2010 to 171.66.16.34. Redistribution subject to ASME license or copyright; see http://www.asme.org/terms/Terms_Use.cfm

For a power-hardening law $\epsilon_P = B\Sigma^n$, where (n, B) are material parameters, the effective stress and strain at the maximum pressure difference are

$$\Sigma = \left(\frac{2\beta_1}{3nB}\right)^{1/n} \quad \epsilon_P = \frac{2\beta_1}{3n} \tag{60}$$

with the corresponding pressure

$$\Delta P_{\max} = \frac{2\left(\frac{h_0}{r_0}\right)}{1 + \frac{2}{3}\mu}\left(\frac{2\beta_1}{3enB}\right)^{1/n}. \tag{61}$$

Recalling that β_1 is given in (34) we find that the level of nonassociativity has a considerable influence on the plastic response of the elemental spherical shell. Thus, the pair ($\mu = 0.5, \eta = 1.5 \Rightarrow \beta_1 = 1.5$) produces an instability strain ϵ_P which is three times higher than the one obtained with ($\mu = 1.5, \eta = 0 \Rightarrow \beta_1 = 0.5$). The corresponding ratio of pressures (61) is $3^{1/n}$ which for a typical value of $n = 2$ is ~ 1.73.

It is reasonable to expect that the sensitivity of the strength of a single shell to the ratio η/μ will be transmitted to the entire medium even though plastic collapse is not radially homogeneous.

The Mohr-Coulomb Solid. Existing studies on cavity expansion problems in soils are dominated by the elastic-perfectly plastic Mohr-Coulomb model (Chadwick, 1959; Bigoni and Laudiero, 1990; Yu and Houlsby, 1991).

The Mohr-Coulomb solid—in its nonassociated version—is governed by the yield function and flow potential

$$\sigma_e = \bar{\mu}\sigma_1 - \sigma_3 \quad g = \bar{\eta}\sigma_1 - \sigma_3 \tag{62}$$

where (σ_1, σ_3) are, respectively, the largest and smallest principal stresses, and $(\bar{\mu}, \bar{\eta})$ are material parameters. For the spherical cavity problem ($\sigma_1 = \sigma_\theta = \sigma_\varphi, \sigma_3 = \sigma_r$) and the plastic strain rates become

$$\dot{\epsilon}_r^P = -\frac{\sigma_e}{g}\dot{\epsilon}_\theta^P \quad \dot{\epsilon}_\theta^P = \frac{1}{2}\bar{\eta}\frac{\sigma_e}{g}\dot{\epsilon}_P$$

with

$$\sigma_e = \bar{\mu}\sigma_\theta - \sigma_r \quad g = \bar{\eta}\sigma_\theta - \sigma_r. \tag{63}$$

These relations are equivalent to the plastic branch of the Drucker-Prager constitutive law (15) – (17) apart from a rescaling of the material parameters. It follows that the preceding analysis can be adapted to include the nonassociated Mohr-Coulomb solid with strain-hardening.

Spontaneous Growth

The internal pressure approaches an asymptotic limit P_c which, when attained, will induce a spontaneous expansion of the cavity at a constant load $P = P_c$. Cavitation phenomena have been studied extensively (Horgan, 1995) but little seems to be available on cavitation in plastic-hardening pressure sensitive solids. That cavitation pressure can be obtained from the loading path (30) at the limit of $\Sigma_a \to \infty$. For elastic-perfectly plastic solids we integrate the pair (39) and (41) with $\epsilon_{Pa} \to \infty$. We can use also (56) directly with $a/r_i \to 0$ to find the cavitation limit of $t_a = A/R_i$ from

$$\int_{t_a}^1 \left[\exp\left(\frac{1 + \frac{2}{3}\mu}{\mu}\beta_5\Sigma_Y t^{-\alpha_4}\right)\right] t^{2\beta_3}dt = \frac{\exp\left(\frac{\beta_4}{\mu}\Sigma_Y\right)}{2\beta_3 + 1}. \tag{64}$$

The cavitation pressure follows from (54) as

$$P_c = \frac{\Sigma_Y}{\mu}\left[(1 + \tfrac{2}{3}\mu)t_a^{-\alpha_4} - 1\right] \tag{65}$$

for both flow and deformation theories.

The self-similarity of the spontaneous growth state enables a direct evaluation of the cavitation pressure with no need to trace the entire straining history (Fleck et al., 1992). The procedure is particularly helpful with the flow theory (17) where an elaborated step by step incremental routine is required for the complete numerical solution. This analysis can be easily generalized to account for the presence of external pressure, thus increasing the level of P_c.

All field quantities are assumed to depend on the single coordinate $\xi = R/A$, with the time-like differentiation

$$(\dot{}) = \left(\frac{\dot{R}}{A} - \xi\frac{\dot{A}}{A}\right)\frac{d(\ )}{d\xi}. \tag{66}$$

The strain rates are now $\dot{\epsilon}_r = d\dot{R}/dR$ and $\dot{\epsilon}_\theta = \dot{R}/R$ and the constitutive relations (17) take the form

$$\frac{dV}{d\xi} = (V - \xi) \times \left[\frac{d}{d\xi}(\Sigma_r - 2\nu\Sigma_\theta) + \left(-1 + \frac{1}{3}\eta\right)\frac{\Sigma}{G}\cdot\frac{d\epsilon_P}{d\xi}\right] \tag{67a}$$

$$\frac{V}{\xi} = (V - \xi) \times \left[\frac{d}{d\xi}(-\nu\Sigma_r + (1 - \nu)\Sigma_\theta) + \left(\frac{1}{2} + \frac{1}{3}\eta\right)\frac{\Sigma}{G}\cdot\frac{d\epsilon_P}{d\xi}\right] \tag{67b}$$

where $V = \dot{R}/\dot{A}$.

The couple (67) together with the equilibrium requirement

$$\frac{d\Sigma_r}{d\xi} = \frac{2}{\xi}(\Sigma_\theta - \Sigma_r) \tag{68}$$

provide three equations for $\Sigma_r, \Sigma_\theta, V$ as unknowns. Integration can start at the remote linear elastic field where

$$\xi \to \infty: \Sigma_r = -\frac{C}{\xi^3} \quad \Sigma_\theta \to \frac{C}{2\xi^3} \quad V \to \frac{3(1 + \nu)C}{2\xi^2} \tag{69}$$

and C is an unknown constant. At the cavity boundary we require

$$\xi = 1 : V = 1 \quad \Sigma_\theta \to \infty \quad \Sigma_r = -P_c. \tag{70}$$

A standard shooting method can be used to solve this two point boundary value problem.

Alternatively, we may exploit the coordinate transformation

$$X = \frac{V}{\xi} \tag{71}$$

and eliminate ξ between (67b) and (68) to obtain

$$\Sigma_r' = \frac{(X - 1)(\Sigma - \mu\Sigma_r)\left(\alpha_1 + \beta_1\frac{\Sigma}{G}\epsilon_P'\right)}{X - \alpha_2(X - 1)(\Sigma - \mu\Sigma_r)}. \tag{72}$$

Similarly, Eq. (67a) is transformed to

$$X' = (X - 1)\left[\alpha_3(\mu\Sigma_r' - 1) - \frac{3}{2}\cdot\frac{\Sigma}{G}\epsilon_P'\right] \tag{73}$$

where $(\ )' = d(\ )/d\Sigma$.

Downloaded 04 May 2010 to 171.66.16.34. Redistribution subject to ASME license or copyright; see http://www.asme.org/terms/Terms_Use.cfm

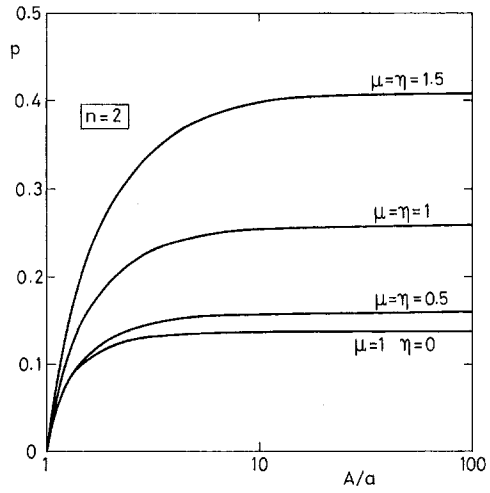


Fig. 1 Pressure-expansion curves for a power-law material. $\epsilon_P = B\,\Sigma^n$ with $B = 100$ and $n = 2$. $\nu = 0.3$. Results are for the deformation theory.

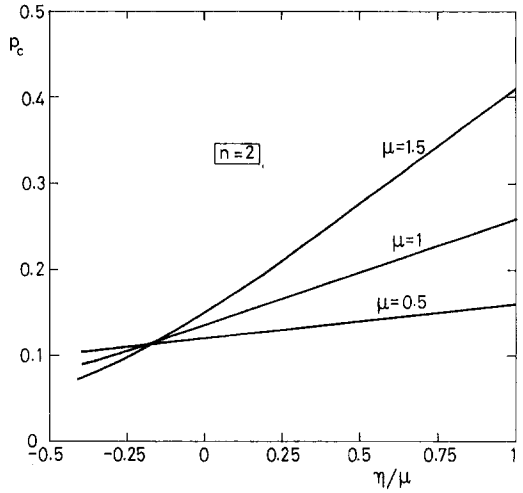


Fig. 3 Variation of the cavitation pressure with level of non-associativity for a power-law material. $\epsilon_P = B\,\Sigma^n$ with $B = 100$ and $n = 2$. $\nu = 0.3$. Results for deformation and flow theories are practically the same.

The system (72)–(73) is simpler to integrate numerically in comparison with (67)–(69). In the far-field $X = (1 + \nu)\Sigma$, $\Sigma_r = -\frac{2}{3}\Sigma$, and integration can start with any reasonable choice of Σ in the remote elastic zone. At the cavity $\Sigma \to \infty$ $X \to 1$ and $\Sigma_r = -P_c$.

For the associated flow rule ($\Sigma = G$) Eq. (73) integrates exactly to

$$\ln(1 - X) = -\alpha_3(\Sigma - \mu\Sigma_r) - \tfrac{3}{2}\epsilon_P. \tag{74}$$

Inserting this relation in (72) gives exactly Eq. (38) with the cavity data $X = 1$ $\Sigma \to \infty$. This shows formally that the cavitation limit of the loading history is the self-similar field of spontaneous growth. A similar analysis can be made for the nonassociated deformation theory (with hardening), and for the nonassociated flow theory with the elastic-perfectly plastic response. For the latter case we deduce from (49) and (67)

$$\frac{dV}{d\xi} + 2\beta_3\frac{V}{\xi} = (V - \xi)\alpha_4\beta_5\left(P + \frac{\Sigma_Y}{\mu}\right)\xi^{-\alpha_4^{-1}}. \tag{75}$$

The solution of this equation together with the cavity and interface conditions leads again to (64).

The similarity solution can be extended to include inertia effects: Radial motion is governed by the equation (ρ being the density)

$$\frac{d\sigma_r}{dR} + \frac{2}{R}(\sigma_r - \sigma_\theta) = \rho\ddot{R} \tag{76}$$

which can be rewritten in the nondimensionalized form

$$\frac{d\Sigma_r}{d\xi} + \frac{2}{\xi}(\Sigma_r - \Sigma_\theta) = \frac{\rho\dot{A}^2}{E}(V - \xi)\frac{dV}{d\xi}. \tag{77}$$

Conservation of matter requires that $\dot{\rho} + \rho\mathbf{I}\cdot\cdot\mathbf{D} = 0$ or, in a rate form,

$$\frac{\dot{\rho}}{\rho} + \dot{\epsilon}_r + 2\dot{\epsilon}_\theta = 0 \tag{78}$$

Hence, in steady growth,

$$(V - \xi)\frac{d\ln\dfrac{\rho}{\rho_0}}{d\xi} + \frac{dV}{d\xi} + 2\frac{V}{\xi} = 0, \tag{79}$$

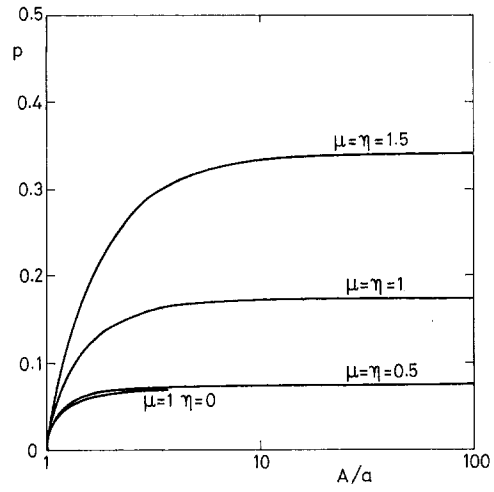


Fig. 2 Pressure-expansion curves for an elastic-perfectly plastic material. $\Sigma_Y = 0.01$. $\nu = 0.3$. Results are for both flow and deformation theories.

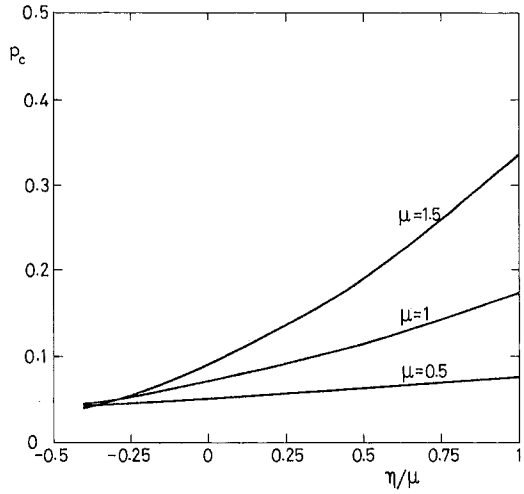


Fig. 4 Variation of the cavitation pressure with level of nonassociativity for an elastic-perfectly plastic material. $\Sigma_Y = 0.01$. $\nu = 0.3$. Results are for both flow and deformation theories.

Downloaded 04 May 2010 to 171.66.16.34. Redistribution subject to ASME license or copyright; see http://www.asme.org/terms/Terms_Use.cfm

where ρ_0 is material density in the undeformed state. The governing system consists now of (77), (79) and (67) or their analogue for the deformation theory.

In the absence of hardening we can replace (67) in the plastic zone by

$$\frac{dV}{d\xi} + 2\beta_3 \frac{V}{\xi} = (V - \xi) \times \left[(1 - 2\nu\beta_3) \frac{d\Sigma_r}{d\xi} - 2(\nu - (1 - \nu)\beta_3) \frac{d\Sigma_\theta}{d\xi} \right] \quad (80)$$

along with the yield condition

$$(1 + \tfrac{2}{3}\mu)\Sigma_\theta - (1 - \tfrac{1}{3}\mu)\Sigma_r = \Sigma_Y. \quad (81)$$

Relations (80)–(81) are valid also with the deformation theory and it follows that both theories will predict identical stresses and strain rates (but different $\dot{\epsilon}_P$) in dynamic spontaneous growth when the material is elastic-perfectly plastic. A full analysis of dynamic spontaneous growth goes beyond the scope of this paper.

Numerical Examples

Equation (30) has been integrated numerically for the power-law material $\epsilon_P = B\Sigma^n$ with $B = 100$ and $n = 2$ (which are representative for soils). Typical pressure-expansion curves are displayed in Fig. 1 and it is clearly seen that a cavitation limit is approached with increasing cavity strain A/a. The cavitation pressure is higher for larger values of μ and η. Similar conclusions hold for the elastic-perfectly plastic model (Fig. 2). The curves in Fig. 2 were evaluated from (39) and (41) with a yield stress of $\Sigma_Y = Y/E = 0.01$. These ideally plastic results are valid, as we have already explained, for both flow and deformation theories.

The variation of the cavitation pressure P_c with the level of nonassociativity η/μ is depicted in Fig. 3 for the power-law material, and in Fig. 4 for the elastic-perfectly plastic model. In the latter case flow and deformation theories give identical values for the cavitation pressure. With the hardening model (Fig. 3) the differences in P_c predicted by the two theories are practically negligible. Thus, the limiting pressure obtained from the deformation theory loading path (30) is virtually the same as the one given by the flow theory spontaneous growth Eqs. (72)–(73). It can be concluded from Figs. 3–4 that the cavitation pressure increases with η, but the dependence on μ is more complex with a possible inversion for negative values of η. However, deviations from normality always reduce the cavitation pressure.

The upshot of these sample calculations appears to be a considerable sensitivity of material response to the relative pressure dependence of the yield surface and the flow potential. For the associated case ($\eta = \mu$), in particular, there is a remarkable strengthening of the medium with increasing μ. The ratio of the cavitation pressures for $\mu = 1.5$ and $\mu = 0.5$ is over 2.5 for $n = 2$, and over 4.5 for the elastic-perfectly plastic material.

Acknowledgment

We are indebted to Drs M. D. Bolton and E. Detournay for helpful discussions. Part of this research was supported by the fund for the promotion of research at the Technion and by funding from the Schlumberger Laboratory, Cambridge, England.

References

Bigoni, D., and Laudiero, F., 1989, "The Quasi-Static Finite Cavity Expansion in a Non-Standard Elasto-Plastic Medium," *Int. J. Mech. Sci.*, Vol. 31, No. 11–12, pp. 825–837.

Chadwick, P., 1959, "The Quasi-Static Expansion of a spherical Cavity in Metals and Ideal Soils," *Quart. J. Mech. Appl. Math.*, Vol. 12, Part 1, pp. 52–71.

Drucker, D. C., and Prager, W., 1952, "Soil Mechanics and Plastic Analysis or Limit Design," *Quart. Appl. Math.*, Vol. 10, No. 2, pp. 157–165.

Durban, D., and Baruch, M., 1974, "Behaviour of an Incrementally Elastic Thick Walled Sphere under Internal and External Pressure," *Int. J. Non-Linear Mech.*, Vol. 9, pp. 105–119.

Durban, D., and Baruch, M., 1976, "On the Problem of a Spherical Cavity in an Infinite Elasto-Plastic Medium," ASME JOURNAL OF APPLIED MECHANICS, Vol. 43, pp. 633–638.

Fleck, N. A., Otoyo, H., and Needleman, A., 1992, "Indentation of Porous Solids," *Int. J. Solids Struct.*, Vol. 29, No. 13, pp. 1613–1636.

Horgan, C. O., and Polignone, D. A., 1995, "Cavitation in Nonlinearly Elastic Solids: A Review," ASME *Appl. Mech. Rev.*, Vol. 48, pp. 471–485.

Hughes, J. M. O., Wroth, C. P., and Windle, D., 1977, "Pressuremeter Tests in Sands," *Geotechnique*, Vol. 27, pp. 455–477.

Pye, Ch. N., 1995, "The Influence of Constitutive Models on Self-Boring Pressuremeter Interpretation in Clay," *Can. Geotechnique J.*, Vol. 32, No. 3, pp. 420–427.

Randolph, M. F., Carter, J. P., and Wroth, C. P., 1979, "Driven Piles in Clay—The Effects of Installation and Subsequent Consolidation," *Geotechnique*, Vol. 29, pp. 361–393.

Rudnicki, J. W., and Rice, J. R., 1975, "Conditions for the Localization of Deformation in Pressure-Sensitive Dilatant Materials," *J. Mech. Phys. Solids*, Vol. 23, pp. 371–394.

Wood, D. M., 1990, "Strain-Dependent Moduli and Pressuremeter Tests," *Geotechnique*, Vol. 40, No. 3, pp. 509–512.

Wroth, C. P., 1984, "The Interpretation of In Situ Soil Tests," *Geotechnique*, Vol. 34, pp. 449–489.

Yu, H. S., and Houlsby, G. T., 1991, "Finite Cavity Expansion in Dilitant Soils: Loading Analysis," *Geotechnique*, Vol. 41, No. 2, pp. 173–183.

Downloaded 04 May 2010 to 171.66.16.34. Redistribution subject to ASME license or copyright; see http://www.asme.org/terms/Terms_Use.cfm

Scale Effects in Media With Periodic and Nearly Periodic Microstructures, Part I: Macroscopic Properties

M. W. Schraad[1]

N. Triantafyllidis
Fellow ASME.

Department of Aerospace Engineering,
The University of Michigan,
Ann Arbor, MI 48109-2118

Traditional averaging and homogenization techniques, developed to predict the macroscopic properties of heterogeneous media, typically ignore microstructure related scale effects—that is, the influence of the size of the representative volume, relative to the size of the unit cell. This issue is presently investigated by exploring the behavior of a nonlinearly elastic, planar, lattice model, which is subjected to general macroscopic deformations. For these materials, scale effects may be due to nonuniformities in the macroscopic strain field throughout the specimen, or alternatively, to the presence of microstructural imperfections that may be either geometric or constitutive in nature. For the case of macroscopic strain nonuniformities, it is shown that the microstructure related scale effects can be accounted for by the presence of higher order gradient terms in the macroscopic strain energy density of the model. For the case of microstructural imperfections, the difference between the respective macroscopic properties of the perfect and imperfect models are shown to depend on the relative size of the specimen, and on the imperfection amplitude and wavelength, while being nearly insensitive to the imposed macroscopic strain. For all of the cases considered, several analytical approximations are proposed to predict the influence of scale on the macroscopic properties, and the accuracy of each method is examined.

1 Introduction

The standard approach to the design of any structure, requires a continuum description of the engineering material that will be used for its fabrication. Modern material science can tailor, to an unprecedented degree, the microstructure of engineering materials to give them the desired macroscopic properties. In response to these technological advances, there has been a renewed and strong interest in solid mechanics for predicting the macroscopic (continuum) properties of engineering materials based on their microstructure. The corresponding methodologies are frequently termed "averaging" or "homogenization" techniques.

There is voluminous literature in engineering and applied physics, spanning well over 100 years of research, which is devoted primarily to the averaging or homogenization problem involved in predicting the macroscopic properties of linearly elastic materials under small strains. For these problems, the microgeometries considered are general, and countless averaging techniques, both deterministic and statistical, have been developed to date. In addition, beginning with the work of Voigt (1889), various bounding techniques have also been developed to give accurate estimates of the overall properties of elastic composites. All of these methods have subsequently been extended to include more general constitutive laws, ranging from small strain elastoplasticity (see Hill, 1965), to finite strain elasticity (see Talbot and Willis, 1985). All of these classical averaging techniques ignore the "scale effect" (i.e., the influence of the size of the representative volume, relative to the characteristic length of the underlying microstructure). The quantification of this scale effect, however, is important to a variety of technological applications, including dispersion in wave propagation problems, current problems involving nanoscale sized structures, and the prediction of localized failure mechanisms in composites, to state only a few.

To correct this deficiency, a number of phenomenological remedies have been proposed, which involve the relaxation of the "local action" hypothesis of classical continuum mechanics. This hypothesis dictates that only the first gradient of the deformation enters the constitutive law. Continuum models that violate the local action hypothesis are termed "nonlocal," and can be classified into several different categories: micropolar or "Cosserat" type models, integral type models, and higher order gradient type models. Although the majority of the previously mentioned averaging techniques are phenomenological, some effort has recently been dedicated to deriving macroscopic higher order gradient theories based on micromechanical models. For the case of linear elasticity, the microgeometries considered in these derivations are general (see Drugan and Willis, 1996). In addition, for the case of nonlinear materials under finite deformations, analogous nonlocal models have recently been derived for periodic media (see Bardenhagen and Triantafyllidis (1994) for materials with discrete microstructures; and Triantafyllidis and Bardenhagen (1996) for microstructured continua).

The present work is motivated by engineering applications involving periodic, and nearly periodic, ductile composites, under finite macroscopic strains. Of interest here is the quantification of the scale effect on the macroscopic properties and on the failure mechanisms of these materials. For this class of applications one can unambiguously identify a scale parameter, which characterizes the size of the specimen, relative to the characteristic microstructural length. To quantify the above-

[1] Currently at Group T-3, Mail Stop B216, Theoretical Division, Los Alamos National Laboratory, Los Alamos, NM 87545.

Contributed by the Applied Mechanics Division of THE AMERICAN SOCIETY OF MECHANICAL ENGINEERS for publication in the ASME JOURNAL OF APPLIED MECHANICS.

Discussion on the paper should be addressed to the Technical Editor, Professor Lewis T. Wheeler, Department of Mechanical Engineering, University of Houston, Houston, TX 77204-4792, and will be accepted until four months after final publication of the paper itself in the ASME JOURNAL OF APPLIED MECHANICS.

Manuscript received by the ASME Applied Mechanics Division, Oct. 30, 1996; final revision, Apr. 7, 1997. Associate Technical Editor: S. Kyriakides.

Copyright © 1997 by ASME

Downloaded 04 May 2010 to 171.66.16.34. Redistribution subject to ASME license or copyright; see http://www.asme.org/terms/Terms_Use.cfm

mentioned scale effects under general finite macroscopic strains, a simple model is proposed, for which the microstructure is idealized as a nonlinear, planar, lattice model, with a square, six-element unit cell. The first part of this work explores the influence of scale on the overall properties of the lattice models. The second part investigates the microstructure related scale effects on the onset of failure in these materials.

More specifically, in the first part of this work, the influence of scale on the macroscopic properties of the material are investigated at finite levels of strain. For the perfectly periodic model, there is only one relevant scale, characterized by the "geometric" scale parameter ϵ, which is defined to be the ratio of the size of the unit cell h, to the size of the representative volume H on which the macroscopic properties are defined. The macroscopic energy density W, for models with perfectly periodic microstructure, depends solely on the imposed macroscopic deformation gradient $\mathbf{F}$, and is independent of the geometric scale parameter ϵ. In engineering applications there are two different sources for the scale dependence of the macroscopic properties: the nonuniformity of the imposed macroscopic strain, and the imperfections which are inevitably present in any nearly periodic composite, due to inaccuracies in the manufacturing process. The scale parameters, resulting from the strain gradient and microstructural imperfections, are related to the geometric scale parameter ϵ. Consequently, a strain gradient parameter κ, and an imperfection amplitude parameter δ are defined, where κH and $\delta\epsilon$ are the dimensionless "deformation" and "imperfection" scale parameters, respectively. The scale dependence of the macroscopic quantities (i.e., the strain energy density, the stresses, and the incremental moduli) is made explicit through their dependence on the parameters ϵ, κ, and δ.

Detailed numerical investigations are conducted to determine the influence of both the deformation and imperfection scale parameters on the macroscopic properties of the lattice models. To study the effects of nonuniform strains, bending deformations, which are superimposed onto the uniform uniaxial strains, are considered. Here, the influence of scale is explored by examining the strain energy density of the material. To study the effects of microstructural imperfections, two different types are considered: geometric and constitutive. In addition, for each type of imperfection, the amplitude is held constant, and the effects of various regular, as well as random imperfection shapes are examined. In this case, the scale effects are quantified through a scalar parameter which measures the stress deviation of the imperfect model from its perfectly periodic counterpart.

Moreover, in the interest of gaining additional insight into how the macroscopic properties are influenced by the strain gradient and imperfection amplitude parameters, analytical approximations are proposed for small values of κ and δ. For each case investigated, the analytical results of the proposed approximations are compared with the results of numerical calculations involving the exact equilibrium equations of the entire micromechanical model. The proposed analytical approximations are accurate for adequately large values of κ and δ, and for finite macroscopic strains. As expected, these approximations break down once an instability strain is approached (for details, see Part II of this work).

The presentation is concluded with a detailed discussion of the results pertaining to scale effects on the macroscopic properties. Issues concerning the onset of failure for the lattice models, and the corresponding microstructure related scale effects, are the subject of the investigation in Part II.

2 Model Description

Consider the discrete, planar, lattice model, shown in Fig. 1(a). This model, which is a representative volume of a larger microstructured medium, is a perfectly periodic assembly of unit cells. In the reference (undeformed) configuration these unit cells are squares, each cell having common dimensions

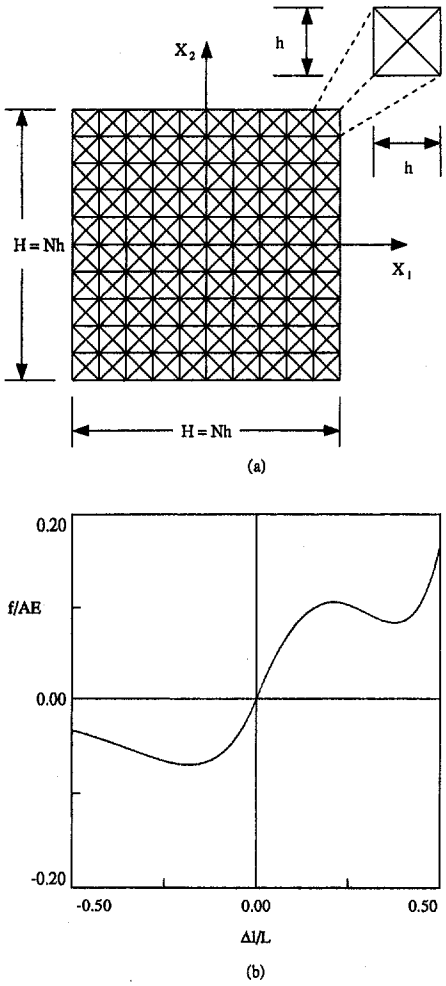


Fig. 1 The discrete planar lattice model. (a) Perfectly periodic microstructure with geometric scale parameter $\epsilon = h/H = 0.1$. (b) Nondimensional force-elongation response for the base element of the unit cell with $\mathcal{A} = 1$, $E = 1$, $a = -7/2$, and $b = 7/2$.

$h \times h$, where h is the characteristic microstructural length of the material. The geometric scale parameter ϵ is defined as the ratio of this characteristic microstructural length h, to the length H that defines the size of the representative volume ($V = H \times H$). For convenience, the representative volume dimension H is set equal to unity for all models. Therefore, $\epsilon = h/H = 1/N$, where N is the number of unit cells in each row or column of the representative volume. If the cross-sectional areas of the model elements are scaled appropriately, this is equivalent to fixing the unit cell dimensions, and varying the size of the representative volume.

Each of the unit cells consists of four nodes (one at each vertex) connected by six one-dimensional, nonlinearly elastic elements. Each node possesses two translational degrees-of-freedom and is capable of transmitting forces, but cannot transmit moments. As a result, the elements are stressed axially, but do not support shear forces or bending moments.

The reference position vector (in the undeformed configuration) for each node is denoted by $\mathbf{X}$ and the current position vector (in the deformed configuration) is denoted by $\mathbf{x}$. The relative position vector of the nodes for each element is defined by $\Delta\mathbf{X} = \epsilon\boldsymbol{\Delta}$ in the reference configuration and by $\Delta\mathbf{x} = \epsilon\boldsymbol{\Delta} + \Delta\mathbf{u}$ in the current configuration. Here, $\boldsymbol{\Delta}$ is the dimensionless relative position vector of the element nodes in the reference configuration, and $\Delta\mathbf{u}$ is the relative displacement vector of the element nodes in the current configuration. Therefore, the element length in the reference configuration L is given by

Downloaded 04 May 2010 to 171.66.16.34. Redistribution subject to ASME license or copyright; see http://www.asme.org/terms/Terms_Use.cfm

$$L = (\Delta \mathbf{X} \cdot \Delta \mathbf{X})^{1/2} = \epsilon(\boldsymbol{\Delta} \cdot \boldsymbol{\Delta})^{1/2}, \quad (1)$$

and the element length in the current configuration l is given by

$$l = (\Delta \mathbf{x} \cdot \Delta \mathbf{x})^{1/2}. \quad (2)$$

Due to the finite deformations of the lattice models, nonlinear kinematic relations are required. In one dimension, all nonlinear strain measures are equivalent. Here, for convenience, the Lagrangian strain e is adopted:

$$e = \frac{1}{2}\left[\left(\frac{l}{L}\right)^2 - 1\right]. \quad (3)$$

The element strain energy $\mathcal{E}$ is taken to be

$$\mathcal{E} = AEL[\tfrac{1}{2}e^2 + (\operatorname{sgn} e)\tfrac{1}{3}ae^3 + \tfrac{1}{4}be^4], \quad (4)$$

where $A = \mathcal{A}\epsilon$ is the cross-sectional area of the element, E is the initial tangent modulus of the material, and the quantities a and b are material constants. The cross-sectional areas of the elements scale with the size of the unit cell to provide a stress-strain response which is independent of the geometric scale parameter ϵ, for all perfectly periodic models. The nondimensional force versus elongation (i.e., f/EA versus $(l - L)/L$, where $f = d\mathcal{E}/dl$) response for the base element of the unit cell, with $\mathcal{A} = 1$, $E = 1$, $a = -7/2$, and $b = 7/2$, is shown in Fig. 1(b). These constants are adopted here, and for all subsequent applications, because they give rise to a macroscopic stress-strain response with a broad nonlinear range, and a maximum load at a finite level of strain for all the load paths considered.

The lattice models are subjected to general in-plane deformations, where the displacement vector $\mathbf{u}$ of each constrained node corresponds to a linearly varying, continuous, macroscopic deformation gradient $\mathbf{F}(\mathbf{X})$:

$$\mathbf{u} = (\mathbf{F}_0 - \mathbf{I}) \cdot \mathbf{X} + \tfrac{1}{2}\mathbf{X} \cdot \mathbf{F}_1 \cdot \mathbf{X},$$

$$\text{where} \quad \mathbf{I} + \mathbf{u} \otimes \nabla = \mathbf{F}(\mathbf{X}) = \mathbf{F}_0 + \mathbf{F}_1 \cdot \mathbf{X}. \quad (5)$$

Here, $\mathbf{F}_0 = (1/V)\int_V \mathbf{F}(\mathbf{X})\,dV$ is the average macroscopic deformation gradient tensor, and $\mathbf{F}_1 = \mathbf{F} \otimes \nabla$ is the (constant) second-order deformation gradient tensor which characterizes the nonuniformity of the macroscopic strain in the representative volume of the material. In addition to the geometric scale parameter ϵ, which characterizes the relative size of the specimen under investigation, a deformation scale parameter, which characterizes the spatial variations in the imposed strain field, can be defined by the dimensionless parameter κH. Here, κ is the strain gradient parameter defined to be the norm of the second-order deformation gradient tensor (i.e., $\kappa \equiv \|\mathbf{F} \otimes \nabla\| = [(\mathbf{F} \otimes \nabla)_{ijk}(\mathbf{F} \otimes \nabla)_{ijk}]^{1/2}$).

The average deformation gradient tensor $\mathbf{F}_0$ can be decomposed into the product of the tensor of principal stretch ratios $\mathbf{U}$, and an orientation tensor $\mathbf{R}$, such that

$$\mathbf{F}_0 = \mathbf{R}^T \cdot \mathbf{U} \cdot \mathbf{R}, \quad (6)$$

where

$$\mathbf{U} = \begin{bmatrix} \lambda_1 & 0 \\ 0 & \lambda_2 \end{bmatrix} \quad \text{and} \quad \mathbf{R} = \begin{bmatrix} \cos\theta & \sin\theta \\ -\sin\theta & \cos\theta \end{bmatrix}, \quad (7)$$

and where θ indicates the orientation of the principal strains with respect to the initial axes of material orthotropy. The principal stretch ratios λ_1 and λ_2 are parameterized in terms of a single load parameter λ and a load path angle ϕ:

$$\lambda_1 = 1 + \lambda\cos\phi \quad \text{and} \quad \lambda_2 = 1 + \lambda\sin\phi. \quad (8)$$

Thus, setting $\theta = 0$, and letting ϕ range from 0 to 2π, all possible orthotropic deformations, which involve all combinations of biaxial tension and compression, are produced. Various amounts of shear are superimposed by letting θ vary between 0 and $\pi/2$, thereby encompassing all possible macroscopic deformations.

To investigate the influence of microstructural imperfections on the macroscopic properties of the model, the initially periodic microstructural geometry and the initially uniform element material properties of the lattice are perturbed. For each type of imperfection, both regular and random shapes are considered. An imperfection scale parameter, which characterizes the relative size of the imperfection in the material microstructure, can be defined by the dimensionless parameter $\delta\epsilon$, where δ is the corresponding imperfection amplitude parameter.

For example, "geometric" imperfections are produced by perturbing the initially periodic internal nodal position vectors. A regular imperfection in the reference position vector $\mathbf{X} = (X_1, X_2)$ of an interior node is given by the new perturbed reference position vector $\bar{\mathbf{X}}$, defined by

$$\bar{\mathbf{X}} = \mathbf{X} + \delta\epsilon H \sin\left[\frac{m_1\pi}{H}\left(X_1 + \frac{H}{2}\right)\right] \times \sin\left[\frac{m_2\pi}{H}\left(X_2 + \frac{H}{2}\right)\right](\mathbf{e}_1 + \mathbf{e}_2), \quad (9)$$

while a random imperfection is produced by

$$\bar{\mathbf{X}} = \mathbf{X} + \delta\epsilon H(r_1\mathbf{e}_1 + r_2\mathbf{e}_2). \quad (10)$$

Here, m_1 and m_2 are the wave numbers of the regular imperfection shape, and r_1 and r_2 are random numbers between -1 and 1.

"Constitutive" imperfections are produced by perturbing the initially uniform internal element cross-sectional areas. A regular imperfection in the cross-sectional area $A = \mathcal{A}\epsilon$ of an interior element centered at (X_1, X_2) is given by the new perturbed cross-sectional area $\bar{A}$, defined by

$$\bar{A} = \mathcal{A}\epsilon\left\{1 + \delta\sin\left[\frac{m_1\pi}{H}\left(X_1 + \frac{H}{2}\right)\right] \times \sin\left[\frac{m_2\pi}{H}\left(X_2 + \frac{H}{2}\right)\right]\right\}, \quad (11)$$

while a random imperfection is produced by

$$\bar{A} = \mathcal{A}\epsilon(1 + \delta r), \quad (12)$$

where r is, again, a random number between -1 and 1. These imperfections affect the constitutive law of each element, and are equivalent to similar imperfections involving the initial tangent modulus of the material E, or the material constants a and b.

Notice that for both types of imperfection, the boundary nodes are kept in their initially perfect positions, and the elements which lie on the model boundaries maintain their originally uniform cross-sectional areas. As an example, the reference configurations for planar lattice models with $\epsilon = 0.1$ and regular ($m_1 = m_2 = 2$) and random geometric imperfections are shown in Fig. 2(a) and Fig. 2(b), respectively. Here, the imperfection amplitude parameter for both imperfection shapes is $\delta = 0.25$.

3 Macroscopic Properties

The macroscopic properties of the planar lattice are defined on the representative volume of the model. For problems involving nonuniform deformations, linearly varying strain fields are imposed by prescribing displacements at every node in the lattice model. The resulting strain energy density is found in terms

Downloaded 04 May 2010 to 171.66.16.34. Redistribution subject to ASME license or copyright; see http://www.asme.org/terms/Terms_Use.cfm

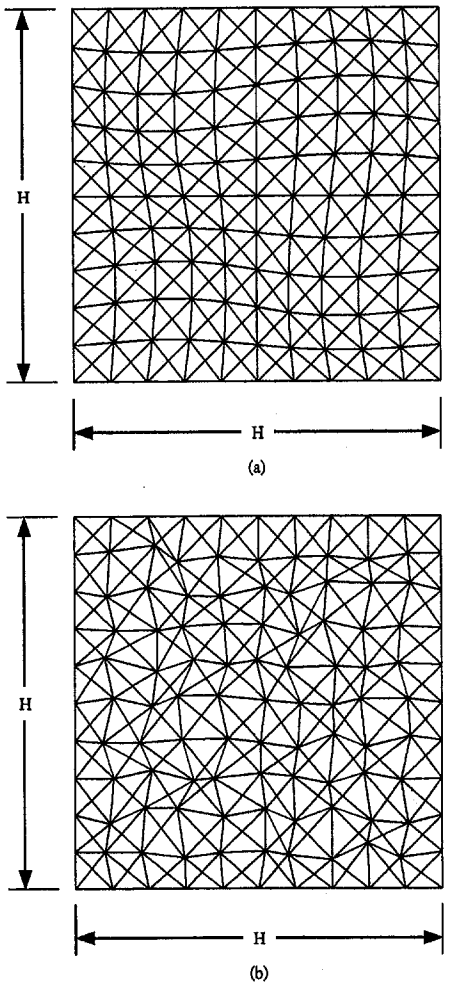


Fig. 2 Reference configurations for a planar lattice model with $\epsilon = 0.1$ and (*a*) regular ($m_1 = m_2 = 2$) and (*b*) random geometric imperfections of 25 percent amplitude ($\delta = 0.25$)

of the average and second-order deformation gradient tensors $\mathbf{F}_0$ and $\mathbf{F}_1$, respectively. For problems involving microstructural imperfections, displacements corresponding to uniform deformations are prescribed on the boundaries of the representative volume, and the equilibrium strain energy density is determined in terms of the average deformation gradient tensor $\mathbf{F}_0$, and the imperfection amplitude parameter δ.

The exact strain energy density W is defined to be the representative volume average of the total strain energy $\mathcal{E}$, which is the sum of the element strain energies $\mathcal{E}^{\text{el}}$:

$$W = \frac{1}{V}\,\mathcal{E} = \frac{1}{V}\sum_{\text{cell}=1}^{N^2}\left[\sum_{\text{el}=1}^{6}\mathcal{E}^{\text{el}}(e^{\text{el}})\right]_{\text{cell}}. \tag{13}$$

This exact strain energy density is used to determine the exact macroscopic first Piola-Kirchhoff stress tensor $\mathbf{\Pi}$, which is defined by

$$\mathbf{\Pi}^T = \frac{\partial W}{\partial \mathbf{F}_0} = \frac{1}{V}\sum_{\text{cell}=1}^{N^2}\left[\sum_{\text{el}=1}^{6}\frac{\partial \mathcal{E}^{\text{el}}}{\partial \mathbf{u}}\cdot\frac{\partial \mathbf{u}}{\partial \mathbf{F}_0}\right]_{\text{cell}}, \tag{14}$$

and the exact macroscopic incremental moduli tensor $\mathbf{L}$, which is given by

$$\mathbf{L} = \frac{\partial^2 W}{\partial \mathbf{F}_0 \partial \mathbf{F}_0} = \frac{1}{V}\sum_{\text{cell}=1}^{N^2}\left[\sum_{\text{el}=1}^{6}\frac{\partial \mathbf{u}}{\partial \mathbf{F}_0}\cdot\frac{\partial^2 \mathcal{E}^{\text{el}}}{\partial \mathbf{u}\partial \mathbf{u}}\cdot\frac{\partial \mathbf{u}}{\partial \mathbf{F}_0}\right]_{\text{cell}}. \tag{15}$$

The simplification of the second derivative of the total strain energy with respect to the average deformation gradient tensor $\partial^2\mathcal{E}/\partial\mathbf{F}_0\partial\mathbf{F}_0$ in Eq. (15) is made as follows. Consider the equilibrium equations,

$$\delta\mathbf{u}\cdot\frac{\partial \mathcal{E}}{\partial \mathbf{u}} = 0 \quad \text{in} \quad V \quad \text{and} \quad \delta\mathbf{u} = \mathbf{0} \quad \text{on} \quad \partial V, \tag{16}$$

where ∂V denotes the boundary of the representative volume. Since the second derivative of the displacement vector with respect to the average deformation gradient tensor $\partial^2\mathbf{u}/\partial\mathbf{F}_0\partial\mathbf{F}_0$ is a kinematically admissible field (i.e., $\mathbf{u} = (\mathbf{F}_0 - \mathbf{I})\cdot\mathbf{X}$ on $\partial V \Rightarrow \partial^2\mathbf{u}/\partial\mathbf{F}_0\partial\mathbf{F}_0 = \mathbf{0}$ on ∂V), it follows from Eq. (16) that

$$\frac{\partial^2 \mathcal{E}}{\partial \mathbf{F}_0 \partial \mathbf{F}_0} = \frac{\partial \mathbf{u}}{\partial \mathbf{F}_0}\cdot\frac{\partial^2 \mathcal{E}}{\partial \mathbf{u}\partial \mathbf{u}}\cdot\frac{\partial \mathbf{u}}{\partial \mathbf{F}_0}. \tag{17}$$

The derivative of the displacement vector with respect to the average deformation gradient tensor $\partial\mathbf{u}/\partial\mathbf{F}_0$ in Eqs. (14) and (15) is found by taking the derivative of the equilibrium equations with respect to the average deformation gradient tensor,

$$\delta\mathbf{u}\cdot\frac{\partial^2 \mathcal{E}}{\partial \mathbf{u}\partial \mathbf{u}}\cdot\frac{\partial \mathbf{u}}{\partial \mathbf{F}_0} = \mathbf{0} \quad \text{in} \quad V \quad \text{and} \quad \frac{\partial \mathbf{u}}{\partial \mathbf{F}_0} = \mathbf{X} \quad \text{on} \quad \partial V, \tag{18}$$

and solving the resulting equations for $\partial\mathbf{u}/\partial\mathbf{F}_0$.

For the case of a lattice model with perfectly periodic microstructure ($\delta = 0$), subjected to uniform deformations ($\mathbf{F} \otimes \nabla = \mathbf{0}$), the macroscopic properties W, $\mathbf{\Pi}$, and $\mathbf{L}$ do not depend on ϵ, that is, on the relative size of the representative volume. However, when spatial variations in the strain field are imposed or microstructural imperfections are present, the macroscopic properties depend on the geometric scale parameter ϵ, the strain gradient parameter κ, and the imperfection amplitude parameter δ.

The goals of the present work are threefold. First, to study the influence of scale, due to nonuniform deformations, on the exact strain energy density of the perfectly periodic lattice models. Second, to investigate the influence of scale, due to microstructural imperfections, on the macroscopic stress-strain response of the nearly periodic lattice models. And third, to derive analytical approximations for the macroscopic properties of lattice models which are subjected to nonuniform deformations or possess geometric and constitutive microstructural imperfections, and to compare these approximations with their exact counterparts.

3.1 Approximation for Nonuniform Deformations. Consider a planar lattice model with perfectly periodic microstructure ($\delta = 0$), subjected to overall, nonuniform deformations ($\mathbf{F} \otimes \nabla \neq \mathbf{0}$). The scale effects, which are due to the spatial variations in the strain field within the representative volume, are approximated by considering the asymptotic expansion of the exact strain energy density. The expansion used here is based on an extension of the continuum calculations of Born and Huang (1954) for the elastic properties of perfect crystals. These continuum calculations, involving only first-order gradient terms, result in an expression for the strain energy density which neglects the characteristic microstructural length, and its role in determining the overall behavior of the material. Bardenhagen and Triantafyllidis (1994) have extended this formulation to include higher order gradient terms, which result in an energy density that depends on the geometric scale parameter ϵ.

Following this higher order gradient method, the current relative position vector of the element nodes can be expanded, using the Taylor series, as

$$\Delta\mathbf{x} = \epsilon\mathbf{F}\cdot\mathbf{\Delta} + \frac{\epsilon^2}{2}(\mathbf{F} \otimes \nabla):(\mathbf{\Delta} \otimes \mathbf{\Delta}) + O(\epsilon^3). \tag{19}$$

Substitution of the expansion (19) and the kinematic relations (1)–(3) into the definition of the strain energy density (13),

Downloaded 04 May 2010 to 171.66.16.34. Redistribution subject to ASME license or copyright; see http://www.asme.org/terms/Terms_Use.cfm

and subsequent expansion of the result in terms of ascending powers of the geometric scale parameter ϵ, yields

$$W = \frac{1}{V}\int_V \left[\bar{W} + \frac{\epsilon^2}{2}(\mathbf{F}\otimes\nabla):\mathbf{B}:(\mathbf{F}\otimes\nabla) + O(\epsilon^4)\right] dV, \quad (20)$$

where $\bar{W}$ is defined by

$$\bar{W}(\mathbf{F}) = \frac{1}{V}\sum_{el=1}^{6} \mathcal{E}^{el}(\bar{e}^{el}(\mathbf{F})), \quad (21)$$

and the average element strain $\bar{e}^{el}$ is given by

$$\bar{e}^{el}(\mathbf{F}) = \frac{1}{2}\left[\frac{(\mathbf{F}\cdot\boldsymbol{\Delta}^{el})\cdot(\mathbf{F}\cdot\boldsymbol{\Delta}^{el})}{\boldsymbol{\Delta}^{el}\cdot\boldsymbol{\Delta}^{el}} - 1\right]. \quad (22)$$

In addition, the components of the tensor $\mathbf{B}$ are found, from the same expansion, to be

$$B_{ijklmn} = -\frac{1}{12}\frac{1}{V}\sum_{el=1}^{6}\left\{\frac{\partial^2\mathcal{E}^{el}(\bar{e}^{el}(\mathbf{F}))}{\partial\bar{e}^{el}\partial\bar{e}^{el}}\frac{F_{ip}\Delta_p^{el}F_{lq}\Delta_q^{el}}{(\boldsymbol{\Delta}^{el}\cdot\boldsymbol{\Delta}^{el})^2} + \frac{\partial\mathcal{E}^{el}(\bar{e}^{el}(\mathbf{F}))}{\partial\bar{e}^{el}}\frac{\delta_{il}}{\boldsymbol{\Delta}^{el}\cdot\boldsymbol{\Delta}^{el}}\right\}\Delta_j^{el}\Delta_k^{el}\Delta_m^{el}\Delta_n^{el}. \quad (23)$$

The second-order ($O(\epsilon^2)$) and higher order terms in the continuum expression for the macroscopic strain energy density depend on the relative size of the representative volume. The fact that more than one continuum strain energy density can be found for the same discrete model is a known phenomenon in mathematical physics (see, for example, the discussion in Kunin, 1982). The various continuum strain energy densities, which differ by a null Lagrangian, produce identical Euler-Lagrange (equilibrium) equations as discussed in Triantafyllidis and Bardenhagen (1993) for one-dimensional; and Bardenhagen and Triantafyllidis (1994) for two and three-dimensional, nonlinearly elastic lattice networks. It will be shown that the exact strain energy density of the representative volume converges, within an accuracy of $O(\epsilon^4)$, to the continuum approximation given in Eq. (20), thus justifying the particular choice for the $O(\epsilon^2)$ term used in that expression. The proof of the corresponding convergence result for the simpler one-dimensional lattice model is given in Appendix A.

3.2 Approximations for Microstructural Imperfections. Next, consider a planar lattice model, with either geometric or constitutive microstructural imperfections ($\delta \neq 0$), subjected to boundary displacements which correspond to uniform macroscopic deformations ($\mathbf{F}\otimes\nabla = \mathbf{0}$). These microstructural imperfections cause spatial variations in the strain field which affect the macroscopic properties of the material. Three different approximations, which estimate the effects of these imperfections on the macroscopic properties, will be considered, and the macroscopic stress-strain response predicted by these approximations will be compared to the exact solution.

The first approximation is the standard "Voigt" approximation (see Voigt, 1889), which uses the average deformation gradient tensor $\mathbf{F}_0$ in place of the actual macroscopic deformation gradient tensor $\mathbf{F}(\mathbf{X})$ in the definition (13) for the strain energy density. Therefore, the approximate strain energy density becomes

$$\bar{W}_V = W(\delta, \mathbf{F}_0), \quad (24)$$

and the approximate macroscopic stress and incremental moduli tensors are defined in the same manner that was given in Eqs. (14) and (15), respectively, where the use of the average macroscopic deformation gradient tensor in place of the actual deformation gradient tensor is retained.

The second approximation is a standard linearization approximation, according to which the macroscopic properties are expanded about the perfect solution. Terms higher than first order in the imperfection amplitude parameter δ are neglected, resulting in approximate macroscopic properties that are linear in the imperfection amplitude parameter. For the strain energy density, this approximation gives

$$\bar{W}_L = W_0 + \delta W_1; \quad W_0 = W|_{\delta=0} \quad \text{and} \quad W_1 = \left.\frac{dW}{d\delta}\right|_{\delta=0}, \quad (25)$$

where W_0 is the strain energy density of the perfectly periodic model. Similarly, the macroscopic stress tensor of the imperfect model, as derived by the linearization approximation, is given by

$$\bar{\boldsymbol{\Pi}}_L = \boldsymbol{\Pi}_0 + \delta\boldsymbol{\Pi}_1; \quad \boldsymbol{\Pi}_0^T = \frac{1}{V}\left(\frac{\partial\mathcal{E}}{\partial\mathbf{u}}\cdot\frac{\partial\mathbf{u}}{\partial\mathbf{F}_0}\right)\Big|_{\delta=0} \quad \text{and}$$

$$\boldsymbol{\Pi}_1^T = \frac{1}{V}\left(\frac{\partial^2\mathcal{E}}{\partial\mathbf{u}\partial\delta}\cdot\frac{\partial\mathbf{u}}{\partial\mathbf{E}_0}\right)\Big|_{\delta=0}, \quad (26)$$

where $\boldsymbol{\Pi}_0$ is the macroscopic stress tensor of the perfectly periodic model. In addition, similar expressions can be found for the approximate macroscopic incremental moduli tensor.

The third and last approximation considered is an improvement of the previously mentioned standard linearization approximation, and is termed the displacement linearization approximation. According to this approximation, only the displacement field is expanded about the perfect solution, and terms higher than first order in the imperfection amplitude parameter δ are neglected, resulting in an approximate displacement field that is linear in the imperfection amplitude parameter. For the strain energy density, this approximation gives

$$\bar{W}_{DL} = W(\delta, \mathbf{u}_L(\delta)). \quad (27)$$

Here, the displacement field is approximated as

$$\mathbf{u}_L(\delta) = \mathbf{u}_0 + \delta\mathbf{u}_1; \quad \mathbf{u}_0 = \mathbf{u}|_{\delta=0} \quad \text{and} \quad \mathbf{u}_1 = \left.\frac{d\mathbf{u}}{d\delta}\right|_{\delta=0}, \quad (28)$$

where $\mathbf{u}_0$ is the uniform displacement field of the perfectly periodic model. Again, the macroscopic stress and incremental moduli tensors are defined in the same manner that was given in Eqs. (14) and (15), respectively, where the use of the linearized displacement field in place of the exact displacement field is retained.

It should be mentioned, once again, at this point, that certain simplifications must be made to obtain Eq. (26). Equilibrium is again considered, and arguments similar to those presented in equations (16)–(18) are used to make these simplifications.

Two interesting and general results are obtained by considering the asymptotic expansion of the macroscopic properties. For models with arbitrary geometric imperfections, the first-order terms in the expansions of the macroscopic properties are identically zero for all deformations satisfying the prescribed displacement boundary conditions (see Appendix B). Since the first-order terms are zero (i.e., the effects of geometric imperfections are second order in the imperfection amplitude parameter δ), the linearization approximation gives the macroscopic properties of the perfectly periodic model as an approximation for the macroscopic properties of the imperfect model.

Furthermore, for models with either geometric or constitutive microstructural imperfections, the respective macroscopic properties of the lattice models, as predicted by the Voigt and the linearization approximations, differ only by terms that are sec-

Downloaded 04 May 2010 to 171.66.16.34. Redistribution subject to ASME license or copyright; see http://www.asme.org/terms/Terms_Use.cfm

ond order in the imperfection amplitude parameter δ (see Appendix C). Therefore, the standard linearization approximation does not provide any additional information beyond that which is already known from the solution for the perfectly periodic model, or can be obtained, to the first order, from the Voigt approximation.

4 Results

Analyses have been performed for lattice models with various geometric scale parameters and microstructural imperfections, subjected to different uniform and nonuniform deformations. Results are presented which illustrate the more typical microstructure related scale effects on the macroscopic properties of the planar lattice models. The material parameters used for the base element of the perfect unit cell in these analyses were given in Section 2 (see also Fig. 1(b)).

Scale effects, which are due to nonuniform deformations, are studied first by examining the influence of linearly varying strain fields (i.e., strain fields with constant second order deformation gradient tensor $\mathbf{F}_1$), on the exact strain energy density of perfectly periodic lattice models with geometric scale parameters ranging from $\epsilon = 1.00$ to $\epsilon = 0.04$ ($N = 1$ to $N = 25$). The exact strain energy density is also compared to the approximate strain energy density, derived in Section 3.1. Next, scale effects, which are due to microstructural imperfections, are explored by studying the differences in the exact macroscopic stress-strain response of models with perfectly periodic microstructures and their counterparts with geometrically irregular and constitutively nonuniform microstructures. For models with imperfect microstructures, the macroscopic properties depend on the geometric scale parameter ϵ, the imperfection amplitude parameter δ, the imperfection shape (defined by the wave numbers m_1 and m_2 for regular imperfections), and the imposed macroscopic deformation (defined by the principal stretch ratios λ_1 and λ_2, and the orientation angle θ). Studies concerning the influence of each one of these parameters on the macroscopic stress-strain response of the imperfect lattice models are presented. Lastly, the predictions for the macroscopic stress-strain response of models with imperfect microstructures, obtained using the Voigt and the displacement linearization approximations, are investigated and compared to the exact solutions. It should be mentioned here that all of the statements concerning convergence, made in the following discussion, refer to apparent convergence based upon the relevant numerical results.

4.1 Scale Effects due to Nonuniform Deformations. To investigate the scale effects on the macroscopic properties of the representative volume, which result from imposing spatially varying strain fields, the exact strain energy density W is determined for a perfectly periodic model subjected to various macroscopically nonuniform deformations. The exact strain energy density is then compared to its approximate continuum counterpart obtained from the expansion given in Eq. (20). Of interest here is the convergence of the exact strain energy density to its continuum average as the geometric scale parameter ϵ approaches zero.

To measure the accuracy of the first correction due to the imposed strain gradient, that is, the accuracy of the $O(\epsilon^2)$ term in Eq. (20), a function $f(\epsilon)$ is defined as

$$f(\epsilon) = \frac{W - (1/V)\int_V \bar{W}\, dV}{(\epsilon^2/2)(\mathbf{F} \otimes \nabla) \vdots (1/V)\int_V \mathbf{B}\, dV \vdots (\mathbf{F} \otimes \nabla)}. \quad (29)$$

According to Eq. (20), the numerator in Eq. (29) is $O(\epsilon^2)$, and since the exact strain energy density converges to its continuum average as the relative size of the representative volume increases, the function $f(\epsilon)$ should converge to one as the geometric scale parameter ϵ approaches zero (recall the discussion in Section 3.1 regarding the correct $O(\epsilon^2)$ term, and the derivation in Appendix A of this term for a one-dimensional model).

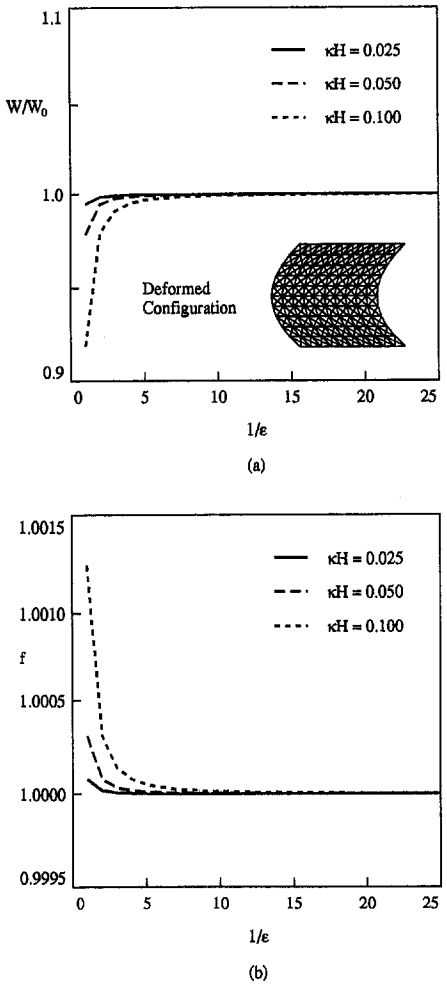


Fig. 3 (a) Scale effects, due to nonuniform deformations, on the exact strain energy density of a perfectly periodic lattice model. (b) Corresponding convergence of the function $f(\epsilon)$ to one as the geometric scale parameter ϵ approaches zero.

Several different values for the average and second-order deformation gradient tensors $\mathbf{F}_0$ and $\mathbf{F}_1$ have been considered. Some typical results are depicted in Fig. 3 and correspond to the macroscopic deformation defined by

$$\mathbf{F}_0 = \begin{bmatrix} 1.05 & 0 \\ 0 & 1 \end{bmatrix}, \quad (\mathbf{F} \otimes \nabla)_{122} = \kappa$$

$$\text{and all other } (\mathbf{F} \otimes \nabla)_{ijk} = 0, \quad (30)$$

where the macroscopic strain gradient parameter is defined as the norm of the second-order deformation gradient tensor $\kappa \equiv \|\mathbf{F} \otimes \nabla\|$. The second-order deformation gradient considered in Eq. (30) adds bending to the uniform uniaxial strain defined by $\mathbf{F}_0$, as shown by the deformed configuration in the inset of Fig. 3(a) for $\kappa H = 2.5$ (a relatively high value of the deformation scale parameter used to show the effects of $\mathbf{F} \otimes \nabla$). Figure 3($a$) shows the scale effects associated with the resulting nonuniform deformation on the exact strain energy density of a perfectly periodic lattice model, and Fig. 3(b) shows the corresponding convergence of the function $f(\epsilon)$ for values of the dimensionless deformation scale parameter ranging from $\kappa H = 0.025$ (solid line) to $\kappa H = 0.100$ (dotted line).

Downloaded 04 May 2010 to 171.66.16.34. Redistribution subject to ASME license or copyright; see http://www.asme.org/terms/Terms_Use.cfm

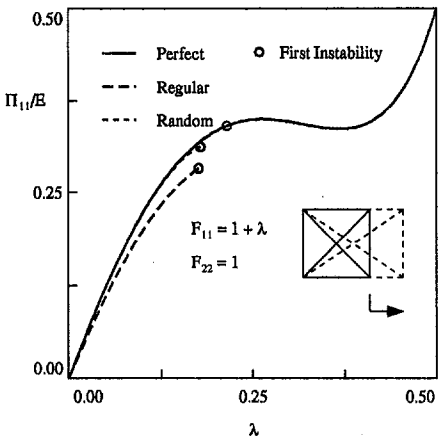


Fig. 4 Effects of regular ($m_1 = m_2 = 1$) and random constitutive imperfections of 25 percent amplitude ($\delta = -0.25$) on the macroscopic stress-strain response of an initially perfectly periodic lattice model with $\epsilon = 0.04$, subjected to uniaxial extension with no lateral contraction ($\phi = \theta = 0$)

As expected, the results show that as the geometric scale parameter approaches zero, the exact strain energy density of the lattice model converges to its continuum average, and therefore, the function $f(\epsilon)$ converges to one. Notice that the convergence of the strain energy density is quite rapid, and that the accuracy of the second-order term in the continuum expansion of the strain energy density at predicting the difference between the exact value and its continuum average improves as the relative size of the representative volume increases.

4.2 Scale Effects due to Microstructural Imperfections. To investigate the scale effects on the macroscopic properties of the lattice, which are associated with the presence of imperfections in the microstructure, the exact macroscopic stress-strain response of a model with perfectly periodic microstructure is compared to the exact response of models with geometric and constitutive microstructural imperfections. For example, Fig. 4 shows the effects of a regular ($m_1 = m_2 = 1$) and a random constitutive imperfection (dashed and dotted lines, respectively) of 25 percent amplitude ($\delta = -0.25$) on the macroscopic stress-strain response of an initially periodic lattice model with $\epsilon = 0.04$ (solid line), subjected to uniaxial extension with no lateral contraction ($\phi = \theta = 0$ in Eqs. (7) and (8)). For models with microstructural imperfections, the range of deformation is limited by the onset of failure, which is defined as the first maximum load encountered along the principal equilibrium path. An investigation of the influence of scale on the onset of failure for this model is presented in Part II of this work.

For lattice models with microstructural imperfections, the macroscopic properties depend on the geometric scale parameter ϵ, as well as on the imperfection amplitude parameter δ, the imperfection shape, and the imposed macroscopic deformation. To study the influence of these controlling parameters on the macroscopic properties of the model, a dimensionless stress deviation parameter D, which measures the deviation of the macroscopic stresses of the imperfect lattice models from their perfect counterparts, is defined as

$$D = \frac{\|\mathbf{\Pi}_{\text{per}} - \mathbf{\Pi}_{\text{imp}}\|}{\|\mathbf{\Pi}_{\text{per}}\|}, \tag{31}$$

where $\mathbf{\Pi}_{\text{per}}$ and $\mathbf{\Pi}_{\text{imp}}$ are the exact macroscopic first Piola-Kirchhoff stress tensors of the perfectly periodic and the imperfect lattice models, respectively. The limit of the stress deviation parameter as the geometric scale parameter approaches zero is denoted by D_0 (i.e., $D_0 = \lim_{\epsilon \to 0} D$). Scale effects on the macroscopic stress-strain response of the models, which are due to microstructural imperfections, are studied by examining the dependence of this stress deviation parameter D on the geometric scale parameter ϵ. The dependence of the stress deviation limit D_0 on the imperfection amplitude parameter δ and the imposed macroscopic deformation (defined by $\mathbf{F}_0$) are also explored.

The effects of geometric imperfections on the stress deviation parameter are studied first. Figure 5(a) shows the scale effects, due to microstructural imperfections, on D for a lattice model with regular ($m_1 = m_2 = 1, 2, 3, 4$, depicted by the solid, dashed, dotted, and dashed-dotted lines, respectively) and random geometric imperfections of 25 percent amplitude ($\delta = 0.25$), subjected to uniaxial extension with no lateral contraction ($\phi = \theta = 0$ and $\lambda = 0.05$). For models with regular geometric imperfections, the stress deviation parameter converges exponentially to zero as the geometric scale parameter decreases (i.e., $D_0 = 0$). This is expected, since the wavelengths of the imperfection shape are fixed, while the relative size of the imperfection $\delta\epsilon$ decreases to zero. The rate at which the stress deviation parameter approaches zero decreases as the wave numbers associated with the regular imperfection shape increase. For models with random geometric imperfections, the stress deviation parameter converges to some nonzero asymptotic limit as the geometric scale parameter decreases (i.e., $D_0 \neq 0$). Here, the imperfection wavelengths are of the order of

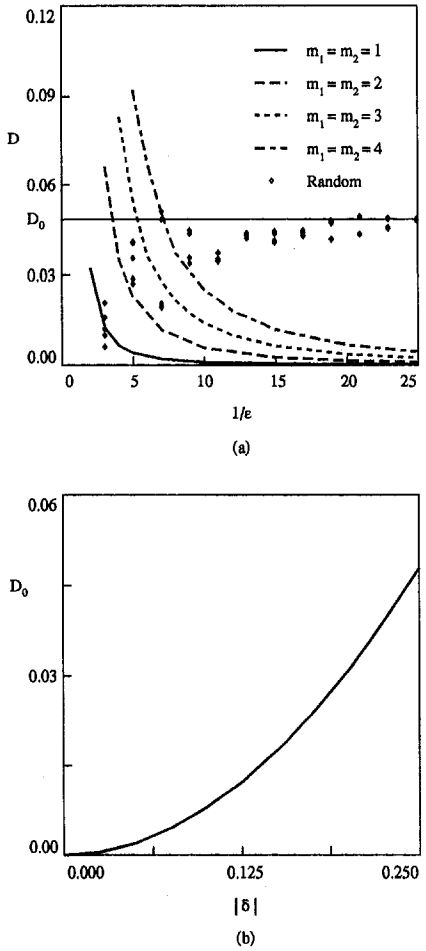


Fig. 5 (a) Scale effects, due to microstructural imperfections, on the stress deviation parameter D for a lattice model with regular and random geometric imperfections of 25 percent amplitude ($\delta = 0.25$), subjected to uniaxial extension with no lateral contraction ($\phi = \theta = 0$ and $\lambda = 0.05$). (b) Corresponding stress deviation limit D_0 as a function of the imperfection amplitude parameter δ.

Downloaded 04 May 2010 to 171.66.16.34. Redistribution subject to ASME license or copyright; see http://www.asme.org/terms/Terms_Use.cfm

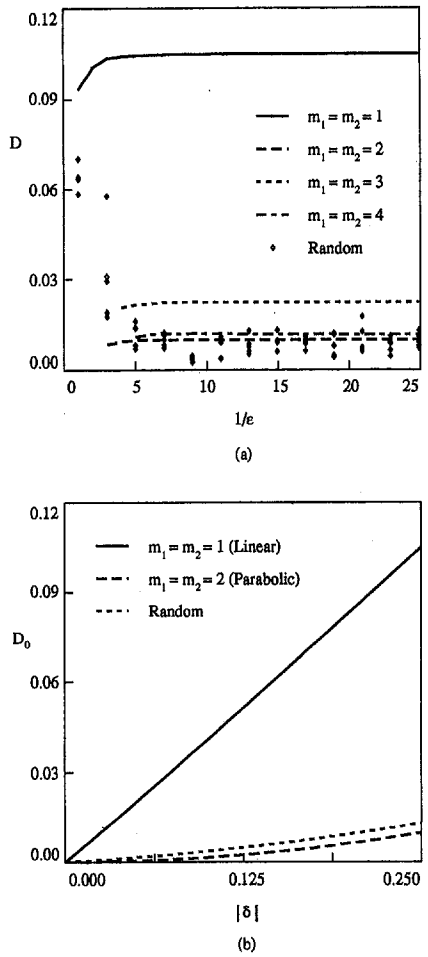


Fig. 6 (*a*) Scale effects, due to microstructural imperfections, on the stress deviation parameter *D* for a lattice model with regular and random constitutive imperfections of 25 percent amplitude ($\delta = -0.25$), subjected to uniaxial extension with no lateral contraction ($\phi = \theta = 0$ and $\lambda = 0.05$). (*b*) Corresponding stress deviation limit D_0 as a function of the imperfection amplitude parameter δ.

the unit cell dimensions, therefore, the microstructural geometry remains highly irregular, even as the geometric scale parameter decreases. The stress deviation limit D_0 is plotted as a function of the imperfection amplitude parameter δ in Fig. 5(b) for the lattice model with random geometric imperfections. As expected, the results show that the stress deviation limit curve is parabolic ($D_0 \sim |\delta|^2$). Recall that the effects of arbitrary geometric microstructural imperfections on the macroscopic properties of the lattice models are second order in the imperfection amplitude parameter δ, as shown in Appendix B.

The effects of constitutive imperfections on the stress deviation parameter are studied next. Figure 6(a) shows the scale effects on D, due to microstructural imperfections, for a lattice model with regular ($m_1 = m_2 = 1, 2, 3, 4$, depicted by the solid, dashed, dotted, and dashed-dotted lines, respectively) and random constitutive imperfections of 25 percent amplitude ($\delta = -0.25$), subjected to uniaxial extension with no lateral contraction ($\phi = \theta = 0$ and $\lambda = 0.05$). As in the case for models with geometric imperfections, the stress deviation parameters for models with constitutive imperfections converge to asymptotic limits as the geometric scale parameter approaches zero. In this case, however, the limits are all nonzero, and depend on the shape of the imperfection. For models with regular constitutive imperfections with $m_1 = m_2 = 1$, all of the element cross-sectional areas (except those that lie along the boundary of the representative volume) are decreased (since $\delta < 0$) and the overall effect on the macroscopic stress-strain response is first order (hence, the much higher asymptotic limit for the stress deviation parameter). As the wave numbers associated with the regular imperfection shapes increase, the asymptotic limits of the stress deviation parameters approach some constant value. Note that for regular imperfections, this constant value is approached from different directions depending on whether the wave numbers of the corresponding imperfection shape are even or odd (i.e., depending on whether the effects are first order or second order in the imperfection amplitude parameter δ). It is to this same value that the stress deviation parameter converges for models with random constitutive imperfections. The stress deviation limit D_0 is plotted as a function of the imperfection amplitude parameter δ in Fig. 6(b) for a lattice model with regular ($m_1 = m_2 = 1, 2$, depicted by the solid and dashed lines, respectively) and random (dotted line) constitutive imperfections. For the model with $m_1 = m_2 = 1$, the linear curve implies that the effects of these imperfections are first order in the imperfection amplitude parameter. For the model with $m_1 = m_2 = 2$ the parabolic curve implies that the effects are second order. And, for the model with random imperfections, the results indicate that the effects are first order, although the initial slope is much smaller than the one for the $m_1 = m_2 = 1$ case.

It is expected that a given microstructure will have a combination of both geometric and constitutive microstructural imperfections. The stress deviation limit D_0 is plotted as a function of the imperfection amplitude parameter δ in Fig. 7 for a lattice model with a combination of random geometric and constitutive imperfections (solid line), subjected to uniaxial extension with no lateral contraction ($\phi = \theta = 0$ and $\lambda = 0.05$). The combined effect of these imperfections is shown to compare closely with the sum of the effects for each imperfection considered separately (dashed-dotted line).

All of the above results are for a given loading direction and a fixed magnitude of strain ($\phi = \theta = 0$ and $\lambda = 0.05$). The influence of the particular load path and magnitude of strain on the stress deviation limit is addressed next. The stress deviation limit D_0 is plotted as a function of the principal stretch ratios λ_1 and λ_2 in Fig. 8(a) for pure biaxial deformations ($\theta = 0$), and in Fig. 8(b) for deformations including shear ($\theta = \pi/8$). For both deformations a lattice model with regular ($m_1 = m_2 = 1$) constitutive imperfections of 25 percent amplitude ($\delta = -0.25$) is considered. Both figures show that, for any load path, the stress deviation limit D_0 remains between nine and ten percent for levels of deformation approaching the onset of failure. This implies that the effects of constitutive imperfec-

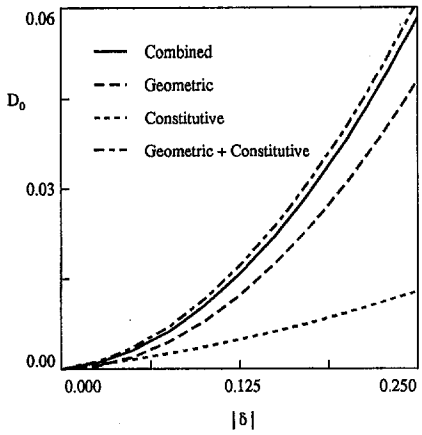


Fig. 7 The stress deviation limit D_0 as a function of the imperfection amplitude parameter δ for a lattice model with random geometric imperfections, random constitutive imperfections, and a combination of random geometric and constitutive imperfections of 25 percent amplitude ($\delta = -0.25$), subjected to uniaxial extension with no lateral contraction ($\phi = \theta = 0$ and $\lambda = 0.05$).

Downloaded 04 May 2010 to 171.66.16.34. Redistribution subject to ASME license or copyright; see http://www.asme.org/terms/Terms_Use.cfm

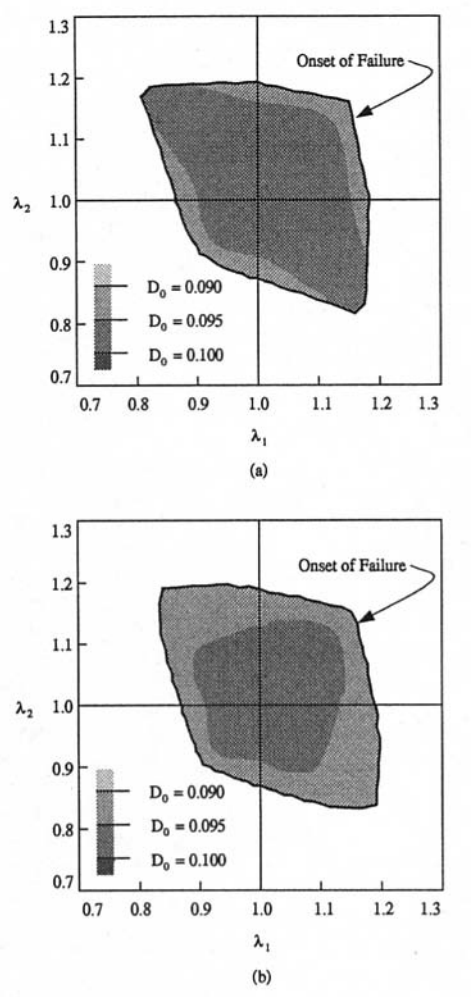


Fig. 8 The stress deviation limit D_0 as a function of the principal stretch ratios λ_1 and λ_2 for a lattice model with regular ($m_1 = m_2 = 1$) constitutive imperfections of 25 percent amplitude ($\delta = -0.25$), subjected to (*a*) pure biaxial deformations ($\theta = 0$) and (*b*) deformations including shear ($\theta = \pi/8$)

tions on the macroscopic properties are almost insensitive to the state of strain in the lattice models. Similar results are found for constitutive imperfections with random shapes and for arbitrary geometric imperfections as well.

The final topic of interest pertains to the accuracy of the proposed analytical approximations. The exact stress-strain response for lattice models with imperfect microstructures is compared to the response predicted by the Voigt and the displacement linearization approximations derived in Section 3.2. To illustrate how well the proposed approximations predict the macroscopic stress-strain response, regular ($m_1 = m_2 = 1$) constitutive imperfections of 25 percent amplitude ($\delta = -0.25$) are considered for models with $\epsilon = 0.04$. To quantify the error of the analytical approximations, a stress error measure $\mathcal{D}$, which quantifies the difference between the exact and approximate macroscopic stress tensor norms, is defined as

$$\mathcal{D} = \frac{\|\mathbf{\Pi}_{ex} - \mathbf{\Pi}_{app}\|}{\|\mathbf{\Pi}_{ex}\|}, \tag{32}$$

where $\mathbf{\Pi}_{ex}$ and $\mathbf{\Pi}_{app}$ are the exact and approximate macroscopic stress tensors of the imperfect lattice models, respectively.

The approximations are analyzed for a lattice model subjected to a series of boundary conditions encompassing both pure biaxial deformations and deformations including shear. The stress error measure $\mathcal{D}$ for the Voigt approximation is plotted as a function of the principal stretch ratios λ_1 and λ_2 in Fig. 9(*a*) for pure biaxial deformations ($\theta = 0$), and in Fig. 9(*b*) for deformations including shear ($\theta = \pi/8$). The stress error measure for the displacement linearization approximation is shown in Fig. 10(*a*) for pure biaxial deformations, and in Fig. 10(*b*) for deformations including shear. The results show that the errors for both approximations are less than one percent, for models with relatively large imperfection amplitude parameters, and for a broad range of macroscopic strains approaching the onset of failure. The displacement linearization approximation is found to be more accurate than the Voigt approximation by roughly an order of magnitude. The accuracy of both approximations improves even further as the imperfection amplitude parameter decreases, or as the imperfection shape changes resulting in the smaller second-order ($O(\delta^2)$) effects.

This section is concluded with a note on the computational efficiency and the corresponding usefulness of the proposed approximation methods. Recall, that to obtain the stress state of an imperfect lattice model at a finite level of strain, many numerical solutions (one for each increment along the particular load path) involving the entire micromechanical model are required. The proposed approximation methods, on the other hand, require only one solution involving the entire model, to determine the displacement correction terms due to the imperfection. Moreover, the assembly of the corresponding stiffness matrix, for the entire lattice model, only requires information

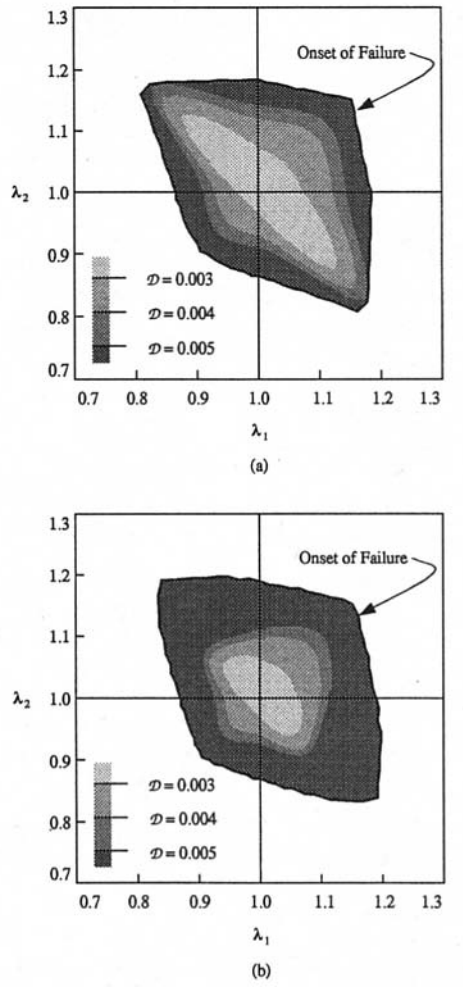


Fig. 9 Voigt approximation stress error measure $\mathcal{D}$ as a function of the principal stretch ratios λ_1 and λ_2 for a lattice model with $\epsilon = 0.04$ and regular ($m_1 = m_2 = 1$) constitutive imperfections of 25 percent amplitude ($\delta = -0.25$), subjected to (*a*) pure biaxial deformations ($\theta = 0$) and (*b*) deformations including shear ($\theta = \pi/8$)

Downloaded 04 May 2010 to 171.66.16.34. Redistribution subject to ASME license or copyright; see http://www.asme.org/terms/Terms_Use.cfm

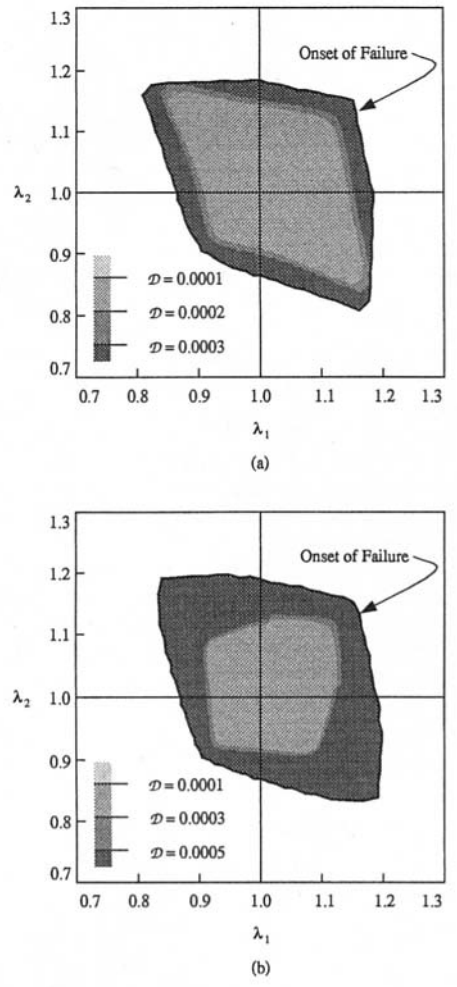


Fig. 10 Displacement linearization approximation stress error measure $\mathcal{D}$ as a function of the principal stretch ratios λ_1 and λ_2 for a lattice model with $\epsilon = 0.04$ and regular ($m_1 = m_2 = 1$) constitutive imperfections of 25 percent amplitude ($\delta = -0.25$), subjected to (*a*) pure biaxial deformations ($\theta = 0$) and (*b*) deformations including shear ($\theta = \pi/8$)

about the state of the unit cell at the strain level in question. These computational advantages become important in the case of microstructured continua, where the size and the complexity of the models are orders of magnitude higher.

5 Conclusions

The present work addresses the influence of scale on the macroscopic properties of nonlinearly elastic materials under finite macroscopic strain. Of interest here are materials with periodic and nearly periodic microstructures, for which a geometric scale parameter ϵ can be unambiguously defined as the ratio of the unit cell size, to the overall size of the representative volume. In the interest of computational efficiency, a kinematically and constitutively nonlinear lattice is proposed as the basic model for this investigation. The results obtained from the study of this simple nonlinear lattice model are indicative of the types of behavior seen in more realistic (both in the geometric and constitutive sense) solids.

The macroscopic properties of a perfectly periodic lattice model, subjected to a uniform macroscopic strain field, are independent of the geometric scale parameter ϵ. The scale effect on the macroscopic properties of the model are due either to nonuniformities in the imposed macroscopic strain field, or to the presence of geometric or constitutive microstructural imperfections. The influence of scale on the exact macroscopic properties under these two conditions is investigated, and analytical methods are proposed in each case to approximate these effects.

Regarding the influence of macroscopic strain nonuniformities on the macroscopic properties, previous work has shown that the $O(\epsilon^2)$ correction to the average macroscopic strain energy density is not unique, and that the various corrections differ by a null Lagrangian (see Bardenhagen and Triantafyllidis, 1994). The present work, which is based on exact calculations involving the strain energy density of the representative volume, clarifies this ambiguity by showing which of these correction terms is appropriate. Consequently, the proper expression for the macroscopic strain energy density, which is correct to $O(\epsilon^2)$, involves only the gradient of the macroscopic strain ($\mathbf{F} \otimes \nabla$), which is the form selected for most empirical calculations in nonlinear solids, where scale effects have to be included (see the discussion in Bardenhagen and Triantafyllidis, 1994).

Concerning both geometric and constitutive microstructural imperfections, the influence of scale, imperfection amplitude, and imperfection shape have all been investigated by examining the dependence of the dimensionless stress deviation parameter D on the corresponding geometric scale and imperfection parameters (i.e., on ϵ, δ, m_1, and m_2). It is shown that geometric imperfections produce a second-order ($O(\delta^2)$) effect on the macroscopic properties, while constitutive imperfections produce either a first-order or second-order effect, according to whether or not the imperfection changes the average initial stiffness of the lattice model (i.e., according to whether the wave numbers of the corresponding imperfection shape are odd or even, respectively).

The investigation is concluded by proposing two different approximation methods for calculating the macroscopic properties of the imperfect lattice models (a straightforward averaging and a direct linearization method). The accuracies of these approximation methods are verified for all macroscopic strains (up to the onset of failure in the model), and both methods are shown to be highly accurate, even for large imperfection amplitudes, and are also shown to be insensitive to the magnitude and orientation of the macroscopic strain.

All of the results of this investigation are valid for finite strains smaller than those corresponding to the onset of failure in the representative volume of the model. The issues of defining a failure surface in macroscopic strain space for these models, and the dependence of this failure surface on the relative size of the specimen under investigation, is the topic of Part II of this work.

Acknowledgments

The present work was partially funded, initially by Alcoa, and subsequently by AFOSR under Grant DOD-G-F49620-94-1-0402. The authors would like to express their appreciation for this financial assistance, and their gratitude to Dr. Owen Richmond of the Alcoa Technical Center for his interest and encouragement, and for sharing his ideas on the subject of stability as it relates to microstructured materials.

References

Bardenhagen, S., and Triantafyllidis, N., 1994, "Derivation of higher order gradient continuum theories in 2, 3-D non-linear elasticity from periodic lattice models," *J. Mech. Phys. Solids,* Vol. 42, pp. 111–139.

Born, M., and Huang, K., 1954, *Dynamical Theory of Crystal Lattices,* Oxford University Press, Oxford, UK, Chapter 3.

Drugan, W. J., and Willis, J. R., 1996, "A micromechanics-based nonlocal constitutive equation and estimates of representative volume element size for elastic composites," *J. Mech. Phys. Solids,* Vol. 44, pp. 497–524.

Hill, R., 1965, "Continuum micro-mechanics in elastoplastic polycrystals," *J. Mech. Phys. Solids,* Vol. 13, pp. 89–101.

Kunin, I. A., 1982, *Elastic Media with Microstructure I, One-Dimensional Models,* Springer, Berlin.

Triantafyllidis, N., and Bardenhagen, S., 1993, "On higher order gradient continuum theories in 1-D nonlinear elasticity. Derivation from and comparison to the corresponding discrete models," *J. Elasticity,* Vol. 33, pp. 259–293.

Downloaded 04 May 2010 to 171.66.16.34. Redistribution subject to ASME license or copyright; see http://www.asme.org/terms/Terms_Use.cfm

Triantafyllidis, N., and Bardenhagen, S., 1996, "The influence of scale size on the stability of periodic solids and the role of associated higher order gradient continuum models," *J. Mech. Phys. Solids,* Vol. 44, pp. 1891–1928.

Voigt, W., 1889, "Über die Beziehung zwischen den beiden Elastizitätskonstanten isotroper Körper," *Wied. Ann.,* Vol. 38, pp. 573–587.

Talbot, D. R. S., and Willis, J. R., 1985, "Variational principles for nonlinear inhomogeneous media," *IMA J. Appl. Math.,* Vol. 35, pp. 39–54.

APPENDIX A

Strain Energy Density Convergence Result in One Dimension

Of interest here is the derivation of the second-order ($O(\epsilon^2)$) correction to the strain energy density of the lattice model. The expansion of the exact strain energy density W, in terms of ascending powers of the geometric scale parameter ϵ, can be written as

$$W = W_0 + \frac{\epsilon^2}{2} W_2 + O(\epsilon^4), \tag{33}$$

where the $O(\epsilon^0)$ term, $W_0 = (1/L)\int_0^L W dX$ is the average strain energy density. Here, the absence of any odd order terms in the geometric scale parameter ϵ (i.e., W_1, W_3, ...) is due to the symmetry of the microstructure. Of interest is the limit of the second-order term W_2 (which is the lowest order term in the macroscopic strain energy density which contains scale information) as the geometric scale parameter ϵ approaches zero.

From Eq. (33), the second-order term W_2 is defined as

$$W_2 = \lim_{\epsilon \to 0} \left[\frac{W - (1/L)\int_0^L W dx}{\epsilon^2/2} \right] = \frac{1}{L}\int_0^L \left[\frac{\epsilon W_i - \int_{X_i}^{X_{i+1}} W dX}{\epsilon^3/2} \right] dX, \tag{34}$$

where $W_i = W(e_i(X))$ is the strain energy density of element i, $e_i(X)$ is the strain of element i, and X_i and X_{i+1} are the reference positions for the element nodes.

Let the displacement of each node correspond to a continuous, macroscopic deformation gradient $F(X)$ such that

$$u = (F_0 - 1)X + \tfrac{1}{2}F_1 X^2 + \tfrac{1}{6}F_2 X^3. \tag{35}$$

Here, $F_0 = (1/L)\int_0^L F(X)dX$ is the average macroscopic deformation gradient, and F_1 and F_2 are second and third-order deformation gradients, respectively.

Using Eq. (35) for the displacements, the element strains can be written as

$$e_i(X) = \frac{u(X_{i+1}) - u(X_i)}{\epsilon} = \frac{\partial u(X_{i+1/2})}{\partial X} + \frac{\epsilon^2}{24} F_2. \tag{36}$$

Substitution of the element strain relation (36) into $W(e_i(X))$ and subsequent expansion yields

$$W(e_i(X)) = W(e(X_i)) + \frac{\epsilon}{2}\frac{dW(e(X_i))}{dX} + \frac{\epsilon^2}{8}\frac{d^2W(e(X_i))}{dX^2} + \frac{\epsilon^2}{24}\frac{dW(e(X_i))}{de} F_2. \tag{37}$$

Expansion of $\int_{X_i}^{X_{i+1}} W(e(X))dX$ yields

$$\int_{X_i}^{X_{i+1}} W(e(X))dX = \epsilon W(e(X_i)) + \frac{\epsilon^2}{2}\frac{dW(e(X_i))}{dX} + \frac{\epsilon^3}{6}\frac{d^2W(e(X_i))}{dX^2}. \tag{38}$$

And finally, substitution of the expansions (37) and (38) into the relation for the second-order strain energy density term (34), and subsequent simplification gives

$$W_2 = \frac{1}{L}\int_0^L \left[-\frac{1}{12}\frac{d^2W}{de^2}\left(\frac{\partial^2 u}{\partial X^2}\right)^2 \right] dX, \tag{39}$$

which can be written as

$$W_2 = \frac{1}{L}\int_0^L \left[\frac{\partial^2 u}{\partial X^2} B \frac{\partial^2 u}{\partial X^2} \right] dX, \quad \text{where} \quad B = -\frac{1}{12}\frac{\partial^2 W}{\partial e^2}. \tag{40}$$

The additional term included in Eq. (23) involving $\partial \mathcal{E}^{el}/\partial \bar{e}^{el}$ results from using the nonlinear Lagrangian strain measure defined by Eq. (22). The remaining differences between Eqs. (23) and (40) are due to the fact that only a one-dimensional model was considered here.

APPENDIX B

Effects of Geometric Imperfections on the Macroscopic Properties

Of interest here are the effects of geometric microstructural imperfections on the macroscopic properties, and in particular the dependence of these properties on the imperfection amplitude parameter δ. To determine this dependence, the expansion of the exact strain energy density of the lattice model is considered. The first-order term in the expansion of the strain energy density is

$$W_1 = \left.\frac{dW}{d\delta}\right|_{\delta=0} = \left.\left(\frac{\partial W}{\partial \delta} + \frac{\partial W}{\partial \mathbf{u}}\cdot\frac{\partial \mathbf{u}}{\partial \delta}\right)\right|_{\delta=0}. \tag{41}$$

Consider a planar lattice model with arbitrary geometric microstructural imperfections. For this model it can be shown, after some lengthy but straightforward algebra (which takes into account the fact that the boundary nodes are unperturbed), that

$$\left.\frac{\partial W}{\partial \delta}\right|_{\delta=0} = 0. \tag{42}$$

Also, from the equilibrium equations,

$$\delta\mathbf{u}\cdot\frac{\partial \mathcal{E}}{\partial \mathbf{u}} = 0 \quad \text{in} \quad V \quad \text{and} \quad \delta\mathbf{u} = \mathbf{0} \quad \text{on} \quad \partial V, \tag{43}$$

it follows that

$$\frac{\partial W}{\partial \mathbf{u}}\cdot\frac{\partial \mathbf{u}}{\partial \delta} = 0, \tag{44}$$

since $\partial\mathbf{u}/\partial\delta$ is a kinematically admissible field (i.e., $\mathbf{u} = (\mathbf{F}_0 - \mathbf{I})\cdot\mathbf{X}$ on $\partial V \Rightarrow \partial\mathbf{u}/\partial\delta = \mathbf{0}$ on ∂V).

From Eqs. (42) and (44), it follows that for lattice models with arbitrary geometric microstructural imperfections, the first-order term in the expansion of the exact strain energy density W_1 is identically zero. And, since $\mathbf{\Pi}^T = \partial W/\partial \mathbf{F}_0$ and $\mathbf{L} = \partial^2 W/\partial \mathbf{F}_0 \partial \mathbf{F}_0$, it follows that

$$\mathbf{\Pi}_1 = \mathbf{0} \quad \text{and} \quad \mathbf{L}_1 = \mathbf{0}, \tag{45}$$

for deformations satisfying the prescribed displacement boundary conditions. Therefore, the effects of arbitrary geometric imperfections are second order in the imperfection amplitude parameter δ.

Downloaded 04 May 2010 to 171.66.16.34. Redistribution subject to ASME license or copyright; see http://www.asme.org/terms/Terms_Use.cfm

APPENDIX C

$O(\delta)$ Coincidence of the Voigt and Linearization Approximations

Of interest here is the comparison of the predictions for the macroscopic properties obtained using the Voigt and the standard linearization approximations. Consider a planar lattice model with arbitrary geometric or constitutive microstructural imperfections. Recall that the macroscopic strain energy density, as given by the Voigt approximation, is

$$\bar{W}_V = W(\delta, \mathbf{u}_0) = W|_{\delta=0} + \delta \left.\frac{\partial W}{\partial \delta}\right|_{\delta=0} + O(\delta^2), \quad (46)$$

and the strain energy density, as given by the linearization approximation, is

$$\bar{W}_L = W|_{\delta=0} + \delta \left.\frac{dW}{d\delta}\right|_{\delta=0}$$

$$= W|_{\delta=0} + \delta \left.\left(\frac{\partial W}{\partial \delta} + \frac{\partial W}{\partial \mathbf{u}} \cdot \frac{\partial \mathbf{u}}{\partial \delta}\right)\right|_{\delta=0}. \quad (47)$$

From the equilibrium equations it follows that

$$\frac{\partial W}{\partial \mathbf{u}} \cdot \frac{\partial \mathbf{u}}{\partial \delta} = 0. \quad (48)$$

Therefore, the strain energy density, as given by the linearization approximation, becomes

$$\bar{W}_L = W|_{\delta=0} + \delta \left.\frac{\partial W}{\partial \delta}\right|_{\delta=0}, \quad (49)$$

which differs from the strain energy density as given by the Voigt method $\bar{W}_V$ by $O(\delta^2)$. Similar results hold for the average stresses and incremental moduli tensors.

Downloaded 04 May 2010 to 171.66.16.34. Redistribution subject to ASME license or copyright; see http://www.asme.org/terms/Terms_Use.cfm

Scale Effects in Media With Periodic and Nearly Periodic Microstructures, Part II: Failure Mechanisms

M. W. Schraad[1]

N. Triantafyllidis
Fellow ASME.

Department of Aerospace Engineering,
The University of Michigan,
Ann Arbor, MI 48109-2118

Using the nonlinearly elastic planar lattice model presented in Part I, the influence of scale (i.e., the size of the representative volume, relative to the size of the unit cell) on the onset of failure in periodic and nearly periodic media is investigated. For this study, the concept of a microfailure surface is introduced—this surface being defined as the locus of first instability points found along radial load paths through macroscopic strain space. The influence of specimen size and microstructural imperfections (both geometric and constitutive) on these failure surfaces is investigated. The microfailure surface determined for the infinite model with perfectly periodic microstructure, is found to be a lower bound for the failure surfaces of perfectly periodic, finite models, and an upper bound for the failure surfaces of finite models with microstructural imperfections. The concept of a macrofailure surface is also introduced—this surface being defined as the locus of points corresponding to the loss of ellipticity in the macroscopic (homogenized) moduli of the model. The macrofailure surface is easier to construct than the microfailure surface, because it only requires calculation of the macroscopic properties for the unit cell, at each loading state along the principal equilibrium path. The relation between these two failure surfaces is explored in detail, with attention focused on their regions of coincidence, which are of particular interest due to the possible development of macroscopically localized failure modes.

1 Introduction

The influence of scale on the macroscopic properties of microstructured media was the subject of Part I of this investigation. Of primary interest in Part II is the influence of scale on the onset of failure in these materials. Defining failure in composite and microstructured media can be a relatively daunting and intricate task. The complexity involved stems from the multitude of simultaneously occurring failure mechanisms, some of which are present, even at negligible levels of loading. In the present investigation attention is restricted to ductile solids with periodic and nearly periodic microstructures, since in addition to the existence of a well-defined geometric scale parameter ϵ (which characterizes the size of representative volume, relative to the size of the unit cell), one can also define the onset of failure as the first buckling-type instability encountered along a load path which begins from the undeformed stress-free state.

In addition to the influence of the geometric and imperfection scales introduced in Part I, the onset of failure investigation involved in Part II explores the influence of a new scale, characterized by the parameter ω_c, which is associated with the resulting instability mode (ω_c is defined as the ratio of the unit cell size, to the wavelength of first bifurcation mode shape at criticality). This critical mode shape scale establishes whether the onset of failure is a global ($\omega_c \to 0$) or local ($\omega_c \neq 0$) phenomenon. With regard to the different length scales involved, there are three fundamental questions which need to be addressed for this general class of rate-independent periodic ductile solids, when subjected to general macroscopic finite strain loadings. First, what is the critical mode shape scale parameter ω_c associated with such a medium, for a given macroscopic loading, in the absence of boundary effects? Second, under what conditions can the failure of these materials be predicted from the macroscopic properties found in Part I? And third, what is the influence of the geometric scale, the imperfection shape, and the imperfection amplitude, on the critical load and bifurcation mode shape at the onset of failure?

The present work is closely related to earlier research, conducted by one of the authors, on the stability of finitely strained periodic composites. The issues concerning the critical mode shape scale parameter were first investigated using exact calculations involving ω_c, for the case of axially deformed layered composites under plane-strain conditions, by Triantafyllidis and Maker (1985). Subsequent work by Geymonat, Müller, and Triantafyllidis (1993) illustrated the completeness of the Bloch wave representation for capturing the first instability in finitely strained, perfectly periodic composites in three dimensions, and proved that in the case for which $\omega_c \to 0$, the first instability can also be determined from the macroscopic properties of the infinite medium, as the first loss of ellipticity in the homogenized moduli of the material. Lastly, the concepts of micro and macrofailure surfaces for finitely strained periodic media were introduced by Triantafyllidis and Schnaidt (1993) for the case of biaxially stressed truss models. All of this work, however, concerns perfectly periodic media of infinite extent. The influence of the geometric scale, and the effects of microstructural imperfections on the onset of failure in these materials were not previously addressed (since the corresponding calculations

[1] Currently at Group T-3, Mail Stop B216, Theoretical Division, Los Alamos National Laboratory, Los Alamos, NM 87545.

Contributed by the Applied Mechanics Division of THE AMERICAN SOCIETY OF MECHANICAL ENGINEERS for publication in the ASME JOURNAL OF APPLIED MECHANICS.

Discussion on the paper should be addressed to the Technical Editor, Professor Lewis T. Wheeler, Department of Mechanical Engineering, University of Houston, Houston, TX 77204-4792, and will be accepted until four months after final publication of the paper itself in the ASME JOURNAL OF APPLIED MECHANICS.

Manuscript received by the ASME Applied Mechanics Division, Oct. 30, 1996; final revision, Apr. 7, 1997. Associate Technical Editor: S. Kyriakides.

Copyright © 1997 by ASME

Downloaded 04 May 2010 to 171.66.16.34. Redistribution subject to ASME license or copyright; see http://www.asme.org/terms/Terms_Use.cfm

are orders of magnitude more complicated). These topics, therefore, are the subject of the present investigation.

It should be mentioned at this point that the stability of periodic lattice-type structures, and the use of continuum models for the investigation of their behavior, is not a novel idea. The investigation of the stability for both the resulting continuum (macroscopic) models, as well as for the exact (microscopic) models, has been the subject of a number of previous investigations (see, for example, Forman and Hutchinson, 1970, for an investigation involving reticulated shell structures, and Elyada and Babcock, 1987, for a similar study of truss columns, etc.). The traditional approach to these problems, thus far, has involved the study of the exact (microscopic) model of a particular material or structure, when subjected to specific loading conditions (see, for example, Anderson, 1981, for a general formulation of the stability problem for periodic truss structures). In cases when a continuum model has also been used, no systematic investigation of the validity of the nonlinear continuum (macroscopic) model, under all possible macroscopic strains, has been presented. Furthermore, an investigation of scale effects in such problems, which requires the comparison of solutions to boundary value problems with fixed macroscopic dimensions and loading, but with a variety of unit cell sizes, has not been undertaken, thus far, to the best of the authors' knowledge. Moreover, although some work has already been devoted to the subject of imperfection sensitivity in the exact models (see, for example, Anderson, 1986), a systematic investigation of the influence of geometric and constitutive microstructural imperfections on the first buckling-type instability in this class of materials remains to be initiated. Finally, on the experimental side, the only consistent investigation of scale effects on the failure of periodic composites, known to the authors, was undertaken by Greszuck (1975), who tested a series of self-similar fiber-reinforced composites under axial compression.

The method used to address the previously posed questions concerning the geometric and imperfection scale dependence of the failure mechanisms of ductile media with periodic microstructures under finite strains involves the nonlinear periodic lattice model introduced in Part I. For this idealized model, a microscopic failure surface, which corresponds to the onset of the first local instability mode, and a macroscopic failure surface, which corresponds to the first loss of ellipticity in the macroscopic (homogenized) behavior of the model, are defined in macroscopic strain space. In view of the relative simplicity of the lattice model, detailed investigations are conducted to find the critical mode shape scale parameter ω_c, and to determine the influence of the geometric and imperfection scales on the shape of the corresponding failure surfaces, for all possible states of macroscopic strain. The relation between the micro and macrofailure surfaces is explored further, with attention focused on their regions of coincidence, which are of particular interest due to the possibility of macroscopically localized instability modes developing at the onset of failure.

A sequence of calculations is proposed which allows the construction of the failure surfaces for the perfectly periodic medium. The methodology proceeds from the simplest calculations involved in the construction of the macrofailure surface for the perfectly periodic infinite model, to the more complex calculations used to construct the microfailure surface. This methodology also illustrates how to bound the actual failure surface of a real (imperfect) microstructured medium, for which the onset of failure calculations in an actual application would be prohibitively time-consuming. The proposed methodology is applicable to periodic media, with both discrete and continuum microstructures.

2 Failure Mechanisms

The ultimate failure of ductile solids with periodic microstructures can be related to the onset of a buckling-type instability. Consequently, for the idealized lattice models considered here, failure is defined as the loss of stability in the model's behavior. Of particular interest is the first instance of instability, which for the nonlinearly elastic model, coincides with the first loss of positive definiteness in the incremental stiffness matrix of the model. For a perfectly periodic lattice model, the onset of the first instability corresponds to a bifurcation in the principal equilibrium solution (i.e., the solution for which all unit cells deform identically), while for a lattice model with microstructural imperfections, the first instability corresponds to a maximum load.

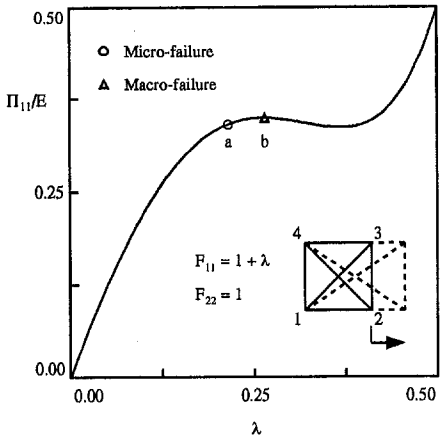


Fig. 1 Micro and macrofailure points, corresponding to the initial bifurcation in the principal equilibrium solution and the loss of ellipticity in the macroscopic material behavior, respectively, for an infinite lattice model ($\epsilon \to 0$) with perfectly periodic microstructure ($\delta = 0$), subjected to uniaxial extension with no lateral contraction ($\phi = \theta = 0$)

The representative volume of the perfectly periodic model, which is comprised of $N \times N$ unit cells (see Fig. 1(a) of Part I), is subjected to a macroscopic strain characterized by the deformation gradient tensor $\mathbf{F}_0(\lambda)$ defined in Eqs. (6)–(8) of Part I. This macroscopic loading is imposed by prescribing the boundary displacements to the representative volume (Dirichlet boundary conditions) for the case of finite-sized specimens.

The loading of the lattice models follows radial paths through macroscopic strain space. Each load path is parameterized by the scalar load parameter λ, and corresponds to a macroscopic deformation gradient tensor $\mathbf{F}_0(\lambda)$, with a fixed principal macroscopic strain orientation angle θ, and a fixed ratio of principal macroscopic stretch ratios characterized by a constant load path angle ϕ (see the definitions in Eqs. (6) and (7) of Part I). As the load parameter increases from zero ($\lambda = 0$ corresponds to the stable undeformed stress-free configuration), the principal equilibrium solution remains stable until a critical value, denoted by λ_c and termed the "critical load," is reached, at which the model first loses stability. A microfailure surface for the representative volume can thus be defined in macroscopic strain space. This failure surface corresponds to the locus of all critical principal stretch ratios $(\lambda_1(\lambda_c), \lambda_2(\lambda_c))$, which are calculated for a fixed principal strain orientation angle θ.

Of interest in the present work is the influence of scale and the effects of imperfections on the previously defined failure surfaces. For a finite-sized lattice model, comprised of $N \times N$ unit cells, the relevant scale is characterized by the geometric scale parameter $\epsilon = h/H = 1/N$, defined in Part I. For an infinite specimen (i.e., for $\epsilon \to 0$) with perfectly periodic microstructure, a different scale parameter becomes relevant—namely, the bifurcation mode shape scale parameter ω, which is defined as the ratio of the unit cell size, to the wavelength of the bifurcation eigenmode. In the remainder of this section, the theoretical aspects of the onset of failure calculations are developed, initially for the infinite lattice model with perfectly periodic microstructure, and then for the finite lattice models.

Downloaded 04 May 2010 to 171.66.16.34. Redistribution subject to ASME license or copyright; see http://www.asme.org/terms/Terms_Use.cfm

2.1 Infinite Periodic Model—Microfailure Surface. Consider first the construction of the microfailure surface for the infinite lattice model with perfectly periodic microstructure. The corresponding calculations are considerably less involved than those required to construct the corresponding failure surface for the finite model, because they are based on the incremental response of the unit cell along the principal equilibrium solution. Although the corresponding methodology, which is based on Bloch wave theory, has been presented in Triantafyllidis and Schnaidt (1993) for the case of discrete models, and by Triantafyllidis and Bardenhagen (1996) for continuum models, the calculations are briefly outlined here for reasons of completeness.

By definition, for each load path defined by the macroscopic deformation gradient tensor $\mathbf{F}_0(\lambda)$, the critical load parameter λ_c corresponds to the first instance of instability in the infinite model, which also coincides with the first singular point in the incremental stiffness matrix of the system. As a result, the incremental equilibrium of the model, at the critical principal state, admits a nontrivial solution in the absence of externally imposed loading. The relationship between the increments in the nodal force vectors $\dot{\mathbf{f}}_p$, exerted by all elements of node p that do not belong to the unit cell, and the corresponding displacement increment vectors $\dot{\mathbf{u}}_q$, at node q of the unit cell (see the insert of Fig. 1), is

$$\dot{\mathbf{f}}_p = \mathbb{K}_{pq} \cdot \dot{\mathbf{u}}_q, \quad 1 \le p, q \le 4, \tag{1}$$

where

$$\mathbf{K}_{pq} = \begin{bmatrix} K_{2p-1,2q-1} & K_{2p-1,2q} \\ K_{2p,2q-1} & K_{2p,2q} \end{bmatrix} \quad \text{and} \quad K_{ij} = \frac{\partial^2 \mathcal{E}_{\text{cell}}}{\partial u_i \, \partial u_j}. \tag{2}$$

Recall from Part I, that $\mathcal{E}_{\text{cell}}$ is the total strain energy of the unit cell, and u_i are the corresponding eight displacement degrees-of-freedom ($\mathbf{u}_p = (u_{2p-1}, u_{2p})$, where u_{2p-1} and u_{2p} are the X_1 and X_2 displacements, respectively, of node p). The derivative of the strain energy $\mathcal{E}_{\text{cell}}$ is evaluated at the stressed state defined by $\mathbf{F}_0(\lambda)$, and consequently, all components of the stiffness matrix $\mathbf{K}_{pq}$ of the unit cell are functions of the macroscopic deformation gradient tensor $\mathbf{F}_0(\lambda)$.

It can be shown (see, for example, Lomont, 1959, for analysis pertaining to the stability of lattice systems) that at the critical load defined by λ_c, the displacement increment vector $\dot{\mathbf{u}}(X_1, X_2)$ can always assume the following form:

$$\dot{\mathbf{u}}(X_1, X_2) = \exp[i(\omega_1 X_1 + \omega_2 X_2)/h]\mathbf{p}(X_1, X_2), \tag{3}$$

where $i = \sqrt{-1}$, ω_1/h and ω_2/h are the wave numbers of the corresponding bifurcation eigenmode along the X_1 and X_2 directions, respectively, and $\mathbf{p}(X_1, X_2)$ is a periodic function of X_1 and X_2, with the same spatial periodicity as the unit cell (i.e., $\mathbf{p}(X_1 + n_1 h, X_2 + n_2 h) = \mathbf{p}(X_1, X_2)$, where n_1 and n_2 are arbitrary integers).

The representation of $\dot{\mathbf{u}}$ given in Eq. (3) implies the following relationships between the nodal force and displacement increment vectors of the unit cell:

$$\dot{\mathbf{u}}_2 = \mu_1 \dot{\mathbf{u}}_1, \quad \dot{\mathbf{u}}_3 = \mu_1 \mu_2 \dot{\mathbf{u}}_1, \quad \dot{\mathbf{u}}_4 = \mu_2 \dot{\mathbf{u}}_1; \tag{4}$$

and

$$\dot{\mathbf{f}}_2 = -\mu_1 \dot{\mathbf{f}}_1, \quad \dot{\mathbf{f}}_3 = \mu_1 \mu_2 \dot{\mathbf{f}}_1, \quad \dot{\mathbf{f}}_4 = -\mu_2 \dot{\mathbf{f}}_1; \tag{5}$$

where

$$\mu_1 = \exp(i\omega_1), \quad \text{and} \quad \mu_2 = \exp(i\omega_2). \tag{6}$$

Introducing relations (4) and (5) into the incremental force-displacement relation (1), the following equivalent system can be obtained solely in terms of $\dot{\mathbf{u}}_1$:

$$\hat{\mathbf{K}}(\lambda, \boldsymbol{\omega}) \cdot \dot{\mathbf{u}}_1 = \mathbf{0}, \quad \text{where} \quad \boldsymbol{\omega} = (\omega_1, \omega_2), \tag{7}$$

and where $\hat{\mathbf{K}}$ is a reduced, 2×2, Hermitian matrix (i.e., $\hat{\mathbf{K}}^T = \bar{\hat{\mathbf{K}}}$, where $\bar{\hat{\mathbf{K}}}$ is the complex conjugate of $\hat{\mathbf{K}}$). The matrix $\hat{\mathbf{K}}$ is the stability matrix of the infinite model with perfectly periodic microstructure, which is strained by $\mathbf{F}_0(\lambda)$, and subjected to the quasi-periodic condition defined in Eq. (3). Let $\lambda_m(\boldsymbol{\omega})$ denote the minimum root of the equation $\det(\hat{\mathbf{K}}(\lambda, \boldsymbol{\omega})) = 0$, for a fixed dimensionless wave number vector $\boldsymbol{\omega}$, that is,

$$\lambda_m(\boldsymbol{\omega}) = \text{min root of } \{\det[\hat{\mathbf{K}}(\lambda, \boldsymbol{\omega})] = 0\}. \tag{8}$$

Thus, $\lambda_m(\boldsymbol{\omega})$ defines a critical load parameter surface in dimensionless wave number space, and therefore, the critical load parameter λ_c is defined as the minimum value of $\lambda_m(\boldsymbol{\omega})$ over all dimensionless wave number vectors $\boldsymbol{\omega}$ (i.e., for $0 \le \omega_1, \omega_2 \le 2\pi$):

$$\lambda_c = \min_{0 \le \omega_1, \omega_2 \le 2\pi} \lambda_m(\boldsymbol{\omega}) = \lambda_m(\boldsymbol{\omega}_c). \tag{9}$$

There are two important characteristics of the critical load parameter surface $\lambda_m(\boldsymbol{\omega})$ which require discussion at this point. The first has to do with the symmetries of this surface in the dimensionless wave number domain. Notice that for situations involving pure biaxial deformation (i.e., for load paths with $\theta = 0$), the principal equilibrium solution is symmetric with respect to both the X_1 and X_2 coordinate axes, as well as point-symmetric about the center of the unit cell. These symmetries imply the following relationships for the stability matrix $\hat{\mathbf{K}}(\lambda, \boldsymbol{\omega})$, defined in Eq. (7), for $\theta = 0$:

$$\hat{\mathbf{K}}(\lambda, \omega_1, \omega_2) = \hat{\mathbf{K}}(\lambda, 2\pi - \omega_1, \omega_2) = \hat{\mathbf{K}}(\lambda, \omega_1, 2\pi - \omega_2) = \hat{\mathbf{K}}(\lambda, 2\pi - \omega_1, 2\pi - \omega_2). \tag{10}$$

The same symmetry relations that hold for the stability matrix $\hat{\mathbf{K}}(\lambda, \boldsymbol{\omega})$ also hold for the critical load parameter surface, and hence, $\lambda_m(\boldsymbol{\omega})$ is only calculated for the domain $0 \le \omega_1, \omega_2 \le \pi$.

For instances when the principal strain axes are oriented at an angle $\theta \neq 0$ with respect to the initial axes of material orthotropy, the principal equilibrium solution is only point-symmetric about the center of the unit cell. This symmetry implies the following relationship for the stability matrix $\hat{\mathbf{K}}(\lambda, \boldsymbol{\omega})$ for $\theta \neq 0$:

$$\hat{\mathbf{K}}(\lambda, \omega_1, \omega_2) = \hat{\mathbf{K}}(\lambda, 2\pi - \omega_1, 2\pi - \omega_2). \tag{11}$$

Again, the same symmetry relationship should also hold for the critical load parameter surface, and thus $\lambda_m(\boldsymbol{\omega})$ is only calculated in the domain $0 \le \omega_1 + \omega_2 \le 2\pi$.

The second important characteristic of the critical load parameter surface $\lambda_m(\boldsymbol{\omega})$ concerns the presence of a singularity at the origin of the dimensionless wave number domain (i.e., at $\boldsymbol{\omega} = (0, 0)$). Notice that two different types of bifurcation eigenmodes are mapped in the neighborhood of the origin: the periodic modes (since the eigenmode corresponding to $\omega_1 = \omega_2 = 0$ has wavelengths in each direction which are commensurate with the corresponding unit cell size), and the long wavelength modes, (i.e., the modes with wavelengths $L_i \gg h$, since the corresponding dimensionless wave numbers $(\omega_1, \omega_2) = (2\pi h/L_1, 2\pi h/L_2) \to (0, 0)$). The critical load for a long wavelength mode does not, in general, coincide with the critical load of a periodic mode, and hence, the critical load parameter surface $\lambda_m(\boldsymbol{\omega})$ is singular at the origin (see Fig. 3).

Since the geometric scale parameter is identically zero for the infinite model (i.e., $\epsilon \to 0$), the relevant scale parameter is ω, which is defined as the magnitude of the dimensionless wave number vector,

Downloaded 04 May 2010 to 171.66.16.34. Redistribution subject to ASME license or copyright; see http://www.asme.org/terms/Terms_Use.cfm

$$\omega = \|\boldsymbol{\omega}\| = [(\omega_1)^2 + (\omega_2)^2]^{1/2}, \tag{12}$$

and is termed the "mode shape scale" parameter.

Two different situations are distinguished, according to whether or not the corresponding critical mode shape scale parameter ω_c is zero at the critical load λ_c. For $\omega_c \neq 0$, the onset of failure is termed "local," because the critical eigenmode has a wavelength commensurate with the unit cell size. For $\omega_c \to 0$ (i.e., when the critical load parameter surface has a singularity at the origin, and hence, $\lambda_m(0, 0)$ cannot be defined—which is always the case for the lattice model under investigation), the onset of failure is termed "global," because the critical eigenmode has a wavelength which is much larger than the unit cell size. For the latter case, the failure mode depends on the overall properties of the lattice at the loading state in question, and therefore, the critical load for this case can be found with considerably less effort by investigating the macroscopic (homogenized) properties of the model. Consequently, one can extend this approach, and construct a new failure surface for the model, which is based on the macroscopic properties. The resulting failure surface, which is a more easily obtainable upper bound for the computationally intensive, exact, or "microfailure" surface, is termed the "macrofailure" surface, and is defined immediately below.

2.2 Infinite Periodic Model—Macrofailure Surface. The macrofailure surface, determined for the infinite lattice model, is defined in macroscopic strain space using the loss of ellipticity of the macroscopic (homogenized) moduli tensor $\mathbf{L}(\lambda)$, defined in Eq. (15) of Part I, as the onset of failure criterion. More specifically, the macroscopic critical load, denoted by λ_e, is defined as the minimum value of the load parameter λ along a given load path (i.e., for fixed ϕ and θ) for which the rank two tensor $\mathbf{n} \cdot \mathbf{L}(\lambda) \cdot \mathbf{n}$ (termed the "acoustic tensor") loses positive definiteness, that is,

$$\lambda_e = \text{min root of } \{d(\lambda) = 0\}, \tag{13}$$

where

$$d(\lambda) = \min_{\|\mathbf{n}\|=1} \det (L_{ijkl}(\lambda) n_j n_l). \tag{14}$$

As shown by Triantafyllidis and Schnaidt (1993) for materials with discrete periodic microstructures, and by Geymonat, Müller, and Triantafyllidis (1993) for general periodic continua, the macroscopic critical load is always greater than or equal to the microscopic critical load (i.e., $\lambda_e \geq \lambda_c$), with the equality achieved when $\omega_c \to 0$. Hence, the macrofailure surface for an infinite lattice model with perfectly periodic microstructure provides an upper bound for the corresponding microfailure surface.

Notice that the construction of the macrofailure surface is based on a simple algebraic manipulation of the macroscopic (homogenized) incremental moduli tensor $\mathbf{L}(\lambda)$, which is calculated only once at each increment along the load path of interest. Alternatively, the construction of the microfailure surface requires, at each increment, the calculation of the reduced stiffness matrix $\hat{\mathbf{K}}(\lambda, \boldsymbol{\omega})$, for a sufficient number of dimensionless wave number vectors $\boldsymbol{\omega}$ (to adequately cover the dimensionless wave number domain, and accurately predict the critical load and bifurcation mode shape). Consequently, the calculation of the macrofailure surface is considerably less intensive computationally than the calculation of the corresponding microfailure surface. In general, the ratio of the two calculation times is roughly equal to the number of grid points used to cover the dimensionless wave number domain, which for the calculations reported here is of the order of 10^3 to 10^4.

The locus of points in macroscopic strain space for which the micro and macrofailure surfaces coincide (i.e., the points for which $\omega_c \to 0$), is of particular interest here for two reasons. First, it determines a range of validity for the failure predictions obtained from the macroscopic properties determined by homogenization theory, since for the macroscopic strains in question, a local instability does not precede an instability which is global in nature. And second, for the critical load states for which the first instability in the infinite medium with perfectly periodic microstructure is global in nature, the post-bifurcation failure mode is likely to develop into a macroscopically localized mode of failure (of the shear band or kink band type). As discussed in detail in Triantafyllidis and Bardenhagen (1996), the determination of the range of deformations, defined by $\mathbf{F}_0(\lambda)$, for which the micro and macrofailure surfaces do not coincide, is based on calculations involving the higher order gradient homogenized moduli tensor $\mathbf{B}$, introduced in Eq. (23) of Part I.

According to Triantafyllidis and Bardenhagen (1996), a sufficient condition, which ensures that the micro and macrofailure surfaces do not coincide, is based on the sign of the "failure surface separation parameter" β. This scalar parameter is the minimum eigenvalue of the stiffness matrix, for a model subjected to a rank one macroscopic deformation gradient (i.e., subjected to $\mathbf{F} = \boldsymbol{\alpha} \otimes \mathbf{n}$), and is defined by

$$\beta = B_{ijklmn}(\lambda_e) \alpha_i^e n_j^e n_k^e \alpha_l^e n_m^e n_n^e, \tag{15}$$

where the vectors $\mathbf{n}^e$ and $\boldsymbol{\alpha}^e$ are determined from the following conditions, respectively,

$$\det (L_{ijkl}(\lambda_e) n_j^e n_l^e) = 0, \quad L_{ijkl}(\lambda_e) n_j^e \alpha_k^e n_l^e = 0. \tag{16}$$

Here, $\mathbf{n}^e$ is the unit vector for which the acoustic tensor $\mathbf{n} \cdot \mathbf{L}(\lambda) \cdot \mathbf{n}$ first loses positive definiteness, and $\boldsymbol{\alpha}^e$ is the corresponding eigenvector of the acoustic tensor at the macroscopic critical load λ_e. When the failure surface separation parameter β is less than zero, it can be shown that the first instability in the perfectly periodic lattice is local in nature, and therefore, the micro and macrofailure surfaces do not coincide. The proposed sufficient condition is based on the macroscopic properties of the model, and provides the means to determine, in a computationally efficient manner, the region of the macrofailure surface which cannot be reached due to the occurrence of a prior, local instability.

2.3 Failure Surfaces for Finite Models. Following the determination of the micro and macrofailure surfaces for the infinite lattice model with perfectly periodic microstructure—which are based on calculations involving only the unit cell—attention is focused on the failure surfaces for finite size specimens comprised of $N \times N$ unit cells. Of interest here is the influence of the geometric scale parameter $\epsilon = h/H = 1/N$, as well as the effects of microstructural imperfections on these failure surfaces. The imperfections considered are the same geometric and constitutive perturbations defined in Eqs. (9)–(12) of Part I. For all of the finite models considered, the construction of the failure surfaces requires the consideration of the entire representative volume, as opposed to just the unit cell, as in the case of infinite models. The onset of failure is defined by the loss of positive definiteness of the corresponding stiffness matrix $\mathbf{K}$, evaluated along the principal equilibrium solution corresponding to the macroscopic deformation defined by $\mathbf{F}_0(\lambda)$, that is,

$$\lambda_c = \text{min root of } \{\det (\mathbf{K}(\lambda)) = 0\}, \tag{17}$$

where

$$\mathbf{K} = \frac{\partial^2 \mathcal{E}}{\partial \mathbf{u} \partial \mathbf{u}}, \tag{18}$$

and where $\mathcal{E}(\mathbf{u})$ is the total strain energy of the representative volume, expressed as a function of the internal degrees-of-freedom $\mathbf{u}$ (recall that Dirichlet boundary conditions are considered). For perfectly periodic specimens, the onset of failure is due to a bifurcation in the principal equilibrium solution, while

Downloaded 04 May 2010 to 171.66.16.34. Redistribution subject to ASME license or copyright; see http://www.asme.org/terms/Terms_Use.cfm

for imperfect specimens, it corresponds to the solution reaching a limit point (i.e., a maximum load).

3 Results

For all of the numerical calculations reported here, the same material parameters that were proposed in Part I for the base element of the unit cell, have been used. The equilibrium solutions for both the unit cell, and for the finite representative volume specimens are determined using an incremental Newton-Raphson algorithm. The critical load parameter surface $\lambda_m(\boldsymbol{\omega})$, determined for the infinite model with perfectly periodic microstructure, and the critical load λ_c, determined for the finite sized specimens, are found using a straightforward bisection method. The results pertaining to the micro and macrofailure surfaces for the infinite model are presented and discussed first, followed by the corresponding failure surfaces for finite specimens with both perfectly periodic and imperfect microstructures.

3.1 Failure Surfaces for the Infinite Model. Of interest here is the comparison between the micro and macrofailure surfaces for the perfectly periodic model of infinite extent (to avoid the influence of the model boundaries), as well as the dependence of these failure surfaces on the imposed macroscopic strain. As an illustration, the microfailure (first bifurcation) and macrofailure (maximum load) points for an infinite lattice model with perfectly periodic microstructure, subjected to uniaxial extension ($\theta = \phi = 0$), are shown along the principal equilibrium path in Fig. 1. The corresponding failure surfaces can be constructed using the loci of failure points for all load paths with the same fixed value of the orientation angle θ.

The micro and macrofailure surfaces for the perfectly periodic, infinite model, are depicted in principal macroscopic strain space in Fig. 2 with solid and dashed lines, respectively (recall that λ_1 and λ_2 are the principal stretch ratios which correspond to the macroscopic deformation defined by $\mathbf{F}_0(\lambda)$). The results in Fig. 2(a) correspond to a macroscopic deformation with principal macroscopic strain axes aligned with the initial axes of orthotropy ($\theta = 0$), while the results in Fig. 2(b) correspond to a macroscopic deformation with principal macroscopic strain axes oriented at an angle $\theta = \pi/8$ with respect to the axes of orthotropy. Note the locations of the first bifurcation and maximum load points, labeled a and b in the uniaxial extension case shown in Fig. 1, on the corresponding failure surfaces shown in Fig. 2(a). Also notice from Fig. 2(a), that for $\theta = 0$, the macrofailure surface considerably overestimates the critical strains for certain loading directions (approximately for $-\pi/4 \leq \phi \leq \pi/8$ and $3\pi/8 \leq \phi \leq 3\pi/4$).

The stable domain of deformation (i.e., the set of points contained within the microfailure surface), increases as the principal axes of macroscopic strain rotate with respect to the initial axes of orthotropy, while the discrepancy between the micro and macrofailure surfaces decreases significantly, as one can see for the case when $\theta = \pi/8$ shown in Fig. 2(b). The strong dependence of the shape of the failure surfaces on the orientation angle θ is one important result of this investigation. Another important result pertains to the fact that these failure surfaces are always closed, and always contain the origin $\lambda_1 = \lambda_2 = 1$. This implies that if the periodic lattice model is adequately strained, it will always lose stability, for any load path starting from the undeformed stress-free configuration. The fact that the model becomes unstable upon finite straining is a result of the constitutive law chosen to represent the element behavior, which always reaches a maximum load at some finite level of strain. Not all failure surfaces for finitely strained periodic media are closed, as one can see by the example given in Triantafyllidis and Bardenhagen (1996) for a fiber-reinforced composite material.

Recall from the discussion in Section 2.1 that the calculations involved in the construction of the microfailure surface require

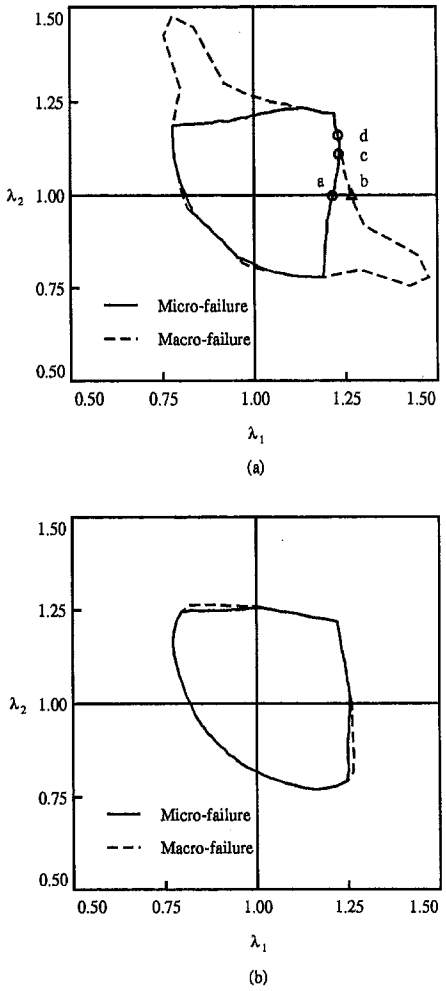


Fig. 2 Micro and macrofailure surfaces, corresponding to the initial bifurcation in the principal equilibrium solution and the loss of ellipticity in the macroscopic model behavior, respectively, in macroscopic strain space, for an infinite lattice model ($\epsilon \to 0$) with perfectly periodic microstructure ($\delta = 0$), subjected to (a) pure biaxial deformations ($\theta = 0$) and (b) deformations including shear ($\theta = \pi/8$)

the determination of the critical load parameter λ_c for each load path, which in turn requires the determination of the critical load parameter surface $\lambda_m(\boldsymbol{\omega})$. Two typical critical load parameter surfaces are depicted in Fig. 3, with Fig. 3(a) corresponding to point c on the microfailure surface shown in Fig. 2(a), and with Fig. 3(b) corresponding to point d on the same surface. The micro and macrofailure surfaces do not coincide at point c, thus, the critical load λ_c, which corresponds to the minimum value of $\lambda_m(\boldsymbol{\omega})$ over all dimensionless wave number vectors $\boldsymbol{\omega}$, occurs for $\omega_1 = \omega_2 = \pi$; while at point d, where the micro and macrofailure surfaces coincide, the minimum occurs at the origin of the dimensionless wave number domain (i.e., at $\omega_1 \to 0$ and $\omega_2 = 0$).

The results for the last portion of the investigation involving the infinite lattice model, pertain to the type of instability mode encountered (e.g., local or global), and verify the validity of the sufficiency condition for the micro and macrofailure surface separation, based on the parameter β introduced in Section 2.2. The microfailure surfaces shown in Fig. 4 correspond to the same macroscopic straining of the model along the initial axes of orthotropy ($\theta = 0$), as was considered for the failure surfaces presented in Fig. 2(a). More specifically, the microfailure surface depicted in Fig. 2(a) is reploted in Fig. 4(a), with a solid line representing those critical points for which the instability mode is global in nature (i.e., for which $\omega_c \to 0$), and with

Downloaded 04 May 2010 to 171.66.16.34. Redistribution subject to ASME license or copyright; see http://www.asme.org/terms/Terms_Use.cfm

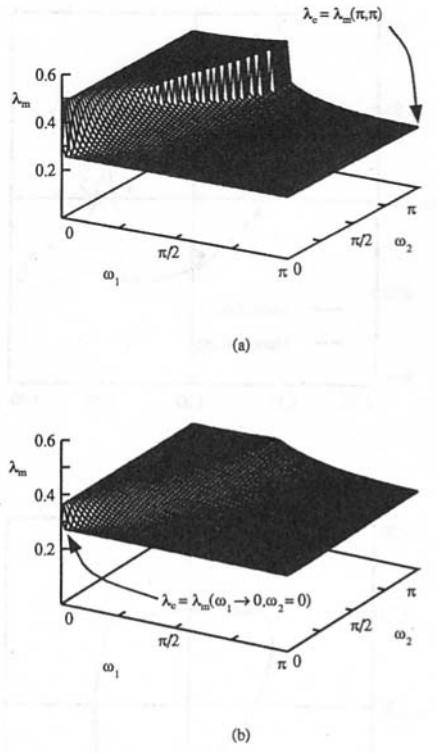


Fig. 3 Critical load parameter surface, determined using Bloch wave theory, for an infinite lattice model ($\epsilon \to 0$) with perfectly periodic microstructure ($\delta = 0$), subjected to (*a*) pure biaxial extension with $\phi = 25$ deg and (*b*) pure biaxial extension with $\phi = 35$ deg

a dotted line representing those critical points for which the instability mode is local in nature (i.e., for which $\omega_c \neq 0$). Notice that for the lattice model considered here, the critical mode shape scale parameter is equal to the same value ($\omega_c = \sqrt{2}\pi$) for all critical points for which the micro and macrofailure surfaces do no coincide. The corresponding bifurcation eigenmodes are always antiperiodic in both coordinate directions, with $\lambda_c = \lambda_m(\pi, \pi)$.

Given the computational advantages associated with determining the macrofailure surface, and the importance of determining the points for which the first instability is accurately predicted by that failure criterion, the failure surface separation parameter β, introduced in Eq. (15), has been calculated and plotted in Fig. 4(b) for all critical points on the macrofailure surface previously shown in Fig. 2(a). The dashed portion of this surface corresponds to those critical points for which $\beta < 0$, while the solid portion corresponds to those critical points for which $\beta \geq 0$. As expected from the discussion of the sufficiency condition, which ensures the onset of a local instability mode when $\beta < 0$, the range of load paths for which $\beta < 0$ is a proper subset of the range for which the micro and macrofailure surfaces do not coincide.

3.2 Failure Surfaces for the Finite Models.

(a) Perfectly Periodic Model—Influence of Scale. The influence of the relative size of the representative volume, which is characterized by the geometric scale parameter ϵ, on the failure surface of the lattice model with perfectly periodic microstructure, is investigated next for finite-sized specimens, subjected to pure biaxial deformations ($\theta = 0$). The results of the corresponding calculations are plotted in Fig. 5, with a dotted line representing the failure surface of a coarse 5×5 unit cell model ($\epsilon = 0.2$), with a dashed line representing the failure surface of a more refined 10×10 unit cell model ($\epsilon = 0.1$), and with a solid line representing the failure surface of the

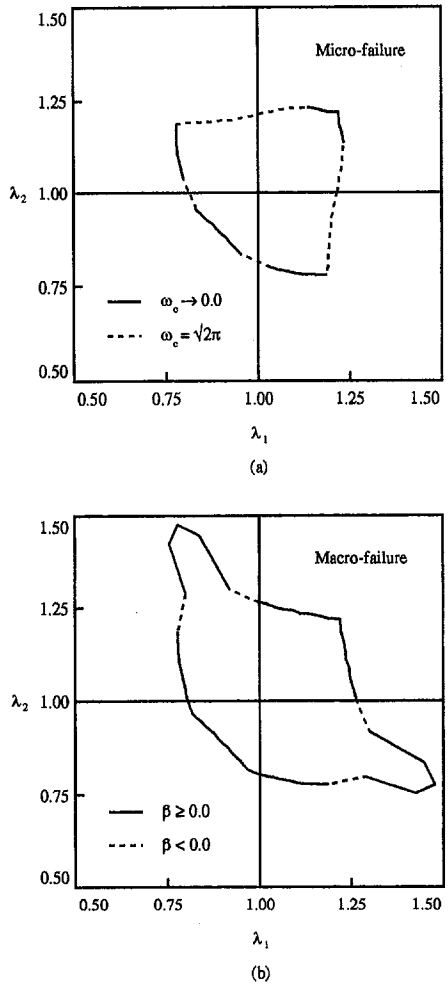


Fig. 4 (*a*) Values of the critical bifurcation mode shape scale parameter ω_c, for an infinite lattice model ($\epsilon \to 0$) with perfectly periodic microstructure ($\delta = 0$), subjected to pure biaxial deformations ($\theta = 0$). (*b*) Corresponding values of the failure criterion β based on the higher order gradient macroscopic (homogenized) moduli.

corresponding infinite model (i.e., for $\epsilon \to 0$). The latter surface coincides, by definition, with the microfailure surface shown in Fig. 2(a). As expected, the failure surfaces of the finite-sized

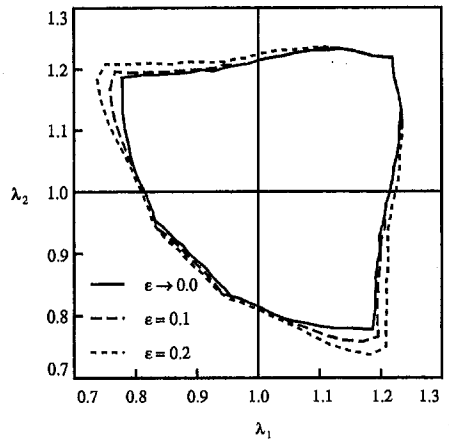


Fig. 5 Scale effects on the microfailure surfaces of perfectly periodic lattice models ($\delta = 0$), subjected to pure biaxial deformations ($\theta = 0$). Note that the microfailure surface, determined using Bloch wave theory for the infinite model, provides a lower bound for the failure surfaces of the finite models.

Downloaded 04 May 2010 to 171.66.16.34. Redistribution subject to ASME license or copyright; see http://www.asme.org/terms/Terms_Use.cfm

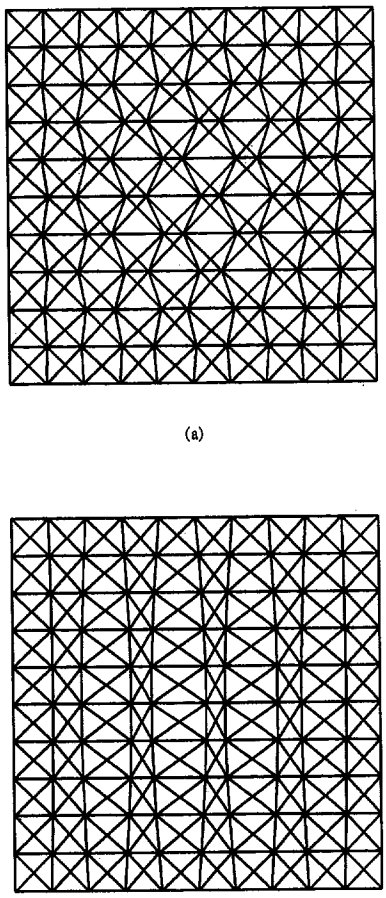


Fig. 6 Bifurcation mode shapes for a finite lattice model ($\epsilon = 0.1$) with perfectly periodic microstructure ($\delta = 0$), subjected to (*a*) pure biaxial extension with $\phi = 25$ deg and (*b*) pure biaxial extension with $\phi = 35$ deg

models converge monotonically to the failure surface of the infinite model, as the geometric scale parameter ϵ converges to zero (due to the progressive reduction in the stiffening influence of the prescribed displacement boundary conditions). Moreover, the influence of the geometric scale parameter ϵ on the failure surface is negligible only in a small subset of the range of deformations for which the micro and macrofailure surfaces for the infinite model coincide, namely, for the range near the balanced biaxial extension load path (compare the coincident regions of the failure surfaces in Fig. 5 with the appropriate portion of the microfailure surface shown in Fig. 4(*a*), for which $\omega_c \to 0$).

Additional information about the nature of the eigenmode at the onset of failure (i.e., whether the instability mode is local or global in nature), for the finite model with perfectly periodic microstructure, can be obtained from information about the critical mode shape scale parameter ω_c, for the corresponding infinite model shown Fig. 4(*a*). The eigenmodes shown in Figs. 6(*a*) and 6(*b*) are for a finite lattice model with $\epsilon = 0.1$, and correspond to the failure points labeled *c* and *d* on the failure surface of the infinite model shown in Fig. 2(*a*) (i.e., for load paths with $\phi = 25$ deg and $\phi = 35$ deg, respectively). As expected from the corresponding critical load parameter surfaces shown in Fig. 3(*a*) and Fig. 3(*b*), the shape of the eigenmode for the local instability corresponding to point *c*, is antiperiodic (with a wavelength equal to two unit cell lengths in each direction) near the center of the model (i.e., away from the boundaries), as shown in Fig. 6(*a*); while the shape of the eigenmode for the global instability corresponding to point *d*, varies smoothly over the entire specimen as shown in Fig. 6(*b*).

(b) Imperfect Models—Influence of Imperfections. The final part of this investigation addresses the influence of microstructural imperfections on the failure surfaces of finite lattice models. The imperfections considered are either geometric or constitutive in nature, and are described by Eqs. (9)—(12) of Part I. With regard to the failure surfaces of the finite model with perfectly periodic microstructure, the results presented here correspond to pure biaxial deformations along the initial axes of orthotropy ($\theta = 0$). In addition, all of the calculations correspond to a 25×25 unit cell model ($\epsilon = 0.04$), since for this, or any smaller values of the geometric scale parameter ϵ, there is no appreciable influence on the corresponding failure surfaces (for $\epsilon = 0.04$ the failure surface of the finite model with perfectly periodic microstructure nearly coincides with the failure surface of the infinite model).

As expected from general imperfection sensitivity theory for the buckling of elastic structures (see, for example, Budiansky, 1974), the maximum load for the lattice model with microstructural imperfections is lower than the load corresponding to the initial bifurcation point for its perfectly periodic counterpart. This phenomenon occurs when the post-bifurcation equilibrium solution of a perfect structure is subcritical (i.e., when the solution occurs under a decreasing applied load). For lattice structures with individual elements which exhibit a maximum load (as in the present case), one can show that the corresponding bifurcated equilibrium solutions are subcritical under either load or displacement control, since they emerge under decreasing load and decreasing displacement (see Triantafyllidis and Bardenhagen, 1993). Consequently, the imperfect structure exhibits a critical load along any load path through strain space. Moreover, the general theory of elastic stability dictates that the maximum load of the imperfect structure decreases with increasing amplitude of imperfection. Hence, the failure surfaces for the imperfect, finite lattice models, with a given imperfection shape, are contained within (i.e., bounded from above by) the failure surface for the corresponding perfectly periodic model. Furthermore, the failure surfaces for the imperfect models contract monotonically with increasing imperfection amplitude parameter δ.

The influence of the imperfection amplitude parameter δ on the failure surface of the perfectly periodic, finite model is shown in Fig. 7(*a*) and Fig. 7(*b*) for regular ($m_1 = m_2 = 2$) geometric and constitutive imperfections, respectively. The choice of imperfection shape is motivated by the desire to leave the initial average stiffness of the model unchanged. The results correspond to two different values of the imperfection amplitude parameter: $\delta = 0.1$ and $\delta = 0.25$, represented by dashed and dotted lines, respectively. The maximum discrepancy between the critical load parameter λ_c, determined for the perfectly periodic and imperfect models, occurs for both geometric and constitutive imperfections, for a deformation corresponding to pure balanced biaxial extension ($\phi = \pi/4$). The maximum reduction in the critical load due to geometric imperfections is approximately 8.5 percent for an imperfection amplitude corresponding to $\delta = 0.1$, and is approximately 17 percent for $\delta = 0.25$, as seen in Fig. 7(*a*). The corresponding reductions due to constitutive imperfections are approximately 19 percent and 36 percent, respectively. The main conclusion drawn from this portion of the investigation is that for an adequately large, but fixed amplitude of imperfection, the regular constitutive imperfections have a stronger influence on the microfailure surfaces than their geometric counterparts.

For a fixed imperfection amplitude parameter (for the calculations considered here $\delta = 0.25$) the influence of the imperfection shape on the failure surface of the finite models, subjected to pure biaxial deformations ($\theta = 0$) is shown in Fig. 8(*a*) for the case of geometric imperfections, and in Fig. 8(*b*) for the

Downloaded 04 May 2010 to 171.66.16.34. Redistribution subject to ASME license or copyright; see http://www.asme.org/terms/Terms_Use.cfm

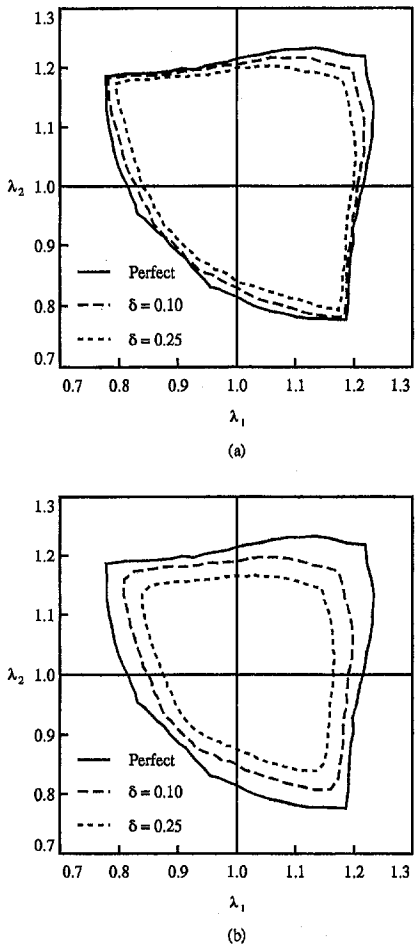


Fig. 7 Sensitivity of the microfailure surface to the magnitude of the imperfection amplitude parameter δ, for finite lattice models ($\epsilon = 0.04$) with regular ($m_1 = m_2 = 2$); (*a*) geometric imperfections and (*b*) constitutive imperfections, subjected to pure biaxial deformations ($\theta = 0$). Note that the microfailure surface determined for the perfectly periodic model, provides an upper bound for the failure surfaces of the imperfect models.

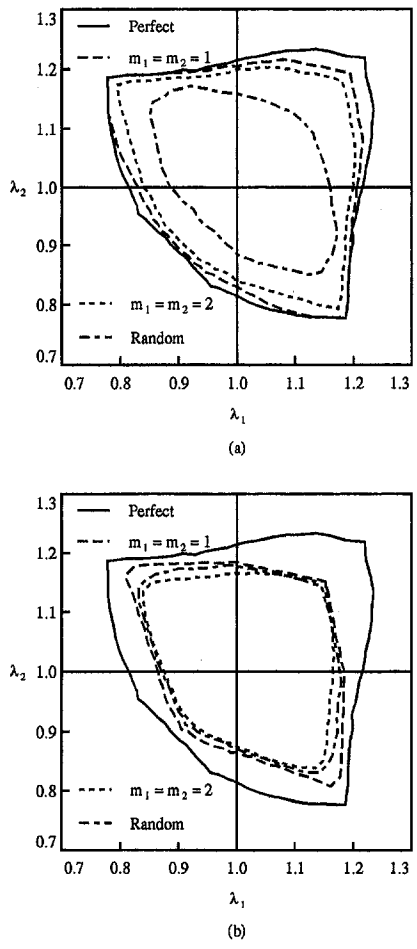


Fig. 8 Sensitivity of the micro-failure surface to the imperfection shape for finite lattice models ($\epsilon = 0.04$) with (*a*) geometric imperfections and (*b*) constitutive imperfections of 25 percent amplitude ($\delta = 0.25$), subjected to pure biaxial deformations ($\theta = 0$)

case of constitutive imperfections. For the case of geometric imperfections, the maximum load decreases with increasing imperfection wave number (i.e., with decreasing imperfection wavelength) and hence, the corresponding failure surfaces are contained within (i.e., bounded from above by) the failure surface of the perfectly periodic model, accordingly. The most contracted failure surface corresponds to a geometric imperfection with a random shape, and shows a significant reduction in the critical load (up to 50 percent, compared with 17 percent for the case of a model with regular $m_1 = m_2 = 2$ geometric imperfections, subjected to balanced biaxial extension), as seen in Fig. 8(a).

In contrast to the strong influence of the geometric imperfection shape on the failure surface of the finite model, the influence of the constitutive imperfection shape is less pronounced (the maximum reduction in the critical load is on the order of 36 percent), as seen in Fig. 8(b). Also, in contrast to the results presented in Fig. 8(a), the critical loads for the models with constitutive imperfections do not decrease monotonically with the wavelength of the regular imperfection shape (notice that the failure surface for the model with random constitutive imperfections is nested between the failure surfaces for the models with regular imperfections). One should also notice at this point, that unlike the results presented in Fig. 7 for models with regular imperfections, where for a fixed imperfection amplitude parameter δ, the constitutive imperfections resulted in a more contracted failure surface, the opposite is true for models with random imperfections (i.e., for a given imperfection amplitude, a random geometric imperfection weakens the model more than a random constitutive imperfection).

4 Conclusions

In the second part of this work, attention is focused on the influence of scale on the stability of microstructured media. Using the same nonlinearly elastic lattice model introduced in Part I, failure is defined as the onset of the first instability encountered along a radial load path through macroscopic strain space. Failure surfaces are then constructed using the locus of failure points for all load paths corresponding to a fixed value of the principal macroscopic strain orientation angle. Subsequently, the influence of the geometric scale and microstructural imperfection parameters on the failure surfaces of the model are investigated.

For the case of an infinite lattice model with perfectly periodic microstructure, the relevant scale is characterized by the mode shape scale parameter ω, which is defined as the ratio of the unit cell size, to the wavelength of the first instability mode. Using Bloch wave theory on the deformed configuration of the unit cell, the microfailure surface for the model is constructed in macroscopic strain space. In addition, the critical value of the mode shape scale parameter ω_c is determined for each point on the microfailure surface. The critical points for which $\omega_c \neq 0$ correspond to local first instability modes, while the points for which $\omega_c = 0$ correspond to first instability modes which are global in nature.

Downloaded 04 May 2010 to 171.66.16.34. Redistribution subject to ASME license or copyright; see http://www.asme.org/terms/Terms_Use.cfm

For the infinite model with perfectly periodic microstructure, the concept of a macrofailure surface is also introduced. This surface is defined as the locus of all points in macroscopic strain space for which the macroscopic (homogenized) response of the model loses ellipticity. The corresponding calculations are based on the determination of the overall properties of the unit cell at a given state of deformation, and are considerably less intensive computationally than the Bloch wave calculations involved in the determination of the corresponding microfailure surface. It can be shown that the two failure surfaces coincide when the critical mode shape scale parameter ω_c approaches zero. Consequently, the microfailure surface is always contained within (i.e., bounded from above by) the more easily obtainable macrofailure surface. The range of deformations for which the two surfaces coincide (i.e., the range for which $\omega_c \to 0$) is the range of deformations which are expected to result in post-failure behavior of the model involving a catastrophic macroscopic localization of deformation.

For the case of finite sized specimens, the failure surface is also a function of the geometric scale parameter ϵ (i.e., the ratio of the size of unit cell, to the size of representative volume). Due to the stiffening influence of the imposed Dirichlet boundary conditions, the failure surfaces for the perfectly periodic, finite models are bounded from below by the microfailure surfaces of the infinite model, and converge monotonically to the infinite model failure surface as the geometric scale parameter approaches zero. For specimen sizes with $\epsilon < 0.04$ ($N > 25$) the geometric scale effects become negligible.

Of particular importance is the influence of microstructural imperfections on the failure surfaces of the finite models. For a regular (smoothly varying) imperfection shape with a fixed wavelength, the failure surfaces for the imperfect models are bounded from above by the failure surface of the corresponding perfectly periodic model, and contract monotonically with increasing imperfection amplitude. For finite models with geometric imperfections of fixed amplitude, the failure surfaces also contract monotonically with increasing wave number (i.e., with decreasing wavelength), with the most contracted surface corresponding to the random imperfection shape. This result does not hold for the case of models with constitutive imperfections.

The proposed methodology of introducing a failure surface to study the effects of scale on the failure of ductile media with periodic or nearly periodic microstructures is general. Furthermore, the failure surfaces introduced here can be defined in either macroscopic strain or macroscopic stress space. The relatively simple lattice model, which admits computationally efficient solutions, provides considerable insight into the stability problems of more complicated microstructured media. The extreme sensitivity of the shape of the failure surfaces to the macroscopic load orientation has been established. Moreover, the failure surface calculations give the critical mode shape scale (e.g., local or global) at the onset of failure. What is more important, is that the failure surface for the infinite model with perfectly periodic microstructure, determined using Bloch wave theory, provides an upper bound for the failure surfaces of the more realistic imperfect models.

The sequence of calculations proposed to establish the failure surfaces for the perfectly periodic medium proceed from the simplest (construction of the macrofailure surface for the perfectly periodic infinite model), to the more complex (construction of the microfailure surface), and illustrate how to bound the actual failure surface of a real (imperfect) microstructured medium, for which the failure calculations in an actual application would be prohibitively time consuming. The ideas developed here are intended for applications involving more realistic microstructured materials (i.e., materials with more complicated microgeometries, such as honeycombs, foams, and layered and fiber-reinforced composite materials) and more complicated constitutive behavior (e.g., rate-independent elastoplastic behavior). Work in that direction has already been initiated, starting with applications involving aluminum honeycombs (Triantafyllidis and Schraad, 1998) and fiber-reinforced composites (Triantafyllidis and Bardenhagen, 1996). Calculations for the onset of failure in these applications only require knowledge of the current tangent moduli, just as in the case of the nonlinearly elastic material. The potential unloading associated with plasticity becomes important only in the postbifurcation and localization portion of the material response, thus justifying the nonlinearly elastic simplification adopted in the present work.

Acknowledgments

The present work was partially funded initially by Alcoa and subsequently by AFOSR under Grant DOD-G-F49620-94-1-0402. The authors would like to express their appreciation for this financial assistance, and their gratitude to Dr. Owen Richmond of the Alcoa Technical Center for his interest and encouragement and for sharing his ideas on the subject of stability as it relates to microstructured materials.

References

Anderson, M. S., 1981, "Buckling of periodic lattice structures," *AIAA J.*, Vol. 19, pp. 782–788.

Anderson, M. S., 1986, "Natural vibration and buckling of general periodic lattice structures," *AIAA J.*, Vol. 24, pp. 163–169.

Budiansky, B., 1974, "Theory of buckling and post-buckling behavior of elastic structures," *Advances in Applied Mechanics*, C. H. Yih, ed., Academic Press, New York, pp. 1–65.

Elyada, D., and Babcock, C., 1987, "Buckling and nonlinear response of imperfect three-legged truss columns," *AIAA J.*, Vol. 25, 324–330.

Forman, S., and Hutchinson, J. W., 1970, "Buckling of reticulated shell structures," *Int. J. Solids Structures*, Vol. 6, pp. 909–932.

Geymonat, G., Müller, S., and Triantafyllidis, N., 1993, "Homogenization of nonlinearly elastic materials, microscopic bifurcation and macroscopic loss of rank-one convexity," *Arch. Rat. Mech. Anal.*, Vol. 122, pp. 231–290.

Greszczuk, L. B., 1975, "Microbuckling failure in circular fiber-reinforced composites," *AIAA J.*, Vol. 13, pp. 1311–1318.

Lomont, J. S., 1959, *Applications of finite groups*, Academic Press, New York.

Triantafyllidis, N., and Bardenhagen, S., 1993, "On higher order gradient continuum theories in 1-D nonlinear elasticity: Derivation from and comparison to the corresponding discrete models," *J. Elasticity*, Vol. 33, pp. 259–293.

Triantafyllidis, N., and Bardenhagen, S., 1996, "The influence of scale size on the stability of periodic solids and the role of associated higher order gradient continuum models," *J. Mech. Phys. Solids*, Vol. 44, pp. 1891–1928.

Triantafyllidis, N., and Maker, B. N., 1985, "On the Comparison Between Microscopic and Macroscopic Instability Mechanisms in a Class of Fiber-Reinforced Composites," ASME JOURNAL OF APPLIED MECHANICS, Vol. 52, pp. 794–800.

Triantafyllidis, N., and Schnaidt, W. C., 1993, "Comparison of microscopic and macroscopic instabilities in a class of two-dimensional periodic composites," *J. Mech. Phys. Solids*, Vol. 41, pp. 1533–1565.

Triantafyllidis, N., and Schraad, M. W., 1998, "Onset of failure in aluminum honeycombs under general in-plane loading," *J. Mech. Phys. Solids*, to appear.

Downloaded 04 May 2010 to 171.66.16.34. Redistribution subject to ASME license or copyright; see http://www.asme.org/terms/Terms_Use.cfm

Enhanced Elastic Buckling Loads of Composite Plates With Tailored Thermal Residual Stresses

S. F. Müller de Almeida[1]
Instituto Technológico de Aeronáutica,
Department of Mechanical Engineering,
12.228-900 Sao Jose dos Campos–SP,
Brazil

J. S. Hansen
University of Toronto,
Institute of Aerospace Studies,
4925 Dufferin Street,
Downsview, ON M3H 5T6,
Canada

Thermal residual stresses introduced during the manufacturing process and their effect on the buckling load of stringer reinforced composite plates is investigated. The principal idea is to include stiffeners on the perimeter of the plate and thereby, during manufacture, induce a favorable thermal residual-stress state in the structure; these stresses arise by considering the difference in thermal expansion coefficients and elastic properties of the plate and the stiffeners. In this manner, it is shown that thermal residual stresses can be tailored to significantly enhance the performance of the structure. The analysis is taken within the context of an enhanced Reissner-Mindlin plate theory and the finite element technique is used to analyze the problem. A 16 node bi-cubic Lagrange element is implemented in a FORTRAN code to determine the buckling load of the composite plate in the presence of thermal residual stresses. Three different plate-stiffener geometries are used as illustrations. The analyses indicate that buckling loads can be significantly increased by properly tailoring the thermal residual stresses. Therefore it may be concluded that an evaluation of these stresses and a judicious analysis of their effects must be included in the design procedure for this class of composite structure.

Introduction

Considerable research has been published investigating thermal effects on the buckling response of composite structures (Sai Ram and Sinha, 1992; Sun and Hsu, 1990). These investigations typically deal with stresses developed by a constrained laminated plate subjected to a temperature change. These problems have direct practical application only if the structure constraining the plate is not affected by the temperature change; this is often not the case for aerospace structures. On the other hand, very significant thermal residual stresses may be introduced in composite structures during the manufacturing process; the thermal residual stresses in co-cured reinforced plates/shells are, in general, different from those of plates/shells produced by secondary bonding. The presence of such manufacturing stresses may significantly affect the structural response but they are seldom taken into account during the design and analysis of such structures.

The objective of this work is to investigate the effect of manufacturing-introduced thermal residual stresses on the buckling response of composite plates. An innovative approach to the problem is introduced; it is proposed that not only must these stresses be taken into account but they can also be tailored to enhance the performance of the structure.

The existence of the thermal residual stresses is a consequence of the anisotropy of advanced composite materials. The thermal expansion coefficient of unidirectional graphite/epoxy composites, for example, is typically nearly zero in the direction of the fibers and relatively large in the transverse direction (Table 1). The cure process is usually carried out in an autoclave at elevated temperatures from 120 to 180°C or in the case of thermoplastic composites the consolidation process is carried out at temperatures as high as 380°C. Considering that the laminates are stress free at an elevated temperature (cure or consolidation temperature), thermal residual stresses develop during cooling to room temperature due to a variation of thermal expansion coefficients of the lamina in a plate. The in-plane thermal residual stress resultants are zero for a symmetrically laminated composite plate in the absence of external constraints. However, if the plate is nonuniform (stringer reinforced) these stress resultants are in general nonzero.

Composite plates used in the aerospace industry are usually reinforced along the direction of the most critical loading. Typically, there exists a mismatch between the thermal expansion coefficients of the reinforcement and the plate. If the reinforcement is constructed primarily of 0 deg plies to take advantage of the anisotropy of composite laminates, they are likely to have a thermal expansion coefficient lower than that of the plate. In that case, the plate may contain considerable tensile thermal residual stresses while the stringers are under compression. The existence of these thermal residual stresses affect the structural behavior of the composite part.

The magnitude of the thermal residual stresses depends on a number of factors: plate geometry and construction, physical properties of the materials used, cure (or consolidation) temperature, etc. Of course, the effect of the thermal stresses on the structural behavior also depends on those variables. This effect may be quite significant as will be demonstrated herein. Therefore, the design variables must be chosen such that a favorable residual stress distribution is present in the structure; the thermal residual stresses should be tailored to enhance a particular characteristic of the structure.

A finite element formulation is used to analyze the problem. A 16 node bi-cubic Lagrange element is implemented within the context of an enhanced Reissner-Mindlin plate theory to

[1] Currently on leave at UTIAS.

Contributed by the Applied Mechanics Division of THE AMERICAN SOCIETY OF MECHANICAL ENGINEERS for publication in the ASME JOURNAL OF APPLIED MECHANICS.

Discussion on the paper should be addressed to the Technical Editor, Professor Lewis T. Wheeler, Department of Mechanical Engineering, University of Houston, Houston, TX 77204-4792, and will be accepted until four months after final publication of the paper itself in the ASME JOURNAL OF APPLIED MECHANICS.

Manuscript received by the ASME Applied Mechanics Division, Sept. 24, 1996; final revision, Feb. 10, 1997. Associate Technical Editor: J. N. Reddy.

Copyright © 1997 by ASME

Downloaded 04 May 2010 to 171.66.16.34. Redistribution subject to ASME license or copyright; see http://www.asme.org/terms/Terms_Use.cfm

Table 1 Material properties used for T300/5208 graphite-epoxy

Property	Value
Longitudinal modulus of elasticity, E_1	154500 MPa
Transversal modulus of elasticity, E_2	11130 MPa
In-plane Poisson's ratio, ν_{12}	0.304
In-plane shear modulus, G_{12}	6980 MPa
Transversal shear modulus, G_{13}	6980 MPa
Transversal shear modulus, G_{23}	3360 MPa
Longitudinal thermal expansion coefficient, α_1	-0.17×10^{-6}/°C
Transversal thermal expansion coefficient, α_2	23.1×10^{-6}/°C
Ply thickness, t	0.15 mm

determine the buckling response of the plate. Three different stiffened-plate geometries are used to illustrate the thermal residual-stress effects. The calculations indicate that the buckling load can be significantly increased by properly tailoring the residual stresses.

Formulation of Problem

The problem under consideration has three main elements. All calculations are based on laminated Reissner-Mindlin plate theory. Full nonlinear strain-displacement relations are assumed; however, the nonlinearities only play a role in the calculation of the buckling solution. The analysis is quite general, with the only restriction being no membrane-bending coupling exists. This is because this coupling will cause thermally induced out-of-plane deformations as a result of the cure/consolidation and this deformation state leads to totally different analysis requirements. (Such a "plate" would no longer be a plate but would be a shell.)

The first element is the calculation of the thermally induced effects due to the cure/consolidation. This aspect of the problem is solved in a general form with the only restrictions being that there is no membrane-bending coupling and that the analysis is linear. Both these assumptions are reasonable within the present context and should not be considered major restrictions. It should also be noted that in this calculation the plate-stiffener assembly is assumed to be completely unconstrained; thus residual stresses arise only from thermal coefficient of expansion mismatches either through the thickness of the laminate or due to spatial variations in the thermal coefficient of expansion.

The second element is the calculation of the prebuckling state of the plate-stiffener assembly. In the application of the boundary conditions it is assumed that there are no mechanically induced stresses imposed on the system by virtue of the boundary conditions. This assumption is consistent with physical reality. The loading state in the prebuckling problem is assumed to result from the application of a uniform displacement applied on the plate boundary of interest. This calculation is assumed linear with no membrane-bending coupling; the results of this calculation are nonuniform displacement fields with associated stress and strain fields. Because of the nonuniformity of the prebuckling state the buckling problem does not exhibit the inherent simplicity of classical buckling problems in which the buckling load is directly related to uniform stress resultants.

The third and final element is the buckling calculation. This calculation follows the traditional approach in that a full nonlinear formulation is undertaken. The problem is solved by separating the solution into a combined thermal/prebuckling state and the buckling state. Individually these states are assumed linear while the nonlinearity in the problem contributes to the interaction of the thermal/prebuckling and the buckling states. The linearized buckling problem is an eigenvalue problem which yields buckling loads and associated buckling modes. It should be noted that the buckling loads are not obtained directly; rather the buckling load is the total force required to produce the critical displacement at the loaded plate edge. Such a model is typical of the manner in which plates are loaded in actual experimental configurations.

In the next section the basic equations of the problem are presented. Also the solution of each of the three elements described above is discussed in detail.

Basic Equations. Consider a composite laminated plate subjected to in-plane compressive loads as depicted in Fig. 1. Each lamina is assumed to be orthotropic, homogeneous, linear elastic, and is oriented at an angle θ with respect to the y-axis. Also, the plate may be nonuniform and thermal residual stresses due to the cure or consolidation process may be present. The total potential energy of the plate is

$$\pi_p = \tfrac{1}{2}\int_v \{\bar{\epsilon}\}^T\{\bar{\sigma}\}\,dv - \int_s \{\bar{f}\}^T\{\bar{u}\}\,ds \tag{1}$$

where v is the plate volume and s is its plate surface (edges), $\{\bar{\epsilon}\}$ are the strains, $\{\bar{\sigma}\}$ the stresses, $\{\bar{u}\}$ the displacements, and $\{\bar{f}\}$ the edge tractions. The first integral is the strain energy of the plate. Throughout this work, an overbar indicates a quantity defined for an arbitrary point (x, y, z) in the plate while quantities without the overbar are defined in the x-y plane at the plate middle surface.

The present formulation assumes Mindlin plate hypotheses (Mindlin, 1951). Therefore, the in-plane displacement fields $\bar{u}$, $\bar{v}$ are assumed to vary linearly through the plate thickness and the transverse displacement $\bar{w}$ is assumed constant through the plate thickness. That is

$$\begin{aligned}\bar{u}(x, y, z) &= u(x, y) + z\psi_x(x, y)\\ \bar{v}(x, y, z) &= v(x, y) + z\psi_y(x, y)\\ \bar{w}(x, y, z) &= w(x, y)\end{aligned} \tag{2}$$

where u, v and w are the displacements along directions x, y, and z, respectively, and ψ_x and ψ_y are rotations of the cross section.

The strain can be represented as the sum of linear and nonlinear components, respectively,

$$\{\bar{\epsilon}\} = \{\bar{\epsilon}^L\} + \{\bar{\epsilon}^N\}. \tag{3}$$

Using the nonlinear strain-displacement relations (Novozhilov, 1953) the linear strain components are given by

$$\begin{aligned}\bar{\epsilon}_x^L &= u_{,x} + z\kappa_{xx}\\ \bar{\epsilon}_y^L &= v_{,y} + z\kappa_{yy}\\ \bar{\gamma}_{xy}^L &= u_{,y} + v_{,x} + z\kappa_{xy}\end{aligned}$$

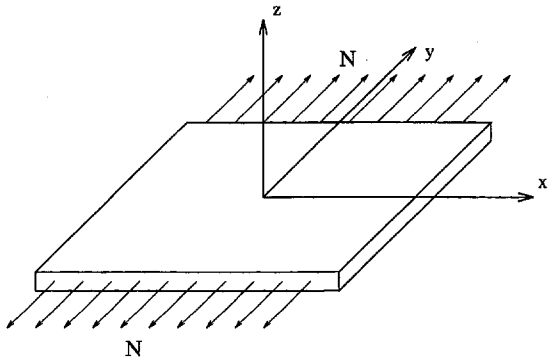


Fig. 1 Plate geometry

Downloaded 04 May 2010 to 171.66.16.34. Redistribution subject to ASME license or copyright; see http://www.asme.org/terms/Terms_Use.cfm

$$\bar{\gamma}_{xz}^{L} = w_{,x} + \psi_x$$
$$\bar{\gamma}_{yz}^{L} = w_{,y} + \psi_y \tag{4}$$

where κ_{ij} are the middle-surface curvatures of the plate

$$\kappa_{xx} = \psi_{x,x}$$
$$\kappa_{yy} = \psi_{y,y}$$
$$\kappa_{xy} = \psi_{x,y} + \psi_{y,x}. \tag{5}$$

Also, let $\{\epsilon\}$ be the vector of in-plane linear strain components:

$$\{\epsilon\}^T = [u_{,x} \quad v_{,y} \quad u_{,y} + v_{,x}]. \tag{6}$$

The nonlinear strain components can be expressed in terms of the displacements as

$$\bar{\epsilon}_x^N = \tfrac{1}{2}[(u_{,x}^2 + v_{,x}^2 + w_{,x}^2) + 2z(u_{,x}\psi_{x,x} + v_{,x}\psi_{y,x}) + z^2(\psi_{x,x}^2 + \psi_{y,x}^2)]$$
$$\bar{\epsilon}_y^N = \tfrac{1}{2}[(u_{,y}^2 + v_{,y}^2 + w_{,y}^2) + 2z(u_{,y}\psi_{x,y} + v_{,y}\psi_{y,y}) + z^2(\psi_{x,y}^2 + \psi_{y,y}^2)]$$
$$\bar{\gamma}_{xy}^N = (u_{,x}u_{,y} + v_{,x}v_{,y} + w_{,x}w_{,y}) + z(u_{,x}\psi_{x,y} + u_{,y}\psi_{x,x} + v_{,x}\psi_{y,y} + v_{,y}\psi_{y,x}) + z^2(\psi_{x,x}\psi_{x,y} + \psi_{y,x}\psi_{y,y})$$
$$\bar{\gamma}_{xy}^N = (u_{,x}\psi_x + v_{,x}\psi_y) + z(\psi_x\psi_{x,x} + \psi_y\psi_{y,x})$$
$$\bar{\gamma}_{yz}^N = (u_{,y}\psi_x + v_{,y}\psi_y) + z(\psi_x\psi_{x,y} + \psi_y\psi_{y,y}) \tag{7}$$

where a subscript following a comma indicates partial differentiation with respect to that variable.

The strains at any point in the plate are expressed in terms of the middle-surface strain components using Eqs. (4), (5), (6), and (7). Therefore, we define a middle-surface linear strain vector, $\{e\}$, and a vector of the components of the nonlinear strain terms, $\{e_G\}$ as

$$\{e\}^T = [u_{,x} \; v_{,y} \; u_{,y} + v_{,x} \; \kappa_{xx} \; \kappa_{yy} \; \kappa_{xy} \; w_{,x} + \psi_x \; w_{,y} + \psi_y] \tag{8}$$

$$\{e_G\}^T = [u_{,x} \; u_{,y} \; v_{,x} \; v_{,y} \; w_{,x} \; w_{,y} \; \psi_{x,x} \; \psi_{x,y} \; \psi_{y,x} \; \psi_{y,y} \; \psi_x \; \psi_y]. \tag{9}$$

Thermal Problem. The first step in the analysis is the computation of the thermal residual stresses in the plate. These residual stresses arise only from thermal coefficient of expansion mismatches either through the thickness of the laminate or due to spatial variations in the thermal coefficient of expansion.

As previously discussed, the following assumptions are used:

1 the plate is totally unconstrained;
2 no mechanical loads are applied;
3 the laminate is such that no membrane-bending coupling exists;
4 the strain-displacement relations are linear.

The stress-strain relation adopted involves the thermal effects directly and is

$$\{\bar{\sigma}\} = [\bar{Q}]\{\{\bar{\epsilon}\} - \Delta T\{\bar{\alpha}\}\} \tag{10}$$

where $[\bar{Q}]$ are the material stiffnesses in structural coordinates while $\{\bar{\alpha}\}$ is the vector of total strains; $\{\bar{\alpha}\}$ is the vector of structural thermal coefficients of expansion; and ΔT is the change in temperature. The expressions for $[\bar{Q}]$ and $\{\bar{\alpha}\}$ in terms of the lamina elastic properties at an arbitrary angle are given by Jones (1975) and are not reproduced here.

It is to be noted that $[\bar{Q}]$, $\{\bar{\alpha}\}$ are in general functions of temperature and that at elevated temperatures viscoelastic/creep effects are to be expected. These aspects are not included in the present work but may be important in actual design situations. Results are presented for a range of ΔT and these illustrate that the effects being investigated are significant for a broad range of ΔT. Furthermore, if viscoelastic/creep effects are assumed to cause a stress state that corresponds to an "equivalent lower temperature cure" based on room temperature material properties the present results will be representative of such a situation.

In the absence of external loads, the total potential energy of the plate for the thermal problem, π_p^t, can be computed from Eqs. (1) and (10) as

$$\pi_p^t = \tfrac{1}{2}\int_v \{\bar{\epsilon}\}^T[\bar{Q}]\{\bar{\epsilon}\}dv - \Delta T\int_v \{\bar{\epsilon}\}^T[\bar{Q}]\{\bar{\alpha}\}dv. \tag{11}$$

The linear strains at any point in the plate can be described in terms of the middle-surface linear strains using Eqs. (6) and (5). Therefore, the previous expression for the total potential energy of the plate for the thermal problem can be integrated through the thickness (with respect to z) and in turn expressed in terms of the middle-surface strain vector, $\{e\}$, defined in Eq. (8).

After some algebra it may be shown that Eq. (11) can be rewritten as

$$\pi_p^t = \tfrac{1}{2}\int_A \{e\}^T[\mathcal{D}]\{e\}dA - \Delta T\int_A (\{\epsilon\}\{N\}_t + \{\kappa\}\{M\}_t)dA \tag{12}$$

where matrix $[\mathcal{D}]$ represents the constitutive relation between the stress resultants and the middle-surface strains, and $\{N\}_t$ and $\{M\}_t$ are thermal load vectors.

Matrix $[\mathcal{D}]$ is defined by

$$[\mathcal{D}] = \begin{bmatrix} [A] & [B] & [0] \\ [B] & [D] & [0] \\ [0] & [0] & [A^*] \end{bmatrix} \tag{13}$$

where

$$(A_{ij}, B_{ij}, D_{ij}) = \sum_{k=1}^{K}\int_{z_{k-1}}^{z_k} [\bar{Q}_{ij}]_k(1, z, z^2)dz \quad i,j = 1,2,6 \tag{14}$$

and:

$$A_{ij}^* = \sum_{k=1}^{K}\int_{z_{k-1}}^{z_k} [\bar{Q}_{ij}]_k dz \quad i,j = 4,5 \tag{15}$$

where K is the total number of lamina in the laminate and z_{k-1}, z_k are the bottom and top coordinates of the kth layer with respect to the plate middle surface.

The thermal load vectors are defined as (Jones, 1975)

$$\{N\}_t = \Delta T\sum_{k=1}^{K}[\bar{Q}]_k\{\bar{\alpha}\}_k(z_k - z_{k-1}) \tag{16}$$

and

$$\{M\}_t = \Delta T\sum_{k=1}^{K}[\bar{Q}]_k\{\bar{\alpha}\}_k\frac{(z_k^2 - z_{k-1}^2)}{2}. \tag{17}$$

The thermal load vectors defined above must not be confused with the thermal residual stress resultants. The thermal load vectors can only introduce actual thermal residual stresses in the plate in the presence of some external constraint or due to thermal coefficient of expansion mismatches throughout the plate.

The thermal problem may be solved by computing the displacement field that minimizes Eq. (12). After this field is obtained, the thermal residual stresses can be obtained from Eq. (10).

For the sake of completeness, the equations presented in this subsection include bending-membrane coupling terms. In the absence of bending-membrane coupling, matrix $[B]$ and the

Downloaded 04 May 2010 to 171.66.16.34. Redistribution subject to ASME license or copyright; see http://www.asme.org/terms/Terms_Use.cfm

thermal load vector $\{M\}_t$ are identically zero. As a consequence, the bending thermal residual stress-resultants vector is also identically zero. As noted above all the calculations to be completed are based on $[B] \equiv 0$.

Prebuckling Problem. The second step is the calculation of the prebuckling state of the plate-stiffener assembly. The loading state in the prebuckling problem is assumed to result from the application of a uniform displacement applied on the plate boundary of interest.

The following assumptions are made:

1 the applied load results from a uniform displacement applied to the loaded edge;
2 application of boundary conditions does not induce any mechanical loads;
3 the composite laminate is such that no membrane-bending coupling exists;
4 the problem is linear.

In this case, the stress-strain relation is

$$\{\bar{\sigma}\} = [\bar{Q}]\{\bar{\epsilon}\} \tag{18}$$

where $[\bar{Q}]$ are the material stiffnesses in structural coordinates.

Thus, the total potential energy of the plate in the prebuckling state, π_p^0, can be computed from Eq. (1) as

$$\pi_p^0 = \tfrac{1}{2}\int_v \{\bar{\epsilon}\}^T[\bar{Q}]\{\bar{\epsilon}\}\,dv \tag{19}$$

where $\{\bar{u}\}$ are the displacements. It should be noted that the applied load results from the specified boundary conditions, then there is no explicit work term due to external forces.

Again, the strain at any point in the plate can be described in terms of the middle-surface linear strains. Therefore, the previous expression for the total potential energy of the plate for the prebuckling state can be integrated through the thickness (with respect to z) and in turn expressed in terms of the middle-surface strain vector, $\{e\}$, defined in Eq. (8).

Following a similar procedure to the one used in the thermal problem analysis Eq. (19) can be rewritten as

$$\pi_p^0 = \tfrac{1}{2}\int_A \{e\}^T[\mathcal{D}]\{e\}\,dA \tag{20}$$

where matrix $[\mathcal{D}]$ is the same as in the thermal problem and is defined in (13).

The displacement field in the prebuckling state may be found by minimizing the potential energy (20). After this field is obtained, the prebuckling stresses can be obtained from Eq. (18).

Buckling Problem. The third and final step is the buckling calculation. For this calculation a full nonlinear formulation is undertaken. The problem is solved by separating the solution into a combined thermal/prebuckling state and the buckling state. Individually these states are assumed linear while the nonlinearity in the problem contributes to the interaction of the thermal/prebuckling and the buckling states. Therefore, the stresses at any point in the plate are given by

$$\{\bar{\sigma}\} = [\bar{Q}]\{\bar{\epsilon}\} + \{\bar{\sigma}_0\} + \{\bar{\sigma}_R\} \tag{21}$$

where $\{\bar{\sigma}_0\}$ are the stresses in the prebuckling state and $\{\bar{\sigma}_R\}$ are the thermal residual stresses. Matrix $[\bar{Q}]$ represents the stress-strain relations in reference axes xyz for the particular lamina considered.

The strain energy of the plate can now be computed by substituting Eq. (3) and (21) into Eq. (1). Neglecting higher-order terms and using the fact that $\{\bar{\sigma}_0\}$ and $\{\bar{\sigma}_R\}$ represent states of equilibrium, yields the result

$$U = \tfrac{1}{2}\int_v \{\bar{\epsilon}^L\}^T[\bar{Q}]\{\bar{\epsilon}^L\}\,dv + \int_v \{\bar{\epsilon}^N\}^T\{\bar{\sigma}_0\}\,dv + \int_v \{\bar{\epsilon}^N\}^T\{\bar{\sigma}_R\}\,dv. \tag{22}$$

The strains at any point in the plate can be described in terms of the middle-surface strains using Eqs. (4), (5), and (7). Therefore, the previous expression for the strain energy can be integrated through the thickness (with respect to z) and in turn expressed in terms of the middle-surface strain vector, $\{e\}$, and the components of the nonlinear strain terms, $\{e_G\}$ defined, respectively, in Eqs. (8) and (9).

After some algebra it may be shown that Eq. (22) can be rewritten as

$$U = \tfrac{1}{2}\int_A \{e\}^T[\mathcal{D}]\{e\}\,dA + \int_A \{e_G\}^T[\mathcal{D}_G^0]\{e_G\}\,dA + \int_A \{e_G\}^T[\mathcal{D}_G^R]\{e_G\}\,dA \tag{23}$$

where matrix $[\mathcal{D}]$ represents the constitutive relation between the stress resultants and the middle-surface strains as given in Eq. (13).

The terms in Eqn. (23) involving the subscript G refer to the strain energy due to the coupling between linear and nonlinear terms. The linear terms refer to either one of two stress states: the thermal residual stresses indicated by superscript R or to the prebuckling state indicated by superscript 0. It can be shown that matrix $[\mathcal{D}_G]$ is given by

$$[\mathcal{D}_G^S] = \begin{bmatrix}
N_x^s & N_{xy}^s & 0 & 0 & 0 & 0 & M_x^s & M_{xy}^s & 0 & 0 & Q_x^s & 0 \\
N_{xy}^s & N_y^s & 0 & 0 & 0 & 0 & M_{xy}^s & M_y^s & 0 & 0 & Q_x^s & 0 \\
0 & 0 & N_x^s & N_{xy}^s & 0 & 0 & 0 & 0 & M_x^s & M_{xy}^s & 0 & Q_y^s \\
0 & 0 & N_{xy}^s & N_y^s & 0 & 0 & 0 & 0 & M_{xy}^s & M_y^s & 0 & Q_y^s \\
0 & 0 & 0 & 0 & N_x^s & N_{xy}^s & 0 & 0 & 0 & 0 & 0 & 0 \\
0 & 0 & 0 & 0 & N_{xy}^s & N_y^s & 0 & 0 & 0 & 0 & 0 & 0 \\
M_x^s & M_{xy}^s & 0 & 0 & 0 & 0 & L_x^s & L_{xy}^s & 0 & 0 & T_x^s & 0 \\
M_{xy}^s & M_y^s & 0 & 0 & 0 & 0 & L_{xy}^s & L_y^s & 0 & 0 & T_y^s & 0 \\
0 & 0 & M_x^s & M_{xy}^s & 0 & 0 & 0 & 0 & L_x^s & L_{xy}^s & 0 & T_x^s \\
0 & 0 & M_{xy}^s & M_y^s & 0 & 0 & 0 & 0 & L_{xy}^s & L_y^s & 0 & T_y^s \\
Q_x^s & Q_x^s & 0 & 0 & 0 & 0 & T_x^s & T_y^s & 0 & 0 & 0 & 0 \\
0 & 0 & Q_y^s & Q_y^s & 0 & 0 & 0 & 0 & T_x^s & T_y^s & 0 & 0
\end{bmatrix} \tag{24}$$

where $S = R$ or 0 indicating the thermal residual stresses or the prebuckling stresses, respectively. The following stress resultants were used in the definition of matrix $[\mathcal{D}_G]$:

$$(N_{ij}^S, M_{ij}^S, L_{ij}^S) = \sum_{k=1}^{K}\int_{z_{k-1}}^{z_k} \bar{\sigma}_{ij}(1, z, z^2)\,dz \quad ij = xx, yy, xy \tag{25}$$

and

$$(Q_i^S, T_i^S) = \sum_{k=1}^{K}\int_{z_{k-1}}^{z_k} \bar{\sigma}_{iz}(1, z)\,dz \quad i = x, y. \tag{26}$$

It should be noted that L_{ij}^S are higher-order moments of the stress about the plate middle surface. Since Mindlin plate hypotheses were assumed, these stress resultants are identically zero for single layer plates under in-plane loads. However, for the case of laminated plates under in-plane loads L_{ij}^S are, in general, nonzero even for symmetric laminates. Also, the kine-

Downloaded 04 May 2010 to 171.66.16.34. Redistribution subject to ASME license or copyright; see http://www.asme.org/terms/Terms_Use.cfm

matic hypotheses assumed imply that the stress resultants T_i^S are identically zero for symmetrically laminated plates. They may be nonzero for nonsymmetric laminates and/or out-of-plane loads.

Finite Element Formulation

A finite element formulation was developed to solve the problem described in the previous section. A 16-node isoparametric bi-cubic element using Lagrange interpolation functions (Zienkiewicz and Taylor, 1989) was implemented in a FORTRAN code. Figure 2 shows the geometry of the element. The element has five degrees-of-freedom per node (u, v, w, ψ_x, and ψ_y) with a total of 80 degrees-of-freedom per element. The displacements at an arbitrary point within the domain of the pth element is given by

$$\{\delta\}^T = [u\ v\ w\ \psi_x\ \psi_y] = [N]\{\delta\}_p \tag{27}$$

where $[N]$ is a matrix of interpolation functions. Matrix $[N]$ has dimensions 5 by 80. Vector $\{\delta\}_p$ contains the 80 element nodal variables arranged as

$$\{\delta\}_p^T = [u_1\ y_1\ w_1\ \psi_{x_1}\ \psi_{y_1}\ u_2\ \ldots\ \psi_{y_{15}}\ u_{16}\ v_{16}\ w_{16}\ \psi_{x_{16}}\ \psi_{y_{16}}]. \tag{28}$$

The vector of strains at the middle surface of the plate can be expressed as

$$\{e\} = [B]\{\delta\}_p \tag{29}$$

where matrix $[B]$ is an 8-by-80 matrix that contains derivatives of the interpolation functions N_i with respect to variables x and y. Matrix $[B]$ can be derived from Eqs. (4), (5), (27), and (29). The derivatives of the interpolation functions with respect to coordinates x and y were computed in terms of derivatives of the interpolation functions with respect to the element coordinates ξ and η, shown in Fig. 2, using mapping techniques (Zienkiewicz and Taylor, 1989). Therefore, a general isoparametric element is implemented.

Similarly, the vector of components of the nonlinear strain terms, $\{e_G\}$, can be computed as

$$\{e_G\} = [B_G]\{\delta\}_p \tag{30}$$

where matrix $[B_G]$ is a 12-by-80 matrix that contains derivatives of the interpolation functions N_i with respect to variables x and y. Matrix $[B_G]$ can be derived from Eqs. (9), (27), and (30). Again, mapping techniques were used to derive expressions to compute matrix $[B_G]$ for a general quadrilateral element.

The element stiffness matrix and element geometric stiffness matrix (Zienkiewicz and Taylor, 1989) can be computed from the matrices defined above. The stiffness matrix of the pth element is given by

$$[K]_p = \int_{A_p} [B]^T[\mathcal{D}][B]dA \tag{31}$$

where the area integration is carried out numerically using Gauss quadrature (Bathe and Wilson, 1976) with 16 integration points. A shear correction factor of $\frac{5}{6}$ is used for all laminates. It should also be noted that the present finite element formulation does not suffer from shear locking; no special techniques of reduced integration are required (Heppler and Hansen, 1986).

The element geometric stiffness matrix for the pth element is given by

$$[K_G^S]_p = \int_{A_p} [B_G]^T[\mathcal{D}_G^S][B_G]dA \quad \text{where} \quad S = R \ \text{or}\ 0. \tag{32}$$

The superscript S indicates either the geometric stiffness matrix due to the residual thermal stresses, $[K_G^R]_p$, or the geometric stiffness matrix due to prebuckling state, $[K_G^0]_p$. Matrix $[K_G^R]_p$ is computed assuming a thermal loading corresponding to the difference between the room temperature and the cure or consolidation temperature. Matrix $[K_G^0]_p$ is computed for a unit positive displacement.

Variable λ characterizes the intensity of the prebuckling load. The geometric stiffness matrices are also computed numerically using Gauss quadrature with 16 integration points.

The expression for the plate strain energy can now be rewritten using an approximation based on the finite element discretization. Equation (23) becomes

$$U_N = \tfrac{1}{2}\sum_{p=1}^{N}\{\delta\}_p^T[K]_p\{\delta\}_p + \tfrac{1}{2}\sum_{p=1}^{N}\{\delta\}_p^T[K_G^R]_p\{\delta\}_p - \tfrac{1}{2}\sum_{p=1}^{N}\lambda\{\delta\}_p^T[K_G^0]_p\{\delta\}_p \tag{33}$$

where N is the total number of elements in the model.

Global matrices consistent with the boundary conditions of the problem can then be generated using standard finite element techniques (Zienkiewicz and Taylor, 1989). Applying Trefftz criterion yields an eigenvalue problem for λ in terms of the vector of unknown nodal displacements, $\{\delta\}$,

$$\{[K] + [K_G^R] - \lambda[K_G^0]\}\{\delta\} = \{0\} \tag{34}$$

where $[K]$, $[K_G^R]$, and $[K_G^0]$ are the global matrices for the plate. The least eigenvalue λ corresponds to the buckling load of the plate.

The solution procedure for the problem includes the following steps:

1 computation of the stiffness matrices ($[K]_p$);
2 solution of the thermoelastic problem to obtain the stress resultants due to the cure temperature (N_{ij}^R, M_{ij}^R, L_{ij}^R, Q_i^R, T_i^R) at the Gauss points;
3 computation of the thermal geometric stiffness matrices ($[K_G^R]_p$);
4 solution of the prebuckling problem to compute the stress resultants due to the prebuckling load (N_{ij}^0, M_{ij}^0, L_{ij}^0, Q_i^0, T_i^0) at the Gauss points;
5 computation of the prebuckling geometric stiffness matrices ($[K_G^0]_p$);
6 solution of the eigenvalue problem, Eq. (34).

The implemented software allows the prebuckling load to be applied as a set of edge tractions, a set of prescribed displacements or a uniform thermal loading. The eigenvalue problem is solved using the subspace iteration algorithm (Bathe and Wilson, 1976).

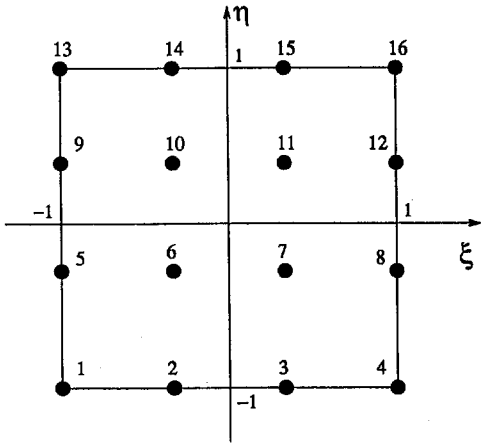
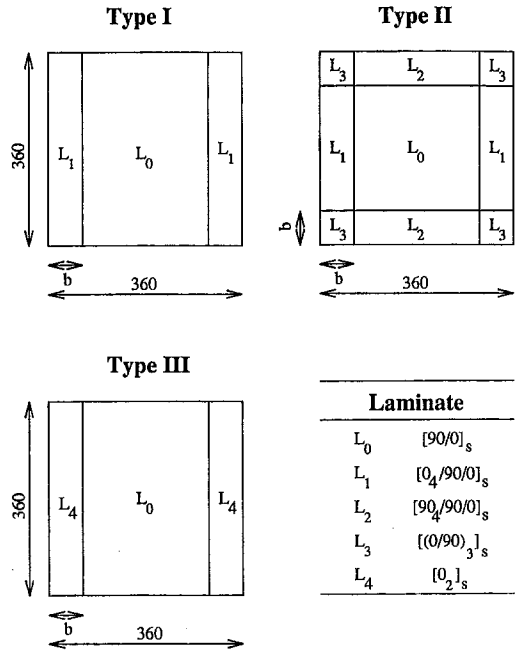


Fig. 2 Bi-cubic Lagrangian isoparametric element

Downloaded 04 May 2010 to 171.66.16.34. Redistribution subject to ASME license or copyright; see http://www.asme.org/terms/Terms_Use.cfm



Laminate	
L_0	$[90/0]_s$
L_1	$[0_4/90/0]_s$
L_2	$[90_4/90/0]_s$
L_3	$[(0/90)_3]_s$
L_4	$[0_2]_s$

Fig. 3 Types of reinforced plates analyzed

Buckling Load of Plates With Tailored Thermal Residual Stresses

The current numerical procedure is suitable for the evaluation of the nonlinear behavior of composite laminates under compressive loads in the presence of thermal residual stresses. Since this work aims at assessing the effect of thermal residual stresses on the buckling load of composite plates, only the analyses of symmetric laminates will be considered. Nonsymmetric laminates in general yield out-of-plane deflections under the action of compressive in-plane loads and there is not a characteristic load that correspond to the loss of stability of the prebuckling state (Singh, Venkateswara Rao, and Iyengar, 1994). The thermal residual stresses also affect the behavior of nonsymmetric laminates but this issue is beyond the scope of this work.

In order to illustrate the effect of the thermal residual stresses on the buckling load of symmetric composite plates we consider a square graphite/epoxy plate with reinforcement that introduces nonzero thermal residual stress resultants. The basic laminate for the analysis is a $[90/0]_s$. Since only symmetric plates are considered, the reinforcement is always placed symmetrically on the edges of the plate. Figure 3 depicts the three plate reinforcement geometries analyzed in this work.

The reinforcement used for plates types I and II consists of four unidirectional plies of width b placed on a $[90/0]_s$ laminate. In plate type I the reinforcement is placed on both sides of the plate with the fibers parallel to the loading direction. In plate type II the reinforcement is placed around the perimeter of the plate forming a symmetric frame. Figure 3 shows the geometry and lamination sequence for each of the configurations considered.

Table 2 Plate descriptions

Designation	Type	b (mm)
R18	I	18
R27	I	27
R45	I	45
R63	I	63
F18	II	18
F27	II	27
F45	II	45
F63	II	63
M0	III	0
M1	III	45
M2	III	90
M3	III	135
M4	III	180

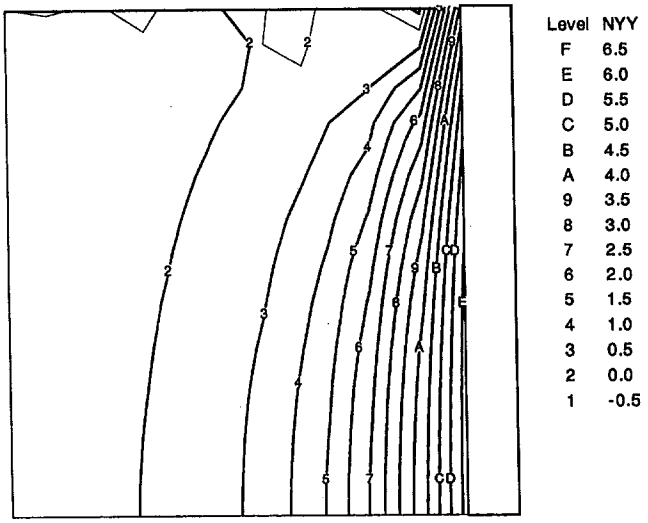


Fig. 4(*a*) Distribution of thermal residual stress resultants N_y^R on plate R18 for a temperature difference of 150°C

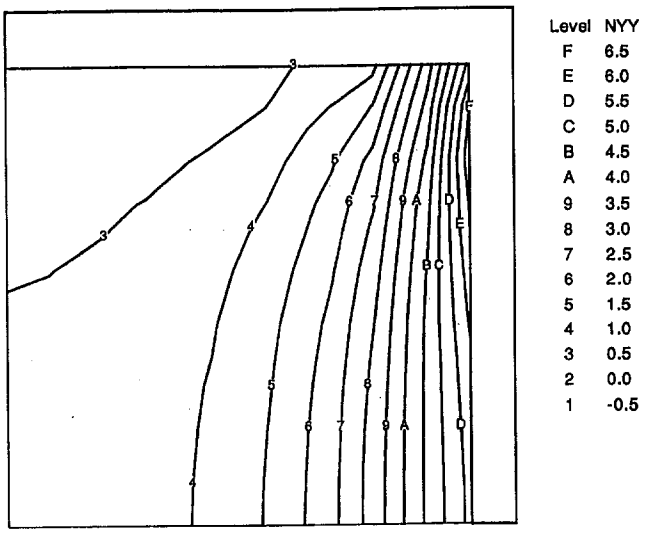


Fig. 4(*b*) Distribution of thermal residual stress resultants N_y^R on plate F18 for a temperature difference of 150°C

Plate types I and II were chosen for analyses because they present different distributions of thermal residual stress resultants. In plate type I the thermal residual stress resultants are particularly high near the edges of the reinforcement. They tend to be zero at the center of the plate due to Saint Venant effects. On the other hand, plate type II is stretched everywhere in both directions due to the frame constraint. Both of these configurations can be easily manufactured and are of practical significance. Direct comparison of the buckling loads for the different configurations may, however, be misleading because their total mass depends on the type of reinforcement and on the width b. In order to present a realistic comparison, the buckling loads for plates types I and II are normalized with respect to a uniform $[90/0]_s$ plate having the same mass as the reinforced plate. That is, the lamina thickness of the reference $[90/0]_s$ plate is taken such that the total mass of the plates are the same.

The third plate configuration considered, plate type III, consists of a $[90/0]_s$ laminate combined with two laminates $[0_4]$

Downloaded 04 May 2010 to 171.66.16.34. Redistribution subject to ASME license or copyright; see http://www.asme.org/terms/Terms_Use.cfm

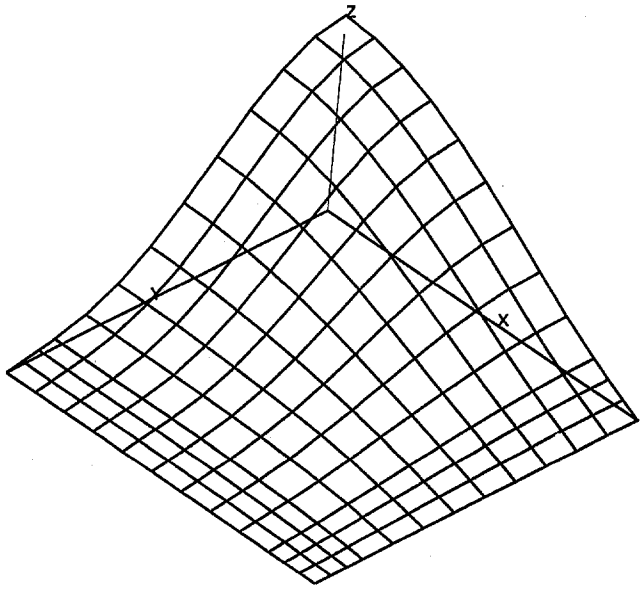


Fig. 5(*a*) Buckling mode for plate F27 for a temperature difference of 0°C

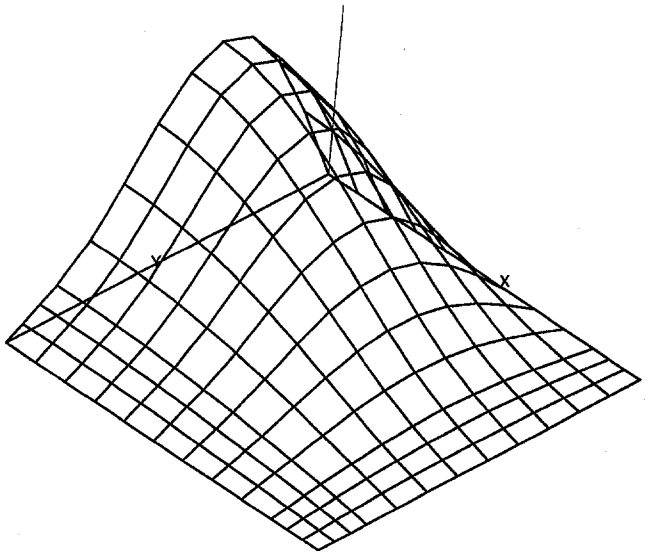


Fig. 5(*b*) Buckling mode for plate F27 for a temperature difference of 60°C

of width b along the edges parallel to the direction of the applied load, forming a square plate as shown in Fig. 3. Unlike plates type I and II, the total mass of plates type III is independent of the width b and equal to the total mass of a uniform $[90/0]_s$ laminate of the same thickness. Direct comparisons of buckling loads can be made in this case. The analyses of plates type III provide a better insight into the problem but these plates are impractical because of the low-strength interface between the two laminates.

The material considered for all analyses is graphite/epoxy T300/5208. The material properties used are given in Table 1, after Adams, Bowles, and Herakovich (1988). The finite element code implemented assumes that the material properties do not vary with temperature. Therefore, a linear thermoelastic problem is solved to compute the thermal residual stress resultants. This approximation is appropriate for most engineering applications and represents an upper bound to reality. A more realistic analysis would account for the variation of the material properties with temperature (Adams, Bowles, and Herakovich, 1988) and incorporate a thermochemical model of the cure process (Ciriscioli and Springer, 1990) or a model of the consolidation process (Domb and Hansen, 1994).

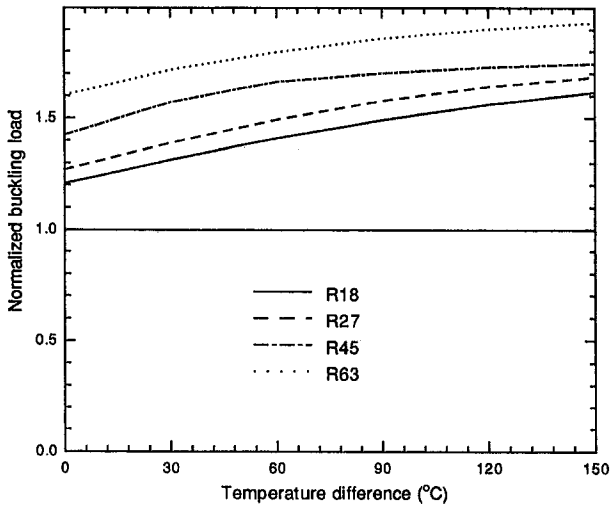


Fig. 6 Normalized buckling loads of plates R18, R27, R45, and R63 as a function of the temperature difference T

The boundary conditions used for the solution of the thermoelastic problem simply eliminate plate rigid-body motions; they do not impose any other external constraint on the plate. In the case of symmetric laminates and in order to improve numerical efficiency, all out-of-plane degrees-of-freedom may be constrained; however, this is not a necessity. The implemented finite element code supports uniform pressure and edge traction loading of each element. It also allows prescribed degrees-of-freedom at each node and a uniform temperature over the entire plate. The boundary conditions imposed in the prebuckling calculation simulates the compression of the plate in a test machine. The edges are assumed simply supported. The out-of-plane displacement w is constrained along the entire perimeter of the plate. The in-plane displacements normal to the edges are constrained. The prebuckling load is applied by prescribing a unit displacement along the y-direction on the upper edge of the plate ($y = 180$ mm). The software computes the prebuckling stress resultants and the reaction forces corresponding to the prescribed displacements.

The plate is discretized into 16 elements arranged in a 4×4 rectangular array. The model uses a total of 169 nodes and

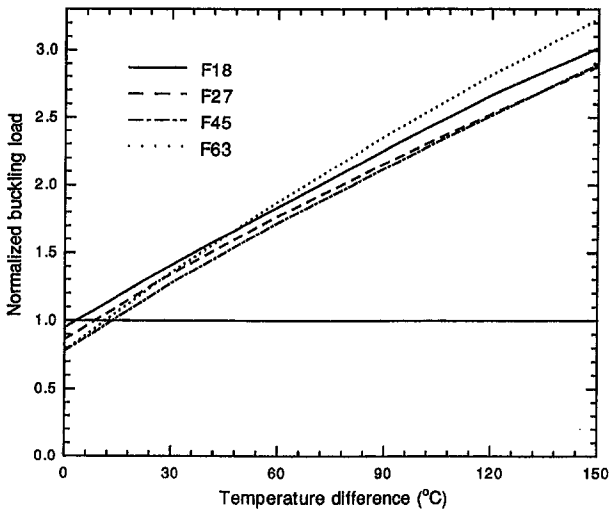


Fig. 7 Normalized buckling loads of plates F18, F27, F45, and F63 as a function of the temperature difference T

Downloaded 04 May 2010 to 171.66.16.34. Redistribution subject to ASME license or copyright; see http://www.asme.org/terms/Terms_Use.cfm

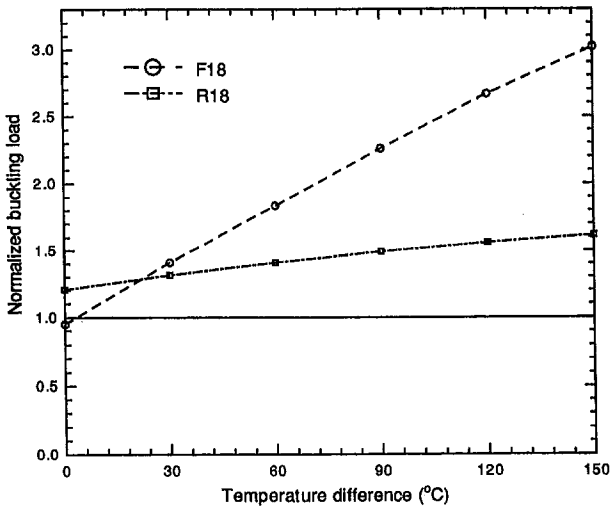


Fig. 8(*a*) Comparison of the normalized buckling loads of plates F18 and R18 as a function of the temperature difference *T*

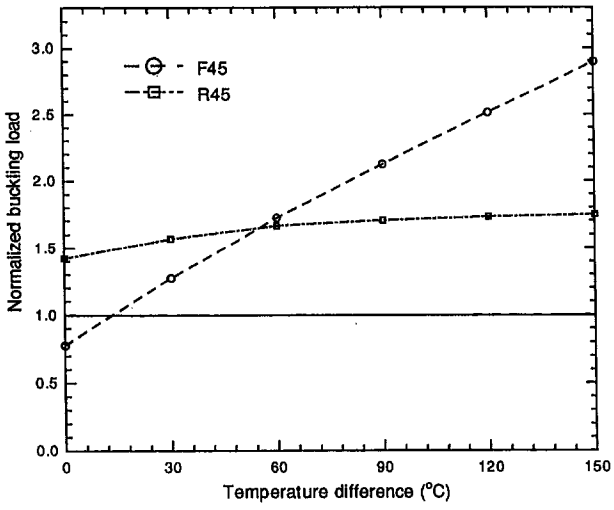


Fig. 8(*c*) Comparison of the normalized buckling loads of plates F45 and R45 as a function of the temperature difference *T*

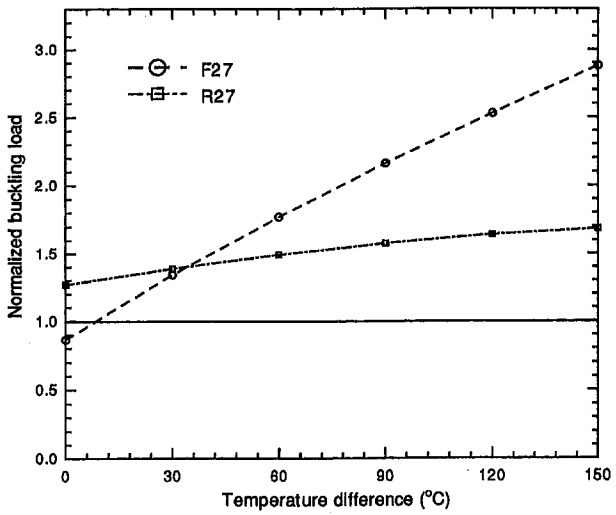


Fig. 8(*b*) Comparison of the normalized buckling loads of plates F27 and R27 as a function of the temperature difference *T*

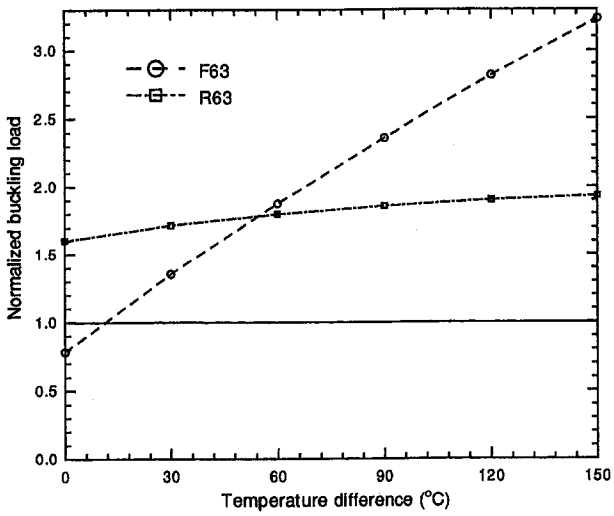


Fig. 8(*d*) Comparison of the normalized buckling loads of plates F63 and R63 as a function of the temperature difference *T*

takes advantage of the symmetry of the problem. Only one fourth of the plate is modeled and two different models are generated: one for symmetric buckling modes and other for antisymmetric buckling modes along the y-direction. The plate buckling load corresponds to the lowest eigenvalue of the two models.

The types of plates analyzed in this work and the nomenclature used to designate them are given in Table 2. Four different values of the reinforcement width b are used in the analyses of plates types I and II: 18, 27, 45, and 63 mm. These figures are also used to identify each plate as shown in the table. These values correspond to a reinforcement width of 10 percent, 15 percent, 25 percent, and 35 percent of the total plate width, respectively.

Plates type III are analyzed for five different values of b. The cases $b = 0$ mm and $b = 180$ mm correspond to uniform plates $[90/0]_s$ (plate M0) and $[0_4]$ (plate M4), respectively. The intermediate values of b, 45, 90, and 135 mm (plates M1, M2, and M3, respectively) correspond to plates involving both laminates $[90/0]_s$ and $[0_4]$. The proportion of laminate $[0_4]$ in the plate increases linearly from 0 percent to 100 percent from plate M0 to plate M4.

The buckling loads of all plates described in Table 2 were calculated using the finite element model described above. The study is limited to assess the influence of the type of reinforcement, its width, and the effect of temperature on the buckling load. In what follows, the temperature difference, T, should be understood as the difference between the temperature at which the plate and reinforcement are stress free (cure, or consolidation, or secondary bonding temperature) and the operating temperature of the structure.

The type of reinforcement affects primarily the distribution of thermal residual stress resultants. This fact is illustrated in Figs. 4(a) and 4(b) that show only one fourth of the plate because of the symmetry of the problem. They compare the distribution of thermal residual stress resultants N_y^R on plates F18 and R18 for a temperature difference of 150°C. It can be seen that in plate R18 the distribution of the stress resultant N_y^R exhibits large gradients near the edge of the reinforcement and is negative at the center of the plate. Plate F18, that uses a reinforcement in the form of a frame around the perimeter of the plate, presents a smoother distribution than plate R18. Also, the stress resultant N_y^R is positive everywhere contributing to an enhance of its behavior in compression.

The existence of the thermal residual stresses affect the buckling load and they may also affect the buckling mode of the plate. The thermal residual stresses vary linearly with the temperature difference. However, the thermal residual stresses affect each buckling mode differently. Therefore, as the temperature difference is changed the buckling mode may also change.

Downloaded 04 May 2010 to 171.66.16.34. Redistribution subject to ASME license or copyright; see http://www.asme.org/terms/Terms_Use.cfm

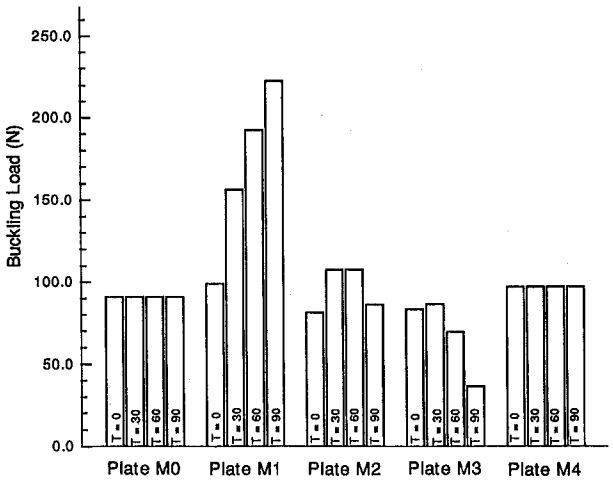


Fig. 9 Buckling loads of plates M0, M1, M2, M3 and M4 for different values of the temperature difference T

As an example, Figs. 5(a) and 5(b) show the buckling modes for plate F27 for $T = 0$°C and $T = 60$°C, respectively. Again, only one fourth of the plate is shown because of the use of symmetry. It can be seen that the buckling mode is symmetric for $T = 0$°C and antisymmetric for $T = 60$°C.

The normalized buckling loads for plates with reinforcement type I is given in Fig. 6. The buckling loads of the plates increase by about 30 percent as the temperature difference increases from 0 deg to 150 deg.

Figure 7 shows the normalized buckling loads for plates with reinforcement type II. It can be seen that the buckling loads increase dramatically with temperature difference. The buckling load for $T = 150$°C is typically more than three times the value for $T = 0$°C. It is also interesting to note that for $T = 0$°C the normalized buckling loads of these plates are less than unity. This means that if the temperature difference is zero the uniform $[90/0]_s$ plate is a more efficient structure in buckling than the plate with reinforcement type II. On the other hand, as the temperature difference increases the reinforced plate becomes far more efficient because of the effect of the thermal residual stresses.

The structural efficiencies of plates with reinforcement types I and II are compared in Fig. 8 as a function of the temperature difference. Figure 8(a) shows the results for $b = 18$ mm, comparing the normalized buckling loads of plates R18 and F18. For temperature differences lower than 30°C reinforcement type I is advantageous. For higher temperature differences the thermal residual stresses induced by the frame construction increase the buckling load significantly compensating for the additional mass in the plate.

A similar trend can be seen in Figs. 8(b)–8(d) comparing reinforcements type I and II for $b = 27$, 45, and 63 mm, respectively. Again, at low-temperature differences, reinforcement type I is more effective and above a certain temperature reinforcement type II is more effective. The temperature difference at which this transition occurs is in the range 30°C to 60°C for the plates studied.

The buckling loads of plates with reinforcement type III are compared in Fig. 9 for different values of temperature difference. Plates M0 and M4 are uniform plates, therefore their buckling loads do not depend on the temperature difference. On the other hand, the thermal residual stresses present on plates M1, M2, and M3 strongly influence their buckling loads. The figure shows that the thermal residual stresses have a beneficial effect on the buckling behavior of plate M1. However, the buckling load of plate M2 initially increases with the temperature difference and then starts decreasing. Also, the thermal residual stresses have a detrimental effect on the buckling load of plate M3. In fact, if this plate is cured (or consolidated) above a critical temperature (corresponding to $T \approx 100$°C) it buckles when cooling down to room temperature in the absence of mechanical loads.

Conclusions

The analyses presented here demonstrate that the existence of thermal residual stresses due to the cure or consolidation of composite laminates may strongly affect the structural behavior of a composite plate. Therefore, an evaluation of these stresses and a judicious analysis of their possible effects must be included in the design procedure for this type of composite structure.

Moreover, with the use of appropriate design practices the thermal residual stresses may be tailored to enhance certain aspects of the structural behavior of composite structures. This involves the choice of the lamina orientation, the position and geometry of the reinforcement, and the fabrication process. An optimization procedure can be combined with the present formulation to determine the design parameters that maximize the structural performance of the plate.

The simple cases analyzed in this work were specifically chosen to demonstrate the potential buckling-load increase that can be achieved by tailoring the thermal residual stresses. However, the actual design of composite structures requires a comprehensive analysis of the overall structural behavior of the plate. Tensile thermal residual stresses are beneficial for the buckling and vibration behavior of plates; however, they may have detrimental effects on the strength and damage tolerance of a plate. Therefore, the maximum possible gain in the buckling load is limited by requirements on the overall performance of the structure. The existence of the thermal residual stresses must be taken into account in the optimization procedure of the structure. Their magnitude and distribution may be tailored to maximize the performance of the structure.

Acknowledgments

The first author acknowledges CNPq (Brazilian National Research Council) for the financial support received for this work under grant 200692/82-8. Additional support came from NSERC (Natural Sciences and Engineering Research Council Canada) grant OGP0003663.

References

Adams, D. S., Bowles, D. E., and Herakovich, C. T., 1988, "Thermally induced transverse cracking in graphite-epoxy cross-ply laminates," *Environmental effects on composite materials,* Vol. 3, ed., G. S. Springer, ed., Technomic, Lancaster, PA, pp. 247–274.

Bathe, K.-J., and Wilson, E. L., 1976, *Numerical methods in finite element analysis,* Prentice-Hall, Englewood Cliffs, NJ.

Ciriscioli, P. R., and Springer, G. S., 1990, "Smart autoclave cure of composites," Technomic, Lancaster, PA.

Domb, M. M., and Hansen, J. S., 1994, "Development of free edge effect during processing of semicrystalline thermoplastic composites," *AIAA J.,* Vol. 31, No. 5, pp. 1029–1033.

Heppler, G. R., and Hansen, J. S., 1986, "A Mindlin Element for Thick and Deep Shells," *Computer Methods in Applied Mechanics and Engineering,* V. 54, No. 1, Jan., pp. 21–47.

Jones, R. M., 1975, *Mechanics of Composite Materials,* McGraw-Hill, New York.

Mindlin, R. D., 1951, "Influence of Rotary Inertia and Shear on Flexural Motions of Isotropic Elastic Plates," ASME JOURNAL OF APPLIED MECHANICS, Vol. 18, pp. 31–38.

Novozhilov, V. V., 1953, *Foundations of the non-linear theory of elasticity,* Graylock, Rochester, NY.

Sai Ram, K. S., and Sinha, P. K., 1992, "Hygrothermal effects on the buckling of composite laminated plates," *Composite Structures,* Vol. 21, pp. 233–247.

Singh, G., Venkateswara Rao, G., and Iyengar, N. G. R., 1994, "Thermal post-buckling behavior of laminated composite plates," *AIAA J.,* Vol. 32, No. 6, pp. 1336–1338.

Sun, L. X., and Hsu, T. R., 1990, "Thermal buckling of laminated composite plates with transverse shear deformation," *Int. J. Computers & Structures,* Vol. 36, pp. 893–899.

Zienkiewicz, O. C., and Taylor, R. L., 1989, *The finite element method,* 4th ed., McGraw-Hill, New York.

Downloaded 04 May 2010 to 171.66.16.34. Redistribution subject to ASME license or copyright; see http://www.asme.org/terms/Terms_Use.cfm

Micromechanical Modeling of Creep Behavior in Particle-Reinforced Silicone-Rubber Composites

Chao-Hsun Chen
Associate Professor.

Chaing-Ho Cheng
Former Graduate Student.

Institute of Applied Mechanics,
National Taiwan University,
Taipei 10764, Taiwan R.O.C.

A micromechanically based composite model is proposed to study the viscoelastic behavior of solid-filled rubber composites. A nonlinear So-Chen's (1991) mechanical model which describes the viscoelastic behavior of the rubber matrix is proposed to relate volume-average deformation and stress within the two-phase composite inclusion to the remote (macroscopic) fields. The influence of the volume fractions of inclusions on the overall creep strain of a rubber-matrix composite is investigated at the level of dilute concentration. The creep rate of the rubber matrix, which depends nonlinearly on the creep strain and the primary creep and secondary creep resulting from the viscous flow of creep deformation, is also considered in addition to the usual steady-state, or secondary, creep. The method developed for the calculation of the incremental process is based upon Eshelby's (1957) equivalence principle of an inhomogeneity-transformation problem and Mori-Tanaka's (1973) idea of mean-field stress. In order to examine the applicability of the model as well as the nonlinear stretch parameter, a series of experiments on solid-filled silicone rubbers has been carried out, which included constant rate of tensile tests and creep tests. It is demonstrated that this simple, albeit approximate micromechanical modeling is capable of predicting the volume fraction dependence of the time dependent creep, with characteristic consistency with the known elastic behavior.

1 Introduction

For nonlinear vicoelastic material, even under very small strain conditions, the stress-strain relationship is still nonlinear and the Boltzmann's superimposition method can no longer be applied. We can find suitable nonlinear elements to form the nonlinear mechanical model, such as So-Chen's (1991) nonlinear four-element Burger's (NFEB) model (Fig. 1), which can well describe the nonlinear mechanical behavior. They treated each individual molecular chain as the "entropy spring" and employed the rubber elasticity formula to replace the linear spring. Also, from the concept of the nonlinear activation energy jump over the energy barrier, they employed Eyring's activation energy dashpot to replace Newton's dashpot.

This paper is concerned with the quantitative determination of the time-dependent creep of a rubber-matrix composite, where solid particles are homogeneously dispersed in the rubber matrix. The particles are assumed to remain elastic, but at elevated temperature the rubber matrix may undergo both primary (transient) and the secondary (steady-state) creep. The creep rate of rubbers usually depends nonlinearly on the stress. The matrix and particles will be taken to be perfectly bonded together, without any void nucleation or growth. Here the composite as a whole is isotropic, and its overall creep behavior will be affected by the volume function of the particles. When such a composite is subjected to a constant, external stress, the initial response is elastic, and its overall elastic strain can be determined from its effective moduli.

Contributed by the Applied Mechanics Division of THE AMERICAN SOCIETY OF MECHANICAL ENGINEERS for publication in the ASME JOURNAL OF APPLIED MECHANICS.

Discussion on this paper should be addressed to the Technical Editor, Professor Lewis T. Wheeler, Department of Mechanical Engineering, University of Houston, Houston, TX 77204-4792, and will be accepted until four months after final publication of the paper itself in the ASME JOURNAL OF APPLIED MECHANICS.

Manuscript received by the ASME Applied Mechanics Division, Aug. 18, 1994; final revision, Aug. 31, 1995. Associate Technical Editor: R. Abeyaratne.

As the stress-strain relation of the solid-filled rubber composite is highly nonlinear, we have used the secant elastic moduli in our theoretical derivation to capture the elastic modulus of every loading status. The theory makes use of a linear comparison material, whose elastic moduli at every instant is chosen to coincide with the average secant moduli of the rubber matrix to reflect its nonlinear state. Following Eshelby's (1957) equivalent-inclusion principle and Mori-Tanaka's (1973) mean-field method, the composite is subsequently replaced by the comparison material filled with equivalent transformation strains. This approach allows one to find the average stress of the matrix in terms of the macroscopic stress, and then by appealing to the constitutive equation of the rubber matrix, the overall stress-strain relation of the two-phase system can be easily determined.

This paper is organized as follows: the constitutive equations of the rubber matrix will be briefly recapitulated first, and then the initial stress state of the rubber matrix, suitable for the calculation of the initial creep rate, will be derived. The micromechanical principles involved in assessing the stress variation of the matrix following an incremental creep will be established subsequently, and the overall creep will be presented at the end. This result will then be checked by comparison with results from a series of experiments for glassbead-reinforced silicone rubber specimens.

2 Neo-Hookean Rubber Elasticity and the Associated Secant Moduli

Let λ_i be the principal stretches of deformation associated with the Cauchy-Green deformation tensor so that, for a Neo-Hookean material characterized by a single constant μ, the principal Cauchy stress components σ_{kk} are determined by (Truesdell and Noll, 1965):

$$\sigma_{kk} = \mu\lambda_k^2 - p, \quad k = 1, 2, 3, \tag{2.1}$$

Copyright © 1997 by ASME

Downloaded 04 May 2010 to 171.66.16.34. Redistribution subject to ASME license or copyright; see http://www.asme.org/terms/Terms_Use.cfm

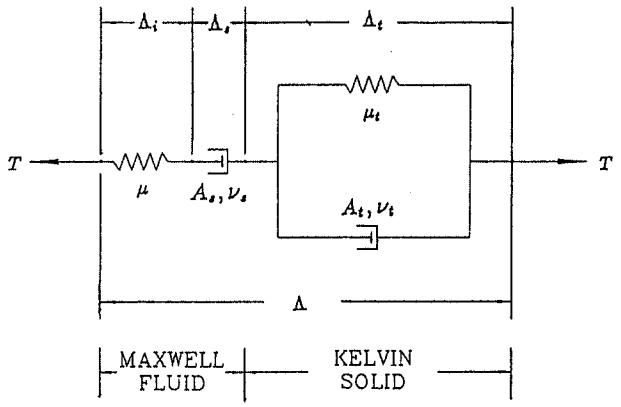


Fig. 1 So-Chen's nonlinear four-element burger's model

where p is an unknown hydrostatic stress. The above equation is augmented by the constant volume constraint relation:

$$\lambda_1\lambda_2\lambda_3 = 1. \tag{2.2}$$

Consider now the following generalized tensile loading:

$$\sigma_{11} = P, \quad \sigma_{22} = \sigma_{33} = Q, \tag{2.3}$$

where Q vanishes for a simple tensile loading. It follows from (2.1) and (2.2) that the associated deformation is

$$\lambda_1 = \lambda(R) = M(R) + \frac{R}{3\mu M(R)} \tag{2.4}$$

$$\lambda_2 = \lambda_3 = \sqrt{\lambda}^{-1} \tag{2.5}$$

$$M(R) = \left\{\frac{1}{2} + \left[\frac{1}{4} - \left(\frac{R}{3\mu}\right)^3\right]^{1/2}\right\}^{1/3} \tag{2.6}$$

$$R = P - Q \tag{2.7}$$

and

$$R = \mu\left(\lambda^2 - \frac{1}{\lambda}\right). \tag{2.8}$$

It is clear from the above that the desired material constant μ may be deduced by fitting (2.8) to an experimentally measured curve for the simple tension test

$$R = P = \sigma_{11} = \sigma, \quad Q = 0, \tag{2.9}$$

recalling that the three principal engineering strains ϵ_{kk} are related to the principal stretches by $\epsilon_{kk} = \lambda_k - 1$.

The generalized tensile loading (2.3) and the strains may be made to satisfy the linear elasticity relations. The secant shear modulus, μ^s, and secant bulk modulus, κ^s, follow from the usual definitions. We have

$$\kappa^s = \frac{1}{3}\left(\frac{R + 3Q}{\lambda + 2\lambda^{-1/2} - 3}\right) \tag{2.10}$$

$$\mu^s = \frac{1}{2}\left(\frac{R}{\lambda - \lambda^{-1/2}}\right). \tag{2.11}$$

For rubbers, nonlinear behavior exhibits even under small strains. The linear mechanical model can not be applied to such materials directly.

So-Chen's (1991) NFEB model is employed here to describe the nonlinear viscoelastic behavior of the elastomers. The total nonlinear stretch Λ can be expressed as follows:

$$\Lambda(t) = \frac{T}{\mu} + A_s \sinh(\nu_s T)t + \frac{T}{\mu_t}\left\{1 - \frac{2}{\nu_t T}\tan^{-1}\left[\tanh\left(\frac{\nu_t T}{2}\right)\exp(-A_t\nu_t\mu_t t)\right]\right\} \tag{2.12}$$

where

$$\Lambda = \lambda - \frac{1}{\lambda^2}. \tag{2.13}$$

There are six material parameters, namely, μ, A_s, ν_s, μ_t, A_t, and ν_t, in the nonlinear model as well as in Eq. (2.12). In general, some experimental data from the two creep curves using the method of least squares are required to determine these six parameters. This equation will be proved correct by experimental results.

Equation (2.12) leads to the total nonlinear stretch rate, $\dot{\Lambda}$, as

$$\dot{\Lambda} = A_s \sinh(\nu_s T) + \frac{2A_t \tanh\left(\frac{\nu_t T}{2}\right)\exp(-\nu_t\mu_t A_t t)}{1 - \left[\tanh\left(\frac{\nu_t T}{2}\right)\exp(-\nu_t\mu_t A_t t)\right]^2}. \tag{2.14}$$

Equation (2.13) can be recasted as

$$\dot{\lambda} = \frac{\dot{\Lambda}}{1 + \frac{2}{\lambda^3}}. \tag{2.15}$$

At the initial stage, the rubber matrix satisfies the incompressibility constraint. When the creep behavior starts, the incompressible constraint no longer holds. As its difference is still small compared to the total deformation, for convenience of computation, here, we approximate the relation between true stress, σ, and engineering stress, T, by using the incompressible constraint of rubber elasticity as

$$T = \sigma\lambda_2\lambda_3 \approx \frac{\sigma}{\lambda_1} = \frac{\sigma}{\lambda}. \tag{2.16}$$

Substituting Eqs. (2.14) and (2.16) into Eq. (2.15) leads to the stretch rate, $\dot{\lambda}$, as

$$\dot{\lambda} = \left\{A_s \sinh\left(\nu_s\frac{\sigma}{\lambda}\right) + \frac{2A_t \tanh\left(\frac{\nu_t\sigma}{2\lambda}\right)\exp(-\nu_t\mu_t A_t t)}{1 - \left[\tanh\left(\frac{\nu_t\sigma}{2\lambda}\right)\exp(-\nu_t\mu_t A_t t)\right]^2}\right\} \Big/ \left(1 + \frac{2}{\lambda^3}\right) = F(\sigma, \lambda, t). \tag{2.17}$$

As the matrix phase in a composite system often exits in a triaxial stress state, we can generalize Eq. (2.17) to uniaxial systems for an isotropic and incompressible material by employing the plastic flow idea. Therefore, the effective stretch rate, $\dot{\lambda}_e$, can be generalized as a function of Von-Misses's effective stress, σ_e, effective stretch, λ_e, and time, t, as

$$\dot{\lambda}_e = F(\sigma_e, \lambda_e, t). \tag{2.18}$$

Downloaded 04 May 2010 to 171.66.16.34. Redistribution subject to ASME license or copyright; see http://www.asme.org/terms/Terms_Use.cfm

The differentiation of Eq. (2.2) can be written as

$$\frac{d\lambda_1}{\lambda_1} + \frac{d\lambda_2}{\lambda_2} + \frac{d\lambda_3}{\lambda_3} = 0 \tag{2.19}$$

or

$$d(\ln \lambda_1) + d(\ln \lambda_2) + d(\ln \lambda_3) = 0. \tag{2.19a}$$

For small deformation, Eq. (2.19*a*) can be reduced to the linear elasticity relation

$$d\epsilon_{11} + d\epsilon_{22} + d\epsilon_{33} = 0. \tag{2.20}$$

Equations (2.19*a*) and (2.20) show that for large deformation we can replace ϵ_i with $\ln \lambda_i$ and replace ϵ_e with $\ln \lambda_e$. By these analogous results, in the principle direction we have assumed the effective stress, σ_e, and effective stretch, λ_e, relation of large deformation is as follows:

$$\sigma_e = \frac{1}{\sqrt{2}}[(\sigma_{11} - \sigma_{22})^2 + (\sigma_{22} - \sigma_{33})^2 + (\sigma_{33} - \sigma_{11})^2]^{1/2} \tag{2.21a}$$

$$\ln \lambda_e = \frac{\sqrt{2}}{3}[(\ln \lambda_1 - \ln \lambda_2)^2 + (\ln \lambda_2 - \ln \lambda_3)^2 + (\ln \lambda_3 - \ln \lambda_1)^2]^{1/2}. \tag{2.21b}$$

Substituting Eqs. (2.21*a*) and (2.21*b*) into Eq. (2.18), we have the effective stretch rate $\dot{\lambda}_e$ relation. Following the Prandtl-Reuss flow rule idea, we have assumed that the flow rule of large deformation is

$$d(\ln \lambda_i) = \frac{3}{2}\frac{d(\ln \lambda_e)}{\sigma_e}\sigma'_{ii}, \quad i = 1 \sim 3, \tag{2.22}$$

where $\boldsymbol{\sigma}'$ is the deviatoric stress. Equation (2.22) can be rewritten as

$$d\epsilon_{ii} = d\lambda_i = \frac{3}{2}\frac{d\lambda_e}{\lambda_e}\frac{\lambda_i}{\sigma_e}\sigma'_{ii} = \frac{3}{2}\frac{F(\lambda_e, \sigma_e t)\lambda_i}{\lambda_e \sigma_e}\sigma'_{ii}dt \tag{2.23}$$

or

$$\dot{\epsilon}_{ii} = \frac{3}{2}\frac{F(\lambda_e, \sigma_e, t)\lambda_i}{\lambda_e \sigma_e}\sigma'_{ii}. \tag{2.24}$$

3 The Initial Stress of the Rubber Matrix

Consider a representative volume of a glass bead-reinforced silicone rubber which is assumed to be statistically homogeneous and macroscopically isotropic. The silicone rubber is referred to as the matrix, and the volume fraction of the glass bead is denoted by f_1. Following the exposition of Tandon and Weng (1988) and Weng (1990), we introduce an identically shaped of comparison sample made of pure silicone rubber. Let the composite and the pure silicone rubber comparison sample both be subjected to the boundary traction, which will give rise to a uniform generalized tensile state

$$\bar{\boldsymbol{\sigma}} = (\bar{P}, \bar{Q}), \quad \bar{R} = \bar{P} - \bar{Q}. \tag{3.1}$$

The strain, $\boldsymbol{\epsilon}^o$, in the comparison sample is related to the above by

$$\bar{\boldsymbol{\sigma}} = \mathbf{C}_o^s \boldsymbol{\epsilon}^o, \tag{3.2}$$

The average strain, $\boldsymbol{\epsilon}^{(o)}$, $\boldsymbol{\sigma}^o$ in the matrix of the composite cannot be the same as $\boldsymbol{\epsilon}^o$, $\bar{\boldsymbol{\sigma}}$ and may be represented by

$$\boldsymbol{\sigma}^{(o)} = \bar{\boldsymbol{\sigma}} + \tilde{\boldsymbol{\sigma}} = \mathbf{C}_o^s \boldsymbol{\epsilon}^{(o)} = \mathbf{C}_o^s(\boldsymbol{\epsilon}^o + \tilde{\boldsymbol{\epsilon}}). \tag{3.3}$$

The introduction of an equivalent transformation strain, $\boldsymbol{\epsilon}^*$, combined with Mori-Tanaka's concept, leads to the identity

$$\boldsymbol{\sigma}^{(1)} = \mathbf{C}_1(\boldsymbol{\epsilon}^o + \tilde{\boldsymbol{\epsilon}} + \boldsymbol{\epsilon}^p) = \mathbf{C}_o^s(\boldsymbol{\epsilon}^o + \tilde{\boldsymbol{\epsilon}} + \boldsymbol{\epsilon}^p - \boldsymbol{\epsilon}^*) \tag{3.4}$$

where $\boldsymbol{\epsilon}^p$ and $\boldsymbol{\epsilon}^*$ are related by

$$\boldsymbol{\epsilon}^p = \mathbf{S}_o^s \boldsymbol{\epsilon}^* \tag{3.5}$$

in which $\mathbf{S}_o^s$ is the Eshelby tensor (calculated in the elastic comparison material) associated with spherical inclusions and $\mathbf{C}_o^s$.

Finally, since $\bar{\boldsymbol{\sigma}}$ of (3.1) is also the uniform stress of the composite, we have

$$\bar{\boldsymbol{\sigma}} = f_1 \boldsymbol{\sigma}^{(1)} + (1 - f_1)\boldsymbol{\sigma}^{(o)}, \tag{3.6}$$

where f_1 is the volume fraction of the glass bead. Following the above equations (3.3), (3.4), (3.5), and (3.6) we have

$$\boldsymbol{\epsilon}^* = (\mathbf{A}^{-1} - (1 - f_1)\mathbf{S}^s - f_1\mathbf{I})^{-1} \cdot \boldsymbol{\epsilon}^o \tag{3.7}$$

$$\mathbf{A}^{-1} = \mathbf{I} - \mathbf{C}_o^{s^{-1}}\mathbf{C}_1. \tag{3.8}$$

The total strain of the composite is given by the weighted average of those strains of the matrix and inclusion, i.e.,

$$\bar{\boldsymbol{\epsilon}} = (1 - f_1)\boldsymbol{\epsilon}^{(o)} + f_1\boldsymbol{\epsilon}^{(1)} = f_1\boldsymbol{\epsilon}^* + \boldsymbol{\epsilon}^o. \tag{3.9}$$

Substituting (3.7) into the above and using (3.2), we finally conclude that

$$\bar{\boldsymbol{\sigma}} = \mathbf{C}^s \bar{\boldsymbol{\epsilon}}, \tag{3.10}$$

where

$$\mathbf{C}^s = C_o^s[\mathbf{I} + f_1(\mathbf{A}^{-1} - (1 - f_1)\mathbf{S}^s - f_1\mathbf{I})^{-1}]^{-1} \tag{3.11}$$

and $\bar{C}^s$ is but the secant elasticity tensor for the composite at the stress level (3.1).

For convenience of measurement in the simple tension test, we need to use the relation between the engineering stress, T, and true stress, $\bar{\sigma}_{11}$, as

$$T = \bar{\sigma}_{11}(1 + \bar{\epsilon}_{33})(1 + \bar{\epsilon}_{22}). \tag{3.12}$$

The final product of this section is the composite stress-strain relations (3.11). The secant elasticity tensor, $\bar{C}^s$, however, depends on $\bar{\boldsymbol{\sigma}}$ via $\boldsymbol{\sigma}^{(o)}$, the stress of the matrix of the composite. Thus, an iteration procedure must be improvised to facilitate the computation. We use the simpler hard-bead approximation to illustrate the procedure described as follows. Using (2.10) and (2.11), μ_o^s and κ_o^s are derived; therefore, C_o^s is obtained. Using (3.7), (3.9), and (3.11), $\bar{C}^s$ and $\bar{\boldsymbol{\epsilon}}$ are derived, respectively. Finally, via (3.3), we have $\boldsymbol{\sigma}^{(o)}$. Then, we go back to (2.10) and (2.11) to check $\mathbf{C}_o^s$. By this iteration procedure, we can have the stress-strain solution of this composite system.

4 The Micromechanics of Creep Behavior in Solid-Filled Rubber Composites

As the stress-strain relation of the solid-filled rubber composites is highly nonlinear, to capture the elastic response for each time increment, we have used the secant moduli approach in our theoretical derivation. In Section 3 we made use of a linear comparison material, whose elastic moduli at every instant is chosen to coincide with the secant moduli of the rubber matrix to reflect its nonlinear state. Following Eshelby's (1957) equivalent-inclusion principle and Mori-Tanaka's (1973) mean stress by the comparison material filled with equivalent transformation strains, the secant moduli, $\mathbf{C}_o^s$, of different volume fractions of solid-filled rubber composites under any loading status can be expressed in terms of the functions of stress of the rubber matrix, $\boldsymbol{\sigma}^{(o)}$. From Section 3, we have the stress distribution of the rubber matrix, $\boldsymbol{\sigma}^{(o)}$, and the strain of the matrix, $\boldsymbol{\epsilon}^{(o)}$, under a given stress, $\bar{\boldsymbol{\sigma}}$, individually, as

Downloaded 04 May 2010 to 171.66.16.34. Redistribution subject to ASME license or copyright; see http://www.asme.org/terms/Terms_Use.cfm

$$\boldsymbol{\sigma}^{(o)} = \mathbf{C}_o^s(\mathbf{A}^{-1} - \mathbf{S}_o^s) \times [\mathbf{A}^{-1} - (1 - f_1)\mathbf{S}_o^s - f_1\mathbf{I}]^{-1}\mathbf{C}_o^{s^{-1}}\bar{\boldsymbol{\sigma}}, \quad (4.1a)$$

$$\boldsymbol{\epsilon}^{(o)} = (\mathbf{A}^{-1} - \mathbf{S}_o^s) \times [\mathbf{A}^{-1} - (1 - f_1)\mathbf{S}_o^s - f_1\mathbf{I})]^{-1}\mathbf{C}_o^{s^{-1}}\bar{\boldsymbol{\sigma}}, \quad (4.1b)$$

$$\mathbf{A} = \mathbf{I} - \mathbf{C}_o^{s^{-1}}\mathbf{C}_1. \quad (4.1c)$$

Substitution of Eqs. (4.1*a*) and (4.1*b*) into Eqs. (2.17) and (2.24) leads to the creep rate of the rubber matrix. Under a given $\bar{\boldsymbol{\sigma}}$, the initial creep rate of the rubber matrix then can be calculated, and this, over a time increment dt, generates an incremental creep strain

$$d\boldsymbol{\epsilon}^c = \dot{\boldsymbol{\epsilon}}dt. \quad (4.2)$$

Such is also the case for any subsequent time increment. Our concern now is the nature of the stress redistribution between the inclusions and rubber matrix following an incremental creep, with $\bar{\boldsymbol{\sigma}}$ kept constant.

In general, an incremental creep in the rubber matrix is also accompanied by a stress reduction, which has to be carried over by the elastic inclusions to maintain a constant $\bar{\boldsymbol{\sigma}}$. For a nonlinear matrix experiencing both primary and secondary creep, the determination of a precise solution for such a problem is not simple. Here we use the approximate method suggested previously by the writers Zhu and Weng (1987, 1989, 1990), which was originally formulated for the self-consistent determination of the time-dependent creep of polycrystals (Weng, 1981). This model takes the constraint power of the matrix to be elastic and, therefore, is more suitable for a small creep strain range. Since our matrix is rubber material, its stress-strain relation is highly nonlinear, so the secant moduli approach is employed here. Also, in our creep test, we can only fix a constant loading force instead of the constant loading stress, $\bar{\boldsymbol{\sigma}}$. Due to the large deformation of the rubber matrix, the loading stress, $\bar{\boldsymbol{\sigma}}$, increases as the creep deformation increases. The stress increment, $d\bar{\boldsymbol{\sigma}}$, is due to the reduction of the cross-section area of the specimen. This stress increment doesn't cause the elastic strain to increase, but it does contribute to the stretch rate, $\dot{\lambda}$, of the next time-increment stage. Therefore, the stress increment, $d\bar{\boldsymbol{\sigma}}$, needs to be included for each time increment stage.

For solid-filled rubber composites, we have also employed the same idea, of that within the time interval dt, when there is a creep strain $d\boldsymbol{\epsilon}^c$ of the rubber matrix then $d\bar{\boldsymbol{\epsilon}}$ will also increase. As a result, the cross-section area A will decrease, causing $d\boldsymbol{\sigma}$, in turn, to increase. Therefore, from (4.1*a*) $d\boldsymbol{\sigma}^{(o)}$ will also increase. At the next time-step, the increase of $d\boldsymbol{\sigma}^{(o)}$ must be included in the calculation of $d\boldsymbol{\epsilon}^c$.

To estimate the average stress variations in both phases, we first take the inclusions out and let the matrix creep homogeneously over a short time dt. The inclusions are now subjected to a boundary traction corresponding to a homogeneous stress, $\mathbf{C}_1 d\epsilon^c$, so that they fit perfectly into the deformed holes.

A negative traction, $-\mathbf{C}_1 d\epsilon^c$, is now applied to the bonded interfaces to remove the unwanted traction discontinuity. This is equivalent to having an Eshelby's "stress-free" strain,

$$d\boldsymbol{\epsilon}^* = -d\boldsymbol{\epsilon}^c, \quad (4.3)$$

in the context of the inhomogeneity/transformation problem (see also Mura, 1987). Then, by means of Mori and Tanaka's (1973) concept of mean-field approximation, the average stress variation in the rubber matrix can be written as

$$d\boldsymbol{\sigma}^{(o)} = d\tilde{\boldsymbol{\sigma}} = \mathbf{C}_o^s d\tilde{\boldsymbol{\epsilon}}, \quad (4.4)$$

in parallel with (3.3). Similarly, in parallel with (3.4), the mean-stress variation of the inclusions can be cast as

$$d\boldsymbol{\sigma}^{(1)} = d\tilde{\boldsymbol{\sigma}} + d\boldsymbol{\sigma}^p = \mathbf{C}_1(d\tilde{\boldsymbol{\epsilon}} + d\boldsymbol{\epsilon}^{pt} - d\boldsymbol{\epsilon}^*), = \mathbf{C}_o^s(d\tilde{\boldsymbol{\epsilon}} + d\boldsymbol{\epsilon}^{pt} - d\boldsymbol{\epsilon}^* - d\boldsymbol{\epsilon}^{**}), \quad (4.5)$$

noting that a stress-free transformation strain, $d\boldsymbol{\epsilon}^*$, already exists in the inclusion. Strain $d\boldsymbol{\epsilon}^{**}$ is Eshelby's equivalent transformation strain, and, together with $d\boldsymbol{\epsilon}^*$, they form the total transformation strain, such that

$$d\boldsymbol{\epsilon}^p = \mathbf{S}_o^s(d\boldsymbol{\epsilon}^* + d\boldsymbol{\epsilon}^{**}). \quad (4.6)$$

The boundary condition $d\bar{\boldsymbol{\sigma}} = \Sigma f_r d\boldsymbol{\sigma}^{(r)} = 0$ further leads to

$$d\tilde{\boldsymbol{\sigma}} = -f_1 d\boldsymbol{\sigma}^{pt}, \quad (4.7)$$

or

$$d\tilde{\boldsymbol{\epsilon}} = -f_1[d\boldsymbol{\epsilon}^p - (d\boldsymbol{\epsilon}^* + d\boldsymbol{\epsilon}^{**})] = -f_1(\mathbf{S}_o^s - \mathbf{I})(d\boldsymbol{\epsilon}^* + d\boldsymbol{\epsilon}^{**}). \quad (4.8)$$

To find the overall strain variation over dt, we recall that a uniform creep strain, $d\boldsymbol{\epsilon}^c$, took place before the inclusions were placed back into the deformed holes. It follows that

$$d\bar{\boldsymbol{\epsilon}}^c = d\boldsymbol{\epsilon}^c + (1 - f_1)d\tilde{\boldsymbol{\epsilon}} + f_1(d\tilde{\boldsymbol{\epsilon}} + d\boldsymbol{\epsilon}^p) = d\boldsymbol{\epsilon}^c + f_1(d\boldsymbol{\epsilon}^* + d\boldsymbol{\epsilon}^{**}), \quad (4.9)$$

where the strain increment, $d\boldsymbol{\epsilon}^c$, is the inclusion's deformation after the inclusion is taken out. Meanwhile, the composite now has the uniform deformation strain, $d\bar{\boldsymbol{\epsilon}}^c$. Therefore, we need to add $d\bar{\boldsymbol{\epsilon}}^c$ to form the total strain increment, $d\bar{\bar{\boldsymbol{\epsilon}}}^c$. Using Eqs. (4.5), (4.6), and (4.8), $d\boldsymbol{\epsilon}^* + d\boldsymbol{\epsilon}^{**}$ then can be derived as

$$d\boldsymbol{\epsilon}^* + d\boldsymbol{\epsilon}^{**} = \mathbf{B}_1 d\boldsymbol{\epsilon}^*, \quad (4.10)$$

where

$$\mathbf{B}_1 = (\mathbf{I} - (1 - f_1)\mathbf{A}\mathbf{S}_o^s - f_1\mathbf{A})^{-1}(\mathbf{I} - \mathbf{A}) \quad (4.10a)$$

$$\mathbf{A} = (\mathbf{I} - \mathbf{C}_o^{s^{-1}}\mathbf{C}_1). \quad (4.10b)$$

Substituting Eqs. (4.3) and (4.10) into Eq. (4.9) leads to

$$d\bar{\bar{\boldsymbol{\epsilon}}}^c = (\mathbf{I} - f_1\mathbf{B}_1)d\boldsymbol{\epsilon}^c. \quad (4.11)$$

Therefore, the stress increment of the matrix, $d\boldsymbol{\sigma}^{(o)}$, and the strain increment of the matrix, $d\boldsymbol{\epsilon}^{(o)}$, then can be derived as

$$d\boldsymbol{\sigma}^{(o)} = f_1\mathbf{C}_o^s(\mathbf{S}_o^s - \mathbf{I})\mathbf{B}_1 d\boldsymbol{\epsilon}^c \quad (4.12)$$

$$d\boldsymbol{\epsilon}^{(o)} = f_1(\mathbf{S}_o^s - \mathbf{I})\mathbf{B}_1 d\boldsymbol{\epsilon}^c + d\boldsymbol{\epsilon}^c. \quad (4.13)$$

The total creep strain of the composite system, $\bar{\bar{\boldsymbol{\epsilon}}}$, and the rubber matrix, $\bar{\bar{\boldsymbol{\epsilon}}}^{(o)}$, after a time increment can be written as

$$\boldsymbol{\epsilon}(t + dt) = \boldsymbol{\epsilon}(t) + d\boldsymbol{\epsilon}(t) \quad (4.14)$$

$$\boldsymbol{\epsilon}^{(o)}(t + dt) = \boldsymbol{\epsilon}^{(o)}(t) + d\boldsymbol{\epsilon}^{(o)}(t). \quad (4.15)$$

The stress increment, $d\bar{\boldsymbol{\sigma}}$, due to the reduction of the cross-section area, is

$$d\bar{\sigma}_{11} = \frac{T}{(1 + \bar{\epsilon}_{22} + d\bar{\epsilon}_{22})^2} - \frac{T}{(1 + \bar{\epsilon}_{22})^2} \quad (4.17)$$

$$d\bar{\sigma}_{22} = 0 = d\bar{\sigma}_{33}. \quad (4.17a)$$

Due to the reduction of the cross-section area, from Eq. (4.1) we can get the stress increments of the rubber matrix as

$$d\bar{\boldsymbol{\sigma}}^{(o)} = \mathbf{C}_o^s(\mathbf{A}^{-1} - \mathbf{S}_o^s) \times (\mathbf{A}^{-1} - (1 - f_1)\mathbf{S}_o^s - f_1\mathbf{I})^{-1}\mathbf{C}_o^{s^{-1}}d\bar{\boldsymbol{\sigma}}. \quad (4.18)$$

Therefore, the total stress of the rubber matrix after a time increment is

$$\boldsymbol{\sigma}^{(o)}(t + dt) = \boldsymbol{\sigma}^{(o)}(t) + d\boldsymbol{\sigma}^{(o)}(t) + d\bar{\boldsymbol{\sigma}}^{(o)}(t). \quad (4.19)$$

By using Eqs. (4.15) and (4.19), the effective stress, $\sigma_e^{(o)}(t +$

Downloaded 04 May 2010 to 171.66.16.34. Redistribution subject to ASME license or copyright; see http://www.asme.org/terms/Terms_Use.cfm

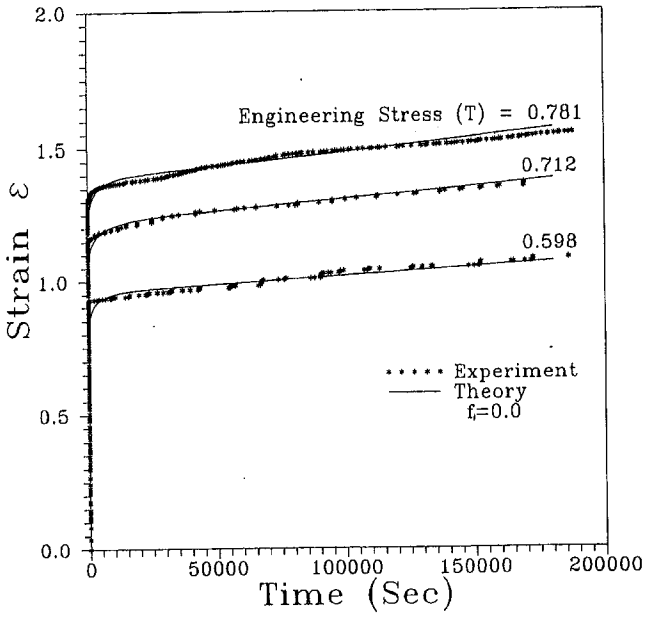


Fig. 2 The creep strain ϵ_{11} versus time curve of $f_1 = 0.00$

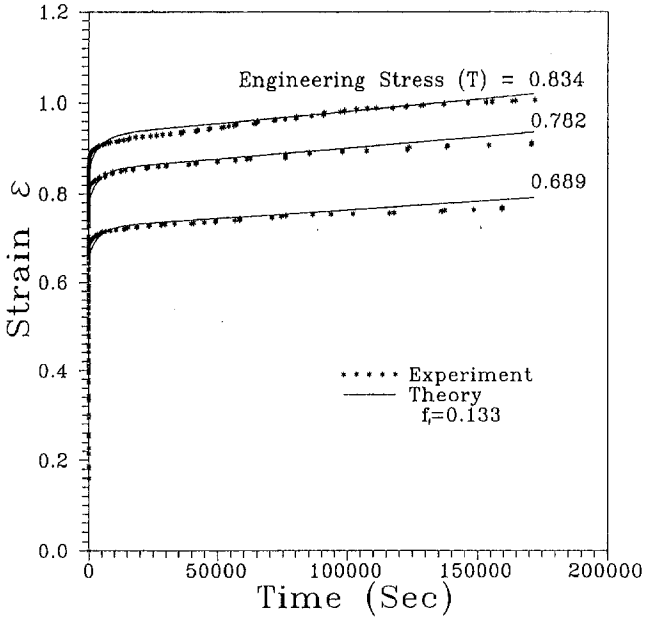


Fig. 3 The creep strain ϵ_{11} versus time curve of $f_1 = 0.13$

dt), and $\lambda_e^{(o)}(t + dt)$ then can be derived. By substituting the results of $\sigma_e^{(o)}$ and $\lambda_e^{(o)}$ into Eqs. (2.31) and (2.38), we can have the strain increment of the rubber matrix $d\boldsymbol{\epsilon}^c$. Once the result of $d\boldsymbol{\epsilon}^c$ is obtained, the procedures for deriving Eqs. (4.3)–(4.19) will be repeated to get the quantities of $\bar{\boldsymbol{\epsilon}}(t)$, $\boldsymbol{\sigma}^{(o)}(t)$ and $\boldsymbol{\epsilon}^{(o)}(t)$ for every time increment. Therefore, by using the small time-increment approach, we can predict the creep history of the solid-filled rubber composites.

5 Experiments

The basic elastomers were prepared from silicone rubber cured with the hardener T409103 (from Wacker-Chemie GmbH). The material was cast into sheets measuring 150 by 150 by 2 mm. The particulate composites were obtained by adding glass spheres of 66 to 88 mm in diameter in quantities necessary to obtain volume fractions of 13.3 percent and 21 percent in the silicone mixture. The Young's modulus of the glass beads was 68500 Mpa. The Poisson's ratio of the glass beads was 0.24. The shear modulus of the silicone rubber μ was found to be 0.4 Mpa by the aid of Eq. (2.8) and the method of least squares with the data obtained from simple tensile tests. Tensile and creep specimens of gauge lengths 20 mm (by ASTM D412) were cut from the sheets. All the specimens were kept in a desiccator for 15 days for post curing and to stabilize their properties. All the tensile and creep tests were performed in a laboratory environment of 50 percent relative humidity (RH) and at 25°C.

6 Results and Discussions

We assume in our calculations that the inclusions and the matrix take the properties of the glass beads and the silicone rubber, respectively, at room temperature. Based on two creep curves tested at 0.781 MPa and 0.712 MPa, the creep properties of the silicone rubber at room temperature were found to be μ = 0.4 MPa, μ_t = 3 MPa, $A_t = 8.4 \times 10^{-6}$ 1/sec, ν_t = 7.83 1/MPa,

$$A_s = 5.2 \times 10^{-7} \text{ 1/sec} \quad \text{and} \quad \nu_s = 2.0 \text{ 1/MPa}.$$

The quantitative accuracy of the present theory can to some extent be assessed by comparison between its predicted results and the experimental results. Such a comparison is shown in Figs. 2–4. The volume fractions of 0 percent, 13.3 percent, and 21 percent of glass bead-reinforced silicone rubber were under three different constant creep test loads, where the solid line represents the theoretical predictions, and the symbols represent the experimental results. The results show that filling of the glass beads had a reinforcing effect. The solution turns out to be in very good agreement with the experimental results.

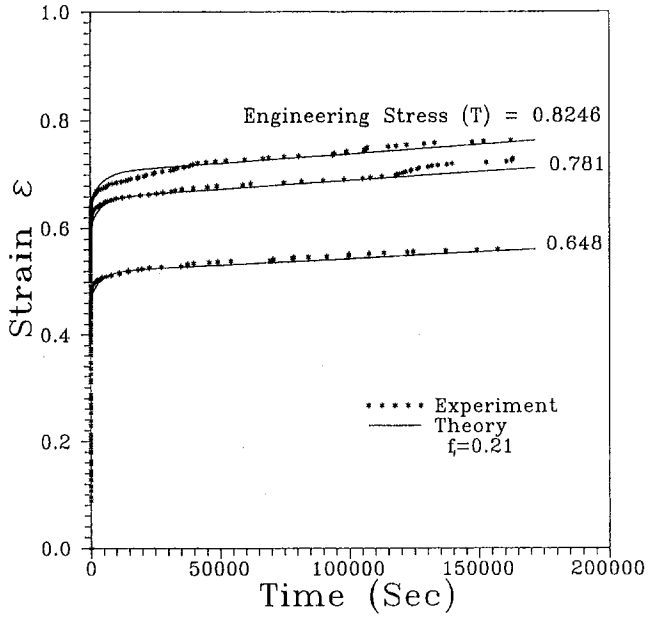


Fig. 4 The creep strain ϵ_{11} versus time curve of $f_1 = 0.21$

Acknowledgments

The authors wish to express their thanks to Prof. Yih-Hsing Pao for his many helpful suggestions. This work was supported by the National Science Council of R.O.C. under grant NSC-80-0405-E002-13.

References

Eshelby, J. D., 1957, "The Determination of the Elastic Field of an Ellipsoidal Inclusion and Related Problems," *Proceedings of Royal Society, London*, Vol. A241, pp. 376–396.

Downloaded 04 May 2010 to 171.66.16.34. Redistribution subject to ASME license or copyright; see http://www.asme.org/terms/Terms_Use.cfm

Mori, T., and Tanaka, K., 1973, "Average Stress in Matrix and Average Elastic Energy of Materials with Misfitting Inclusions," *Acta Metallurgica,* Vol. 21, pp. 571–574.

Prandtl, L., 1925, "Spannungsverteilung in Plastichen Koerpern.," *Proc. 1st Internat. Congr. Appl. Mech.,* Deflt, pp. 43–54.

Reuss, E., 1930, "Beruecksichtigung der elastichen Formaenderungen in der Plasizitaetstheorie," *Zeits. Angew. Math. Mech.,* Vol. 10, pp. 266–274.

So, H., and Chen, U. D., 1991, "A Nonlinear Mechanical Model for Solid-Filled Rubbers," *Polymer Engineering and Science,* Vol. 31, pp. 410–416.

Tandon, G. P., and Weng, G. J., 1988, "A Theory of Particle-Reinforced Plasticity," ASME JOURNAL OF APPLIED MECHANICS, Vol. 55, pp. 126–135.

Truesdell, C., and Noll, W., 1965, "The non-linear field theories of mechanics," *Encyclopedia of Physics,* V. III/3, S. Flgge, ed., Springer-Verlag, Berlin.

Weng, G. J., 1990, "The overall elastoplastic stress-strain relation of dual-phase metals," *J. Mech. Phys. Solids,* Vol. 38, pp. 419–441.

Weng, G. J., 1981, "Self-Consistent Determination of Time-Dependent Behavior of Metals," ASME JOURNAL OF APPLIED MECHANICS, Vol. 48, pp. 41–46.

Zhao, Y. H., Tandon, G. P., and Weng, G. J., 1989, "Elastic Moduli for a Class of Porous Materials," *Acta Mechanica,* Vol. 76, pp. 105–130.

Zhu, Z. G., and Weng, G. J., 1987, "Micromechanics of Time-Dependent Deformation in a Dispersion Hardened Polycrystal," *Acta Mechanica,* Vol. 69, pp. 295–313.

Zhu, Z. G., and Weng, G. J., 1990, "Creep Anisotropy of MetalMatrix Composite Containing Dilute Concentration of Aligned Spheroidal Inclusions," *Mechanics of Materials,* Vol. 9, pp. 93–105.

Zhu, Z. G., and Weng, G. J., 1989, "Creep Deformation of Particle Strengthened Metal Matrix Composites," ASME *Journal of Engineering Materials and Technology,* Vol. 111, pp. 99–105.

Downloaded 04 May 2010 to 171.66.16.34. Redistribution subject to ASME license or copyright; see http://www.asme.org/terms/Terms_Use.cfm

Linear Elastic Behavior of a Low-Density Kelvin Foam With Open Cells

W. E. Warren
Department of Civil Engineering,
Texas A&M University,
College Station, TX 77843-3136
Fellow ASME.

A. M. Kraynik
Engineering Sciences Center,
Department 9112, MS 0834,
Sandia National Laboratories,
Albuquerque, NM 87185-0834

A micromechanical analysis for the linear elastic behavior of a low-density foam with open cells is presented. The foam structure is based on the geometry of a Kelvin soap froth with flat faces: 14-sided polyhedral cells contain six squares and eight hexagons. Four struts meet at every joint in the perfectly ordered, spatially periodic, open-cell structure. All of the struts and joints have identical shape. Strut-level force-displacement relations are expressed by compliances for stretching, bending, and twisting. We consider arbitrary homogeneous deformations of the foam and present analytic results for the force, moment, and displacement at each strut midpoint and the rotation at each joint. The effective stress-strain relations for the foam, which has cubic symmetry, are represented by three elastic constants, a bulk modulus, and two shear moduli, that depend on the strut compliances. When these compliances are evaluated for specific strut geometries, the shear moduli are nearly equal and therefore the elastic response is nearly isotropic. The variational results of Hashin and Shtrikman are used to calculate the effective isotropic shear modulus of a polycrystal that contain grains of Kelvin foam.

Introduction

Strong connections between mechanical behavior and cell structure of foams are accepted widely but understood poorly. The practical desire to engineer foamed materials and predict performance motivates investigation of structure-property-processing relations that represent accurately mechanics at the cell level—both the fluid mechanics associated with structure formation during processing and the solid mechanics that determines macroscopic mechanical response of the final structure. This article addresses the latter through micromechanical analysis. A stimulating review by Weaire and Fortes (1994) discusses common issues relating to stress and strain in liquid and solid foams. Other useful surveys on the mechanics of cellular solids include Progelhof and Throne (1979), Gibson and Ashby (1988), and Kraynik and Warren (1994).

Thin films that separate adjacent cells are virtually absent in low-density open-cell foams where slender struts meet predominately at four-way joints and adjacent struts have different orientations. The struts, e.g., in a flexible polyurethane foam, originate as liquid in Plateau borders that form along the edges of polyhedral cells. Surface tension, viscous flow, and other physical chemical mechanisms control the evolving strut geometry during foam formation when gas bubbles grow and deform in highly viscous liquid that eventually solidifies.

Previous micromechanical models of elastic behavior for open-cell foams have invoked only one or two strut-level deformation mechanisms: stretching and bending. The current analysis also includes torsion and bending moments at strut midpoints—both occur in more representative foam geometries. Previous investigations have considered mechanically isolated struts (Gent and Thomas, 1959; Lederman, 1971; Kanakkanatt, 1973), isolated joints (Menges and Knipschild, 1975, 1982; Warren and Kraynik, 1988, 1991), or isolated cells (Budiansky and Kimmel, 1987). These approaches must invoke ad hoc assumptions to balance strut-level forces and distortions since they do not consider explicitly a connected foam structure.

Ko (1965) considered two fully connected structures based on different closest packed arrangements of uniform spheres: hexagonal (hex) and face-centered cubic (fcc), which give cell geometries corresponding to a trapezo-rhombic dodecahedron and rhombic dodecahedron, respectively. Both of these structures have some four-way joints and some eight-way joints, but the strut alignment differs in a very significant way. In the hex foam, some struts line up through the entire structure. In the fcc foam, each strut and a neighbor form an aligned pair. Ko determined the effective Young's modulus in the direction of aligned struts for each structure and found $E_{\text{hex}} \propto \phi$ and $E_{\text{fcc}} \propto \phi^2$, where ϕ, the relative foam density, is very small. Linear versus quadratic ϕ dependence indicates that strut stretching or strut bending, respectively, controls the macroscopic response. Ko's analysis illustrates the strong relationship between cell geometry, strut deformation mechanisms, and foam stiffness.

We consider a perfectly ordered foam whose geometry is based on the regular tetrakaidecahedron, as shown in Fig. 1. We refer to this idealized structure as an open-cell Kelvin foam following the classic work on soap froth geometry (Thomson, 1887). The Kelvin cell is the only polyhedral bubble known that fills space to form a dry soap foam (one that contains very little liquid) with perfect order; i.e., all cells have identical shape and orientation, only their positions differ. Other polyhedra that fill space, such as cubes, do not satisfy the minimal energy conditions embodied in Plateau's laws (Plateau, 1873).

Dement'ev and Tarakanov (1970a) were the first to model an open-cell foam with the tetrakaidecahedron. They considered uniaxial compression along a ⟨100⟩ axis of the structure, neglected strut bending, and predicted an effective Young's modulus of $E_{\langle 100\rangle} = E\phi/9$ where E is the modulus of the foamed material. Even when bending terms are neglected, the analysis presented below gives a different coefficient for $E_{\langle 100\rangle}$: 2/3 instead of 1/9. In a subsequent paper, Dement'ev and Tarakanov (1970b) considered bending and obtained $E_{\langle 100\rangle} = (4\sqrt{2}/9)E\phi^2$, which is consistent with our analysis when the struts have uniform square cross section. Choi and Lakes (1995)

Contributed by the Applied Mechanics Division of THE AMERICAN SOCIETY OF MECHANICAL ENGINEERS for publication in the ASME JOURNAL OF APPLIED MECHANICS.

Discussion on the paper should be addressed to the Technical Editor, Professor Lewis T. Wheeler, Department of Mechanical Engineering, University of Houston, Houston, TX 77204-4792, and will be accepted until four months after final publication of the paper itself in the ASME JOURNAL OF APPLIED MECHANICS.

Manuscript received by the ASME Applied Mechanics Division, July 22, 1996; final revision, Apr. 21, 1997. Associate Technical Editor: J. T. Jenkins.

Copyright © 1997 by ASME

Downloaded 04 May 2010 to 171.66.16.34. Redistribution subject to ASME license or copyright; see http://www.asme.org/terms/Terms_Use.cfm

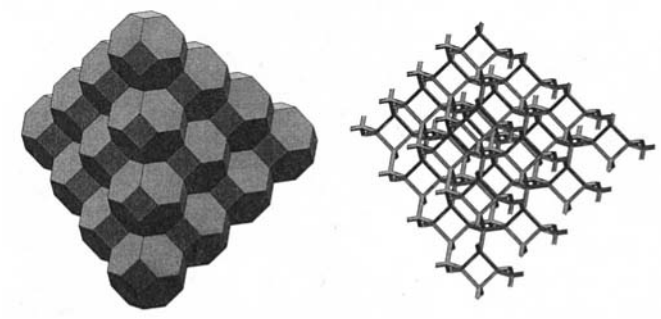


Fig. 1 Kelvin cells are based on regular tetrakaidecahedra. These fourteen-sided polyhedra sit on a body-centered-cubic lattice and fill space. The ⟨100⟩ directions are perpendicular to squares and the ⟨111⟩ directions are perpendicular to hexagons. A Kelvin foam with open cells is composed of struts meeting at four-way joints. The strut axes coincide with edges of the underlying polyhedra.

got a different result for $E_{\langle 100\rangle}$, which can be attributed to their pseudo three-dimensional calculation.

We analyze linear elastic behavior of an open-cell Kelvin foam by relating forces and distortions at the strut level to macroscopic response. The cell centers lie on a body centered cubic (bcc) lattice. Figure 2 shows 12 struts and six joints in a representative volume (unit cell) of foam. All undeformed struts and joints are identical to within a translation and rotation and the struts have mirror symmetry about the midplane between joints. We only consider struts with a straight axis and isotropic transverse response. Cubic symmetry of the foam requires three effective elastic constants, which are expressed in terms of compliances for each strut-level deformation mechanism. The compliances and elastic constants are then related to foam density for specific strut geometries. The shear modulus of an isotropic polycrystal with individual randomly oriented grains composed of Kelvin foam are estimated using variational results of Hashin and Shtrikman (1962).

Analysis

A local variable $\mathcal{P}$, such as stress or displacement, in a spatially periodic medium satisfies

$$\mathcal{P}(\mathbf{x}) = \mathcal{P}(\mathbf{x} + n_1\mathbf{b}_x + n_2\mathbf{b}_y + n_3\mathbf{b}_z) \tag{1}$$

where $\mathbf{x}$ is position, n_1, n_2, n_3 are arbitrary integers, and $\mathbf{b}_x$, $\mathbf{b}_y$, $\mathbf{b}_z$ are lattice vectors. For an undeformed Kelvin foam, the lattice vectors are chosen as

$$\begin{aligned}\mathbf{b}_x &= 2\sqrt{2}\mathcal{L}(-\mathbf{e}_x + \mathbf{e}_y + \mathbf{e}_z)\\ \mathbf{b}_y &= 2\sqrt{2}\mathcal{L}(+\mathbf{e}_x - \mathbf{e}_y + \mathbf{e}_z)\\ \mathbf{b}_z &= 2\sqrt{2}\mathcal{L}(+\mathbf{e}_x + \mathbf{e}_y - \mathbf{e}_z)\end{aligned} \tag{2}$$

where $\mathcal{L}$ is the strut half-length, and the $\mathbf{e}_\alpha$ are basis vectors of a Cartesian coordinate system with $\alpha = x, y, z$. The lattice vectors of a deformed foam differ from (2) by homogeneous displacements that correspond to the macroscopic strain.

The Kelvin foam is centrosymmetric; geometric features at $\mathbf{x}$ match those at $-\mathbf{x}$ when the origin is fixed at a cell center. This symmetry property is preserved under arbitrary homogeneous deformation, consequently, the response of the entire foam can be represented by the response of six struts and three joints.

We investigate mechanical equilibrium by isolating each joint as a free body and considering the resultant force $\mathbf{F}$ and moment $\mathbf{M}$ at strut midpoints. Each unique joint is labeled x, y, or z according to the normal axis of the square *faces* shown in Fig. 3. The term face refers to the flat surfaces on the underlying tetrakaidecahedron. Each edge of the polyhedron corresponds to a strut axis and each vertex corresponds to the center of a joint. The unit vectors $\mathbf{e}_{i\alpha}$ directed along the axis of strut $i = 1, 2, 3, 4$ from the center of joint $\alpha = x, y, z$ are given by

$$\begin{aligned}&\sqrt{2}\mathbf{e}_{1x} = +\mathbf{e}_y + \mathbf{e}_z, \quad \sqrt{2}\mathbf{e}_{1y} = +\mathbf{e}_z + \mathbf{e}_x, \quad \sqrt{2}\mathbf{e}_{1z} = +\mathbf{e}_x + \mathbf{e}_y\\ &\sqrt{2}\mathbf{e}_{2x} = -\mathbf{e}_y + \mathbf{e}_z, \quad \sqrt{2}\mathbf{e}_{2y} = -\mathbf{e}_z + \mathbf{e}_x, \quad \sqrt{2}\mathbf{e}_{2z} = -\mathbf{e}_x + \mathbf{e}_y\\ &\sqrt{2}\mathbf{e}_{3x} = +\mathbf{e}_x - \mathbf{e}_z, \quad \sqrt{2}\mathbf{e}_{3y} = +\mathbf{e}_y - \mathbf{e}_x, \quad \sqrt{2}\mathbf{e}_{3z} = +\mathbf{e}_z - \mathbf{e}_y\\ &\sqrt{2}\mathbf{e}_{4x} = -\mathbf{e}_x - \mathbf{e}_z, \quad \sqrt{2}\mathbf{e}_{4y} = -\mathbf{e}_y - \mathbf{e}_x, \quad \sqrt{2}\mathbf{e}_{4z} = -\mathbf{e}_z - \mathbf{e}_y\end{aligned}$$

which we represent in the more concise notation

$$\begin{aligned}\sqrt{2}\mathbf{e}_{1\alpha} &= +\mathbf{e}_{(\alpha+1)} + \mathbf{e}_{(\alpha-1)}\\ \sqrt{2}\mathbf{e}_{2\alpha} &= -\mathbf{e}_{(\alpha+1)} + \mathbf{e}_{(\alpha-1)}\\ \sqrt{2}\mathbf{e}_{3\alpha} &= +\mathbf{e}_\alpha - \mathbf{e}_{(\alpha-1)}\\ \sqrt{2}\mathbf{e}_{4\alpha} &= -\mathbf{e}_\alpha - \mathbf{e}_{(\alpha-1)}.\end{aligned} \tag{3}$$

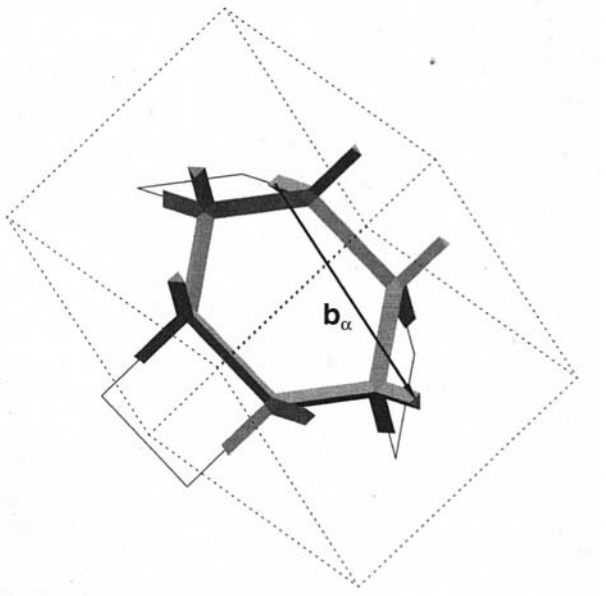


Fig. 2 Representative piece of open-cell Kelvin foam and unit cell with edges (dotted line) defined by lattice vectors b_α. Strut midsections that fit together to fill space are connected by lattice vectors.

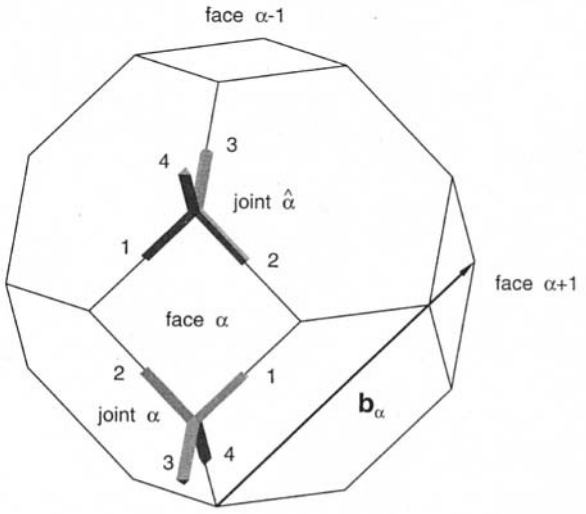


Fig. 3 Two unique joints are associated with each face α, which is labeled according to its normal direction. Each joint contains four half-struts of length $\mathcal{L}$. Lattice vectors b_α span similar points within the spatially periodic structure.

Downloaded 04 May 2010 to 171.66.16.34. Redistribution subject to ASME license or copyright; see http://www.asme.org/terms/Terms_Use.cfm

Joints x, y, and z are located at $\sqrt{2}\mathcal{L}(2, 0, -1)$, $\sqrt{2}\mathcal{L}(-1, 2, 0)$, and $\sqrt{2}\mathcal{L}(0, -1, 2)$; i.e., joint α is located at $\sqrt{2}\mathcal{L}(2\mathbf{e}_\alpha - \mathbf{e}_{(\alpha-1)})$. Struts 1α and 2α lie in the $(\alpha + 1)(\alpha - 1)$ plane. The strut midpoint forces $\mathbf{F}_{i\alpha}$ are defined as

$$\begin{aligned}\mathbf{F}_{1\alpha} &= P_{1\alpha}\mathbf{e}_{1\alpha} + Q_{1\alpha 2}\mathbf{e}_{2\alpha} + Q_{1\alpha\alpha}\mathbf{e}_\alpha\\ \mathbf{F}_{2\alpha} &= P_{2\alpha}\mathbf{e}_{2\alpha} + Q_{2\alpha 1}\mathbf{e}_{1\alpha} + Q_{2\alpha\alpha}\mathbf{e}_\alpha\\ \mathbf{F}_{3\alpha} &= P_{3\alpha}\mathbf{e}_{3\alpha} + Q_{3\alpha 4}\mathbf{e}_{4\alpha} + Q_{3\alpha(\alpha+1)}\mathbf{e}_{(\alpha+1)}\\ \mathbf{F}_{4\alpha} &= P_{4\alpha}\mathbf{e}_{4\alpha} + Q_{4\alpha 3}\mathbf{e}_{3\alpha} + Q_{4\alpha(\alpha+1)}\mathbf{e}_{(\alpha+1)}.\end{aligned} \tag{4}$$

The P (axial) components are parallel to the strut and the Q (shear) components are transverse. The strut midpoint moments $\mathbf{M}_{i\alpha}$ are represented as

$$\begin{aligned}\mathbf{M}_{1\alpha} &= T_{1\alpha}\mathbf{e}_{1\alpha} + S_{1\alpha 2}\mathbf{e}_{2\alpha} + S_{1\alpha\alpha}\mathbf{e}_\alpha\\ \mathbf{M}_{2\alpha} &= T_{2\alpha}\mathbf{e}_{2\alpha} + S_{2\alpha 1}\mathbf{e}_{1\alpha} + S_{2\alpha\alpha}\mathbf{e}_\alpha\\ \mathbf{M}_{3\alpha} &= T_{3\alpha}\mathbf{e}_{3\alpha} + S_{3\alpha 4}\mathbf{e}_{4\alpha} + S_{3\alpha(\alpha+1)}\mathbf{e}_{(\alpha+1)}\\ \mathbf{M}_{4\alpha} &= T_{4\alpha}\mathbf{e}_{4\alpha} + S_{4\alpha 3}\mathbf{e}_{3\alpha} + S_{4\alpha(\alpha+1)}\mathbf{e}_{(\alpha+1)}\end{aligned} \tag{5}$$

where the T (torsional) components are parallel and the S (bending) components are transverse to the strut. Mechanical equilibrium at joint α requires

$$\begin{aligned}\mathbf{0} &= \sum_{i=1}^{4}\mathbf{F}_{i\alpha}\\ \mathbf{0} &= \sum_{i=1}^{4}\{\mathcal{L}\mathbf{e}_{i\alpha}\times\mathbf{F}_{i\alpha} + \mathbf{M}_{i\alpha}\}.\end{aligned} \tag{6}$$

Joint $\hat{\alpha}$ with strut vectors $\hat{\mathbf{e}}_{i\alpha} = -\mathbf{e}_{i\alpha}$ is obtained by rotating joint α around the α axis by 180 deg; i.e., joint $\hat{\alpha}$ is located at $\sqrt{2}\mathcal{L}(2\mathbf{e}_\alpha + \mathbf{e}_{(\alpha-1)})$. The forces and moments for joint $\hat{\alpha}$ satisfy

$$\hat{\mathbf{F}}_{i\alpha} = -\mathbf{F}_{i\alpha}, \quad \hat{\mathbf{M}}_{i\alpha} = \mathbf{M}_{i\alpha} \tag{7}$$

which are consistent with centrosymmetry and spatial periodicity. The equilibrium equations for the α joints lead to

$$\begin{aligned}\mathbf{F}_{1\alpha} &= -\mathbf{F}_{4(\alpha-1)}, \quad \mathbf{F}_{2\alpha} = \mathbf{F}_{3(\alpha-1)},\\ \mathbf{M}_{1\alpha} &= -\mathbf{M}_{4(\alpha-1)}, \quad \mathbf{M}_{2\alpha} = -\mathbf{M}_{3(\alpha-1)}.\end{aligned} \tag{8}$$

These identities provide the following relations between force and moment coefficients:

$$\begin{aligned}&P_{4\alpha} = P_{1(\alpha+1)}, \quad Q_{4\alpha 3} = -Q_{1(\alpha+1)2}, \quad Q_{4\alpha(\alpha+1)} = -Q_{1(\alpha+1)(\alpha+1)}\\ &P_{3\alpha} = P_{2(\alpha+1)}, \quad Q_{3\alpha 4} = -Q_{2(\alpha+1)1}, \quad Q_{3\alpha(\alpha+1)} = Q_{2(\alpha+1)(\alpha+1)}\\ &T_{4\alpha} = T_{1(\alpha+1)}, \quad S_{4\alpha 3} = -S_{1(\alpha+1)2}, \quad S_{4\alpha(\alpha+1)} = -S_{1(\alpha+1)(\alpha+1)}\\ &T_{3\alpha} = -T_{2(\alpha+1)}, \quad S_{3\alpha 4} = S_{2(\alpha+1)1}, \quad S_{3\alpha(\alpha+1)} = -S_{2(\alpha+1)(\alpha+1)}.\end{aligned} \tag{9}$$

We use (7) and (9) to associate 36 unknown force and moment components with six representative struts, 1α and 2α.

Strut Midpoint Displacement. The displacement of a strut midpoint with respect to an adjacent joint is related to the strut midpoint force $\mathbf{F}$ through a stretching compliance $\mathcal{M}$ and a bending compliance $\mathcal{N}$, to the strut midpoint moment $\mathbf{M}$ through a compliance $\mathcal{N}_M$, and to the joint rotation. All compliances are constant since all struts are assumed to have identical shape and isotropic moment of inertia. Specifically, the strut-midpoint displacement $\mathbf{\Delta}_{i\alpha}$ with respect to joint α has the general representation

$$\begin{aligned}\mathbf{\Delta}_{i\alpha} = \mathcal{M}(\mathbf{F}_{i\alpha}\cdot\mathbf{e}_{i\alpha})\mathbf{e}_{i\alpha} + \mathcal{N}(\mathbf{e}_{i\alpha}\times\mathbf{F}_{i\alpha})\times\mathbf{e}_{i\alpha}\\ + \mathcal{N}_M\mathbf{M}_{i\alpha}\times\mathbf{e}_{i\alpha} + \mathcal{L}\mathbf{\Psi}_\alpha\times\mathbf{e}_{i\alpha}\end{aligned} \tag{10}$$

where $\mathbf{\Psi}_\alpha = \Psi_{\alpha x}\mathbf{e}_x + \Psi_{\alpha y}\mathbf{e}_y + \Psi_{\alpha z}\mathbf{e}_z$ is the infinitesimal rotation of joint α. Relations similar to (10) for strut midpoint displacements $\hat{\mathbf{\Delta}}_{i\alpha}$ associated with joint $\hat{\alpha}$ lead to

$$\mathbf{\Delta}_{i\alpha} + \hat{\mathbf{\Delta}}_{i\alpha} = \mathcal{L}(\mathbf{\Psi}_\alpha - \hat{\mathbf{\Psi}}_\alpha)\times\mathbf{e}_{i\alpha}. \tag{11}$$

Strut Connectivity and Joint Rotation. To enforce strut connectivity throughout the foam, the midpoint displacements satisfy compatibility conditions that require the net displacement around any face to vanish. For the Kelvin foam, it is sufficient to consider three different square faces. For the face with normal $\mathbf{e}_\alpha$, this condition requires

$$\begin{aligned}\mathbf{\Delta}_{1\alpha} - \mathbf{\Delta}_{2\alpha} + \mathbf{\Delta}_{3(\alpha-1)} - \mathbf{\Delta}_{4(\alpha-1)} + \hat{\mathbf{\Delta}}_{1\alpha} - \hat{\mathbf{\Delta}}_{2\alpha}\\ + \hat{\mathbf{\Delta}}_{3(\alpha-1)} - \hat{\mathbf{\Delta}}_{4(\alpha-1)} = \mathbf{0}\end{aligned} \tag{12}$$

and provides

$$\begin{aligned}(\mathbf{\Psi}_\alpha - \hat{\mathbf{\Psi}}_\alpha)\times(\mathbf{e}_{1\alpha} - \mathbf{e}_{2\alpha}) + (\mathbf{\Psi}_{(\alpha-1)} - \hat{\mathbf{\Psi}}_{(\alpha-1)})\\ \times(\mathbf{e}_{1\alpha} + \mathbf{e}_{2\alpha}) = \mathbf{0}.\end{aligned} \tag{13}$$

The relative rotation between two ends of a strut is proportional to the moment $\mathbf{M}$ at the strut midpoint through a torsional compliance $\mathcal{J}_T$ and a bending compliance $\mathcal{J}_B$, where $\mathcal{J}_T$ and $\mathcal{J}_B$ are constant. There are nine nonredundant relative joint rotations of the form

$$\begin{aligned}\mathbf{\Psi}_{(\alpha-1)} - \mathbf{\Psi}_\alpha &= \mathcal{J}_T T_{1\alpha}\mathbf{e}_{1\alpha} + \mathcal{J}_B(S_{1\alpha 2}\mathbf{e}_{2\alpha} + S_{1\alpha\alpha}\mathbf{e}_\alpha)\\ \hat{\mathbf{\Psi}}_{(\alpha-1)} - \mathbf{\Psi}_\alpha &= \mathcal{J}_T T_{2\alpha}\mathbf{e}_{2\alpha} + \mathcal{J}_B(S_{2\alpha 1}\mathbf{e}_{1\alpha} + S_{2\alpha\alpha}\mathbf{e}_\alpha).\end{aligned} \tag{14}$$

Equations (13) and (14) indicate that joints at opposite corners of each square (or hexagon) have the same rotation

$$\mathbf{\Psi}_\alpha = \hat{\mathbf{\Psi}}_\alpha \tag{15}$$

and provide the additional relations

$$\begin{aligned}S_{1\alpha\alpha} &= S_{2\alpha\alpha}\\ \mathcal{J}_B S_{1\alpha 2} &= \mathcal{J}_T T_{2\alpha}\\ \mathcal{J}_B S_{2\alpha 1} &= \mathcal{J}_T T_{1\alpha}.\end{aligned} \tag{16}$$

Equations (11) and (15) indicate that joints at opposite corners of each face have opposite displacement

$$\mathbf{\Delta}_{i\alpha} = -\hat{\mathbf{\Delta}}_{i\alpha}. \tag{17}$$

The rigid-body rotation of the entire foam is given by $\mathbf{\Omega}$, where

$$\mathbf{\Omega} = \omega_{yz}\mathbf{e}_x + \omega_{zx}\mathbf{e}_y + \omega_{xy}\mathbf{e}_z \tag{18}$$

is the dual vector of the usual antisymmetric infinitesimal rotation tensor for homogeneous deformation. Symmetry requires that the component of joint rotation parallel to $\mathbf{e}_{(\alpha-1)}$ is equal to that component of rigid-body rotation for the entire foam

$$\Psi_{\alpha(\alpha-1)} = \omega_{\alpha(\alpha+1)}. \tag{19}$$

This restriction and (14) provide additional relations between the other components of $\mathbf{\Psi}_\alpha$ and the strut midpoint torques

$$\begin{aligned}\sqrt{2}(\Psi_{\alpha(\alpha+1)} - \omega_{(\alpha-1)\alpha}) &= -\mathcal{J}_T(T_{1\alpha} - T_{2\alpha})\\ \sqrt{2}(\Psi_{\alpha\alpha} - \omega_{(\alpha+1)(\alpha-1)}) &= -\mathcal{J}_T(T_{1(\alpha+1)} + T_{2(\alpha+1)})\end{aligned} \tag{20}$$

and between the strut midpoint moments and torques

$$S_{1\alpha\alpha} = -\sqrt{2}\Gamma(T_{1(\alpha+1)} + T_{2(\alpha+1)}) \tag{21}$$

where $\Gamma = \mathcal{J}_T/\mathcal{J}_B$. The number of unknown moment components is reduced from 18 to 6 with (16) and (21).

Solution of the Equilibrium Equations. The 18 scalar equilibrium equations from (6) reduce to a system with 24 unknown force and moment components by using (9), (16),

Downloaded 04 May 2010 to 171.66.16.34. Redistribution subject to ASME license or copyright; see http://www.asme.org/terms/Terms_Use.cfm

and (21). This system of equations together with (20) determine all components of the joint rotations and the strut midpoint forces and moments in terms of the six axial force components $P_{1\alpha}$ and $P_{2\alpha}$. The results are expressed as

$$2Q_{1\alpha 2} = 2Q_{2\alpha 1} = (P_{1\alpha} + P_{2\alpha}) - (P_{1(\alpha-1)} + P_{2(\alpha-1)})$$

$$\sqrt{2}\mathcal{L}(Q_{1\alpha\alpha} + Q_{2\alpha\alpha}) = -\sqrt{2}\mathcal{A}(T_{1\alpha} - T_{2\alpha}) = \mathcal{L}(P_{1(\alpha+1)} - P_{2(\alpha+1)})$$

$$\sqrt{2}\mathcal{L}(Q_{1\alpha\alpha} - Q_{2\alpha\alpha}) = -\sqrt{2}\mathcal{A}(T_{1\alpha} + T_{2\alpha}) = \mathcal{L}(P_{1(\alpha-1)} - P_{2(\alpha-1)}) \quad (22)$$

where $\mathcal{A} = 1 + 5\Gamma = 1 + 5\mathcal{I}_T/\mathcal{I}_B$. The axial force combinations $P_{1\alpha} \pm P_{2\alpha}$ are determined from homogeneous deformations of the foam.

Homogeneous Deformation. A homogeneous deformation is imposed on the entire Kelvin foam by displacing lattice vectors according to

$$\mathbf{u}_\alpha = \mathbf{E}\mathbf{b}_\alpha + \boldsymbol{\Omega} \times \mathbf{b}_\alpha - \mathbf{b}_\alpha \quad (23)$$

where $\mathbf{E}$ is the symmetric uniform strain tensor with components $\epsilon_{\alpha\beta}$, and the dual vector $\boldsymbol{\Omega}$ of the antisymmetric rotation tensor is defined in (18). The lattice displacements $\mathbf{u}_\alpha$ can also be expressed in terms of strut midpoint displacements (see Fig. 4) as

$$\mathbf{u}_\alpha = \boldsymbol{\Delta}_{1\alpha} - \boldsymbol{\Delta}_{3\alpha} + \boldsymbol{\Delta}_{3(\alpha+1)} - \boldsymbol{\Delta}_{2(\alpha+1)} + \boldsymbol{\Delta}_{2(\alpha-1)} - \boldsymbol{\Delta}_{4(\alpha-1)}. \quad (24)$$

Equating (23) and (24), making use of the constitutive relations in (10) together with the joint-rotation relations in (13) and (14) and the equilibrium relations in (22) provide, finally, a consistent set of six scalar equations in terms of 12 unknowns: $P_{1\alpha}$, $P_{2\alpha}$, and $\epsilon_{\alpha\beta}$. The strut midpoint forces can be expressed in terms of strain on the foam as

$$P_{1\alpha} + P_{2\alpha} = \frac{2\mathcal{L}}{\mathcal{M}(3\mathcal{N} + \mathcal{M})} \times [(\mathcal{N} - \mathcal{M})\epsilon_{\alpha\alpha} + (\mathcal{N} + \mathcal{M})(\epsilon_{(\alpha+1)(\alpha+1)} + \epsilon_{(\alpha-1)(\alpha-1)})]$$

$$P_{1\alpha} - P_{2\alpha} = \frac{4\mathcal{L}\epsilon_{(\alpha+1)(\alpha-1)}}{(\mathcal{M} + \mathcal{N} + \mathcal{L}^2\mathcal{I})} \quad (25)$$

where $\mathcal{I} = \mathcal{I}_T/2\mathcal{A} = \mathcal{I}_T/2(1 + 5\Gamma) = \mathcal{I}_T\mathcal{I}_B/2(\mathcal{I}_B + 5\mathcal{I}_T)$.

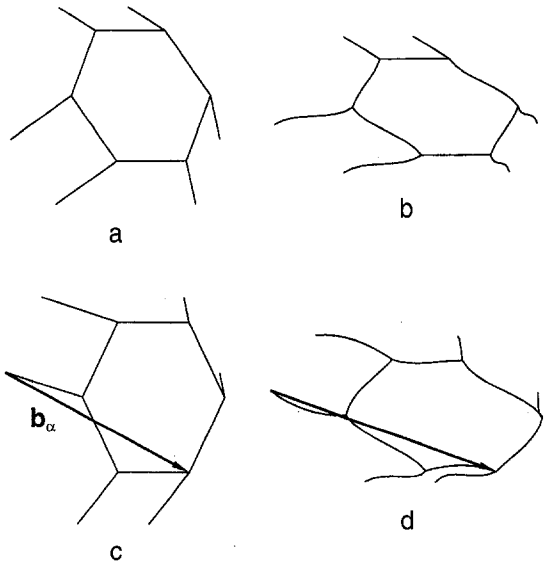


Fig. 4 Shown are 12 connected struts associated with the unit cell of various Kelvin foams. When (*a*) is compressed along a ⟨100⟩ axis to form (*b*), by "pushing on a square face," the struts only stretch and bend. There is no twisting and the bending moment is zero at each strut midpoint. When (*c*) is compressed along a ⟨111⟩ axis to form (*d*), by "pushing on a hexagonal face," the struts stretch, bend, and twist. The bending moment is finite at some strut midpoints. Lattice vectors b_α connect similar points within the spatially periodic structure. Midpoint displacements in Eq. (24) are summed along struts that form a connected path between similar points.

Effective Stress

The effective stress $\boldsymbol{\sigma}$ for the spatially periodic foam is given by the volume average of local stress $\boldsymbol{\sigma}'$ as (Nemat-Nasser and Hori, 1993)

$$\boldsymbol{\sigma} = \frac{1}{\mathcal{V}}\int_{\mathcal{V}_S} \boldsymbol{\sigma}'\, dv \quad (26)$$

where $\mathcal{V} = 64\sqrt{2}\mathcal{L}^3$ is the volume of the unit cell and $\mathcal{V}_S$ refers to the region occupied by solid struts. The pressure in the gas-filled region outside $\mathcal{V}_S$ is taken to be zero so the corresponding volume integral vanishes. Using the divergence theorem, (26) can be written as a surface integral

$$\boldsymbol{\sigma} = \frac{1}{\mathcal{V}}\int_{\partial\mathcal{V}_S} \mathbf{x}\mathbf{t}\, ds \quad (27)$$

where $\mathbf{t}$ is the surface traction and $\partial\mathcal{V}_S$ is the boundary of $\mathcal{V}_S$. To evaluate (27), consider representative foam structures whose boundaries include midplanes between joints, as shown in Fig. 2. The traction is zero everywhere on $\partial\mathcal{V}_S$ but the strut midsections; the contribution to the integral in (27) from each strut midsection is $\mathbf{x}\mathbf{F}$, which leads to

$$\boldsymbol{\sigma} = \frac{1}{\mathcal{V}}\sum \mathbf{x}\mathbf{F} \quad (28)$$

$$= \frac{\sqrt{2}}{64\mathcal{L}^3}(\mathbf{b}_x\mathbf{F}_{1x} + \mathbf{b}_y\mathbf{F}_{1y} + \mathbf{b}_z\mathbf{F}_{1z}). \quad (29)$$

The summation in (28) is over all strut midpoints on $\partial\mathcal{V}_S$; there are 12 such midpoints for the object in Fig. 2. The final result is obtained by recognizing that pairs of strut midpoints are connected by lattice vectors and forces on the body at those midpoints act in opposite directions.

Components of the symmetric stress tensor $\boldsymbol{\sigma}$ evaluate to

$$\sigma_{\alpha\alpha} = \frac{(\mathcal{N} + 3\mathcal{M})\epsilon_{\alpha\alpha} + (\mathcal{N} - \mathcal{M})(\epsilon_{(\alpha+1)(\alpha+1)} + \epsilon_{(\alpha-1)(\alpha-1)})}{8\sqrt{2}\mathcal{L}\mathcal{M}(3\mathcal{N} + \mathcal{M})}$$

$$\sigma_{\alpha(\alpha+1)} = \sigma_{(\alpha+1)\alpha} = \frac{\epsilon_{\alpha(\alpha+1)}}{4\sqrt{2}\mathcal{L}(\mathcal{M} + \mathcal{N} + \mathcal{L}^2\mathcal{I})}. \quad (30)$$

These relations provide three independent elastic constants, as expected from cubic symmetry of a Kelvin foam. The constants can be represented as a bulk modulus for volume compression κ and two shear moduli μ_1 and μ_2, which take the form

$$\kappa = \frac{1}{3}(c_{11} + 2c_{12}) = \frac{1}{24\sqrt{2}\mathcal{L}\mathcal{M}} \quad (31)$$

$$\mu_1 = \frac{1}{2}(c_{11} - c_{12}) = \frac{1}{4\sqrt{2}\mathcal{L}(\mathcal{M} + 3\mathcal{N})} \quad (32)$$

$$\mu_2 = c_{44} = \frac{1}{8\sqrt{2}\mathcal{L}(\mathcal{M} + \mathcal{N} + \mathcal{L}^2\mathcal{I})} \quad (33)$$

Downloaded 04 May 2010 to 171.66.16.34. Redistribution subject to ASME license or copyright; see http://www.asme.org/terms/Terms_Use.cfm

where the c_{ij} are elastic constants used by Love (1944) and Nye (1992).

In general, the Kelvin foam exhibits anisotropic shear response since μ_1 and μ_2 have different forms and μ_1 does not even involve torsion. Despite this, we will show in the next section that μ_1 and μ_2 are nearly equal for low-density foams with strut shapes and material properties of interest. But first, consider uniaxial compression along $\langle 100 \rangle$ and $\langle 111 \rangle$ axes of the Kelvin foam, which correspond to distortions where strut twisting is absent or maximized. The Young's moduli are given by

$$E_{\langle 100 \rangle} = \frac{3\mu_1}{1 + \mu_1/(3\kappa)} \to 3\mu_1$$

$$E_{\langle 111 \rangle} = \frac{3\mu_2}{1 + \mu_2/(3\kappa)} \to 3\mu_2. \tag{34}$$

The asymptotic forms recall the linear relation between Young's modulus and shear modulus for an incompressible material; a low-density Kelvin foam is nearly incompressible since $\mathcal{M} \ll \mathcal{N}$. Figure 4 illustrates strut-level distortions. Compression along the z-axis corresponds to pushing on a square face. The strain is given by $\epsilon_{zz} = -\epsilon$, $\epsilon_{xx} = \epsilon_{yy} \approx \epsilon/2$, $\epsilon_{xy} = \epsilon_{yz} = \epsilon_{zx} = 0$. There is no strut twisting, consistent with the absence of $\mathcal{G}$ in $E_{\langle 100 \rangle}$ and μ_1. Struts stretch when they lie in the xy-plane (on the pushed square face). The other struts bend but the bending moment vanishes at their midpoint. Some struts twist whenever the compression axis is not aligned with a $\langle 100 \rangle$ axis. Twisting is most evident for compression along a $\langle 111 \rangle$ axis, which corresponds to pushing on a hexagonal face. This occurs, for example, when the strains are given by $\epsilon_{xy} = \epsilon_{yz} = \epsilon_{zx} = -\gamma$ and $\epsilon_{xx} = \epsilon_{yy} = \epsilon_{zz} = 0$. Struts bend but do not twist when they lie on the pushed hexagonal face; the other struts bend and twist. All of the strut-level forces and distortions can be calculated from results presented in the previous section.

Results for Specific Strut Geometries

Bulk Modulus. The Kelvin foam exhibits isotropic elastic response for pure volume change, as guaranteed by cubic symmetry. The struts experience axial deformation that corresponds to affine joint displacement; there is no bending so the effective bulk modulus κ only depends on $\mathcal{M}$. To relate effective elastic constants to foam density, we consider slender struts with Young's modulus E, total length 2ℓ, and uniform cross section of area A, which gives

$$\phi = \frac{3A}{8\sqrt{2}\,\ell^2} + O\left(\frac{A^{3/2}}{\ell^3}\right) \tag{35}$$

$$\mathcal{M} = \frac{\ell}{EA} \tag{36}$$

$$\kappa = \tfrac{1}{9} E\phi \tag{37}$$

when $\phi \ll 1$. Unique among the strut compliances, $\mathcal{M}$ does not depend on cross section shape, consequently, neither does κ. The relation between κ and ϕ in (37) is always obtained when stress transfer involves only axial deformation of struts (Christensen, 1986). This general behavior is revealed by rewriting (31) as

$$\kappa = \frac{1}{9}\frac{\ell^3}{\mathcal{V}_J}\frac{4}{\ell\mathcal{M}} \tag{38}$$

where $\mathcal{V}_J$ is the volume of foam occupied per joint; for a Kelvin foam $\mathcal{V}_J = \mathcal{V}/6$. The foam density and axial compliance are given by

$$\phi = \frac{4\ell A}{\mathcal{V}_J}$$

$$\frac{4}{\ell\mathcal{M}} = E\frac{\mathcal{V}_J}{\ell^3}\phi \tag{39}$$

which leads to (37). Notice that terms involving $\mathcal{V}_J$ cancel when (38) and (39) are combined, therefore (37) does not depend on the specific foam geometry. In contrast, the shear modulus is more sensitive to strut shape and foam topology.

Shear Modulus. To calculate the shear moduli, we evaluate bending compliances by modeling the struts as Euler beams. The torsional compliance is obtained from classical torsion theory. This gives

$$\frac{1}{\ell\mathcal{N}} = \frac{3EI}{\ell^4} \to \frac{3}{16}E\left(\frac{q^2}{A}\right)\left(\frac{\mathcal{V}_J}{\ell^3}\right)^2\phi^2 \tag{40}$$

$$\ell^2\mathcal{G}_B = \frac{2\ell^3}{EI} = 6\mathcal{N} \tag{41}$$

$$\ell^2\mathcal{G} = \tfrac{1}{2}\mathcal{N}(1 + \mathcal{G}) \tag{42}$$

where

$$\mathcal{G} = \frac{\mathcal{G}_T - \mathcal{G}_B}{5\mathcal{G}_T + \mathcal{G}_B}$$

and q is the radius of gyration of a strut with moment of inertia $I = q^2A$. The parameters q^2/A and $\mathcal{G}$, which depend on strut shape, are contained in Table 1 for different strut cross sections: circle, square, equilateral triangle, and Plateau border. The last shape is most representative of real struts and recalls the gas-liquid stage during processing; the strut cross section is a hypercycloid, which corresponds to the space between three identical, mutually tangent circles. The square is included to compare with previous results (Dement'ev and Tarakanov, 1970b) even though square cross section is inconsistent with typical foam structures where struts are shared by three neighboring foam cells. From Table 1, the parameter $\mathcal{G}$ has narrow range given by $0 \le \mathcal{G} < 2/13$ when Poisson's ratio for the strut material satisfies $0 \le \nu \le 1/2$.

Using (40) and (42), the shear moduli for low-density foams with $\phi \ll 1$ and $\mathcal{M} \ll \mathcal{N}$ are given by

$$\mu_1 \to \frac{16\sqrt{2}}{9}E\left(\frac{q^2}{A}\right)\phi^2$$

$$\mu_2 \to \frac{\mu_1}{1 + \mathcal{G}/3}. \tag{43}$$

Table 1 Compliance parameters for slender struts with uniform cross section and the corresponding isotropic Young's modulus for a low-density Kelvin foam ($\phi \ll 1$) with incompressible struts ($\nu = 1/2$); $\bar{E}$ is calculated from variational results of Hashin and Shtrikman (1962). The value of $\mathcal{G}$ for the Plateau border is based on calculations by Warren, Neilsen, and Kraynik (1997).

Strut Shape	$\frac{q^2}{A}$	$\mathcal{G}$	$\frac{\bar{E}}{E\phi^2}$
circle	$\frac{1}{4\pi} = 0.07958$	$\frac{\nu}{6+5\nu}$	0.593
square	$\frac{1}{12} = 0.08333$	$\frac{10.0+64\nu}{374.0+320\nu}$	0.619
equilateral triangle	$\frac{1}{6\sqrt{3}} = 0.09623$	$\frac{2+5\nu}{28+25\nu}$	0.710
Plateau border	$\frac{20\sqrt{3}-11\pi}{6(2\sqrt{3}-\pi)^2} = 0.1338$	$\frac{7.0+10\nu}{53.0+50\nu}$	0.979

Downloaded 04 May 2010 to 171.66.16.34. Redistribution subject to ASME license or copyright; see http://www.asme.org/terms/Terms_Use.cfm

The elastic response is isotropic when $\mathcal{G} = 0$, which occurs for circular struts with $\nu = 0$. Incompressible struts with Plateau border shape cause the most anisotropy: $\mu_2/\mu_1 = 0.951$ when $\mathcal{G} = 2/13$. These results indicate that a low-density Kelvin foam exhibits weak anisotropy for strut shapes and material properties of interest.

Equation (43) indicates that torsion is a very important strut-level deformation mechanism for shear response. The second shear modulus is substantially larger, $\mu_2 = (3/2)\mu_1$, if the struts have infinite torsional rigidity ($\mathcal{J} = 0$ or $\mathcal{G} = -1$).

Elastic Properties of an Isotropic Polycrystal

Since the elastic properties of a Kelvin foam are not isotropic, it is interesting to consider a composite material with polycrystalline structure and isotropic behavior. The individual grains are composed of Kelvin foam and have random orientation and arbitrary shape. Bounds on the effective elastic properties of this polycrystal can be calculated from the variational results of Hashin and Shtrikman (1962), which improve upon the upper bound of Voigt (1910) and the lower bound of Reuss (1929). Chapman and Higdon (1994) provide additional perspective and results for a periodic bicontinous porous medium with overlapping spherical microstructure.

The various bounds on the shear modulus μ expressed in terms of elastic constants for cubic material in the grains, are given by

$$\mu_V = \frac{1}{5}(2\mu_1 + 3\mu_2) \to \mu_1 \frac{1 + 2\mathcal{G}/15}{1 + \mathcal{G}/3} \tag{44}$$

$$\mu_R = \frac{5\mu_1\mu_2}{3\mu_1 + 2\mu_2} \to \mu_1 \frac{1}{1 + \mathcal{G}/5} \tag{45}$$

$$\mu_U = \mu_1 + 3\left(\frac{5}{\mu_2 - \mu_1} - 4h_1\right)^{-1} \to \mu_1 \frac{1 + 16\mathcal{G}/75}{(1 + \mathcal{G}/3)(1 + 2\mathcal{G}/25)} \tag{46}$$

$$\mu_L = \mu_2 + 2\left(\frac{5}{\mu_1 - \mu_2} - 6h_2\right)^{-1} \to \mu_1 \frac{1 + 2\mathcal{G}/25}{1 + 7\mathcal{G}/25} \tag{47}$$

where

$$h_i = \frac{3(\kappa + 2\mu_i)}{5\mu_i(3\kappa + 4\mu_i)}.$$

The low-density forms of these quantities are graphed in Fig. 5 to emphasize that while the Voigt bound μ_V and Reuss bound μ_R are relatively close, the Hashin-Shtrikman bounds are indistinguishable on the same scale. The shear modulus of the polycrystal can be represented accurately by the mean value of the Hashin-Shtrikman bounds, μ_U and μ_L, and a corresponding range

$$\bar{\mu}/\mu_1 = \frac{1 + 37\mathcal{G}/75 + 112\mathcal{G}^2/1875 + 2\mathcal{G}^3(1 \pm 1)/1875}{(1 + \mathcal{G}/3)(1 + 2\mathcal{G}/25)(1 + 7\mathcal{G}/25)}. \tag{48}$$

The effective isotropic Young's modulus $\bar{E}$ for incompressible struts with Plateau border shape is

$$\bar{E} = 0.979E\phi^2. \tag{49}$$

The correction from (48) to the numerical coefficient in (49) falls in the sixth decimal place. When correlating experimental data, Progelhof and Throne (1979) and Gibson and Ashby (1988) chose a coefficient of one, which is convenient because $\bar{E} = E$ when $\phi = 1$. Our results support this choice when $\phi \ll 1$. The numerical factor is quite sensitive to strut shape through the parameter q^2/A; it is 40 percent smaller for circular struts and 38 percent smaller for square struts (see Table 1).

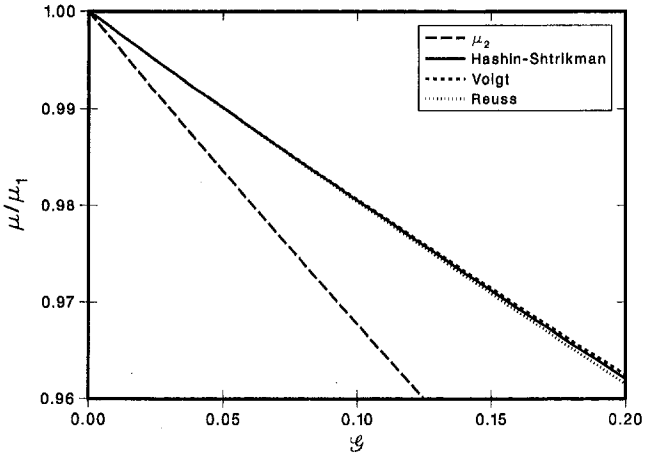


Fig. 5 Variational bounds on the isotropic shear modulus of a polycrystal with grains of Kelvin foam. The solid curve is $\bar{\mu}$, the mean of the upper and lower bounds of Hashin and Shtrikman (1962); the individual curves are indistinguishable on this scale.

Comparison With Other Models of an Open-Cell Foam

The affine theory of Gent and Thomas (1959) for randomly oriented struts that do not bend, predicts the stiffest response in shear (see Christensen, 1986)

$$\mu \to \tfrac{1}{15} E\phi. \tag{50}$$

A foam composed of simple cubic cells with six-way joints exhibits highly anisotropic behavior (Warren and Kraynik, 1988) with

$$\mu_1 = \frac{1}{2}(c_{11} - c_{12}) = \frac{1}{8\mathcal{LM}} \to \frac{1}{4} E\phi$$

$$\mu_2 = c_{44} = \frac{1}{8\mathcal{LN}} \to \frac{3}{2} E\left(\frac{q^2}{A}\right)\phi^2. \tag{51}$$

The stiffness is greatest for deformations along the ⟨100⟩ axes; bending is absent because struts are aligned end to end. In contrast, deformation along the ⟨111⟩ directions maximizes bending and minimizes stiffness, producing softer response than a Kelvin foam, even though struts do not twist in a simple cubic foam.

Large stiffness—associated with axial load transfer in struts aligned end to end—is also exhibited by the structure based on hexagonal-closest packing that was analyzed by Ko (1965). The effective Young's modulus parallel to the aligned struts is

$$E_{\text{hex}} \to \tfrac{1}{6} E\phi. \tag{52}$$

The shear modulus also varies with orientation from linear to quadratic dependence on ϕ. In contrast, aligned struts are found only in pairs in Ko's other structure, which is based on face-centered-cubic packing. Young's modulus in the direction of alignment is given by

$$E_{\text{fcc}} \to 14\sqrt{3}E\left(\frac{q^2}{A}\right)\phi^2. \tag{53}$$

The shear modulus is proportional to ϕ^2 in all directions; strut bending dominates stretching, despite the presence of eight-way joints and aligned strut pairs.

Downloaded 04 May 2010 to 171.66.16.34. Redistribution subject to ASME license or copyright; see http://www.asme.org/terms/Terms_Use.cfm

Warren and Kraynik (1988) analyzed an isolated tetrahedral joint and assumed the representative foam volume to be a regular tetrahedron. Regular tetrahedra do not pack to fill space, so their results were not considered to apply to a connected structure. Tetrahedral joints do fill space when arranged like carbon atoms in diamond; however, the resulting structure lacks the characteristic cell geometry based on polyhedra that is distinctive of foams. The unit cell in the diamond structure contains two identical joints with different orientation; adjacent joints are rotated 180 deg about the axis of shared struts. As a consequence of this symmetry, the displacement of strut midpoints is affine and moments vanish at these points. The same conditions were used to obtain force-displacement relations for the isolated tetrahedral joint; so those results carry over to the diamond structure, which has cubic symmetry and elastic constants given by

$$\mu_1 = \frac{1}{2}(c_{11} - c_{12}) = \frac{\sqrt{3}}{32\mathcal{L}\mathcal{N}}$$

$$\mu_2 = c_{44} = \frac{3\sqrt{3}}{32\mathcal{L}(2\mathcal{M} + \mathcal{N})}$$

$$\bar{\mu} \to \frac{(3656 \pm 128)\sqrt{3}}{2079} E\left(\frac{q^2}{A}\right)\phi^2. \qquad (54)$$

The diamond structure is more anisotropic than the Kelvin foam since $\mu_2/\mu_1 \to 3$. As measured by $\bar{\mu}$, the mean Hashin-Shtrikman bounds, the diamond structure is also stiffer than the Kelvin foam.

Discussion

The Kelvin cell is a natural starting point for developing micromechanical models of open-cell foams. It forms the simplest space-filling structure with four struts meeting at every joint. All of the struts and all of the joints have identical shape. The relatively compact analytic results that have been presented also reflect the fact that struts are modeled as straight beams with isotropic transverse response. Even though we have only evaluated elastic constants for struts with uniform cross section, all results expressed in terms of strut compliance are valid for struts with nonuniform cross section. The only restriction is symmetry about the midplane between joints and isotropic bending compliance.

Struts can bend, stretch, and twist when the Kelvin foam is subjected to homogeneous deformations. Strut torsion and finite bending moments at strut midpoints have not been discussed in previous studies that are based on even simpler views of foam geometry. Twisting is undoubtedly an important strut-level deformation mechanism in three-dimensional foams with more realistic structure.

Hydrostatic compression of a Kelvin foam with straight struts does not induce bending or twisting. Only axial loading of struts is involved, consequently, the foam is much stiffer under pure dilatation than under shear. The response of the Kelvin foam to pure volume distortion also corresponds to affine displacement of joints. Strut bending and twisting are suppressed by the symmetry of the joints. Gibson and Ashby (1988) found large scatter in experimental data for Poisson's ratio of foam μ_f but proposed 1/3 as a reasonable value. Our analysis gives $\nu_f \to 1/2$ when $\phi \ll 1$; and, ν_f decreases as ϕ increases. However, the densities required to get Poisson's ratio approaching 1/3 correspond to very thick struts and joints; our analysis is not valid in that regime. More complex structures that contain, for example, struts of different length meeting at many different angles or struts that are curved along their axis, will have less symmetry than the Kelvin foam. The resulting bending and twisting of struts will give softer response under hydrostatic compression. Choi and Lakes (1995) indicate that re-entrant foam structure with struts that are bent initially can have negative Poisson's ratio.

Strut twisting exhibits strong dependence on orientation of the Kelvin foam and vanishes entirely when principal directions of deformation coincide with ⟨100⟩ axes of the cell. In view of this, the weak anisotropy of the elastic response is surprising.

Finite element methods are being used to extend micromechanical analysis to large deformations. Results for open-cell foams based on the Weaire-Phelan structure (Weaire and Phelan, 1994) and other tetrahedrally close-packed (t.c.p.) systems (Rivier, 1994), and random structure, will be reported elsewhere (Neilsen and Kraynik, 1998). Parallel studies on the microrheology of soap froth and emulsions (Reinelt and Kraynik, 1993, 1996; Kraynik and Reinelt, 1996a–d) are leading to systematic understanding of structure-property relations for a broad range of foamed materials.

Acknowledgments

Sandia is a multiprogram laboratory operated by Sandia Corporation, a Lockheed Martin Company, for the U.S. Department of Energy under contract #DE-AC04-94AL85000. This work was also supported by the Dow Chemical Company under a Cooperative Research and Development Agreement (CRADA).

We thank J. J. L. Higdon for useful discussions on effective isotropic properties.

Note Added in Proof

During the review process, a complementary analysis of this problem came to our attention: Zhu, H. X., Knott, J. F., and Mills, N. J., 1997, "Analysis of the Elastic Properties of Open-Cell Foams with Tetrakaidecahedral Cells," *Journal of Mechanics and Physics of Solids,* Vol. 45, pp. 319–343.

References

Budiansky, B., and Kimmel, E., 1987, "Elastic Moduli of Lungs," ASME JOURNAL OF APPLIED MECHANICS, Vol. 54, pp. 351–358.

Choi, J. B., and Lakes, R. S., 1995, "Analysis of Elastic Modulus of Conventional Foams and of Re-Entrant Foam Materials with a Negative Poisson's Ratio," *International Journal of Mechanical Sciences,* Vol. 37, pp. 51–59.

Christensen, R. M., 1986, "Mechanics of Low Density Materials," *Journal of Mechanics and Physics of Solids,* Vol. 34, pp. 563–578.

Dement'ev, A. G., and Tarakanov, O. G., 1970a, "Effect of Cellular Structure on the Mechanical Properties of Plastic Foams," *Mekhanika Polimerov,* Vol. 4, pp. 594–602; translation *Polymer Mechanics,* Vol. 6, pp. 519–525.

Dement'ev, A. G., and Tarakanov, O. G., 1970b, "Model Analysis of the Cellular Structure of Plastic Foams of the Polyurethane Type," *Mekhanika Polimerov,* Vol. 5, pp. 859–865; translation *Polymer Mechanics,* Vol. 6, pp. 744–749.

Gent, A. N., and Thomas, A. G., 1959, "The Deformation of Foamed Elastic Materials," *Journal of Applied Polymer Science,* Vol. 1, pp. 107–113.

Gibson, L. J., and Ashby, M. F., 1988, *Cellular Solids,* Pergamon, Oxford.

Hashin, Z., and Shtrikman, S., 1962, "A Variational Approach to the Theory of the Elastic Behavior of Polycrystals," *Journal of the Mechanics and Physics of Solids,* Vol. 10, pp. 343–352.

Chapman, A. M., and Higdon, J. J. L., 1994, "Effective Elastic Properties for a Periodic Bicontinuous Porous Medium," *Journal of the Mechanics and Physics of Solids,* Vol. 42, pp. 283–305.

Kanakkanatt, S. V., 1973, "Mechanical Anisotropy of Open-Cell Foams," *Journal of Cellular Plastics,* Vol. 9, pp. 50–53.

Ko, W. L., 1965, "Deformations of Foamed Elastomers," *Journal of Cellular Plastics,* Vol. 1, pp. 45–50.

Kraynik, A. M., and Reinelt, D. A., 1996a, "The Linear Elastic Behavior of Dry Soap Foams," *Journal of Colloid and Interface Science,* Vol. 181, pp. 511–520.

Kraynik, A. M., and Reinelt, D. A., 1996b, "The Linear Elastic Behavior of a Bidisperse Weaire-Phelan Soap Foam," *Chemical Engineering Communications,* Vol. 148–150, pp. 409–420.

Kraynik, A. M., and Reinelt, D. A., 1996c, "Elastic-Plastic Behavior of a Kelvin Foam," *Forma,* Vol. 11, pp. 255–270.

Kraynik, A. M., and Reinelt, D. A., 1996d, "The Microrheology of Wet Foams," *Proceedings of XIIth International Congress on Rheology,* edited by A. Ait-Kadi, J. M. Dealy, D. F. James, and M. C. Williams, eds., Quebec City, Canada, August 18–23, pp. 625–626.

Downloaded 04 May 2010 to 171.66.16.34. Redistribution subject to ASME license or copyright; see http://www.asme.org/terms/Terms_Use.cfm

Kraynik, A. M., and Warren, W. E., 1994, "The Elastic Behavior of Low-Density Cellular Plastics," *Low Density Cellular Plastics,* N. C. Hilyard and A. C. Cunningham, eds., Chapman and Hall, London, pp. 187–225.

Lederman, J. M., 1971, "The Prediction of the Tensile Properties of Flexible Foams," *Journal of Applied Polymer Science,* Vol. 15, pp. 693–703.

Love, A. E. H., 1994, *A Treatise on the Mathematical Theory of Elasticity,* Dover, New York.

Menges, G., and Knipschild, F., 1975, "Estimation of Mechanical Properties for Rigid Polyurethane Foams," *Polymer Engineering and Science,* Vol. 15, pp. 623–627.

Menges, G., and Knipschild, F., 1982, "Stiffness and Strength-Rigid Plastic Foams," *Mechanics of Cellular Plastics,* N. C. Hilyard, ed., Macmillan, New York, pp. 27–72.

Neilsen, M. K., and Kraynik, A. M., 1998, manuscript in preparation.

Nemat-Nasser, S., and Hori, M., 1993, *Micromechanics: Overall Properties of Heterogeneous Materials,* North Holland, Amsterdam.

Nye, J. F., 1985, *Physical Properties of Crystals,* Clarendon Press, Oxford.

Plateau, J. A. F., 1873, *Statique Experimentale et Theorique des Liquides Soumis aux Seules Forces Moleculaires,* Gauthier-Villars, Paris.

Progelhof, R. C., and Throne, J. L., 1979, "Young's Modulus of Uniform Density Thermoplastic Foam," *Polymer Engineering and Science,* Vol. 19, pp. 493–499.

Reinelt, D. A., and Kraynik, A. M., 1993, "Large Elastic Deformations of Three-Dimensional Foams and Highly Concentrated Emulsions," *Journal of Colloid and Interface Science,* Vol. 159, pp. 460–470.

Reinelt, D. A., and Kraynik, A. M., 1996, "Simple Shearing Flow of a Dry Kelvin Soap Foam," *Journal of Fluid Mechanics,* Vol. 311, pp. 327–343.

Rivier, N., 1994, "Kelvin's Conjecture on Minimal Surfaces and the Counterexample of Weaire and Phelan," *Philosophical Magazine Letters,* Vol. 69, pp. 297–303.

Thomson, W. (Lord Kelvin), 1887, "On the Division of Space with Minimum Partitional Energy," *Philosophical Magazine,* Vol. 24, pp. 503–514.

Warren, W. E., Neilsen, M. K., and Kraynik, A. M., 1997, "Torsional Rigidity of a Plateau Border," in press.

Warren, W. E., and Kraynik, A. M., 1988, "The Linear Elastic Properties of Open-Cell Foams," ASME JOURNAL OF APPLIED MECHANICS, Vol. 55, pp. 341–347.

Warren, W. E., and Kraynik, A. M., 1991, "The Nonlinear Elastic Behavior of Open-Cell Foams," ASME JOURNAL OF APPLIED MECHANICS, Vol. 58, pp. 376–381.

Weaire, D., and Fortes, M. A., 1994, "Stress and Strain in Liquid and Solid Foams," *Advances in Physics,* Vol. 43, pp. 685–738.

Weaire, D., and Phelan, R., 1994, "A Counterexample to Kelvin's Conjecture on Minimal Surfaces," *Philosophical Magazine Letters,* Vol. 69, pp. 107–110.

Downloaded 04 May 2010 to 171.66.16.34. Redistribution subject to ASME license or copyright; see http://www.asme.org/terms/Terms_Use.cfm

A Multicontinuum Approach to Structural Analysis of Linear Viscoelastic Composite Materials

M. R. Garnich
Engineering Mechanics Group,
Battelle—Pacific Northwest
National Laboratory,
Richland, WA 99352

A. C. Hansen
Department of Mechanical Engineering,
University of Wyoming,
Laramie, WY 82071

A "multicontinuum" approach to structural analyses of composites is described. A continuum field is defined to represent each constituent material along with the traditional continuum field associated with the composite. Finite element micromechanics is used to establish relationships between composite and constituent field variables. These relationships uncouple the micromechanics from structural solutions and render an efficient means of extracting constituent information during the course of a finite element structural analysis. Equations are developed for the case of a linear elastic reinforcing material embedded in a linear viscoelastic matrix and verified by comparison with results of finite element micromechanics.

1 Introduction

The analysis of composite material structures is complicated by the microstructural presence of two or more distinctly different materials and their microstructural interaction. The traditional approach to structural analysis is to ignore microstructural details by homogenizing them into an effective set of properties for a single continuum. Though very successful for noncomposite structural materials, the traditional approach has been found inadequate for describing or predicting many types of composite material behavior. Inadequacies are most frequently associated with inelastic material behaviors and predictions of material damage and failure. The inability to predict such phenomena can often be traced to a lack of information about constituent material response. The goal of this work is to develop a theory and associated numerical algorithm for extracting the continuum stress and strain fields for the constituents in a linear viscoelastic composite during the course of a routine structural analysis.

The modern approach to acquiring microstructural information is to employ numerical methods to perform micromechanical analyses. However, micromechanical analyses of single points are often computationally intensive. Therefore, it is generally impractical to use detailed micromechanical models in conjunction with structural analyses where there are often thousands of material points. Some investigators have employed simplified micromechanical models in an attempt to reduce the computational burden and allow some degree of coupling with structural analyses. Aboudi (1991) has developed a coupled micromechanical approach known as the Method of Cells in which the reinforcement is assumed to exist in a doubly periodic rectangular array. The unit cell model consists of four rectangular regions. This simplification of the microstructure facilitates efficient analytical expressions for the deformation behavior of the unit cell. However, these expressions must be solved at every step for each material point in an analysis, and despite the simplification, bring a significant computational cost. Also, assumed periodicity and simplified inclusion shape can produce poor results in some cases (see, e.g., Brockenbrough et al., 1991). In a similar vein, Pecknold and Rahman (1994) also employed a rectangular array micromechanics model that they formulated using mechanics of materials. They presented their micromechanics model as a cost effective tradeoff in conjunction with a hierarchical modeling approach to structural analysis of thick composites. Ravichandran and Seetharaman (1993) developed a model for predicting steady-state creep rates in composites by assuming a periodic array of rigid cubic inclusions and report good results except at intermediate volume fractions where the creep rates were significantly overestimated. Based primarily on Eshelby's (1957) work, Dvorak and Benveniste (1992) and Dvorak (1992) have developed a transformation theory for the micromechanical analysis of composites. Dvorak et al. (1994) implemented the theory in a numerical setting and made comparisons with finite element micromechanics results. Though elegant, the method was shown to be only marginally more efficient than the comparison finite element model as it relies on basically the same type of discretization procedures. These various studies stand as evidence of the trend toward the use of micromechanics models to either develop or verify constitutive laws for structural analysis of composites.

Coupled approaches, in which a micromechanics model is associated with each material point in a structural analysis, tend to be inefficient because they produce large amounts of information, such as microstructural displacements, that are of no direct use to the structural analyst. Hence, micromechanics has been used largely as a tool for investigating the constitutive behavior of composite materials and much less as a means of enhancing structural analyses. Such micromechanical investigations of constitutive behavior reveal the importance of microstructural variables in predicting the macroscopic response of the composite.

The traditional single continuum by itself does not provide a good framework for incorporating microstructure related variables into the structural solution process. For example, the viscous relaxation of a matrix material can cause significant exchange of load with an elastic fibrous reinforcement. Though a single continuum can be made to model the macroscopic deformation associated with such phenomena, it provides no means for monitoring variables associated with the phenomena itself (i.e., constituent stresses and strains). Micromechanics can readily model such behavior for a point, but as discussed previously, is generally impractical for use in structural analyses. To establish a more general framework for structural analysis of composites, Garnich and Hansen (1996) have introduced the concept of a multicontinuum. They have defined continuum fields for each material constituent and produced continuum results for fiber and matrix materials in a linear thermal-elastic

Contributed by the Applied Mechanics Division of THE AMERICAN SOCIETY OF MECHANICAL ENGINEERS for publication in the ASME JOURNAL OF APPLIED MECHANICS.

Discussion on the paper should be addressed to the Technical Editor, Professor Lewis T. Wheeler, Department of Mechanical Engineering, University of Houston, Houston, TX 77204-4792, and will be accepted until four months after final publication of the paper itself in the ASME JOURNAL OF APPLIED MECHANICS.

Manuscript received by the ASME Applied Mechanics Division, Oct. 7, 1996; final revision, Feb. 10, 1997. Associate Technical Editor: J. N. Reddy.

Copyright © 1997 by ASME

Downloaded 04 May 2010 to 171.66.16.34. Redistribution subject to ASME license or copyright; see http://www.asme.org/terms/Terms_Use.cfm

binary composite. Here, the concept is developed for the case of a linear viscoelastic composite in which a linear elastic reinforcing material is embedded in a linear viscoelastic matrix material.

The present work utilizes the concept of a "representative volume element" (RVE) as described by Hill (1963). The RVE concept and its limitations are formally discussed in detail by Nemat-Nasser and Hori (1993). For the present work it is assumed that any conditions necessary to validate the RVE concept are met and that volume averaging of constituent behavior within the RVE serves to define the effective properties of the composite.

The concept of volume averaging a small region about some point in a body is implicit to the definitions of stress and strain at a point in a continuum. For the special case of linear elastic and linear viscoelastic constituent materials (or phases) in a composite undergoing small strains and displacements under quasi-static loads and deformations, Hashin (1965) showed that the relationships between average stress and average strain in an RVE can be written in standard index notation as

$$\bar{\sigma}_{ij}(t) = \int_0^t C_{ijkl}(t-\tau)\frac{d\bar{\epsilon}_{kl}(\tau)}{d\tau}\,d\tau, \tag{1}$$

$$\bar{\epsilon}_{ij}(t) = \int_0^t D_{ijkl}(t-\tau)\frac{d\bar{\sigma}_{kl}(\tau)}{d\tau}\,d\tau, \tag{2}$$

where C_{ijkl} are the effective relaxation moduli of the composite, D_{ijkl} are the effective creep compliances, and t is time. Equations (1) and (2) are the familiar hereditary integral forms of the constitutive law for a linear viscoelastic material. Thus, a basis for small strain constitutive laws for heterogeneous materials consisting of perfectly bonded linear phases is established.

Micromechanics can be used to determine the average stresses and strains associated with a RVE. Many micromechanical models assume periodicity of the microstructural geometry. For example, unidirectional fibrous composites are commonly assumed to have the fibers arranged in hexagonal or square arrays. Under this assumption, a RVE which contains many fibers will contain the same characteristic periodicity in microstress and strain fields because of the assumed macroscopically uniform fields. Hence, a small part of the RVE (enough to contain one characteristic unit of the periodic behavior) becomes representative of the RVE. Such characteristic subvolumes of the RVE are termed "unit cells" and micromechanical models based on such periodicity are referred to as "unit cell models."

In the remainder of this paper, both direct tensor notation and the "Voigt" double index notation (Mehrabadi and Cowen, 1990) are employed. In direct notation, vectors are denoted by lower case boldface Arabic characters while second-order tensors are lower case boldface Greek characters and fourth-order tensors are denoted by bolded upper case characters. Unbolded characters denote scalars. In Voigt notation, fourth-order tensors are contracted to 6×6 matrices whose components are specified by pairs of subscript indices, second-order tensors are contracted to 6×1 vectors whose components are identified by a single subscript index. The notation $[\ \ ]^T$ denotes the transpose of the matrix $[\ \ ]$.

2 A Linear Viscoelastic Multicontinuum

Equations are developed for a multicontinuum in which inelastic deformations occur. Specifically, a composite consisting of a linear isotropic viscoelastic matrix reinforced by aligned transversely isotropic linear elastic fibers is modeled. The development is restricted to linearity so, as with linear elasticity, the volume average stresses and strains yield exact constitutive relations.

The constitutive law for the material is formulated in terms of hereditary integrals that are exploited by use of a recursive relation that allows an incremental numerical evaluation. A simple Euler approximation is utilized at each time step. A unique decomposition of constituent strains is employed to derive a system of equations that are exact relations between incremental composite stresses and strains and those of the constituents. Although the theory is valid for thermorheologically simple materials (Schapery 1974), for simplicity reduced time is not introduced so that thermal expansion properties in the composite are assumed independent of temperature. In the constituents, thermal expansion properties are independent of time and temperature.

The governing equations are implemented in a standard displacement based finite element program. Multicontinuum stress and strain histories are generated and compared with those determined from finite element micromechanics.

2.1 Strain Decompositions. The eventual solution for constituent variables relies on the following decompositions of constituent strains. First, let

$$\boldsymbol{\epsilon}_\beta(t) = \boldsymbol{\epsilon}_\beta^e(t) + \boldsymbol{\epsilon}_\beta^f(t), \tag{3}$$

such that

$$\boldsymbol{\sigma}_\beta(t) = \mathbf{C}_\beta[\boldsymbol{\epsilon}_\beta^e(t) - \theta(t)\boldsymbol{\alpha}_\beta], \tag{4}$$

where $\mathbf{C}_\beta$ is the elastic stiffness tensor for constituent β. Also, $\boldsymbol{\epsilon}_\beta$, $\boldsymbol{\sigma}_\beta$, and $\boldsymbol{\alpha}_\beta$ are the continuum strain, stress, and thermal expansion tensors, respectively, for constituent β. The scalar θ is the temperature relative to a reference temperature in the composite. The above implies that $\boldsymbol{\epsilon}_\beta^f(t)$ is a "flow" strain that does not contribute to stress in Eq. (4). Now consider the existence of two clearly identifiable sources of elastic strain in the constituents. The rationale for such a decomposition is discussed later. For now, let

$$\boldsymbol{\epsilon}_\beta^e(t) = \boldsymbol{\epsilon}_\beta^{e'}(t) + \boldsymbol{\epsilon}_\beta^{e''}(t), \tag{5}$$

such that

$$\sum_\beta \phi_\beta \mathbf{C}_\beta \boldsymbol{\epsilon}_\beta^{e''}(t) = \mathbf{0}, \tag{6}$$

where ϕ_β represents the volume fraction of constituent β.

Consider now the well-known summation rules (see, e.g., Hill, 1963):

$$\boldsymbol{\sigma}(t) = \sum_\beta \phi_\beta \boldsymbol{\sigma}_\beta(t), \tag{7}$$

and

$$\boldsymbol{\epsilon}(t) = \sum_\beta \phi_\beta \boldsymbol{\epsilon}_\beta(t). \tag{8}$$

Substituting Eqs. (4) through (6) into (7) gives

$$\boldsymbol{\sigma}(t) = \sum_\beta \phi_\beta \mathbf{C}_\beta[\boldsymbol{\epsilon}_\beta^{e'}(t) - \theta(t)\boldsymbol{\alpha}_\beta]. \tag{9}$$

Also, substituting Eqs. (3) and (5) into Eq. (8) allows one to write

$$\boldsymbol{\epsilon}(t) = \sum_\beta \phi_\beta[\boldsymbol{\epsilon}_\beta^{e'}(t) + \boldsymbol{\epsilon}_\beta^{e''}(t) + \boldsymbol{\epsilon}_\beta^f(t) + \theta(t)\boldsymbol{\alpha}_\beta - \theta(t)\boldsymbol{\alpha}_\beta]. \tag{10}$$

Noting Eq. (9) it is seen from Eq. (10) that the total composite strain not associated with any *composite* stress, in terms of constituent strains, is

$$\boldsymbol{\epsilon}^*(t) = \sum_\beta \phi_\beta[\boldsymbol{\epsilon}_\beta^{e''}(t) + \boldsymbol{\epsilon}_\beta^f(t) + \theta(t)\boldsymbol{\alpha}_\beta]. \tag{11}$$

The above stress-free composite strain relation is a key to the numerical solution of constituent variables developed later. Also, it should be noted that $\boldsymbol{\epsilon}_\beta^{e''}(t)$ is an elastic strain in constituent β that, although contributing to the stress in constituent β,

Downloaded 04 May 2010 to 171.66.16.34. Redistribution subject to ASME license or copyright; see http://www.asme.org/terms/Terms_Use.cfm

does not contribute to stress in the composite. Hence $\boldsymbol{\epsilon}_\beta^{e''}(t)$ occurs entirely due to exchange of load between constituents in a RVE, and not due to any external load on the RVE.

For consistency with the constituent strain decompositions, let

$$\boldsymbol{\epsilon}(t) = \boldsymbol{\epsilon}^e(t) + \boldsymbol{\epsilon}^f(t), \tag{12}$$

and define

$$\boldsymbol{\epsilon}^f(t) = \boldsymbol{\epsilon}^*(t) - \theta(t)\hat{\boldsymbol{\alpha}}, \tag{13}$$

so that for the composite the stress is expressed in the same form as Eq. (4), i.e.,

$$\boldsymbol{\sigma}(t) = \mathbf{C}[\boldsymbol{\epsilon}^e(t) - \theta(t)\hat{\boldsymbol{\alpha}}]. \tag{14}$$

In the above, $\hat{\boldsymbol{\alpha}}$ is the initial ($t = 0$) composite thermal expansion coefficient and Eq. (13) implies that the associated thermal expansion is contained in $\boldsymbol{\epsilon}^e(t)$. Note the composite thermal expansion is time dependent even though the constituent thermal expansions are constant. This is caused by the mismatch in constituent thermal expansions that results in stresses, and therefore creep strains, at the microstructural level in a viscoelastic composite.

2.2 Constitutive Laws. The present theory is developed only for linear constitutive laws. Therefore, for demonstration purposes, the composite is assumed to consist of a linear viscoelastic matrix with a linear elastic reinforcing material. The reinforcement and matrix materials are denoted by subscripts r and m, respectively. The constitutive law for the reinforcement is

$$\boldsymbol{\sigma}_r(t) = \mathbf{C}_r[\boldsymbol{\epsilon}_r(t) - \theta(t)\boldsymbol{\alpha}_r], \tag{15}$$

where $\mathbf{C}_r$ is the elastic stiffness tensor, $\boldsymbol{\alpha}_r$ is a constant thermal expansion tensor, and $\theta(t)$ is the temperature relative to a reference temperature in the composite that corresponds to a stress-free state in the constituents. The reinforcement is assumed to consist of transversely isotropic fibers, aligned uniaxially in the composite.

For the linear viscoelastic matrix, an integral form of the constitutive law is used:

$$\boldsymbol{\epsilon}_m(t) = \int_{0^-}^{t} \mathbf{D}_m(t-\tau)\dot{\boldsymbol{\sigma}}_m d\tau + \theta(t)\boldsymbol{\alpha}_m, \tag{16}$$

where for an arbitrary function $\omega(\tau)$,

$$\dot{\omega} \equiv \frac{d\omega(\tau)}{d\tau}.$$

In the above, $\mathbf{D}_m(t)$ is the creep compliance tensor. At $t = 0^-$ (an arbitrarily small time before $t = 0$), the composite and constituents are assumed to be in a stress-free reference state. At $t = 0^+$, there may be finite loads, thus permitting instantaneous loads at time $t = 0$. The components of $\mathbf{D}_m(t)$ can be defined in the exponential form:

$$D_{ij}(t) = D_{ij}^0 + \sum_{L=1}^{N} D_{ij}^L \exp\left[\frac{-t}{\prod_{ij}^L}\right], \tag{17}$$

where the symbol $\prod$ denotes time constants associated with each exponential term and N is the number of exponential terms required to properly characterize the time dependence of the material behavior.

For the present case the matrix is assumed isotropic, and the following exponential form of the uniaxial creep compliance is used to characterize the viscoelastic response (Flügge, 1967).

$$J_m(t) = J_m^0 + \sum_{L=1}^{N} J_m^L \exp\left[\frac{t}{\prod_m^L}\right] \tag{18}$$

In the above, superscripts are indices, not exponents. The $\prod_m^L$ are the time constants associated with each of the N exponential terms and the J_m^L are the corresponding creep coefficients. Although the theory readily admits time-dependent bulk behavior, for simplicity the bulk response is assumed purely elastic, i.e.,

$$K_m(t) = K_m. \tag{19}$$

Then, in Voigt double-index notation (Mehrabadi and Cowen, 1990) the isotropic creep compliance tensor is defined by

$$D_{m,ij}(t) = \begin{bmatrix} D_{m,11}(t) & D_{m,12}(t) & D_{m,12}(t) & 0 & 0 & 0 \\ D_{m,12}(t) & D_{m,11}(t) & D_{m,12}(t) & 0 & 0 & 0 \\ D_{m,12}(t) & D_{m,12}(t) & D_{m,11}(t) & 0 & 0 & 0 \\ 0 & 0 & 0 & D_{m,44}(t) & 0 & 0 \\ 0 & 0 & 0 & 0 & D_{m,44}(t) & 0 \\ 0 & 0 & 0 & 0 & 0 & D_{m,44}(t) \end{bmatrix}, \tag{20}$$

where

$$D_{m,11}(t) = J_m(t),$$

$$D_{m,12}(t) = \frac{1}{2}\left[\frac{1}{3K_m} - J_m(t)\right],$$

and

$$D_{m,44}(t) = 2[D_{m,11}(t) - D_{m,12}(t)].$$

The above three equations are readily derivable by analogy to the isotropic linear elastic compliance tensor.

For a composite consisting of the above constituents, the following constitutive law applies:

$$\boldsymbol{\epsilon}(t) = \int_{0^-}^{t} \mathbf{D}(t-\tau)\dot{\boldsymbol{\sigma}} d\tau + \int_{0^-}^{t} \boldsymbol{\alpha}(t-\tau)\dot{\theta} d\tau. \tag{21}$$

To define $\mathbf{D}(t)$ and $\boldsymbol{\alpha}(t)$ in Eq. (21), the components of the compliance tensor for a transversely isotropic composite in Voigt double-index notation are

$$D_{ij}(t) = \begin{bmatrix} D_{11}(t) & D_{12}(t) & D_{12}(t) & 0 & 0 & 0 \\ D_{12}(t) & D_{22}(t) & D_{23}(t) & 0 & 0 & 0 \\ D_{12}(t) & D_{23}(t) & D_{22}(t) & 0 & 0 & 0 \\ 0 & 0 & 0 & D_{44}(t) & 0 & 0 \\ 0 & 0 & 0 & 0 & D_{55}(t) & 0 \\ 0 & 0 & 0 & 0 & 0 & D_{55}(t) \end{bmatrix}, \tag{22}$$

where

$$D_{44}(t) = 2(D_{22}(t) - D_{23}(t)).$$

In the above, $D_{44}(t)$ is the transverse shear compliance and, as implied, the fibers are aligned in the 1-direction. For thermal expansion,

$$\alpha_i(t) = [\alpha_1(t) \quad \alpha_2(t) \quad \alpha_2(t) \quad 0 \quad 0 \quad 0]^T. \tag{23}$$

The components of Eq. (22) can also be defined in the form of Eq. (17) while the components of Eq. (23) are similarly defined by

$$\alpha_i(t) = \alpha_i^0 + \sum_{K=1}^{M} \alpha_i^K \exp\left[-\frac{t}{\prod_i^K}\right]. \tag{24}$$

Given the material constants of the constituents, a finite element micromechanics model can be used to generate the material constants for the composite in Eqs. (17) and (24). For demonstration purposes, a hexagonal packing unit cell model for a unidirectional fibrous composite described by Garnich and Hansen (1996), was employed in the present study to generate data for three creep tests that completely define the five independent creep compliance functions for the transversely isotropic composite. The creep data were used to define the five indepen-

Downloaded 04 May 2010 to 171.66.16.34. Redistribution subject to ASME license or copyright; see http://www.asme.org/terms/Terms_Use.cfm

dent functions found in Eq. (22). These resulting data were then fitted to a sum of exponentials to yield the constants in Eq. (17) using a nonlinear least-squares curve fitting algorithm found in Press et al. (1989). Similarly, a constant temperature thermal expansion will result in a strain history that defines the constants in Eq. (24). The assumed material constants associated with Eqs. (15), (18)–(20), and (22)–(24) are listed in Appendix A.

2.3 Composite Solution Algorithm. Here, an incremental procedure for determining the stress and strain history of an integration point in a finite element model of a composite structure is described. The procedure for an approximate incremental solution of Eq. (21) has been described for isotropic materials by Krishnaswamy et al. (1990) and is generalized here for orthotropic materials. The explicit time-stepping procedure for the structural displacement solution is equivalent to the one described by Hughes and Taylor (1978). To avoid confusion in what follows, all summations over indices are explicit, i.e., there is *no* implied summation over repeated indices.

Consider an increment in time between steps n and $n+1$, and define $\Delta t = t_{n+1} - t_n$. Then, after interchanging the summation and integration, an incremental form of Eq. (21) using the notation of Eqs. (22) and (23) is

$$\Delta\epsilon_i = \sum_{j=1}^{6}\left(\int_{0^-}^{t_{n+1}} D_{ij}(t_{n+1}-\tau)\dot{\sigma}_j d\tau - \int_{0^-}^{t_n} D_{ij}(t_n-\tau)\dot{\sigma}_j d\tau\right) + \int_{0^-}^{t_{n+1}} \alpha_i(t_{n+1}-\tau)\dot{\theta}\,d\tau - \int_{0^-}^{t_n} \alpha_i(t_n-\tau)\dot{\theta}\,d\tau. \quad (25)$$

In the above, an increment in strain is given by a sum of integral difference pairs of the form

$$\Delta I = \int_{0^-}^{t_{n+1}} Q(t_{n+1}-\tau)\dot{\xi}\,d\tau - \int_{0^-}^{t_n} Q(t_n-\tau)\dot{\xi}\,d\tau, \quad (26)$$

where the functions $Q(t)$ are defined by Eqs. (17) and (24). In Appendix B, an equation is derived for an explicit approximation of ΔI based on small Δt where $\dot{\xi}$ is assumed constant over the interval. Using the form of Eq. (B11) in conjunction with Eqs. (17) and (24), Eq. (25) becomes

$$\Delta\epsilon_i = \sum_{j=1}^{6}\left[D_{ij}^0\Delta\sigma_j + \sum_{L=1}^{N}\left(1-\exp\left[\frac{-\Delta t}{\Pi_{ij}^L}\right]\right)\times\left(D_{ij}^L\Pi_{ij}^L\frac{\Delta\sigma_j}{\Delta t} - P_{ij}^L(t_n)\right)\right] + \alpha_i^0\Delta\theta + \sum_{K=1}^{M}\left(1-\exp\left[\frac{-\Delta t}{\Pi_i^K}\right]\right)\left(\alpha_i^K\Pi_i^K\frac{\Delta\theta}{\Delta t} - \zeta_i^K(t_n)\right), \quad (27)$$

where, according to equation (B6), the $P_{ij}^L(t_n)$ and $\zeta_i^K(t_n)$ are known from

$$P_{ij}^L(t_n) = P_{ij}^L(t_{n-1})\exp\left[\frac{-\Delta\hat{t}}{\Pi_{ij}^L}\right] + D_{ij}^L\Pi_{ij}^L\frac{\Delta\hat{\sigma}_j}{\Delta\hat{t}}\left(1-\exp\left[\frac{-\Delta\hat{t}}{\Pi_{ij}^L}\right]\right), \quad (28)$$

and

$$\zeta_i^K(t_n) = \zeta_i^K(t_{n-1})\exp\left[\frac{-\Delta\hat{t}}{\Pi_i^K}\right] + \alpha_i^K\Pi_i^K\frac{\Delta\hat{\theta}}{\Delta\hat{t}}\left(1-\exp\left[\frac{-\Delta\hat{t}}{\Pi_i^K}\right]\right). \quad (29)$$

In the above, $\Delta\hat{t}$, $\Delta\hat{\sigma}$, and $\Delta\hat{\theta}$ are increments for the previous time step. The temperature history is assumed known from an uncoupled thermal problem and therefore $\Delta\theta$ in Eq. (27) is known. Finally, a solution to (27) is realized by making an Euler approximation to the strain increment over Δt. That is, the inelastic part of the total strain increment is assumed independent of $\Delta\sigma_j$ and is denoted as $\Delta\epsilon_j^*$. The elastic strain increment associated with $\Delta\sigma_j$ is assumed independent of time and occurs instantaneously at the end of the time step when the structural solution permits explicit calculation of $\Delta\sigma_j$. Therefore, to determine $\Delta\epsilon_j^*$, it is assumed that $\Delta\sigma_j = 0$ and Eq. (27) becomes

$$\Delta\epsilon_i^* = -\sum_{j=1}^{6}\sum_{L=1}^{N}\left(1-\exp\left[\frac{-\Delta t}{\Pi_{ij}^L}\right]\right)P_{ij}^L(t_n) + \alpha_i^0\Delta\theta + \sum_{K=1}^{M}\left(1-\exp\left[\frac{-\Delta t}{\Pi_i^K}\right]\right)\left(\alpha_i^K\Pi_i^K\frac{\Delta\theta}{\Delta t} - \zeta_i^K(t_n)\right). \quad (30)$$

Note, the above implies N is the same for each $D_{ij}(t)$ and M is the same for each $\alpha_i(t)$. The strain increment $\Delta\epsilon_i^*$ is stress free and includes thermal strain but is not equal to the total strain increment $\Delta\epsilon_i$.

In the context of a structural problem formulated with the finite element method, $\Delta\epsilon_i^*$ is the stress-free increment in strain at an integration point. Using well-known finite element procedures (e.g., Levy and Pifko, 1981) fictitious element nodal loads, which are associated with $\Delta\epsilon_i^*$ and the elastic material properties, are determined by numerical integration over the element volume. The structure incremental displacements are determined as a function of the elastic structure stiffness and the "total" increment in load. That is, if the material elastic stiffness matrix is $[C]$, the strain-displacement matrix is $[B]$, the vector of incremental external loads is $\{\Delta F\}$, and the vector of structure incremental nodal displacements is $\{\Delta U\}$, then the structure elastic stiffness matrix is $[K] = \int_V [B]^T[C][B]dV$ and

$$[K]\{\Delta U\} = \int_V [B]^T[C]\{\Delta\epsilon^*\}dV + \{\Delta F\}. \quad (31)$$

The increment in displacements is solved for and is used to update the total strain and stress in the composite. Then, using Eqs. (12) and (14) the total composite flow strain, $\boldsymbol{\epsilon}^f(t)$, can be calculated.

2.4 Constituent Solutions. Consider the time increment Δt and the stress-free composite strain increment $\Delta\boldsymbol{\epsilon}^*$ of Eq. (30). Because the change in stress is zero, the associated incremental form of Eq. (9) for the present binary composite is

$$\mathbf{0} = \phi_r\mathbf{C}_r(\Delta\boldsymbol{\epsilon}_r^{e'} - \Delta\theta\boldsymbol{\alpha}_r) + \phi_m\mathbf{C}_m(\Delta\boldsymbol{\epsilon}_m^{e'} - \Delta\theta\boldsymbol{\alpha}_m). \quad (32)$$

The above is the same form as Eq. (6) and therefore the terms in parenthesis satisfy the definition of $\Delta\boldsymbol{\epsilon}_r^{e''}$ and $\Delta\boldsymbol{\epsilon}_m^{e''}$ and must individually be zero because by definition these terms are distinct from $\Delta\boldsymbol{\epsilon}_r^{e''}$ and $\Delta\boldsymbol{\epsilon}_m^{e''}$. Therefore, for $\Delta\boldsymbol{\sigma} = \mathbf{0}$, instead of the single Eq. (32), there are two conditions:

$$\Delta\boldsymbol{\epsilon}_r^{e'} = \Delta\theta\boldsymbol{\alpha}_r,$$

and

$$\Delta\boldsymbol{\epsilon}_m^{e'} = \Delta\theta\boldsymbol{\alpha}_m. \quad (33)$$

Combining Eqs. (3) and (5), utilizing the above result, and noting that $\Delta\boldsymbol{\epsilon}_r^f = 0$, the corresponding strain increments in the constituents are

Downloaded 04 May 2010 to 171.66.16.34. Redistribution subject to ASME license or copyright; see http://www.asme.org/terms/Terms_Use.cfm

$$\Delta\boldsymbol{\epsilon}_r^* = \Delta\theta\boldsymbol{\alpha}_r + \Delta\boldsymbol{\epsilon}_r^{e''},$$

and

$$\Delta\boldsymbol{\epsilon}_m^* = \Delta\theta\boldsymbol{\alpha}_m + \Delta\boldsymbol{\epsilon}_m^{e''} + \Delta\boldsymbol{\epsilon}_m^{f}. \tag{34}$$

Substituting Eq. (34) into an incremental form of Eq. (8), noting Eq. (6), and rearranging terms yields

$$\Delta\boldsymbol{\epsilon}^* = \Delta\theta(\phi_r\boldsymbol{\alpha}_r + \phi_m\boldsymbol{\alpha}_m) + \phi_m(\mathbf{I} - \mathbf{C}_r^{-1}\mathbf{C}_m)\Delta\boldsymbol{\epsilon}_m^{e''} + \phi_m\Delta\boldsymbol{\epsilon}_m^{f}, \tag{35}$$

where $\mathbf{I}$ is the identity tensor. Recall, $\Delta\boldsymbol{\epsilon}^*$ is the stress-free strain increment that is known from the composite solution (see Eq. (30)).

Now recall Eq. (16), the constitutive law for the viscoelastic matrix, and specialize it to the present incremental form for a stress-free strain increment in the composite.

$$\Delta\boldsymbol{\epsilon}_m^* = \int_{0^-}^{t_{n+1}} \mathbf{D}_m(t_{n+1} - \tau)\dot{\boldsymbol{\sigma}}_m^* d\tau - \int_{0^-}^{t_n} \mathbf{D}_m(t_n - \tau)\dot{\boldsymbol{\sigma}}_m^* d\tau + \Delta\theta\boldsymbol{\alpha}_m. \tag{36}$$

In the above, the components of $\mathbf{D}_m(t)$ are defined by Eqs. (18) through (20). The matrix stress rate $\dot{\boldsymbol{\sigma}}_m^*$ is, like $\Delta\boldsymbol{\epsilon}_m^*$, associated with the constant *composite* stress strain increment. Therefore, recalling Eqs. (4), (5), and (33), $\dot{\boldsymbol{\sigma}}_m^*$ must be defined by

$$\dot{\boldsymbol{\sigma}}_m^* = \mathbf{C}_m \frac{d\boldsymbol{\epsilon}_m^{e''}}{dt}. \tag{37}$$

The integral difference pair in Eq. (36) is of the same form as those of the composite and the same solution procedure using the equations of Appendix B can be applied to yield

$$\Delta\boldsymbol{\epsilon}_m^* = \left(\mathbf{D}_m^0 + \sum_{L=1}^{N} \mathbf{D}_m^L \frac{\prod_m^L}{\Delta t}\left(1 - \exp\left[\frac{-\Delta t}{\prod_m^L}\right]\right)\right)\Delta\boldsymbol{\sigma}_m^* - \sum_{L=1}^{N}\left(1 - \exp\left[\frac{-\Delta t}{\prod_m^L}\right]\right)\boldsymbol{\gamma}^L(t_n) + \Delta\theta\boldsymbol{\alpha}_m, \tag{38}$$

where

$$\Delta\boldsymbol{\sigma}_m^* = \mathbf{C}_m\Delta\boldsymbol{\epsilon}_m^{e''}, \tag{39}$$

and again noting results of Appendix B,

$$\boldsymbol{\gamma}^L(t_n) = \boldsymbol{\gamma}^L(t_{n-1})\exp\left[\frac{-\Delta\hat{t}}{\prod_m^L}\right] + \mathbf{D}_m^L\prod_m^L\left(1 - \exp\left[\frac{-\Delta\hat{t}}{\prod_m^L}\right]\right)\frac{\Delta\hat{\boldsymbol{\sigma}}_m}{\Delta\hat{t}}, \tag{40}$$

with initial condition

$$\boldsymbol{\gamma}^L(0^+) = \boldsymbol{\sigma}_m(0^+). \tag{41}$$

Again, terms with "hats" are for the previous time step. Equations (34), (35), (38), and (39) are solvable for the unknown constituent variables $\Delta\boldsymbol{\epsilon}_m^*$, $\Delta\boldsymbol{\epsilon}_m^{e''}$, $\Delta\boldsymbol{\epsilon}_m^{f}$, and $\Delta\boldsymbol{\sigma}_m^*$. For example,

$$\Delta\boldsymbol{\sigma}_m^* = \mathbf{H}\Delta\boldsymbol{\mu}, \tag{42}$$

where

$$\mathbf{H} = \left(\mathbf{C}_r^{-1} - \mathbf{D}_m^0 - \sum_{L=1}^{N}\mathbf{D}_m^L\left(1 - \exp\left[\frac{-\Delta t}{\prod_m^L}\right]\right)\frac{\prod_m^L}{\Delta t}\right)^{-1},$$

Table 1 Computational procedure for multicontinuum solution of linear viscoelastic structural problems

1. For the initial ($t = 0$) loads $\{F_*\}$, determine the initial displacements $\{U_*\}$ from $[K]\{U_*\} = \{F_*\}$. Initialize integration point "flow" strains for the composite, $\{\varepsilon'\} = \{0\}$, and the matrix, $\{\varepsilon'_m\} = \{0\}$.
2. Using element displacements, $\{u\}$, determine total strains for the composite from $\{\varepsilon\} = [B]\{u\}$, total strains for the matrix from equation (45), and matrix stress from equations (3) and (4).
3. Determine the stress free change in composite strain $\{\Delta\varepsilon^*\}$ from equation (30).
4. Determine $\{\Delta\varepsilon'\}$ from an incremental form of equation (13) and update the total $\{\varepsilon'\}$.
5. Determine $\{\Delta\sigma_m^*\}$ from equation (42), $\{\Delta\varepsilon'_m\}$ from equation (43), and update the total $\{\varepsilon'_m\}$.
6. Determine the increment in structure displacements using equation (31) and update the total displacements $\{U\}$.
7. If solution is not complete return to step 2.

and

$$\Delta\boldsymbol{\mu} = \left(\frac{\Delta\theta}{\phi_m}(\phi_r\boldsymbol{\alpha}_r + \phi_m\boldsymbol{\alpha}_m) - \frac{\Delta\boldsymbol{\epsilon}^*}{\phi_m} - \sum_{L=1}^{N}\mathbf{D}_m^L\left(1 - \exp\left[\frac{-\Delta t}{\prod_m^L}\right]\right)\boldsymbol{\gamma}^L(t_n)\right).$$

Using the above result, the increment in flow strain for the matrix is easily calculated from

$$\Delta\boldsymbol{\epsilon}_m^f = (\mathbf{C}_r^{-1} - \mathbf{C}_m^{-1})\Delta\boldsymbol{\sigma}_m^* + \frac{\Delta\boldsymbol{\epsilon}^*}{\phi_m} - \frac{\Delta\theta}{\phi_m}(\phi_r\boldsymbol{\alpha}_r + \phi_m\boldsymbol{\alpha}_m). \tag{43}$$

The total flow strain in the matrix is updated using

$$\boldsymbol{\epsilon}_m^f(t_{n+1}) = \boldsymbol{\epsilon}_m^f(t_n) + \Delta\boldsymbol{\epsilon}_m^f. \tag{44}$$

Then, combined with the composite results of the previous section, the total strain in the matrix is determined using Eqs. (3), (4), (7), (8), (12), and (14) as

$$\boldsymbol{\epsilon}_m = \frac{1}{\phi_m}(\mathbf{C}_m - \mathbf{C}_r)^{-1}\{(\mathbf{C} - \mathbf{C}_r)\boldsymbol{\epsilon} + \theta(\phi_r\mathbf{C}_r\boldsymbol{\alpha}_r + \phi_m\mathbf{C}_m\boldsymbol{\alpha}_m - \mathbf{C}\hat{\boldsymbol{\alpha}}) + \phi_m\mathbf{C}_m\boldsymbol{\epsilon}_m^f - \mathbf{C}\boldsymbol{\epsilon}^f\}. \tag{45}$$

From here, all other constituent variables are readily determined using Eqs. (3), (4), (8), and (15).

The basic steps of the computational procedure used for the multicontinuum solution of linear viscoelastic problems are shown in Table 1 using the matrix notation associated with Eq. (31). Note, that steps 2–5 describe integration point calcula-

Downloaded 04 May 2010 to 171.66.16.34. Redistribution subject to ASME license or copyright; see http://www.asme.org/terms/Terms_Use.cfm

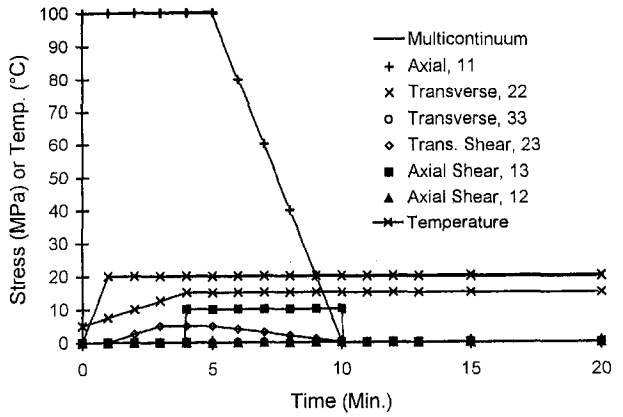


Fig. 1 Composite stress and applied temperature history for the combined loading. Lines indicate multicontinuum data and symbols indicate associated finite element micromechanics model results.

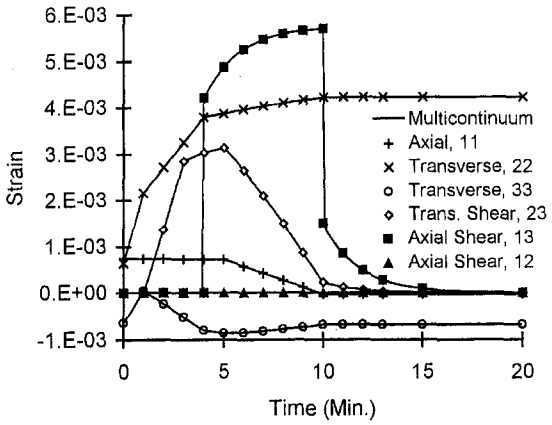


Fig. 3 Matrix strain results for the combined loading. Lines indicate multicontinuum results and symbols indicate finite element micromechanics model results.

tions that must be performed for every integration point in the structure. The vectors $\{\epsilon^f\}$ and $\{\epsilon_m^f\}$ must be stored for the previous time step at all integration points to perpetuate the algorithm and at any other time to permit post calculation of constituent results as desired.

2.5 Numerical Results. The equations developed in the previous section were implemented in a standard displacement based finite element program. Effectively, equations (42) through (45) were embedded in the solution algorithm for the composite represented by Eqs. (30) and (31). A standard eight-node three-dimensional solid element as described by Cook et al. (1989) was employed. A single element model of cubic geometry was used in all simulations. Boundary conditions that would generate specific histories of uniform stress or strain could then be easily specified. For the results presented here, small time steps were specified to exclude numerical error due to time-step approximations as a complicating issue in the quantitative comparisons.

In all plots of stress or strain histories, the solid lines represent results of the multicontinuum theory, while the discrete symbols are volume average values extracted from the finite element micromechanics model. A combined load simulation was performed to verify the theory as well as the numerical implementation. A single element model was stress controlled by specifying nodal load histories that result in uniform states of stress. The applied composite stress history is shown in Fig. 1 along with the temperature load history. The associated composite strain histories are shown in Fig. 2. Finally, the matrix and reinforcement strain histories are shown in Fig. 3 and Fig. 4, respectively. In all cases there is effectively exact agreement between the finite element micromechanics and the multicontinuum results.

3 Computational Costs

The multicontinuum theory is intended to be a computationally effective means of bringing constituent information to the analysis of composite structures. As such, it is relevant to examine the computational resources required. For comparison, consider the use of finite element micromechanics models as solutions coupled to the structural finite element model. The cost of the composite structural model is the same in both cases so the comparison is restricted to the cost of producing constituent information. For the finite element micromechanics model used in this study, the simulation of one material point for 50 minutes of viscoelastic behavior, required approximately 2500 seconds of processing time. In contrast, the single element structural model representing eight material (integration) points required less than one second devoted to the multicontinuum calculations. Therefore, for a single material point, the multicontinuum model required roughly four orders of magnitude less processing time. In fact, the cost of multicontinuum calculations are but a small percentage of the cost of the composite structural solution. The more significant cost of the multicontinuum approach is data storage. Because there are three continuum fields there can be nearly three times as much data generated for postprocessing. However, in general only two of the fields need be saved as the third can be readily extracted as a function of the

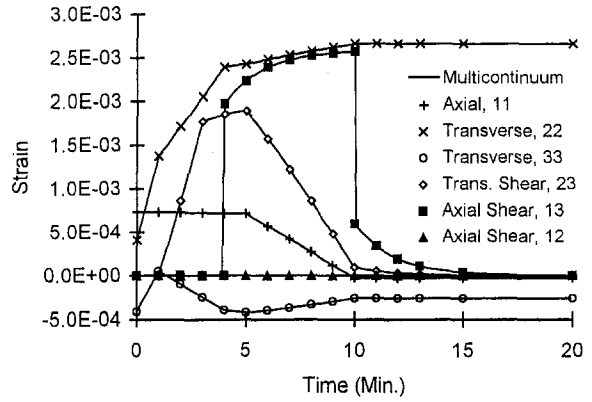


Fig. 2 Composite strain results for the combined loading. Lines indicate multicontinuum results and symbols indicate finite element micromechanics model results.

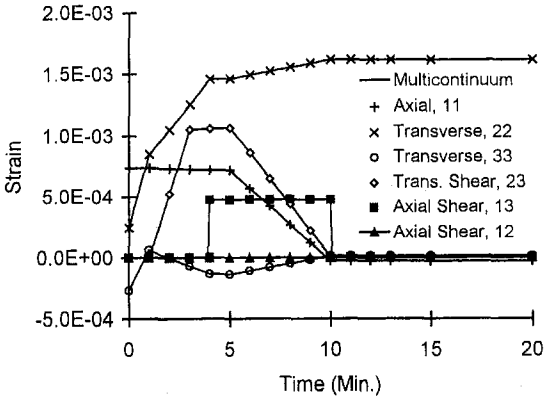


Fig. 4 Reinforcement strain results for the combined loading. Lines indicate multicontinuum results and symbols indicate finite element micromechanics model results.

Downloaded 04 May 2010 to 171.66.16.34. Redistribution subject to ASME license or copyright; see http://www.asme.org/terms/Terms_Use.cfm

other two. Even assuming double the storage, the postprocessing data storage requirements are small compared to the requirements associated with maintaining even a modest micromechanics model at each integration point.

In summary, the processing cost is considered negligible, while the increase in storage costs are the same order as is associated with conventional single continuum structural analysis. Though significant, the additional storage is perhaps the minimum that can be expected when bringing micromechanical information to bear on a structural problem.

4 Discussion

The multicontinuum theory provides a rational framework for incorporating a larger number of constitutive and field variables in composite structural analysis. It does so by conceptually superimposing multiple continuum fields associated with the constituent materials. In this way, the known constitutive behaviors of the individual phases are incorporated into the analysis without the cost of explicitly modeling microstructural details as with the coupled micromechanics approach. And yet, the effect of microstructural details are present in the analysis because micromechanics is used to establish relations between the constituent and composite variables. However, because the micromechanics is a preprocessing step in establishing these relations, it does not impose any direct computational burden on subsequent structural analyses.

In the multicontinuum, the composite response is decomposed by rigorous relations to the summed responses of the constituents. Not only does this approach produce constituent information but the composite constitutive law is forced to be consistent with those of the constituents through a micromechanics model that should properly emulate the microstructural interaction of the constituents. Because the micromechanics model is uncoupled from the structural analysis, it can be of high complexity with minimal simplifying assumptions. For example, random fiber unit cells can be utilized in materials where the effect of reinforcement distribution is important to accurate modeling of the constitutive response.

For the case of linear thermal viscoelasticity, the classic decomposition of strains into elastic and inelastic parts was extended by decomposing the elastic strains of the constituents into parts defined by the microstructural interaction that exchanges load between the constituents with no change in load on the composite. These strain decompositions yielded equations that relate the constituent constitutive laws with the incremental composite solution process and thus yield constituent stress and strain increments rigorously tied to those of the composite.

The results indicate the value of constituent information. Consider the constituent strain histories in Figs. 3 and 4, and the available constituent stress histories not shown. Clearly this information is a valuable addition to the composite data shown in Figs. 1 and 2 that is normally available from structural analysis programs.

Acknowledgment

This work was supported by Battelle–Pacific Northwest National Laboratory and NASA (Grant #NGT 40050) through the Wyoming Planetary and Space Sciences Center.

References

Aboudi, J., 1991, *Mechanics of Composite Materials: A Unified Micromechanics Approach,* Elsevier, Amsterdam.

Brockenbrough, J. R., Suresh, S., and Wienecke, H. A., 1991, "Deformation of Metal Matrix Composites with Continuous Fibers: Geometrical Effects of Fiber Distribution and Shape," *Acta Metall. Mater.,* Vol. 39, No. 5, pp. 735–752.

Cook, R. D., Malkus, D. S., Plesha, M. E., 1989, *Concepts and Applications of Finite Element Analysis,* John Wiley and Sons, New York.

Dvorak, G. J., 1992, "Transformation Field Analysis of Inelastic Composite Materials," *Proc. R. Soc. London,* Vol. 437, pp. 311–327.

Dvorak, G. J. and Benveniste, Y. 1992, "On Transformation Strains and Uniform Fields in Multiphase Elastic Media," *Proc. R. Soc. London,* Vol. 437, pp. 291–310.

Dvorak, G. J., Bahei-El-Din, Y. A., Wafa, A. M., 1994, "Implementation of the Transformation Field Analysis for Inelastic Composite Materials," *Comput. Mech.,* Vol. 14, pp. 201–228.

Eshelby, J. D., 1957, "The Determination of the Elastic Field of an Ellipsoidal Inclusion and Related Problems," *Proc. R. Soc. London,* Vol. 241, pp. 376–396.

Flügge, W., 1967, *Viscoelasticity,* Blaisdell, Waltham, MA.

Garnich, M. R., and Hansen, A. C., 1996, "A Multicontinuum Theory for Thermal-Elastic Structural Analysis of Composites," *J. Compo. Mater.,* Vol. 31, No. 1, pp. 71–86.

Hashin, Z., 1965, "Viscoelastic Behavior of Heterogeneous Media," ASME JOURNAL OF APPLIED MECHANICS, Vol. 32, pp. 630–636.

Hill, R., 1963, "Elastic Properties of Reinforced Solids: Some Theoretical Principles," *J. Mech. Phys. Solids,* Vol. 11, pp. 357–372.

Hughes, T. J. R., Taylor, R. L., 1978, "Unconditionally Stable Algorithms for Quasi-Static Elasto/Visco-Plastic Finite Element Analysis," *Comput. & Struct.,* Vol. 8, pp. 169–173.

Krishnaswamy, P., Tuttle, M. E., and Emery, A. F., 1990, "Finite Element Modeling of Crack Tip Behavior in Viscoelastic Materials, Part I: Linear Behavior," *Int. J. Num. Meth. Engng.,* Vol. 30, pp. 371–387.

Levy, A., and Pifko, A. B., 1981, "On Computational Strategies for Problems Involving Plasticity and Creep," *Int. J. Num. Meth. Engng.,* Vol. 17, pp. 747–771.

Mehrabadi, M. M., and Cowen, S. C., 1990, Eigentensors of Linear Anisotropic Elastic Materials, *J. Mech. Appl. Math.,* Vol. 43, pp. 15–41.

Nemat-Nasser, S., and Hori, M., 1993, *Micromechanics: Overall Properties of Heterogeneous Materials,* Elsevier, Amsterdam.

Pecknold, D. A., and Rahman, S., 1994, "Micromechanics-Based Structural Analysis of Thick Laminated Composites," *Computers and Struct.,* Vol. 51, No. 2, pp. 163–179.

Press, W. H., Flannery, B. P., Teukolsky, S. A., and Vetterling, W. T., 1989, *Numerical Recipes, The Art of Scientific Computing (FORTRAN Version),* Cambridge University Press, Cambridge, UK.

Ravichandran, K. S., and Seetharaman, V., 1993, "Prediction of Steady State Creep Behavior of Two Phase Composites," *Acta Metall. et Mater.,* Vol. 41, No. 12, pp. 3351–3361.

Schapery, R. A., 1974, "Viscoelastic Behavior and Analysis of Composite Materials," *Composite Materials,* Vol. 2, G. P. Sendeckyj, ed., Academic Press, New York, pp. 85–168.

APPENDIX A

Material Properties for a Linear Viscoelastic Composite

The relative magnitudes of the constants and degree of anisotropy of the fibers was intended to be representative of a graphite epoxy system with 60 percent fiber by volume.

The elastic material constants for the fibers are listed in Table A1. Here, $\nu_{r,12}$ and $\nu_{r,13}$ are the so-called "major Poisson's ratio" and are the negative ratio of strain in the transverse direction to strain in the axial direction due to load in the axial direction. Material constants defining the matrix material behavior associated with Eqs. (18) and (19) are listed in Table A2.

Table A1 Linear elastic reinforcement (fiber) material constants

Young's Moduli (GPa)	Poisson's Ratios	Shear Moduli (GPa)	Expansion Coef. (10^{-6}/°C)
$E_{r,11} = 220.60$	$\nu_{r,23} = 0.28$	$G_{r,23} = 5.516$	$\alpha_{r,11} = -0.36$
$E_{r,22} = 13.354$	$\nu_{r,13} = 0.20$	$G_{r,13} = 26.00$	$\alpha_{r,22} = 18.00$
$E_{r,33} = 13.354$	$\nu_{r,12} = 0.20$	$G_{r,12} = 26.00$	$\alpha_{r,33} = 18.00$

Table A2 Linear viscoelastic matrix material constants

J_m^0 $(GPa)^{-1}$	J_m^1 $(GPa)^{-1}$	Π_m^1 (Sec.)	K_m (MPa)	α_m (10^{-6}/°C)
0.32472	-0.0830	107.0	4309.4	40.0

Downloaded 04 May 2010 to 171.66.16.34. Redistribution subject to ASME license or copyright; see http://www.asme.org/terms/Terms_Use.cfm

The components of Eq. (17) associated with the matrix material (Eq. (20)) are

$$D^0_{m,ij} = \begin{bmatrix} .3247 & -.1237 & -.1237 & 0 & 0 & 0 \\ -.1237 & .3247 & -.1237 & 0 & 0 & 0 \\ -.1237 & -.1237 & .3247 & 0 & 0 & 0 \\ 0 & 0 & 0 & .8968 & 0 & 0 \\ 0 & 0 & 0 & 0 & .8968 & 0 \\ 0 & 0 & 0 & 0 & 0 & .8968 \end{bmatrix} (\text{GPa})^{-1},$$

$$D^1_{m,ij} = \begin{bmatrix} -.0830 & .0415 & .0415 & 0 & 0 & 0 \\ .0415 & -.0830 & .0415 & 0 & 0 & 0 \\ .0415 & .0415 & -.0830 & 0 & 0 & 0 \\ 0 & 0 & 0 & -.2490 & 0 & 0 \\ 0 & 0 & 0 & 0 & -.2490 & 0 \\ 0 & 0 & 0 & 0 & 0 & -.2490 \end{bmatrix} (\text{GPa})^{-1},$$

and

$$\prod^1_{m,ij} = \begin{bmatrix} 1.783 & 1.783 & 1.783 & 0 & 0 & 0 \\ 1.783 & 1.783 & 1.783 & 0 & 0 & 0 \\ 1.783 & 1.783 & 1.783 & 0 & 0 & 0 \\ 0 & 0 & 0 & 1.783 & 0 & 0 \\ 0 & 0 & 0 & 0 & 1.783 & 0 \\ 0 & 0 & 0 & 0 & 0 & 1.783 \end{bmatrix} (\text{Min.}).$$

The matrix material definition is completed by specifying the constant thermal expansion coefficient vector.

$$\alpha_{m,i} = [40.0 \quad 40.0 \quad 40.0 \quad 0 \quad 0 \quad 0]^T \times 10^{-6}(^\circ\text{C})^{-1}.$$

The following arrays define the constants for the composite as in Eqs. (17) and (22).

$$\prod^1_{ij} = \begin{bmatrix} 1.380 & 1.399 & 1.399 & 0 & 0 & 0 \\ 1.399 & 1.785 & 1.797 & 0 & 0 & 0 \\ 1.399 & 1.797 & 1.785 & 0 & 0 & 0 \\ 0 & 0 & 0 & 1.794 & 0 & 0 \\ 0 & 0 & 0 & 0 & 1.823 & 0 \\ 0 & 0 & 0 & 0 & 0 & 1.823 \end{bmatrix} (\text{Min.})$$

$$\prod^2_{ij} = \begin{bmatrix} 1.279 & 1.293 & 1.293 & 0 & 0 & 0 \\ 1.293 & 1.478 & 1.571 & 0 & 0 & 0 \\ 1.293 & 1.571 & 1.478 & 0 & 0 & 0 \\ 0 & 0 & 0 & 1.520 & 0 & 0 \\ 0 & 0 & 0 & 0 & 1.713 & 0 \\ 0 & 0 & 0 & 0 & 0 & 1.713 \end{bmatrix} (\text{Min.})$$

The following vectors associated with Eqs. (23) and (24) define the composite thermal expansion behavior.

$$\prod^1_i = \begin{bmatrix} 1.408 \\ 1.420 \\ 1.420 \\ 0 \\ 0 \\ 0 \end{bmatrix} (\text{Min.}), \quad \prod^2_i = \begin{bmatrix} 1.309 \\ 1.325 \\ 1.325 \\ 0 \\ 0 \\ 0 \end{bmatrix} (\text{Min.})$$

$$\alpha^0_i = \begin{bmatrix} .5919\text{E}-7 \\ .3196\text{E}-4 \\ .3196\text{E}-4 \\ 0 \\ 0 \\ 0 \end{bmatrix} (^\circ\text{C})^{-1},$$

$$\alpha^1_i = \begin{bmatrix} .7630\text{E}-7 \\ -.5114\text{E}-6 \\ -.5114\text{E}-6 \\ 0 \\ 0 \\ 0 \end{bmatrix} (^\circ\text{C})^{-1},$$

$$\alpha^2_i = \begin{bmatrix} .4846\text{E}-7 \\ -.3303\text{E}-6 \\ -.3303\text{E}-6 \\ 0 \\ 0 \\ 0 \end{bmatrix} (^\circ\text{C})^{-1}$$

APPENDIX B

Recursive Relation for Hereditary Integral Evaluation

Consider an integral of the form

$$P^L(t_n) = Q^L \int_{0^-}^{t_n} \exp\left[\frac{-(t_n - \tau)}{\Pi^L}\right] \frac{d\xi(\tau)}{d\tau} d\tau, \quad \text{(B1)}$$

where the superscripts are indices and not exponents. Now consider a small step

$$\Delta t = t_{n+1} - t_n, \quad \text{(B2)}$$

and write

$$D^0_{ij} = \begin{bmatrix} .749\text{E}-5 & -.201\text{E}-5 & -.201\text{E}-5 & 0 & 0 & 0 \\ -.201\text{E}-5 & .135\text{E}-3 & -.600\text{E}-4 & 0 & 0 & 0 \\ -.201\text{E}-5 & -.600\text{E}-4 & .135\text{E}-3 & 0 & 0 & 0 \\ 0 & 0 & 0 & .390\text{E}-3 & 0 & 0 \\ 0 & 0 & 0 & 0 & .259\text{E}-3 & 0 \\ 0 & 0 & 0 & 0 & 0 & .259\text{E}-3 \end{bmatrix} (\text{MPa})^{-1}$$

$$D^1_{ij} = \begin{bmatrix} -.140\text{E}-7 & .781\text{E}-7 & .781\text{E}-7 & 0 & 0 & 0 \\ .781\text{E}-7 & -.107\text{E}-4 & .921\text{E}-5 & 0 & 0 & 0 \\ .781\text{E}-7 & .921\text{E}-5 & -.107\text{E}-4 & 0 & 0 & 0 \\ 0 & 0 & 0 & -.397\text{E}-4 & 0 & 0 \\ 0 & 0 & 0 & 0 & -.396\text{E}-4 & 0 \\ 0 & 0 & 0 & 0 & 0 & -.396\text{E}-4 \end{bmatrix} (\text{MPa})^{-1}$$

$$D^2_{ij} = \begin{bmatrix} -.929\text{E}-8 & .489\text{E}-7 & .489\text{E}-7 & 0 & 0 & 0 \\ .489\text{E}-7 & -.560\text{E}-5 & .548\text{E}-5 & 0 & 0 & 0 \\ .489\text{E}-7 & .548\text{E}-5 & -.560\text{E}-5 & 0 & 0 & 0 \\ 0 & 0 & 0 & -.222\text{E}-4 & 0 & 0 \\ 0 & 0 & 0 & 0 & -.224\text{E}-4 & 0 \\ 0 & 0 & 0 & 0 & 0 & -.224\text{E}-4 \end{bmatrix} (\text{MPa})^{-1}$$

Downloaded 04 May 2010 to 171.66.16.34. Redistribution subject to ASME license or copyright; see http://www.asme.org/terms/Terms_Use.cfm

$$P^L(t_{n+1}) = Q^L \int_{0^-}^{t_{n+1}} \exp\left[\frac{-(t_{n+1}-\tau)}{\Pi^L}\right] \frac{d\xi(\tau)}{d\tau}\, d\tau. \quad \text{(B3)}$$

Use equation (B2) to rewrite (B3) as

$$P^L(t_{n+1}) = Q^L \exp\left[\frac{-\Delta t}{\Pi^L}\right] \times \int_{0^-}^{t_{n+1}} \exp\left[\frac{-(t_n-\tau)}{\Pi^L}\right] \frac{d\xi(\tau)}{d\tau}\, d\tau, \quad \text{(B4)}$$

and break up the integral to give

$$P^L(t_{n+1}) = \exp\left[\frac{-\Delta t}{\Pi^L}\right]\left(P^L(t_n) + Q^L \int_{t_n}^{t_{n+1}} \exp\left[\frac{-(t_n-\tau)}{\Pi^L}\right] \frac{d\xi(\tau)}{d\tau}\, d\tau\right). \quad \text{(B5)}$$

Now assume Δt is small so that $d\xi(t)/dt$ is well approximated as a constant over the interval and given by $\Delta\xi/\Delta t$. The remaining integral can then be evaluated and after some simplification the following recursive relation is determined.

$$P^L(t_{n+1}) = P^L(t_n) \exp\left[\frac{-\Delta t}{\Pi^L}\right] + Q^L \Pi^L \frac{\Delta\xi}{\Delta t}\left(1 - \exp\left[\frac{-\Delta t}{\Pi^L}\right]\right). \quad \text{(B6)}$$

At time $t = 0^-$ in Eq. (B1), it is assumed that $P^L(0^-) = 0$. For finite ξ at $t = 0^+$ (i.e., infinite $d\xi/dt$ at $t = 0$), Eq. (B1) can be written as

$$P^L(0^+) = Q^L \int_{0^-}^{0^+} \exp\left[\frac{-(0^+-\tau)}{\Pi^L}\right] \frac{d(\xi(0^+)H(\tau))}{d\tau}\, d\tau, \quad \text{(B7)}$$

where $H(t)$ is the Heaviside unit step function. Noting that the derivative of $H(t)$ is $\delta(t)$, the Dirac Delta function, Eq. (B7) simplifies to the initial condition:

$$P^L(0^+) = Q^L \xi(0^+). \quad \text{(B8)}$$

Now consider beginning with the integral difference pair

$$\Delta I = \int_0^{t_{n+1}} Q(t_{n+1} - \tau) \frac{d\xi(\tau)}{d\tau}\, d\tau - \int_0^{t_n} Q(t_n - \tau) \frac{d\xi(\tau)}{d\tau}\, d\tau, \quad \text{(B9)}$$

where

$$Q(t-\tau) = Q^0 + \sum_L Q^L \exp\left[\frac{-(t-\tau)}{\Pi^L}\right]. \quad \text{(B10)}$$

Substituting Eq. (B10) into (B9) and following steps analogous to the derivation represented by Eqs. (B1) through (B6) gives the following approximation of ΔI:

$$\Delta I = Q^0 \Delta\xi + \sum_L \left(1 - \exp\left[\frac{-\Delta t}{\Pi^L}\right]\right) \times \left(Q^L \Pi^L \frac{\Delta\xi}{\Delta t} - P^L(t_n)\right). \quad \text{(B11)}$$

Note that $P^L(t_n)$ is known via Eq. (B6) for the previous step, so if $\Delta\xi$ is known, then ΔI can be evaluated explicitly.

Downloaded 04 May 2010 to 171.66.16.34. Redistribution subject to ASME license or copyright; see http://www.asme.org/terms/Terms_Use.cfm

Fracture Mechanics of Composites With Residual Thermal Stresses

J. A. Nairn
Material Science and Engineering,
University of Utah,
Salt Lake City, UT 84112

The problem of calculating the energy release rate for crack growth in an arbitrary composite in the presence of residual stresses is considered. First, a general expression is given for arbitrary, mixed traction, and displacement boundary conditions. This general result is then applied to a series of specific problems including statistically homogeneous composites under traction or displacement boundary conditions, delamination of double cantilever beam specimens, and microcracking in the transverse plies of laminates. In many examples, the energy release rate in the presence of residual stresses can be reduced to finding the effect of damage on the effective mechanical properties of the composite. Because these effective properties can be evaluated by isothermal stress analysis, the effect of residual stresses on the energy release rate can be evaluated without recourse to any thermal elasticity stress analyses.

Introduction

When a composite comprised of materials having disparate thermal expansion coefficients is subjected to a uniform change in temperature, it will develop residual thermal stresses. If that composite develops cracks, either as a result of the residual thermal stresses or of some subsequently applied mechanical tractions, the residual and mechanical stresses will change to accommodate the fracture surfaces. One effect of the redistribution of residual thermal stresses is a change in the effective thermal expansion coefficient of the composite (Hashin, 1988). Additionally, the redistribution of residual and mechanical stresses releases strain energy that can drive crack propagation—the energy release rate for crack growth.

The goal of this paper is to evaluate the effect of residual thermal stresses on the energy release rate for crack growth in composites. The redistribution of residual and mechanical stresses caused by cracks can be viewed as similar elasticity problems but with different boundary conditions. Because of their similarity, it is often possible to explicitly account for the effect of residual thermal stresses without doing a thermal elasticity analysis of the composite. Some general energy release rate expressions including residual thermal stresses are derived in the first section of this paper. The general results are for an arbitrary composite under arbitrary, mixed traction, and displacement boundary conditions. Next, the general expressions are applied to statistically homogeneous composites, double cantilever beam delamination specimens, and microcracked laminates. The simplest possible energy release rate expressions are derived. In some examples, the energy release depends on knowledge of both the mechanical and residual stress states, but, in some important practical examples, the energy release rate can be expressed in terms of the effect of cracks on the *effective* composite mechanical properties. These effective mechanical properties can be derived using elasticity analyses that ignore residual stresses.

Contributed by the Applied Mechanics Division of THE AMERICAN SOCIETY OF MECHANICAL ENGINEERS for publication in the ASME JOURNAL OF APPLIED MECHANICS.

Discussion on the paper should be addressed to the Technical Editor, Professor Lewis T. Wheeler, Department of Mechanical Engineering, University of Houston, Houston, TX 77204-4792, and will be accepted until four months after final publication of the paper itself in the ASME JOURNAL OF APPLIED MECHANICS.

Manuscript received by the ASME Applied Mechanics Division, Nov. 11, 1996; final revision, Apr. 7, 1997. Associate Technical Editor: R. Becker.

General Theory

Consider an arbitrary, multiphase composite subjected a uniform temperature change of $\Delta T = T$ and to any mixed traction and displacement boundary conditions. Let the surface be $S = S_T \cup S_u$, where S_T is that part of the surface subjected to traction boundary conditions

$$\boldsymbol{T} = \boldsymbol{T}^0 = \boldsymbol{\sigma}^0 \hat{n} \tag{1}$$

where $\boldsymbol{\sigma}^0$ is the surface applied stress (note: all tensors are written in roman boldface) and $\hat{n}$ is a unit normal to the surface. S_u is that part of the surface subjected to displacement boundary conditions

$$\boldsymbol{u} = \boldsymbol{u}^0 = \boldsymbol{\epsilon}^0 \boldsymbol{x} \tag{2}$$

where $\boldsymbol{\epsilon}^0$ is the surface strain and $\boldsymbol{x}$ is a position vector on the surface. $\boldsymbol{T}^0$ and $\boldsymbol{u}^0$ are the boundary conditions; in general they may depend on position. Note also that tractions and displacements may be applied over the same portions of the surface provided they are applied along different coordinates. For example, one section of the surface may have traction in the x direction but fixed displacement in the y direction. Similar to Rosen and Hashin (1970), the full thermal elasticity problem can be treated as a superposition of two problems. First, let $\boldsymbol{\sigma}^m$ and $\boldsymbol{\epsilon}^m$, with tractions $\boldsymbol{T}^m$ and displacements $\boldsymbol{u}^m$, be the solution to the isothermal ($T = 0$) elasticity problem:

$$\boldsymbol{\sigma}^m \hat{n} = \boldsymbol{T}^0 \quad \text{on} \quad S_T \tag{3}$$

$$\boldsymbol{u}^m = \boldsymbol{u}^0 \quad \text{on} \quad S_u \tag{4}$$

$$\boldsymbol{\sigma}^m = \mathbf{C}\boldsymbol{\epsilon}^m \quad \text{and} \quad \boldsymbol{\epsilon}^m = \mathbf{S}\boldsymbol{\sigma}^m \tag{5}$$

where $\mathbf{C}$ and $\mathbf{S}$ are the stiffness and compliance tensors. In a composite, $\mathbf{C}$ and $\mathbf{S}$ will depend on position. As the solution to an elasticity problem, $\boldsymbol{\sigma}^m$ satisfies equilibrium and $\boldsymbol{\epsilon}^m$ satisfies compatibility. Second, let $\boldsymbol{\sigma}^r$ and $\boldsymbol{\epsilon}^r$, with tractions $\boldsymbol{T}^r$ and displacements $\boldsymbol{u}^r$, be the solution to the thermal elasticity problem:

$$\boldsymbol{\sigma}^r \hat{n} = 0 \quad \text{on} \quad S_T \tag{6}$$

$$\boldsymbol{u}^r = 0 \quad \text{on} \quad S_u \tag{7}$$

$$\boldsymbol{\sigma}^r = \mathbf{C}(\boldsymbol{\epsilon}^r - \boldsymbol{\alpha}T) \quad \text{and} \quad \boldsymbol{\epsilon}^r = \mathbf{S}\boldsymbol{\sigma}^r + \boldsymbol{\alpha}T \tag{8}$$

where $\boldsymbol{\alpha}$ is the position-dependent thermal expansion tensor, $\boldsymbol{\sigma}^r$

Copyright © 1997 by ASME

Downloaded 04 May 2010 to 171.66.16.34. Redistribution subject to ASME license or copyright; see http://www.asme.org/terms/Terms_Use.cfm

satisfies equilibrium, and $\boldsymbol{\epsilon}^r$ satisfies compatibility. Note that $\boldsymbol{T}^r$ may be nonzero on S_u and $\boldsymbol{u}^r$ may be nonzero on S_T. A superposition of the above two solutions, $\boldsymbol{\sigma} = \boldsymbol{\sigma}^m + \boldsymbol{\sigma}^r$ and $\boldsymbol{\epsilon} = \boldsymbol{\epsilon}^m + \boldsymbol{\epsilon}^r$, solves the complete thermal elasticity problem

$$\boldsymbol{\sigma}\hat{n} = \boldsymbol{T}^0 \quad \text{on} \quad S_T \tag{9}$$

$$\boldsymbol{u} = \boldsymbol{u}^0 \quad \text{on} \quad S_u \tag{10}$$

$$\boldsymbol{\sigma} = \mathbf{C}(\boldsymbol{\epsilon} - \boldsymbol{\alpha}T) \quad \text{and} \quad \boldsymbol{\epsilon} = \mathbf{S}\boldsymbol{\sigma} + \boldsymbol{\alpha}T. \tag{11}$$

$\boldsymbol{\sigma}^m$ and $\boldsymbol{\epsilon}^m$ are the mechanical stresses and strains while $\boldsymbol{\sigma}^r$ and $\boldsymbol{\epsilon}^r$ are the residual thermal stresses and strains.

The internal energy is the volume integral of stress dotted into strain relative to the free-expansion strains. This energy can be expressed in terms of mechanical and residual stresses:

$$U = \tfrac{1}{2}\int_V \boldsymbol{\sigma}\cdot(\boldsymbol{\epsilon} - \boldsymbol{\alpha}T)dV$$

$$= \tfrac{1}{2}\int_V \boldsymbol{\sigma}^m\mathbf{S}\boldsymbol{\sigma}^m dV + \int_V \boldsymbol{\sigma}^m\mathbf{S}\boldsymbol{\sigma}^r dV + \tfrac{1}{2}\int_V \boldsymbol{\sigma}^r\mathbf{S}\boldsymbol{\sigma}^r dV. \tag{12}$$

Assuming traction-free crack surfaces and using the divergence theorem, the mechanical stress term in Eq. (12) may be written in terms of mechanical surface tractions, $\boldsymbol{T}^m$, and displacements, $\boldsymbol{u}^m$, as

$$\tfrac{1}{2}\int_V \boldsymbol{\sigma}^m\mathbf{S}\boldsymbol{\sigma}^m dV = \tfrac{1}{2}\int_{S_T} \boldsymbol{T}^0\cdot\boldsymbol{u}^m dS + \tfrac{1}{2}\int_{S_u} \boldsymbol{T}^m\cdot\boldsymbol{u}^0 dS. \tag{13}$$

For the cross term in Eq. (12), the displacements caused by the residual thermal stresses can be considered as virtual displacements to the mechanical strains or $\delta\boldsymbol{u} = \boldsymbol{u}^r$. They correctly have $\boldsymbol{u}^r = 0$ on S_u. By virtual work

$$\int_V \boldsymbol{\sigma}^m\cdot\boldsymbol{\epsilon}^r dV = \int_{S_T} \boldsymbol{T}^0\cdot\boldsymbol{u}^r dS. \tag{14}$$

But also, $\boldsymbol{\epsilon}^r = \mathbf{S}\boldsymbol{\sigma}^r + \boldsymbol{\alpha}T$, giving

$$\int_V \boldsymbol{\sigma}^m\mathbf{S}\boldsymbol{\sigma}^r dV = \int_{S_T} \boldsymbol{T}^0\cdot\boldsymbol{u}^r dS - \int_V \boldsymbol{\sigma}^m\cdot\boldsymbol{\alpha}T dV. \tag{15}$$

Analogously, the residual tractions, $\boldsymbol{T}^r$, can be considered as virtual forces on the mechanical stresses; $\boldsymbol{\sigma}^r$ obeys equilibrium and $\boldsymbol{T}^r = 0$ on S_T. Thus, again by virtual work

$$\int_V \boldsymbol{\epsilon}^m\cdot\boldsymbol{\sigma}^r dV = \int_V \boldsymbol{\sigma}^m\mathbf{S}\boldsymbol{\sigma}^r dV = \int_{S_u} \boldsymbol{T}^r\cdot\boldsymbol{u}^0 dS. \tag{16}$$

Finally, for the pure residual stress term in Eq. (12),

$$\tfrac{1}{2}\int_V \boldsymbol{\sigma}^r\mathbf{S}\boldsymbol{\sigma}^r dV = \tfrac{1}{2}\int_V (\boldsymbol{\sigma}^r\cdot\boldsymbol{\epsilon}^r - \boldsymbol{\sigma}^r\cdot\boldsymbol{\alpha}T)dV$$

$$= \tfrac{1}{2}\left(\int_S \boldsymbol{T}^r\cdot\boldsymbol{u}^r dS - \int_V \boldsymbol{\sigma}^r\cdot\boldsymbol{\alpha}T dV\right). \tag{17}$$

But, over the entire surface, either $\boldsymbol{T}^r = 0$ or $\boldsymbol{u}^r = 0$, giving

$$\tfrac{1}{2}\int_V \boldsymbol{\sigma}^r\mathbf{S}\boldsymbol{\sigma}^r dV = -\tfrac{1}{2}\int_V \boldsymbol{\sigma}^r\cdot\boldsymbol{\alpha}T dV. \tag{18}$$

Combining Eqs. (13), (15), (16), and (18) gives

$$U = \tfrac{1}{2}\int_{S_T} \boldsymbol{T}^0\cdot\boldsymbol{u}^m dS + \tfrac{1}{2}\int_{S_u} \boldsymbol{T}^m\cdot\boldsymbol{u}^0 dS$$

$$+ \int_{S_u} \boldsymbol{T}^r\cdot\boldsymbol{u}^0 dS - \tfrac{1}{2}\int_V \boldsymbol{\sigma}^r\cdot\boldsymbol{\alpha}T dV \tag{19}$$

$$\int_V \boldsymbol{\sigma}^m\cdot\boldsymbol{\alpha}T = \int_{S_T} \boldsymbol{T}^0\cdot\boldsymbol{u}^r dS - \int_{S_u} \boldsymbol{T}^r\cdot\boldsymbol{u}^0 dS. \tag{20}$$

For fracture mechanics analysis we need to evaluate the energy release rate defined as

$$G = \frac{dW}{dA} - \frac{dU}{dA} \tag{21}$$

where W is external work and A is fracture area. The external work is caused by the action of the mechanical tractions on S_T applied over the *total* displacements. Thus

$$\frac{dW}{dA} = \frac{d}{dA}\left(\int_{S_T} \boldsymbol{T}^0\cdot(\boldsymbol{u}^m + \boldsymbol{u}^r)dS\right). \tag{22}$$

Combining this result with Eqs. (19) and (20) gives

$$G = G_{\text{mech}} + \frac{VT}{2}\left(2\frac{d\langle\boldsymbol{\sigma}^m\cdot\boldsymbol{\alpha}\rangle}{dA} + \frac{d\langle\boldsymbol{\sigma}^r\cdot\boldsymbol{\alpha}\rangle}{dA}\right) \tag{23}$$

where G_{mech} is the mechanical energy release rate or the energy release rate when $T = 0$,

$$G_{\text{mech}} = \frac{d}{dA}\left(\tfrac{1}{2}\int_{S_T} \boldsymbol{T}^0\cdot\boldsymbol{u}^m dS - \tfrac{1}{2}\int_{S_u} \boldsymbol{T}^m\cdot\boldsymbol{u}^0 dS\right), \tag{24}$$

and angle brackets indicates a volume-averaged quantity

$$\langle f(x, y, z)\rangle = \frac{1}{V}\int_V f(x, y, z)dV. \tag{25}$$

Note that the full, thermodynamic internal energy in thermal elasticity includes heat capacity terms. The energy associated with residual stresses that exist under zero traction (or zero displacement), can be viewed as contributing to the effective constant pressure (or constant volume) heat capacity of the composite (Rosen and Hashin, 1970). Here the residual stress energy contributes to the total energy release rate for crack growth. The heat capacity terms associated with individual phases, however, can be ignored when calculating energy release rates because they drop out when the derivative with respect to crack area is evaluated.

The result in Eq. (23) includes nothing specific about composites. The result for a composite with n phases is

$$G = G_{\text{mech}} + \frac{VT}{2}\sum_{i=1}^{n} v_i\boldsymbol{\alpha}^{(i)}\cdot\left(2\frac{d\overline{\boldsymbol{\sigma}^{(im)}}}{dA} + \frac{d\overline{\boldsymbol{\sigma}^{(ir)}}}{dA}\right) \tag{26}$$

where superscript (i) means a property of phase i; v_i is the volume fraction of phase i, and the overbar indicates a phase-averaged quantity integrated over the volume of phase i, V_i:

$$\overline{\boldsymbol{\sigma}^{(im)}} = \frac{1}{Vv_i}\int_{V_i} \boldsymbol{\sigma}^m dV \tag{27}$$

In deriving Eq. (26), it was assumed that the component thermal expansion tensors in each phase are independent of position within that phase. This situation always holds for composites with isotropic phases. For composites with anisotropic phases at variable orientations, each orientation must be considered as a separate phase for analysis by Eq. (26). When anisotropic phases are aligned, such as in unidirectional, carbon-fiber reinforced composites, the anisotropic phase can be considered as a single phase.

Although the general result in Eq. (26) depends on both mechanical and thermal stresses, in some important special cases, the energy release rate can be expressed solely in terms of mechanical properties and stresses. For example, in many fracture situations, cracks will propagate such that failure is by pure mode I fracture or pure opening mode fracture. For example, it has been suggested that regardless of external loading conditions that delamination always proceeds by mode I fracture

Downloaded 04 May 2010 to 171.66.16.34. Redistribution subject to ASME license or copyright; see http://www.asme.org/terms/Terms_Use.cfm

(Charalambides et al., 1992). Under pure mode I crack growth, energy release rate is related to mode I stress intensity factor by

$$G_I \propto K_I^2. \tag{28}$$

In linear thermal elasticity, K_I must be linearly related to applied load and temperature change. If we thus consider uniformly scaling all applied tractions and displacements to be

$$\boldsymbol{T}^{\text{app}} = P\boldsymbol{T}^0 \quad \text{and} \quad \boldsymbol{u}^{\text{app}} = P\boldsymbol{u}^0 \tag{29}$$

where P is a scalar multiplier, stress intensity must have the form

$$K_I = c_1 P + c_2 T \tag{30}$$

where c_1 and c_2 are some constants that depend on material properties and geometry of the crack. The energy release rate must therefore have the form

$$G_I \propto (c_1 P + c_2 T)^2. \tag{31}$$

Comparing Eq. (31) to Eq. (26) we can prove that

$$\frac{TV}{2}\frac{\sum_{i=1}^{n} v_i \boldsymbol{\alpha}^{(i)} \cdot \dfrac{d\overline{\boldsymbol{\sigma}^{(im)}}}{dA}}{G_{\text{mech}}} = \frac{\sum_{i=1}^{n} v_i \boldsymbol{\alpha}^{(i)} \cdot \dfrac{d\overline{\boldsymbol{\sigma}^{(ir)}}}{dA}}{\sum_{i=1}^{n} v_i \boldsymbol{\alpha}^{(i)} \cdot \dfrac{d\boldsymbol{\sigma}^{(im)}}{dA}} \tag{32}$$

Substitution back into Eq. (26) gives

$$\frac{G_I}{G_{\text{mech}}} = \left(1 + \frac{TV}{2}\frac{\sum_{i=1}^{n} v_i \boldsymbol{\alpha}^{(i)} \cdot \dfrac{d\overline{\boldsymbol{\sigma}^{(im)}}}{dA}}{G_{\text{mech}}}\right)^2. \tag{33}$$

Remarkably, the energy release rate including residual thermal stresses depends only on the results from a mechanical stress analysis. Thus, the effect of residual stresses can be determined without any need for solving a thermal elasticity problem. Although this result was derived for pure mode I crack growth, analogous expressions hold for pure mode II or III crack growth.

Examples

Uniform Traction, Statistically Isotropic Composite. A useful model for evaluating effective properties of composite materials is to consider a statistically homogeneous composite (Hashin, 1963; 1969). Such composites are analyzed by averaging over a representative volume element; this element must be chosen large enough to have all averaged results representative of the averaged results for the entire composite (Hashin, 1963; 1969). Here we also consider the representative volume element to have cracks that are representative of the entire composite. Such a representative volume element is then subjected to a *uniform* traction or a traction that arises from a surface stress, $\boldsymbol{\sigma}^0$, that is independent of position. By the average strain theorem (Hill, 1963; Hashin 1963; 1969), the only remaining integral in G_{mech} reduces to

$$\tfrac{1}{2}\int_S \boldsymbol{T}^0 \cdot \boldsymbol{u}^m dS = \frac{V}{2}\boldsymbol{\sigma}^0 \cdot (\langle \boldsymbol{\epsilon}^m \rangle - \mathbf{D}^m) = \frac{V}{2}\boldsymbol{\sigma}^0 \cdot \mathbf{S}^* \boldsymbol{\sigma}^0 \tag{34}$$

where $\mathbf{S}^*$ is the effective compliance tensor of the composite (Hashin, 1963; 1969). The tensor $\mathbf{D}^m$ is related to the crack-opening mechanical displacements and is defined by

$$D_{ij}^m = \frac{1}{2V}\int_{S_c} (u_j^m n_i + u_i^m n_j) dS \quad (i, j = x, y, \text{or } z) \tag{35}$$

where S_c is total crack surface area. The effective composite compliance is defined in terms of the *apparent* average strain which is the bulk average strain reduced by the crack-opening tensor (Aboudi, 1994); thus

$$\mathbf{S}^* \boldsymbol{\sigma}^0 = \langle \boldsymbol{\epsilon}^m \rangle - \mathbf{D}^m. \tag{36}$$

Substituting Eq. (34) into Eq. (26) the energy release rate becomes

$$G = \frac{V}{2}\left[\boldsymbol{\sigma}^0 \cdot \frac{d\mathbf{S}^*}{dA}\boldsymbol{\sigma}^0 + T\sum_{i=1}^{n} v_i \boldsymbol{\alpha}^{(i)} \cdot \left(2\frac{d\overline{\boldsymbol{\sigma}^{(im)}}}{dA} + \frac{d\overline{\boldsymbol{\sigma}^{(ir)}}}{dA}\right)\right]. \tag{37}$$

For pure mode I (or II, or III) crack growth the energy release rate becomes

$$\frac{G_I}{G_{\text{mech}}} = \left(1 + T\frac{\sum_{i=1}^{n} v_i \boldsymbol{\alpha}^{(i)} \cdot \dfrac{d\overline{\boldsymbol{\sigma}^{(im)}}}{dA}}{\boldsymbol{\sigma}^0 \cdot \dfrac{d\mathbf{S}^*}{dA}\boldsymbol{\sigma}^0}\right)^2 \tag{38}$$

Finally, for a two-phase composite (a composite with two isotropic phases or two aligned anisotropic phases) we have

$$v_1 \frac{d\overline{\boldsymbol{\sigma}^{(1m)}}}{dA} + v_2 \frac{d\overline{\boldsymbol{\sigma}^{(2m)}}}{dA} = 0 \tag{39}$$

$$\mathbf{S}^{(1)} v_1 \frac{d\overline{\boldsymbol{\sigma}^{(1m)}}}{dA} + \mathbf{S}^{(2)} v_2 \frac{d\overline{\boldsymbol{\sigma}^{(2m)}}}{dA} = \frac{d\langle \boldsymbol{\epsilon}^m \rangle}{dA} = \frac{d\mathbf{S}^*}{dA}\boldsymbol{\sigma}^0 + \frac{d\mathbf{D}^m}{dA}. \tag{40}$$

For pure mode fracture we can derive

$$G_I = \frac{V}{2}\frac{\left[(\boldsymbol{\sigma}^0 + T(\boldsymbol{\alpha}^{(1)} - \boldsymbol{\alpha}^{(2)})(\mathbf{S}^{(1)} - \mathbf{S}^{(2)})^{-1}) \cdot \dfrac{d\mathbf{S}^*}{dA}\boldsymbol{\sigma}^0 + T(\boldsymbol{\alpha}^{(1)} - \boldsymbol{\alpha}^{(2)})(\mathbf{S}^{(1)} - \mathbf{S}^{(2)})^{-1} \cdot \dfrac{d\mathbf{D}^m}{dA}\right]^2}{\boldsymbol{\sigma}^0 \cdot \dfrac{d\mathbf{S}^*}{dA}\boldsymbol{\sigma}^0}. \tag{41}$$

The energy release rate depends only on the effective compliance tensor and the mechanically induced crack-opening displacement tensor. Note the $\mathbf{D}^m$ only affects the energy release rate when there are residual thermal stresses; in the absence of residual stresses, G_I depends only on $\mathbf{S}^*$.

Uniform Displacement, Statistically Isotropic Composite. For uniform displacement ($\boldsymbol{u}^0 = \boldsymbol{\epsilon}^0 \boldsymbol{x}$ where $\boldsymbol{\epsilon}^0$ is independent of position) applied to a statistically homogeneous composite, use of the average stress theorem leads to

$$G_{\text{mech}} = -\frac{V}{2}\frac{d\langle \boldsymbol{\sigma}^m \rangle}{dA} \cdot \boldsymbol{\epsilon}^0 = -\frac{V}{2}\boldsymbol{\epsilon}^0 \cdot \frac{d\mathbf{C}^*}{dA} \cdot \boldsymbol{\epsilon}^0 \tag{42}$$

where $\mathbf{C}^*$ is the effective stiffness tensor of the composite. For a better analogy with the uniform traction results, some terms can be re-expressed as

Downloaded 04 May 2010 to 171.66.16.34. Redistribution subject to ASME license or copyright; see http://www.asme.org/terms/Terms_Use.cfm

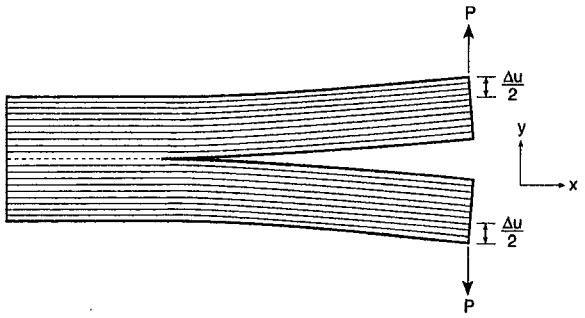


Fig. 1 A double cantilever beam specimen using unidirectional composites. The fiber direction (indicated by the internal lines) is parallel to the delamination crack growth. The specimen is point loaded by loads of P. The total deflection between the loading points is Δu.

$$\boldsymbol{\alpha}^{(i)} \cdot \overline{\boldsymbol{\sigma}^{(im)}} = -\mathbf{M}^{(i)} \cdot \overline{\boldsymbol{\epsilon}^{(im)}} \tag{43}$$

$$\boldsymbol{\alpha}^{(i)} \cdot \overline{\boldsymbol{\sigma}^{(ir)}} = -\mathbf{M}^{(i)} \cdot \overline{\boldsymbol{\epsilon}^{(ir)}} + \boldsymbol{\alpha}^{(i)} \cdot \mathbf{M}^{(i)} \mathbf{T} \tag{44}$$

where $\mathbf{M} = -\mathbf{C}\boldsymbol{\alpha}$ is the stress-temperature tensor. Incorporating these results into the Eq. (26) and ignoring the constant term $\boldsymbol{\alpha}^{(i)} \cdot \mathbf{M}^{(i)} T$, which drops out upon differentiation, the energy release rate is

$$G = -\frac{V}{2}\left[\boldsymbol{\epsilon}^0 \cdot \frac{d\mathbf{C}^*}{dA}\boldsymbol{\epsilon}^0 + T\sum_{i=1}^{n} v_i \mathbf{M}^{(i)} \cdot \left(2\frac{d\overline{\boldsymbol{\epsilon}^{(im)}}}{dA} + \frac{d\overline{\boldsymbol{\epsilon}^{(ir)}}}{dA}\right)\right]. \tag{45}$$

This result is identical to the uniform traction results (see Eq. (37)) except for a sign change and physical meanings of all symbols. The sign change is required because G is positive and, in general, $\mathbf{C}^*$ decreases with crack growth. By an explicit analogy to the results for uniform traction, the energy release rate for pure mode crack growth becomes

$$\frac{G_I}{G_{\text{mech}}} = \left(1 + T\frac{\sum_{i=1}^{n} v_i \mathbf{M}^{(i)} \cdot \frac{d\overline{\boldsymbol{\epsilon}^{(im)}}}{dA}}{\boldsymbol{\epsilon}^0 \cdot \frac{d\mathbf{C}^*}{dA}\boldsymbol{\epsilon}^0}\right)^2 \tag{46}$$

Delamination. Figure 1 shows a double cantilever beam specimen made from a unidirectional composite. The fibers run parallel to the x direction. This problem differs from the previous sections in two respects. First, the specimen is not statistically homogeneous because there is only one macroscopic delamination crack. Second, although there is only traction loading, the tractions are not uniform (i.e., they depend on position). The tractions can be written as

$$\boldsymbol{T}^0 = P[\delta(\boldsymbol{x} - \boldsymbol{x}_{\text{upper}}) - \delta(\boldsymbol{x} - \boldsymbol{x}_{\text{lower}})] \tag{47}$$

where $\delta(\boldsymbol{x})$ is the Dirac delta function and $\boldsymbol{x}_{\text{upper}}$ and $\boldsymbol{x}_{\text{lower}}$ are the locations of the upper and lower load points. Substitution into Eqs. (24) and (33) (because the crack growth is pure mode I) gives

$$G_I = \frac{P^2}{2}\frac{dC_m}{dA}\left(1 + \frac{TV}{2}\frac{\sum_{i=1}^{n} v_i \boldsymbol{\alpha}^{(i)} \cdot \frac{d\overline{\boldsymbol{\sigma}^{(im)}}}{dA}}{\frac{P^2}{2}\frac{dC_m}{dA}}\right)^2 \tag{48}$$

where $C_m = \Delta u^m / P$ is the mechanical load-point compliance. The leading term is G_{mech} or the energy release rate in the absence of residual stresses.

Proceeding for a two-phase unidirectional composite (fibers as phase 1 and matrix as phase 2) with aligned transversely isotropic phases, we can write

$$\sum_{i=1}^{n} v_i \boldsymbol{\alpha}^{(i)} \cdot \frac{d\overline{\boldsymbol{\alpha}^{(im)}}}{dA} = v_1[\overline{\sigma_{xx}^{(1m)}}\,\alpha_A^{(1)} + (\overline{\sigma_{yy}^{(1m)}} + \overline{\sigma_{zz}^{(1m)}})\alpha_T^{(1)}] + v_2[\overline{\sigma_{xx}^{(2m)}}\,\alpha_A^{(2)} + (\overline{\sigma_{yy}^{(2m)}} + \overline{\sigma_{zz}^{(2m)}})\alpha_T^{(2)}] \tag{49}$$

Now, double-cantilever beams specimens without residual stresses can be well analyzed using beam analyses (Hashemi et al., 1990). Within the assumptions of a beam analysis $\overline{\sigma_{yy}^{(im)}}$ and $\overline{\sigma_{zz}^{(im)}}$ are identically zero while $\overline{\sigma_{xx}^{(im)}}$ will net to zero by virtue of a balance between tension and compression stresses within the beam. The energy release rate for delamination becomes simply

$$G = \frac{P^2}{2}\frac{dC_m}{dA} \tag{50}$$

In other words, within the assumptions of beam analyses, residual stresses have no effect on delamination. Residual stresses are present in both the fiber and the matrix, but they release no energy as the delamination propagates.

Microcracked Laminate. Figure 2 shows an edge view of a symmetric $2n$-ply laminate under a uniaxial load of σ_0 in the x direction in which the central 90-deg ply group has through-the-width cracks separated by a distance s. This geometry is appropriate for analysis of a microcracked laminate with periodic microcracks in the 90-deg plies having a density $D = 1/s$ (Nairn and Hu, 1994). This problem differs from previous examples in three respects. First, the tractions are nonuniform: σ_0 is applied to the uncracked plies, but there is zero traction on the cracked 90-deg plies. Second, there are more then two phases. Although the plies themselves are composites, here each ply is treated as a homogeneous, anisotropic material. The general laminate, which may have plies at many orientations or may even be a hybrid laminate, is thus a multiphase composite. Third, we incorporate information about the laminated structure of the composite into the analysis. The key structural information we use is that the x and y direction strains of all uncracked plies are equal and that $\overline{\sigma_{zz}^{(im)}} = \overline{\sigma_{zz}^{(ir)}} = 0$ in all plies.

From Eq. (23), we can immediately write

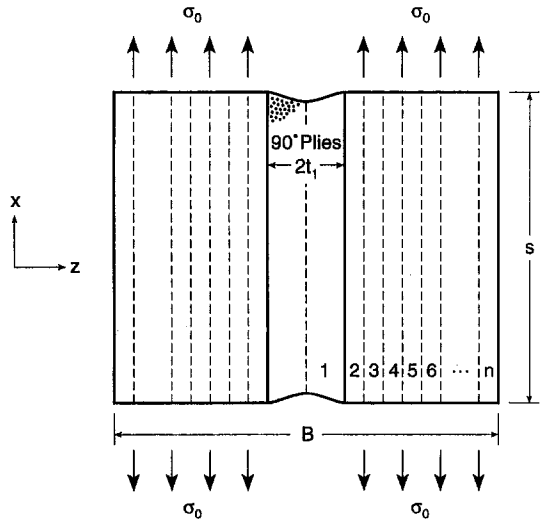


Fig. 2 An edge view of a microcracked laminate. The microcracks occur in the central 90 deg plies; they are located at the top and bottom of the 90 deg plies are are separated by a distance s. Each ply has thickness t_i; the total symmetric laminate thickness is B.

Downloaded 04 May 2010 to 171.66.16.34. Redistribution subject to ASME license or copyright; see http://www.asme.org/terms/Terms_Use.cfm

$$G = \frac{V}{2}\frac{d}{dA}\left(\frac{\sigma_0^2}{E_{xx}^*} + T(2\langle \boldsymbol{\sigma}^m \cdot \boldsymbol{\alpha}\rangle + \langle \boldsymbol{\sigma}^r \cdot \boldsymbol{\alpha}\rangle)\right) \quad (51)$$

where E_{xx}^* is the effective laminate modulus in the x direction. The first term is the energy release rate in the absence of residual stresses. Furthermore, by Eq. (20) we can write

$$\langle \boldsymbol{\sigma}^m \cdot \boldsymbol{\alpha} T\rangle = \sigma_0 \langle \epsilon_{xx}^r \rangle_u = \sigma_0 \alpha_{xx}^* T \quad (52)$$

where α_{xx}^* is the effective laminate thermal expansion coefficient in the x direction and $\langle \epsilon_{xx}^r \rangle_u$ is the volume averaged residual strain in the *uncracked* plies only. This term appears because the tractions are applied only to the uncracked plies. Equation (52) is similar to Levin's analysis for thermal expansion coefficient of a composite (Levin, 1967; Rosen and Hashin, 1970) except that it is applied here under conditions of nonuniform traction.

The energy release rate will be analyzed first using a plane stress analysis in which $\sigma_{yy}^{(im)} = \sigma_{yy}^{(ir)} = 0$ in all plies. From Eq. (52),

$$\sigma_0 \alpha_{xx}^* = \sum_{i=1}^{n} v_i \overline{\sigma_{xx}^{(im)}}\, \alpha_{xx}^{(i)}, \quad (53)$$

where $v_i = 2t_i/B$ is the total volume fraction of ply i including both sides of the symmetric laminate. By force balance and iso-strain in the uncracked plies

$$\sum_{i=1}^{n} v_i \overline{\sigma_{xx}^{(im)}} = \sigma_0 \quad \text{and} \quad \overline{\sigma_{xx}^{(im)}} = \frac{E_{xx}^{(i)}\sigma_0}{E_{xx}^*} \quad \text{for} \quad i \neq 1. \quad (54)$$

Using these results, the effective x-direction thermal expansion coefficient can be expressed as

$$\alpha_{xx}^* = \alpha_{xx}^{(i)} - \frac{(1 - v_1)\Delta\alpha_{xx} E_{xx}^{(u)}}{E_{xx}^*} \quad (55)$$

where

$$\Delta\alpha_{xx} = \alpha_{xx}^{(1)} - \alpha_{xx}^{(u)}, \quad E_{xx}^{(u)} = \frac{\sum_{i=2}^{n} v_i E_{xx}^{(i)}}{1 - v_1},$$

$$\text{and} \quad \alpha_{xx}^{(u)} = \frac{\sum_{i=2}^{n} v_i \alpha_{xx}^{(i)} E_{xx}^{(i)}}{\sum_{i=2}^{n} v_i E_{xx}^{(i)}}. \quad (56)$$

$E_{xx}^{(u)}$ and $\alpha_{xx}^{(u)}$ are the rule-of-mixtures x-direction modulus and thermal expansion coefficient of the uncracked plies. The residual strain energy term is

$$\langle \boldsymbol{\sigma}^r \cdot \boldsymbol{\alpha} T\rangle = \sum_{i=1}^{n} v_i \overline{\sigma_{xx}^{(ir)}}\, \alpha_{xx}^{(i)} T. \quad (57)$$

By force balance of residual stresses and iso-strain in the uncracked plies

$$\sum_{i=1}^{n} v_i \overline{\sigma_{xx}^{(ir)}} = 0 \quad \text{and} \quad \overline{\sigma_{xx}^{(ir)}} = E_{xx}^{(i)}(\alpha_{xx}^* - \alpha_{xx}^{(i)})T \quad \text{for} \quad i \neq 1. \quad (58)$$

Using these results, the residual strain energy term is

$$\langle \boldsymbol{\sigma}^r \cdot \boldsymbol{\alpha} T\rangle = \text{constant} - \alpha_{xx}^*(1 - v_1)T^2 \Delta\alpha_{xx} E_{xx}^{(u)}. \quad (59)$$

The "constant" term is not evaluated because it drops out when finding the energy release rate.

Substituting Eqs. (52), (55), and (59) into Eq. (51) gives

$$G = \frac{V}{2}(\sigma_0 - \Delta\alpha_{xx} E_{xx}^{(u)}(1 - v_1)T)^2 \frac{d}{dA}\left(\frac{1}{E_{xx}^*}\right). \quad (60)$$

The energy release rate in the presence of residual thermal stresses depends only on one effective property—E_{xx}^*; that property can be evaluated by an isothermal stress analysis. If we imagine formation of a complete new microcrack midway between two existing microcracks, we have

$$V = BWs = \frac{BW}{D} \quad \text{and} \quad dA = 2t_1 W = v_1 BW. \quad (61)$$

The integrated energy release rate for formation of a complete microcrack is

$$G = \frac{1}{2v_1 D}(\sigma_0 - \Delta\alpha_{xx} E_{xx}^{(u)}(1 - v_1)T)^2 \Delta\left(\frac{1}{E_{xx}^*}\right) \quad (62)$$

where $\Delta(1/E_{xx}^*)$ is the change in the effective x-direction modulus caused by the new microcrack. An energy release expression mathematically identical to Eq. (62) is given in a different form in Nairn et al. (1993) and Nairn and Hu (1994) and in the identical form in Nairn (1995). In Nairn et al. (1993), Nairn and Hu (1994), and Nairn (1995), however, the energy release rate was the specific result of a thermal elasticity analysis. Here the energy release rate is derived as a general result. The accuracy of finding G is only limited to the accuracy in finding E_{xx}^*. In Nairn (1995), variational mechanics was used to bound E_{xx}^* and an average of those bounds gave a virtually exact solution for G.

A better connection with laminated plate theory can be derived by considering a generalized plane-strain analysis of a cracked laminate instead of the previous plane stress analysis. In the generalized plane-strain analysis, it is assumed that the y-direction strain in all plies is $-\nu_{xy}^* \sigma_0/E_{xx}^*$ where ν_{xy}^* is the effective x–y Poisson's ratio of the cracked laminate. The resulting new analysis will correct the plane stress analysis to account for differential Poisson's ratios between the plies. The corrections are generally small, but can be accomplished in a straightforward analysis.

Equations (51) and (52) are unchanged in the generalized plane-strain analysis. Starting from Eq. (52),

$$\sigma_0 \alpha_{xx}^* = \sum_{i=1}^{n} (v_i \overline{\sigma_{xx}^{(im)}}\, \alpha_{xx}^{(i)} + v_i \overline{\sigma_{yy}^{(im)}}\, \alpha_{yy}^{(i)}). \quad (63)$$

By force balance and iso-strain in the uncracked plies

$$\sum_{i=1}^{n} v_i \overline{\sigma_{xx}^{(im)}} = \sigma_0 \quad \text{and} \quad \sum_{i=1}^{n} v_i \overline{\sigma_{yy}^{(im)}} = 0 \quad (64)$$

$$\overline{\sigma_{xx}^{(im)}} = (Q_{11}^{(i)} - \nu_{xy}^* Q_{12}^{(i)})\frac{\sigma_0}{E_{xx}^*} \quad \text{for} \quad i \neq 1 \quad (65)$$

$$\overline{\sigma_{yy}^{(im)}} = (Q_{12}^{(i)} - \nu_{xy}^* Q_{22}^{(i)})\frac{\sigma_0}{E_{xx}^*} \quad \text{for} \quad i \neq 1 \quad (66)$$

where $Q_{kj}^{(i)}$ $(k, j = 1, 2, 6)$ are the suitably rotated elements of the in-plane stiffness matrix for ply i (Tsai, 1987). Using these results, the effective x-direction thermal expansion coefficient becomes

$$\alpha_{xx}^* = \alpha_{xx}^{(1)} + \frac{1}{E_{xx}^*}\sum_{i=2}^{n} v_i[(\alpha_{xx}^{(i)} - \alpha_{xx}^{(1)})Q_{11}^{(i)} + (\alpha_{yy}^{(i)} - \alpha_{yy}^{(1)})Q_{12}^{(i)}]$$

$$- \frac{\nu_{xy}^*}{E_{xx}^*}\sum_{i=2}^{n} v_i[(\alpha_{xx}^{(i)} - \alpha_{xx}^{(1)})Q_{12}^{(i)} + (\alpha_{yy}^{(i)} - \alpha_{yy}^{(1)})Q_{22}^{(i)}]. \quad (67)$$

Now consider the laminate created by removing the cracked plies and joining the remaining plies; call it the "uncracked"

Downloaded 04 May 2010 to 171.66.16.34. Redistribution subject to ASME license or copyright; see http://www.asme.org/terms/Terms_Use.cfm

laminate. By laminated plate analysis of the *symmetric* uncracked laminate (Tsai, 1987), it can be shown that

$$\sum_{i=2}^{n} v_i Q_{kj}^{(i)} = \frac{A_{kj}^{(u)}}{B} \tag{68}$$

$$\sum_{i=2}^{n} v_i (\alpha_{xx}^{(i)} Q_{11}^{(i)} + \alpha_{yy}^{(i)} Q_{12}^{(i)}) = \frac{1}{B} (A_{11}^{(u)} \alpha_{xx}^{(u)} + A_{12}^{(u)} \alpha_{yy}^{(u)}) \tag{69}$$

$$\sum_{i=2}^{n} v_i (\alpha_{xx}^{(i)} Q_{12}^{(i)} + \alpha_{yy}^{(i)} Q_{22}^{(i)}) = \frac{1}{B} (A_{12}^{(u)} \alpha_{xx}^{(u)} + A_{22}^{(u)} \alpha_{yy}^{(u)}) \tag{70}$$

where $A_{kj}^{(u)}$ are the elements of the laminated plate theory $[A]$ matrix for the uncracked laminate and $\alpha_{xx}^{(u)}$ and $\alpha_{yy}^{(u)}$ are the thermal expansion coefficients for the uncracked laminate defined by

$$\alpha_{xx}^{(u)} = B[a_{11}^{(u)} \sum_{i=2}^{n} v_i (\alpha_{xx}^{(i)} Q_{11}^{(i)} + \alpha_{yy}^{(i)} Q_{12}^{(i)}) + a_{12}^{(u)} \sum_{i=2}^{n} v_i (\alpha_{xx}^{(i)} Q_{12}^{(i)} + \alpha_{yy}^{(i)} Q_{22}^{(i)})] \tag{71}$$

$$\alpha_{yy}^{(u)} = B[a_{12}^{(u)} \sum_{i=2}^{n} v_i (\alpha_{xx}^{(i)} Q_{11}^{(i)} + \alpha_{yy}^{(i)} Q_{12}^{(i)}) + a_{22}^{(u)} \sum_{i=2}^{n} v_i (\alpha_{xx}^{(i)} Q_{12}^{(i)} + \alpha_{yy}^{(i)} Q_{22}^{(i)})]. \tag{72}$$

Here $a_{kj}^{(u)}$ are elements of the laminated plate theory $[a]$ matrix which is the inverse of the $[A]$ matrix. Using these results, the effective x-direction thermal expansion coefficient can be expressed as

$$\alpha_{xx}^{*} = \alpha_{xx}^{(1)} - \frac{(1 - v_1)\Delta_1}{E_{xx}^{*}} + \frac{\nu_{xy}^{*}(1 - v_1)\Delta_2}{E_{xx}^{*}} \tag{73}$$

where

$$\Delta_1 = \frac{1}{B(1 - v_1)} [A_{11}^{(u)}(\alpha_{xx}^{(1)} - \alpha_{xx}^{(u)}) + A_{12}^{(u)}(\alpha_{yy}^{(1)} - \alpha_{yy}^{(u)})] \tag{74}$$

$$\Delta_2 = \frac{1}{B(1 - v_1)} [A_{12}^{(u)}(\alpha_{xx}^{(1)} - \alpha_{xx}^{(u)}) + A_{22}^{(u)}(\alpha_{yy}^{(1)} - \alpha_{yy}^{(u)})]. \tag{75}$$

Note that $A_{kj}^{(u)}/(B(1 - v_1))$ are the elements of the normalized, x–y plane stiffness matrix for the uncracked laminate (Tsai, 1987). By a similar analysis but with σ_0 applied in the y direction, the effective y-direction thermal expansion coefficient can be expressed as

$$\alpha_{yy}^{*} = \alpha_{yy}^{(1)} - \frac{(1 - v_1)\Delta_2}{E_{yy}^{*}} + \frac{\nu_{xy}^{*}(1 - v_1)\Delta_1}{E_{xx}^{*}}. \tag{76}$$

The residual strain energy term is

$$\langle \boldsymbol{\sigma}^{r} \cdot \boldsymbol{\alpha} T \rangle = \sum_{i=1}^{n} (v_i \overline{\sigma_{xx}^{(ir)}} \alpha_{xx}^{(i)} T + v_i \overline{\sigma_{yy}^{(ir)}} \alpha_{yy}^{(i)} T). \tag{77}$$

By force balance of residual stresses and iso-strain in the uncracked plies

$$\sum_{i=1}^{n} v_i \overline{\sigma_{xx}^{(ir)}} = 0 \quad \text{and} \quad \sum_{i=1}^{n} v_i \overline{\sigma_{yy}^{(ir)}} = 0 \tag{78}$$

$$\overline{\sigma_{xx}^{(ir)}} = Q_{11}^{(i)}(\alpha_{xx}^{*} - \alpha_{xx}^{(i)})T + Q_{12}^{(i)}(\alpha_{yy}^{*} - \alpha_{yy}^{(i)})T \quad \text{for} \quad i \neq 1 \tag{79}$$

$$\overline{\sigma_{yy}^{(ir)}} = Q_{12}^{(i)}(\alpha_{xx}^{*} - \alpha_{xx}^{(i)})T + Q_{22}^{(i)}(\alpha_{yy}^{*} - \alpha_{yy}^{(i)})T \quad \text{for} \quad i \neq 1. \tag{80}$$

Using these results, the residual strain energy term is

$$\langle \boldsymbol{\sigma}^{r} \cdot \boldsymbol{\alpha} T \rangle = \text{constant} - \alpha_{xx}^{*}(1 - v_1)T^2\Delta_1 - \alpha_{yy}^{*}(1 - v_1)T^2\Delta_2. \tag{81}$$

The "constant" term is not evaluated because it drops out when finding the energy release rate.

Substituting Eqs. (52), (73), (76), and (81) into Eq. (51) gives

$$G = \frac{V}{2}\left[(\sigma_0 - (1 - v_1)T\Delta_1)^2 \frac{d}{dA}\left(\frac{1}{E_{xx}^{*}}\right) + 2(1 - v_1)T\Delta_2(\sigma_0 - (1 - v_1)T\Delta_1)\frac{d}{dA}\left(\frac{\nu_{xy}^{*}}{E_{xx}^{*}}\right) + (1 - v_1)^2T^2\Delta_2^2 \frac{d}{dA}\left(\frac{1}{E_{yy}^{*}}\right)\right]. \tag{82}$$

The energy release rate depends only on E_{xx}^{*}, E_{yy}^{*}, and ν_{xy}^{*}, all of which can be evaluated by an isothermal stress analysis. Equation (82) is exact for any damage mode in a microcracked laminate. If the damage is mode I propagation of a new microcrack between the existing microcracks, we can use Eq. (31) to derive an exact relation between laminate effective properties:

$$\frac{\dfrac{d}{dA}\left(\dfrac{\nu_{xy}^{*}}{E_{xx}^{*}}\right)}{\dfrac{d}{dA}\left(\dfrac{1}{E_{xx}^{*}}\right)} = \frac{\dfrac{d}{dA}\left(\dfrac{1}{E_{yy}^{*}}\right)}{\dfrac{d}{dA}\left(\dfrac{\nu_{xy}^{*}}{E_{xx}^{*}}\right)}. \tag{83}$$

Interestingly, an analysis of fracture in the presence of residual thermal stresses has lead to a relation between effective mechanical properties. Using Eq. (83) the mode I microcracking energy release is

$$G_I = \frac{V}{2} \times \frac{\left[(\sigma_0 - (1 - v_1)T\Delta_1)\dfrac{d}{dA}\left(\dfrac{1}{E_{xx}^{*}}\right) + (1 - v_1)T\Delta_2 \dfrac{d}{dA}\left(\dfrac{\nu_{xy}^{*}}{E_{xx}^{*}}\right)\right]^2}{\dfrac{d}{dA}\left(\dfrac{1}{E_{xx}^{*}}\right)}. \tag{84}$$

The mode I energy release rate depends only on E_{xx}^{*} and ν_{xy}^{*}. McCartney (1994) derived results that appear equivalent to Eqs. (82) and (83). McCartney's results, however, were a specific result of an approximate generalized, plane-strain, thermal elasticity analysis of a microcracked laminate. The results here were derived by a very different path and are exact provided exact results for E_{xx}^{*}, ν_{xy}^{*}, and E_{yy}^{*} are known.

The previous results were for uniaxial loading. It is trivial to extend the analysis to generalized in-plane loading of the microcracked laminate. The energy release rate becomes

$$G = \boldsymbol{\sigma}^{\text{eff}} \cdot \frac{d}{dA} \begin{pmatrix} \dfrac{1}{E_{xx}^{*}} & -\dfrac{\nu_{xy}^{*}}{E_{xx}^{*}} & 0 \\ -\dfrac{\nu_{xy}^{*}}{E_{xx}^{*}} & \dfrac{1}{E_{yy}^{*}} & 0 \\ 0 & 0 & \dfrac{1}{G_{xy}^{*}} \end{pmatrix} \boldsymbol{\sigma}^{\text{eff}} \tag{85}$$

Downloaded 04 May 2010 to 171.66.16.34. Redistribution subject to ASME license or copyright; see http://www.asme.org/terms/Terms_Use.cfm

where G_{xy}^* is the effective in-plane shear modulus and $\boldsymbol{\sigma}^{\text{eff}}$ is the effective in-plane applied stressed defined by

$$\boldsymbol{\sigma}^{\text{eff}} = (\sigma_{x0} - (1 - \upsilon_1)T\Delta_1, \sigma_{y0} - (1 - \upsilon_1)T\Delta_2, \tau_{xy0}). \quad (86)$$

Here σ_{x0}, σ_{y0}, and τ_{xy0} are the applied in-plane stresses.

Discussion

In many examples considered, the energy release rate for crack growth, G, was reduced to an expression that depends only on the effective compliance ($\mathbf{S}^*$) or stiffness ($\mathbf{C}^*$) tensors and the phase average mechanical stresses. Because these terms can be evaluated by isothermal elasticity methods (Hashin 1963; 1969), it is often possible to include the effect of residual thermal stresses on the energy release rate without ever evaluating the thermal stresses. In other words, no thermal elasticity analysis of the composite is required. This result, however, does not imply that the effect of residual thermal stresses is a trivial extension of isothermal fracture mechanics analysis. For example, the isothermal energy release rate for microcracking of a laminate depends only on the E_{xx}^*. In contrast, the energy release rate in the presence of residual stresses depends on E_{xx}^*, ν_{xy}^*, and E_{yy}^*. Thus, in general, the fracture mechanics analysis of a composite with residual thermal stresses will require more isothermal elasticity analysis of composite properties than the corresponding isothermal fracture mechanics analysis.

The discussion here was confined to residual thermal stresses, but identical results could be derived for other types of residual stresses. For example, fiber-reinforced polymer-matrix composites can develop residual stresses due to differential moisture absorption between the fibers and the matrix (Tsai, 1987). The results for moisture-induced residual stresses can be generated from the results given here by replacing $\boldsymbol{\alpha}$ by the moisture expansion tensor and T by the moisture concentration. Residual stresses induced by nonuniform temperature (T a function of position) are more complicated. The general theory derived here up to Eq. (23) still applies when there is nonuniform T. Many subsequent simplifications, however, only hold for uniform T.

The energy release rate in the presence of residual stresses depends on derivatives of mechanical terms like

$$\frac{d\mathbf{S}^*}{dA}, \quad \frac{d\mathbf{C}^*}{dA}, \quad \text{and} \quad \frac{d\overline{\boldsymbol{\sigma}^{(im)}}}{dA}. \quad (87)$$

Many damage mechanics models have been developed that give effective properties as a function damage. The results in this paper could easily be incorporated into such models to simultaneously give the energy release rate for damage growth. An important observation, however, is that the ability of a damage analysis to predict effective properties is *necessary* but not *sufficient* justification for use of that analysis to calculate energy release rate. The problem is that calculating derivatives of effective properties is a harder problem than calculating the average property itself. Analyses that are accurate to within a few percent for effective properties may be grossly in error when calculating the derivative. Thus any damage mechanics analysis that seeks to calculate energy release rate must be verified to have accurate *derivatives* of the required terms. Experimentally this verification can be done by comparing fracture experiments to fracture mechanics predictions. In contrast, experimental verification based on effective property predictions, such as modulus reductions, are inadequate tests of energy release rate models.

Acknowledgments

This work was supported, in part, by a grant from the Mechanics of Materials program at NSF (CMS-9401772), and, in part, under McDonnell Douglas contract NAMP-1294-1544.

References

Aboudi, J., 1994, "Interfacial Damage," *Damage Mechanics of Composite Materials,* Ramesh Talreja, ed., Elsevier, Amsterdam, pp. 245–294.

Charalambides, M., Kinloch, A. J., Wang, Y., and Williams, J. G., 1992, "On the Analysis of Mixed-Mode Failure," *Int. J. Fract.,* Vol. 54, pp. 269–291.

Hashemi, S., Kinloch, A. J., and Williams, J. G., 1990, "The Analysis of Interlaminar Fracture in Uniaxial Fibre Reinforced Polymer Composites," *Proc. R. Soc. Lond.,* Vol. A347, pp. 173–199.

Hashin, Z., 1963, "Theory of Mechanical Behavior of Heterogeneous Media," ASME *Applied Mechanics Reviews,* Vol. 17, pp. 1–9.

Hashin, Z., 1969, "Theory of Composite Materials," *Mechanics of Composite Materials,* Pergamon Press, New York, pp. 201–242.

Hashin, Z., 1988, "Thermal Expansion Coefficients of Cracked Laminates," *Comp. Sci. & Tech.,* Vol. 31, pp. 247–260.

Hill, R., 1963, "Elastic Properties of Reinforced Solids: Some Theoretical Principles," *J. Mech. Phys. Solids,* Vol. 11, pp. 357–372.

Levin, V. M., 1967, "On the Coefficients of Thermal Expansion in Heterogeneous Materials," *Mechanics of Solids,* Vol. 2, pp. 58–61.

McCartney, L. N., 1994, "The Prediction of Non-Uniform Cracking in Biaxially Loaded Cross-Ply Laminates," National Physical Laboratory, Teddington, United Kingdom, Report DMM(A) 142.

Nairn, J. A., Hu, S., and Bark, J. S., 1993, "A Critical Evaluation of Theories for Predicting Microcracking in Composite Laminates," *J. Mat. Sci.,* Vol. 28, pp. 5099–5111.

Nairn, J. A., and Hu, S., 1994, "Micromechanics of Damage: A Case Study of Matrix Microcracking," *Damage Mechanics of Composite Materials,* Ramesh Talreja, ed., Elsevier, Amsterdam, pp. 187–243.

Nairn, J. A., 1995, "Some New Variational Mechanics Results on Composite Microcracking," *Proc. 10th Int'l Conf. on Comp. Mat.,* Vol. I, pp. 423–430.

Rosen, B. W., and Hashin, Z., 1970, "Effective Thermal Expansion Coefficients and Specific Heats of Composite Materials," *Int. J. Engng. Sci.,* Vol. 8, pp. 157–173.

Tsai, T. W., 1987, *Composites Design,* Think Composites, Dayton, OH.

Downloaded 04 May 2010 to 171.66.16.34. Redistribution subject to ASME license or copyright; see http://www.asme.org/terms/Terms_Use.cfm

J. L. Grenestedt

S. Hallstrom

Department of Aeronautics,
Division of Lightweight Structures,
Kungl Tekniska Hogskolan
(Royal Institute of Technology)
S-100 44 Stockholm, Sweden

Crack Initiation From Homogeneous and Bimaterial Corners

Fracture initiated at a corner between two different isotropic materials is considered. A "small" crack, well within the region dominated by the asymptotic stress fields of the noncracked corner, is modeled and the stress intensities associated with the tip of the small crack are determined. Different criteria for the direction of crack propagation are studied.

Introduction

The stress fields around a sharp corner are generally singular and fracture is likely to initiate there. The problem is of engineering relevance and the present investigation was initiated with application in mind: marine vessels constructed of sandwich panels in which the panels' sandwich core blocks are butt joined to each other with structural putty, often have insufficiently filled joints and thus bi or tri-material corners, surrounded by both core material, putty, and perhaps skin material, result, Fig. 1. Cracks often initiate in these regions.

The major goals of the current project are to determine when cracks initiate, the direction in which they propagate, and where the cracks propagate—in the core, in the putty, or in the bimaterial interface. A further goal is to tailor the properties of the putty to reduce the risk of crack initiation. It is interesting to note is that in a composite material sandwich vessel, structural putty often contributes five to eight percent to the total hull weight (Sjögren et al., 1984), and there is thus a good incentive to tailor putty properties, including weight.

Initiation of cracks at corners have been addressed by, e.g., Leicester (1969), Carpinteri (1987), Seweryn (1994), and Grenestedt et al. (1996) for Mode I stress fields and Hallström and Grenestedt (1996) for mixed mode cases. The stress state near a corner tip can in essence be written $\sigma_{ij} = Qr^{\lambda-1}f_{ij}(\theta)$, where Q can be considered a generalized stress intensity factor. Fracture in brittle materials can be conjectured to occur when this factor reaches a certain value, Q_{cr}, characteristic for the material but dependent on the exponent λ. The approach can be justified only by massive experimentation, using specimens of various geometric shapes and sizes.

To predict the direction of crack propagation from a corner, the stress intensity factors at the tip of a small crack emanating from the tip of the corner are determined. When the crack is so small that the stress field in the structure is virtually unaffected by the crack, save for a region close to the crack, then the stress intensity factors at the tip of the crack depend linearly on the corner stress intensity factor Q of the noncracked corner. The relation between the crack and corner stress intensities are determined in the paper.

When the stress state at the noncracked corner, and the stress state at the tip of a small crack emanating from the tip of the corner, have been determined, different criteria for predicting direction of crack growth can be examined and compared. An interesting feature is that it may be possible to find a corner configuration which can distinguish between four similar but different criteria: (1) cracks propagate in the direction of maximum energy release rate G, (2) cracks propagate in a direction such that $K_{II} = 0$ at the crack tip, (3) cracks propagate in the direction of maximum K_I, or (4) cracks propagate in a direction perpendicular to the maximum circumferential stress of the corner without a crack. The criteria (1) and (2) were used, e.g., by Hutchinson and Suo (1991) to determine the direction of kinking of cracks, and it was shown that the two criteria predict the same direction within a few degrees at most. Erdogan and Sih (1963) introduced criterion (4), which gives a prediction which differs slightly more from criteria (1) and (2). For the kinking of a crack in an isotropic homogeneous solid loaded in Mode II, the four criteria predict the kink angles (1) 75.6 deg, (2) 77.33 deg, (3) 76.58 deg, and (4) 70.53 deg, respectively, where for the kinked crack the data of Melin (1994) was used. The difference between the first three criteria is so small that experimental verification is practically impossible. Unfortunately, the same is true for the corner configurations studied; the three criteria predict virtually the same angle also for the corners studied. The fourth criterion though predicts very different crack angles.

Stress Fields at Noncracked Bimaterial Corners

In the following, plane strain and the geometry shown in Fig. 2 is assumed. The geometry is described by the two angles γ and φ. The asymptotic stress fields of corners have been studied by, among others, Williams (1952), Bogy (1968, 1971), Bogy and Wang (1971), Hein and Erdogan (1971), Theocaris (1974), and Lin and Hartmann (1989). The solution is readily obtained by using an Airy stress function $\Phi = \mathrm{Re}[r^{\lambda+1}h(\theta)]$ in cylindrical coordinates r, θ centered at the corner tip. The approach is outlined in Appendix A. The stress state in the singularity dominated zone close to the corner can be written

$$\sigma_{11} = \sum_m \mathrm{Re}[Q_m r^{\lambda_m - 1} f^m_{11}(\theta)]$$

$$\sigma_{22} = \sum_m \mathrm{Re}[Q_m r^{\lambda_m - 1} f^m_{22}(\theta)]$$

$$\sigma_{12} = \sum_m \mathrm{Re}[Q_m r^{\lambda_m - 1} f^m_{12}(\theta)] \qquad (1)$$

where the singularities λ_m generally are complex as are also the stress intensity factors Q_m and the functions f^m_{ij}. These stress intensity factors are similar to K_I, K_{II} of ordinary cracks, or the complex stress intensity factor $K = K_1 + iK_2$ of some bimaterial cracks with oscillating singularities. The singularities λ_m are roots to the characteristic equation, given in Appendix A. Presently we concentrate on the strongest singularity, which is

Contributed by the Applied Mechanics Division of THE AMERICAN SOCIETY OF MECHANICAL ENGINEERS for publication in the ASME JOURNAL OF APPLIED MECHANICS.

Discussion on this paper should be addressed to the Technical Editor, Professor Lewis T. Wheeler, Department of Mechanical Engineering, University of Houston, Houston, TX 77204-4792, and will be accepted until four months after final publication of the paper itself in the ASME JOURNAL OF APPLIED MECHANICS.

Manuscript received by the ASME Applied Mechanics Division, Nov. 6, 1996; final revision, Mar. 28, 1997. Associate Technical Editor: I. M. Daniel.

Copyright © 1997 by ASME

Downloaded 04 May 2010 to 171.66.16.34. Redistribution subject to ASME license or copyright; see http://www.asme.org/terms/Terms_Use.cfm

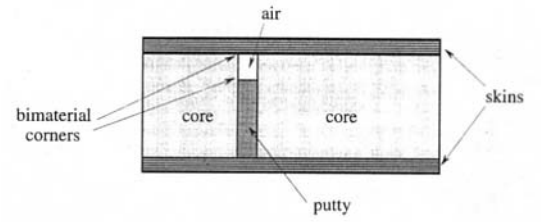


Fig. 1 Example of bimaterial corners occurring by a nonproperly filled butt joint with an air inclusion in a sandwich structure

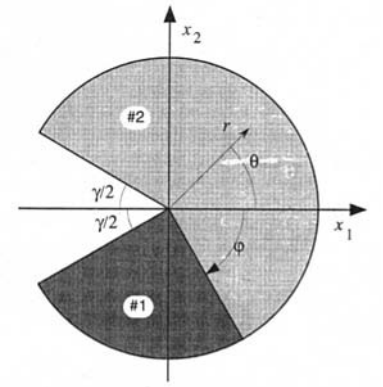


Fig. 2 Geometry of a general bimaterial corner. The x_1-axis bisects the traction-free wedge surfaces.

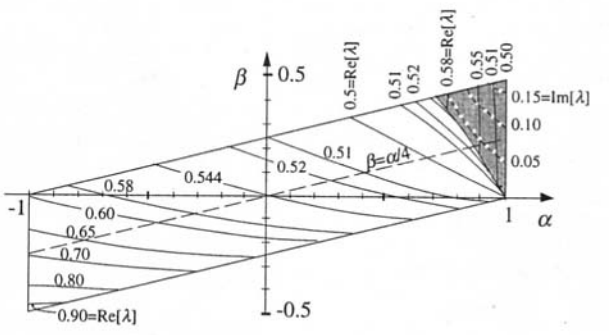


Fig. 3 Strongest singularity of 90 deg bimaterial corner (γ = 90 deg, φ = 45 deg) versus Dundurs' parameters. Within the shaded area λ is complex.

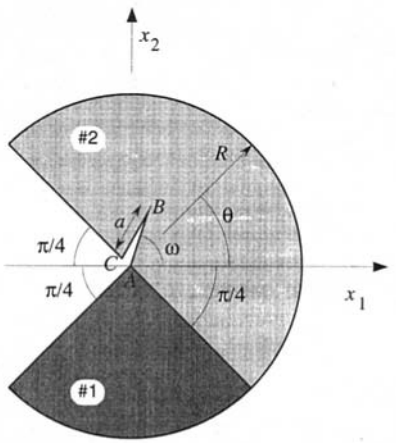


Fig. 4 Geometry of 90 deg bimaterial corner with small crack of length *a* extending from the tip of the corner. Crack stress intensity factor *K* is calculated for the tip of the crack, located at *B*. This *K* is related to the corner stress intensity factor *Q* for the noncracked corner, i.e., when *A* = *C*, subjected to the same far-field loading.

the singularity λ_m with the smallest real part and fulfilling $\mathrm{Re}[\lambda_m] > 0$ (required for a bounded total strain energy). Other terms will be ignored and we subsequently drop the index m.

The elastic bimaterial corner problem is affected by two, rather than three, nondimensional material parameters, referred to as Dundurs' (1968, 1969) elastic mismatch parameters α and β,

$$\alpha = \frac{\mu_1(\kappa_2 + 1) - \mu_2(\kappa_1 + 1)}{\mu_1(\kappa_2 + 1) + \mu_2(\kappa_1 + 1)} = \frac{\bar{E}_1 - \bar{E}_2}{\bar{E}_1 + \bar{E}_2},$$

$$\beta = \frac{\mu_1(\kappa_2 - 1) - \mu_2(\kappa_1 - 1)}{\mu_1(\kappa_2 + 1) + \mu_2(\kappa_1 + 1)} \tag{2}$$

where μ_i is shear modulus and ν_i is Poisson's ratio, and for plane-strain $\bar{E}_i = E_i/(1 - \nu_i^2)$ and $\kappa_i = 3 - 4\nu_i$. Especially note that $\beta = \alpha/4$ when $\nu_1 = \nu_2 = \frac{1}{3}$. In plane strain, the range of Dundurs' parameters is within the parallelogram enclosed by $\alpha = \pm 1$ and $\alpha - 4\beta = \pm 1$, assuming non-negative Poisson's ratios.

The x_1-x_2-coordinates are defined in Fig. 2, with the x_1-axis bisecting the traction-free corner. For a one-material (as opposed to a bimaterial) corner the stress state with the strongest singularity is symmetric about the x_1-axis. The stress intensity factors will for any corner be normalized such that the opening stress ahead of the corner tip is

$$(\sigma_{22})_{\theta=0} = \mathrm{Re}[Qr^{\lambda-1}]. \tag{3}$$

For a corner with nonoscillating stresses, λ, Q, and f are real. The oscillating case will be further dealt with in the next section.

Most of the present work is concentrated on the practically important bimaterial corner with γ = 90 deg and φ = 45 deg. The singularities of this corner have been well studied by, e.g., Bogy (1971), and a representation of the strongest singularity as a function of the elastic mismatch parameters is given in Fig. 3. Note that for this corner geometry, $\mathrm{Re}[\lambda] \geq 0.5$ for all material combinations.

Oscillating Stress Fields at Noncracked Corner

The stress singularity λ fulfills an eigenvalue equation of the form

$$\mathbf{M}(\lambda)\mathbf{c} = 0 \tag{4}$$

where $\mathbf{M}$ is an 8×8 matrix and $\mathbf{c}$ an eight dimensional vector (see Appendix A). The $\mathbf{M}$ matrix contains only real numbers apart from possibly λ. This means that $(\mathbf{M}(\lambda))^* = \mathbf{M}(\lambda^*)$ where the asterisk denotes complex conjugation. Using this relation in the conjugate of Eq. (4) reveals that if λ is an eigenvalue then so is λ*, i.e., the strongest singularity (the singularity λ with the smallest real part and fulfilling $\mathrm{Re}[\lambda_m] > 0$) is not unique if it is complex. This is similar to crack problems, where the strongest singularity is not unique; mode I and mode II

Table 1 Material data used in the analysis. The *E* and *ν* are the exact values used for the finite element analysis, whereas the *α* and *β* are approximate.

α	β	E_1/E_2	ν_1	ν_2
0.8	0	11.05	0.2353	0.48
0.5	0	3.394	0.3125	0.45
0	0	1	0.3333	0.3333
-0.5	0	0.2946	0.45	0.3125
-0.8	0	0.09052	0.48	0.2353
0.8	0.2	9	0.3333	0.3333
0.5	0.125	3	0.3333	0.3333
-0.5	-0.125	0.3333	0.3333	0.3333
-0.8	-0.2	0.1111	0.3333	0.3333

Downloaded 04 May 2010 to 171.66.16.34. Redistribution subject to ASME license or copyright; see http://www.asme.org/terms/Terms_Use.cfm

Table 2 Stress intensity factors K for cracks extending in the interface ($\omega = -\varphi = -45$ deg) from 90 deg bimaterial corners and various α and with $\beta = 0$. The factor ϕ was interpolated from data in Hutchinson et al. (1987).

α (β=0)	ϕ	$\frac{K_1}{Qa^{\lambda-1/2}}$	$\frac{K_2}{Qa^{\lambda-1/2}}$
0.8	0.0970	1.42	-0.983
0.5	0.066	1.74	-0.854
0	0	1.89	-0.767
-0.5	-0.106	1.94	-0.678
-0.8	-0.2270	1.92	-0.613

singularities have the same strength. For the corners, the stresses associated with the strongest singularity can still be written as in Eq. (3) but with a complex stress intensity factor $Q = Q_1 + iQ_2$, where Q_1 and Q_2 are independent stress intensity factors for two different "modes." Oscillating singularities result when λ is complex, which occurs for α and β values within the shaded region in Fig. 3, which approximately is $\beta \geq 1.5(1 - \alpha)$.

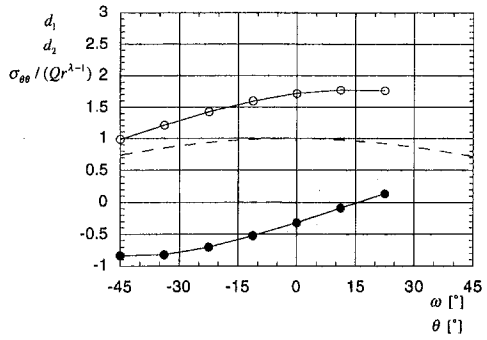
Stress Fields at the Tip of a Small Crack Emerging From the Tip of a Corner

At the tip of a corner in a structure subjected to increasing loads, a small crack as pictured in Fig. 4 is likely to develop. Presently, it is assumed that there exists only one crack and that it starts from the very tip of the noncracked corner. The crack is further assumed to be sharp, and to at least initially extend straight in a radial direction. The mechanics of this crack is studied in this section. A small crack, well within the region dominated by the asymptotic stress fields of the noncracked corner, is modeled and the stress intensities associated with the tip of the small crack determined. In this formulation there is only one length parameter involved, the length a of the crack. The other relevant parameters are the (nondimensional) material constants α, β, the stress intensity factor Q, the (nondimensional) singularity λ, and the two angles γ and φ. The stresses by the tip of the crack will be governed by the two stress intensity factors K_I and K_{II}($K_{III} = 0$ since plane strain is assumed) if the crack propagates in either of the surrounding materials, and by the complex stress intensity factor $K = K_1 + iK_2$ if it propagates in the interface. In the latter case, the definition of Hutchinson et al. (1987) is used for the stress intensity factor, such that the stresses straight ahead of the crack are $(\sigma_{\theta\theta} + i\sigma_{r\theta})_{\theta=\omega} = \rho^{-i\epsilon}K/\sqrt{2\pi\rho}$, where $\epsilon = \ln[(1 - \beta)/(1 + \beta)]/2\pi$ and ρ is distance ahead of the crack tip in the direction of the crack. The sign of the exponent differs from that of Hutchinson et al. because material 1 and 2 are interchanged. The conventional (nonoscillating) crack-tip fields are recovered when the elastic mismatch vanishes, so only the complex stress intensity factor will be used here. The dimensions of the stress intensity factors are, respectively, $MT^{-2}L^{-1/2-i\epsilon}$ for K and

Table 3 Stress data for the case $\beta = 0$. Stress intensity factors (d_1 and d_2, Eq. (5)) and energy release rate ($d_1^2 + d_2^2$, Eq. (7)) at the tip of a small crack emerging from a corner, as functions of the angle ω of the small crack. Tangential stress $\sigma_{\theta\theta}$ of the noncracked corner as function of the angle θ.

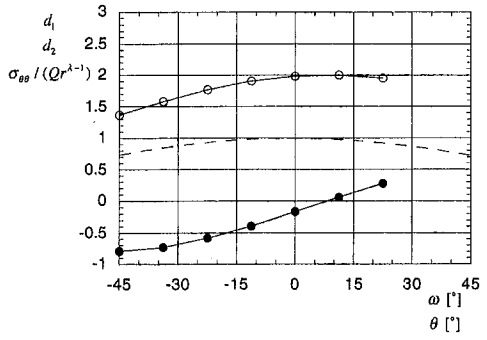
α (β=0)	λ	angle [°]	d_1	d_2	$d_1^2 + d_2^2$	$\frac{\sigma_{\theta\theta}}{Qr^{\lambda-1}}$
0.8	0.50853	-45+	0.985	-0.832	1.66	0.737
		-33.75	1.21	-0.819	2.14	0.850
		-22.5	1.43	-0.703	2.53	0.935
		-11.25	1.60	-0.529	2.83	0.986
		0	1.72	-0.317	3.05	1
		11.25	1.77	-0.0889	3.15	0.976
		22.5	1.76	0.137	3.13	0.918
0.5	0.52173	-45+	1.37	-0.789	2.50	0.735
		-33.75	1.58	-0.731	3.03	0.847
		-22.5	1.77	-0.586	3.47	0.932
		-11.25	1.91	-0.392	3.78	0.984
		0	1.98	-0.171	3.97	1
		11.25	2.00	0.0590	4.00	0.978
		22.5	1.95	0.279	3.88	0.921
0.0	0.54448	-45+	1.89	-0.767	4.17	0.730
		-33.75	2.10	-0.630	4.80	0.841
		-22.5	2.26	-0.448	5.31	0.927
		-11.25	2.36	-0.233	5.63	0.981
		0	2.39	0	5.74	1
		11.25	2.36	0.233	5.63	0.981
		22.5	2.26	0.448	5.31	0.927
-0.5	0.56856	-45+	2.83	-0.662	8.46	0.725
		-33.75	2.97	-0.313	8.94	0.834
		-22.5	3.04	-0.0924	9.24	0.921
		-11.25	3.03	0.126	9.21	0.978
		0	2.96	0.339	8.85	1
		11.25	2.81	0.538	8.21	0.985
		22.5	2.61	0.710	7.34	0.934
-0.8	0.58406	-45+	4.50	-0.368	20.35	0.722
		-33.75	4.34	0.412	18.98	0.830
		-22.5	4.14	0.601	17.47	0.917
		-11.25	3.87	0.729	15.51	0.976
		0	3.56	0.831	13.40	1
		11.25	3.23	0.918	11.31	0.987
		22.5	2.89	0.988	9.35	0.938

Downloaded 04 May 2010 to 171.66.16.34. Redistribution subject to ASME license or copyright; see http://www.asme.org/terms/Terms_Use.cfm



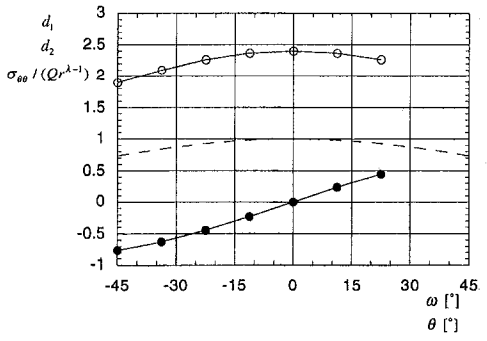
α=0.8, β=0

Fig. 5(Pt. 1)



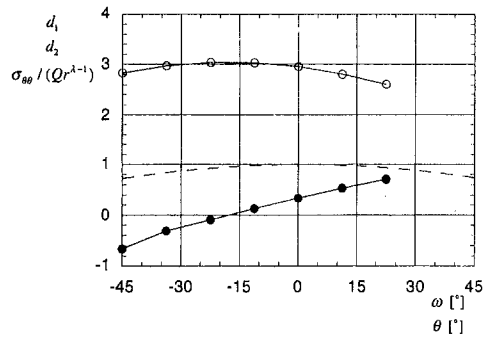
α=0.5, β=0

Fig. 5(Pt. 2)



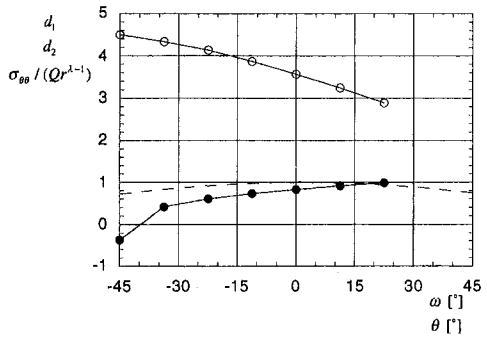
α=0, β=0

Fig. 5(Pt. 3)



α=-0.5, β=0

Fig. 5(Pt. 4)



α=-0.8, β=0

Fig. 5(Pt. 5)

Fig. 5 Stress intensity factors at the tip of a small crack emerging from a corner, plotted against angle ω of the small crack, for material combinations with $\beta = 0$. Open symbols are $d_1 = K_I/(Qa^{\lambda-1/2})$, closed symbols are $d_2 = K_{II}/(Qa^{\lambda-1/2})$. Dashed line is normalized tangential stress around the noncracked corner $\sigma_{\theta\theta}/(Qr^{\lambda-1})$, plotted versus polar coordinate θ.

$MT^{-2}L^{-\lambda_R}L^{-i\lambda_I}$ for Q, where $\lambda_R = \mathrm{Re}[\lambda]$ and $\lambda_I = \mathrm{Im}[\lambda]$. Linearity ($K$ and Q depend linearly on applied load) and dimensional considerations (the length a of the crack is the only length parameter) require the stress intensity factor K to be related to the stress intensity factor Q and the crack length a according to

$$K = d_1 Q a^{\lambda-1/2-i\epsilon} + i d_2^* Q^* a^{\lambda^*-1/2-i\epsilon} \tag{5}$$

where the generally complex influence coefficients d_1 and d_2 depend only on the angle ω of the crack, the Dundurs parameters α and β, and the geometry of the corner (i.e., γ and φ). The energy release rate for the small crack is obtained from the K above. For an interface crack (Malyshev and Salganik 1965),

$$G = \frac{1-\beta^2}{\hat{E}} KK^*, \quad \text{where} \quad \hat{E} = \frac{2\bar{E}_1\bar{E}_2}{\bar{E}_1 + \bar{E}_2}. \tag{6}$$

When the crack propagates in either of the two materials (not in the interface), λ is real and the energy release rate is

$$G = Q^2 a^{2\lambda-1}(d_1^2 + d_2^2)/\bar{E} \tag{7}$$

where $\bar{E} = E/(1-\nu^2)$ is the plane-strain tensile modulus of the material in which the crack propagates. Note that when $\mathrm{Re}\,[\lambda] > 0.5$, i.e., when the singularity is weaker than that of a sharp crack, then $K \to 0$ and $G \to 0$ when $a \to 0$. $\mathrm{Re}[\lambda] \geq 0.5$ for the homogeneous corner for all γ, and for the bimaterial corner with $\gamma = 90$ deg and $\varphi = 45$ deg for all material combinations, see Fig. 3.

The coefficients d_i were determined numerically, for which purpose a p-version (increasing polynomial degree of shape functions for increased precision) of the finite element method, the STRIPE[1] finite element package of Andersson et al. (1995), was used. d_1 and d_2 were calculated only for bimaterial corners with $\gamma = 90$ deg and $\varphi = 45$ deg, and only for configurations with real λ (of the noncracked corner). The restriction to real λ is not severe for the present geometry since rather few material combinations lead to complex λ, see Fig. 3. The finite element model had the general shape given in Fig. 4, i.e., a corner with a short crack of length a emerging from the center of a circular region with radius R. The radius R should be so large that the fact that R/a is finite has a negligible effect on crack-tip stress intensities. In the numerical analysis, $R/a = 50$ was used in general. $R/a = 200$ was used to obtain an estimate of the effect of finite R/a and the difference was negligible. The effect of R/a is also dealt with in Appendix B. The asymptotic stress field around the noncracked corner was determined analytically and the corresponding displacements were given as boundary condition on the circular part of the boundary for the finite element analysis. The finite element mesh had a high degree of refinement in the vicinity of the corner and crack tips, and a fair number of elements on the circular boundary such that the boundary conditions could be given with good accuracy. The

[1] STRIPE was developed at the Aeronautical Research Institute of Sweden.

Downloaded 04 May 2010 to 171.66.16.34. Redistribution subject to ASME license or copyright; see http://www.asme.org/terms/Terms_Use.cfm

Table 4 Stress data for the case $\beta = \alpha/4$ ($\nu_1 = \nu_2 = 1/3$). Stress intensity factors (d_1 and d_2, Eq. (5)) and energy release rate ($d_1^2 + d_2^2$, Eq. (7)) at the tip of a small crack emerging from a corner, as functions of the angle ω of the small crack. Tangential stress $\sigma_{\theta\theta}$ of the noncracked corner as function of the angle θ.

α (β=α/4)	λ	angle [°]	d_1	d_2	$d_1^2 + d_2^2$	$\frac{\sigma_{\theta\theta}}{Qr^{\lambda-1}}$
0.8	0.50807	-33.75	2.17	-1.62	7.30	0.597
		-22.5	2.61	-1.29	8.46	0.770
		-11.25	2.91	-0.913	9.32	0.907
		0	3.10	-0.501	9.85	1
		11.25	3.17	-0.0844	10.03	1.044
		22.5	3.12	0.310	9.86	1.037
0.5	0.50490	-33.75	1.63	-1.02	3.70	0.781
		-22.5	1.91	-0.824	4.31	0.890
		-11.25	2.11	-0.582	4.78	0.965
		0	2.23	-0.313	5.09	1
		11.25	2.28	-0.0342	5.21	0.995
		22.5	2.25	0.234	5.14	0.950
0.0	0.54448	-33.75	2.10	-0.630	4.80	0.841
		-22.5	2.26	-0.448	5.31	0.927
		-11.25	2.36	-0.233	5.63	0.981
		0	2.39	0	5.74	1
		11.25	2.36	0.233	5.63	0.981
		22.5	2.26	0.448	5.31	0.927
-0.5	0.60441	-33.75	2.87	-0.126	8.23	0.856
		-22.5	2.88	0.0169	8.31	0.933
		-11.25	2.84	0.193	8.12	0.983
		0	2.74	0.377	7.68	1
		11.25	2.59	0.550	7.00	0.982
		22.5	2.38	0.697	6.15	0.928
-0.8	0.65160	-33.75	3.93	0.605	15.80	0.856
		-22.5	3.68	0.659	13.96	0.930
		-11.25	3.39	0.729	12.02	0.980
		0	3.08	0.797	10.10	1
		11.25	2.75	0.856	8.30	0.986
		22.5	2.42	0.901	6.66	0.936

polynomial degree of the shape functions, p, of the finite elements was gradually increased until the numerical accuracy of the extracted stress intensity factors of the crack were believed to be significant to three or four digits for the given geometry; this does not account for possibly larger errors due to finite R/a. For most cases, p was gradually increased to nine. The number of elements in the models was in the order of 100 plus mesh grading by the crack and corner tips, which gave another 30–50 elements. The number of elements can be kept this small due to the high polynomial degree of the shape functions; see, e.g., Andersson et al. (1995) for details.

For values of ω close to $-\varphi$, there will be a sharp wedge-shaped region between the interface and the crack and the finite element method is likely to have trouble calculating the stress fields accurately. For this reason, the stress intensity factors for the interface crack were calculated and the stress intensities for cracks in either of the surrounding materials a small angle off from the interface were extracted using the results of Hutchinson et al. (1987) on cracks paralleling an interface. Hutchinson et al. express the stress intensity factors K_I and K_{II} at the tip of a crack, which is parallel and close to an interface, as a function of the stress intensity which would result if the crack were located in the interface. Their expression is, save for a difference in sign of the exponent due to a slightly different geometrical definition,

$$K_I + iK_{II} = \frac{1}{\sqrt{1+\alpha}} e^{-i\phi} K \tag{8}$$

when the interface crack is not oscillating ($\beta = \epsilon = 0$) and $\omega > -\varphi$. Hutchinson et al. (1987) tabulate ϕ (not to be confused with φ) which is a function of α and β. Presently, only configurations with nonoscillating interface cracks were studied using this method.

The material data used for the calculations are given in Table 1. The results from the calculations with $\beta = 0$ are presented in Tables 2 and 3 and Fig. 5 for the five different bimaterial configurations $\alpha = 0.8$, $\alpha = 0.5$, $\alpha = 0$, $\alpha = -0.5$, and $\alpha = -0.8$. The results from the calculations with $\beta = \alpha/4$ (obtained with $\nu_1 = \nu_2 = \frac{1}{3}$) and the same α are presented in Table 4 and Fig. 6. For most of the configurations and angles ω analyzed, the wedges on either side of the small crack are non-singular. In cases these edges are singular, mesh grading was used also at the edges. None of the configurations studied has logarithmic singularities which are stronger than those analyzed.

The tangential stress, normalized as $\sigma_{\theta\theta}/(Qr^{\lambda-1})$, ahead of the corner tip when no crack is present, is also given in Tables 3 and 4, and in Figs. 5 and 6.

Direction of Crack Propagation

Four criteria for direction of crack growth were discussed in the Introduction: (1) cracks propagate in the direction of maximum energy release rate G, (2) cracks propagate in a direction such that $K_{II} = 0$ at the crack tip, (3) cracks propagate in the direction of maximum K_I, or (4) cracks propagate in a direction perpendicular to the maximum circumferential stress. For crack kinking (a short crack extending from a global crack, generally in an angle to the global crack) in a one-material, these four criteria predict angles which differ very little.

The tangential stresses $\sigma_{\theta\theta}/(Qr^{\lambda-1})$ for the nine bimaterial configurations investigated are given in Tables 3 and 4, and plotted in Figs. 5 and 6. As seen in the figures, the angles θ for maximum tangential stress are for all corners considered close to 0 deg, with the exception $\alpha = 0.8$, $\beta = 0.2$, for which the maximum tangential stress occurs approximately for $\theta = 15$ deg.

In Figs. 5 and 6 the stress intensities at the crack tips of the cracks are plotted versus angles of the cracks ω. The conclusions from these figures can be summarized as follows: The three crack direction criteria based on energy release rate and stress intensity factors predict virtually the same direction of crack propagation from a 90 deg bimaterial corner ($\gamma = 90$ deg, $\varphi = 45$ deg). The angles ω for which crack-tip stress intensities were calculated range from $\omega = -\pi/4$ to $\omega = \pi/8$ with the interval $\pi/16$. For these discrete angles, K_I and G are maximum

Downloaded 04 May 2010 to 171.66.16.34. Redistribution subject to ASME license or copyright; see http://www.asme.org/terms/Terms_Use.cfm

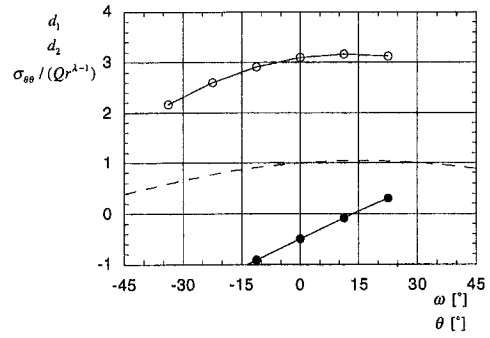


Fig. 6(Pt. 1)

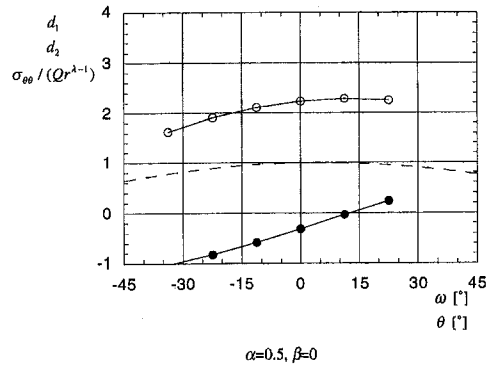


Fig. 6(Pt. 2)

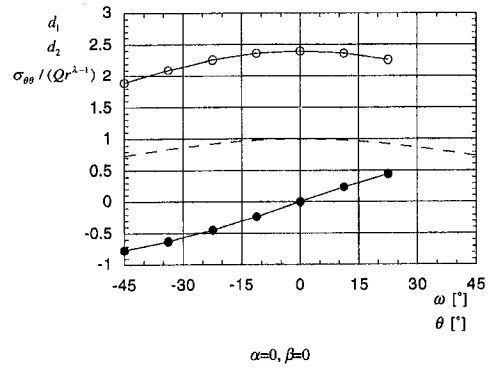


Fig. 6(Pt. 3)

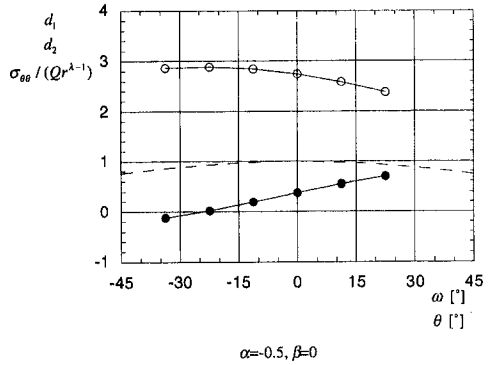


Fig. 6(Pt. 4)

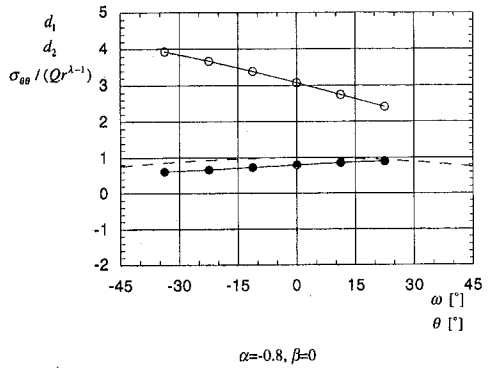


Fig. 6(Pt. 5)

Fig. 6 Stress intensity factors at the tip of a small crack emerging from a corner, plotted against angle ω of the small crack, for material combinations with $\beta = \alpha/4$. Open symbols are $d_1 = K_I/(Qa^{\lambda-1/2})$, closed symbols are $d_2 = K_{II}/(Qa^{\lambda-1/2})$. Dashed line is normalized tangential stress around the noncracked corner $\sigma_{\theta\theta}/(Qr^{\lambda-1})$, plotted versus polar coordinate θ.

for the same angle, i.e., criteria (1) and (3) predict the same angle when only these discrete angles are considered. Criterion (2) predicts virtually the same angles as criteria (1) and (3) except for the case $\alpha = -0.8$, $\beta = 0$, for which criteria (1) and (3) predict crack growth in or just by the interface, or possibly in material 1, whereas criterion (2) predicts crack growth a few degrees in to material 2. The three criteria (1–3) predict crack angles ranging from approximately -45 deg (i.e., an interface crack) or less for $\alpha = -0.8$, $\beta = 0$, to approximately 15 deg for $\alpha = 0.8$, $\beta = 0$. The maximum tangential stress criterion predicts vastly different angles.

The three curves of K_I and G versus the angle of the crack ω, and $\sigma_{\theta\theta}$ versus polar coordinate θ, are quite flat near their maxima. A physical significance of this is that slight material inhomogeneities may make a crack propagate in a directions which quite significantly differs from the angle for maximum K_I, G, or $\sigma_{\theta\theta}$.

A further significance of the fact that $\sigma_{\theta\theta}$ versus θ is quite flat is that even if criterion (4) is poor at predicting the angle of crack propagation, it may be fairly good at predicting loads for crack initiation. The difference in tangential stress at the angle for maximum $\sigma_{\theta\theta}$, and tangential stress at the angle for maximum K_I, is only a few percent (zero to five percent) except for the configurations with $\alpha = -0.8$; in these cases the difference is almost 30 percent.

Preliminary experiments, performed on slabs of expanded polymer foams glued together and pulled apart, indicate that the angles predicted by the fracture mechanics criteria are in better agreement to the experiments than are the maximum tangential stress criterion. For the configurations modeled, there is probably too little difference in predicted angles between the three criteria based on fracture mechanics (maximum G, $K_{II} = 0$, and maximum K_I) for judging from experiments which criterion is the better.

Summary and Conclusions

Fracture initiated at a corner between two different isotropic materials were studied. Different criteria for the direction of crack propagation from the tip of the corner were compared. Three criteria based on fracture mechanics of a small crack extending from the tip of the corner (maximum G, $K_{II} = 0$, and maximum K_I) predicted virtually the same angle of crack propagation for the nine configurations studied. A criterion based on stresses around the noncracked corner (maximum $\sigma_{\theta\theta}$) predicted quite different angles. Preliminary experiments suggest that the fracture mechanics approaches are in better agreement with experiments.

Acknowledgments

Professor J. W. Hutchinson is gratefully acknowledged for fruitful discussions. The work of JLG was supported by the

Downloaded 04 May 2010 to 171.66.16.34. Redistribution subject to ASME license or copyright; see http://www.asme.org/terms/Terms_Use.cfm

Swedish Research Council for Engineering Sciences (TFR), and the work of SH was supported by Brite/EuRam project BE-5781.

References

Andersson, B., Falk, U., Babuska, I., and von Petersdorff, T., 1995, "Reliable Stress and Fracture Mechanics Analysis of Complex Components Using a h–p Version of FEM," *International Journal for Numerical Methods in Engineering,* Vol. 38, pp. 2135–2163.

Bogy, D. B., 1968, "Edge-Bonded Dissimilar Orthogonal Elastic Wedges Under Normal and Shear Loading," ASME JOURNAL OF APPLIED MECHANICS, Vol. 35, pp. 460–466.

Bogy, D. B., 1971, "Two Edge-Bonded Elastic Wedges of Different Materials and Wedge Angles Under Surface Tractions," ASME JOURNAL OF APPLIED MECHANICS, Vol. 38, pp. 377–386.

Bogy, D. B., and Wang, K. C., 1971, "Stress singularities at interface corners in bonded dissimilar isotropic elastic materials," *Int. J. Solids Structures,* Vol. 7, pp. 993–1005.

Carpinteri, A., 1987, "Stress-Singularity and Generalized Fracture Toughness at the Vertex of Re-Entrant Corners," *Eng. Fract. Mech.,* Vol. 26, No. 1, pp. 143–155.

Dundurs, J., 1968, "Analogy between Concentrated Forces and Edge Dislocations," *Journal of Applied Physics,* Vol. 39, No. 9, pp. 4152–4156.

Dundurs, J., 1969, "Elastic Interaction of Dislocations With Inhomogeneities," *Mathematical Theory of Dislocations,* ASME, New York.

Erdogan, F., and Sih, G. C., 1963, "On the crack extension in plates under plane loading and transverse shear," *J. Bas. Engng.,* Vol. 85, pp. 519–527.

Grenestedt, J. L., Hallström, S., and Kuttenkeuler, J., 1996, "On Cracks Emanating from Wedges in Expanded PVC Foam," *Eng. Fract. Mech.,* Vol. 54, No. 4, pp. 445–456.

Hallström, S., and Grenestedt, J. L., 1996, "Mixed Mode Fracture of Cracks and Wedge Shaped Notches in Expanded PVC Foam," *International Journal of Fracture,* accepted for publication.

Hein, V. L., and Erdogan, F., 1971, "Stress singularities in a two-material wedge," *Int. J. Fracture Mech.,* Vol. 7, pp. 317–330.

Hutchinson, J. W., Mear, M. E., and Rice, J. R., 1987, "Cracks Paralleling an Interface Between Dissimilar Materials," ASME JOURNAL OF APPLIED MECHANICS, Vol. 54, pp. 828–832.

Hutchinson, J. W., and Suo, Z., 1991, "Mixed Mode Cracking in Layered Materials," *Advances in Applied Mechanics,* Vol. 29.

Leicester, R. H., 1969, "The Size Effect of Notches," *Proc. 2nd Australasian Conf. Mech. of Structures and Materials,* pp. 4.1–4.20.

Lin, K. Y., and Hartmann, H. H., 1989, "Numerical analysis of stress singularities at a bonded anisotropic wedge," *Eng. Fract. Mech.,* Vol. 32, pp. 211–224.

Malyshev, B. M., and Salganik, R. L., 1965, "The strength of adhesive joints using the theory of cracks," *Int. J. Fracture Mech.,* Vol. 1, pp. 114–128.

Melin, S., 1994, "Accurate Data for Stress Intensity Factors at Infinitesimal Kinks," ASME JOURNAL OF APPLIED MECHANICS, Vol. 61, pp. 467–470.

Seweryn, A., 1994, "Brittle Fracture Criterion for Structures with Sharp Notches," *Eng. Fract. Mech.,* Vol. 47, No. 5, pp. 673–681.

Sjögren, J., Celsing, C.-G., Olsson, K.-A., Levander, C.-G., and Hellbratt, S.-E., 1984, "Swedish Development of MCMV Hull Design and Production," *Proc. RINA Symp.,* London.

Theocaris, P. S., 1974, "The order of singularity at a multi-wedge corner of a composite plate," *Int. J. Engng. Sci.,* Vol. 12, pp. 107–120.

Williams, M. L., 1952, "Stress Singularities Resulting from Various Boundary Conditions in Angular Plates in Extension," ASME JOURNAL OF APPLIED MECHANICS, Vol. 19, pp. 526–528.

APPENDIX A

Analytical Determination of Stress Fields at the Non-cracked Corner

The stresses at a bimaterial corner can be derived by assuming the existence of an Airy stress function

$$\Phi_I = \mathrm{Re}[r^{\lambda+1}h_1(\theta)] \text{ in material I}$$

$$\Phi_{II} = \mathrm{Re}[r^{\lambda+1}h_{II}(\theta)] \text{ in material II} \qquad \text{(A1)}$$

in polar coordinates (r, θ) where λ in general is complex. A general solution to the biharmonic equation and the *ansatz* above is

$$h(\theta) = c_1 \cos[(\lambda - 1)\theta] + c_2 \sin[(\lambda - 1)\theta] + c_3 \cos[(\lambda + 1)\theta] + c_4 \sin[(\lambda + 1)\theta] \qquad \text{(A2)}$$

where the numbers c_i generally are complex. The stresses are

$$\sigma_{rr} = \frac{1}{r}\frac{\partial\Phi}{\partial r} + \frac{1}{r^2}\frac{\partial^2\Phi}{\partial\theta^2} = \mathrm{Re}\left[r^{\lambda-1}\left\{(\lambda + 1)h + \frac{d^2h}{d\theta^2}\right\}\right]$$

$$\sigma_{\theta\theta} = \frac{\partial^2\Phi}{\partial r^2} = \mathrm{Re}[\lambda(\lambda + 1)r^{\lambda-1}h]$$

$$\sigma_{r\theta} = -\frac{\partial}{\partial r}\left(\frac{1}{r}\frac{\partial\Phi}{\partial\theta}\right) = -\mathrm{Re}\left[\lambda r^{\lambda-1}\frac{dh}{d\theta}\right] \qquad \text{(A3)}$$

and the displacements

$$u_r(r, \theta) = \mathrm{Re}\left[r^\lambda \frac{(1 + \nu)}{E}[(3 - \lambda - 4\nu)\{\sin[(\lambda - 1)\theta]c_2 + \cos[(\lambda - 1)\theta]c_1\} - (1 + \lambda)\{\sin[(\lambda + 1)\theta]c_4 + \cos[(\lambda + 1)\theta]c_3\}]\right]$$

$$u_\theta(r, \theta) = \mathrm{Re}\left[r^\lambda \frac{1 + \nu}{E}[(3 + \lambda - 4\nu)\{\sin[(\lambda - 1)\theta]c_1 - \cos[(\lambda - 1)\theta]c_2\} + (\lambda + 1)\{\sin[(\lambda + 1)\theta]c_3 - \cos[(\lambda + 1)\theta]c_4)\}]\right] + \vartheta r \qquad \text{(A4)}$$

which are valid for plane strain. The tip of the corner is assumed fixed and ϑ is rigid-body rotation, which, without loss of generality, is set to zero.

The corner surfaces are traction free, thus

$$h_I(-\pi + \gamma/2) = 0$$

$$\frac{dh_I}{d\theta}(-\pi + \gamma/2) = 0$$

$$h_{II}(\pi - \gamma/2) = 0$$

$$\frac{dh_{II}}{d\theta}(\pi - \gamma/2) = 0 \qquad \text{(A5)}$$

and tractions and deformations are continuous over the bimaterial border, thus

$$h_I(-\varphi) = h_{II}(-\varphi)$$

$$\frac{dh_I}{d\theta}(-\varphi) = \frac{dh_{II}}{d\theta}(-\varphi)$$

$$u_r^I(r, -\varphi) = u_r^{II}(r, -\varphi)$$

$$u_\theta^I(r, -\varphi) = u_\theta^{II}(r, -\varphi). \qquad \text{(A6)}$$

The boundary conditions collectively can be written in matrix form

$$\mathbf{M}(\lambda)\mathbf{c} = 0 \qquad \text{(A7)}$$

where $\mathbf{M}$ is an 8×8 matrix and $\mathbf{c}$ an eight-dimensional vector. A nontrivial solution requires the vanishing of the determinant of the matrix (both real and imaginary parts), which determines λ. The eigenvector (null space) of the eigenvalue problem gives the solution to the corner stress field, save for a scaling factor which in general is complex. The scaling factor is determined from the definition in Eq. (3). Recall that λ in general is complex.

In case the singularity λ is complex, there exist two different stress states which have the same strength of the singularity. These can e.g. be obtained from

Downloaded 04 May 2010 to 171.66.16.34. Redistribution subject to ASME license or copyright; see http://www.asme.org/terms/Terms_Use.cfm

$$\Phi^a = \mathrm{Re}[r^{\lambda+1}h(\theta)]$$

$$\Phi^b = \mathrm{Im}[r^{\lambda+1}h(\theta)] \quad \text{(A8)}$$

in each material. The full solution is a linear combination of these.

APPENDIX B

Size of Finite Element Model

A cracked infinite corner shaped continuum was simulated by a finite-size disk loaded by applied boundary displacements according to the singular solution of the noncracked corner. Errors due to finite size of the disk are introduced when a small crack extending from the corner tip is introduced. The size of the finite element disk should be so large that the stress intensities at the tip of the crack differ little from those obtained by an infinite continuum. The order of magnitude of the error is estimated by calculating the strain energy within a disk of radius R, and comparing this with the energy released when a crack grows from the corner tip to a length a. The strain energy within a disk of radius R and included angle 2π-γ and without crack is

$$W_{\text{w/o crack}} = \int_0^R \int_{-(\pi-\gamma/2)}^{\pi-\gamma/2} S_{\alpha\beta\gamma\delta}\sigma_{\alpha\beta}\sigma_{\gamma\delta} r d\theta dr \propto R^{2\lambda_R} \quad \text{(B1)}$$

where Eq. (1) was used. The released energy is

$$\Delta W_{\text{crack}} = \int_0^a G(a)da \propto \int_0^a a^{2(\lambda_R - 1/2)}da \propto a^{2\lambda_R} \quad \text{(B2)}$$

where Eqs. (5) – (7) were used. We believe that the error scale as

$$e \equiv \frac{\Delta W_{\text{crack}}}{W_{\text{w/o crack}}} \propto \left(\frac{a}{R}\right)^{2\lambda_R}. \quad \text{(B3)}$$

Apparently e has linear scaling to a/R for a sharp crack, and approaches quadratic scaling when the corner opens up, i.e. when λ approaches 1.

Downloaded 04 May 2010 to 171.66.16.34. Redistribution subject to ASME license or copyright; see http://www.asme.org/terms/Terms_Use.cfm

Theoretical Transient Analysis of the Interaction Between a Dynamically Propagating In-Plane Crack and Traction-Free Boundaries

Chwan-Huei Tsai
Associate Professor,
Department of Mechanical Engineering,
Huafan University,
Taipei Hsien, Taiwan 223,
Republic of China

Chien-Ching Ma
Professor,
Department of Mechanical Engineering,
National Taiwan University,
Taipei, Taiwan 10617,
Republic of China

In this study, the transient response of a propagating in-plane crack interacting with half-plane boundaries is investigated in detail. The reflected waves which are generated from traction-free boundaries will interact with the propagating crack and make the problem extremely difficult to analyze. The complete transient solutions are constructed by superimposing fundamental solutions in the Laplace transform domain. The fundamental solutions represent the responses of applying exponentially distributed loadings in the Laplace transform domain on the surface of a half-plane or the propagating crack faces. We focus our attention on the determination of the dynamic stress intensity factor. The dynamic stress intensity factors of a propagating crack in a configuration with boundaries and subjected to dynamic loadings are obtained in an explicit closed form. The transient solutions obtained in this study are in agreement with the experimental results from the literature. Some interesting phenomena observed in the published experimental works are also identified and discussed. It is concluded that the reflected waves generated from the boundary parallel to the crack have much stronger influence on the propagating crack than those generated from the boundary perpendicular to the crack. When the reflected waves generated from the boundary parallel to the crack return to the moving crack tip, the stress intensity factor will increase rapidly.

1 Introduction

Most existing analyses of cracked bodies are quasi-static. However, there are numerous situations in which the material inertia becomes significant and must be taken into account. Inertial effects can arise either from applying dynamic loading to a cracked solid or from rapid crack propagation. The inherent time dependence of a dynamic fracture process results in mathematical models that are more complex than equivalent quasi-static models. The phenomena of crack propagation, arrest, and branching are very important subjects in the area of dynamic fracture analysis. In a series of papers, Freund (1972a, b, 1973, 1974) developed an important analytical method for evaluating the transient stress field and dynamic stress intensity factor of a propagating semi-infinite crack in an infinite medium. Freund proposed a superposition method in the time domain to study the dynamic effect of crack propagation, some fundamental solutions were obtained and were used to develop the solution for the negation of the stress distribution on the prospective fracture plane. His method is valid for the loading condition of step stress pulse applied on the crack faces, but without considering the reflected waves generated from boundaries.

The interaction of reflected waves with a moving crack has only been discussed in a series of experimental works by Ravi-Chandar and Knauss (1982, 1984a, b, c, d), Ravichandran and Clifton (1989), and Kim (1985). Experimental results indicated that the effect of reflected waves dominates the stability of crack propagation. The possibility of arrest, acceleration, or branching of the propagating crack is influenced by the reflected waves generated from boundaries of specimen. It seems difficult to obtain the analytical solution of the problem of interaction of reflected waves with a propagating crack by using conventional methodology.

In recent years, a powerful and efficient methodology based on superimposing the fundamental solution in the Laplace transform domain was proposed by Tsai and Ma (1991, 1992, 1997) to solve many complicated and difficult problems. Using this superposition methodology, Ma and Chen (1994) and Ma and Ing (1995) investigated the transient response of antiplane semi-infinite cracks in a configuration with boundaries. The solutions to applying an exponentially distributed traction at the surface of a half-plane and at a semi-infinite crack face in the Laplace transform domain are considered as the fundamental solutions. The reflected and diffracted fields generated from the half-plane and crack tip can be obtained by superimposing these fundamental solutions as shown in the Appendix. In this study, the superposition method that is used to solve the stationary crack problem is extended to solve the transient response of a propagating crack interacting with reflected waves generated from traction-free boundaries.

In this paper, transient stress intensity factors for a semi-infinite crack embedded in a half-plane subjected to a sudden impact on the crack faces are analyzed. The orientations of the half-plane boundary are parallel to the crack and perpendicular to the crack. The reflected waves will induce mixed-mode stress intensity factors and influence the crack propagation path for the crack which is parallel to the boundary. The numerical results obtained in this study show that reflected waves gener-

Contributed by the Applied Mechanics Division of THE AMERICAN SOCIETY OF MECHANICAL ENGINEERS for publication in the ASME JOURNAL OF APPLIED MECHANICS.

Discussion on this paper should be addressed to the Technical Editor, Professor Lewis T. Wheeler, Department of Mechanical Engineering, University of Houston, Houston, TX 77204-4792, and will be accepted until four months after final publication of the paper itself in the ASME JOURNAL OF APPLIED MECHANICS.

Manuscript received by the ASME Applied Mechanics Division, July 26, 1996; final revision, Mar. 14, 1997. Associate Technical Editor: W. J. Drugan.

Copyright © 1997 by ASME

Downloaded 04 May 2010 to 171.66.16.34. Redistribution subject to ASME license or copyright; see http://www.asme.org/terms/Terms_Use.cfm

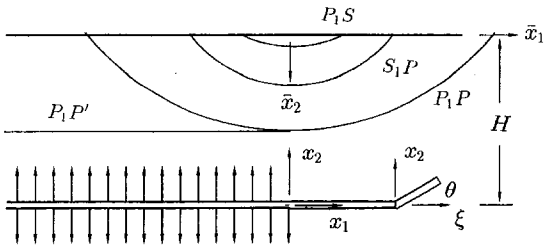


Fig. 1 Configuration and coordinate systems of a semi-infinite crack which is parallel to the half-plane boundary

ated from the boundary parallel to the crack have much stronger influence on the propagating crack than those generated from the boundary perpendicular to the crack. When the reflected waves generated from the boundary parallel to the crack return to the moving crack tip, the stress intensity factor will increase rapidly. Finally, the analytical solution of a propagating crack in a rectangular finite plate subjected to impact loading on the crack faces is obtained without considering the diffracted waves generated from plate corners. The experimental results obtained by Ravi-Chandar and Knauss (1982, 1984b) are discussed and are compared with the analytical result in light of the theoretical analysis in this study.

2 Crack Propagation and Interaction With a Half-Plane

For the convenience of the following derivation, some useful symbols are defined as follows:

$$\alpha_\pm = \alpha_\pm(\lambda) = [a \pm \lambda(1 \mp av)]^{1/2},$$

$$\alpha^0_\pm = \alpha^0_\pm(\lambda) = (a \mp \lambda)^{1/2},$$

$$\alpha = \alpha(\lambda) = \alpha_+(\lambda)\alpha_-(\lambda), \quad \alpha^0 = \alpha^0(\lambda) = \alpha^0_+(\lambda)\alpha^0_-(\lambda),$$

$$\beta_\pm = \beta_\pm(\lambda) = [b \pm \lambda(1 \mp bv)]^{1/2},$$

$$\beta^0_\pm = \beta^0_\pm(\lambda) = (b \mp \lambda)^{1/2},$$

$$\beta = \beta(\lambda) = \beta_+(\lambda)\beta_-(\lambda), \quad \beta^0 = \beta^0(\lambda) = \beta^0_+(\lambda)\beta^0_-(\lambda),$$

$$R = R(\lambda) = (b^2(1 - \lambda v)^2 - 2\lambda^2)^2 + 4\lambda^2\alpha\beta$$
$$= \kappa(d - \lambda)^2(c_1 - \lambda)(c_2 + \lambda)S_+(\lambda)S_-(\lambda),$$

$$\kappa = 4(1 - a^2v^2)^{1/2}(1 - b^2v^2)^{1/2} - (2 - b^2v^2)^2, \quad d = 1/v,$$

$$a_1 = a/(1 + av), \quad b_1 = b/(1 + bv), \quad c_1 = c/(1 + cv),$$

$$a_2 = a/(1 - av), \quad b_2 = b/(1 - bv), \quad c_2 = c/(1 - cv),$$

$$S_\pm = S_\pm(\lambda)$$
$$= \exp\left(\frac{-1}{\pi}\int_{a_{2,1}}^{b_{2,1}} \tan^{-1}\left[\frac{4\xi^2|\alpha||\beta|}{(b^2(1 \pm \xi v)^2 - 2\xi^2)^2}\right]\frac{d\xi}{\xi \pm \lambda}\right),$$

$$R^0 = R^0(\lambda) = R(\lambda)|_{v=0}, \quad S^0_\pm = S^0_\pm(\lambda) = S_\pm(\lambda)|_{v=0}, \quad (1)$$

where a $(=1/v_l)$, b $(=1/v_s)$, c $(=1/v_r)$, and d $(=1/v)$ are the slownesses of longitudinal wave, shear wave, Rayleigh wave, and moving crack tip, respectively, v_l, v_s, v_r, and v are the corresponding speeds of the longitudinal wave, shear wave, Rayleigh wave, and the moving crack tip.

We consider a semi-infinite crack embedded in a half-plane whose boundary is parallel to the crack as shown in Fig. 1 and embedded in a half-plane whose boundary is perpendicular to the crack as shown in Fig. 2. The distance from the crack tip to the boundary parallel to the crack is denoted as H and to the boundary perpendicular to the crack is denoted as L. The coordinate system (x_1, x_2) is attached to the stationary crack tip, and the alternative coordinate system $(\bar{x}_1, \bar{x}_2)$ is fixed at $x_1 = 0$, $x_2 = H$ (or $x_1 = L$, $x_2 = 0$). At time $t = 0$, a uniform pressure of magnitude σ_0 is suddenly applied to the crack faces. After a delay time t_d, the crack begins to extend at a constant velocity v, and the moving coordinate system (ξ, x_2) is attached to the moving crack tip. The relation between x_1 and ξ is $x_1 = \xi + v(t - t_d)$.

After a uniformly distributed impact is suddenly applied to the stationary crack faces, a diffracted longitudinal wave (denoted by P_1) and a shear wave (denoted by S_1) will be emitted from the stationary crack tip. The P_1 wave will be reflected from the traction-free boundary of the half-plane and hence generate the reflected longitudinal wave and shear wave which are denoted by P_1P wave and P_1S wave. Similarly, the S_1 wave will be reflected from the boundary of the half-plane and the reflected longitudinal wave (S_1P) and shear wave (S_1S) will be generated. After a delay time t_d, the crack begins to propagate with a constant speed v. The diffracted longitudinal wave (P_2) and shear wave (S_2) will be emitted from the moving crack tip at time $t = t_d$. The diffracted waves P_2 and S_2 will also be reflected from the boundary of the half-plane and generate reflected longitudinal waves (P_2P, S_2P) and shear waves (P_2S, S_2S). All these reflected waves will interact with the moving crack tip at later times, and make the problem extremely difficult to analyze.

Before reflected waves return to the propagating crack tip, the problem can be viewed as a semi-infinite crack propagating in an unbounded medium; the solution has been obtained by Freund (1973) by using another method. We focus our attention on the reflected waves for the first time. The reflected effect for the second time, third time, etc., will not be discussed in this study.

The diffracted waves include two parts, the first one is induced from the stationary crack tip and the second one is generated from the moving crack tip. Before the stress waves which are emitted from the propagating crack tip return to the moving crack tip, the stress intensity factors are shown in Section 2.1. After the P_2P, P_2S, S_2P, and S_2S waves reach the crack tip, the stress intensity factors can be obtained approximately by taking the problem for a uniformly extending crack (i.e., At time $t = 0$, the crack tip is located at $x_1 = -vt_d$ and extends at a constant speed v without delay time) which is shown in Section 2.2.

2.1 Stress Intensity Factors due to the Stress Waves Generated From the Stationary Crack.

2.1.1 Diffracted Waves in Infinite Medium. Consider a stationary semi-infinite crack embedded in a half-plane as

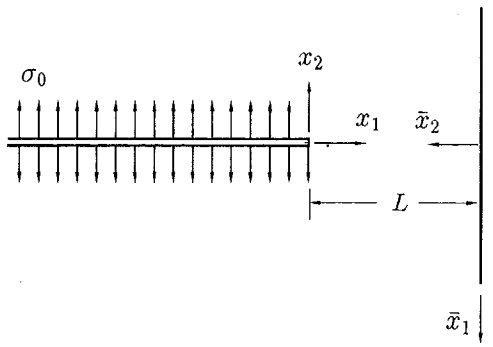


Fig. 2 Configuration and coordinate systems of a semi-infinite crack which is perpendicular to the half-plane boundary

Downloaded 04 May 2010 to 171.66.16.34. Redistribution subject to ASME license or copyright; see http://www.asme.org/terms/Terms_Use.cfm

shown in Fig. 1. At time $t = 0$, a uniform pressure with magnitude σ_0 is suddenly applied at the crack faces. The waves emitted from the stationary crack can be expressed in the Laplace transform domain as follows (Thau and Lu, 1971):

$$\bar{\sigma}_{22}^{D} = \frac{A_0}{2\pi i p}\int \frac{(b^2-2\lambda^2)^2}{2\lambda\alpha_+^0(c-\lambda)S_-^0}\, e^{-p\alpha^0 x_2 + p\lambda x_1} + \frac{2\lambda\alpha_-^0\beta^0}{(c-\lambda)S_-^0}\, e^{-p\beta^0 x_2 + p\lambda x_1} d\lambda, \quad (2)$$

$$\bar{\sigma}_{12}^{D} = \frac{A_0}{2\pi i p}\int \frac{-\alpha_-^0(b^2-2\lambda^2)}{(c-\lambda)S_-^0}\, e^{-p\alpha^0 x_2 + p\lambda x_1} + \frac{\alpha_-^0(b^2-2\lambda^2)}{(c-\lambda)S_-^0}\, e^{-p\beta^0 x_2 + p\lambda x_1} d\lambda, \quad (3)$$

where

$$A_0 = \frac{\omega_0}{(b^2-a^2)}, \quad \omega_0 = \frac{\sigma_0\sqrt{a}}{cS_+^0(0)},$$

p is the Laplace transform parameter. The first and second terms of (2) and (3) represent the diffracted P_1 wave and S_1 wave generated from the stationary crack tip, respectively. The solution is exactly the same as that for a semi-infinite crack in an unbounded medium. The corresponding stress intensity factor in the time domain is

$$K_I = \frac{2\sqrt{2}}{\sqrt{\pi}}\,\omega_0\sqrt{t}\,. \quad (4)$$

2.1.2 Stress Intensity Factors due to Reflected Waves From the Boundary Parallel to the Crack. The diffracted waves emitted from the stationary crack will be reflected from the boundary at $x_2 = H$. From Eqs. (2) and (3), it is obvious that the traction which must be applied at $x_2 = H$ to eliminate the stresses $\bar{\sigma}_{22}^{D}$ and $\bar{\sigma}_{12}^{D}$ is represented by the exponential function $e^{p\lambda x_1}$. The fundamental solutions for normal traction $e^{p\lambda x_1}$ and tangential traction $e^{p\lambda x_1}$ applied at the surface of the half-plane can be obtained from the Appendix by taking $v \to 0$, $\xi \to \bar{x}_1$, $\eta \to \lambda$. Then the stresses $\bar{\sigma}_{22}^{R}$ and $\bar{\sigma}_{12}^{R}$ induced by reflected waves can be obtained by superimposing the fundamental solutions of (A4), (A5), (A9), and (A10).

If the crack starts to propagate before the reflected wave P_1P returns to the crack tip (i.e., $t_d < 2aH$), the moving coordinate system (ξ, x_2) should be introduced to perform the superposition procedure for the propagating crack. The stresses induced on the propagating crack faces by $\bar{\sigma}_{22}^{R}$ and $\bar{\sigma}_{12}^{R}$ must be eliminated. Applying the transformation principle between the two different coordinate systems as mentioned in Appendix Eqs. (A22) and (A23), $\bar{\sigma}_{22}^{R}$ and $\bar{\sigma}_{12}^{R}$ can be obtained as

$$\bar{\sigma}_{22}^{R} = \frac{A_0}{2\pi i p}\int \frac{-(b^2-2\bar{\lambda}^2)^2((b^2-2\bar{\lambda}^2)^2 - 4\bar{\lambda}^2\bar{\alpha}^0\bar{\beta}^0)}{2\bar{\lambda}\bar{\alpha}_+^0(c-\bar{\lambda})\bar{S}_-^0\bar{R}^0(1-\lambda v)^2} \times e^{-2p\alpha H + p\lambda(\xi - vt_d)} d\lambda + \frac{A_0}{2\pi i p}\int \frac{-8\bar{\lambda}\bar{\alpha}^0\bar{\beta}^0(b^2-2\bar{\lambda}^2)^2}{\bar{\alpha}_+^0(c-\bar{\lambda})\bar{S}_-^0\bar{R}^0(1-\lambda v)^2} \times e^{-p\alpha H - p\beta H + p\lambda(\xi - vt_d)} d\lambda + \frac{A_0}{2\pi i p}\int \frac{2\bar{\lambda}\bar{\alpha}_-^0\bar{\beta}^0((b^2-2\bar{\lambda}^2)^2 - 4\bar{\lambda}^2\bar{\alpha}^0\bar{\beta}^0)}{(c-\bar{\lambda})\bar{S}_-^0\bar{R}^0(1-\lambda v)^2} \times e^{-2p\beta H + p\lambda(\xi - vt_d)} d\lambda, \quad (5)$$

$$\bar{\sigma}_{12}^{R} = \frac{A_0}{2\pi i p}\int \frac{-\bar{\alpha}_-^0(b^2-2\bar{\lambda}^2)((b^2-2\bar{\lambda}^2)^2 - 4\bar{\lambda}^2\bar{\alpha}^0\bar{\beta}^0)}{(c-\bar{\lambda})\bar{S}_-^0\bar{R}^0(1-\lambda v)^2} \times e^{-2p\alpha H + p\lambda(\xi - vt_d)} d\lambda + \frac{A_0}{2\pi i p}\int \frac{2\bar{\alpha}_-^0(b^2-2\bar{\lambda}^2)((b^2-2\bar{\lambda}^2)^2 - 4\bar{\lambda}^2\bar{\alpha}^0\bar{\beta}^0)}{(c-\bar{\lambda})\bar{S}_-^0\bar{R}^0(1-\lambda v)^2} \times e^{-p\alpha H - p\beta H + p\lambda(\xi - vt_d)} d\lambda + \frac{A_0}{2\pi i p}\int \frac{-\bar{\alpha}_-^0(b^2-2\bar{\lambda}^2)((b^2-2\bar{\lambda}^2)^2 - 4\bar{\lambda}^2\bar{\alpha}^0\bar{\beta}^0)}{(c-\bar{\lambda})\bar{S}_-^0\bar{R}^0(1-\lambda v)^2} \times e^{-2p\beta H + p\lambda(\xi - vt_d)} d\lambda \quad (6)$$

where

$$\bar{\lambda} = \frac{\lambda}{1-\lambda v}, \quad \bar{\alpha}^0 = \alpha^0(\bar{\lambda}), \quad \bar{\alpha}_\pm^0 = \alpha_\pm^0(\bar{\lambda}),$$

$$\bar{\beta}^0 = \beta^0(\bar{\lambda}), \quad \bar{\beta}_\pm^0 = \beta_\pm^0(\bar{\lambda}), \quad \bar{S}^0 = S^0(\bar{\lambda}), \quad \bar{R}^0 = R^0(\bar{\lambda}).$$

It is obvious that the tractions which should be applied to the propagating crack faces to eliminate the stresses $\bar{\sigma}_{22}^{R}$ and $\bar{\sigma}_{12}^{R}$ induced by reflected waves are represented by the function $e^{p\lambda\xi}$. Since the stress intensity factor for applying normal traction $e^{p\eta\xi}$ at the propagating crack faces has been obtained in (A16) and (A21), the stress intensity factors induced from reflected waves can be obtained by superimposing the fundamental solution as follows:

$$\bar{K}_I = \frac{1}{2\pi i p^{3/2}}\int H_1(\lambda)e^{-2p\alpha H - p\lambda v t_d} + H_2(\lambda)e^{-p\alpha H - p\beta H - p\lambda v t_d} + H_3(\lambda)e^{-2p\beta H - p\lambda v t_d} d\lambda, \quad (7)$$

$$\bar{K}_{II} = \frac{1}{2\pi i p^{3/2}}\int H_4(\lambda)e^{-2p\alpha H - p\lambda v t_d} + H_5(\lambda)e^{-p\alpha H - p\beta H - p\lambda v t_d} + H_6(\lambda)e^{-2p\beta H - p\lambda v t_d} d\lambda, \quad (8)$$

where

$$H_1(\lambda) = -(b^2-2\bar{\lambda}^2)^2((b^2-2\bar{\lambda}^2)^2 - 4\bar{\lambda}^2\bar{\alpha}^0\bar{\beta}^0)\alpha_+ J(\lambda)/2\sqrt{1-av}\,\bar{\lambda}\bar{\alpha}_+^0,$$

$$H_2(\lambda) = -8\bar{\lambda}\bar{\alpha}_-^0\bar{\beta}^0(b^2-2\bar{\lambda}^2)^2\alpha_+ J(\lambda)/\sqrt{1-av},$$

$$H_3(\lambda) = 2\bar{\lambda}\bar{\alpha}_-^0\bar{\beta}^0((b^2-2\bar{\lambda}^2)^2 - 4\bar{\lambda}^2\bar{\alpha}^0\bar{\beta}^0)\alpha_+ J(\lambda)/\sqrt{1-av},$$

$$H_4(\lambda) = -\bar{\alpha}_-^0(b^2-2\bar{\lambda}^2)((b^2-2\bar{\lambda}^2)^2 - 4\bar{\lambda}^2\bar{\alpha}^0\bar{\beta}^0)\beta_+ J(\lambda)/\sqrt{1-bv},$$

$$H_5(\lambda) = -2H_4(\lambda), \quad H_6(\lambda) = H_4(\lambda),$$

$$J(\lambda) = \sqrt{2}A_0/((c-\bar{\lambda})\bar{S}_-^0\bar{R}^0(1-\lambda v)^2(c_2+\lambda)S_+).$$

Inverting to the time domain by using the Cagniard-de Hoop method, the stress intensity factors of the propagating crack induced by reflected P_1P, P_1S, S_1P, and S_1S waves can be obtained as follows:

$$K_I = \frac{1}{\pi^{3/2}}\int_{T_{P_1P}}^{t}\sqrt{t-\tau}\,\mathrm{Im}\left[H_1(\lambda_1)\frac{\partial\lambda_1}{\partial\tau}\right]d\tau + \frac{1}{\pi^{3/2}}\int_{T_{P_1S}}^{t}\sqrt{t-\tau}\,\mathrm{Im}\left[H_2(\lambda_2)\frac{\partial\lambda_2}{\partial\tau}\right]d\tau + \frac{1}{\pi^{3/2}}\int_{T_{S_1S}}^{t}\sqrt{t-\tau}\,\mathrm{Im}\left[H_3(\lambda_3)\frac{\partial\lambda_3}{\partial\tau}\right]d\tau, \quad (9)$$

$$K_{II} = \frac{1}{\pi^{3/2}}\int_{T_{P_1P}}^{t}\sqrt{t-\tau}\,\mathrm{Im}\left[H_4(\lambda_1)\frac{\partial\lambda_1}{\partial\tau}\right]d\tau + \frac{1}{\pi^{3/2}}\int_{T_{P_1S}}^{t}\sqrt{t-\tau}\,\mathrm{Im}\left[H_5(\lambda_2)\frac{\partial\lambda_2}{\partial\tau}\right]d\tau + \frac{1}{\pi^{3/2}}\int_{T_{S_1S}}^{t}\sqrt{t-\tau}\,\mathrm{Im}\left[H_6(\lambda_3)\frac{\partial\lambda_3}{\partial\tau}\right]d\tau \quad (10)$$

where

$$\lambda_1 = \frac{vt_d t - 4va^2H^2 + i2H\sqrt{t^2 - a^2(vt - vt_d)^2 - 4a^2H^2}}{v^2t_d^2 + 4H^2 - 4a^2v^2H^2},$$

Downloaded 04 May 2010 to 171.66.16.34. Redistribution subject to ASME license or copyright; see http://www.asme.org/terms/Terms_Use.cfm

$$\lambda_3 = \frac{vt_d t - 4vb^2H^2 + i2H\sqrt{t^2 - b^2(vt - vt_d)^2 - 4b^2H^2}}{v^2t_d^2 + 4H^2 - 4b^2v^2H^2}, \quad (11)$$

and λ_2 is the solution of $\alpha H + \beta H + \lambda v t_d = t$. The arrival time for each wavefront is

$$T_{P_1P} = \frac{-a^2v^2t_d + \sqrt{a^2v^2t_d^2 + 4a^2H^2 - 4a^4v^2H^2}}{1 - a^2v^2},$$

$$T_{S_1S} = \frac{-b^2v^2t_d + \sqrt{b^2v^2t_d^2 + 4b^2H^2 - 4b^4v^2H^2}}{1 - b^2v^2}, \quad (12)$$

and T_{P_1S} is the corresponding time t at which the imaginary part of λ_2 begins to vanish.

The physical meaning of the terms in (9) and (10) following the sequence represent the stress intensity factors due to the contribution of reflected P_1P, $P_1S + S_1P$, and S_1S waves, respectively. It is noted that the P_1S wave and S_1P wave reach the propagating crack tip at the same time. The wave fronts of the above-mentioned reflected waves are shown in Fig. 1.

If the crack remains stationary after the reflected waves return to the crack tip, λ_1, λ_2, and λ_3 will be all pure imaginary numbers. Then, the integral result of (9) comes only from the contributions of the pole $\lambda_1 = 0$ of the first term, and the stress intensity factor can be reduced to the simple form

$$K_I = \frac{2\sqrt{2}\omega_0}{\sqrt{\pi}}\sqrt{t - 2Ha}. \quad (13)$$

Combining the incident effect due to diffracted P_1 and S_1 waves, the stress intensity factor is

$$K_I = \frac{2\sqrt{2}\omega_0}{\sqrt{\pi}}\sqrt{t} + \frac{2\sqrt{2}\omega_0}{\sqrt{\pi}}\sqrt{t - 2Ha}, \quad 2Ha < t < 4Ha. \quad (14)$$

2.1.3 Stress Intensity Factors due to Reflected Waves From the Boundary Perpendicular to the Crack. If the crack is perpendicular to the half-plane boundary as shown in Fig. 2, the diffracted waves emitted from the stationary crack tip will be reflected from the boundary at $x_1 = L$. It is obvious that the traction which must be applied at $x_1 = L$ to eliminate the stresses $\bar{\sigma}_{11}^D$ and $\bar{\sigma}_{12}^D$ can be represented by the exponential functions $e^{-p\alpha^0|\bar{x}_1|}$, $e^{-p\beta^0|\bar{x}_1|}$. The fundamental solutions for applying normal traction and tangential traction $e^{-p\alpha^0|\bar{x}_1|}$ or $e^{-p\beta^0|\bar{x}_1|}$ to the surface of a half-plane were solved by Tsai and Ma (1991); the reflected waves can be obtained by superimposing these fundamental solutions. Then, by using the same procedure as given from (5) to (12), the stress intensity factor of the propagating crack induced by reflected waves from the boundary of half-plane can be expressed as follows:

$$K_I(t) = \frac{\sqrt{2}A_0}{\pi^{3/2}}\int_{T_{P_1P}}^{t}\sqrt{t-\tau}\,\mathrm{Im}\left[\frac{(b^2 - 2\bar{\lambda}_1^2)^2((b^2 - 2\bar{\alpha}^{0^2})^2 - 4\bar{\lambda}_1\bar{\alpha}^{0^2}\beta^0(\bar{\alpha}^0))\alpha_+(\lambda_1)}{2\bar{\lambda}_1\bar{\alpha}_-^0(c + \bar{\lambda}_1)S_+^0(\bar{\lambda}_1)R^0(\bar{\alpha}^0)(1 - \lambda_1 v)\sqrt{1 - av}(c_2 + \lambda_1)S_+(\lambda_1)}\frac{\partial\lambda_1}{\partial\tau}\right]d\tau$$

$$+ \frac{2\sqrt{2}A_0}{\pi^{3/2}}\int_{T_{P_1S}}^{t}\sqrt{t-\tau}\,\mathrm{Im}\left[\frac{-4(b^2 - 2\alpha^{02}(\bar{\beta}^0))(\alpha_+^0(\alpha^0(\bar{\beta}^0))\bar{\beta}^0\bar{\lambda}_2^2\alpha_+(\lambda_2)}{\alpha^0(\bar{\beta}^0)(c + \alpha^0(\bar{\beta}^0))S_+^0(\alpha^0(\bar{\beta}^0))(1 - \lambda_2 v)\sqrt{1 - av}(c_2 + \lambda_2)S_+(\lambda_2)}\frac{\partial\lambda_2}{\partial\tau}\right]d\tau$$

$$+ \frac{2\sqrt{2}A_0}{\pi^{3/2}}\int_{T_{S_1P}}^{t}\sqrt{t-\tau}\,\mathrm{Im}\left[\frac{-4(b^2 - 2\bar{\lambda}_3^2)(b^2 - 2\bar{\alpha}^{0^2})\alpha_+^0(\beta^0(\bar{\alpha}^0))\bar{\alpha}^0\bar{\lambda}_3\alpha_+(\lambda_3)}{(c + \beta^0(\bar{\alpha}^0))S_+^0(\beta^0(\bar{\alpha}^0))R^0(\bar{\alpha}^0)(1 - \lambda_3 v)\sqrt{1 - av}(c_2 + \lambda_3)S_+(\lambda_3)}\frac{\partial\lambda_3}{\partial\tau}\right]d\tau$$

$$+ \frac{2\sqrt{2}A_0}{\pi^{3/2}}\int_{T_{S_1S}}^{t}\sqrt{t-\tau}\,\mathrm{Im}\left[\frac{(-2\bar{\alpha}_+^0\bar{\beta}^0\bar{\lambda}_4(b^2 - 2\bar{\lambda}^2)^2 + 8\bar{\alpha}_+^0\bar{\beta}^{0^3}\bar{\lambda}_4^2\alpha^0(\bar{\beta}^0))\alpha_+(\lambda_4)}{(c + \bar{\lambda}_4)S_+^0(\bar{\lambda}_4)R^0(\bar{\beta}^0)(1 - \lambda_4 v)\sqrt{1 - av}(c_2 + \lambda_4)S_+(\lambda_4)}\frac{\partial\lambda_4}{\partial\tau}\right]d\tau, \quad (16)$$

where

$$\lambda_1 = \frac{\tau}{2L + vt_d}, \quad \lambda_4 = \frac{\tau}{2L + vt_d},$$

$$\lambda_2 = \frac{a^2vL^2 - b^2vL^2 - \tau L - \tau vt_d}{a^2v^2L^2 - b^2v^2L^2 - v^2t_d^2 - 2Lvt_d} + \frac{[(a^2vL^2 - b^2vL^2 - \tau L - \tau vt_d)^2 - (a^2v^2L^2 - b^2v^2L^2 - v^2t_d^2 - 2Lvt_d)(a^2L^2 - b^2L^2 - \tau^2)]^{1/2}}{a^2v^2L^2 - b^2v^2L^2 - v^2t_d^2 - 2Lvt_d},$$

$$\lambda_3 = \frac{b^2vL^2 - a^2vL^2 - \tau L - \tau vt_d}{b^2v^2L^2 - a^2v^2L^2 - v^2t_d^2 - 2Lvt_d} + \frac{[(b^2vL^2 - a^2vL^2 - \tau L - \tau vt_d)^2 - (b^2v^2L^2 - a^2v^2L^2 - v^2t_d^2 - 2Lvt_d)(b^2L^2 - a^2L^2 - \tau^2)]^{1/2}}{b^2v^2L^2 - a^2v^2L^2 - v^2t_d^2 - 2Lvt_d}.$$

The arrival time of each wavefront is

$$T_{P_1P} = a_1(2L + vt_d), \quad T_{P_1S} = \frac{aL + bL + bvt_d}{1 + bv},$$

$$T_{S_1P} = \frac{aL + bL + avt_d}{1 + av}, \quad T_{S_1S} = b_1(2L + vt_d). \quad (17)$$

The physical meanings of the four terms in (15) are the induced dynamic stress intensity factors due to the reflected P_1P, P_1S, S_1P, and S_1S waves generated from the vertical boundary.

2.2 Stress Intensity Factors due to Stress Waves From the Propagating Crack.

2.2.1 Diffracted Waves in Infinite Medium. Consider a semi-infinite crack embedded in a half-plane as shown in Fig. 1. At time $t = 0$, the crack tip is located at $x_1 = -vt_d$ and extends at a constant speed v. At this instant, a dynamic uniform pressure with magnitude σ_0 is suddenly applied to the crack

Downloaded 04 May 2010 to 171.66.16.34. Redistribution subject to ASME license or copyright; see http://www.asme.org/terms/Terms_Use.cfm

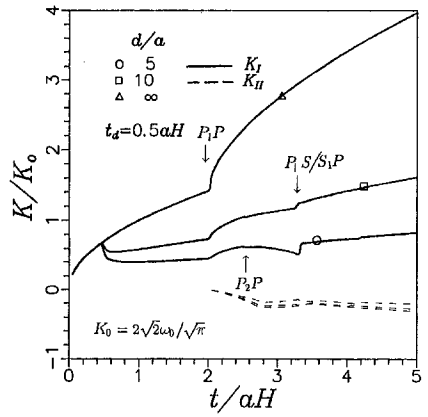


Fig. 3 Stress intensity factors of a propagating crack subjected to a uniform pressure. The half-plane boundary is parallel to the crack.

faces. The pressure continues to be applied along the newly extending crack faces $-vt_d < x_1 < 0$; after the crack tip pass through the point $x_1 = 0$, the pressure is only applied at the crack faces for $x_1 < 0$ and does not cover the newly created crack faces. The uniform pressure can be expressed as

$$\bar{\sigma}_{22} = \frac{\sigma_0}{2\pi i}\int \frac{1}{p\lambda(1-\lambda v)} e^{p\lambda(\xi - vt_d)} d\lambda. \tag{18}$$

The emitted stress fields of the propagating crack can be obtained by superimposing the fundamental solution (A14) as follows:

$$\bar{\sigma}_{22} = \frac{1}{2\pi ip}\int \frac{(b^2(1-\lambda v)^2 - 2\lambda^2)^2}{\kappa d^2 \alpha_+(1-\lambda v)^2(c_1-\lambda)S_-(\lambda)} F_1(\lambda) e^{-p\alpha x_2 + p\lambda\xi}$$
$$+ \frac{4\lambda^2\alpha_-(\lambda)\beta}{\kappa d^2(1-\lambda v)^2(c_1-\lambda)S_-(\lambda)} F_1(\lambda) e^{-p\beta x_2 + p\lambda\xi} d\lambda, \tag{19}$$

$$\bar{\sigma}_{12} = \frac{1}{2\pi ip}\int \frac{-2\lambda\alpha_-(\lambda)(b^2(1-\lambda v)^2 - 2\lambda^2)}{\kappa d^2(1-\lambda v)^2(c_1-\lambda)S_-(\lambda)} F_1(\lambda) e^{-p\alpha x_2 + p\lambda\xi}$$
$$+ \frac{2\lambda\alpha_-(\lambda)(b^2(1-\lambda v)^2 - 2\lambda^2)}{\kappa d^2(1-\lambda v)^2(c_1-\lambda)S_-(\lambda)} F_1(\lambda) e^{-p\beta x_2 + p\lambda\xi} d\lambda, \tag{20}$$

Table 1 Arrival times at which reflected waves reach the moving crack tip. The half-plane boundary is parallel to the crack.

v	$P_1P(P_2P)$	$P_1S(P_2S)/S_1P(S_2P)$	$S_1S(S_2S)$
$0v_l$	2.00(2.50)aH	2.73(3.23)aH	3.46(3.95)aH
$0.1v_l$	2.01(2.51)aH	2.75(3.26)aH	3.50(4.02)aH
$0.2v_l$	2.02(2.54)aH	2.80(3.33)aH	3.63(4.19)aH

where

$$F_1(\lambda) = \frac{\sigma_0\alpha_+(0)}{c_2 S_+^0(0)\lambda} + \frac{\sigma_0\alpha_+(d)e^{-pt_d}}{(c_2+d)S_+(d)(d-\lambda)}. \tag{21}$$

The stress intensity factor can also be obtained by superimposing the fundamental solution (A16) as follows:

$$\bar{K}_I = \frac{\sigma_0\sqrt{2}}{2\pi ip^{2/3}} \times \int \frac{\alpha_+(\lambda)}{\sqrt{1-av}(c_2+\lambda)S_+(\lambda)\lambda(1-\lambda v)} e^{-p\lambda vt_d} d\lambda. \tag{22}$$

Because only the poles $\lambda = 0$ and d contribute to the integral in (22), the stress intensity factor for the unbounded medium in the time domain is

$$K_I = \frac{2\sqrt{2}\alpha_+(d)}{\sqrt{\pi}\sqrt{1-av}(c_2+d)S_+(d)} \times (\omega_0\sqrt{t} - \sqrt{t-t_d}H(t-t_d)). \tag{23}$$

2.2.2 Stress Intensity Factors due to Reflected Waves From the Boundary Parallel to the Crack. The incident and diffracted waves emitted from the propagating crack will be reflected from the horizontal boundary at $x_2 = H$. From Eqs. (19) and (20), it is obvious that the tractions which must be applied at $x_2 = H$ to eliminate the stresses $\bar{\sigma}_{22}^D$ and $\bar{\sigma}_{12}^D$ are represented by the exponential function $e^{p\lambda\xi}$. The reflected waves generated from the half-plane boundary can be obtained by superimposing the fundamental solutions (A4), (A5), (A9), and (A10). From a similar procedure to that indicated in the case of stationary crack, the stress intensity factors can be obtained as

$$\bar{K}_I = \frac{\sqrt{2}A_0}{2\pi ip^{3/2}}\int \frac{-(b^2(1-\lambda v)^2 - 2\lambda^2)^2((b^2(1-\lambda v)^2 - 2\lambda^2)^2 - 4\alpha\beta\lambda^2)}{\sqrt{1-av}R^2} F_1(\lambda) e^{-2p\alpha H} d\lambda$$
$$+ \frac{\sqrt{2}A_0}{2\pi ip^{3/2}}\int \frac{-16\lambda^2\alpha\beta(b^2(1-\lambda v)^2 - 2\lambda^2)^2}{\sqrt{1-av}R^2} F_1(\lambda) e^{-p\alpha H - p\beta H} d\lambda$$
$$+ \frac{\sqrt{2}A_0}{2\pi ip^{3/2}}\int \frac{4\alpha\beta\lambda^2((b^2(1-\lambda v)^2 - 2\lambda^2)^2 - 4\alpha\beta\lambda^2)}{\sqrt{1-av}R^2} F_1(\lambda) e^{-2p\beta H} d\lambda. \tag{24}$$

$$\bar{K}_{II} = \frac{\sqrt{2}A_0}{2\pi ip^{3/2}}\int \frac{-2\lambda\alpha_-\beta_+((b^2(1-\lambda v)^2 - 2\lambda^2)^2 - 4\lambda^2\alpha\beta)}{\sqrt{1-bv}R^2} F_1(\lambda) e^{-2p\alpha H} d\lambda$$
$$+ \frac{\sqrt{2}A_0}{2\pi ip^{3/2}}\int \frac{4\lambda\alpha_-\beta_+(b^2(1-\lambda v)^2 - 2\lambda^2)((b^2(1-\lambda v)^2 - 2\lambda^2)^2 - 4\lambda^2\alpha\beta)}{\sqrt{1-bv}R^2} F_1(\lambda) e^{-p\alpha H - p\beta H} d\lambda$$
$$+ \frac{\sqrt{2}A_0}{2\pi ip^{3/2}}\int \frac{-2\lambda\alpha_-\beta_+((b^2(1-\lambda v)^2 - 2\lambda^2)^2((b^2(1-\lambda v)^2 - 2\lambda^2)^2 - 4\lambda^2\alpha\beta)}{\sqrt{1-bv}R^2} F_1(\lambda) e^{-2p\beta H} d\lambda. \tag{25}$$

Downloaded 04 May 2010 to 171.66.16.34. Redistribution subject to ASME license or copyright; see http://www.asme.org/terms/Terms_Use.cfm

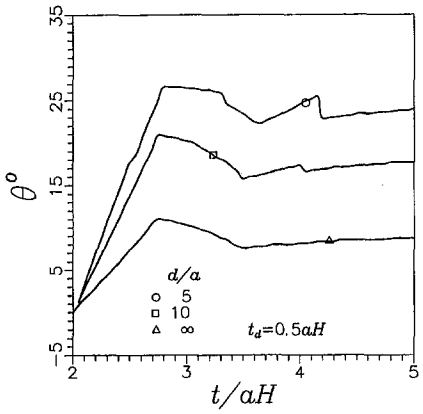


Fig. 4 Possible branching angle θ of a propagating crack subjected to uniform pressure. The half-plane boundary is parallel to the crack.

By using the Cagniard-de Hoop method, the stress intensity factors can be obtained in the time domain; the expressions are omitted here. The arrival times for P_2P and S_2S waves are $T_{P_2P} = 2\sqrt{a_1a_2}H$ and $T_{S_2S} = 2\sqrt{b_1b_2}H$, respectively, and $T_{P_2S} = T_{S_2P}$ is the corresponding time t at which the imaginary part of λ begins to vanish and $\alpha(\lambda)H + \beta(\lambda)H = t$ is satisfied.

2.2.3 Stress Intensity Factors due to Reflected Waves From the Boundary Perpendicular to the Crack. In a similar way, the stress intensity factor induced by the reflected waves generated from the vertical boundary can be obtained as follows:

$$T_{P_2P} = 2a_1L, \quad T_{P_2S} = \frac{a}{1 + bv} + b_1L,$$

$$T_{S_2P} = \frac{b}{1 + av} + a_1L, \quad T_{S_2S} = 2b_1L. \tag{28}$$

3 Numerical Results

We now perform a numerical investigation of the dynamic stress intensity factor for a propagating crack interacting with stress waves reflected from boundaries. In this study, Poisson's ratio ν is assumed to be equal to 0.25, which gives ratios of the slownesses $b = \sqrt{3}a$ and $c = 1.884a$. A semi-infinite crack embedded parallel to the boundary of a half-plane as shown in Fig. 1 is considered first. At time $t = 0$, a uniform loading with magnitude σ_0 is applied to the crack faces. The stress gradually intensifies at the crack tip, and crack propagation may be initiated only after some delay time t_d. It is assumed that the crack begins to propagate straight with constant speed $v = 0$, $0.1v_l$, $0.2v_l$ after a delay time $t_d = 0.5aH$. The pressure does not expand over the newly created crack faces, but it continues to act on the original crack faces.

The diffracted waves emitted from the crack tip will be reflected from the boundaries and interact with the propagating crack tip. The transient responses of mixed-mode dynamic stress intensity factors are calculated as shown in Fig. 3. The arrival times of reflected waves reaching the propagating crack tip are shown in Table 1. The analytical solutions presented in this study are valid until the P_1P wave is reflected twice from the boundary and returns to the moving crack tip. It is found that the mode I stress intensity factors increase rapidly after the reflected P_1P wave reaches the crack tip. The mixed-mode stress intensity factors will lead to crack branching and kinking from the original crack direction. The criterion of minimum strain energy density proposed by Sih (1972) is introduced to predict the crack growth direction. The possible branching angle with respect to the original crack direction is obtained as shown in Fig. 4. It is found that the angles θ are all positive which means that the crack will propagate upward and extrude out of the half-plane surface.

The diffracted waves generated from the moving crack tip are smaller than those from the stationary crack; at the time that the stress waves generated from the moving crack tip return back to crack tip, the stress intensity factor will experience slight variation. Because the tensile effect of a reflected P_2P wave will decay gradually, the incremental rate of stress intensity factor change will decrease after the P_2P wave arrives at the crack tip (i.e., about time $t = 2.5aH$). But at a later time (about time $t = 3.3aH$), the P_1S wave which carries a strong tensile effect reaches the crack tip and will enlarge the stress intensity factor.

$$\begin{aligned}
\bar{K}_I = {} & \frac{\sqrt{2}}{2\pi i p^{3/2}} \int \frac{((b^2 - 2a^2)(1 - \tilde{\lambda}v)^2 + 2\tilde{\lambda}^2)(b^2(1 - \tilde{\lambda}v)^2 - 2\tilde{\lambda}^2)\tilde{\alpha}_-(b^2 - 2\bar{\alpha}^{0^2})(b^2 - 2\lambda^2)}{\kappa d^2(1 - \tilde{\lambda}v)^2\tilde{\alpha}^0(c_1 - \tilde{\lambda})S_-(\tilde{\lambda})(1 - \bar{\lambda}v)(1 - \lambda v)R^0(\bar{\alpha}^0)} F_2(\tilde{\lambda}) e^{-2p\lambda L'} \\
& + \frac{4\tilde{\lambda}(b^2(1 - \tilde{\lambda}v)^2 - 2\tilde{\lambda}^2)\tilde{\alpha}_-\bar{\alpha}^0\beta^0(\bar{\alpha}^0)(b^2 - 2\bar{\lambda}^2)}{\kappa d^2(1 - \tilde{\lambda}v)^2(c_1 - \tilde{\lambda})S_-(\tilde{\lambda})(1 - \bar{\lambda}v)(1 - \lambda v)R^0(\bar{\alpha}^0)} F_2(\bar{\lambda}) e^{-2p\lambda L'} d\lambda \\
& + \frac{\sqrt{2}}{2\pi i p^{3/2}} \int \frac{-8\bar{\lambda}^2\bar{\beta}^{0^2}((b^2 - 2a^2)(1 - \tilde{\lambda}v)^2 + 2\tilde{\lambda}^2)(b^2(1 - \tilde{\lambda}v)^2 - 2\tilde{\lambda}^2)}{\kappa d^2(1 - \tilde{\lambda}v)^2\tilde{\alpha}_+(c_1 - \tilde{\lambda})S_-^0(\tilde{\lambda})(1 - \alpha^0(\bar{\beta}^0)v)R^0(\bar{\beta}^0)(1 - \lambda v)} F_2(\tilde{\lambda}) e^{-p\lambda L' - p\alpha^0(\bar{\beta}^0)(1 - \lambda v)L'} d\lambda \\
& + \frac{\sqrt{2}}{2\pi i p^{3/2}} \int \frac{8\tilde{\lambda}^2\tilde{\beta}\tilde{\alpha}_+(b^2 - 2\beta^0(\bar{\alpha}^0)^2)(b^2 - 2\bar{\lambda}^2)\bar{\lambda}}{\kappa d^2(1 - \tilde{\lambda}v)^2(c_1 - \tilde{\lambda})S_-^0(\tilde{\lambda})(1 - \beta^0(\bar{\alpha}^0)v)R^0(\bar{\alpha}^0)(1 - \lambda v)} F_2(\tilde{\lambda}) e^{-p\lambda L' - p\beta^0(\bar{\alpha}^0)(1 - \lambda v)L'} d\lambda \\
& + \frac{\sqrt{2}}{2\pi i p^{3/2}} \int \frac{16\tilde{\lambda}^2\tilde{\beta}^0\tilde{\alpha}_-\bar{\beta}^{0^2}\alpha^0(\bar{\beta}^0)\bar{\lambda} + 4\tilde{\lambda}(b^2(1 - \tilde{\lambda}v)^2 - 2\tilde{\lambda}^2)\tilde{\alpha}_-\bar{\lambda}\bar{\beta}^0(b^2 - 2\bar{\lambda}^2)}{\kappa d^2(1 - \tilde{\lambda}v)^2(c_1 - \tilde{\lambda})S_-^0(\tilde{\lambda})(1 - \bar{\lambda}v)(1 - \lambda v)R^0(\bar{\beta}^0)} F_2(\tilde{\lambda}) e^{-2p\lambda L'} d\lambda,
\end{aligned} \tag{26}$$

where

$$\tilde{\alpha} = \alpha(\tilde{\lambda}), \quad \tilde{\beta} = \beta(\tilde{\lambda}), \quad L' = L + vt_d,$$

$$\bar{\lambda} = \frac{\lambda}{1 + \lambda v}, \quad F_2(\tilde{\lambda}) = \frac{\alpha_+(\lambda)}{\sqrt{1 - av}(c_2 + \lambda)S_+(\lambda)} F_1(\tilde{\lambda}). \tag{27}$$

$\tilde{\lambda}$ expressed in the first and fourth terms in (26) are

$$\tilde{\lambda} = \frac{-\lambda}{1 - 2\lambda v}$$

and $\tilde{\lambda}$ expressed in the second and third terms in (26) are

$$\tilde{\lambda} = \frac{-\alpha^0(\bar{\beta}^0)}{1 - \alpha^0(\bar{\beta}^0)v}, \quad \tilde{\lambda} = \frac{-\beta^0(\bar{\alpha}^0)}{1 - \beta^0(\bar{\alpha}^0)v}.$$

By using the Cagniard-de Hoop method, the stress intensity factors are obtained in the time domain; the results are omitted here. The arrival times are

Downloaded 04 May 2010 to 171.66.16.34. Redistribution subject to ASME license or copyright; see http://www.asme.org/terms/Terms_Use.cfm

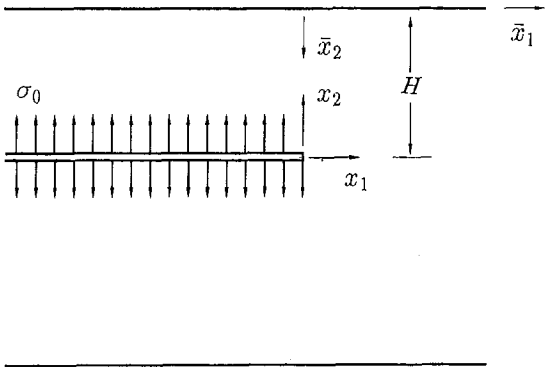


Fig. 5 Configuration and coordinate systems of a semi-infinite crack embedded in a finite strip

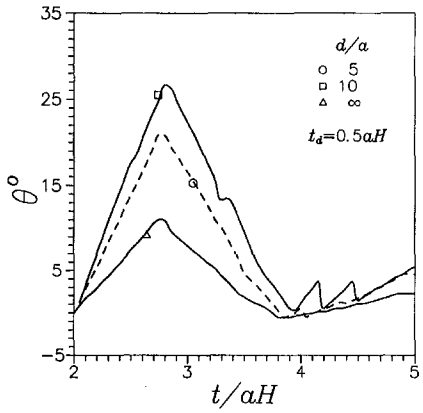


Fig. 7 Possible branching angle θ of a propagating crack subjected to uniform pressure in a finite strip

If the asymmetrical strip shown in Fig. 5 is considered, and the distance between the crack and the bottom of the strip is $1.4H$, the mixed-mode dynamic stress intensity factors can be obtained as shown in Fig. 6. The mixed mode stress will make the propagating crack deviate from the original crack direction. The possible kinking angle with respect to the original crack direction is obtained and shown in Fig. 7. The direction of the crack propagation is always toward the top side, which is consistent with the curved path of the propagating crack obtained by Ravi-Chandar and Knauss (1984d).

A semi-infinite crack embedded in a half-plane, as shown in Fig. 2, is considered next. With the same loading condition as the previous problem, the transient history of mode I stress intensity factor induced only from the reflected waves is calculated and shown in Fig. 8. Because the influence of the reflected waves from the boundary perpendicular to the crack on the stress intensity factor is very weak, the transient solutions (4) and (23) are excluded from Fig. 8 in order to emphasize the reflected effect. This figure shows clearly that the influence on the stress intensity factor due to reflected waves from the boundary perpendicular to the crack is much smaller than that from the boundary parallel to the crack. The numerical results are consistent with the experimental results obtained by Ravi-Chandar and Knauss (1984d) in that the influence of reflected waves generated from the frontal surface is very weak. It is worthwhile to note that the first few reflected waves produce a compression effect. The arrival times of the reflected waves are shown in Table 2. The analytical solutions of this study are valid until the reflected P_1P wave is reflected twice from the vertical boundary and returns to the moving crack tip.

Finally, experimental results reported by Ravi-Chandar and Knauss are simulated and compared with the present theoretical analysis. For the experimental set-up, a long edge crack was cut into a rectangular specimen of Homalite-100 along a symmetrical line as shown in Fig. 9. The specimen was then subjected to suddenly applied uniformly distributed pressure on the crack surfaces. The time variation of this pressure distribution was approximated very well by a linear increment in magnitude up until the rise time t_r after application, and then constant magnitude thereafter. From the experimental data presented, the loading rise time t_r was approximate 25 μs, independent of the final magnitude of the applied pressure. The time history of the applied loading can be expressed as $\sigma_0 t/t_r H(t) - \sigma_0(t - t_r)/t_r H(t - t_r)$, so that the transient effect can be obtained by superposition of the solutions for the linearly increased pressure.

The properties of Homalite-100 given by Ravi-Chandar and Knauss (1984d) are $\rho = 1230$ kg/m^3, $\nu = 0.31$, and $E = 4550$ MN/m^2, which yield the wave speeds $v_l = 2057$ m/s, $v_s = 1176$ m/s, and $v_R = 1081$ m/s. Two different loading conditions will be discussed in detail; we choose $\sigma_0 = 1.10$ MPa (2.46 MPa) which makes $t_d = 56$ μs (28 μs) and crack extending speed $v = 240$ m/s (363 m/s). The transient stress intensity factors are calculated by neglecting the diffracted waves generated from the corner of the plate and results are shown in Fig. 10. The theoretical predictions are in agreement with experimental results. The first reflected wave generated from the boundary arrives at the propagating crack tip at $t = 150$ μs and causes the stress intensity factor to increase very quickly. At about time $t = 170$ μs to 200 μs, the experiment shows a short duration period of constant value of stress intensity factor. This phenomenon is attributed to the arrival of the reflected P_2P. But a short

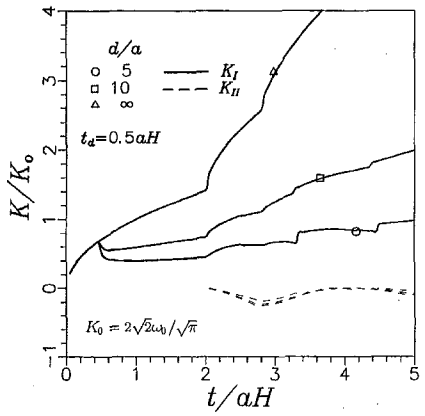


Fig. 6 Stress intensity factors of a propagating crack subjected to uniform pressure in a finite strip

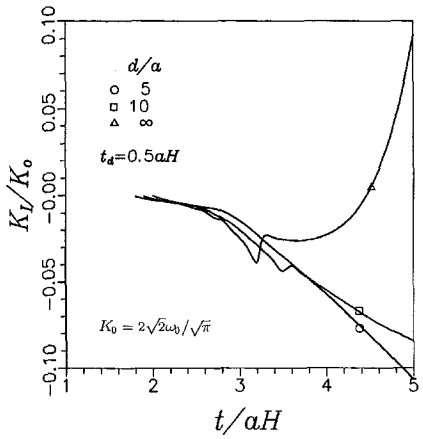


Fig. 8 Stress intensity factors of a propagating crack subjected to uniform pressure. The half-plane boundary is perpendicular to the crack.

Downloaded 04 May 2010 to 171.66.16.34. Redistribution subject to ASME license or copyright; see http://www.asme.org/terms/Terms_Use.cfm

Table 2 Arrival times at which reflected waves reach the moving crack tip. The half-plane boundary is perpendicular to the crack.

v	$P_1P(P_2P)$	$P_1S(P_2S)$	$S_1P(S_2P)$	$S_1S(S_2S)$
$0v_l$	$2.00(2.50)aL$	$2.73(3.23)aL$	$2.73(3.23)aL$	$3.46(3.95)aL$
$0.1v_l$	$1.86(2.32)aL$	$2.40(2.83)aL$	$2.53(2.98)aL$	$3.03(3.45)aL$
$0.2v_l$	$1.75(2.17)aL$	$2.16(2.53)aL$	$2.36(2.78)aL$	$2.70(3.07)aL$

time later, the P_1S wave and S_1P wave reach the crack tip, the stress intensity factor will increase again and branching is observed in the experiment.

4 Conclusions

The phenomena of crack propagation, arrest, and branching are the most important subjects in the areas of dynamic fracture analysis. The interaction of reflected waves with a propagating crack subjected to dynamic loading had previously only been investigated in experimental works. It seems difficult to obtain the analytical solutions by using well-known conventional methods. The fundamental solutions for a half-plane and a propagating crack are used to solve the problem of the interaction of stress waves and a moving crack. The reflected and diffracted fields can be constructed by superimposing the fundamental solutions in the Laplace transform domain. A superposition methodology is used in this study to solve this complicated problem. It is shown to be both powerful and efficient in solving complicated dynamic fracture problems of finite dimensions.

In this study, we focus our attention on the contribution of the reflected waves generated from plane boundaries. An explicit result for the dynamic stress intensity factor is obtained in a closed form which is valid before the reflected waves for the second time return to the crack tip. For the finite crack problem, the diffracted waves generated from the other crack tip reach the propagating crack tip will influence the stress intensity factor. But according to the study of a stationary center crack by Sih et al. (1972), the influence is very small before the time $t = 2.5al$, where l is the crack length. Thus, if the crack length $l = 2H$, the present solutions are remain acceptable during the time interval $t = 5aH$. Because uniform step loading or high-ramp loading are unusual and the reflected tensile waves occurring require the shorter pulse for the crack close to the surface, the reflected effect due to practical loading should be weaker than the theoretical results.

If the medium is a half-plane or a asymetrical finite strip, the mixed-mode stress intensity factors will induce a curved crack path. The theoretical results and numerical calculations provided in this study are consistent with the experimental work done by Ravi-Chandar and Knauss (1982, 1984d). There are many unanswered questions in dynamic fracture mechanics. This work may provide a useful technique for further investigation in more complicated dynamic loadings and configurations.

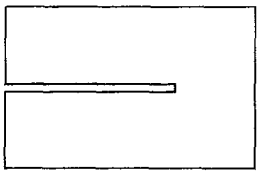


Fig. 9 Configuration of an edge crack specimen investigated by Ravi-Chandar and Knauss (1982, 1984b)

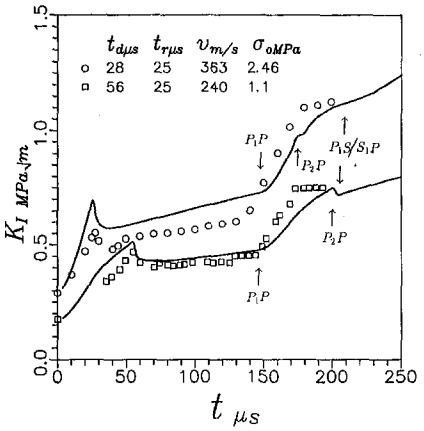


Fig. 10 Stress intensity factors of theoretical prediction and experimental results of Ravi-Chandar and Knauss (1982, 1984b)

Acknowledgment

The authors gratefully acknowledge the financial support of this research by the National Science Council (Republic of China) under Grant NSC 81-0401-E211-503 to Huafan University.

References

Freund, L. B., 1972a, "Crack Propagation in an Elastic Solid Subjected to General Loading—I. Constant Rate of Extension," *Journal of the Mechanics and Physics of Solids,* Vol. 20, pp. 129–140.

Freund, L. B., 1972b, "Crack Propagation in an Elastic Solid Subjected to General Loading—II. Non-uniform Rate of Extension," *Journal of the Mechanics and Physics of Solids,* Vol. 20, pp. 141–152.

Freund, L. B., 1973, "Crack Propagation in an Elastic Solid Subjected to General Loading—III. Stress Wave Loading," *Journal of the Mechanics and Physics of Solids,* Vol. 21, pp. 47–61.

Freund, L. B., 1974, "Crack Propagation in an Elastic Solid Subjected to General Loading—IV. Obliquely Incident Stress Pulse," *Journal of the Mechanics and Physics of Solids,* Vol. 22, pp. 137–147.

Kim, K. S., 1985, "Dynamic Fracture Under Normal Impact Loading of the Crack Faces," ASME JOURNAL OF APPLIED MECHANICS, Vol. 52, pp. 585–592.

Ma, C. C., and Chen, S. K., 1994, "Exact Transient Full-Field Analysis of an Antiplane Subsurface Crack Subjected to Dynamic Impact Loading," ASME JOURNAL OF APPLIED MECHANICS, Vol. 61, pp. 649–655.

Ma, C. C., and Ing, Y. S., 1995, "Transient Analysis of Dynamic Crack Propagation with Boundary Effect," ASME JOURNAL OF APPLIED MECHANICS, Vol. 62, pp. 1029–1038.

Ravi-Chandar, K., and Knauss, W. G., 1982, "Dynamic Crack-tip Stresses Under Stress Wave Loading—A Comparison of Theory and Experiment," *International Journal of Fracture,* Vol. 20, pp. 209–222.

Ravi-Chandar, K., and Knauss, W. G., 1984a, "An Experimental Investigation into Dynamic Fracture: I. Crack Initiation and Arrest," *International Journal of Fracture,* Vol. 25, pp. 247–262.

Ravi-Chandar, K., and Knauss, W. G., 1984b, "An Experimental Investigation into Dynamic Fracture: II. Microstructural Aspects," *International Journal of Fracture,* Vol. 26, pp. 65–80.

Ravi-Chandar, K., and Knauss, W. G., 1984c, "An Experimental Investigation into Dynamic Fracture: III. On Steady-State Crack Propagation and Crack Branching," *International Journal of Fracture,* Vol. 26, pp. 141–154.

Ravi-Chandar, K., and Knauss, W. G., 1984d, "An Experimental Investigation into Dynamic Fracture: IV. On the Interaction of Stress Waves With Propagating Cracks," *International Journal of Fracture,* Vol. 26, pp. 189–200.

Ravichandran, G., and Clifton, R. J., 1989, "Dynamic Fracture Under Plane Wave Loading," *International Journal of Fracture,* Vol. 40, pp. 157–201.

Sih, G. C., Embley, G. T., and Ravera, R. S., 1972, "Impact Response of a Finite Crack in Plane Extension," *International Journal of Solids and Structures,* Vol. 8, pp. 977–993.

Thau, S. A., and Lu, T. H., 1971, "Transient Stress Intensity Factors for a Finite Crack in an Elastic Solid Cause by a Dilatational Wave," *International Journal of Solids and Structures,* Vol. 7, pp. 731–750.

Tsai, C. H., and Ma, C. C., 1991, "Exact Transient Solutions of Buried Dynamic Point Forces and Displacement Jumps for an Elastic Half Space," *International Journal of Solids and Structures,* Vol. 28, pp. 955–974.

Tsai, C. H., and Ma, C. C., 1992, "Transient Analysis of a Semi-infinite Crack Subjected to Dynamic Concentrated Forces," ASME JOURNAL OF APPLIED MECHANICS, Vol. 59, pp. 804–811.

Tsai, C. H., and Ma, C. C., 1997, "Transient Analysis of a Propagating In-Plane Crack in a Finite Geometry body Subjected to Static Loadings," ASME JOURNAL OF APPLIED MECHANICS, accepted for publication.

Downloaded 04 May 2010 to 171.66.16.34. Redistribution subject to ASME license or copyright; see http://www.asme.org/terms/Terms_Use.cfm

APPENDIX

A1 Fundamental Solution of a Half-Plane

The solution of applying an exponentially distributed loading in the Laplace transform domain to the surface of a half-plane is denoted as the fundamental solution of the half-plane. The coordinates system (ξ, x_2) moving with a constant speed v is attached at the surface of half-plane. For the boundary conditions

$$\bar{\sigma}_{22}(\xi, 0, p) = e^{p\eta\xi}, \quad -\infty < \xi < \infty, \tag{A1}$$

$$\bar{\sigma}_{12}(\xi, 0, p) = 0, \quad -\infty < \xi < \infty, \tag{A2}$$

where η is an arbitrary imaginary number, the solutions for stresses can be obtained as

$$\bar{\sigma}_{11} = \frac{((b^2 - 2a^2)(1 - \eta v)^2 + 2\eta^2)(b^2(1 - \eta v)^2 - 2\eta^2)}{R(\eta)} \times e^{-p\alpha x_2 + p\eta\xi} + \frac{4\eta^2\alpha\beta}{R(\eta)} e^{-p\beta x_2 + p\eta\xi}, \tag{A3}$$

$$\bar{\sigma}_{12} = \frac{-2\eta\alpha(b^2(1 - \eta v)^2 - 2\eta^2)}{R(\eta)} e^{-p\alpha x_2 + p\eta\xi} + \frac{2\eta\alpha(b^2(1 - \eta v)^2 - 2\eta^2)}{R(\eta)} e^{-p\beta x_2 + p\eta\xi}, \tag{A4}$$

$$\bar{\sigma}_{22} = \frac{(b^2(1 - \eta v)^2 - 2\eta^2)^2}{R(\eta)} e^{-p\alpha x_2 + p\eta\xi} + \frac{4\alpha\beta\eta^2}{R(\eta)} e^{-p\beta x_2 + p\eta\xi}. \tag{A5}$$

For the boundary conditions

$$\bar{\sigma}_{22}(\xi, 0, p) = 0, \quad -\infty < \xi < \infty, \tag{A6}$$

$$\bar{\sigma}_{12}(\xi, 0, p) = e^{p\eta\xi}, \quad -\infty < \xi < \infty, \tag{A7}$$

solutions for stresses are

$$\bar{\sigma}_{11} = \frac{-2\eta\beta((b^2 - 2a^2)(1 - \eta v)^2 + 2\eta^2)}{R(\eta)} e^{-p\alpha x_2 + p\eta\xi} + \frac{-2\eta\beta((b^2(1 - \eta v)^2 - 2\eta^2)}{R(\eta)} e^{-p\beta x_2 + p\eta\xi}, \tag{A8}$$

$$\bar{\sigma}_{12} = \frac{4\eta^2\alpha\beta}{R(\eta)} e^{-p\alpha x_2 + p\eta\xi} + \frac{(b^2(1 - \eta v)^2 - 2\eta^2)^2}{R(\eta)} e^{-p\beta x_2 + p\eta\xi}, \tag{A9}$$

$$\bar{\sigma}_{22} = \frac{-2\eta\beta(b^2(1 - \eta v)^2 - 2\eta^2)}{R(\eta)} e^{-p\alpha x_2 + p\eta\xi} + \frac{2\eta\beta(b^2(1 - \eta v)^2 - 2\eta^2)}{R(\eta)} e^{-p\beta x_2 + p\eta\xi}. \tag{A10}$$

A2 Fundamental Solution of a Propagating Crack

The solution of an exponentially distributed loading in the Laplace transform domain applied at the propagating crack faces is denoted as the fundamental solution of propagating crack. Consider a semi-infinite crack propagating with constant speed $v = 1/d$ in an unbounded medium. The coordinate system (ξ, x_2) is attached to the moving crack tip and is also moving with the constant speed v. Consider the boundary conditions of mode I

$$\bar{\sigma}_{22}(\xi, 0, p) = e^{p\eta\xi} \quad \text{for} \quad -\infty < \xi < 0, \tag{A11}$$

$$\bar{\sigma}_{12}(\xi, 0, p) = 0 \quad \text{for} \quad -\infty < \xi < \infty, \tag{A12}$$

$$\bar{u}_2(\xi, 0, p) = 0 \quad \text{for} \quad 0 < \xi < \infty, \tag{A13}$$

where η is a complex number, under the condition that $\mathrm{Re}(\eta) > \mathrm{Re}(\lambda)$, the stresses can be obtained as follows:

$$\bar{\sigma}_{ij} = \frac{1}{2\pi i} \int [S_{ij}^1(\lambda) e^{-p\alpha x_2 + p\lambda\xi} + S_{ij}^2(\lambda) e^{-p\beta x_2 + p\lambda\xi}] d\lambda, \tag{A14}$$

where

$$\begin{aligned}
S_{11}^1(\lambda) &= -((b^2 - 2a^2)(1 - \lambda v)^2 + 2\lambda^2) \times (b^2(1 - \lambda v)^2 - 2\lambda^2)\alpha_+(\eta) G(\eta, \lambda)/\alpha_+(\lambda), \\
S_{11}^2(\lambda) &= 4\lambda^2\beta(\lambda)\alpha_-(\lambda)\alpha_+(\eta) G(\eta, \lambda), \\
S_{12}^1(\lambda) &= 2\lambda(b^2(1 - \lambda v)^2 - 2\lambda^2)\alpha_-(\lambda)\alpha_+(\eta) G(\eta, \lambda), \\
S_{12}^2(\lambda) &= -S_{12}^1(\lambda), \\
S_{22}^1(\lambda) &= -(b^2(1 - \lambda v)^2 - 2\lambda^2)^2\alpha_+(\eta) G(\eta, \lambda)/\alpha_+(\lambda), \\
S_{22}^2 &= -S_{11}^2, \\
G(\eta, \lambda) &= 1/(\kappa(d - \lambda)^2(c_1 - \lambda)(c_2 + \eta) \times S_-(\lambda) S_+(\eta)(\lambda - \eta)).
\end{aligned} \tag{A15}$$

The corresponding mode I stress intensity factor is

$$\bar{K}_I = \frac{-\sqrt{2}}{\sqrt{p}} \frac{\alpha_+(\eta)}{\sqrt{1 - av}(c_2 + \eta) S_+(\eta)}. \tag{A16}$$

If the boundary conditions are

$$\bar{\sigma}_{22}(\xi, 0, p) = 0, \quad -\infty < \xi < \infty, \tag{A17}$$

$$\bar{\sigma}_{12}(\xi, 0, p) = e^{p\eta\xi}, \quad -\infty < \xi < 0, \tag{A18}$$

$$\bar{u}_1(\xi, 0, p) = 0, \quad 0 < \xi < \infty, \tag{A19}$$

the solution of stresses is expressed as in Eq. (A14) with

$$\begin{aligned}
S_{11}^1(\lambda) &= 2\lambda(b^2(1 - \lambda v)^2 - 2\alpha^2)\beta_-(\lambda)\beta_+(\eta) G(\eta, \lambda), \\
S_{11}^2(\lambda) &= S_{11}^1(\lambda), \\
S_{12}^1(\lambda) &= -4\lambda^2\alpha(\lambda)\beta_-(\lambda)\beta_+(\eta) G(\eta, \lambda), \\
S_{12}^2(\lambda) &= -(b^2(1 - \lambda v)^2 - 2\lambda^2)^2\beta_+(\eta) G(\eta, \lambda)/\beta_+(\lambda), \\
S_{22}^1(\lambda) &= 2\lambda(b^2(1 - \lambda v)^2 - 2\lambda^2)\beta_-(\lambda)\beta_+(\eta) G(\eta, \lambda), \\
S_{22}^2(\lambda) &= -S_{22}^1(\lambda).
\end{aligned} \tag{A20}$$

The corresponding mode II stress intensity factor is

$$\bar{K}_{II} = -\frac{\sqrt{2}}{\sqrt{p}} \frac{\beta_+(\eta)}{\sqrt{1 - bv}(c_2 + \eta) S_+(\eta)}. \tag{A21}$$

A3 Coordinates Transformation Principle of Stresses

The physical quantities must be expressed in the same coordinate system, so that the superposition method can be performed successfully. If the stress $\bar{\sigma}_{ij}$ expressed in the fixed coordinate system (x_1, x_2) is

$$\bar{\sigma}_{ij}(x_1, x_2, p) = p^n \int F(\lambda) e^{-p\alpha^0 x_2 + p\lambda x_1} d\lambda, \tag{A22}$$

then it can be transformed to the moving coordinate system (ξ, x_2) by the form

$$\bar{\sigma}_{ij}(\xi, x_2, p) = p^n \int (1 - \lambda v)^{n-1} F\left(\frac{\lambda}{1 - \lambda v}\right) e^{-p\alpha x_2 + p\lambda\xi} d\lambda, \tag{A23}$$

where $\xi = x_1 - vt$. The stresses of (A22) and (A23) can be proved to be equivalent in the time domain.

Downloaded 04 May 2010 to 171.66.16.34. Redistribution subject to ASME license or copyright; see http://www.asme.org/terms/Terms_Use.cfm

Y. Shindo
Professor,
Department of Materials Processing,
Graduate School of Engineering,
Tohoku University,
Sendai 980-77, Japan

I. Ohnishi
Toyota Motor Corporation,
1 Toyota-cho,
Toyota 471, Japan

S. Tohyama
Graduate Student,
Department of Materials Processing,
Graduate School of Engineering,
Tohoku University,
Sendai 980-77, Japan

Flexural Wave Scattering at a Through Crack in a Conducting Plate Under a Uniform Magnetic Field

Following a classical plate bending theory of magneto-elasticity, we consider the scattering of time-harmonic flexural waves by a through crack in a conducting plate under a uniform magnetic field normal to the crack surface. An incident wave giving rise to moments symmetric about the crack plane is applied. It is assumed that the plate has the electric and magnetic permeabilities of the free space. By the use of Fourier transforms we reduce the problem to solving a pair of dual integral equations. The solution of the dual integral equations is then expressed in terms of a Fredholm integral equation of the second kind. The dynamic moment intensity factor versus frequency is computed and the influence of the magnetic field on the normalized values is displayed graphically. It is found that the existence of the magnetic field produces higher singular moments near the crack tip.

Introduction

In recent years, interest in magnetic fracture mechanics has grown appreciably in view of its importance in the field of applied superconductivity. The components of a magnetic fusion reactor frequently are subjected to strong magnetic fields that can have an undesirable effect on the integrity of the structure (Shindo et al., 1989; Shindo, 1991). From the requirements for the fusion experimental reactor, the maximum magnetic field is 12 T (tesla). The dynamic behavior of an electrically conducting elastic plate is sufficiently affected by the presence of the strong magnetic field. In the previous paper, Shindo et al. (1993) have considered the scattering of time-harmonic flexural waves by a through crack in a perfectly conducting plate under a uniform magnetic field to show the effect of induced current, and have found that the existence of the magnetic field produces lower singular moments near the crack tip. For conductors with finite electric conductivity, through the interaction of conduction currents with the velocity field of mechanical waves, there is magnetic damping on the wave motion. The magnetic damping by induced current is significant in magnetoelastic interactions. Considerable work has been done to consider the transient wave problem and investigate the magneto-elastodynamic problem for an infinite, isotropic, elastic conductor with a penny-shaped crack (Shindo, 1982).

In this investigation, the scattering of time-harmonic flexural waves by a through crack in a conducting plate under a uniform magnetic field is analyzed to show the effect of induced current. Since our interest lies primarily with the motion of the cracked plate, the electrical behavior will be assumed to be quasi-stationary while the mechanical behavior is dynamical. This is a small conductivity and high-frequency approximation (Dunkin and Eringen, 1963). Classical plate bending theory for magneto-elastic interactions in conducting bodies is applied. A limitation of the theory is that both the crack and incident wave length must be large in comparison with the plate thickness. The plate is engulfed by a uniform magnetic field directed normal to the crack and subjected to incident waves that generate vibratory motion in the transverse direction of the plate. Fourier transforms are used to reduce the magneto-elastic crack problem to a pair of dual integral equations which can be further reduced to a Fredholm integral equation of the second kind (Shindo et al., 1993) that is amenable to numerical calculations. Dynamic moment intensity factors are determined for different wave frequencies and amplitudes of the magnetic field. Allowing the magnetic field to tend to zero, we have the purely elastic problem, which has been studied by Sih and Chen (1977). Mindlin's plate theory of magneto-elasticity can be made, of course, but our purpose here is to demonstrate the nature of the magneto-elastic coupling using the simplest theory.

Magneto-Elastic Thin Plate Bending

We consider an electrically conducting elastic plate of thickness $2h$ with finite electric conductivity. The coordinate axes x and y are in the middle plane of the plate and the z-axis is perpendicular to this plane. It is assumed that the plate has the electric and magnetic permeabilities $\epsilon = \epsilon_0 = 8.85 \times 10^{-12}$ F/m, $\kappa = \kappa_0 = 1.26 \times 10^{-6}$ H/m, respectively, with ϵ_0 and κ_0 being the free space permeabilities. The conducting plate is permeated by a static uniform magnetic field $\mathbf{H}_0$. We consider small perturbations characterized by the displacement vector $\mathbf{u}$ produced in the plate. The magnetic and electric fields may be expressed in the form

$$\left.\begin{aligned}\mathbf{H} &= \mathbf{H}_0 + \mathbf{h}\\ \mathbf{E} &= \mathbf{0} + \mathbf{e}\end{aligned}\right\} \tag{1}$$

where $\mathbf{H}$ and $\mathbf{E}$ are the magnetic and electric field intensity vectors, and $\mathbf{h}$ and $\mathbf{e}$ are the fluctuating fields and result from the velocity field of mechanical waves. The normalized fluctuating fields are assumed to be of the same order of magnitude as the normalized particle displacement.

The frequencies associated with mechanical vibrations or waves are much smaller than those associated with electromagnetic waves of the same wave length. Thus when dealing with dynamic mechanical problems it may be expedient to drop dis-

Contributed by the Applied Mechanics Division of THE AMERICAN SOCIETY OF MECHANICAL ENGINEERS for publication in the ASME JOURNAL OF APPLIED MECHANICS.

Discussion on the paper should be addressed to the Technical Editor, Professor Lewis T. Wheeler, Department of Mechanical Engineering, University of Houston, Houston, TX 77204-4792, and will be accepted until four months after final publication of the paper itself in the ASME JOURNAL OF APPLIED MECHANICS.

Manuscript received by the ASME Applied Mechanics Division, Apr. 21, 1995; final revision, Apr. 24, 1997. Associate Technical Editor: M. Taya.

Copyright © 1997 by ASME

Downloaded 04 May 2010 to 171.66.16.34. Redistribution subject to ASME license or copyright; see http://www.asme.org/terms/Terms_Use.cfm

placement currents from Maxwell's equations. Neglecting displacement currents compared to the conduction currents, we have the following linearized field equations (Shindo et al., 1993):

$$\text{curl } \mathbf{h} = \mathbf{j} \tag{2}$$

$$\text{curl } \mathbf{e} = -\kappa_0 \mathbf{h}_{,t} \tag{3}$$

$$\text{div } \mathbf{h} = 0 \tag{4}$$

$$\text{div } \mathbf{e} = 0 \tag{5}$$

$$\left.\begin{aligned} \sigma_{x,x} + \tau_{yx,y} + \tau_{zx,z} + (\mathbf{j} \times \mathbf{B}_0)_x &= \rho u_{x,tt} \\ \tau_{xy,x} + \sigma_{y,y} + \tau_{zy,z} + (\mathbf{j} \times \mathbf{B}_0)_y &= \rho u_{y,tt} \\ \tau_{xz,x} + \tau_{yz,y} + \sigma_{z,z} + (\mathbf{j} \times \mathbf{B}_0)_z &= \rho u_{z,tt} \end{aligned}\right\} \tag{6}$$

where a comma denotes partial differentiation with respect to the coordinate or the time t, $\mathbf{j}$ is the current density, $\mathbf{B}_0 = \kappa_0 \mathbf{H}_0$ is the magnetic induction, ρ is the mass density, (σ_x, σ_y, σ_z, $\tau_{xy} = \tau_{yx}$, $\tau_{yz} = \tau_{zy}$, $\tau_{zx} = \tau_{xz}$) are the elastic stress components, and (u_x, u_y, u_z) are the components of $\mathbf{u}$. In a moving conductor the current is determined by Ohm's law as

$$\mathbf{j} = \sigma(\mathbf{e} + \mathbf{u}_{,t} \times \mathbf{B}_0) \tag{7}$$

where σ is the electric conductivity. The Eq. (7) and the Lorentz force in (6) are the coupling terms between the elastic medium and electromagnetic field. The mechanical constitutive equations are taken to be the usual Hooke's law

$$\left.\begin{aligned} \sigma_x &= \lambda(u_{x,x} + u_{y,y} + u_{z,z}) + 2\mu u_{x,x} \\ \sigma_y &= \lambda(u_{x,x} + u_{y,y} + u_{z,z}) + 2\mu u_{y,y} \\ \sigma_z &= \lambda(u_{x,x} + u_{y,y} + u_{z,z}) + 2\mu u_{z,z} \\ \tau_{xy} &= \mu(u_{x,y} + u_{y,x}) \\ \tau_{yz} &= \mu(u_{y,z} + u_{z,y}) \\ \tau_{xz} &= \mu(u_{z,x} + u_{x,z}) \end{aligned}\right\} \tag{8}$$

where λ, μ are the Lamé constants. Outside the plate the external fields are solutions of

$$\text{curl } \mathbf{h}^e = 0 \tag{9}$$

$$\text{curl } \mathbf{e}^e = -\kappa_0 \mathbf{h}^e_{,t} \tag{10}$$

$$\text{div } \mathbf{h}^e = 0 \tag{11}$$

$$\text{div } \mathbf{e}^e = 0 \tag{12}$$

where the superscript e denotes the external value of the quantity so labeled.

From Eqs. (2)–(6) and (7), we have the field equations:

$$h_{z,y} - h_{y,z} = \sigma\{e_x + \kappa_0(H_{0z}u_{y,t} - H_{0y}u_{z,t})\} \tag{13}$$

$$h_{x,z} - h_{z,x} = \sigma\{e_y + \kappa_0(H_{0x}u_{z,t} - H_{0z}u_{x,t})\} \tag{14}$$

$$h_{y,x} - h_{x,y} = \sigma\{e_z + \kappa_0(H_{0y}u_{x,t} - H_{0x}u_{y,t})\} \tag{15}$$

$$e_{z,y} - e_{y,z} = -\kappa_0 h_{x,t} \tag{16}$$

$$e_{x,z} - e_{z,x} = -\kappa_0 h_{y,t} \tag{17}$$

$$e_{y,x} - e_{x,y} = -\kappa_0 h_{z,t} \tag{18}$$

$$h_{x,x} + h_{y,y} + h_{z,z} = 0 \tag{19}$$

$$e_{x,x} + e_{y,y} + e_{z,z} = 0 \tag{20}$$

$$\sigma_{x,x} + \tau_{xy,y} + \tau_{xz,z} = \rho u_{x,tt} + \sigma[-\kappa_0 H_{0z} e_y + \kappa_0 H_{0y} e_z + \kappa_0^2\{(H_{0z}^2 + H_{0y}^2)u_{x,t} - H_{0x}H_{0z}u_{z,t} - H_{0x}H_{0y}u_{y,t}\}] \tag{21}$$

$$\tau_{xy,x} + \sigma_{y,y} + \tau_{yz,z} = \rho u_{y,tt} + \sigma[-\kappa_0 H_{0x} e_z + \kappa_0 H_{0z} e_x + \kappa_0^2\{(H_{0x}^2 + H_{0z}^2)u_{y,t} - H_{0x}H_{0y}u_{x,t} - H_{0y}H_{0z}u_{z,t}\}] \tag{22}$$

$$\tau_{xz,x} + \tau_{yz,y} + \sigma_{z,z} = \rho u_{z,tt} + \sigma[-\kappa_0 H_{0y} e_x + \kappa_0 H_{0x} e_y + \kappa_0^2\{(H_{0x}^2 + H_{0y}^2)u_{z,t} - H_{0y}H_{0z}u_{y,t} - H_{0x}H_{0z}u_{x,t}\}] \tag{23}$$

where (H_{0x}, H_{0y}, H_{0z}), (e_x, e_y, e_z) and (h_x, h_y, h_z) are the components of $\mathbf{H}_0$, $\mathbf{e}$, and $\mathbf{h}$.

By using magnetoelastic thin plate theory (Ambartsumian et al., 1971, 1975; Fung, 1965; Shindo, 1991), the rectangular displacement components u_x, u_y, and u_z; the x, y-components of $\mathbf{e}$; and the z-component of $\mathbf{h}$ may be expressed as follows:

$$u_x = -zw_{,x}, \quad u_y = -zw_{,y}, \quad u_z = w(x, y, t) \tag{24}$$

$$e_x = \varphi(x, y, t), \quad e_y = \psi(x, y, t), \quad h_z = f(x, y, t) \tag{25}$$

in which $w(x, y, t)$ represents the deflection of the middle plane of the plate, φ, ψ, f are the functions of x, y, t. Assuming the hypotheses (24) and (25), the three-dimensional magneto-elasticity problem reduces substantially to a two-dimensional problem of magneto-elasticity of the plate. Substituting Eqs. (24) and (25) into Eqs. (13), (14), and (20) yields

$$h_{x,z} = f_{,x} + \sigma\{\psi + \kappa_0(H_{0x}w_{,t} + zH_{0z}w_{,xt})\} \tag{26}$$

$$h_{y,z} = f_{,y} - \sigma\{\psi + \kappa_0(H_{0y}w_{,t} + zH_{0z}w_{,yt})\} \tag{27}$$

$$e_{z,z} = -\varphi_{,x} - \psi_{,y}. \tag{28}$$

The linearized electromagnetic boundary conditions are also obtained as

$$\left.\begin{aligned} h_x(x, y, \pm h, t) &= h_x^e(x, y, \pm h, t) \\ h_y(x, y, \pm h, t) &= h_y^e(x, y, \pm h, t) \\ h_z(x, y, t) &= h_z^e(x, y, \pm h, t) \\ e_x(x, y, t) &= e_x^e(x, y, \pm h, t) \\ e_y(x, y, t) &= e_y^e(x, y, \pm h, t) \\ e_z(x, y, \pm h, t) &= e_z^e(x, y, \pm h, t). \end{aligned}\right\} \tag{29}$$

Taking into account the boundary conditions (29) and integrating the representations (26)–(28) with respect to z, we obtain the remaining electromagnetic field components as

$$h_x = \frac{h_x(x, y, h, t) + h_x(x, y, -h, t)}{2} + z\{f_{,x} + \sigma(\psi + \kappa_0 H_{0x}w_{,t})\} + \sigma\kappa_0 H_{0z}\frac{z^2 - h^2}{2}w_{,xt} \tag{30}$$

$$h_y = \frac{h_y(x, y, h, t) + h_y(x, y, -h, t)}{2} + z\{f_{,y} - \sigma(\varphi - \kappa_0 H_{0y}w_{,t})\} + \sigma\kappa_0 H_{0z}\frac{z^2 - h^2}{2}w_{,yt} \tag{31}$$

$$e_z = \frac{e_z(x, y, h, t) + e_z(x, y, -h, t)}{2} - z(\varphi_{,x} + \psi_{,y}). \tag{32}$$

Therefore, all the electromagnetic field components are represented by means of the four desired functions φ, ψ, f, w.

With Eqs. (24), the elastic stress components (8) become

$$\sigma_x = -z\frac{E}{1 - \nu^2}(w_{,xx} + \nu w_{,yy}) \tag{33}$$

$$\sigma_y = -z\frac{E}{1 - \nu^2}(w_{,yy} + \nu w_{,xx}) \tag{34}$$

Downloaded 04 May 2010 to 171.66.16.34. Redistribution subject to ASME license or copyright; see http://www.asme.org/terms/Terms_Use.cfm

$$\tau_{xy} = -z\frac{E}{1+\nu}w_{,xy} \tag{35}$$

where E is the Young's modulus and ν is the Poisson's ratio.

The bending and twisting moments per unit length (M_{xx}, M_{yy}, $M_{xy} = M_{yx}$) and the vertical shear forces per unit length (Q_x, Q_y) can be expressed in terms of $w(x, y, t)$ as

$$\left.\begin{aligned} M_{xx} &= \int_{-h}^{h} z\sigma_x dz = -D(w_{,xx} + \nu w_{,yy}) \\ M_{yy} &= \int_{-h}^{h} z\sigma_y dz = -D(w_{,yy} + \nu w_{,xx}) \\ M_{xy} = M_{yx} &= \int_{-h}^{h} z\tau_{xy} dz = -(1-\nu)Dw_{,xy} \end{aligned}\right\} \tag{36}$$

$$\left.\begin{aligned} Q_x &= \int_{-h}^{h} \tau_{xz} dz = -D(w_{,xx} + w_{,yy})_{,x} \\ Q_y &= \int_{-h}^{h} \tau_{yz} dz = -D(w_{,xx} + w_{,yy})_{,y}. \end{aligned}\right\} \tag{37}$$

The stress boundary conditions on the plate surfaces are

$$\tau_{xz} = \tau_{yz} = \sigma_z = 0 \quad (z = \pm h). \tag{38}$$

By virtue of Eqs. (24), (25) and (33)–(35), and taking account of the boundary conditions (38), we obtain the stress components from Eqs. (21) and (22) as

$$\begin{aligned} \tau_{xz} = -z\sigma\Big\{ & \kappa_0 H_{0z}\psi - \kappa_0 H_{0y} \\ & \times \frac{e_z(x, y, h, t) + e_z(x, y, -h, t)}{2} + \kappa_0^2 H_{0x} H_{0z} w_{,t} \Big\} \\ & + \frac{h^2 - z^2}{2}\Big\{ \rho w_{,xtt} - \frac{E}{1-\nu^2}(w_{,xx} + w_{,yy})_{,x} \\ & + \sigma\kappa_0 H_{0y}(\varphi_{,x} + \psi_{,y} + \sigma\kappa_0^2(H_{0z}^2 + H_{0y}^2)w_{,xt} \\ & - \sigma\kappa_0^2 H_{0x} H_{0y} w_{,yt}\Big\} \end{aligned} \tag{39}$$

$$\begin{aligned} \tau_{yz} = -z\sigma\Big\{ & \kappa_0 H_{0x}\frac{e_z(x, y, h, t) + e_z(x, y, -h, t)}{2} \\ & - \kappa_0 H_{0z}\varphi + \kappa_0^2 H_{0y} H_{0z} w_{,t}\Big\} \\ & + \frac{h^2 - z^2}{2}\Big\{ \rho w_{,ytt} - \frac{E}{1-\nu^2}(w_{,xx} + w_{,yy})_{,y} \\ & + \sigma\kappa_0 H_{0x}(\varphi_{,x} + \psi_{,y} + \sigma\kappa_0^2(H_{0x}^2 + H_{0z}^2)w_{,yt} \\ & - \sigma\kappa_0^2 H_{0x} H_{0y} w_{,xt}\Big\}. \end{aligned} \tag{40}$$

Substituting Eqs. (24), (25) and (30)–(32) into the equations (13), (14), and (18), and integrating the equations with respect to z from $-h$ to h, we have

$$f_{,x} + \sigma(\psi + \kappa_0 H_{0x} w_{,t}) = \frac{h_x(x, y, h, t) - h_x(x, y, -h, t)}{2h} \tag{41}$$

$$f_{,y} + \sigma(\varphi + \kappa_0 H_{0y} w_{,t}) = \frac{h_y(x, y, h, t) - h_y(x, y, -h, t)}{2h}. \tag{42}$$

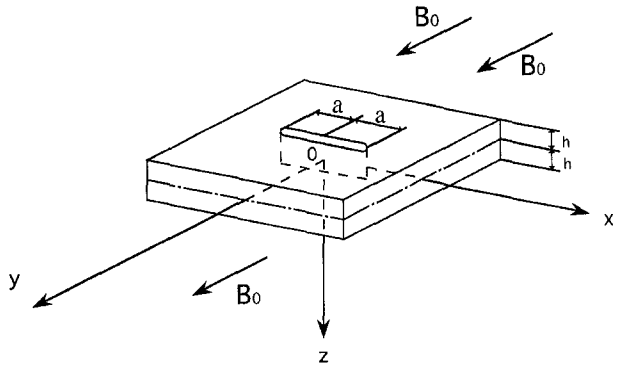


Fig. 1 An electrically conducting plate with a through crack

$$\psi_{,x} - \varphi_{,y} = -\kappa_0 f_{,t} \tag{43}$$

Substituting Eqs. (24), (25), (39), and (40) into Eq. (23), integrating the equations with respect to z from $-h$ to h, and taking into account the boundary conditions (38), we also have the equation of motion for a thin plate under the influence of magnetic field

$$\begin{aligned} & D(w_{,xxxx} + 2w_{,xxyy} + w_{,yyyy}) - \tfrac{2}{3}\rho h^3(w_{,xx} + w_{,yy})_{,tt} \\ & - \tfrac{2}{3}h^3\sigma\kappa_0(H_{0y}\varphi_{,xx} - H_{0x}\varphi_{,xy} + H_{0y}\psi_{,xy} - H_{0x}\psi_{,yy}) \\ & - 2h\sigma\kappa_0\{H_{0y}(\varphi - \kappa_0 H_{0y} w_{,t}) - H_{0x}(\psi + \kappa_0 H_{0x} w_{,t})\} \\ & + 2\rho h w_{,tt} = 0 \end{aligned} \tag{44}$$

where $D = 4\mu h^3/3(1-\nu)$ is the flexural rigidity of the plate.

Problem Statement and Method of Solution

Consider an electrically conducting elastic plate having a through crack of length $2a$ as shown in Fig. 1. The crack is located on the line $y = 0$, $|x| < a$ and the cracked plate is permeated by the magnetic field of magnetic induction $B_0 = \kappa_0 H_0$ normal to the crack surface. An incident wave giving rise to moments symmetric about the crack plane $y = 0$ is applied:

$$w^i = w_{i0}\exp\{i(ky - \omega t)\} \tag{45}$$

where the superscript i stands for the incident component, w_{i0} is the amplitude of the input wave, k is the wave number, and ω is the circular frequency. We further assume a quasi-static electromagnetic state (small conductivity, high frequency, $|k|^2 \gg \sigma\kappa_0\omega$). Mathematically this is accomplished by dropping $\mathbf{h}_{,t}$ from Maxwell's Eqs. (2)–(5) while retaining all other time derivatives. Thus we obtain the dispersion relation (Ambartsumian, 1971, 1975)

$$\frac{2\rho h}{D}\omega^2 = k^4 - \frac{2i\omega h\sigma}{D}(\kappa_0 H_0)^2 = k_1^4. \tag{46}$$

Consider the definition of

$$\Omega^2 = Dk^4/2\rho h, \quad c_2^2 = \mu/\rho, \quad h_c = \kappa_0 H_0^2/\mu \tag{47}$$

then the combination of Eqs. (46) and (47) gives

$$\omega^2 - \Omega^2 + ic_2^2 h_c \sigma\kappa_0\omega = 0. \tag{48}$$

The deflection arising from the scattered wave w^s may be added onto that for the incident wave w^i to yield the total wave field:

$$w(x, y, t) = w^i(x, y, t) + w^s(x, y, t) \tag{49}$$

where the superscript s stands for the scattered component. Only one quarter of the plate needs to be considered because of symmetry. For a stress-free crack surface, the thin plate theory

Downloaded 04 May 2010 to 171.66.16.34. Redistribution subject to ASME license or copyright; see http://www.asme.org/terms/Terms_Use.cfm

requires the vanishing of the bending moment M_{yy} and equivalent shear V_y given by

$$V_y = Q_y + M_{xy,x}. \tag{50}$$

The conditions to be specified on the crack for the scattered field become

$$V_y^s = M_{xy,x}^s + Q_y^s = 0 \quad (y = 0, \quad 0 \le x < \infty) \tag{51}$$

$$e_y^s = 0 \quad (y = 0, \quad 0 \le x < \infty) \tag{52}$$

$$\left.\begin{array}{ll} M_{yy}^s = -M_{yy}^i = -Dw_{i0}k^2 \exp(-i\omega t) & (y = 0, \quad 0 \le x < a) \\ u_y^s = 0 & (y = 0, \quad a \le x < \infty). \end{array}\right\} \tag{53}$$

In what follows, the exponential time factor $\exp(-iwt)$ would be omitted as it always appears with the quantity $Dw_{i0}k^2$ as indicated in Eq. (53).

Assuming a quasi-static electromagnetic state, which is realized by dropping the term $f_{,t}$ and retaining other time derivatives in Eqs. (41)–(44), and neglecting rotational inertia and resultant external moments, we obtain

$$\psi_{,x} - \varphi_{,y} = 0 \tag{54}$$

$$f_{,x} + \sigma\psi = \frac{h_x(x, y, h, t) - h_x(x, y, -h, t)}{2h} \tag{55}$$

$$f_{,y} - \sigma(\varphi - \kappa_0 H_0 w_{,t}) = \frac{h_y(x, y, h, t) - h_y(x, y, -h, t)}{2h} \tag{56}$$

$$D(w_{,xxxx} + 2w_{,xxyy} + w_{,yyyy}) - 2h\sigma\kappa_0 H_0(\varphi - \kappa_0 H_0 w_{,t}) + 2\rho h w_{,tt} = 0. \tag{57}$$

The field Eqs. (9)–(12) in the vacuum can be written as

$$\left.\begin{array}{l} h_{x,xx}^e + h_{x,yy}^e + h_{x,zz}^e = 0 \\ h_{y,xx}^e + h_{y,yy}^e + h_{y,zz}^e = 0 \\ h_{z,xx}^e + h_{z,yy}^e + h_{z,zz}^e = 0 \end{array}\right\} \tag{58}$$

$$\left.\begin{array}{l} e_{x,xx}^e + e_{x,yy}^e + e_{x,zz}^e = 0 \\ e_{y,xx}^e + e_{y,yy}^e + e_{y,zz}^e = 0. \end{array}\right\} \tag{59}$$

The electromagnetic boundary conditions can be obtained from Eqs. (29) as

$$\left.\begin{array}{l} h_x(x, y, \pm h, t) = h_x^e(x, y, \pm h, t) \\ h_y(x, y, \pm h, t) = h_y^e(x, y, \pm h, t) \\ f(x, y, t) = h_z^e(x, y, \pm h, t) \end{array}\right\} \tag{60}$$

$$\left.\begin{array}{l} \varphi(x, y, t) = e_x^e(x, y, \pm h, t) \\ \psi(x, y, t) = e_y^e(x, y, \pm h, t). \end{array}\right\} \tag{61}$$

From Eq. (9), we have

$$\left.\begin{array}{l} h_{z,y}^e - h_{y,z}^e = 0 \\ h_{x,z}^e - h_{z,x}^e = 0 \\ h_{y,x}^e - h_{x,y}^e = 0. \end{array}\right\} \tag{62}$$

To solve the field equations, we use the Fourier transforms (Sneddon, 1951). We assume that the solution $w(x, y, t)$ is of the form

$$w(x, y) = \frac{2}{\pi}\sum_{j=1}^{3}\int_0^\infty A_j(\alpha)\exp\{-\gamma_j(\alpha)y\}\cos(\alpha x)d\alpha \tag{63}$$

where $A_j(\alpha)$ and $\gamma_j(\alpha)$ $(j = 1, 2, 3)$ are the unknown functions to be determined later. In Eq. (63), the summation has only three terms which give the exact solution. It can be shown that the solutions (h_x^e, h_y^e, h_z^e) satisfying Eqs. (58) are given by

$$\left.\begin{array}{l} h_x^e = \dfrac{2}{\pi}\displaystyle\sum_{j=1}^{3}\int_0^\infty a_{1j}(\alpha)\exp\{-\gamma_j(\alpha)y\} \\ \qquad \times \exp[-\{\alpha^2 - \gamma_j^2(\alpha)\}^{1/2}z]\sin(\alpha x)d\alpha \ (z \ge h) \\ \qquad = \dfrac{2}{\pi}\displaystyle\sum_{j=1}^{3}\int_0^\infty a_{2j}(\alpha)\exp\{-\gamma_j(\alpha)y\} \\ \qquad \times \exp[\{\alpha^2 - \gamma_j^2(\alpha)\}^{1/2}z]\sin(\alpha x)d\alpha (z \le -h) \end{array}\right\} \tag{64}$$

$$\left.\begin{array}{l} h_y^e = \dfrac{2}{\pi}\displaystyle\sum_{j=1}^{3}\int_0^\infty b_{1j}(\alpha)\exp\{-\gamma_j(\alpha)y\} \\ \qquad \times \exp[-\{\alpha^2 - \gamma_j^2(\alpha)\}^{1/2}z]\cos(\alpha x)d\alpha (z \ge h) \\ \qquad = \dfrac{2}{\pi}\displaystyle\sum_{j=1}^{3}\int_0^\infty b_{2j}(\alpha)\exp\{-\gamma_j(\alpha)y\} \\ \qquad \times \exp[\{\alpha^2 - \gamma_j^2(\alpha)\}^{1/2}z]\cos(\alpha x)d\alpha (z \le -h) \end{array}\right\} \tag{65}$$

$$\left.\begin{array}{l} h_z^e = \dfrac{2}{\pi}\displaystyle\sum_{j=1}^{3}\int_0^\infty c_{1j}(\alpha)\exp\{-\gamma_j(\alpha)y\} \\ \qquad \times \exp[-\{\alpha^2 - \gamma_j^2(\alpha)\}^{1/2}z]\cos(\alpha x)d\alpha (z \ge h) \\ \qquad = \dfrac{2}{\pi}\displaystyle\sum_{j=1}^{3}\int_0^\infty c_{2j}(\alpha)\exp\{-\gamma_j(\alpha)y\} \\ \qquad \times \exp[\{\alpha^2 - \gamma_j^2(\alpha)\}^{1/2}z]\cos(\alpha x)d\alpha (z \le -h) \end{array}\right\} \tag{66}$$

where the unknowns $a_{1j}(\alpha)$, $a_{2j}(\alpha)$, $b_{1j}(\alpha)$, $b_{2j}(\alpha)$, $c_{1j}(\alpha)$, and $c_{2j}(\alpha)$ $(j = 1, 2, 3)$ are to be evaluated from the boundary conditions (60) at $|z| = h$.

Making use of Eqs. (62), (64)–(66), and (60) renders the magnetic intensity components $h_x(x, y, \pm h, t)$, $h_y(x, y, \pm h, t)$, $f(x, y, t)$

$$\left.\begin{array}{l} h_x(x, y, \pm h, t) = \pm\dfrac{2}{\pi}\displaystyle\sum_{j=1}^{3}\int_0^\infty \frac{\alpha}{\{\alpha^2 - \gamma_j^2(\alpha)\}^{1/2}} c_{1j}(\alpha)\exp\{-\gamma_j(\alpha)y\} \times \exp[-\{\alpha^2 - \gamma_j^2(\alpha)\}^{1/2}h]\sin(\alpha x)d\alpha \\ h_y(x, y, \pm h, t) = \pm\dfrac{2}{\pi}\displaystyle\sum_{j=1}^{3}\int_0^\infty \frac{\gamma_j(\alpha)}{\{\alpha^2 - \gamma_j^2(\alpha)\}^{1/2}} c_{1j}(\alpha)\exp\{-\gamma_j(\alpha)y\} \times \exp[-\{\alpha^2 - \gamma_j^2(\alpha)\}^{1/2}h]\cos(\alpha x)d\alpha \\ f(x, y, t) = \dfrac{2}{\pi}\displaystyle\sum_{j=1}^{3}\int_0^\infty c_{1j}(\alpha)\exp\{-\gamma_j(\alpha)y\} \times \exp[-\{\alpha^2 - \gamma_j^2(\alpha)\}^{1/2}h]\cos(\alpha x)d\alpha. \end{array}\right\} \tag{67}$$

Downloaded 04 May 2010 to 171.66.16.34. Redistribution subject to ASME license or copyright; see http://www.asme.org/terms/Terms_Use.cfm

Substituting Eqs. (63) and (67) into Eqs. (55) and (56), we also obtain the functions $\varphi(x, y)$ and $\psi(x, y)$ as

$$\varphi(x, y) = -\frac{1}{\sigma}\frac{2}{\pi}\sum_{j=1}^{3}\int_0^\infty \gamma_j(\alpha)\frac{\{\alpha^2 - \gamma_j^2(\alpha)\}^{1/2}h + 1}{\{\alpha^2 - \gamma_j^2(\alpha)\}^{1/2}h} \times c_{1j}(\alpha)\exp\{-\gamma_j(\alpha)y\} \times \exp[-\{\alpha^2 - \gamma_j^2(\alpha)\}^{1/2}h]\cos(\alpha x)d\alpha - i\omega\kappa_0 H_0\frac{2}{\pi}\sum_{j=1}^{3}\int_0^\infty A_j(\alpha) \times \exp\{-\gamma_j(\alpha)y\}\cos(\alpha x)d\alpha \quad (68)$$

$$\psi(x, y) = \frac{1}{\sigma}\frac{2}{\pi}\sum_{j=1}^{3}\int_0^\infty \alpha\frac{\{\alpha^2 - \gamma_j^2(\alpha)\}^{1/2}h + 1}{\{\alpha^2 - \gamma_j^2(\alpha)\}^{1/2}h} c_{1j}(\alpha) \times \exp\{-\gamma_j(\alpha)y\} \times \exp[-\{\alpha^2 - \gamma_j^2(\alpha)\}^{1/2}h]\sin(\alpha x)d\alpha. \quad (69)$$

Eq. (54) leads to the determination of $c_{1j}(\alpha)$ as

$$c_{1j}(\alpha) = \frac{i\omega\sigma\kappa_0 H_0\gamma_j(\alpha)\{\alpha^2 - \gamma_j^2(\alpha)\}^{1/2}h}{\{\alpha^2 - \gamma_j^2(\alpha)\}[\{\alpha^2 - \gamma_j^2(\alpha)\}^{1/2}h + 1]} \times \exp[\{\alpha^2 - \gamma_j^2(\alpha)\}^{1/2}h]A_j(\alpha) \quad (j = 1, 2, 3). \quad (70)$$

From Eqs. (68) and (70), we obtain

$$\varphi(x, y) = -i\omega\kappa_0 H_0\frac{2}{\pi}\sum_{j=1}^{3}\int_0^\infty \frac{\gamma_j^2(\alpha)}{\alpha^2 - \gamma_j^2(\alpha)} \times A_j(\alpha)\exp\{-\gamma_j(\alpha)y\}\cos(\alpha x)d\alpha - i\omega\kappa_0 H_0\frac{2}{\pi}\sum_{j=1}^{3}\int_0^\infty A_j(\alpha) \times \exp\{-\gamma_j(\alpha)y\}\cos(\alpha x)d\alpha. \quad (71)$$

Substituting Eqs. (63) and (71) into Eq. (57) yields

$$\gamma_j^6(\alpha) - 3\alpha^2\gamma_j^4(\alpha) + \left(3\alpha^4 + \frac{a_0}{D}\right)\gamma_j^2(\alpha) + \frac{2\rho h}{D}\omega^2\alpha^2 - \alpha^6 = 0 \quad (72)$$

where $a_0 = -2i\omega h\sigma(\kappa_0 H_0)^2 - 2\rho h\omega^2$. Substituting Eq. (63) into Eq. (57), we obtain $\varphi(x, y)$ as

$$\varphi(x, y) = \frac{D}{2h\sigma\kappa_0 H_0}\frac{2}{\pi}\sum_{j=1}^{3}\int_0^\infty [\{\alpha^2 - \gamma_j^2(\alpha)\}^2 - k^4] \times A_j(\alpha)\exp\{-\gamma_j(\alpha)y\}\cos(\alpha x)d\alpha. \quad (73)$$

From Eqs. (54) and (73), we also obtain $\psi(x, y) = e_y(x, y)$ as

$$e_y(x, y) = -\frac{-D}{2h\sigma\kappa_0 H_0}\frac{2}{\pi}\sum_{j=1}^{3}\int_0^\infty \frac{1}{\alpha}[\{\alpha^2 - \gamma_j^2(\alpha)\}^2 - k^4] \times \gamma_j(\alpha)A_j(\alpha)\exp\{-\gamma_j(\alpha)y\}\sin(\alpha x)d\alpha. \quad (74)$$

The boundary conditions (51) and (52) render

$$\sum_{j=1}^{3} g_j(\alpha)\gamma_j(\alpha)A_j(\alpha) = 0 \quad (75)$$

$$\sum_{j=1}^{3} h_j(\alpha)\gamma_j(\alpha)A_j(\alpha) = 0 \quad (76)$$

in which $g_j(\alpha)$ and $h_j(\alpha)$ are known as

$$\left.\begin{aligned} g_j(\alpha) &= -(2 - \nu)\alpha^2 + \gamma_j^2(\alpha) \quad (j = 1, 2, 3) \\ h_j(\alpha) &= \{\alpha^2 - \gamma_j^2(\alpha)\}^2 - k^4 \quad (j = 1, 2, 3). \end{aligned}\right\} \quad (77)$$

Application of the boundary conditions (53) gives rise to a pair of dual integral equations:

$$\left.\begin{aligned} \int_0^\infty B(\alpha)F(\alpha)\cos(\alpha x)d\alpha &= \frac{\pi}{2}\frac{M_{iy}}{D} \quad (0 \le x < a) \\ \int_0^\infty B(\alpha)\cos(\alpha x)d\alpha &= 0 \quad (a \le x < \infty) \end{aligned}\right\} \quad (78)$$

in which M_{iy} and $F(\alpha)$ are known as

$$M_{iy} = Dw_{i0}k^2 \quad (79)$$

$$F(\alpha) = \frac{1}{\alpha}\frac{G_1(\alpha) - G_2(\alpha) - G_3(\alpha)}{T_1(\alpha)T_2(\alpha) - S_2(\alpha)T_2(\alpha) - S_1(\alpha)T_1(\alpha)} \quad (80)$$

$$\left.\begin{aligned} G_1(\alpha) &= \{\gamma_1^2(\alpha) - \nu\alpha^2\}\frac{T_1(\alpha)T_2(\alpha)}{\gamma_1(\alpha)} \\ G_2(\alpha) &= \{\gamma_1^2(\alpha) - \nu\alpha^2\}\frac{S_2(\alpha)T_2(\alpha)}{\gamma_2(\alpha)} \\ G_3(\alpha) &= \{\gamma_1^2(\alpha) - \nu\alpha^2\}\frac{S_1(\alpha)T_1(\alpha)}{\gamma_3(\alpha)} \end{aligned}\right\} \quad (81)$$

$$\left.\begin{aligned} S_1(\alpha) &= h_1(\alpha) - \frac{h_2(\alpha)}{g_2(\alpha)}g_1(\alpha) \\ S_2(\alpha) &= h_1(\alpha) - \frac{h_3(\alpha)}{g_3(\alpha)}g_1(\alpha) \\ T_1(\alpha) &= h_2(\alpha) - \frac{h_3(\alpha)}{g_3(\alpha)}g_2(\alpha) \\ T_2(\alpha) &= h_3(\alpha) - \frac{h_2(\alpha)}{g_2(\alpha)}g_3(\alpha). \end{aligned}\right\} \quad (82)$$

The unknown $B(\alpha)$ is related to $A_j(\alpha)$ $(j = 1, 2, 3)$ as follows:

$$B(\alpha) = \sum_{j=1}^{3}\gamma_j(\alpha)A_j(\alpha). \quad (83)$$

The second of Eqs. (78) would be satisfied if $B(\alpha)$ is taken as (Copson, 1961)

$$B(\alpha) = \frac{\pi}{2}\frac{M_{iy}}{DF_1}a^2\int_0^1 \xi^{1/2}\Phi_1(\xi)J_0(a\alpha\xi)d\xi \quad (84)$$

where $J_0(\ \ )$ is the zero-order Bessel function of the first kind, $\Phi_1(\xi)$ is the unknown function to be determined later, and

$$F_1 = \lim_{\alpha\to\infty} F(\alpha). \quad (85)$$

Inserting Eq. (84) into the first of Eqs. (78) yields a Fredholm integral equation of the second kind:

$$\Phi_1(\xi) + \int_0^1 K_1(\xi, \eta)\Phi_1(\eta)d\eta = \xi^{1/2} \quad (86)$$

where the kernel $K_1(\xi, \eta)$ is given by

$$K_1(\xi, \eta) = (\xi\eta)^{1/2}\int_0^\infty \alpha\left[\frac{1}{F_1}F(\alpha/a) - 1\right]J_0(\alpha\xi)J_0(\alpha\eta)d\alpha. \quad (87)$$

The moment intensity factor is defined by

Downloaded 04 May 2010 to 171.66.16.34. Redistribution subject to ASME license or copyright; see http://www.asme.org/terms/Terms_Use.cfm

Table 1 Material properties of gaphite

Material	Density ρ (kg/m^3)	Electrical conductivity σ (mho/m)	Shear modulus μ (N/m^2)
Graphite	2250	1.25×10^5	1.96×10^9

$$K_I = \lim_{x \to a^+} \{2\pi(x-a)\}^{1/2} M_{yy}(x, 0, t)$$

$$= M_0 \left(\frac{k}{k_1}\right)^2 (\pi a)^{1/2} \Phi_1(1) = M_0 M_2 (\pi a)^{1/2} \Phi_1(1) \quad (88)$$

in which $M_0 = Dw_{i0}k_1^2$ and $M_2 = (k/k_1)^2$. Keep in mind that the factor $\exp(-i\omega t)$ has been suppressed. The $1/(x-a)^{1/2}$ type of singularity for the magneto-elastic moments is the same as that in the classical case.

Discussion of Results

The elastodynamic plate solution (Sih and Chen, 1977) is recovered when the magnetic field tends to zero. In the limit as $\omega \to 0$, the corresponding static solution of $K_I = M_0(\pi a)^{1/2}$ is obtained. The considered conductor is graphite. The material properties are given in Table 1. Computed are the numerical values of $\Phi_1(1)$ in Eq. (86) for $\nu = 0.3$. The ratio k/k_1 in Eq. (88) is known from ω in Eq. (46) which can be further reduced to

$$(k/k_1)^4 = \frac{2i\Gamma_h}{\pi(\omega/\omega_0)} + 1 \quad (89)$$

in which $\Gamma_h = h_c c_2 h \sigma \kappa_0$, $h_c = \kappa_0 H_0^2/\mu$, $\omega_0 = \pi c_2/2h$ is the cut-off frequency and $c_2 = (\mu/\rho)^{1/2}$ is the shear wave speed. The normalized magnetic field of $\Gamma_h = 0.0$, 0.005, 0.01, and 0.02 ($c_2 h \sigma \kappa_0 = 0.5$) corresponds, respectively, to magnetic induction $B_0 = \kappa_0 H_0 = 0.0$, 5, 7, and 10T (tesla).

Based on the above information, a plot of the normalized moment intensity factor $|K_I/M_0(\pi a)^{1/2}|$ is given in Fig. 2 for the ratio $a/h = 5$ and four different values of Γ_h mentioned earlier. The dashed curve obtained for the case of $\Gamma_h = 0.0$ coincides with the purely elastic case. The quantity $|K_I/M_0(\pi a)^{1/2}|$ for $\Gamma_h = 0.0$ decays as the frequency increases. As the two curves for $\Gamma_h \neq 0.0$ possess higher amplitude than that for $\Gamma_h = 0.0$, the magnetic field is seen to increase the local moment with increasing Γ_h. Such an effect dies out at high frequency. Figure 3 shows the result for the ratio $a/h = 10$. The same gross effect is observed. The determination of the moment intensity factor K_I requires the solution of the function $\Phi_1(\xi)$ and the ratio k/k_1, and the normalized moment intensity factor is given by $K_I/M_0(\pi a)^{1/2} = (k/k_1)^2 \Phi_1(1) = \{2i\Gamma_h/\pi(\omega/\omega_0) + 1\}^{1/2} \Phi_1(1)$ which has a singularity when the frequency approaches zero. When there is no magnetic field $\Gamma_h = 0$, there is no singularity. Note that K_I approaches zero as $\omega/\omega_0 \to 0$, since the coefficient $M_0 M_2 = Dw_{i0}k^2 = Dw_{i0}\{(2\rho h/D)\omega_0(2i\Gamma_h/\pi + \omega/\omega_0)(\omega/\omega_0)\}^{1/2}$ in Eq. (88) is zero for $\omega/\omega_0 = 0$. The same data for $|K_I/M_0(\pi a)^{1/2}|$ is plotted against Γ_h in Figs. 4 and 5. Note that $|K_I/M_0(\pi a)^{1/2}|$ approaches unity as $\omega/\omega_0 \to 0$ at $\Gamma_h = 0.0$ and tends to increase with increasing Γ_h.

In conclusion, evaluated in this work is the amplification of the moment intensity factor of a through crack in a thin plate subjected to a steady-state magnetic field normal to the crack and an incident flexural wave. A quasistatic electromagnetic field is assumed for the plate and classical plate bending theory

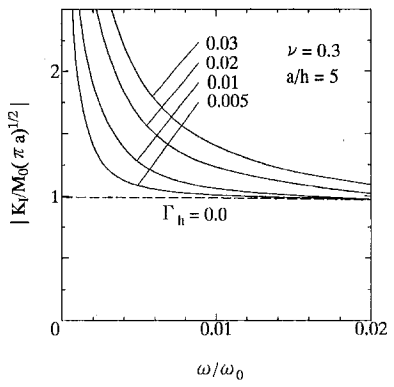


Fig. 2 Dynamic bending moment intensity factor $|K_I/M_0(\pi a)^{1/2}|$ versus ω/ω_0 ($a/h = 5$)

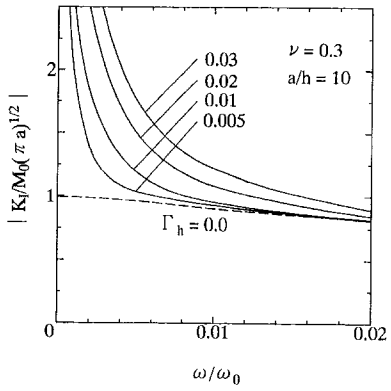


Fig. 3 Dynamic bending moment intensity factor $|K_I/M_0(\pi a)^{1/2}|$ versus ω/ω_0 ($a/h = 10$)

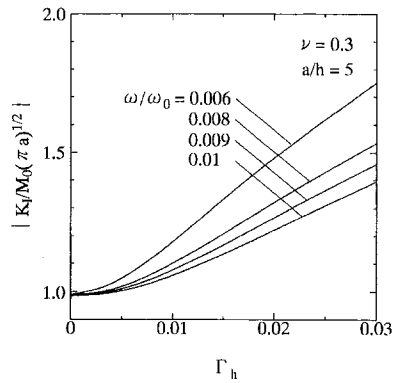


Fig. 4 Dynamic bending moment intensity factor $|K_I/M_0(\pi a)^{1/2}|$ versus Γ_h ($a/h = 5$)

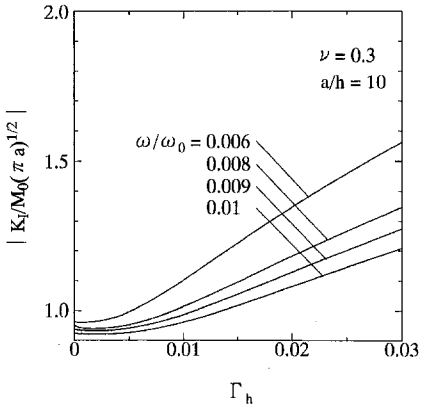


Fig. 5 Dynamic bending moment intensity factor $|K_I/M_0(\pi a)^{1/2}|$ versus Γ_h ($a/h = 10$)

Downloaded 04 May 2010 to 171.66.16.34. Redistribution subject to ASME license or copyright; see http://www.asme.org/terms/Terms_Use.cfm

is extended to include dynamic magneto-elastic effects. Significant increase in the local moment intensity factor occurs at low wave frequency and the magnetic field effect dies out gradually as the frequency is increased. All results are based on linear magneto-elasticity assuming a coupling between the induced current and deformation.

References

Ambartsumian, S. A., Bagdasarian, G. E., and Belubekian, M. V., 1971, "On the Three-Dimensional Problem of Magnetoelastic Plate Vibrations," *Journal of Applied Mathematics and Mechanics (PMM),* Vol. 35, pp. 184–195.

Ambartsumian, S. A., Bagdasarian, G. E., and Belubekian, M. V., 1975, "On the Equations of Magnetoelastic Thin Plate," *Journal of Applied Mathematics and Mechanics (PMM),* Vol. 39, pp. 922–926.

Copson, E. T., 1961, "On Certain Dual Integral Equations," *Proceedings of Glasgow Mathematical Association,* Vol. 5, pp. 19–24.

Dunkin, J. W., and Eringen, A. C., 1963, "On the Propagation of Waves in an Electromagnetic Elastic Solid," *International Journal of Engineering Science,* Vol. 1, pp. 461–495.

Fung, Y. C., 1965, *Foundation of Solid Mechanics,* Prentice-Hall, Englewood Cliffs, NJ.

Shindo, Y., 1982, "Sudden Twisting of an Infinite Elastic Conductor with a Penny-Shaped Crack in a Constant Axial Magnetic Field," *ZAMM,* Vol. 62, pp. 599–607.

Shindo, Y., Tamura, H., and Horiguchi, K., 1989, "Transient Response of Cracked Materials in a Strong Magnetic Field," *Fusion Engineering and Design,* Vol. 9, pp. 81–85.

Shindo, Y., 1991, "Magneto-Mechanical Behavior of First Wall Materials," *Fusion Engineering and Design,* Vol. 16, pp. 317–322.

Shindo, Y., Ohnishi, I., and Suzuki, S., 1993, "Dynamic Singular Moments in a Perfectly Conducting Plate with a Through Crack under a Magnetic Field," *Mechanics of Electromagnetic Materials and Structures,* J. S. Lee, G. A. Maugin, and Y. Shindo, eds., ASME, AMD-Vol. 161, MD-Vol. 42, pp. 87–97.

Sih, G. C., and Chen, E. P., 1977, "Dynamic Analysis of Cracked Plates in Bending and Extension," *Plates and Shells with Cracks* (Mechanics of Fracture 3), G. C. Sih, ed., Noordhoff, Leyden, pp. 231–272.

Sneddon, I. N., 1951, *Fourier Transforms,* McGraw-Hill, New York.

Downloaded 04 May 2010 to 171.66.16.34. Redistribution subject to ASME license or copyright; see http://www.asme.org/terms/Terms_Use.cfm

Viscoelastic Model of Finitely Deforming Rubber and Its Finite Element Analysis

Seung Jo Kim
Professor.

Kyeong Su Kim[1]

Jin Yeon Cho
Research Assistant.

Department of Aerospace Engineering,
Seoul National University,
San 56-1, Shillim-Dong, Kwanak-Ku,
Seoul 151-742, Republic of Korea

A viscoelastic model of finitely deforming rubber is proposed and its nonlinear finite element approximation and numerical simulation are carried out. This viscoelastic model based on continuum mechanics is an extended model of Johnson and Quigley's one-dimensional model. In the extended model, the kinematic configurations and measures based on continuum mechanics are rigorously defined and by using these kinematic measures, constitutive relations are introduced. The obtained highly nonlinear equations are approximated by the nonlinear finite element method, where a mixture of the total and updated Lagrangian descriptions is used. To verify the theory and the computer code, uniaxial stretch tests are simulated for various stretch rates and compared with actual experiments. As a practical example, an axisymmetric rubber plate under various time-dependent pressure loading conditions is analyzed.

Introduction

Rubber-like materials have been increasingly used in various engineering applications, like the vibration-isolation devices, energy-storage devices, tires and adhesive joint, etc. and recently in the aerospace application like the O-ring (Salita 1987) and the flexseal. The flexseal is the major component of the TVC (Thrust Vector Control) System which is equipped in a large rocket booster. (Prins et al., 1992).

Generally, rubber-like materials show the incompressible hyperelastic behavior and often exhibit time-dependent behavior due to their inherent viscous effects. To describe these viscoelastic behavior, many theories have been proposed over the years. Treloar (1975) observed relaxation and creep effects during the uniaxial, biaxial, and simple shear tests. The earlier work of Green and Tobolsky (1946) demonstrated that the classical relaxation theories can be expressed in terms of the molecular structure theory and the chemical rate theory. And they obtained a time-dependent behavior from the sum of an elastic component and a strain-history-dependent component. Bernstein et al. (1963) proposed the BKZ elastic-fluid model. McGuirt and Lianis (1970) observed isothermal and nonisothermal viscoelastic behaviors of a SBR (Stylene-Butadiene-Rubber) and proposed a history-integral constitutive model. Goldberg and Lianis (1970) showed that a history-integral constitutive model is equivalent to a BKZ elastic-fluid model. A different approach was taken by Christensen (1970) who emphasized on the viscoelastic generalization of the kinetic theory of rubber elasticity applicable to the stress-imposed problems. He showed that the type and degree of nonlinearity is very different under relaxation conditions from those involved during creep conditions. Keren, Partom, and Rosenberg (1984) presented the PH model (Phases Model), which is a type of generalized Maxwell model with linear springs and nonlinear dashpots. They implemented it into a two-dimensional finite difference code and carried out the numerical simulation of compression tests. Recently, Johnson and Quigley (1992) proposed a phenomenological one-dimensional model which is referred to as the JQ model in this paper. Material constants of the JQ model can be easily determined by the uniaxial stretch-relaxation test. The JQ model can predict step-strain relaxation test accurately and be easily implemented by conventional numerical techniques. The JQ model has many possibilities in application of the model. However, in spite of these advantages, the JQ model is not yet established as a constitutive model based on rigorous continuum mechanics. The finite viscoelasticity theory needs rigorous kinematical definitions. Since rubber-like material suffers extreme finite deformation, its kinematics should be firmly described. Otherwise, mechanical meaning of motion is apt to be misunderstood and as a result, the finite viscoelastic behaviour of rubber-like materials cannot be properly depicted.

In this work, the foundation based on continuum mechanics is provided for the phenomenological JQ model and its efficient finite element formulation is proposed. The basic contents are as follows:

(i) Kinematics: Kinematical configurations in this work are identified and kinematical measures (e.g., deformation gradients, strain measures) based on continuum mechanics are introduced.

(ii) Constitutive equations: Elastic state law and flow rule are stated. To satisfy the incompressible condition, a penalty-type Mooney-Rivlin energy function is adopted, as in Fried and Johnson (1988) and Johnson and Quigley (1992). It is assumed that there exists an elastic potential which describes the recoverable energy at each time. Under this assumption, elastic state law is derived from the elastic potential. The proposed flow rule is reduced to the JQ flow model in one-dimensional problems.

(iii) Variational formulation and finite element approximation: A mixed Lagrangian description is stated in this section where a mixture of total and updated Lagrangian descriptions is used.

(iv) Numerical example: To verify this work, the simulated results are compared with measured data in McGuirt and Lianis (1970). The comparison shows good agreement. For a practical example, a pressurized rubber plate is analyzed.

Kinematics

In accordance with very large viscoelastic deformations, a new kinematical configuration is introduced. In this study, three kinematical configurations are used. They are reference, current,

[1] Currently Engineer of Samsung Aerospace Company.

Contributed by the Applied Mechanics Division of THE AMERICAN SOCIETY OF MECHANICAL ENGINEERS for publication in the ASME JOURNAL OF APPLIED MECHANICS.

Discussion on the paper should be addressed to the Technical Editor, Professor Lewis T. Wheeler, Department of Mechanical Engineering, University of Houston, Houston, TX 77204-4792, and will be accepted until four months after final publication of the paper itself in the ASME JOURNAL OF APPLIED MECHANICS.

Manuscript received by the ASME Applied Mechanics Division, Aug. 29, 1996; final revision, Apr. 10, 1997. Associate Technical Editor: I. M. Daniel.

Copyright © 1997 by ASME

Downloaded 04 May 2010 to 171.66.16.34. Redistribution subject to ASME license or copyright; see http://www.asme.org/terms/Terms_Use.cfm

and virtual viscoconfigurations. In developing this work, it is assumed that each particle of an actual body consists of an internal elastic part and an internal viscoelastic part, which is similar to the three-parameter Maxwell model in Caddell (1980) as shown in Fig. 1. Compatibility condition requires that three deformations (i.e., actual deformation, deformation of internal elastic part, deformation of internal viscoelastic part) coincide with one another. Deformation of an internal viscoelastic part is decomposed into pure viscous deformation and elastic deformation through the virtual viscoconfiguration as in Fig. 2. This is similar to the method adopted in finite elastoplasticity. Physically, virtual viscoconfiguration corresponds to the pure viscously deformed shape of an internal viscoelastic part.

Material body B moves through Euclidean space R^3. To trace the motion of body B we establish an absolutely fixed frame of reference. Then each point X in the body B can be identified by their corresponding reference position $\mathbf{X}$ through the map

$$\chi_o : B \to R^3$$
$$\mathbf{X} = \chi_o(X). \tag{1}$$

The image of this mapping $\chi_o(B)$ is denoted by B_o, which is called the reference configuration. The spatial position $\mathbf{x}$ of a particle X at time t is given by a relation as

$$\mathbf{x} = \chi(\mathbf{X}, t) = \mathbf{X} + \mathbf{u}$$
$$\mathbf{X} \in B_o, \quad t \geq 0 \tag{2}$$

where χ is a continuous invertible map from B_o into R^3 and $\mathbf{u}$ denotes a displacement. The image $\chi(\mathbf{X}, t)$ is called the current configuration B_t at time t. And χ also can be understood as a deformation of reference configuration into current configuration. Since the motion of an internal elastic part is equivalent to the actual motion, Eq. (2), corresponding to an actual motion, can be applied directly to the motion of an internal elastic part. So the kinematical relation of an elastic part can be described by Eq. (2) for an actual motion of body.

Similarly, we introduce a virtual viscoconfiguration. To describe the viscous motion rigorously, viscous deformation must be precisely incorporated in kinematics. The pure viscous motion can be identified by a relation as

$$\mathbf{x}_L = \chi_L(\mathbf{X}, t) = \mathbf{X} + \mathbf{u}_L$$
$$\mathbf{X} = B_o, \quad t \geq 0 \tag{3}$$

where χ_L is a continuous invertible map from B_o into R^3 and $\mathbf{u}_L$ denotes a displacement for pure viscous motion. The image $\chi_L(\mathbf{X}, t)$ is called the virtual viscoconfiguration B_{L_t} at time t. The virtual viscoconfiguration can be imagined roughly and conceptually as a stress-free configuration of the internal viscoelastic part in a three-parameter Maxwell model. And a mapping from B_{L_t} to B_t can be determined under given χ and χ_L. At a certain time, the corresponding motion is as follows:

$$\mathbf{x} = \chi(\mathbf{X}, t) = \hat{\chi}(\chi_L(\mathbf{X}, t)). \tag{4}$$

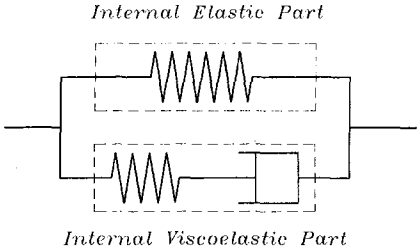


Fig. 1 Three-parameter Maxwell model

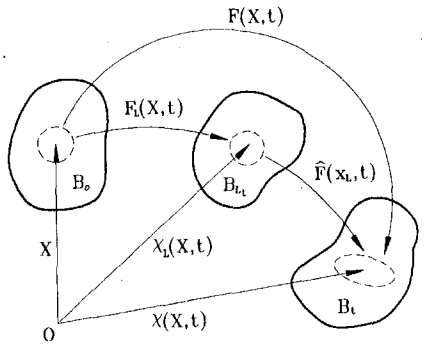


Fig. 2 Configurations in finite viscoelasticity

This motion is interpreted as an elastic deformation of an internal viscoelastic part and also can be considered in terms of displacements.

$$\mathbf{x} = \mathbf{x}_L + \hat{\mathbf{u}} = \mathbf{X} + \mathbf{u}_L + \hat{\mathbf{u}} \tag{5}$$

where $\hat{\mathbf{u}}$ denotes displacement for an elastic deformation of internal viscoelastic part.

From the defined configurations, deformation gradients can be obtained and used in measuring the local deformation. The actual deformation gradient is obtained by differentiation of current configuration with respect to reference configuration.

$$\mathbf{F} = \frac{\partial \mathbf{x}}{\partial \mathbf{X}} \tag{6}$$

It also describes the deformation of an internal elastic part. To locally describe the pure viscous motion of the internal viscoelastic part, a pure viscous deformation gradient is required. It is as follows:

$$\mathbf{F}_L = \frac{\partial \mathbf{x}_L}{\partial \mathbf{X}}. \tag{7}$$

The deformation of the virtual viscoconfiguration (i.e., elastic deformation of the internal viscoelastic part of a particle) is described by the following deformation gradient:

$$\hat{\mathbf{F}} = \frac{\partial \mathbf{x}}{\partial \mathbf{x}_L}. \tag{8}$$

And from Eqs. (6)–(8) the relation of deformation gradients can be expressed as

$$\mathbf{F} = \hat{\mathbf{F}}\mathbf{F}_L. \tag{9}$$

The above relation shows that the internal viscoelastic part of a particle is deformed through $\mathbf{F}_L$ (pure viscous motion) and $\hat{\mathbf{F}}$ (elastic motion). It should be remembered that the actual deformation is equal to the deformation of an internal viscoelastic part. This results in classical multiplicative decomposition which is generally adopted in finite elastoplasticity. But in this work, this decomposition has the physical meaning different from finite elastoplasticity. It means that deformation of the internal viscoelastic part is decomposed multiplicatively into the pure viscous deformation and the elastic deformation.

In this work, the following strain measures are defined in terms of deformation gradients:

$$\mathbf{E} = \tfrac{1}{2}(\mathbf{F}^T\mathbf{F} - \mathbf{I}) \tag{10}$$

$$\mathbf{E}_L = \tfrac{1}{2}(\mathbf{F}_L^T\mathbf{F}_L - \mathbf{I}) \tag{11}$$

$$\hat{\mathbf{E}} = \tfrac{1}{2}(\hat{\mathbf{F}}^T\hat{\mathbf{F}} - \mathbf{I}) \tag{12}$$

Downloaded 04 May 2010 to 171.66.16.34. Redistribution subject to ASME license or copyright; see http://www.asme.org/terms/Terms_Use.cfm

where $\mathbf{E}$ is the classical Green strain tensor and describes actual deformation. But other strain measures $\mathbf{E}_L$ and $\hat{\mathbf{E}}$ have some different physical meanings. In this framework, strain measures $\mathbf{E}_L$ and $\hat{\mathbf{E}}$ are not actual strains but virtual strains. They are pseudo-kinematic measures which have roles as internal variables. Conceptually $\mathbf{E}_L$ has the meaning of an imaginary pure viscous deformation and $\hat{\mathbf{E}}$ possesses the concept of elastic deformation of an internal viscoelastic part in the three-parameter Maxwell model. It should be noted that unlike $\mathbf{E}$ and $\mathbf{E}_L$, $\hat{\mathbf{E}}$ is not a Lagrange measure, since it can only be measured in the intermediate virtual viscoconfiguration but not in the reference configuration.

Constitutive Equations

Elastic State Law. Let us assume the existence of an elastic potential. The potential describes the recoverable energy storage at each time. To enforce the incompressibility condition by a penalty-type method, two modified Mooney-Rivlin energy density functions are used in the elastic potential as

$$W = W_E + J_L W_L, \tag{13}$$

where J_L denotes the determinant of $\mathbf{F}_L$ and W_E and W_L are two modified Mooney-Rivlin energy density functions. Their forms assume the following:

$$W_E = C_{E1}(I_1^{(E)} - 3I_3^{(E)^{1/3}}) + C_{E2}(I_2^{(E)} - 3I_3^{(E)^{2/3}}) + \frac{K_E}{2}(\ln I_3^{(E)})^2 \tag{14}$$

$$W_L = C_{L1}(I_1^{(L)} - 3I_3^{(L)^{1/3}}) + C_{L2}(I_2^{(L)} - 3I_3^{(L)^{2/3}}) + \frac{K_L}{2}(\ln I_3^{(L)})^2 \tag{15}$$

where $I_k^{(E)}$ and $I_k^{(L)}(1 \le k \le 3)$ are the invariants of $\mathbf{F}^T\mathbf{F}$ and $\hat{\mathbf{F}}^T\hat{\mathbf{F}}$, respectively. Cs and Ks are material constants. If a large number is chosen for the values of the bulk moduli K_E and K_L, a nearly incompressible condition can be satisfied. The Cauchy-Green deformation tensor $\mathbf{F}^T\mathbf{F}$ is a Lagrange measure, but $\hat{\mathbf{F}}^T\hat{\mathbf{F}}$ is not. Physically, $\hat{\mathbf{F}}^T\hat{\mathbf{F}}$ means the deformation of virtual viscoconfiguration.

The elastic state law is as follows:

$$\mathbf{S} = \frac{\partial W}{\partial \mathbf{E}} = \frac{\partial W_E}{\partial \mathbf{E}} + \frac{\partial J_L W_L}{\partial \mathbf{E}} \tag{16}$$

where $\mathbf{S}$ denotes the second Piola-Kirchhoff stress which is thermodynamically conjugate to the Green strain. Since W_L is a function of $\hat{\mathbf{E}}$ only (i.e., $\hat{\mathbf{F}}^T\hat{\mathbf{F}} = 2\hat{\mathbf{E}} - \mathbf{I}$) and J_L is independent of $\mathbf{E}$, it can be rewritten as

$$\mathbf{S} = \frac{\partial W}{\partial \mathbf{E}} = \frac{\partial W_E}{\partial \mathbf{E}} + J_L \frac{\partial W_L}{\partial \hat{\mathbf{E}}} \frac{\partial \hat{\mathbf{E}}}{\partial \mathbf{E}}. \tag{17}$$

And the relation of $\hat{\mathbf{E}}$ and $\mathbf{E}$ is obtained from Eqs. (10)–(12),

$$\hat{\mathbf{E}} = \mathbf{F}_L^{-T}(\mathbf{E} - \mathbf{E}_L)\mathbf{F}_L^{-1}. \tag{18}$$

Since $\mathbf{F}_L$ and $\mathbf{E}_L$ is independent of $\mathbf{E}$, the elastic state law is rewritten as follows:

$$\mathbf{S} = \frac{\partial W}{\partial \mathbf{E}} = \frac{\partial W_E}{\partial \mathbf{E}} + J_L \mathbf{F}_L^{-1} \frac{\partial W_L}{\partial \hat{\mathbf{E}}} \mathbf{F}_L^{-T}. \tag{19}$$

From the relation of the second Piola-Kirchhoff stress, the Cauchy stress $\boldsymbol{\sigma}$ can be derived.

$$\boldsymbol{\sigma} = J^{-1}\mathbf{F}\mathbf{S}\mathbf{F}^T = J^{-1}\mathbf{F}\frac{\partial W_E}{\partial \mathbf{E}}\mathbf{F}^T + \hat{J}^{-1}\hat{\mathbf{F}}\frac{\partial W_L}{\partial \hat{\mathbf{E}}}\hat{\mathbf{F}}^T \tag{20}$$

where J, $\hat{J}$ denote $\det \mathbf{F}$ and $\det \hat{\mathbf{F}}$, respectively. If the viscoelastic part in a particle is absent, W_L is zero. Therefore, the Cauchy stress $\boldsymbol{\sigma}_E$ for an elastic part only is reduced to the first term on the right-hand side of Eq. (20). Conversely, the Cauchy stress $\boldsymbol{\sigma}_L$ for the viscoelastic part is also obtained by the same method. It can be expressed by the second term on the right-hand side of Eq. (20). Hence it is understood that the total Cauchy stress is the summation of the Cauchy stresses induced from the elastic part and the viscoelastic part, and the elastic potential is the summation of the recoverable energy reserved in the elastic part and the viscoelastic part.

Flow Rule. From the phenomenological observation [Johnson and Quigley (1992)] of the stress relaxation test, a flow rule in three dimensions is proposed. The flow rule is written as

$$\frac{\partial \overline{W_L}}{\partial \hat{\mathbf{F}}^{-1}} = -\eta_L \frac{\partial^2 \overline{W_L}}{\partial \hat{\mathbf{F}}^{-1}\partial \hat{\mathbf{F}}^{-1}} : \left.\frac{d\hat{\mathbf{F}}^{-1}}{dt}\right|_{B_t \text{ fixed}} \tag{21}$$

where η_L denotes the damping coefficient and $\overline{W_L}$ assumes the form as follows:

$$\overline{W_L} = C_{L1}(\bar{I}_1^{(L)} - 3\bar{I}_3^{(L)^{1/3}}) + C_{L2}(\bar{I}_2^{(L)} - 3\bar{I}_3^{(L)^{2/3}}) + \frac{K_L}{2}(\ln \bar{I}_3^{(L)})^2 \tag{22}$$

where $\bar{I}_k^{(L)}(1 \le k \le 3)$ are invariants of $\hat{\mathbf{F}}^{-T}\hat{\mathbf{F}}^{-1}$. It is noted that in uniaxial stretch problems, the flow rule is reduced to the JQ flow model with the assumption of incompressibility.

Variational Formulation and Finite Element Approximation

We restrict ourselves to quasi-static problems where inertia force is neglected. In a referential description, the force equilibrium equation is written by the first Piola-Kirchhoff stress as follows:

$$\text{Div } \mathbf{T} + \mathbf{f}_o = \mathbf{0} \tag{23}$$

where $\mathbf{T}$ is the first Piola-Kirchhoff stress and $\mathbf{f}_o$ denotes the force per unit volume in the reference configuration. Using the principle of virtual work, the variational form of the equilibrium equation is reduced to

$$\int_{B_o} \delta\boldsymbol{\chi}(\text{Div } \mathbf{T} + \mathbf{f}_o) dV_o = 0 \tag{24}$$

where $\delta\boldsymbol{\chi}$ denotes any kinematically admissible variation in $\boldsymbol{\chi}$. By using the Green-Gauss divergence theorem with the relation of the first and the second Piola-Kirchhoff stresses as shown in Gurtin (1981), it can be changed to

$$\int_{B_o} \mathbf{S} : \mathbf{F}^T\delta\mathbf{F} dV_o = \int_{B_o} \mathbf{f}_o\delta\boldsymbol{\chi} dV_o + \int_{\partial B_o} \delta\boldsymbol{\chi}\mathbf{T}\mathbf{N} dA_o \tag{25}$$

where $\mathbf{N}$ is the outward unit normal vector in the reference configuration and $\mathbf{TN}$ is the traction force at the boundary of the reference configuration. For the displacement-based finite element approximation, Eq. (25) is rewritten in terms of displacements by the substitution of the elastic state law (17).

$$\int_{B_o} \frac{\partial W_E}{\partial \mathbf{E}} : \left(\mathbf{I} + \frac{\partial \mathbf{u}}{\partial \mathbf{X}}\right)^T \frac{\partial \delta\mathbf{u}}{\partial \mathbf{X}} dV_o + \int_{B_o} J_L \frac{\partial W_L}{\partial \hat{\mathbf{E}}} : \left(\mathbf{I} + \frac{\partial \hat{\mathbf{u}}}{\partial \mathbf{x}_L}\right)^T \frac{\partial \delta\mathbf{u}}{\partial \mathbf{X}} \frac{\partial \mathbf{X}}{\partial \mathbf{x}_L} dV_o = \int_{B_o} \mathbf{f}_o\delta\mathbf{u} dV_o + \int_{\partial B_o} \hat{\boldsymbol{\sigma}}\delta\mathbf{u} dA_o \tag{26}$$

Downloaded 04 May 2010 to 171.66.16.34. Redistribution subject to ASME license or copyright; see http://www.asme.org/terms/Terms_Use.cfm

where $\hat{\boldsymbol{\sigma}}$ denotes **TN**. The second integral term on the left-hand side of the above equation can be described in B_{L_t} by the change of variables. From the relations (5) and (7), $J_L dV_o$ is equal to dV_{L_t} and $\delta\mathbf{u} = \delta\mathbf{u}_L + \delta\hat{\mathbf{u}}$. Since the virtual viscoconfiguration $\boldsymbol{\chi}_L$ is determined from the flow rule, the integral domain expressed in B_{L_t} and $\mathbf{u}_L$ are determined. And, as a consequence, it is kinematically admissible that $\mathbf{u}_L$ is set to be fixed during the variation of $\mathbf{u}$ without loss of generality. Therefore, the variational form of the equilibrium equation at time t can be expressed in alternative form.

$$\int_{B_o} \frac{\partial W_E}{\partial \mathbf{E}} : \left(\mathbf{I} + \frac{\partial \mathbf{u}}{\partial \mathbf{X}}\right)^T \frac{\partial \delta\mathbf{u}}{\partial \mathbf{X}}\, dV_o + \int_{B_{L_t}} \frac{\partial W_L}{\partial \hat{\mathbf{E}}} : \left(\mathbf{I} + \frac{\partial \hat{\mathbf{u}}}{\partial \mathbf{x}_L}\right)^T \frac{\partial \delta\hat{\mathbf{u}}}{\partial \mathbf{x}_L}\, dV_{L_t} = \int_{B_o} \mathbf{f}_o \delta\mathbf{u}\, dV_o + \int_{\partial B_o} \hat{\boldsymbol{\sigma}}\delta\mathbf{u}\, dA_o \quad (27)$$

where $\delta\mathbf{u} = \delta\hat{\mathbf{u}}$. It is noted that in the alternative variational form, the total Lagrangian and the similar method of the updated Lagrangian formulation are used together. Through the alternative variational form, the finite element discretization is realized. We call this alternative variational form the mixed Lagrangian description formulation. The unknown displacement functions are interpolated by linear shape functions as follows:

$$\mathbf{u} = \psi_N(\mathbf{X})\mathbf{u}^N \quad (28)$$

$$\mathbf{u}_L = \psi_N(\mathbf{X})\mathbf{u}_L^N \quad (29)$$

$$\hat{\mathbf{u}} = \phi_N(\mathbf{x}_L)\hat{\mathbf{u}}^N \quad (30)$$

where $\psi_N(\mathbf{X}^K) = \delta_{NK}$ and $\phi_N(\mathbf{x}_L^K) = \delta_{NK}$. Then from $\delta\mathbf{u} = \delta\hat{\mathbf{u}}$ and Eqs. (28)–(30), the following relation is obtained:

$$\psi_N(\mathbf{X})\delta\mathbf{u}^N = \phi_N(\mathbf{X} + \psi_M(\mathbf{X})\mathbf{u}_L^M)\delta\hat{\mathbf{u}}^N. \quad (31)$$

Since $\mathbf{x}_L^K = \mathbf{X}^K + \psi_M(\mathbf{X}^K)\mathbf{u}_L^M$, at node K the above relation is reduced to

$$\delta\mathbf{u}^K = \delta\hat{\mathbf{u}}^K. \quad (32)$$

Therefore, the discretized equation can be written in component form as follows:

$$\int_{B_o} \frac{\partial W_E}{\partial E_{ij}} \frac{\partial \psi_N}{\partial X_j}\left(\delta_{ki} + u_k^M \frac{\partial \psi_M}{\partial X_i}\right)\delta u_k^N dV_o + \int_{B_{L_t}} \frac{\partial W_L}{\partial \hat{E}_{ij}} \frac{\partial \phi_N}{\partial x_{L_j}}\left(\delta_{ki} + \hat{u}_k^M \frac{\partial \phi_M}{\partial x_{L_i}}\right)\delta u_k^N dV_{L_t} = \int_{B_o} f_{o_k}\psi_N \delta u_k^N dV_o + \int_{\partial B_o} \hat{\sigma}_k \psi_N \delta u_k^N dA_o, \quad \forall \delta u_k^N. \quad (33)$$

For node N and displacement k, it can be simplified in a similar way in Oden (1972).

$$\int_{B_o} \frac{\partial W_E}{\partial u_k^N} dV_o + \int_{B_{L_t}} \frac{\partial W_L}{\partial \hat{u}_k^N} dV_{L_t} = \int_{B_o} f_{o_k}\psi_N \mathrm{d}V_o + \int_{\partial B_o} \hat{\sigma}_k \psi_N dA_o \quad (34)$$

The resulting discretized equation can be solved by the Newton-Raphson method via the incremental method. In the application of the Newton-Raphson method, it should be noted that $\partial \hat{u}_k^N / \partial u_k^N$ is equal to the identity.

In the conventional integration scheme of the flow rule, the evolved field values are obtained at gauss points. However, in

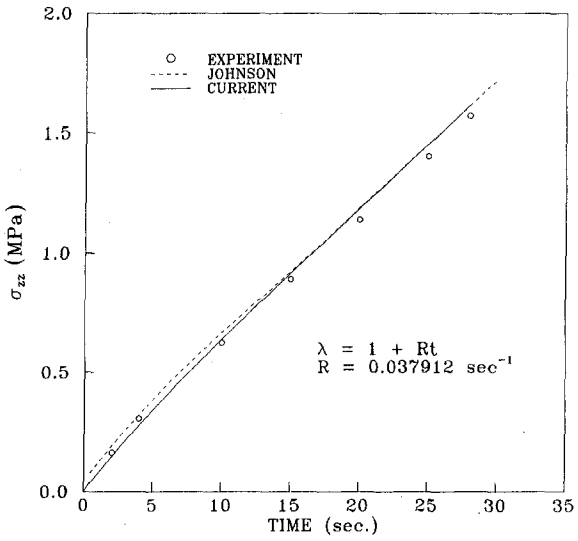


Fig. 3(*a*)

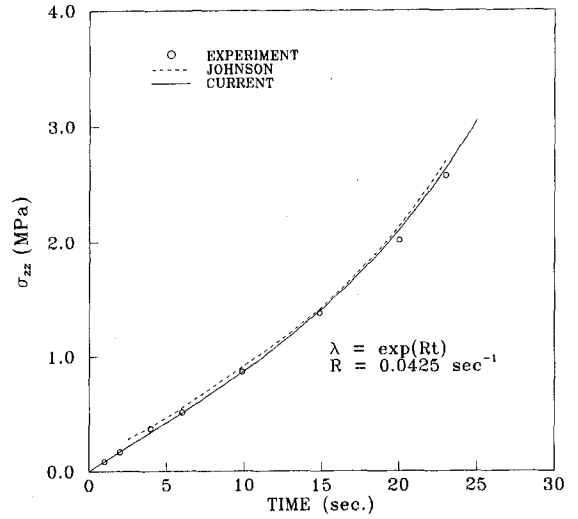


Fig. 3(*b*)

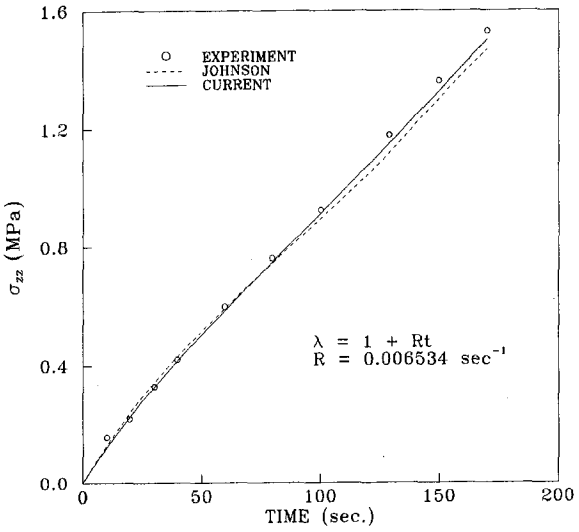


Fig. 3(*c*)

Fig. 3 The comparison of the predicted results and the measure data for uniaxial stretch tests at various stretch rates (λ is stretch ratio)

Downloaded 04 May 2010 to 171.66.16.34. Redistribution subject to ASME license or copyright; see http://www.asme.org/terms/Terms_Use.cfm

this work, a different approach is adopted in the time integration of the flow rule to obtain directly the virtual viscoconfiguration. The flow rule is recast to variational form as follows:

$$\int_{B_t} \frac{\partial \overline{W_L}}{\partial \hat{\mathbf{F}}^{-1}} : \delta \hat{\mathbf{F}}^{-1} dV_t = -\eta_L \int_{B_t} \left(\frac{\partial^2 \overline{W_L}}{\partial \hat{\mathbf{F}}^{-1} \partial \hat{\mathbf{F}}^{-1}} : \left. \frac{d\hat{\mathbf{F}}^{-1}}{dt} \right|_{B_t \text{ fix}} \right) : \delta \hat{\mathbf{F}}^{-1} dV_t. \quad (35)$$

It is noted that the current configuration $\mathbf{x}$ is fixed in variation and time differentiation. For simplicity, the intermediate displacement $\tilde{\mathbf{u}} = \mathbf{u}_L - \mathbf{u}$ is used. Then the following relations are obtained:

$$\hat{\mathbf{F}}^{-1} = \frac{\partial \mathbf{x}_L}{\partial \mathbf{x}} = \mathbf{I} + \frac{\partial \tilde{\mathbf{u}}}{\partial \mathbf{x}} \quad (36)$$

$$\delta \hat{\mathbf{F}}^{-1} = \frac{\partial \delta \mathbf{x}_L}{\partial \mathbf{x}} = \frac{\partial \delta \tilde{\mathbf{u}}}{\partial \mathbf{x}} \quad (37)$$

$$\left. \frac{d\hat{\mathbf{F}}^{-1}}{dt} \right|_{B_t \text{ fix}} = \frac{\partial}{\partial \mathbf{x}} \left(\frac{d\tilde{\mathbf{u}}}{dt} \right). \quad (38)$$

In terms of displacement $\tilde{\mathbf{u}}$, the variational form of the flow rule is rewritten as

$$\int_{B_t} \frac{\partial \overline{W_L}}{\partial \hat{\mathbf{F}}^{-1}} : \frac{\partial \delta \tilde{\mathbf{u}}}{\partial \mathbf{x}} dV_t = -\eta_L \int_{B_t} \left(\frac{\partial^2 \overline{W_L}}{\partial \hat{\mathbf{F}}^{-1} \partial \hat{\mathbf{F}}^{-1}} : \frac{\partial}{\partial \mathbf{x}} \left(\frac{d\tilde{\mathbf{u}}}{dt} \right) \right) : \frac{\partial \delta \tilde{\mathbf{u}}}{\partial \mathbf{x}} dV_t. \quad (39)$$

The unknown displacement function for $\tilde{\mathbf{u}}$ is interpolated by linear shape functions as follows:

$$\tilde{\mathbf{u}} = \xi_M(\mathbf{x}) \tilde{\mathbf{u}}^M \quad (40)$$

where $\xi_N(\mathbf{x}^K) = \delta_{NK}$. Then substitution of interpolation functions to Eq. (39) yields a discretized equation in component form as shown below.

$$-\eta_L \int_{B_t} \frac{\partial^2 \overline{W_L}}{\partial \hat{F}_{ij}^{-1} \partial \hat{F}_{kl}^{-1}} \frac{\partial \xi_M}{\partial x_j} \frac{\partial \xi_N}{\partial x_l} \dot{\tilde{u}}_k^N \delta \tilde{u}_i^M dV_t = \int_{B_t} \frac{\partial \overline{W_L}}{\partial \hat{F}_{ij}^{-1}} \frac{\partial \xi_M}{\partial x_j} \delta \tilde{u}_i^M dV_t, \quad \forall \delta \tilde{u}_a^M \quad (41)$$

From Eqs. (36) and (40), the following relation is obtained:

$$\frac{\partial \hat{F}_{ij}^{-1}}{\partial \tilde{u}_a^M} = \delta_{ai} \frac{\partial \xi_M}{\partial x_j}. \quad (42)$$

With the aid of the above relation, we can simplify Eq. (41). Moreover, since the above relation holds for all $\delta \tilde{u}_a^M$, the following result is obtained for node M and displacement a:

$$\int_{B_t} \frac{\partial \overline{W_L}}{\partial \tilde{u}_a^M} dV_t = -\eta_L \int_{B_t} \frac{\partial^2 \overline{W_L}}{\partial \tilde{u}_a^M \partial \tilde{u}_b^N} \dot{\tilde{u}}_b^N dV_t \quad (43)$$

By Eqs. (28)–(30), it is obtained that

$$\xi_N(\mathbf{x}) \tilde{\mathbf{u}}^N = \xi_N(\mathbf{X} + \psi_M(\mathbf{X}) \mathbf{u}^M) \tilde{\mathbf{u}}^N = \psi_N(\mathbf{X}) \mathbf{u}_L^N - \psi_N(\mathbf{X}) \mathbf{u}^N. \quad (44)$$

From Eqs. (40) and (44), the nodal displacements at node K are related as

$$\tilde{\mathbf{u}}^K = \mathbf{u}_L^K - \mathbf{u}^K. \quad (45)$$

Recalling that $\mathbf{x}$ is fixed in time differentiation, the time derivative of $\tilde{\mathbf{u}}$ is equal to the time derivative of $\mathbf{u}_L$ (i.e., $\dot{\tilde{\mathbf{u}}}^K = \dot{\mathbf{u}}_L^K$).

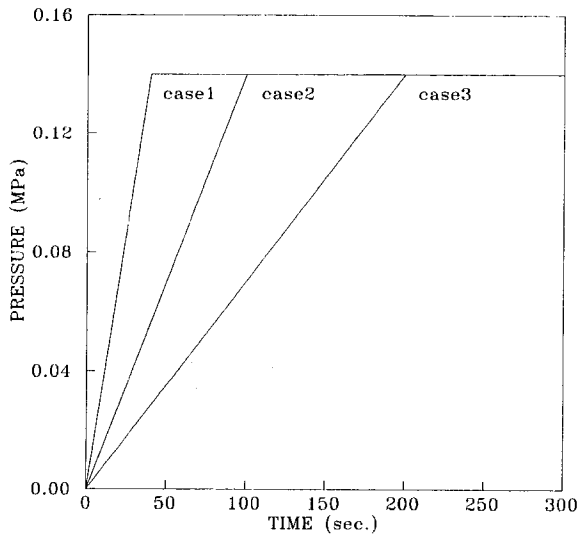


Fig. 4(a)

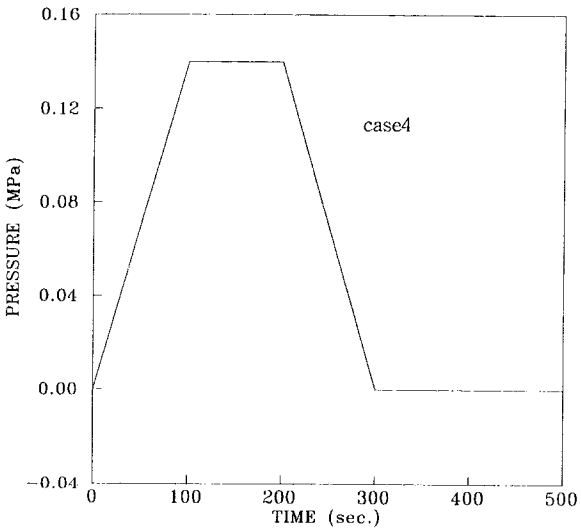


Fig. 4(b)

Fig. 4 Applied time-dependent pressure loading cycles

Therefore $\dot{\tilde{u}}_b^N$ can be replaced by $\dot{u}_{L_b}^N$. With the relation, the discretized form reduces to

$$\int_{B_t} \frac{\partial \overline{W_L}}{\partial \tilde{u}_a^M} dV_t = -\eta_L \int_{B_t} \frac{\partial^2 \overline{W_L}}{\partial \tilde{u}_a^M \partial \tilde{u}_b^N} \dot{u}_{L_b}^N dV_t. \quad (46)$$

The discretized form (46) of the flow rule is integrated by the forward Euler method. It is noted that virtual viscoconfiguration is obtained from the above flow rule. And the updated virtual viscoconfiguration is used in the equilibrium equation to obtain the current configuration. Again the obtained current configuration is used in the flow rule.

Numerical Examples

In the computational experiments, the linear isoparametric three-node axisymmetric triangular elements are used. As stated above, the penalty-type method is adopted to satisfy the nearly incompressible condition. Since the bulk moduli affect the numerical stability and degree of incompressibility, the parametric study on the bulk moduli K_F and K_L is performed. From the parametric study, the bulk moduli K_F, K_L are chosen optimally. From the optimally chosen bulk moduli, the nearly incompressible condition is achieved. Other material constants are deter-

Downloaded 04 May 2010 to 171.66.16.34. Redistribution subject to ASME license or copyright; see http://www.asme.org/terms/Terms_Use.cfm

mined from the uniaxial stretch relaxation tests. For the detail procedure of the determination of constants, Johnson and Quigley's paper (1992) can be referred. The following material constants are used in this work:

$$C_{E1} = 0.11509 \text{ MPa}, \quad C_{E2} = 0.1473 \text{ MPa},$$

$$C_{L1} = 3.87 \text{ kPa}, \quad C_{L2} = 76.6 \text{ kPa}$$

$$K_L = 5.0\text{E}7, \quad K_E = 2.5\text{E}8, \quad \eta_L = 22.7 \text{ sec}.$$

To verify the agreements between the experiments and ours, uniaxial stretch tests are simulated at various stretch rates by the developed finite element code. The predicted results are compared with the experimental data in McGuirt and Lianis (1970) and is shown in Fig. 3. The comparison of the predicted results and the measured data shows good agreement. Moreover, rate-dependent behaviors are clearly shown.

For a practical example, finite viscoelastic analyses of the pressurized circular rubber plate are performed where the hinged boundary condition and time-dependent pressure loadings (case 1-4) are imposed. The finite element model for a circular plate is shown in Fig. 5 in its original shape. The applied time-dependent pressure loading cycles are shown in Fig. 4.

For the pressure loading cycle of case 1, the actual current deformed shapes and virtual pure viscously deformed shapes (virtual viscoconfiguration) are shown at each time in Fig. 5. The difference of the two deformed shapes at each time is due to the elastic potential energy in the viscoelastic part. As the applied pressure loading is converged at final value, the difference of the two deformed shapes is diminished and converged to zero at last. This fact explains the relaxation phenomena of viscoelastic rubber.

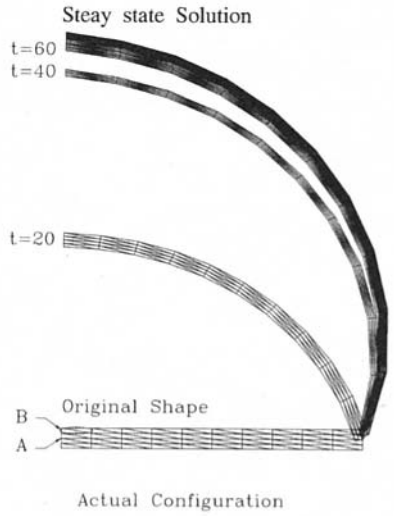


Fig. 5(*a*)

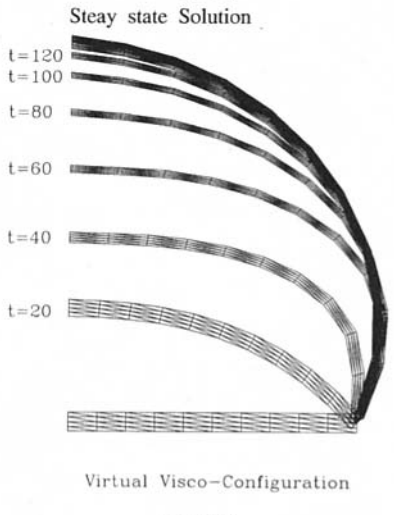


Fig. 5(*b*)

Fig. 5 The deformed shapes of an axisymmetric rubber plate under the time-dependent pressure loading (case 1)

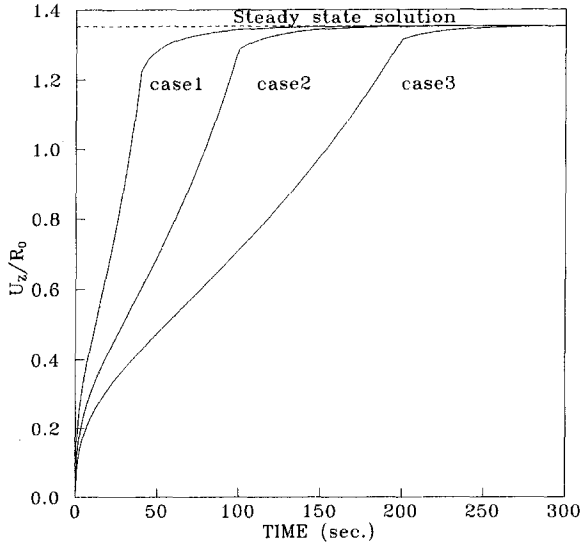


Fig. 6(*a*)

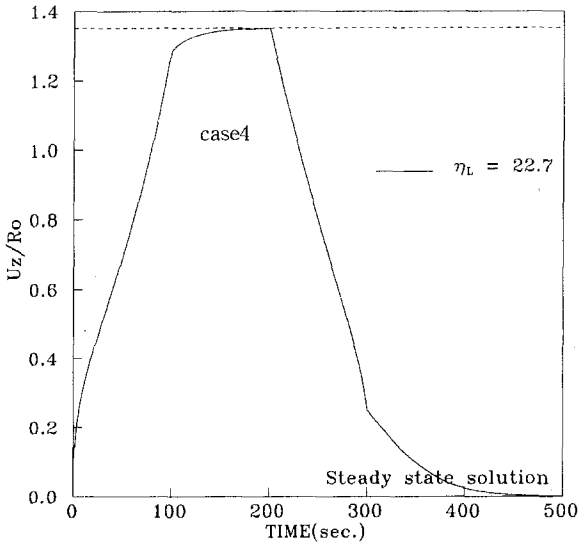


Fig. 6(*b*)

Fig. 6 The vertical displacement at node A versus time

To show the time-dependent responses of the plate, the vertical displacement at A and the radial stresses averaged over the element B are plotted versus the time of the respective loading cycle in Figs. 6 and 7. The rapid changes of stresses at the outset in Fig. 7 describe the glassy responses. From the case 1-3, it can be observed that the behaviors of the plate are very different for the different loading rates but the solutions converge to the steady-state solution with no regard to loading rates. Also, it is observed that the viscous effects diminish as the loading rate decreases. In case 4, the rubber plate bulges into a spherical shape and returns slowly to its original shape, showing the viscous effects. This example clearly shows the characteristics of finite viscoelasticity.

Conclusion

In this paper, rigorous kinematics based on continuum mechanics are developed for rubber finite viscoelasticity. In kine-

Downloaded 04 May 2010 to 171.66.16.34. Redistribution subject to ASME license or copyright; see http://www.asme.org/terms/Terms_Use.cfm

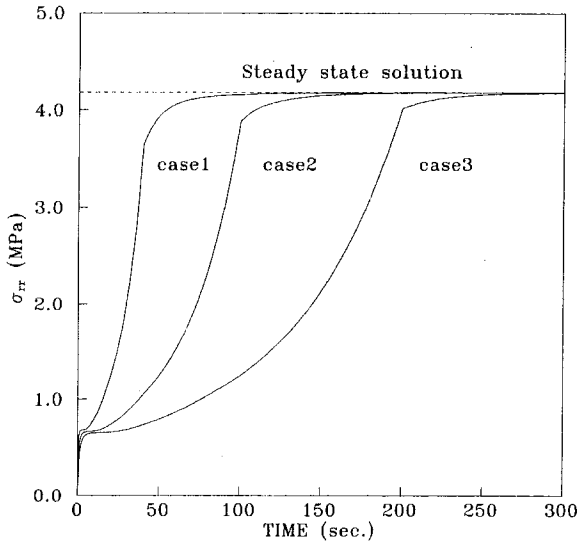


Fig. 7(*a*)

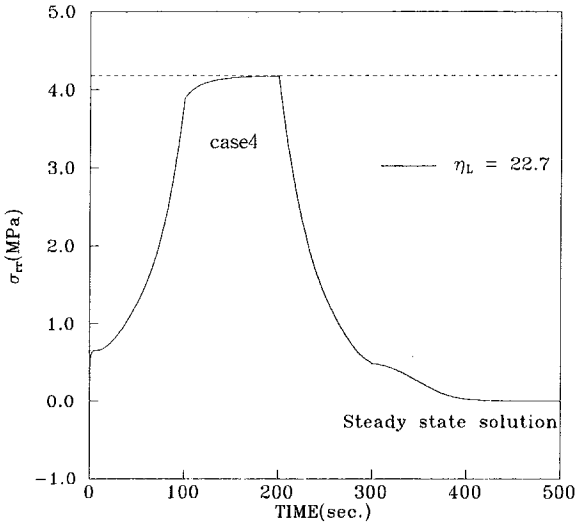


Fig. 7(*b*)

Fig. 7 The radial stresses at elements B versus time

matics, a new virtual viscoconfiguration is introduced to describe the viscous motion precisely. By using the developed kinematics, Johnson and Quigley's one-dimensional model, which predicts the stretch-relaxation tests precisely, is extended by the continuum approach. The extended constitutive model is implemented in nonlinear finite element approximation.

To satisfy the nearly incompressible condition, the penalty-type method using the modified Mooney-Rivlin energy function is adopted. And to obtain directly the virtual viscoconfiguration, the flow rule is recast to a variational form. By using the recast variational form, the virtual viscoconfiguration is obtained successfully. In the equilibrium equation, the total and similar method of the updated Lagrangian descriptions are used together. The mixture of total and updated Lagrangian descriptions reduces the numerical burdens (e.g., obtaining the stresses and deformation gradients at gauss points). Furthermore, the scheme reduces the system of nonlinear equations to a much-simplified form. From the rigorous constitutive analysis in the three-dimensional space, it is known that the developed kinematics and constitutive model conform well to the theory of large deformation.

Finite viscoelastic time-dependent behaviors are clearly shown in numerical examples and predicted results show good agreement with the experiments. Therefore, the developed finite viscoelasticity model and numerical technique can be efficiently used to analyze the viscoelastic deformations of the mechanical systems made of rubber (e.g., Flexseal, O-ring, etc.).

References

Bernstein, B., Kearsley, E. A., and Zapas, L. J., 1963, "A study of stress relaxation with finite strain," *Trans. Soc. Rheol.*, Vol. 7, pp. 391–410.

Caddell, R. M., 1980, *Deformation and Fracture of Solids*, Prentice-Hall, Englewood Cliffs, NJ.

Christensen, R. M., 1970, "A Nonlinear Theory of Viscoelasticity for Application to Elastomers," ASME JOURNAL OF APPLIED MECHANICS, Vol. 37, pp. 53–60.

Fried, I., and Johnson, A. R., 1988, "Nonlinear computation of axisymmetric solid rubber deformation," *Comput. Methods Appl. Mech. Eng.*, Vol. 67, pp. 241–253.

Goldberg, W., and Lianis, G., 1970, "Stress Relaxation in Combined Torsion-Tension," ASME JOURNAL OF APPLIED MECHANICS, Vol. 37, pp. 53–60.

Green, M. S., and Tobolsky, A. V., 1946, "A new approach to the theory of relaxing polymeric media," *J. Chem. Phys.*, Vol. 14, No. 2, pp. 80–92.

Gurtin, M. E., 1981, *An Introduction to Continuum Mechanics*, Academic Press, New York, p. 178.

Johnson, A. R., and Quigley, C. J., 1992, "A viscohyperelastic maxwell model for rubber viscoelasticity," *Rubber Chem. Technol.*, Vol. 65, pp. 137–153.

Keren, B., Partom, Y., and Rosenberg, Z., 1984, "Nonlinear viscoelastic response in two dimensions—Numerical modeling and experimental verification," *Polym. Eng. Sci.*, Vol. 24, No. 18, pp. 1409–1416.

Lianis, G., 1963, "Constitutive equations of viscoelastic solids under finite deformation," Purdue University Report, AA&ES, pp. 63–110.

McGuirt, C. W., and Lianis, G., 1970, "Constitutive equations for viscoelastic solids under finite uniaxial and biaxial deformations," *Trans. Soc. Rheol.*, Vol. 14, p. 117.

Oden, J. T., 1972, *Finite Elements of Nonlinear Continua*, McGraw-Hill, New York.

Prins, W., Meyer, S., and Cox, P., 1992, "Advanced solid rocket motor nozzle thrust vector control flexseal development status," AIAA/SAE/ASME/ASEE 28th Joint Propulsion Conference and Exhibit.

Salita, M., 1987, "A simple finite-element model of O-ring deformation and activation during squeeze and pressurization." AIAA/SAE/ASME 23rd Joint Propulsion Conference.

Treloar, L. R. G., 1975, *The Physics of Rubber Elasticity*, 3rd ed., Oxford University Press, Oxford, UK.

Downloaded 04 May 2010 to 171.66.16.34. Redistribution subject to ASME license or copyright; see http://www.asme.org/terms/Terms_Use.cfm

Post-buckling Analysis of Multiply Delaminated Composite Plates

Haiying Huang
Graduate Research Assistant.

G. A. Kardomateas
Professor,
Mem. ASME.

School of Aerospace Engineering,
Georgia Institute of Technology,
Atlanta, GA 30332-0150

This paper presents an elastic post-buckling analysis of an axially loaded beam-plate with two central across-the-width delaminations located at arbitrary depths. The analysis is based on the nonlinear beam equations, combined with the appropriate kinematic continuity and equilibrium conditions. A perturbation technique is employed, which transforms the nonlinear equations into a sequence of linear equations. An asymptotic solution of the post-buckling behavior of the plate is thus obtained. It is shown that with two delaminations, both the maximum deflection and the internal load of the first buckled (top) subplate increase as the external load increases. Of particular interest is the redistribution of load among subplates, which keeps the increase rate of internal load of the top buckled subplate much less than that of the external load. In other words, the load of the buckled subplate is close to the critical value even though the externally applied load is much larger than the critical load. In addition to the two-delamination configuration, a single delamination case is studied based on the present approach in order to verify the accuracy of the method. Also, a comparison with available finite element results is performed.

Introduction

Due to the weak interlaminar toughness of composite materials, delaminations can be easily introduced into the interface region by impact loading, fatigue, or poor manufacture. In this event, the critical load of a delaminated composite plate will be less than the corresponding pure plate without delaminations; however, buckling of the plate does not necessarily indicate its failure. In order to determine the ultimate load capacity of a delaminated composite material, the elastic post-buckling analysis of the delaminated plate is called for.

Numerous papers have been published on the prediction of the critical load of composite plates with one or multiple delaminations. However, because the nonlinearity introduced by large deformation makes the description of the post-buckling behavior extremely complex, the post-buckling behavior that ultimately governs the performance characteristics of the composite structure is not yet as well studied and understood. Kardomateas (1989, 1993) analyzed the post-buckling of composite plates with one delamination as well as the possible delamination growth behavior. An elastic buckling and post-buckling analysis of an axially loaded column with an across-the-width delamination symmetrically located at an arbitrary depth was presented by Roorda and Sakthykanapathy (1989). Also, Yin et al. (1986) investigated the ultimate axial load capacity of a plate with a single delamination. The shear buckling and post-buckling behavior of delaminated composite plates were also analyzed and the effects of delamination on shear properties were studied by Suemasu (1991). For the more complex configuration of multiple delaminations, Kutlu and Chang (1992) did some extensive investigations on the compression responses of laminate composites containing multiple delaminations, both analytically and experimentally. The compression behavior of composite panels with through-width, equal size, equally spaced multiple delaminations were also investigated analytically by Suemasu (1993) by applying the Rayleigh-Ritz approximation method. Sheinman and Soffer (1991) and Sheinman et al. (1993) developed a system composed of partial nonlinear differential equations in terms of the transverse and axial displacements to analyze the post-buckling behavior of multiply delaminated beams or long plates under cylindrical bending. A finite element method based on layerwise laminated composite plate theory was presented by Lee et al. (1995) to formulate and solve the post-buckling problem of laminated composites with delaminations.

Unlike the previously published papers, which were mostly based on finite element analysis, this paper presents an asymptotic solution for the post-buckling analysis of composite plates containing two central delaminations. It should be noted that the approach is also applicable to the case of a single delamination. Because of the nonlinearity of the post-buckling behavior, the perturbation method is introduced to transform the nonlinear problem into a linear problem. It should also be noted that good agreements were obtained between the calculation results from the present method and previously published data, both for two-delamination problems and one-delamination problems. Some interesting conclusions are drawn. The interaction among subplates is also studied and it is found that the redistribution of load among the subplates keeps the buckled subplate close to the critical load.

Formulation

The model of a delaminated plate employed in the analysis is shown in Fig. 1. A plate of half-length L, thickness T, and width W has two pre-existing central delaminations. It is assumed that the delaminations will not propagate under axial compressive load. Both ends of the plate are clamped and the external load is symmetrically applied. Because of the symmetry of the structure, only the left half can be considered. The half-plate is divided into five subplates, each having a size parameter pair (L_i, t_i), L_i and t_i being the length and thickness of the ith plate, respectively. The coordinate systems for each subplate are also shown in Fig. 1. Points A and B are the crack tips. The first, shallow (top) delamination will be denoted as delamina-

Contributed by the Applied Mechanics Division of THE AMERICAN SOCIETY OF MECHANICAL ENGINEERS for publication in the ASME JOURNAL OF APPLIED MECHANICS.

Discussion on this paper should be addressed to the Technical Editor, Professor Lewis T. Wheeler, Department of Mechanical Engineering, University of Houston, Houston, TX 77204-4792, and will be accepted until four months after final publication of the paper itself in the ASME JOURNAL OF APPLIED MECHANICS.

Manuscript received by the ASME Applied Mechanics Division, Sept. 20, 1996; final revision, Feb. 7, 1997. Associate Technical Editor: S. Kyriakides.

Copyright © 1997 by ASME

Downloaded 04 May 2010 to 171.66.16.34. Redistribution subject to ASME license or copyright; see http://www.asme.org/terms/Terms_Use.cfm

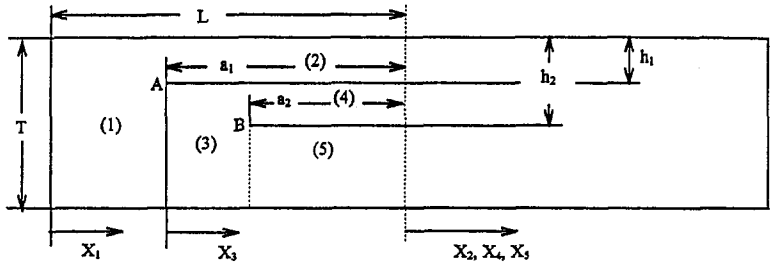


Fig. 1 Definition of the geometry for the multiple delamination problem

tion I and the second deep one as delamination II. The sizes and locations of these two delaminations are defined by their lengths a_i and depths h_i. Notice that $t_1 = T$, $t_2 = h_1$, $t_3 = T - h_1$, $t_4 = h_2 - h_1$, $t_5 = T - h_2$, and $L_1 = L - a_1$, $L_2 = a_1$, $L_3 = a_1 - a_2$ and $L_4 = L_5 = a_2$.

According to the nonlinear beam theory, the differential equations for subplates 1–5 are (e.g., Dym, 1974):

$$D_i \frac{d^2\theta_i}{dx_i^2} + P_i \sin\theta_i = 0, \tag{1a}$$

with boundary conditions

$$\theta_i(0) = 0, \quad i = 1, 2, 4, 5. \tag{2}$$

Notice that for $i = 2, 4, 5$, this is due to symmetry, whereas $\theta_1(0) = 0$ is due to the clamped end where D_i is the bending stiffness of the plate, $D_i = E_{11}I/(1 - \nu_{12}\nu_{21})$ for orthotropic materials.

Referring to Fig. 2, the equilibrium conditions are as follows: At the section of point A,

$$M_1 - M_2 - M_3 - P_2\frac{t_3}{2} + P_3\frac{t_2}{2} = 0, \tag{3a}$$

$$P_2 + P_3 = P_1. \tag{3b}$$

At the section of point B,

$$M_3 - M_4 - M_5 - P_4\frac{t_5}{2} + P_5\frac{t_4}{2} = 0, \tag{3c}$$

$$P_4 + P_5 = P_3. \tag{3d}$$

The kinematic continuity conditions are as follows: At point A,

$$\theta_1(L_1) = \theta_2(-L_2) = \theta_3(0) = \theta_A, \tag{3e}$$

$$u_2^A = u_3^A. \tag{3f}$$

At point B,

$$\theta_3(L_3) = \theta_4(-L_4) = \theta_5(-L_5) = \theta_B, \tag{3g}$$

$$u_4^B = u_5^B. \tag{3h}$$

In these relations $M_i = D_i\, d\theta_i/dx_i$, and u is the displacement along the x direction. The displacements at points A and B are due to the rotation of the cross section about the midplane and the shortening of the midplane under compression and bending, so we can write

$$u_2^A = \frac{1}{2}\int_{-L_2}^{0}\theta_2^2 dx_2 + \frac{P_2L_2}{WEt_2} + \theta_A\frac{t_2}{2}, \tag{3i}$$

$$u_3^A = \frac{1}{2}\int_{-L_5}^{0}\theta_5^2 dx_5 + \frac{1}{2}\int_{0}^{L_3}\theta_3^2 dx_3 + \frac{P_3L_3}{WEt_3} + \frac{P_5L_5}{WEt_5} - \theta_B\frac{t_4}{2} - \theta_A\frac{t_3}{2}, \tag{3j}$$

$$u_4^B = \frac{1}{2}\int_{-L_4}^{0}\theta_4^2 dx_4 + \frac{P_4L_4}{WEt_4} + \theta_B\frac{t_4}{2}, \tag{3k}$$

$$u_5^B = \frac{1}{2}\int_{-L_5}^{0}\theta_5^2 dx_5 + \frac{P_5L_5}{WEt_5} + \theta_B\frac{t_5}{2}, \tag{3l}$$

where W is the width of the plate.

Equation (1a) looks very simple; however, it is actually very difficult to solve because of the nonlinearity of the sine function. The perturbation method is a very powerful technique for solving nonlinear differential equations. In order to take advantage of the perturbation method, it is neccessary to modify Eq. (1a) into a form such that the perturbation expansion of its solution will result in a series of linear equations that can be solved iteratively. Using Taylor's formula to expand the sine function, i.e.,

$$\sin\theta = \theta - \frac{\theta^3}{6} + O(\theta^5),$$

and substituting into (1a) gives differential equations for each subplate 1–5 in the form

$$D_i\frac{d^2\theta_i}{dx^2} + P_i\left(\theta_i - \frac{\theta_i^3}{6}\right) = 0. \tag{1b}$$

To implement the perturbation technique, a straightforward expansions of the solutions θ_i and P_i are constructed first (e.g., Bush, 1990):

$$\theta_i = \theta_i^{(0)} + \epsilon^{0.5}\theta_i^{(1)} + \epsilon^{1.5}\theta_i^{(2)} + O(\epsilon^{2.5}), \tag{4a}$$

$$P_i = P_i^{(0)} + \epsilon^{0.5}P_i^{(1)} + \epsilon^{1.5}P_i^{(2)} + O(\epsilon^{2.5}), \tag{4b}$$

where ϵ is a small perturbation parameter. The asymptotic sequence $\{\epsilon^{0.5}, \epsilon^{1.5}, \epsilon^{2.5}, \ldots\}$ was chosen as opposed to the more

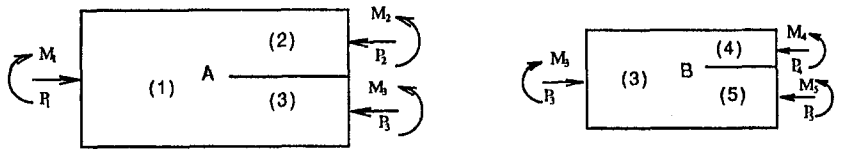


Fig. 2 Internal load conditions at the sections of points A and B

Downloaded 04 May 2010 to 171.66.16.34. Redistribution subject to ASME license or copyright; see http://www.asme.org/terms/Terms_Use.cfm

usually used $\{\epsilon^0, \epsilon^1, \epsilon^2, \ldots\}$ because it will generate the linear differential equations such that the second-order equation would include the first-order term and thus can be solved iteratively.

Now the initial position is the prebuckling state of uniform compression, so $\theta_i^{(0)} = 0$ and $P_i^{(0)} = \bar{P}t_i/T$, where $\bar{P}$ is the applied external load.

Substituting (4) into (1*b*) and dividing by $\epsilon^{0.5}$, yields

$$D_i \frac{d^2\theta_i^{(1)}}{dx_i^2} + (P_i^{(0)} + \epsilon^{0.5}P_i^{(1)})\theta_i^{(1)} + \epsilon\left[D_i \frac{d^2\theta_i^{(2)}}{dx_i^2} + (P_i^{(0)} + \epsilon^{0.5}P_i^{(1)})\theta_i^{(2)} - (P_i^{(0)} + \epsilon^{0.5}P_i^{(1)}) \frac{\theta_i^{(1)2}}{6} + \epsilon^{0.5}P_i^{(2)}\theta_i^{(1)} \right] + O(\epsilon^2) = 0. \quad (5)$$

The boundary conditions and compatibility conditions are also processed in a similar fashion. Next, two groups of linear equations are obtained by a proper grouping of the terms of powers of ϵ, based on the following.

Since ϵ is a very small number, $\{1, \epsilon^{0.5}\}$ are very large compared to $\{\epsilon, \epsilon^{1.5}\}$. In turn, $\{\epsilon, \epsilon^{1.5}\}$ are very large compared to $\{\epsilon^2, \epsilon^{2.5}\}$, etc. Therefore, starting from Eq. (5), the first-order terms are selected to be both $\{O(1)$ *and* $O(\epsilon^{0.5})\}$, and the second-order terms are both $\{O(\epsilon)$ and $O(\epsilon^{1.5})\}$, i.e., unlike the conventional asymptotic expansions, the term "first-order terms" means to include terms *up to* $\epsilon^{0.5}$ [which, again, means both $O(\epsilon^0)$ and $O(\epsilon^{0.5})$] and the term "second order terms" means to include terms up to $\epsilon^{1.5}$ (which, again, means both $O(\epsilon)$ and $O(\epsilon^{1.5})$). This methodology for constructing the asymptotic solution is essentially a matter of proper grouping of the terms, or, in other words, proper selection of what is retained, and it is necessary to achieve the solution since the traditional approach would not be successful.

Thus, the following two groups of linear equations are obtained:

First-Order, i.e., up to $O(\epsilon^{0.5})$.

$$D_i \frac{d^2\theta_i^{(1)}}{dx_i^2} + (P_i^{(0)} + \epsilon^{0.5}P_i^{(1)})\,\theta_i^{(1)} = 0, \quad (6a)$$

$$\theta_i^{(1)}(0) = 0 \quad \text{for} \quad i = 1, 2, 4, 5. \quad (6b)$$

At the section of point A, by using (3*e*),

$$\theta_1^{(1)}(L_1) = \theta_2^{(1)}(-L_2) = \theta_3^{(1)}(0), \quad (6c)$$

and by applying (3*f*) and (3*i*, *j*),

$$\frac{1}{2}\int_{-L_5}^{0} \theta_5^{(1)2}dx_5 + \frac{1}{2}\int_0^{L_3} \theta_3^{(1)2}dx_3 + \epsilon^{-0.5}\frac{P_5^{(1)}L_5}{WEt_5} + \epsilon^{-0.5}\frac{P_3^{(1)}L_3}{WEt_3} = \frac{1}{2}\int_{-L_2}^{0} \theta_2^{(1)2}dx_2 + \epsilon^{-0.5}\frac{P_2^{(1)}L_2}{WEt_2} + \epsilon^{-0.5}\theta_5^{(1)}(-L_5)\frac{t_5}{2} + \epsilon^{-0.5}\theta_3^{(1)}(0)\frac{T}{2}, \quad (6d)$$

and by applying (3*a*, *b*),

$$P_2^{(1)} + P_3^{(1)} = 0, \quad (6e)$$

$$-D_1\frac{d\theta_1^{(1)}}{dx_1} + D_2\frac{d\theta_2^{(1)}}{dx_2} + D_3\frac{d\theta_3^{(1)}}{dx_3} = P_3^{(1)}\frac{t_2}{2} - P_2^{(1)}\frac{t_3}{2}. \quad (6f)$$

At the section of point B, by applying (3*g*),

$$\theta_3^{(1)}(L_3) = \theta_4^{(1)}(-L_4) = \theta_5^{(1)}(-L_5), \quad (6g)$$

and now by applying (3*h*) and using (3*k*, *l*),

$$\frac{1}{2}\int_{-L_5}^{0} \theta_5^{(1)2}dx_5 + \epsilon^{-0.5}\frac{P_5^{(1)}L_5}{WEt_5} = \frac{1}{2}\int_{-L_4}^{0} \theta_4^{(1)2}dx_4 + \epsilon^{-0.5}\frac{P_4^{(1)}L_4}{WEt_4} + \epsilon^{-0.5}\theta_5^{(1)}(-L_5)\frac{t_4 + t_5}{2}, \quad (6h)$$

and by applying (3*c*, *d*),

$$P_4^{(1)} + P_5^{(1)} = P_3^{(1)}, \quad (6i)$$

$$-D_3\frac{d\theta_3^{(1)}}{dx_3} + D_4\frac{d\theta_4^{(1)}}{dx_4} + D_5\frac{d\theta_5^{(1)}}{dx_5} = P_5^{(1)}\frac{t_4}{2} - P_4^{(1)}\frac{t_5}{2}. \quad (6j)$$

Second order, i.e. up to $O(\epsilon^{1.5})$. Substituting (4) into (1*b*) gives

$$D_i \frac{d^2\theta_i^{(2)}}{dx_i^2} + (P_i^{(0)} + \epsilon^{0.5}P_i^{(1)})\theta_i^{(2)} = (P_i^{(0)} + \epsilon^{0.5}P_i^{(1)})\frac{\theta_i^{(1)3}}{6} - \epsilon^{0.5}P_i^{(2)}\theta_i^{(1)}, \quad (7a)$$

$$\theta_i^{(2)}(0) = 0 \quad \text{for} \quad i = 2, 4, 5. \quad (7b)$$

At the section of point A, by applying (3*e*),

$$\theta_1^{(2)}(L_1) = \theta_2^{(2)}(-L_2) = \theta_3^{(2)}(0), \quad (7c)$$

and now by applying (3*f*) and using (3*i*, *j*),

$$\int_{-L_5}^{0} \theta_5^{(1)}\theta_5^{(2)}dx_5 + \int_0^{L_3} \theta_3^{(1)}\theta_3^{(2)}dx_3 + \epsilon^{-0.5}\frac{P_5^{(2)}L_5}{WEt_5} + \epsilon^{-0.5}\frac{P_3^{(2)}L_3}{WEt_3} = \int_{-L_2}^{0} \theta_2^{(1)}\theta_2^{(2)}dx_2 + \epsilon^{-0.5}\frac{P_2^{(2)}L_2}{WEt_2} + \epsilon^{-0.5}\theta_5^{(2)}(-L_5)\frac{t_4}{2} + \epsilon^{-0.5}\theta_3^{(2)}(0)\frac{T}{2}, \quad (7d)$$

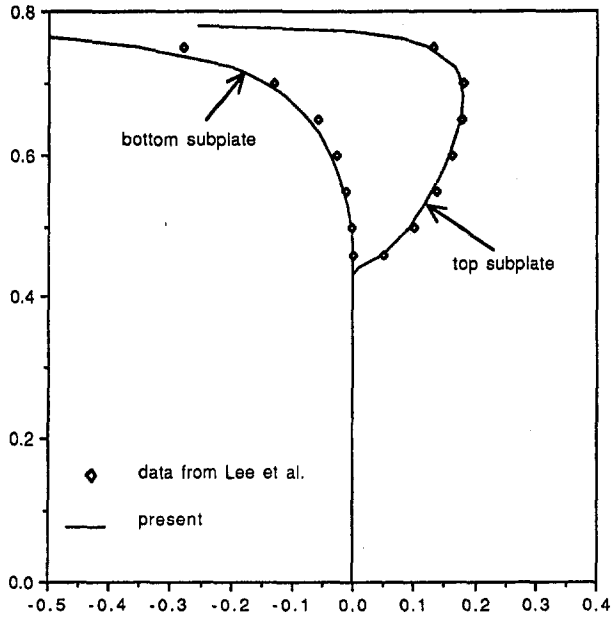


Fig. 3 Deflection-load curve of a plate with a single delamination: $\bar{h}$ = 0.2 and $\bar{a}$ = 0.3. Horizontal axis is w_i and vertical axis is $\bar{P}$.

Downloaded 04 May 2010 to 171.66.16.34. Redistribution subject to ASME license or copyright; see http://www.asme.org/terms/Terms_Use.cfm

Table 1 Post-buckling behavior of a plate with two equal-length delaminations

$\bar{P}$		0.2	0.3	0.4	0.5	0.6	0.7
Lee et al. (1995)	$\bar{W}_2$	0.06	0.13	0.18	0.20	0.22	0.21
Lee et al. (1995)	$\bar{W}_5$	0.0	−0.01	−0.02	−0.05	−0.095	−0.2
Present	$\bar{W}_2$	0.0635	0.1399	0.1838	0.2138	0.2298	0.2187
Present	$\bar{W}_5$	−0.0025	−0.0125	−0.0293	−0.0561	−0.1046	−0.2095
Present	$\bar{P}_2$	1.0088	1.0218	1.0334	1.0474	1.0679	1.1028

and by applying $(3a, b)$,

$$P_2^{(2)} + P_3^{(2)} = 0, \tag{7e}$$

$$-D_1 \frac{d\theta_1^{(2)}}{dx_1} + D_2 \frac{d\theta_2^{(2)}}{dx_2} + D_3 \frac{d\theta_3^{(2)}}{dx_3} = P_3^{(2)} \frac{t_2}{2} - P_2^{(2)} \frac{t_3}{2}. \tag{7f}$$

At the section of point B, by applying $(3g)$,

$$\theta_3^{(2)}(L_3) = \theta_4^{(2)}(-L_4) = \theta_5^{(2)}(-L_5), \tag{7g}$$

and now by applying $(3h)$ and using $(3k, l)$,

$$\int_{-L_5}^{0} \theta_5^{(1)}\theta_5^{(2)} dx_5 + \epsilon^{-0.5} \frac{P_5^{(2)} L_5}{WEt_5} = \int_{-L_4}^{0} \theta_4^{(1)}\theta_4^{(2)} dx_4 + \epsilon^{-0.5} \frac{P_4^{(2)} L_4}{WEt_4} + \epsilon^{-0.5}\theta_5^{(2)}(-L_5) \frac{t_4 + t_5}{2}, \tag{7h}$$

and, finally, by applying $(3c, d)$,

$$P_4^{(2)} + P_5^{(2)} = P_3^{(2)}, \tag{7i}$$

$$-D_3 \frac{d\theta_3^{(2)}}{dx_3} + D_4 \frac{d\theta_4^{(2)}}{dx_4} + D_5 \frac{d\theta_5^{(2)}}{dx_5} = P_5^{(2)} \frac{t_4}{2} - P_4^{(2)} \frac{t_5}{2}. \tag{7j}$$

The general solution for the first-order differential Eq. $(6a)$ is

$$\theta_i^{(1)} = A_i^{(1)} \sin \lambda_i x_i + B_i^{(1)} \cos \lambda_i x_i, \tag{8a}$$

with

$$\lambda_i = \sqrt{(P_i^{(0)} + \epsilon^{0.5} P_i^{(1)})/D_i}, \tag{8b}$$

where $A_i^{(1)}$, $B_i^{(1)}$, $i = 1, 2, 3, 4, 5$ and $P_i^{(1)}$, $i = 2, 3, 4, 5$ are unknowns; i.e., 14 unknowns. $P_1^{(1)} = 0$ because $P_1 = \bar{P}$ is a constant. Substituting (8) into boundary condition $(6b)$, the number of unknowns reduces to ten. Solving the ten compatibility condition equations $(6c-j)$ by the Newton's continuation method, allows determining $\theta_i^{(1)}$.

To solve the second-order system of equations, substitute $\theta_i^{(1)}$ from $(8a)$ into Eq. $(7a)$, then the general solutions for Eq. $(7a)$ are

$$\theta_i^{(2)} = A_i^{(2)} \sin \lambda_i x_i + B_i^{(2)} \cos \lambda_i x_i - \frac{C_i^{(1)}}{2\lambda_i} x_i \cos \lambda_i x_i + \frac{C_i^{(2)}}{2\lambda_i} x_i \sin \lambda_i x_i - \frac{C_i^{(3)}}{8\lambda_i^2} \sin 3\lambda_i x_i - \frac{C_i^{(4)}}{8\lambda_i^2} \cos 3\lambda_i x_i \tag{9a}$$

where

$$C_i^{(1)} = \frac{\lambda_i^2 A_i^{(1)}}{8} (A_i^{(1)2} + B_i^{(1)2}) - \epsilon^{0.5} A_i^{(1)} \frac{P_i^{(2)}}{D_i}, \tag{9b}$$

$$C_i^{(2)} = \frac{\lambda_i^2 B_i^{(1)}}{8} (A_i^{(1)2} + B_i^{(1)2}) - \epsilon^{0.5} B_i^{(1)} \frac{P_i^{(2)}}{D_i}, \tag{9c}$$

and

$$C_i^{(3)} = \frac{\lambda_i^2 A_i^{(1)}}{24} (3B_i^{(1)2} - A_i^{(1)2}), \tag{9d}$$

$$C_i^{(4)} = \frac{\lambda_i^2 B_i^{(1)}}{24} (B_i^{(1)2} - 3A_i^{(1)2}). \tag{9e}$$

So again we have 14 unknowns. Introducing Eq. $(9a)$ into $(7b)$ and $(7c-j)$, the 14 unknowns are easy to calculate because all the equations are linear. Then the asymptotic solutions for the post-buckling deformation quantities are expressed as

$$\theta_i = \epsilon^{0.5}\theta_i^{(1)} + \epsilon^{1.5}\theta_i^{(2)} + O(\epsilon^{2.5}). \tag{10}$$

Although $\theta_i^{(1)}$ and $\theta_i^{(2)}$ are functions of ϵ as $\epsilon^{0.5}$ appears in both the first and second-order equations, θ_i is not a function of ϵ as long as ϵ is chosen to be a small value.

Finally, the deflection $W(x)$ can be obtained by integrating Eq. (10) and using boundary conditions and compatibility conditions, i.e.,

$$W_1(0) = 0; \quad W_2(-L_2) = W_3(0) = W_1(L_1), \tag{11a}$$

$$W_4(-L_4) = W_5(-L_5) = W_3(L_3). \tag{11b}$$

Results

A simple computer code was written according to the preceding theory. Delaminations of different sizes and locations were investigated. The calculation results are presented both in tables and graphs. The parameters are nondimensionalized as

$$\bar{h}_i = h_i/T; \quad \bar{a}_i = a_i/L; \quad \bar{P} = P/P_{cr}^0; \quad \bar{W}_i = W_i/T.$$

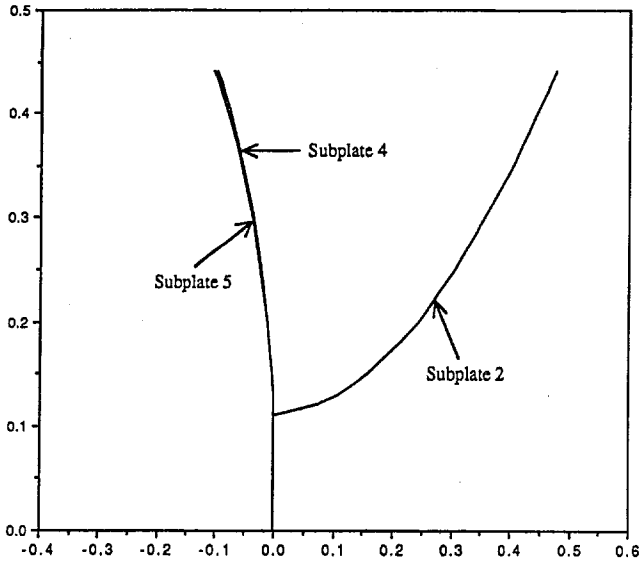


Fig. 4 Load-deflection curve for a two-delamination configuration, in which delamination I is long

Downloaded 04 May 2010 to 171.66.16.34. Redistribution subject to ASME license or copyright; see http://www.asme.org/terms/Terms_Use.cfm

Notice that P_{cr}^0 is the critical load of the plate without delamination and W_i represents the maximum deflection of the ith subplate with the upward direction as its positive direction. In Figs. 3, 4, and 5, the horizontal axis is $\bar{w}_i$ and the vertical axis is $\bar{P}$.

Single Delamination. To verify the accuracy of the present method, an example employed by Lee et al. (1995) is revisited. The material being used is T300/5208 graphite/epoxy with typical material parameters $E_{11} = 181$ Gpa, $E_{22} = 10.3$ Gpa, $G_{12} = G_{13} = 7.17$ Gpa, and $\nu_{12} = \nu_{13} = 0.28$. A plate containing a single through-the-width delamination at its center with $\bar{t} = 0.2$ and $\bar{a} = 0.3$ is considered. The thickness-to-span ratio is assumed to be $T/L = 1/400$. Figure 3 presents the calculation results as well as the plotted data from finite element study in Fig. 3 (Lee et al., 1995), which shows that they are in good agreement.

Two Delaminations. To further verify this method, a two-delamination example by Lee et al. (1995) is reconsidered. The example considers two delaminations symmetrically located with respect to midplane and both delaminations are assumed to have the same length. The material properties of the composite material in the study are as follows: $E_{11} = 10.9$ Gpa, $E_{22} = 7.58$ Gpa, $G_{12} = G_{13} = 2.48$ Gpa, $\nu_{21} = 0.31$, $\nu_{13} = 0.22$. The post-buckling analysis results for $\bar{h}_1 = 0.125$, $\bar{h}_2 = 0.75$ and $\bar{a}_1 = \bar{a}_2 = 0.3$ are listed in Table 1, as well as data extracted from a figure presented by Lee et al. (1995). In this example, the second delamination remains closed. The composite plate behaves as if it contains the upper delamination only. Another interesting observation is the load redistribution among subplates. $\bar{P}_2$ in Table 1 is the ratio between the current axial load in subplate 2 and its critical load. It is clearly shown in Table 1 that the increase of $\bar{P}_2$ is not proportional to that of $\bar{P}$. This is because the stiffness of subplate 2 will decrease when it buckles and the load is distributed through the thickness of the plate in relation to the thickness and stiffness properties of each subplate. As a result, the load redistribution keeps the load of the buckled subplate at a level close to the critical load.

A delaminated plate has a variety of buckling modes, including the global mode, which does not involve lamina separation, the local mode, which involves buckling of the surface subplate only (thin film mode), and the general mode, which is the coupled mode of the global mode and the local mode. It has been mentioned by other researchers that a plate with long delaminations behaves differently from that with short delaminations. To investigate the effect of delamination size on the post-buckling behavior of plates, two configurations involving two delaminations are considered: (1) long delamination: $\bar{h}_1 = 0.2$, $\bar{h}_2 = 0.5$, $\bar{a}_1 = 0.6$ and $\bar{a}_2 = 0.3$; (2) short delamination: $\bar{h}_1 = 0.2$, $\bar{h}_2 = 0.5$, $\bar{a}_1 = 0.3$, and $\bar{a}_2 = 0.3$. Figures 4 and 5 are the load-deflection curves of these two configurations, respectively. For the long delamination case, subplate 2 buckles first when the external load $\bar{P}$ is larger than the critical load $\bar{P}_{cr} = 0.1103$. As the external load $\bar{P}$ increases, the maximum deflection of subplate 2 increases, too. However, the maximum deflections of subplate 4 and 5 are kept at a small level. In fact, the whole structure stays in local buckling mode even when the external load reaches the second eigenvalue. In contrast, the plate with short delamination behaves differently. At the initial post-buckling state, the plate behaves in a local buckling mode. However, the maximum deflections of subplates (4) and (5) become large as $\bar{P}$ increases further, which indicates a switch to a global buckling mode. When $\bar{P}$ reaches 0.71, the global buckling mode becomes dominant. For a small increment of external load, that is $\bar{P}$ going from 0.71 to 0.72, the deflection increases abruptly and the whole structure collapses.

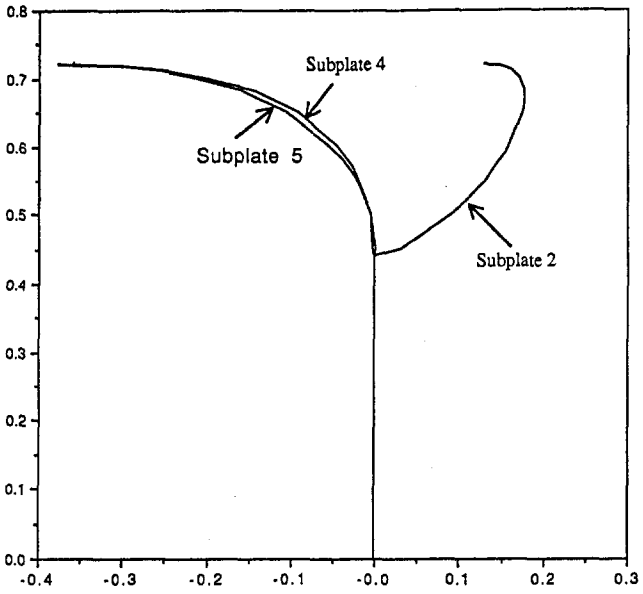


Fig. 5 Load-deflection curve for a two-delamination configuration, in which delamination I is short

Acknowledgment

The financial support of the Office of Naval Research, Ship Structures and Systems, S&T Division, Grant N00014-91-J-1892, and the interest and encouragement of the Grant Monitor, Dr. Y. D. S. Rajapakse, are both gratefully acknowledged.

References

Bush, A. W., 1990, *Perturbation Methods for Engineers and Scientists,* Teesside Polytechnic, U.K.

Dym, C. L., 1974, *Stability Theory and Its Applications to Structural Mechanics,* Noordhoff, Leyden.

Kardomateas, G. A., 1993, "The Initial Post-buckling and Growth Behavior of Internal Delaminations in Composite Plates," ASME JOURNAL OF APPLIED MECHANICS, Vol. 60, pp. 903–910.

Kardomateas, G. A., 1989, "Large deformation effects in the post buckling behavior of composites with thin delaminations," *AIAA Journal,* Vol. 27, No. 5, pp. 624–631.

Kutlu, Z., and Chang, F. K., 1992, "Modeling compressive failure of delaminated composites containing multiple through-the-width delaminations," *J of Composite Materials,* Vol. 26, No. 3, pp. 350–387.

Lee, J., Gurdal, Z., and Griffin, O. H., 1995, "Post buckling of laminated composites with delaminations," *AIAA Journal,* Vol. 33, No. 10, pp. 1963–1970.

Roorda, J., and Sakthykanapathy, S., 1989, "Delaminations: buckling and growth in a one dimensional model," *Res Mechanica,* Vol. 28, No. 1–4, pp. 91–112.

Sheinman, I., Adan, M., and Altus, E., 1993, "Postbuckling analysis of multiple delaminated beams," *International Journal of Solids and Structures,* Vol. 30, No. 10, pp. 1289–1300.

Sheinman, I., and Soffer, M., 1991, "Post buckling analysis of composite delaminated beams," *Int. J. Solids Structures,* Vol. 27, No. 5, pp. 639–646.

Suemasu, H., 1991, "Analytical study of shear buckling and postbuckling behaviors of composite plates with delaminations," *JSME International Journal,* Series 1, Vol. 34, No. 2, pp. 135–142.

Suemasu, H., 1993, "Post buckling behavior of composite panels with multiple delaminations," *J of Composite Materials,* Vol. 27, No. 11, pp. 1077–1097.

Yin, W. L., Sallam, S., and Simitses, G. J., 1986, "Ultimate axial load capacity of a delaminated beam-plate," *AIAA Journal,* Vol. 24, No. 1, pp. 123–128.

Downloaded 04 May 2010 to 171.66.16.34. Redistribution subject to ASME license or copyright; see http://www.asme.org/terms/Terms_Use.cfm

Cheng Chang-qing
Ph.D. Candidate.

Shen Ya-peng
Professor.

The State Key Laboratory of Mechanical Structural Strength and Vibration, Xi'an Jiaotong University, Xi'an, 710049, P. R. China

Stability Analysis of Piezoelectric Circular Cylindrical Shells

A study on the problem of linear buckling of piezoelectric circular cylindrical shells subjected to external pressure as well as on an electric field is presented. In this paper, the structure is treated as a three-dimensional one. The results reveal that the piezoelectric effect has significant effect on the critical load, while the stress due to the uniformly applied electric field alone is not likely to cause elastic buckling. In addition, they can also be used to assess the limitation of shell theories in predicting buckling of piezoelectric smart shell structures.

Introduction

In recent years, smart structures with piezoelectric sensors and actuators have attracted serious attention for they can sense and alter the mechanical response during in-service operation. On the other hand, light-weight shell-type structures may be one of the most popularly used structures in space vehicles. For these reasons, shell-type smart structures have become the subject of focus for many researchers. Tzou and his co-workers published a series of papers on finite element and analytical analysis of piezoelectric shell-type continua (e.g., Tzou and Gadre, 1989; Tzou, 1992; Tzou and Tseng, 1991; Tzou et al., 1994). Using the first-order shear theory, Miller and Abramovich (1995) studied an analytically thick shell with distributed self-sensing piezoelectric actuators. In addition to the aforementioned approximate analysis, exact studies of piezoelectric circular cylindrical shells (Chen et al., 1996) and piezothermoelastic shells (Tzou and Ye, 1994; Chen and Shen, 1996a) were also performed.

As we know, loss of stability is of primary concern for these shell-type structures; to the author's knowledge, however, few publication are about the stability of piezoelectric shells. Baumhauer and Tiersten (1973) developed a general theory which can be employed into the linear stability analysis of piezoelectric media. Recently, Chen and Shen (1996b) presented general nonlinear theories for the buckling, post-buckling, and dynamic stability of piezoelectric shells.

The objective of this paper is to study the buckling of piezoelectric circular cylindrical shells based upon a three-dimensional approach. A piezoelectric cylindrical shell of infinite length subjected to external pressure and electric field is studied. The effect of the piezoelectric effect on the buckling load are studied. The results provide a means of assessing the limitations of shell theories in predicting buckling of piezoelectric shell structures and are helpful for understanding the electric and mechanical behavior of these smart structures.

Contributed by the Applied Mechanics Division of THE AMERICAN SOCIETY OF MECHANICAL ENGINEERS for publication in the ASME JOURNAL OF APPLIED MECHANICS.

Discussion on the paper should be addressed to the Technical Editor, Professor Lewis T. Wheeler, Department of Mechanical Engineering, University of Houston, Houston, TX 77204-4792, and will be accepted until four months after final publication of the paper itself in the ASME JOURNAL OF APPLIED MECHANICS.

Manuscript received by the ASME Applied Mechanics Division, Sept. 19, 1996; final revision, Mar. 11, 1997. Associate Technical Editor: S. Kyriakides.

Basic Equation

The buckling equation of equilibrium in the Lagrangian description has the form of (see, for example, Washizu, 1982)

$$(\sigma_{KL}\delta_{Ki} + \sigma^0_{KL}u_{i,K})_{,L} = 0 \tag{1}$$

where the body force is assumed to be absent, σ_{KL} is the second Piola Kirchhoff stress tensor, δ_{Ki} is the Kronecker delta, σ^0_{KL} is the prebuckling stress, and u_i is the mechanical displacement in the Euler frame. The capital case Latin indices and the lower case Latin indices refer to the Lagrange and Euler configurations, respectively.

The charge equation of electrostatics of a perturbed state in a Lagrange frame is (Baumhauer and Tiersten, 1973; Chen and Shen, 1996b)

$$D_{K,K} = 0 \tag{2}$$

where D_K is the electric displacement of Lagrange frame form, and it is related to the ordinary electric displacement D_i by

$$D_K = JX_{K,i}D_i \tag{3}$$

where J is the Jacobian and $X_{K,i}$ is the deformation gradient.

Equations (1) and (2) can be expressed in the cylindrical coordinate system as

$$\frac{\partial}{\partial r}\left[\sigma^0_r u_{r,r} + \sigma^0_{r\theta}\frac{u_{r,\theta} - u_\theta}{r} + \sigma^0_{rz}u_{r,z} + \sigma_r\right]$$

$$+ \frac{\partial}{r\partial\theta}\left[\sigma^0_{r\theta}u_{r,r} + \sigma^0_\theta\frac{u_{r,\theta} - u_\theta}{r} + \sigma^0_{\theta z}u_{r,z} + \sigma_{r\theta}\right]$$

$$+ \frac{\partial}{\partial z}\left[\sigma^0_{zr}u_{r,r} + \sigma^0_{\theta z}\frac{u_{r,\theta} - u_\theta}{r} + \sigma^0_z u_{r,z} + \sigma_{zr}\right]$$

$$+ \frac{1}{r}\left(\sigma^0_r u_{r,r} + \sigma^0_{r\theta}\frac{u_{r,\theta} - u_\theta}{r} + \sigma^0_{zr}u_{r,z} - \sigma^0_{r\theta}u_{\theta,r}\right.$$

$$\left. - \sigma^0_\theta\frac{u_r + u_{\theta,\theta}}{r} - \sigma^0_{\theta z}u_{\theta,z} + \sigma_r - \sigma_\theta\right) = 0 \tag{4}$$

Copyright © 1997 by ASME

Downloaded 04 May 2010 to 171.66.16.34. Redistribution subject to ASME license or copyright; see http://www.asme.org/terms/Terms_Use.cfm

$$\frac{\partial}{\partial r}\left[\sigma_r^0 u_{\theta,r} + \sigma_{r\theta}^0 \frac{u_r + u_{\theta,\theta}}{r} + \sigma_{rz}^0 u_{\theta,z} + \sigma_{r\theta}\right]$$

$$+ \frac{\partial}{r\partial\theta}\left[\sigma_{r\theta}^0 u_{\theta,r} + \sigma_\theta^0 \frac{u_r + u_{\theta,\theta}}{r} + \sigma_{\theta z}^0 u_{\theta,z} + \sigma_{\theta\theta}\right]$$

$$+ \frac{\partial}{\partial z}\left[\sigma_{zr}^0 u_{\theta,r} + \sigma_{\theta z}^0 \frac{u_r + u_{\theta,\theta}}{r} + \sigma_z^0 u_{\theta,z} + \sigma_{zz}\right]$$

$$+ \frac{1}{r}\left(\sigma_r^0 u_{\theta,r} + \sigma_{r\theta}^0 \frac{u_r + u_{\theta,\theta}}{r} + \sigma_{zr}^0 u_{\theta,z} + \sigma_{r\theta}^0 u_{r,r} + \sigma_{\theta\theta}^0 \frac{u_{r,\theta} - u_\theta}{r} + \sigma_{\theta z}^0 u_{r,z} + 2\sigma_{r\theta}\right) = 0 \quad (5)$$

$$\frac{\partial}{\partial r}\left[\sigma_r^0 u_{z,r} + \sigma_{r\theta}^0 \frac{u_{z,\theta}}{r} + \sigma_{rz}^0 u_{z,z} + \sigma_{zr}\right]$$

$$+ \frac{\partial}{r\partial\theta}\left[\sigma_{r\theta}^0 u_{z,r} + \sigma_\theta^0 \frac{u_{z,\theta}}{r} + \sigma_{\theta z}^0 u_{z,z} + \sigma_{\theta z}\right]$$

$$+ \frac{\partial}{\partial z}\left[\sigma_{zr}^0 u_{z,r} + \sigma_{\theta z}^0 \frac{u_{z,\theta}}{r} + \sigma_z^0 u_{z,z} + \sigma_{zz}\right]$$

$$+ \frac{1}{r}\left(\sigma_r^0 u_{z,r} + \sigma_{r\theta}^0 \frac{u_{z,\theta}}{r} + \sigma_{zr}^0 u_{z,z} + \sigma_{zr}\right) = 0 \quad (6)$$

$$D_{r,r} + \frac{D_{\theta,\theta}}{r} + D_{z,z} + \frac{D_r}{r} = 0 \quad (7)$$

in which u_r, u_θ, and u_z are the mechanical displacements in the radial, the circumferential, and the axial directions, and D_r, D_θ, and D_z are the corresponding electric displacements in the Lagrangian description.

The linear constitutive equations coupling piezoelectric materials are given by

$$\{\sigma\} = [C]\{\varepsilon\} - [e]^T\{E\}$$

$$\{D\} = [e]\{\varepsilon\} + [\epsilon]\{E\} \quad (8)$$

where superscript T means transpose of a matrix, $[C]$ is the elastic constant matrix, $[e]$ the piezoelectric stress coefficient matrix, $[\epsilon]$ the dielectric matrix, $\{\varepsilon\}$ the strain vector, and $\{E\}$ is the electric field which can be described in terms of a scalar function as

$$E_r = -\varphi_{,r}; \quad E_\theta = -\frac{\varphi_{,\theta}}{r}; \quad E_z = -\varphi_{,z} \quad (9)$$

where φ is the increment of the electric potential from an initial state. And the relation between the strain and the mechanical displacement are

$$\varepsilon_r = u_{r,r}; \quad \varepsilon_\theta = \frac{u_{\theta,\theta} + u_r}{r}; \quad \varepsilon_z = u_{z,z}$$

$$\gamma_{\theta z} = u_{\theta,z} + \frac{u_{z,\theta}}{r}; \quad \gamma_{zr} = u_{r,z} + u_{z,r};$$

$$\gamma_{r\theta} = u_{\theta,r} + \frac{u_{r,\theta} - u_\theta}{r}. \quad (10)$$

All the matrices in Eq. (8) are shown in the Appendix.

Prebuckling Analysis

The piezoelectric circular cylindrical shell considered in this paper is of infinite length and is subjected to axisymmetric pressure and applied electric voltage in the radial direction. R_1 and R_2 are the inner and outer radii, respectively (shown in Fig. 1). Exact study (Chen et al., 1996) has shown that the linear variation assumption of the electric potential in the radial direction is reasonable even for a thick piezoelectric shell. Therefore, the electric field in the radial direction is assumed to be uniform in this paper. And, the charge equation of electrostatics is then thought to be approximately satisfied without further investigation. Under these considerations such as infinite length, axisymmetric state, and uniform electric field (E_r^0) as well as outer pressure (Q_r^0) in the radial direction, the prebuckling study is simple.

Substituting Eq. (9) and (10) into the following constitutive equation,

$$\begin{Bmatrix} \sigma_r^0 \\ \sigma_\theta^0 \\ \sigma_{r\theta}^0 \end{Bmatrix} = \begin{bmatrix} C_{11} & C_{12} & \\ C_{12} & C_{22} & \\ & & C_{66} \end{bmatrix} \begin{Bmatrix} \varepsilon_r^0 \\ \varepsilon_\theta^0 \\ \gamma_{r\theta}^0 \end{Bmatrix} - \begin{bmatrix} e_{33} & \\ e_{31} & \\ & e_{15} \end{bmatrix} \begin{Bmatrix} E_r^0 \\ 0 \end{Bmatrix}, \quad (11)$$

and then into the equilibrium equation

$$\sigma_{r,r}^0 + \frac{\sigma_r^0 - \sigma_\theta^0}{r} = 0, \quad (12)$$

we have

$$C_{11} u_{r,rr}^0 + C_{11}\frac{u_{r,r}^0}{r} - C_{22}\frac{u_r^0}{r^2} = (e_{33} - e_{31})\frac{E_r^0}{r}, \quad (13)$$

where the superscript zero denotes the prebuckling state. With the given boundary conditions, the displacement solution of Eq. (13) can be obtained directly.

When $C_{22} \neq C_{11}$ which is the case studied in present paper, we have

$$u_r^0 = A_1 r^\beta + A_2 r^{-\beta} + \frac{(e_{33} - e_{31})E_r^0}{(1 - \beta^2)C_{11}} r \quad (14)$$

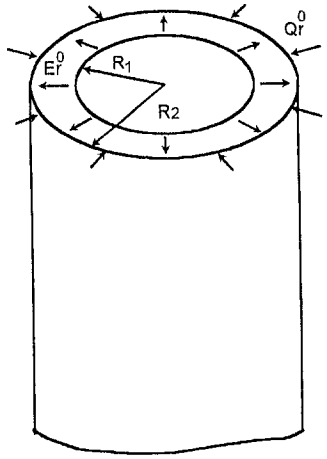


Fig. 1 Configuration of the circular cylindrical shell

Downloaded 04 May 2010 to 171.66.16.34. Redistribution subject to ASME license or copyright; see http://www.asme.org/terms/Terms_Use.cfm

in which

$$A_1 = \frac{\tilde{P}c^{\beta+1} - \tilde{Q}}{(1 - c^{2\beta})(\beta C_{11} + C_{12})R_2^{\beta-1}};$$

$$A_2 = \frac{(\tilde{Q}c^{\beta-1} - \tilde{P})R_1^{\beta+1}}{(1 - c^{2\beta})(-\beta C_{11} + C_{12})R_2^{\beta-1}}$$

$$\tilde{P} = -e_{33}E_r^0 + \frac{C_{11} + C_{12}}{C_{11} - C_{22}}(e_{33} - e_{31})E_r^0$$

$$\tilde{Q} = Q_r^0 - e_{33}E_r^0 + \frac{C_{11} + C_{12}}{C_{11} - C_{22}}(e_{33} - e_{31})E_r^0$$

$$c = \frac{R_1}{R_2}; \quad \beta = \sqrt{\frac{C_{22}}{C_{11}}}. \tag{15}$$

Accordingly, the prebuckling stress can be obtained and the nonzero ones are given by

$$\sigma_r^0 = \frac{1}{1 - c^{2\beta}}\left[(\tilde{P}c^{\beta+1} - \tilde{Q})\left(\frac{r}{R_2}\right)^{\beta-1} + (\tilde{Q}c^{\beta-1} - \tilde{P})\left(\frac{R_1}{r}\right)^{\beta+1}\right] + \frac{C_{11} + C_{12}}{C_{11} - C_{22}}(e_{33} - e_{31})E_r^0 - e_{33}E_r^0$$

$$\sigma_\theta^0 = \frac{\beta}{1 - c^{2\beta}}\left[(\tilde{P}c^{\beta+1} - \tilde{Q})\left(\frac{r}{R_2}\right)^{\beta-1} - (\tilde{Q}c^{\beta-1} - \tilde{P})\left(\frac{R_1}{r}\right)^{\beta+1}\right] + \frac{C_{11} + C_{12}}{C_{11} - C_{22}}(e_{33} - e_{31})E_r^0. \tag{16}$$

Buckling Equations and Solution

With the prebuckling analysis, the linear buckling equations for the piezoelectric circular cylindrical shell can be derived. Since the structure is of infinite length, the axial direction is not taken into consideration. As a result, the three-dimensional equations (4)–(7) reduce to two-dimensional ones.

In virtue of the constitutive Eq. (8) and the strain-displacement and electric field-electric potential relations, the stress and the electric displacement can be expressed in terms of the increments of the mechanical displacements and the electric potential as

$$\sigma_r = C_{11}u_{r,r} + \frac{C_{12}}{r}(u_r + u_{\theta,\theta}) + e_{33}\varphi_{,r} \tag{17}$$

$$\sigma_\theta = C_{12}u_{r,r} + \frac{C_{22}}{r}(u_r + u_{\theta,\theta}) + e_{31}\varphi_{,r} \tag{18}$$

$$\sigma_{r\theta} = C_{66}\left(\frac{\partial u_\theta}{\partial r} + \frac{u_{r,\theta} - u_\theta}{r}\right) + e_{15}\frac{\varphi_{,\theta}}{r} \tag{19}$$

$$D_r = e_{33}u_{r,r} + e_{31}\frac{u_r + u_{\theta,\theta}}{r} - \epsilon_{33}\varphi_{,r} \tag{20}$$

$$D_\theta = e_{15}\left(u_{\theta,r} + \frac{u_{r,\theta} - u_\theta}{r}\right) - \epsilon_{11}\frac{\varphi_{,\theta}}{r}. \tag{21}$$

Substituting Eqs. (17)–(21) into Eqs. (4), (5), and (7), and neglecting variables related to the axial direction yield the two-dimensional buckling equations governing the infinitely long piezoelectric shell

$$\left[(C_{11} + \sigma_r^0)\frac{\partial^2}{\partial r^2} + \left(C_{11} + r\frac{\partial \sigma_r^0}{\partial r} + \sigma_r^0\right)\frac{\partial}{r\partial r} + (-C_{22} - \sigma_\theta^0)\frac{1}{r^2} + (C_{66} + \sigma_\theta^0)\frac{\partial^2}{r^2\partial\theta^2}\right]u_r + \left[(C_{12} + C_{66})\frac{\partial^2}{r\partial r\partial\theta} + (-C22 - C66 - 2\sigma_\theta^0)\frac{\partial}{r^2\partial\theta}\right]u_\theta + \left[e_{33}\frac{\partial^2}{\partial r^2} + (e_{33} - e_{31})\frac{\partial}{r\partial r} + e_{15}\frac{\partial^2}{r^2\partial\theta^2}\right]\varphi = 0 \tag{22}$$

$$\left[(C_{12} + C_{66})\frac{\partial^2}{r\partial r\partial\theta} + (C_{22} + C_{66} + 2\sigma_\theta^0)\frac{\partial}{r^2\partial\theta}\right]u_r + \left[(C_{66} + \sigma_r^0)\frac{\partial^2}{\partial r^2} + \left(C_{66} + r\frac{\partial \sigma_r^0}{\partial r} + \sigma_r^0\right)\frac{\partial}{r\partial r} + (-C_{66} - \sigma_\theta^0)\frac{1}{r^2} + (C_{22} + \sigma_\theta^0)\frac{\partial^2}{r^2\partial\theta^2}\right]u_\theta + \left[(e_{31} + e_{15})\frac{\partial^2}{r\partial r\partial\theta} + e_{15}\frac{\partial}{r^2\partial\theta}\right]\varphi = 0 \tag{23}$$

$$\left[e_{33}\frac{\partial^2}{\partial r^2} + (e_{31} + e_{33})\frac{\partial}{r\partial r} + e_{15}\frac{\partial^2}{r^2\partial\theta^2}\right]u_r + \left[(e_{31} + e_{15})\frac{\partial^2}{r\partial r\partial\theta} - e_{15}\frac{\partial}{r^2\partial\theta}\right]u_\theta - \left[\epsilon_{33}\frac{\partial^2}{\partial r^2} + \epsilon_{33}\frac{\partial^2}{r\partial r} + \epsilon_{11}\frac{\partial^2}{r^2\partial\theta^2}\right]\varphi = 0. \tag{24}$$

Additionally, the boundary conditions on the inner and outer surfaces need to be formulated. The boundary conditions associated with Eq. (1) are given by

$$\sigma_{KL}\delta_{Ki}N_L^0 + \sigma_{KL}^0 u_{i,K}N_L^0 = \bar{T}_i \tag{25}$$

where N_L^0 is the unit vector normal outward to surface of the prebuckling state and $\bar{T}_i$ is the traction increment vector acting on the bounding surface. Indeed, the magnitude of the traction (hydrostatic pressure) remains invariant under deformation while its direction changes, which is always normal to the surface at which it acts.

Since the inner and outer surface of the shell is subjected to electric potential, the boundary conditions related to Eq. (2) is

$$\varphi = 0. \tag{26}$$

It should be noted that it is not necessary to assume the variation of the electric potential increment to be linear in this part.

Taking into account the neglecting of all variables in the axial direction and the assumption that the piezoelectric retains its shape before buckling (i.e., $N_r^0 = 1$, $N_\theta^0 = 0$), Eq. (25) can be written in the cylindrical coordinate system as

$$\sigma_r + \sigma_r^0 u_{r,r} = \bar{T}_r; \quad \sigma_{r\theta} + \sigma_r^0 u_{\theta,r} = \bar{T}_\theta \tag{27}$$

in which we have made use of the fact that $\sigma_{r\theta}^0$ is vanished.

Downloaded 04 May 2010 to 171.66.16.34. Redistribution subject to ASME license or copyright; see http://www.asme.org/terms/Terms_Use.cfm

Because the traction increments $\bar{T}_r$ and $\bar{T}_\theta$ are due to the variation of the unit normal during the deformation, we have (see, Fig. 2)

$$\bar{T}_r = -Q_r^0 N_r; \quad \bar{T}_\theta = -Q_r^0 N_\theta \tag{28}$$

where N_r and N_θ are the increments of the unit normal during the deformation and when linear buckling is considered they are determined by the displacement field as (see, Kuang, 1989)

$$N_p = u_{i,k} N_i^0 N_k^0 N_p^0 - u_{k,p} N_k^0. \tag{29}$$

Following Eq. (29), we arrive at

$$N_r = 0; \quad N_\theta = \frac{u_\theta - u_{r,\theta}}{r}. \tag{30}$$

Substituting Eq. (30) into (28) and then into (27) yields

$$\sigma_r + \sigma_r^0 u_{r,r} = 0$$

$$\sigma_{r\theta} + \sigma_r^0 u_{\theta,r} = -Q_r^0 \frac{u_\theta - u_{r,\theta}}{r}. \tag{31}$$

Combining Eqs. (17)–(19) and (31) produces the boundary conditions on the outer surface

$$\left(C_{11}\frac{\partial}{\partial r} + C_{12}\frac{1}{r} - Q_r^0\frac{\partial}{\partial r}\right)u_r + C_{12}\frac{\partial}{r\partial\theta}u_\theta + e_{33}\frac{\partial}{\partial r}\varphi = 0$$

$$(C_{66} - Q_r^0)\frac{\partial^2}{\partial r\partial\theta}u_r + \left[C_{66}\left(\frac{\partial}{\partial r} - \frac{1}{r}\right) + \frac{Q_r^0}{r} - Q_r^0\frac{\partial}{\partial r}\right]u_\theta + e_{15}\frac{\partial}{r\partial\theta}\varphi = 0 \tag{32}$$

and those on the inner surface

$$\left(C_{11}\frac{\partial}{\partial r} + C_{12}\frac{1}{r}\right)u_r + C_{12}\frac{\partial}{r\partial\theta}u_\theta + e_{33}\frac{\partial}{\partial r}\varphi = 0$$

$$C_{66}\frac{\partial^2}{\partial r\partial\theta}u_r + C_{66}\left(\frac{\partial}{\partial r} - \frac{1}{r}\right)u_\theta + e_{15}\frac{\partial}{r\partial\theta}\varphi = 0. \tag{33}$$

A set of displacement and electric potential functions for the solution of the buckling equations is assumed to be

$$u_r = F_r(r)\cos k\theta; \quad u_\theta = F_\theta(r)\sin k\theta;$$
$$\varphi = F_\varphi(r)\cos k\theta \tag{34}$$

in which k is the number of the buckling half-wave in the circumferential direction.

Substituting Eq. (34) into (22)–(24), (32), and (33), we arrive at the following linear homogeneous ordinary differential equations governing the buckling problem, i.e., the equilibrium equation and the charge equation of electrostatics

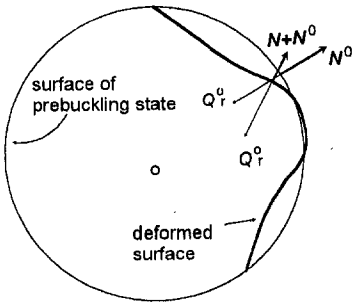


Fig. 2 Tractions on the deformed shell

Table 1 Comparison of the critical pressure $Q_{cr}R_2^3/[10C_{66}(R_2 - R_1)^3]$ for the composite shell obtained by different methods

R_2/R_1	Present	Simplified Elasticity*	Classic Shell Theory*
1.10	0.2693	0.2728 (1.3%)	0.2930 (8.9%)
1.15	0.2697	0.2769 (2.7%)	0.3119 (15.6%)
1.20	0.2671	0.2784 (4.2%)	0.3308 (23.8%)
1.25	0.2623	0.2780 (6.0%)	0.3495 (33.2%)
1.30	0.2561	0.2762 (7.8%)	0.3681 (43.7%)
1.40	0.2420	0.2696 (11.4%)	0.4046 (67.2%)

* Kardomateas (1993).

$$\left[(C_{11} + \sigma_r^0)\frac{\partial^2}{\partial r^2} + \left(C_{11} + r\frac{\partial\sigma_r^0}{\partial r} + \sigma_r^0\right)\frac{\partial}{r\partial r} + (-C_{22} - \sigma_\theta^0)\frac{1}{r^2} - (C_{66} + \sigma_\theta^0)\frac{k^2}{r^2}\right]F_r + k\left[(C_{12} + C_{66})\frac{\partial}{r\partial r} - (C_{22} + C_{66} + 2\sigma_\theta^0)\frac{1}{r^2}\right]F_\theta + \left[e_{33}\frac{\partial^2}{\partial r^2} + (e_{33} - e_{31})\frac{\partial}{r\partial r} - e_{15}\frac{k^2}{r^2}\right]F_\varphi = 0 \tag{35}$$

$$\left[-k(C_{12} + C_{66})\frac{\partial}{r\partial r} - (C_{22} + C_{66} + 2\sigma_\theta^0)\frac{k}{r^2}\right]F_r + \left[(C_{66} + \sigma_r^0)\frac{\partial^2}{\partial r^2} + \left(C_{66} + r\frac{\partial\sigma_r^0}{\partial r} + \sigma_r^0\right)\frac{\partial}{r\partial r} + (-C_{66} - \sigma_\theta^0)\frac{1}{r^2} - (C_{22} + \sigma_\theta^0)\frac{k^2}{r^2}\right]F_\theta - k\left[(e_{31} + e_{15})\frac{\partial}{r\partial r} + e_{15}\frac{1}{r^2}\right]F_\varphi = 0 \tag{36}$$

$$\left[e_{33}\frac{\partial^2}{\partial r^2} + (e_{31} + e_{33})\frac{\partial}{r\partial r} - k^2 e_{15}\frac{1}{r^2}\right]F_r + k\left[(e_{31} + e_{15})\frac{\partial}{r\partial r} - e_{15}\frac{1}{r^2}\right]F_\theta - \left[\epsilon_{33}\frac{\partial^2}{\partial r^2} + \epsilon_{33}\frac{\partial^2}{r\partial r} - k^2\epsilon_{11}\frac{1}{r^2}\right]F_\varphi = 0, \tag{37}$$

the boundary conditions on the outer surface

$$\left(C_{11}\frac{\partial}{\partial r} + C_{12}\frac{1}{r} - Q_r^0\frac{\partial}{\partial r}\right)F_r + C_{12}\frac{k}{r}F_\theta + e_{33}\frac{\partial}{\partial r}F_\varphi = 0$$

$$-k(C_{66} - Q_r^0)\frac{\partial}{\partial r}F_r + \left[C_{66}\left(\frac{\partial}{\partial r} - \frac{1}{r}\right) + \frac{Q_r^0}{r} - Q_r^0\frac{\partial}{\partial r}\right]F_\theta - ke_{15}\frac{1}{r}F_\varphi = 0$$

$$F_\varphi = 0, \tag{38}$$

and the boundary conditions on the inner surface

Downloaded 04 May 2010 to 171.66.16.34. Redistribution subject to ASME license or copyright; see http://www.asme.org/terms/Terms_Use.cfm

$$\left(C_{11}\frac{\partial}{\partial r}+C_{12}\frac{1}{r}\right)F_r+C_{12}\frac{k}{r}F_\theta+e_{33}\frac{\partial}{\partial r}F_\varphi=0$$

$$-kC_{66}\frac{\partial}{\partial r}F_r+C_{66}\left(\frac{\partial}{\partial r}-\frac{1}{r}\right)F_\theta-ke_{15}\frac{1}{r}F_\varphi=0$$

$$F_\varphi=0. \tag{39}$$

It should be noted that in the derivation of Eqs. (35)–(39), the assumption that strain is negligible when compared to rotation used by Lekhnitskii (1981) and Kardomateas (1993) is not employed in this paper. As a result, present buckling formulations are more general and can be applied to thick shell analysis.

The eigenvalue problem (35)–(39) can be solved by numerical method. The standard Euler method for a two-point value problem is used to provide results. And the convergence of the method has been investigated during our numerical study.

Numerical Results and Discussion

In order to validate our derived formulations, an infinitely long composite circular cylindrical shell subjected to outer pressure is studied, which was also investigated by Kardomateas (1993). The inner radium is $R_1 = 1$ m with material properties given in the Appendix. The minimum eigenvalue is obtained when $k = 2$, which is usually termed as the critical value or buckling value. The critical pressure of the elastic composite shell provided by present exact study, the elasticity solution, and the classical shell theory prediction of Kardomateas (1993) is presented in Table 1 for various outer to inner radium ratios. As we can see, only when the shell is not very thick the simplified elasticity solutions of Kardomateas (1993) coincide well with present results. The reason may be that an assumption that strain is small compared to the rotation is employed in the simplified elasticity solutions while no such assumption is used in present derivation. Therefore, the assumption is only suitable for thin to moderately thick shells.

The second example is an infinitely long circular cylindrical shell made of piezoelectric ceramics. Its material properties are listed in the Appendix for an inner radium $R_1 = 1$ m. When only an electric field is applied in the radial directions, the critical value leading to buckling is $E_r^0 = 9.815 \times 10^{10}(\text{Volt}\cdot\text{m}^{-1})$ for $R_2 = 1.1$ m. Considering that the damage electric field of piezoelectric ceramic is always between 10^5 and $10^6(\text{Volt}\cdot\text{m}^{-1})$, the critical electric field is so large that piezoelectric shell is damaged before losing its stability. In other words, the uniform electric field alone is not likely to cause elastic buckling. Furthermore, we have found that the electric field hardly has any effect on the critical pressure (not shown here) when the electric field is below the damage value. The buckling pressure loads (marked by Q_{cr}^p) of the piezoelectric shell are shown in Table 2. When the effect of piezoelectric material is neglected, i.e., the piezoelectric shell is treated as an elastic orthotropic shell, the critical value of the pressure load (marked by Q_{cr}^c) is also listed in it. Table 2 shows that although the effect of the electric field on the critical pressure is negligible, the piezoelectric effect affects it greatly.

Table 2 Critical pressures $[(Q_{cr}^p, Q_{cr}^c)R_2^3]/[C_{11}(R_2 - R_1)^3]$ for the piezoelectric circular cylindrical shell

R_2/R_1	$Q_{cr}^p R_2^3/[C_{11}(R_2 - R_1)^3]$	$Q_{cr}^c R_2^3/[C_{11}(R_2 - R_1)^3]$
1.10	0.2839	0.2143
1.15	0.2922	0.2204
1.20	0.2991	0.2252
1.30	0.3092	0.2318
1.40	0.3156	0.2353

From the previous results, it can be concluded that for an infinitely long piezoelectric circular cylindrical shell, the uniform electric field alone will not cause elastic buckling, while the piezoelectric effect has a significant effect on the buckling pressure loading.

Acknowledgment

This project is supported by the National Natural Science Foundation of China and the Doctoral Education Foundation of China.

Reference

Baumhauer, J. C., and Tiersten, H. F., 1973, "Nonlinear electroelastic equations for small fields superposed on a bias," *J. Acoustic Society of America,* Vol. 54, No. 4, pp. 1017–1033.

Chen, C. Q., and Shen, Y. P., 1996, "Piezothermoelasticity analysis for circular cylindrical shell under the state of axisymmetric deformation," *Int. J. Engineering Science,* Vol. 34, No. 13, pp. 1585–1600.

Chen, C. Q., Shen, Y. P., and Wang, X. M., 1996a, "Exact solution of orthotropic cylindrical shell with piezoelectric layers under cylindrical bending," *Int. J. Solids and Structures,* Vol. 33, No. 30, pp. 4481–4494.

Chen, C. Q., and Shen, Y. P., 1996b, "Incremental variational principles for finitely deformed piezothermoelastic media," *Acta Solids Mechnica Sinica,* submitted for publication.

Lekhnitskii, S. G., 1981, *Theory of elasticity of an anisotropic elastic body,* Mir Publishers, Moscow, Russia.

Miller, S. E., and Abramovich, H., 1995, "A self-sensing piezolaminated actuator model for shells using a first shear deformation theory," *J. Intelligent Material Systems and Structures,* Vol. 6, pp. 624–638.

Kardomateas, G. A., 1993, "Buckling of Thick Orthtropic Cylindrical Shells Under External Pressure," ASME JOURNAL OF APPLIED MECHANICS, Vol. 60, pp. 195–202.

Kuang, Z. B., 1989, *Foundation of nonlinear continuum mechanics,* Xi'an Jiaotong University Press, Xi'an, China.

Tzou, H. S., 1992, "Anew distributed sensors and actuator theory for intelligent shells," *J. Sound Vibration,* Vol. 153, pp. 335–349.

Tzou, H. S., and Gadar, M., 1989, "Theoretical analysis of a multilayered thin shell coupled with piezoelectric shell actuators for distributed vibration controls," *J. Sound Vibration,* Vol. 132, pp. 433–450.

Tzou, H. S., and Tseng, C. L., 1991, "Distributed Modal Identification and Vibration Control of Continua: Piezoelectric Element Formulation and Analysis, ASME *Journal of Dynamic Systems, Measurement, and Control,* Vol. 113, pp. 500–505.

Tzou, H. S., and Ye, R., 1994, "Piezothermoelasticity and Precision Control of Piezoelectric Systems, ASME *Journal of Vibration and Acoustics,* Vol. 116, pp. 489–495.

Tzou, H. S., Zhong, J. P., and Holkamp, J. J., 1994, "Spatially distributed orthogonal piezoelectric shell actuators: theory and application," *J. Sound Vibration,* Vol. 177, pp. 363–378.

Washizu, K., 1982, *Variational methods in elasticity and plasticity,* Pergamon Press, 3rd ed., New York.

APPENDIX

The constitutive relations of Eqs. (8) in the cylindrical coordinate system are

$$\begin{Bmatrix}\sigma_r\\ \sigma_\theta\\ \sigma_z\\ \sigma_{\theta z}\\ \sigma_{zr}\\ \sigma_{r\theta}\end{Bmatrix}=\begin{bmatrix}C_{11}&C_{12}&C_{13}&&&\\ C_{12}&C_{22}&C_{23}&&&\\ C_{13}&C_{23}&C_{33}&&&\\ &&&C_{44}&&\\ &&&&C_{55}&\\ &&&&&C_{66}\end{bmatrix}\begin{Bmatrix}\varepsilon_r\\ \varepsilon_\theta\\ \varepsilon_z\\ \gamma_{\theta z}\\ \gamma_{zr}\\ \gamma_{r\theta}\end{Bmatrix}-\begin{bmatrix}e_{33}&0&0\\ e_{31}&0&0\\ e_{32}&0&0\\ 0&0&0\\ 0&0&e_{24}\\ 0&e_{15}&0\end{bmatrix}\begin{Bmatrix}E_r\\ E_\theta\\ E_z\end{Bmatrix}$$

Downloaded 04 May 2010 to 171.66.16.34. Redistribution subject to ASME license or copyright; see http://www.asme.org/terms/Terms_Use.cfm

$$\begin{Bmatrix} D_r \\ D_\theta \\ D_z \end{Bmatrix} = \begin{bmatrix} e_{33} & e_{31} & e_{32} & 0 & 0 & 0 \\ 0 & 0 & 0 & 0 & 0 & e_{15} \\ 0 & 0 & 0 & 0 & e_{24} & 0 \end{bmatrix} \begin{Bmatrix} \varepsilon_r \\ \varepsilon_\theta \\ \varepsilon_z \\ \gamma_{\theta z} \\ \gamma_{zr} \\ \gamma_{r\theta} \end{Bmatrix} + \begin{bmatrix} \epsilon_{33} & & \\ & \epsilon_{11} & \\ & & \epsilon_{22} \end{bmatrix} \begin{Bmatrix} E_r \\ E_\theta \\ E_z \end{Bmatrix} . \quad \text{(A1)}$$

The elements of an elastic constant matrix for the composite shell of infinite length are given by

$$C_{11} = 17.448 \times 10^9 \text{ Pa}, \quad C_{12} = 6.8938 \times 10^9 \text{ Pa}$$
$$C_{22} = 60.819 \times 10^9 \text{ Pa}, \quad C_{66} = 5.7 \times 10^9 \text{ Pa}. \quad \text{(A2)}$$

And the material propertises of the piezoelectric material are

$$C_{11} = 11.5 \times 10^{10} \text{ Pa}, \quad C_{12} = 7.43 \times 10^{10} \text{ Pa}$$
$$C_{22} = 13.9 \times 10^{10} \text{ Pa}, \quad C_{66} = 2.56 \times 10^{10} \text{ Pa}$$
$$e_{31} = -5.2\text{C} \cdot \text{m}^{-2}, \quad e_{33} = 15.1\text{C} \cdot \text{m}^{-2}, \quad e_{15} = 12.7\text{C} \cdot \text{m}^{-2}$$
$$\epsilon_{11} = 6.46 \times 10^{-9} \text{ F} \cdot \text{m}^{-1},$$
$$\epsilon_{33} = 5.62 \times 10^{-9} \text{ F} \cdot \text{m}^{-1}, \quad \text{(A3)}$$

in which C is Coulomb and F is Faraday. Other elements in Eq. (A1), which are not given in (A2) and (A3), are not related to the case of infinitely long circular cylindrical shell.

Downloaded 04 May 2010 to 171.66.16.34. Redistribution subject to ASME license or copyright; see http://www.asme.org/terms/Terms_Use.cfm

Total Deformation, Plane-Strain Contact Analysis of Macroscopically Homogeneous, Compositionally Graded Materials With Constant Power-Law Strain Hardening

A. E. Giannakopoulos
Department of Materials Science and Engineering, Massachusetts Institute of Technology, Cambridge, MA 02139

Plane-strain contact analysis is presented for compositionally graded materials with power-law strain hardening. The half-space, $y \leq 0$, is modeled as an incompressible, nonlinear elastic material. The effective stress, σ_e, and the effective total strain, ϵ_e, are related through a power-law model, $\sigma_e = K_0 \epsilon_e^{\mu}$; $0 < \mu \leq min\ (1, (1 + k))$. The material property K_0 changes with depth, $|y|$, as $K_0 = A|y|^k$; $A > 0$, $0 \leq |k| < 1$. This material description attempts to capture some features of the plane-strain indentation of elastoplastic or steady-state creeping materials that show monotonically increasing or decreasing hardness with depth. The analysis starts with the solution for the normal line load (Flamant's problem) and continues with the rigid, frictionless, flat-strip problem. Finally, the general solution of normal indentation of graded material by a convex, symmetric, rigid, and frictionless two-dimensional punch is given. Applications of the present results range from surface treatments of engineering structures, protective coatings for corrosion and fretting fatigue, settling of beam-type foundations in the context of soil and rock mechanics, to bioengineering as well as structural applications such as contact of railroad tracks.

1 Introduction

The stress and deformation fields in elastic half-spaces subjected to normal line loads have been examined extensively in the past. Extension to plane normal contact by symmetric rigid indenters such as flat strips, cylinders, and wedges were also examined previously (see Johnson (1985) for a comprehensive review).

An important extension of these problems involves the study of indentation of compositionally graded materials by point forces and other cylindrical indenters (strips, wedges, etc.), and penetration of geo-materials such as solids and rocks, where the elastic and/or plastic properties vary as a function of depth beneath the surface. The composite itself may be of two or more different materials such as particle reinforced ceramics or metals and cellular materials (graded porosity). This topic has major applications in a wide variety of scientific and technological areas which include:

- the synthesis (diffusion, plasma-spaying, molecular beam epitaxy, and chemical vapor deposition) of advanced coating for structural components to guard against tribological damage (e.g., fretting fatigue, wear),
- structural porous or cellular materials with gradients in porocity for wings and fuselags of aerospace vehicles, as well as in bioengineering models of teeth, bones, wood, etc.,
- geotechnical analysis of settlement and stability of foundations,
- earth removing devices like excavator teeth on deposits of inhomogeneous soils, clay rocks, and various ores,
- carburization and nitriding of steels on the surfaces of components subjected to repeated contact, for hardness enhancement due to carbon or nitrogen concentration, and
- impact and penetration of potential armor materials made of compositionally graded materials by projectiles.

A few general solutions exist for graded elastic substrates with Young's modulus varying with depth, $|y|$, as $E = E_0|y|^k$; $0 \leq k < 1$; $k = 0$ representing the homogeneous case and $k = 1$ denoting the so-called "Gibson soil." Holl (1940), Hruban (1958), and Lekhniskii (1962) considered deformation of line loads normal to an elastic half-space wherein the elastic modulus varies as a power-law function of depth from a value zero at the indented surface. In that work, radial stress fields were constructed for the particular cases of Poisson ratio $\nu = 1/(1 + k)$. Ching-Hua (1961) presented the general formulation of two-dimensional nonhomogeneous elastic isotropic medium. Gibson (1967), Brown and Gibson (1972), and Awojobi and Gibson (1973) presented plane-strain results for linearly nonhomogeneous ($k = 1$) isotropic elastic half-space. The additional issue of incompressibility ($\nu = 0.5$) was addressed by Hruban (1958) and Calladine and Greenwood (1978). Booker et al. (1985) studied the response of an elastic nonhomogeneous half-space subject to line loads, as well as the strip-type, rigid, and frictionless punch problem. In that formulation, the Poisson ratio was kept spacially invariant ($\nu = 0.25$) and a power-law variation with depth was assumed for the Young's modulus ($0 \leq k < 1$).

Contributed by the Applied Mechanics Division of THE AMERICAN SOCIETY OF MECHANICAL ENGINEERS for publication in the ASME JOURNAL OF APPLIED MECHANICS.

Discussion on this paper should be addressed to the Technical Editor, Professor Lewis T. Wheeler, Department of Mechancial Engineering, University of Houston, Houston, TX 77204-4792, and will be accepted until four months after final publication of the paper itself in the ASME JOURNAL OF APPLIED MECHANICS.

Manuscript received by the ASME Applied Mechanics Division, Oct. 29, 1996; final revision, Apr. 16, 1997. Associate Technical Editor: R. Becker.

Copyright © 1997 by ASME

Downloaded 04 May 2010 to 171.66.16.34. Redistribution subject to ASME license or copyright; see http://www.asme.org/terms/Terms_Use.cfm

Obviously, the power-law variation of material properties is a mathematical idealization which may be useful as a first approximation in the analysis of contact and indentation of inhomogeneous materials, much in the spirit of classic fracture mechanics analysis where total deformation power-law type of elasticity was used to examine near-tip fields (e.g., HRR singular fields). As for the homogenization problem, it is tacitly assumed that the micromechanical lengths are much smaller than the bulk contact lengths. Some of the above shortcomings have been quantified numerically and will be discussed in the conclusions. In any case, there are indeed actual materials (artificial and natural) that follow very closely these idealizations. Such materials are sandy soils and normally consolidated clay deposites ($k = 0.5$, O'Neill and Dobry (1980)), microcracked rocks, diffusion bonded materials (Ilschner and Cherradi, 1994), fiber composite multilayered materials, teeth, and bones. In these materials, the present nonlinear elastic analysis is very relevant.

It is the objective of this paper to extend the analytical solutions to inhomogeneous, nonlinear elastic substrates for plane contact problems by symmetric indentors (e.g., strips, cylinders, wedges). In this respect, the problem includes the additional nonlinearity due to local material behavior. The other nonlinearities are the inhomogeneity of mechanical properties and the contact analysis itself.

In the following, the normal line load was solved first. Subsequently, the general plane contact problem was approximated by superposition of the line load solution and solved. Complete solution was given for the flat strip punch and approximate solution was given for the wedge punch.

2 Problem Formulation

The material was modeled to be homogeneously incompressible ($\nu = 0.5$, everywhere), with a power-law strain hardening between the effective stress and the total effective strain. The strain-hardening coefficient was taken to be spatially constant but the amplitude varied as a power law with depth. The material was assumed to be locally isotropic. Such material description approximates a graded substrate with hardness (or yield strength) that increases or decreases monotonically with depth. The plane indenters were taken to be rigid, convex, and symmetric. The contact radius was assumed to be frictionless. The material was considered to be initially stress-free and without body forces. However, the inhomogeneous variation of the stress-strain amplitude may account for the residual stresses, assuming simple changes in the yield strength with depth due to the constraint effect of the residual stresses. Small strain isothermal analysis was carried out using cylindrical coordinates (r, θ, z), as shown in Fig. 1 ($r \geq 0$; $-\pi/2 \leq \theta \leq \pi/2$).

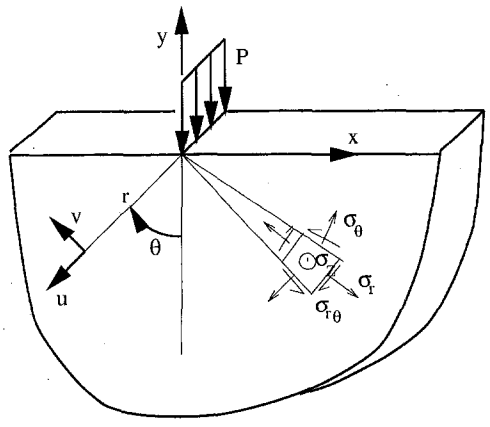


Fig. 1 The coordinate system, the displacement, and the stress directions for the plane line load and contact problem

A power-law total deformation plasticity is a useful model because it can capture most of the loading history of incremental plasticity (if the stress paths are nearly proportional), steady-state creep (if primary creep is of lesser importance), nonlinear elasticity (if strain rotations are small). Therefore, the present analysis can be easily extended to approximate the above cases which cover broad classes of materials such as metals and polymers, under different range of temperature or strain rates.

In the plane-strain problem, the effective (Mises) stress, σ_e, and the total effective strain, ϵ_e, are

$$\sigma_e = [(\sigma_\theta - \sigma_z)^2 + (\sigma_\theta - \sigma_r)^2 + (\sigma_r - \sigma_z)^2 + 6\sigma_{r\theta}^2]^{1/2}/\sqrt{6}, \quad (1)$$

$$\epsilon_e = [(\epsilon_\theta - \epsilon_z)^2 + (\epsilon_\theta - \epsilon_r)^2 + (\epsilon_r - \epsilon_z)^2 + 6\gamma_{r\theta}^2]^{1/2}/\sqrt{6}, \quad (2)$$

in obvious notation for the stress and strain components in the chosen coordinate system. Then, the constitutive law reads as

$$\sigma_e = K_0 \epsilon_e^\mu, \quad (3)$$

where μ is the strain-hardening coefficient and K_0 is the amplitude characterizing the material at a specific point. Note that $0 < \mu < 1$, with $\mu = 1$ approaching linear elasticity and $K_0 > 0$, so that $d^2\epsilon_e/d\sigma_e^2 > 0$, as indicated in Fig. 2. The strain-hardening coefficient, μ, is assumed to be spatially constant.

The inhomogeneity (continuous gradiation of mechanical properties) of the problem is introduced by asuming a spatial variation of K_0 with depth,

$$K_0 = A|y|^k = Ar^k \cos^k \theta, \quad (4)$$

with $A > 0$ (A has dimensions of stress $\times$ length^{-k}) and $0 \leq |k| < 1$, a dimensionless constant describing the rate of change of the amplitude of the stress-strain law and characterizing the composition (and to some extend the residual stresses) of the graded substrate. For $0 \leq k < 1$, hardness increases with depth, whereas for $-1 < k \leq 0$, hradness decreases with depth. Clearly, this is an idealization that facilitates the analytic part of this work and should be viewed only as a method to unveil the trends.

The strain-displacement relations are given as

$$\epsilon_r = \frac{\partial u}{\partial r}, \quad (5)$$

$$\epsilon_\theta = \frac{1}{r}\frac{\partial v}{\partial \theta} + \frac{u}{r}, \quad (6)$$

$$\epsilon_z = 0, \quad (7)$$

$$2\gamma_{r\theta} = \frac{\partial v}{\partial r} - \frac{u}{r} + \frac{1}{r}\frac{\partial u}{\partial \theta}, \quad (8)$$

where u and v are the displacements along the r and θ direction (Fig. 1).

Assuming associative flow rule, the plane stress-strain relations read as

$$\sigma_r - \sigma_z = \epsilon_r K_0 \epsilon_e^{\mu-1}, \quad (9)$$

$$\sigma_\theta - \sigma_z = \epsilon_\theta K_0 \epsilon_e^{\mu-1}, \quad (10)$$

$$\sigma_{r\theta} = \gamma_{r\theta} K_0 \epsilon_e^{\mu-1}, \quad (11)$$

$$\sigma_z = (\sigma_r + \sigma_\theta)/2. \quad (12)$$

The incompressibility condition reads as

$$\epsilon_r + \epsilon_\theta = 0. \quad (13)$$

Downloaded 04 May 2010 to 171.66.16.34. Redistribution subject to ASME license or copyright; see http://www.asme.org/terms/Terms_Use.cfm

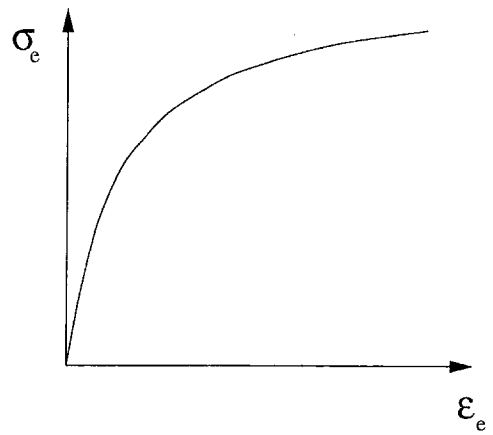


Fig. 2 The stress-strain relation between effective stress and effective strain, $\sigma_e = K_0\epsilon_e^\mu$, $K_0 > 0$, $0 < \mu \le \min(1, (1 + k))$

In the absence of body forces, the equilibrium equations are

$$\frac{\partial}{\partial r}[r\sigma_r] + \frac{\partial \sigma_{r\theta}}{\partial \theta} = \sigma_\theta, \tag{14}$$

$$\frac{\partial \sigma_\theta}{\partial \theta} + r\frac{\partial \sigma_{r\theta}}{\partial r} + 2\sigma_{r\theta} = 0. \tag{15}$$

3 The Normal Line Load at the Surface

The problem to be solved is shown in Fig. 1. The applied normal line load is P (dimensions force $\times$ length^{-1}). The boundary conditions exclude tractions acting on the free surface, $y = 0$.

$$\sigma_\theta = \sigma_{r\theta} = 0; \quad \theta = \pm\pi/2, \quad r > 0. \tag{16}$$

Following Arutiunian (1959), assume that the displacements can be given as

$$u = f_1(r)X_{,\theta}(\theta) + f_{0,\theta}(\theta), \tag{17}$$

$$v = f_2(r)X(\theta) - f_0(\theta). \tag{18}$$

The comma denotes differentiation with respect to the function's argument. The functions f_0, f_1, f_2, and X are singe-valued and continuous in the space $r > 0$ and $-\pi/2 \le \theta \le \pi/2$.

Assume that

$$\sigma_{r\theta} = 0; \quad \text{everywhere}, \tag{19}$$

$$\sigma_\theta = 0; \quad \text{everywhere}. \tag{20}$$

Then, both boundary conditions, Eq. (16), are automatically satisfied. This will render all fields to be radial and pointing to the location of application of the load ($r = 0$). Equilibrium Eq. (15) will also be automatically satisfied. From the constitutive Eq. (11),

$$\gamma_{r\theta} = 0. \tag{21}$$

Equation (21) together with (8), (13), (17), and (18) decouple into a system of three ordinary equations

$$f_{0,\theta\theta}(\theta) + f_0(\theta) = 0, \tag{22}$$

$$X_{,\theta\theta}(\theta) + \lambda^2 X(\theta) = 0, \tag{23}$$

$$r^2 f_{1,rr}(r) + rf_{1,r}(r) - [1 - \lambda^2]f_1(r) = 0, \tag{24}$$

and

$$f_2(r) = -(rf_{1,r}(r) + f_1(r)), \tag{25}$$

with λ a parameter to be defined ($0 < \lambda^2 < 1$). At $r \to \infty$, u and v must be finite. Then solving (24), without loss of generality,

$$f_1(r) = r^{-\sqrt{1-\lambda^2}}. \tag{26}$$

Note that in the linear case, $\mu = 1$, $\lambda = 1$ and $f_1(r) = \ln(r)$. This case has been examined by Calladine and Greenwood (1978) and will not be elaborated further.

The nonzero strains are

$$\epsilon_r = -\epsilon_\theta = -\sqrt{1 - \lambda^2}\, r^{-(1+\sqrt{1-\lambda^2})} X_{,\theta}(\theta) \tag{27}$$

and the effective strain is

$$\epsilon_e = |\epsilon_r| = \sqrt{1 - \lambda^2}\, r^{-(1+\sqrt{1-\lambda^2})} |X_{,\theta}(\theta)|. \tag{28}$$

The nonzero stresses are

$$\sigma_r = -2K_0[\sqrt{1 - \lambda^2}\, r^{-(1+\sqrt{1-\lambda^2})}]^\mu |X_{,\theta}(\theta)|^\mu, \tag{29}$$

$$\sigma_z = \sigma_r/2. \tag{30}$$

In order to satisfy the remaining equilibrium Eq. (14),

$$\sqrt{1 - \lambda^2} = \frac{1 + k}{\mu} - 1, \tag{31}$$

where for $0 \le k < 1$, $0 < \mu < 1$ and for $-1 < k \le 0$, $0 < \mu < 1 + k$.

To prevent overall rotations, $v = 0$ at $\theta = 0$. Then, the solution of (22) is

$$f_0(\theta) = D_6 \sin\theta, \tag{32}$$

and the solution of (23) is

$$X(\theta) = D_4\theta; \quad \frac{\mu}{1 + k} = \frac{1}{2}, \tag{33}$$

$$X(\theta) = D_4 \sin\lambda\theta; \quad \frac{\mu}{1 + k} > \frac{1}{2}, \tag{34}$$

$$X(\theta) = D_4 \sinh|\lambda|\theta; \quad \frac{\mu}{1 + k} < \frac{1}{2}. \tag{35}$$

Therefore,

$$X_{,\theta}(\theta) = D_4; \quad \frac{\mu}{1 + k} = \frac{1}{2}, \tag{36}$$

$$X_{,\theta}(\theta) = D_4\lambda \cos\lambda\theta; \quad \frac{\mu}{1 + k} > \frac{1}{2}, \tag{37}$$

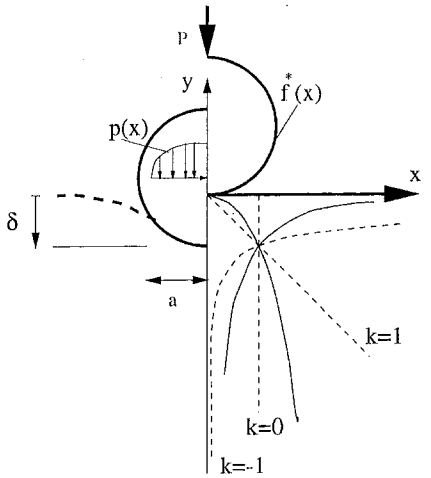


Fig. 3 The plane contact problem. Geometry of the indenter and contact pressure, $p(x)$, along the surface segment, $|x| \le a$.

Downloaded 04 May 2010 to 171.66.16.34. Redistribution subject to ASME license or copyright; see http://www.asme.org/terms/Terms_Use.cfm

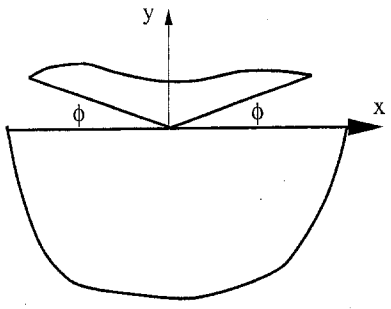


Fig. 4 The geometry of the wedge indenter

$$X_{,\theta}(\theta) = D_4|\lambda|\cosh|\lambda|\theta; \quad \frac{\mu}{1+k} < \frac{1}{2}. \tag{38}$$

From overall equilibrium,

$$P = -\int_{-\pi/2}^{\pi/2} \sigma_r r \cos\theta d\theta \tag{39}$$

(the line force is taken positive towards the half-space, Fig. 1). Using (39) with (29) and (36)–(38), we obtain

$$D_4 = \frac{P^{1/\mu}}{A^{1/\mu}\sqrt{1-\lambda^2}J^{1/\mu}}, \tag{40}$$

with

$$J = 4\int_0^{\pi/2} \cos^{k+1}\theta d\theta; \quad \frac{\mu}{1+k} = \frac{1}{2}, \tag{41}$$

$$J = 4\lambda^{\mu}\int_0^{\pi/2} \cos^{\mu}\lambda\theta\cos^{k+1}\theta d\theta; \quad \frac{\mu}{1+k} > \frac{1}{2}, \tag{42}$$

$$J = 4|\lambda|^{\mu}\int_0^{\pi/2} \cosh^{\mu}|\lambda|\theta\cos^{k+1}\theta d\theta; \quad \frac{\mu}{1+k} < \frac{1}{2}. \tag{43}$$

Note that $J > 0$ and $X_{,\theta}(\theta) \geq 0$ $(0 \leq \theta \leq \pi/2)$.

Combining the above results, we obtain $(0 \leq \theta \leq \pi/2)$

$$u = r^{-\sqrt{1-\lambda^2}}X_{,\theta}(\theta) + D_6\cos\theta, \tag{44}$$

$$v = -\left|\frac{1+2}{\mu} - 2\right| r^{-\sqrt{1-\lambda^2}}X(\theta) - D_6\sin\theta. \tag{45}$$

D_6 is essentially the vertical deformation far away from the origin $(r \to \infty)$. Without loss of generality, we can take it to be zero, $D_6 = 0$. Then, $u \geq 0$ and $v \leq 0$; $0 \leq \theta \leq \pi/2$.

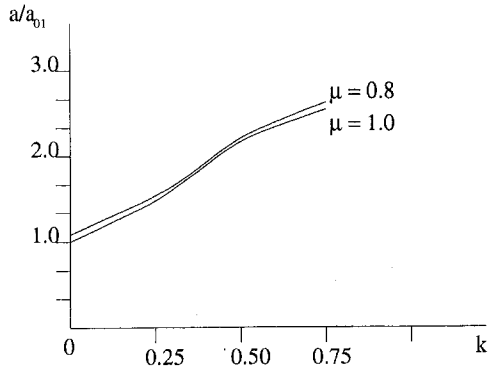


Fig. 5 The normalized contact radius a/a_{01} as a function of k and μ. a_{01} is the contact radius for $k = 0$ and $\mu = 1$ (homogeneous, linear case). In all cases the penetration depth was kept constant $(\delta/a_{01} = 0.316)$.

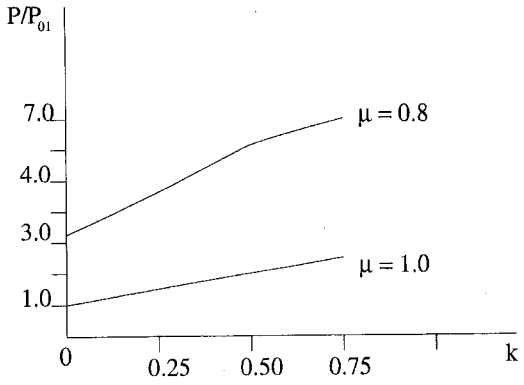


Fig. 6 The normalized applied line load P/P_{01} as a function of k and μ. P_{01} is the applied load for $k = 0$ and $\mu = 1$ (homogeneous, linear case). In all cases the penetration depth was kept constant $(\delta/a_{01} = 0.316)$.

The displacements at the boundary of the half-plane $(\theta = \pm\pi/2)$ are

$$u(-\pi/2) = u(\pi/2) = r^{-\sqrt{1-\lambda^2}}X_{,\theta}(\pi/2), \tag{46}$$

$$v(-\pi/2) = v(\pi/2) = -\left|\frac{1+k}{\mu} - 2\right| r^{-\sqrt{1-\lambda^2}}X(\pi/2). \tag{47}$$

Equation (47) gives the surface sinking-in due to the line load and Eq. (46), the surface radial expansion due to incompressibility.

The nonzero stresses are

$$\sigma_r = -\frac{2A(1-\lambda^2)^{\mu/2}}{r}\cos^k\theta X_{,\theta}^{\mu}(\theta), \tag{48}$$

$$\sigma_z = \sigma_r/2, \tag{49}$$

which are compressive everywhere.

Note that the stress singularity is r^{-1}, as for the homogeneous $(k = 0)$ and for the linear $(\mu = 1)$ cases. The strain singularity is $r^{-(1+\sqrt{1-\lambda^2})}$, which is stronger than the stress singularity for $0 < k < 1$ and weaker for $-1 < k < 0$ than the homogeneous case $(k = 0)$ as well as the corresponding linear case $(\mu = 1)$. A similar argument holds for the displacement singularity, $r^{-\sqrt{1-\lambda^2}}$.

4 The General Plane Contact Problem

We will assume a plane, convex, symmetric, rigid indenter, decribed by the function $f^*(x)$, Fig. 3. Obviously, $f^*(x) =$

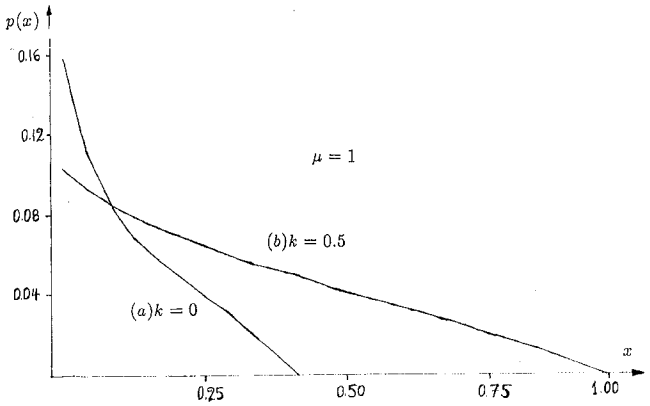


Fig. 7 Contact stress distribution, $p(x)$, for $\mu = 1$, $A = 1$, $\tan\phi = 0.1$. The same indentation depth is applied. (a) $k = 0$, $h/a = 0.3273$, $P = 2.6248 \times 10^{-2}$, $p_{av} = P/(2a) = 0.02863$. (b) $k = 0.5$, $h/a = 0.15$, $P = 4.5342 \times 10^{-2}$, $p_{av} = P/(2a) = 0.02267$.

Downloaded 04 May 2010 to 171.66.16.34. Redistribution subject to ASME license or copyright; see http://www.asme.org/terms/Terms_Use.cfm

$f^*(-x), f^*(x) \geq 0$. The contact is assumed to be frictionless ($\sigma_{r\theta} = 0$ at $\theta = \pm\pi/2$) and cohesionless. A monotonic contact region $|x| \leq a$, $y = 0$ will be developed (Fig. 3). A normal contact pressure, $p(x)$, will result such that $p(x) = p(-x)$ along the contact segment. The vertical displacement at contact is

$$|v| = \delta - f^*(x), \tag{50}$$

where δ is the indentation depth of the punch ($\delta \geq 0$). Incrementally, $d\delta dP \geq 0$, $dad\delta \geq 0$ and $p(|x| \leq a) \geq 0$, the zero values when and only $\delta = 0$.

If sinking-in at the contact perimeter is the dominant deformation, then the problem can be approximated using superposition of the point force solution given by (47). This will put a constrain in the values of μ for the above assumption to be valid (typically, $\mu > \frac{1}{4}$). Following Arutiunian (1959), we retain the principal term of the superposition of displacements due to forces of magnitude $p(s)ds$.

$$|v| \approx \left|\frac{1+k}{\mu} - 2\right| X^* \left(\int_{-a}^{a} \frac{p(s)}{|s-x|\sqrt{1-x^2}}\, ds \right)^{1/\mu}, \tag{51}$$

with

$$X^* = X(\theta = \pi/2; P = 1). \tag{52}$$

Equation (51) is a singular Fredholm integral equation of the first kind with respect to the unkown function $p(x)$ ($p(x) = p(-x)$). Overall equilibrium requires

$$P = \int_{-a}^{a} p(x)dx. \tag{53}$$

4.1 The Flat Punch Problem. The solution for the flat strip problem is relatively simple, since $f^*(x) = 0$. In this case the contact is complete, that is a is known. The contact pressure is directly derived from Eq. (51) (which becomes an Abel type of integral equation)

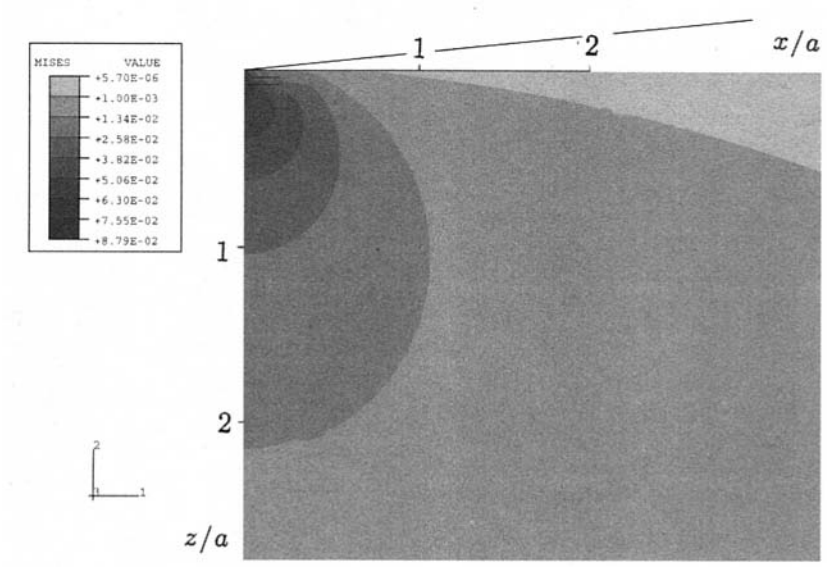


Fig. 8(*a*)

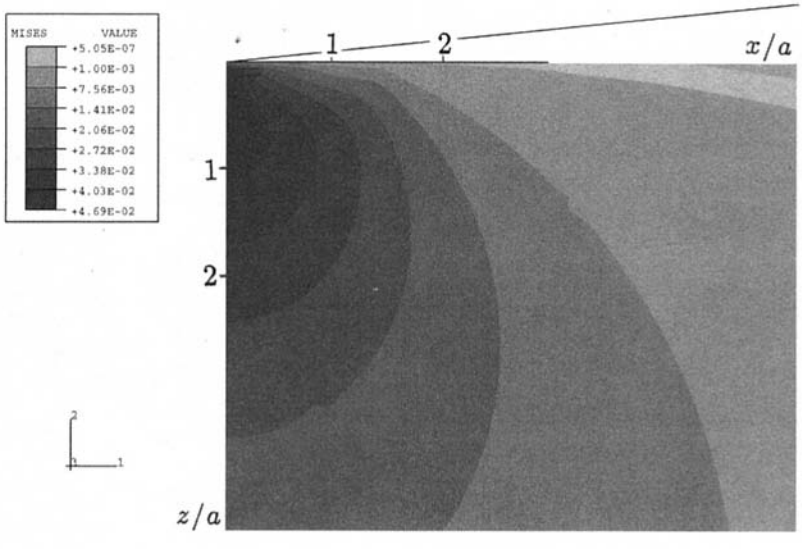


Fig. 8(*b*)

Fig. 8 Mises stress, σ_e, for $\mu = 1$, $A = 1$, $\tan\phi = 0.1$. The same indentation depth is applied. (*a*) $k = 0$, $h/a = 0.3273$, $P = 2.6248 \times 10^{-2}$, $p_{av} = P/(2a) = 0.02863$. (*b*) $k = 0.5$, $h/a = 0.15$, $P = 4.5342 \times 10^{-2}$, $p_{av} = P/(2a) = 0.02267$.

Downloaded 04 May 2010 to 171.66.16.34. Redistribution subject to ASME license or copyright; see http://www.asme.org/terms/Terms_Use.cfm

$$p(x) = \left(\frac{\delta}{\left|\frac{1+k}{\mu} - 2\right| X^*}\right)^{\mu} \frac{\sin\frac{\pi\mu}{2(1+k)}}{\pi(a^2 - x^2)^{\mu/(2(1+k))}}. \quad (54)$$

Note that at the contact perimeter, the contact pressure is singular, $x^{-\mu/(2(1+k))}$. For $0 < k < 1$, this singularity is milder than that of the homogeneous and linear cases ($x^{-\mu/2}$, $x^{-1/2}$, respectively). For $-1 < k < 0$, the singularity is stronger than for the homogeneous and linear cases.

The force-depth ($P - \delta$) relation is given by

$$P = \left(\frac{\delta}{\left|\frac{1+k}{\mu} - 2\right| X^*}\right)^{\mu} \times \frac{\sqrt{\pi}\, a^{1-(\mu/(1+k))}}{\Gamma\left(\frac{\mu}{2(1+k)}\right)\Gamma\left(\frac{3\mu/(1+k) - 1}{2}\right)}, \quad (55)$$

where $\Gamma(\ )$ is the Gamma function (Magnus and Oberhettinger, 1954). Note that P is related with δ in a nonlinear way. For linear strain-hardening and homogeneous case ($\mu = 1, k = 0$), the results approach the classic strip solution, $p(x) = P/(\pi\sqrt{a^2 - x^2})$ (Johnson, 1985). For the homogeneous case ($k = 0$), the results of Arutiunian (1959) are recovered.

4.2 The General Punch Solution. Denote by $w(x)$ the positive function

$$w(x) = \left(\frac{\delta - f^*(x)}{\left|\frac{1+k}{\mu} - 2\right| X^*}\right)^{1/(1+k)}. \quad (56)$$

Since the contact is nonconformal and incomplete, we need a condition to determine the contact segment, a. This condition requires $p(\pm a) = 0$. The contact pressure is then given by superposition of the flat punch problem following Sneddon's general methodology

$$p(x) = Q(\mu, k)\left(\int_x^a \frac{u^{\mu/(k+1)}du}{(u^2 - x^2)^{\mu/(2(1+k))}} \int_0^u \frac{w_{,xx}(s)ds}{(u^2 - s^2)^{\mu/(2(1+k))}} + w_{,x}(0+)\int_x^a \frac{du}{(u^2 - x^2)^{\mu/(2(1+k))}}\right), \quad (57)$$

with

$$Q(\mu, k) = \Gamma\left(\frac{1 - \mu/(1+k)}{2}\right) \times \Gamma\left(\frac{\mu}{2(1+k)}\right)\frac{\sin^2\frac{\pi\mu}{2(1+k)}}{(2\pi^{5/2})}. \quad (58)$$

The relation between contact segment, a, versus depth, δ, is given by

$$\frac{d}{da}\int_0^a \frac{w(s)ds}{(a^2 - s^2)^{\mu/(2(1+k))}} = 0. \quad (59)$$

For a round-tip indenter, $w_{,x}(0) = 0$, and Eq. (57) simplifies accordingly.

The force-depth ($P - \delta$) relation is given by the equilibrium equation

$$P = \frac{\sin^2\frac{\pi\mu}{2(1+k)}}{\pi}\int_0^a \frac{w(s)ds}{(a^2 - s^2)^{\mu/(2(1+k))}}. \quad (60)$$

A limitation of the present analysis comes from neglecting of piles up at the contact perimeter where the present superposition arguments will definitely fail (e.g., for $\mu < \frac{1}{4}$). This limitation, however, will not be of major concern for the moderate and high strain-hardening often found in graded materials.

4.3 The Wedge Indenter. The wedge indenter is described by the function $f^*(x) = |x| \tan\phi$ (Fig. 4). Taking only the right part, due to symmetry,

$$f^*(x+) = x\tan\phi. \quad (61)$$

Then,

$$w(x) = \left(\frac{\delta - x\tan\phi}{\left|\frac{1+k}{\mu} - 2\right| X^*}\right)^{1/(1+k)}. \quad (62)$$

The applied force can be evaluated by noting that

$$\int_0^a \frac{(\delta - s\tan\phi)^{1/(1+k)}ds}{(a^2 - s^2)^{\mu/(2(1+k))}}$$

can be expressed in terms of Hypergeometric functions (the final result is not shown here due to its excessive length).

Regarding the contact pressure, $p(x)$, for the homogeneous and linear case ($k = 0, \mu = 1$), we obtain the classic logarithmic singularity as $x \to 0$. For $0 < \mu < 1$ and/or $0 \le k < 1$, the contact pressure is finite at $x = 0$. The loss of singularity is due to the nonlinear strain-hardening, as well as to the inhomogeneous variation of the stress-strain amplitude. For small values of k, we can approximate the pressure at $x = 0$ as

$$p(0) \approx \frac{\Gamma\left(\frac{1-\mu}{2}\right)\Gamma(\mu/2)\sin^2\frac{\pi\mu}{2}}{2\pi^{5/2}} \frac{\tan\phi}{\left|\frac{1}{\mu} - 2\right| X^*} a^{1-\mu}, \quad (63)$$

where X, X^* are evaluated for $k \approx 0$.

The analytic results can be further pursued by integrating Eqs. (57) and (60). The contact radius, a, was computed iteratively by enforcing $p(a) = 0$. The results were obtained for constant penetration depth δ, wedge angle ϕ, and material constant A. Figure 5 shows the evolution of contact radius a with

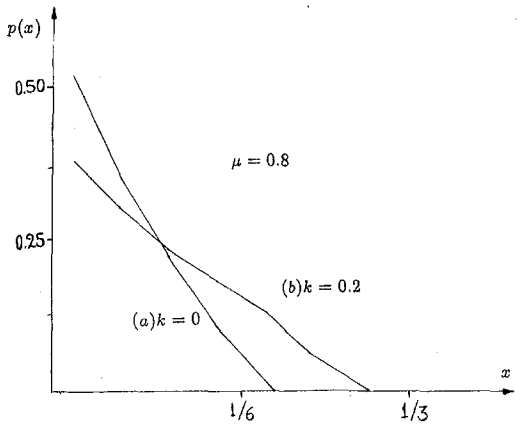


Fig. 9 Contact stress distribution, $p(x)$, for $\mu = 0.8$, $A = 1$, $\tan\phi = 0.1$. The same indentation depth is applied. (a) $k = 0$, $h/a = 0.24$, $P = 4.9843 \times 10^{-2}$, $p_{av} = P/(2a) = 0.1196$. (b) $k = 0.2$, $h/a = 0.1718$, $P = 5.3517 \times 10^{-2}$, $p_{av} = P/(2a) = 0.1218$.

Downloaded 04 May 2010 to 171.66.16.34. Redistribution subject to ASME license or copyright; see http://www.asme.org/terms/Terms_Use.cfm

k and μ. The results were normalized with the contact radius a_{01}, that is the contact radius for $k = 0$ and $\mu = 1$ (homogeneous, linear case). To simplify the numerics, the value of $\delta/a_{01} = 0.316$ was chosen. Figure 6 shows the evolution of the applied line force P with k and μ. The results were normalized with the applied line force P_{01}, that is the line force for $k = 0$ and $\mu = 1$ (homogeneous, linear case). Note that the contact area spreads with increasing k and μ. The relative load is also increasing with k and μ due to incompressibility.

4.4 Numerical Examples. The general two-dimensional problem was modeled with finite elements using the ABAQUS general purpose code. A mesh of 4747 four-noded elements and 5058 nodes was used. The details of the meshing are extensively described in Giannakopoulos and Suresh (1997). A new material code had to be developed for the purposes of the present work. Near incompressible conditions were enforced by underintegration and hourglass control of the element deformation modes. A rigid, frictionless wedge indenter was modeled with $\tan \phi = 0.1$. The parameter $A = 1$, with consistent dimensions. Two sets of cases were solved.

In the first set, the strain-hardening exponent was $\mu = 1$ with $k = 0$ (homogeneous case) and $k = 0.5$. For comparison, the same indentation depth, h, was applied. For $k = 0$, $h/a = 0.3273$, the total fore was $P = 2.6248 \times 10^{-2}$ and the average pressure was $p_{av} = P/(2a) = 0.02863$. For $k = 0.5$, $h/a = 0.15$, the total fore was $P = 4.5342 \times 10^{-2}$ and the average pressure was $p_{av} = P/(2a) = 0.02267$. It is clear that for the same indentation depth, the contact radius, a, increases and the average pressure, p_{av}, decreases in accord with the theoretical predictions. The contact stress distribution, $p(x)$, is shown in Fig. 7. Note that the stress singularity dissappears with increasing k, as predicted by the theory. The effective Mises stress, σ_e, is shown in Fig. 8(a) for $k = 0$ and in Fig. 8(b) for $k = 0.5$. It is clear that the inhomogeneity (from soft surface to stiff substrate) relaxes the singular stresses significantly.

In the second set, the strain-hardening exponent was $\mu = 0.8$ with $k = 0$ (homogeneous case) and $k = 0.2$. For comparison, the same indentation depth, h, was applied. For $k = 0$, $h/a = 0.24$, the total fore was $P = 4.9843 \times 10^{-2}$ and the average pressure was $p_{av} = P/(2a) = 0.1196$. For $k = 0.2$, $h/a =$

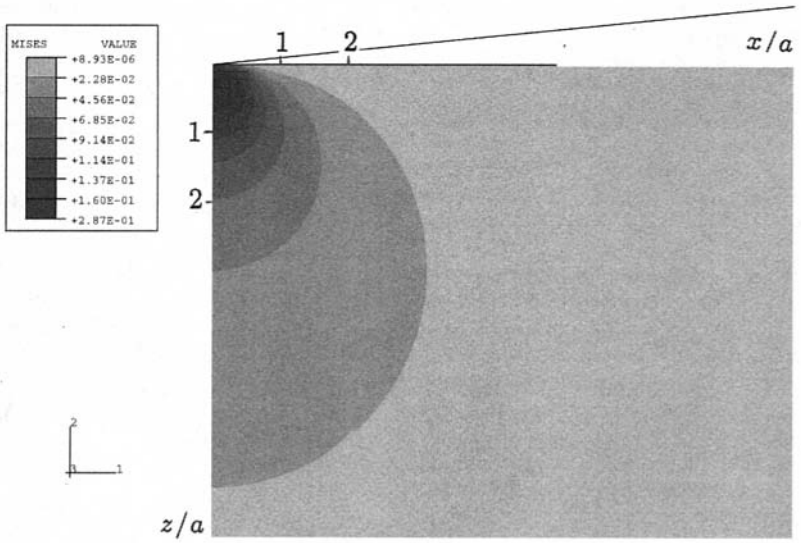


Fig. 10(a)

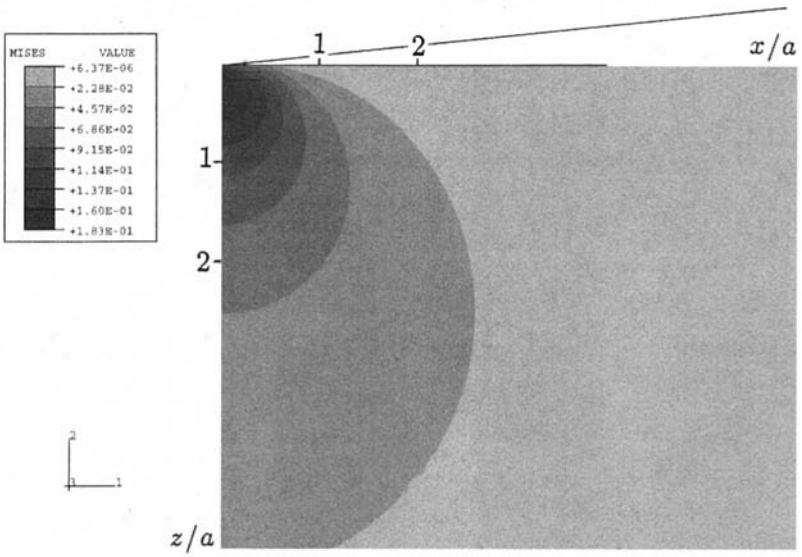


Fig. 10(b)

Fig. 10 Mises stress, σ_e, for $\mu = 0.8$, $A = 1$, $\tan \phi = 0.1$. The same indentation depth is applied. (a) $k = 0$, $h/a = 0.24$, $P = 4.9843 \times 10^{-2}$, $p_{av} = P/(2a) = 0.1196$. (b) $k = 0.2$, $h/a = 0.1718$, $P = 5.3517 \times 10^{-2}$, $p_{av} = P/(2a) = 0.1218$.

Downloaded 04 May 2010 to 171.66.16.34. Redistribution subject to ASME license or copyright; see http://www.asme.org/terms/Terms_Use.cfm

0.1718, the total fore was $P = 5.3517 \times 10^{-2}$ and the average pressure was $p_{av} = P/(2a) = 0.1218$. The contact stress distribution, $p(x)$, is shown in Fig. 9. The effective Mises stress, σ_e, is shown in Fig. 10(a) for $k = 0$ and in Fig. 10(b) for $k = 0.2$. It can be seen that the trends of the theory are again proven.

In all previous cases (Figs. 7–10), the results can become universal (within the selected k, μ, and A parameters), if all length are normalized by the contact radius, a, and all stresses by the average pressure, $p_{av} = P/(2a)$.

5 Conclusions

The present work provides solutions for the plane (two-dimensional) contact analysis of compositionally graded materials with power-law strain-hardening and incompressibility, $\sigma_e = A|y|^k \epsilon_e^\mu$. The present model approximates a graded substrate with hardness (or yield strength) that increases monotonically with depth in a power-law way. The problem includes the nonlinearity of the spatial variation of the constitutive relation (k), in addition to the stress-strain (μ) and contact analysis nonlinearities.

The line force (Flamant) problem was solved initially. All fields were found explicitly. The stress field was found to be radial with r^{-1} singularity. The strains and displacements exhibited a different type of singularity. The restrictions for μ and k are $0 \le |k| < 1$ and $0 < \mu \le \min(1, (1 + k))$.

Next, the rigid punch contact problem was solved. The punch was taken to be convex and symmetric. Frictionless and adhesionless contact conditions were assumed. The flat-strip punch problem was first solved. The contact pressure and the force-depth relation were derived explicitly. It was found that the contact stresses exhibit an $r^{-\mu/(2(1+k))}$ singularity at the contact perimeter. The force-depth relation was nonlinear, $P \propto \delta^\mu$.

The flat punch problem was subsequently used to solve the general punch shape problem. The additional contact condition of zero contact pressure at the contact edge provides the depth-contact segment ($\delta - a$) relation. Overall equilibrium provides the force-depth ($P - \delta$) relation. The general forms were cast in integral form.

The particular case of a sharp wedge was finally examined. The force-depth relation was derived. For $0 \le k < 1$, the contact pressure turns out to be nonsingular at the wedge line. This is due to the nonlinear strain-hardening and the inhomogeneous variation of the stress-strain amplitude. The particular type of inhomogenity makes the solution for the wedge indenter nonsingular. This is in contrast to the homogenous case where a logarithmic stress singularity is present in the vicinity of the wedge line. For small values of k, an aproximate solution for the contact pressure at the wedge tip was given.

Finally, general finite element codes were developed and some numerical examples with the wedge indenter were solved fully.

It should be pointed out that the presence of residual (self-equilibrated) stresses will not alter the current results and may be simply superposed to the present solutions.

Two main limitations of the present analysis are the use of deformation instead of incremental plastic theory and the constant strain-hardening exponent with depth. The problem is further complicated in the case of macroscopically inhomogeneous media. Regarding the inhomogeneity, finite element results and experiments, Jørgensen et al. (1997), have shown that, if the contact radius a is larger than about five times the characteristic material length (e.g., layer thickness), then the homogeneous approximation is good. Comparing incremental versus total deformation elastoplastic finite element results, it can be concluded that macroscopic relations like force-depth, contact area-depth, and contact stress distributions are captured well with the total deformation analysis. Regarding the stress fields, the difference between total deformation and incremental elastoplasticity is small for sharp indentors but considerable for spherical indentors. However, a relatively high strain-hardening ($\mu > 0.3$) gives close results in all cases.

Regarding the variation of strain-hardening with depth, it was found that a constitutive law of the type $\sigma_e = A|y + b|^k \epsilon_e^{\mu(1+c\sin z)}$ did not affect the results much, provided that $0 \le b \le 0.2a$ and $|c| \le 0.1$. Stronger and more frequent variations of the material parameters will produce large microstress variations arround the average values captured by the present analysis. The present contact analysis is limited from problems related to heterogeneity, preexisting residual stresses, microasperities, microflaws, and friction. It is not, of course, possible for this work to cover in detail such broad scopes that took other fields much effort and time to achieve. Despite the above limitations, the results of the present analysis can be very useful as a first step in the understanding of the elastoplastic contact of continuously graded materials with hardness that increases or decreases continuously with depth and provide useful guidelines in the design of such materials for contact and indentation related applications. What has been gained from this analysis from a practical point of view is that graded properties offer many optimization possibilities for contact related problems and further work on these lines is justified.

Acknowledgments

The work was carried out in the Laboratory for Experimental and Computational Micromechanics of the Department of Materials Science and Engineering at M.I.T.

References

ABAQUS, 1996, *User's Manual,* Version 5.5, Hibbit, Karlson and Sorensen, Pawtucket, RI.

Arutiunian, N. Kh., 1959, "The plane contact problem in the theory of creep," *PMM,* Vol. 23, pp. 1283–1313.

Awojobi, A. O., and Gibson, R. E., 1973, "Plane strain and axially symmetric problems of a linearly non-homogeneous elastic half-space," *Quart. J. of Mech. and Appl. Math.,* Vol. 26, pp. 285–302.

Booker, J. R., Balaam, N. P., and Davis, E. H., 1985, "The behavior of an elastic non-homogeneous half-space. Part I—Line and point loads. Part II—Circular and strip footings," *Int. J. Num. Anal. Meth. Geomech.,* Vol. 9, pp. 353–381.

Brown, P. T., and Gibson, R. E., 1972, "Surface settlement of a deep elastic stratum whose modulus increases with depth," *Canadian Geotech. Journal,* Vol. 9, pp. 467–476.

Calladine, C. R., and Greenwood, J. A., 1978, "Line and point loads on a nonhomogeneous incompressible elastic half-space," *Quart. J. of Mech. and Appl. Math.,* Vol. 31, pp. 507–529.

Ching-Hua, D., 1961, "The two-dimensional problems of the non-homogeneous isotropic medium," *Problems of Continuum Mechanics,* Akad. Nauk. SSSR, pp. 104–108.

Giannakopoulos, A. E., and Suresh, S., 1997, "Indentation of solids with a gradient in elastic properties: Part II. Axisymmetric indenters," *Int. J. Solids and Structures,* Vol. 34, pp. 2393–2498.

Gibson, R. E., 1967, "Some results concerning displacements in a non-homogeneous elastic half-space," *Geotechnique,* Vol. 17, pp. 58–67.

Holl, D. L., 1940, "Stress transmition in earths," *Proc. Highway Res. Board,* Vol. 20, pp. 709–721.

Hruban, K., 1958, "The basic problem of a non-linear and non-homogeneous half-space," *Non-homogeneity in Elasticity and Plasticity IUTAM Symposium,* Warsaw, Pergamon Press, pp. 53–61.

Ilschner, B., and Cherradi, N., eds., 1994, *3rd Int. Symp. on Structural and Functional Gradient Materials,* Lausanne, Switzerland.

Johnson, K. L., 1985, *Contact Mechanics,* Cambridge University Press, Cambridge, UK.

Jørgensen, O., Giannakopoulos, A. E., and Suresh, S., 1997, "Large spherical indentation of composite laminates with controlled gradients in elastic anisotropy," MIT Report Nav-PGS-96-1, *Int. J. Solids and Structures,* in press.

Lekhnitskii, S. G., 1962, "Radial distribution of stress in a wedge and in a half-plane with variable modulus of elasticity," *PMM,* Vol. 26, pp. 146–151.

Magnus, W., and Oberhettinger, F., 1954, *Formulas and Theorems for the Functions of Mathematical Physics,* Chelsea, New York.

O'Neill, M. W., and Dobry, R., eds., 1980, *Dynamic Response of Pile Foundations: Analytical Aspects,* ASCE, New York.

Downloaded 04 May 2010 to 171.66.16.34. Redistribution subject to ASME license or copyright; see http://www.asme.org/terms/Terms_Use.cfm

Wing Kam Liu
Professor of Mechanical and Civil Engineering,
Department of Mechanical Engineering,
Northwestern University,
2145 Sheridan Road,
Evanston, IL 60208
Fellow ASME

R. A. Uras
Engineer,
Reactor Engineering Division,
Argonne National Laboratory,
9700 S. Cass Avenue, Bldg. 208,
Argonne, IL 60439
Mem. ASME

Y. Chen[1]
Post-Doctoral Fellow,
Department of Mechanical Engineering,
Northwestern University,
2145 Sheridan Road,
Evanston, IL 60208

Enrichment of the Finite Element Method With the Reproducing Kernel Particle Method

The reproducing kernel particle method (RKPM) has attractive properties in handling high gradients, concentrated forces, and large deformations where other widely implemented methodologies fail. In the present work, a multiple field computational procedure is devised to enrich the finite element method with RKPM, and RKPM with analytical functions. The formulation includes an interaction term that accounts for any overlap between the fields, and increases the accuracy of the computational solutions in a coarse mesh or particle grid. By replacing finite element method shape functions at selected nodes with higher-order RKPM window functions, RKPM p-enrichment is obtained. Similarly, by adding RKPM window functions into a finite element method mesh, RKPM hp-enrichment is achieved analogous to adaptive refinement. The fundamental concepts of the multiresolution analysis are used to devise an adaptivity procedure.

1 Introduction

The finite element method (FEM) has been one of the most widely used techniques in the computational mechanics in the past two decades. Recently, particle methods have increasingly been attracting attention. Several different particle methods with unique advantages and disadvantages have been proposed, including smooth particle hydrodynamics (SPH) (Gingold and Monaghan, 1977; Lucy, 1977) diffuse elements (Nayroles et al., 1992), element-free Galerkin (EFG) methods (Belytschko et al., 1994a–c), particle in-cell methods (PIC) (Sulsky et al., 1996), reproducing kernel particle methods (RKPM) (Liu et al., 1993; Liu and Oberste-Brandenburg, 1993; Liu et al., 1995a, b, 1996a–c, 1997a, b; Liu and Chen, 1995), and wavelet particle methods (WPM) (Liu and Oberste-Brandenburg, 1993; Liu and Chen, 1995). Because of the importance of this class of methods, a special volume of Computer Methods in Applied Mechanics and Engineering dedicated to *Meshless Methods,* was published by North-Holland in Dec. 1996 (Liu, Belytschko, and Oden, 1996).

Particle methods such as RKPM employ a grid of particles eliminating the need for a mesh (as in FEM) and several difficulties associated with it such as mesh entanglement in large deformation problems. However, in contrast to SPH, RKPM is capable of properly treating the domain boundaries with a correction term. Hence, solution accuracy is improved, and phase errors are avoided (Liu and Chen, 1995).

This paper is aimed at developing procedures to couple RKPM with other methods, and at introducing adaptive refinement concepts for RKPM and FEM-RKPM coupling. A multiple field procedure is proposed to combine RKPM with known analytical forms to enhance computational accuracy. The effectiveness of the multiple field RKPM is shown for the case of FEM-RKPM coupling where total solution error can be reduced by employing FEM at the essential boundary.

Through proper formulation, the traditional FEM can be treated as a special case of RKPM establishing a natural way to blend these two methods. Thus, the so-called RKPM *p*-enrichment and *hp*-enrichment becomes easier to implement. Moreover, there are no compatibility problems along the element boundary, and no restrictions are required in choosing a higher order window function. The enrichment concept can be applied in refining the grid through adaptivity. Thus, local phenomena such as high concentration regions in the domain can be captured efficiently. Multiresolution concept can be used to establish criteria in determining critical regions for local refinement. At the end of each refinement level, the wavelet function is computed for the current grid, and the highest wavelet function values are determined. The simplest criterion for an adaptive refinement is the identification of the particles whose wavelet values are within a prescribed percentage of the maximum wavelet value. In problems with smooth solutions, this criterion appears to be computationally efficient due to a relatively small number of additional particles. A second criterion is based on a prescribed percentage of the number of particles with the highest wavelet values. The number of additional particles is greater than the previous criterion, and is expected to yield faster convergence in problems with high concentrations.

The organization of this paper is as follows. In Section 2, the fundamental concepts in the development of RKPM are briefly reviewed, the reproducing conditions and the construction of an appropriate correction function are introduced, and shape functions suitable for a Galerkin formulation are derived. The guidelines for a multiple-field RKPM, and coupling procedures between RKPM and FEM, and RKPM and analytical solutions are described, and are implemented in example problems in Section 3. Section 4 is devoted to adaptivity through RKPM enrichment, and multiresolution analysis. The sample problems are designed to clarify the implementation of adaptivity with RKPM, and enrichment of FEM with a wavelet-based RKPM. Conclusions are stated in Section 5.

[1] Currently Senior Stress Analyst, L. J. Broutman & Associates, Ltd., Chicago, IL 60616.

Contributed by the Applied Mechanics Division of THE AMERICAN SOCIETY OF MECHANICAL ENGINEERS for publication in the ASME JOURNAL OF APPLIED MECHANICS.

Discussion on this paper should be addressed to the Technical Editor, Professor Lewis T. Wheeler, Department of Mechancial Engineering, University of Houston, Houston, TX 77204-4792, and will be accepted until four months after final publication of the paper itself in the ASME JOURNAL OF APPLIED MECHANICS.

Manuscript received by the ASME Applied Mechanics Division, Dec. 5, 1996; final revision, May 6, 1997. Associate Technical Editor: L. T. Wheeler.

Copyright © 1997 by ASME

Downloaded 04 May 2010 to 171.66.16.34. Redistribution subject to ASME license or copyright; see http://www.asme.org/terms/Terms_Use.cfm

2 Fundamentals of RKPM

2.1 Preliminaries. In mathematical physics, the solution to a differential equation can be expressed as

$$u^R(\mathbf{x}) = \int_{-\infty}^{+\infty} u(\mathbf{y})\phi(\mathbf{x} - \mathbf{y})d\mathbf{y} \tag{1}$$

where ϕ is a kernel function, and acts like a projection operator, and u^R is the *reproduced* solution of $u(x)$. This form is one of the fundamental developments in many interpolation methods, and will be referred to as the reproducing kernel method. Widely used methods such as smooth particle hydrodynamics (SPH), and wavelet methods also belong to this class of methods. One major drawback of these methods is the need for a special boundary treatment in finite domains. Through a proper construction of a boundary correction function, the artificial boundaries required by the SPH and wavelet methods can be eliminated, and the accuracy of the discrete solution is improved (Liu, 1995; Liu et al., 1995b).

In a finite domain, Eq. (1) can be written as

$$u^R(\mathbf{x}) = \int_{\Omega} u(\mathbf{y})\bar{\phi}(\mathbf{x}; \mathbf{x} - \mathbf{y})d\mathbf{y}, \tag{2}$$

where Ω denotes the domain, and the modified kernel function, $\bar{\phi}$, is given as

$$\bar{\phi}(\mathbf{x}; \mathbf{x} - \mathbf{y}) = C(\mathbf{x}; \mathbf{x} - \mathbf{y})\phi(\mathbf{x} - \mathbf{y}), \tag{3}$$

where $C(\mathbf{x}; \mathbf{x} - \mathbf{y})$ is the boundary correction function.

In problems involving finite domains, the SPH method yields amplitude and phase errors mainly due to the boundary effects. This phenomenon can be attributed to the failure of satisfying the completeness requirements. The correction function, $C(\mathbf{x}; \mathbf{x} - \mathbf{y})$, is constructed to alleviate the difficulties mentioned above. Since the integral defined in Eq. (2) is too complicated to be carried out analytically, it is generally discretized either by a mesh (as in the finite element method), or by a grid of particles (SPH methods). The class of methods involving mesh-free Lagrangian particles concerned with the solution of Eq. (2) are referred to as reproducing kernel particle methods (RKPM).

2.2 Reproducing Conditions and Correction Function. In a Galerkin finite element formulation, the space of admissible functions, V^h, consists of all linear combinations of shape functions N_A, $A = 1, \ldots,$ neq (neq is the number of equations, i.e., the total number of unknowns):

$$V^h = \{N_1, \ldots, N_{\text{neq}}\}. \tag{4}$$

In order to guarantee the convergence of the approximate Galerkin solution with successive mesh refinements, the shape functions have to be complete, i.e., capable of spanning the linear field exactly (Hughes, 1987).

In RKPM, the space of admissible functions can be defined by a set of arbitrary window functions generated from the translations of a single function

$$V_\phi^h = \{\phi_1, \ldots, \phi_{np} | \phi_j(x) = \phi(x - x_j), j \in [1, np]\} \tag{5}$$

where np is the total number of particles.

An arbitrarily selected window function may not satisfy the completeness requirements, possibly jeopardizing important convergence characteristics of the method. Therefore, it is necessary to restore completeness of the function space by introducing the following *reproducing conditions* for the discretized system (Liu, 1995; Liu et al., 1995b):

$$\tilde{m}_0(x) = 1 \quad \text{and} \quad \tilde{m}_k(x) = 0 \quad \text{for} \quad k \geq 1 \tag{6}$$

where

$$\tilde{m}_k(x) = \sum_{j=1}^{np} (x - x_j)^k \phi(x - x_j)\Delta x_j \tag{7}$$

which represents the kth-order discretized moment of the window function over the entire domain.

If the selected window functions do not automatically satisfy the reproducing conditions in Eq. (6), then a correction function, as in Eq. (3) is constructed such that

$$\bar{\phi}(x; x - y) = C(x; x - y)\phi(x - y) = \sum_{k=0}^{n} \beta_k(x)(x - y)^k \phi(x - y) \tag{8}$$

where n is the order of the discretized field to be satisfied exactly. The unknown coefficients $\beta_k(x)$ are to be selected such that the modified kernel function, $\bar{\phi}(x; x - y)$ fulfills the completeness requirements. The reproducing conditions, Eq. (7), are imposed on Eq. (8) up to order n to determine the corresponding unknown functions, $\beta_k(x)$:

$$\begin{bmatrix} \tilde{m}_0(x) & \tilde{m}_1(x) & \cdots & \tilde{m}_n(x) \\ \tilde{m}_1(x) & \tilde{m}_2(x) & \cdots & \tilde{m}_{n+1}(x) \\ \vdots & \vdots & \ddots & \vdots \\ \tilde{m}_n(x) & \tilde{m}_{n+1}(x) & \cdots & \tilde{m}_{2n}(x) \end{bmatrix} \begin{bmatrix} \beta_0(x) \\ \beta_1(x) \\ \vdots \\ \beta_n(x) \end{bmatrix} = \begin{bmatrix} 1 \\ 0 \\ \vdots \\ 0 \end{bmatrix}. \tag{9}$$

Through this procedure, the correction function and consequently the modifed kernel function are determined, and they can be used in the formulation without compromising important convergence characteristics.

2.3 Shape Functions. The ultimate goal in most computational methods is the development of interpolation functions. In order to obtain suitable RKPM interpolation functions, Eq. (2) is discretized using np particles:

$$u^{R_h}(x) = \sum_{j=1}^{np} N^{\text{RKPM}}(x, x_j)u(x_j) \tag{10}$$

where

$$N^{\text{RKPM}}(x, x_j) = C(x; x - x_j)\phi(x - x_j)\Delta x_j. \tag{11}$$

The versatility of the interpolation functions in Eq. (11) is threefold: (i) they can be used in a Galerkin formulation; (ii) their derivatives can be obtained by direct differentiation; and (iii) the built-in window function allows flexibility to enhance convergence and accuracy.

2.4 RKPM as an Enrichment Tool. RKPM interpolation functions, as given in Eq. (11), are very similar in form to FEM shape functions. Favorable features of FEM such as easier handling of boundaries can complement RKPM in boundary value problems. In problems with known analytical forms, RKPM can be enhanced for accuracy in coarse grids. Moreover, adaptive refinement procedures can be devised to replace and/or add RKPM particles onto an FEM mesh.

These concepts are introduced and explored in detail in the following sections.

3 Multiple-Field RKPM

Multiple-field RKPM can be viewed as a generalization of the multiple-scale method. Thus, fields representing different scales in the problem are incorporated into the formulation, and any overlap between fields is automatically eliminated. Consequently, consistency of solutions is achieved.

The concept of multiple-field RKPM is explained for a two-scale decomposition of $u(x)$:

$$u(x) = v(x) + w(x) \tag{12}$$

where $v(x)$ and $w(x)$ are the solutions to different scales or different fields. It will be assumed that $v(x)$ and $w(x)$ represent the primary and secondary scales/fields of the total solution,

Downloaded 04 May 2010 to 171.66.16.34. Redistribution subject to ASME license or copyright; see http://www.asme.org/terms/Terms_Use.cfm

$u(x)$. A sampling projection operator can be defined such that the primary scale/field is reproduced exactly, i.e.,

$$v(x) = Pv(x). \tag{13}$$

The same projection operator, P, is applied to Eq. (12) to obtain

$$Pu(x) = Pv(x) + Pw(x) \tag{14}$$

which further is simplified by using Eq. (13) to

$$Pu(x) = v(x) + Pw(x). \tag{15}$$

The primary field, $v(x)$, can be solved for from Eq. (15), and substituted into Eq. (12) to obtain

$$u(x) = Pu(x) - Pw(x) + w(x) \tag{16}$$

where Pu is the projected solution and Pw is the interaction term, and Eq. (16) can be interpreted as a general expression for a multiple-scale analysis. In particular, if there is no overlapping of scales between $v(x)$ and $w(x)$, then by the property of the projection operator, the interaction term is zero. By repeated applications of Eq. (16), multiple-scale methods can be developed within the framework of a multilevel data structure.

Two sample cases are presented to clarify the concept of projection: coupling of FEM with RKPM, and coupling of RKPM with analytical forms.

3.1 Coupling of RKPM With FEM. In order to couple FEM and RKPM over the domain of the problem, Ω, two subdomains are defined, Ω_{2a} is the FEM subdomain, and Ω_a is the RKPM subdomain. If the solutions in FEM and RKPM subdomains are

$$u^{\text{FEM}}(x) = Pu(x) = \sum_{j=1}^{NP} N_j(x)u(x_j) \tag{17}$$

and

$$w(x) = Qw(x) = \int_{\Omega_a} \bar{\phi}(x_j; x_j - y)w(y)dy, \tag{18}$$

respectively, then the the multiple-field solution given in Eq. (16) becomes

$$u(x) = \sum_{j=1}^{NP} N_j(x)u(x_j) + \int_{\Omega_a} [\bar{\phi}(x; x - y) - \sum_{j=1}^{NP} N_j(x)\bar{\phi}(x_j; x_j - y)]w(y)dy, \tag{19}$$

where $N_j(x)$ is the FEM shape function and NP is the number of FEM nodes. To take full advantage of the adaptive hp-finite element method with wavelet enrichment, $w(x)$ should not intersect with any essential boundary conditions. A similar approach in enforcing the essential boundary conditions in meshless approximations is presented by Krongauz and Belytschko (1995). However, in their method, a special function is required along the boundary between the finite elements and the meshless domain.

A simple one-dimensional case with the following equilibrium equation is considered to demonstrate the effect of coupling between the RKPM and the FEM:

$$u_{,xx}(x) + f(x) = 0 \tag{20}$$

with the boundary conditions

$$u(0) = 0 \tag{21}$$

$$u_{,x}(1) = 0 \tag{22}$$

and the forcing term

$$f(x) = 1. \tag{23}$$

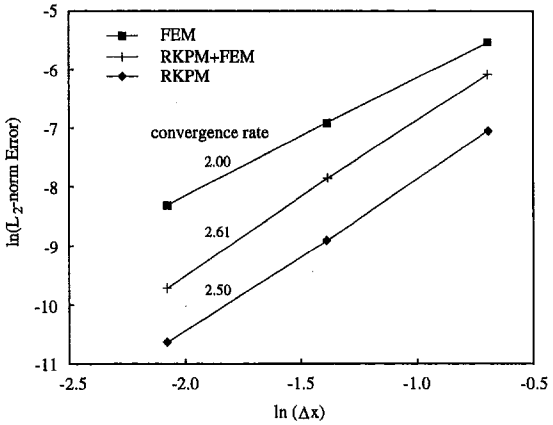


Fig. 1 The convergence plot for RKPM-FEM coupling

The analytical solution for this boundary value problem can be determined as

$$u(x) = x - \tfrac{1}{2}x^2. \tag{24}$$

The L_2-Norm results for FEM, FEM with RKPM, and RKPM are presented in Fig. 1. The third-order spline employed as window function in RKPM yields higher accuracy as well as increased convergence rate than FEM. The coupling of RKPM and FEM is achieved by discretizing the end with the essential boundary condition by FEM whereas the rest of the domain is discretized by RKPM. A good compromise between a loss of accuracy and an increase in convergence rate is observed.

3.2 Coupling of RKPM With Analytical Functions. The multiple-field formulation for coupling between RKPM and analytical function is similar to that of the FEM and RKPM coupling.

The projection operator in the RKPM domain is expressed in terms of modified window functions

$$u^{\text{RKPM}}(x) = Pu(x) = \int_{\Omega_a} \bar{\phi}(x_j; x_j - y)u(y)dy \tag{25}$$

and the analytical solution is given by

$$w(x) = Qw(x) = cf(x), \tag{26}$$

where c is a coefficient to be determined and $f(x)$ is a given analytical function.

Coupled multiple field formulation for RKPM and an analytical function is obtained by substituting Eqs. (25) and (26) into Eq. (16) to yield

$$u(x) = \int_{\Omega} \bar{\phi}_a(x; x - y)u(y)dy + c[f(x) - \int_{\Omega} \bar{\phi}_a(x; x - y)f(y)dy]. \tag{27}$$

The advection-diffusion equation is used to demonstrate the concept of the multiple-field RKPM. The governing equation is

$$u_{,xx}(x) - au_{,x}(x) = b(x) \tag{28}$$

with the boundary conditions

$$u(0) = 1 \tag{29}$$

$$u(1) = -1 \tag{30}$$

and the body force

$$b(x) = 2a[2ax^2 - ax - 1]e^{-a(1/2-x)^2}. \tag{31}$$

Downloaded 04 May 2010 to 171.66.16.34. Redistribution subject to ASME license or copyright; see http://www.asme.org/terms/Terms_Use.cfm

Table 1 L_2-Norm errors of the boundary layer problem

	Multiple Field RKPM Eq. (33)	RKPM	Multiple Field RKPM Eq. (34)
26 Nodes	0.09592	0.16720	0.22998
51 Nodes	0.03926	0.06196	0.08282
101 Nodes	0.01250	0.01754	0.02300
201 Nodes	0.00421	0.00492	0.00639

In this example, the advection parameter, a, is chosen as 200 to ensure a sharp boundary layer formation at the boundary $x = 1$.

The analytical solution is given as

$$u(x) = \frac{2}{1 - e^{a}}(e^{ax} - 1) + (1 - e^{a/4}) + e^{-a(1/2-x)^2}. \quad (32)$$

The analytical expressions for the boundary layer term to be coupled with RKPM are

$$w(x) = c_e f(x) = c_e(1 - e^{ax}) \quad (33)$$

and

$$w(x) = c_p(1 - ax^2), \quad (34)$$

where c_e and c_p are the unknowns to be determined.

There are several important observations made from this numerical example. In problems with abrupt changes in the solution such as a boundary layer, a coarse grid with uniform spacing is inadequate even though RKPM is employed. The results reveal oscillations in the transition region from the far-field solution to the boundary solution. The use of an appropriate function (in the current example, Eq. (33)) induces a slight reduction in the amplitude of oscillations. However, the overall L_2-Norm error is significantly smaller than that of RKPM (refer to Table 1, and Fig. 2). A more generic form such as a polynomial form, Eq. (34), yields inaccurate solutions over the entire domain although the order of error appears to be comparable to that of RKPM (refer to Table 1). As depicted in Fig. 2, fast convergence is observed with all three approaches. The far-field to boundary layer oscillations observed for 26, 51, and 101 grid points completely disappear when 201 particles are used. The difference in solutions obtained from three approaches diminish with successive grid refinements.

An efficient way of eliminating the difficulties in transition regions is the choice of nonuniform spacing between particles. One other obvious approach is the addition of extra particles into the grid. The adaptive refinement procedure will be explained in the next section. Figures 3 and 4 depict the comparisons of the solutions using multiple-field RKPM with an exponential boundary layer, standard RKPM, multiple-field RKPM with a parabolic boundary layer, and the analytical solution.

In all cases, a total of 51 particles are used. As it can be seen in Fig. 3, the results of a straightforward uniform grid reveals oscillations, and the choice of the form of the boundary layer is very important. The parabolic form is not only inadequate to represent the boundary layer, but it also causes severe deterioration of the solution over the entire domain. The multiple-field RKPM with an exponential boundary layer performs better than that of the standard RKPM, yet yields an oscillatory response in the transition region.

The situation depicted in Fig. 4 is entirely different, although the total number of particles is the same as in the previous case. The distribution of the particles is modified by concentrating more particles in the transition region: 21 particles in $0 \le x \le 0.5$, 10 particles in $0.5 \le x \le 0.9$, and 20 particles in $0.9 \le x \le 1.0$. The improvement in results is remarkable although the importance of the form of the boundary layer is still apparent over the whole domain.

Finally, the influence of the interaction term, $Pw(x)$ in Eq. (16), on the solution is also investigated. This term vanishes if there is no overlap between the different fields in the domain. However, its effect cannot be ignored in the present problem where boundary layer solutions are imposed on the RKPM solution. The computational results show that its absence induces a significant loss in accuracy and fails to represent the boundary layer appropriately especially when a coarse particle grid is selected. Considerable grid refinement is necessary to alleviate the adverse effects. It should be noted that the improvement through grid refinement is expected since an RKPM solution with a finer grid becomes adequate in representing the solution in the domain.

4 Enhanced Accuracy Through Enrichment

4.1 FEM to RKPM. The FEM shape functions introduced in Eq. (4) belong to a function space which satisfies the completeness requirement. Therefore, an enforcement of the reproducing conditions is not needed in an FEM mesh. Some of the shortcomings of FEM such as mesh entanglement, inability to represent high gradients, etc., can be alleviated using RKPM (Liu and Oberste-Brandenburg, 1993; Liu and Chen, 1995; Liu et al., 1995b–f). Consequently, complementing FEM with RKPM in such problems appears to be a viable alternative. Several enrichment procedures as well as a wavelet-based adaptivity approach are presented here.

4.2 FEM With RKPM p-Enrichment. Considering the useful properties associated with an approach utilizing a window function, the function space, V^h can be modified by replacing one of the shape functions with a higher-order window function

$$V^h = \{N_1, \ldots, N_{p-1}, \phi_p, N_{p+1}, \ldots, N_{\text{neq}}\}. \quad (35)$$

This concept is described in Fig. 5. The completeness requirement is satisfied everywhere in the domain except under the support of ϕ_p in region $\bar{\Omega}$. The generalized reproducing conditions, Eqs. (7), have to be enforced on ϕ_p only in $\bar{\Omega}$. This type of enrichment of FEM with RKPM will be referred to as FEM with p-enrichment. This development can be extended by substituting several shape functions with window functions. The generalized reproducing conditions are imposed on these window functions only within their compact support.

4.3 FEM With RKPM hp-Enrichment. A different enrichment can be achieved by inserting an additional node in the domain of interest and a higher-order $\phi_{\text{neq}+1}(x)$ window function in V^h as shown in Fig. 6. Similar to the FEM with RKPM p-enrichment, reproducing conditions are required in $\bar{\Omega}$. However, unlike the traditional hp finite elements, the additional

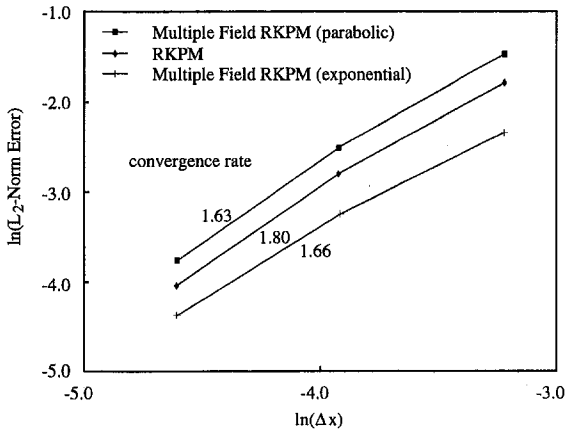


Fig. 2 L_2-Norm error plot of the boundary layer problem

Downloaded 04 May 2010 to 171.66.16.34. Redistribution subject to ASME license or copyright; see http://www.asme.org/terms/Terms_Use.cfm

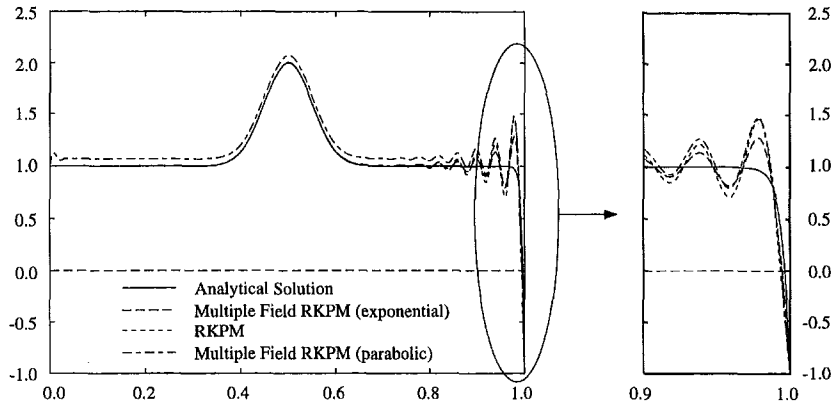


Fig. 3 Boundary layer problem with a uniform particle grid

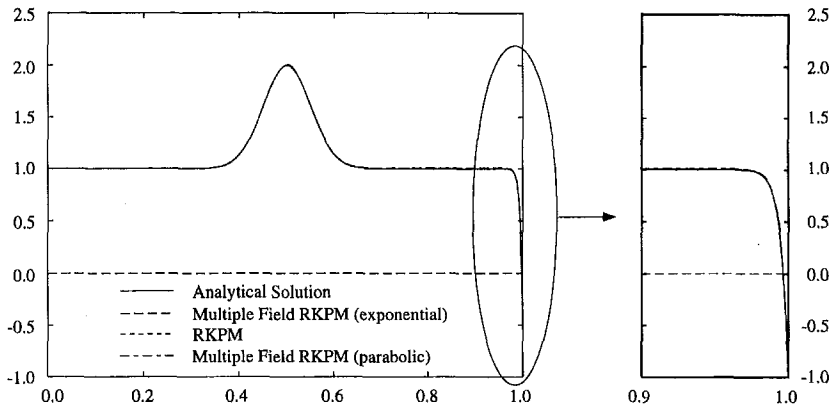


Fig. 4 Boundary layer problem with a nonuniform particle grid

window V^h can cover some of the finite element nodes and no special adjustment of the higher-order window function is needed along the interelement boundary.

The coupling of FEM and RKPM, and the effect of reproducing conditions are demonstrated in Figs. 7. The test grid has six RKPM particles and five FEM nodes. The RKPM shape functions are third-order splines, and FEM shape functions are linear Lagrange interpolants (as shown in Fig. 7(a)). The reproducing conditions are applied on RKPM shape functions to obtain the modified shape functions presented in Fig. 7(b).

The same concept of enrichment through the addition of particles to an existing computational grid (FEM or RKPM) can be extended to two dimensions. As depicted in Fig. 8, a particle p defined through a window function ϕ_p and its support, $\bar{\Omega}_p$, is added to the original grid. The reproducing conditions are applied to all additional particles to obtain completeness in the computational grid.

4.4 Adaptivity Through Multiresolution Analysis. In this section, an adaptivity procedure based on a multiresolution analysis is devised. The regions where additional nodes/particles are needed are determined through a wavelet decomposition.

4.4.1 Adaptivity Criteria via Wavelet Solution. The reproducing equation, Eq. (2), can be discretized for a given dilation parameter, a, as

$$u_a(\mathbf{x}) = u(a; \mathbf{x}) = \sum_{j=1}^{np} u(\mathbf{x}_j)\bar{\phi}_a(\mathbf{x} - \mathbf{x}_j)\Delta\mathbf{x}_j. \quad (36)$$

Based on the current grid, the next level of fine scale discretization is obtained by using a finer scale window function, $\bar{\phi}_{2a}$:

$$u_{2a}(\mathbf{x}) = \sum_{j=1}^{np} u(\mathbf{x}_j)\bar{\phi}_{2a}(\mathbf{x} - \mathbf{x}_j)\Delta\mathbf{x}_j. \quad (37)$$

Consequently, the wavelet solution for the current grid is defined as

$$\psi(\mathbf{x}) = u_a(\mathbf{x}) - u_{2a}(\mathbf{x}). \quad (38)$$

Due to its construction, the wavelet solution, ψ represents the difference between the scales of the current and the next refinement levels. This information appears to be adequate in determining the regions for refinement. The criteria for adaptivity can be a certain number of particles with the highest ψ values and/or a predetermined percentage of the maximum ψ

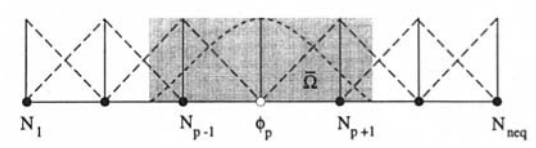


Fig. 5 FE with RKPM *p*-enrichment

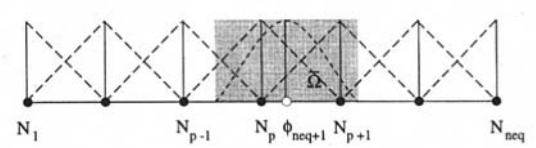


Fig. 6 FE with RKPM *hp*-enrichment

Downloaded 04 May 2010 to 171.66.16.34. Redistribution subject to ASME license or copyright; see http://www.asme.org/terms/Terms_Use.cfm

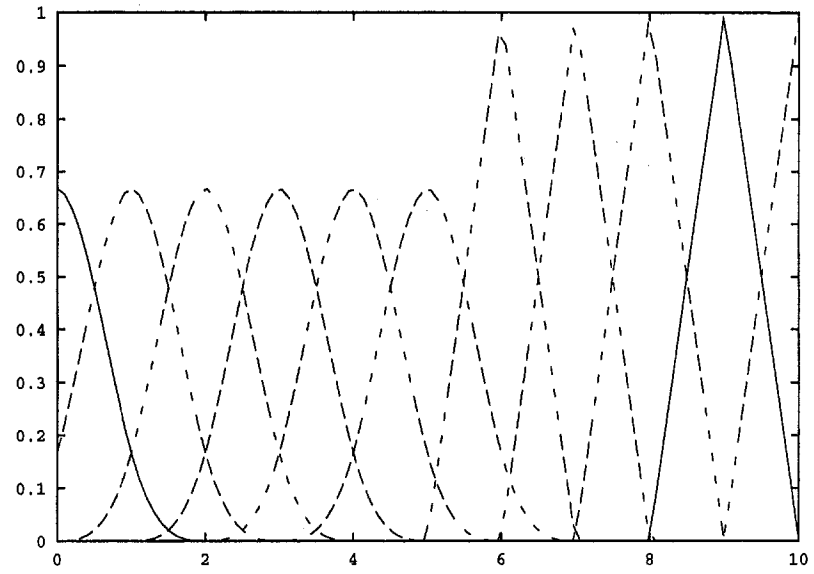


Fig. 7(*a*) Before

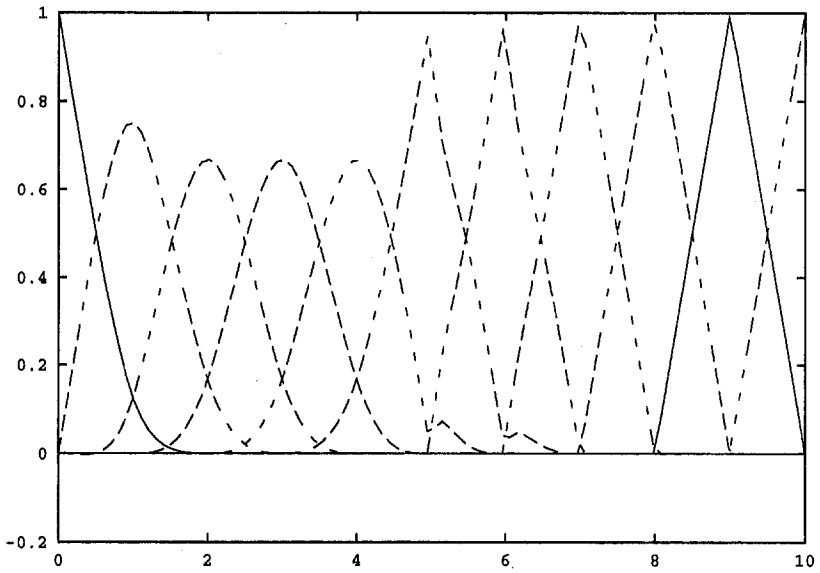


Fig. 7(*b*) After

Fig. 7 The FEM shape functions, and the RKPM window functions, before and after imposing the reproducing conditions

value. The particles falling into one or both categories are identified as critical and their immediate surroundings are subjected to a particle refinement. Adaptivity based on the first criterion requires a large number of additional particles, and may be interpreted as a conservative approach. From the numerical examples discussed below, the first approach is found to be effective in problems with high gradients, and performs well even if the initial grid is very coarse. Similarly, the second criterion is

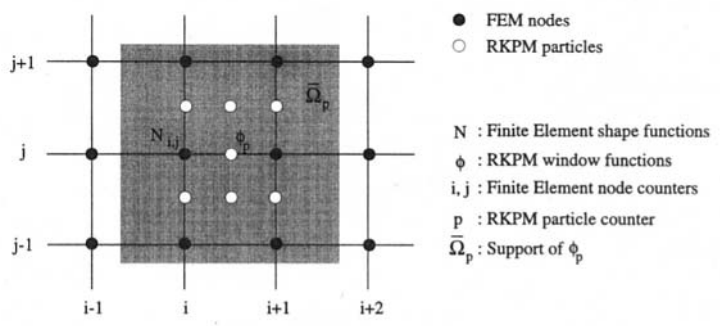


Fig. 8 Enrichment concept in two dimensions

Downloaded 04 May 2010 to 171.66.16.34. Redistribution subject to ASME license or copyright; see http://www.asme.org/terms/Terms_Use.cfm

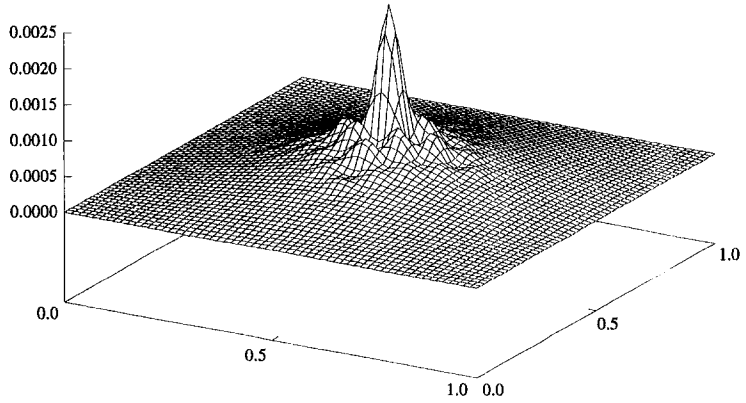


Fig. 9(*a*) Overall solution after initial grid

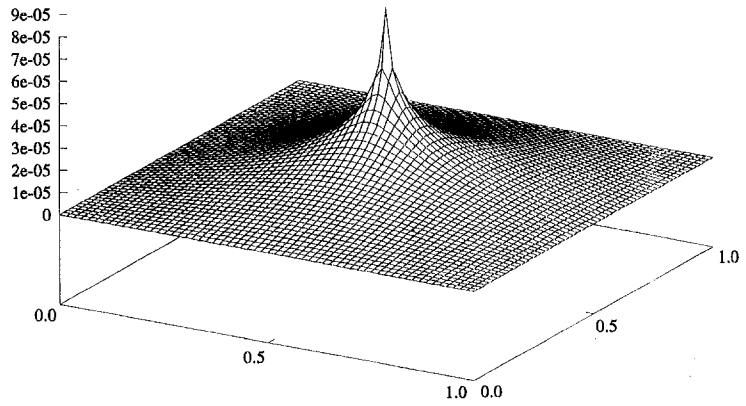


Fig. 9(*b*) Overall solution after ninth level adaptivity

Fig. 9 Adaptivity based on wavelet solutions for RKPM

found to be very efficient due to a smaller number of additional particles. In problems with slowly varying gradients, convergence is obtained after only a few levels of adaptive refinements even though a very coarse initial grid is selected. However, the more conservative criterion is recommended to properly account for sharp gradients in coarse grids.

4.4.2 Adaptivity Procedure. The multiresolution adaptivity procedure described in the previous section is outlined as follows:

- An initial grid of particles is selected, and the computations are performed to determine the unknown variables.
- The finer-scale solution, Eq. (37), is evaluated for the current grid.
- The wavelet solution, ψ, is computed using Eq. (38).
- The grid locations of highest values of ψ are determined based on the criteria described earlier.
- Additional particles are inserted in the vicinity of particles with high ψ values.
- If necessary, boundary conditions are imposed on the additional particles.
- New particle dilation parameters are defined based on the new grid.
- The solution for the new grid is computed, and checked for convergence.
- The adaptivity is continued until the desired accuracy level is reached which is determined through selected error criteria on important system variables at critical locations.

Table 2 Convergence to analytical solution with successive adaptivity

Adaptivity Level	Midpoint Displacement Analytical $= 0.8029 \cdot 10^{-4}$	Number of Particles in the Grid
0	$65.52 \cdot 10^{-4}$	441
1	$17.07 \cdot 10^{-4}$	545
2	$4.439 \cdot 10^{-4}$	649
3	$1.153 \cdot 10^{-4}$	753
4	$0.7408 \cdot 10^{-4}$	857
5	$0.9800 \cdot 10^{-4}$	897
6	$0.9841 \cdot 10^{-4}$	921
7	$0.8844 \cdot 10^{-4}$	958
8	$0.8350 \cdot 10^{-4}$	980
9	$0.8057 \cdot 10^{-4}$	1005
10	$0.8060 \cdot 10^{-4}$	1009

4.5 Adaptivity in RKPM With RKPM. The wavelet-based RKPM adaptivity concept is demonstrated in a problem with an analytical solution. The governing equation for a square domain with an external load applied is given as

$$u_{xx} + u_{yy} = -f(x) \quad (x, y) \in \Omega \tag{39}$$

where

$$f(x) = \begin{cases} 1 & \bar{x} - \bar{a} \le x \le \bar{x} + \bar{a},\ \bar{y} - \bar{a} \le y \le \bar{y} + \bar{a} \\ 0 & \text{otherwise} \end{cases} \tag{40}$$

where $\bar{x} = 0.5$ and $\bar{y} = 0.5$. The load is applied on the area, $\bar{a}$ by $\bar{a}$, centered at $(\bar{x}, \bar{y})$. The boundary conditions are given as

$$u(0, y) = 0 \quad u(1, y) = 0 \quad 0 \le y \le 1$$
$$u(x, 0) = 0 \quad u(x, 1) = 0 \quad 0 \le x \le 1 \tag{41}$$

The analytical solution is given by

Downloaded 04 May 2010 to 171.66.16.34. Redistribution subject to ASME license or copyright; see http://www.asme.org/terms/Terms_Use.cfm

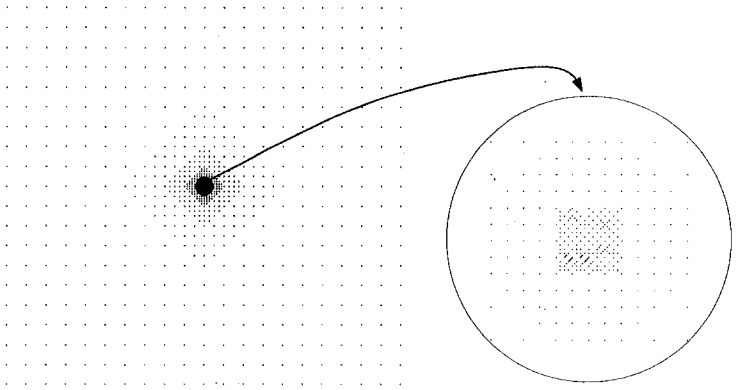


Fig. 10 RKPM particle distribution after ten levels of adaptivity

$$u(x, y) = \frac{16}{\pi^4} \sum_{i,j=1,3,5,\ldots}^{\infty} \frac{1}{(i^2 + j^2)ij} \sin \frac{i\pi}{2} \sin \frac{j\pi}{2} \sin \frac{i\pi\bar{a}}{2} \times \sin \frac{j\pi\bar{a}}{2} \sin (i\pi x) \sin (j\pi y). \quad (42)$$

The governing equation given in Eq. (39) is solved using RKPM with cubic splines as window functions. Since the analytical solution for the concentrated load case exhibits extremely slow convergence, the area parameter, $\bar{a}$, is chosen as $\frac{1}{200}$ to mimic the concentrated load. The initial grid consists of 11 particles in each direction (121 particles in total). The wavelet solution for adaptive refinement is obtained by following the procedure outlined in Section 4.4.1. In this example, the adaptivity criterion based on a predetermined percentage of the maximum wavelet value failed to converge to the analytical solution. Therefore, the criterion referred to as conservative in Section 4.4.1, is adopted to allow more particles in the concentration region. Although this approach yields convergent solutions, the rate is rather slow and an oscillating behavior is observed around the analytical solution from one adaptivity level to the next. The difficulties encountered in applying both adaptivity criteria are attributed to the inadequacy of the solution obtained from the initial coarse grid in representing the overall response in the domain.

A second study is then conducted with an initial 21 by 21 grid (441 particles). The particle insertion algorithm is designed to insert additional particles in the vicinity of each critical particle. Since the algorithm avoids any duplication of the existing particles, the total number of additional particles depends on the relative location of the critical particles prior to the refinement. Further control over the total number of additional particles as well as over particle clustering is accomplished through a proximity parameter which limits the insertion process to a preset distance from each critical particle. In the current example, 25 particles are selected as critical at the first adaptivity level, and the proximity parameter is arbitrarily set to $\frac{1}{64}$th of the initial interparticle distance. A larger particle number appears to be unnecessary since the convergence is mainly influenced by the initial approximation as indicated earlier. In order to limit the insertion process only to the high-gradient region, the number of critical particles is reduced to nine after the fourth, to five after the seventh, and to one after the ninth adaptivity levels. As depicted in Fig. 9, and tabulated in Table 2, the results obtained by the initial grid are about two orders higher than the analytical solution. The results show that by the fifth adaptivity level (857 particles), the error in the value of the solution at the center is about 7.7 percent. The refinement at the first four levels of adaptivity assigns additional particles in the region near the applied force where oscillations are observed (see Fig. 9(a)). As oscillations are eliminated with successive levels of adaptivity, the order of computational results approached the analytical solution, and particles are added only in the immediate neighborhood of the applied force. At the sixth and seventh levels, just after the computational results reached the same order as the analytical solution, a slight overshoot in the midpoint response is observed. However, the following adaptivity levels yield a uniform convergence to the analytical solution. It is remarkable that the solution after the tenth level is only within 0.3 percent with a total of 1005 particles in the grid mostly concentrated near the forcing function. The final particle distribution in the computational grid is depicted in Fig. 10.

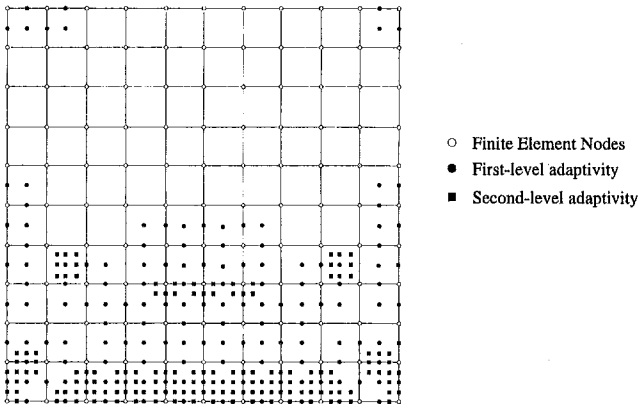


Fig. 11 Particle distribution and two levels of adaptivity

The investigation of a 41 × 41 grid indicates that there is no substantial improvement in the initial solution. Hence it is not worth the computational effort required to solve a system even larger than ten levels of adaptivity with a 21 × 21 initial grid.

4.6 Adaptivity in FEM Through RKPM. The enrichment and adaptivity concepts are demonstrated in a two-dimensional example. Instead of using an actual FEM mesh, FEM shape functions are emulated by an appropriate selection of the dilation parameter. Thus, the third-order spline used for RKPM is reduced to a form corresponding to Lagrange interpolants of FEM.

The governing equation and boundary conditions are stated as follows:

$$u_{xx} + u_{yy} = 0 \quad (x, y) \in \Omega \quad (43)$$

$$u(0, y) = 0 \quad u(\pi, y) = 0 \quad 0 \le y \le \pi$$

$$u(x, 0) = x(\pi - x) \quad u(x, \pi) = 0 \quad 0 \le x \le \pi. \quad (44)$$

The analytical solution is given as

Downloaded 04 May 2010 to 171.66.16.34. Redistribution subject to ASME license or copyright; see http://www.asme.org/terms/Terms_Use.cfm

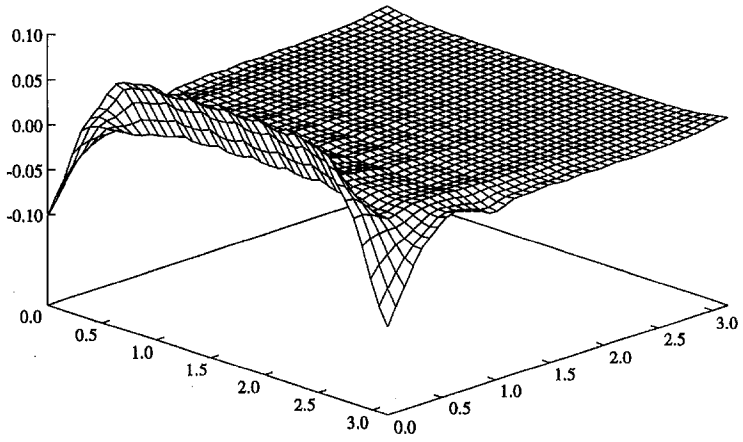


Fig. 12(*a*) Wavelet solution obtained with the 11 × 11 FE mesh

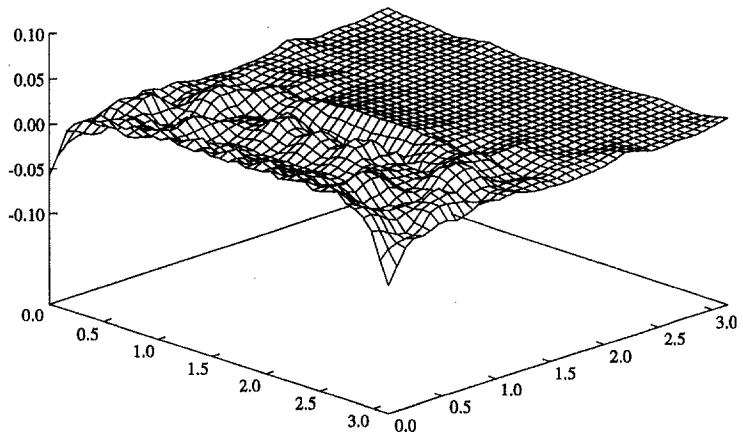


Fig. 12(*b*) Wavelet solution after first level adaptivity

$$u(x, y) = \frac{8}{\pi} \sum_{n=1}^{\infty} \frac{1}{(2n-1)^3} \frac{\sinh (2n-1)(\pi - y)}{\sinh (2n-1)\pi} \times \sin (2n-1)x. \quad (45)$$

An 11 × 11 finite element mesh is selected as the initial computational grid. By using the wavelet solution, the critical particles are identified for refinement. Both adaptivity procedures introduced in Section 4.4.1 are employed with high degrees of success. RKPM is applied through the additional particles whereas the original FEM nodes are kept without a modification. Only two additional levels of adaptivity are required to obtain convergence to the analytical solution. The initial finite element mesh, and the particle distribution after two levels of adaptivity is depicted in Fig. 11.

The wavelet solutions for the initial mesh and two levels of adaptivity, and the final solution are presented in Figs. 12. The amplitude of the wavelet solution is reduced following each refinement level as the computational results approach the analytical solution.

5 Conclusions

In this paper, the convergence characteristics inherent in an FEM formulation are recovered by introducing a correction function in RKPM. The coupling between FEM and RKPM are performed through a so-called multiple field formulation as well as by imposing the completeness or reproducing conditions. The appropriate blending between RKPM and other computational methods as well as analytical functions are also achieved through the same multiple-field RKPM formulation. The solution can further be divided into several fields representing different scales within the same problem. Examples show that a multiple-field RKPM with FEM yields more accurate solutions than FEM of the same order of approximation.

The concept of enrichment of FEM with RKPM is taken to a broader spectrum by introducing an adaptive grid refinement approach. Using the multiresolution analysis, a wavelet-based adaptivity approach is devised, and the associated refinement criteria are established. The effectiveness of this method is shown through an example featuring an FEM mesh refined by particles.

Acknowledgments

The support of this research by Office of Naval Research (ONR), and Air Force Office of Scientific Research (AFOSR) to Northwestern University is gratefully acknowledged. A part of this work (R. A. Uras) was supported by the U.S. Department of Energy, Technology Support Program, under contract W-31-109-Eng-38.

Downloaded 04 May 2010 to 171.66.16.34. Redistribution subject to ASME license or copyright; see http://www.asme.org/terms/Terms_Use.cfm

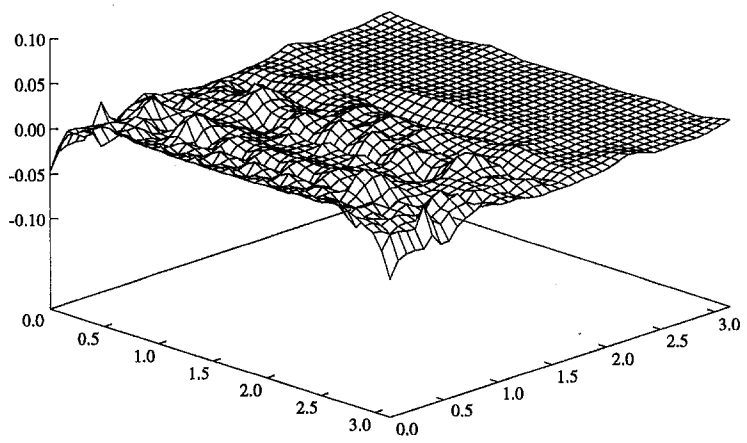


Fig. 12(*c*) Wavelet solution after second level adaptivity

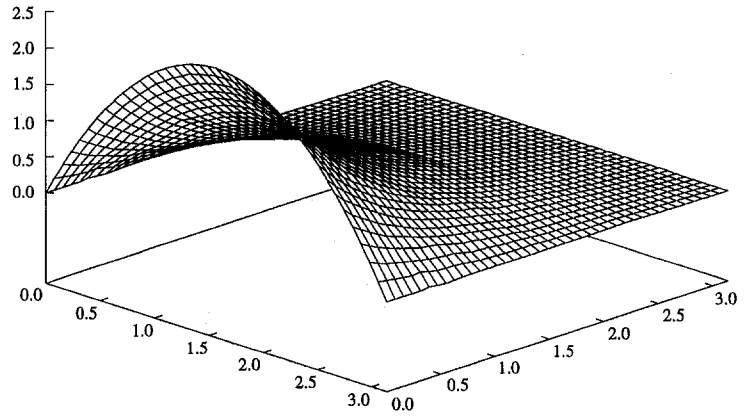


Fig. 12(*d*) Overall solution after second level adaptivity

Fig. 12 Coupling of FEM and RKPM through adaptivity

References

Belytschko, T., Lu, Y. Y., and Gu, L., 1994a, "Element Free Galerkin Methods," *International Journal for Numerical Methods in Engineering,* Vol. 37, pp. 229–256.

Belytschko, T., Lu, Y. Y., and Gu, L., 1994b, "A New Implementation of the Element Free Galerkin Method," *Computer Methods in Applied Mechanics and Engineering,* Vol. 113, pp. 397–414.

Belytschko, T., Gu, L., and Lu, Y. Y., 1994c, "Fracture and Crack Growth by EFG Methods," *Modeling Simul. Mater. Sci. Eng.,* Vol. 2, pp. 519–534.

Gingold, R. A., and Monaghan, J. J., 1977, "Smoothed Particle Hydrodynamics: Theory and Application to Non-Spherical Stars," *Mon. Not. Roy. Astron. Soc.,* Vol. 181, pp. 375–389.

Hughes, T. J. R., 1987, *The Finite Element Method,* Prentice-Hall Inc., Englewood Cliffs, NJ.

Krongauz, Y., and Belytschko, T., 1996, "Enforcement of Essential Boundary Conditions in Meshless Approximation using Finite Element Method," *Computer Methods in Applied Mechanics and Engineering,* accepted for publication.

Liu, W. K., and Oberste-Brandenburg, C., 1993, "Reproducing Kernel and Wavelet Particle Methods," *Aerospace Structures: Nonlinear Dynamics and System Response,* J. P. Cusumano, C. Pierre, and S. T. Wu, eds., ASME, New York, pp. 39–56.

Liu, W. K., Adee, J., and Jun, S., 1993a, "Reproducing Kernel Particle Methods for Elastic and Plastic Problems," *Advanced Computational Methods for Material Modeling,* D. J. Benson and R. A. Asaro, eds., ASME, New York, pp. 175–190.

Liu, W. K., 1995, "Feature Article on An Introduction to Wavelet Reproducing Kernel Particle Methods," *USACM Bulletin,* Vol. 8, No. 1, pp. 3–16.

Liu, W. K., and Chen, Y., 1995, "Wavelet and Multiple Scale Reproducing Kernel Methods," *International Journal for Numerical Methods in Fluids,* Vol. 21, pp. 901–932.

Liu, W. K., Jun, S., Li, S., Adee, J., and Belytschko, T., 1995a, "Reproducing Kernel Particle Methods for Structural Dynamics," *International Journal of Numerical Methods for Engineering,* Vol. 38, pp. 1655–1679.

Liu, W. K., Jun, S., and Zhang, Y. F., 1995b, "Reproducing Kernel Particle Methods," *International Journal of Numerical Methods in Fluids,* Vol. 20, pp. 1081–1106.

Liu, W. K., Belytschko, T., and Oden, J. T., eds., 1996, "Meshless Methods," *Computer Methods in Applied Mechanics and Engineering,* Vol. 139.

Liu, W. K., Chen, Y., Chang, C. T., and Belytschko, T., 1996a, "Advances in Multiple Scale Kernel Particle Methods," *Computational Mechanics* (An International Journal, A Special Feature Article for the 10th Anniversary Volume of Computational Mechanics), Vol. 18, 73–111.

Liu, W. K., Chen, Y., Jun, S., Chen, J. S., Belytschko, T., Pan, C., Uras, R. A., and Chang, C. T., 1996b "Overview and Applications of the Reproducing Kernel Particle Methods," *Archives of Computational Methods in Engineering, State of the Art Reviews,* Vol. 3, pp. 3–80.

Liu, W. K., Chen, Y., Uras, R. A., and Chang, T. C., 1996c, "Generalized Multiple Scale Reproducing Kernel Particle Methods," *Computer Methods in Applied and Engineering,* Vol. 139, pp. 91–157.

Liu, W. K., Jun, S., Sihling, D. T., Chen, Y., and Hao, W., 1997a, "Multiresolution Reproducing Kernel Particle Method for Computational Fluid Dynamics," *International Journal of Numerical Methods in Fluids,* Vol. 24, pp. 1391–1415.

Liu, W. K., Li, S., and Belytschko, T., 1997b, "Moving Least Square Kernel Galerkin Method (I) Methodology and Convergence," *Computer Methods in Applied Mechanics and Engineering,* Vol. 143, pp. 113–154.

Lucy, L., 1977, "A Numerical Approach to Testing the Fission Hypothesis," *Astronomical Journal,* Vol. 82, pp. 1013–1024.

Sulsky, D., and Schreyer, H. L., 1996, "Axisymmetric Form of the Material Point Method with Applications to Upsetting and Taylor Impact Problems," *Computer Methods in Applied Mechanics and Engineering,* Vol. 139, pp. 409–430.

Downloaded 04 May 2010 to 171.66.16.34. Redistribution subject to ASME license or copyright; see http://www.asme.org/terms/Terms_Use.cfm

W. R. Qualls
Senior Process Development Engineer,
Memory Technologies Group,
3M Company,
St. Paul, MN
Mem. ASME

J. K. Good
Professor,
Noble Research Fellow,
Department of Mechanical and
Aerospace Engineering,
Oklahoma State University,
Stillwater, OK 74078
Mem. ASME

Thermal Analysis of a Round Roll

A method for calculating the internal stress distribution in a wound roll subjected to a homogeneous temperature change is presented. The nonlinear constitutive behavior apparent in the stack-wise direction of the roll is represented by a function dependent upon pressure that is incrementally updated during the analysis. In addition to the mechanics of the model, procedures for measuring the circumferential and radial coefficients of thermal expansion are described. Particular examples are presented that show, by comparison with experimental data, the model described herein accurately predicts interlayer pressures in a wound pack. In addition, the marked effect of the core expansion coefficient on the stress distribution is shown and this example illustrates the potential for optimizing the selection of core materials such that the effects of environmental changes on roll structure are minimized.

Introduction

Wound rolls subjected to changes in climatic conditions respond mechanically to equilibrate the internal stresses in the structure. The stress state in the wound roll can be drastically altered by processes involving even the slightest change in strain. As Hakiel (1987) points out, the internal stress distributions are the quantitative source by which roll quality and its susceptibility to damage and defect are determined. When the stress state of a wound roll is sufficiently altered, the roll is subject to defect during subsequent manufacturing, transportation, or handling operations. As many defects occur in finished or near-finished products, the loss in capital can be substantial. Consequently, environmental factors have plagued the winding and converting industry for years. Often the response is to apply extensive climatic controls during production processes, and in several cases, during transportation. These controls can be costly; however, the necessity to ship and store products across and through climatic extremes has provided the incentive to invest in this preventative technology. Even though this approach has, in many cases, been successful, it is not an economical solution. From a mechanics point of view, the solution to this problem resides in the structural combination of thermal expansion coefficients, elastic moduli, and roll geometry. If all significant variables can be combined into a mathematical formulation, then the winding process, core selection, and roll geometry may be optimized such that significant savings could be realized by relaxing stringent environmental controls.

Tramposch (1967) was the first in the literature to provide a mathematical solution to the thermoelastic winding problem. Pfeiffer (1966) and Hakiel (1987) have since shown the radial modulus, E_r, of a wound roll is a function of the radial pressure. They have also shown the radial pressure profile within a roll to be quite dependent upon the radial modulus. Since Tramposch assumed the material properties of the roll structure were constant, the roll structure was not realistically represented. Connolly and Winarski (1984) later published an orthotropic thermoelastic model employing constant material properties. An exact solution to this problem was also presented along with several qualitative remarks. As with the work of Tramposch, the results of Connolly and Winarski must be questioned and their conclusions reviewed due to the assumption of constant moduli. Most recently, Willett and Poesch (1988) published a nonlinear winding model with many similarities to that which Hakiel developed in 1985. Though Willett and Poesch were not the first to solve the nonlinear problem and include a radial modulus written as a function of radial pressure, their initial formulation included the effect of a homogeneous temperature change. Despite their focus on the thermoelastic problem, no thermal analysis nor solution techniques involving such were presented in their published work.

A review of literature has revealed a void in work focusing on thermal analysis of wound roll structures. All relevant works have either assumed constant material properties which yield questionable results or neglected to present numerical examples. Additionally, no publication has experimentally determined material properties needed for such an analysis nor experimentally verified the analysis technique. The focus of this work will be to fill this void. A nonlinear orthotropic thermoelastic wound roll model will be derived using practical assumptions and well-known solution techniques. The governing equations will be generated in terms of the radial stress. Furthermore, the authors will outline methods for measuring coefficients of thermal expansion relative to the wound structure and then provide experimental verification of the developed model. Finally, the influence of the core expansion properties will be demonstrated and a discussion will take place regarding the optimization of the core selection process.

Solution Methodology

Most of the winding models found in the literature have been derived using a stress formulation cast in terms of radial stress. The advantage of a radial stress formulation in wound roll modeling is that the radial stresses can be used to infer roll quality. Good and Vaidyanathan (1995) showed that the radial stress could be used to calculate the torque capacity of a wound roll which was found useful in predicting propensity for interlayer slippage, a mechanism that can initiate roll defects such as crepe wrinkles and starring. For this reason the thermoelastic model derived herein is written with the radial stress as the primary variable. Derivation begins with the equilibrium and compatibility equations in polar coordinates along with constitutive laws governing material behavior. The equilibrium expression for an axisymmetric formulation is

Contributed by the Applied Mechanics Division of THE AMERICAN SOCIETY OF MECHANICAL ENGINEERS for publication in the ASME JOURNAL OF APPLIED MECHANICS.

Discussion on the paper should be addressed to the Technical Editor, Professor Lewis T. Wheeler, Department of Mechanical Engineering, University of Houston, Houston, TX 77204-4792, and will be accepted until four months after final publication of the paper itself in the ASME JOURNAL OF APPLIED MECHANICS.

Manuscript received by the ASME Applied Mechanics Division, Mar. 27, 1996; final revision, Dec. 19, 1996. Associate Technical Editor: I. M. Daniel.

Copyright © 1997 by ASME

Downloaded 04 May 2010 to 171.66.16.34. Redistribution subject to ASME license or copyright; see http://www.asme.org/terms/Terms_Use.cfm

$$r\frac{\partial \sigma_r}{\partial r} + \sigma_r - \sigma_\theta = 0 \tag{1}$$

where r is the radius and σ_r and σ_θ are the radial and circumferential stresses, respectively. The authors have chosen to use an elastic constitutive relation similar to that used by Hakiel (1987) but modified to include thermal influences. The wound roll is then taken to be governed by the stress-strain relationships in (2) and (3).

$$\epsilon_r = \frac{1}{E_r}\sigma_r - \frac{\upsilon_{r\theta}}{E_\theta}\sigma_\theta + \alpha_r \Delta T \tag{2}$$

$$\epsilon_\theta = \frac{1}{E_\theta}\sigma_\theta - \frac{\upsilon_{\theta r}}{E_r}\sigma_r + \alpha_\theta \Delta T \tag{3}$$

The subscripts r and θ refer to the radial and circumferential directions; E is the elastic modulus; ϵ is normal strain; ΔT is the change in temperature; ν is Poisson's ratio; and α is a coefficient of thermal expansion. The circumferential stress, σ_θ, is eliminated from the process by solving the equilibrium equation for σ_θ and substituting the result into (2) and (3). This yields expressions for the radial and circumferential strain, as shown below.

$$\epsilon_r = \frac{1}{E_r}\sigma_r - \frac{\upsilon_{r\theta}}{E_\theta}\left(r\frac{\partial \sigma_r}{\partial r} + \sigma_r\right) + \alpha_r \Delta T \tag{4}$$

$$\epsilon_\theta = \frac{1}{E_\theta}\left(r\frac{\partial \sigma_r}{\partial r} + \sigma_r\right) - \frac{\upsilon_{\theta r}}{E_r}\sigma_r + \alpha_\theta \Delta T \tag{5}$$

Equations (4) and (5) are then substituted into the compatibility equation, shown in (6).

$$r\frac{\partial \epsilon_\theta}{\partial r} + \epsilon_\theta - \epsilon_r = 0 \tag{6}$$

When the right-hand side of Eq. (5) is substituted into compatibility equation (6), a partial derivative operates on all terms. Two assumptions are now made which simplify the governing differential equation and limit the scope of this study. First, it is assumed that the circumferential material properties, E_θ, $\nu_{r\theta}$, and α_θ are constants and the derivatives of such identically zero. It should be noted that both Hakiel (1987) and Willett and Poesch (1988) also assumed E_θ and $\nu_{r\theta}$ constants in their work. Hakiel experimentally verified his winding model, thereby demonstrating the validity of this assumption.

The second assumption takes the roll to be subjected to a homogeneous temperature change. Since the temperature change is assumed uniform, derivatives of the temperature are then zero. Returns are twofold as a transient thermal analysis would require solution to the conduction problem and assessment of thermal conductivities for the core and the wound pack.

Using the above assumptions, the result of substituting Eqs. (4) and (5) into compatibility Eq. (6) yields (7), the governing equation written in terms of the radial stress, σ_r.

$$\frac{r^2}{E_\theta}\frac{\partial^2 \sigma_r}{\partial r^2} + \left(\frac{3r}{E_\theta} - \frac{r\nu_{\theta r}}{E_r} + \frac{r\nu_{r\theta}}{E_\theta}\right)\frac{\partial \sigma_r}{\partial r} + \left(-\frac{r}{E_r}\frac{\partial \nu_{\theta r}}{\partial r} - r\nu_{\theta r}\left(-\frac{1}{E_r^2}\frac{\partial E_r}{\partial r}\right) + \frac{1}{E_\theta} - \frac{\nu_{\theta r}}{E_r} - \frac{1}{E_r} + \frac{\nu_{r\theta}}{E_\theta}\right)\sigma_r = (\alpha_r - \alpha_\theta)\Delta T \tag{7}$$

Further simplification of (7) encompasses an assumption regarding the behavior of Poisson's ratios in the wound structure. Willett and Poesch (1988) addressed this issue of employing isotropic values for Poisson's ratios and found that the common assumption of isotropy in Poisson's ratio is incorrect. They also investigated the validity of using Maxwell's relation, shown in Eq. (8), in wound roll modeling. In an experiment Willett and Poesch measured the radial Poisson's ratio, $\nu_{\theta r}$, to be 0.07. This value was significantly less than that resulting from an assumption of isotropy in Poisson's ratio, but was greater than that predicted by orthotropic theory or Maxwell's relation. Willett and Poesch did not provide an explanation for this behavior and furthermore did not comment on the effect of this parameter on the solution. Hakiel (1988) and Zabaras et al. (1994) have shown that $\nu_{\theta r}$ can be estimated from Maxwell's relation by a successful comparison of predicted radial pressures to those acquired experimentally. In lieu of the work by Hakiel and Zabaras et al., the present authors have chosen to employ Maxwell's relation shown below.

$$\frac{\upsilon_{\theta r}}{E_r} = \frac{\upsilon_{r\theta}}{E_\theta} \tag{8}$$

Substituting (8) into expression (7) yields that shown in (9).

$$\frac{r^2}{E_\theta}\frac{\partial^2 \sigma_r}{\partial r^2} + \frac{3r}{E_\theta}\frac{\partial \sigma_r}{\partial r} + \left(-\frac{r}{E_r}\frac{\partial}{\partial r}\left(\frac{E_r \nu_{r\theta}}{E_\theta}\right) - r\frac{E_r \nu_{r\theta}}{E_\theta} \times \left(-\frac{1}{E_r^2}\frac{\partial E_r}{\partial r}\right) + \frac{1}{E_\theta} - \frac{1}{E_r}\right)\sigma_r = (\alpha_r - \alpha_\theta)\Delta T \tag{9}$$

Since E_θ and $\nu_{r\theta}$ have been assumed constant, the above equation becomes

$$\frac{r^2}{E_\theta}\frac{\partial^2 \sigma_r}{\partial r^2} + \frac{3r}{E_\theta}\frac{\partial \sigma_r}{\partial r} + \left(-\frac{r}{E_r}\frac{\nu_{r\theta}}{E_\theta}\frac{\partial (E_r)}{\partial r} - r\frac{E_r \nu_{r\theta}}{E_\theta} \times \left(-\frac{1}{E_r^2}\frac{\partial E_r}{\partial r}\right) + \frac{1}{E_\theta} - \frac{1}{E_r}\right)\sigma_r = (\alpha_r - \alpha_\theta)\Delta T, \tag{10}$$

which readily simplifies to

$$r^2\frac{\partial^2 \sigma_r}{\partial r^2} + 3r\frac{\partial \sigma_r}{\partial r} + \left(1 - \frac{E_\theta}{E_r}\right)\sigma_r = E_\theta(\alpha_r - \alpha_\theta)\Delta T, \tag{11}$$

a second-order differential equation in radial stress.

Two boundary conditions must be applied for a solution. At the core-roll interface, continuity of displacement is prescribed. Mathematical representation of the inner boundary condition is shown in (12) and (13) where E_c is the core stiffness, u is radial displacement, and the subscript c denotes the core. The deformation of the core is taken to be equivalent to the deformation of the innermost layer in the wound roll. Note, expression (13) is derived from (12) by normalizing with the inner roll radius.

$$u_c = u_{\text{mat'l}} \tag{12}$$

$$\frac{\sigma_r}{E_c} + \alpha_c \Delta T = \epsilon_\theta \tag{13}$$

The constitutive relation for the circumferential strain is used to cast (13) in terms of stress. Then, the circumferential stress is eliminated by employing the equilibrium equation. Once terms are collected, the inner boundary condition can be written, as shown in (14), in a form convenient for numerical solution.

$$r\frac{\partial \sigma_r}{\partial r} + \sigma_r\left(1 - \upsilon - \frac{E_\theta}{E_c}\right) = E_\theta(\alpha_c - \alpha_r)\Delta T \tag{14}$$

Downloaded 04 May 2010 to 171.66.16.34. Redistribution subject to ASME license or copyright; see http://www.asme.org/terms/Terms_Use.cfm

where

$$\upsilon \equiv \upsilon_{r\theta}. \tag{15}$$

The outer boundary condition takes advantage of the traction-free outer roll surface and is thusly written as

$$\sigma_r(r = r_{\text{out}}) = 0. \tag{16}$$

Using the finite difference method, the governing equation in (7) is discretized at N number of locations along the roll radii. Once the derivatives are replaced with central difference approximations, the governing equation takes the following form.

$$\left(\frac{r^2}{h^2} - \frac{3r}{2h}\right)\sigma_r(i-1) + \left(\frac{-2r^2}{h^2} + 1 - \frac{E_\theta}{E_r}\right)\sigma_r(i) + \left(\frac{r^2}{h^2} + \frac{3r}{2h}\right)\sigma_r(i+1) = E_\theta(\alpha_r - \alpha_\theta)\Delta T \tag{17}$$

where

$$h = \frac{r_{\text{out}} - r_{\text{in}}}{N} \tag{18}$$

and r_{in} and r_{out} refer to the inside and outside roll radii, respectively. Equation (17) is written once at all interior points in the roll for a total of N-2 times. With the inner and outer boundary conditions supplying the remaining two equations, a solution is possible. The boundary value problem has now been reduced to a simultaneous set of equations with N unknowns. Assembling these equations in matrix form yields a tri-diagonal system as shown below.

$$[A]\{\sigma_r\} = \{B\} \tag{19}$$

The system is solved efficiently by a Gaussian elimination routine consisting of (N-1) forward and (N-1) backward substitutions.

Before moving on, several points must be made concerning the thermoelastic model and the process of accounting for nonlinearities. First, the governing equation in (7) can be likened to that presented by Willett and Poesch (1988) with good agreement. Next, the reader should note the thermoelastic problem differs from the winding model in that the thermal solution is not one of accretion. That is, the system of equations in (19) must only be solved once for any prescribed temperature change. However, since the radial modulus is nonlinear, the temperature change should be divided into a number of small discrete increments, defined in this work as NSteps, and the intermediate problem solved at each step. Subdividing the temperature change allows the nonlinear term to be updated, thus providing a more accurate solution than would have been obtained if a one step solution sequence had been used. Since the wound roll is highly nonlinear, foreknowledge of the radial stress profile is required before a thermal analysis can take place. As a result, this model is most conveniently linked to an elastic wound roll model, such as that described by Hakiel (1987), or to a nonlinear viscoelastic model, such as that presented by Qualls and Good (1995). Either model can be used to provide the initial values of the total radial pressure and thus the radial modulus at the interior points. Changes in the radial stress distribution due to temperature would then be computed using expression (19) at each NStep and these changes superposed with the previous results.

Experimental Verification

In this section, predicted results will be compared to radial stresses measured in a roll subjected to various homogeneous temperature changes. Prior to this comparison, procedures for measuring the radial and machine direction coefficients of thermal expansion will be discussed and measured results presented. These material properties are used as input to the thermal model and the predicted results will then be compared to those measured in a wound roll using pull tabs. A pull tab is constructed from a narrow strip of stainless steel feeler gage sandwiched in a folded section of brass shim. Pull tabs are inserted into the winding roll at various radii and the force required to partially extract the feeler gage provides a measure of the radial pressure within the roll.

Machine Direction Coefficient of Thermal Expansion. The procedure used to measure the machine direction (MD) coefficient of thermal expansion is as follows. A 15.24 cm wide sample of 63.5 μm polyethylene approximately 88.9 cm in length was cut from a continuous strip. Two lines perpendicular to the machine direction and 76.2 cm apart were accurately marked on the sample and the sample was folded in half as to make the two lines overlay. The free ends were then clamped and vertically suspended, as shown in Fig. 1, in an environmental chamber with a variable reluctance displacement transducer (LVDT) capable of resolving 2.5 μm attached to the bottom side. With the sample thusly configured, the temperature of the chamber was varied from −1.1° to 65.6°C in 5.55°C increments. Once thermal equilibrium was reached, a measure of the displacement was taken using the attached LVDT. A plot of the sample strain versus temperature is shown in Fig. 2. The slope of this curve is equal to the coefficient of thermal expansion and this value was easily determined by the method of least squares. The results are summarized in Table 1, where the MD coefficient of thermal expansion is shown for two different temperature ranges. Notice the expansion coefficients slightly differ for each of the prescribed ranges. This outcome is expected as the curve in Fig. 2 possesses a slight curvature. Coefficients of thermal expansion obtained during this test agree very well with tabulated values referenced from the Plastics Design Library (1990), where the expansion coefficient of low density polyethylene is given as (2.52E-04 < α_θ < 3.6E-04 cm/cm/°C) for a range of 0° to 50°C.

Radial Coefficient of Thermal Expansion. To measure the radial expansion coefficient of the wound roll, a planar stack of 63.5 μm polyethylene consisting of a sufficient number of layers to form a 2.54 cm sample was prepared such that the interaction of asperities and layer-to-layer contact could be assessed. Had only a single layer been chosen, the thermal response of the composite wound structure might not be accurately represented. The stack was placed between two parallel

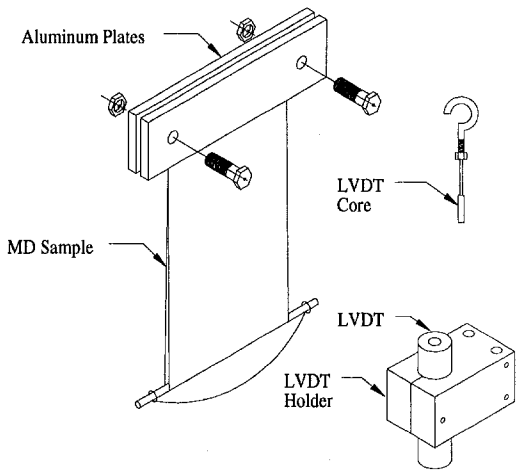


Fig. 1 Machine direction sample used for measuring the coefficient of thermal expansion

Downloaded 04 May 2010 to 171.66.16.34. Redistribution subject to ASME license or copyright; see http://www.asme.org/terms/Terms_Use.cfm

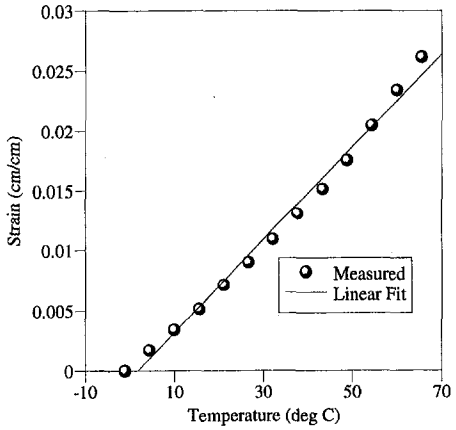


Fig. 2 Machine direction strain versus temperature for 63.5 μm polyethylene

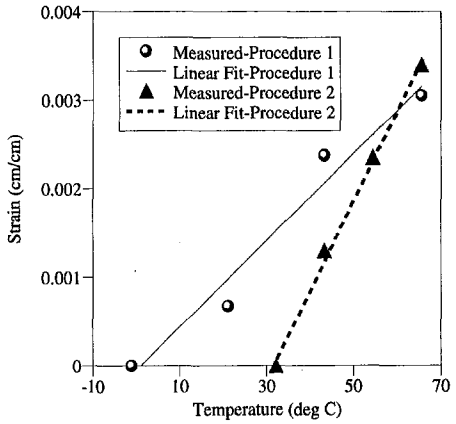


Fig. 3 Comparison of measured radial strain versus temperature using procedures #1 and #2 for 63.5 μm polyethylene

metal platens. The weight of the upper platen was approximately 125 N and produced a compressive stress of approximately 6.9 kPa. A LVDT was mounted to the platen pair to provide measurement of stack displacement. The platens and stack were placed in an environmental chamber and subjected to a fixed temperature of 65.6°C. The sample was initially soaked for a period of five days to eliminate the majority of sample creep. Displacement of the stack was then measured and a correction for platen expansion applied. The temperature of the chamber was decreased 22.2°C and the sample was soaked for approximately 24 hours to allow sufficient time for thermal equilibrium. This process was repeated over a temperature range of −1.11° to 65.6°C. Figure 3 displays measured sample strain plotted as a function of temperature. Again, the slope of the curve is equivalent to the thermal expansion coefficient which was found to be 4.878E-05 cm/cm/°C. As shown in Fig. 3, the experimental data are not well represented by the straight line fit as data tend to be slightly erratic. Consequently, an alternative experimental procedure was designed to corroborate the measured information.

For this alternate procedure, a materials testing system was utilized with a temperature chamber mounted between the crossheads. A sample stack was placed between opened platens. An initial temperature of 65.6°C was prescribed and the sample was allowed to soak for a period of 24 hours. After equilibrium was reached, a small load was applied by brining the platens into contact with the sample. When the load reached 8.9 N, corresponding to a pressure of 491 Pa, a measurement of platen position was recorded via extensiometer. The platens were promptly reopened to remove all loads from the sample. This process was repeated for a temperature range of 32.2° to 65.6°C in 11.11°C increments. The measured displacement was corrected for frame and platen expansion and the results are presented in Fig. 3. As seen, the measured strains appear much more linear with temperature than in the previous case. In this case, the radial expansion coefficient was found to be 1.010E-04 cm/cm/°C which is approximately two times that found using the foregoing procedure. It now seems appropriate to determine the influence of the radial expansion coefficient on the solution since two differing measured values have been presented.

Table 1 Machine direction coefficient of thermal expansion over specified temperature ranges

Temperature range	MD thermal expansion coefficient
−1.1° to 65.56°C	3.870E-04 cm/cm/°C
−1.1° to 43.33°C	3.348E-04 cm/cm/°C

To determine the effect of the radial coefficient of thermal expansion on predicted radial pressures, a sensitivity study was prepared. For this study, the thermoelastic model was used in calculating predicted wound roll pressure changes. For fixed values of the machine direction expansion coefficient, the radial expansion coefficient was varied and the resulting pressures changes calculated. Defining a proportionality constant, K, equal to the ratio of the α_θ to α_r, the predicted radial pressures can be plotted for various values of K. Listed in the caption of Fig. 4 are the material properties, analysis parameters, and the winding stress, T_w, chosen for this sensitivity analysis. Figure 4 displays predicted radial pressure distributions for homogeneous temperature changes of ±11.1°C. Notice that the stress distributions are only significantly influenced by K when the value of K is very near one. Furthermore, this study shows that the thermal model is relatively insensitive to changes in the radial expansion term when $K > 3.3$. Experimental data suggest that K ranges from 3.3 to 6.8 for the material used in this study. As a result, differences in the measured values of the radial expansion coefficient by the two procedures described above are not considered significant and the value determined by procedure #2 will be used in all subsequent calculations.

Winding Experiments. With the thermoelastic material properties determined, the final and perhaps the most rigorous evaluation of the numerical model may be performed. By comparing computer simulated results to measured radial pressures, the accuracy of the thermoelastic model can be verified. For a

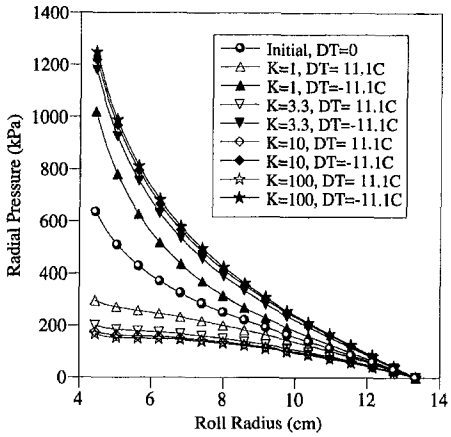


Fig. 4 Influence of the radial expansion coefficient on interlayer pressures, using $K = \alpha_\theta/\alpha_r$, α_θ = 3.348E-04 cm/cm/°C, α_c = 10.8E-06 cm/cm/°C, Ec = 1.9E07 kPa, $E_r = 167\sigma_r$ kPa, E_θ = 1.724E05 kPa, ν = 0.3, NSteps = 10, N = 30, and T_w = 689.5 kPa

Downloaded 04 May 2010 to 171.66.16.34. Redistribution subject to ASME license or copyright; see http://www.asme.org/terms/Terms_Use.cfm

comparison to be made, a roll imbedded with pull tabs was subjected to known changes in temperature. Since polyethylene was chosen for this experiment, special consideration of viscoelastic behavior must be taken in account as increases in temperature often produce accelerated creep rates. To reduce the viscoelastic influences in the ensuing thermal experiment, a roll that was no longer displaying transient stress distributions was used. A roll of this type is often termed "viscoelastically dead." When a dead roll is subjected to a decrease in temperature, then it follows that the roll will remain dead. However, when a dead roll is subjected to an increase in temperature, the roll may become viscoelastically active at the elevated temperature, provided the roll remains at the elevated temperature for a sufficient amount of time.

In the following discussion, an experiment will be described wherein a dead roll is subjected to an increase in temperature for the purpose of verifying the thermoelastic model. An increase in temperature was imposed such that the radial pressures in the roll would decrease, thus allowing for pressure measurement via embedded pull tabs. In addition, it will be shown that thermal equilibrium, in a polyethylene roll of dimensions 15.24 cm in. width and 26.7 cm in. diameter, is reached within 24 hours. As a result, the time for any viscoelastic behavior was minimal. Hence, any changes in stress measured within the first 24 hours after an imposed temperature change will be assumed to be purely thermoelastic. This assumption is later verified by successful comparison with experimental data.

Radial pressures in a roll of 63.5 μm polyethylene wound under controlled conditions were measured for a period of approximately nine months after winding. During the first two months, changes in radial pressure were documented. However, for the later seven months of storage, periodic measures of roll pressure showed no variation. To ensure thermal equilibrium of the roll during experimentation, a duplicate roll was wound under similar winding conditions and imbedded with thermocouples. Both rolls were placed in an environmental chamber. Roll temperatures were increased 5.5, 11.1, and 16.7°C from an initial ambient temperature of 21.1°C. Thermal equilibrium was reached in all cases within 24 hours of the prescribed change. Figure 5 shows the measured radial pressures at room temperature just after winding, after nine months (6E + 06 seconds) of storage, and after the roll was subjected to 5.5°C increments in temperature. As can be seen, a drastic change in roll stress has been documented. Also note, the changes in roll pressure due to temperature variation are much larger than those resulting from viscoelastic relaxation. Thus, the assumption that the changes in roll pressure are predominately thermoelastic is supported by this evidence.

Figure 5 shows that for an increase in temperature of 16.7°C, the radial pressures decreased 80 percent from the initial values.

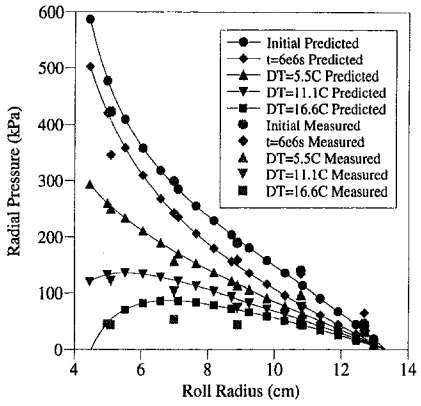


Fig. 5 Experimental verification of thermoelastic model using NSteps = 10, N = 50, T_w = 689.5 kPa, and material properties listed in Table 2

Table 2 Material properties used for verification of thermal model

Property	Value
Core expansion coefficient	α_c = 10.8E-06 cm/cm/°C
Radial expansion coefficient	α_r = 1.01E-04 cm/cm/°C
MD expansion coefficient	α_θ = 3.35E-04 cm/cm/°C
Web-Poisson's ratio	ν = 0.3
Core-Poisson's ratio	ν_c = 0.33
Core stiffness	E_c = 1.9E07 kPa
Radial modulus	$E_r = 167\sigma_r$ kPa
MD modulus	E_θ = 1.724E05 kPa

Rolls transported via freight truck or rail car may be subjected to more extreme changes than those depicted here. For example, rolls wound in a controlled environment may be transported to various locations in the dead of winter or in the middle of summer. These rolls may be exposed to temperatures ranging from −17.8° to 48.9°C. As a result, the quality of the roll structure may be compromised in the process.

The thermoelastic model will now be compared to the measured results by using the experimentally determined material properties. In addition to the elastic and thermoelastic material properties, the viscoelastic properties of polyethylene will be needed for this comparison since the roll pressures at the onset of thermal testing were not equal to those just after winding. Radial and circumferential creep properties used for this comparison were taken from measurements published by Qualls and Good (1995) and are given below.

$$J_r(t) = 4.435\text{E-}06\text{-}2.9516\text{E-}06e^{(-t/2.78\text{E+}03)} - 1.4852\text{E-}06e^{(-t/2.613\text{E+}05)}\ \text{kPa}^{-1}$$

$$J_\theta(t) = 3.874\text{E-}06\text{-}1.5267\text{E-}06e^{(-t/5.8101\text{E+}02)} - 2.3460\text{E-}06e^{(-t/1.2194\text{E+}05)}\ \text{kPa}^{-1}$$

Here $J_r(t)$ and $J_\theta(t)$ are, respectively, the radial and circumferential creep compliances in the time domain and the time, t, is given in seconds. To compare the results effectively, the viscoelastic algorithm outlined by Qualls and Good (1995) was used to calculate the pressures in the roll prior to thermal testing. These pressures are then used to evaluate the nonlinear radial modulus throughout the roll for input to the thermal model. Predicted pressure profiles are shown in Fig. 5, along with values measured immediately after winding, after the roll was stored for nine months (6E + 06 seconds), and for post storage temperature changes of 5.5, 11.1, and 16.7°C. In all cases, the predicted and measured pressures show excellent agreement. Consequently, the thermoelastic model is considered experimentally verified and may be used with confidence in subsequent simulations.

Finally, an example is presented which illustrates the influence of the core expansion coefficient on the roll structure. Using the material properties listed in Table 2 and winding parameters like those described above, Fig. 6 was generated for various values of α_c. In this example, the core pressures in a roll having been wound onto a core with α_c = 10.8E-06 cm/cm/°C have been decreased to zero when subjected to an increase in temperature of 16.7°C. However, when the same roll is wound under identical parameters onto a core with α_c = 5.4E-04 cm/cm/°C and subjected to the same temperature change, the pressures in the roll do not drastically change. More subtle changes may be obtained for other values of the core expansion coefficient as illustrated in this figure. As shown, by altering the expansion coefficient of the core, the change in radial stress may be compensated for by introducing a designed expansion at the core. Additionally, this example demonstrates the possibility for improved wound roll designs by proper selection of core materials.

Downloaded 04 May 2010 to 171.66.16.34. Redistribution subject to ASME license or copyright; see http://www.asme.org/terms/Terms_Use.cfm

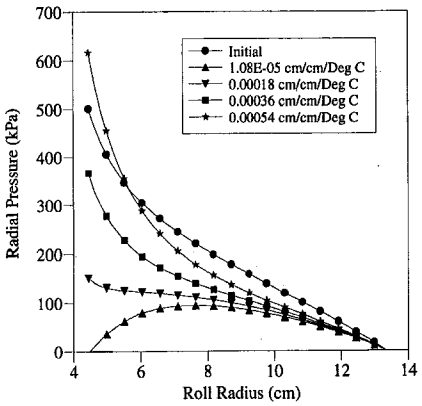


Fig. 6 Predicted effect of core expansion coefficient on an elastic roll structure using α_θ = 3.348E-04 cm/cm/°C, α_r = 1.01E-04 cm/cm/°C, Ec = 1.903E7 kPa, E_r = 167 σ_r kPa, E_θ = 1.724E05 kPa, NSteps = 10, N = 50, T_w = 620.5 kPa, and ΔT = 16.7°C

Summary

In review, a numerical method that may be used to predict the updated stress distribution in a wound roll subjected to a homogeneous temperature change has been developed. Procedures were outlined to evaluate the radial and MD coefficients of thermal expansion; in addition, measured properties were presented. The measured expansion coefficients were then used to predict the stress distribution in a roll subjected to known changes in temperature. Pressures measured in a roll subjected of temperature changes of 5.5°, 11.1°, and 16.7°C were compared to those predicted by the thermoelastic model with good correlation.

References

Connolly, D., and Winarski, D. J., 1984, "Stress Analysis of Wound Magnetic Tape," ASLE Special Publication SP-16, Oct., pp. 172–182.

Good, J. K., and Vaidyanathan, N., 1995, "The Importance of Torque Capacity in Predicting Crepe Wrinkles and Starring in Wound Rolls," *Proceedings of the Third International Conference on Web Handling,* Oklahoma State University.

Hakiel, Z., 1987, "Nonlinear Model for Wound Roll Stresses," *Tappi Journal,* Vol. 70, May, No. 5, pp. 113–117.

Pfeiffer, J. D., 1966, "Internal Pressures in a Wound Roll," *Tappi Journal,* Vol. 49, Aug., No. 8.

Plastics Design Library, 1990, *The Effect of Temperature and Other Related Factors on Plastics,* Vol. I, Book B, Plastics Design Library, New York.

Qualls, W. R., and Good, J. K., 1995, "A Nonlinear Orthotropic Viscoelastic Winding Model," *Proceedings of the Third International Conference on Web Handling,* Oklahoma State University, June.

Tramposch, H., 1967, "Anisotropic Relaxation of Internal Forces in a Wound Reel of Magnetic Tape," ASME JOURNAL OF APPLIED MECHANICS, Vol. 44, pp. 888–894.

Willett, M. S., and Poesch, W. L., 1988, "Determining the Stress Distributions in Wound Reels of Magnetic Tape Using a Nonlinear Finite-Difference Approach," ASME JOURNAL OF APPLIED MECHANICS, Vol. 55, pp. 365–371.

Zabaras, N., Liu, S., Koppuzha, J., and Donaldson, E., 1994, "A Hypoelastic Model for Computing the Stresses in Centerwound Rolls of Magnetic Tape," ASME JOURNAL OF APPLIED MECHANICS, Vol. 61, pp. 290–295.

Downloaded 04 May 2010 to 171.66.16.34. Redistribution subject to ASME license or copyright; see http://www.asme.org/terms/Terms_Use.cfm

Boundary Element Solution for Free Edge Stresses in Composite Laminates

G. Davì
Associate Professor.

A. Milazzo
Research Engineer.

Dipartimento di Meccanica e Aeronautica,
Universita di Palermo,
Viale delle Scienze,
I-90128 Palermo, Italy

The edge-stress problem in multilayered composite laminates under uniform axial extension is analyzed through an alternative method based on a boundary integral formulation. The basic equations of the formulation are discussed and solved by the multiregion boundary element method. Generalized orthotropic elasticity analytic fundamental solutions are employed to establish the integral equations governing the problem. The formulation is absolutely general with regard to the laminate stacking sequence and the section geometry and it does not require any aprioristic assumption on the elastic response nature. This makes the formulation suitable for an investigation of the singular behavior of the stress field at the free edge in composite laminates. The interlaminar normal and shear stress distributions are examined in detail with the aim of calculating the stress singularity at the interlaminar free edge. The singularity parameters, i.e., power and strength, are determined for two family of laminates in order to ascertain the effectiveness of the method for the free edge-stress problem.

1 Introduction

It is well recognized that the stress field in laminated composites evidences an inherently three-dimensional behavior showing high interlaminar gradients along the free edges. This behavior was theoretically predicted on the basis of the works by Bogy (1968) and Kuo and Bogy (1974a, b) and it was actually observed by Pipes and Pagano (1970). Several studies have been devoted to the calculation of the stresses arising at the interface between the laminate layers where the phenomenon reveals itself with the presence of a mathematical singularity in the model solution. Even if the physical mechanism of the laminate response cannot present singularities, the solution of the laminate linear elastic model, which generally expects this singular behavior, is very important. Indeed, certain parameters describing the overall characteristics of the free edge delamination can be extracted from the solution of this model for a useful application to technical problems. Both finite difference (Pipes and Pagano, 1970) and finite elements (Rybicki, 1971; Wang and Crossman, 1977; Spilker and Chou, 1980; Raju and Crews, 1981; Whitcomb et al., 1982; Giavotto et al., 1983; Wang and Yuan, 1983; Chan and Ochoa, 1990; Chen et al., 1996; Lessard et al., 1996) have been employed as numerical techniques to evaluate the interlaminar stress field. They require a remarkable computational effort associated with lengthy extrapolation procedures in order to obtain accurate predictions near the free edge regions. Other analysis schemes have been implemented to obtain the laminate response. The perturbation method (Hsu and Herakovich, 1977), complex stress potentials coupled with eigenfunction (Wang and Choi, 1982a, b; Zwiers et al, 1982) and polynomial expansion (Yin, 1994a, b), series solution (Pipes and Pagano, 1974; Wang and Dickson, 1978), Reissner's variational principle (Pagano, 1978a, b), and the force balance method coupled with the minimum complementary energy principle (Kassapoglou and Lagace, 1986; Lin et al., 1995) have been used. These methods often rest on assumptions about the problem unknowns which enforce the stress field nature assuming or negating the presence of a singular trend on the basis of aprioristic hypotheses. Moreover some elasticity relations are fulfilled in an average sense whereas the problem demands a description in a pointwise fashion. From this point of view boundary integral equations seem to be a powerful tool to deal with layered body elastostatics and in particular with the composite laminate free edge problem. The first boundary integral solution for anisotropic bodies is due to Wilson and Cruse (1978) who used the three-dimensional anisotropic point load solution. This approach is rather cumbersome to use because no general closed form is available for the fundamental solution (Wideberg and Benitez, 1995). Many efforts have successfully been made in the field of two-dimensional anisotropic linear elasticity problems where the integral equation kernels are directly available and boundary element method solutions have been presented for different problems (e.g., Wu et al., 1992; Tan et al., 1992). It is not known to the authors that any attempt has been made to apply the boundary integral equation representation to the composite laminate three-dimensional elastic response. Recently an alternative direct boundary integral formulation for general composite laminates under axial extension was presented by Davì (1991 and 1996). The formulation employs an explicit representation of the fundamental solution due to a load distributed along a line expressly derived on the basis of the Lekhnitskii theory of the anisotropic elastic body. Due to the exact fulfilling of the equilibrium equations, strain compatibility, traction boundary conditions, and interface continuity conditions, the method proposed is numerically consistent and is able to give a correct and attractive solution to the problem. In this paper the stress field arising in composite laminates is investigated in some detail by using a numerical solution of the formulation by the boundary element method. The aim is to ascertain the ability of the method for calculating free edge stresses in composite laminates and hence describing the stress singularity at the free edge exploiting the advantages of boundary integral formulations and solutions in treating singular elasticity problems (Cruse, 1995).

2 Basic Equations

Consider a laminated composite consisting of M generalized orthotropic elastic layers perfectly bonded at the interface. The

Contributed by the Applied Mechanics Division of THE AMERICAN SOCIETY OF MECHANICAL ENGINEERS for publication in the ASME JOURNAL OF APPLIED MECHANICS.

Discussion on this paper should be addressed to the Technical Editor, Professor Lewis T. Wheeler, Department of Mechanical Engineering, University of Houston, Houston, TX 77204-4792, and will be accepted until four months after final publication of the paper itself in the ASME JOURNAL OF APPLIED MECHANICS.

Manuscript received by the ASME Applied Mechanics Division, Apr. 26, 1996; final revision, May 23, 1997. Associate Technical Editor: J. N. Reddy.

Copyright © 1997 by ASME

Downloaded 04 May 2010 to 171.66.16.34. Redistribution subject to ASME license or copyright; see http://www.asme.org/terms/Terms_Use.cfm

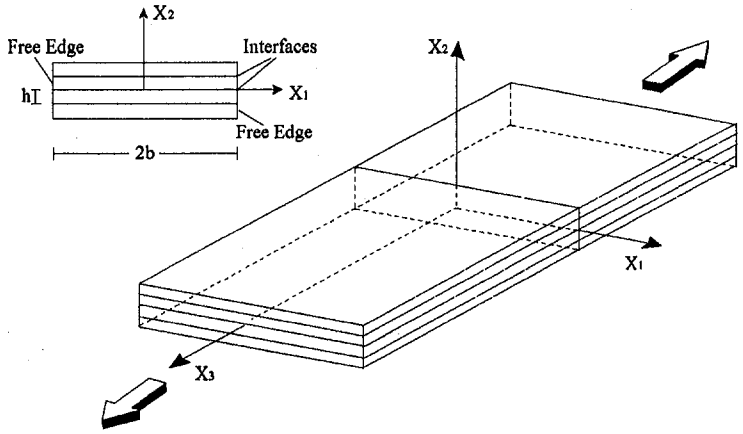


Fig. 1 Laminate configuration

laminate, having constant cross section Ω and length l, is referred to the coordinate system x_i, $i = 1, 2, 3$, as shown in Fig. 1. Each layer of constant cross section Ω_e bounded by the contour Γ_e has one of the material symmetry planes parallel to the x_3-axis. The laminate is subjected to uniform extensional strain ϵ_0 along the x_3-axis. By virtue of Saint Venant's principle, the solution of the elasticity problem outlined can be expressed in terms of displacements s_i as follows (Lekhnitskii, 1963; Pipes and Pagano, 1970):

$$s_1 = u_1(x_1, x_2) \tag{1a}$$

$$s_2 = u_2(x_1, x_2) \tag{1b}$$

$$s_3 = u_3(x_1, x_2) + \epsilon_0 x_3 \tag{1c}$$

where u_1, u_2, and u_3 are unknown functions depending on x_1 and x_2 only. The strain tensor is independent of the x_3 coordinate and the strain-displacement, stress-strain, and equilibrium equations which govern the behavior of each layer are

$$\boldsymbol{\epsilon} = \begin{bmatrix} \epsilon_{11} \\ \epsilon_{22} \\ \epsilon_{12} \\ \epsilon_{31} \\ \epsilon_{32} \end{bmatrix} = \begin{bmatrix} \partial/\partial x_1 & 0 & 0 \\ 0 & \partial/\partial x_2 & 0 \\ \partial/\partial x_2 & \partial/\partial x_1 & 0 \\ 0 & 0 & \partial/\partial x_1 \\ 0 & 0 & \partial/\partial x_2 \end{bmatrix} \begin{bmatrix} u_1 \\ u_2 \\ u_3 \end{bmatrix} = \mathbf{Du} \tag{2a}$$

$$\epsilon_{33} = \epsilon_0 \tag{2b}$$

$$\boldsymbol{\sigma} = \begin{bmatrix} \sigma_{11} \\ \sigma_{22} \\ \sigma_{12} \\ \sigma_{31} \\ \sigma_{32} \end{bmatrix} = \begin{bmatrix} E_{11} & E_{12} & 0 & E_{14} & 0 \\ E_{12} & E_{22} & 0 & E_{24} & 0 \\ 0 & 0 & E_{33} & 0 & E_{35} \\ E_{14} & E_{24} & 0 & E_{44} & 0 \\ 0 & 0 & E_{35} & 0 & E_{55} \end{bmatrix} \boldsymbol{\epsilon} + \begin{bmatrix} E_{16} \\ E_{26} \\ 0 \\ E_{46} \\ 0 \end{bmatrix} \epsilon_0 = \mathbf{E}\boldsymbol{\epsilon} + \mathbf{Q}\epsilon_0 \tag{3a}$$

$$\sigma_{33} = [E_{16} \quad E_{26} \quad 0 \quad E_{46} \quad 0]\,\boldsymbol{\epsilon} + E_{66}\epsilon_0 = \mathbf{Q}^T\boldsymbol{\epsilon} + E_{66}\epsilon_0 \tag{3b}$$

$$\mathbf{D}^T\boldsymbol{\sigma} = \mathbf{0} \quad \text{in} \quad A_e \tag{4}$$

$$\mathbf{D}_n\boldsymbol{\sigma} = \mathbf{t} \quad \text{on} \quad \Gamma_e \tag{5}$$

where $\boldsymbol{\epsilon}$, $\boldsymbol{\sigma}$, $\mathbf{u}$, and $\mathbf{t}$ indicate the strains, stresses, displacements, and tractions, respectively. The operator $\mathbf{D}_n$ is defined as

$$\mathbf{D}_n = \begin{bmatrix} \alpha_1 & 0 & \alpha_2 & 0 & 0 \\ 0 & \alpha_2 & \alpha_1 & 0 & 0 \\ 0 & 0 & 0 & \alpha_1 & \alpha_2 \end{bmatrix} \tag{6}$$

where α_1 and α_2 are the direction cosines of the outward normal $\mathbf{n}$ to the section boundary Γ_e.

3 Integral Equation Formulation

The generic prismatic ply within the laminate, having cross section Ω_e with boundary Γ_e, is loaded on its lateral surface by the traction system $\mathbf{t}$. Consider an elementary part of the prismatic ply between two sections having an infinitesimal distance dx_3 between them, and let $\boldsymbol{\tau}$ be the tractions which act on the cross section

$$\boldsymbol{\tau}^T = [\sigma_{31} \quad \sigma_{32} \quad \sigma_{33}]. \tag{7}$$

Let $\mathbf{s}_j$ be another system of displacements associated with some particular body forces $\mathbf{f}_j$ and suitable traction boundary conditions $\mathbf{t}_j$. The external elementary work done by the tractions $\mathbf{t}$ and $\boldsymbol{\tau}$ through the displacements $\mathbf{s}_j$ is (Giavotto et al., 1983)

$$dL_{12} = \left(\int_{\Gamma_e} \mathbf{s}_j^T \mathbf{t}\, d\Gamma_e + \frac{\partial}{\partial x_3} \int_{\Omega_e} \mathbf{s}_j^T \boldsymbol{\tau}\mathbf{d}\, \Omega_e \right) dx_3. \tag{8}$$

Analogously, the external elementary work done by the body forces $\mathbf{f}_j$ and tractions $\mathbf{t}_j$ and $\boldsymbol{\tau}_j$ through the displacements $\mathbf{s}$ is

$$dL_{21} = \left(\int_{\Gamma_e} \mathbf{t}_j^T \mathbf{s}\, d\Gamma_e + \int_{\Omega_e} \mathbf{f}_j^T \mathbf{s}\, d\Omega_e + \frac{\partial}{\partial x_3} \int_{\Omega_e} \boldsymbol{\tau}_j^T \mathbf{s}\, d\Omega_e \right) dx_3. \tag{9}$$

Since from the reciprocal work theorem $dL_{12} = dL_{21}$, from Eqs. (8) and (9) follows

$$\int_{\Gamma_e} (\mathbf{t}_j^T \mathbf{s} - \mathbf{s}_j^T \mathbf{t})\, d\Gamma_e + \int_{\Omega_e} \mathbf{f}_j^T \mathbf{s}\, d\Omega_e = \int_{\Omega_e} \frac{\partial}{\partial x_3} (\mathbf{s}_j^T \boldsymbol{\tau} - \boldsymbol{\tau}_j^T \mathbf{s})\, d\Omega_e. \tag{10}$$

Equation (10) is the expression of Betti's reciprocity theorem inherent to the present problem. In the following, in order to use Eq. (10) as a starting point for the boundary integral formulation, let us assume $\mathbf{s}_j$ independent on the x_3 coordinate

$$\mathbf{s}_j = \mathbf{u}_j(x_1, x_2). \tag{11}$$

Downloaded 04 May 2010 to 171.66.16.34. Redistribution subject to ASME license or copyright; see http://www.asme.org/terms/Terms_Use.cfm

With this assumption, since also the tractions τ and τ_j are constant along the longitudinal axis, the domain integral on the right-hand side of Eq. (10) reduces to the work for unit length done by the normal stress σ_{33j} on the axial strain ϵ_0. Thus, taking into account the strain-displacement and stress-strain relations and observing that $\epsilon_{33j} = 0$, Eq. (10) becomes

$$\int_{\Gamma_e} (\mathbf{t}_j^T \mathbf{s} - \mathbf{u}_j^T \mathbf{t}) d\Gamma_e + \int_{\Omega_e} \mathbf{f}_j^T \mathbf{s} d\Omega_e = -\epsilon_0 \int_{\Omega_e} \boldsymbol{\epsilon}_j^T \mathbf{Q} d\Omega_e. \quad (12)$$

Again, taking into account that

$$\int_{\Omega_e} \mathbf{f}_j d\Omega_e + \int_{\Gamma_e} \mathbf{t}_j d\Gamma_e = 0, \quad (13)$$

Eq. (12) can be written as

$$\int_{\Gamma_e} (\mathbf{t}_j^T \mathbf{u} - \mathbf{u}_j^T \mathbf{t}) d\Gamma_e + \int_{\Omega_e} \mathbf{f}_j^T \mathbf{u} d\Omega_e = -\epsilon_0 \int_{\Omega_e} \boldsymbol{\epsilon}_j^T \mathbf{Q} d\Omega_e. \quad (14)$$

The integral relation (14) is the basis to derive directly the integral equations employed in the present method. Let the body forces $\mathbf{f}_j$ be a concentrated load distributed along a line parallel to the longitudinal axis and applied in the j direction. Thus, indicating with P_0 the load application point in the ply cross section, the load $\mathbf{f}_j$ can be characterized as

$$\mathbf{f}_j = \mathbf{c}_j(P_0)\delta(P - P_0) \quad (15)$$

where δ is the Dirac function and the vector $\mathbf{c}_j$ contains the concentrated load components. Under these assumptions, Eq. (14) gives (Rizzo, 1967; Cruse, 1974; Davì, 1996)

$$\mathbf{c}_j^T \mathbf{u}(P_0) + \int_{\Gamma_e} (\mathbf{t}_j^T \mathbf{u} - \mathbf{u}_j^T \mathbf{t}) d\Gamma_e = -\epsilon_0 \int_{\Omega_e} \boldsymbol{\epsilon}_j^T \mathbf{Q} d\Omega_e \quad (16)$$

where the vector $\mathbf{c}_j$ can be expressed in terms of the boundary tractions as

$$\mathbf{c}_j = \int_{\Omega_e} \mathbf{f}_j d\Omega_e = -\int_{\Gamma_e} \mathbf{t}_j^T d\Gamma_e. \quad (17)$$

The domain integral on the right-hand side of Eq. (16) can be also transformed into an equivalent boundary integral by divergence theorem:

$$\int_{\Omega_e} \boldsymbol{\epsilon}_j^T \mathbf{Q} d\Omega_e = \int_{\Gamma_e} \mathbf{u}_j^T \mathbf{q} d\Gamma_e \quad (18)$$

where

$$\mathbf{q}^T = [E_{16}\alpha_1 \quad E_{26}\alpha_2 \quad E_{46}\alpha_1]. \quad (19)$$

Substituting Eq. (18) into Eq. (16) the integral equation representation is obtained in its final form where the boundary only character of the formulation is recovered,

$$\mathbf{c}_j^T \mathbf{u}(P_0) + \int_{\Gamma_e} (\mathbf{t}_j^T \mathbf{u} - \mathbf{u}_j^T \mathbf{t}) d\Gamma_e = -\epsilon_0 \int_{\Gamma_e} \mathbf{u}_j^T \mathbf{q} d\Gamma_e. \quad (20)$$

For P_0 belonging to the ply section boundary, Eq. (20) provides the relations linking the displacements and the tractions on the boundary of each layer. These integral equations, coupled with the prescribed boundary data and the interface continuity conditions, should be sufficient to solve the problem in terms of the boundary unknowns only. The problem can be solved numerically by the conventional boundary element method. On the boundary of the generic layer the unknown displacements $\mathbf{u}$ and tractions $\mathbf{t}$, involved in Eq. (20), are interpolated with the corresponding nodal values $\boldsymbol{\delta}$ and $\mathbf{p}$ using appropriate shape functions. The resulting discretized equations for the kth layer within the laminate can be written as

$$\mathbf{H}_k \boldsymbol{\delta}_k + \mathbf{G}_k \mathbf{p}_k = \mathbf{B}_k \quad k = 1, 2 \ldots M \quad (21)$$

where the matrices $\mathbf{H}_k$ and $\mathbf{G}_k$ are the influence matrices for the displacements and tractions, respectively, and $\mathbf{B}_k$ contains the contribution of the prescribed strain ϵ_0. For the generic kth layer, Eq. (21) presents six unknowns for each node, namely three nodal displacements and three nodal tractions, while only three independent integral equations can be written specializing $j = 1, 2, 3$ in Eq. (20). The extra relations needed to solve the problem are obtained by applying the appropriate continuity and equilibrium conditions at the common boundary between the contiguous layers k and $k + 1$, i.e., at the kth laminate interface. Once the unknown boundary data are determined, Eq. (20) should be sufficient to characterize the elastic response of the laminate. The strain field at each point P_0 of the generic ply can be calculated by differentiation of Eq. (20) with respect to the coordinates of the load point P_0 and then, using the stress-strain relations (3), the stresses can be expressed as

$$\sigma = \mathbf{E}\left\{\int_{\Gamma_e} \mathbf{T}\mathbf{u} d\Gamma_e - \int_{\Gamma_e} \mathbf{U}\mathbf{t} d\Gamma_e + \epsilon_0 \int_{\Gamma_e} \mathbf{U}\mathbf{q} d\Gamma_e\right\} + \mathbf{Q}\epsilon_0 \quad (22a)$$

$$\sigma_{33} = \mathbf{Q}^T\left\{\int_{\Gamma_e} \mathbf{T}\mathbf{u} d\Gamma_e - \int_{\Gamma_e} \mathbf{U}\mathbf{t} d\Gamma_e + \epsilon_0 \int_{\Gamma_e} \mathbf{U}\mathbf{q} d\Gamma_e\right\} + E_{66}\epsilon_0 \quad (22b)$$

where the kernels $\mathbf{T}$ and $\mathbf{U}$ are obtained by applying the strain operator $\mathbf{D}$ to the matrices $[t_{ij}]^T$ and $[u_{ij}]^T$, respectively (Banerjee and Butterfield, 1981).

4 Fundamental solutions

The fundamental singular solution for the generalized orthotropic elasticity problem can be obtained according to the theory of anisotropic elasticity (Lekhnitskii, 1963). The fundamental solution in an infinite generalized orthotropic elastic space due to an infinitely long line load parallel to the x_3-axis is governed by the following equilibrium equation, expressed in terms of displacements:

$$\mathbf{D}^T \mathbf{E} \mathbf{D} \mathbf{u}_j(P, P_0) + \mathbf{c}_j \delta(P - P_0) = \mathbf{0}, \quad (23)$$

in which P is a field point, P_0 is the point of the x_1x_2-plane where the load is applied, and δ indicates the Dirac function. These fundamental solutions $\mathbf{u}_j(P, P_0)$ (Kayupov and Kuriyagawa, 1996) are related to the compliances of the considered ply, and more specifically they depend on the roots λ_i of the following characteristic equation:

$$\{C_{11}C_{44} - C_{14}^2\}\lambda^3 + \{2C_{14}(C_{24} + C_{35}) - C_{11}C_{55} - C_{44}(2C_{12} + C_{33})\}\lambda^2 + \{C_{22}C_{44} + C_{55}(2C_{12} + C_{33}) - (C_{24} + C_{35})^2\}\lambda - C_{22}C_{55} = 0 \quad (24)$$

where the C_{rs} coefficients are defined as

$$[C_{rs}] = \mathbf{E}^{-1}. \quad (25)$$

An explicit analytical closed form for the problem fundamental solution can be deduced integrating Eq. (23) on the basis of the Lekhnitskii complex stress potential theory under the hypothesis of distinct and positive in sign roots λ_i of the Eq. (24) (Davì, 1996). The fundamental displacements are given by

Downloaded 04 May 2010 to 171.66.16.34. Redistribution subject to ASME license or copyright; see http://www.asme.org/terms/Terms_Use.cfm

$$\mathbf{u}_j = \begin{bmatrix} u_{1j} \\ u_{2j} \\ u_{3j} \end{bmatrix} = \begin{bmatrix} \varphi_1 B_{11} & \varphi_2 B_{12} & \varphi_3 B_{13} \\ \psi_1 B_{21} & \psi_2 B_{22} & \psi_3 B_{23} \\ \varphi_1 B_{31} & \varphi_2 B_{32} & \varphi_3 B_{33} \end{bmatrix} \begin{bmatrix} A_{1j} \\ A_{2j} \\ A_{3j} \end{bmatrix} \tag{26}$$

where for $j = 1$ and $j = 3$ the functions φ_i and ψ_i are

$$\varphi_i(P, P_0) = -(\ln r_i)/2\pi \tag{27a}$$

$$\psi_i(P, P_0) = -(\tan^{-1}(\sqrt{\lambda_i}\, y/x))/2\pi\sqrt{\lambda_i} \tag{27b}$$

while for $j = 2$ one has to set

$$\varphi_i(P, P_0) = -(\tan^{-1}(\sqrt{\lambda_i}\, y/x))\sqrt{\lambda_i}/2\pi \tag{28a}$$

$$\psi_i(P, P_0) = (\ln r_i)/2\pi. \tag{28b}$$

In the previous relations the following definitions are valid:

$$x = x_1(P) - x_1(P_0) \tag{29a}$$

$$y = x_2(P) - x_2(P_0) \tag{29b}$$

$$r_i = \sqrt{x^2 + \lambda_i y^2} \tag{29c}$$

$$B_{1i} = C_{11} - C_{12}/\lambda_i + C_{14}\gamma_i \tag{30a}$$

$$B_{2i} = C_{12} - C_{22}/\lambda_i + C_{24}\gamma_i \tag{30b}$$

$$B_{3i} = C_{14} - C_{24}/\lambda_i + C_{44}\gamma_i \tag{30c}$$

$$\gamma_i = (C_{14}\lambda_i - C_{24} - C_{35})/(C_{55} - C_{44}\lambda_i). \tag{31}$$

For $j = 1$ and $j = 3$ the coefficients A_{ij} are given by

$$\mathbf{A}_j = \begin{bmatrix} A_{1j} \\ A_{2j} \\ A_{3j} \end{bmatrix} = \begin{bmatrix} \frac{1}{\sqrt{\lambda_1}} & \frac{1}{\sqrt{\lambda_2}} & \frac{1}{\sqrt{\lambda_3}} \\ \frac{B_{21}}{\sqrt{\lambda_1}} & \frac{B_{22}}{\sqrt{\lambda_2}} & \frac{B_{23}}{\sqrt{\lambda_3}} \\ \frac{\gamma_1}{\sqrt{\lambda_1}} & \frac{\gamma_2}{\sqrt{\lambda_2}} & \frac{\gamma_3}{\sqrt{\lambda_3}} \end{bmatrix}^{-1} \begin{bmatrix} c_{1j} \\ 0 \\ c_{3j} \end{bmatrix} \tag{32}$$

while for $j = 2$ they are

$$\mathbf{A}_2 = \begin{bmatrix} A_{12} \\ A_{22} \\ A_{32} \end{bmatrix} = \begin{bmatrix} B_{11}\sqrt{\lambda_1} & B_{12}\sqrt{\lambda_2} & B_{13}\sqrt{\lambda_3} \\ \frac{1}{\sqrt{\lambda_1}} & \frac{1}{\sqrt{\lambda_2}} & \frac{1}{\sqrt{\lambda_3}} \\ B_{31}\sqrt{\lambda_1} & B_{32}\sqrt{\lambda_2} & B_{33}\sqrt{\lambda_3} \end{bmatrix}^{-1} \begin{bmatrix} 0 \\ c_{22} \\ 0 \end{bmatrix}. \tag{33}$$

The traction kernels can be expressed as

$$\mathbf{t}_j = \mathbf{D}_n\mathbf{E}\mathbf{D}\mathbf{u}_j = \begin{bmatrix} t_{1j} \\ t_{2j} \\ t_{3j} \end{bmatrix} = \begin{bmatrix} \Lambda_1 & \Lambda_2 & \Lambda_3 \\ \Pi_1 & \Pi_2 & \Pi_3 \\ \gamma_1\Lambda_1 & \gamma_2\Lambda_2 & \gamma_3\Lambda_3 \end{bmatrix} \begin{bmatrix} A_{1j} \\ A_{2j} \\ A_{3j} \end{bmatrix} \tag{34}$$

where for $j = 1$ and $j = 3$

$$\Lambda_i = -(x\alpha_1 + y\alpha_2)/2\pi r_i^2 \tag{35a}$$

$$\Pi_i = (x\alpha_2 - \lambda_i y\alpha_1)/2\pi\lambda_i r_i^2 \tag{35b}$$

while for $j = 2$

$$\Lambda_i = (\lambda_i y\alpha_1 - x\alpha_2)/2\pi r_i^2 \tag{36a}$$

$$\Pi_i = -(x\alpha_1 + y\alpha_2)/2\pi r_i^2. \tag{36b}$$

The kernels $\mathbf{U} = [U_{ij}]$ and $T = [T_{ij}]$ involved in the integral relations (22a) and (22b), providing the stresses at the source point, are defined in terms of their columns as follows:

$$\mathbf{T}_j = \begin{bmatrix} T_{1j} \\ T_{2j} \\ T_{3j} \\ T_{4j} \\ T_{5j} \end{bmatrix} = \begin{bmatrix} \eta_1 & \eta_2 & \eta_3 \\ -\eta_1 & -\eta_2 & -\eta_3 \\ \frac{\lambda_1 + 1}{\lambda_1}\mu_1 & \frac{\lambda_2 + 1}{\lambda_2}\mu_2 & \frac{\lambda_3 + 1}{\lambda_3}\mu_3 \\ \gamma_1\eta_1 & \gamma_2\eta_2 & \gamma_3\eta_3 \\ \gamma_1\mu_1 & \gamma_2\mu_2 & \gamma_3\mu_3 \end{bmatrix} \begin{bmatrix} A_{1j} \\ A_{2j} \\ A_{3j} \end{bmatrix} \tag{37}$$

$$\mathbf{U}_j = \begin{bmatrix} U_{1j} \\ U_{2j} \\ U_{3j} \\ U_{4j} \\ U_{5j} \end{bmatrix} = \begin{bmatrix} B_{11}\zeta_1 & B_{12}\zeta_2 & B_{13}\zeta_3 \\ B_{21}\zeta_1 & B_{22}\zeta_2 & B_{23}\zeta_3 \\ (B_{11}\lambda_1 - B_{21})\chi_1 & (B_{12}\lambda_2 - B_{22})\chi_2 & (B_{13}\lambda_3 - B_{23})\chi_3 \\ B_{31}\zeta_1 & B_{32}\zeta_2 & B_{33}\zeta_3 \\ B_{31}\lambda_1\chi_1 & B_{32}\lambda_2\chi_2 & B_{33}\lambda_3\chi_3 \end{bmatrix} \times \begin{bmatrix} A_{1j} \\ A_{2j} \\ A_{3j} \end{bmatrix} \tag{38}$$

where for $j = 1$ and $j = 3$ one has to set

$$\eta_i = -\frac{(x^2 - \lambda_i y^2)\alpha_1 + 2xy\alpha_2}{r_i^4} \tag{39a}$$

$$\mu_i = -\frac{2\lambda_i xy\alpha_1 - (x^2 - \lambda_i y^2)\alpha_2}{r_i^4} \tag{39b}$$

$$\zeta_i = \frac{x}{r_i^2} \tag{39c}$$

$$\chi_i = \frac{y}{r_i^2} \tag{39d}$$

while for $j = 2$ one has to set

$$\eta_i = \frac{2\lambda_i xy\alpha_1 - (x^2 - \lambda_i y^2)\alpha_2}{r_i^4} \tag{40a}$$

$$\mu_i = -\frac{\lambda_i(x^2 - \lambda_i y^2)\alpha_1 + 2xy\alpha_2}{r_i^4} \tag{40b}$$

$$\zeta_i = -\lambda_i \frac{y}{r_i^2} \tag{40c}$$

$$\chi_i = \frac{x}{r_i^2}. \tag{40d}$$

The case of plies having the orthotropic principal directions coincident with the laminate reference axes (Mantic and Paris, 1995) is recovered through a suitable limit procedure applied to the previous relations (Davì and Milazzo, 1996). For P_0

Downloaded 04 May 2010 to 171.66.16.34. Redistribution subject to ASME license or copyright; see http://www.asme.org/terms/Terms_Use.cfm

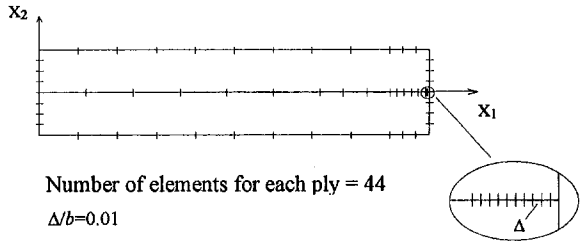


Fig. 2 Boundary element method discretization for a quarter of the laminate section

belonging to Ω_e the fundamental solutions are in general obtained by setting $c_{ij}(P_0) = \delta_{ij}$ where δ_{ij} is the Kronecker delta, such that for P_0 on a smooth boundary Γ_e one has $c_{ij}(P_0) = \delta_{ij}/2$.

5 Applications

A computer code has been developed to calculate laminate behavior by using the present method. The code allows to consider absolutely general lay-ups and section geometries and it was implemented with the following features. The influence coefficients are computed numerically by Gaussian quadrature, assuming linear interpolation of the unknown boundary data. An adaptive integration scheme has been applied which allows one to numerically take the kernel singularities into account (Davì, 1989). According to Eq. (17) the coefficients $\mathbf{c}_j$ at the layer's corners are also computed by using Gaussian quadrature. The enforcement of the traction-free boundary condition $\sigma_{12} = 0$ at the intersection between the interface and the free edge requires some remarks (Whithcomb et al., 1982). Due to the symmetry of the stress tensor, at the interface corner point one actually has five unknown quantities, namely three nodal displacements and only two nodal tractions, against a number of six integral equations written at this point for the two contiguous plies. The traction-free boundary condition has been therefore implemented in the computer code by considering at the interface corner a linear combination given by the sum of the two integral equations obtained at this point for a load acting in the $j = 1$ direction. By doing so all the boundary conditions, equilibrium equations and interface continuity conditions are exactly satisfied and the numerical solution obtained is therefore consistent. Several four-ply symmetric configurations were analyzed using the graphite/epoxy material elastic properties:

$$E_{LL} = 137.9 \text{ GPa}; \quad E_{TT} = E_{SS} = 14.5 \text{ GPa}$$

$$G_{LT} = G_{LS} = G_{TS} = 5.9 \text{ GPa}$$

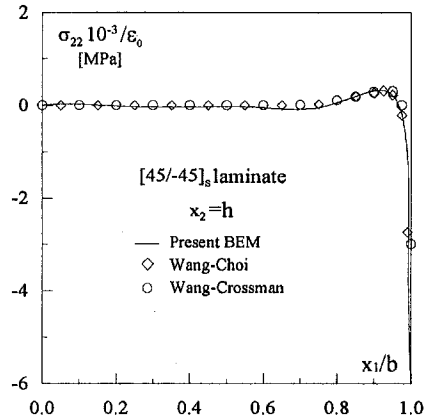


Fig. 3 The σ_{22} distribution for the $[45/-45]_s$ laminate

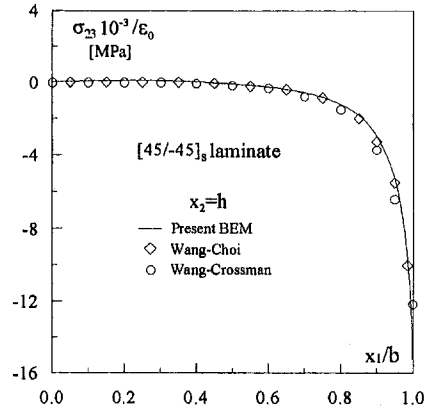


Fig. 4 The σ_{23} distribution for the $[45/-45]_s$ laminate

$$\nu_{LT} = \nu_{LS} = \nu_{TS} = 0.21 \tag{41}$$

where the subscripts L, T, and S refer to the along fiber, transverse, and thickness directions, respectively. Each individual ply has thickness h and width $16h$. By virtue of the problem symmetries only a quarter of the laminate cross section has been considered in the analysis (Pipes and Pagano, 1970) and the basic discretization shown in Fig. 2 was employed. The accuracy of the solution was tested comparing the present results for a $[45/-45]_s$ angle-ply laminate with the finite element solution of Wang and Crossman (1977) and the analytical solution of Wang and Choi (1982b). The results for the interlaminar stresses σ_{22} and σ_{23} at the interface $x_2 = h$ of the $[45/-45]_S$ laminate are shown in Figs. 3 and 4. The present results compare very well with the previous findings and evidence the good efficiency of the technique employed. The execution of the computer code for this typical application took only 29.8 seconds on a Pentium personal computer. The boundary element solution for the $[45/-45]_s$ laminate evidences steep gradients in the stress field which confirm the singular trend of the stresses near the free edge. This singular trend can be clearly evidenced by examining the through-thickness distributions of the boundary layer stresses. As an example the distributions of the most dominant interlaminar shear stress σ_{23} along the x_2 direction are shown in Fig. 5. These distributions well describe the singular behavior of the stress field near the free edge and are in good agreement with the solution of Wang and Choi (1982b) who expressly assume the singular term in their model. This singular

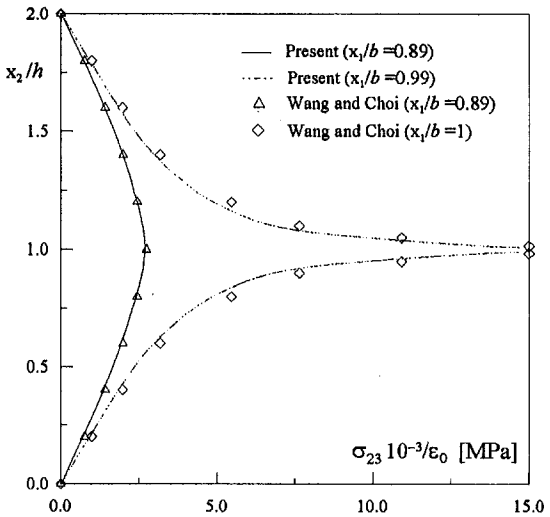


Fig. 5 Through-thickness distribution of σ_{23} for the $[45/-45]_s$ laminate

Downloaded 04 May 2010 to 171.66.16.34. Redistribution subject to ASME license or copyright; see http://www.asme.org/terms/Terms_Use.cfm

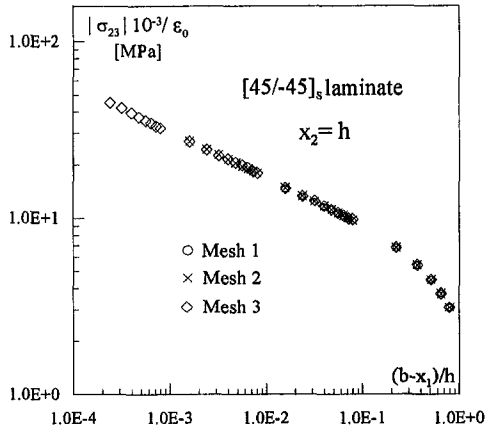


Fig. 6 Convergence analysis

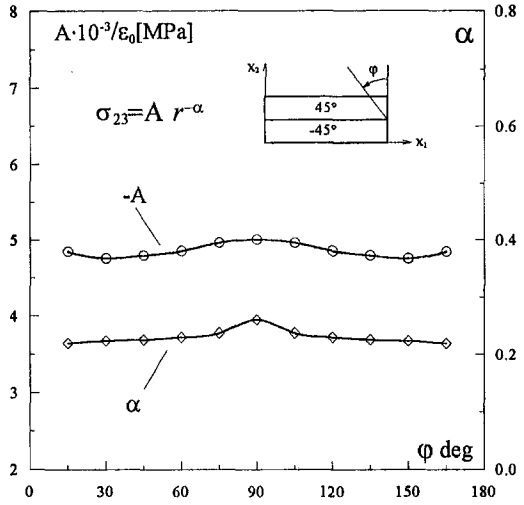


Fig. 7 Angular variation of singularity power and strength for the [45/−45]$_s$ laminate

behavior, already outlined by other researchers (Pipes and Pagano, 1970; Raju and Crews, 1981; Withcomb et al., 1982; Wang and Choi, 1982a; Zwiers et al., 1982; Wang and Yuan, 1983), is here investigated in some detail exploiting the well-established capability of the boundary element solutions to predict singular trends in the elastic response (Cruse 1995; Ioka et al., 1995). It is well known that in the proximity of a singularity point the stress field components can be approximated by

$$\sigma \cong Ar^{-\alpha} \tag{42}$$

or

$$\log \sigma \cong \log A - \alpha \log r \tag{43}$$

where α and A are the power and the strength of the singularity and r is the normalized distance from the singularity point. The stress singularity can be numerically assessed if the data obtained from the problem solution are well fitted by Eq. (42) or (43). This procedure was employed to ascertain the singularity parameters by the finite element method (Raju and Crews, 1981). The first step for the present singularity analysis was a convergence study in order to ensure a correct boundary element modelization for the cross section. This study was performed for the typical $[45/-45]_S$ configuration employing three different meshes. As the aim is to check for the singularity parameter convergence the three meshes were obtained starting from the basic discretization of Fig. 2 and subdividing the interface element contiguous to the free edge of subsequent mesh into ten elements. The results obtained for the three meshes are presented in the log-log diagram of Fig. 6 in terms of σ_{23} interlaminar stress. The choice of the σ_{23} stress in the singularity analysis is due to the requirement of treating with a predominant stress to obtain a good approximation via Eq. (43) and hence reliable predictions of the singular behavior at the free edge. For the three meshes the data relative to the free edge region are very well fitted by the Eq. (43) as proved by the absolute value of the correlation coefficient (given in Table 1) in the least-square procedure employed to determine the value of the singularity parameters α and A. The performed convergence study, given in Table 1, demonstrates that a useful singularity prediction can be obtained with the basic discretization of Fig. 2 whose results can be treated as converged values. On this basis, in order to check the accuracy of the procedure, the singularity power and strength were calculated along radial lines starting from the free edge of the $[45/-45]_S$ laminate. The results of this analysis are shown in Fig. 7 and, according to the finite element prediction (Raju and Crews, 1981), they suggest that the singularity characteristic values are accurate for $\varphi = 90$ deg, i.e., along the interface where the σ_{23} stress is more predominant than along the other directions. Two laminate families, namely the $[\theta/\theta - 90]_S$ and the $[\theta/-\theta]_S$, were analyzed and the results obtained are shown in Figs. 8 and 9, respectively. The singularity parameters for the two laminate families can be computed by applying the log-linear procedure to all the configurations considered. In Fig. 10 the singularity power and strength for the laminates belonging to the $[\theta/\theta - 90]_S$ family are plotted versus the θ parameter for 0 deg $\leq \theta \leq$ 90 deg. The same quantities are shown in Fig. 11 for the $[\theta/-\theta]_S$ laminates. For all the configurations considered the singularity power is the same whereas the singularity strength depends on the ply orientation. The $\theta = 15$ deg condition seems to be the hardest for both of the

Table 1 Convergence study results

Mesh	1	2	3
α	.2618	.2627	.2630
$\lvert A\rvert$	4.964	5.009	5.028
$\frac{\alpha_{i+1}-\alpha_i}{\alpha_i}100$		.34	.11
$\frac{\lvert A\rvert_{i+1}-\lvert A\rvert_i}{\lvert A\rvert_i}100$		.91	.38
Coeff. Corr.	.9989	.9991	.9996

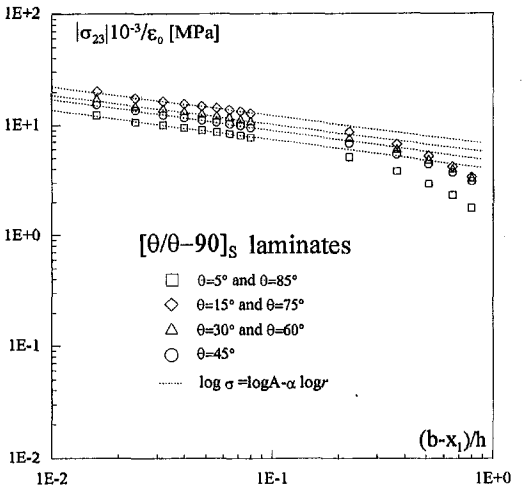


Fig. 8 Log-log plot and log-linear approximation for σ_{23} along interface ($x_2 = h$) for the $[\theta/\theta - 90]_s$ laminate family

Downloaded 04 May 2010 to 171.66.16.34. Redistribution subject to ASME license or copyright; see http://www.asme.org/terms/Terms_Use.cfm

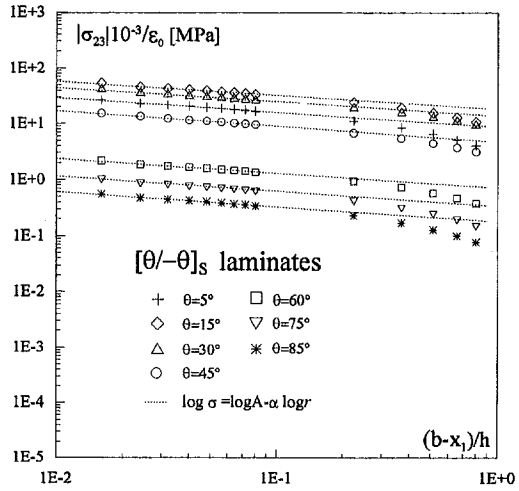


Fig. 9 Log-log plot and log-linear approximation for σ_{23} along interface ($x_2 = h$) for the $[\theta/-\theta]_s$ laminate family

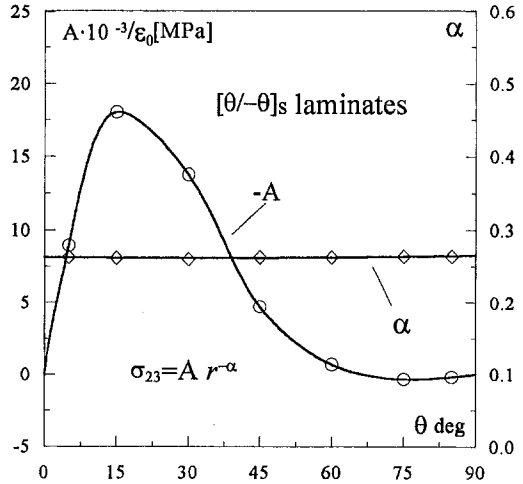


Fig. 11 Singularity power α and strength A for the $[\theta/-\theta]_s$ laminate family

investigated composite laminate families in agreement with the studies present in the literature (Raju and Crews, 1981; Herakovich et al., 1985).

6 Conclusions

An alternative integral equations based method was employed to determine the response of composite laminates under axial extension with particular emphasis on the interlaminar stress field. The stress equilibrium equations, strain compatibility, traction boundary conditions, and ply interface continuity conditions are all exactly satisfied in the formulation and the solution of the model by the boundary element method thus gives numerically consistent elastic solutions. The proposed method does not present aprioristic assumptions and, with respect to other numerical techniques, it has significant computational advantages which make it possible to perform systematic investigations about the behavior of general laminates. Accuracy and convergence studies have been accomplished in order to validate the ability of the method to predict the stress singular trend at the interlaminar free edge. In the present paper the singularity was investigated for several four-ply symmetric laminate layups, even if the method can be applied to more complex configurations with general stacking sequence. Two laminate families were considered and the singularity power and strength were calculated for both. The results obtained show that the two laminate families present the same singularity power value whereas the singularity strength depends on the laminate layup. The results obtained prove that the formulation proposed appears to give a solution for the laminate problem that characterizes the stress distribution near an interface corner accurately and efficiently, and they also show close agreement with the existing numerical solutions in the literature. Due to the reduction in dimension the present boundary element solution requires significantly reduced computational effort. The excellent solution accuracy and efficiency provides a solid basis for further developments of the present method. These will focus on the extension of the present results to more complex configurations with particular care devoted to the application in other loading modes.

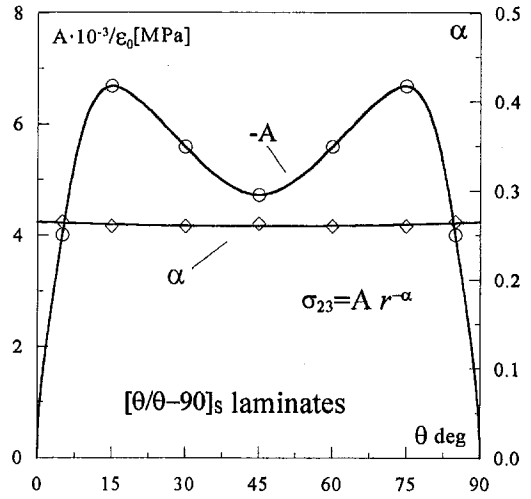


Fig. 10 Singularity power α and strength A for the $[\theta/\theta - 90]_s$ laminate family

References

Banerjee, P. K., and Butterfield, R., 1981, *Boundary Element Methods in Engineering Science,* McGraw-Hill, Maidenhead, U.K.

Bogy, D. B., 1968, "Edge-Bonded Dissimilar Orthogonal Elastic Wedges Under Normal and Shear Loading," ASME JOURNAL OF APPLIED MECHANICS, Vol. 35, pp. 460–466.

Chan, W. S., and Ochoa, O. O., 1990, "Delamination characterization of laminates under tension, bending and torsion loads," *Computational Mechanics,* Vol. 6, pp. 393–405.

Chen, D. J., Shah, D. K., and Chan, W. S., 1996, "Interfacial Stress Estimation Using Least-Square Extrapolation and Local Stress Smoothing in Laminated Composites," *Computers & Structures,* Vol. 58, pp. 765–774.

Cruse, T. A., 1974, "An Improved Boundary-Integral Equation Method for Three Dimensional Elastic Stress Analysis," *Computers & Structures,* Vol. 4, pp. 741–754.

Cruse, T. A., 1995, "BIE Fracture Mechanics Analysis. 25 Years of Developments," *Proceedings of the International Conference on Computational Engineering Science,* S. N. Atluri, G. Yagawa, and T. A. Cruse, eds., Springer-Verlag, New York, pp. 2848–2855.

Davì, G., 1989, "A general boundary integral formulation for the numerical solution of bending multilayer sandwich plates," *Proceedings of the 11th International Conference on Boundary Element Methods,* C. A. Brebbia and J. J. Connors, eds., Computational Mechanics Publications, Southampton, UK, Vol. 1, pp. 25–35.

Davì, G., 1991, "La trave multistrato in materiale composito sollecitata a sforzo normale," *Aerotecnica Missili e Spazio,* Vol. 70, pp. 13–18.

Davì, G., 1996, "Stress Fields in general composite laminates," *AIAA Journal,* Vol. 34, pp. 2604–2608

Davì, G., and Milazzo A., 1996, "Stress Fields in composite cross-ply laminates," *Proceedings of the 11th International Conference on Boundary Element Technology,* R. C. Ertekin, C. A. Brebbia, M. Tanaka, and R. Shaw, eds., Computational Mechanics Publications, Southampton, UK, pp. 175–185.

Giavotto, V., Borri, M., Mantegazza, P., Ghiringhelli, G. L., Caramaschi, V., Maffioli, G. C., and Mussi, F., 1983, "Anisotropic beam theory and applications," *Computers & Structures,* Vol. 16, pp. 403–413.

Herakovich, C. T., Post, D., Buczek, M. B., and Czarnek, R., 1985, "Free Edge Strain Concentrations in Real Composite Laminates: Experimental-Theoretical Correlation," ASME JOURNAL OF APPLIED MECHANICS, Vol. 52, pp. 787–793.

Downloaded 04 May 2010 to 171.66.16.34. Redistribution subject to ASME license or copyright; see http://www.asme.org/terms/Terms_Use.cfm

Hsu, P. W., and Herakovich, C. T., 1977, "Edge effect in angle-ply composite laminates," *Journal of Composite Materials,* Vol. 11, pp. 422–428.

Ioka, S., Kubo, S., and Ohji, K., 1995, "Free-edge stress singularity and its disappearance in bonded dissimilar materials," *Proceedings of the International Conference on Computational Engineering Science,* S. N. Atluri, G. Yagawa, and T. A. Cruse, eds., Springer-Verlag, New York, pp. 2389–2394.

Kassapoglou, C., and Lagace, P. A., 1986, "An Efficient Method for the Calculation of Interlaminar Stresses in Composite Materials," ASME JOURNAL OF APPLIED MECHANICS, Vol. 53, pp. 744–750.

Kayupov, M. A., and Kuriyagawa, M., 1996, "Stress and Displacement Discontinuiy Boundary Elements in an Anisotropic Medium," *Proceedings of the 11th International Conference on Boundary Element Technology,* R. C. Ertekin, C. A. Brebbia, M. Tanaka, and R. Shaw, eds., Computational Mechanics Publications, Southampton, UK, pp. 193–202.

Kuo, M. C., and Bogy, D. B., 1974a, "Plane Solution for the Displacement and Traction-Displacement Problems for Anisotropic Elastic Wedges," ASME JOURNAL OF APPLIED MECHANICS, Vol. 41, pp. 197–202.

Kuo, M. C., and Bogy, D. B., 1974b, "Plane Solution for Traction Problems on Orthotropic Unsymmetrical Wedges and Symmetrical Twinned Wedges," ASME JOURNAL OF APPLIED MECHANICS, Vol. 41, pp. 203–208.

Lekhnitskii, S. G., 1963, *Theory of Elasticity of an Anisotropic Body,* Holden-Day, San Francisco.

Lessard, L. B., Schmidt, A. S., and Shokrieh, M. M., 1996, "Three-Dimensional Stress Analysis of Free-Edge Effects in a Simple Composite Cross-Ply Laminate," *International Journal of Solids and Structures,* Vol. 33, pp. 2243–2259.

Lin, C. C., Hsu, C. Y., and Ko, C. C., 1995, "Interlaminar stresses in general laminates with straight free edges," *AIAA Journal,* Vol. 33, pp. 1471–1476.

Mantic, V., and Paris, F., 1995, "Explicit formulae of the integral kernels and C-matrix in the 2D Somigliana identity for orthotropic materials," *Engineering Analysis with Boundary Elements,* Vol. 15, pp. 283–288.

Pagano, N. J., 1978a, "Stress fields in composite laminates," *International Journal of Solids and Structures,* Vol. 14, pp. 385–400.

Pagano, N. J., 1978b, "Free edge stress fields in composite laminates," *International Journal of Solids and Structures,* Vol. 14, pp. 401–406.

Pipes, R. B., and Pagano, N. J., 1970, "Interlaminar stresses in composite laminates under uniform axial extension," *Journal of Composite Materials,* Vol. 4, pp. 538–548.

Pipes, R. B., and Pagano, N. J., 1974, "Interlaminar Stresses in Composite Laminates: An Approximate Elasticity Solution," ASME JOURNAL OF APPLIED MECHANICS, Vol. 41, pp. 668–672.

Raju, I. S., and Crews, J. H., Jr., 1981, "Interlaminar stress singularities at a straight free edge in composite laminate," *Computers & Structures,* Vol. 14, pp. 21–28.

Rizzo, F. J., 1967, "An Integral Equation Approach to Boundary Value Problem of Classical Elastostatics," *Quarterly Journal of Applied Mathematics,* Vol. 25, pp. 83–95.

Rybicki, E. F., 1971, "Approximate three-dimensional solutions for symmetric laminates under inplane loading," *Journal of Composite Materials,* Vol. 5, pp. 354–360.

Spilker, R. L., and Chou, S. C., 1980, "Edge effect in symmetric composite laminates: Importance of satisfying the traction free edge," *Journal of Composite Materials,* Vol. 14, pp. 2–19.

Tan, C. L., Gao, Y. L., and Afagh, F. F., 1992, "Boundary Element Analysis of Interface Cracks Between Dissimilar Anisotropic Materials," *International Journal of Solids and Structures,* Vol. 29, pp. 3201–3220.

Wang, A. S. D., and Crossman, F. W., 1977, "Some new results on edge effect in symmetric composite laminates," *Journal of Composite Materials,* Vol. 1, pp. 92–106.

Wang, J. T. S., and Dickson, J. N., 1978, "Interlaminar stresses in symmetric composite laminates," *Journal of Composite Materials,* Vol. 12, pp. 390–402.

Wang, S. S., and Choi, I., 1982a, "Boundary-Layer Effects in Composite Laminates: Part I—Free Edge Stress Singularities," ASME JOURNAL OF APPLIED MECHANICS, Vol. 49, pp. 541–548.

Wang, S. S., and Choi, I., 1982b, "Boundary Layer Effects in Composite Laminates: Part II—Free Edge Stress Solutions and Basic Characteristics," ASME JOURNAL OF APPLIED MECHANICS, Vol. 49, pp. 549–560.

Wang, S. S., and Yuan, F. G., 1983, "A Hybrid Finite Element Approach to Composite Laminate Elasticity Problems With Singularities," ASME JOURNAL OF APPLIED MECHANICS, Vol. 50, pp. 835–844.

Whitcomb, J. D., Raju, I. S., and Goree, J. G., 1982, "Reliability of the finite element method for calculating free edge stresses in composite laminates," *Computers & Structures,* Vol. 15, pp. 23–37.

Wideberg, J., and Benitez, F. G., 1995, "Elastic stress and displacement distribution in an orthotropic multilayered system due to a concentrated load," *Engineering Analysis with Boundary Elements,* Vol. 16, pp. 19–27.

Wilson, R. B., and Cruse, T. A., 1978, "Efficient Implementation of Anisotropic Three Dimensional Boundary-Integral Equation Stress Analysis," *International Journal of Numerical Methods in Engineering,* Vol. 12, pp. 1383–1397.

Wu, K. C., Chiu, Y. T., and Hwu, Z. H., 1992, "A New Boundary Integral Equation Formulation for Linear Elastic Solids," ASME JOURNAL OF APPLIED MECHANICS, Vol. 59, pp. 344–348.

Yin, W. L., 1994a, "Free Edge Effects in Anisotropic Laminates Under Extension, Bending, and Twisting: Part I—A Stress Function Based Variational Approach," ASME JOURNAL OF APPLIED MECHANICS, Vol. 61, pp. 410–415.

Yin, W. L., 1994b, "Free Edge Effects in Anisotropic Laminates Under Extension, Bending, and Twisting: Part II—Eigenfunction Analysis and the Results for Symmetric Laminates," ASME JOURNAL OF APPLIED MECHANICS, Vol. 61, pp. 416–421.

Zwiers, R. I., Ting, T. C. T., and Spilker, R. L., 1982, "On the Logarithmic Singularity of Free-Edge Stress in Laminated Composite Under Uniform Extension," ASME JOURNAL OF APPLIED MECHANICS, Vol. 49, 561–569.

Downloaded 04 May 2010 to 171.66.16.34. Redistribution subject to ASME license or copyright; see http://www.asme.org/terms/Terms_Use.cfm

Koiter-Based Solution for the Initial Post-buckling Behavior of Moderately Thick Orthotropic and Shear Deformable Cylindrical Shells Under External Pressure

G. A. Kardomateas
Professor,
School of Aerospace Engineering,
Georgia Institute of Technology,
Atlanta, GA 30332-0150

The initial post-buckling behavior of moderately thick orthotropic shear deformable cylindrical shells under external pressure is studied by means of Koiter's general post-buckling theory. To this extent, the objective is the calculation of imperfection sensitivity by relating to the initial post-buckling behavior of the perfect structure, since it is generally recognized that the presence of small geometrical imperfections in some structures can lead to significant reductions in their buckling strengths. A shear deformation theory, which accounts for transverse shear strains and rotations about the normal to the shell midsurface, is employed to formulate the shell equations. The initial post-buckling analysis indicates that for several combinations and geometric dimensions, the shell under external pressure will be sensitive to small geometrical imperfections and may buckle at loads well below the bifurcation predictions for the perfect shell. On the other hand, there are extensive ranges of geometrical dimensions for which the shell is insensitive to imperfections, and, therefore it would exhibit stable post-critical behavior and have a load-carrying capacity beyond the bifurcation point. The range of imperfection sensitivity depends strongly on the material anisotropy, and also on the shell thickness and whether the end pressure loading is included or not. For example, for the circumferentially reinforced graphite/epoxy example case studied, it was found that the structure is not sensitive to imperfections for values of the Batdorf length parameter $\tilde{z}$ above $\simeq 270$, whereas for the axially reinforced case the structure is imperfection-sensitive even at the high range of length values; for the isotropic case, the structure is not sensitive to imperfections above $\tilde{z} \simeq 1000$.

Introduction

Recent studies on the buckling of moderately thick orthotropic shells under external pressure have pointed to the importance of the effects of orthotropy and thickness in lowering the critical load and rendering classical shell theory estimates, in some cases quite non-conservative, in comparison to isotropic thin shell construction (e.g., Kardomateas, 1993; Kardomateas and Chung, 1994; Simitses et al., 1993). It is natural to consider next the extent to which these effects influence the imperfection sensitivity of the shell.

This can be achieved in an efficient manner by applying Koiter's (1945, 1963) general post-buckling theory, according to which, the slope of the secondary curve and the degradation of the critical loads with imperfections are described by means of the value and sign of the coefficient of the post-buckled state, b. A comprehensive survey by Hutchinson and Koiter (1970) provides a very useful bibliography, together with an overview of the achievements and goals of this theory. In addition to Koiter's original work, several papers have produced variations of the theory with a bias towards virtual work (Budiansky and Hutchinson, 1964; Budiansky, 1974).

The other approach to calculating the imperfection sensitivity is the formulation and solution of the full nonlinear imperfect shell problem. A solution methodology for the analysis of an isotropic, geometrically imperfect, thin, circular cylindrical shell loaded by uniform axial compression, based on the Galerkin procedure, was described by Sheinman and Simitses (1983).

Regarding applications of Koiter's theory to shells, several papers have been published, mostly based on isotropic classical thin shell formulations (e.g., Hutchinson, 1968). Hutchinson and Frauenthal (1969) studied the post-buckling and imperfection sensitivity of stringer reinforced cylindrical shells. Regarding external pressure loading, Budiansky and Amazigo (1968) studied an isotropic thin shell under hydrostatic pressure on the basis of the nonlinear Kármán-Donnell theory and found that these shells may be sensitive to imperfections in some instances and insensitive in others. Also, a much earlier post-buckling shell analysis was made by Koiter (1956) on the basis of his general formulation in terms of displacements.

The purpose of the present paper is to extend these earlier studies on the initial post-buckling behavior by including material orthotropy and basing the analysis on a shear deformation shell theory rather than a classical Donnell-based formulation. This is because the construction of the shell structure involves

Contributed by the Applied Mechanics Division of THE AMERICAN SOCIETY OF MECHANICAL ENGINEERS for publication in the ASME JOURNAL OF APPLIED MECHANICS.

Discussion on the paper should be addressed to the Technical Editor, Professor Lewis T. Wheeler, Department of Mechanical Engineering, University of Houston, Houston, TX 77204-4792, and will be accepted until four months after final publication of the paper itself in the ASME JOURNAL OF APPLIED MECHANICS.

Manuscript received by the ASME Applied Mechanics Division, Aug. 21, 1996; final revision, Mar. 22, 1997. Associate Technical Editor: S. Kryiakides.

Copyright © 1997 by ASME

Downloaded 04 May 2010 to 171.66.16.34. Redistribution subject to ASME license or copyright; see http://www.asme.org/terms/Terms_Use.cfm

advanced composite materials and moderate shell wall thickness where shear effects are more pronounced rendering classical shell theories inadequate. Besides the anisotropy, composite shells have most often one other important distinguishing feature, namely extensional-to-shear modulus ratio much larger than that of their metal counterparts.

In this regard, several improved shell theories have been formulated (e.g., Naghdi and Cooper, 1956; Mirsky and Herrmann, 1957; Dong and Tso, 1972; Whitney and Sun, 1974; Reddy and Liu, 1985). Most of these refined theories focused on their application to vibration problems and can be categorized into two basic groups: one with in-plane displacements approximated by linear variations in the thickness direction and the other by cubic polynomials. The first group requires the so-called shear correction factors as first suggested by Mindlin (1951) for homogeneous isotropic plates to account for the nonuniform distribution of transverse shear stresses and strains across the thickness. The second group, also called higher-order theories, uses higher-order approximations for shear stresses and strains and does not use shear correction factors but calls for a more involved analysis. The present paper is based on the simpler Timoshenko-Mindlin kinematic hypothesis with shear correction factors. Although the formulation reduces in general to the numerical solution of a standard two-point boundary value problem for ordinary differential equations, a simple closed-form solution can be derived by considering the limit of a very long cylindrical shell. It should also be mentioned that an orthotropic ring under external pressure does not exhibit imperfection sensitivity (Fu and Waas, 1995). It will be shown in this paper that an orthotropic shell under external pressure has wide ranges of length in which it is imperfection sensitive, and these ranges depend on the anisotropy of the material.

Basic Equations

Consider an orthotropic circular cylindrical shell of thickness h, mean radius R, and length l. The shell is referred to a coordinate system x, θ, and z, in which x and θ are in the axial and circumferential directions of the shell and z is in the direction of the outward normal to the middle surface. The corresponding displacements at the middle surface are designated by u, v, and w and the rotations of a normal to the middle surface in the θz and xz-planes respectively are denoted by ϕ and ψ. The nonlinear strain-displacement relations are

$$\epsilon_x = u_{,x} + \tfrac{1}{2}w_{,x}^2, \tag{1a}$$

$$\epsilon_\theta = \frac{v_{,\theta} + w}{R} + \frac{1}{2R^2}\, w_{,\theta}^2, \tag{1b}$$

$$\gamma_{x\theta} = v_{,x} + \frac{u_{,\theta}}{R} + \frac{1}{R}\, w_{,x}w_{,\theta}, \tag{1c}$$

$$\gamma_{\theta z} = \phi + \frac{w_{,\theta}}{R}; \quad \gamma_{xz} = \psi + w_{,x}, \tag{1d}$$

and the bending strains (or curvature) relationships are

$$\kappa_x = \psi_{,x}; \quad \kappa_\theta = \frac{\phi_{,\theta}}{R}; \quad \kappa_{x\theta} = \phi_{,x} + \frac{\psi_{,\theta}}{R}. \tag{1e}$$

Notice that based on the Timoshenko-Mindlin kinematic hypothesis, the displacement field $\bar{u}$, $\bar{v}$, $\bar{w}$ at an arbitrary point, is represented by

$$\bar{u}(x, \theta, z) = u(x, \theta) + z\psi(x, \theta), \tag{2a}$$

$$\bar{v}(x, \theta, z) = v(x, \theta) + z\phi(x, \theta), \tag{2b}$$

$$\bar{w}(x, \theta, z) = w(x, \theta). \tag{2c}$$

In these equations, a comma denotes differentiation with respect to the corresponding coordinate; ϵ_x, ϵ_θ, and $\gamma_{x\theta}$ are the inplane strains; $\gamma_{\theta z}$ and γ_{xz} are transverse shear strains. Notice that for the classical shell theory, $\psi = -w_{,x}$ and $\phi = -w_{,\theta}/R$, therefore $\gamma_{xz} = \gamma_{\theta z} = 0$.

One thing should be mentioned at this point. The shallow classical shell theory equations were chosen because of their simplicity and for the desire to stay with the simplest possible shell formulation for purposes of clarity of the presentation of the initial post-buckling behavior. Although the classical shallow shell theory has been shown to provide poor accuracy for low n (e.g., Brush and Almroth, 1975), this paper employs a shear deformable theory, and for this case it has been shown with a few examples (Kardomateas and Philobos, 1995) that the first-order shear deformation theory ($n = 2$) gives critical loads very close to the three-dimensional elasticity solution, although the classical shell theory would give, for these examples, critical loads noticably above the elasticity ones.

Asymptotic Expansions for the Post-buckling Behavior of the Perfect Shell. In the post-critical regime, the structure suffers deviations in the displacement profile from the buckling mode $\mathbf{V}_1 = \{u^{(1)}, v^{(1)}, w^{(1)}\}$, and simultaneously, p will deviate from p_c, the critical pressure. Define $\eta = p/p_c$. Then, the displacements of the structure in the initial post-buckling phase can be written as

$$\mathbf{V} = \eta\mathbf{V}_0 + \xi\mathbf{V}_1 + \xi^2\mathbf{V}_2 + \xi^3\mathbf{V}_3 + \xi^4\mathbf{V}_4 + \ldots \tag{3a}$$

where η depends on ξ. In this expansion $\mathbf{V}_0$ is associated with the prebuckling state, $\mathbf{V}_1$ describe a normalized buckling mode, and the remaining terms are orthogonal to the buckling mode. For example,

$$u = \eta u_0 + \xi u^{(1)} + \xi^2 u^{(2)} + \xi^3 u^{(3)} + \xi^4 u^{(4)} + \ldots. \tag{3b}$$

Also, similar expansions are assumed for the resultant forces and moments. For example,

$$N_x = \eta N_{x0} + \xi N_x^{(1)} + \xi^2 N_x^{(2)} + \xi^3 N_x^{(3)} + \xi^4 N_x^{(4)} + \ldots. \tag{3c}$$

Substituting into the nonlinear strain displacement Eqs. (1) give the strains in the form

$$\epsilon_{ij} = \eta\epsilon_{ij}^0 + \xi\epsilon_{ij}^{(1)} + \xi^2\epsilon_{ij}^{(2)} + \xi^3\epsilon_{ij}^{(3)} + \xi^4\epsilon_{ij}^{(4)} + \ldots. \tag{3d}$$

Second-Order Strains. In the following we shall use e_{ij} to denote the linear strains, for example $e_x = u_{,x}$.

Using the asymptotic expansion (3) and the nonlinear strain-displacement relations (1) gives the second-order strains in the abbreviated form:

$$\epsilon^{(2)} = e^{(2)} + L(\mathbf{V}_1). \tag{4a}$$

Specifically, the second-order normal strains are

$$\epsilon_x^{(2)} = u_{,x}^{(2)} + L_x(\mathbf{V}_1); \quad \epsilon_\theta^{(2)} = \frac{v_{,\theta}^{(2)} + w^{(2)}}{R} + L_\theta(\mathbf{V}_1), \tag{4b}$$

where

$$L_x(\mathbf{V}_1) = \frac{1}{2}\, w_{,x}^{(1)2}; \quad L_\theta(\mathbf{V}_1) = \frac{1}{2R^2}\, w_{,\theta}^{(1)2}. \tag{4c}$$

The second-order shear strains are

$$\gamma_{x\theta}^{(2)} = v_{,x}^{(2)} + \frac{u_{,\theta}^{(2)}}{R} + L_{x\theta}(\mathbf{V}_1), \tag{5a}$$

$$\gamma_{\theta z}^{(2)} = \phi^{(2)} + \frac{w_{,\theta}^{(2)}}{R}; \quad \gamma_{xz}^{(2)} = \psi^{(2)} + w_{,x}^{(2)}, \tag{5b}$$

Downloaded 04 May 2010 to 171.66.16.34. Redistribution subject to ASME license or copyright; see http://www.asme.org/terms/Terms_Use.cfm

where

$$L_{x\theta}(\mathbf{V}_1) = \frac{1}{R} w_{,x}^{(1)} w_{,\theta}^{(1)}; \quad L_{\theta z}(\mathbf{V}_1) = L_{xz}(\mathbf{V}_1) = 0. \quad (5c)$$

The third or fourth-order strains can be found in a similar fashion.

Stress Resultants. In the first-order shear deformation shell theory considered, the generalized stress σ consists of the five force resultants N_x, N_θ, $N_{x\theta}$, Q_{xz}, and $Q_{\theta z}$ and the three moment resultants M_x, M_θ, and $M_{x\theta}$. The generalized strain ϵ represents the five membrane strains ϵ_x, ϵ_θ, $\gamma_{x\theta}$, γ_{xz}, $\gamma_{\theta z}$ and the three bending strains κ_x, κ_θ, and $\kappa_{x\theta}$. The generalized displacement consists of the five midpoint linear and angular displacements u, v, w, ϕ, and ψ.

For orthotropy, the stress resultants are related to the strain components by

$$\sigma = \begin{bmatrix} N_x \\ N_\theta \\ Q_{\theta z} \\ Q_{xz} \\ N_{x\theta} \\ M_x \\ M_\theta \\ M_{x\theta} \end{bmatrix} = \begin{bmatrix} c_{11} & c_{12} & 0 & 0 & 0 & 0 & 0 & 0 \\ c_{12} & c_{22} & 0 & 0 & 0 & 0 & 0 & 0 \\ 0 & 0 & k_2^2 c_{44} & 0 & 0 & 0 & 0 & 0 \\ 0 & 0 & 0 & k_1^2 c_{55} & 0 & 0 & 0 & 0 \\ 0 & 0 & 0 & 0 & c_{66} & 0 & 0 & 0 \\ 0 & 0 & 0 & 0 & 0 & D_{11} & D_{12} & 0 \\ 0 & 0 & 0 & 0 & 0 & D_{12} & D_{22} & 0 \\ 0 & 0 & 0 & 0 & 0 & 0 & 0 & D_{66} \end{bmatrix} \times \begin{bmatrix} \epsilon_x \\ \epsilon_\theta \\ \gamma_{\theta z} \\ \gamma_{xz} \\ \gamma_{x\theta} \\ \kappa_x \\ \kappa_\theta \\ \kappa_{x\theta} \end{bmatrix} = C.\epsilon, \quad (6a)$$

where c_{ij} are the stiffness constants (we have used the notation $1 \equiv x$ (axial), $2 \equiv \theta$, $3 \equiv z$ (radial), $4 \equiv \theta z$, $5 \equiv xz$ and $6 \equiv x\theta$) and k_1^2, k_2^2 are the shear correction factors. These constants are expressed in terms of the moduli and Poisson's ratios of the material and the thickness h of the shell as follows:

$$c_{11} = \frac{hE_x}{1 - \nu_{x\theta}\nu_{\theta x}}; \quad c_{12} = \frac{h\nu_{x\theta}E_\theta}{1 - \nu_{x\theta}\nu_{\theta x}}; \quad c_{22} = \frac{hE_\theta}{1 - \nu_{x\theta}\nu_{\theta x}}, \quad (6b)$$

$$c_{66} = hG_{x\theta}; \quad c_{55} = hG_{xz}; \quad c_{44} = hG_{\theta z}; \quad D_{ij} = \frac{h^2}{12} c_{ij}. \quad (6c)$$

As far as the shear correction factors, results will be presented for the usual values of $k_1^2 = k_2^2 = \frac{5}{6}$. A discussion of various methods for determining these factors can be found in Dong and Nelson (1972) and Whitney (1973).

We shall use s_{ij} to denote the generalized stresses corresponding to the generalized linear strains, i.e., $s = C.e$. Using the asymptotic expansions for the strains gives the stresses as

$$\sigma_{ij} = \eta s_0 + \xi s_{ij}^{(1)} + \xi^2 \sigma_{ij}^{(2)} + \xi^3 \sigma_{ij}^{(3)} + \ldots. \quad (7a)$$

Notice that

$$\sigma_{ij}^0 = s_{ij}^0; \quad \sigma_{ij}^{(1)} = s_{ij}^{(1)}. \quad (7b)$$

For example, the second-order resultant force N_x is

$$N_x^{(2)} = c_{11} u_{,x}^{(2)} + c_{12} \frac{v_{,\theta}^{(2)} + w^{(2)}}{R} + c_{11} L_x(\mathbf{V}_1) + c_{12} L_\theta(\mathbf{V}_1), \quad (7c)$$

or, in abbreviated form,

$$\sigma^{(2)} = s^{(2)} + C.L(\mathbf{V}_1). \quad (7d)$$

The third-order generalized stresses can also be found in a similar fashion.

The relationship $\eta(\xi)$. In this subsection, we shall use the abbreviation $\frac{1}{2}\sigma\epsilon$ to denote the strain energy of the shell, which can be written in the form of an integral over the volume, V:

$$\frac{1}{2}\sigma\epsilon = \frac{1}{2}\int_0^l \int_0^{2\pi} (N_x\epsilon_x + N_\theta\epsilon_\theta + N_{x\theta}\gamma_{x\theta} + Q_{xz}\gamma_{xz} + Q_{\theta z}\gamma_{\theta z} + M_x\kappa_x + M_\theta\kappa_\theta + M_{x\theta}\kappa_{x\theta}) R d\theta dx. \quad (8a)$$

Also, we shall denote by Ω the work done by the uniform fluid pressure (which remains always normal to the surface as the shell deforms); this is the product of the pressure and the change in the volume enclosed by the shell. An expression in terms of the displacements can be found in Brush and Almroth (1975):

$$\Omega = p \int_0^l \int_0^{2\pi} \left[w + \frac{1}{2R} (v^2 - vw_{,\theta} + v_{,\theta} w + w^2) \right] R d\theta dx. \quad (8b)$$

A complete and extensive presentation of the $\eta(\xi)$ relationship is given in Budiansky (1974), in which use is made of Frechet derivatives. The formal definition given for Frechet derivatives of any order is entirely equivalent to the familiar process of "taking variations" in the calculus of variations. We shall use prime to denote Frechet derivatives and the subscript c means evaluation at the critical state.

If we set now

$$\eta = 1 + a\xi + b\xi^2, \quad (9a)$$

we can find the coefficients a, b for the case of linear stress-strain relations, quadratic strain-displacement relations, and quadratic shortening-displacement relations, as follows (Budiansky, 1974):

$$a = -\frac{3}{2} \frac{\sigma^{(1)}(\epsilon_c'' V_1^2)}{\sigma_c^0(\epsilon_c'' V_1^2) - (\Omega_c'' V_1^2)}, \quad (9b)$$

$$b = -\frac{2\sigma^{(1)}(\epsilon_c'' V_1 V_2) + \sigma^{(2)}(\epsilon_c'' V_1^2)}{\sigma_c^0(\epsilon_c'' V_1^2) - (\Omega_c'' V_1^2)}. \quad (9c)$$

Notice that the second term in the denominator is due to the hydrostatic loading and it would not exist in a dead-loading situation. Also, the variable V is identified as the set of functions u, v, w. The Frechet derivatives of the generalized strains are found to be

$$\epsilon_x'' V_1 V_2 = w_{,x}^{(1)} w_{,x}^{(2)}; \quad \epsilon_x'' V_1^2 = w_{,x}^{(1)2}, \quad (10a)$$

$$\epsilon_\theta'' V_1 V_2 = w_{,\theta}^{(1)} w_{,\theta}^{(2)}/R^2; \quad \epsilon_\theta'' V_1^2 = w_{,\theta}^{(1)2}, \quad (10b)$$

$$\gamma_{x\theta}'' V_1 V_2 = \frac{1}{R}(w_{,x}^{(1)} w_{,\theta}^{(2)} + w_{,x}^{(2)} w_{,\theta}^{(1)}); \quad \gamma_{x\theta}'' V_1^2 = 2w_{,x}^{(1)} w_{,\theta}^{(1)}/R. \quad (10c)$$

All the other components of the generalized strain result in zero Frechet second derivatives.

Downloaded 04 May 2010 to 171.66.16.34. Redistribution subject to ASME license or copyright; see http://www.asme.org/terms/Terms_Use.cfm

Also, the second Frechet derivative of the external work is

$$\Omega_c'' V_1^2 = p_c \iint (v^{(1)2} - v^{(1)} w_{,\theta}^{(1)} + v_{,\theta}^{(1)} w^{(1)} + w^{(1)2}) d\theta dx. \quad (10d)$$

It is also to be noted that the derivation of the relationship $\eta(\xi)$ makes use of the orthogonality conditions

$$s^{(2)} e^{(1)} = s^{(1)} e^{(2)} = s^0(\epsilon_c'' V_1 V_2) = 0. \quad (10e)$$

The First-Order Displacement Field

The governing equations of equilibrium and boundary conditions for the shear deformable orthotropic shell can be derived from the principle of virtual work, namely $\delta I = \delta\Omega$, by integrating by parts and setting the coefficients of δu, δv, δw, $\delta\phi$, and $\delta\psi$ to zero separately. Thus, one obtains

$$RN_{x,x} + N_{x\theta,\theta} = 0, \quad (11a)$$

$$RN_{x\theta,x} + N_{\theta,\theta} - p(v - w_{,\theta}) = 0, \quad (11b)$$

$$RM_{x,x} + M_{x\theta,\theta} - RQ_{xz} = 0, \quad (11c)$$

$$RM_{x\theta,x} + M_{\theta,\theta} - RQ_{\theta z} = 0, \quad (11d)$$

$$RQ_{xz,x} + Q_{\theta z,\theta} - N_\theta + R(N_x w_{,x})_{,x} + \frac{1}{R}(N_\theta w_{,\theta})_{,\theta} + (N_{x\theta} w_{,\theta})_{,x} + (N_{x\theta} w_{,x})_{,\theta} - p(v_{,\theta} + w) - pR = 0. \quad (11e)$$

Denoting prescribed quantities by *, the boundary conditions at $x = 0, l$ for the general case of a shell in which the end loading N_x^* or M_x^* may be nonzero, are

Either	Or
$u = u^*$	$N_x = N_x^*$
$v = v^*$	$N_{x\theta} = 0$
$w = w^*$	$N_x w_{,x} + N_{x\theta}\frac{w_{,\theta}}{R} + Q_{xz} = 0$
$\psi = \psi^*$	$M_x = M_x^*$
$\phi = \phi^*$	$M_{x\theta} = 0.$

We shall consider in the present paper a shell loaded by external pressure in a simply supported configuration and in which there are no prescribed end forces or moments. The boundary conditions in this case are simply

$$v = w = \phi = 0; \quad N_x = M_x = 0; \quad \text{at } x = 0, l. \quad (11f)$$

In the prebuckling state, the axially symmetric distribution of external forces produces stresses identical at all cross sections. For external pressure,

$$N_{\theta 0} = -pR; \quad N_{x0} = -\alpha pR/2; \quad N_{x\theta 0} = 0. \quad (12a)$$

The parameter α is used to conveniently allow for end pressure loading; if the pressure contributes to axial stress through end plates, $\alpha = 1$, whereas if the pressure only acts laterally, $\alpha = 0$. We shall also use the superscript c to refer to the critical state, i.e., $N_{\theta 0}^c = -p_c R$.

Substituting the asymptotic expansions (3) into the equilibrium Eqs. (11), retaining the first-order terms and then using the constitutive relations (6) to express the first-order resultant forces and moments in terms of the first-order displacements gives the following five partial differential equations for the displacements:

$$Rc_{11}u_{,xx}^{(1)} + \frac{c_{66}}{R}u_{,\theta\theta}^{(1)} + (c_{12} + c_{66})v_{,x\theta}^{(1)} + c_{12}w_{,x}^{(1)} = 0, \quad (13a)$$

$$(c_{12} + c_{66})u_{,x\theta}^{(1)} + Rc_{66}v_{,xx}^{(1)} + \frac{c_{22}}{R}v_{,\theta\theta}^{(1)} - p_c v^{(1)} + \left(\frac{c_{22}}{R} + p_c\right)w_{,\theta}^{(1)} = 0, \quad (13b)$$

$$RD_{11}\psi_{,xx}^{(1)} + D_{66}\frac{\psi_{,\theta\theta}^{(1)}}{R} + (D_{12} + D_{66})\phi_{,x\theta}^{(1)} - Rk_1^2 c_{55}(\psi^{(1)} + w_{,x}^{(1)}) = 0, \quad (13c)$$

$$RD_{66}\phi_{,xx}^{(1)} + D_{22}\frac{\phi_{,\theta\theta}^{(1)}}{R} + (D_{12} + D_{66})\psi_{,x\theta}^{(1)} - k_2^2 c_{44}(R\phi^{(1)} + w_{,\theta}^{(1)}) = 0, \quad (13d)$$

$$-c_{12}u_{,x}^{(1)} - \left(\frac{c_{22}}{R} + p_c\right)(v_{,\theta}^{(1)} + w^{(1)}) + R(N_{x0}^c + k_1^2 c_{55})w_{,xx}^{(1)} + (N_{\theta 0}^c + k_2^2 c_{44})\frac{w_{,\theta\theta}^{(1)}}{R} + Rk_1^2 c_{55}\psi_{,x}^{(1)} + k_2^2 c_{44}\phi_{,\theta}^{(1)} = 0, \quad (13e)$$

and the first-order boundary conditions are

$$v^{(1)} = w^{(1)} = \phi^{(1)} = 0 \quad \text{at} \quad x = 0, l. \quad (13f)$$

$$c_{11}u_{,x}^{(1)} + \frac{c_{12}}{R}(v_{,\theta}^{(1)} + w^{(1)}) = 0;$$

$$D_{11}\psi_{,x}^{(1)} + \frac{D_{12}}{R}\phi_{,\theta}^{(1)} = 0 \quad \text{at} \quad x = 0, l \quad (13g)$$

The first-order displacement field is set in the form

$$u^{(1)}(x, \theta) = U_1 \sin n\theta \cos \lambda x;$$

$$v^{(1)}(x, \theta) = V_1 \cos n\theta \sin \lambda x, \quad (14a)$$

$$w^{(1)}(x, \theta) = W_1 \sin n\theta \sin \lambda x, \quad (14b)$$

$$\psi^{(1)}(x, \theta) = \Psi_1 \sin n\theta \cos \lambda x;$$

$$\phi^{(1)}(x, \theta) = \Phi_1 \cos n\theta \sin \lambda x. \quad (14c)$$

By setting

$$\lambda = \frac{m\pi}{l}, \quad (14c)$$

the boundary conditions (13f,g) are satisfied. Then, substituting into the differential equations (13a–e) gives a system of five linear algebraic homogeneous equations as follows:

$$\left(Rc_{11}\lambda^2 + \frac{c_{66}}{R}n^2\right)U_1 + (c_{12} + c_{66})n\lambda V_1 - c_{12}\lambda W_1 = 0, \quad (15a)$$

$$(c_{12} + c_{66})n\lambda U_1 + \left(Rc_{66}\lambda^2 + \frac{c_{22}}{R}n^2 + p_c\right)V_1 - \left(\frac{c_{22}}{R} + p_c\right)nW_1 = 0, \quad (15b)$$

$$Rk_1^2 c_{55}\lambda W_1 + \left(RD_{11}\lambda^2 + \frac{D_{66}}{R}n^2 + Rk_1^2 c_{55}\right)\Psi_1 + (D_{12} + D_{66})n\lambda\Phi_1 = 0, \quad (15c)$$

Downloaded 04 May 2010 to 171.66.16.34. Redistribution subject to ASME license or copyright; see http://www.asme.org/terms/Terms_Use.cfm

$$k_2^2 c_{44} n W_1 + (D_{12} + D_{66}) n\lambda\Psi_1 + \left(RD_{66}\lambda^2 + \frac{D_{22}}{R} n^2 + Rk_2^2 c_{44}\right)\Phi_1 = 0, \quad (15d)$$

$$c_{12}\lambda U_1 + \left(\frac{c_{22}}{R} + p_c\right) n V_1 - \left[\frac{c_{22}}{R} + R(N_{x0}^c + k_1^2 c_{55})\lambda^2 + (N_{\theta 0}^c + k_2^2 c_{44})\frac{n^2}{R} + p_c\right] W_1 - Rk_1^2 c_{55}\lambda\Psi_1 - k_2^2 c_{44} n\Phi_1 = 0. \quad (15e)$$

Setting the five-by-five determinant to zero gives a quadratic equation; the minimum positive root is the critical pressure, p_c. The buckling modes, i.e., the constants U_1, V_1, W_1, Ψ_1, and Φ_1, are subsequently obtained by choosing the normalization $W_1 = h$, where h is the shell thickness.

Second-Order Displacements

Substituting the asymptotic expansions (3) into the equilibrium Eqs. (11), retaining the ξ^2 terms and using the anticipated result that $p = p_c + O(\xi^2)$, gives the second-order equilibrium equations as follows:

$$RN_{x,x}^{(2)} + N_{x\theta,\theta}^{(2)} = 0, \quad (16a)$$

$$RN_{x\theta,x}^{(2)} + N_{\theta,\theta}^{(2)} - p_c(v^{(2)} - w_{,\theta}^{(2)}) = 0, \quad (16b)$$

$$RM_{x,x}^{(2)} + M_{x\theta,\theta}^{(2)} - RQ_{xz}^{(2)} = 0, \quad (16c)$$

$$RM_{x\theta,x}^{(2)} + M_{\theta,\theta}^{(2)} - RQ_{\theta z}^{(2)} = 0, \quad (16d)$$

$$RQ_{xz,x}^{(2)} + Q_{\theta z,\theta}^{(2)} - N_\theta^{(2)} + R(N_{x0}^c w_{,x}^{(2)} + N_x^{(1)} w_{,x}^{(1)})_{,x} + \frac{1}{R}(N_{\theta 0}^c w_{,\theta}^{(2)} + N_\theta^{(1)} w_{,\theta}^{(1)})_{,\theta} + (N_{x\theta}^{(1)} w_{,x}^{(1)})_{,\theta} + (N_{x\theta}^{(1)} w_{,\theta}^{(1)})_{,x} - p_c(v_{,\theta}^{(2)} + w^{(2)}) = 0. \quad (16e)$$

Substituting the resultant force-displacement relations gives the following differential equations for the second-order displacement field:

$$Rc_{11}u_{,xx}^{(2)} + \frac{c_{66}}{R} u_{,\theta\theta}^{(2)} + (c_{12} + c_{66})v_{,x\theta}^{(2)} + c_{12}w_{,x}^{(2)} + Rc_{11}w_{,x}^{(1)} w_{,xx}^{(1)} + \frac{c_{66}}{R} w_{,x}^{(1)} w_{,\theta\theta}^{(1)} + \frac{c_{12} + c_{66}}{R} w_{,\theta}^{(1)} w_{,x\theta}^{(1)} = 0, \quad (17a)$$

$$(c_{12} + c_{66})u_{,x\theta}^{(2)} + Rc_{66}v_{,xx}^{(2)} + \frac{c_{22}}{R} v_{,\theta\theta}^{(2)} - p_c v^{(2)} + \left(\frac{c_{22}}{R} + p_c\right) w_{,\theta}^{(2)} + c_{66}w_{,\theta}^{(1)} w_{,xx}^{(1)} + (c_{12} + c_{66})w_{,x}^{(1)} w_{,x\theta}^{(1)} + \frac{c_{22}}{R^2} w_{,\theta}^{(1)} w_{,\theta\theta}^{(1)} = 0, \quad (17b)$$

$$RD_{11}\psi_{,xx}^{(2)} + D_{66}\frac{\psi_{,\theta\theta}^{(2)}}{R} + (D_{12} + D_{66})\phi_{,x\theta}^{(2)} - Rk_1^2 c_{55}(\psi^{(2)} + w_{,x}^{(2)}) = 0, \quad (17c)$$

$$RD_{66}\phi_{,xx}^{(2)} + D_{22}\frac{\phi_{,\theta\theta}^{(2)}}{R} + (D_{12} + D_{66})\psi_{,x\theta}^{(2)} - k_2^2 c_{44}(R\phi^{(2)} + w_{,\theta}^{(2)}) = 0, \quad (17d)$$

$$-Rc_{12}u_{,x}^{(2)} - (c_{22} + p_c R)(v_{,\theta}^{(2)} + w^{(2)}) + R^2(N_{x0}^c + k_1^2 c_{55})w_{,xx}^{(2)} + (N_{\theta 0}^c + k_2^2 c_{44})w_{,\theta\theta}^{(2)} + R^2 k_1^2 c_{55}\psi_{,x}^{(2)} + Rk_2^2 c_{44}\phi_{,\theta}^{(2)} - \frac{Rc_{12}}{2} w_{,x}^{(1)2} - \frac{c_{22}}{2R} w_{,\theta}^{(1)2} + [Rc_{11}u_{,x}^{(1)} + c_{12}(v_{,\theta}^{(1)} + w^{(1)})]Rw_{,xx}^{(1)} + [Rc_{11}u_{,xx}^{(1)} + c_{12}(v_{,x\theta}^{(1)} + w_{,x}^{(1)})]Rw_{,x}^{(1)} + \left[c_{12}u_{,x}^{(1)} + \frac{c_{22}}{R}(v_{,\theta}^{(1)} + w^{(1)})\right]w_{,\theta\theta}^{(1)} + \left[c_{12}u_{,x\theta}^{(1)} + \frac{c_{22}}{R}(v_{,\theta\theta}^{(1)} + w_{,\theta}^{(1)})\right]w_{,\theta}^{(1)} + c_{66}R\left[2\left(v_{,x}^{(1)} + \frac{u_{,\theta}^{(1)}}{R}\right)w_{,x\theta}^{(1)} + \left(v_{,x\theta}^{(1)} + \frac{u_{,\theta\theta}^{(1)}}{R}\right)w_{,x}^{(1)} + \left(v_{,xx}^{(1)} + \frac{u_{,x\theta}^{(1)}}{R}\right)w_{,\theta}^{(1)}\right] = 0. \quad (17e)$$

Furthermore, the second-order boundary conditions are

$$v^{(2)} = w^{(2)} = \phi^{(2)} = 0 \quad \text{at} \quad x = 0, l. \quad (17f)$$

$$N_x^{(2)} = c_{11}u_{,x}^{(2)} + \frac{c_{12}}{R}(v_{,\theta}^{(2)} + w^{(2)}) + \frac{c_{11}}{2} w_{,x}^{(1)2} + \frac{c_{12}}{2R^2} w_{,\theta}^{(1)2} = 0 \quad (17g)$$

$$M_x^{(2)} = D_{11}\psi_{,x}^{(2)} + \frac{D_{12}}{R}\phi_{,\theta}^{(2)} = 0 \quad \text{at} \quad x = 0, l \quad (17h)$$

The quadratic terms involving the first-order displacements on the right-hand sides of the equations give rise to nonhomogeneous terms which are either independent of the θ coordinate or vary as $\cos 2n\theta$ or $\sin 2n\theta$. Thus, the second-order displacement is sought in the separated form:

$$u^{(2)}(x, \theta) = U_{20}(x) + U_{22}(x)\cos 2n\theta;$$
$$v^{(2)}(x, \theta) = V_{20}(x) + V_{22}(x)\sin 2n\theta, \quad (18a)$$
$$w^{(2)}(x, \theta) = W_{20}(x) + W_{22}(x)\cos 2n\theta;$$

$$\psi^{(2)}(x, \theta) = \Psi_{20}(x) + \Psi_{22}(x)\cos 2n\theta, \quad (18b)$$

$$\Phi^{(2)}(x, \theta) = \Phi_{20}(x) + \Phi_{22}(x)\sin 2n\theta. \quad (18c)$$

Notice that this second-order displacement field satisfies the orthogonality requirements (15a,b), namely, $s^{(2)}e^{(1)} = s^0(\epsilon_c'' V_1 V_2) = 0$, since

$$\int_0^{2\pi} \cos n\theta d\theta = \int_0^{2\pi} \sin n\theta d\theta = \int_0^{2\pi} \cos n\theta \cos 2n\theta d\theta = \int_0^{2\pi} \sin n\theta \cos 2n\theta d\theta = 0.$$

Substituting (18) into (17) gives in terms of

$$b_1 = R^2\left[c_{11}U_1\lambda + \frac{c_{12}}{R}(V_1 n - W_1)\right]W_1\lambda^2 + \left[c_{12}U_1\lambda + \frac{c_{22}}{R}(V_1 n - W_1)\right]W_1 n^2, \quad (19a)$$

Downloaded 04 May 2010 to 171.66.16.34. Redistribution subject to ASME license or copyright; see http://www.asme.org/terms/Terms_Use.cfm

$$b_2 = -R^2\left[c_{11}U_1\lambda + \frac{c_{12}}{R}\left(V_1 n - \frac{W_1}{2}\right)\right]W_1\lambda^2 - c_{66}R\left(V_1\lambda + \frac{U_1 n}{R}\right)W_1\lambda n, \quad (19b)$$

$$b_3 = -\left[c_{12}U_1\lambda + \frac{c_{22}}{R}\left(V_1 n - \frac{W_1}{2}\right)\right]W_1 n^2 - c_{66}R\left(V_1\lambda + \frac{U_1 n}{R}\right)W_1\lambda n, \quad (19c)$$

$$b_4 = 2c_{66}R\left(V_1\lambda + \frac{U_1 n}{R}\right)W_1\lambda n, \quad (19d)$$

two sets of ordinary differential equations, one set for the functions in the θ-independent terms of (18) and another set for the functions in the θ-dependent terms.

The first set consists of the following five ordinary differential equations for $U_{20}(x)$, $V_{20}(x)$, $W_{20}(x)$, $\Psi_{20}(x)$, and $\Phi_{20}(x)$:

$$Rc_{11}U''_{20}(x) + c_{12}W'_{20}(x) + [(c_{12} + c_{66})n^2 - R^2c_{11}\lambda^2 - c_{66}n^2]\frac{W_1^2}{4R}\lambda \sin 2\lambda x = 0, \quad (20a)$$

$$Rc_{66}V''_{20}(x) - p_cV_{20}(x) = 0, \quad (20b)$$

$$D_{11}\Psi''_{20}(x) - k_1^2c_{55}[\Psi_{20}(x) + W'_{20}(x)] = 0, \quad (20c)$$

$$D_{66}\Phi''_{20}(x) - k_2^2c_{44}\Phi_{20}(x) = 0, \quad (20d)$$

$$R^2(k_1^2c_{55} + N^c_{x0})W''_{20}(x) - (c_{22} + p_cR)W_{20}(x) - Rc_{12}U'_{20}(x) + R^2k_1^2c_{55}\Psi'_{20}(x) + \tfrac{1}{2}[(b_1 + b_3)\sin^2\lambda x + (b_2 + b_4)\cos^2\lambda x] = 0. \quad (20e)$$

Also, the corresponding boundary conditions (17) give at the ends of the shell:

$$V_{20} = W_{20} = \Phi_{20} = 0; \quad \text{at} \quad x = 0, l, \quad (20f)$$

and

$$\Psi'_{20} = 0; \quad c_{11}U'_{20} = -c_{11}\lambda^2\frac{W_1^2}{4}; \quad \text{at} \quad x = 0, l. \quad (20g)$$

Likewise, the second set consists of the following five ordinary differential equations for $U_{22}(x)$, $V_{22}(x)$, $W_{22}(x)$, $\Psi_{22}(x)$, and $\Phi_{22}(x)$:

$$Rc_{11}U''_{22}(x) - \frac{c_{66}}{R}4n^2U_{22}(x) + (c_{12} + c_{66})2nV'_{22}(x) + c_{12}W'_{22}(x) + [(c_{12} + c_{66})n^2 + R^2c_{11}\lambda^2 + c_{66}n^2] \times \frac{W_1^2}{4R}\lambda \sin 2\lambda x = 0, \quad (21a)$$

$$Rc_{66}V''_{22}(x) - \left(\frac{c_{22}}{R}4n^2 + p_c\right)V_{22}(x) - (c_{12} + c_{66})2nU'_{22}(x) - \left(\frac{c_{22}}{R} + p_c\right)2nW_{22}(x) + \left[(c_{12} + c_{66})\lambda^2\cos^2\lambda x - c_{66}\lambda^2\sin^2\lambda x - \frac{c_{22}}{R^2}n^2\sin^2\lambda x\right]\frac{W_1^2}{2}n = 0, \quad (21b)$$

$$RD_{11}\Psi''_{22}(x) - \left(\frac{D_{66}}{R}4n^2 + Rk_1^2c_{55}\right)\Psi_{22}(x) + (D_{12} + D_{66})2n\Phi'_{22}(x) - Rk_1^2c_{55}W'_{22}(x) = 0, \quad (21c)$$

$$RD_{66}\Phi''_{22}(x) - \left(\frac{D_{22}}{R}4n^2 + Rk_2^2c_{44}\right)\Phi_{22}(x) - (D_{12} + D_{66})2n\Psi'_{22}(x) + k_2^4c_{44}2nW_{22}(x) = 0, \quad (21d)$$

$$R^2(k_1^2c_{55} + N^c_{x0})W''_{22}(x) - [(k_2^2c_{44} + N^c_{\theta 0})4n^2 + c_{22} + p_cR]W_{22}(x) - Rc_{12}U'_{22}(x) - (c_{22} + p_cR)2nV_{22}(x) + R^2k_1^2c_{55}\Psi'_{22}(x) + Rk_2^2c_{44}2n\Phi_{22}(x) + \tfrac{1}{2}[(b_3 - b_1)\sin^2\lambda x + (b_4 - b_2)\cos^2\lambda x] = 0. \quad (21e)$$

Also, the conditions at the ends are

$$V_{22} = W_{22} = \Phi_{22} = 0; \quad \text{at} \quad x = 0, l, \quad (21f)$$

and

$$\Psi'_{22} = 0; \quad c_{11}U'_{22} = c_{11}\lambda^2\frac{W_1^2}{4}; \quad \text{at} \quad x = 0, l. \quad (21g)$$

However, due to symmetry only half of the shell need be considered in the solution procedure. Indeed, the symmetry of the shell deformation imposes for $0 \le x \le l/2$:

$$U(l - x) = -U(x); \quad V(l - x) = V(x); \quad W(l - x) = W(x), \quad (22a)$$

$$\Psi(l - x) = -\Psi(x); \quad \Phi(l - x) = \Phi(x). \quad (22b)$$

Therefore, at the midpoint of the shell, i.e., at $x = l/2$, $u = v' = w' = \psi = \phi' = 0$ allows solving for half the shell length and replacing the conditions (20f,g) at $x = l$ with

$$U_{20} = V'_{20} = W'_{20} = \Psi_{20} = \Phi'_{20} = 0 \quad \text{at} \quad x = l/2 \quad (22c)$$

and also allows replacing the conditions (21f, g) at $x = l$, with

$$U_{22} = V'_{22} = W'_{22} = \Psi_{22} = \Phi'_{22} = 0 \quad \text{at} \quad x = l/2. \quad (22d)$$

Solution Details. The two-point boundary value problem for half of the shell is solved separately for the θ-independent and the θ-dependent functions by the relaxation method (Press et al, 1989), in which the five coupled ordinary differential equations are replaced by finite difference equations on a mesh of points that spans half the length of the shell. The method produces a matrix equation to be solved, but the matrix takes a special, "block diagonal" form, that allows it to be inverted far more efficiently both in time and storage than would be possible for a general matrix.

In the implementation of the method for the functions of the θ-independent term of (18), ten functions of x are defined as follows: $y_1 = V_{20}$, $y_2 = W_{20}$, $y_3 = \Psi'_{20}$, $y_4 = U'_{20}$, $y_5 = \Phi_{20}$, $y_6 = U_{20}$, $y_7 = V'_{20}$, $y_8 = W'_{20}$, $y_9 = \Psi_{20}$, and $y_{10} = \Phi'_{20}$. The ten first-order coupled ordinary differential equations for the ten y's are $y'_1 = y_7$, Eq. (20a), $y'_2 = y_8$, Eq. (20b), $y'_9 = y_3$, Eq. (20c), $y'_6 = y_4$, Eq. (20d), $y'_5 = y_{10}$, and Eq. (20e). The corresponding ten boundary conditions are Eqs. (20f,g) at $x = 0$ and (22c) at $x = l/2$.

It should be noted that in order to exploit the reduced storage allowed by operating on blocks, the functions should be defined in such order so as pivot elements can be found among the first five rows of the matrix. This means that the five boundary conditions at the first point must contain some dependence on the first five dependent variables y_1, y_2, y_3, y_4, and y_5. An

Downloaded 04 May 2010 to 171.66.16.34. Redistribution subject to ASME license or copyright; see http://www.asme.org/terms/Terms_Use.cfm

examination of the boundary conditions $(20f,g)$ shows that defining the y_i's as outlined would satisfy this requirement. Regarding other details of the method, an equally spaced mesh of 241 points was employed and the procedure turned out to be highly efficient with rapid convergence. As an initial guess for the iteration process, the closed-form solution for a very long cylinder (as outlined below) was used for the displacements. An investigation of the convergence showed that essentially the same results were produced with even three times as many mesh points.

In a similar fashion, the procedure involves solving a separate two-point boundary value problem for the U_{22}, V_{22}, etc., i.e., by defining $y_1 = V_{22}$, $y_2 = W_{22}$, $y_3 = \Psi'_{22}$, $y_4 = U'_{22}$, $y_5 = \Phi_{22}$, $y_6 = U_{22}$, $y_7 = V'_{22}$, $y_8 = W'_{22}$, $y_9 = \Psi_{22}$, and $y_{10} = \Phi'_{22}$ and using the differential equations $(21a-e)$ together with the boundary conditions $(21f,g)$ and $(22d)$.

Initial Post-buckling Variation of Pressure

Once the second-order displacement field is determined from the solution of the foregoing two-point boundary value problem, the post-buckling coefficient, b, can be determined from (9) and (10).

Notice first that the coefficient $a = 0$, as expected, since

$$\sigma^{(1)}(\epsilon_c'' V_1^2) = \int_0^{2\pi}\int_0^{l}\left(N_x^{(1)} w_{,x}^{(1)2} + N_\theta^{(1)}\frac{w_{,\theta}^{(1)2}}{R^2} + 2N_{x\theta}^{(1)}\frac{w_{,x}^{(1)} w_{,\theta}^{(1)}}{R}\right)dxd\theta. \quad (23a)$$

Substituting the first-order resultant forces and moments in terms of the first-order displacement field by using $(6a)$ and integrating with respect to θ involves the integrals

$$\int_0^{2\pi}\cos n\theta \sin^2 n\theta d\theta = \int_0^{2\pi}\cos^3 n\theta d\theta = \int_0^{2\pi}\sin n\theta \sin 2n\theta d\theta = 0. \quad (23b)$$

Therefore,

$$\sigma^{(1)}(\epsilon_c'' V_1^2) = 0. \quad (23c)$$

This verifies that the initial variation of pressure after buckling is

$$\eta = p/p_c = 1 + b(\delta/h)^2, \quad (24)$$

where, since the buckling modes were normalized so that W_1 is equal to the shell thickness, h, the general perturbation variable ξ has been replaced by δ/h, the maximum amplitude of the buckling mode over the shell thickness.

Returning to the post-buckling coefficient, b, the denominator term in $(9c)$ is

$$\sigma_c^0(\epsilon_c'' V_1^2) = -\int_0^{2\pi}\int_0^{l}\left(N_{x0}^c w_{,x}^{(1)2} + N_{\theta 0}^c\frac{w_{,\theta}^{(1)2}}{R^2} + 2N_{x\theta 0}^c\frac{w_{,x}^{(1)} w_{,\theta}^{(1)}}{R}\right)dxd\theta. \quad (25a)$$

Substituting the first-order displacement field (14) and integrating with respect to θ gives

$$\sigma_c^0(\epsilon_c'' V_1^2) = -\left(N_{x0}^c\lambda^2 + N_{\theta 0}^c\frac{n^2}{R^2}\right)W_1^2\frac{\pi L}{2}dx. \quad (25b)$$

The first term in the numerator in $(9c)$ becomes

$$\sigma^{(1)}(\epsilon_c'' V_1 V_2) = \int_0^{2\pi}\int_0^{l}\left[N_x^{(1)} w_{,x}^{(1)} w_{,x}^{(2)} + N_\theta^{(1)}\frac{w_{,\theta}^{(1)} w_{,\theta}^{(2)}}{R^2} + \frac{N_{x\theta}^{(1)}}{R}(w_{,x}^{(1)} w_{,\theta}^{(2)} + w_{,x}^{(2)} w_{,\theta}^{(1)})\right]dxd\theta. \quad (26a)$$

Substituting the first-order resultant forces in terms of the first-order displacement fields by use of $(6a)$ and (1) and integrating with respect to θ gives

$$\sigma^{(1)}(\epsilon_c'' V_1 V_2) = \int_0^{l}\left[f_1(x)\frac{\sin 2\lambda x}{2} - W_{22}(x)n(b_2 n\sin^2\lambda x + b_3\lambda\cos^2\lambda x)\right]W_1\pi dx, \quad (26b)$$

where

$$f_1(x) = W'_{20}(x)(b_1\lambda + b_3 n) + W'_{22}(x)\frac{b_3 n - b_1\lambda}{2}. \quad (26c)$$

Finally, the second term in the numerator in $(9c)$ is

$$\sigma^{(2)}(\epsilon_c'' V_1^2) = \int_0^{2\pi}\int_0^{l}\left(N_x^{(2)} w_{,x}^{(1)2} + N_\theta^{(2)}\frac{w_{,\theta}^{(1)2}}{R^2} + 2N_{x\theta}^{(2)}\frac{w_{,x}^{(1)} w_{,\theta}^{(1)}}{R}\right)dxd\theta. \quad (27a)$$

Substituting the first and second-order resultant forces and moments in terms of the first and second-order displacement fields by using $(6a)$ and (4) and integrating with respect to θ gives

$$\sigma^{(2)}(\epsilon_c'' V_1^2) = \int_0^{l}\left[f_2(x)\lambda^2\cos^2\lambda x + f_3(x)\frac{n^2}{R^2}\sin^2\lambda x + f_4(x)\frac{n\lambda}{R}\sin 2\lambda x\right]\pi\frac{W_1^2}{2}dx, \quad (27b)$$

where

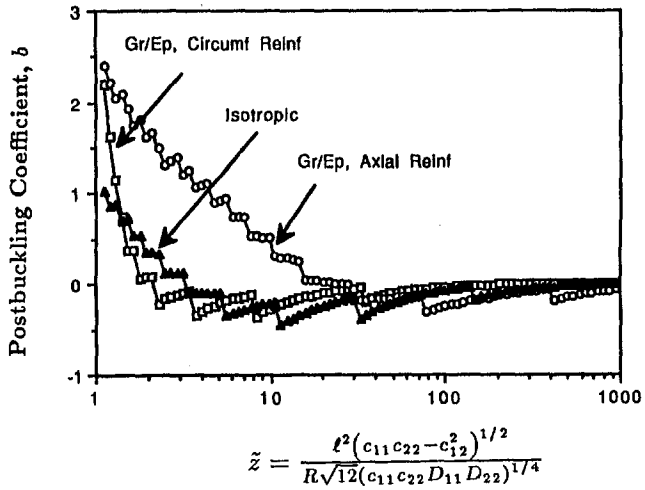
$$f_2(x) = c_{11}[2U'_{20}(x) - U'_{22}(x)] + \frac{c_{12}}{R}[2W_{20}(x) - 2nV_{22}(x) - W_{22}(x)] + \frac{c_{11}}{4}W_1^2\lambda^2\cos^2\lambda x + \frac{c_{12}}{4R^2}W_1^2 n^2\sin^2\lambda x, \quad (27c)$$

$$f_3(x) = c_{12}[2U'_{20}(x) - U'_{22}(x)] + \frac{c_{22}}{R}[2W_{20}(x) - 2nV_{22}(x) - W_{22}(x)] + \frac{c_{12}}{4}W_1^2\lambda^2\cos^2\lambda x + \frac{c_{22}}{4R^2}W_1^2 n^2\sin^2\lambda x, \quad (27d)$$

and

$$f_4(x) = c_{66}\left[V'_{22}(x) - U_{22}(x)\frac{2n}{R}\right] + \frac{c_{66}}{4R}W_1^2 n\lambda\sin 2\lambda x. \quad (27e)$$

Downloaded 04 May 2010 to 171.66.16.34. Redistribution subject to ASME license or copyright; see http://www.asme.org/terms/Terms_Use.cfm



$$\tilde{z} = \frac{\ell^2\left(c_{11}c_{22}-c_{12}^2\right)^{1/2}}{R\sqrt{12}(c_{11}c_{22}D_{11}D_{22})^{1/4}}$$

Fig. 1 Post-buckling coefficient, b, calculated from the shear deformable theory, for the cases of circumferentially reinforced, axially reinforced graphite/epoxy, and isotropic material, in a shell under lateral external pressure only

One additional term is from the effect of the external pressure

$$\Omega'' V_1^2 = p\int_0^{2\pi}\int_0^{l}(v^{(1)2} - v^{(1)}w_{,\theta}^{(1)} + v_{,\theta}^{(1)}w^{(1)} + w^{(1)2})\,d\theta dx. \tag{27e}$$

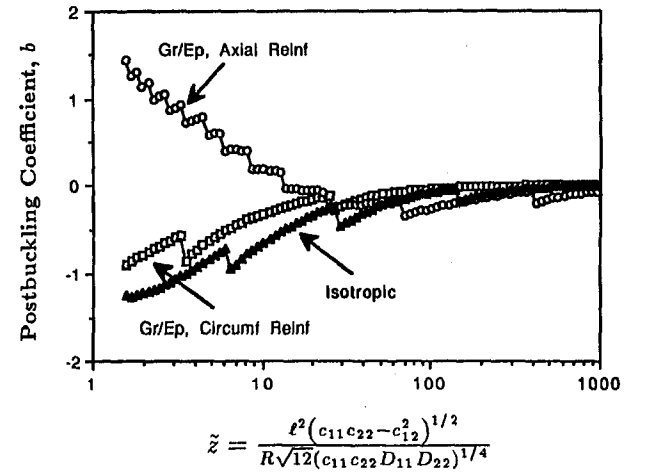
Substituting the first-order displacement field and integrating gives

$$\Omega'' V_1^2 = p(V_1^2 - 2V_1W_1n + W_1^2)\frac{\pi L}{2}. \tag{27e}$$

A standard method of numerical integration is used to calculate the post-buckling coefficient b from these expressions. The character of the post-buckling behavior in the initial stages after buckling hinges on the sign and magnitude of b. If b is positive, the applied load (external pressure) increases to values above the critical load p_c with increasing buckling deflection. However, if b turns out to be negative, then the equilibrium load falls with increasing buckling deflection and the post-buckling behavior is unstable.

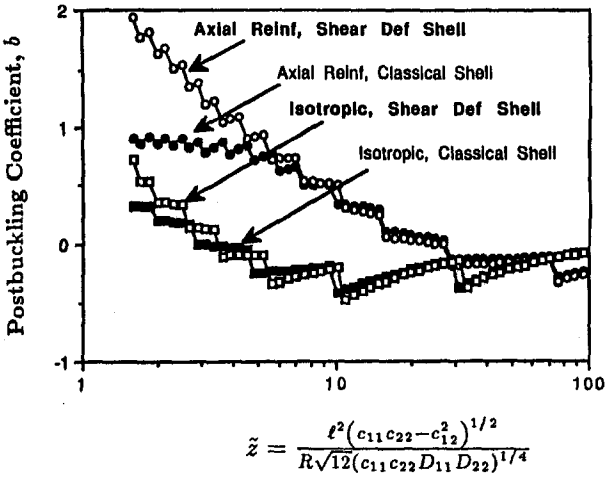
Results and Discussion

Let us consider a shell being made of unidirectional graphite/epoxy with the following typical properties for the material (1 is along the fibers, 2 is the in-plane transverse, and 3 is the out-of-plane transverse direction): moduli in GN/m^2 $E_1 = 140.0$, $E_2 = 9.1$, $G_{12} = G_{23} = G_{31} = 4.3$, and Poisson's ratio $\nu_{12} = 0.300$. The shear correction factors are assumed to be $k_1^2 = k_2^2 = \frac{5}{6}$. The shell has a mean radius of $R = 1$ m. Two cases of shell thickness are considered in the following, one corresponding to radii ratio $R_2/R_1 = 1.05$ and another thicker construction with $R_2/R_1 = 1.10$. Also, two cases of loading are considered: lateral only external pressure loading, i.e., no axial load and $\alpha = 0$ in (12a), and external pressure with hydrostatic end loading, i.e., with axial compressive loads determined from (12a) with $\alpha = 1$.



$$\tilde{z} = \frac{\ell^2\left(c_{11}c_{22}-c_{12}^2\right)^{1/2}}{R\sqrt{12}(c_{11}c_{22}D_{11}D_{22})^{1/4}}$$

Fig. 2 Post-buckling coefficient, b, from the shear deformable shell theory for the case of hydrostatic end loading



$$\tilde{z} = \frac{\ell^2\left(c_{11}c_{22}-c_{12}^2\right)^{1/2}}{R\sqrt{12}(c_{11}c_{22}D_{11}D_{22})^{1/4}}$$

Fig. 3 The effect of transverse shear on the postbuckling coefficient, b, for lateral external pressure loading

The Batdorf parameter has been used as a convenient nondimensional parameter to present results for shell buckling and post-buckling. For isotropic cylindrical shells, this is only a function of the geometry and is defined as $\tilde{z} = l^2/Rh$ where l is the length, R is the mean radius, and h the thickness of the shell. Analogues for anisotropy have been derived by Nemeth (1994) by performing a nondimensionalization of the shell buckling equations and it was shown that, for anisotropic shells, the Batdorf parameter depends not only on the geometry but

Table 1 Effect of the anisotropy Post-buckling coefficient, b

Lateral External Pressure Only, $R = 1$m, $R_2/R_1 = 1.10$, $k_1^2 = k_2^2 = 5/6$

$\tilde{z}$*	b Circumf† Reinf	b Axial‡ Reinf	b Isotropic**
2	0.0847	1.6421	0.3483
5	−0.2170	0.9241	−0.0949
10	−0.2681	0.5118	−0.2075
23	−0.0839	0.0152	−0.2052
53	−0.0934	−0.1460	−0.1940
120	−0.0232	−0.2119	−0.0474
271	0.0001	−0.0916	−0.0618
615	0.0064	−0.1102	−0.0101
1,395	0.0078	−0.0339	0.0043
3,162	0.0081	−0.0036	0.0075

* Batdorf Parameter for orthotropy, $\tilde{z} = l^2(c_{11}c_{22} - c_{12}^2)^{1/2}/[R\sqrt{12}(c_{11}c_{22}D_{11}D_{22})^{1/4}]$.
† Gr/Ep, Circumferential Reinforcement, moduli in GN/m^2: $E_x = 9.1$, $E_\theta = 140.0$, $G_{x\theta} = G_{\theta z} = G_{xz} = 4.3$, and Poisson's ratio $\nu_{x\theta} = 0.020$.
‡ Gr/Ep, Axial Reinforcement, moduli in GN/m^2: $E_x = 140.0$, $E_\theta = 9.1$, $G_{x\theta} = G_{\theta z} = G_{xz} = 4.3$, and Poisson's ratio $\nu_{x\theta} = 0.300$.
** For Isotropic, $E = 140.0$ GN/m^2, and $\nu = 0.300$.

Downloaded 04 May 2010 to 171.66.16.34. Redistribution subject to ASME license or copyright; see http://www.asme.org/terms/Terms_Use.cfm

Table 2 Effect of hydrostatic end loading post-buckling coefficient, b

$R = 1\text{m}$, $R_2/R_1 = 1.10$, $k_1^2 = k_2^2 = 5/6$

$\tilde{z}$*	b	b	b	b
	Circumf Reinf†		Axial reinf‡	
	Lateral only	w/End pressure	Lateral only	w/End pressure
2	0.0847	−0.7760	1.6421	1.1391
5	−0.2170	−0.6034	0.9241	0.5963
10	−0.2681	−0.3189	0.5118	0.1941
23	−0.0839	−0.1283	0.0152	−0.0664
53	−0.0934	−0.0975	−0.1460	−0.1767
120	−0.0232	−0.0286	−0.2119	−0.2207
271	0.0001	−0.0035	−0.0916	−0.0968
615	0.0064	0.0039	−0.1102	−0.1111
1,395	0.0078	0.0059	−0.0339	−0.0353
3,162	0.0081	0.0006	−0.0036	−0.0050

* Batdorf Parameter for orthotropy, $\tilde{z} = l^2(c_{11}c_{22} - c_{12}^2)^{1/2}/[R\sqrt{12}(c_{11}c_{22}D_{11}D_{22})^{1/4}]$.
† Gr/Ep, Circumferential Reinforcement, moduli in GN/m²: $E_x = 9.1$, $E_\theta = 140.0$, $G_{x\theta} = G_{\theta z} = G_{xz} = 4.3$, and Poisson's ratio $\nu_{x\theta} = 0.020$.
‡ Gr/Ep, Axial Reinforcement, moduli in GN/m²: $E_x = 140.0$, $E_\theta = 9.1$, $G_{x\theta} = G_{\theta z} = G_{xz} = 4.3$, and Poisson's ratio $\nu_{x\theta} = 0.300$.

also on the stiffness constants. In particular, for an orthotropic cylindrical shell, the Batdorf parameter becomes

$$\tilde{z} = \frac{l^2(c_{11}c_{22} - c_{12}^2)^{1/2}}{R\sqrt{12}(c_{11}c_{22}D_{11}D_{22})^{1/4}}, \tag{28}$$

where c_{ij} and D_{ij} are defined in (6b, c).

The post-buckling coefficient b is calculated following the solution of the two-point boundary value problem for the second-order displacements, as has already been outlined. If b is negative, the shell is imperfection-sensitive and the load carrying capacity diminishes following buckling. Also, the degree of imperfection-sensitivity is governed by the magnitude of b. If, on the other hand, b is positive, the structure retains some ability to support increased loads once bifurcation has taken place.

In all cases considered the structure buckles at $m = 1$, whereas n depends on the shell length, l, becoming equal to 2 for very long shells. The transition from one value of n to the next lower causes an abrupt change in b which explains the lack of smoothness of the b versus l curves in Figs. 1, 2, and 3. Budiansky and Amazigo (1968), in their isotropic classical shell solution, defined $\zeta = n^2l^2/\pi^2R^2$ and found the critical load by making the simplifying assumption that ζ may vary continuously and executing a formal minimization of the pressure function of ζ; this led to smooth b versus l curves.

Table 1 and Fig. 1 give b, calculated from the shear deformable theory, for the cases of circumferentially reinforced, axially reinforced graphite/epoxy, and isotropic material in a shell under lateral external pressure only, and for radii ratio, $R_2/R_1 = 1.10$. The main conclusion is that the regions of imperfection sensitivity are strongly dependent on the anisotropy of the material. For the circumferentially reinforced case, it can be concluded that the critical pressure (at the bifurcation point) ought to be reliable above $\tilde{z} \simeq 270$, whereas for the axially reinforced case the structure is imperfection-

Table 3 Effect of the transverse shear post-buckling coefficient, b

Graphite/Epoxy, Circumferential Reinforcement, moduli GN/m²: $E_x = 9.1$, $E_\theta = 140.0$, $G_{x\theta} = G_{\theta z} = G_{xz} = 4.3$, and Poisson's ratio $\nu_{x\theta} = 0.020$
Lateral External Pressure Only, $R = 1\text{m}$, $R_2/R_1 = 1.10$, $k_1^2 = k_2^2 = 5/6$

$\tilde{z}$*	b	b
	Shear Def Shell	Classical Shell
8	0.874	−0.3852	−0.1918
10	0.977	−0.2681	−0.1598
16	1.236	−0.1418	−0.0990
23	1.482	−0.0839	−0.0604
53	2.250	−0.0934	−0.0748
120	3.386	−0.0232	−0.0196
222	4.605	−0.0033	−0.0020
271	5.088	0.0001	0.0010
615	7.664	0.0064	0.0067
1,395	11.543	0.0078	0.0080
3,162	17.379	0.0081	0.0082

* Batdorf Parameter for orthotropy, $\tilde{z} = l^2(c_{11}c_{22} - c_{12}^2)^{1/2}/[R\sqrt{12}(c_{11}c_{22}D_{11}D_{22})^{1/4}]$.

Table 4 Effect of thickness post-buckling coefficient, b

Lateral External Pressure Only, $R = 1\text{m}$, $k_1^2 = k_2^2 = 5/6$

l/R	b (n)	b (n)	b (n)	b (n)
	Circumf Reinf†		Axial Reinf‡	
	$R_2/R_1 = 1.05$	$R_2/R_1 = 1.10$	$R_2/R_1 = 1.05$	$R_2/R_1 = 1.10$
0.4	−0.1680 (6)	0.3775 (7)	0.9958 (15*)	1.7581 (15*)
0.5	−0.2319 (5*)	−0.1457 (5*)	0.7619 (12*)	1.3482 (12*)
0.7	−0.2347 (4*)	−0.2095 (4*)	0.3978 (9*)	0.9284 (9*)
1.0	−0.1011 (4)	−0.2511 (3)	0.0358 (7)	0.3097 (6)
2.0	−0.0328 (3)	−0.1373 (2)	−0.1616 (5)	−0.1627 (4)
4.0	−0.0133 (2*)	−0.0102 (2*)	−0.0833 (4)	−0.1570 (3)
5.0	−0.0054 (2*)	−0.0004 (2*)	−0.1045 (3*)	−0.0958 (3*)
6.0	−0.0019 (2*)	0.0037 (2*)	−0.0662 (3*)	−0.0566 (3*)
8.0	0.0007 (2*)	0.0067 (2*)	−0.0284 (3)	−0.0985 (2)
10.0	0.0015 (2*)	0.0075 (2*)	−0.0121 (3)	−0.0535 (2)

* Denotes buckling at the same same (n, m) for both R_2/R_1 ratios of 1.05 and 1.10.
† Gr/Ep, Circumferential Reinforcement, moduli in GN/m²: $E_x = 9.1$, $E_\theta = 140.0$, $G_{x\theta} = G_{\theta z} = G_{xz} = 4.3$, and Poisson's ratio $\nu_{x\theta} = 0.020$.
‡ Gr/Ep, Axial Reinforcement, moduli in GN/m²: $E_x = 140.0$, $E_\theta = 9.1$, $G_{x\theta} = G_{\theta z} = G_{xz} = 4.3$, and Poisson's ratio $\nu_{x\theta} = 0.300$.

Table 5 Range of imperfection sensitivity (negative b)*

$R = 1\text{m}$, $k_1^2 = k_2^2 = 5/6$

	Lateral External Pressure Only			
	$R_2/R_1 = 1.10$		$RT_2/R_1 = 1.05$	
	$\tilde{z}$	(l/R)	$\tilde{z}$	(l/R)
Circumf Reinf†	2.3–269.6	(0.47–5.07)	1.7–1,045	(0.29–7.15)
Axial Reinf‡	>27.0	(>1.6)	>25.0	(>1.1)
Isotropic**	3.4–952.3	(0.58–9.75)	>3.8	(>0.44)
	w/Hydrostatic End Loading			
	$R_2/R_1 = 1.10$		$R_2/R_1 = 1.051$	
	$\tilde{z}$	(l/R)	$\tilde{z}$	(l/R)
Circumf Reinf†	<353.5	(<5.81)	<1,866	(<9.55)
Axial Reinf‡	>13.1	(>1.12)	>14.1	(>0.83)
Isotropic**	<1,081	(<10.39)	All values	(All values)

* For values of $\tilde{z} = l^2(c_{11}c_{22} - c_{12}^2)^{1/2}/[R\sqrt{12}(c_{11}c_{22}D_{11}D_{22})^{1/4}]$, examined from 1.0 to 3000.
† Gr/Ep, Circumferential Reinforcement, moduli in GN/m²: $E_x = 9.1$, $E_\theta = 140.0$, $G_{x\theta} = G_{\theta z} = G_{xz} = 4.3$, and Poisson's ratio $\nu_{x\theta} = 0.020$.
‡ Gr/Ep, Axial Reinforcement, moduli in GN/m²: $E_x = 140.0$, $E_\theta = 9.1$, $G_{x\theta} = G_{\theta z} = G_{xz} = 4.3$, and Poisson's ratio $\nu_{x\theta} = 0.300$.
** For Isotropic, modulus $E = 140.0$ GN/m², and Poisson's ratio $\nu = 0.300$.

Downloaded 04 May 2010 to 171.66.16.34. Redistribution subject to ASME license or copyright; see http://www.asme.org/terms/Terms_Use.cfm

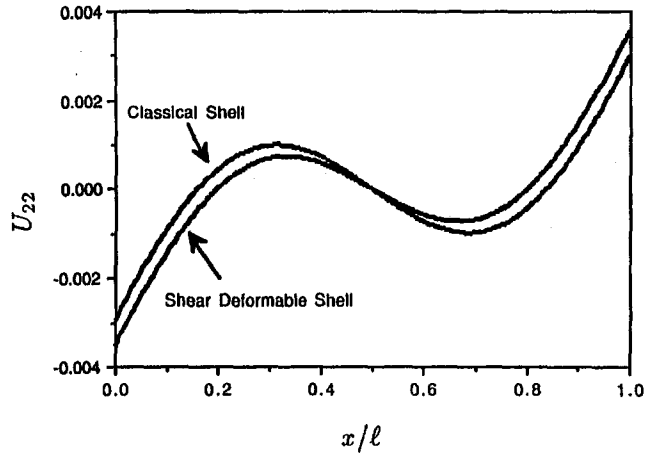


Fig. 4(*a*) $U_{22}(x)$ for both the shear deformable and the classical shell theory (lateral only external pressure)

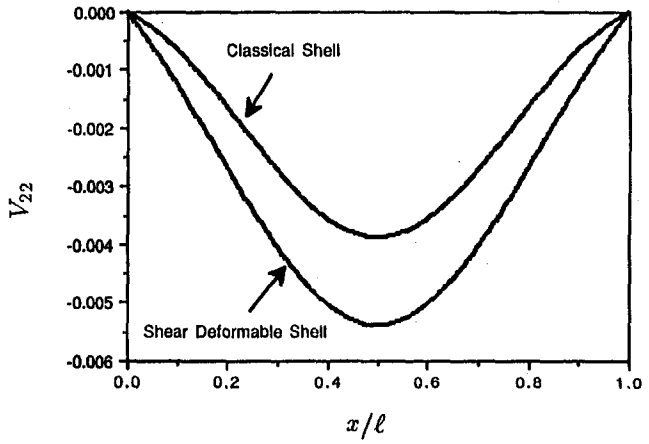


Fig. 4(*b*) $V_{22}(x)$ for both the shear deformable and the classical shell theory

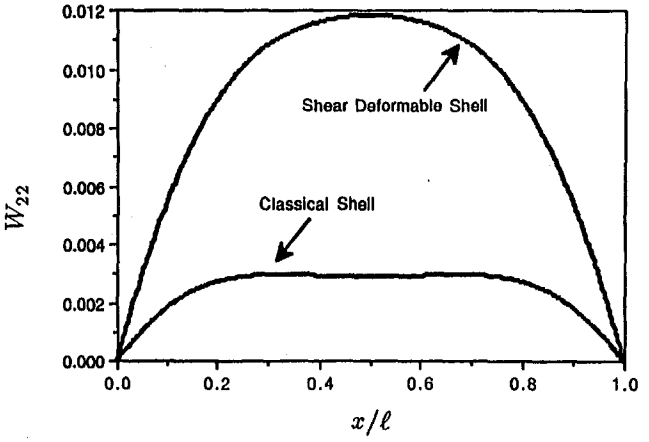


Fig. 4(*c*) $W_{22}(x)$ for both the shear deformable and the classical shell theory

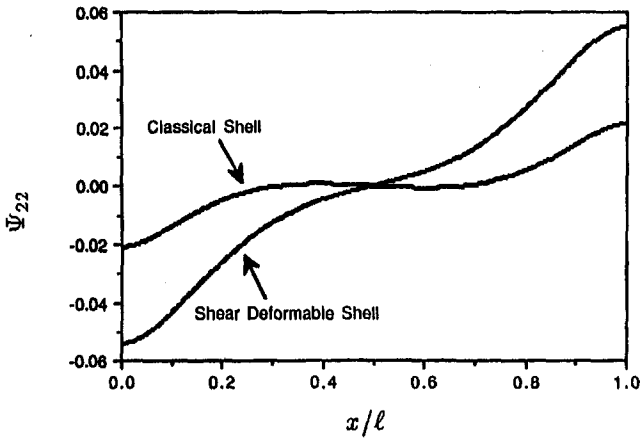


Fig. 4(*d*) $\Psi_{22}(x)$ for both the shear deformable and the classical shell theory

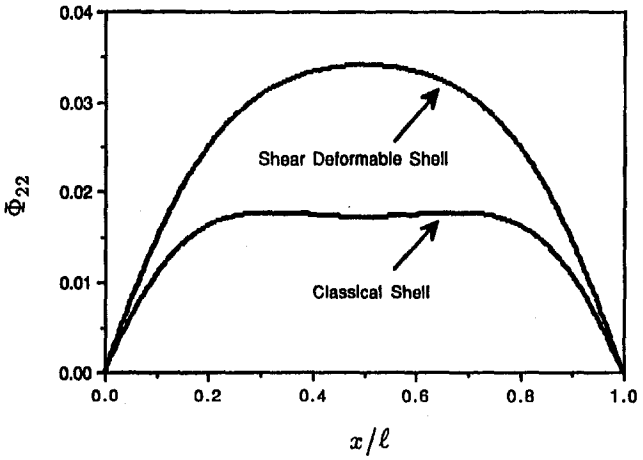


Fig. 4(*e*) $\Phi_{22}(x)$ for both the shear deformable and the classical shell theory

sensitive even at the high range of length values, and therefore reduction in the buckling pressure from the bifurcation values should be anticipated; for the isotropic case, the bifurcation pressure ought to be reliable above $\bar{z} \simeq 1{,}000$. For the rather short shells, i.e., small values of $\bar{z}$, the circumferentially reinforced case shows a large amount of imperfection-sensitivity above $\bar{z} \simeq 2.3$ (and up to $\simeq$270), whereas the axially reinforced case exhibits no imperfection-sensitivity below $\bar{z} \simeq 27$. One interesting observation from Fig. 1 is that the absolute maximum of the negative range of the postbuckling coefficient, b, is reached in the isotropic case.

Figure 2 and Table 2 give the results for the postbuckling coefficient b from the shear deformable shell theory for the case of hydrostatic end loading. The major changes occur for the rather short shells, i.e., for $\bar{z}$ less than $\simeq$25, for which the pressure loading of the ends causes an increase of the imperfection sensitivity (smaller values of b) in comparison with the lateral-only external pressure loading.

The results in Table 3 and in Fig. 3 illustrate the effect of transverse shear on the post-buckling coefficient for lateral external pressure loading. Compared to the results from the classical shell theory, i.e., neglecting the transverse shear effects, it can be concluded that this effect leads to a decrease in the value of b and hence increases the imperfection sensitivity of the shell; however, this effect is negligible for longer shells, specifically for $\bar{z}$ above $\simeq$100.

The effect of thickness is illustrated in Table 4, in which two cases of thickness are considered, a relatively thinner shell with $R_2/R_1 = 1.05$, and a relatively thicker shell with $R_2/R_1 = 1.10$. The shells have the same mean radius $R = 1$ m. Since the Batdorf number $\bar{z}$ depends on the shell thickness, it seems advisable to use the length ratio l/R for comparison purposes in this table. One main point is that for the same length, the thinner and thicker shells may buckle at different values of n. If the shells buckle at the same n (these cases are denoted by an asterisk in the data in Table 4), then it can be concluded that the values of the post-buckling coefficient are larger for the thicker shell and therefore, the thicker shell is less sensitive to imperfections. However, if at the same length, the thicker shell buckles at a smaller n, then b can be smaller and the thicker

Downloaded 04 May 2010 to 171.66.16.34. Redistribution subject to ASME license or copyright; see http://www.asme.org/terms/Terms_Use.cfm

shell can be more imperfection-sensitive. Therefore, the thicker shells are less sensitive to imperfections only if they buckle at the same value of n as the thinner shells (of the same length, l, and mean radius, R) with which they are compared.

One of the most useful data in this problem of a shell under external pressure, is the range of imperfection sensitivity, expressed in terms of the range of values of $\bar{z}$, or equivalently, the range of values of l/R, for which the post-buckling coefficient b is negative, and these data are given in Table 5. A range of $\bar{z}$ from 1 to 3,000 was examined. As can be seen, the range of imperfection sensitivity depends on the material anisotropy, the thickness and whether the end pressure loading is included or not. For example, the isotropic case with hydrostatic end loading is always imperfection-sensitive for $R_2/R_1 = 1.05$, but not for the thicker $R_2/R_1 = 1.10$, in which case it shows a positive b and hence lack of imperfection-sensitivity for $\bar{z}$ above $\simeq$ 1,100.

Finally, in order to illustrate the effect of transverse shear on the second-order displacement field, Figs. 4*a–e* show the functions $U_{22}(x)$, $V_{22}(x)$, $W_{22}(x)$, $\Psi_{22}(x)$, and $\Phi_{22}(x)$ for both the shear deformable and the classical shell theory. The case selected was lateral only external pressure, graphite/epoxy with circumferential reinforcement, radii ratio $R_2/R_1 = 1.10$, and length parameter $\bar{z} = 10$. For this case the structure is imperfection-sensitive with calculated $b = -0.2681$ from the shear deformable shell, and $b = -0.1598$ from the classical shell theory.

Long Cylindrical Shell Limit

If we make the assumption of an infinitely long cylinder, we may ignore boundary conditions at the ends of the shell and the solutions to the differential Eqs. (20) may then be sought in the form of periodic functions of the axial coordinate. Specifically,

$$U_{20} = \tilde{U}_{20} \sin 2\lambda x; \quad V_{20} = \tilde{V}_{20} \cos 2\lambda x;$$

$$W_{20} = \tilde{W}^*_{20} + \tilde{W}_{20} \cos 2\lambda x, \tag{29a}$$

$$\Psi_{20} = \tilde{\Psi}_{20} \sin 2\lambda x; \quad \Phi_{20} = \tilde{\Phi}_{20} \cos 2\lambda x. \tag{29b}$$

Then, substituting into the differential Eqs. (20), gives $\tilde{W}^*_{20}$ from

$$(c_{22} + p_c R)\tilde{W}^*_{20} = (b_1 + b_2 + b_3 + b_4)/4, \tag{30a}$$

where the b_i's are given in Eqs. (19) and λ is the buckling mode from (14*c*). Also, $\tilde{V}_{20} = \tilde{\Phi}_{20} = 0$, and $\tilde{U}_{20}$, $\tilde{W}_{20}$, and $\tilde{\Psi}_{20}$ are found from the linear equations:

$$4\lambda^2 R c_{11}\tilde{U}_{20} + 2\lambda c_{12}\tilde{W}_{20} = \left(\frac{c_{12}}{R} n^2 - R c_{11}\lambda^2\right)\frac{W_1^2\lambda}{4}, \tag{30b}$$

$$2k_1^2 c_{55}\lambda\tilde{W}_{20} - (4D_{11}\lambda^2 + k_1^2 c_{55})\tilde{\Psi}_{20} = 0, \tag{30c}$$

$$2\lambda c_{12} R\tilde{U}_{20} + [c_{22} + p_c R + (k_1^2 c_{55} + N^c_{x0})4\lambda^2 R^2]\tilde{W}_{20} - 2\lambda c_{12} k_1^2 c_{55} R^2 \tilde{\Psi}_{20} = (b_2 + b_4 - b_1 - b_3)/4. \tag{30d}$$

In a similar fashion, solutions to the differential Eqs. (21) are set in the form

$$U_{22} = \tilde{U}_{22} \sin 2\lambda x; \quad V_{22} = \tilde{V}^*_{22} + \tilde{V}_{22} \cos 2\lambda x;$$

$$W_{22} = \tilde{W}^*_{22} + \tilde{W}_{22} \cos 2\lambda x, \tag{31a}$$

$$\Psi_{22} = \tilde{\Psi}_{22} \sin 2\lambda x; \quad \Phi_{22} = \tilde{\Phi}^*_{22} + \tilde{\Phi}_{22} \cos 2\lambda x. \tag{31b}$$

Then, substituting into (21), gives $\tilde{V}^*_{22}$, $\tilde{W}^*_{22}$, and $\tilde{\Phi}^*_{22}$ from

$$\left(\frac{c_{22}}{R} 4n^2 + p_c\right)\tilde{V}^*_{22} + \left(\frac{c_{22}}{R} + p_c\right)2n\tilde{W}^*_{22} = \left(c_{12}\lambda^2 - \frac{c_{22}}{R^2} n^2\right)\frac{W_1^2 n}{4}, \tag{32a}$$

$$2nk_2^2 c_{44}\tilde{W}^*_{22} - \left(\frac{D_{22}}{R} 4n^2 + R k_2^2 c_{44}\right)\tilde{\Phi}^*_{22} = 0, \tag{32b}$$

$$(c_{22} + p_c R)2n\tilde{V}^*_{22} + [(k_2^2 c_{44} + N^c_{\theta 0})4n^2 + c_{22} + p_c R]\tilde{W}^*_{22} - 2nRk_2^2 c_{44}\tilde{\Phi}^*_{22} = (b_3 + b_4 - b_1 - b_2)/4. \tag{32c}$$

Also, $\tilde{U}_{22}$, $\tilde{V}_{22}$, $\tilde{W}_{22}$, $\tilde{\Psi}_{22}$, and $\tilde{\Phi}_{22}$ are found from the linear equations:

$$4\left(Rc_{11}\lambda^2 + \frac{c_{66}}{R} n^2\right)\tilde{U}_{22} + 4\lambda n(c_{12} + c_{66})\tilde{V}_{22} + 2\lambda\tilde{W}_{22} = \left(\frac{c_{12} + 2c_{66}}{R} n^2 + Rc_{11}\lambda^2\right)\frac{W_1^2\lambda}{4}, \tag{33a}$$

$$4\lambda n(c_{12} + c_{66})\tilde{U}_{22} + \left(\frac{c_{22}}{R} 4n^2 + 4\lambda^2 R c_{66} + p_c\right)\tilde{V}_{22} + 2n\left(\frac{c_{22}}{R} + p_c\right)\tilde{W}_{22} = \left[(c_{12} + 2c_{66})\lambda^2 + \frac{c_{22}}{R^2} n^2\right]\frac{W_1^2 n}{4}, \tag{33b}$$

$$2\lambda k_1^2 c_{55} R\tilde{W}_{22} - \left(\frac{D_{66}}{R} 4n^2 + Rk_1^2 c_{55} + 4\lambda^2 R D_{11}\right)\tilde{\Psi}_{22} - 4\lambda n(D_{12} + D_{66})\tilde{\Phi}_{22} = 0, \tag{33c}$$

$$2nk_2^2 c_{44}\tilde{W}_{22} - 4\lambda n(D_{12} + D_{66})\tilde{\Psi}_{22} - \left(4\lambda^2 R D_{66} + \frac{D_{22}}{R} 4n^2 + Rk_2^2 c_{44}\right)\tilde{\Phi}_{22} = 0, \tag{33d}$$

$$2\lambda c_{12} R\tilde{U}_{22} + 2n(c_{22} + p_c R)\tilde{V}_{22} + [(k_2^2 c_{44} + N^c_{\theta 0})4n^2 + c_{22} + p_c R + (k_1^2 c_{55} + N^c_{x0})4\lambda^2 R^2]\tilde{W}_{22} - 2\lambda k_1^2 c_{55} R^2\tilde{\Psi}_{22} - 2nRk_2^2 c_{44}\tilde{\Phi}_{22} = (b_4 + b_1 - b_2 - b_3)/4. \tag{33e}$$

The post-buckling coefficient b can now be calculated by substituting into the full expressions for the displacement field, Eqs. (18), and then into the formulas (9) and (10). This closed-form solution for the second-order displacement field for a very long cylindrical shell, besides being a useful quickly obtainable solution, can be used as the initial guess for the relaxation method which is employed to solve the differential equations for the second-order displacements for a cylindrical shell of finite length.

A comparison of this long shell limit solution for the post-buckling coefficient, b, is given in Fig. 5(*a*) for the graphite/epoxy shell with circumferential reinforcement and in Fig. 5(*b*) for the the graphite/epoxy shell with axial reinforcement (lateral external pressure only and $R_2/R_1 = 1.10$). In both cases, the long shell limit essentially converges to the solution outlined in the previous sections for a shell of finite length, when the length values become large, i.e., in the first case for $\bar{z}$ beyond about 100 and the second case for $\bar{z}$ beyond about 400.

Conclusions

1 Koiter's general post-buckling theory is used to study the initial post-buckling behavior of moderately thick, orthotropic, shear deformable cylindrical shells under external pressure. A

Downloaded 04 May 2010 to 171.66.16.34. Redistribution subject to ASME license or copyright; see http://www.asme.org/terms/Terms_Use.cfm

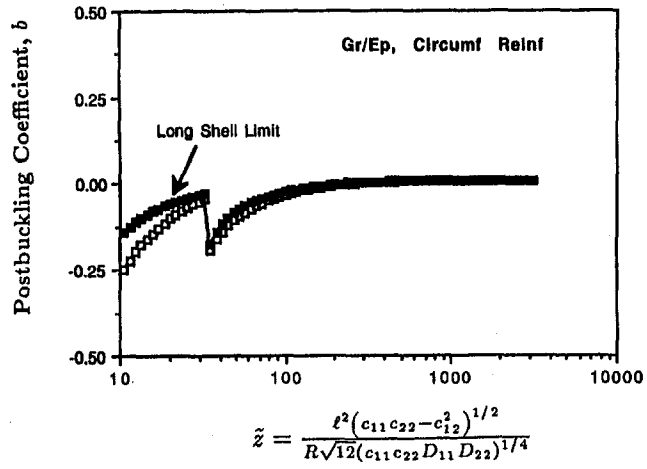


Fig. 5(*a*) The long cylinder limit closed-form solution for the initial postbuckling coefficient, *b*, in comparison to the finite length solution for a graphite/epoxy with circumferential reinforcement

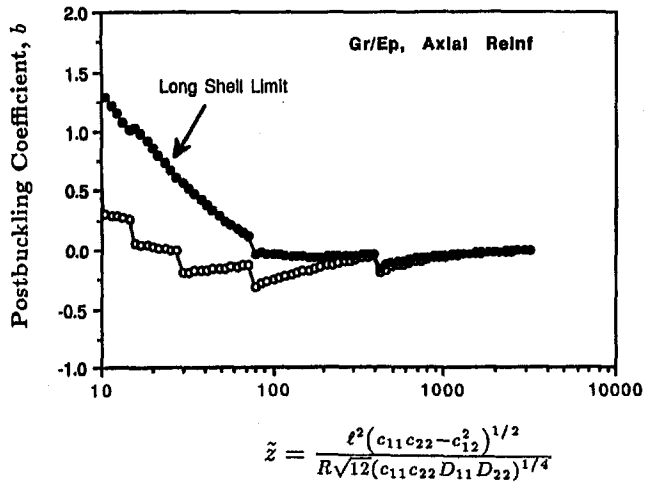


Fig. 5(*b*) The long cylinder limit closed-form solution for the initial postbuckling coefficient, *b*, in comparison to the finite length solution for a graphite/epoxy with axial reinforcement

shear deformation theory, which accounts for transverse shear strains and rotations about the normal to the shell midsurface, is employed to formulate the shell equations.

2 The range of imperfection sensitivity depends strongly on the material anisotropy, on the wall thickness, and on whether the end pressure loading is included or not.

3 For the circumferentially reinforced graphite/epoxy example case studied, it was found that the structure is not sensitive to imperfections for values of the Batdorf length parameter $\tilde{z}$ above $\simeq$270, whereas for the axially reinforced case the structure is imperfection-sensitive even at the high range of length values; for the isotropic case, the structure is not sensitive to imperfections above $\tilde{z} \simeq 1000$.

4 For the same length, a thicker shell is less sensitive to imperfections if it buckles at the same number of wave numbers (n, m) as the thinner construction.

5 Transverse shear effects lead to an increase in the imperfection sensitivity of the shell; however, this effect is significant only for relatively short shells.

6 If the hydrostatic pressure loading of the ends is included, major changes would occur for rather short shells, for which an increase of the imperfection sensitivity is observed in comparison to the lateral only external pressure loading.

7 A closed-form long-shell limit solution for the initial postbuckling coefficient, b, is derived and shown to properly converge to the solution for a shell of finite length, when the values of $\tilde{z}$ become large.

Acknowledgment

The financial support of the Office of Naval Research, Ship Structures and Systems, S&T Division, Grant N00014-91-J-1892, and the interest and encouragement of the Grant Monitor, Dr. Y. D. S. Rajapakse, are both gratefully acknowledged.

References

Budiansky, B., 1974, "Theory of Buckling and Post-Buckling Behavior of Elastic Structures," *Advances in Applied Mechanics,* Vol. 14, pp. 1–65.

Budiansky, B., and Amazigo, J. C., 1968, "Initial Post-buckling Behavior of Cylindrical Shells Under External Pressure," *Journal of Mathematics and Physics,* Vol. 47, No. 3, pp. 223–235.

Budiansky, B., and Hutchinson, J. W., 1964, "Dynamic Buckling of Imperfection-Sensitive Structures," *Proceedings XI International Congress of Applied Mechanics,* H. Görtler, ed, Springer, Munich, pp. 636–651.

Brush, D. O., and Almroth, B. O., 1975, *Buckling of Bars, Plates, and Shells,* McGraw-Hill, New York, pp. 159–161.

Dong, S. B., and Nelson, R. B., 1972, "On Natural Vibrations and Waves in Laminated Orthotropic Plates," ASME JOURNAL OF APPLIED MECHANICS, Vol. 39, pp. 739–745.

Dong, S. B., and Tso, F. K. W., 1972, "On a Laminated Orthotropic Shell Theory Including Transverse Shear Deformation," ASME JOURNAL OF APPLIED MECHANICS, Vol. 39, pp. 1091–1097.

Fu, L., and Waas, A. M., 1995, "Initial Post-buckling Behavior of Thick Rings Under Uniform External Hydrostatic Pressure," ASME JOURNAL OF APPLIED MECHANICS, Vol. 62, pp. 338–345.

Hutchinson, J. W., 1968, "Buckling and Initial Postbuckling Behavior of Oval Cylindrical Shells Under Axial Compression," ASME JOURNAL OF APPLIED MECHANICS, Vol. 35, pp. 66–72.

Hutchinson, J. W., and Frauenthal, J. C., 1969, "Elastic Postbuckling Behavior of Stiffened and Barreled Cylindrical Shells," ASME JOURNAL OF APPLIED MECHANICS, Vol. 36, pp. 784–790.

Hutchinson, J. W., and Koiter, W. T., 1970, "Postbuckling theory," ASME *Appl. Mech. Rev.* Vol. 23, pp. 1353–1366.

Kardomateas, G. A., 1993, "Buckling of Thick Orthotropic Cylindrical Shells Under External Pressure," ASME JOURNAL OF APPLIED MECHANICS, Vol. 60, 1993, pp. 195–202.

Kardomateas, G. A., and Chung, C. B., 1994, "Buckling of Thick Orthotropic Cylindrical Shells Under External Pressure Based on Non-Planar Equilibrium Modes," *International Journal of Solids and Structures,* Vol. 31, No. 16, pp. 2195–2210.

Kardomateas, G. A., and Philobos, M. S., 1995, "Buckling of Thick Orthotropic Cylindrical Shells Under Combined External Pressure and Axial Compression," *AIAA Journal,* Vol. 33, No. 10, pp. 1946–1953.

Koiter, W. T., 1945, *On the Stability of Elastic Equilibrium* (in Dutch), thesis, Delft, Amsterdam; English transl. (a) NASA TT-F10, 833 (1967), (b) AFFDL-TR-70-25 (1970).

Koiter, W. T., 1956, "Buckling and Postbuckling Behavior of a Cylindrical Panel Under Axial Compression," NLR Rep. No. S476. Rep. Trans. Nat. Aero. Res. Inst. Vol. 20, Nat. Aero. Res. Inst., Amsterdam.

Koiter, W. T., 1963, "Elastic Stability and Post-Buckling Behavior," *Non-Linear Problems,* R. E. Langer ed., University of Wisconsin Press, Madison, WI.

Mindlin, R. D., 1951, "Influence of Rotatory Inertia and Shear on Flexural Motions in Isotropic Elastic Plates" ASME JOURNAL OF APPLIED MECHANICS, Vol. 18, pp. 31–38.

Mirsky, I., and Herrmann, G., 1957, "Nonaxially symmetric motion of cylindrical shells," *J. Acoust. Soc. Am.,* Vol. 29, pp. 1116–1123.

Naghdi, P. M., and Cooper, R. M., 1956, "Propagation of elastic waves in cylindrical shells including the effects of transverse shear and rotatory inertia," *J. Acoust. Soc. Am.* Vol. 28, pp. 56–63.

Nemeth, M. P., 1994, "Nondimensional Parameters and Equations for Buckling of Anisotropic Shallow Shells," ASME JOURNAL OF APPLIED MECHANICS, Vol. 61, pp. 664–669.

Press, W. H., Flannery, B. P., Teukolsky, S. A., and Vetterling, W. T., 1989, *Numerical Recipes,* Cambridge University Press, Cambridge, UK.

Reddy, J. N., and Liu, C. F., 1985, "A Higher-Order Shear Deformation Theory of Laminated Elastic Shells," *Int. J. Eng. Sci.,* Vol. 23, No. 3, pp. 319–330.

Sheinman, I., and Simitses, G. J., 1983, "Buckling and Postbuckling of Imperfect Cylindrical Shells Under Axial Compression," *Computers & Structures,* Vol. 17, No. 2, pp. 277–285.

Simitses, G. J., Tabiei, A., and Anastasiadis, J. S., 1993, "Buckling of Moderately Thick, Laminated Cylindrical Shells Under Lateral Pressure," *Composites Engineering,* Vol. 3, No. 5, pp. 409–417.

Whitney, J. M., 1973, "Shear Correction Factors for Orthotropic Laminates Under Static Load," ASME JOURNAL OF APPLIED MECHANICS, Vol. 40. pp. 302–304.

Whitney, J. M., and Sun, C. T., 1974, "A Refined Theory for Laminated Anisotropic Cylindrical Shells," ASME JOURNAL OF APPLIED MECHANICS, Vol. 41, pp. 471–476.

Downloaded 04 May 2010 to 171.66.16.34. Redistribution subject to ASME license or copyright; see http://www.asme.org/terms/Terms_Use.cfm

In-Plane Stress and Displacement Distributions in a Spinning Annular Disk Under Stationary Edge Loads

Jen-San Chen
Associate Professor.

Jhi-Lu Jhu
Graduate Student.

Department of Mechanical Engineering,
National Taiwan University
Taipei, Taiwan 107,
Republic of China

It is well known that the in-plane stress and displacement distributions in a stationary annular disk under stationary edge tractions can be obtained through the use of Airy stress function in the classical theory of linear elasticity. By using Lame's potentials, this paper extends these solutions to the case of a spinning disk under stationary edge tractions. It is also demonstrated that the problem of stationary disk-spinning load differs from the problem of spinning disk-stationary load not only by the centrifugal effect, but also by additional terms arising from the Coriolis effect. Numerical simulations show that the amplitudes of the stress and displacement fields grow unboundedly as the rotational speed of the disk approaches the critical speeds. As the rotational speed approaches zero, on the other hand, the in-plane stresses and displacements are shown, both numerically and analytically, to recover the classical solutions derived through the Airy stress function.

Introduction

Designers of spur gears, grinding wheels, and circular saw blades are often interested in the dynamic stresses induced in a rotating disk under space-fixed in-plane edge loads. In gearboxes and grinding wheels, the in-plane vibration is transmitted through the bearing to the machine casing, where it may produce unwanted noise. In the wood cutting industry, it is well known that the bending vibration and stability of the spinning disk are significantly affected by the in-plane stress distribution induced by the cutting forces on the outer rim (Chen, 1994; Shen and Song, 1996). In these analyses, the in-plane stress distribution is obtained, in additional to the components due to the centrifugal effect, by assuming that both the disk and the edge load are fixed in space. This assumption is acceptable when the rotation speed of the disk is relatively low. In the very high speed range, on the other hand, it is not certain whether it is appropriate to ignore the effect of relative motion between the spinning disk and the space-fixed edge load on the in-plane stress distribution.

It is well known that the natural frequencies of the in-plane radial and torsional vibrations of a spinning disk depend on the rotation speed. Bhuta and Jones (1963) investigated the axisymmetric planar vibration of a rotating full disk and found that the effect of rotation is generally to lower the natural frequencies. The same problem was studied by Doby (1969) with different formulation. Burdess et al. (1987) generalized the analysis to asymmetric in-plane vibration, and discussed the properties of both the forward and backward traveling circumferential waves. In most of these works, the disk is assumed to be full. Chen and Jhu (1996) studied the in-plane vibration of spinning annular disks and investigated the effects of clamping ratio on the natural frequencies and stability of the disks. All these analyses demonstrate the existence of certain critical rotation speed at which one of the natural frequencies vanishes.

Contributed by the Applied Mechanics Division of THE AMERICAN SOCIETY OF MECHANICAL ENGINEERS for publication in the ASME JOURNAL OF APPLIED MECHANICS.

Discussion on the paper should be addressed to the Technical Editor, Professor Lewis T. Wheeler, Department of Mechanical Engineering, University of Houston, Houston, TX 77204-4792, and will be accepted until four months after final publication of the paper itself in the ASME JOURNAL OF APPLIED MECHANICS.

Manuscript received by the ASME Applied Mechanics Division, June 26, 1995; final revision, May 22, 1997. Associate Technical Editor: N. C. Perkins.

The in-plane stress distribution in a stationary annular disk under stationary edge tractions can be readily calculated by using the Airy stress function (Coker and Filon, 1957). On the other hand, the problem of a spinning disk under stationary edge loads has never been studied before. This problem is much more complex than the classical one with a nonrotating disk as a result of the Coriolis terms associated with the relative motion between the spinning disk and the stationary edge loads. In order to avoid the difficulties imposed by the Coriolis terms and the in-plane stresses due to centrifugal effect, Srinivasan and Ramamurti (1980) investigated a relevant problem of a stationary disk under a rotating concentrated edge load. Leung and Pinnington (1987) conducted experiments to measure the in-plane response of a stationary disk under rotating edge loads.

In the present paper we derive the analytical solutions for the in-plane stress and displacement distributions in a spinning disk under stationary edge tractions. The equations of in-plane vibration of the spinning disk with respect to the inertial frame are first derived. Lame's potentials are used to simplify the highly coupled equations. Numerical examples of stress and displacement distributions for a typical radius ratio are demonstrated. As the rotational speed of the disk approaches zero, the in-plane stresses and displacements are shown analytically to recover the solutions derived through the Airy stress function in the classical theory of linear elasticity.

Equations of Motion

Figure 1 shows an elastic annular disk spinning at constant speed Ω. The material of the disk is assumed to be homogeneous and isotropic with mass density ρ, Young's modulus E, and Poisson ratio ν. The spinning disk is clamped at inner radius $r = a$, and is subject to nonrotating edge tractions $\hat{\sigma}_{rr}$ and $\hat{\sigma}_{r\eta}$ at the outer radius $r = b$. (r, η) are the polar coordinates of a point on the spinning disk with respect to an inertial frame. If the disk is thin, plane stress conditions can be assumed and the equilibrium equations in the radial and tangential directions in terms of in-plane displacements u_r and u_θ can be written with respect to the body-fixed coordinate system (r, θ) (Burdess et al., 1987),

Copyright © 1997 by ASME

Downloaded 04 May 2010 to 171.66.16.34. Redistribution subject to ASME license or copyright; see http://www.asme.org/terms/Terms_Use.cfm

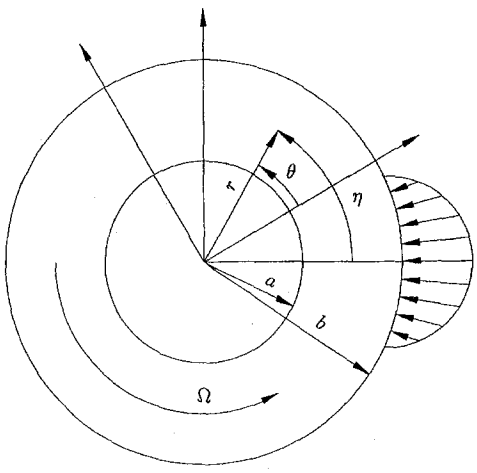


Fig. 1 A spinning annular disk under stationary edge load

$$\frac{E}{\rho(1-\nu^2)}(L_{11}u_r + L_{12}u_\theta) = \ddot{u}_r - 2\Omega\dot{u}_\theta - \Omega^2(u_r + r) \quad (1)$$

$$\frac{E}{\rho(1-\nu^2)}(L_{21}u_r + L_{22}u_\theta) = \ddot{u}_\theta + 2\Omega\dot{u}_r - \Omega^2 u_\theta \quad (2)$$

where the differential operators are defined as

$$L_{11} = \frac{\partial^2}{\partial r^2} + \frac{1}{r}\frac{\partial}{\partial r} - \frac{1}{r^2} + \frac{1-\nu}{2r^2}\frac{\partial^2}{\partial\theta^2} \quad (3)$$

$$L_{12} = \frac{1+\nu}{2}\frac{1}{r}\frac{\partial^2}{\partial r\partial\theta} - \frac{3-\nu}{2}\frac{1}{r^2}\frac{\partial}{\partial\theta} \quad (4)$$

$$L_{21} = \frac{1+\nu}{2}\frac{1}{r}\frac{\partial^2}{\partial r\partial\theta} + \frac{3-\nu}{2}\frac{1}{r^2}\frac{\partial}{\partial\theta} \quad (5)$$

$$L_{22} = \frac{1-\nu}{2}\left(\frac{\partial^2}{\partial r^2} + \frac{1}{r}\frac{\partial}{\partial r} - \frac{1}{r^2}\right) + \frac{1}{r^2}\frac{\partial^2}{\partial\theta^2}. \quad (6)$$

Equations (1) and (2) can be rewritten with respect to the inertial frame (r, η) by using the transformations

$$\dot{u}_r(r,\theta) = \frac{\partial u_r(r,\eta)}{\partial t} + \Omega\frac{\partial u_r(r,\eta)}{\partial\eta} \quad (7)$$

$$\dot{u}_\theta(r,\theta) = \frac{\partial u_\eta(r,\eta)}{\partial t} + \Omega\frac{\partial u_\eta(r,\eta)}{\partial\eta} \quad (8)$$

where

$$\eta = \theta + \Omega t. \quad (9)$$

It is convenient at this stage to introduce some dimensionless variables (denoted with an asterisk),

$$r^* = \frac{r}{b}, \quad \zeta = \frac{a}{b}, \quad u_r^* = \frac{u_r}{b}, \quad u_\eta^* = \frac{u_\eta}{b},$$

$$\Omega^* = \Omega b\sqrt{\frac{\rho}{E}}, \quad t^* = \frac{t}{b}\sqrt{\frac{E}{\rho}}$$

$$\sigma_{rr}^* = \frac{\sigma_{rr}}{E}, \quad \sigma_{r\eta}^* = \frac{\sigma_{r\eta}}{E}, \quad \sigma_{\eta\eta}^* = \frac{\sigma_{\eta\eta}}{E}$$

The equations of motion in terms of the dimensionless variables defined above with respect to the inertial frame can be written as follows:

$$\frac{1}{(1-\nu^2)}(L_{11}^* u_r^* + L_{12}^* u_\eta^*) = \left(\frac{\partial^2 u_r^*}{\partial t^{*2}} + 2\Omega^*\frac{\partial^2 u_r^*}{\partial t^*\partial\eta} + \Omega^{*2}\frac{\partial^2 u_r^*}{\partial\eta^2}\right) - 2\Omega^*\left(\frac{\partial u_\eta^*}{\partial t^*} + \Omega^*\frac{\partial u_\eta^*}{\partial\eta}\right) - \Omega^{*2}(u_r^* + r^*) \quad (10)$$

$$\frac{1}{(1-\nu^2)}(L_{21}^* u_r^* + L_{22}^* u_\eta^*) = \left(\frac{\partial^2 u_\eta^*}{\partial t^{*2}} + 2\Omega^*\frac{\partial^2 u_\eta^*}{\partial t^*\partial\eta} + \Omega^{*2}\frac{\partial^2 u_\eta^*}{\partial\eta^2}\right) + 2\Omega^*\left(\frac{\partial u_r^*}{\partial t^*} + \Omega^*\frac{\partial u_r^*}{\partial\eta}\right) - \Omega^{*2}u_\eta^*. \quad (11)$$

The differential operators L_{11}^*, L_{12}^*, L_{21}^*, and L_{22}^* are similar to those in Eqs. (3)–(6) with r and θ being replaced by r^* and η, respectively. The dimensionless boundary conditions with respect to the inertial frame are

$$u_r^* = u_\eta^* = 0 \quad \text{at } r^* = \zeta \quad (12a, b)$$

$$\frac{1}{1-\nu^2}\left[\frac{\partial u_r^*}{\partial r^*} + \nu\left(\frac{u_r^*}{r^*} + \frac{1}{r^*}\frac{\partial u_\eta^*}{\partial\eta}\right)\right] = \hat{\sigma}_{rr}^*(\eta)$$

$$\frac{1}{2(1+\nu)}\left(\frac{1}{r^*}\frac{\partial u_r^*}{\partial\eta} + \frac{\partial u_\eta^*}{\partial r^*} - \frac{u_\eta^*}{r^*}\right) = \hat{\sigma}_{r\eta}^*(\eta) \quad \text{at } r^* = 1. \quad (13a, b)$$

In the following discussion we drop all the asterisks for brevity.

It is noted that both the differential Eqs. (10) and (11), and the boundary conditions (12) and (13) are inhomogeneous. The superposition principle (Stakgold, 1979) permits us to decompose the problem into two simpler parts; one with inhomogeneous equations and homogeneous boundary conditions, and the other with homogeneous equations and inhomogeneous boundary conditions. The solution of the original problem can be obtained by reassembling these solutions of the simpler problems. For the first part, the forcing term $r\Omega^2$ in the inhomogeneous Eq. (10) is due to the centrifugal effect. When the steady-state solutions are concerned, this term is dominant compared to other contribution from the term $u_r\Omega^2$. Therefore, the solution of the first problem is the same as the classical problem of a freely spinning disk, and is well documented in the literature (Ono et al., 1991). On the other hand, the second problem has never been solved in the literature, and will be the subject of the following discussion.

Lame's Potentials

The homogeneous parts of Eqs. (10) and (11) can be simplified if Lame's potentials ϕ and ψ are introduced (Eringen and Suhubi, 1975):

$$u_r = \frac{\partial\phi}{\partial r} + \frac{1}{r}\frac{\partial\psi}{\partial\eta} \quad (14)$$

$$u_\eta = \frac{1}{r}\frac{\partial\phi}{\partial\eta} - \frac{\partial\psi}{\partial r}. \quad (15)$$

As a consequence, the stress components can also be represented as

Downloaded 04 May 2010 to 171.66.16.34. Redistribution subject to ASME license or copyright; see http://www.asme.org/terms/Terms_Use.cfm

$$\sigma_{rr} = \frac{\nu}{1-\nu^2}\nabla^2\phi + \frac{1}{1+\nu}\left(\frac{\partial^2\phi}{\partial r^2} - \frac{1}{r^2}\frac{\partial\psi}{\partial\eta} + \frac{1}{r}\frac{\partial^2\psi}{\partial r\partial\eta}\right) \quad (16)$$

$$\sigma_{r\eta} = \frac{1}{2(1+\nu)}\left(\frac{2}{r}\frac{\partial^2\phi}{\partial r\partial\eta} - \frac{2}{r^2}\frac{\partial\phi}{\partial\eta} - \frac{\partial^2\psi}{\partial r^2} + \frac{1}{r}\frac{\partial\psi}{\partial r} + \frac{1}{r^2}\frac{\partial^2\psi}{\partial\eta^2}\right) \quad (17)$$

$$\sigma_{\eta\eta} = \frac{\nu}{1-\nu^2}\nabla^2\phi + \frac{1}{1+\nu}\left(\frac{1}{r}\frac{\partial\phi}{\partial r} + \frac{1}{r^2}\frac{\partial^2\phi}{\partial\eta^2} + \frac{1}{r^2}\frac{\partial\psi}{\partial\eta} - \frac{1}{r}\frac{\partial^2\psi}{\partial r\partial\eta}\right). \quad (18)$$

It is assumed that the edge traction is applied for a long time and the steady state prevails as seen by an observer in the inertial frame. Substituting Eqs. (14) and (15) into homogeneous parts of Eqs. (10) and (11) and neglecting all the temporal derivatives result in the following equations:

$$\frac{\partial G}{\partial r} + \frac{1}{r}\frac{\partial H}{\partial\eta} = 0 \quad (19)$$

$$\frac{1}{r}\frac{\partial G}{\partial\eta} - \frac{\partial H}{\partial r} = 0 \quad (20)$$

where

$$G = \lambda_1^2\nabla^2\phi - \Omega^2\frac{\partial^2\phi}{\partial\eta^2} + \Omega^2\phi - 2\Omega^2\frac{\partial\psi}{\partial\eta} \quad (21)$$

$$H = \lambda_2^2\nabla^2\psi - \Omega^2\frac{\partial^2\psi}{\partial\eta^2} + \Omega^2\psi + 2\Omega^2\frac{\partial\phi}{\partial\eta}. \quad (22)$$

λ_1 and λ_2 are two constants depending on the Poisson ratio,

$$\lambda_1^2 = \frac{1}{1-\nu^2}, \quad \lambda_2^2 = \frac{1}{2(1+\nu)}. \quad (23a, b)$$

It is noted that for the problem of a fixed disk described by an observer rotating with speed Ω, Eqs. (21) and (22) should read (Srinivasan and Ramamurti, 1980)

$$G = \lambda_1^2\nabla^2\phi - \Omega^2\frac{\partial^2\phi}{\partial\eta^2},$$

$$H = \lambda_2^2\nabla^2\psi - \Omega^2\frac{\partial^2\psi}{\partial\eta^2}. \quad (24a, b)$$

As a consequence, the problem of a stationary disk under rotating edge loads differs from the problem of a rotating disk under stationary edge loads not only by the centrifugal effect, but also by additional terms arising from Coriolis effect. It is noted that for the problem of a stationary disk under rotating edge loads, the equilibrium equations are decoupled into equations for ϕ and ψ, respectively, and have been investigated by Srinivasan and Ramamurti (1980).

The general solutions for G and H in Eqs. (19) and (20) can be expressed in the form

$$G = A_0 + \sum_{n=1}^{\infty}[(A_n r^n + B_n r^{-n})\cos n\eta + (A_n' r^n + B_n' r^{-n})\sin n\eta] \quad (25)$$

$$H = A_0' + \sum_{n=1}^{\infty}[(A_n' r^n - B_n' r^{-n})\cos n\eta + (-A_n r^n + B_n r^{-n})\sin n\eta] \quad (26)$$

where A_n, B_n, A_n', and B_n' are undetermined constants. Equations (21) and (22) are two inhomogeneous equations for ϕ and ψ. Since the corresponding solutions must be periodic in η, the solutions for ϕ and ψ can be expressed in Fourier series as

$$\phi(r,\eta) = \Phi_{0c} + \sum_{n=1}^{\infty}\Phi_{nc}(r)\cos n\eta + \Phi_{ns}(r)\sin n\eta \quad (27)$$

$$\psi(r,\eta) = \Psi_{0c} + \sum_{n=1}^{\infty}\Psi_{nc}(r)\cos n\eta + \Psi_{ns}(r)\sin n\eta. \quad (28)$$

Since the Fourier components are orthogonal, the solutions can be treated separately for different Fourier component.

Case $n = 0$: This case corresponds to the spinning disk under uniform traction. Φ_{0c} and Ψ_{0c} can be solved as

$$\Phi_{0c} = c_0 J_0(\beta_{01}r) + e_0 Y_0(\beta_{01}r) + A_0\frac{1}{\Omega^2} \quad (29)$$

$$\Psi_{0c} = -d_0' J_0(\beta_{02}r) - f_0' Y_0(\beta_{02}r) + A_0'\frac{1}{\Omega^2} \quad (30)$$

where J and Y are Bessel functions of the first and the second kinds, respectively. β_{01} and β_{02} are defined as

$$\beta_{01} = \frac{\Omega}{\lambda_1} \quad \text{and} \quad \beta_{02} = \frac{\Omega}{\lambda_2}. \quad (31)$$

Constants A_0 and A_0' do not affect the displacement and the stress fields in the spinning disk and can be ignored.

Case $n \geq 2$: The general solutions for this case are

$$\Phi_{nc} = c_n J_n(\beta_{n1}r) + d_n s_{n1} J_n(\beta_{n2}r) + e_n Y_n(\beta_{n1}r) + f_n s_{n1} Y_n(\beta_{n2}r) + \frac{A_n r^n}{(1+n)^2\Omega^2} + \frac{B_n r^{-n}}{(1-n)^2\Omega^2} \quad (32)$$

$$\Psi_{ns} = c_n s_{n2} J_n(\beta_{n1}r) + d_n J_n(\beta_{n2}r) + e_n s_{n2} Y_n(\beta_{n1}r) + f_n Y_n(\beta_{n2}r) - \frac{A_n r^n}{(1+n)^2\Omega^2} + \frac{B_n r^{-n}}{(1-n)^2\Omega^2} \quad (33)$$

$$\Phi_{ns} = c_n' J_n(\beta_{n1}r) + d_n' s_{n1} J_n(\beta_{n2}r) + e_n' Y_n(\beta_{n1}r) + f_n' s_{n1} Y_n(\beta_{n2}r) + \frac{A_n' r^n}{(1+n)^2\Omega^2} + \frac{B_n' r^{-n}}{(1-n)^2\Omega^2} \quad (34)$$

$$\Psi_{nc} = -c_n' s_{n2} J_n(\beta_{n1}r) - d_n' J_n(\beta_{n2}r) - e_n' s_{n2} Y_n(\beta_{n1}r) - f_n' Y_n(\beta_{n2}r) + \frac{A_n' r^n}{(1+n)^2\Omega^2} - \frac{B_n' r^{-n}}{(1-n)^2\Omega^2}. \quad (35)$$

β_{n1} and β_{n2} are positive real roots of the following quartic equation:

$$\lambda_1^2\lambda_2^2\beta^4 - (\lambda_1^2 + \lambda_2^2)(1+n^2)\Omega^2\beta^2 + (1-n^2)^2\Omega^4 = 0. \quad (36)$$

s_{n1} and s_{n2} are defined as

$$s_{n1} = \frac{2n\Omega^2}{(1+n^2)\Omega^2 - \lambda_1^2\beta_{n2}^2} \quad \text{and}$$

$$s_{n2} = \frac{2n\Omega^2}{(1+n^2)\Omega^2 - \lambda_2^2\beta_{n1}^2}. \quad (37a, b)$$

It is noted that constants s_{n1} and s_{n2} are independent of Ω because β_{n1} and β_{n2} are proportional to Ω. Again, the terms associated with constants A_n, A_n', B_n, B_n' will not affect the stress and displacement fields of the loaded disk and can be ignored.

Downloaded 04 May 2010 to 171.66.16.34. Redistribution subject to ASME license or copyright; see http://www.asme.org/terms/Terms_Use.cfm

Case $n = 1$: The solution for this case can not be generalized from the case $n \geq 2$, because one of the two β's vanishes. The general solution for this case can be found as

$$\Phi_{1c} = d_1 s_{11} J_1(\beta_{12} r) + f_1 s_{11} Y_1(\beta_{12} r) + A_1 \frac{r}{2\Omega^2} + B_1 \frac{r \ln r}{\lambda_1^2 + \lambda_2^2} + \chi_1 r + \chi_2 \frac{1}{r} \quad (38)$$

$$\Psi_{1s} = d_1 J_1(\beta_{12} r) + f_1 Y_1(\beta_{12} r) + B_1 \frac{1}{\lambda_1^2 + \lambda_2^2} \left(r \ln r + \frac{\lambda_1^2 - \lambda_2^2}{2r\Omega^2} \right) + \chi_1 r + \chi_2 \frac{1}{r} \quad (39)$$

$$\Phi_{1s} = d_1' s_{11} J_1(\beta_{12} r) + f_1' s_{11} Y_1(\beta_{12} r) + A_1' \frac{r}{2\Omega^2} + B_1' \frac{r \ln r}{\lambda_1^2 + \lambda_2^2} + \chi_1' r + \chi_2' \frac{1}{r} \quad (40)$$

$$\Psi_{1c} = -d_1' J_1(\beta_{12} r) - f_1' Y_1(\beta_{12} r) - B_1' \frac{1}{\lambda_1^2 + \lambda_2^2} \left(r \ln r + \frac{\lambda_1^2 - \lambda_2^2}{2r\Omega^2} \right) - \chi_1' r - \chi_2' \frac{1}{r}. \quad (41)$$

β_{12} from Eq. (36) and s_{11} from Eq. (37a) are found to be

$$\beta_{12} = \frac{\sqrt{3 - \nu}}{\lambda_2} \Omega \quad \text{and} \quad s_{11} = -\frac{1 - \nu}{2}.$$

Unlike the cases for $n \neq 1$, the terms associated with constants A_1, B_1, A_1', and B_1' contribute to the stress and displacement fields of the spinning disk. On the other hand, the homogeneous solutions associated with constants χ_1, χ_2, χ_1', and χ_2' are irrelevant to the stress and displacement fields, and can be ignored.

Stress and Displacement Fields

After obtaining the solutions for ϕ and ψ we can write the general expressions of the in-plane stress and displacement fields for a spinning disk under stationary edge loads. It is assumed that the edge load on the outer boundary can be expanded in the following Fourier series:

$$\hat{\sigma}_{rr}(\eta) = \sum_{n=0}^{\infty} p_n \cos n\eta + p_n' \sin n\eta \quad (42)$$

$$\hat{\sigma}_{r\eta}(\eta) = \sum_{n=0}^{\infty} q_n' \cos n\eta + q_n \sin n\eta. \quad (43)$$

The above traction boundary conditions can be divided into two parts. The first part involves only symmetric $\hat{\sigma}_{rr}(\eta)$ and antisymmetric $\hat{\sigma}_{r\eta}(\eta)$ (i.e., $p_n' = q_n' = 0$ in Eqs. (42), (43)), and the second part involves only antisymmetric $\hat{\sigma}_{rr}(\eta)$ and symmetric $\hat{\sigma}_{r\eta}(\eta)$. The complete solution may be obtained by reassembling these two solutions. For the first problem with $p_n' = q_n' = 0$, the stress and displacement fields of the loaded disk are

$$(1 - \nu^2)\sigma_{rr}(r, \eta) = B_1(2\mu_1 r^{-1} - \mu_2 r^{-3}) \cos \eta + \sum_{n=0}^{\infty} \cos n\eta \{ c_n[(\kappa_{n1} r^{-2} - \beta_{n1}^2) J_n(\beta_{n1} r) + \kappa_{n2} r^{-1} J_{n+1}(\beta_{n1} r)] + d_n[(\kappa_{n3} r^{-2} - s_{n1}\beta_{n2}^2) J_n(\beta_{n2} r) + \kappa_{n4} r^{-1} J_{n+1}(\beta_{n2} r)] + e_n[(\kappa_{n1} r^{-2} - \beta_{n1}^2) Y_n(\beta_{n1} r) + \kappa_{n2} r^{-1} Y_{n+1}(\beta_{n1} r)] + f_n[(\kappa_{n3} r^{-2} - s_{n1}\beta_{n2}^2) Y_n(\beta_{n2} r) + \kappa_{n4} r^{-1} Y_{n+1}(\beta_{n2} r)] \} \quad (44)$$

$$(1 - \nu^2)\sigma_{r\eta}(r, \eta) = -B_1(\mu_0\mu_1 r^{-1} + \mu_2 r^{-3}) \sin \eta + \sum_{n=0}^{\infty} \sin n\eta [c_n \{ (\tfrac{1}{2}\mu_0 s_{n2}\beta_{n1}^2 - \kappa_{n1} r^{-2}) J_n(\beta_{n1} r) - \kappa_{n5} r^{-1} J_{n+1}(\beta_{n1} r) \} + d_n[(\tfrac{1}{2}\mu_0\beta_{n2}^2 - \kappa_{n3} r^{-2}) J_n(\beta_{n2} r) - \kappa_{n6} r^{-1} J_{n+1}(\beta_{n2} r)] + e_n \{ (\tfrac{1}{2}\mu_0 s_{n2}\beta_{n1}^2 - \kappa_{n1} r^{-2}) Y_n(\beta_{n1} r) - \kappa_{n5}\beta_{n1} r^{-1} Y_{n+1}(\beta_{n1} r) \} + f_n[(\tfrac{1}{2}\mu_0\beta_{n2}^2 - \kappa_{n3} r^{-2}) Y_n(\beta_{n2} r) - \kappa_{n6} r^{-1} Y_{n+1}(\beta_{n2} r)] \} \quad (45)$$

$$(1 - \nu^2)\sigma_{\eta\eta}(r, \eta) = B_1(2\nu\mu_1 r^{-1} + \mu_2 r^{-3}) \cos \eta + \sum_{n=0}^{\infty} \cos n\eta \{ c_n[(-\kappa_{n1} r^{-2} - \nu\beta_{n1}^2) J_n(\beta_{n1} r) - \kappa_{n2} r^{-1} J_{n+1}(\beta_{n1} r)] + d_n[(-\kappa_{n3} r^{-2} - \nu s_{n1}\beta_{n2}^2) J_n(\beta_{n2} r) - \kappa_{n4} r^{-1} J_{n+1}(\beta_{n2} r)] + e_n[(-\kappa_{n1} r^{-2} - \nu\beta_{n1}^2) Y_n(\beta_{n1} r) - \kappa_{n2} r^{-1} Y_{n+1}(\beta_{n1} r)] \} + f_n[(-\kappa_{n3} r^{-2} - \nu s_{n1}\beta_{n2}^2) Y_n(\beta_{n2} r) - \kappa_{n4} r^{-1} Y_{n+1}(\beta_{n2} r)] \} \quad (46)$$

$$u_r(r, \eta) = \cos \eta \left\{ \frac{A_1}{2\Omega^2} + B_1 \left[\mu_1(1 + 2 \ln r) + \frac{1}{2} \frac{\mu_2}{\mu_0} r^{-2} \right] \right\} + \sum_{n=0}^{\infty} \cos n\eta \{ c_n[\kappa_{n8} r^{-1} J_n(\beta_{n1} r) - \beta_{n1} J_{n+1}(\beta_{n1} r)] + d_n[\kappa_{n7} r^{-1} J_n(\beta_{n2} r) - s_{n1}\beta_{n2} J_{n+1}(\beta_{n2} r)] + e_n[\kappa_{n8} r^{-1} Y_n(\beta_{n1} r) - \beta_{n1} Y_{n+1}(\beta_{n1} r)] + f_n[\kappa_{n7} r^{-1} Y_n(\beta_{n2} r) - s_{n1}\beta_{n2} Y_{n+1}(\beta_{n2} r)] \} \quad (47)$$

$$u_\eta(r, \eta) = -\sin \eta \left\{ \frac{A_1}{2\Omega^2} + B_1 \left[\mu_1(1 + 2 \ln r) - \frac{1}{2} \frac{\mu_2}{\mu_0} r^{-2} \right] \right\} + \sum_{n=0}^{\infty} \sin n\eta \{ c_n[s_{n2}\beta_{n1} J_{n+1}(\beta_{n1} r) - \kappa_{n8} r^{-1} J_n(\beta_{n1} r)] + d_n[\beta_{n2} J_{n+1}(\beta_{n2} r) - \kappa_{n7} r^{-1} J_n(\beta_{n2} r)] + e_n[s_{n2}\beta_{n1} Y_{n+1}(\beta_{n1} r) - \kappa_{n8} r^{-1} Y_n(\beta_{n1} r)] + f_n[\beta_{n2} Y_{n+1}(\beta_{n2} r) - \kappa_{n7} r^{-1} Y_n(\beta_{n2} r)] \} \quad (48)$$

where the constants μ's and κ's are defined as follows:

$$\mu_0 = 1 - \nu, \quad \mu_1 = (\lambda_1^2 + \lambda_2^2)^{-1}, \quad \mu_2 = \mu_0\mu_1(\lambda_1^2 - \lambda_2^2)\Omega^{-2}$$

$$\kappa_{n1} = \mu_0(1 + s_{n2})(n^2 - n), \quad \kappa_{n2} = \mu_0(1 - n s_{n2})\beta_{n1},$$

$$\kappa_{n3} = \mu_0(1 + s_{n1})(n^2 - n), \quad \kappa_{n4} = -\mu_0(n - s_{n1})\beta_{n2},$$

$$\kappa_{n5} = -\mu_0(n - s_{n2})\beta_{n1}, \quad \kappa_{n6} = \mu_0(1 - n s_{n1})\beta_{n2},$$

$$\kappa_{n7} = n(1 + s_{n1}), \quad \kappa_{n8} = n(1 + s_{n2}).$$

The terms containing constants d_0, f_0, c_1, and e_1, which have not been defined before, in Eqs. (44)–(48) should be ignored. Their presence in Eqs. (44)–(48) is solely to make the equations more compact. Equations (44)–(48) are in analogy with the classical solutions derived through the Airy stress function for a stationary annular disk under stationary edge loads (Coker and Filon, 1957). From boundary conditions (42) and (43), together with the zero displacement conditions (12) on the inner radius, one can determine the constants in Eqs. (44)–(48) uniquely.

When the traction boundary conditions involve only antisymmetric $\hat{\sigma}_{rr}(\eta)$ and symmetric $\hat{\sigma}_{r\eta}(\eta)$, i.e., $p_n = q_n = 0$, the equations for stress and displacement can be obtained from Eqs. (44)–(48) by replacing c_n, e_n, d_n, f_n, A_1, and B_1 with their primed counterparts, bearing in mind that the terms containing

Downloaded 04 May 2010 to 171.66.16.34. Redistribution subject to ASME license or copyright; see http://www.asme.org/terms/Terms_Use.cfm

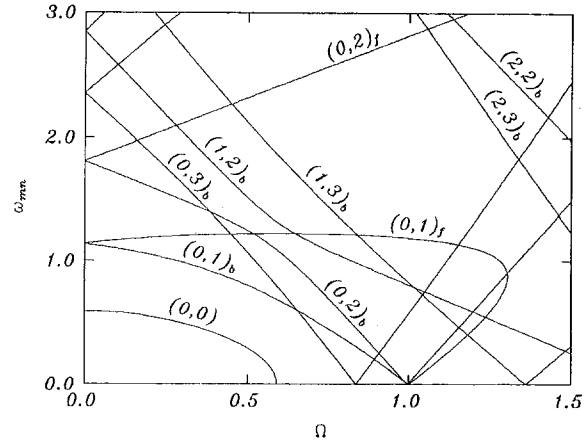


Fig. 2 Natural frequencies of in-plane vibration for a freely spinning disk with radius ratio 0.3

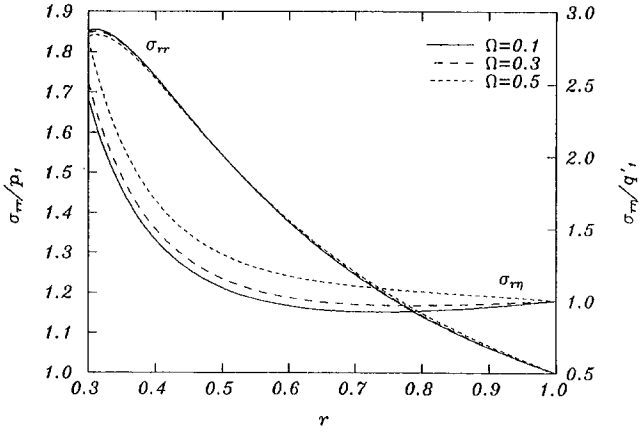


Fig. 4 The curves denoted σ_{rr} represent normal stress distribution for a disk under normal edge traction $\hat{\sigma}_{rr} = p_1 \cos \eta$. The curves denoted $\sigma_{r\eta}$ represent shear stress distribution for a disk under shear edge traction $\hat{\sigma}_{r\eta} = q'_1 \cos \eta$.

constants c'_0, e'_0, c'_1, and e'_1 should be ignored. In the meantime cos $n\eta$ in Eqs. (44), (46), (47) should be replaced by sin $n\eta$, while sin $n\eta$ in Eqs. (45), (48) should be replaced by $-\cos n\eta$.

Numerical Examples

Before presenting the stress and displacement distributions, we first examine the natural frequencies of the in-plane vibration of the freely spinning disk (Chen and Jhu, 1996). Figure 2 shows the relation between dimensionless natural frequency ω_{mn} and dimensionless rotational speed Ω for radius ratio $\zeta = 0.3$. For simplicity, only the modes with less than four nodal diameters are shown in Fig. 2. The definition of ω_{mn} is the same as that of Ω, i.e., multiplying the physical natural frequency by $b\sqrt{\rho/E}$. The Poisson ratio is assumed to be 0.3. The mode label $(m, n)_f$ represents the forward traveling modes with m nodal circles and n nodal diameters. Similarly, the subscript "b" represents a backward traveling wave. The critical speed Ω_{cn} is defined as the rotational speed at which the natural frequency of the mode $(0, n)_b$ vanishes. The first critical speed in Fig. 2 is $\Omega_{c0} = 0.591$ corresponding to the mode (0, 0). Beyond this critical speed the natural frequency ω_{00} becomes purely imaginary, and divergence instability is induced. The critical speeds corresponding to the modes with $n = 1, 2, 3$ are 0.998, 0.995, and 0.836, respectively. It is noted that mode (0, 0) is a torsional mode which involves displacement u_η only, while mode (1, 0) (beyond the range of Fig. 2) is a radial mode which involves displacement u_r only (Chen and Jhu, 1996). All the modes with nodal diameters involve both torsional and radial vibrations at the same time.

The curves denoted σ_{rr} in Figs. 3 to 5 represent the normal stress distributions along the radius from inner to outer boundary for a disk under normal edge tractions $\hat{\sigma}_{rr}(\eta) = p_n \cos n\eta$, where $n = 0$, 1, and 2, respectively, for three rotational speeds ($\Omega = 0.1, 0.3, 0.5$). On the other hand, the curves denoted $\sigma_{r\eta}$ in Figs. 3 to 5 represent the shear stress distributions for a disk under tangential edge tractions $\hat{\sigma}_{r\eta}(\eta) = q'_n \cos n\eta$. The scales for σ_{rr} and $\sigma_{r\eta}$ are different, as shown in these figures. In general, the amplitude of the stress field increases significantly as Ω increases. However, Figs. 3 and 4 show that the stress field is much more susceptible to tangential edge traction than to normal edge traction in the cases of $n = 0$ and 1.

It is noted that numerical difficulties arise in solving the constants in Eqs. (44) – (48) as the rotational speed approaches zero. More specifically, the constants c_n, d_n approach infinite and e_n, f_n approach zero as Ω approaches zero. In order to compare the above results with the case of a nonrotating disk, we obtain the solutions for $\Omega = 0$ separately through the use of the Airy stress function in the classical theory of linear elasticity. We find that the curves for $\Omega = 0$ are indistinguishable from the curves for $\Omega = 0.1$ in Figs. 3 through 5.

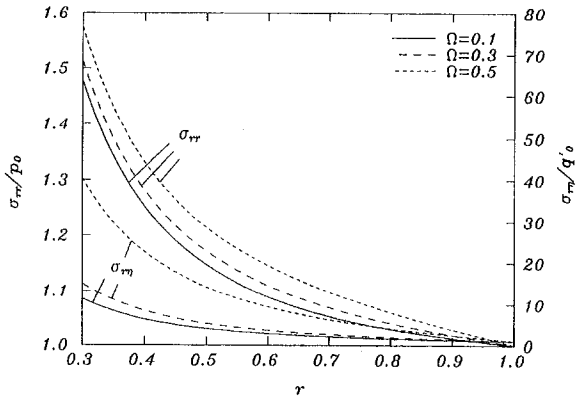


Fig. 3 The curves denoted σ_{rr} represent normal stress distribution along the radius for a disk under uniform normal edge traction $\hat{\sigma}_{rr} = p_0$. The curves denoted $\sigma_{r\eta}$ represent shear stress distribution for a disk under shear edge traction $\hat{\sigma}_{r\eta} = q'_0$.

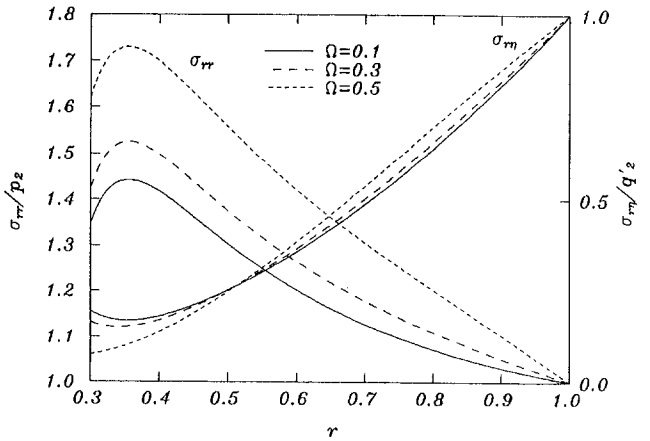


Fig. 5 The curves denoted σ_{rr} represent normal stress distribution for a disk under normal edge traction $\hat{\sigma}_{rr} = p_2 \cos 2\eta$. The curves denoted $\sigma_{r\eta}$ represent shear stress distribution for a disk under shear edge traction $\hat{\sigma}_{r\eta} = q'_2 \cos 2\eta$.

Downloaded 04 May 2010 to 171.66.16.34. Redistribution subject to ASME license or copyright; see http://www.asme.org/terms/Terms_Use.cfm

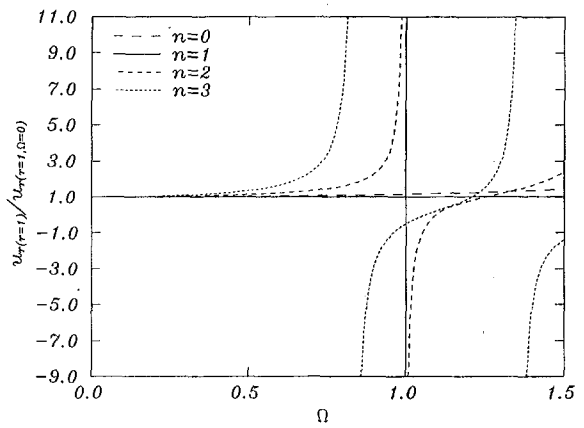


Fig. 6 Effect of rotational speed Ω on the displacement at the outer radius for a spinning disk under normal edge traction $\hat{\sigma}_{rr} = p_n \cos n\eta$

Figure 6 shows the displacement ratio $u_r/u_{r(\Omega=0)}$ at point ($r = 1$, $\eta = 0$) as function of Ω when the spinning disk is under normal edge traction $\hat{\sigma}_{rr}(\eta) = p_n \cos n\eta$. Similarly, Fig. 7 shows the relation between $u_\eta/u_{\eta(\Omega=0)}$ and Ω when the disk is under tangential edge traction $\hat{\sigma}_{r\eta}(\eta) = q_n' \cos n\eta$. For the case when the disk is under uniform normal edge traction ($n = 0$), the steady-state displacement is rather small even when the disk is spinning beyond the critical speed, as shown in Fig. 6. On the other hand, when the disk is under uniform tangential traction, the displacement grows unboundedly as Ω approaches Ω_{c0}. Steady-state response does not exist when the disk is spinning beyond the critical speed and under uniform tangential traction. This phenomenon reflects the fact that mode (0, 0) is of torsional nature. For the case when $n \geq 1$, on the other hand, either normal or tangential edge load tends to induce unbounded displacement as long as Ω is close to Ω_{cn}. It is noted in Fig. 6 that while u_r jumps to $\pm\infty$ as Ω approaches Ω_{c1}, the radial displacement is rather insentive to the rotation speed when Ω is away from Ω_{c1}.

Special Case as Ω Approaches Zero

From the above numerical calculations, we observe that the stress and displacement distributions for a spinning disk under stationary edge loads recover the classical solutions of a stationary disk under stationary edge loads as Ω approaches zero. In this section we show in an analytical manner that formulae (44)–(48) can indeed recover the classical formulae derived through the Airy stress function. Since numerical experience shows that constants c_n and d_n approach infinite, while e_n and f_n approach zero as Ω approaches zero, additional analyses are needed in this limit case.

Case $n = 0$: When the rotational speed Ω approaches zero, Bessel functions $J_0(x)$ and $Y_0(x)$ can be approximated by $1 - x^2/4$ and $2 \ln x/\pi$, respectively. Consequently, the nontrivial solutions for Φ_{0c} and Ψ_{0c} can be reduced to

$$\Phi_{0c} = \hat{c}_0 r^2 + \hat{e}_0 \ln r \tag{49}$$

$$\Psi_{0c} = \hat{d}_0' r^2 + \hat{f}_0' \ln r \tag{50}$$

where

$$\hat{c}_0 = -\frac{\Omega^2}{4\lambda_1^2} c_0, \quad \hat{e}_0 = \frac{2}{\pi} e_0, \quad \hat{d}_0' = \frac{\Omega^2}{4\lambda_2^2} d_0', \quad \hat{f}_0' = -\frac{2}{\pi} f_0'.$$

The stress and displacement fields deduced from Eqs. (49) and (50) recover the classical solutions deduced from the Airy stress function.

Case $n \geq 2$: In this case Bessel functions $J_n(x)$ and $Y_n(x)$ can be approximated as

$$J_n(x) \approx \frac{x^n}{2^n n!} - \frac{x^{n+2}}{2^{n+2}(n+1)!} \tag{51}$$

$$Y_n(x) \approx \frac{2^n (n-1)!}{-\pi x^n} + \frac{2^{n-2}(n-2)!}{-\pi x^{n-2}}. \tag{52}$$

For the problem with $p_n' = q_n' = 0$, the matrix equation for determining constants c_n, d_n, e_n, f_n can be reduced to

$$\begin{bmatrix} g_{11} + \beta_{n1}^2 h_{11} & g_{12} + \beta_{n2}^2 h_{12} & g_{13} + \beta_{n1}^2 h_{13} & g_{14} + \beta_{n2}^2 h_{14} \\ g_{21} + \beta_{n1}^2 h_{21} & g_{22} + \beta_{n2}^2 h_{22} & g_{23} + \beta_{n1}^2 h_{23} & g_{24} + \beta_{n2}^2 h_{24} \\ g_{31} + \beta_{n1}^2 h_{31} & g_{32} + \beta_{n2}^2 h_{32} & g_{33} + \beta_{n1}^2 h_{33} & g_{34} + \beta_{n2}^2 h_{34} \\ g_{41} + \beta_{n1}^2 h_{41} & g_{42} + \beta_{n2}^2 h_{42} & g_{43} + \beta_{n1}^2 h_{43} & g_{44} + \beta_{n2}^2 h_{44} \end{bmatrix} \times \begin{Bmatrix} \hat{c}_n \\ \hat{d}_n \\ \hat{e}_n \\ \hat{f}_n \end{Bmatrix} = \begin{Bmatrix} 0 \\ 0 \\ p_n \\ q_n \end{Bmatrix} \tag{53}$$

where $\hat{c}_n$, $\hat{d}_n$, $\hat{e}_n$, $\hat{f}_n$ are defined as

$$\hat{c}_n = \frac{\beta_{n1}^n c_n}{2^n n!}, \quad \hat{d}_n = \frac{\beta_{n2}^n d_n}{2^n n!}, \quad \hat{e}_n = \frac{2^n n! e_n}{\pi \beta_{n1}^n}, \quad \hat{f}_n = \frac{2^n n! f_n}{\pi \beta_{n2}^n}.$$

The constants g_{ij} and h_{ij} are given in Appendix. Since β_{n1} and β_{n2} are proportional to Ω, the terms containing constants h_{ij} are relatively unimportant in comparing with the terms containing constants g_{ij}. However, the terms containing h_{ij} should not be left out of matrix Eq. (53) entirely because the determinant of matrix g_{ij} vanishes. If we subtract the first row of Eq. (53) by the second row, and subtract the third row by the fourth row, we obtain two equations

$$[2g_{11} r^{n-1} + O(\beta_{n1}^2)]\hat{c}_n + [2g_{12} r^{n-1} + O(\beta_{n1}^2)]\hat{d}_n + O(\beta_{n1}^2)\hat{e}_n + O(\beta_{n1}^2)\hat{f}_n = 0 \tag{54}$$

$$[2g_{31} r^{n-1} + O(\beta_{n1}^2)]\hat{c}_n + [2g_{32} r^{n-1} + O(\beta_{n1}^2)]\hat{d}_n + O(\beta_{n1}^2)\hat{e}_n + O(\beta_{n1}^2)\hat{f}_n = p_n - q_n. \tag{55}$$

$O(\beta_{n1}^2)$ represents the terms proportional to β_{n1}^2, and are relatively small as Ω approaches zero. Therefore, as Ω approaches zero the terms containing $\hat{e}_n$ and $\hat{f}_n$ can be neglected in Eqs. (54) and (55). Since determinant $\begin{vmatrix} g_{11} & g_{12} \\ g_{31} & g_{32} \end{vmatrix} = 0$, the ratio between $\hat{c}_n$ and $\hat{d}_n$ approaches a constant value, i.e.,

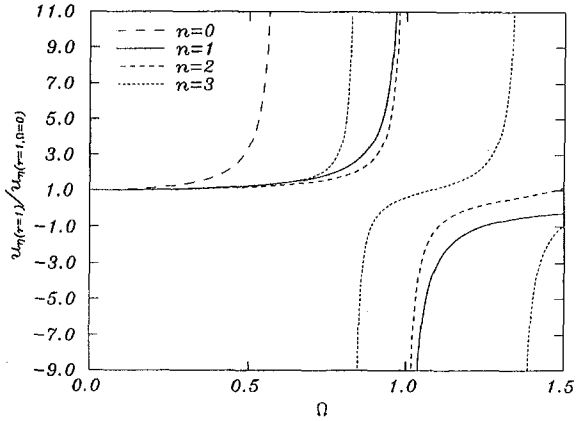


Fig. 7 Effect of rotational speed Ω on the displacement at the outer radius for a spinning disk under tangential edge traction $\hat{\sigma}_{r\eta} = q_n' \cos n\eta$

Downloaded 04 May 2010 to 171.66.16.34. Redistribution subject to ASME license or copyright; see http://www.asme.org/terms/Terms_Use.cfm

$$\frac{\hat{c}_n}{\hat{d}_n} = -\frac{g_{12}}{g_{11}} = \frac{(1-\nu-2s_{n1})\beta_{n2}^2}{(2-s_{n2}+\nu s_{n2})\beta_{n1}^2}, \tag{56}$$

while the constants $\hat{c}_n$ and $\hat{d}_n$ approach infinite as Ω approaches zero. It is noted that while the values of $\hat{c}_n$ and $\hat{d}_n$ depend on the boundary conditions p_n and q_n, the ratio in Eq. (56) is independent of the boundary conditions. This fact has also been verified numerically. By a similar procedure, with adding rows instead of subtracting, we conclude that the ratio between $\hat{e}_n$ and $\hat{f}_n$ approaches a constant value,

$$\frac{\hat{e}_n}{\hat{f}_n} = -\frac{g_{14}}{g_{13}} = \frac{(-1+\nu-2s_{n1})\beta_{n2}^2}{(2+s_{n2}-\nu s_{n2})\beta_{n1}^2}. \tag{57}$$

With the observations from Eqs. (56), (57), and the approximations (51), (52), the classical solutions for a stationary annular disk under stationary in-plane edge load can be recovered from solutions (44)–(48).

Case $n = 1$: In this case Bessel function $J_1(x)$ can be obtained from Eq. (51), while $Y_1(x)$ can be approximated as

$$Y_1(x) \approx \frac{x \ln x}{\pi} - \frac{(\ln 2 - \gamma)x}{\pi} - \frac{2}{\pi x} - \frac{x}{2\pi}$$

where γ denotes Euler's constant defined by

$$\gamma = \lim_{n\to\infty}\left(1 + \frac{1}{2} + \frac{1}{3} + \ldots + \frac{1}{n} - \ln n\right) = 0.5772\ldots.$$

As Ω approaches zero, the matrix equation for determining constants d_1, f_1, A_1, and B_1 can be reduced to

$$\begin{bmatrix} t_{11}+\beta_{12}^2 w_{11} & t_{12}+\beta_{12}^2 w_{12} & 1 & t_{14}+\Omega^2 w_{14} \\ t_{21}+\beta_{12}^2 w_{21} & t_{22}+\beta_{12}^2 w_{22} & -1 & t_{24}+\Omega^2 w_{24} \\ \beta_{12}^2 w_{31} & t_{32}+\beta_{12}^2 w_{32} & 0 & t_{34}+\Omega^2 w_{34} \\ \beta_{12}^2 w_{41} & t_{42}+\beta_{12}^2 w_{42} & 0 & t_{44}+\Omega^2 w_{44} \end{bmatrix} \times \begin{Bmatrix} \hat{d}_1 \\ \hat{f}_1 \\ \hat{A}_1 \\ \hat{B}_1 \end{Bmatrix} = \begin{Bmatrix} 0 \\ 0 \\ p_1 \\ q_1 \end{Bmatrix} \tag{58}$$

where $\hat{d}_1, \hat{f}_1, \hat{A}_1$, and $\hat{B}_1$ are defined as

$$\hat{d}_1 = \frac{\beta_{12}}{2} d_1, \quad \hat{f}_1 = \frac{2}{\pi\beta_{12}} f_1, \quad \hat{A}_1 = \frac{1}{2\Omega^2} A_1, \quad \hat{B}_1 = \frac{1}{\Omega^2} B_1.$$

t_{ij} and w_{ij} are defined in the Appendix. After adding the first two rows, and adding the last two rows of Eq. (58), one obtains

$$O(\beta_{12}^2)\hat{d}_1 + [2t_{12} + O(\beta_{12}^2)]\hat{f}_1 + [2t_{14} + O(\Omega^2)]\hat{B}_1 = 0 \tag{59}$$

$$O(\beta_{12}^2)\hat{d}_1 + [2t_{32} + O(\beta_{12}^2)]\hat{f}_1 + [2t_{34} + O(\Omega^2)]\hat{B}_1 = p_1 + q_1 \tag{60}$$

By following the similar argument as that used in the previous case for $n \geq 2$, we can conclude that the ratio between $\hat{f}_1$ and $\hat{B}_1$ approaches a constant value

$$\frac{\hat{f}_1}{\hat{B}_1} = -\frac{t_{14}}{t_{12}} = \frac{2(1+\nu)^2\Omega^2}{(3-\nu)\beta_{12}^2}. \tag{61}$$

With the observation from Eq. (61), the classical solutions for a stationary annular disk under stationary in-plane edge load can be recovered from Eqs. (44)–(48).

Conclusions and Discussions

The steady-state in-plane response of a spinning annular disk under stationary edge traction is investigated analytically. The results of this study can be summarized as follows.

1 The problem of a spinning disk-stationary load differs from the problem of a stationary disk-spinning load not only by the centrifugal effect, but also by the terms arising from the Coriolis effect.

2 While the equilibrium equations for the stationary disk-spinning load system can be decoupled by using Lame's potentials, the equations for the spinning disk-stationary load system cannot be completely decoupled. This renders the problem of a spinning disk-stationary load much more complicated.

3 The general solutions for the steady-state stress and displacement distributions are derived explicitly in the series form. These formulae are in analogy with the solutions for a stationary disk under stationary edge load, which are derived through the use of the Airy stress function in the classical theory of linear elasticity.

4 When the spinning disk is under uniform normal edge traction, the displacement response is rather small even when the rotational speed Ω is beyond the critical speed Ω_{c0}. When the disk is under uniform tangential edge traction, on the other hand, the displacement grows unboundedly as Ω approaches Ω_{c0}. This observation reflects the fact that the mode (0, 0) is of torsional nature.

5 As the rotational speed approaches zero, the solutions for the spinning disk-stationary load system are shown, both numerically and analytically, to recover the classical solutions derived through the Airy stress function for the stationary disk-stationary load system.

It is interesting to compare the physical in-plane critical speed Ω_{in} to the physical out-of-plane critical speed Ω_{out} of a spinning disk. It is noted that Ω_{in} is independent of the thickness h of the disk,

$$\Omega_{\text{in}} = \frac{\Omega_{\text{in}}^c}{b}\sqrt{\frac{E}{\rho}},$$

where Ω_{in}^c is the lowest dimensionless in-plane critical speed. On the other hand, Ω_{out} is dependent upon the thickness (Chen, 1997),

$$\Omega_{\text{out}} = \frac{\Omega_{\text{out}}^c}{b^2}\sqrt{\frac{Eh^2}{12\rho(1-\nu^2)}},$$

where Ω_{out}^c is the lowest dimensionless out-of-plane critical speed. The ratio of these two physical critical speeds are

$$\frac{\Omega_{\text{in}}}{\Omega_{\text{out}}} = \frac{\Omega_{\text{in}}^c b}{\Omega_{\text{out}}^c h}\sqrt{12(1-\nu^2)}.$$

For a typical saw blade, we assume $b = 200$ mm, $h = 1$ mm, $\nu = 0.27$, and clamping ratio 0.5. The dimensionless critical speeds are $\Omega_{\text{in}}^c = 0.6$ and $\Omega_{\text{out}}^c = 8$, respectively (Chen and Jhu, 1996; Chen, 1997). A rough estimate based on these parameters gives us the critical speed ratio 50. In other words, in saw blade application, the out-of-plane vibration is dominant. On the other hand, in the design of spur gears and grinding wheels, the outer radius decreases while the thickness increases, say $b = 40$ mm and $h = 10$ mm. Consequently, the critical speed ratio is in the order of one. Apparently, both the in-plane and out-of-plane vibrations ought to be taken into account in these applications.

While the formulations and numerical examples presented in this paper are for a plane-stress problem, the same approach works equally well in solving a plane-strain problem with appropriate substitution in elastic constants. The corresponding plane-strain problem represents a spinning long cylinder, constrained on both ends, subject to edge loads on the outer surface with force direction perpendicular to the spinning axis and load variation independent of the axial coordinate.

References

Bhuta, P. G., and Jones, J. P., 1963, "Symmetric Planar Vibrations of a Rotating Disc," *Journal of Acoustical Society of America*, Vol. 35, No. 7, pp. 982–989.

Downloaded 04 May 2010 to 171.66.16.34. Redistribution subject to ASME license or copyright; see http://www.asme.org/terms/Terms_Use.cfm

Burdess, J. S., Wren, T., and Fawcett, J. N., 1987, "Plane Stress Vibrations in Rotating Discs," *Proceedings of Institution of Mechanical Engineers,* Vol. 201, pp. 37–44.

Chen, J.-S., 1994, "Stability Analysis of a Spinning Elastic Disk Under a Stationary Concentrated Edge Load," ASME JOURNAL OF APPLIED MECHANICS, Vol. 61, pp. 788–792.

Chen, J.-S., 1997, "Parametric Resonance of a Spinning Disk Under Space-Fixed Pulsating Edge Loads," ASME JOURNAL OF APPLIED MECHANICS, Vol. 64, pp. 139–143.

Chen, J.-S., and Jhu, J.-L., 1996, "On the In-Plane Vibration and Stability of a Spinning Annular Disk," *Journal of Sound and Vibration,* Vol. 195, No. 4, pp. 585–593.

Coker, E. G., and Filon, L. N. G., 1957, *A Treatise on Photo-Elasticity,* Cambridge University Press, London.

Doby, R., 1969, "On the Elastic Stability of Coriolis-Coupled Oscillations of a Rotating Disc," *Journal of Franklin Institute,* Vol. 288, No. 3, pp. 203–212.

Eringen, A. C., and Suhubi, W. S., 1975, *Elastodynamics,* Vol. II, Academic Press, New York.

Leung, R. C. N., and Pinnington, R. J., 1987, "Vibration of a Rotating Disc Subjected to an In-Plane Force at Its Rim, or at Its Centre," *Journal of Sound and Vibration,* Vol. 114, No. 2, pp. 281–295.

Ono, K., Chen, J.-S., and Bogy, D. B., 1991, "Stability Analysis of the Head-Disk Interface in a Flexible Disk Drive," ASME JOURNAL OF APPLIED MECHANICS, Vol. 58, pp. 1005–1014.

Shen, I. Y., and Song, Y., 1996, "Stability and Vibration of a Rotating Circular Plate Subjected to Stationary In-Plane Edge Loads," ASME JOURNAL OF APPLIED MECHANICS, Vol. 63, pp. 121–127.

Srinivasan, V., and Ramamurti, V., 1980, "Dynamic Response of an Annular Disk to a Moving Concentrated, In-Plane Edge Load," *Journal of Sound and Vibration,* Vol. 72, No. 2, pp. 251–262.

Stakgold, Ivar, 1979, *Green's Function and Boundary Value Problems,* John Wiley and Sons, New York.

APPENDIX

For the case of $n \geq 2$

$$g_{11} = -g_{21} = \kappa_{n8}\zeta^{n-1}, \quad g_{12} = -g_{22} = \kappa_{n7}\zeta^{n-1},$$

$$g_{13} = g_{23} = (1 - s_{n2})\zeta^{-n-1}, \quad g_{14} = g_{24} = (s_{n1} - 1)\zeta^{-n-1},$$

$$g_{31} = -g_{41} = \frac{\kappa_{n1}}{1 - \nu^2}, \quad g_{32} = -g_{42} = \frac{\kappa_{n3}}{1 - \nu^2},$$

$$g_{33} = g_{43} = -\frac{(n + 1)(1 - s_{n2})}{1 + \nu},$$

$$g_{34} = g_{44} = \frac{(n + 1)(1 - s_{n1})}{1 + \nu},$$

$$h_{11} = -\frac{(n + 2 + ns_{n2})\zeta^{n+1}}{4(n + 1)},$$

$$h_{12} = -\frac{[n + (2 + n)s_{n1}]\zeta^{n+1}}{4(n + 1)},$$

$$h_{13} = \frac{(n - 2 - ns_{n2})\zeta^{-n+1}}{4n(n - 1)},$$

$$h_{14} = \frac{[(n - 2)s_{n1} - n]\zeta^{-n+1}}{4n(n - 1)},$$

$$h_{21} = \frac{[n + (2 + n)s_{n2}]\zeta^{n+1}}{4(n + 1)}, \quad h_{22} = \frac{(n + 2 + ns_{n1})\zeta^{n+1}}{4(n + 1)},$$

$$h_{23} = \frac{(n + 2s_{n2} - ns_{n2})\zeta^{-n+1}}{4n(n - 1)}, \quad h_{24} = -\frac{(n - 2 - ns_{n1})\zeta^{-n+1}}{4n(n - 1)}$$

$$h_{31} = \frac{-n(1 - \nu)s_{n2} + (n - 2)\nu - n - 2}{4(1 - \nu^2)},$$

$$h_{32} = -\frac{(-n\nu + 2\nu + n + 2)s_{n1} + n(1 - \nu)}{4(1 - \nu^2)}$$

$$h_{33} = \frac{n(1 - \nu)s_{n2} + (n + 2)\nu - n + 2}{4n(1 - \nu^2)},$$

$$h_{34} = \frac{(n\nu + 2\nu - n + 2)s_{n1} + n(1 - \nu)}{4n(1 - \nu^2)}$$

$$h_{41} = \frac{\kappa_{n8}}{4(1 + \nu)}, \quad h_{42} = \frac{\kappa_{n7}}{4(1 + \nu)},$$

$$h_{43} = -\frac{1 - s_{n2}}{4(1 + \nu)}, \quad h_{44} = \frac{1 - s_{n1}}{4(1 + \nu)}.$$

For the case of $n = 1$

$$t_{11} = -t_{21} = \frac{1 + \nu}{2}, \quad t_{12} = t_{22} = -\frac{3 - \nu}{2\zeta^2},$$

$$t_{14} = t_{24} = \frac{1 + \nu}{2(3 - \nu)\zeta^2}$$

$$t_{32} = t_{42} = \frac{3 - \nu}{1 + \nu}, \quad t_{34} = t_{44} = \frac{-1}{3 - \nu}$$

$$w_{11} = \frac{(1 - 3\nu)\zeta^2}{16},$$

$$w_{12} = \frac{(1 + \nu)\ln\zeta}{4} + \frac{2(1 + \nu)(\ln\beta_{12} - \ln 2 + \gamma) - (3 - \nu)}{8}$$

$$w_{14} = w_{24} = \frac{2(1 - \nu^2)(1 + 2\ln\zeta)}{3 - \nu}, \quad w_{21} = \frac{(5 + \nu)\zeta^2}{16}$$

$$w_{22} = \frac{-(1 + \nu)\ln\zeta}{4} - \frac{2(1 + \nu)(\ln\beta_{12} - \ln 2 + \gamma) + (3 - \nu)}{8},$$

$$w_{31} = w_{41} = \tfrac{1}{8}, \quad w_{32} = w_{42} = \frac{(1 - \nu)^2}{4(1 - \nu^2)},$$

$$w_{34} = \frac{4}{3 - \nu}, \quad w_{44} = \frac{-2(1 + \nu)}{3 - \nu}.$$

Downloaded 04 May 2010 to 171.66.16.34. Redistribution subject to ASME license or copyright; see http://www.asme.org/terms/Terms_Use.cfm

Derivation of Plate Theory Accounting Asymptotically Correct Shear Deformation

V. G. Sutyrin
Department of Mechanical Engineering,
Wayne State University,
Detroit, MI 48202
Mem. ASME.

The focus of this paper is the development of linear, asymptotically correct theories for inhomogeneous orthotropic plates, for example, laminated plates with orthotropic laminae. It is noted that the method used can be easily extended to develop nonlinear theories for plates with generally anisotropic inhomogeneity. The development, based on variational-asymptotic method, begins with three-dimensional elasticity and mathematically splits the analysis into two separate problems: a one-dimensional through-the-thickness analysis and a two-dimensional "plate" analysis. The through-the-thickness analysis provides elastic constants for use in the plate theory and approximate closed-form recovering relations for all truly three-dimensional displacements, stresses, and strains expressed in terms of plate variables. In general, the specific type of plate theory that results from variational-asymptotic method is determined by the method itself. However, the procedure does not determine the plate theory uniquely, and one may use the freedom appeared to simplify the plate theory as much as possible. The simplest and the most suitable for engineering purposes plate theory would be a "Reissner-like" plate theory, also called first-order shear deformation theory. However, it is shown that construction of an asymptotically correct Reissner-like theory for laminated plates is not possible in general. A new point of view on the variational-asymptotic method is presented, leading to an optimization procedure that permits a derived theory to be as close to asymptotical correctness as possible while it is a Reissner-like. This uniquely determines the plate theory. Numerical results from such an optimum Reissner-like theory are presented. These results include comparisons of plate displacement as well as of three-dimensional field variables and are the best of all extant Reissner-like theories. Indeed, they even surpass results from theories that carry many more generalized displacement variables. Although the derivation presented herein is inspired by, and completely equivalent to, the well-known variational-asymptotic method, the new procedure looks different. In fact, one does not have to be familiar with the variational-asymptotic method in order to follow the present derivation.

1 Introduction

For engineering structures, laminated composite materials provide excellent opportunities for structural simplicity as well as elastic couplings for potential optimization of design criteria. Although plates made of such materials have been used for some time in a variety of engineering applications, simple and efficient methods for analyzing plates with anisotropy and nonhomogeneity are still needed. This is partly due to rapid changes taking place in manufacturing technology for composite materials and partly to ever-increasing demands for accuracy and efficiency. The balance of accuracy and simplicity inherent in Reissner-like plate theories makes them quite desirable for engineering analysis. Therefore, the intent of this paper is to present a means to obtain the best possible Reissner-like theory for laminated plates. It should be also noted that the new method used for derivations is not restricted to the subject of present paper.

1.1 Background. Much of what is done in engineering analysis of laminated plates is based on classical plate theory (CPT) which, although adequate for many engineering applications for thin enough plates, has well-known limitations due to the Kirchhoff hypothesis. Many attempts have been made to improve classical theory by taking into account nonclassical behavior such as transverse shear deformation and transverse normal stresses. From the time laminated fiber-reinforced composites were first introduced, numerous works have been published, the objectives of which include the improvement of CPT for laminated plate applications. This subject is discussed at length in review papers by Librescu and Reddy (1989), Noor and Burton (1989), Liew et al. (1995), and Reissner (1985).

The present paper presents an improved derivation of the analysis presented by Sutyrin and Hodges (1995, 1996). Some parts of those papers are reproduced here to make the present paper self-contained for the benefit of the reader. One need not to read the previous paper in order to follow the derivation below. Also, the detailed historical discussion of the problem presented by Sutyrin and Hodges (1995, 1996) is only briefly summarized below.

Since Kirchhoff introduced his plate theory in the last century, scientists and engineers have not stopped searching for a more accurate and efficient two-dimensional theory through application of reduction methods applied to three-dimensional elasticity. The most popular such refinement, often called first-order shear deformation theory, was proposed by E. Reissner in the 1940s, who probably took the main idea of through-the-thickness line element rotation degrees-of-freedom from analogous beam derivation by Timoshenko in the 1920s. The Reissner equations are quite simple, have a clear mechanical

Contributed by the Applied Mechanics Division of THE AMERICAN SOCIETY OF MECHANICAL ENGINEERS for publication in the ASME JOURNAL OF APPLIED MECHANICS.

Discussion on the paper should be addressed to the Technical Editor, Professor Lewis T. Wheeler, Department of Mechanical Engineering, University of Houston, Houston, TX 77204-4792, and will be accepted until four months after final publication of the paper itself in the ASME JOURNAL OF APPLIED MECHANICS.

Manuscript received by the ASME Applied Mechanics Division, Sept. 15, 1995; final revision, Feb. 11, 1997. Associate Technical Editor: J. N. Reddy.

Copyright © 1997 by ASME

Downloaded 04 May 2010 to 171.66.16.34. Redistribution subject to ASME license or copyright; see http://www.asme.org/terms/Terms_Use.cfm

sense, are easy for finite element implementation, and are loved by engineers. However, they do not provide sufficiently accurate through-the-thickness distributions of stresses, strains, and displacements, a very important issue for fatigue, fracture, or brittle-ductile failure prediction in composite materials.

The search for both a two-dimensional plate theory and accurate "recovering relations" that allow a user to recover three-dimensional distributions of the quantities from the two-dimensional plate solution, has been intensely investigated for years. Berdichevsky (1979) was probably the first who clearly realized that different recovering relations can be compared to each other by mean of their asymptotical correctness (see below for an explanation of what is meant by asymptotical correctness). It becomes clear that the Kirchhoff's theory is asymptotically correct up to the zeroth order. V. L. Berdichevsky has constructed the asymptotically correct recovering relations up to the second order for Reissner-like equations of isotropic homogeneous plates. However, the extension of this result to the general anisotropic inhomogeneous case appeared to be a nontrivial issue. Significant contributions were made by Hodges et al. (1992–1995). A practical version of one of these theories, termed the "neo-classical" plate theory (NCPT), often provides accurate results. However, there are results reported for which the correlation of NCPT with the exact solution is not good. Successful construction of a second-order asymptotically correct plate theory has not been achieved up to now.[1] The problem is that the straightforward application of the variational-asymptotic technique leads to a theory with higher derivatives, which is asymptotically correct but not useful because of its being overly complex. One must stay in the framework of Reissner-like equations in order to get practical and meaningful results.

One of the main results of this paper is the proof of that an asymptotically correct Reissner-like second-order theory does not exist in the truly general case. That is probably the reason of why such a theory has not been found. However, having known that asymptotical correctness is the most important criterion for the theory to be accurate we propose the technique that allows to make the theory as close to asymptotical correctness as possible.

1.2 Present Approach. The second-order asymptotically correct Reissner-like theory has been developed by Sutyrin and Hodges (1995). The derivation was started from the main two-dimensional to three-dimensional exchange rule

$$u_\alpha = v_\alpha - h\zeta v_{3,\alpha} + h\phi^\nu_\alpha(\zeta)\gamma_\nu + w_\alpha \quad u_3 = v_3 + w_3 \quad (1)$$

which contains in front of the nonclassical shear degree-of-freedom, γ, a function $\phi(\zeta)$ to be found from the condition of asymptotical correctness for plate theory. It turns out that the final results happen to be independent of $\phi(\zeta)$. This at first surprising fact immediately became trivial, after we had realized that the warping, w, adjusts to make sum $h\phi^\nu_\alpha(\zeta)\gamma_\nu + w_\alpha$ to be the same up to a given order for any choice of $\phi(\zeta)$. Although $\phi(\zeta)$ seems to be the essential key of the derivation of asymptotically correct theory, the result independence of $\phi(\zeta)$ suggests that there must be a way to derive everything without introducing $\phi(\zeta)$ at all. This way has been found. It seems to be the most simple and efficient way to derive an asymptotically correct theory and it is represented here.

A linear theory for orthotropic plates is presented. However, there appear to be no obstacles to develop a nonlinear theory for plates with arbitrary physical properties. In this paper, we use some forms of tensor notation that are not in common use but are suitable for the purpose of the present investigation. The approach to be presented is actually equivalent to the variational-asymptotic method, combined with a change of variables implemented in a number of papers Berdichevsky (1979), Berdichevsky and Starosel'skii (1983), and Le (1986). However, the new procedure itself looks different and one need not be familiar with the variational-asymptotic method in order to follow the present derivation.

The essence of this new approach is that we look directly for the recovering relations that keep the two-dimensional energy Reissner-like and still give an asymptotically correct theory.

We begin with the three-dimensional formulation of the problem. Next, the notion of asymptotical correctness is defined. Classical theory is then presented, along with asymptotically correct recovering relations. The first-order shear deformation theory is then presented, first for homogeneous, isotropic plates and then in its general form. Finally, some numerical results are presented.

2 Original Three-Dimensional Formulation of the Problem

In this paper we consider only linear plate theory. Let a Cartesian system of coordinates, x_i, be chosen in such a way that x_α: $\{x_1, x_2\}$ denotes lengths along orthogonal straight lines in the mid-surface of the undeformed plate, and $x_3 \equiv h\zeta$ is the distance in the normal direction, where $-(1/2) \le \zeta \le (1/2)$ and h is the thickness of the plate. Throughout the analysis, Greek indices assume values 1 or 2; Latin indices assume values 1, 2, and 3; and repeated indices are summed over their ranges.

Asymptotical methods presuppose the existence of small parameters. In a linear theory one supposes the strain to be small. In addition to this, we consider the thickness of the plate h as a small quantity relative to the characteristic length associated with the in-plane deformation. The deformed state of plate is described by three spatial displacements, u_i, as functions of x_i. In order to explicitly introduce h into the equations, we replace the coordinate x_3 by $h\zeta$ and consider the displacement as a function of ζ, h and the plate coordinates x_α:

$$u_i(x_i) = u_i(x_\alpha, \zeta, h). \quad (2)$$

In this notation, the strain measures are

$$2\epsilon_{\alpha\beta} = u_{\alpha,\beta}(x_\alpha, \zeta, h) + u_{\beta,\alpha}(x_\alpha, \zeta, h)$$

$$2\epsilon_{\alpha 3} = \frac{1}{h} u_{\alpha,\zeta}(x_\alpha, \zeta, h) + u_{3,\alpha}(x_\alpha, \zeta, h)$$

$$\epsilon_{33} = \frac{1}{h} u_{3,\zeta}(x_\alpha, \zeta, h) \quad (3)$$

Here and below $\bullet_{,\alpha} \equiv \bullet_{,x_\alpha} \equiv \partial\bullet/\partial x_\alpha$ and $\bullet_{,\zeta} \equiv \partial\bullet/\partial\zeta$. One should note that ζ is treated differently from all other Greek letters, since it is the notation for an independent variable.

The strain energy density of a laminated plate, each lamina of which is made of orthotropic material, is written as

$$U = \tfrac{1}{2}D_\perp(\epsilon_{33} + C^{\gamma\delta}\epsilon_{\gamma\delta})^2 + \tfrac{1}{2}D^{\alpha\beta}_\angle(2\epsilon_{\alpha 3})(2\epsilon_{\beta 3}) + \tfrac{1}{2}D^{\alpha\beta\gamma\delta}_\parallel\epsilon_{\alpha\beta}\epsilon_{\gamma\delta} \quad (4)$$

where $D_\perp$, $D^{\alpha\beta}_\angle$, and $D^{\alpha\beta\gamma\delta}_\parallel$ are the dimensional material constants for transverse, shear, and in-plane energies, respectively; $C^{\gamma\delta}$ are the generalized dimensionless two-dimensional Poisson's ratios. This way of writing the energy density, taken from Berdichevsky (1979), is unusual, but it is a natural way to facilitate development of a plate theory. All the material constants may be functions of the transverse coordinate ζ.

The total elastic energy functional to be minimized is then

$$\int_S h\langle U\rangle + \mathcal{P} \to \min \quad (5)$$

[1] No one has tried to go further than the second order, and it is indeed probably pointless because the complexity of such a theory would be comparable with that of three-dimensional theory.

Downloaded 04 May 2010 to 171.66.16.34. Redistribution subject to ASME license or copyright; see http://www.asme.org/terms/Terms_Use.cfm

where $\mathcal{P}$ is the potential energy due to applied external forces; $\langle \bullet \rangle$ denotes the integral through the dimensionless thickness, ζ; S is the area occupied by plate in the $\{x_1, x_2\}$-plane. Both strain and potential energies are needed to derive an asymptotically correct theory, and we work with the total potential energy without splitting it into the strain and applied-load parts. Thus, the functional to be minimized can be represented as

$$\int_S J - \int_{\partial S} \langle P^i_\partial u_i \rangle \to \min \tag{6}$$

where

$$J = h\langle U \rangle - h\langle F^i(x_j) u_i(x_\alpha, \zeta, h) \rangle - P^i_+(x_\alpha) u^+_i(x_\alpha, h) - P^i_-(x_\alpha) u^-_i(x_\alpha, h). \tag{7}$$

Here $P_\pm$, F, and P_∂ are the applied external forces, and ∂S is the boundary of S. The notations $\bullet^\pm \equiv \bullet_\pm \equiv \bullet|_{\zeta=\pm 1/2}$ are introduced here.

The applied-load term written explicitly in Eq. (6) accounts for applied loads on the edges of the plate. In this paper, we do not consider the edge-zone problem. This is an important subject in its own right and will be treated in a later paper. Therefore, we drop the $\int_{\partial S}$ terms everywhere. As a first approximation for the actual plate boundary conditions the ones developed below can be used.

Also, the present development is not applicable if the displacement is prescribed on either the upper or lower surface of the plate. One must derive another theory in this case.

3 Definition of an Asymptotically Correct Theory

3.1 Small Parameters. Asymptotical methods rest on the existence of small parameters. In a linear theory one supposes the strain to be small. In addition to this, we consider the thickness of the plate h to be smaller than the wavelength of any deformation of the plate. Denoting this wavelength by l, this means that $\bullet_{,\alpha} = (1/l)O(\bullet)$ and that (h/l) is considered to be small relative to unity.

3.2 Definitions. To be complete, any plate theory must consist of three major parts that can be defined as follows:

1 *The main exchange rules:* A definition of the two-dimensional variables in terms of three-dimensional ones, along with a set of relations that represent the form of the three-dimensional variables in terms of two-dimensional ones, representing a sort of one-to-one correspondence between two-dimensional and three-dimensional variables. As examples of main exchange rules, see Eqs. (10)–(12) or Eqs. (38)–(40).

2 *The two-dimensional (or plate) energy:* The total potential energy as a function only of two-dimensional plate variables from which the complete two-dimensional theory can be derived.

3 *The recovering relations:* Approximations of the original three-dimensional variables (functions to be found) in terms of the two-dimensional plate variables.

Recovering relations always enable one to express the three-dimensional variables as a series with respect to (h/l). However, those series are, in general, not explicit expansions of three-dimensional variables with respect to (h/l). This is because the two-dimensional quantities that appear explicitly in the recovering relations may also depend on (h/l), since the two-dimensional plate energy may depend on (h/l). We use term *the final expansion* to denote the result obtained after first expanding all quantities pertaining to the two-dimensional theory and then substituting them into the recovering relations.

The final expansion does not necessarily coincide with the expansion of three-dimensional variables obtained from an exact three-dimensional solution of any problem. This leads us to the definition of an asymptotically correct theory.

Definition: An *asymptotically correct plate theory of a given order* is one for which the asymptotic expansion of the exact solution coincides up to the given order with the final expansion.

The following remarks must be mentioned here.

- There is no unique asymptotically correct plate theory of a given order.
- The form of the recovering relations and two-dimensional equations depends on how the two-dimensional variables are chosen.
- There is no universal rule to extract two-dimensional variables.

We also use that two different plate theories are said to be *equivalent* if each of them can be transferred to the other by a change of two-dimensional variables, and two plate theories are *asymptotically equivalent* if they have same final expansions up to given order.

It is clear that the final expansions for equivalent theories are coincident, but two asymptotically equivalent plate theories may have different final expansions in higher-order terms that are not asymptotically correct.

We discuss below how to develop plate theories that are asymptotically equivalent and correct up to the second order.

4 The Necessary Condition for Asymptotical Correctness

Supposing the recovering relations are known, we can write them symbolically:

$$\mathbf{u}(x_\alpha, \zeta, h) = \mathcal{R}[\mathbf{v}(x_\alpha, h), \zeta, h] \tag{8}$$

where $\mathbf{v}$ is a set of all plate (two-dimensional) variables, $\mathbf{u}$ is the set of all three-dimensional displacement variables, and $\mathcal{R}$ is a given functional.

In order to derive the two-dimensional energy, one has to substitute Eq. (8) into Eq. (7), making use of Eqs. (3) and (4), and drop higher-order terms. The resulting two-dimensional energy density

$$\mathcal{E} = \text{main part of } J$$

is a function of the two-dimensional strains, which we denote as $\boldsymbol{\epsilon}$.

To formulate the necessary conditions for a plate theory to be asymptotically correct let us represent the exact three-dimensional displacement in the form

$$\mathbf{u}(x_\alpha, \zeta, h) = \mathcal{R}[\mathbf{v}(x_\alpha), \zeta, h] + \boldsymbol{w}(x_\alpha, \zeta, h) \tag{9}$$

where the warping $\boldsymbol{w}$ is the difference between the recovering relations and exact values of displacements.

Substituting Eq. (9) into Eq. (7), one obtains an expression that depends on the two-dimensional strains, $\boldsymbol{\epsilon}$, and warping, $\boldsymbol{w}$. Thus, the total potential can be split into three parts:

1 The first part depends on two-dimensional strains, $\boldsymbol{\epsilon}$, only and has the asymptotical order which is intended to be made correct.

2 The second part consists of the leading interaction terms between $\boldsymbol{\epsilon}$ and $\boldsymbol{w}$. It has the same asymptotical order as the first part.

3 The third part contains only higher-order terms and can be dropped.

The necessary condition for the theory to be asymptotically correct is that the second part of the total potential energy is equal to zero for any admissible warping and two-dimensional variables.

All of this is equivalent to the variational-asymptotic method, presented by Berdichevsky (1979) and successfully applied in a number of publications (see Berdichevsky and Starosel'skii,

Downloaded 04 May 2010 to 171.66.16.34. Redistribution subject to ASME license or copyright; see http://www.asme.org/terms/Terms_Use.cfm

1983; Le, 1986). Although it is not the usual way to present the variational-asymptotic method, we found the present way to be more convenient for the purposes of present work.

5 Classical Theory

The most trivial plate theory of zeroth order can be constructed with the following choice of the main exchange rules:

$$v_i(x_\alpha) = \langle u_i(x_\alpha, \zeta)\rangle \tag{10}$$

$$u_i(x_\alpha, \zeta, h) = v_i(x_\alpha, h) + w_i(x_\alpha, \zeta, h) \tag{11}$$

$$\langle w_i(x_\alpha, \zeta, h)\rangle = 0. \tag{12}$$

The recovering relations are (see Berdichevsky, 1979)

$$u_\alpha = v_\alpha - h\zeta v_{3,\alpha}$$

$$u_3 = v_3 + hD_e^{\gamma\delta}(\zeta)A_{\gamma\delta} + hD_b^{\gamma\delta}(\zeta)B_{\gamma\delta} \tag{13}$$

where A and B are two-dimensional in-plane and bending plate measures of deformation, respectively,

$$A_{\gamma\delta} = \tfrac{1}{2}(v_{\gamma,\delta} + v_{\delta,\gamma}), \quad B_{\gamma\delta} = -hv_{3,\gamma\delta}. \tag{14}$$

Tensors $D_e^{\gamma\delta}(\zeta)$ and $D_b^{\gamma\delta}(\zeta)$ are the integrals of the following equations:

$$D_{e,\zeta}^{\gamma\delta} = -C^{\gamma\delta} \quad \langle D_e^{\gamma\delta}\rangle = 0$$

$$D_{b,\zeta}^{\gamma\delta} = -\zeta C^{\gamma\delta} \quad \langle D_b^{\gamma\delta}\rangle = 0. \tag{15}$$

The plate two-dimensional total energy is

$$\mathcal{E}_{cl} = E_{cl} + P_{cl}$$

where strain, E_{cl}, and potential, P_{cl}, energies are

$$E_{cl} = \tfrac{1}{2}hE_e^{\alpha\beta\gamma\delta}A_{\alpha\beta}A_{\gamma\delta} + \tfrac{1}{2}hE_b^{\alpha\beta\gamma\delta}B_{\alpha\beta}B_{\gamma\delta} + hE_{eb}^{\alpha\beta\gamma\delta}A_{\alpha\beta}B_{\gamma\delta}$$

$$P_{cl} = -f^i v_i + m^\alpha v_{3,\alpha} \tag{16}$$

with

$$E_e^{\alpha\beta\gamma\delta} = \langle D_\parallel^{\alpha\beta\gamma\delta}\rangle$$

$$E_{eb}^{\alpha\beta\gamma\delta} = \langle \zeta D_\parallel^{\alpha\beta\gamma\delta}\rangle$$

$$E_b^{\alpha\beta\gamma\delta} = \langle \zeta^2 D_\parallel^{\alpha\beta\gamma\delta}\rangle$$

$$f^i = P_+^i + P_-^i + h\langle F^i\rangle$$

$$m^\alpha = \tfrac{1}{2}h(P_+^\alpha - P_-^\alpha) + h^2\langle \zeta F^\alpha\rangle. \tag{17}$$

The complete plate functional to be minimized is

$$\int_S (E_{cl} + P_{cl}) + \int_{\partial S} (-f^i{}_\partial v_i + m_\partial^\alpha v_{3,\alpha}) \tag{18}$$

where

$$f^i{}_\partial = h\langle P_\partial^i\rangle \quad m_\partial^\alpha = h^2\langle \zeta P_\partial^\alpha\rangle. \tag{19}$$

In order to verify that the presented theory is asymptotically correct up to the order $(h/l)^0$, let us write the true three-dimensional displacements in the form[2]

$$u_\alpha = \underset{l\epsilon}{v_\alpha} - \underset{l\epsilon}{h\zeta v_{3,\alpha}} + \underset{l(h/l)^2\epsilon}{w_\alpha}$$

$$u_3 = \underset{h(h/l)^{-2}\epsilon}{v_3} + \underset{h\epsilon}{hD_e}: A + \underset{h\epsilon}{hD_b}: B + \underset{h(h/l)\epsilon}{w_3} \tag{20}$$

where w is the warping, satisfying by Eq. (12). The asymptotical order of each term is written under it here.

[2] The notations ":" or "·" that denotes contracting with respect to two or one indices is introduced here ($D_b: B \equiv D_b^{\gamma\delta}B_{\gamma\delta}$, for example). We also sometimes drop the indices of a tensor if an expression is clear without them (for example, $D_\parallel^{\alpha\beta\gamma\delta}$, $D_\parallel^{\alpha\beta}$, and $D_\parallel$ denote the same objects).

The strains, calculated from Eq. (20), are[3]

$$\epsilon_{\alpha\beta} = \underset{\epsilon}{A_{\alpha\beta}} + \underset{\epsilon}{\zeta B_{\alpha\beta}} + \underset{(h/l)^2\epsilon}{w_{\underline{\alpha,\beta}}} \tag{21}$$

$$2\epsilon_{\alpha 3} = \underset{(h/l)\epsilon}{\frac{1}{h}w_{\alpha,\zeta}} + \underset{(h/l)\epsilon}{hD_e}: A_{,\alpha} + \underset{(h/l)\epsilon}{hD_b}: K_{,\alpha} + \underset{(h/l)^2\epsilon}{w_{3,\alpha}} \tag{22}$$

$$\epsilon_{33} = \underset{(h/l)\epsilon}{\frac{1}{h}w_{3,\zeta}} + \underset{\epsilon}{D_{e,\zeta}}: A + \underset{\epsilon}{D_{b,\zeta}}: B\,. \tag{23}$$

Note that only the terms of order $(h/l)^0\epsilon$ are asymptotically correct.

After substituting Eq. (20) into the three-dimensional energy density Eq. (4) one gets

$$U = D_\parallel^{\alpha\beta\gamma\delta}(A_{\alpha\beta} + \zeta B_{\alpha\beta})(A_{\gamma\delta} + \zeta B_{\gamma\delta})$$
$$+ \tfrac{1}{2}D_\perp[\underline{\underline{(D_{e,\zeta}^{\gamma\delta} + C^{\gamma\delta})}}A_{\gamma\delta} + \underline{\underline{(D_{b,\zeta}^{\gamma\delta} + \zeta C^{\gamma\delta})}}B_{\gamma\delta}$$
$$+ \frac{1}{h}w_{3,\zeta} + hC^{\gamma\delta}D_{e\underline{\gamma}}: A_{,\underline{\delta}} + hC^{\gamma\delta}D_{b\underline{\gamma}}: B_{,\underline{\delta}} + C^{\gamma\delta}w_{\underline{\gamma,\delta}}]^2$$
$$+ D_\perp^{\alpha\beta}\left(\frac{1}{h}w_{\alpha,\zeta} + hD_e: A_{,\alpha} + hD_b: B_{,\alpha} + w_{3,\alpha}\right)(\alpha \to \beta)$$
$$+ D_\parallel^{\alpha\beta\gamma\delta}(A_{\alpha\beta} + \zeta B_{\alpha\beta})w_{\underline{\gamma,\delta}} + \tfrac{1}{2}D_\parallel^{\alpha\beta\gamma\delta}w_{\underline{\alpha,\beta}}w_{\underline{\gamma,\delta}}. \tag{24}$$

The double underlined terms are equal to zero due to Eqs. (15). They are the only terms that produce part 2 of the energy which needs to be made equal zero.

The two-dimensional equilibrium equations are

$$-N_{,\beta}^{\alpha\beta} = f^\alpha \quad M_{,\alpha\beta}^{\alpha\beta} = f^3 + m_{,\alpha}^\alpha \tag{25}$$

where

$$N^{\alpha\beta} = \frac{\partial E_{cl}}{\partial A_{\alpha\beta}} \quad M^{\alpha\beta} = h\frac{\partial E_{cl}}{\partial B_{\alpha\beta}}. \tag{26}$$

The choice of variables, Eq. (10), with the main exchange rule, Eq. (11), is not unique. Plate displacement might be the displacement of the middle plane, for example, or it can be the displacement of either the upper or lower surface.

With any choice of two-dimensional variables, any theory that keeps the asymptotically leading terms asymptotically correct is always asymptotically equivalent to the theory described above.

6 Order of Quantities

Since the problem under consideration is linear, the orders of all quantities can be synchronously increased or decreased, and we have to make some agreement of how to assign the orders. We assume the order of plate deformations A and B to be ϵ. The order of any quantity can be expressed as $(h/l)^n\epsilon$. We have already used this notation in Eqs. (20)–(23).

Material coefficients are treated as independent of h quantities. We denote their characteristic value by μ to facilitate understanding of some expressions, but no expansion with respect to μ is considered.

From the classical equations it can also be derived that

$$f^3 \sim \mu\left(\frac{h}{l}\right)^2\epsilon \quad f^\alpha \sim \mu\left(\frac{h}{l}\right)\epsilon \quad m^\alpha \sim \mu h\left(\frac{h}{l}\right)\epsilon \tag{27}$$

[3] The underlining of indices indicates the operation of symmetrization with respect to underlined indices. For example, $w_{\underline{\alpha,\beta}} \equiv \tfrac{1}{2}(w_{\alpha,\beta} + w_{\beta,\alpha})$.

Downloaded 04 May 2010 to 171.66.16.34. Redistribution subject to ASME license or copyright; see http://www.asme.org/terms/Terms_Use.cfm

and

$$P_{\pm}^{3} \sim hF^{3} \sim \mu\left(\frac{h}{l}\right)^{2}\epsilon \quad P_{\pm}^{\alpha} \sim hF^{\alpha} \sim \mu\left(\frac{h}{l}\right)\epsilon. \quad (28)$$

We construct a Reissner-like theory to produce quantities of order $(h/l)^2\epsilon$ that are asymptotically correct.

7 First-Order Shear Deformation Theory Equations

First-order shear deformation theory suggested by Reissner (1944, 1945) is based on five two-dimensional variables to be found: three displacements, v_i, and two rotations, θ_α. The plate energy depends on three kinds of strain:

$$A_{\alpha\beta} = v_{\underline{\alpha,\beta}}\text{—in-plane deformation} \quad (29)$$

$$K_{\alpha\beta} = h\theta_{\underline{\alpha,\beta}}\text{—bending deformation} \quad (30)$$

$$\gamma_\alpha = \theta_\alpha + v_{3,\alpha}\text{—transverse shear deformation.} \quad (31)$$

The two-dimensional equilibrium equations are

$$-N^{\alpha\beta}_{,\beta} = f^{\alpha} \quad (32)$$

$$-M^{\alpha\beta}_{,\beta} + Q^{\alpha} = m^{\alpha} \quad (33)$$

$$-Q^{\alpha}_{,\alpha} = f^{3} \quad (34)$$

where

$$N^{\alpha\beta} = \frac{\partial \mathcal{E}}{\partial A_{\alpha\beta}} \quad M^{\alpha\beta} = h\frac{\partial \mathcal{E}}{\partial K_{\alpha\beta}} \quad Q^{\alpha} = \frac{\partial \mathcal{E}}{\partial \gamma_\alpha} \quad (35)$$

and where the total strain-potential energy

$$\mathcal{E} = E_R + P_R$$

with the strain energy density being

$$E_R = \tfrac{1}{2}hE_e^{\alpha\beta\gamma\delta}A_{\alpha\beta}A_{\gamma\delta} + \tfrac{1}{2}hE_b^{\alpha\beta\gamma\delta}K_{\alpha\beta}K_{\gamma\delta} + hE_{eb}^{\alpha\beta\gamma\delta}A_{\alpha\beta}K_{\gamma\delta} + \tfrac{1}{2}hG^{\alpha\beta}\gamma_\alpha\gamma_\beta \quad (36)$$

and the potential energy density of the applied loads being

$$P_R = -f^i v_i - m^\alpha\theta_\alpha. \quad (37)$$

Here[4] $E_{(e;b)}$, f^i, and m^α are given by Eq. (17), and G is the tensor of transverse shear stiffnesses.

The Reissner equations are very attractive, since each term has a clear physical meaning, and it is convenient to base finite element methods on them. Unfortunately, Reissner's original recovering relations are written in terms of stresses only. Thus, it is difficult to judge their asymptotical correctness. To do so in the present framework requires that the Reissner equations be complemented with appropriate recovering relations. The first successful attempt for homogeneous plates was made by Berdichevsky (1979). He started from the following main exchange rules

$$v_i = \langle u_i \rangle, \quad \theta_\alpha = \frac{1}{h}\langle 12\zeta u_\alpha\rangle \quad (38)$$

$$u_\alpha = v_\alpha + h\zeta\theta_\alpha + w_\alpha, \quad u_3 = v_3 + w_3 \quad (39)$$

$$\langle w_i \rangle = 0, \quad \langle \zeta w_\alpha\rangle = 0 \quad (40)$$

and proved that the two-dimensional total energy

$$\mathcal{E}_R = \tfrac{1}{2}hE_e^{\alpha\beta\gamma\delta}A_{\alpha\beta}A_{\gamma\delta} + \tfrac{1}{2}hE_b^{\alpha\beta\gamma\delta}K_{\alpha\beta}K_{\gamma\delta} + hE_{eb}^{\alpha\beta\gamma\delta}A_{\alpha\beta}K_{\gamma\delta} + \tfrac{1}{2}hG^{\alpha\beta}\gamma_\alpha\gamma_\beta$$

$$P_e\colon A + P_b\colon K - f^i v_i - m^\alpha\theta_\alpha \quad (41)$$

where

$$P_e = \tfrac{1}{2}h(P_3^{+} - P_3^{-})C \quad (42)$$

$$P_b = \tfrac{1}{10}h(P_3^{+} + P_3^{-})C \quad (43)$$

with the recovering relations

$$u_\alpha = v_\alpha - h\zeta v_{3,\zeta} - 5h\left(\frac{\zeta^3}{3} - \frac{\zeta}{4}\right)\gamma_\alpha + h^2\frac{1}{2}\left(\zeta^2 - \frac{1}{12}\right)C\colon A_{,\alpha} + h^2\frac{1}{2}\left(\frac{\zeta^3}{3} - \frac{\zeta}{20}\right)C\colon K_{,\alpha} \quad (44)$$

$$u_3 = v_3 - h\zeta C\colon A - h\tfrac{1}{2}(\zeta^2 - \tfrac{1}{20})C\colon K \quad (45)$$

gives a theory which is asymptotically correct up to the second order. The term $P_e\colon A + P_b\colon K$ in Eq. (41) is the contribution to the energy from external forces.[5]

The above theory was derived under the assumption of upper and lower surface in-plane traction and body forces set equal to zero. This result can be extended to a special case of inhomogeneity, namely, if all the material coefficients are proportional to the same function of through-the-thickness coordinate, ζ. Although the latter case is impractical, it can be used as a test problem for debugging purposes. Another special case is pointed by Atılgan and Hodges (1992). No other asymptotically correct theories for laminated plates are known to the author.

Taking into account the beauty of the Reissner equations, we try to find the recovering relations for them in the generic case that are as close to asymptotical correctness as possible. For the purpose of our discussion, let us call any two-dimensional plate theory containing Eqs. (29)–(35) and (41) a *Reissner-like theory.*

8 Reissner-Like Theory for Orthotropic Plates

In this section we present a Reissner-like theory for orthotropic laminated plates. All the expressions given here are derived in the next section.

The strain and potential energies are represented by Eqs. (36) and (37) with $E_{(e;b)}$, f, and m given by Eq. (17). Quantities $P_{(e;b)}$ are

$$P_{(e;b)} = -P_{\pm}^{3}hD_{(e;b)}^{\pm} - h^2\langle F^3 D_{(e;b)}\rangle + (h^2P_{\pm}^{\alpha}H_{(e;b)\alpha}^{\nu\pm} + h^3\langle F^\alpha H_{(e;b)\alpha}^{\nu}\rangle)_{,\nu} \quad (46)$$

with recovering relations being

$$u_\alpha = v_\alpha - h\zeta v_{3,\alpha} + h^2H_{e\alpha}^{\nu}\colon A_{,\nu} + h^2H_{b\alpha}^{\nu}\colon B_{,\nu} + hR_\alpha$$

$$u_3 = v_3 + hD_e\colon A + hD_b\colon B + h^3J_e^{\mu\nu}\colon A_{,\mu\nu} + h^3J_b^{\mu\nu}\colon B_{,\mu\nu} + hR_3 \quad (47)$$

where

$$D_{(e;b)} = \bar{D}_{(e;b)}(\zeta) + D_{(e;b)}^{0}$$

$$H_{(e;b)\alpha}^{\nu} = \bar{H}_{(e;b)\alpha}^{\nu}(\zeta) + H_{(e;b)\alpha}^{0\nu} - \zeta\delta_\alpha^\nu D_{(e;b)}^{0} \quad (48)$$

and where $\bar{D}_{(e;b)}(\zeta)$, $\bar{H}_{(e;b)\alpha}^{\nu}(\zeta)$, $J_{(e;b)}(\zeta)$, $R_\alpha(\zeta)$, and $R_3(\zeta)$ are the solutions of the equations

[4] Notation $E_{(e;b)}$ is read as either E_e or E_b, or E_{eb}.

[5] Actually some parts of this contribution come from the three-dimensional strain energy and some from the three-dimensional potential energy. That is why we work with the total potential energy without splitting it into the strain and applied-load parts.

Downloaded 04 May 2010 to 171.66.16.34. Redistribution subject to ASME license or copyright; see http://www.asme.org/terms/Terms_Use.cfm

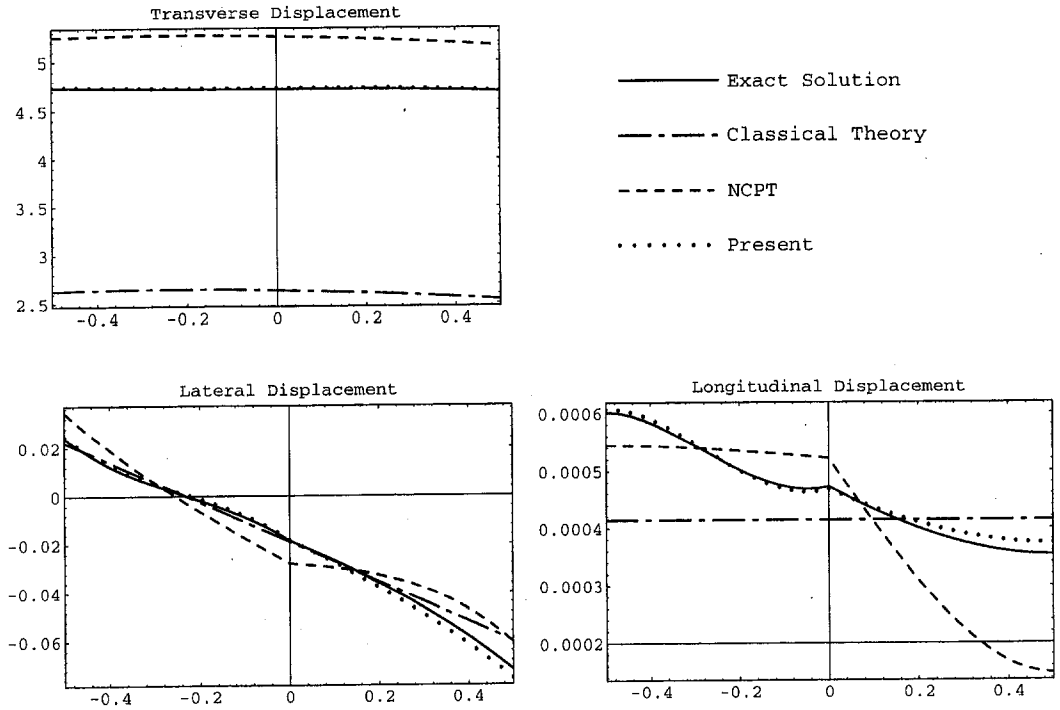


Fig. 1 Distribution of the displacement components versus the through-the-thickness coordinate from the kinematic recovery relations for an infinite two-layer plate with layup [−0.5 deg, 89.5 deg]. The quotient of the thickness by the width of the plate is equal to 0.25.

$$\bar{D}^{\gamma\delta}_{e,\zeta} = -C^{\gamma\delta}, \quad \bar{D}^{\gamma\delta}_{b,\zeta} = -\zeta C^{\gamma\delta}, \quad \langle \bar{D}^{\gamma\delta}_{(e;b)} \rangle = 0 \tag{49}$$

$$\bar{H}^{\nu}_{(e;b)\alpha,\zeta} = \bar{L}^{\ \nu}_{(e;b)\alpha} - \delta^{\nu}_{\alpha}\bar{D}_{(e;b)}, \quad \langle \bar{H}^{\nu}_{(e;b)\alpha} \rangle = 0 \tag{50}$$

$$[D_{\perp}(J^{\mu\nu}_{(e;b),\zeta} + C^{\alpha\mu}H^{\nu}_{(e;b)\alpha})]_{,\zeta} + D^{\alpha\mu}_{\angle}\bar{L}^{\ \nu}_{(e;b)\alpha} = \langle D^{\alpha\mu}_{\angle}\bar{L}^{\ \nu}_{(e;b)\alpha} \rangle,$$
$$\langle J^{\mu\nu}_{(e;b)} \rangle = 0 \tag{51}$$

$$[D_{\perp}(J^{\mu\nu}_{(e;b),\zeta} + C^{\alpha\mu}H^{\nu}_{(e;b)\alpha})]|_{\zeta=\pm 1/2} = 0$$

$$(D^{\alpha\beta}_{\angle}R_{\beta,\zeta})_{,\zeta} + hF^{\alpha} = f^{\alpha}, \quad \langle R_{\alpha} \rangle = 0$$

$$(D^{\alpha\beta}_{\angle}R_{\beta,\zeta})|_{\zeta=\pm 1/2} = \pm P^{\alpha}_{\pm} \tag{52}$$

$$[D_{\perp}(R_{3,\zeta} + C^{\alpha\beta}R_{\alpha,\beta})]_{,\zeta} + D^{\alpha\beta}_{\angle}R_{\alpha,\beta} + hF^{3} = f^{3} + \langle D^{\alpha\beta}_{\angle}R_{\alpha,\beta} \rangle,$$
$$\langle R_3 \rangle = 0$$

$$[D_{\perp}(R_{3,\zeta} + C^{\alpha\beta}R_{\alpha,\beta})]|_{\zeta=\pm 1/2} = \pm P^{3}_{\pm} \tag{53}$$

and finally where $\bar{L}^{\ \nu}_{(e;b)\alpha}$ are the solution of

$$(D^{\alpha\mu}_{\angle}\bar{L}^{\ \beta\gamma\delta}_{e\mu})_{,\zeta} + D^{\alpha\beta\gamma\delta}_{\parallel} = \langle D^{\alpha\beta\gamma\delta}_{\parallel} \rangle$$

$$(D^{\alpha\mu}_{\angle}\bar{L}^{\ \beta\gamma\delta}_{e\mu})|_{\zeta=\pm 1/2} = 0 \tag{54}$$

$$(D^{\alpha\mu}_{\angle}\bar{L}^{\ \beta\gamma\delta}_{b\mu})_{,\zeta} + \zeta D^{\alpha\beta\gamma\delta}_{\parallel} = \langle \zeta D^{\alpha\beta\gamma\delta}_{\parallel} \rangle$$

$$(D^{\alpha\mu}_{\angle}\bar{L}^{\ \beta\gamma\delta}_{b\mu}) = 0|_{\zeta=\pm 1/2} = 0. \tag{55}$$

Equations (49)–(55) make part 2 of the energy equal zero and provide asymptotical correctness. Constants $D^{0}_{(e;b)}$ and $H^{0}_{(e;b)}$ (Eq. 48) may be arbitrary and are not determined by the condition of asymptotical correctness.

The following expression must be zero in order for the theory to be Reissner-like:

$$E_{*} = \tfrac{1}{2}G^{-1}_{\alpha\beta}(E^{\alpha\nu}_{eb}: A_{,\nu} + E^{\alpha\nu}_{b}: K_{,\nu})(\alpha \to \beta)$$

$$+ \tfrac{1}{2}\langle D^{\alpha\beta}_{\angle}(\zeta)[\bar{L}^{\ \nu}_{e\alpha}(\zeta): A_{,\nu} + \bar{L}^{\ \nu}_{b\alpha}(\zeta): K_{,\nu}][\alpha \to \beta] \rangle$$

$$- \langle D^{\alpha\beta}_{\parallel}(\zeta): (A_{,\beta} + \zeta K_{,\beta})[\bar{H}^{\nu}_{e\alpha}(\zeta): A_{,\nu}$$

$$+ \bar{H}^{\nu}_{b\alpha}(\zeta): K_{,\nu} + (H^{0\nu}_{e\alpha} - \zeta\delta^{\nu}_{\alpha}D^{0}_{e}): A_{,\nu}$$

$$+ (H^{0\nu}_{b\alpha} - \zeta\delta^{\nu}_{\alpha}D^{0}_{b}): K_{,\nu}] \rangle. \tag{56}$$

This is a 12 × 12 quadratic form with respect to $A_{,\nu}$ and $B_{,\nu}$ depending on 33 variables, $D^{0}_{(e;b)}$ (6 variables), $H^{0}_{(e;b)}$ (24 variables), and G (3 variables), if all the above equations are solved. This form contains 78 coefficients, and in the general case it is not possible to make E_{*} zero. However, real plates frequently have some symmetry that can help to drive E_{*} to zero. At least one can numerically minimize the sum of the squares of the 78 coefficients by choosing 33 variables. We will discuss later some of the test calculations we have done so far.

8.1 Computational Notes. In order to solve the system of Eqs. (49)–(55) one should basically have two solvers. One of them has to solve the equation for $f(\zeta)$

$$f(\zeta)_{,\zeta} = g(\zeta) - \langle g(\zeta) \rangle \quad f|_{\zeta=\pm 1/2} = 0 \tag{57}$$

with arbitrary $g(\zeta)$, and another has to give the solution of the equation for $f(\zeta)$

$$f(\zeta)_{,\zeta} = g(\zeta) \quad \langle f(\zeta) \rangle = 0. \tag{58}$$

Using solver Eq. (57), one can start with Eqs. (54), and (55), then solve Eqs. (49) and (50) via Eq. (58). Then the quadratic form Eq. (56) must be minimized to get values of $D^{0}_{(e;b)}$, $H^{0}_{(e;b)}$ and G. After that one is ready to solve Eqs. (54)–(55) using the combination of the solvers in Eqs. (57) and (58). Equations (52)–(53) can also been solved by the combination of solvers in Eqs. (57) and (58), but they depend on external forces and are, therefore, part of the two-dimensional problem.

This procedure is not computationally expensive.

9 Derivation

9.1 Plan of the Derivation. Derivation is performed in two steps. First we derive the second-order asymptotically correct theory starting from the classical main exchange rule with-

Downloaded 04 May 2010 to 171.66.16.34. Redistribution subject to ASME license or copyright; see http://www.asme.org/terms/Terms_Use.cfm

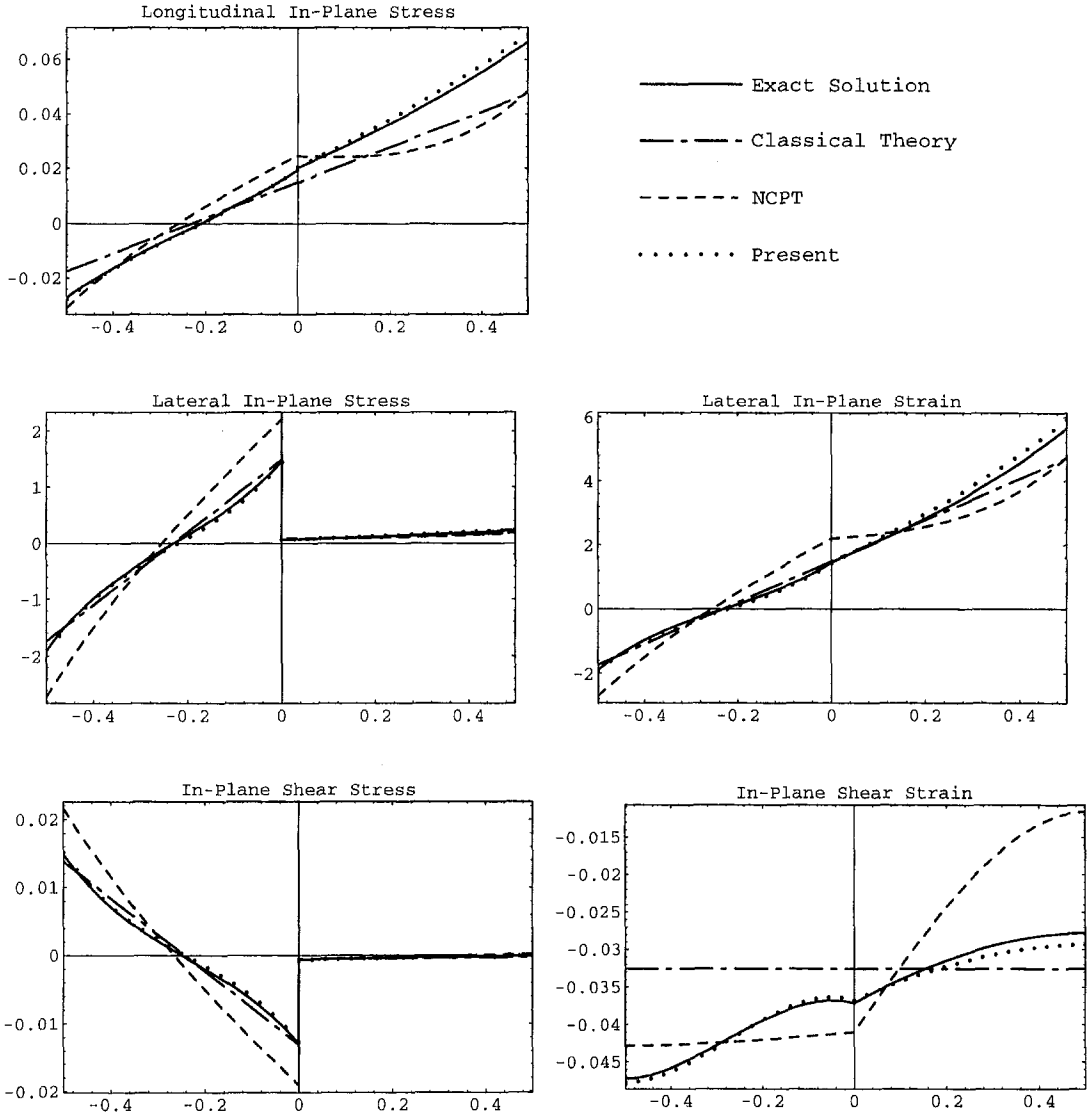


Fig. 2 Distribution of in-plane stresses and strains versus the through-the-thickness coordinate for an infinite two-layer plate with layup [−0.5 deg, 89.5 deg]. The strains were obtained using the kinematic recovery relations. The stresses are obtained from the three-dimensional constitutive equations. The longitudinal in-plane strain is equal to zero identically for each theory. The quotient of the thickness by the width of the plate is equal to 0.25.

out introducing any new degrees-of-freedom.[6] As a result we arrive to the quite complicate plate energy expression which is asymptotically correct, but contains high derivatives of the three classical degrees-of-freedom. Namely, it depends on A, B, $A_{,\nu}$, and $B_{,\nu}$. Straight use of this theory is possible, but cannot be efficient, because of its being overly complex. Besides that, one has to derive extra boundary conditions to cover the high derivatives and this task is not obvious. No one would be satisfied with such a theory. The problem of how to get rid of undesirable high derivatives remaining the theory asymptotically correct has been in the focus of investigators for the last two decades, since the variational-asymptotic method had been introduced.

The condition of asymptotical correctness does not determine the energy expression uniquely. This important observation is paid a special attention. We carefully keep as much freedom as we possibly can, because our intention is to use this freedom later while obtaining the final Reissner-like energy expression. This is a key stone of the present derivation.

The second step is the transformation of the energy obtained to the Reissner-like one. First, in order to introduce Reissner's degrees-of-freedom, we plug B expressed by the identity $B_{\alpha\beta} \equiv K_{\alpha\beta} - h\gamma_{\underline{\alpha,\beta}}$ into the energy. Energy becomes to depend on the same set of the quantities as a Reissner-like plate energy, but with the high derivatives $A_{,\nu}$, $K_{,\nu}$, $\gamma_{,\nu}$ and even $\gamma_{,\mu\nu}$. Now, we can separate all the terms into three parts:

(1) terms with A, K and γ comprising the Reissner-like plate energy,
(2) terms with $A_{,\nu}$, $K_{,\nu}$ and γ that are of the needed asymptotical order, but cannot be kept in the first-order shear deformation theory, and
(3) Terms like $\gamma_{,\nu}$, $\gamma_{,\mu\nu}A_{,\mu\nu}$, and $K_{,\mu\nu}$ of a higher asymptotical order.

The terms from the third group can just be dropped. In order to obtain Reissner-like theory one has to zero the second part. We try to do it using the coefficient freedom mentioned above. See the derivation below to find out how it is actually done.

[6] The reader who is familiar with the variational-asymptotic method should notice that this is equivalent to the three straightforward steps of the variational-asymptotic procedure.

Downloaded 04 May 2010 to 171.66.16.34. Redistribution subject to ASME license or copyright; see http://www.asme.org/terms/Terms_Use.cfm

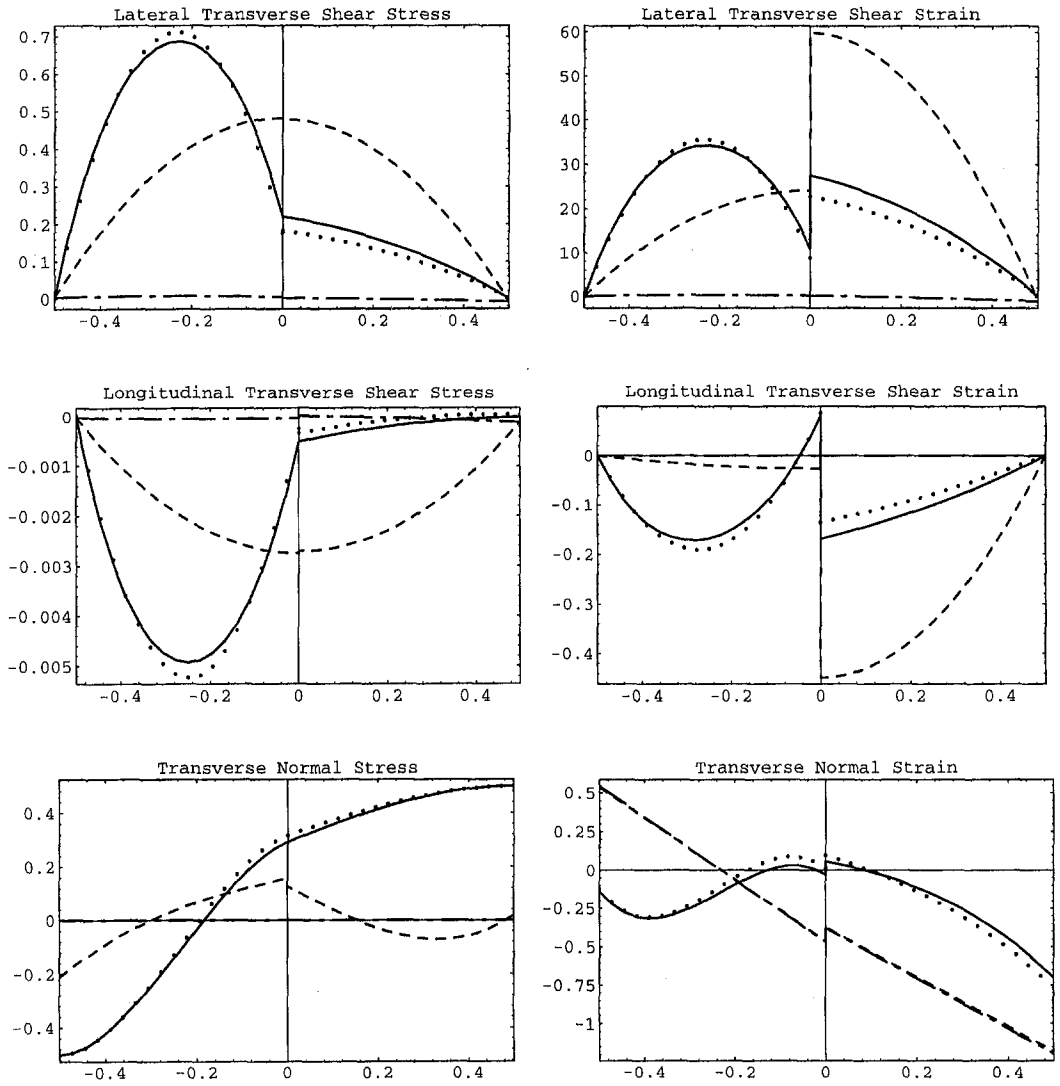


Fig. 3 Distribution of transverse stresses and strains versus the through-the-thickness coordinate for an infinite two-layer plate with layup [−0.5 deg, 89.5 deg]. The strains were obtained using the kinematic recovery relations, and stresses are obtained from the three-dimensional constitutive equations. The quotient of the thickness by the width of the plate is equal to 0.25. The legend is the same as on the previous figures.

9.2 Asymptotically Correct Energy With High Derivatives. In order to shorten all the further expressions, let us introduce the object A^a as a pair of A and B. Quasi-index a can be either e or b. If the quasi-index a equals e then

$$A^e \equiv A$$

and if the quasi-index a equals b then

$$A^b \equiv B.$$

We use the summation rule with respect to this quasi-index. For example,

$$J_a : A^a \equiv J_e : A + J_b : B.$$

Also Eq. (36) can be written in this notation as

$$E_R = \frac{h}{2} A^a : E_{ac} : A^c + \frac{h}{2} \gamma \cdot G \cdot \gamma + P_a : A^a.$$

We assumed here that $E_{ee} \equiv E_e$ and $E_{bb} \equiv E_b$.

We also need a special notation I_c defined as

$$I_e \equiv 1 \quad I_b \equiv \zeta.$$

Let us represent the displacements in the following general form:

$$u_\alpha = \underset{h(h/l)^{-1}\epsilon}{v_\alpha} - \underset{h(h/l)^{-1}\epsilon}{h\zeta v_{3,\alpha}} + \underset{h(h/l)\epsilon}{h\tilde{R}_\alpha} + \underset{h(h/l)\epsilon}{h^2 \tilde{H}^v_{c\alpha} : A^c_{,v}} + \underset{h(h/l)^3\epsilon}{w_\alpha} \tag{59}$$

$$u_3 = \underset{h(h/l)^{-2}\epsilon}{v_3} + \underset{h\epsilon}{hD_c : A^c} + \underset{h(h/l)^2\epsilon}{h\tilde{R}_3} \tag{60}$$

where $\tilde{R}_i(x_\alpha, \zeta)$ are terms coming from external forces, $D_c(\zeta)$, $\tilde{H}_c(\zeta)$, and $\tilde{J}_c(\zeta)$ are functions of ζ to be determined and $\boldsymbol{w}(\zeta, x^\alpha)$ are warping satisfying the constraint

$$\langle \boldsymbol{w} \rangle = 0. \tag{61}$$

In Eqs. (59) and (60), we put *all the possible terms* that are needed to get order $(h/l)^2\epsilon$ in the energy. The orthotropic symmetry of the laminae is taken into account here. It explains the absence of terms with A^a and $A^a_{,\mu\nu}$ in Eq. (59), and the absence of terms with $A^a_{,\mu}$ in Eq. (60).

Strains are defined according to relations Eq. (59), (60)

$$\epsilon_{\alpha\beta} = \underset{\epsilon}{A_{\alpha\beta}} + \underset{\epsilon}{\zeta B_{\alpha\beta}} + \underset{(h/l)^2\epsilon}{h\tilde{R}_{\underline{\alpha,\beta}}} + \underset{(h/l)^2\epsilon}{h^2 \tilde{H}^\nu_{c\underline{\alpha}} : A^c_{,\nu\underline{\beta}}} + \underset{(h/l)^4\epsilon}{w_{\underline{\alpha,\beta}}} \tag{62}$$

Downloaded 04 May 2010 to 171.66.16.34. Redistribution subject to ASME license or copyright; see http://www.asme.org/terms/Terms_Use.cfm

$$2\epsilon_{\alpha 3} = \underset{(h/l)^3\epsilon}{\frac{1}{h} w_{\alpha,\zeta}} + \underset{(h/l)\epsilon}{\tilde{R}_{\alpha,\zeta}} + \underset{(h/l)\epsilon}{h\tilde{L}^{\nu}_{c\alpha}: A^{c}_{,\nu}} + \underset{(h/l)^3\epsilon}{h\tilde{R}_{3,\alpha}} + \underset{(h/l)^3\epsilon}{h^3 \tilde{J}^{\mu\nu}_{c}: A^{c}_{,\mu\nu\alpha}} + \underset{(h/l)^3\epsilon}{w_{3,\alpha}} \quad (63)$$

$$\epsilon_{33} = \underset{(h/l)^4\epsilon}{\frac{1}{h} w_{3,\zeta}} + \underset{\epsilon}{D_{c,\zeta}: A^{c}} + \underset{(h/l)^2\epsilon}{\tilde{R}_{3,\zeta}} + \underset{(h/l)^2\epsilon}{h^2 \tilde{J}^{\mu\nu}_{c,\zeta}: A^{c}_{,\mu\nu}} \quad (64)$$

where the notation

$$\tilde{L}^{\nu}_{c\alpha} = \tilde{H}^{\nu}_{c\alpha,\zeta} + D_c \delta^{\nu}_{\alpha} \quad (65)$$

is introduced. The asymptotical order of each term is written under it here. Equations (14) have also been used. Only terms up to the order $(h/l)^2\epsilon$ are supposed to be asymptotically correct.

Now, one can substitute Eqs. (60)–(64) into the three-dimensional total energy density, Eq. (7), and get

$$\begin{aligned} J = E_{cl} + P_{cl} + h\Big\langle & \frac{1}{2} D_{\perp}[(D_{c,\zeta} + I_c C): A^{c}]^2 \\ & + D_{\perp}[(D_{c,\zeta} + I_c C): A^{c}] \times [h^2 \tilde{J}^{\mu\nu}_{c,\zeta}: A^{c}_{,\mu\nu} + \tilde{R}_{3,\zeta} \\ & + C^{\alpha\beta} w_{\underline{\alpha,\beta}} + C^{\alpha\beta}(h\tilde{R}_{\underline{\alpha,\beta}} + h^2 \tilde{H}^{\nu}_{c\alpha}: A^{c}_{,\nu\beta})] \\ & + D_{\perp} \frac{1}{h} w_{3,\zeta}[(D_{c,\zeta} + I_c C): A^{c}] \\ & + D_{\perp} \frac{1}{h} w_{3,\zeta}[h^2 \tilde{J}^{\mu\nu}_{c,\zeta}: A^{c}_{,\mu\nu} + \tilde{R}_{3,\zeta} + C^{\alpha\beta}(h\tilde{R}_{\underline{\alpha,\beta}} \\ & + h^2 \tilde{H}^{\nu}_{c\alpha}: A^{c}_{,\nu\beta})] + \tfrac{1}{2} D^{\alpha\beta}_{\angle}(h\tilde{L}^{\nu}_{c\alpha}: A^{c}_{,\nu} + \tilde{R}_{\alpha,\zeta})(\alpha \to \beta) \\ & + D^{\alpha\beta}_{\angle} \frac{1}{h} w_{\beta,\zeta}(h\tilde{L}^{\nu}_{c\alpha}: A^{c}_{,\nu}) + D^{\alpha\beta}_{\angle} w_{3,\beta}(h\tilde{L}^{\nu}_{c\alpha}: A^{c}_{,\nu}) \\ & + D^{\alpha\beta\gamma\delta}_{\parallel}(A_{\gamma\delta} + \zeta B_{\gamma\delta}) \times (h\tilde{R}_{\underline{\alpha,\beta}} + h^2 \tilde{H}^{\nu}_{c\underline{\alpha}}: A^{c}_{,\nu\underline{\beta}} + w_{\underline{\alpha,\beta}}) \Big\rangle \\ & - P^{\alpha}_{\pm}(h^2 \tilde{H}^{\nu}_{c\alpha}: A^{c}_{,\nu} + w_{\alpha})^{\pm} - \langle hF^{\alpha}(h^2 \tilde{H}^{\nu}_{c\alpha}: A^{c}_{,\nu} + w_{\alpha})\rangle \\ & - P^{3}_{\pm}(hD_c: A^{c} + w_3)^{\pm} - \langle hF^{3}(hD_c: A^{c} + w_3)\rangle. \end{aligned} \quad (66)$$

Notation $P_{\pm}(\bullet)^{\pm}$ means $P_{+}(\bullet)^{+} + P_{-}(\bullet)^{-}$ here. All the higher-order terms are dropped here.

Let us start the investigation with the interaction term between w_3 and A^c:

$$\langle D_{\perp} w_{3,\zeta}[(D_{c,\zeta} + I_c C): A^{c}]\rangle. \quad (67)$$

This must be zero for any admissible function $w_3(\zeta)$ satisfied by Eq. (61). One can derive that

$$[D_{\perp}((D_{c,\zeta} + I_c C): A^{c})]_{,\zeta} = \lambda \quad (68)$$

$$[D_{\perp}((D_{c,\zeta} + I_c C): A^{c})]|_{\zeta=\pm(1/2)} = 0 \quad (69)$$

where λ is a Lagrange multiplier that enforces the constraint $\langle w_3\rangle = 0$, Eq. (61).

In order to calculate λ one can integrate Eq. (68) through the range of ζ and take into account Eq. (69). It makes λ equal to zero. This procedure is kept in the all similar derivations below. In other words, the calculated value of Lagrange multipliers that enforce the constraint Eq. (61), is always substituted in the expressions below.

Since A^c can be arbitrary,

$$D_{c,\zeta} + I_c C = 0. \quad (70)$$

The solution of this equations can be written as

$$D_c(\zeta) = \bar{D}_c(\zeta) + D^{0}_{c} \quad \langle \bar{D}_c\rangle = 0 \quad (71)$$

where $\bar{D}_c$ are the same as in classical theory (see Eq. (15)) and D^0_c are arbitrary constants that are to be determined later.

The analogous derivation shows that the following equations cause other terms of the energy containing w_3 to vanish,

$$[D_{\perp}(\tilde{J}^{\mu\nu}_{c,\zeta} + C^{\alpha\mu}\tilde{H}^{\nu}_{c\alpha})]_{,\zeta} + D^{\alpha\mu}_{\angle}\tilde{L}^{\nu}_{c\alpha} = \langle D^{\alpha\mu}_{\angle}\tilde{L}^{\nu}_{c\alpha}\rangle$$

$$[D_{\perp}(\tilde{J}^{\mu\nu}_{c,\zeta} + C^{\alpha\mu}\tilde{H}^{\nu}_{c\alpha})]|_{\zeta=\pm(1/2)} = 0 \quad (72)$$

$$[D_{\perp}(\tilde{R}_{3,\zeta} + C^{\alpha\beta}\tilde{R}_{\alpha,\beta})]_{,\zeta} + D^{\alpha\beta}_{\angle}\tilde{R}_{\alpha,\beta} + hF^{3} = f^{3} + \langle D^{\alpha\beta}_{\angle}\tilde{R}_{\alpha,\beta}\rangle$$

$$[D_{\perp}(\tilde{R}_{3,\zeta} + C^{\alpha\beta}\tilde{R}_{\alpha,\beta})]|_{\zeta=\pm(1/2)} = \pm P^{3}_{\pm}. \quad (73)$$

Let us collect the terms containing w_α in Eq. (66)

$$\begin{aligned} -P^{\alpha}_{\pm} w^{\pm}_{\alpha} - h\langle F^{\alpha} w_{\alpha}\rangle + \langle & D^{\alpha\beta}_{\angle} w_{\beta,\zeta}(\tilde{R}_{\alpha,\zeta} + h\tilde{L}^{\nu}_{c\alpha}: A^{c}_{,\nu}) \\ & - hD^{\alpha\beta\gamma\delta}_{\parallel} w_{\alpha}(A_{\gamma\delta,\beta} + \zeta B_{\gamma\delta,\beta})\rangle. \end{aligned} \quad (74)$$

The integration by parts takes place in the last term here.

To complete the analysis of these equations, let us notice that if $\tilde{L}_c$ are known, $\tilde{H}_c$ from Eq. (65) are given by

$$\tilde{H}^{\beta}_{c\alpha}(\zeta) = \bar{H}^{\beta}_{c\alpha}(\zeta) + H^{0\beta}_{c\alpha} - \zeta\delta^{\beta}_{\alpha} D^{0}_{c} \quad (75)$$

where $\bar{H}_c$ is the solution of

$$\bar{H}_{c,\zeta} = \bar{L}_c - I\bar{D}_c \quad \langle \bar{H}_c\rangle = 0 \quad (76)$$

that is the same as Eq. (50). Here, $\bar{D}_c$ and D^0_c come from Eq. (71) and H^0_c is arbitrary constant to be determined later.

Equations for $\tilde{R}_\alpha(\zeta)$ can also be obtained from Eq. (74)

$$-(D^{\alpha\beta}_{\angle}\tilde{R}_{\beta,\zeta})_{,\zeta} - (hF^{\alpha} - f^{\alpha}) = 0$$

$$(D^{\alpha\beta}_{\angle}\tilde{R}_{\beta,\zeta})|_{\zeta=\pm(1/2)} = \pm P^{\alpha}_{\pm}. \quad (77)$$

The solution of Eq. (77) is

$$\tilde{R}_{\alpha}(\zeta) = \bar{R}_{\alpha}(\zeta) + R^{0}_{\alpha} \quad \langle \bar{R}_{\alpha}\rangle = 0 \quad (78)$$

where $R^0_\alpha = \langle \tilde{R}_\alpha(\zeta)\rangle$ is arbitrary constant, to be determined later.

Expressions for D_c, $\tilde{L}_c$, and $\tilde{H}_c$ contain 30 arbitrary constants:

- $6 = 2 \times 3$ of D^0_c (each D^0_c is a 2×2 symmetric matrix which has three different coefficients).
- $24 = 2 \times 12$ of H^0_c (each $H^{0\beta\gamma\delta}_{c\mu}$ is symmetrical with respect to γ and δ which makes three coefficients for each of four possible choices of μ and β).

If Eqs. (70), (72)–(73), and (77) are satisfied, the energy, Eq. (66), reduces to

$$\begin{aligned} J = E_{cl} + P_{cl} & - P^{\alpha}_{\pm}(h^2 \tilde{H}^{\nu}_{c\alpha}: A^{c}_{,\nu})^{\pm} - \langle hF^{\alpha}(h^2 \tilde{H}^{\nu}_{c\alpha}: A^{c}_{,\nu})\rangle \\ & - P^{3}_{\pm}(hD_c: A^{c})^{\pm} - \langle hF^{3}(hD_c: A^{c})\rangle \\ & + h\langle \tfrac{1}{2} D^{\alpha\beta}_{\angle}(h\tilde{L}^{\nu}_{c\alpha}: A^{c}_{,\nu} + \tilde{R}_{\alpha,\zeta})(\alpha \to \beta) \\ & - hD^{\alpha\beta\gamma\delta}_{\parallel}(A_{\gamma\delta,\beta} + \zeta B_{\gamma\delta,\beta}) \times (\tilde{R}_{\alpha} + h\tilde{H}^{\nu}_{c\alpha}: A^{c}_{,\nu})\rangle. \end{aligned} \quad (79)$$

Here the term with $D_\parallel$ is obtained through the integration by parts with respect to x^α.

9.3 Extracting Reissner-Like Energy. Now we are ready to carry out the second step of the derivation. In order to introduce two new shear degrees-of-freedom, θ_α, let us perform the following transformations with the energy, Eq. (79):

1 Exchange B with K and γ by

$$B_{\alpha\beta} = K_{\alpha\beta} - h\gamma_{\underline{\alpha,\beta}} \quad (80)$$

which follows from Eq. (31) and second expression in Eqs. (14).

Downloaded 04 May 2010 to 171.66.16.34. Redistribution subject to ASME license or copyright; see http://www.asme.org/terms/Terms_Use.cfm

2 Exchange $v_{3,\alpha}$, which enters in P_{cl}, with γ and θ by

$$v_{3,\alpha} = \gamma_\alpha - \theta_\alpha \tag{81}$$

which is Eq. (31) written in another way.

3 Add and subtract the term $(h/2)\gamma \cdot G \cdot \gamma$ where G is an unknown tensor to be determined later. Such a term is a necessary part of the first-order shear deformation energy. The added term and other appropriate terms comprise the first-order shear deformation energy. The subtracted one goes to the second part[7] of the energy denoted as E_*.

4 Perform integration by parts on all the terms like $A\gamma_{,\nu}$ to make them look like $A_{,\nu}\gamma$. Then part E_* become a quadratic form with respect $A_{,\nu}$, $K_{,\nu}$, and γ.

5 Substitute in E_* the expression for γ

$$\gamma_\alpha = G^{-1}_{\alpha\mu}\left(hE^{\mu\nu}_{eb}\colon A_{,\nu} + hE^{\mu\nu}_{b}\colon K_{,\nu} + \frac{1}{h}\, m^\mu \right) \tag{82}$$

derived from Eq. (33) by dropping all higher-order terms. This makes E_* a quadratic form with respect to $A_{,\nu}$ and $K_{,\nu}$ only.

In the course of these transformations we continually drop all higher-order terms and finally get the Reissner-like energy presented by Eqs. (41) and (46), and the following expression for the E_* part of the energy:

$$\begin{aligned} E_* = \langle & \tfrac{1}{2} D^{\alpha\beta}_{\angle}(\bar{L}^{\ \nu}_{e\alpha}\colon A_{,\nu} + \bar{L}^{\ \nu}_{b\alpha}\colon K_{,\nu})(\alpha \to \beta) \\ & + \tfrac{1}{2} G^{-1}_{\alpha\beta}(E^{\alpha\nu}_{eb}\colon A_{,\nu} + E^{\alpha\nu}_{b}\colon K_{,\nu})(\alpha \to \beta) \\ & - D^{\alpha\beta}_{\parallel}\colon (A_{,\beta} + \zeta K_{,\beta})(\bar{H}^{\nu}_{e\alpha}\colon A_{,\nu} + \bar{H}^{\nu}_{b\alpha}\colon K_{,\nu} \\ & + (H^{0\nu}_{e\alpha} - \zeta\delta^\nu_\alpha D^0_e)\colon A_{,\alpha} + (H^{0\nu}_{b\alpha} - \zeta\delta^\nu_\alpha D^0_b)\colon K_{,\alpha})\rangle. \end{aligned} \tag{83}$$

This can be rewritten in the form

$$E_* = \tfrac{1}{2} A_{,\mu}\colon E^{\mu\nu}_{*e}\colon A_{,\nu} + \tfrac{1}{2} K_{,\mu}\colon E^{\mu\nu}_{*b}\colon K_{,\nu} + A_{,\mu}\colon E^{\mu\nu}_{*eb}\colon K_{,\nu} \tag{84}$$

with

$$\begin{aligned} E^{\mu\nu\alpha\beta\gamma\delta}_{*e} &= \langle \bar{L}^{\ \mu\alpha\beta}_{e\eta} D^{\eta\theta}_{\angle} \bar{L}^{\ \nu\gamma\delta}_{e\theta}\rangle + E^{\eta\mu\alpha\beta}_{e} G^{-1}_{\eta\theta} E^{\theta\nu\gamma\delta}_{e} \\ &\quad - 2\langle (\bar{H}^{\mu\alpha\beta}_{e\eta} + H^{0\mu\alpha\beta}_{e\eta} - \zeta\delta^\mu_\eta D^{0\alpha\beta}_e) D^{\eta\nu\gamma\delta}_{\parallel}\rangle \\ E^{\mu\nu\alpha\beta\gamma\delta}_{*b} &= \langle \bar{L}^{\ \mu\alpha\beta}_{b\eta} D^{\eta\theta}_{\angle} \bar{L}^{\ \nu\gamma\delta}_{b\theta}\rangle + E^{\eta\mu\alpha\beta}_{b} G^{-1}_{\eta\theta} E^{\theta\nu\gamma\delta}_{b} \\ &\quad - 2\langle \zeta(\bar{H}^{\mu\alpha\beta}_{b\eta} + H^{0\mu\alpha\beta}_{b\eta} - \zeta\delta^\mu_\eta D^{0\alpha\beta}_b) D^{\eta\nu\gamma\delta}_{\parallel}\rangle \\ E^{\mu\nu\alpha\beta\gamma\delta}_{*eb} &= \langle \bar{L}^{\ \mu\alpha\beta}_{e\eta} D^{\eta\theta}_{\angle} \bar{L}^{\ \nu\gamma\delta}_{b\theta}\rangle + E^{\eta\mu\alpha\beta}_{e} G^{-1}_{\eta\theta} E^{\theta\nu\gamma\delta}_{b} \\ &\quad - \langle (\bar{H}^{\mu\gamma\delta}_{b\eta} + H^{0\mu\gamma\delta}_{b\eta} - \zeta\delta^\mu_\eta D^{0\gamma\delta}_b) D^{\eta\nu\alpha\beta}_{\parallel}\rangle \\ &\quad - \langle \zeta(\bar{H}^{\mu\alpha\beta}_{e\eta} + H^{0\mu\alpha\beta}_{e\eta} - \zeta\delta^\mu_\eta D^{0\alpha\beta}_e) D^{\eta\nu\gamma\delta}_{\parallel}\rangle. \end{aligned} \tag{85}$$

This expression is explicit form of Eq. (56).

Note, that explicit definition of two-dimensional variables following from Eqs. (47) is

$$\begin{aligned} \langle u_\alpha\rangle &= v_\alpha + h^2 H^{0\nu}_{e\alpha}\colon A_{,\nu} + h^2 H^{0\nu}_{b\alpha}\colon B_{,\nu} \\ \langle u_3\rangle &= v_3 + hD^0_e\colon A + hD^0_b\colon B. \end{aligned} \tag{86}$$

Equations (86) are hardly ever used in practice and presented here for the completeness only.

This finishes the derivation.

10 Numerical Results

In this section we give a few sample results to illustrate the power of the theory. For our numerical calculations, we choose a fiber-reinforced composite material which has the following material properties:

$$E_L = 25 \times 10^6 \text{ psi} \quad E_T = 10^6 \text{ psi}$$

$$G_{LT} = 0.5 \times 10^6 \text{ psi} \quad G_{TT} = 0.2 \times 10^6 \text{ psi}$$

$$\nu_{LT} = \nu_{TT} = 0.25$$

where E and G denote the Young's and shear three-dimensional moduli, respectively, L signifies the direction parallel to the fibers and T the transverse direction. These properties, along with a ply angle, allow the calculation of the material tensors, $D_\perp$, $D_\angle$, and $D_\parallel$.

The test problem is the bending of a simply-supported infinite plate under a sinusoidal load equally distributed on the upper and lower surfaces. This problem has a known exact solution by Pagano (1969, 1970) in which all the quantities are proportional either sines or cosines of the dimensionless lateral space variable. The coefficients in front of the sine and cosine terms are functions of ζ, and they can be compared with the results from the present theory as well as from NCPT.

The results for one-layer layup [15 deg] and two-layer layup [15 deg, −15 deg] have been presented by Sutyrin and Hodges (1995) and showed very good agreement with the exact analytical solution.

In this paper we present the results for the case known as the most challenging problem—cross-ply layout [0 deg, 90 deg].[8]

Figure 1 shows the distributions of the displacement through the thickness for the cross-ply plate calculated from the recovering relations.

Figure 2 and 3 shows the distributions of the stress and strain calculated by plugging the recovering relations into the three-dimensional constitutive equations.

Although many quantities are not smooth through the thickness, the results from the new theory show excellent agreement with the exact solution, even for thick enough plate ($h/l = 0.25$). Such an excellent agreement has not been obtained with any first-order shear deformation theory within the author's knowledge. Indeed, it is even better than that of many higher-order and layerwise theories. This is especially remarkable considering that through-the-thickness integration of the three-dimensional equilibrium equations was not required to get a good agreement for even transverse strain and stress.

Figure 4 shows relative error for the four-layer cross-ply case [90 deg, 0 deg, 90 deg, 0 deg].[9] It should be noticed that the accuracy of the present approach depends on how well one is able to drive E_* to zero, but does not depend on number of layers.

11 Concluding Remarks

A complete Reissner-like first-order shear deformation two-dimensional plate theory is developed for orthotropic plates which is as close to asymptotical correctness as can be obtained. In the course of developing this theory, several new observations were made:[10]

- A new technique for derivation of a plate theory is presented. Although this technique is inspired by the variational-asymptotic method of Berdichevsky (1979), the present method involves a different derivation procedure and can be understood without reference to the variational-asymptotic method.

[7] See subsection "Plan of the derivation."

[8] Rather than write a new version of our *Mathematica* (Wolfram, 1991) implementation of Pagano's exact solution for cross-ply laminates, we consider a plate, the layup of which is very close to being cross-ply: [−0.5 deg, 89.5 deg].

[9] Again we actually used [90.5 deg, 0.5 deg, 90.5 deg, 0.5 deg] layup to get Pagano's exact solution for cross-ply laminates.

[10] These concluding remarks are partly repetitive of the ones by Sutyrin and Hodges (1995, 1996).

Downloaded 04 May 2010 to 171.66.16.34. Redistribution subject to ASME license or copyright; see http://www.asme.org/terms/Terms_Use.cfm

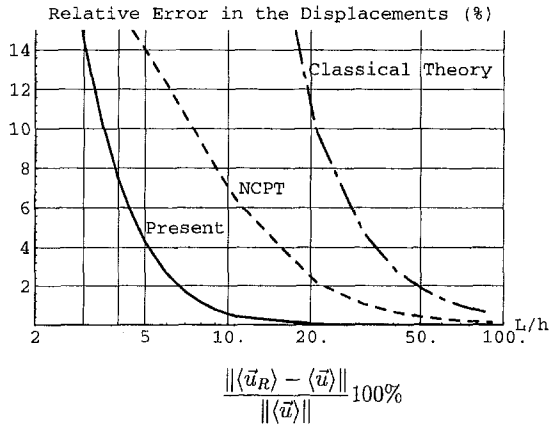


Fig. 4 Relative displacement errors versus the thickness parameter—the quotient of the width of the plate by its thickness. The horizontal axis is logarithmic. $\vec{u}$ is the three-dimensional exact vector displacement, $\vec{u}_R$ is the three-dimensional vector displacement obtaining by the recovery relations of a plate theory. The case of four-layer cross-ply layup [90.5 deg, 0.5 deg, 90.5 deg, 0.5 deg].

- The condition for any plate or shell theory to be asymptotically correct is formulated. This condition requires that certain coefficients in the full three-dimensional energy, as expressed in terms the two-dimensional variables, vanish.
- An asymptotically correct form of the theory for homogeneous plates is presented.
- For the most general inhomogeneity of plates, an asymptotically correct Reissner-like theory may not exist. However, it is shown that a minimization procedure can always be applied to bring such a theory as close as possible to asymptotical correctness. That minimization procedure is implemented in *Mathematica* (Wolfram, 1991) code.
- Numerical results obtained from the present theory, including both two-dimensional and three-dimensional quantities for a variety of particular cases of laminated plates, are presented. The accuracy of these results is superior to that of any extant first-order shear deformation theory known to authors. Indeed, the theory gives accurate *transverse* stresses and strains without employing integration of three-dimensional equilibrium equations.
- The generalization of new technique to the nonlinear theory is straightforward.

Future work to be done includes development of a nonlinear theory, extension to shells, and application of this methodology to creation of a new generation of simple and accurate finite elements.

Acknowledgments

This work was supported, in part, by the U.S. Army Research Office through the Center of Excellence for Rotorcraft Technology (Dr. Gary L. Anderson, technical monitor) at Georgia Tech where the author was Visiting Scholar in the early stages of this work. Technical discussions with Profs. Victor L. Berdichevsky (Wayne State University) and Dewey H. Hodges (Georgia Institute of Technology) are gratefully acknowledged.

References

Atilgan, A. R., and Hodges, D. H., 1992, "On the strain energy of laminated composite plates," *International Journal of Solids and Structures,* Vol. 29, pp. 2527–2543.

Berdichevsky, V. L., 1979, "Variational-asymptotic method of construction a theory of shell," *PMM,* Vol. 43, pp. 664–687.

Berdichevsky, V. L., and Starosel'skii, L. A., 1983, "On the theory of curvilinear Timoshenko-type rods," *Prikl. Matem. Mekhan.,* Vol. 47, pp. 809–817.

Hodges, D. H., Lee, B. W., and Atilgan, A. R., 1992, "Application of the variational-asymptotical method to laminated composite plates," *Proceedings of the 33rd Structures, Structural Dynamics, and Materials Conference,* Dallas, TX, AIAA Paper 92-2357, pp. 514–524.

Hodges, D. H., Lee, B. W., and Atilgan, A. R., 1993, "Application of the variational-asymptotical method to laminated composite plates," *AIAA Journal,* Vol. 31, pp. 1674–1683.

Le, K. C., 1986, "High-frequency longitudinal vibrations of elastic rods," *PMM,* Vol. 50, pp. 335–341.

Lee, B. W., Sutyrin, V. G., and Hodges, D. H., 1993, "A variable-order laminated plate theory based on the variational-asymptotical method," *Proceedings of the 34th Structures, Structural Dynamics and Materials Conference,* La Jolla, CA, AIAA Paper 93-1617, pp. 2721–2732.

Librescu, L., and Reddy, J. N., 1989, "A few remarks concerning several refined theories of anisotropic composite laminated plates," *International Journal of Engineering Science,* Vol. 27, pp. 515–527.

Liew, K. M., Xiang, Y., and Kitipornchai, S., 1995, "Research on Thick Plate Vibration—A Literature Survey," *Journal of Sound and Vibration,* Vol. 180, No. 1, pp. 163–176.

Noor, A. K., and Burton, W. S., 1989, "Assessment of shear deformation theories for multilayered composite plates," *Applied Mechanics Reviews,* Vol. 41, pp. 1–13.

Pagano, N. J., 1969, "Exact solutions for composite laminates in cylindrical bending," *Journal Composite Materials,* Vol. 3, p. 398.

Pagano, N. J., 1970, "Influence of shear coupling in cylindrical bending of anisotropic laminates," *Journal Composite Materials,* Vol. 4, p. 330.

Reissner, E., 1944, "On the theory of bending of elastic plates," *Journal of Mathematics and Physics,* Vol. 23, pp. 184–191.

Reissner, E., 1945, "The effect of transverse shear deformation on the bending of elastic plates," ASME JOURNAL OF APPLIED MECHANICS, Vol. 12, pp. A69–A77.

Reissner, E., 1985, "Reflections on the Theory of Elastic Plates," ASME *Appl. Mech. Rev.,* Vol. 38, pp. 1453–1463.

Sutyrin, V. G., and Hodges, D. H., 1995, "On Asymptotically Correct Plate Theory," *Proceedings of the 36th Structures, Structural Dynamics and Materials Conference,* New Orleans, LA, Apr. 10–13, AIAA Paper 95-1373-CP, pp. 1800–1811.

Sutyrin, V. G., and Hodges, D. H., 1996, "On Asymptotically Correct Linear Plate Theory," *International Journal of Solid and Structures,* Vol. 33, No. 25, pp. 3649–3671.

Wolfram, S., 1991, *Mathematica,* 2nd ed., Addison-Wesley, Reading, MA.

Downloaded 04 May 2010 to 171.66.16.34. Redistribution subject to ASME license or copyright; see http://www.asme.org/terms/Terms_Use.cfm

Air Entrainment During Steady-State Web Winding

M. B. Keshavan

J. A. Wickert

Department of Mechanical Engineering,
Carnegie Mellon University,
Pittsburgh, PA 15213-3890

As a web is wound at speed onto a roll, a thin layer of air becomes entrapped between it and the incoming web stream. The resulting spiral-shaped air bearing separates adjacent web layers and can extend many wraps into the roll. The air entrained during the winding process increases the propensity for lateral interlayer slippage and damage to the edges of the web. In the present paper, an in situ technique is developed for measuring the thickness of the entrained air film during winding, and parameter studies quantify the effects of such winding variables as tension, width, transport speed, and surface roughness. With a view towards evaluating different transport designs and operating conditions, three measures of air entrainment are discussed: (i) the cumulative thickness of all air layers, (ii) the thickness of the outermost air layer at the nip, and (iii) the rate at which air bleeds from the roll once it comes to rest. Measured values of the first two metrics are compared with those predicted by a derived two-dimensional reduced-order model for steady-state winding. The analysis treats the two bounding configurations of symmetric and asymmetric stacking of web layers by specifying appropriate cross-web pressure profiles.

1 Introduction

Continuous sheets of paper, cloth, polymer, sheet metal, magnetic tape, laminated packaging, and other thin materials are encountered in diverse products and industries. The term "web" describes a flat and flexible material that is transported at speed and under tension as it is manufactured or subsequently used. In paper mills, for instance, webs are guided through such processes as drying, coating, and slitting prior to becoming a final product. Plastic and metal sheet goods are processed in a similar fashion. From the standpoint of consumer applications, in magnetic and optical tape drives used for computer and video data storage, thin tape is guided through its transport system by rollers, spindles, flanges, and air bearings. In each of these cases, winding and unwinding are integral operations to the degree that wound rolls provide the most economical and convenient format for material storage.

As webs become thinner and more flexible, and as operating speeds and quality requirements grow, the process of air entrainment can limit the efficiency and precision at which webs are transported and wound. Figure 1 depicts the prototypical winding process in which a web of thickness t and width b is wound onto the roll under tension T. Air within the boundary layer surrounding the web, and moving tangentially with it at speed V, becomes entrapped between the incoming stream and those layers that are already on the roll. Some of this air squeezes out immediately at the "nip"—defined as the point of tangency between the far-field web stream and the roll—and some of it flows laterally across the web, but a significant fraction becomes entrapped within the roll itself. As a result, the outermost wraps, numbering between several and several dozen, are normally not in direct mechanical contact with their adjacent neighboring layers. Instead, they remain separated from one another by a spiral-shaped self-pressurized air film.

Poor contact between layers on the roll's periphery can lead to lateral sliding of the web (that is, out of the roll's plane), staggered wrapping, and damage to the web's edges. These problems become particularly acute following sudden acceleration or deceleration of the roll. The quality of web winding can be measured by the number and amplitude of lateral shifts, and each grows significantly with V as suggested in Fig. 2 for the case of commercial magnetic tape. Vibration, misalignment of guides and other transport components, and preferential bleeding of entrained air across one edge of the web are some of the excitation sources that produce such stack shifting. In Fig. 2, for instance, typical shift heights δ are on the order of several hundred t, with concomitant wear, damage, and wrinkling occurring to the edges of those poorly supported layers.

Air entrainment also generates uneven stresses within the roll because of the additional radial compliance afforded by the air layers. Notwithstanding nominally uniform winding tension, the uneven contact pressure between layers can lead to poor roll hardness and localized buckling of internal layers. As entrained air bleeds out once the roll is brought to rest, the resulting loss of wound-in tension can lead to roll collapse. Polymer and paper rolls, for instance, have time-dependent constitutive characteristics, and their internal stresses relax as the rolls are stored for days, months, or even years. Models that assume the roll to be linearly elastic with polar orthotropy (Tramposch, 1965; Altmann, 1968) predict that given sufficient time, the uneven stresses introduced during winding will relax, exposing the roll to damage through core collapse. In their stress analysis, Willett and Poesch (1988) incorporated some effects of air entrainment by including the air layer's compliance when approximating the roll's radial elastic modulus. Subsequently, Benson (1995) extended that modeling capability to include finite radial deformation arising from compression under large interlayer contact pressure.

The open literature on flexible media mechanics includes investigations of moving web and air-bearing systems—so-called foil bearings (Wickert, 1993)—which date to early studies on the guiding of magnetic tape (Eshel and Elrod, 1965; Licht, 1968). With regard to the problem at hand, published literature is restricted to heuristic lumped parameter models (Smith and von Behren, 1989) and to measurements of web-roller interactions (Jones, 1992; Ducotey and Good, 1995) which treat entrained air within the context of the apparent traction between the web and roller.

Design-specific solutions to air entrainment, including packing and lay-on rollers, have been engineered for a variety of

Contributed by the Applied Mechanics Division of THE AMERICAN SOCIETY OF MECHANICAL ENGINEERS for publication in the ASME JOURNAL OF APPLIED MECHANICS.

Discussion on the paper should be addressed to the Technical Editor, Professor Lewis T. Wheeler, Department of Mechanical Engineering, University of Houston, Houston, TX 77204-4792, and will be accepted until four months after final publication of the paper itself in the ASME JOURNAL OF APPLIED MECHANICS.

Manuscript received by the ASME Applied Mechanics Division, Nov. 4, 1996; final revision, Apr. 7, 1997. Associate Technical Editor: R. Becker.

Copyright © 1997 by ASME

Downloaded 04 May 2010 to 171.66.16.34. Redistribution subject to ASME license or copyright; see http://www.asme.org/terms/Terms_Use.cfm

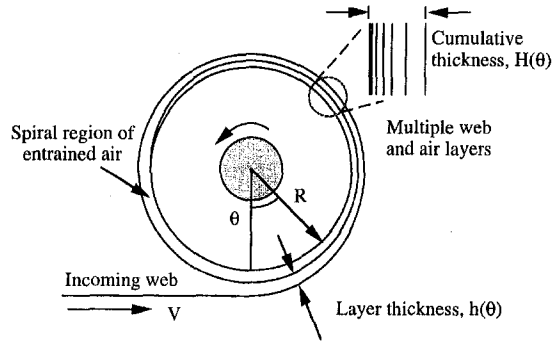


Fig. 1 Illustration of web winding. Air becomes entrapped between the incoming web stream and the roll, forming a spiral-shaped air bearing which can extend many wraps into the roll.

technologies, but often through cut-and-try approaches. With views in the present study to a broader understanding of air entrainment and to the design of web transport systems, the air film thickness during winding is determined experimentally using a laboratory-scale test bed. Over a range of operating conditions, parameter studies detail the effects of tension and speed on the cumulative air film thickness, and the thickness at the nip. A model for steady-state web winding is developed, and it is shown to predict and bound experimentally measured values over the technologically relevant range of the model's dimensionless governing parameters.

2 Measurement of Air Entrainment

A schematic of the web transport test bed is shown in Fig. 3, along with the laser interferometer that was used to measure the air film thickness with resolution in the submicron range. In characterizing the film, two quantities are defined:

- $h(\theta)$ for $\theta \geq 0$ and arbitrarily large, which is the thickness of the air film between any two adjacent web layers, and
- $H(\theta)$ for $\theta \in [0, 2\pi)$, which is the combined or cumulative thickness of all layers at a particular circumferential location. The number of such layers is unknown in advance.

The test web's tension and velocity are controlled during steady winding, and during the transient start-up and shut-down phases of operation. All tests were conducted with an opaque $t = 11$ μm thick, $b = 8$ mm wide, polyethylene-terephthalate web. The web was wound at tensions between 0.28 and 1.12 N with a settle time of 250 ms, and at speeds between 2 and 7 m/s within a one percent tolerance.

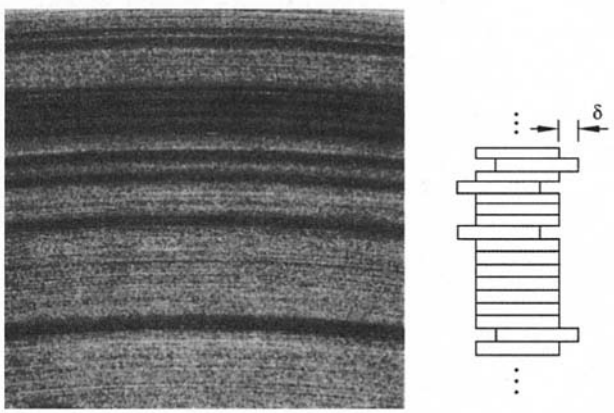


Fig. 2 Photograph of a magnetic tape roll that was wound at $T = 0.56$ N and $V = 4.6$ m/s, indicating lateral shifting or "scrambling" of layers which occurs for low tension and high speed operation; $t = 11$ μm

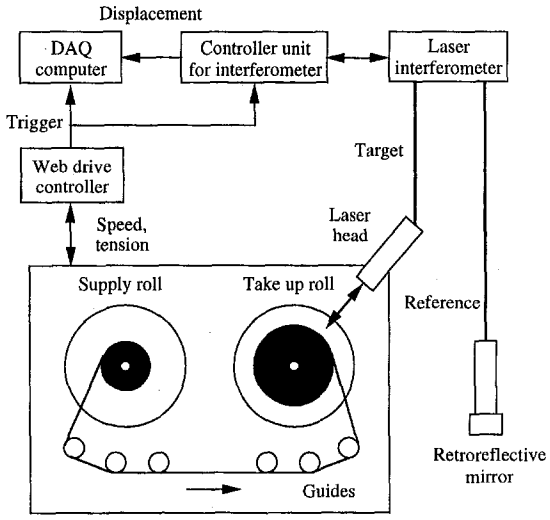


Fig. 3 Apparatus for measuring the thickness of the entrained air film during winding

The radius of the take-up roll was measured by using a commercial dual-fiber laser interferometer in which the reference beam reflected from a retroreflective mirror, and the target beam was directed at the centerline of the web on the take-up roll. In each measurement, the roll's radius was recorded as it changed from its value during steady winding (when the entrained air film was fully developed), to the smaller value reached after the roll had come to rest (when the air film was fully collapsed). During steady winding, when the radius of the take-up roll reached the preset value $R = 2$ cm, the interferometer data, tension, velocity, and the angular positions of the supply and take-up rolls were recorded for ten seconds at the sampling rate of 500 Hz. Three distinct phases occur during a typical shut-down event:

- *Steady winding.* Prior to shut-down, the rate at which air is entrained within the take-up roll is balanced by the rate at which it bleeds across the two sides of the web. Owing to the accretion of web layers during this phase, the roll's radius grows linearly at a rate proportional to V and t. Such steady growth is modulated by the roll's eccentricity and run-out, the profile of which varies from roll to roll, and even from test to test for a given roll. However, the eccentricity profile remains sensibly constant during the several rotations which are relevant to the tests conducted here. Although the amount of air entrained within the roll is a function of its nominal radius, which does grow steadily during winding, the net change in radius during the shut-down event is small when compared to R. As a result, the air entrainment process is treated as being steady immediately prior to shut-down.
- *Deceleration.* As the roll decelerates, but prior to the instant at which it comes to complete rest, the rate of air inflow at the nip decreases. During this 200–300 ms interval, the entrained air film begins to break down, and air bleeds from both the web's edges and the nip. As a result of this leakage, the roll's radius decreases, but that quantity of interest is superposed on radius changes deriving from eccentricity, accretion of web layers, and roll overshoot.
- *Rest.* Once the roll has come to rest, all further changes in its radius are attributed entirely to the bleeding of entrained air. Depending on the tension and speed at which the web was initially wound, and its width and surface roughness, several seconds can elapse between the times when the roll comes to rest and when all air has bled from it.

The cumulative thickness is identified from the measured radius after correcting time records for the effects of eccentricity

Downloaded 04 May 2010 to 171.66.16.34. Redistribution subject to ASME license or copyright; see http://www.asme.org/terms/Terms_Use.cfm

and accretion (or depletion) of web layers. Typical results for H and the roll's angular velocity are shown in Fig. 4 as functions of the roll's angular position following shut-down. In this case at least, little air bled from the roll until it had gone through approximately four revolutions, at which point the angular velocity had fallen only some 15 percent from its value during steady winding. During the rapid deceleration between four and six revolutions, the air film collapsed rapidly, and the roll came to rest after 6.8 revolutions. Overall, $H = 20$ μm of air bled from the roll following shut-down, and at least for this event, approximately two-thirds of it occurred as the roll decelerated, with the remainder having bled once the roll came to rest.

Air entrainment during winding was characterized for seven transport speeds between 2.3 and 6.9 m/s (90–270 in/s), and for three tensions between 0.28 and 0.84 N (1–3 oz). These parameter values are representative of those used in present-day high-density magnetic tape drives which are used for computer and video data storage. Obtained through the discussed procedure, typical time decay profiles that represent the bleeding of entrained air from the take-up roll are shown in Fig. 5 for the lowest and highest speeds. Two quantities of interest are identified from this figure: (i) the cumulative air film thickness obtained as the ordinate value at shut-down, and (ii) the rate at which air bled from the roll once it came to rest. The latter provides a measure of both the settling time that is required for the roll to stabilize, and the efficiency at which air bleeds from the roll. Both quantities are strong functions of the web's width and surface roughness. As expected in Fig. 5, more air was entrained at the higher running speed, with H more than doubling as the speed was increased by a factor of three. Notably, in each case, several seconds elapsed—even after the roll had stopped rotating—before the entrained air had fully bled from the wound roll.

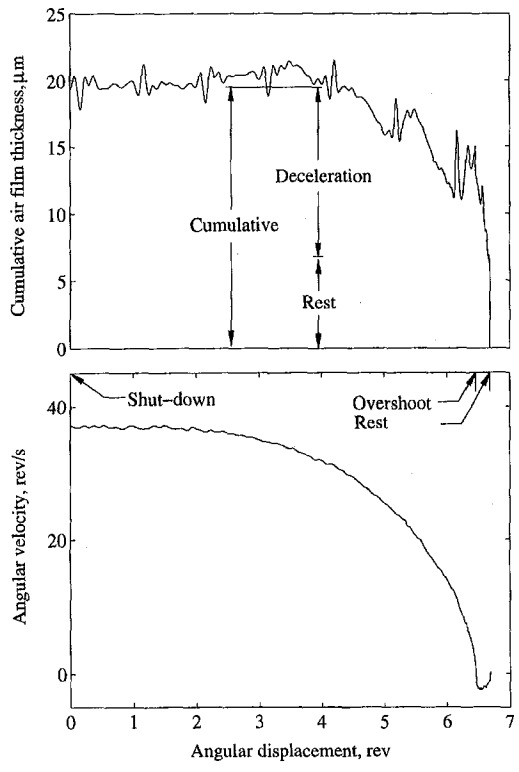


Fig. 4 Measured cumulative film thickness, and the take-up roll's angular velocity, as functions of the roll's rotation angle following shut-down. Some two-thirds of the air bled from the roll during deceleration, and the remainder bled after it had come to rest; $T = 0.56$ N, $V = 4.6$ m/s, and $\theta = 30$ deg.

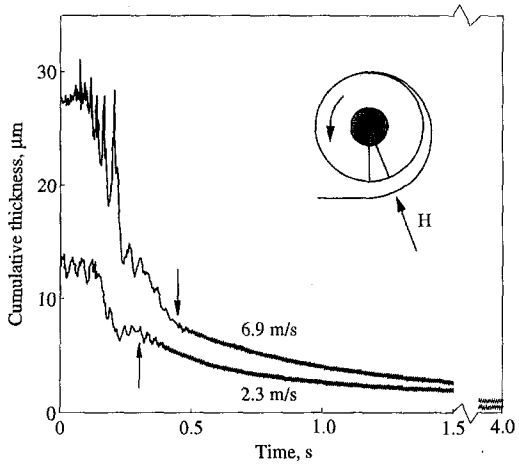


Fig. 5 Measured cumulative thicknesses as functions of time following shut-down from steady winding; $T = 0.84$ N, $V = 2.3$ m/s and 6.9 m/s, and $\theta = 10$ deg. The arrows denote the instants at which the take-up roll came to rest in each case.

3 Steady-State Winding Model

The model and film thickness measurements are discussed in dimensionless form to the degree that similarity between geometrically equivalent web winding applications exists when the appropriate dimensionless parameters are equal. The independent dimensionless variables that are most important in setting H and h are combinations of the roll's nominal radius; the web's tension, velocity, width, and surface roughness ϵ; the viscosity μ of the surrounding fluid; and the ambient pressure p_a. Inertial, centrifugal, and elastic effects are judged to be small, and variations of such environmental factors as temperature and humidity from their ambient values are likewise not considered in the following reduced-order model. Straightforward dimensional analysis suggests the functional relationship $H^* = g(\epsilon^*, b^*, \Pi^*, C^*)$ for the cumulative film thickness at specified θ, and an analogous expression for h^*. Here, all length quantities denoted by the asterisk superscript are nondimensionalized with respect to R. The operating and compressibility parameters are defined $\Pi^* = \mu bV/T$ and $C^* = T/Rbp_a$ respectively. When a particular web is considered, for which the roughness and width ratios are fixed and C^* is negligible, this dependence simplifies to $H^* \approx f(\Pi^*)$. With the film thickness so represented, experimental and model results are applicable in a consistent set of units to any geometrically similar configuration within the context of the modeled parameters.

3.1 Inlet Region. At the nip, air pressure between the web stream and the roll increases from ambient, so that the pressurized inlet region can be treated as a flux source from the standpoint of the interior bearing region. By way of analogy, geometric similarity between a conventional foil bearing and the present system is evident at the converging wedge formed at the inlet (Knox and Sweeney, 1971). One difference between these systems, however, is the absence of the circumferential exit region in the air entrainment process; instead, outward air flow occurs only through side leakage over the bearing's interior. The inlet region is hence modeled following the asymptotic solution of Eshel and Elrod (1965). For the parameter range of interest, the inlet pressure rise is roughly five percent over ambient, so that the effects of compressibility there are negligible (Eshel, 1968). In this manner, the nip thickness is given approximately by $h_0^* = 3.37(\Pi^*)^{2/3}$ with the corresponding inlet mass air flow rate being $M_i^{(1)} = \rho V h_0 b$, where ρ is the density of air.

The film thickness h_0 at the nip was found through cumulative thickness measurements taken at a number of circumferential

Downloaded 04 May 2010 to 171.66.16.34. Redistribution subject to ASME license or copyright; see http://www.asme.org/terms/Terms_Use.cfm

positions on the take-up roll. For specified operating conditions, H decreases monotonically with θ since air bleeds from the web's edges and the interlayer pressure grows. Although h_0 cannot be measured directly by using the present technique, it is determined through H found for a set of distinct θ around the roll. With these results extrapolated to $\theta = 360$ deg, the nip film thickness is obtained as $h_0 = H(0 \text{ deg}) - \hat{H}(360 \text{ deg})$, where the accent denotes an estimated or extrapolated quantity. Figure 6 depicts the variation of the cumulative thickness H around the roll, beginning some $\theta = 10$ deg from the nip and proceeding in 30 deg increments to 240 deg. Measurements for $\theta < 10$ deg are not recommended since the point of the web stream's tangency to the roll does shift slightly during winding. Behavior in the nip region can be highly variable since the nip's location itself is a function of the roll radius. The upper bound on θ was imposed in turn by inaccessibility of the interferometer's fiber optic leads. In Fig. 7, the measured and predicted results for h_0^* are compared over a one-order-of-magnitude range in Π^*. With a root-mean-square error of four percent, agreement between the measured and predicted results supports the approximations made in the inlet model, which forms one boundary condition in treating the pressurized interior region.

3.2 Roll Interior. Downstream from the nip and extending into the roll, the air film decreases monotonically in thickness owing to leakage of entrained air across the web's edges. Further, the interlayer pressure grows with θ, as is necessary to maintain the pressure differential required to preserve the web's nearly circular configuration. This spiral-shaped region can encompass several dozen wraps in a typical application (although the full extent is unknown a priori) and it terminates once asperity-level contact is established between adjacent layers.

The interior is modeled as a cascade of finite width stepped bearings as sketched in Fig. 8(*a*), where h_n denotes the dimensional film thickness of wrap n. This piecewise constant representation of h, while only an approximation, is specified since n is normally large (several dozen) in application, and since it captures the measured data with reasonable accuracy as described below. Alternative piecewise polynomial or exponential distributions can also be specified.

Cross-web bending stiffness and the effects of anticlastic curvature can become important in the related technology of foil bearings, which are formed from adjacent rigid and flexible surfaces. In that case, the web's surface can deform significantly near its edges relative to the rigid surface, locally lowering the film thickness. By contrast, in the multiwrap air entrainment process, both bearing surfaces are flexible, and to the degree that adjacent web layers will deform by sensibly equal amounts, the film thickness is expected to remain more uniform in the cross-web direction than in a comparable foil bearing. Since the number of layers separated by air before contact occurs is normally large, and since the cumulative thickness is established primarily by the outermost layers, these effects are neglected in the first approximation.

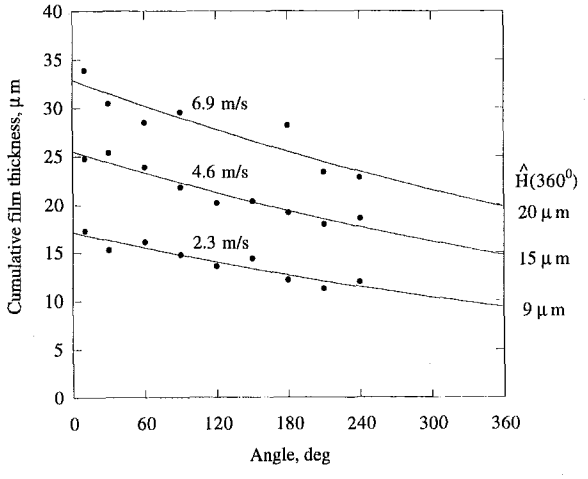


Fig. 6 Cumulative thickness measured at different circumferential locations around the roll. The film thickness at the nip is estimated as the difference between the values at 0 deg (measured) and 360 deg (extrapolated); $T = 0.28$ N, and $V = 2.3$, 4.6, and 6.9 m/s.

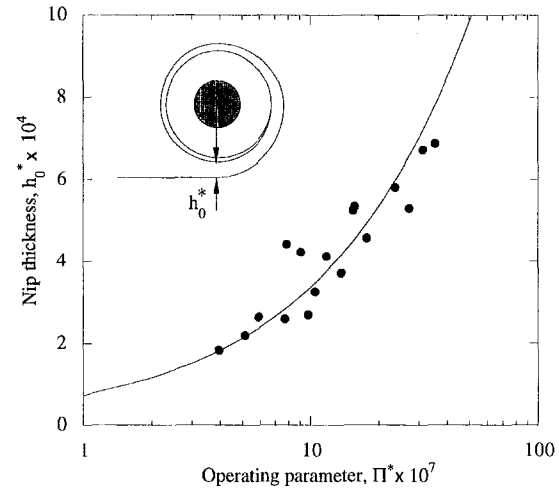


Fig. 7 Comparison between measured (●) and predicted (——) film thicknesses at the nip as a function of the operating parameter. Speeds ranged between 2.3 and 6.9 m/s, and tensions between 0.28 and 0.84 N; $\mu = 1.8 \times 10^{-5}$ Ns/m², $b = 8$ mm, and $\theta = 10$ deg.

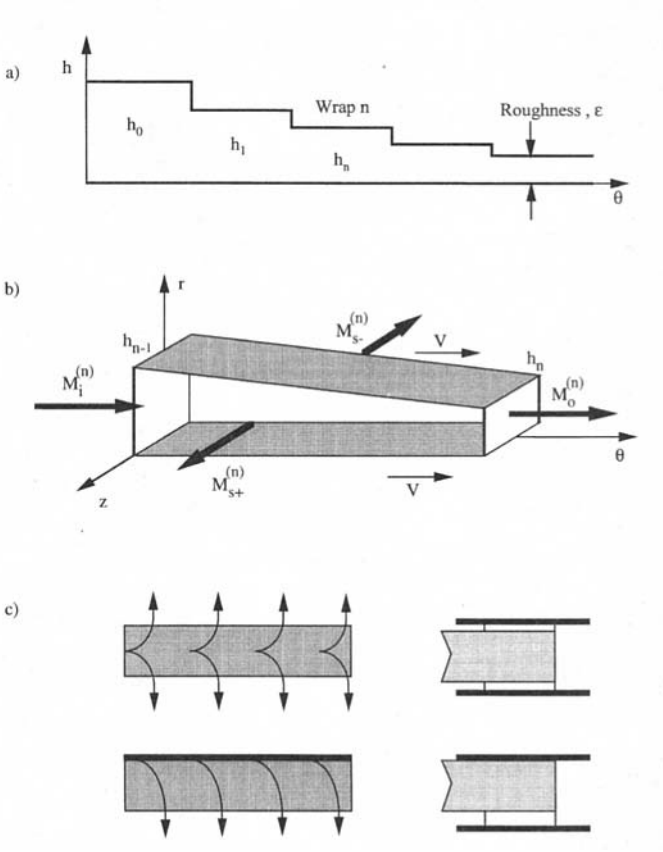


Fig. 8 Model of air entrainment during steady winding. (*a*) Piecewise constant representation of the film thickness, with contact occurring when it falls to the level of the asperity heights. (*b*) Control volume of a typical wrap indicating in-flow, outflow, and side leakages. (*c*) Symmetric and asymmetric winding configurations.

Downloaded 04 May 2010 to 171.66.16.34. Redistribution subject to ASME license or copyright; see http://www.asme.org/terms/Terms_Use.cfm

The two-dimensional pressure distribution within the interior is expressed $p(\theta, z) = p_\theta p_z$ as the product of separable gauge pressures along, and across, the web, respectively. Pressure in the winding direction grows linearly through $p_\theta = (\frac{1}{2} + \theta/2\pi)(T/Rb)$. In this representation, the accretion of each new web layer does not modify the internal tension of the web layers floating beneath it, just as the web transport test-bed maintains tension levels within a few percent of the bias value, but the pressure increments by T/Rb for each interior wrap.

Single term expansions, which satisfy the pressure's boundary conditions, are used to approximate the cross-web pressure distribution. Through this approach, potential asymmetry in side leakage can be incorporated. Two idealized treatments for cross-web air flow are considered:

- *Symmetric side leakage.* In this case, the mass flow rates $M_{s+}^{(n)}$ and $M_{s-}^{(n)}$ in Fig. 8(*b*) are identical. The cross-web pressure distribution is parabolic, symmetric about the web's centerline, and satisfies ambient pressure boundary conditions along the two edges, as indicated by the streamlines in Fig. 8(*c*). Such behavior is expected when web layers stack evenly with similar clearances between the edges of the web and each guiding flange. The resulting pressure distribution is taken as $p_z = \frac{3}{2}(1 - (2z/b)^2)$.
- *Asymmetric side leakage.* When web layers stack preferentially against one flange, air flows across only one side. The cross-web pressure distribution remains parabolic but satisfies the ambient condition along one edge, and zero gradient along the other. This situation is also sketched in Fig. 8(*c*), and the pressure distribution in this case becomes $p_z = \frac{9}{8}(1 - 4z/3b - \frac{4}{3}(z/b)^2)$.

In each case, the leading coefficients in p_z are determined through the normalization $(1/b)\int_{-b/2}^{b/2} p_z dz = 1$. This condition ensures that the average gauge pressure acting on the interior of the nth web wrap is nT/Rb. Experimental web transport systems fall between these two limiting cases, and in that sense, the symmetric and asymmetric leakage models are expected to bound measured behavior.

Entrained air satisfies the integral forms of mass and momentum conservation for a compressible fluid over each control volume, namely, a single web wrap. The density ρ of air can vary in the winding direction and is in general a function of pressure. Assuming ideal gas behavior, this functional dependence can be expressed as $p = \rho R_g T_g$, where R_g is the ideal gas constant and T_g is the air temperature. While effects of air compressibility are relatively unimportant for the inlet model, compressibility is included when treating the roll interior, where the interlayer pressure grows with the number of wound wraps. Several dozen wraps into the interior, the pressure can assume values greater than ambient.

A typical wrap is shown in Fig. 8(*b*), where $M_i^{(n)}$ and $M_o^{(n)}$ represent the mass in and out flow rates in the down-web direction, and $M_{s+}^{(n)}$ and $M_{s-}^{(n)}$ are the mass fluxes associated with side leakage. Flow in the winding direction is driven primarily by shear in the presence of a small adverse pressure gradient, and $M_i^{(n)}$ and $M_o^{(n)}$ are consequently written

$$M_i^{(n)} = U(\rho h)_{n-1} b - \int_{-b/2}^{b/2} \frac{(\rho h)_{n-1}^3}{12\mu R} p_{,\theta}(2n\pi, z)dz \quad (1)$$

$$M_o^{(n)} = U(\rho h)_n b - \int_{-b/2}^{b/2} \frac{(\rho h)_n^3}{12\mu R} p_{,\theta}(2(n-1)\pi, z)dz. \quad (2)$$

On the other hand, the side leakage terms are dominated by pressure gradient in the absence of lateral motion of the web layers, and they are expressed by

$$M_{s\pm}^{(n)} = \mp \int_{2(n-1)\pi}^{2n\pi} \frac{\rho h^3 R}{12\mu} p_{,z}(\theta, \pm b/2)d\theta \quad (3)$$

where the film thickness in each case is taken as the average of values in the neighboring layers. Imposition of the continuity condition $M_i^{(n)} - M_o^{(n)} = M_{s+}^{(n)} + M_{s-}^{(n)}$ and the use of the equation of state for an ideal gas lead to the recursive algebraic cubic equation

$$\left(1 + \frac{6}{5}C^*\{n + 0.5\} - \frac{6n\pi^2}{\kappa b^{*2}}\right) r_n^{*3} - \left(\frac{18n\pi^2}{\kappa b^{*2}}\right) r_n^{*2} - \left(\frac{18n\pi^2}{\kappa b^{*2}} + \frac{24\pi\Pi^*}{h_{n-1}^{*2}}\{1 + (n + 0.5)C^*\}\right) r_n^* + \left(-\frac{6n\pi^2}{\kappa b^{*2}} + \frac{24\pi\Pi^*}{h_{n-1}^{*2}}\{1 + (n - 0.5)C^*\} - 1 - \frac{6}{5}C^*\{n - 0.5\}\right) = 0 \quad (4)$$

in the film thickness ratio $r_n^* = h_n/h_{n-1}$. Here the factor $\kappa = 1$ (or 4) for symmetric (or asymmetric) side flow. When the bearing's fluid is approximated as being incompressible, $C^* = 0$ in Eq. (4).

4 Discussion

The topography of the material used in the present tests is shown in Fig. 9. Since the measured roughness is known to be a strong function of the length scale (Majumdar and Bhushan, 1990) and since side flow occurs on dimensions comparable to the width of the web, the roughness measurements capture some longer wavelength components. The surface measurement shown in Fig. 9 was obtained using a field of view of some 0.25 mm^2 with a noncontact optical interferometer, and with the web sample placed under its nominal operating tension. Peak-to-valley backside roughness in this case is approximately 250 nm, which is the value used in the illustrative calculations below.

For values of the operating and compressibility parameters which are typical of the experiments conducted, Fig. 10 depicts model predictions for the interlayer h_n^* and cumulative thicknesses H^* as a function of the wrap number. Here $\Pi^* = 3.5 \times 10^{-6}$, $\epsilon^* = 1.25 \times 10^{-5}$, and $C^* = 1.73 \times 10^{-2}$. Contact between adjacent layers occurs once h_n^* falls below the peak-to-valley asperity level ϵ^*, and H^* is found as the sum of all individual layer thicknesses. In the case of symmetric S side flow, the entrained region comprises fewer wraps than when one edge contacts a guiding flange. With the same value of ϵ^*, H^* increases for asymmetric stacking A by a factor of approximately 2.4, while the number of wraps before contact occurs increases from 21 to 48. The measured thickness value is expected to fall between 12 and 29, which are the ordinate values in Fig. 10 for S and A, respectively. Further, since the side flow has magnitude of order $\mathcal{O}(h^{*3})$, while the circumferential flow is only $\mathcal{O}(h^*)$, h_n^* drops steeply over the first wrap. For subsequent layers, h^* diminishes more gradually, and in the limit of very large n, r_n^* approaches unity.

Figure 11 demonstrates the dependence of H^* on Π^* for the compressibility parameter assuming values for three different tensions, chosen so as to cover the entire parameter range of interest. At least for the model parameters shown in Fig. 11, the effect of fluid compressibility is negligible with indiscernible distinction between the model predictions. Specifically, the coefficient of the highest-order term in Eq. (4) changes by 0.3 percent for asymmetric leakage, and by less than 0.1 percent for symmetric leakage, when compressibility is ignored. Although the interlayer air pressure for the inner wraps can be significant in relation to the ambient value, the pressure gradient

Downloaded 04 May 2010 to 171.66.16.34. Redistribution subject to ASME license or copyright; see http://www.asme.org/terms/Terms_Use.cfm

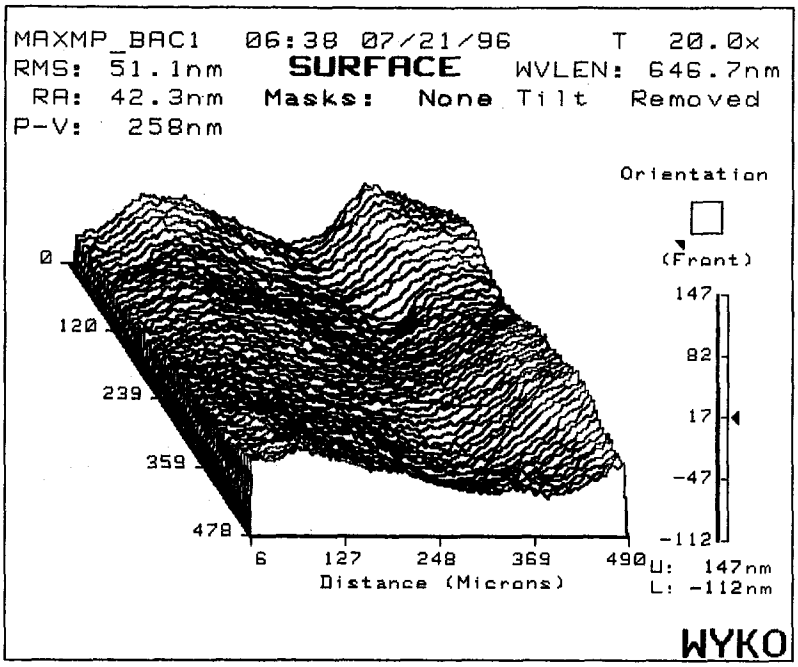


Fig. 9 Measured surface topography of the experimental web material measured using three-dimensional optical profilometry; T = 0.84 N and ϵ = 250 nm

in the winding direction is comparatively small; variation in the wrap-to-wrap air density is likewise small. Figure 11 shows that the film thickness decreases with tension for a fixed running speed, and likewise grows as the transport speed is increased with tension held constant. For the technologically relevant high-speed and low-tension applications, some 10–30 μm of air was entrained within the roll. The predictions by the model of the cumulative thickness for the cases of symmetric and asymmetric side flow provide upper and lower bounds to the experimentally measured values. The measured values are skewed towards the predictions of the symmetric side leakage model, particularly for the higher values of the operating parameter, as is indicative of air bleeding from both edges of the web layers in the tests conducted.

The variation of H^* with the width ratio b^* for a specific Π^* is depicted in Fig. 12, where the cumulative thickness is expected to double as the width ratio is doubled. All tests were conducted with webs of identical width for purposes of the test stand's design, so a full parameter study in b^* is not available,

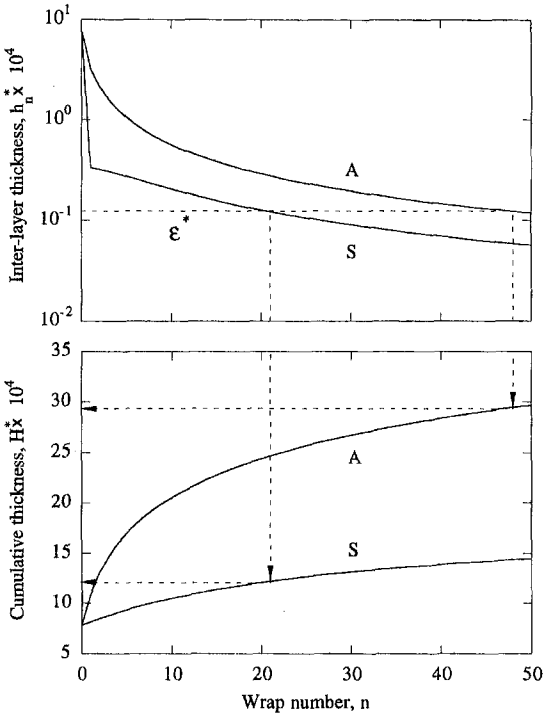


Fig. 10 Predicted interlayer and cumulative film thicknesses as functions of the wrap number for the symmetric and asymmetric side leakage models. The arrows indicate the number of wraps before contact occurs, and the cumulative thicknesses predicted by the two models; $\Pi^* = 3.5 \times 10^{-6}$, $\epsilon^* = 1.25 \times 10^{-5}$, and $C^* = 1.73 \times 10^{-2}$.

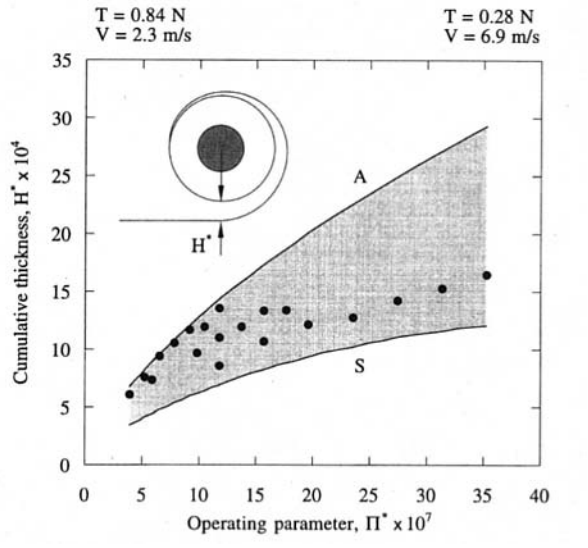


Fig. 11 Comparison between measured (●) and predicted (——) values of the cumulative thickness as a function of the operating parameter for $C^* = 1.73 \times 10^{-2}$, 3.45×10^{-2}, and 5.18×10^{-2}, respectively. The model predictions are insensitive to C^*. The symmetric and asymmetric leakage models bound the measured values (shaded region). The test parameters are the same as in Fig. 7.

Downloaded 04 May 2010 to 171.66.16.34. Redistribution subject to ASME license or copyright; see http://www.asme.org/terms/Terms_Use.cfm

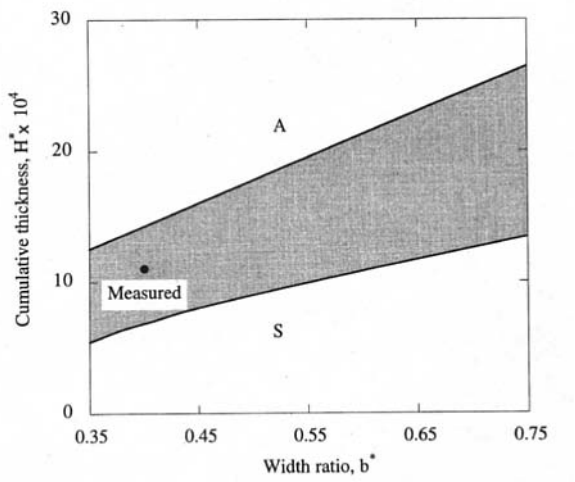


Fig. 12 Measured (●) and predicted (——) values of the cumulative thickness as a function of the width ratio; $\Pi^* = 1.2 \times 10^{-6}$ and $C^* = 3.45 \times 10^{-2}$

but the result for the available case $b^* = 0.38$ does provide pleasing agreement with the model.

5 Summary

An experimental technique was developed for the in situ characterization of air entrainment during winding. With a view towards geometrically similar configurations, four dimensionless parameters—the operating parameter $\Pi^* = \mu Vb/T$, the width ratio $b^* = b/R$, the roughness ratio $\epsilon^* = \epsilon/R$, and the compressibility parameter $C^* = T/Rbp_a$—are useful in representing measured results within the context of the modeled quantities. The cumulative thickness of all air layers and the thickness of the outermost air layer at the nip were determined over a one order-of-magnitude range of Π^*. Experiments indicate that the outermost air layer accounts for some 30–50 percent of the cumulative thickness of the entrained air film, and for the material and operating conditions studied here, H is typically on the order of several tens of microns.

The derived model predicts the number of wraps, the interlayer thickness, and the cumulative thickness during steady-state winding as functions of the winding parameters. Two limiting cases encountered in typical winding configurations were treated in order to provide upper and lower bounds for measured values of the film thickness. The experimental technique and the model establish a quantitative procedure for evaluating candidate solutions to the air entrainment problem, either through selection of the web's properties or operating conditions, or through the design of the web's path and transport components.

Acknowledgment

This work is supported by the National Science Foundation and the Data Storage Systems Center under grant numbers ECD-8907068 and DMI-9622258, the NSIC/ARPA Ultra High Density Magnetic Tape Program, the Minnesota Mining and Manufacturing Company, and by Imation Corporation. The authors appreciate the efforts of Mike Trcka and Tom Zevin from Datatape Incorporated for the mechanical design of the web transport test bed, and of Priyadarshee Mathur, Marc Bodson, and William Messner from Carnegie Mellon for implementation of the speed and tension controller.

References

Altmann, H. C., 1968, "Formulas for Computing the Stresses in Center Wound Rolls," *TAPPI Journal,* Vol. 51, pp. 176–179.

Benson, R. C., 1995, "A Nonlinear Wound Roll Model Allowing for Large Deformation," ASME JOURNAL OF APPLIED MECHANICS, Vol. 62, pp. 853–859.

Bhushan, B., 1992, *Mechanics and Reliability of Flexible Magnetic Media,* Springer-Verlag, New York, pp. 91–93.

Ducotey, K. S., and Good, J. K., 1995, "The Importance of Traction in Web Handling," ASME *Journal of Tribology,* Vol. 117, pp. 679–684.

Eshel, A., and Elrod, H. G., Jr., 1965, "The Theory of the Infinitely Wide, Perfectly Flexible, Self-Acting Foil Bearing," ASME *Journal of Basic Engineering,* Vol. 87, pp. 831–836.

Eshel, A., 1968, "Compressibility Effects on the Infinitely Wide, Perfectly Flexible, Foil Bearing," ASME *Journal of Lubrication Technology,* Vol. 90, pp. 221–225.

Jones, D. P., 1992, "Air Entrainment as a Mechanism for Low Traction on Rollers and Poor Stacking of Polyester Film Reels, and Its Reduction," *Web Handling,* ASME Press, AMD-Vol. 149, pp. 123–131.

Knox, K. L., and Sweeney, T. L., 1971, "Fluid Effects Associated with Web Handling," *Industrial and Engineering Chemistry Process Design and Development,* Vol. 10, pp. 201–206.

Licht, L., 1968, "An Experimental Study of Elastohydrodynamic Lubrication of Foil Bearings," ASME *Journal of Lubrication Technology,* Vol. 90, pp. 199–220.

Majumdar, A., and Bhushan, B., 1990, "Role of Fractal Geometry in Roughness Characterization and Contact Mechanics of Surfaces," ASME *Journal of Tribology,* Vol. 112, pp. 205–216.

Smith, D. P., and Von Behren, R. A., 1989, "Squeeze-Film Analysis of Tape Winding Effects in Data Cartridge," *Tribology and Mechanics of Magnetic Storage Systems,* ASME/STLE Conference Proceedings, Vol. 6, pp. 88–92.

Tramposch, H., 1965, "Relaxation of Internal Forces in a Wound Reel of Magnetic Tape," ASME JOURNAL OF APPLIED MECHANICS, Vol. 32, pp. 865–873.

Wickert, J. A., 1993, "Free Linear Vibration of Self-Pressurized Foil Bearings," ASME *Journal of Vibration and Acoustics,* Vol. 115, pp. 145–151.

Willett, M. S., and Poesch, W. L., 1988, "Determining the Stress Distributions in Wound Reels of Magnetic Tape Using a Nonlinear Finite-Difference Approach," ASME JOURNAL OF APPLIED MECHANICS, Vol. 55, pp. 365–371.

Downloaded 04 May 2010 to 171.66.16.34. Redistribution subject to ASME license or copyright; see http://www.asme.org/terms/Terms_Use.cfm

K. Y. Volokh

O. Vilnay

Faculty of Civil Engineering,
Technion—Israel Institute of Technology,
Haifa 32000, Israel

Different Features of a Stability Problem of Underconstrained Structures

Stability problem of bearing pin-jointed assemblies, in which the number of equilibrium equations is greater than the equilibrium matrix rank (underconstrained structures), is investigated. Local and overall stability of initial and loaded states are discussed. Theoretical considerations are accompanied by numerical examples.

1 Introduction

Pin-jointed assemblies in which nodal displacements do not produce elongations of members are traditionally called *mechanisms* or *kinematic chains.* These assemblies cannot bear external load.

On the contrary pin-jointed assemblies in which nodal displacements produce elongations of members are traditionally called *structures.* These assemblies can bear external load.

A specific class of pin-jointed assemblies called *underconstrained structures* can bear external load even though displacements exist which do not produce elongations of members. (The classification presented above is valid for small displacements.)

Some interest in the theory of underconstrained structures arised lately (Tarnai, 1980; Vilnay, 1990; Calladine and Pellegrino, 1991; Kuznetsov, 1991) in spite of the fact that such structures are used in engineering practice for a long time: cable nets, *tensegric* structures, and so on. The linear analysis of underconstrained structures, where the features of underconstrained structures behavior are clarified, is investigated in Volokh and Vilnay (1997a). It is shown that the rigidity of underconstrained structures is provided by initial equilibrium state or prestressing in contrast to conventional structures in which the rigidity is provided by the elastic properties of the system. This difference is because of the lack of members (or constraints) of underconstrained structures as compared to conventional structures. (The term "underconstrained structures" is derived from the lack of constraints.)

The present paper emphasizes the problem of the analysis of stability of underconstrained structures.

2 Initial Overall Stability

Arbitrary assembly of pin-jointed bars is in equilibrium if the following statical conditions are satisfied:

$$\mathbf{A}_0\mathbf{P}_0 = \mathbf{Q}_0. \tag{1}$$

$\mathbf{A}_0$ is an m by n initial configuration equilibrium matrix, $\mathbf{P}_0$ is an n-dimensional vector of initial member forces; $\mathbf{Q}_0$ is an m-dimensional vector of initial external loads.

In the particular case in which $\mathbf{Q}_0 = \mathbf{0}$, the self-stress state for nontrivial solution of Eq. (1) is obtained.

For simplicity, initial elongations and displacements are defined as zeros, indicating, generally, reference origin but not the physical absence of deformations. In fact, the deformed configuration is considered as an initial one.

Under external load $\mathbf{Q}$ Eq. (1) has to be replaced by

$$(\mathbf{A}_0 + \mathbf{A})(\mathbf{P}_0 + \mathbf{P}) = \mathbf{Q}_0 + \mathbf{Q} \tag{2}$$

in which the values without indexes are increments of the corresponding initial values.

By using Eq. (1) and linearizing Eq. (2) the last one takes the form

$$\mathbf{A}_0\mathbf{P} + \mathbf{A}\mathbf{P}_0 = \mathbf{Q}. \tag{3}$$

By adding Hooke's law and kinematic equations,

$$\mathbf{P} = \mathbf{S}\Delta \tag{4}$$

$$\mathbf{A}_0^{\mathrm{T}}\mathbf{U} = \Delta \tag{5}$$

where $\mathbf{S}$ is the uncoupled stiffness matrix and $\mathbf{U}$ is m-dimensional vector of nodal displacements and Δ is n-dimensional vector of member elongations, a closed system of Eqs. (3)–(5) of the unknown vectors $\mathbf{U}$, $\mathbf{P}$, Δ is obtained.

Since after linearization perturbated equilibrium matrix $\mathbf{A}$ elements depend linearly upon nodal displacements, the second term on the left-hand side of Eq. (3) takes the form

$$\mathbf{A}\mathbf{P}_0 = \mathbf{D}\mathbf{U}$$

$$\mathbf{D} \equiv \mathbf{D}(\mathbf{P}_0) \tag{6}$$

$\mathbf{D}$ is an m by m matrix where the elements are linear combinations of the initial member forces presented by vector $\mathbf{P}_0$ components.

By using Eqs. (4)–(6), Eq. (3) takes the form

$$\mathbf{K}\mathbf{U} = \mathbf{Q} \tag{7}$$

$$\mathbf{K} = \mathbf{A}_0\mathbf{S}\mathbf{A}_0^{\mathrm{T}} + \mathbf{D} \tag{8}$$

$\mathbf{K}$ is an m by m stiffness matrix.

Matrix $\mathbf{K}$ must be positive definite in order to provide overall stability of the initial equilibrium state.

In the case of conventional fully constrained structures, the first term on the right-hand side of Eq. (8) is of rank m. Taking into account that the first term elements are significantly larger than the second ones it is possible to neglect the second term on the right-hand side of Eq. (8). Positive definiteness of $\mathbf{S}$ provides positive definiteness of $\mathbf{K}$ and so initial equilibrium state of fully constrained conventional structures is always stable.

In the case of nonconventional underconstrained structures, the situation is more subtle. This is because the second term on the right-hand side of Eq. (8) cannot be neglected since rank $(\mathbf{A}_0\mathbf{S}\mathbf{A}_0^{\mathrm{T}}) < m$. Generally speaking, it is necessary to check positive definiteness of matrix $\mathbf{K}$ by using both terms of Eq. (8). This straightforward approach is rough and abundant. Simplification of the problem is reached in the following manner:

Contributed by the Applied Mechanics Division of THE AMERICAN SOCIETY OF MECHANICAL ENGINEERS for publication in the ASME JOURNAL OF APPLIED MECHANICS.

Discussion on this paper should be addressed to the Technical Editor, Professor Lewis T. Wheeler, Department of Mechanical Engineering, University of Houston, Houston, TX 77204-4792, and will be accepted until four months after final publication of the paper itself in the ASME JOURNAL OF APPLIED MECHANICS.

Manuscript received by the ASME Applied Mechanics Division, Oct. 13, 1995; final revision, Jan. 25, 1997 Associate Technical Editor: S. Kyriakides.

Copyright © 1997 by ASME

Downloaded 04 May 2010 to 171.66.16.34. Redistribution subject to ASME license or copyright; see http://www.asme.org/terms/Terms_Use.cfm

Let the displacement vectors be resolved into two mutually orthogonal vectors

$$\mathbf{U} = \mathbf{U}^k + \mathbf{U}^e. \tag{9}$$

$\mathbf{U}^k$ are "kinematic" displacement vectors, which do not produce member elongations, and $\mathbf{U}^e$ are "elastic" displacement vectors, which do produce members elongations. It is obvious from the homogeneous Eq. (5) that "kinematic" displacement vectors are presented in the form

$$\mathbf{U}^k = z_1\mathbf{e}_1 + \ldots + z_{m-r}\mathbf{e}_{m-r} \tag{10}$$

or

$$\mathbf{U}^k = \mathbf{WZ}$$

$$\mathbf{W} = \{\mathbf{e}_1, \ldots, \mathbf{e}_{m-r}\}, \quad \mathbf{Z} = \{z_1, \ldots, z_{m-r}\}^T. \tag{11}$$

$\mathbf{e}_i$ is the vector of matrix $\mathbf{A}_0^T$ nullspace, z_i is the arbitrary scalar, r is the matrix $\mathbf{A}_0^T$ rank.

The "elastic" displacement vector belongs to the orthogonal complement subspace of $\mathcal{R}^m$ and it takes the form

$$\mathbf{U}^e = z_{m-r+1}\mathbf{e}_{m-r+1} + \ldots + z_m\mathbf{e}_m \tag{12}$$

or

$$\mathbf{U}^e = \tilde{\mathbf{W}}\tilde{\mathbf{Z}}$$

$$\tilde{\mathbf{W}} = \{\mathbf{e}_{m-r+1}, \ldots, \mathbf{e}_m\}, \quad \tilde{\mathbf{Z}} = \{z_{m-r+1}, \ldots, z_m\}^T. \tag{13}$$

$\mathbf{e}_i$ is the vector of matrix $\mathbf{A}_0^T$ row space and z_i is an arbitrary scalar.

By substituting Eqs. (9), (11), and (13), Eq. (7) takes the form

$$\mathbf{A}_0\mathbf{S}\mathbf{A}_0^T\tilde{\mathbf{W}}\tilde{\mathbf{Z}} + \mathbf{D}\tilde{\mathbf{W}}\dot{\tilde{\mathbf{Z}}} + \mathbf{DWZ} = \mathbf{Q}. \tag{14}$$

Arbitrary vectors of the null space and the row space may be presented in the form:

$$\mathbf{V} = \mathbf{WY} \tag{15}$$

$$\tilde{\mathbf{V}} = \tilde{\mathbf{W}}\tilde{\mathbf{Y}}$$

$$\mathbf{Y} = \{y_1, \ldots, y_{m-r}\}^T, \quad \tilde{\mathbf{Y}} = \{y_{m-r+1}, \ldots, y_m\}^T \tag{16}$$

Multiplying scalarly Eq. (14) by vectors $\mathbf{V}^T$, $\tilde{\mathbf{V}}^T$, it is possible to obtain correspondingly

$$\mathbf{Y}^T(\mathbf{W}^T\mathbf{D}\tilde{\mathbf{W}}\tilde{\mathbf{Z}} + \mathbf{W}^T\mathbf{DWZ}) = \mathbf{Y}^T\mathbf{W}^T\mathbf{Q} \tag{17}$$

$$\tilde{\mathbf{Y}}^T(\tilde{\mathbf{W}}^T\mathbf{A}_0\mathbf{S}\mathbf{A}_0^T\tilde{\mathbf{W}}\tilde{\mathbf{Z}} + \tilde{\mathbf{W}}^T\mathbf{D}\tilde{\mathbf{W}}\dot{\tilde{\mathbf{Z}}} + \tilde{\mathbf{W}}^T\mathbf{DWZ}) = \tilde{\mathbf{Y}}^T\tilde{\mathbf{W}}^T\mathbf{Q}. \tag{18}$$

The physical sense of the projecting is the utilization of the principle of virtual work. Since Eqs. (17), (18) should be satisfied under arbitrary vectors $\mathbf{Y}$, $\tilde{\mathbf{Y}}$, the equations can be rewritten in the form

$$(\mathbf{K}^e + \tilde{\mathbf{W}}^T\mathbf{D}\tilde{\mathbf{W}})\tilde{\mathbf{Z}} + \tilde{\mathbf{W}}^T\mathbf{DWZ} = \tilde{\mathbf{W}}^T\mathbf{Q} \tag{19}$$

$$\mathbf{W}^T\mathbf{D}\tilde{\mathbf{W}}\tilde{\mathbf{Z}} + \mathbf{K}^k\mathbf{Z} = \mathbf{W}^T\mathbf{Q} \tag{20}$$

where

$$\mathbf{K}^e = \tilde{\mathbf{W}}^T\mathbf{A}_0\mathbf{S}\mathbf{A}_0^T\tilde{\mathbf{W}} \tag{21}$$

$$\mathbf{K}^k = \mathbf{W}^T\mathbf{DW}. \tag{22}$$

After some transformations Eqs. (19), (20) take the form

$$\{\mathbf{K}^e + \tilde{\mathbf{W}}^T\mathbf{D}\tilde{\mathbf{W}} - \tilde{\mathbf{W}}^T\mathbf{DW}(\mathbf{K}^k)^{-1}\mathbf{W}^T\mathbf{D}\tilde{\mathbf{W}}\}\tilde{\mathbf{Z}} = \{\tilde{\mathbf{W}}^T - \tilde{\mathbf{W}}^T\mathbf{DW}(\mathbf{K}^k)^{-1}\mathbf{W}^T\}\mathbf{Q} \tag{23}$$

$$\{\mathbf{K}^k - \mathbf{W}^T\mathbf{D}\tilde{\mathbf{W}}(\mathbf{K}^e + \tilde{\mathbf{W}}^T\mathbf{D}\tilde{\mathbf{W}})^{-1}\tilde{\mathbf{W}}^T\mathbf{DW}\}\mathbf{Z} = \{\mathbf{W}^T - \mathbf{W}^T\mathbf{D}\tilde{\mathbf{W}}(\mathbf{K}^e + \tilde{\mathbf{W}}^T\mathbf{D}\tilde{\mathbf{W}})^{-1}\tilde{\mathbf{W}}^T\}\mathbf{Q}. \tag{24}$$

By using the estimate

$$\|\mathbf{K}^e\| \approx \|\mathbf{S}\| \gg \|\mathbf{K}^k\| \approx \|\mathbf{D}\| \approx \|\mathbf{P}_0\| \tag{25}$$

where norms indicate, for example, maximum absolute values of elements, and neglecting small values, Eqs. (23) and (24) take the form

$$\mathbf{K}^e\tilde{\mathbf{Z}} = \tilde{\mathbf{R}}\mathbf{Q} \tag{26}$$

$$\mathbf{K}^k\mathbf{Z} = \mathbf{RQ} \tag{27}$$

where

$$\tilde{\mathbf{R}} = \tilde{\mathbf{W}}^T - \tilde{\mathbf{W}}^T\mathbf{DW}(\mathbf{K}^k)^{-1}\mathbf{W}^T \tag{28}$$

$$\mathbf{R} = \mathbf{W}^T - \mathbf{W}^T\mathbf{D}\tilde{\mathbf{W}}(\mathbf{K}^e)^{-1}\tilde{\mathbf{W}}^T. \tag{29}$$

This means that $\mathbf{K}^k$ is an $m - r$ by $m - r$ "kinematic" stiffness matrix and $\mathbf{K}^e$ is an r by r "elastic" stiffness matrix.

The two matrices $\mathbf{K}^k$ and $\mathbf{K}^e$ must be positive definite to provide overall stability of initial equilibrium state. Matrix $\mathbf{K}^e$ is always positive definite due to its framework. It is implied that $\det(\mathbf{K}^e + \tilde{\mathbf{W}}^T\mathbf{D}\tilde{\mathbf{W}}) \neq 0$, otherwise the state is unstable.

Matrix $\mathbf{K}^k$ positive definiteness must be checked under initial configuration design.

Suppose that the initial forces are induced due to prestressing. In this case, solution of homogeneous Eq. (1) is presented in the form

$$\mathbf{P}_0 = t_1\mathbf{p}_1 + \ldots + t_{n-r}\mathbf{p}_{n-r} \tag{30}$$

t_i is an arbitrary scalar and $\mathbf{p}_i$ is the matrix $\mathbf{A}_0$ nullspace basis vector.

In this case the "kinematic" stiffness matrix takes the form

$$\mathbf{K}^k = t_1\mathbf{K}_1^k + \ldots + t_{n-r}\mathbf{K}_{n-r}^k \tag{31}$$

$$\mathbf{K}_i^k = \mathbf{W}^T\mathbf{D}(\mathbf{p}_i)\mathbf{W}. \tag{32}$$

If the set of parameters t_i leads to positive definiteness of matrix $\mathbf{K}^k$, initial overall stability is provided. Generally speaking, an appropriate set of the parameters could be found under the design of a structure with the help of an algorithm such as that of Calladine-Pellegrino (1991) (CP procedure). The idea of the above algorithm can be described briefly as follows:

For this purpose, it is necessary to maximize parameter e by varying t_i under constraints

$$\mathbf{b}_j^T\Big(\sum_{i=1}^{n-r} t_i\mathbf{K}_i^k\Big)\mathbf{b}_j \geq e \geq 0, \quad j = 1, \ldots l \tag{33}$$

$$t_i^- \leq t_i \leq t_i^+. \tag{34}$$

$\mathbf{b}_j$ is the vector of m-dimensional Euclidian space $\mathcal{R}^m$; t_i^-, t_i^+ are lower and upper boundaries for parameter t_i.

On first iteration, $\mathbf{b}_j$s are selected as unit base vectors in $\mathcal{R}^m$ and $l = m$. Under replacing parameters t_i by subtraction of two positive values, the initial problem is nothing but linear programming problem. If its solution $\{t_1^{(1)}, \ldots, t_{n-r}^{(1)}\}$ leads to positive definite $\mathbf{K}^k$ (all eigenvalues are positive) then the procedure is finished. Otherwise, existing unit vectors $\mathbf{b}_j$ are completed by m new vectors which are eigenvectors of matrix:

$$\overset{(1)}{\mathbf{K}}{}^k = \sum_{i=1}^{n-r} t_i^{(1)}\mathbf{K}_i^k$$

and all the calculations are repeated.

The new solution of the linear programming problem $\{t_1^{(2)}, \ldots, t_{n-r}^{(2)}\}$ leads to a new matrix

Downloaded 04 May 2010 to 171.66.16.34. Redistribution subject to ASME license or copyright; see http://www.asme.org/terms/Terms_Use.cfm

$$\overset{(2)}{\mathbf{K}}{}^{\mathbf{k}} = \sum_{i=1}^{n-r} t_i^{(2)} \mathbf{K}_i^{\mathbf{k}}$$

in which its positive definiteness is checked and so on.

Finally two cases are possible: (a) where a suitable set of nonzero parameters t_i is found or (b) where the found set is comprised of zeros. The latter means that the structure is unstable and can not be stiffened by prestressing.

The assembly shown in Fig. 1 is comprised of 12 members which form a regular quadratic net in plane. Nodes A, B, C, D are of the same height. The initial equilibrium matrix is 12 × 12 but of rank 11. It is easy to find self-stress distributions which satisfy the homogeneous Eq. (1). The initial force projections on the x-axis of members 1–6 should be equal to each other in order to satisfy the nodal equilibrium equations. This argument is valid also for members 7–12 in the y direction. The signs of the force values must be different for the two families of members (1–6 and 7–12) in order to satisfy the nodal equilibrium equations in the z-direction. For example, members 1–6 are under tension and members 7–12 are under compression.

This means that the assembly possesses "kinematic" displacements and may be a mechanism or underconstrained structure. The latter takes place when the self-stress state is stable and matrix $\mathbf{K}^{\mathbf{k}}$ is positive definite. It is easy to observe without any calculation that the assembly is not stable. If it were stable under a given distribution of self-stresses, the matrix $\mathbf{K}^{\mathbf{k}}$ eigenvalues would be positive. Let us, for instance, change the signs of the initial member forces so that members 1–6 are under compression and members 7–12 are under tension. In this case, the matrix $\mathbf{K}^{\mathbf{k}}$ eigenvalue signs are changed too and, consequently, the matrix becomes negative definite, which implies that the new state is unstable. This means that the stability depends upon the numeration of members: If tensioned members are numerated from 1 to 6, the assembly will be stable, otherwise, it will be unstable. This conclusion contradicts the physical sense since the concept of stability is invariant to the transformation of the notation. Finally, initial assumption of the stability of the initial state of the assembly is invalid, and the assembly is an unstable mechanism.

This example emphasizes that the existence of a self-stress state is not enough to indicate that the assembly is a stable structure.

Consider the assembly shown in Fig. 2 (Volokh and Vilnay, 1997b). This assembly was created by adding nodes E, F, G, H and members 13–22 to the previous one. The assembly possesses 24 degrees-of-freedom and 22 members. Consequently, the initial equilibrium matrix is of the 24 × 22 dimension. Again the assembly is a mechanism or an underconstrained structure since the equilibrium matrix rank is smaller than the number of degrees-of-freedom. The rank of the above equilibrium matrix is found to be 19.

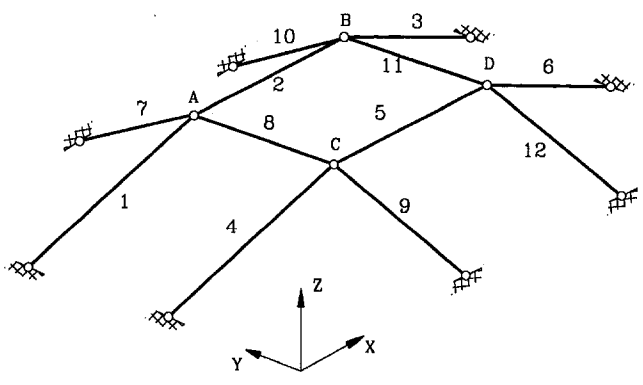


Fig. 1 12-bar assembly

Thus, the self-stress state is obtained with the accuracy of the three unknown parameters $\mathbf{t} = \{t_1, t_2, t_3\}$. These nonzero parameters may be obtained by the described CP-procedure to provide the initial overall stability. For example, in the case of the nodal heights,

$$h_A = h_B = h_C = h_D = 10, \quad h_E = h_F = h_G = h_H = 8.2,$$

the following distribution of the initial member forces leads to matrix $\mathbf{K}^{\mathbf{k}}$ positive definiteness

$$P_{01} = P_{03} = P_{04} = P_{06} = 523.54$$

$$P_{02} = P_{05} = 468.28$$

$$P_{013} = P_{015} = P_{016} = P_{018} = 310.28$$

$$P_{014} = P_{017} = 287.03$$

$$P_{019} = P_{020} = P_{021} = P_{022} = 117.68$$

$$P_{07} = P_{09} = P_{010} = P_{012} = -786.68$$

$$P_{08} = P_{011} = -703.646 \qquad (*)$$

where minus indicates compression.

In the case of changing the heights of the nodes to

$$h_A = h_B = h_C = h_D = 20, \quad h_E = h_F = h_G = h_H = 18.2,$$

the new assembly will not be in equilibrium under the initial member forces given by formula (*). It is possible to change only some of the initial member forces, in order to equilibrate the assembly. If the member forces values are changed as follows,

$$P_{013} = P_{015} = P_{016} = P_{018} = 279.59$$

$$P_{014} = P_{017} = 258.64$$

$$P_{019} = P_{020} = P_{021} = P_{022} = 235.37,$$

and the rest remain the same, the structure will become unstable and it is necessary then to find another distribution of initial member forces to stabilize it.

As a whole, it is evident that the assembly shown in Fig. 2 can be stiffened by prestressing and can be defined as an underconstrained structure.

3 Loaded State Overall Stability

Instability of a loaded state can be interpreted in the traditional way; a bifurcation of the equilibrium problem. In the case of the bifurcation of the equilibrium state, nonzero perturbations $\mathbf{A}'$, $\mathbf{P}'$ exist,

$$(\mathbf{A}_0 + \mathbf{A} + \mathbf{A}')(\mathbf{P}_0 + \mathbf{P} + \mathbf{P}') = \mathbf{Q}_0 + \mathbf{Q}, \qquad (35)$$

by expanding Eq. (35) and omitting values of higher order

$$\mathbf{A}_0\mathbf{P}' + \mathbf{A}'(\mathbf{P}_0 + \mathbf{P}) = \mathbf{0} \qquad (36)$$

where

$$\mathbf{P}' = \mathbf{S}\mathbf{A}_0^{\mathrm{T}}\delta\mathbf{U}^{\mathbf{e}} \qquad (37)$$

$$\mathbf{A}'(\mathbf{P}_0 + \mathbf{P}) = \mathbf{D}'\delta(\mathbf{U}^{\mathbf{e}} + \mathbf{U}^{\mathbf{k}})$$

$$\mathbf{D}' \equiv \mathbf{D}(\mathbf{P}_0) + \mathbf{D}(\mathbf{P}). \qquad (38)$$

This means that equilibrium equations in terms of displacements can be obtained directly from Eqs. (19), (20) with the help of the following replacements:

Downloaded 04 May 2010 to 171.66.16.34. Redistribution subject to ASME license or copyright; see http://www.asme.org/terms/Terms_Use.cfm

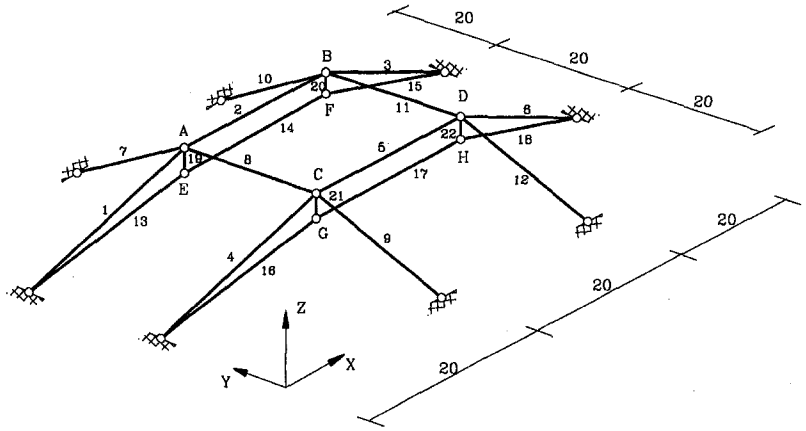


Fig. 2 22-bar assembly

$$\mathbf{Z} \to \delta\mathbf{Z},\ \tilde{\mathbf{Z}} \to \delta\tilde{\mathbf{Z}},\ \mathbf{D} \to \mathbf{D}',\ \mathbf{Q} \to \mathbf{0}$$

which take the form

$$(\mathbf{K}^e + \tilde{\mathbf{W}}^T\mathbf{D}'\tilde{\mathbf{W}})\delta\tilde{\mathbf{Z}} + \tilde{\mathbf{W}}^T\mathbf{D}'\mathbf{W}\,\delta\mathbf{Z} = \mathbf{0} \tag{39}$$

$$\mathbf{W}^T\mathbf{D}'\tilde{\mathbf{W}}\delta\tilde{\mathbf{Z}} + \hat{\mathbf{K}}^k\delta\mathbf{Z} = \mathbf{0} \tag{40}$$

where

$$\hat{\mathbf{K}}^k = \mathbf{W}^T\mathbf{D}'\mathbf{W}. \tag{41}$$

$\mathbf{P}$ is obtained from Eqs. (5), (4), (9), (13), (26),

$$\mathbf{P} = \mathbf{S}\mathbf{A}_0^T\mathbf{U}^e = \mathbf{S}\mathbf{A}_0^T\tilde{\mathbf{W}}(\mathbf{K}^e)^{-1}\tilde{\mathbf{R}}\mathbf{Q}. \tag{42}$$

In the case where the external load $\mathbf{Q}$ grows up proportionally by parameter ν, then member forces take the form $\nu\mathbf{P}$, and consequently

$$\mathbf{D}' \equiv \mathbf{D}(\mathbf{P}_0) + \nu\mathbf{D}(\mathbf{P}).$$

Nonzero displacements appear under such values of parameter ν, which lead to the following equality:

$$\det\begin{bmatrix} \mathbf{K}^e + \tilde{\mathbf{W}}^T\mathbf{D}'\tilde{\mathbf{W}} & \tilde{\mathbf{W}}^T\mathbf{D}'\mathbf{W} \\ \mathbf{W}^T\mathbf{D}'\tilde{\mathbf{W}} & \hat{\mathbf{K}}^k \end{bmatrix} = 0. \tag{43}$$

Estimate (25) indicates that the left upper submatrix elements are significantly larger than the rest. By using Laplace's resolution of the determinant, it is possible to replace approximately Eq. (43) by the following one:

$$\det(\mathbf{K}^e + \tilde{\mathbf{W}}^T\mathbf{D}'\tilde{\mathbf{W}})\det\hat{\mathbf{K}}^k = 0. \tag{44}$$

By using estimate (25) it is obvious that the minimum value of ν is obtained by using equation

$$\det\hat{\mathbf{K}}^k = 0 \tag{45}$$

or equation

$$\det\{\mathbf{K}^k + \nu\mathbf{W}^T\mathbf{D}(\mathbf{P})\mathbf{W}\} = 0. \tag{46}$$

Equation (46) represents the bifurcation of equilibrium problem of underconstrained structures.

It is interesting to compare this equation and the analogous one for conventional fully constrained structures

$$\det\{\mathbf{K} + \nu\mathbf{D}(\mathbf{P})\} = 0. \tag{47}$$

$\mathbf{K}$ is defined by Eq. (8).

The magnitudes of matrix $\mathbf{K}$ elements, which are determined by the elastic properties of the members, are significantly larger than the ones of matrix $\mathbf{K}^k$, which are determined by the values of the initial member forces only. As a consequence of this, the magnitude of the critical parameter ν_{cr} is determined by the elastic properties of the members in the case of fully constrained structures but not in the case of underconstrained structures. It is necessary to note that the increments of the member forces included in the second terms in the braces of Eqs. (46), (47) depend upon the correlations between the member stiffnesses and not upon the magnitude of their stiffnesses. In summary, the influence of the elastic properties of the members on the critical bifurcation load is negligible in the case of underconstrained structures which is in contrast to fully constrained ones.

The displacement modes at the bifurcation point are obtained in the following way: first, the nullspace of the matrix in the braces of Eq. (46) is calculated; this is no other but vector $\delta\mathbf{Z}$ with the accuracy of constant. Secondly, "kinematic" displacements are calculated with the help of Eq. (11) by replacing $\mathbf{Z}$ by $\delta\mathbf{Z}$. Vector $\delta\tilde{\mathbf{Z}}$ and the "elastic" displacements may be obtained from Eq. (39) but they are negligible, and so it is possible to claim (at least in an approximate manner) that the displacements modes at the bifurcation point are purely kinematic.

In the case of the underconstrained truss shown in Fig. 2, where the product of the Young's modulus and cross-section area is the same for all members,

$$E_i S_i = ES,$$

the critical values of the external loads for the four loading cases shown in Fig. 3 were calculated by using Eq. (46). The results take the form

$$\nu_{cr} = 13.1342 \quad \text{for case a;}$$

$$\nu_{cr} = 13.9680 \quad \text{for case b;}$$

$$\nu_{cr} = 85.5169 \quad \text{for case c;}$$

$$\nu_{cr} = 85.5169 \quad \text{for case d.}$$

The modes of displacement for the critical value of the load for case a are presented in Table 1 and Fig. 4.

In order to check the absence of the influence of the member elastic properties on the overall stability, the member stiffness was replaced significantly as follows:

$$E_i S_i \to l_i^3 ES.$$

Nevertheless, the new critical values of the external loads practically coincide with the previous ones

$$\nu_{cr} = 13.4986 \quad \text{for case a;}$$

$$\nu_{cr} = 12.9478 \quad \text{for case b;}$$

$$\nu_{cr} = 86.4936 \quad \text{for case c;}$$

Downloaded 04 May 2010 to 171.66.16.34. Redistribution subject to ASME license or copyright; see http://www.asme.org/terms/Terms_Use.cfm

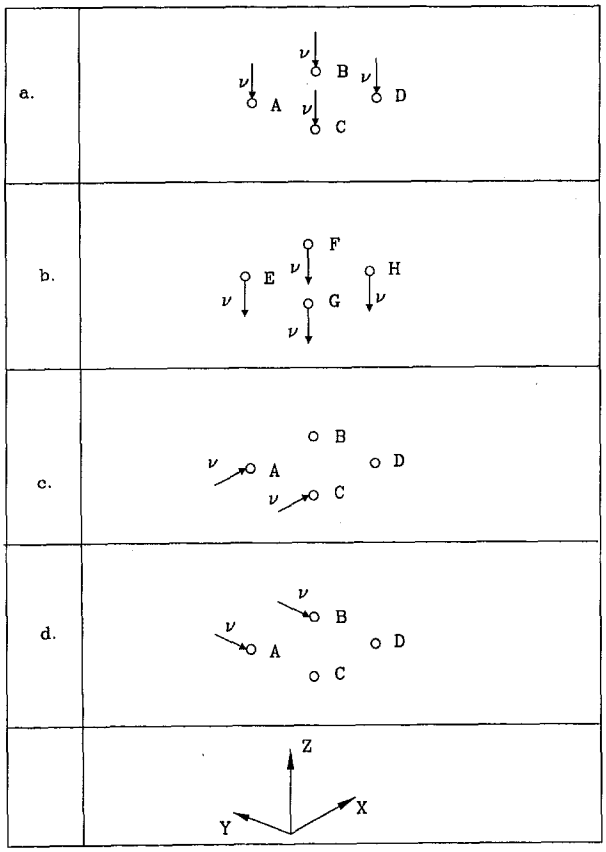


Fig. 3 Cases of loading

$$\nu_{cr} = 86.4936 \quad \text{for case d.}$$

4 Initial and Loaded States Local Stability

A local stability problem may be formulated as the loss of stability of one member which unconditionally leads to a general collapse of an underconstrained structure. Figure 5 and the following arguments show that the local stability problem can be formulated as a classical Euler's bifurcation problem for a hingely supported column. Let us cut member i with member force P_i with ajacent members as shown in Fig. 5(a). This fragment of the structure must be in equilibrium. To replace action of the adjacent members on the nodes by summary load, it is necessary to consider the equilibrium of the nodes (Fig. 5(b)). Evidently, the equilibrium of the nodes is satisfied where the sums of the adjacent member forces equal the member force P_i in the opposite direction. By these means the ith member is under external load P_i (Fig. 5(c)) and, consequently, Euler's classical problem takes a place (Fig. 5(d)). Thus, stability of the ith member is defined by

Table 1

Nodes/displacement direction	x	y	z
A	0.15	−0.15	−0.30
B	0.15	0.15	0.30
C	−0.15	−0.15	0.30
D	−0.15	0.15	−0.30
E	0.12	−0.09	−0.30
F	0.12	0.09	0.30
G	−0.12	−0.09	0.30
H	−0.12	0.09	−0.30

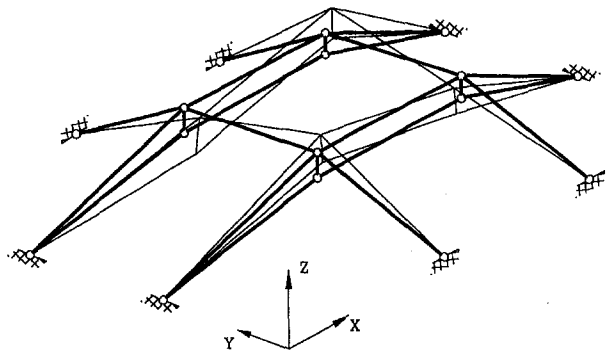


Fig. 4 Buckling mode

$$P_i = \frac{\pi^2 E_i I_i}{l_i^2}.$$

Since P_i may be due to prestressing or external load, this approach to local stability does not differ for initial and loaded states.

In the case of the assembly shown in Fig. 2, where dimensions are given in meters, the prestressing forces calculated by using formulae (*) are given in kilograms and the compressed members 7, 9, 10, 12 are made of steel with circular cross sections, the moment of inertia takes the form

$$I = I_7 = I_9 = I_{10} = I_{12} = \frac{\pi r^4}{4}$$

where r is the radius of the cross sections. In the case where Young's modulus is the same to all members,

$$E = E_7 = E_9 = E_{10} = E_{12} = 2.1 \cdot 10^6 \text{ kg/cm}^2,$$

it is possible to obtain a critical radius to the members, taking into account that the member length is 2236 cm

$$r^{cr} = \sqrt[4]{\frac{786.68 \cdot 4 \cdot 2236^2}{\pi^3 \cdot 2.1 \cdot 10^6}} \cong 4 \text{ cm}.$$

5 Conclusions

1 The stability of the initial state of underconstrained structures is not provided automatically. The formal existence of a self-stress state does not indicate that the structure is stable. This is contrary to the conventional fully constrained structures.

2 Overall stability of loaded underconstrained structures is affected by the initial equilibrium state or prestressing, not by the elastic properties of the system as in conventional structures.

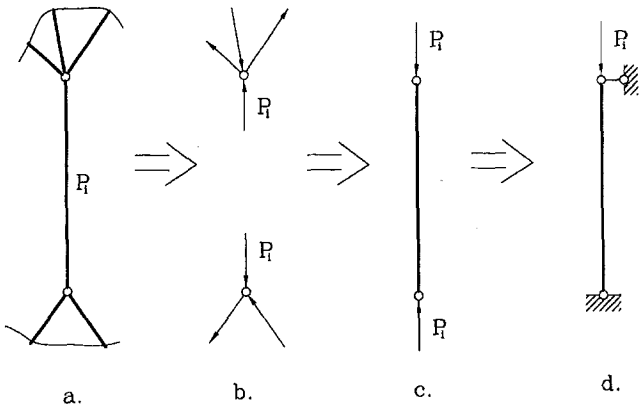


Fig. 5 On the formulation of the local stability problem

Downloaded 04 May 2010 to 171.66.16.34. Redistribution subject to ASME license or copyright; see http://www.asme.org/terms/Terms_Use.cfm

3 Local stability of underconstrained structures is affected by elastic properties of members and can be formulated in the classical Euler's manner.

Acknowledgment

One of the authors (K. Y. V.) is grateful to the Lady Davis Fellowship Trust for support.

References

Calladine, C. R., and Pellegrino, S., 1991, "First Order Infinitesimal Mechanisms," *International Journal of Solids and Structures,* Vol. 27, pp. 505–515.

Kuznetsov, E. N., 1991, *Underconstrained Structural Systems,* Springer-Verlag, New York.

Tarnai, T., 1980, "Simultanious Static And Kinematic Indeterminacy Of Space Trusses With Cyclic Symmetry," *International Journal of Solids and Structures,* Vol. 16, pp. 347–359.

Vilnay, O., 1990, *Cable Nets and Tensegric Shells: Analysis and Design Applications,* Ellis Horwood, UK.

Volokh, K., Yu., Vilnay, O., 1997a, " 'Natural,' 'Kinematic,' and 'Elastic' Displacements Of Underconstrained Structures," *International Journal of Solids and Structures,* Vol. 34, pp. 911–930.

Volokh, K., Yu., and Vilnay, O., 1997b, "New Classes of Reticulated Underconstrained Structures," *International Journal of Solids and Structures,* Vol. 34, pp. 1093–1104.

Downloaded 04 May 2010 to 171.66.16.34. Redistribution subject to ASME license or copyright; see http://www.asme.org/terms/Terms_Use.cfm

S. I. Barry

G. N. Mercer

School of Mathematics and Statistics,
University College,
University of New South Wales,
Canberra ACT 2600, Australia

C. Zoppou

Engineering Branch,
ACT Electricity and Water,
Canberra ACT 2601, Australia

Approximate and Analytic Solutions for Deformation of Finite Porous Filters

The deformation, using linear poroelasticity, of a two-dimensional box of porous material due to fluid flow from a line source is considered as a model of certain filtration processes. Analytical solutions for the steady-state displacement, pressure, and fluid velocity are derived when the side walls of the filter have zero solid stress. A numerical solution for the case where the porous material adheres to the side walls is also found. It will be shown, however, that simpler approximate solutions can be derived which predict the majority of the deformation behavior of the filter.

Introduction

When fluid flows through a porous filter, the solid matrix may deform. This may increase or decrease the porosity of the filter and hence change the filtration properties. Hence there is a coupling between the fluid flow and the deformation of the solid which is complicated by the presence of solid boundaries.

The problem we consider here is motivated by the design of industrial filters for use in the filtering of freshwater for human consumption and the filtering of sewerage effluent. When the solution passes through the filter, suspended particles are trapped within the pores of the filter. These eventually clog the filter reducing its efficiency. Introduction of a source of fluid within the medium can increase its porosity, prolonging the life of the filter, and hence decreasing the frequency of the cleaning process. A source of fluid may also increase the efficiency of the backwashing process by opening up the pore spaces and allowing a greater fluid flux. Hence a model of the interaction of the fluid flow and the deformation of the filter is required. The model is also applicable to flow in finite regions of soil which undergo subsidence due to fluid withdrawal.

The model described in this paper is based on linear poroelasticity and will predict the solid deformation, fluid pressure, porosity, and fluid flux in a constrained filter. Two different boundary conditions are applied on the constraining walls, first, where the restraining side walls have zero solid contact stress (that is they are slippery) and secondly, where the porous solid adheres to the side walls (the walls are sticky). We will illustrate a method of obtaining an exact analytic solution to the first "slippery" boundary condition, and a numerical solution for the second tethered boundary. A much simpler approximate solution is derived and compared with both solutions. A porous material will neither be perfectly tethered to the boundary nor have completely zero solid contact stress with the boundary wall. Hence the solutions we obtain with these different boundary conditions will form upper and lower bounds on the real deformation. In some applications, an array of fluid sources distributed uniformly at some height z_1 along a strip of porous material may be used. The deformation around a source far from the side boundaries will be equivalent, by symmetry, to that derived using the slippery boundary condition.

Contributed by the Applied Mechanics Division of THE AMERICAN SOCIETY OF MECHANICAL ENGINEERS for publication in the ASME JOURNAL OF APPLIED MECHANICS.

Discussion on the paper should be addressed to the Technical Editor, Professor Lewis T. Wheeler, Department of Mechanical Engineering, University of Houston, Houston, TX 77204-4792, and will be accepted until four months after final publication of the paper itself in the ASME JOURNAL OF APPLIED MECHANICS.

Manuscript received by the ASME Applied Mechanics Division, Dec. 19, 1995; final revision, Apr. 2, 1997. Associate Technical Editor: J. T. Jenkins.

Our solutions will be used to illustrate the general behavior of the porous material under steady-state conditions. We will restrict our study to the case of a square-sided box of porous material since this adequately illustrates both the analytic procedure and the general form of the deformation. Different rectangular geometries can easily be solved using the procedures outlined here.

The general theory of deformable porous materials (poroelasticity) began primarily with the studies of Biot (1941) on the consolidation of soil under loading. This theory has been extended using the theory of mixtures (Kenyon, 1976; Bowen 1980) to model the deformation of arteries, articular cartilage and other soft biological tissues (Mow and Lai, 1980; Mow et al., 1990).

Poroelasticity has been used extensively in the soil science literature, often to study the consolidation of semi-infinite regions of soil under compressive loads (Chiarella and Booker, 1975) or the subsidence of soils due to fluid extraction (Booker and Carter, 1986, 1987). The deformation of layers of porous materials has been considered in relation to soil consolidation (Gibson et al., 1970), cartilage compression (Mak et al., 1987; Suh and Spilker, 1994), diffusive response to an initial deformation (Sachs et al., 1994; Jensen et al., 1994), and due to a point source (Barry et al., 1995a, b). Much of this work involves semi-infinite regions or infinite layers of material. There have been few studies, however, on the deformation in a finite region where two-dimensional effects occur. Armstrong et al., (1984) considered the unconfined compression of articular cartilage but was able to employ symmetry conditions to simplify the deformation. Other studies have considered complex finite element schemes to model intervertebral disks and cartilages with precise geometries and internal properties. We present here a solution applicable to a finite constrained porous material that involves two-dimensional coupling between deformation and pressure.

We will consider a poroelastic medium defined on the region $\hat{x} \in [0, \hat{x}_1]$, $\hat{z} \in [0, \hat{z}_1]$ using a Cartesian coordinate frame $(\hat{x}, \hat{z})$. The nondimensional version of the geometry is shown schematically in Fig. 1. The bottom surface, $\hat{z} = 0$, is rigid and impermeable with the porous material adhering to this boundary. The side walls of the region, $\hat{x} = 0$ and $\hat{x} = \hat{x}_1$, are impermeable and rigid. We consider two cases for these boundaries: first, where the porous medium is tethered to the boundary (zero vertical and horizontal displacement) and second, where the boundary is slippery (zero solid contact stress). The upper surface is considered stress free and permeable. Fluid is pumped into the medium from a line source placed at an arbitrary point $(\hat{x}_0, \hat{z}_0)$.

Copyright © 1997 by ASME

Downloaded 04 May 2010 to 171.66.16.34. Redistribution subject to ASME license or copyright; see http://www.asme.org/terms/Terms_Use.cfm

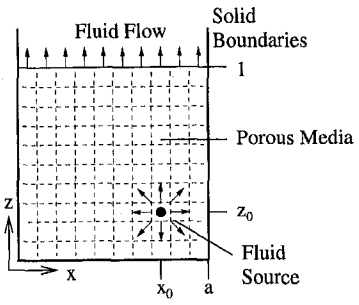


Fig. 1 Schematic diagram of a point source in a two-dimensional box of deformable porous media

We assume in our model that the material is initially homogeneous and isotropic. The deformation will, however, induce inhomogeneities in the medium after the fluid flux is applied. Gravity is neglected as it can be incorporated into the pressure gradient and does not significantly affect the problem considered here. The individual fluid and solid constituents are assumed intrinsically incompressible. Thus compression or expansion of the porous material arises from a change in the relative proportion of these two constituents. The deformations will be considered small so that linear elastic theory can be used. This implies that the boundary conditions are applied at the initial position of the boundaries consistent with the standard infinitesimal elastic assumption. The permeability will be taken as constant throughout the medium. It is expected that as the medium deforms, the permeability will change as a function of the local porosity (Lai and Mow, 1980; Holmes, 1985; Barry and Aldis, 1990). If the deformation is small enough, this additional nonlinearity may be ignored and the permeability taken as a constant. With these assumptions the problem becomes linear and hence amenable to analytical analysis. For clarity, however, we will show results with large displacements since, by linearity, these are simply scaled versions of the true infinitesimal deformations. Despite these limitations the results shown are indicative of relatively large deformation and illustrate the general behavior of the medium when larger fluid pressures are applied. For the filtration application we are modeling, these assumptions are appropriate. Certainly the deformations of a clogged filter will be small enough that the results obtained here will indicate the general pattern of deformation and flow. The effect of the boundary position and the strain-dependent permeability are the most serious limitations of our model. These can be incorporated into the numerical scheme we will outline later but would make an analytic solution impossible. Many industrial filters are also made from layers of different materials. This inhomogeneity would have to be included in a working model of a filter and will be studied at a later date.

In the next section we will briefly discuss the poroelastic equations and boundary conditions appropriate for our problem. We will then nondimensionalize all the variables and derive differential equations for the solid displacement and fluid pressure. A method for obtaining the analytic solution where the side walls are slippery is described and a general numerical scheme outlined. This is followed by the derivation of the approximate solutions which is compared with the exact and numerical solutions.

Governing Equations

In this section we will briefly describe the governing poroelastic equations. A full derivation, using mixture theory, is not included, since other papers (Mow et al., 1990; Holmes, 1985; Barry and Aldis, 1993) adequately cover this material.

The deformation of the solid component of the porous material is governed by standard elasticity theory where the internal body force is due to the gradient of fluid pressure. Hence, if inertial forces are negligible, then the equilibrium equation is

$$\nabla \cdot \hat{\boldsymbol{\sigma}} = \nabla \hat{p} = -\frac{\hat{\mathbf{v}}}{k}, \tag{1}$$

where $\hat{\boldsymbol{\sigma}}$ is the solid "contact stress" tensor (Kenyon, 1976), $\hat{p}$ is the pressure, $\hat{\mathbf{v}}$ is the velocity vector, and k is the permeability. This latter relationship between pressure and velocity is Darcy's law. Note that k includes the fluid viscosity which is often written separately in the soil literature. This conforms to the notation used in the biological literature and often used in poroelasticity.

Conservation of mass can be represented by the equation:

$$\nabla \cdot \hat{\mathbf{v}} = q \equiv f_0 \delta(\hat{x} - \hat{x}_0)\delta(\hat{z} - \hat{z}_0), \tag{2}$$

where δ denotes the Dirac Delta function, f_0 is a measure of the source strength, and $(\hat{x}_0, \hat{z}_0)$ is the position of the line source.

The stress is related to the displacements, $\hat{\mathbf{u}} = (\hat{u}, \hat{v})$, by the relationships

$$\boldsymbol{\sigma} = \lambda e \mathbf{I} + 2\mu \mathbf{e}, \tag{3}$$

$$\mathbf{e} = \tfrac{1}{2}(\nabla \hat{\mathbf{u}} + (\nabla \hat{\mathbf{u}})^T), \tag{4}$$

where λ, μ are the Lamé stress constants, $\mathbf{e}$ is the infinitesimal strain tensor, $\mathbf{I}$ is the identity tensor, and $e = \mathbf{e}_{jj}$ using the tensor summation convention.

Nondimensionalization

We nondimensionalize the poroelastic equations with respect to the height of the box $\hat{z}_1$ and the Lamé stress constant 2μ so that

$$p = \frac{\hat{p}}{2\mu}, \quad x = \frac{\hat{x}}{\hat{z}_1}, \quad z = \frac{\hat{z}}{\hat{z}_1}, \quad u = \frac{\hat{u}}{\hat{z}_1}, \quad \text{and} \quad v = \frac{\hat{v}}{\hat{z}_1}. \tag{5}$$

Three dimensionless parameters,

$$m = 1 + \frac{\lambda}{\mu}, \quad \alpha = \frac{\hat{z}_1 f_0}{2\mu k}, \quad a = \frac{\hat{x}_1}{\hat{z}_1} \tag{6}$$

govern the system where a is the nondimensional width of the box. We note, however, that the parameter α is simply a measure of the strength of the source and, by linearity, plays no part in the relative dynamics of the system.

By substituting the stress relation (3) into Eq. (1) we obtain the following nondimensional equations for the displacement (u, v) and the pressure p:

$$(1 + m)\frac{\partial^2 u}{\partial x^2} + \frac{\partial^2 u}{\partial z^2} + m\frac{\partial^2 v}{\partial x \partial z} = 2\frac{\partial p}{\partial x}, \tag{7}$$

$$\frac{\partial^2 v}{\partial x^2} + (1 + m)\frac{\partial^2 v}{\partial z^2} + m\frac{\partial^2 u}{\partial x \partial z} = 2\frac{\partial p}{\partial z}, \tag{8}$$

$$\frac{\partial^2 p}{\partial x^2} + \frac{\partial^2 p}{\partial z^2} = -\alpha q. \tag{9}$$

The latter equation, for the pressure p, was derived by taking the divergence of Eq. (1) and using Eq. (2).

The boundary conditions applicable to this problem are

$$\text{on} \quad x = 0, a, \quad u = \frac{\partial p}{\partial x} = 0,$$

$$\text{with} \quad v = 0 \quad \text{or} \quad \frac{\partial v}{\partial x} = 0, \tag{10}$$

$$\text{on} \quad z = 0, \quad u = v = \frac{\partial p}{\partial z} = 0, \tag{11}$$

Downloaded 04 May 2010 to 171.66.16.34. Redistribution subject to ASME license or copyright; see http://www.asme.org/terms/Terms_Use.cfm

which correspond to zero horizontal displacement on the side walls (due to a rigid boundary) and zero normal fluid flux (due to an impermeable boundary). The choice of boundary condition on $x = 0, a$ corresponds, respectively, to either zero vertical displacement (tethered boundary) or zero solid shear stress, $\sigma_{xz} = 0$, which reduces to $\partial v/\partial x = 0$. The upper boundary, $z = 1$, is permeable so $p = 0$ and stress free so $\sigma_{xz} = 0$ and $\sigma_{zz} = p$. Thus on the upper boundary

$$\frac{\partial u}{\partial z} + \frac{\partial v}{\partial x} = 0, \tag{12}$$

$$\frac{m-1}{m+1}\frac{\partial u}{\partial x} + \frac{\partial v}{\partial z} = 0. \tag{13}$$

Hou et al. (1989) give a full derivation and discussion of boundary conditions applicable to poroelastic media.

Analytic Solution Method

We derive here a method for obtaining the analytic solution for the deformation and pressure when the side walls have zero solid stress. This method involves use of finite Fourier transforms and hence the resulting solution is expressed as an infinite summation. The solutions can be computed to any degree of accuracy by truncating the infinite series. An algebraic manipulation package is also necessary to compute a set of coefficients. This method can be extended to include the case of sticky side walls; however, this is a much more difficult problem that is not considered here.

The approach we use here is similar to that used for the infinite layer by Barry et al. (1995a, b). To include the boundary conditions on $x = 0, a$ the Hankel transform used in these papers is changed to a finite Fourier transform.

The Eqs. (7) and (8) are rewritten as

$$\frac{\partial^2 u}{\partial x^2} + \frac{\partial^2 u}{\partial z^2} + m\frac{\partial \phi}{\partial x} = 2\frac{\partial p}{\partial x}, \tag{14}$$

$$\frac{\partial^2 v}{\partial x^2} + \frac{\partial^2 v}{\partial z^2} + m\frac{\partial \phi}{\partial z} = 2\frac{\partial p}{\partial z}. \tag{15}$$

The dilatation,

$$\phi = \nabla \cdot \mathbf{u} = \frac{\partial u}{\partial x} + \frac{\partial v}{\partial z}, \tag{16}$$

is a measure of the change in porosity such that $\phi = (\phi^f - \phi_0^f)/(1 - \phi_0^f)$ where the volume fraction of fluid in the medium, ϕ^f, is initially ϕ_0^f.

It can be shown, by taking the divergence of Eq. (1) and nondimensionalizing, that

$$\nabla^2 p = \frac{m+1}{2}\nabla^2\phi. \tag{17}$$

The finite Fourier transforms we will use to simplify Eqs. (14)–(17) to a set of ordinary differential equations are

$$S\{f(x)\} = \int_0^a f(x)\sin\lambda_n x dx,$$

$$C\{f(x)\} = \int_0^a f(x)\cos\lambda_n x dx, \tag{18}$$

where $\lambda_n = n\pi/a$, $n = 0, 1, 2, \ldots$. Standard inversion relations apply (for example, O'Neil, 1983).

We define $\bar{u}(n, z) = S\{u(x, z)\}$ and use the cosine transform for the other variables v, p, ϕ. The correct choice of transform ensures that the slippery boundary conditions on $x = 0, a$ are satisfied. By taking the sine transform of Eq. (14) and the cosine transform of Eqs. (15)–(17) we obtain

$$\frac{\partial^2 \bar{u}}{\partial z^2} - \lambda_n^2\bar{u} = -2\lambda_n\bar{p} + m\lambda_n\bar{\phi}, \tag{19}$$

$$\frac{\partial^2 \bar{v}}{\partial z^2} - \lambda_n^2\bar{v} = 2\frac{\partial \bar{p}}{\partial z} - m\frac{\partial \bar{\phi}}{\partial z}, \tag{20}$$

$$\frac{\partial^2 \bar{p}}{\partial z^2} - \lambda_n^2\bar{p} = \frac{m+1}{2}\left(\frac{\partial^2\bar{\phi}}{\partial z^2} - \lambda_n^2\bar{\phi}\right), \tag{21}$$

$$\frac{\partial^2 \bar{p}}{\partial z^2} - \lambda_n^2\bar{p} = -\alpha\sin(\lambda_n x_0)\delta(z - z_0), \tag{22}$$

with the transformed boundary conditions

$$\text{on } z = 1, \quad \frac{m-1}{2}\bar{\phi} + \frac{\partial \bar{v}}{\partial z} = 0,$$

$$\frac{\partial \bar{u}}{\partial z} - \lambda_n\bar{v} = 0, \quad \bar{p} = 0. \tag{23}$$

$$\text{on } z = 0, \quad \bar{v} = 0, \quad \bar{u} = 0, \quad \partial\bar{p}/\partial z = 0. \tag{24}$$

The solution to Eq. (22) for the pressure is found separately in the regions $z < z_0$ and $z > z_0$. Thus

$$\bar{p} = -\frac{\alpha}{\lambda_n\cosh\lambda_n}\begin{cases}\cosh(\lambda_n z_0)\sinh(\lambda_n(z-1)), & z \in [z_0, 1],\\ \sinh(\lambda_n(z_0-1))\cosh(\lambda_n z), & z \in [0, z_0],\end{cases} \tag{25}$$

where the matching conditions at $z = z_0$, $p(z_0^+) = p(z_0^-)$ and $p'(z_0^+) - p'(z_0^-) = -1$ have been used.

The quantities $\bar{u}$, $\bar{v}$, $\bar{\phi}$ are also divided into solutions in the intervals $z \in [z_0, 1]$ and $z \in [0, z_0]$, denoted with subscripts one and two, respectively. Thus

$$\bar{\phi}_{1,2} = \frac{2}{m+1}\bar{p} + C\cosh(\lambda_n z) + D\sinh(\lambda_n z) \tag{26}$$

$$\bar{u}_1 = E_1\cosh(\lambda_n z) + F_1\sinh(\lambda_n z) + \frac{mC}{2}z\sinh(\lambda_n z) + \frac{mD}{2}z\cosh\lambda_n z - \frac{\alpha A_1}{m+1}z\cosh(\lambda_n(z-1)), \tag{27}$$

$$\bar{u}_2 = E_2\cosh(\lambda_n z) + F_2\sinh(\lambda_n z) + \frac{mC}{2}z\sinh(\lambda_n z) + \frac{mD}{2}z\cosh\lambda_n z - \frac{\alpha A_2}{m+1}z\sinh(\lambda_n z), \tag{28}$$

$$\bar{v}_1 = G_1\cosh(\lambda_n z) + J_1\sinh(\lambda_n z) - \frac{mC}{2}z\cosh(\lambda_n z) - \frac{mD}{2}z\sinh(\lambda_n z) + \frac{\alpha A_1}{m+1}z\sinh(\lambda_n(z-1)), \tag{29}$$

$$\bar{v}_2 = G_2\cosh(\lambda_n z) + J_2\sinh(\lambda_n z) - \frac{mC}{2}z\cosh(\lambda_n z) - \frac{mD}{2}z\sinh(\lambda_n z) + \frac{\alpha A_2}{m+1}z\cosh(\lambda_n z), \tag{30}$$

where C, D, $E_{1,2}$, $F_{1,2}$, $G_{1,2}$, $J_{1,2}$ are complicated expressions which are independent of z and were found from the boundary conditions and by satisfying continuity at $z = z_0$. The algebraic manipulation package Maple was used to find these expressions.

Downloaded 04 May 2010 to 171.66.16.34. Redistribution subject to ASME license or copyright; see http://www.asme.org/terms/Terms_Use.cfm

Numerical Solution

A finite difference numerical scheme was developed to solve Eqs. (7)–(13) for the pressure and displacement. The pressure equation is independent of the displacements and is solved separately. The partial derivatives were discretized using central differencing and the resulting equations solved for the displacement or pressure at the central grid position in terms of the surrounding grid points. This process is then iterated for all points in the medium until convergence to the final solution. A complete description of this scheme, which includes time dependence, can be found in Mercer and Barry (1997). Second-order finite differences were used at all interior points (accurate to order h^2 where h is the grid spacing). Due to the complexity of the boundary condition on the free surface, only first-order differences (accurate to order h) were used on this boundary. Hence the resulting solutions are accurate to order h.

The numerical solution was tested for convergence and was found to be grid independent. The scheme was also tested using known one dimensional solutions and using the analytical solution outlined in the previous section. A 60×60 grid was used to calculate the solutions shown here.

Approximate Solutions

Although the previous analytic and numerical solutions are accurate, a simpler solution that approximately describes the behaviour of the medium would be useful. Different approximations are obtained for the tethered and slippery boundaries.

Stress-Free Boundaries. We assume here that because the solid medium is constrained laterally, the horizontal displacement, u, will be much smaller than the vertical displacement, v. Because the side walls are slippery there is no solid stress restraining the material from uniformly sliding up the walls. This would create vertical displacements which are, to first order, dependent only on z. Any x dependence of v would thus come from asymmetrical fluid flow rather than any inherent elastic response. We thus assume that $(\partial^2 v/\partial x^2) \ll (\partial^2 v/\partial z^2)$ and $u \ll v$. We also assume that the pressure gradient satisfies $\partial p/\partial x \ll \partial p/\partial z$. With these assumptions Eqs. (7)–(9) simplify to become

$$(1 + m)\frac{\partial^2 v}{\partial z^2} = 2\frac{\partial p}{\partial z} \tag{31}$$

$$\frac{\partial^2 p}{\partial z^2} = -\alpha\delta(z - z_0) \tag{32}$$

where we also assume that the source singularity has no x dependence. The boundary conditions with this assumption are the same as Eqs. (10) and (11) with Eqs. (12) and (13) on the top boundary, $z = 1$, replaced by $\partial v/\partial z = 0$.

The solution, obtained by integration, is

$$p = -\alpha\begin{cases} z - 1, & z > z_0, \\ z_0 - 1, & z \le z_0 \end{cases} \tag{33}$$

and

$$v = \frac{-\alpha}{1 + m}\begin{cases} \frac{1}{2}(z^2 + z_0^2) - z, & z > z_0, \\ (z_0 - 1)z, & z \le z_0 \end{cases} \tag{34}$$

This illustrates that below the source the medium has a uniform pressure while above the source the pressure decreases linearly with distance. This is a reasonable result, since the bottom and lower boundaries are impermeable, the fluid source will essentially pressurize the entire region below the source creating a uniform "bath" of fluid.

Tethered Boundaries. We expect that the tethering of the solid material to the side walls will produce a definite gradient $\partial v/\partial x$ within the material. Hence we continue to assume that $u \ll v$ and $(\partial p/\partial x) \ll (\partial p/\partial z)$ but no longer restrict the dependence of the vertical displacement. Equations (7)–(9) hence become

$$\frac{\partial^2 v}{\partial x^2} + (1 + m)\frac{\partial^2 v}{\partial z^2} = 2\frac{\partial p}{\partial z} \tag{35}$$

with the pressure satisfying Eq. (33). The boundary conditions are the same as in the previous approximation.

To find v we take the Fourier sine transform in the x direction giving

$$\frac{\partial^2 \bar{v}}{\partial z^2} - \frac{\lambda_n^2}{1 + m}\bar{v} = -\frac{2\alpha}{1 + m}S\{1\}H(z - z_0) \tag{36}$$

where $S\{1\} = (1/\lambda_n)(1 - (-1)^n)$ and $H(z - z_0)$ denotes a Heaviside step function, that is $H(z - z_0) = 1$ if $z > z_0$ and zero if $z < z_0$. Thus

$$\bar{v} = \frac{2\alpha S\{1\}}{\lambda_n^2 \cosh\hat{\lambda}}\begin{cases} \sinh(\hat{\lambda}(z_0 - 1))\cosh(\hat{\lambda}(z - 1)) - 1, & \\ & z > z_0, \\ \cosh(\hat{\lambda}z_0)\sinh(\hat{\lambda}z), & z \le z_0, \end{cases} \tag{37}$$

where $\hat{\lambda} = \lambda_n/\sqrt{1 + m}$. The final solution can be written as an infinite sum using the inverse sine transform.

These approximate solutions are the "zeroth-order" solution of a singular perturbation expansion with boundary layers along the walls. It is not clear how the higher order terms would be calculated and how the size and location of the boundary layers estimated, due to the complexity and two dimensionality of the problem. It will be shown in the next section, however, that these zeroth-order approximate solutions accurately represent the exact behavior of the medium.

Results and Discussion

We look here at the deformation pattern, pressure and dilatation contours for a source at (0.75, 0.25) with $a = 1$ and $m = 1.5$. This position is chosen since it illustrates the general pattern of flow and deformation, plus it represents the worst comparison between the approximate and the exact solution. The source strength is $\alpha = 1$ throughout. As noted in the Introduction, the solution is linear in α and the results with $\alpha = 1$ are simple scaled versions of the solution for small α. We have not attempted to consider the solutions for a range of possible values of m or a since the general deformation and fluid flow patterns are illustrated using the above parameter values.

In Fig. 2 we compare the exact solution for the deformation with the approximate solution, Eq. (34) for the untethered medium. The deformed state of the grid lines indicated in Fig. 1 are shown. The solid lines indicate the exact solution. The dashed lines indicate a sample of the deformation predicted by the approximate solution. The approximate solution compares very favorably with the exact solution and is accurate, for this worst case, to within ten percent. We note that the vertical deformation calculated from the approximate solution, Eq. (34), appears to give an average of the exact vertical deformation along any horizontal line, with the exact solution almost symmetric around $x = 0.5$. Hence the exact height of the medium at $x = 0.5$ is approximately (within one percent) of that predicted by the approximate solution. We have found that when the source is placed with $x_0 = 0.5$, the approximate solution is within one percent of the exact solution. This comparison of exact and approximate solutions emphasises that the untethered medium simply expands upwards and becomes virtually one dimensional with little dependence on x.

Downloaded 04 May 2010 to 171.66.16.34. Redistribution subject to ASME license or copyright; see http://www.asme.org/terms/Terms_Use.cfm

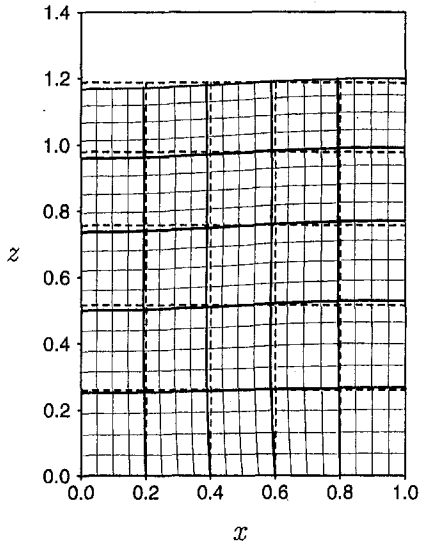


Fig. 2 Deformation grid pattern, due to a line source at (0.75, 0.25), when the side walls, $x = 0, a$ have zero solid stress (slippery walls). The parameters $m = 1.5$, $a = 1$, and $\alpha = 1$. Solid lines indicate the exact deformation pattern while dashed lines indicate the approximate solution via Eq. (34).

In Fig. 3 we illustrate the contours of ϕ for the same conditions as Fig. 2. Although not shown, the approximate solution (34) would imply horizontal contours of ϕ at approximately the same level as that shown. Note that, as expected, the contours are nearly circular near the source and become more linear with increasing height. We would expect that for high aspect ratios, $a > 1$, the deformation would be dominated by the circular dilation. For low aspect ratios, $a < 1$ indicating long thin boxes, the contours in dilatation would become predominantly linear as the flow becomes one dimensional with increasing z. This figure also illustrates that the entire medium is expanded, that is the porosity increases with the greatest increase occurring near the source.

Figure 4 illustrates the pressure contours. Note that these have a similar pattern to the contours of dilatation except that near $z = 1$, the contours are forced (by the boundary condition $p = 0$ at $z = 1$) to become horizontal. This is expected since p and ϕ are related by Eq. (17). These pressure contours are independent of the displacement due to the assumption of constant permeability and hence apply to the tethered boundary solution as well.

Figure 5 illustrates the displacement grid where the boundaries are tethered. The solid lines were obtained using the full numerical solution and the dashed lines the approximate solution. Note that the vertical displacements given by the approximate solution are within ten percent of the full numerical solution. Also note that there is significant horizontal displacements since the source was not centered at $x_0 = 0.5$. The horizontal displacements, u, are largest near the top boundary which is not accounted for by the approximate solution. This is apparent by looking along the grid line at $x = 0.2$. This shows a small horizontal displacement except near $z = 1$ which is due to the complicated boundary conditions at $z = 1$. Any improvement to the approximate solution would thus have to incorporate the region near $z = 1$ where u is no longer negligible. When the source is positioned along the central line, $x_0 = 0.5$, the horizontal displacements are considerably smaller.

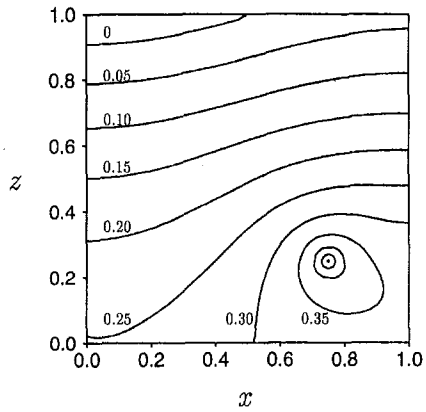


Fig. 3 Contours of dilatation, ϕ, for the same conditions as Fig. 2

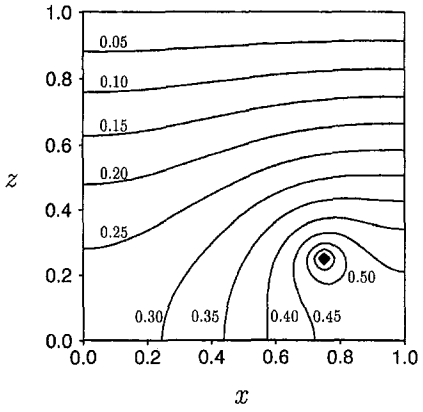


Fig. 4 Contours of pressure for the same conditions as Figs. 2 and 3. These contours also apply to the tethered geometry shown in Figs. 5 and 6.

The contours of dilatation are indicated in Fig. 6. In comparison to the contours in Fig. 3 (the untethered medium), the dilatation for a tethered geometry is more complicated. Most of the medium is still being expanded except in small regions near the upper corners (0, 1) and (1, 1).

To compare the effect of different source positions we have plotted, in Fig. 7, the maximum deformation, v_m, on the top surface, $z = 1$, versus the height of the source, z_0. The solid lines indicate v_m for sources with $x_0 = 0.5$, the dotted lines sources with $x_0 = 0.75$. Dashed lines indicate the approximate solution. The upper set of curves represent the displacements when slippery boundaries are used and the lower set when

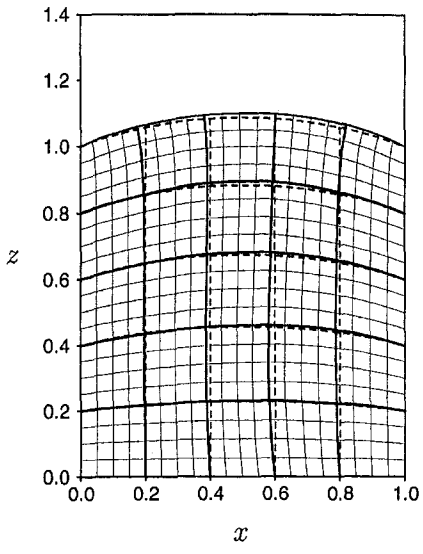


Fig. 5 Deformation grid pattern where the porous material is tethered to the side walls. The conditions are otherwise the same as Fig. 2.

Downloaded 04 May 2010 to 171.66.16.34. Redistribution subject to ASME license or copyright; see http://www.asme.org/terms/Terms_Use.cfm

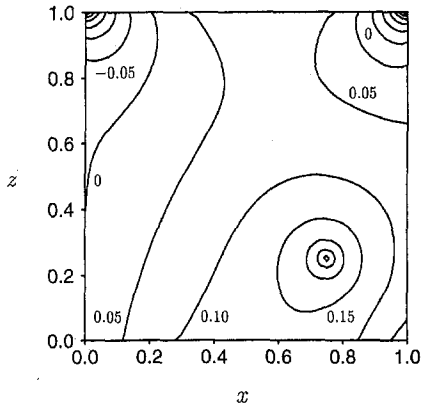


Fig. 6 Contours of dilatation, ϕ, for the same conditions as Fig. 5

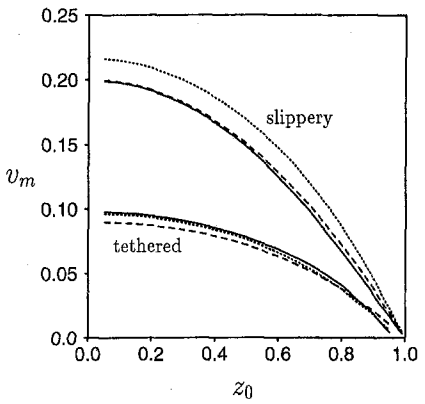


Fig. 7 Maximum surface deformation, v_m, as a function of the height of the source z_0. Solid lines indicate v_m for a source at (0.5, z_0), the dotted lines correspond to a source at (0.75, z_0) and the dashed lines indicate the approximate solution.

tethered boundaries are used. If the mean displacement of the upper boundary had been plotted, rather than v_m, in the upper set of curves then the comparison with the approximate solution would be favourable. The tethering reduces the deformation as expected. As the source approaches the top surface, $z_0 \to 1$, the deformation tends to zero since the fluid flows immediately out of the top surface without deforming the medium.

Conclusions

We have illustrated here analytic, numerical, and approximate solutions for coupled two-dimensional deformation and fluid flow within a porous material. In particular the approximate solutions were shown to be at least within ten percent of the exact solutions and for some source positions to within one percent. Due to their simplicity, these can then be used to estimate deformation and porosity in finite porous material such as filters.

We have illustrated solutions that model the deformation, and fluid flow and can be extended, where necessary, to particular geometries and conditions. Further work on this problem could include an the effects of the aspect ratio, a, and the permeability, $k(\phi)$, on the deformation behavior. Extensions to include time dependence and a model of the concentration of pollutants within the filter are the subject of further research.

Acknowledgments

This research was partially funded by the Australian Capital Territory Electricity and Water Corporation (ACTEW) and the Australian Research Council.

References

Armstrong, C. G., Lai, W. M., and Mow, V. C., 1984, "An Analysis of the Unconfined Compression of Articular Cartilage," ASME *Journal of Biomechanical Engineering,* Vol. 106, pp. 165–173.

Barry, S. I., and Aldis, G. K., 1990, "Comparison of models for flow induced deformation of soft biological tissue," *Journal of Biomechanics,* Vol. 23, pp. 647–654.

Barry, S. I., and Aldis, G. K., 1993, "Radial flow through deformable porous shells," *Journal Australian Mathematical Society, Series B,* Vol. 34, pp. 333–354.

Barry, S. I., Aldis, G. K., and Mercer, G. N., 1995, "Injection of fluid into a layer of deformable porous medium," ASME *Applied Mechanics Reviews,* Vol. 48, pp. 722–726.

Barry, S. I., and Mercer, G. N., 1997, "Deformation and Flow Within a Finite Poroelastic Medium, II—Numerical Method," ASME JOURNAL OF APPLIED MECHANICS, submitted for publication.

Barry, S. I., Zoppou, C., and Mercer, G. N., 1997, "Deformation and fluid flow due to a source in a poroelastic layer," accepted for publication. *Applied Mathematics Modelling.*

Biot, M. A., 1941, "General theory of three-dimensional consolidation," *Journal Applied Physics,* Vol. 12, pp. 155–164.

Booker, J. R., and Carter, J. P., 1986, "Long term subsidence due to fluid extraction from a saturated, anisotropic, elastic soil mass," *Quarterly Journal of Mechanics and Applied Mathematics,* Vol. 39, pp. 85–97.

Booker, J. R., and Carter, J. P., 1987, "Withdrawal of a compressible pore fluid from a point sink in an isotropic elastic half space with anisotropic permeability," *International Journal of Solids and Structures,* Vol. 23, pp. 369–385.

Bowen, R. M., 1980, "Incompressible porous media models by the theory of mixtures," *International Journal of Engineering Science,* Vol. 18, pp. 1129–1148.

Chiarella, C., and Booker, J. R., 1975, "The time-settlement behaviour of a rigid die resting on a deep clay layer," *Quarterly Journal of Mechanics and Applied Mathematics,* Vol. 28, pp. 317–328.

Gibson, R. E., Schiffman, R. L., and Pu, S. L., 1970, "Plane strain and axially symmetric consolidation of a clay layer on a smooth impervious base," *Quarterly Journal of Mechanics and Applied Mathematics,* Vol. 23, pp. 505–520.

Heinrich, G., and Desoyer, K., 1961, "Theorie dreidimensionaler Setzungsvorgaenge in Tonshichten," *Ingenieur-Archiv,* Vol. 30, pp. 225–253.

Holmes, M. H., 1985, "A theoretical analysis for determining the nonlinear hydraulic permeability of a soft tissue from a permeation experiment," *Bulletin of Mathematical Biology,* Vol. 47, pp. 669–683.

Hou, J. S., Holmes, M. H., Lai, W. M., and Mow, V. C., 1989, "Boundary Conditions at the Cartilage-Synovial Fluid Interface for Joint Lubrication and Theoretical Verifications," ASME *Journal of Biomechanical Engineering,* Vol. 111, pp. 78–87.

Jensen, O. E., Glucksberg, M. R., Sachs, J. R., and Grotberg, J. B., 1994, "Weakly Nonlinear Deformation of a Thin Poroelastic Layer With a Free Surface," ASME JOURNAL OF APPLIED MECHANICS, Vol. 61, pp. 729–731.

Kenyon, D. E., 1976, "The theory of an incompressible solid-fluid mixture," *Archives of Rational Mechanical Analysis,* Vol. 62, pp. 131–147.

Lai, W. M., and Mow, V. C., 1980, "Drag induced compression of articular cartilage during a permeation experiment," *Biorheology,* Vol. 17, pp. 111–123.

Mak, A. F., Lai, W. M., and Mow, V. C., 1987, "Biphasic indentation of articular cartilage—I. Theoretical analysis," *Journal of Biomechanics,* Vol. 20, pp. 703–714.

Mow, V. C., Hou, J. S., Owens, J. M., and Ratcliffe, A., 1990, "Biphasic and quasilinear viscoelastic hydrated soft tissues," *Biomechanics of Diarthrodial Joints,* V. C. Mow, A. Ratcliffe, and S. L-Y. Woo, eds., Springer-Verlag, New York, pp. 215–260.

Mow, V. C., and Lai, W. M., 1980, "Recent developments in synovial joint biomechanics," *SIAM Review,* Vol. 22, pp. 275–317.

Sachs, J. R., Glucksberg, M. R., Jensen O. E., and Grotberg, J. B., 1994, "Linear Flow and Deformation in a Poroelastic Disk With a Free Surface," ASME JOURNAL OF APPLIED MECHANICS, Vol. 61, pp. 726–728.

Saxena, S. K., ed., 1978, *Evaluation and Prediction of Subsidence,* ASCE, New York, pp. 1–25.

Spilker, R. L., Suh J.-K., and Mow, V. C., 1992, "A Finite Element Analysis of the Indentation Stress-Relaxation Response of Linear Biphasic Articular Cartilage," ASME *Journal of Biomechanical Engineering,* Vol. 114, pp. 191–201.

Suh, J.-K., and Spilker, R. L., 1994, "Indentation Analysis of Biphasic Articular Cartilage: Nonlinear Phenomena Under Finite Deformation," ASME *Journal of Biomechanical Engineering,* Vol. 116, pp. 1–9.

Terzaghi, K., 1925, *Erdbaumechanik auf Bodenphysikalischen Grundlagen,* Wien, Deutick.

Downloaded 04 May 2010 to 171.66.16.34. Redistribution subject to ASME license or copyright; see http://www.asme.org/terms/Terms_Use.cfm

K. Kumar
Professor,
Department of Aerospace Engineering,
Indian Institute of Technology,
Kanpur 208016, India

J. E. Cochran, Jr.
Professor.

J. A. Cutchins
Professor.

Department of Aerospace Engineering,
Auburn University,
Auburn, AL 36849

Contact Stresses in Cables due to Tension and Torsion

The fundamental theory of wire ropes developed by Costello and Phillips is utilized to obtain closed-form expressions for maximum contact stresses in single strand cables with fibrous cores. These should be useful for gaining an insight into the influence of various parameters of the cable as well as the material properties on its strength and hence design.

Introduction

The first few investigations on estimation of various forces, stresses, and elastic deformations in wire ropes under static loads (Hall, 1951; Hruska, 1951, 1952, 1953; Leissa, 1959; Starkey and Cress, 1959; Bert and Stein, 1962) mark the beginning of a new era directed at theoretical studies. In these analyses, however, several simplifying assumptions of questionable validity were made. Costello, Phillips, and other associates (Costello, 1978, 1983; Costello and Buston, 1982; Costello and Miller, 1979, 1980; Costello and Phillips, 1973, 1974, 1976; Costello and Sinha, 1977a, 1977b) gave a new direction to the subsequent theoretical investigations on cable stresses and deformations. They treated separately the equilibrium of each of the constituent helical wires, although the assumption of no frictional force was kept intact. Their "linearized" relations are applicable to the wire ropes of arbitrary cross sections (Velinsky et al., 1984, 1985; Phillips and Costello, 1985) and enable considerable economy of computational time; however, the analysis remains essentially numerical in character. Perhaps that is why their approach does not provide any direct design insights into the influence of the various cable parameters on cable deformation characteristics unless extensive numerical simulation is undertaken. Recently, the authors successfully utilized some suitable simplifying approximations with an eye on a more thorough utilization of this "linear" theory (Kumar and Cochran, 1987, 1990). This approach led to rather useful closed-form solutions for two different wire rope models. We now extend this theory to develop analytical expressions for critical contact stresses in single strand cables with fibrous cores. The effect of torsional moment is also incorporated in the analysis along with that of simple tension.

It is felt that the explicit nature of the results developed here would be particularly useful in gaining fresh insights into the influence of the various cable parameters, thus facilitating design and rope selection. The better understanding of the contact stresses may also be crucial to modeling of the energy dissipation phenomenon in the cables likely to be exploited in some new proposed applications, e.g., for augmentation of damping in large space structures (Cutchins et al., 1988).

Contributed by the Applied Mechanics Division of THE AMERICAN SOCIETY OF MECHANICAL ENGINEERS for publication in the ASME JOURNAL OF APPLIED MECHANICS.

Discussion on the paper should be addressed to the Technical Editor, Professor Lewis T. Wheeler, Department of Mechanical Engineering, University of Houston, Houston, TX 77204-4792, and will be accepted until four months after final publication of the paper itself in the ASME JOURNAL OF APPLIED MECHANICS.

Manuscript received by the ASME Applied Mechanics Division, Apr. 18, 1994; final revision, Dec. 19, 1994. Associate Technical Editor: J. N. Reddy.

Analysis

The single strand cable under consideration has a fibrous core and is wrapped around helically by an arbitrary number of wires, hereafter denoted by m. The radius of the wire, its helix radius, and helix angle are denoted by R, r, and α, respectively. The case investigated in this paper is that of the cable subjected to an external axial pull or tensile load F, and an axial or torsional moment M. It is assumed that under this loading, the wires retain their helical character. The analysis makes extensive use of several simplifying approximations valid for practical wire rope design situations with the wire helix angle normally lying in the interval $(\pi/3, 2\pi/3)$ and the number of wires in a strand m equal to 5 or greater. Under these constraints, the approximate results obtained after neglecting terms such as $(\frac{1}{2})\cos^6\alpha$, $\sin^4(\pi/m)\cos^4\alpha$ in comparison to unity can be shown to be accurate to within approximately one percent. Some such simplified results developed by Kumar and Cochran (1990) and utilized in the present analysis are stated below:

Geometric Relations.

$$(R/r) \approx \sin\alpha \sin(\pi/m)[1 + (1/2)\cos^2\alpha \sin^2(\pi/m)]$$

$$(R'/r') \approx \sin\alpha' \sin(\pi/m) \times [1 + (1/2)\cos^2\alpha' \sin^2(\pi/m)] \quad (1)$$

where the primes are used to denote the parameter values after deformation due to loading.

Compatibility Relations.

$$\delta\alpha \approx g[\varepsilon(1 + \mu)\sin\alpha\cos\alpha - \beta\sin^2\alpha)]$$

$$\varepsilon_w \approx [\varepsilon - \delta\alpha\cot\alpha] \approx [\varepsilon h + (1/2)\beta g \sin 2\alpha] \quad (2)$$

where

ε_w = longitudinal strain in helical wires
ε = longitudinal strain of the wire rope
β = rotational cable strain, $(r \cdot \tau_s)$
τ_s = the twist angle per unit length of the cable
$\delta\alpha$ = $\alpha' - \alpha$, change in the wire helix angle due to the applied tensile load F and torsional moment M
g = $[1 + (\cos^2\pi/m - \mu)\cos^2\alpha + (1 - 2\mu)\cos^4\alpha]$
h = $[1 - (1 + \mu)\cos^2\alpha - \cos^2\pi/m \cos^4\alpha - \cos^6\alpha]$

Copyright © 1997 by ASME

Downloaded 04 May 2010 to 171.66.16.34. Redistribution subject to ASME license or copyright; see http://www.asme.org/terms/Terms_Use.cfm

Force and Moment Relations for Helical Wires.

$$T_a \approx (\pi R^2 E)\,[\varepsilon h + \beta g \sin\alpha\cos\alpha]$$

$$T_b \approx (1/4)(\pi R^4 E/r^2)\,[\varepsilon(1+2\mu)\sin\alpha\cos\alpha - \beta(1+\mu)\sin^2\alpha]\cos^2\alpha$$

$$G_a \approx [\pi R^4 E/(4r)]\,[(1/2)\varepsilon\sin 2\alpha\,\{\mu_f + \cos 2\alpha + 2(1-\mu)\cos^4\alpha + 2\cos^6\alpha - \sin^2\pi/m\cos^4\alpha\} - \beta\sin^2\alpha\cdot\{\cos 2\alpha + 2(1-\mu)\cos^4\alpha\cos^2\pi/m + 2\cos^6\alpha\}\cdot(1-\mu_f)]$$

$$G_b \approx -[\pi R^4 E/(4r)]\cos^2\alpha\,[\varepsilon\{\mu - (1+\mu)\sin^2\alpha \times (2 + (\cos^2\pi/m - \mu)\cos^2\alpha)\} + \beta\sin^2\alpha\tan\alpha \times \{2 + (\cos^2\pi/m - \mu)\cos^2\alpha + (-\mu + \sin^2\pi/m)\cos^4\alpha\}]$$

$$G_n = 0$$

$$q_n \approx -(\pi R^2 E/r)\cos^2\alpha\,[\varepsilon\{h - (1/4)(1+2\mu) \times \sin^4\alpha\cos^2\alpha\sin^2\pi/m\} + \beta\{g + (1/4)(1+\mu)\sin^4\alpha\sin^2\pi/m\}\sin\alpha\cos\alpha] \quad (3)$$

where

E, μ = modulus of rigidity and Poisson's ratio of the material, respectively
$\mu_f = \mu/(1+\mu)$
T = the resultant internal force on helical wires
G = the resultant internal moment on helical wires
q_n = the component of the resultant intensity of the force on helical wires per unit length along normal direction

and the subscripts a, n and b are used to denote the force and moment components along the axial, normal, and binormal directions, respectively.

The angle θ that locates the line of action of contact loads on a helical wire due to its neighbors is shown in Fig. 1. This angle measured in the plane perpendicular to the length of the wire is given by (Phillips and Costello, 1973)

$$\sin\theta = [1 + \sin^2\alpha'\tan^2\pi/m]^{-1/2}.$$

To be consistent with the earlier approximations resorted to in the analysis, the use of the better expression for θ subsequently given by Costello and Phillips (1974) was considered unnecessary. Further simplifying algebraic manipulations were made to obtain the following approximate expression:

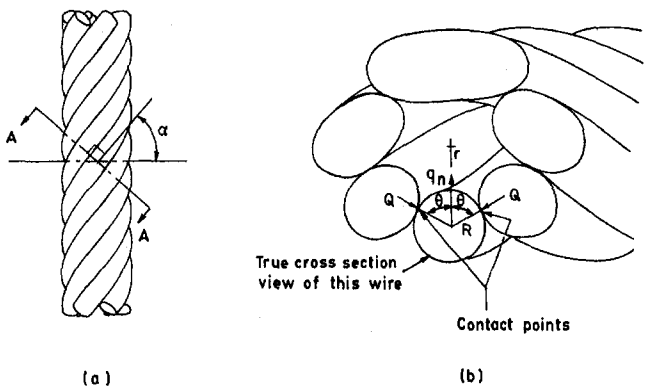


Fig. 1 Geometry of six wire, single strand cable

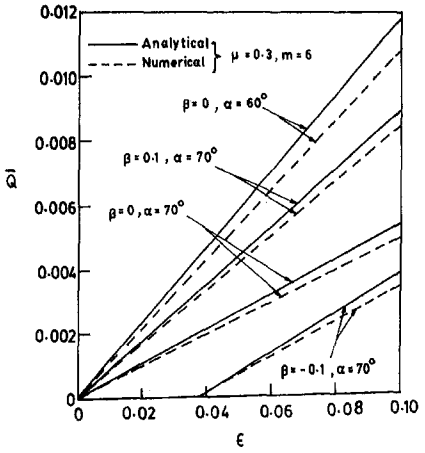


Fig. 2 Typical plots comparing the analytical and more exact numerical contact force results for several loadings

$$\cos\theta \approx \sin\alpha\sin\pi/m\,[1 + (1/2)\sin^2\pi/m\cos^2\alpha]. \quad (4)$$

Then the intensity of compressive forces per unit length along the common line of contact between any two adjacent helical wires, Q is given by

$$q_n = -2Q\cos\theta$$

leading to

$$Q \approx [\pi R^2 E/(2r)]\,(r/R)\cos^2\alpha \times [\varepsilon\{h - (1/4)(1+2\mu)\sin^4\alpha\cos^2\alpha\sin^2\pi/m\} + \beta\{g + (1/4)(1+\mu)\sin^4\alpha\sin^2\pi/m\}] \quad (5)$$

Here, the strains ε and β are related to the tensile force (F) and torsional moment (M) as follows (Kumar and Cochran, 1990):

$$\bar{F} = F_\varepsilon\varepsilon + F_\beta\beta$$
$$\bar{M} = M_\varepsilon\varepsilon + M_\beta\beta \quad (6)$$

where

$$\bar{F} = F/(m\pi R^2 E)$$
$$\bar{M} = M/(m\pi R^3 E)$$
$$F_\varepsilon = h\sin\alpha$$
$$F_\beta = [g - \{(1+\mu)/4\}\sin^2\pi/m\sin^2\alpha\cos^2\alpha]\sin^2\alpha\cos\alpha$$
$$M_\varepsilon = (r/R)\cos\alpha\,[h - (1/4)\sin^2\alpha\sin^2\pi/m]$$

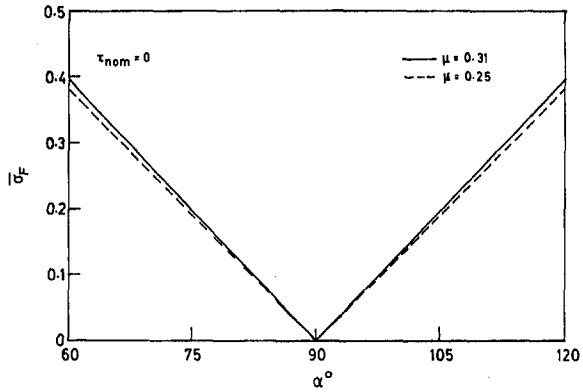


Fig. 3 Typical plots showing the influence of wire helix angle on dimensionless maximum contact stresses due to pure tension

Downloaded 04 May 2010 to 171.66.16.34. Redistribution subject to ASME license or copyright; see http://www.asme.org/terms/Terms_Use.cfm

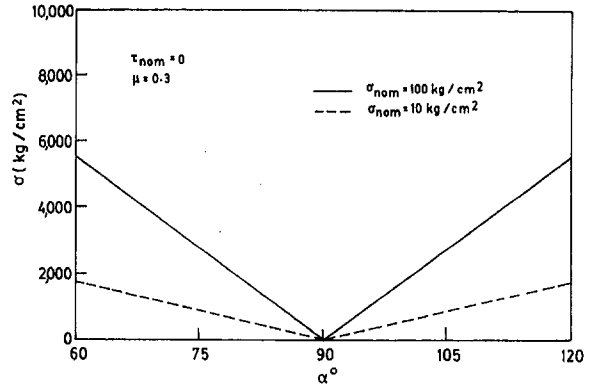


Fig. 4 Typical plots showing the influence of wire helix angle on maximum contact stresses due to pure tension

$$M_\beta = (r/R)\sin\alpha\,[g\cos^2\alpha + (1/4)\sin^4\alpha\sin^2\pi/m \times\{(1-\mu) + (1+3\mu)\cos^2\alpha\}] \quad (7)$$

Solving Eqs. (6) and (7) for ε and β and substituting the resulting expressions into (5) followed by nondimensionalization leads to

$$\bar{Q} \approx Q_F\bar{F} + Q_M\bar{M} \quad (8)$$

where

$$\bar{Q} = Q/(E\pi R)$$

$$Q_F \approx (1/2)(\cos^2\alpha/\sin\alpha)[1 + \mu^2 - \cos^2\alpha + (2+4\mu)\cos^4\alpha]$$

and

$$Q_M \approx (1/16)(1+\mu)(1+\mu+\mu^2)\sin^3 2\alpha\sin\pi/m \times[1-(1-3\mu-\mu^2)\cos^2\alpha].$$

At this stage, to assess the accuracy of the analytical predictions, it may be worthwhile to compare these with those obtained using the more accurate numerical approach adopted by Costello and Phillips (1974). Such a comparision for several typical engineering situations is presented in Fig. 2. It shows the approximate analytical results to be in close agreement with the corresponding numerical solutions. This clearly establishes validity of the approximate analytical approach presented here.

Contact Stresses: To compare the contact stresses, we make use of the following results for the three principal compressive stresses due to the contact force (Seely and Smith, 1952):

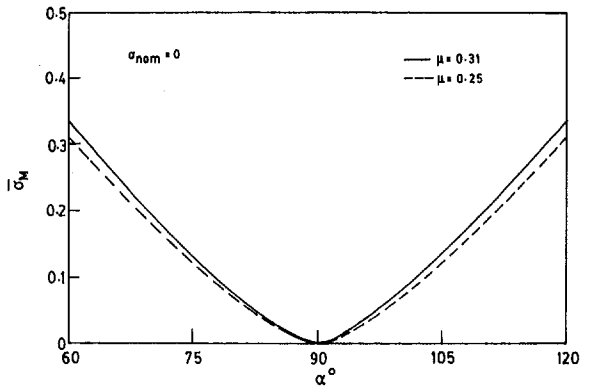


Fig. 5 Typical plots showing the influence of wire helix angle on dimensionless maximum contact stresses due to pure torque loading

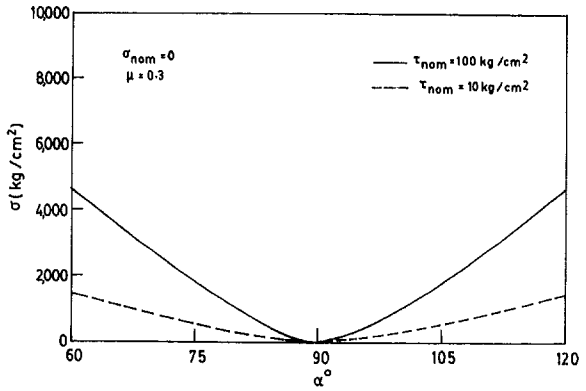


Fig. 6 Typical plots showing the influence of wire helix angle on maximum contact stresses due to pure torque loading

$$\sigma_x = 2\mu\,(p/d)\cdot[\sqrt{\{1+(z/p)^2\}} - (z/p)]$$
$$\sigma_y = (p/d)\cdot[\sqrt{\{1+(z/p)^2\}} - (z/p)]^2/\sqrt{\{1+(z/p)^2\}}]$$
$$\sigma_z = (p/d)/\sqrt{\{1+(z/p)^2\}}$$

where

$\sigma_x, \sigma_y, \sigma_z$ = principal compressive stresses in the axial, tangential, and radial directions, respectively.
z = distance below the surface to the point under consideration
$p = \sqrt{[2Qd/\pi]}$
$d = [2(1-\mu^2)R/E]$.

Since the above compressive stresses are maximum when $z = 0$, i.e., on the surface of the wires at the contact points, we get

$$(\sigma_x)_{\max} = 2\mu\,(p/d) = 2\mu\sqrt{[1/(1-\mu^2)]}\cdot\sqrt{[EQ/\pi R)]}$$

$$(\sigma_y)_{\max} = (\sigma_z)_{\max} = (p/d) = \sqrt{[1/(1-\mu^2)]}\cdot\sqrt{[(EQ/(\pi R)]}.$$

The latter of these is the maximum normal contact stress which we denote by σ; hence

$$\sigma \approx \sqrt{[1/(1-\mu^2)]}\cdot\sqrt{[QE/(\pi R)]}.$$

Substitution of the earlier expression for Q followed by nondimensionalization leads to the following expression for the maximum contact stress:

$$\bar{\sigma} \approx \sqrt{[1/(1-\mu^2)]}\cdot\sqrt{[Q_F\bar{F} + Q_M\bar{M}]} \quad (9)$$

where

$$\bar{\sigma} = \sigma/E.$$

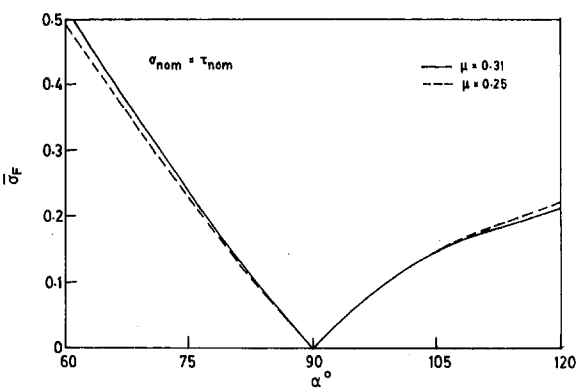


Fig. 7 Typical plots showing the influence of wire helix angle on dimensionless maximum contact stresses due to combined loading

Downloaded 04 May 2010 to 171.66.16.34. Redistribution subject to ASME license or copyright; see http://www.asme.org/terms/Terms_Use.cfm

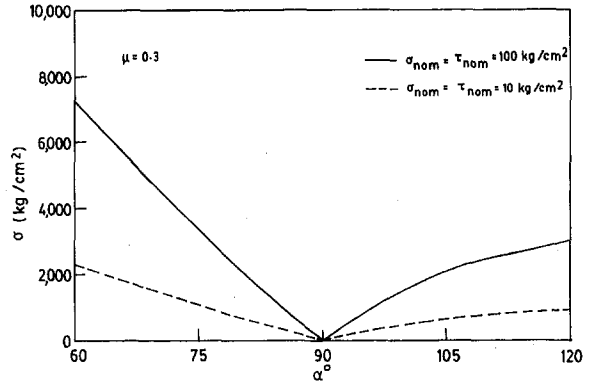


Fig. 8 Typical plots showing the influence of wire helix angle on maximum contact stresses due to combined loading

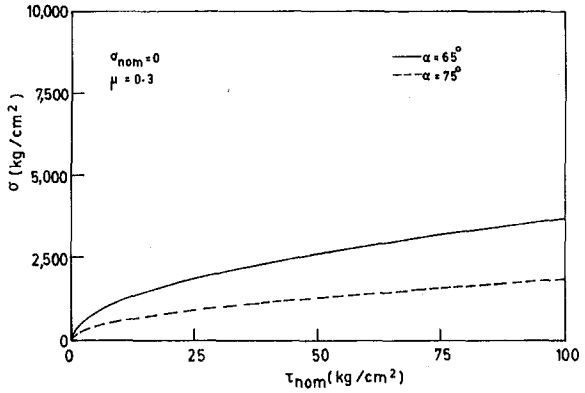


Fig. 10 Typical plots showing the variation of maximum contact stresses with nominal torsional stresses

Alternatively, the expression for the maximum normal contact stress can also be written in more useful dimensional and dimensionless forms as

$$\sigma \approx \sqrt{[E/2]}\,(1+\mu^2)\cos\alpha\,\sqrt{(\sin\alpha)} \times [\{1+2\,(1+2\mu)\cos^4\alpha\}\,\sigma_{\text{nom}} + (1+\mu)^2)\cos\alpha\,\tau_{\text{nom}}]^{1/2} \quad (10)$$

and

$$\bar{\sigma} \approx (1+\mu^2)\cos\alpha\,\sqrt{(\sin\alpha)}\,[\{1+2(1+2\mu)\cos^4\alpha\}\,\bar{\sigma}_{\text{nom}} + (1+\mu)^2\cos\alpha\,\bar{\tau}_{\text{nom}}]^{1/2} \quad (11)$$

where

$$\bar{\sigma}_{\text{nom}} = \sigma_{\text{nom}}/E = F/(m\pi R^2 E) = \bar{F}$$

$$\bar{\tau}_{\text{nom}} = \tau_{\text{nom}}/E = M/(m\pi R^2 r E) = (R/r)\bar{M}.$$

The importance of using $\bar{\tau}_{\text{nom}}$ in place of $\bar{M}$ on the right-hand side is quite evident. This enables us to express the contact stresses directly in terms of the nominal tensile and torsional stresses and explicitly independent of the number of helical wires m.

Applications

1 Effect of Pure Tension: Taking $M = 0$, the governing expression for the maximum contact stress can be approximated to

$$\sigma \approx \sqrt{[E\sigma_{\text{nom}}/2]}\,\cos\alpha\,\sqrt{[\sin\alpha]}\,(1+\mu^2) \times [1+(1+2\mu)\cos^4\alpha] \quad (12)$$

and in the dimensionless form as

$$\bar{\sigma}_F \approx (1/\sqrt{2})\cos\alpha\,\sqrt{[\sin\alpha]}\,(1+\mu^2) \times [1+(1+2\mu)\cos^4\alpha] \quad (13)$$

where

$$\bar{\sigma}_F = \sigma/\sqrt{[E\sigma_{\text{nom}}]} = \sigma/\sqrt{[EF/(m\pi R^2)]}$$

2 Effect of Pure Torsional Moment: Taking $F = 0$, the governing expression for the contact stresses can be approximated to

$$\sigma \approx \sqrt{[E\tau_{\text{nom}}/2]}\,(1+\mu)\,(1+\mu^2)\,\sqrt{[\cos^3\alpha\,\sin\alpha]} \quad (14)$$

and in the dimensionless form as

$$\bar{\sigma}_M \approx (1/\sqrt{2})\,(1+\mu)\,(1+\mu^2)\,\sqrt{[\cos^3\alpha\,\sin\alpha]} \quad (15)$$

where

$$\bar{\sigma}_M = \sigma/\sqrt{[E\tau_{\text{nom}}]} = \sigma/\sqrt{[EM/(m\pi R^2 r)]}$$

3 Conditions for Contact Stresses to be Zero: Using Eq. (8), it is easy to see that for the contact stresses to be zero, the external axial force and moment applied on the wire rope are related according to

$$(\bar{F}/\bar{M}) = -(Q_M/Q_F)$$

which can be alternatively written in the simplified form

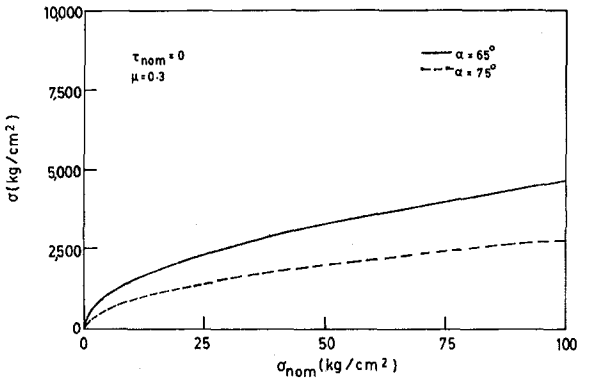


Fig. 9 Typical plots showing the variation of maximum contact stresses with nominal tensile stresses

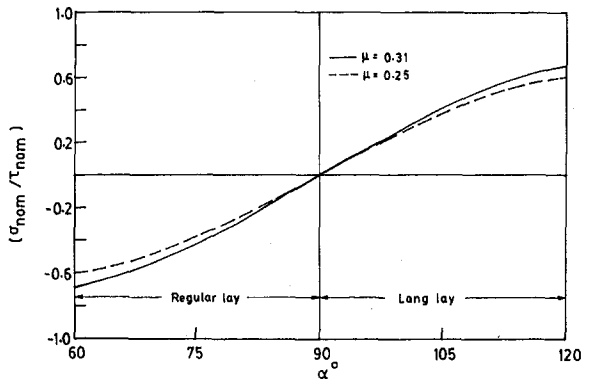


Fig. 11 Typical plots showing the influence of wire helix angle on nominal tensile stress/torsional stress ratio for contact stresses to vanish

Downloaded 04 May 2010 to 171.66.16.34. Redistribution subject to ASME license or copyright; see http://www.asme.org/terms/Terms_Use.cfm

$$(\sigma_{nom}/\tau_{nom}) \approx -(1 + \mu)^2 \sin^3 \alpha \cos \alpha \times [1 - \mu^3 + 3\mu \cos^2 \alpha - 2 \cos^4 \alpha]. \quad (16)$$

Results and Discussion

The analytical expressions developed here are of considerable significance. The explicit results have been obtained in dimensional as well as dimensionless form. These closed-form solutions provide useful information concerning the influence of cable parameters and the material properties. The number of helical wires in the rope does not appear explicitly in the approximate analytical results developed here. However, it significantly affects the contact stresses through the nominal stresses which are strongly dependent on this parameter.

For a better assessment of the effect of the various important parameters on rope design, the plots showing their influence on contact stresses are presented (Figs. 3–11). Figure 3 shows the effect of the helix angle for two extreme situations of the Poisson's ratios for steel, $\mu = 0.25$ and 0.31 when only the tensile force is applied. The maximum dimensionless contact stress $\bar{\sigma}_F$ continually decreases as the helix angle increases from 60 to 90 deg for ropes with regular lay and decreases from 120 to 90 deg in case of lang lay. The Poisson's ratio shows little effect on these stresses, however. The corresponding results presented in dimensional form enable a better appreciation of the order of contact stresses (Fig. 4). Interestingly, the maximum contact stresses are significantly higher than the nominal stress due to the tensile loads. The results showing the influence of pure torsional loading on contact stresses are presented in Figs. 5 and 6. The same general trends are observed with the two types of loadings. The effect of the combined tensile and torsional loadings is shown in Figs. 7 and 8. The result of such a "mixing" is one of reinforcement or cancellation of the maximum contact stresses due to either loading alone, depending upon the direction of the lay of helical wires and that of the axial moment.

More significantly, from the dimensional form of results presented here, it is evident that even for relatively small nominal tensile or torsional stresses or their combination, the contact stresses can be much higher. Figures 9 and 10 provide a better feel of the order of magnitude of the contact stresses that are generated as a result of the varying levels of nominal stresses applied. The maximum contact stresses increase nonlinearly with tensile or torsional stresses. Even for practically feasible levels of nominal stresses, these can and do exceed the elastic limit of the material. Through these results, it seems conceptually possible to explain the phenomenon of relatively higher energy dissipation levels in the ropes subjected to variable loads. This may be attributed to hysteresis energy losses in wires through stresses exceeding the elastic limit as a result of the contact stresses induced. It is evident that the fluctuating moderate loads may give rise to the contact stresses in the material that may reach even its ultimate strength levels causing it to yield and hence considerably enhanced rates of energy dissipation in the process. That may also explain the ever increasing number of broken helical wires especially in the ropes of complex cross section.

Finally, the Fig. 11 focuses on the effect of cable parameters on the nominal tensile stress/torsional stress ratio for which the generally undesirable contact stresses theoretically reduce to zero. This ratio is strongly influenced by the wire helix angle. For the contact stresses to vanish in cables with regular lay, the torsional moment vector must be opposite to that of the tensile load. For the cables with lang lay to have negligible contact stresses, however, the two types of load vectors must have the same axial direction. Thus, the effect of tensile loads on the resulting contact stresses can be largely overcome by introducing torsional moments appropriately. The analysis presented here makes it easy to select the moments that would lead to negligible contact stresses and hence an extended cable life span.

Concluding Remarks

The closed-form expression for critical contact stress has been developed for single strand cables with fibrous cores. Of the two material properties, E and μ, it is only the modulus of rigidity which is shown to have a strong influence on the resulting level of the contact stresses. Evidently the wire helix angle is rather an important design parameter which significantly influences these stresses. For cable designs—with regular or lang lay—the contact stresses are relatively smaller when the helix angles chosen are close to $\pi/2$. Hence such "large" helix angles are likely to promote longer life span. On the other hand, in applications involving the use of the wire ropes for dissipating vibration energy, the smaller helix angles $\sim \pi/3$ or $2\pi/3$ leading to much larger contact stresses may be recommended.

References

Bert, C. W., and Stein, R. A., 1962, "Stress Analysis of Wire Rope in Tension and Torsion," *Wire and Wire Products,* Vol. 37, pp. 769–770; 772–816.

Costello, G. A., 1978, "Analytical Investigation of Wire Rope," ASME *Applied Mechanics Reviews,* Vol. 31, pp. 897–900.

Costello, G. A., 1983, "Stresses in Multilayered Cables," ASME *Journal of Energy Resources Technology,* Vol. 105, pp. 337–340.

Costello, G. A., and Buston, G. J., 1982, "Simplified Bending Theory for Wire-Ropes," *ASCE Journal of the Engineering Mechanics Division,* Vol. 108, pp. 219–227.

Costello, G. A., and Miller, R. E., 1979, "Lay Effect of Wire Rope," *ASCE Journal of Engineering Mechanics Division,* Vol. 105, pp. 597–608.

Costello, G. A., and Miller, R. E., 1980, "Static Response of Reduced Rotation Rope," *ASCE Journal of the Engineering Mechanics Division,* Vol. 106, pp. 623–631.

Costello, G. A., and Phillips, J. W., 1973, "Contact Stresses in Thin Twisted Rods," ASME JOURNAL OF APPLIED MECHANICS, Vol. 40, pp. 629–630.

Costello, G. A., and Phillips, J. W., 1974, "A More Exact Theory for Twisted Wire Cables," *ASCE Journal of the Engineering Mechanics Division,* Vol. 100, pp. 1096–1099.

Costello, G. A., and Phillips, J. W., 1976, "Effective Modulus of Twisted Wire Cables," *ASCE Journal of the Engineering Mechanics Division,* Vol. 102, pp. 171–181.

Costello, G. A., and Sinha, S. K., 1977a, "Torsional Stiffness of Twisted Wire Cables," *ASCE Journal of the Engineering Mechanics Division,* Vol. 103, pp. 766–770.

Costello, G. A., and Sinha, S. K., 1977b, "Static Behavior of Wire Rope," *ASCE Journal of the Engineering Mechanics Division,* Vol. 103, pp. 1011–1022.

Cutchins, M. A., Cochran, J. E., Jr., Kumar, K., Tinker, M. L., and Fitz-Coy, N. G., 1988, "Analysis of Coils of Wire Rope Arranged for Passive Damping," *Proceedings of the Third International Conference on Recent Advances in Structural Dynamics,* Southampton, UK, July 18–22, pp. 469–479.

Hall, H. M., 1951, "Stresses in Small Wire Ropes," *Wire and Wire Products,* Vol. 26, pp. 228; 257–259.

Hruska, F. H., 1951, "Calculations of Stresses in Wire Ropes," *Wire and Wire Products,* Vol. 26, pp. 766–767; 799–801.

Hruska, F. H., 1952, "Radial Forces in Wire Ropes," *Wire and Wire Products,* Vol. 27, pp. 459–463.

Hruska, F. H., 1953, "Tangential Forces in Wire Ropes," *Wire and Wire Products,* Vol. 28, pp. 455–460.

Kumar, K., and Cochran, J. E., Jr., 1987, "Closed-Form Analysis for Elastic Deformations of Multilayered Strands," ASME JOURNAL OF APPLIED MECHANICS, Vol. 54, pp. 898–903.

Kumar, K., and Cochran, J. E., Jr., 1990, "Analytical Estimation for Static Elastic Deformation of Wire Ropes with Fibrous Core," ASME JOURNAL OF APPLIED MECHANICS, Vol. 57, pp. 1000–1003.

Leissa, A. W., 1959, "Contact Stresses in Wire Ropes," *Wire and Wire Products,* Vol. 34, pp. 307–316; 372–373.

Phillips, J. W., and Costello, G. A., 1973, "Contact Stresses in Twisted Wire Cables," *ASCE Journal of the Engineering Mechanics Division,* Vol. 99, pp. 331–341.

Phillips, J. W., and Costello, G. A., 1985, "Analysis of Wire Ropes with Internal-Wire-Rope Cores," ASME JOURNAL OF APPLIED MECHANICS, Vol. 52, pp. 510–516.

Seely, F. B., and Smith, J. O., 1952, *Advanced Mechanics of Materials,* John Wiley and Sons, New York, pp. 365–366.

Starkey, W. L., and Cress, H. A., 1959, "An Analysis of Critical Stresses and Mode of Failure of a Wire Rope," ASME *Journal of Engineering for Industry,* Vol. 81, pp. 307–316.

Velinsky, S. A., Anderson, G. L., and Costello., G. A., 1984, "Wire Rope with Complex Cross Sections," *ASCE Journal of the Engineering Mechanics Division,* Vol. 110, pp. 380–391.

Downloaded 04 May 2010 to 171.66.16.34. Redistribution subject to ASME license or copyright; see http://www.asme.org/terms/Terms_Use.cfm

C. W. Cai
Department of Mechanics,
Zhongshan University,
Guangzhou, P. R. China

H. C. Chan
Head.

Y. K. Cheung

Department of Civil and
Structural Engineering,
The University of Hong Kong,
Hong Kong, China

Localized Modes in Periodic Systems With Nonlinear Disorders

The localized modes of periodic systems with infinite degrees-of-freedom and having one or two nonlinear disorders are examined by using the Lindstedt-Poincare (L-P) method. The set of nonlinear algebraic equations with infinite number of variables is derived and solved exactly by the U-transformation technique. It is shown that the localized modes exist for any amount of the ratio between the linear coupling stiffness k_c and the coefficient γ of the nonlinear disordered term, and the nonsymmetric localized mode in the periodic system with two nonlinear disorders occurs as the ratio k_c/γ, decreasing to a critical value depending on the maximum amplitude.

Introduction

The localized modes in disordered periodic systems have been investigated by several researchers (Hodges, 1982; Pierre and Dowell; Cha and Pierre, 1991). A detailed review of the localization of normal modes was given by Li and Benaroya (1992). The nonlinear localized modes in a perfectly cyclic periodic system was examined with the averaging method of multiple scales (Vakakis et al., 1993). Recently, the U-transformation technique (Cai et al., 1988), was applied to analyze the two and three-dimensional disordered periodic systems for localized modes (Cai et al., 1995).

In the present work, monocoupled periodic systems with infinite degrees-of-freedom and with one or two nonlinear subsystems are considered. The effect of the nonlinear disorders on localized modes is examined by using the Lindstedt-Poincare (L-P) method. The key to the settlement of the question lies in solving the set of nonlinear algebraic equations with infinite number of variables. Such a set of equations is equivalent to imposing a condition to prevent the formation of secular terms. The closed-form solutions of nonlinear algebraic equations describing the localized modes are found by means of the *U*-transformation technique. It is possible to obtain some new results for this problem.

Incidentally, it should be mentioned that the analysis method in the present paper may be extended to the forced oscillation of a system with linear damping.

Governing Equations

Consider the system shown in Fig. 1. It consists of an infinite number of subsystems connected to each other by means of the linear springs having stiffness ϵk_c. Each subsystem consists of a mass M connected to a rigid foundation by a spring with linear stiffness (for ordered ones) or nonlinear stiffness (for disordered ones). In Fig. 1, j_1 and j_2 denote the ordinal number of the disordered subsystem.

It is assumed that the system energy is large enough in order to realize the localized motion mode and that both the coupling stiffness ϵk_c and the coefficient $\epsilon\gamma$ of the cubic term of the nonlinear stiffness in the disordered subsystems are weak, i.e., ϵ is a positive nondimensional small parameter.

This work is aimed at analyzing the mode localization phenomena. The localized mode of the system with infinite number of subsystems is hardly affected by the conditions at infinity. Consequently the system under consideration may be regarded as a cyclic periodic one.

At the outset a cyclic periodic system with N number of subsystems is considered. Then by adopting a limiting process with N approaching infinity, the governing equation will be applicable for a cyclic periodic system with infinite number of subsystems.

Applying Newton's second law to every mass M, we can write the differential equations of motion as follows:

$$M\ddot{\chi}_k + K\chi_k - \epsilon k_c(\chi_{k+1} + \chi_{k-1} - 2\chi_k) = 0 \quad k \neq j_1, j_2$$

$$M\ddot{\chi}_k + K\chi_k - \epsilon k_c(\chi_{k+1} + \chi_{k-1} - 2\chi_k) + \epsilon\gamma\chi_k^3 = 0$$

$$k = j_1, j_2 \quad (2.1)$$

where χ_k denotes the longitudinal displacement of the kth mass and $\chi_{N+1} = \chi_1$, $\chi_0 = \chi_N$ due to cyclic periodicity. The superior double dot denotes the second derivative with respect to the time variable t. K and M denote the stiffness and mass for the ordered subsystems. The nonlinear terms play the role of disorder.

Introducing the time substitution

$$\tau = \omega t \quad (2.2)$$

into Eq. (2.1) results in

$$\omega^2\chi_k'' + \omega_0^2\chi_k = \epsilon\frac{k_c}{M}(\chi_{k+1} + \chi_{k-1} - 2\chi_k) \quad k \neq j_1, j_2$$

$$\omega^2\chi_k'' + \omega_0^2\chi_k = \epsilon\frac{k_c}{M}(\chi_{k+1} + \chi_{k-1} - 2\chi_k) - \epsilon\frac{\gamma}{M}\chi_k^3$$

$$k = j_1, j_2 \quad (2.3)$$

where the prime symbol designates differentiation with respect to τ and

$$\omega_0^2 = \frac{K}{M}. \quad (2.4)$$

The ω in Eqs. (2.2) and (2.3) is the fundamental frequency to be determined. The periodicity condition may be expressed as

Contributed by the Applied Mechanics Division of THE AMERICAN SOCIETY OF MECHANICAL ENGINEERS for publication in the ASME JOURNAL OF APPLIED MECHANICS.

Discussion on this paper should be addressed to the Technical Editor, Professor Lewis T. Wheeler, Department of Mechanical Engineering, University of Houston, Houston, TX 77204-4792, and will be accepted until four months after final publication of the paper itself in the ASME JOURNAL OF APPLIED MECHANICS.

Manuscript received by the ASME Applied Mechanics Division, May 7, 1996; final revision, Dec. 3, 1996. Associate Technical Editor: W. K. Liu.

Copyright © 1997 by ASME

Downloaded 04 May 2010 to 171.66.16.34. Redistribution subject to ASME license or copyright; see http://www.asme.org/terms/Terms_Use.cfm

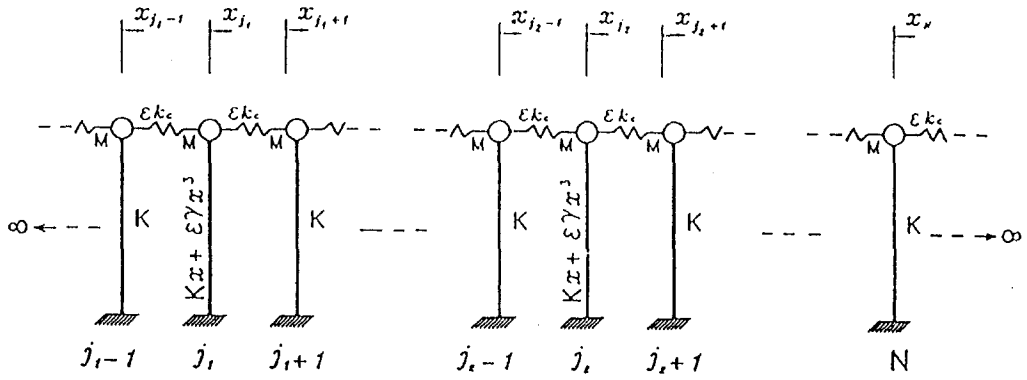


Fig. 1

$$\chi_k(\tau + 2\pi) = \chi_k(\tau) \quad k = 1, 2, \ldots, N. \tag{2.5}$$

According to the L-P method, the solution of Eq. (2.3) is assumed in the form of

$$\chi_k(\tau) = \chi_{k0}(\tau) + \epsilon\chi_{k1}(\tau) + \epsilon^2\chi_{k2}(\tau) + \ldots \quad k = 1, 2, \ldots, N \tag{2.6}$$

and ω is given as

$$\omega = \omega_0 + \epsilon\omega_1 + \epsilon^2\omega_2 + \ldots. \tag{2.7}$$

Substituting Eqs. (2.6) and (2.7) into Eq. (2.3), the coefficients of equal powers of ϵ on both sides of Eq. (2.3) must be equal, i.e.,

$$\omega_0^2\chi_{k0}'' + \omega_0^2\chi_{k0} = 0 \quad k = 1, 2, \ldots, N \tag{2.8a}$$

$$\omega_0^2\chi_{k1}'' + \omega_0^2\chi_{k1} = -2\omega_0\omega_1\chi_{k0}'' + \frac{k_c}{M}(\chi_{k+1,0} + \chi_{k-1,0} - 2\chi_{k,0}) \quad k \neq j_1, j_2$$

$$\omega_0^2\chi_{k1}'' + \omega_0^2\chi_{k1} = -2\omega_0\omega_1\chi_{k0}'' + \frac{k_c}{M}(\chi_{k+1,0} + \chi_{k-1,0} - 2\chi_{k,0}) - \frac{\gamma}{M}\chi_{k,0}^3 \quad k = j_1, j_2 \tag{2.8b}$$

Without loss of generality, we can assume that the initial velocity for each subsystem is zero, i.e.,

$$\chi_{k,j}'(0) = 0 \quad j = 0, 1, \ldots \quad k = 1, 2, \ldots, N. \tag{2.9}$$

Then the solution of Eq. (2.8a) may be expressed as

$$\chi_{k,0} = A_{k0}\cos\tau \quad k = 1, 2, \ldots, N. \tag{2.10}$$

Inserting solution (2.10) into Eq. (2.8b) results in

$$\omega_0^2(\chi_{k1}'' + \chi_{k1}) = \left[2\omega_0\omega_1 A_{k0} + \frac{k_c}{M}(A_{k+1,0} + A_{k-1,0} - 2A_{k,0})\right]\cos\tau \quad k \neq j_1, j_2 \tag{2.11a}$$

$$\omega_0^2(\chi_{k1}'' + \chi_{k1}) = \left[2\omega_0\omega_1 A_{k0} + \frac{k_c}{M}(A_{k+1,0} + A_{k-1,0} - 2A_{k,0}) - \frac{3\gamma}{4M}A_{k,0}^3\right] \times \cos\tau - \frac{\gamma}{4M}A_{k,0}^3\cos 3\tau \quad k = j_1, j_2. \tag{2.11b}$$

In the second equation the identical relation $\cos^3\tau = (\frac{1}{4})(3\cos\tau + \cos 3\tau)$ has been used.

In order to eliminate the secular term from $\chi_{k1}(k = 1, 2, \ldots, N)$ we must set the coefficients of $\cos\tau$ on the right-hand sides of Eqs. (2.11a) and (2.11b) equal to zero, i.e.,

$$2\omega_0\omega_1 A_{k0} + \frac{k_c}{M}(A_{k+1,0} + A_{k-1,0} - 2A_{k,0}) = 0 \quad k \neq j_1, j_2 \tag{2.12a}$$

$$2\omega_0\omega_1 A_{k0} + \frac{k_c}{M}(A_{k+1,0} + A_{k-1,0} - 2A_{k,0}) - \frac{3\gamma}{4M}A_{k,0}^3 = 0 \quad k = j_1, j_2. \tag{2.12b}$$

One can now apply the U-transformation technique to Eqs. (2.12a, b). The U and inverse U transformation may be expressed as

$$A_{k0} = \frac{1}{\sqrt{N}}\sum_{m=1}^{N} e^{i(k-1)m\psi}a_{m,0} \quad k = 1, 2, \ldots, N \tag{2.13a}$$

and

$$a_{m,0} = \frac{1}{\sqrt{N}}\sum_{k=1}^{N} e^{-i(k-1)m\psi}A_{k0} \quad m = 1, 2, \ldots, N \tag{2.13b}$$

where $\psi = 2\pi/N$, $i = \sqrt{-1}$, and $a_{N-m} = \bar{a}_m$ in which the superior bar denotes complex conjugation.

By using the U-transformation, Eqs. (2.12a, b) become

$$2\omega_0\omega_1 a_{m0} + \frac{2k_c}{M}(\cos m\psi - 1)a_{m0} - \frac{3\gamma}{4M}\frac{1}{\sqrt{N}} \times \sum_{k\neq j_1,j_2} e^{-i(k-1)m\psi}A_{k0}^3 = 0 \quad m = 1, 2, \ldots, N. \tag{2.14}$$

Consequently a_{m0} takes the form as

$$a_{m0} = \frac{3\gamma}{8k_c}\left(\omega_0\omega_1\frac{M}{k_c} - 1 + \cos m\psi\right)^{-1}\frac{1}{\sqrt{N}} \times \sum_{j\neq j_1,j_2} e^{-i(j-1)m\psi}A_{j0}^3. \tag{2.15}$$

Substituting Eq. (2.15) into Eq. (2.13a) yields

$$A_{k0} = \frac{3\gamma}{8k_c}\sum_{j\neq j_1,j_2}\left[\frac{1}{N}\sum_{m=1}^{N} e^{i(k-j)m\psi} \times \left(\omega_0\omega_1\frac{M}{k_c} - 1 + \cos m\psi\right)^{-1}\right]A_{j0}^3. \tag{2.16a}$$

Downloaded 04 May 2010 to 171.66.16.34. Redistribution subject to ASME license or copyright; see http://www.asme.org/terms/Terms_Use.cfm

Noting that the imaginary part of the sum of series in the square brackets is equal to zero, Eq. (2.16a) may be rewritten as

$$A_{k0} = \frac{3\gamma}{8k_c} \sum_{j=j_1,j_2} \left[\frac{1}{N} \sum_{m=1}^{N} \cos (k-j)m\psi \times \left(\omega_0\omega_1 \frac{M}{k_c} - 1 + \cos m\psi \right)^{-1} \right] A_{j0}^3. \quad (2.16b)$$

By letting N approach infinity, the limit of the series summation in the square brackets on the right-hand side of Eq. (2.16b) becomes the definite integral (Cai et al., 1988), i.e.,

$$\lim_{N\to\infty} \frac{1}{N} \sum_{m=1}^{N} \cos (k-j)m\psi \left(\omega_0\omega_1 \frac{M}{k_c} - 1 + \cos m\psi \right)^{-1} = \frac{1}{\pi} \int_0^{\pi} \cos (k-j)\theta \left[\omega_0\omega_1 \frac{M}{k_c} - 1 + \cos \theta \right]^{-1} d\theta \equiv \beta_{(k-j)}. \quad (2.17)$$

If

$$\left| \omega_0\omega_1 \frac{M}{k_c} - 1 \right| > 1 \quad (2.18)$$

the definite integral shown in Eq. (2.17) is in existence.

The condition (2.18) is equivalent to

$$\omega^2 > \omega_U^2 \text{ or } \omega^2 < \omega_L^2 \quad (2.19)$$

where $\omega^2 = \omega_0^2 + 2\omega_0\omega_1\epsilon + 0(\epsilon^2)$ and ω_U, ω_L denote the upper and lower limits of the pass band for ordered periodic system ($\gamma = 0$), i.e.,

$$\omega_U^2 = \frac{K}{M} + \frac{4\epsilon k_c}{M}, \quad \omega_L^2 = \frac{K}{M}. \quad (2.20)$$

Equation (2.19) indicates that ω lies in the stop band of the ordered periodic system. Because the frequency corresponding to localized mode must lie in the stop band therefore we have no interest for the case that the integral shown in Eq. (2.17) is not in existence.

Consider now the system having infinite number of subsystems. Consequently Eq. (2.16b) becomes

$$A_{k0} = \frac{3\gamma}{8k_c} [\beta_{(k-j_1)} A_{j_1 0}^3 + \beta_{(k-j_2)} A_{j_2 0}^3] \quad k = 1, 2, \ldots, \infty \quad (2.21)$$

where $\beta_{(k-j)}$ has been defined by Eq. (2.17). Setting $k = j_1$ and j_2, respectively, yield

$$A_{j_1 0} = \frac{3\gamma}{8k_c} [\beta_0 A_{j_1 0}^3 + \beta_{(j_1-j_2)} A_{j_2 0}^3]$$

$$A_{j_2 0} = \frac{3\gamma}{8k_c} [\beta_{(j_2-j_1)} A_{j_1 0}^3 + \beta_0 A_{j_2 0}^3]. \quad (2.22)$$

The unknown amplitudes A_{k0} can be obtained by substituting the nontrivial solution of Eq. (2.22) into Eq. (2.21).

Localized Modes

Before we discuss the solutions of Eq. (2.22), let us calculate the definite integral β_i shown in Eq. (2.17).

$$\beta_0 = \frac{1}{\pi} \int_0^{\pi} \frac{1}{a + \cos\theta} d\theta = \text{sgn}(a) \frac{1}{\sqrt{a^2 - 1}} \quad |a| > 1 \quad (3.1)$$

$$\beta_1 = \beta_{-1} = \frac{1}{\pi} \int_0^{\pi} \frac{\cos\theta}{a + \cos\theta} d\theta = 1 - a\beta_0 \quad |a| > 1 \quad (3.2)$$

$$\beta_2 = \beta_{-2} = \frac{1}{\pi} \int_0^{\pi} \frac{\cos 2\theta}{a + \cos\theta} d\theta = -2a + (2a^2 - 1)\beta_0 \quad |a| > 1 \quad (3.3)$$

$$\beta_3 = \beta_{-3} = \frac{1}{\pi} \int_0^{\pi} \frac{\cos 3\theta}{a + \cos\theta} d\theta = 4a^2 - 1 - a(4a^2 - 3)\beta_0 \quad |a| > 1 \quad (3.4)$$

where

$$a \equiv \omega_0\omega_1 \frac{M}{k_c} - 1. \quad (3.5)$$

It can be verified that

$$\frac{\beta_3}{\beta_2} = \frac{\beta_2}{\beta_1} = \frac{\beta_1}{\beta_0} = \xi \quad (3.6)$$

with

$$\xi = -a + \text{sgn}(a)\sqrt{a^2 - 1} \quad |a| > 1. \quad (3.7)$$

It is obvious that ξ and "a" are of opposite sign and $|\xi| < 1$.

Localized Modes in the System With One Nonlinear Disorder

The periodic system with infinite number of subsystems in which only one subsystem having nonlinear stiffness is considered. The governing Eq. (2.22) can be reduced to

$$A_{j_1 0} = \frac{3\gamma}{8k_c} \beta_0 A_{j_1 0}^3. \quad (3.8)$$

There is a nontrivial solution of the above equation if and only if

$$\frac{3\gamma}{8k_c} \beta_0 A_{j_1 0}^2 = 1. \quad (3.9)$$

Inserting Eq. (3.1) and (3.5) into Eq. (3.9) results in

$$\omega_0\omega_1 = \frac{k_c}{M} \left[1 + \frac{1}{\eta} \sqrt{\eta^2 + 1} \right] \quad (3.10)$$

where

$$\eta = \frac{8k_c}{3\gamma} A_{j_1 0}^{-2}. \quad (3.11)$$

Noting that $\omega^2 = \omega_0^2 + 2\epsilon\omega_0\omega_1 + 0(\epsilon^2)$, it can be proved that if $\gamma > 0$ (hardening spring) $\omega^2 > (K/M) + (4\epsilon k_c/M)$ and $\gamma < 0$ (softening spring) $\omega^2 < (K/M)$. Consequently we can come to the conclusion that if $\gamma > 0$ there is one localized mode with ω greater than ω_U and if $\gamma < 0$ there is one localized mode with ω less than ω_L.

For the localized mode the amplitudes of all subsystems may be obtained from Eqs. (2.21) and (3.8) as

$$A_{j_1+1,0} = A_{j_1-1,0} = \frac{3\gamma}{8k_c} \beta_1 A_{j_1 0}^3 = \xi A_{j_1 0}$$

$$A_{j_1+2,0} = A_{j_1-2,0} = \frac{3\gamma}{8k_c} \beta_2 A_{j_1 0}^3 = \xi^2 A_{j_1 0}$$

$$\ldots$$

$$A_{j_1+k,0} = A_{j_1-k,0} = \frac{3\gamma}{8k_c} \beta_k A_{j_1 0}^3 = \xi^k A_{j_1 0}. \quad (3.12)$$

It indicates that the amplitudes decay exponentially on either side of the nonlinear disorder. The attenuation rate ξ of localized

Downloaded 04 May 2010 to 171.66.16.34. Redistribution subject to ASME license or copyright; see http://www.asme.org/terms/Terms_Use.cfm

mode may be found by substituting Eqs. (3.5) and (3.10) into Eq. (3.7) as

$$\xi = (1 - \sqrt{\eta^2 + 1})/\eta \tag{3.13}$$

ξ is the odd function of nondimensional parameter η. When η approaches zero, ξ also approaches zero. It indicates that if k_c decreases or γ increases or $A_{j_1 0}$ increases, the mode will approach a strongly localized state. The localized lever of the modes is dependent on not only the structural parameters k_c and γ but also the amplitude $A_{j_1 0}$ related to the initial condition or the total energy of system. $A_{j_1 0}$ can be determined by applying the energy conservation to the considered system. Ignoring the $0(\epsilon)$ term it can be proved that the following equation

$$A_{j_1 0}^2 + \sum_{k=1,2\ldots}^{\infty} [A_{j_1+k,0}^2 + A_{j_1-k,0}^2] = \rho^2 \text{ (constant)} \tag{3.14}$$

is a necessary condition for the energy conservation. ρ^2 is an energy-like quantity which is related to the total energy E of the system by $(\frac{1}{2})K\rho^2 + 0(\epsilon) = E$.

Inserting Eqs. (3.12), (3.13), and (3.11) into Eq. (3.14) results in

$$A_{j_1 0}^2 = \sqrt{\rho^4 - \left(\frac{8k_c}{3\gamma}\right)^2} \quad \left|\frac{8k_c}{3\gamma}\right| < \rho^2, \tag{3.15}$$

which indicates that when k_c/γ is given in order that a localized mode would occur, however small the amplitude, the energy constant ρ^2 must be greater than $|8k_c/3\gamma|$. If the system energy is below the required level it is impossible to realize any localized mode. This property is different from that for the linear periodic system.

Localized Modes in the System With Two Nonlinear Disorders

For the system under consideration, the governing Eqs. (2.22) become

$$A_{j_1 0} = \frac{3\gamma}{8k_c}\beta_0(A_{j_1 0}^3 + \xi^n A_{j_2 0}^3) \tag{3.16a}$$

$$A_{j_2 0} = \frac{3\gamma}{8k_c}\beta_0(\xi^n A_{j_1 0}^3 + A_{j_2 0}^3) \tag{3.16b}$$

in which $n = |j_1 - j_2|$ and ξ has been defined by Eqs. (3.7) and (3.5).

Equation (3.16a) minus and plus Eq. (3.16b) yield

$$A_{j_1 0} - A_{j_2 0} = \frac{3\gamma}{8k_c}\beta_0(1 - \xi^n)(A_{j_1 0}^3 - A_{j_2 0}^3) \tag{3.17a}$$

$$A_{j_1 0} + A_{j_2 0} = \frac{3\gamma}{8k_c}\beta_0(1 + \xi^n)(A_{j_1 0}^3 + A_{j_2 0}^3). \tag{3.17b}$$

The above equations are equivalent to

$$A_{j_1 0} = A_{j_2 0} \quad \text{or}$$

$$\frac{3\gamma}{8k_c}\beta_0(1 - \xi^n)(A_{j_1 0}^2 + A_{j_1 0}A_{j_2 0} + A_{j_2 0}^2) = 1 \tag{3.18a}$$

and

$$A_{j_1 0} = -A_{j_2 0} \quad \text{or}$$

$$\frac{3\gamma}{8k_c}\beta_0(1 + \xi^n)(A_{j_1 0}^2 - A_{j_1 0}A_{j_2 0} + A_{j_2 0}^2) = 1, \tag{3.18b}$$

respectively.

The simultaneous Eqs. (3.18a, b) may be divided into three sets of equations, i.e.,

(i) $$A_{j_1 0} = -A_{j_2 0} \tag{3.19a}$$

$$\frac{3\gamma}{8k_c}\beta_0(1 - \xi^n)(A_{j_1 0}^2 + A_{j_1 0}A_{j_2 0} + A_{j_2}^2) = 1 \tag{3.19b}$$

(ii) $$A_{j_1 0} = A_{j_2 0} \tag{3.20a}$$

$$\frac{3\gamma}{8k_c}\beta_0(1 + \xi^n)(A_{j_1 0}^2 - A_{j_1 0}A_{j_2 0} + A_{j_2 0}^2) = 1 \tag{3.20b}$$

(iii) $$\frac{3\gamma}{8k_c}\beta_0(1 - \xi^n)(A_{j_1 0}^2 + A_{j_1 0}A_{j_2 0} + A_{j_2 0}^2) = 1 \tag{3.21a}$$

$$\frac{3\gamma}{8k_c}\beta_0(1 + \xi^n)(A_{j_1 0}^2 - A_{j_1 0}A_{j_2 0} + A_{j_2 0}^2) = 1 \tag{3.21b}$$

Let us discuss in detail the case of $j_2 = j_1 + 1$, i.e., $n = 1$.

(i) The first set of Eqs. (3.19a, b) describes the symmetric localized modes. Inserting Eq. (3.19a) and $n = 1$ into Eq. (3.19b) yields

$$\frac{3\gamma}{8k_c}\beta_0(1 - \xi)A_{j_1 0}^2 = 1. \tag{3.22}$$

Recalling Eq. (3.11), substituting Eqs. (3.1), (3.5), and (3.7) into Eq. (3.22) results in

$$\omega_0\omega_1 = \frac{2k_c}{M}\left[1 + \frac{1}{\eta(\eta + 2)}\right] = \frac{3\gamma}{4M}\left(\eta + \frac{1}{\eta + 2}\right)A_{j_1 0}^2,$$

$$\eta > -1, \tag{3.23}$$

where η is the nondimensional parameter as shown in Eq. (3.11). It is obvious that if $\eta > 0$ (i.e., $\gamma > 0$), $\omega_0\omega_1 > (2k_c/M)$ (i.e., $\omega > \omega_U$); there is a symmetric localized mode with higher frequency (i.e., $\omega > \omega_U$) and if $-1 < \eta < 0$, $\omega < \omega_L$ there is a symmetric localized mode with lower frequency (i.e., $\omega < \omega_L$).

Recalling that $j_2 = j_1 + 1$ and $A_{j_1 0} = -A_{j_2 0}$, the symmetric localized mode can be obtained from Eq. (2.21) as

$$A_{j_1-k,0} = -A_{j_2+k,0} = \frac{3\gamma}{8k_c}(\beta_k - \beta_{k+1})A_{j_1 0}^3 = \xi^k A_{j_1 0}$$

$$k = 0, 1, 2, \ldots, \infty \tag{3.24}$$

which indicates that the amplitudes on either side decay exponentially away from the nonlinear disorders.

The attenuation rate ξ of amplitudes of symmetric mode may be found by substituting Eqs. (3.5) and (3.23) into Eq. (3.7), as

$$\xi = -\frac{\eta}{\eta + 2} \quad \eta > -1. \tag{3.25}$$

The sum of the squares of the amplitudes should be equal to constant ρ^2, i.e.,

$$2A_{j_1 0}^2(1 + \xi^2 + \xi^4 + \ldots + \xi^{2k} + \ldots) = \rho^2$$

or

$$\frac{2}{1 - \xi^2}A_{j_1 0}^2 = \rho^2. \tag{3.26}$$

Inserting Eqs. (3.25) and (3.11) into the above equation results in

$$A_{j_1 0}^2 = \frac{1}{4}\left[\rho^2 - \frac{16k_c}{3\gamma} + \sqrt{\rho^4 + \frac{32k_c}{3\gamma}\rho^2}\right]$$

$$\rho^2 > -\frac{32k_c}{3\gamma} \text{ (for } \gamma < 0) \quad \rho^2 > \frac{4k_c}{3\gamma} \text{ (for } \gamma > 0). \tag{3.27}$$

Downloaded 04 May 2010 to 171.66.16.34. Redistribution subject to ASME license or copyright; see http://www.asme.org/terms/Terms_Use.cfm

In order that the symmetric localized mode may occur, ρ^2 must be greater than max $(-32k_c/3\gamma, 4k_c/3\gamma)$.

The stability analysis of the symmetric localized mode shown in Eqs. (3.24) and (3.25) is investigated by superposing the small perturbations on the mode solution and applying the Floquet theory (Nayfeh and Mook, 1979). It is concluded that when η lies in the region $[0, 2]$, the symmetric localized mode is unstable and when $\eta > 2$ or $-1 < \eta < 0$ the symmetric localized mode is stable. If $\eta \leq -1$, the symmetric localized mode does not exist.

(ii) The second set of equations shown in Eqs. (3.20*a*, *b*) describes the antisymmetric localized modes. Inserting Eq. (3.20*a*) and $n = 1$ in Eq. (3.20*b*) yields

$$\frac{3\gamma}{8k_c}\beta_0(1+\xi)A_{j_10}^2 = 1. \tag{3.28}$$

Substituting Eqs. (3.1), (3.5), and (3.7) into Eq. (3.28) results in

$$\omega_0\omega_1 = \frac{2k_c}{M}\frac{1}{\eta(2-\eta)} = \frac{3\gamma}{4M}\frac{1}{2-\eta}A_{j_10}^2 \quad \eta < 1. \tag{3.29}$$

Recalling $\eta = (8k_c/3\gamma)A_{j_10}^{-2}$, it is concluded that if $\eta < 0$ ($\gamma < 0$), $\omega_0\omega_1 < 0$ ($\omega < \omega_L$) there is an antisymmetric localized mode with lower frequency ($\omega < \omega_L$); and if $0 < \eta < 1$, $\omega_0\omega_1 > (2k_c/M)(\omega > \omega_U)$ there is an antisymmetric localized mode with higher frequency ($\omega > \omega_U$).

The amplitudes for the antisymmetric localized mode can be found by inserting $j_2 = j_1 + 1$ and $A_{j_20} = A_{j_10}$ into Eq. (2.21).

$$A_{j_1-k,0} = A_{j_2+k,0} = \frac{3\gamma}{8k_c}(\beta_k + \beta_{k+1})A_{j_10}^3 = \xi^k A_{j_10}$$
$$k = 0, 1, 2, \ldots, \infty. \tag{3.30}$$

Substituting Eqs. (3.5) and (3.29) into Eq. (3.7) results in

$$\xi = -\frac{\eta}{2-\eta} \quad \eta < 1. \tag{3.31}$$

For the present case Eq. (3.26) is also applicable in which ξ should be defined as in Eq. (3.31) instead of Eq. (3.25). Substituting Eqs. (3.31) and (3.11) into Eq. (3.26) results in

$$A_{j_10}^2 = \frac{1}{4}\left[\rho^2 + \frac{16k_c}{3\gamma} + \sqrt{\rho^4 - \frac{32k_c}{3\gamma}\rho^2}\right]$$

$$\rho^2 > \frac{32k_c}{3\gamma} \text{ (for } \gamma > 0), \quad \rho^2 > -\frac{4k_c}{3\gamma} \text{ (for } \gamma < 0). \tag{3.32}$$

In order that the antisymmetric localized mode may occur ρ^2 must be greater than max $(32k_c/3\gamma, -4k_c/3\gamma)$.

By applying the Floquet theory to stability analysis of the antisymmetric localized mode shown in Eqs. (3.30) and (3.31), it is concluded that when η lies in the region $[-2, 0]$, the antisymmetric localized mode is unstable, and when $\eta < -2$ or $0 < \eta < 1$ the antisymmetric localized mode is stable. If $\eta \geq 1$, it is impossible for the antisymmetric localized mode to occur.

(iii) The third set of equations, i.e., Eq. (3.21*a*, *b*), describes the nonsymmetric localized modes. By inserting Eqs. (3.1), (3.7) and $n = 1$ into Eqs. (3.21*a*), (3.21*b*), it can be proved that the set of Eqs. (3.21*a*, *b*) is equivalent to

$$A_{j_10}A_{j_20} = -\frac{4k_c}{3\gamma} \quad \text{or} \quad A_{j_20} = -\frac{\eta}{2}A_{j_10} \tag{3.33a}$$

$$A_{j_10}^2 + A_{j_20}^2 = \frac{4k_c}{3\gamma}[a + \text{sgn}(a)\sqrt{a^2 - 1}] \tag{3.33b}$$

where "a" is defined as Eq. (3.5).

Without loss of generality, we assume $|A_{j_10}| \geq |A_{j_20}|$ ($|\eta| \leq 2$). Eliminating A_{j_20} from Eq. (3.33*b*) and substituting Eq. (3.5) into it results in

$$\omega_0\omega_1 = \frac{2k_c}{M}\left[1 + \frac{(\eta^2 - 2\eta + 4)^2}{8\eta(\eta^2 + 4)}\right], \quad |\eta| \leq 2 \tag{3.34}$$

where η is given in Eq. (3.11). It is concluded that if $\gamma > 0$ ($\eta > 0$) then $\omega > \omega_U(\omega_0\omega_1 > (2k_c/M)$ therefore the nonsymmetric localized mode with higher frequency ($\omega > \omega_U$) exists and if $\gamma < 0$ ($\eta < 0$) then $\omega < \omega_L(\omega_1 < 0)$, therefore the nonsymmetric localized mode with lower frequency ($\omega < \omega_L$) exists.

The amplitudes for the nonsymmetric mode may also be obtained from Eq. (2.21). For the case of $j_2 = j_1 + 1$, Eq. (2.21) becomes

$$A_{j_1-k,0} = \frac{3\gamma}{8k_c}[\beta_k A_{j_10}^3 + \beta_{k+1}A_{j_20}^3]$$

$$A_{j_2+k,0} = \frac{3\gamma}{8k_c}[\beta_{k+1}A_{j_10}^3 + \beta_k A_{j_20}^3] \quad k = 1, 2, \ldots, \infty. \tag{3.35}$$

Recalling Eqs. (3.6), (3.16*a*, *b*) with $n = 1$, Eq. (3.35) may be rewritten as

$$A_{j_1-k,0} = \xi^k A_{j_10}$$

$$A_{j_2+k,0} = \xi^k A_{j_20} \quad k = 1, 2, \ldots, \infty \tag{3.36}$$

where A_{j_10} and A_{j_20} must satisfy Eq. (3.33*a*).

Substituting Eqs. (3.34) and (3.5) into Eq. (3.7) results in

$$\xi = -\frac{2\eta}{\eta^2 + 4} \quad |\eta| \leq 2. \tag{3.37}$$

Noting Eq. (3.36), the sum of the amplitude squares may be expressed as

$$\frac{1}{1-\xi^2}(A_{j_10}^2 + A_{j_20}^2) = \rho^2. \tag{3.38}$$

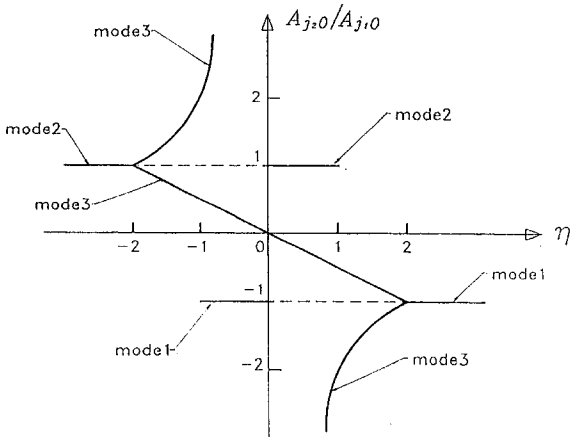


Fig. 2

Downloaded 04 May 2010 to 171.66.16.34. Redistribution subject to ASME license or copyright; see http://www.asme.org/terms/Terms_Use.cfm

Inserting Eqs. (3.37) and (3.33a) in the above equation results in

$$\frac{2k_c}{3\gamma}\frac{(\eta^2+4)^3}{\eta(\eta^4+4\eta^2+16)}=\rho^2 \quad |\eta|\le 2. \qquad (3.39)$$

Recalling $\eta = 8k_c/3\gamma A_{j_1 0}^2$, it is impossible to find the closed-form solution for $A_{j_1 0}^2$ of Eq. (3.39). But it can be proved that if and only if $\rho^2 \ge 32k_c/9\gamma$, the solution of Eq. (3.39) exists, i.e., there are two nonsymmetric localized modes ($A_{j_2 0}/A_{j_1 0}$ and $A_{j_1 0}/A_{j_2 0} = -\eta/2$).

It can be concluded that when $|\eta| \le 2$ in which $\eta \equiv 8k_c/3\gamma A_{\max}^2$ there are two nonsymmetric stable localized modes where one mode is the symmetric image of the other.

The condition for each type of localized mode to occur is shown in Fig. 2.

Conclusion

The mode localization phenomena in periodic system with infinite degrees-of-freedom and two nonlinear disordered subsystems are analyzed by the L-P method with U-transformation technique. The prerequisite for the present work is that the nonlinear disorders and the coupling are weak but different from zero. It is found that the nondimensional parameter η controls the type, number, and stability of the localized modes (see Fig. 2) as follows:

1 When η is less than -2, there is one antisymmetric localized mode which is stable mode.

2 When η lies in the region $[-2, -1]$, there are three localized modes in which two modes are nonsymmetric and stable while the other one is antisymmetric and unstable.

3 When η lies in the region $(-1, 0)$, there are four localized modes in which two nonsymmetric and one symmetric modes are stable while the other antisymmetric mode is unstable.

4 When η lies in the region $(0, 1)$ there are four localized modes in which two nonsymmetric and one antisymmetric modes are stable modes while the other symmetric mode is unstable.

5 When η lies in the region $[1, 2]$ there are three localized modes where two nonsymmetric modes are stable while the other symmetric mode is unstable.

6 When η is greater than 2, there is only one symmetric, stable localized mode.

Recalling $\eta = 8k_c/3\gamma A_{\max}^2$, it is interesting to note that the effect of the maximum amplitude $A_{\max}$ on localized modes is in excess of that of the ratio k_c/γ.

References

Cai, C. W., Cheung Y. K., and Chan, H. C., 1988, "Dynamic Response of Infinite Continuous Beams Subjected to a Moving Force: An Exact Method," *Journal of Sound and Vibration,* Vol. 123, pp. 461–472.

Cai, C. W., Cheung, Y. K., and Chan, H. C., 1995, "Mode Localization Phenomena in Nearly Periodic Systems," ASME JOURNAL OF APPLIED MECHANICS, Vol. 62, pp. 141–149.

Cha, P. D., and Pierre, C., 1991, "Vibration Localization by Disorder in Assemblies of Monocoupled Multimode Component Systems," ASME JOURNAL OF APPLIED MECHANICS, Vol. 58, pp. 1072–1081.

Hodges, C. H., 1982, "Confinement of Vibration by Structural Irregularity," *Journal of Sound and Vibration,* Vol. 82, pp. 411–424.

Li, D., and Benaroya, H., 1992, "Dynamics of Periodic and Near-Periodic Structures," ASME *Applied Mechanics Reviews,* Vol. 45, pp. 447–459.

Nayfeh, A. H., and Mook, D. T., 1979, *Nonlinear Oscillations,* John Wiley and Sons, New York.

Pierre C., and Dowell, E. H., 1987, "Localization of Vibration by Structural Irregularity," *Journal of Sound and Vibration,* Vol. 114, pp. 549–564.

Vakakis, A., Nayfeh, T., and King, M., 1993, "A Multiple-Scales Analysis of Nonlinear, Localized Modes in a Cyclic Periodic System," ASME JOURNAL OF APPLIED MECHANICS, Vol. 60, pp. 388–397.

Downloaded 04 May 2010 to 171.66.16.34. Redistribution subject to ASME license or copyright; see http://www.asme.org/terms/Terms_Use.cfm

A Quasi-Decoupling Approach for Nonclassical Linear Systems in State Space

Gexue Ren
Associate Professor.

Zhaochang Zheng
Professor.

Department of Engineering Mechanics,
Tsinghua University,
100084, Beijing
P. R. China

By adopting the orthogonal transformations provided by the generalized real Schur decomposition, it is shown that every nonclassical linear system in state space can be transformed into block upper triangular form, to which the quasi-decoupling solution can be progressively carried out by solving the either first or second-order component equations with the "back substitution." The distinct characteristics of generalized eigenvalue problems from those of standard ones are discussed. Favorable properties of the proposed method include: no inverting of any system matrix, indiscriminate applicability to both defective and nondefective systems, the simultaneous decoupling of the adjoint problem, and numerical stability. Illustrative examples are also presented.

1 Introduction

By Caughey and O'Kelly's (1965) definition, general linear discrete systems are divided into classical and nonclassical linear systems. Caughey and O'Kelly (1965) gave a sufficient and necessary condition for decoupling classical linear systems with real mode in configuration space or n-space. Liu and Wilson (1992) extended Caughey and O'Kelly's (1965) result to systems with gyroscopic effect or nonclassically damped systems. The first seriously attempted investigation on nonclassical linear systems was considered to be by Inman (1983), as reviewed by Caughey and Ma (1993), and the concept of symmetrizability was introduced in Inman (1983), and Ahmadian and Inman (1984). The necessary and sufficient conditions for nonclassical linear systems to be decoupled and to be solvable in the n-space were given by Caughey and Ma (1993). Recently, Ma and Caughey (1995) gave the necessary and sufficient conditions for nonclassical linear systems to be decoupled with equivalence transformation. In parallel with the decoupling in configuration space, complex mode theory has been developed and used to decouple damped linear systems in state space for decades (see Foss (1958), Meirovitch (1967), and Newland (1989)). The canonical form used in complex mode theory is the Jordan form, so systems with and without defective eigenvalues should be treated differently. No diagonal form is available for defective systems, and the Jordan blocks of the system have to be ascertained in advance, for details refer to Newland (1989). Zhu and Shi (1988) proposed to determine the defectiveness by the rank deficiency in the test matrix. According to Golub and Van Loan (1989), numerically ascertaining Jordan structures is very difficult, especially for large systems. The difficulty may be illustrated by mentioning that theoretical multiple eigenvalues can only be determined to very close eigenvalues in finite arithmetic. Based on the real Schur decomposition, Zheng and Ren (1995, 1996) and Zheng, Ren, and Williams (1997) proposed the dynamic orthogonal decoupling approach for nonclassically damped systems with positive definite mass and stiffness matrices. This method can uniformly be applied to both nondefective and defective systems, and can be completely conducted in the real domain, and there is no need to solve the adjoint or left problem. However, both the complex mode theory and the dynamic orthogonal decoupling approach implicitly assume that the considered generalized eigenvalue problems can be transformed into standard ones. Such transformations may be prevented by the ill-conditioning or rank deficiency in system matrices. By adopting the generalized real Schur decomposition, this paper concentrates on developing a numerical solution path for nonclassical linear systems without any confinement on system matrices, except that they are assumed to be real.

There are also studies on stability criterion for systems with circulatory forces or constraint damping, which are typical nonclassical systems (see Mingory (1970), Huseyin (1978), Techman (1979), Tasso (1980), and Kliem and Pommer (1986)). With the development of computer technology, it might be wise to directly approach the stability problems with appropriate numerical methods for generalized eigenvalue problems.

2 Adopting the Generalized Real Schur Decomposition

The nonclassical linear systems can usually be represented with

$$\mathbf{M}\ddot{x} + (\mathbf{G} + \mathbf{C})\dot{x} + (\mathbf{K} + \mathbf{F})x = f(t) \tag{1}$$

where $\mathbf{M}$, $\mathbf{C}$, and $\mathbf{K}$ are, respectively, n by n mass, damping, and stiffness matrices; $\mathbf{G}$ and $\mathbf{F}$, respectively, n by n gyroscopic matrix and constraint damping matrix or circulatory matrix, both are skew. In most cases, $\mathbf{M}$ is symmetric and at least semipositive definite, but in order to give a general analysis, it is not confined to any assumption in this research. Matrices $\mathbf{C}$ and $\mathbf{K}$ are symmetric. The state-space representation of the dynamic system (1) is not unique, but without loss of generality, it can be denoted as

$$\mathbf{A}\dot{y} + \mathbf{B}y = F(t) \tag{2}$$

where $\mathbf{A}$, $\mathbf{B}$, y, and $F(t)$ take their consistent forms, respectively, for example,

Contributed by the Applied Mechanics Division of THE AMERICAN SOCIETY OF MECHANICAL ENGINEERS for publication in the ASME JOURNAL OF APPLIED MECHANICS.

Discussion on the paper should be addressed to the Technical Editor, Professor Lewis T. Wheeler, Department of Mechanical Engineering, University of Houston, Houston, TX 77204-4792, and will be accepted until four months after final publication of the paper itself in the ASME JOURNAL OF APPLIED MECHANICS.

Manuscript received by the ASME Applied Mechanics Division, May 7, 1996; final revision, Mar. 5, 1997. Associate Technical Editor: N. C. Perkins.

Copyright © 1997 by ASME

Downloaded 04 May 2010 to 171.66.16.34. Redistribution subject to ASME license or copyright; see http://www.asme.org/terms/Terms_Use.cfm

$$\mathbf{A} = \begin{bmatrix} (\mathbf{G} + \mathbf{C}) & \mathbf{M} \\ -\mathbf{M} & \mathbf{0} \end{bmatrix}, \quad \mathbf{B} = \begin{bmatrix} (\mathbf{K} + \mathbf{F}) & 0 \\ 0 & \mathbf{M} \end{bmatrix},$$

$$y = \begin{Bmatrix} x \\ \dot{x} \end{Bmatrix}, \quad F(t) = \begin{Bmatrix} f(t) \\ 0 \end{Bmatrix}. \quad (3a, b, c, d)$$

The stability of the system can be derived from the eigensolution of the generalized eigenvalue problem:

$$\lambda \mathbf{A} y + \mathbf{B} y = 0. \quad (4)$$

By referring to the definition in $(3a, b)$, $\mathbf{A}$ and $\mathbf{B}$ can be expected as very general nonsymmetric matrices. As summarized by Golub and Van Loan (1989), the generalized eigenvalue problems may demonstrate very different features from standard ones. The generalized eigenvalue problem (4) has $2n$ eigenvalues if and only if matrix $\mathbf{A}$ is of full rank $2n$; in case of rank deficiency, the number of the eigenvalues of the generalized eigenvalue problem (4) may be finite, zero, and infinite. However, the standard eigenvalue problem of any $2n$ by $2n$ matrix has $2n$ eigenvalues under any circumstances. If the generalized eigenvalue problem (4) were approached by transforming it to the standard eigenvalue problem of $\mathbf{A}^{-1}\mathbf{B}$ or $\mathbf{A}\mathbf{B}^{-1}$, then at least either $\mathbf{M}$ or $(\mathbf{K} + \mathbf{F})$ should be invertible for respectively guaranteeing an invertible $\mathbf{A}$ or $\mathbf{B}$, and the computed results are subject to perturbations depending on the condition numbers of $\mathbf{A}$ or $\mathbf{B}$. However, the ill-conditioning of single $\mathbf{A}$ or $\mathbf{B}$ may not necessarily mean that the generalized eigenvalue problem is ill-conditioned, as argued by Stewart (1978), and the two matrices formulating the generalized eigenvalue problems should be treated symmetrically in order to avoid unnecessarily introduced numerical sensitivity.

Fortunately, the generalized real Schur decomposition theorem by Stewart (1972) furnishes the orthogonal transformations, which could be used to simplify nonclassical linear systems. The generalized real Schur decomposition asserts that, for any two N by N real matrices $\mathbf{A}$ and $\mathbf{B}$, there exists two orthogonal matrices $\mathbf{Q}$ and $\mathbf{Z}$ such that

$$\mathbf{Q}^T \mathbf{A} \mathbf{Z} = \mathbf{R} \quad (5)$$

$$\mathbf{Q}^T \mathbf{B} \mathbf{Z} = \mathbf{S} \quad (6)$$

where $\mathbf{R}$ is block upper triangular, $\mathbf{S}$ is strict upper triangular, or vice versa. Both can be written in the following conformable block form:

$$\mathbf{R} = \begin{bmatrix} \mathbf{r}_{11} & \mathbf{r}_{12} & \cdots & \mathbf{r}_{1m} \\ & \mathbf{r}_{22} & \cdots & \mathbf{r}_{2m} \\ & & \ddots & \vdots \\ & & & \mathbf{r}_{mm} \end{bmatrix},$$

$$\mathbf{S} = \begin{bmatrix} \mathbf{s}_{11} & \mathbf{s}_{12} & \cdots & \mathbf{s}_{1m} \\ & \mathbf{s}_{22} & \cdots & \mathbf{s}_{2m} \\ & & \ddots & \vdots \\ & & & \mathbf{s}_{mm} \end{bmatrix} \quad (7a, b)$$

where the diagonal blocks $\mathbf{r}_{ii}$ and $\mathbf{s}_{ii}$ $(i = 1, \ldots, m)$ is t_i-by-t_i, and $N = \sum_{i=1}^{m} t_i$ and the maximum of the block sizes t_i $(i = 1, \ldots, m)$ is no larger than 2. In present research $N = 2n$.

The generalized real Schur decomposition can be carried out with the generalized version of the QR algorithm, i.e., the QZ algorithm by Moler and Stewart (1973). In the algorithm, matrices $\mathbf{A}$ and $\mathbf{B}$ are first transformed into Hessenberg-triangular form, followed by successive QZ steps and the checking of the possible deflation until the required Schur forms are obtained. The front end transformation is a counterpart of the transformation to Hessenberg form in the QR algorithm for the standard real Schur decomposition, the aim of which is to reduce the computation in each iteration step. The convergence property of the QZ algorithm is the same as that of the QR algorithm, which "almost always converges" or is "all powerful" as described in Golub and Van Loan (1989), and the speed of the QZ algorithm is not affected by the rank deficiency in matrix $\mathbf{A}$ in Eq. (4). For further information about QZ algorithm, one may refer to the insurmountable presentation by Golub and Van Loan (1989) or the original.

3 The Quasi-Decoupling Property and the Extraction of Eigenvalues

Introducing the following transformation

$$y = \mathbf{Z} z, \quad (8)$$

and premultiplying Eq. (2) with $\mathbf{Q}^T$, and considering Eqs. (5) and (6), we have

$$\mathbf{R}\dot{z} + \mathbf{S}z = \bar{F}(t), \quad (9)$$

where $\bar{F}(t) = \mathbf{Q}^T F(t) = \{\bar{f}_1^T, \bar{f}_2^T, \ldots, \bar{f}_m^T\}^T$. By referring to the block structure of $\mathbf{R}$ and $\mathbf{S}$, the above equation can be rewritten in the following component form:

$$\mathbf{r}_{ii}\dot{z}_i + \mathbf{s}_i z_i = \tilde{f}_i(t) \quad (i = m, \ldots, 1) \quad (10)$$

where $\tilde{f}_i(t) = \tilde{f}_i - \sum_{k=i+1}^{m} (\mathbf{r}_{ik}\dot{z}_k + \mathbf{s}_{ik} z_k)$. By solving the component Eqs. (10) in the reversing order, i.e., from the mth to the first, the solution process is virtually decoupled, because by the time to solve the ith component equation, its inhomogeneous term $\tilde{f}_i(t)$ is already known with the then available mth, ..., $(i + 1)$th component solutions. Since the decoupling is realized by restraining a solution order, a notion similar to the "back substitution" for triangular linear systems, it may be called the quasi-decoupling method.

According to the theory of triangular matrices, the eigenvalue problem associated with (9)

$$\lambda \mathbf{R} z + \mathbf{S} z = 0 \quad (11)$$

is also decoupled into m component eigenvalue problems, which are formulated by the corresponding diagonal blocks of $\mathbf{R}$ and $\mathbf{S}$, i.e.,

$$\lambda \mathbf{r}_{ii} z_i + \mathbf{s}_{ii} z_i = 0 \quad (i = 1, \ldots, m) \quad (12)$$

and the orders of which are either one or two. All eigenvalues of the original eigenvalue problem are comprised of the eigenvalues of the component eigenvalue problems.

Solutions in the frequency domain can also be decoupled with the "back substitution."

4 The Simultaneous Quasi-Decoupling of the Adjoint Problem

The adjoint problem of Eq. (2) can be written as

$$\mathbf{A}^T \dot{y}^* + \mathbf{B}^T y^* = F^*(t). \quad (13)$$

By introducing the transformation $y^* = \mathbf{Q} z^*$, and premultiplying Eq. (14) with $\mathbf{Z}^T$, and by referring to Eqs. (5), (6), we have

$$\mathbf{R}^T \dot{z}^* + \mathbf{S}^T z^* = \bar{F}^*(t) \quad (14)$$

where $\bar{F}^*(t) = \mathbf{Z}^T F^*(t)$, $\mathbf{R}^T$ and $\mathbf{S}^T$ are, in fact, block lower triangular matrices. Again, the the adjoint problem can be quasi-decoupled with the "forward substitution" procedure.

Downloaded 04 May 2010 to 171.66.16.34. Redistribution subject to ASME license or copyright; see http://www.asme.org/terms/Terms_Use.cfm

5 Degeneration to Unsymmetric-Definite Systems

As a special case of Eq. (1), damped gyroscopic systems take the following form:

$$\mathbf{M}\ddot{x} + (\mathbf{G} + \mathbf{C})\dot{x} + \mathbf{K}x = f(t). \tag{15}$$

With positive definite $\mathbf{M}$ and $\mathbf{K}$, the state-space representation (2) for Eq. (15) with notations in Eq. (3) would be of unsymmetric-definite type, for which a solution with $\mathbf{Z} = \mathbf{Q}$ can be obtained such that

$$\mathbf{Q}^T\mathbf{A}\mathbf{Q} = \mathbf{R} \tag{16}$$

$$\mathbf{Q}^T\mathbf{B}\mathbf{Q} = \mathbf{I} \tag{17}$$

where $\mathbf{R}$ is in real Schur form, and $\mathbf{I}$ is the $2n$ by $2n$ unit matrix (see Zheng and Ren (1995, 1996) and Zheng, Ren, and Williams (1997)). Large scale unsymmetric-definite systems can also be solved in the reduced way (see Ren and Zheng (1997) for details).

6 Numerical Examples

Example 1. A system governed by Eq. (1) with

$$\mathbf{M} = \begin{bmatrix} 1 & 0 \\ 0 & 0 \end{bmatrix}, \quad \mathbf{G} = \begin{bmatrix} 0 & \frac{1}{2} \\ -\frac{1}{2} & 0 \end{bmatrix}, \quad \mathbf{C} = \begin{bmatrix} 2 & \frac{1}{2} \\ \frac{1}{2} & 1 \end{bmatrix},$$

$$\mathbf{K} = \begin{bmatrix} 1 & 1 \\ 1 & 1 \end{bmatrix}, \quad \mathbf{F} = \begin{bmatrix} 0 & 1 \\ -1 & 0 \end{bmatrix}.$$

This example is from Newland (1987, 1989), formulating the state-space matrices as

$$\mathbf{A} = \begin{bmatrix} (\mathbf{G} + \mathbf{C}) & \mathbf{M} \\ -\mathbf{I} & \mathbf{0} \end{bmatrix}, \quad \mathbf{B} = \begin{bmatrix} (\mathbf{K} + \mathbf{F}) & \mathbf{0} \\ \mathbf{0} & \mathbf{I} \end{bmatrix}.$$

By a double precision implementation of the QZ algorithm, the matrices for quasi-decoupling the system are given as follows:

$$\mathbf{R} = \begin{bmatrix} -2.00000 & -1.00000 & 1.00000 & 0.000000 \\ -1.00000 & 0.000000 & 0.000000 & 0.000000 \\ 0.000000 & 0.000000 & 1.00000 & 0.000000 \\ 0.000000 & 0.000000 & 1.00000 & 0.000000 \end{bmatrix}$$

$$\mathbf{S} = \begin{bmatrix} -1.00000 & 0.000000 & 2.00000 & 0.000000 \\ 0.000000 & 1.00000 & 0.000000 & 0.000000 \\ 0.000000 & 0.000000 & 1.00000 & 0.000000 \\ 0.000000 & 0.000000 & 0.000000 & 1.00000 \end{bmatrix}$$

$$\mathbf{Q} = \begin{bmatrix} -1.00000 & 0.000000 & 0.000000 & 0.000000 \\ 0.000000 & 0.000000 & -1.00000 & 0.000000 \\ 0.000000 & 1.00000 & 0.000000 & 0.000000 \\ 0.000000 & 0.000000 & 0.000000 & 1.00000 \end{bmatrix}$$

$$\mathbf{Z} = \begin{bmatrix} 1.00000 & 0.000000 & 0.000000 & 0.000000 \\ 0.000000 & 0.000000 & -1.00000 & 0.000000 \\ 0.000000 & 1.00000 & 0.000000 & 0.000000 \\ 0.000000 & 0.000000 & 0.000000 & 1.00000 \end{bmatrix}.$$

From matrices $\mathbf{R}$ and $\mathbf{S}$, the considered system has two component eigenvalue problems:

$$\lambda\mathbf{r}_{11}z_1 + \mathbf{s}_{11}z_1 = 0 \tag{a}$$

$$\lambda\mathbf{r}_{22}z_2 + \mathbf{s}_{22}z_2 = 0 \tag{b}$$

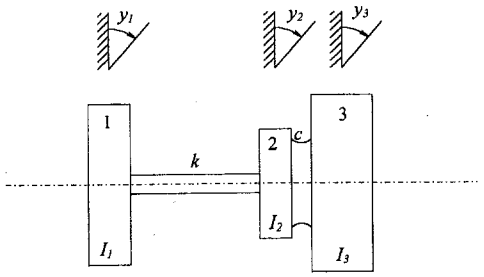


Fig. 1 A simplified torsion model of a propulsion system from Newland (1987)

where

$$\mathbf{r}_{11} = \begin{bmatrix} -2.00000 & -1.00000 \\ -1.00000 & 0.000000 \end{bmatrix}, \quad \mathbf{s}_{11} = \begin{bmatrix} -1.00000 & 0.000000 \\ 0.000000 & 1.00000 \end{bmatrix}$$

$$\mathbf{r}_{22} = \begin{bmatrix} 1.00000 & 0.000000 \\ 1.00000 & 0.000000 \end{bmatrix}, \quad \mathbf{s}_{22} = \begin{bmatrix} 1.00000 & 0.000000 \\ 0.000000 & 1.00000 \end{bmatrix}.$$

Two eigenvalues of the component eigenvalue problem (a) are extracted by directly solving the quadratic characteristic equation, i.e.,

$$|\lambda\mathbf{r}_{11} + \mathbf{s}_{11}| = -(\lambda + 1.00000)^2 = 0 \Rightarrow \lambda_1 = \lambda_2 = -1.00000.$$

In the second component eigenvalue problem (b), the matrix $\mathbf{r}_{22}$ is singular. As mentioned in Section 2, in such a case the generalized eigenvalue problem may demonstrate very different features from those of a standard one. In the current case the second-order eigenproblem (b) only has one eigenvalue, this could be illustrated with its first-order (not second-order) characteristic equation:

$$|\lambda\mathbf{r}_{22} + \mathbf{s}_{22}| = \lambda + 1.00000 = 0 \Rightarrow \lambda_3 = -1.00000.$$

Though the order of $\mathbf{A}$ and $\mathbf{B}$ in this example is 4, the generalized eigenvalue problem (4) of this example possesses only three eigenvalues, rather than four, as it must be in any standard eigenvalue problem of fourth order. The obtained eigenvalues

$$\lambda_1 = \lambda_2 = \lambda_3 = -1.00000$$

are the same as those by Newland (1987, 1989), which were obtained by transforming the quadratic eigenvalue problem of second order to the standard of a 3 by 3 matrix through explicitly eliminating one state variable. The multiple eigenvalues in this example are defective.

Example 2. The torsional model of a marine propulsion system in Fig. 1, from Newland (1987, 1989) is

$$\begin{bmatrix} I_1 & 0 & 0 \\ 0 & I_2 & 0 \\ 0 & 0 & I_3 \end{bmatrix} \begin{Bmatrix} \ddot{y}_1 \\ \ddot{y}_2 \\ \ddot{y}_3 \end{Bmatrix} + \begin{bmatrix} 0 & 0 & 0 \\ 0 & c & -c \\ 0 & -c & c \end{bmatrix} \begin{Bmatrix} \dot{y}_1 \\ \dot{y}_2 \\ \dot{y}_3 \end{Bmatrix}$$

$$+ \begin{bmatrix} k & -k & 0 \\ -k & k & 0 \\ 0 & 0 & 0 \end{bmatrix} \begin{Bmatrix} y_1 \\ y_2 \\ y_3 \end{Bmatrix} = \begin{Bmatrix} f_1(t) \\ f_2(t) \\ f_3(t) \end{Bmatrix}$$

where $I_1 = 3$ kgm^2, $I_2 = 1.5$ kgm^2, $I_3 = 4.5$ kgm^2, $k = 200$ Nm/rad, $c = 135/8$ Nms/rad. This system has the singular stiffness matrix and also has defective multiple eigenvalues. The governing equation is first represented in state space in the form of Eq. (3). The computed $\mathbf{R}$, $\mathbf{S}$, $\mathbf{Q}$, $\mathbf{Z}$ are as follows:

Downloaded 04 May 2010 to 171.66.16.34. Redistribution subject to ASME license or copyright; see http://www.asme.org/terms/Terms_Use.cfm

$$\mathbf{R} = \begin{bmatrix} -2.48506 & -2.53099 & -0.453419 & -0.177677 & 3.40442 & 16.4209 \\ 0.000000 & 0.443782 & -2.80857 & 0.178554 & -0.00495810 & -0.130225 \\ 0.000000 & 0.000000 & 1.29906 & 1.22077 & -0.649800 & -2.36679 \\ 0.000000 & 0.000000 & 0.000000 & -3.00313 & 0.307106 & 1.17766 \\ 0.000000 & 0.000000 & 0.000000 & 0.000000 & 6.21263 & 24.6215 \\ 0.000000 & 0.000000 & 0.000000 & 0.000000 & 0.000000 & -15.3414 \end{bmatrix}$$

$$\mathbf{S} = \begin{bmatrix} -3.86518 & 72.1564 & -339.101 & 1.02934 & -50.1656 & -192.033 \\ 2.32174 & -0.544504 & 11.4196 & 0.0696008 & 1.72198 & 6.59214 \\ 0.000000 & 0.000000 & -12.9906 & -0.0815575 & 0.281150 & -7.99586 \\ 0.000000 & 0.000000 & 0.000000 & 0.177216 \times 10^{-14} & -3.13551 & 0.817669 \\ 0.000000 & 0.000000 & 0.000000 & 0.000000 & 0.109985 \times 10^{-15} & -0.340298 \times 10^{-14} \\ 0.000000 & 0.000000 & 0.000000 & 0.000000 & 0.121535 \times 10^{-17} & -0.316936 \times 10^{-18} \end{bmatrix}$$

$$\mathbf{Q} = \begin{bmatrix} 0.706235 & -0.0233339 & 0.0262265 & -0.124124 \times 10^{-15} & -0.643827 & -0.292381 \\ -0.706235 & 0.0233339 & -0.0262265 & -0.976121 \times 10^{-17} & -0.643827 & -0.292381 \\ 0.176956 \times 10^{-15} & 0.132351 \times 10^{-15} & 0.143725 \times 10^{-15} & 0.165606 \times 10^{-15} & 0.413489 & -0.910509 \\ 0.0310095 & 0.807538 & -0.116562 & -0.577350 & 0.000000 & 0.000000 \\ 0.00710284 & -0.505587 & -0.641092 & -0.577350 & -0.212622 \times 10^{-16} & -0.912158 \times 10^{-16} \\ -0.0381124 & -0.301952 & 0.757654 & -0.577350 & 0.265312 \times 10^{-15} & -0.101033 \times 10^{-16} \end{bmatrix}$$

$$\mathbf{Z} = \begin{bmatrix} -0.0256868 & 0.0932954 & -0.811171 & 0.576748 & 0.000000 & 0.000000 \\ -0.0117673 & -0.161565 & 0.389291 & 0.573132 & 0.177308 & 0.679921 \\ 0.0210470 & -0.00834194 & 0.411017 & 0.580364 & -0.177308 & -0.679921 \\ 0.585011 & 0.599276 & 0.0735384 & 0.0325438 & 0.537489 & -0.0571751 \\ -0.800861 & 0.525206 & 0.0973354 & 0.0162719 & 0.268744 & -0.0285875 \\ -0.123054 & -0.574586 & -0.0814707 & -0.0271198 & 0.758951 & -0.267075 \end{bmatrix}$$

The six eigenvalues of the system are obtained by solving three component eigenproblems:

$$-0.5901 \times 10^{-15} \quad -0.2133 \times 10^{-17} \quad 0.2017 \times 10^{-16}$$

$$-10.00 \quad -2.500 + i11.99 \quad -2.500 - i11.99.$$

As shown in the above, the three zero eigenvalues of the system are computed to high precision, and the computed nonzero eigenvalues are the same as those by Newland (1989). The step-response function $r(t)$ is also obtained in terms of the proposed decoupling approach and the θ-method to solve the decoupled equations. The input is a torque applied to wheel 1 and the output is the torque in the shaft connecting wheel 1 and wheel 2. The obtained result is virtually the same as that by Newland (1989) (see Fig. 2).

7 Conclusions

The quasi-decoupling approach is attempted to provide a solution path for general nonclassical linear systems in state space. The quasi-decoupling for a system and its adjoint problem are attained by following the "back and forward substitution" procedures, a technique similar to that used in solving triangular linear systems. The eigenvalues of the system are extracted by solving the decoupled component eigenvalue problems of order one or two. Due to the adoption of the generalized real Schur form instead of the Jordan form, which is used in complex mode theory, the quasi-decoupling can indiscriminately be applied to both nondefective and defective systems without any confinement on system matrices. Only orthogonal transformations are involved in the quasi-decoupling, so robust real solution algorithms can reasonably be expected.

Further work is needed for other aspects of the proposed approach, such as application to large practical systems, and its relative efficiency with other methods.

Acknowledgment

This work is supported by the National Natural Science Foundation of China.

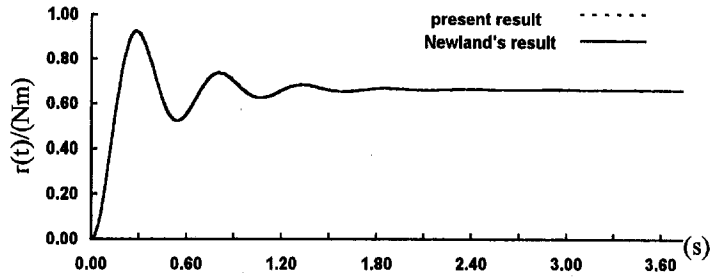


Fig. 2 The step response function of the torque in the shaft connecting wheel 1 and 2 to a step torque (1 Nm) applied on wheel 1 from time zero

Downloaded 04 May 2010 to 171.66.16.34. Redistribution subject to ASME license or copyright; see http://www.asme.org/terms/Terms_Use.cfm

References

Ahmadian, M., and Inman, D. J., 1984, "Classical normal modes in asymmetric nonconservative dynamic systems," *AIAA Journal,* Vol. 22, pp. 1012–1015.

Caughey, T. K., and Ma, F., 1993, "Complex Modes and Solvability of Nonclassical Linear Systems," ASME JOURNAL OF APPLIED MECHANICS, Vol. 60, pp. 26–28.

Caughey, T. K., and O'Kelly, M. E. J., 1965, "Classical Normal Mode in Damped Linear Dynamic System," ASME JOURNAL OF APPLIED MECHANICS, Vol. 32, pp. 583–588.

Foss, K. A., 1958, "Coordinates Which Uncouple the Equations of Damped Linear Dynamic Systems," ASME JOURNAL OF APPLIED MECHANICS, Vol. 25, pp. 361–364.

Golub, G. H., and Van Loan, C. F., 1989, *Matrix computations,* The John Hopkins University Press, Baltimore, MD.

Huseyin, K., 1978, *Vibration and stability of multiple parameter system,* Sijthoff and Noordhoff, Amsterdam.

Inman, D. J., 1983, "Dynamics of Asymmetric Nonconservative Systems," ASME JOURNAL OF APPLIED MECHANICS, Vol. 50, pp. 199–203.

Kliem, W., and Pommer, C., 1986, "On the stability of linear nonconservative systems," *Quarterly Journal of Applied Mathematics,* Vol. XLIII, No. 4, pp. 456–461.

Liu, M., and Wilson, J. M., 1992, "Criterion for decoupling dynamic equation of motion of a linear gyroscopic system," *AIAA Journal,* Vol. 30, pp. 2989–2991.

Ma, F., and Caughey, T. K., 1995, "Analysis of Linear Nonconservative Vibrations," ASME JOURNAL OF APPLIED MECHANICS, Vol. 62, pp. 685–691.

Meirovitch, L., 1967, *Analytical methods in vibrations,* The Macmillan Co., London.

Mingory, D. L., 1970, "A Stability Theorem for Mechanical Systems With Constraint Damping," ASME JOURNAL OF APPLIED MECHANICS, Vol. 37, pp. 253–258.

Moler, C. B., and Stewart, G. W., 1973, "An algorithm for generalized matrix eigenvalue problem," *SIAM Journal on Numerical Analysis,* Vol. 10, pp. 241–256.

Newland, D. E., 1987, "On the modal analysis of non-conservative linear system," *Journal of Sound and Vibration,* Vol. 112, pp. 69–97.

Newland, D. E., 1989, *Mechanical vibration analysis and computation,* Longman Scientific and Technical, Singapore.

Ren, G. X., and Zheng, Z. C., 1997, "A reformulated Arnoldi method for nonclassically damped eigenvalue problem," *International Journal for Numerical Methods in Engineering,* Vol. 40, pp. 3537–3555.

Stewart, G. W., 1972, "On the sensitivity of the eigenvalue problem $Ax = Bx$," *SIAM Journal on Numerical Analysis,* Vol. 9, pp. 669–686.

Stewart, G. W., 1978, "Perturbation theory for the generalized eigenvalue problem," *Recent Advances in Numerical Analysis,* C. de Boor and G. H. Golub, eds., Academic Press, New York.

Tasso, H., 1980, "On the stability of dissipative systems with circulatory forces," *Zeitschrift fur angewandte Mathematik und Physik (ZAMP),* Vol. 31, pp. 536–537.

Teichman, J., 1979, "A stability theorem for systems with circulatory forces," *Zeitschrift fur angewandte Mathematik und Physik (ZAMP),* Vol. 30, pp. 1027–1029.

Zheng, Z. C., and Ren, G. X., 1995, "Dynamic orthogonal decoupling of the non-classically damped dynamic systems," *Proceedings of International Conference on Structural Dynamics, Vibration, Noise and Control,* ed. D. M. Zhu and J. M. Ko, eds., Color Max Commercial Printing Company Ltd., Hong Kong, pp. 125–130.

Zheng, Z. C., and Ren, G. X., 1996, "The analytical approach for large scale non-classically damped dynamic system," *Acta Mechanica Sinica,* Vol. 12, pp. 271–280.

Zheng, Z. C., Ren, G. X., and Williams, F. W., 1997, "The eigenvalue problem for the damped gyroscopic system," *International Journal of Mechanical Science,* Vol. 35, pp. 741–750.

Zhu, D. C., and Shi, G. Q., 1988, "The determination of the defectiveness of linear structural dynamic systems," *Computer and Structure,* Vol. 30, pp. 897–899.

Downloaded 04 May 2010 to 171.66.16.34. Redistribution subject to ASME license or copyright; see http://www.asme.org/terms/Terms_Use.cfm

Three-Dimensional Vibrations of a Beam on an Elastic Half-Space: Resonance Interaction of Vertical-Longitudinal and Lateral Beam Waves

A. V. Metrikine
Wave Dynamics Department,
Mechanical Engineering Institute,
Russian Academy of Sciences,
Nizhny Novgorod, Russia
A. Metrikine@mav.nnov.ru

H. A. Dieterman
Faculty of Civil Engineering,
Delft University of Technology,
Stevinweg 1,
2628 CN Delft, Holland
H.dieterman@ct.tudelft.nl

Three-dimensional vibrations of a Euler-Bernoulli beam on an elastic half-space are investigated. In the model the beam has a finite width and the half-space and beam deflections are equal along the centre line of the beam. It is shown that the vertical and longitudinal beam vibrations are uncoupled from the lateral ones. The dispersion relations for the lateral and vertical-longitudinal waves in the beam are derived and the respective dispersion curves are plotted. These curves can cross each other due to the different equivalent stiffnesses of the half-space in vertical and lateral directions and different vertical and lateral bending stiffnesses of the beam. The existence of a crossing point implies that if the vertical-longitudinal and lateral beam vibrations are coupled for some reason (half-space inhomogeneity, beam asymmetry, etc.), the energy of the vertical vibrations of the beam can be resonantly transferred into the energy of lateral vibrations. This transfer will take place if the frequency of vibrations is close to the frequency determined by the crossing point. The dependency of the frequency of the crossing point on axial compressional stresses in the beam is studied. It is shown that this frequency decreases as the stresses increase.

1 Introduction

Elastic waves generated by a moving train in a railroad track are powerful when the train velocity gets close to the Rayleigh wave velocity in the track subsoil (Filippov, 1961; Bogacz, 1983; Dieterman and Metrikine, 1996). Nowadays this phenomenon has to be taken into account for high-speed trains, especially if they move over soft soils where the surface wave velocity is in order of 150–250 km/h. One of the main consequences of this phenomenon is that the dynamical amplification of the track vibrations under the moving train can cause buckling of the track. Indeed, if rails are almost straight, the compressive stresses (due to temperature) in continuously welded track must be very high to trigger buckling; however, with presence of an initial curvature the critical compressive stresses are reduced substantially. Further the larger the initial curvature, the smaller the temperature at which buckling starts. In practice the buckling usually takes place in lateral direction, so it is of practical importance to analyse the mechanisms which might lead to amplification of the lateral track vibrations.

In this paper we investigate a mechanism by which vertical track vibrations are resonantly transferred into lateral vibrations. To this end three-dimensional vibrations of a Euler-Bernoulli beam on an elastic half-space are considered. The beam has a finite width and the continuous contact with the supporting half-space takes place along the center line of the beam.

Dispersion relations are derived and dispersion curves are plotted for vertical-longitudinal and lateral beam vibrations which are uncoupled in the model under investigation. It is shown that the dispersion curves can have a crossing point. This crossing point determines the critical frequency at which the vertical vibrations of the beam can resonantly amplify the lateral ones.

It is of further interest to investigate the dependency of the critical frequency on axial stresses in the beam. This analysis shows a decreasing of the critical frequency with an increase of the compressional stresses.

2 Model

We consider a Euler-Bernoulli beam with a width $2a$ on an elastic half-space as depicted in Fig. 1.

It is assumed that the half-space displacements and the beam displacements are equal along the center line of the beam. Then the equations of the half-space motion using scalar $\Phi(x, y, z, t)$ and vector $\Psi(x, y, z, t)$ potentials are given as

$$\Delta\Phi = \frac{1}{c_L^2}\frac{\partial^2}{\partial t^2}\Phi, \quad \Delta\Psi = \frac{1}{c_T^2}\frac{\partial^2}{\partial t^2}\Psi, \quad \text{div}\,(\Psi) = 0, \quad (1)$$

where $c_L = \sqrt{(\lambda + 2\mu)/\rho}$ and $c_T = \sqrt{\mu/\rho}$ are the velocities of the compressional and shear waves, respectively, λ and μ are Lamé constants for the elastic half-space, and ρ is its mass density.

The balance of stresses at the surface of the half-space read as follows:

$$2a\tau_{xz}(x, y, 0, t) = \left(m\frac{\partial^2 U^0}{\partial t^2} - 2EA\frac{\partial^2 U^0}{\partial x^2}\right)H(a - |y|),$$

$$2a\tau_{yz}(x, y, 0, t) = \left(m\frac{\partial^2 V^0}{\partial t^2} + 2EI_L\frac{\partial^4 V^0}{\partial x^4}\right)H(a - |y|),$$

Contributed by the Applied Mechanics Division of THE AMERICAN SOCIETY OF MECHANICAL ENGINEERS for publication in the ASME JOURNAL OF APPLIED MECHANICS.

Discussion on the paper should be addressed to the Technical Editor, Professor Lewis T. Wheeler, Department of Mechanical Engineering, University of Houston, Houston, TX 77204-4792, and will be accepted until four months after final publication of the paper itself in the ASME JOURNAL OF APPLIED MECHANICS.

Manuscript received by the ASME Applied Mechanics Division, May 30, 1996; final revision, May 22, 1997. Associate Technical Editor: W. K. Liu.

Copyright © 1997 by ASME

Downloaded 04 May 2010 to 171.66.16.34. Redistribution subject to ASME license or copyright; see http://www.asme.org/terms/Terms_Use.cfm

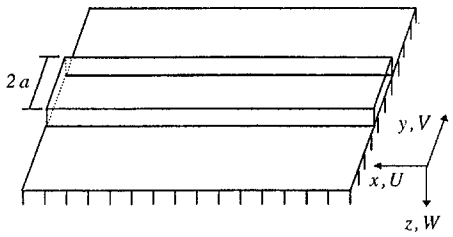


Fig. 1 Model and reference system

$$2a\sigma_{zz}(x, y, 0, t) = \left(m\frac{\partial^2 W^0}{\partial t^2} + 2EI_V\frac{\partial^4 W^0}{\partial x^4}\right)H(a - |y|). \quad (2)$$

Here U^0, V^0, W^0 are the longitudinal, lateral, and vertical beam displacements, m, E, A, $2I_V$, $2I_L$ are the beam mass per unit length, Young's modulus, cross-sectional area, vertical and lateral moments of the cross section inertia, respectively, and $H(\ )$ is the unit step function. We have denoted the moments of inertia as $2I_V$, $2I_L$ to underline that two rails are included into the beam in our model.

The compatibility conditions along the center line of the beam are

$$U(x, 0, 0, t) = U^0(x, t), \quad V(x, 0, 0, t) = V^0(x, t),$$
$$W(x, 0, 0, t) = W^0(x, t), \quad (3)$$

where U, V, $W(x, y, z, t)$ are the half-space displacements in the x, y, z directions, respectively.

3 Dispersion Relations for the Waves in the Beam

To obtain dispersion relations for the waves in the beam we apply the following Fourier transforms with respect to time and horizontal spatial coordinates:

$$\{f(k_1, k_2, z, \omega), \mathbf{g}\} = \int_{-\infty}^{\infty}\int_{-\infty}^{\infty}\int_{-\infty}^{\infty}\{\Phi(x, y, z, t), \Psi\} \times \exp(i(\omega t - k_1 x - k_2 y))dtdxdy$$

$$\{h_x(k_1, \omega), h_y, h_z\} = \int_{-\infty}^{\infty}\int_{-\infty}^{\infty}\{U^0(x, t), V^0, W^0\} \times \exp(i(\omega t - k_1 x))dtdx \quad (4)$$

It gives the following system of equations in the Fourier-domain:

- for the half-space motion (from Eq. (1)),

$$\frac{\partial^2 f}{\partial z^2} + \left(\frac{\omega^2}{c_L^2} - k_1^2 - k_2^2\right)f = 0,$$

$$\frac{\partial^2 \mathbf{g}}{\partial z^2} + \left(\frac{\omega^2}{c_T^2} - k_1^2 - k_2^2\right)\mathbf{g} = 0, \quad \frac{\partial g_z}{\partial z} + ik_1 g_x + ik_2 g_y = 0 \quad (5)$$

- for the stress balance at $z = 0$ (from Eq. (2) using expressions for τ_{xz}, τ_{yz}, σ_{zz} given in Achenbach (1973))

$$\left\{2ik_1\frac{\partial f}{\partial z} + \frac{\partial}{\partial z}\left(ik_2 g_z - \frac{\partial g_y}{\partial z}\right) + ik_1(ik_1 g_y - ik_2 g_x)\right\}_{z=0} = \frac{h_x}{\mu}D_x\frac{\sin(ak_2)}{ak_2},$$

$$\left\{2ik_2\frac{\partial f}{\partial z} - \frac{\partial}{\partial z}\left(ik_1 g_z - \frac{\partial g_x}{\partial z}\right) + ik_2(ik_1 g_y - ik_2 g_x)\right\}_{z=0} = \frac{h_y}{\mu}D_y\frac{\sin(ak_2)}{ak_2},$$

$$\left\{-\frac{\lambda\omega^2}{c_L^2}f + 2\mu\left(\frac{\partial^2 f}{\partial z^2} + i\frac{\partial}{\partial z}(k_1 g_y - k_2 g_x)\right)\right\}_{z=0} = h_z D_z\frac{\sin(ak_2)}{ak_2}, \quad (6)$$

where

$$D_x(k_1, \omega) = -m\omega^2 + 2EAk_1^2, \quad D_y(k_1, \omega) = -m\omega^2 + 2EI_L k_1^4,$$
$$D_z(k_1, \omega) = -m\omega^2 + 2EI_V k_1^4 \quad (7)$$

are the dispersion relations for the longitudinal, lateral, and vertical vibrations of a free beam

- for the compatibility conditions (from Eq. (3))

$$\{h_x(k_1, \omega), h_y, h_z\} = \frac{1}{2\pi}\int_{-\infty}^{\infty}\{u(k_1, k_2, 0, \omega), v, w\}dk_2, \quad (8)$$

where

$$\{u(k_1, k_2, z, \omega), v, w\} = \int_{-\infty}^{\infty}\int_{-\infty}^{\infty}\int_{-\infty}^{\infty}\{U(x, y, z, t), V, W\} \times \exp(i(\omega t - k_1 x - k_2 y))dtdk_1 dk_2$$

are the Fourier images of the displacements of the half-space.

The general solutions of the wave equations in (5), accounting for the proper behavior for large positive values of z, are

$$f = A\exp(-zR_L), \quad \{g_x, g_y, g_z\} = \{B_x, B_y, B_z\}\exp(-zR_T),$$
$$R_{L,T} = \sqrt{k_1^2 + k_2^2 - \omega^2/c_{L,T}^2} \quad (9)$$

provided that the branches in the complex domain are chosen such that the radicals have a positive real part, i.e., $\mathrm{Re}(R_L) > 0$, $\mathrm{Re}(R_T) > 0$.

Substitution of (9) into the last equation of (5) and the balance of stresses given by (6) yields the following set of linear algebraic equations:

$$(ik_1)B_x + (ik_2)B_y + (-R_T)B_z = 0$$
$$(-2ik_1R_L)A + (k_1k_2)B_x + (-k_1^2 - R_T^2)B_y + (-ik_2R_T)B_z = H_x$$
$$(-2ik_2R_L)A + (k_2^2 + R_T^2)B_x + (-k_1k_2)B_y + (ik_1R_T)B_z = H_y$$
$$(2(k_1^2 + k_2^2) - \omega^2/c_T^2)A + (2ik_2R_T)B_x + (-2ik_1R_T)B_y = H_z \quad (10)$$

where

$$\{H_x, H_y, H_z\} = \frac{1}{\mu}\{h_xD_x, h_yD_y, h_zD_z\}\frac{\sin(ak_2)}{ak_2}.$$

When solved for A and $\{B_x, B_y, B_z\}$, the system (10) gives

$$A = \Delta_A/\Delta, \quad \{B_x, B_y, B_z\} = \{\Delta_{B_x}, \Delta_{B_y}, \Delta_{B_z}\}/\Delta,$$

$$\Delta = -R_T\frac{\omega^2}{c_T^2}\left(\left(2k_1^2 + 2k_2^2 - \frac{\omega^2}{c_T^2}\right)^2 - 4(k_1^2 + k_2^2)R_LR_T\right),$$

Downloaded 04 May 2010 to 171.66.16.34. Redistribution subject to ASME license or copyright; see http://www.asme.org/terms/Terms_Use.cfm

$$\Delta_A = -R_T \frac{\omega^2}{c_T^2}\left((-2ik_1R_T)H_x + (-2ik_2R_T)H_y + \left(2k_1^2 + 2k_2^2 - \frac{\omega^2}{c_T^2}\right)H_z\right),$$

$$\Delta_{B_x} = -R_T\left(2k_1k_2\left(2k_1^2 + 2k_2^2 - \frac{\omega^2}{c_T^2} - 2R_LR_T\right)\right)H_x - R_T\left(\left(4k_1^2R_LR_T + \left(\frac{\omega^2}{c_T^2} - 2k_1^2\right)\left(2k_1^2 + 2k_2^2 - \frac{\omega^2}{c_T^2}\right)\right)H_y + \left(2ik_2R_L\frac{\omega^2}{c_T^2}\right)H_z\right),$$

$$\Delta_{B_y} = R_T\left(4k_2^2R_LR_T + \left(\frac{\omega^2}{c_T^2} - 2k_2^2\right)\left(2k_1^2 + 2k_2^2 - \frac{\omega^2}{c_T^2}\right)\right)H_x + R_T\left(\left(2k_1k_2\left(2k_1^2 + 2k_2^2 - \frac{\omega^2}{c_T^2} - 2R_LR_T\right)\right)H_y + \left(2ik_1R_L\frac{\omega^2}{c_T^2}\right)H_z\right),$$

$$\Delta_{B_z} = i(k_1H_y - k_2H_x)\left(\left(2k_1^2 + 2k_2^2 - \frac{\omega^2}{c_T^2}\right)^2 - 4R_LR_T(k_1^2 + k_2^2)\right). \quad (11)$$

In order to obtain equations for the beam vibrations on the half-space we have to apply the compatibility conditions (8). Fourier images of the half-space displacements at the surface have the form (expressions for the elastic space displacements as functions of the scalar and vector potentials are given in Achenbach (1973))

$$u(k_1, k_2, 0, \omega) = ik_1A + ik_2B_z + R_TB_y,$$
$$v(k_1, k_2, 0, \omega) = ik_2A - ik_1B_z - R_TB_x,$$
$$w(k_1, k_2, 0, \omega) = -R_LA + ik_1B_y - ik_2B_x. \quad (12)$$

Now employing (11) we find

$$u(k_1, k_2, 0, \omega) = a_{11}H_x + a_{12}H_y + a_{13}H_z,$$
$$v(k_1, k_2, 0, \omega) = a_{21}H_x + a_{22}H_y + a_{23}H_z,$$
$$w(k_1, k_2, 0, \omega) = a_{31}H_x + a_{32}H_y + a_{33}H_z, \quad (13)$$

where

$$a_{11} = -\frac{1}{R_T}\left(1 + \frac{k_1^2}{\Delta_0}\left(4R_LR_T + 3\frac{\omega^2}{c_T^2} - 4(k_1^2 + k_2^2)\right)\right),$$

$$a_{12} = -\frac{k_1k_2}{R_T\Delta_0}\left(4R_LR_T + 3\frac{\omega^2}{c_T^2} - 4(k_1^2 + k_2^2)\right),$$

$$a_{13} = i\frac{k_1}{\Delta_0}\left(2(k_1^2 + k_2^2) - \frac{\omega^2}{c_T^2} - 2R_LR_T\right),$$

$$a_{21} = a_{12},$$

$$a_{22} = -\frac{1}{R_T}\left(1 + \frac{k_2^2}{\Delta_0}\left(4R_LR_T + 3\frac{\omega^2}{c_T^2} - 4(k_1^2 + k_2^2)\right)\right),$$

$$a_{23} = i\frac{k_2}{\Delta_0}\left(2(k_1^2 + k_2^2) - \frac{\omega^2}{c_T^2} - 2R_LR_T\right),$$

$$a_{31} = -a_{13}, \quad a_{32} = -a_{23}, \quad a_{33} = \frac{\omega^2}{c_T^2}\frac{R_L}{\Delta_0},$$

$$\Delta_0 = \left(2k_1^2 + 2k_2^2 - \frac{\omega^2}{c_T^2}\right)^2 - 4(k_1^2 + k_2^2)R_LR_T.$$

Finally, substituting (13) into the compatibility conditions (8) and using expressions for $\{H_x, H_y, H_z\}$ (see Eq. (10)), we obtain the following equations describing the three-dimensional vibrations of the beam on the elastic half-space

$$h_x = -h_xI_{11}\frac{D_x}{2\pi\mu} + h_zI_{13}\frac{iD_z}{2\pi\mu},$$

$$h_y = -h_yI_{22}\frac{D_y}{2\pi\mu},$$

$$h_z = -h_xI_{31}\frac{iD_x}{2\pi\mu} + h_zI_{33}\frac{D_z}{2\pi\mu}, \quad (14)$$

where

$$I_{11} = -\int_{-\infty}^{\infty} a_{11}\frac{\sin(ak_2)}{ak_2}dk_2 = \int_{-\infty}^{\infty}\frac{1}{R_T}\left(1 + \frac{k_1^2}{\Delta_0}\left(4R_LR_T + 3\frac{\omega^2}{c_T^2} - 4(k_1^2 + k_2^2)\right)\right)\frac{\sin(ak_2)}{ak_2}dk_2,$$

$$I_{13} = I_{31} = \frac{1}{i}\int_{-\infty}^{\infty} a_{13}\frac{\sin(ak_2)}{ak_2}dk_2 = \int_{-\infty}^{\infty}\frac{k_1}{\Delta_0}\left(2(k_1^2 + k_2^2) - \frac{\omega^2}{c_T^2} - 2R_LR_T\right)\frac{\sin(ak_2)}{ak_2}dk_2,$$

$$I_{22} = -\int_{-\infty}^{\infty} a_{22}\frac{\sin(ak_2)}{ak_2}dk_2 = \int_{-\infty}^{\infty}\frac{1}{R_T}\left(1 + \frac{k_2^2}{\Delta_0}\left(4R_LR_T + 3\frac{\omega^2}{c_T^2} - 4(k_1^2 + k_2^2)\right)\right)\frac{\sin(ak_2)}{ak_2}dk_2,$$

$$I_{33} = \int_{-\infty}^{\infty} a_{33}\frac{\sin(ak_2)}{ak_2}dk_2 = \frac{\omega^2}{c_T^2}\int_{-\infty}^{\infty}\frac{R_L}{\Delta_0}\frac{\sin(ak_2)}{ak_2}dk_2. \quad (15)$$

It is evident from (14) that the vertical and longitudinal vibrations (h_z and h_x) are coupled and the lateral (h_y) ones are uncoupled. Mathematically this result has been obtained since a_{12}, a_{21}, a_{23}, a_{32} are odd functions of k_2. Applying the compatibility conditions then the integrals with respect to k_2 over symmetrical limits result in zero.

The uncoupling can be understood also by the following "physical" reasoning. In our model, displacements of the beam can only be caused by the displacement of the half-space along the line $\{y = 0, z = 0\}$ (see compatibility conditions (3)). The excitation of the half-space in x and z-directions is done by forces, symmetrical with respect to the line $\{y = 0, z = 0\}$ (see balance of stresses at the half-space surface (2)). Evidently such forces cannot result in a y-deflection of the line $\{y = 0, z = 0\}$. Therefore the second equation in (14) can not have any members proportional to h_xD_x and h_zD_z at the right side.

It can also be proved by contradiction that a lateral force, symmetrical with respect to the line $\{y = 0, z = 0\}$ cannot cause either x- or z-deflections of the half-space along the line

Downloaded 04 May 2010 to 171.66.16.34. Redistribution subject to ASME license or copyright; see http://www.asme.org/terms/Terms_Use.cfm

of interaction.[1] So at the right sides of the first and third equations in (14) a member proportional to $h_y D_y$ has to be absent.

The Eqs. (14) determine dispersion relations for vertical-longitudinal (first and third equation) and lateral (second equation) waves in the beam on the half-space. According to (14) the frequency ω and the wave number k_1 satisfy the following dispersion relations:

- for vertical-longitudinal waves

$$\left(1 + \frac{1}{2\pi\mu} I_{11} D_x\right)\left(1 - \frac{1}{2\pi\mu} I_{33} D_z\right) - (I_{13})^2 D_x D_z \frac{1}{(2\pi\mu)^2} = 0 \quad (16)$$

- for lateral waves

$$1 + \frac{1}{2\pi\mu} I_{22} D_y = 0. \quad (17)$$

It was shown in (Dieterman and Metrikine, 1996) that waves can propagate in a beam on the half-space with a constant amplitude only if the phase velocity of waves in the beam is smaller than the Rayleigh wave velocity c_R in the half-space. Therefore the equations (16) and (17) might have real pairs of roots $\{\omega, k_1\}$ only if $V_{ph} = \omega/k_1 < c_R$. In this range the equation $\Delta_0 = (2k_1^2 + 2k_2^2 - \omega^2/c_T^2)^2 - 4(k_1^2 + k_2^2)R_L R_T = 0$, which determines the poles of all integrands in (15), does not have any real roots if $V_{ph} \neq 0$ (see (Filippov, 1961; Bogacz, 1983; Dieterman and Metrikine, 1996)) and the integrals I_{11}, I_{13}, I_{22}, I_{31} can be calculated directly using standard programs. The appropriate form for numerical calculations of the integrals is given in the Appendix.

Introducing dimensionless parameters $\beta_T = V_{ph}/c_T$ (V_{ph} is the phase velocity of waves in the beam), $\beta_0 = c_0/c_T$ ($c_0^2 = EA/m$ is the velocity of longitudinal waves in the beam), $K = ak_1$—the ratio of the beam width and a wave length in the beam, $M = m/2\pi\rho a^2$—the beam and the half-space density ratio and $Z_V = I_V/Aa^2$, $Z_L = I_L/Aa^2$—geometrical parameters for vertical and lateral bending deflections, we rewrite the dispersion relations (16) and (17) for numerical analysis in the more appropriate form

$$(1 - MK^2(\beta_T^2 - 2\beta_0^2)I_{11})(1 + MK^2(\beta_T^2 - 2K^2\beta_0^2 Z_V)I_{33}) - M^2K^4(\beta_T^2 - 2\beta_0^2)(\beta_T^2 - 2K^2\beta_0^2 Z_V)(I_{13})^2 = 0 \quad (18)$$

$$1 - MK^2(\beta_T^2 - 2K^2\beta_0^2 Z_L)I_{22} = 0. \quad (19)$$

Now varying β_T in the interval $0 < \beta_T < c_R/c_T$ and for each β_T seeking for the real solution of Eq. (18) and (19) we can find out numerically explicit dispersion relations $\beta_T(K)$ for vertical-longitudinal and lateral waves in the beam.

In Fig. 2 the dispersion curves for vertical-longitudinal (line 1) and lateral (line 2) vibrations are depicted in the plane of the dimensionless parameters $\{\omega a/c_T, ak_1\}$ ($\omega a/c_T = \beta_T K$). The following parameters of the half-space and the beam were used for the calculations: Poisson's ratio of the half-space $\nu = 0.3$; Lamé's constant of the half-space $\mu = 3.27*10^7$ N/m^2; the half-space density $\rho = 1.96*10^3$kg/m^3; the beam mass per unit length $m = 2.089*10^3$ kg/m (we included the mass of the rails, sleepers, and ballast of the size of 2 m × 0.5 m), Young's modulus of the beam $E = 2.06*10^{11}$ N/m^2; the beam cross-sectional area $A = 6.95*10^{-3}$ m^2; the beam width $2a = 1.6$ m; the vertical and lateral moments of inertia of the beam $I_V = 2.07*10^{-5}$ m^4, $I_L = 3.59*10^{-6}$ m^4. The chosen parameters are valid for a description of a railroad track (beam = rails + sleepers) on a subsoil (half-space) (see Kerr and El-Sibaie (1987), Labra (1975), and Patil (1987)).

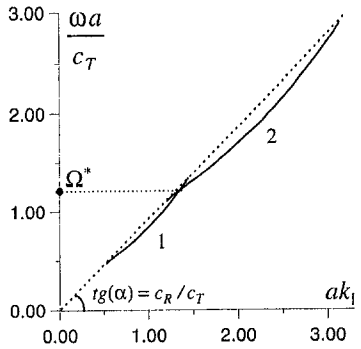


Fig. 2 Dispersion curves for vertical-longitudinal (line 1) and lateral (line 2) vibrations

Figure 2 shows that the dispersion curves have a crossing point $\Omega^* = \omega a/c_T$. The existence of the crossing point implies that if the vertical-longitudinal and lateral beam vibrations are coupled for some reason (half-space inhomogeneity, beam asymmetry with respect to the center line, etc.), the energy of vertical vibrations of the beam can be resonantly transferred into the energy of lateral vibrations. This situation will take place if the frequency of vibrations is close to Ω^*.

4 Effect of Axial Stresses

The phenomenon of the energy transfer from vertical into lateral vibrations can become of more practical importance if the railroad track is axially compressed due to temperature. Indeed, under compressional stresses rail buckling may occur and the larger a misalignment in the rails the smaller the temperature for starting buckling. Therefore lateral vibrations, serving as a dynamical misalignment, should reduce the critical buckling temperature.

To investigate the effect of the compressional stresses on the dispersion curves and the frequency of the crossing point Ω^* we include additional "compressional" members into the equations of the beam vibrations. In this case the boundary conditions at the half-space surface (2) will be rewritten as follows:

$$2a\tau_{xz}(x, y, 0, t) = \left(m\frac{\partial^2 U^0}{\partial t^2} - 2EA\frac{\partial^2 U^0}{\partial x^2}\right)H(a - |y|),$$

$$2a\tau_{yz}(x, y, 0, t) = \left(m\frac{\partial^2 V^0}{\partial t^2} + 2EI_L\frac{\partial^4 V^0}{\partial x^4} + (N - 2s^*)\frac{\partial^2 V^0}{\partial x^2}\right)H(a - |y|),$$

$$2a\sigma_{zz}(x, y, 0, t) = \left(m\frac{\partial^2 W^0}{\partial t^2} + 2EI_V\frac{\partial^4 W^0}{\partial x^4} + N\frac{\partial^2 W^0}{\partial x^2}\right)H(a - |y|), \quad (20)$$

where N is the constant compressional force and s^* is the proportionality constant between the rotational resistance moment and the angle of rotation between rail and tie (per unit length of rail). One method used to determine s^* is to rotate a short section of rail fastened to a rigidized tie and then to record, at the fastener the dependence of the applied torsional moment on the angle of rotation of the rail. Then $s^* = s/d$, where s is the recorded proportionality constant and d is the center-to-center tie spacing (see Kerr and El-Sibaie (1987), Labra (1975), and Frederick, (1978)).

[1] The proof is: Suppose, that there is an x or z-deflection of the line under a lateral force. Then due to the symmetry this deflection will be in the same direction both for positive P and negative $(-P)$ lateral forces. It means that if we apply the force $F = P + (-P) = 0$ we have a nonzero deflection for the linear system.

Downloaded 04 May 2010 to 171.66.16.34. Redistribution subject to ASME license or copyright; see http://www.asme.org/terms/Terms_Use.cfm

Following the same procedure we have used to determine the dispersion relations (18), (19), we obtain the following relations when compressional stresses are taken into account:

$$(1 - MK^2(\beta_T^2 - 2\beta_0^2)I_{11})$$
$$\times (1 + K^2(M(\beta_T^2 - 2K^2\beta_0^2 Z_V) + \tilde{N}_V)I_{33})$$
$$- MK^4(\beta_T^2 - 2\beta_0^2)$$
$$\times (M(\beta_T^2 - 2K^2\beta_0^2 Z_V) + \tilde{N}_V)(I_{13})^2 = 0 \quad (21)$$

$$1 - K^2(M(\beta_T^2 - 2K^2\beta_0^2 Z_L) + \tilde{N}_L)I_{22} = 0 \quad (22)$$

where $\tilde{N}_V = N/2\pi\mu a^2$, $\tilde{N}_L = (N - 2s^*)/2\pi\mu a^2$.

The dispersion curves for vertical-longitudinal (line 1) and lateral (line 2) waves obtained according to (21), (22) are depicted in Figs. 3(*a*) and 3(*b*).

For Fig. 3(*a*) we have taken $N = 0.7^* N_{cr}$ and for Fig. 3(*b*) – $N = N_{cr}$. The critical compresssional force N_{cr} is related to the static lateral buckling (Euler instability) of the beam. It is seen from the Fig. 3(*b*) that in this case the dispersion curve of the lateral waves is tangential to the axes $\omega = 0$. Parameters of the beam and the half-space are taken the same as in the previous section and $s^* = 10^6 N$ (see Kerr and El-Sibaie (1987)). The figures show that the crossing point of the dispersion curves Ω^* still exist in the case of an axially compressed beam and Ω^* depends on the compressional force N. The dependence $\Omega^*(N)$ is depicted in Fig. 4.

It is evident that the critical frequency Ω^* (in the sense of resonance energy transfer) decreases with an increase of the compressional stresses. It can be expected that the phenomenon is even more powerful in this case since the resonance frequency decreases here and the lower a frequency, the weaker the vibrations are damped in many practical situations.

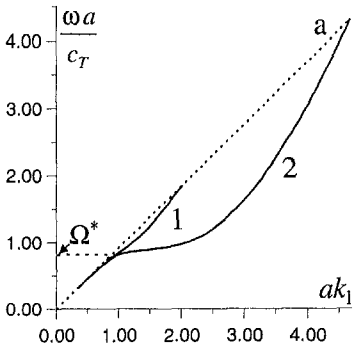


Fig. 3(*a*)

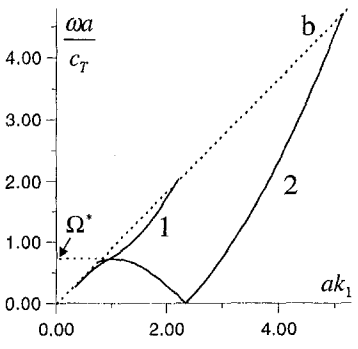


Fig. 3(*b*)

Fig. 3 Dispersion curves for vertical-longitudinal (line 1) and lateral (line 2) vibrations as axial stresses are taken into account (Fig. 3(*a*)—$N = 0.7^* N_{cr}$, Fig. 3(*b*)—$N = N_{cr}$)

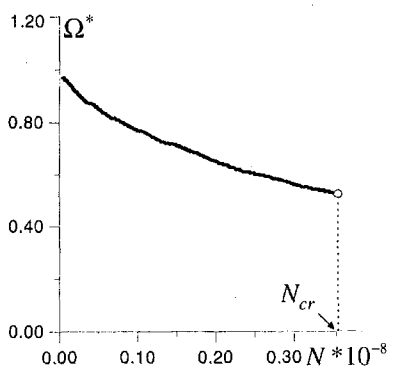


Fig. 4 Dependency of the critical frequency (frequency of the crossing point) on the compressional force

5 Conclusions

In this paper the steady-state three-dimensional vibrations of a beam on an elastic half-space have been investigated. It has been shown that vertical-longitudinal and lateral vibrations of the beam are uncoupled under the following assumptions: (1) stresses at the interface are uniformly distributed along the beam width; (2) displacements of the half-space surface are equal to the beam displacements along the beam center line; (3) vertical, longitudinal, and lateral vibrations of the free beam are uncoupled.

The dispersion relations have been determined for vertical-longitudinal and lateral beam vibrations. The respective dispersion curves were plotted showing the existence of a crossing point. It implies that vertical and lateral waves of the same frequency and wave number can propagate in the beam. Therefore if vibrations of the beam will be coupled for some reason (half-space or beam inhomogeneity, beam asymmetry with respect to center line, etc.) then the energy of vertical vibrations can be resonantly transferred into the energy of lateral vibrations. This situation takes place if the frequency of the beam vibrations is close to the critical frequency determined by the crossing point.

The effect of axial compressional stresses on the beam vibrations has been analyzed. The analysis is important since lateral vibrations serving as an initial misalignment can cause lateral buckling of railroad tracks. It has been shown that the critical frequency decreases with an increase of the compressional axial stresses.

We would like to notice that the model investigated is not unique in the sense of the existence of a crossing point between the dispersion curves. For example, the Rayleigh-Lamb dispersion curves have several crossing points between the symmetric and antisymmetric modes. However, in multimode systems the issue of the crossing point is less important, since practically any source of disturbance generates several modes and the resonance interaction between one of the generated modes and a new (nor excited by the source) mode can not change the system behavior qualitatively. At the same time, if one wants to excite a solitary mode in a multimode system, the existence of a crossing point at the excitation frequency is of great importance—the solitary wave cannot be excited exclusively.

References

Achenbach, J. D., 1973, *Wave propagation in elastic solids,* North-Holland, Amsterdam.

Bogacz, R., 1983, "On dynamics and stability of continuous systems subjected to a distributed moving load," *Ing. Arch.,* Vol. 53, pp. 243–255.

Dieterman, H. A., Metrikine, A. V., 1996, "The Equivalent Stiffness of a Half-Space Interacting With a Beam. Critical Velocities of a Moving Load Along the Beam," *European Journal of Mechanics Solids/A,* Vol. 15, No. 1, pp. 67–90.

Filippov, A. P., 1961, "Steady state vibrations of an infinite beam on an elastic half-space subjected to a moving load," *Izvestija AN SSSR OTN Mechanica I Mashinostroenie,* Vol. 6, pp. 97–105.

Downloaded 04 May 2010 to 171.66.16.34. Redistribution subject to ASME license or copyright; see http://www.asme.org/terms/Terms_Use.cfm

Frederick, C. O., 1978, "The effect of lateral loads on track movement," *Railroad Track Mechanics and Technology,* Pergamon Press, New York.

Kerr, A. D., and El-Sibaie, M. A., 1987, "On the New Equations for the Lateral Dynamics of a Rail-Tie Structure," ASME *Journal of Dynamic Systems, Measurements, and Control,* Vol. 109; pp. 180–185.

Labra, J. J., 1975, "An axially stressed railroad track on an elastic continuum subjected to a moving load," *Acta Mechanica,* Vol. 22, pp. 113–129.

Patil, S. P., 1987, "Natural frequencies of an infinite beam on a simple internal foundation model," *Int. J. Solids Structures,* Vol. 23, pp. 1615–1623.

APPENDIX

Introducing a new variable of integration $\xi = k_2/k_1$, denoting $V_{ph} = \omega/k_1$, $\beta_{L,T} = V_{ph}/c_{L,T}$, $K = ak_1$ and using the even character of integrands we rewrite the integrals I_{11}, I_{13}, I_{22}, I_{31} in the following form:

$$I_{11} = \frac{2}{K}\int_0^\infty F_{11}(\xi)d\xi = \frac{2}{K}\int_0^\infty \frac{1}{R_T(\xi)}\left(1 + \frac{1}{\Delta_0(\xi)}(4R_L(\xi)R_T(\xi) + 3\beta_T^2 - 4(1+\xi^2))\right)\frac{\sin(K\xi)}{\xi}d\xi,$$

$$I_{13} = \frac{2}{K}\int_0^\infty F_{13}(\xi)d\xi = \frac{2}{K}\int_0^\infty \frac{1}{\Delta_0(\xi)}(2(1+\xi^2) - \beta_T^2 - 2R_L(\xi)R_T(\xi))\frac{\sin(K\xi)}{\xi}d\xi,$$

$$I_{22} = \frac{2}{K}\int_0^\infty F_{22}(\xi)d\xi = \frac{2}{K}\int_0^\infty \frac{1}{R_T(\xi)}\left(1 + \frac{\xi^2}{\Delta_0(\xi)}(4R_L(\xi)R_T(\xi) + 3\beta_T^2 - 4(1+\xi^2))\right)\frac{\sin(K\xi)}{\xi}d\xi,$$

$$I_{33} = \frac{2}{K}\int_0^\infty F_{33}(\xi)d\xi = \frac{2}{K}\beta_T^2\int_0^\infty \frac{R_L(\xi)}{\Delta_0(\xi)}\frac{\sin(K\xi)}{\xi}d\xi,$$

$$\Delta_0(\xi) = (2(1+\xi^2) - \beta_T^2)^2 - 4(1+\xi^2)R_L(\xi)R_T(\xi),$$

$$R_{L,T}(\xi) = \sqrt{1+\xi^2-\beta_{L,T}^2}.$$

All the integrals converge as $\xi \to \infty$ since the following asymptotic expressions are valid for $\xi \to \infty$

$$F_{11} \to \left(1 + \frac{\beta_T^2 - 2\beta_L^2}{2\xi^2(\beta_L^2 - \beta_T^2)}\right)\frac{\sin(K\xi)}{\xi^2},$$

$$F_{13} \to \frac{\beta_L^2}{2(\beta_L^2 - \beta_T^2)}\frac{\sin(K\xi)}{\xi^3},$$

$$F_{22} \to -\frac{\beta_T^2}{2(\beta_L^2 - \beta_T^2)}\frac{\sin(K\xi)}{\xi^2},$$

$$F_{33} \to \frac{\beta_T^2}{2(\beta_L^2 - \beta_T^2)}\frac{\sin(K\xi)}{\xi^2}.$$

In the quasi-static case when $\beta_{L,T} \to 0$ the following expressions are adequate to calculate the integrals:

$$F_{11} = \left(1 + \frac{c_L^2/c_T^2 - 2}{2(1+\xi^2)(1 - c_L^2/c_T^2)}\right)\frac{\sin(K\xi)}{\xi\sqrt{1+\xi^2}},$$

$$F_{13} = \frac{\sin(K\xi)}{2\xi(1+\xi^2)(1 - c_L^2/c_T^2)},$$

$$F_{22} = \left(1 + \frac{\xi^2(c_L^2/c_T^2 - 2)}{2(1+\xi^2)(1 - c_L^2/c_T^2)}\right)\frac{\sin(K\xi)}{\xi\sqrt{1+\xi^2}},$$

$$F_{33} = \frac{\sqrt{1+\xi^2}\sin(K\xi)}{2\xi(1+\xi^2)(c_T^2/c_L^2 - 1)}.$$

Downloaded 04 May 2010 to 171.66.16.34. Redistribution subject to ASME license or copyright; see http://www.asme.org/terms/Terms_Use.cfm

Explicit Vibration Solutions of a Cable Under Complicated Loads

P. Yu
Department of Applied Mathematics,
University of Western Ontario,
London, ON N6A 5B7,
Canada

This paper is concerned with the dynamical analysis of a sagged cable having small equilibrium curvature and horizontal supports under both distributed and concentrated loads. The loads are applied in vertical as well as horizontal directions. Based on a free vibration analysis, a transfer matrix method is generalized for solving coupled, nonhomogeneous differential equations to obtain closed-form solutions for the natural frequencies and the associated vibration mode shapes in vertical, horizontal, and longitudinal directions. It is shown that two sets of independent mode shapes associated with two sets of independent frequencies always exist and can be obtained via an equation of one variable only. This method demonstrates its advantages in dealing with interactions of modes in different directions, complex arrangement of concentrated loads, and high-order modes oscillations.

1 Introduction

Cables are commonly employed in a wide range of practical applications in ocean and electrical engineering. The study of oscillations of suspended cables is of great importance to cable structure industry and it has attracted the attention of many researchers. For example, the galloping (a low-frequency large-amplitude oscillation) of overhead transmission lines may cause severe disruptions in the electrical supply and even a cascading collapse of a line's supporting towers. Marine cables may experience vortex-induced oscillations which can accelerate cable fatigue and degrade the performance and positioning of attached instruments such as hydrophones. A better understanding and modeling of cable motions rely on the accurate computation of the cable's *natural frequency* spectrum and vibration *mode shapes.*

Linear theory for bare (with no attached point loads or instruments) suspended, elastic cables with small ratio of the sag to the line's span length was well established for either horizontal (Irvine and Caughey, 1974) or inclined (Triantafyllou, 1984) supports. Irvine (1981) also derived explicit formulas for a taut inclined cable. However, in practice, most of cables have attached point masses or *concentrated loads.* For example, marine cables used as electrical or optical signal transmission lines may have hundreds of attached instruments. Overhead electrical transmission lines may be often equipped with an anti-galloping control device such as *detuning pendulums* which are basically additional masses hanging on the line. These attached concentrated loads greatly complicate the analysis of cable motions. Therefore, numerical methods have been widely used in the study of cables with concentrated loads, in particular, in finding the cable's natural frequencies and vibration mode shapes. The numerical solutions, however, were restricted to the low-order vibration modes of cables due to convergence limitations. Though great progress has been achieved in the study of cable dynamics (e.g., see the review article by Triantafyllou (1991)), the investigation of cables with concentrated loads has received the attention of very few researchers, among them are Irvine (1981), Sergev and Iwan (1981), and Cheng and Perkins (1992a, b).

Contributed by the Applied Mechanics Division of THE AMERICAN SOCIETY OF MECHANICAL ENGINEERS for publication in the ASME JOURNAL OF APPLIED MECHANICS.

Discussion on the paper should be addressed to the Technical Editor, Professor Lewis T. Wheeler, Department of Mechanical Engineering, University of Houston, Houston, TX 77204-4792, and will be accepted until four months after final publication of the paper itself in the ASME JOURNAL OF APPLIED MECHANICS.

Manuscript received by the ASME Applied Mechanics Division, July 26, 1996; final revision, Mar. 5, 1997. Associate Technical Editor: N. C. Perkins.

This research was motivated by an industrial project "Modelling of Conductor Galloping." A simple two-degree-of-freedom model (Yu et al., 1992) and a more comprehensive three-degree-of-freedom model (Yu et al., 1993) have been developed to realistically describe the dynamics of iced cables under side steady wind. These models are established with the natural frequencies and vibration mode shapes obtained using the approach given by Irvine (1981) for bare cables and therefore, are only applicable for the lines with no concentrated loads. In practice, however, many power utilities, especially in North America, have employed add-on devices such as detuning pendulums to control galloping. These control devices may be treated as concentrated loads and thus, the natural frequencies and mode shapes must be recomputed for such a line. In fact, it has been found that continuing to use the natural frequencies and mode shapes of a bare cable for a line equipped with detuning pendulums yields erroneous results (Modelling, 1993).

Furthermore, it has been found that the change of the *static profile* (*equilibrium state*) of a transmission line due to wind changes the line's natural frequencies and mode shapes and therefore, may significantly affect the dynamical analysis. Figure 1 shows a comparison of the results obtained from the three-degree-of-freedom model (Yu et al., 1993) using the data from a most documented field trial performed by Ontario Hydro (Edwards and Madeyski, 1956). In this figure, the vertical axis denotes the *critical wind speed* at which the cable becomes unstable (in the sense of Liapunov asymptotic stability) and galloping is initiated. The horizontal axis represents the ratio q_z/q_y, where q_z is the *horizontal static distributed wind load* and q_y is the vertical static distributed loads which consist of the wind load and the weights of the cable and ice. It is seen that the critical wind speed U_{CV}, predicted by the *vertical model* (assuming no static loads so that the static profile is located in the vertical plane), is quite different from the critical wind speed U_{CI}, obtained from the *inclined model* (the static profile is located in an inclined plane due to horizontal static load). For example, at $q_z/q_y = 0.1$, $U_{CV} = 3.28$ m/s, $U_{CI} = 4.23$ m/s which gives 30 percent error. However, when $q_z/q_y = 0.2$, $U_{CV} = 3.18$ m/s, but $U_{CI} \to \infty$, which implies that the inclined model predicts the line always stable while vertical model indicates the line becoming unstable at a very low wind speed. This shows that the static load, especially the horizontal component, cannot, in general, be neglected in the vibration analysis of cables subjected cross flows.

It has been noted that Irvine (1981) derived the analytical expressions for the natural frequency and mode shapes of a bare cable described by *differential equations.* He also obtained explicit approximate solutions to the case of a cable with vertical

Copyright © 1997 by ASME

Downloaded 04 May 2010 to 171.66.16.34. Redistribution subject to ASME license or copyright; see http://www.asme.org/terms/Terms_Use.cfm

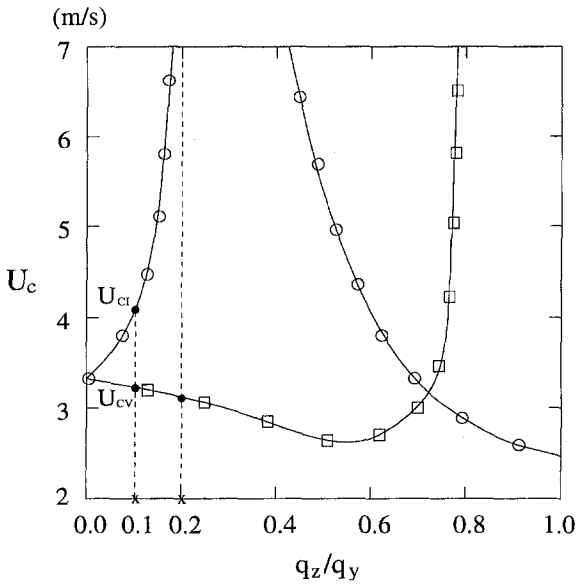


Fig. 1 Effect of horizontal static loads, □: vertical model; ○: inclined model

multiple concentrated loads (masses) by using *difference equations*. The discretion approach makes the derivation and formulas simpler, and give good approximations when the number of multiple loads are not small. However, this method is only applicable for equally linked and equally concentrated loads. To obtain more accurate solutions, Sergev and Iwan (1981) employed a *transfer matrix* approach to derive closed form free vibration solutions for multiple attached point masses by assuming that the cable is *inextensible* (*taut cable*). Recently, Cheng and Perkins (1992a, 1992b) extended the transfer matrix method to consider elastic cables and obtained analytical formulas leading to numerically solve for only two coupled transcendental equations. One common fact noticed from these research results is that the horizontal static distributed loads are neglected so that the static profile is located in the vertical plane. Therefore, the out-plane motion is *decoupled* from the in-plane motion, which greatly simplifies the analysis. However, in case if the horizontal static load cannot be ignored, as has be shown in the galloping analysis, one has to find out-plane and in-plane frequencies and mode shapes by simultaneously solving coupled differential equations. Hence, a new method needs to be developed for solving the general case. It should be noted that all the cases studied before are actually special cases of the general case.

In this paper, the transfer matrix method will be modified and generalized to consider a model of elastic cables with *catenary* static profile. The natural frequencies and mode shapes will be found for the most general case; i.e., there exist static horizontal loads and multiple general concentrated loads which are not necessarily in the vertical direction. The horizontal loads are static *drag* forces, obtained from the measurement of aerodynamic loads. It will be shown that two sets of independent mode shapes associated with two sets of independent frequencies always exist and can be found by solving an equation of one variable only. A practical example is presented to show the applicability of the theory.

2 Equations of Motion

A sagged elastic cable, having span length L_x, with horizontal supports is shown in Fig. 2 where the concentrated loads are denoted by F_i, $i = 1, 2, \ldots n$, each of which deviates from the vertical line by a constant angle θ_i, and their locations are indicated by x_i (or s_i) measured from the left end support of the cable. s is the Lagrangian coordinate indicating a reference distance from the left end support while $\bar{s}$ indicates a new Lagrangian coordinate under vibration.

The equations describing the motion of the cable under both distributed and concentrated loads can be derived (see Fig. 3 for the movement components along the vertical and longitudinal directions) as

$$[(T+\tau)(x'+u')]' = m\ddot{u} + m_i\delta(s-s_i)\ddot{u}$$

$$[(T+\tau)(y_1'+y_2')]' = m\ddot{y}_2 - q_y + \delta(s-s_i)(m_i\ddot{y}_2 + F_i\cos\theta_i)$$

$$[(T+\tau)(z_1'+z_2')]' = m\ddot{z}_2 - q_z + \delta(s-s_i)(m_i\ddot{z}_2 - F_i\sin\theta_i) \quad (1)$$

and

$$\tau(s,t) = AE\left(\frac{d\bar{s}}{ds} - 1\right) \quad \text{(Hooke's Law)} \quad (2)$$

where the prime and dot indicate differentiations with respect to s and t (time), respectively. $T(s)$ and $\tau(s, t)$ represent the static and dynamic tensions of the cable, respectively; q_y and q_z denote respectively the vertical and horizontal static loads per unit length which are assumed spatially uniform along the span. The $x(s)$, $y_1(s)$, and $z_1(s)$ are the static profile while $u(s,t)$, $y_2(s,t)$, and $z_2(s,t)$ are the dynamic movements along the longitudinal, vertical, and horizontal directions, respectively. As shown in Fig. 2, these movements are measured from the static profile. A is the cross-sectional area of the cable and E is

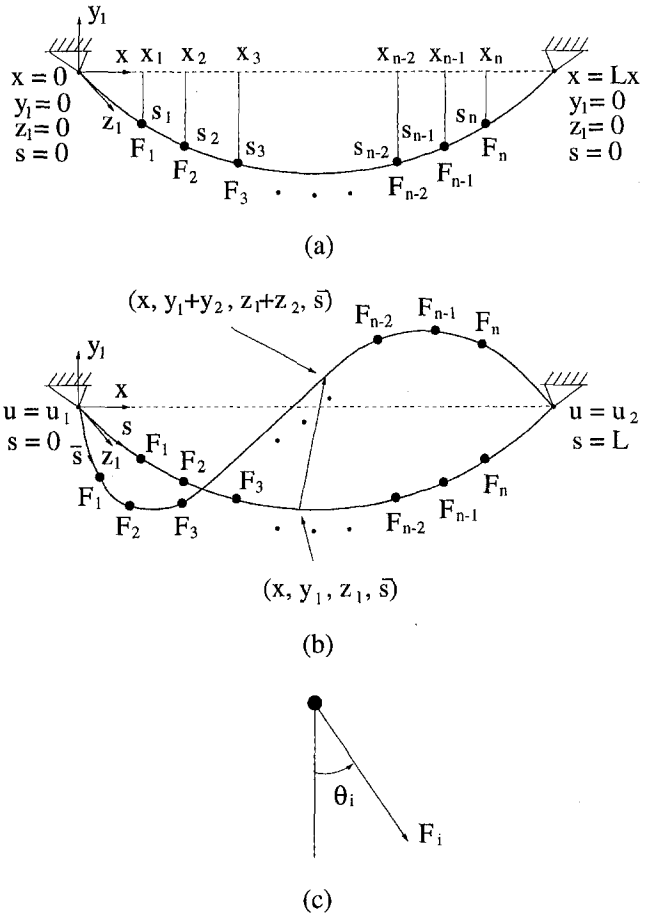


Fig. 2 A sagged cable: (*a*) static profile; (*b*) dynamical motion; and (*c*) concentrated loads

Downloaded 04 May 2010 to 171.66.16.34. Redistribution subject to ASME license or copyright; see http://www.asme.org/terms/Terms_Use.cfm

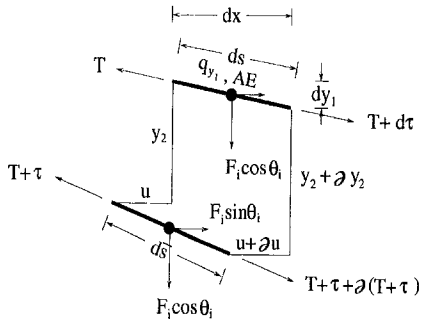


Fig. 3 Differential cable element (projected on $x - y$ plane)

the Young's modulus. δ is a function satisfying $\delta(s - s_i) = 1$ (or 0) if $s = s_i (s \neq s_i)$. Equations (1) and (2) are reduced to two coupled equations studied by Cheng and Perkins (1992b) by assuming $q_z = \theta_i = 0$, which decouples the horizontal motion from the vertical movement, and to one equation considered by Sergev and Iwan (1981) by a further assumption that the cable is inextensible. In this paper, only one assumption is required, that is, the ratio of the sag to the cable's length is small.

Before vibration analysis, the static profile described by x, y_1 and z_1 must be determined. It needs three steps: (1) to find the static profile under the distributed loads only (i.e., $F_i = 0$); (2) to compute the increase of the static tension due to the concentrated loads since usually only the tension under distributed loads is known; and (3) to determine the static profile under both distributed and concentrated loads. The detailed formulations for the three steps can be found in (Yu et al., 1995) and therefore, are not repeated here.

3 Vibration Analysis

The dynamical solutions can be obtained by free vibration analysis on the basis of Eqs. (1) and (2). The dynamic tension increase of a cable with a small ratio of the sag to the cable's length is usually very small compared to the static tension; i.e., $\tau(s, t) \ll T(s)$ and furthermore, one may approximate $\tau(s, t)$ as

$$\tau(s, t) = \tilde{h}(t)\frac{ds}{dx} \tag{3}$$

up to second order. Then by substituting the static profile into the second equation of (1), one can obtain the following equations for the vertical motion:

$$\frac{\partial^2 y_{2i}(s, t)}{\partial s^2} - \left(\frac{m}{H}\right)\frac{\partial^2 y_{2i}(s, t)}{\partial t^2} = \left(\frac{q_y}{H^2}\right)\tilde{h}(t)$$

$$(i = 0, 1, 2, \ldots, n)$$

$$y_{20}(0, t) = y_{2n}(L, t) = 0$$

$$y_{2i}(s_i, t) - y_{2i-1}(s_i, t) = 0$$

$$\frac{\partial y_{2i}(s_i, t)}{ds} - \frac{\partial y_{2i-1}(s_i, t)}{ds} = \left(\frac{m_i}{H}\right)\frac{\partial^2 y_{2i-1}(s_i, t)}{\partial t^2} - \left(\frac{P_i}{H^2}\right)\tilde{h}(t) \tag{4}$$

where H is the horizontal component of the static tension under both the distributed and concentrated loads. Similarly, the third equation of (1) leads to the equations for the horizontal motion, which actually can be obtained from Eq. (4) by changing y to z and setting $P_i = 0$. Equation (2) now becomes

$$\frac{\tilde{h}}{AE}\left(\frac{ds}{dx}\right)^2 = \frac{\partial u}{\partial s} - E_{yi}\frac{\partial y_2}{\partial s} - -E_{zi}\frac{\partial z_2}{\partial s},$$

$$E_{yi} = \frac{q_y}{H}\left[(s - \alpha_i) - \left(\frac{q_z^2}{q^2 q_y}\right)c_i\right],$$

$$E_{zi} = \frac{q_z}{H}\left[(s - \alpha_i) + \left(\frac{q_y}{q^2}\right)c_i\right]. \tag{5}$$

It should be noted due to Eq. (3) that the differential equation describing the longitudinal component has been dropped; i.e., the *longitudinal inertia* is neglected. However, the approximation of the longitudinal motion can still be obtained from Eq. (5). Next, let vibration solutions be

$$u_i(s, t) = \sum_{k=1}^{\infty} U_i^k(s)e^{j\omega_k t}$$

$$y_{2i}(s, t) = \sum_{k=1}^{\infty} Y_i^k(s)e^{j\omega_k t}$$

$$z_{2i}(s, t) = \sum_{k=1}^{\infty} Z_i^k(s)e^{j\omega_k t}$$

$$\tilde{h}(t) = \sum_{k=1}^{\infty} \nu^k e^{j\omega_k t} \tag{6}$$

where $j = \sqrt{-1}$, ω_k is a natural frequency, and $U_i^k(s)$, $Y_i^k(s)$, and $Z_i^k(s)$ are corresponding mode shapes along the longitudinal, vertical, and horizontal directions, respectively.

Substituting Eq. (6) into Eqs. (4) and (5) yields the following ordinary differential equations for a particular frequency (mode) ω_k where the superscripts of $U_i^k(s)$, $Y_i^k(s)$, $Z_i^k(s)$, and ν^k; and the subscripts of ω_k and β_k have been omitted for briefness.

$$\frac{d^2 Y_i(s)}{ds^2} + \beta^2 Y_i(s) = \left(\frac{q_y}{H^2}\right)\nu$$

$$Y_0(0) = Y_n(L) = 0$$

$$Y_i(s_i) - Y_{i-1}(s_i) = 0$$

$$\frac{dY_i(s_i)}{ds} - \frac{dY_{i-1}(s_i)}{ds} = -\beta^2\left(\frac{m_i}{m}\right)Y_{i-1}(s_i) - \left(\frac{P_i}{H^2}\right)\nu \tag{7}$$

and

$$\left(\frac{\nu}{AE}\right)\left(\frac{ds}{dx}\right)^2 = \frac{dU_i(s)}{ds} - E_{yi}\frac{dY_i(s)}{ds} - E_{zi}\frac{dZ_i(s)}{ds} \tag{8}$$

where $\beta = \omega\sqrt{m/H}$, and a similar equation like (7) can be obtained for $Z_i(s)$. The solution to Eq. (7) can be described by

$$Y_i(s) = C_{yi}\cos\beta(s - s_i) + S_{yi}\sin\beta(s - s_i) - C_{y0} \tag{9}$$

where $C_{y0} = -(q_y/\beta^2 H^2)\nu$ is a particular solution, derived from the boundary condition $Y_0(0) = 0$ by substituting Eq. (9) into the first equation of (7). Then the third and fourth equations of (7) lead to

$$\begin{Bmatrix} C_{yi} \\ S_{yi} \end{Bmatrix} = [D_0^i]\begin{Bmatrix} C_{y0} \\ S_{y0} \end{Bmatrix} + \boldsymbol{\gamma}_i\left(\frac{C_{y0}}{q_y}\right) \tag{10}$$

Downloaded 04 May 2010 to 171.66.16.34. Redistribution subject to ASME license or copyright; see http://www.asme.org/terms/Terms_Use.cfm

where

$$[D_0^i] = [D_{i-1}^i][D_0^{i-1}] \quad \text{with} \quad [D_0^0] = I,$$

$$[D_{i-1}^i] = \begin{bmatrix} \cos \beta l_i & \sin \beta l_i \\ -\sin \beta l_i - \beta(m_i/m)\cos \beta l_i & \cos \beta l_i - \beta(m_i/m)\sin \beta l_i \end{bmatrix} \tag{11}$$

ch $l_i = s_i - s_{i-1}$, and I is 2×2 identity matrix. Furthermore, vector $\boldsymbol{\gamma}_i$ is given by the iterative formula

$$\boldsymbol{\gamma}_i = [D_{i-1}^i]\boldsymbol{\gamma}_{i-1} + \begin{Bmatrix} 0 \\ \beta[(m_i/m)q_y + P_i] \end{Bmatrix} \quad \text{with} \quad \boldsymbol{\gamma}_0 = \mathbf{0}. \tag{12}$$

Now substituting Eqs. (9) – (12) into the boundary condition $Y_n(L) = 0$ yields

$$QDS_{y0} = QN_1(C_{y0}/q_y)$$

$$QD = D_0^n(1, 2)\cos \beta(L - s_n) + D_0^n(2, 2)\sin \beta(L - s_n)$$

$$QN_1 = q_y - [q_y D_0^n(1, 1) + \gamma_{n1}]\cos \beta(L - s_n) - [q_y D_0^n(2, 1) + \gamma_{n2}]\sin \beta(L - s_n) \tag{13}$$

where, γ_{n1} and γ_{n2} are components of the vector $\boldsymbol{\gamma}_n$, and $D_0^n(i, j)$ are elements of the matrix $[D_0^n]$. Similarly, the following results can be derived for the horizontal motion:

$$Z_i(s) = C_{zi}\cos \beta(s - s_i) + S_{zi}\sin \beta(s - s_i) - C_{z0}$$

$$\begin{Bmatrix} C_{zi} \\ S_{zi} \end{Bmatrix} = [D_0^i]\begin{Bmatrix} C_{z0} \\ S_{z0} \end{Bmatrix} + \boldsymbol{\zeta}_i\left(\frac{C_{y0}}{q_y}\right) \tag{14}$$

where $C_{z0} = -(q_z/\beta^2 H^2)\nu = q_z(C_{y0}/q_y)$, and

$$QDS_{z0} = QN_2(C_{y0}/q_y)$$

$$QN_2 = q_z - [q_z D_0^n(1, 1) + \zeta_{n1}]\cos \beta(L - s_n) - [q_z D_0^n(2, 1) + \zeta_{n2}]\sin \beta(L - s_n)$$

$$\boldsymbol{\zeta}_i = [D_{i-1}^i]\boldsymbol{\zeta}_{i-1} + \begin{Bmatrix} 0 \\ \beta(m_i/m)q_z \end{Bmatrix} \quad \text{with } \boldsymbol{\zeta}_0 = \mathbf{0}. \tag{15}$$

It can be seen now from Eqs. (9) – (15) that all the variables (or solutions) are expressed in terms of β and ν (or C_{y0}). However, the normalized frequency β ($=\sqrt{m/H\omega}$) can be found without knowing ν (or C_{y0}). To achieve this, integrating Eq. (8) from 0 to L, with the aid of Eqs. (9), (10), and (14), and the boundary conditions $u(0) = u(L) = 0$, yields an equation of two variables β and $\nu(C_{y0})$:

$$0 = (\beta L)\left[\frac{(\beta L)^2}{\lambda^2} - 1\right]\nu + \left(\frac{\nu}{q^2}\right)\sum_{i=0}^{n} SC(\beta)(q_y\boldsymbol{\gamma}_i + q_z\boldsymbol{\zeta}_i) - \left(\frac{\beta H}{q}\right)^2 \sum_{i=0}^{n} SC(\beta)[D_0^i]\left(q_y\begin{Bmatrix} C_{y0} \\ S_{y0} \end{Bmatrix} + q_z\begin{Bmatrix} C_{z0} \\ S_{z0} \end{Bmatrix}\right) + \beta\left(\frac{\beta H}{q}\right)^2 \sum_{i=0}^{n} P_i\left[D_0^i(1, 1)C_{y0} + D_0^i(1, 2)S_{y0} - \left(1 - \frac{\gamma_{i1}}{q_y}\right)C_{y0}\right] \tag{16}$$

where $SC(\beta) = \langle \sin \beta l_{i+1}\ 1 - \cos \beta l_{i+1} \rangle$ is a row vector, and λ^2 is defined as

$$\lambda^2 = \left(\frac{AE}{L_e}\right)\left(\frac{L}{H}\right)^3 q^2 \quad \text{where} \quad L_e = \int_0^L \left(\frac{ds}{dx}\right)^2 dx. \tag{17}$$

The λ^2 is identical to the approximation of the static profile (Yu et al., 1995) if L is replaced by L_x, and then $L_e = \int_0^{L_x} (ds/dx)^3 dx$, defined by Irvine (1981).

Two independent sets of free vibration solutions can now be derived as follows. First let $QD = 0$, it leads to an equation of only one variable β (see Eqs. (11) and (13)), which can be used to solve for the unknown β by applying a simple numerical iteration scheme such as bisection method. Now that $QD = 0$, it is immediately to observe from Eqs. (13) and (15) that $C_{y0} = C_{z0} = \nu = 0$; i.e., $\tau = 0$, while S_{y0} and S_{z0} are remained undetermined. Thus, Eq. (16) is reduced to

$$AS_{y0} + BS_{z0} = 0 \tag{18}$$

where

$$\begin{Bmatrix} A \\ B \end{Bmatrix} = \begin{Bmatrix} -\beta \sum_{i=0}^{n} D_0^i(1, 2)P_i \\ 0 \end{Bmatrix} + \begin{Bmatrix} q_y \\ q_z \end{Bmatrix} \sum_{i=0}^{n} SC(\beta)\begin{Bmatrix} D_0^i(1, 2) \\ D_0^i(2, 2) \end{Bmatrix}. \tag{19}$$

From Eq. (18), two cases should be considered:

(a) $A = B = 0$. This case implies that S_{y0} and S_{z0} can be chosen independently and therefore, only one independent frequency exists but it associates with two independent mode shapes. This particular frequency may be called *repeated frequency*. The corresponding mode shapes can be determined from Eqs. (9), (10), and (14) as

$$Y_i(s) = S_{y0}f_i(s) \quad \text{and} \quad Z_i(s) = S_{z0}f_i(s) \tag{20}$$

where

$$f_i(s) = D_0^i(1, 2)\cos \beta(s - s_i) + D_0^i(2, 2)\sin \beta(s - s_i). \tag{21}$$

Now, back to Eq. (6), it can be found that the vertical and horizontal motions of a particular mode are given by

$$\begin{Bmatrix} y_{2i}(s, t) \\ z_{2i}(s, t) \end{Bmatrix} = \begin{bmatrix} f_i(s) & 0 \\ 0 & f_i(s) \end{bmatrix}\begin{Bmatrix} q_1(t) \\ q_2(t) \end{Bmatrix} = \langle \upsilon_1(\mathbf{s})\upsilon_2(\mathbf{s}) \rangle \begin{Bmatrix} q_1(t) \\ q_2(t) \end{Bmatrix} \tag{22}$$

where $i = 0, 1, 2 \cdots n$, and

$$q_1(t) = S_{y0}e^{j\omega t} \quad \text{and} \quad q_2(t) = S_{z0}e^{j\omega t} \tag{23}$$

which represent oscillations determined from initial conditions. This case ($\tau = 0$) may be called *antisymmetric* case by generalizing the terminology used for cable analysis without concentrated loads (e.g., see Irvine, 1981). The longitudinal mode shape $U_i(s)$ and so free vibration solution $u_i(s, t)$ will be given later together with other cases.

(b) $\max(|A|, |B|) \neq 0$; i.e., at least one of A and B is nonzero. Then Eq. (18) implies that S_{y0} and S_{z0} are dependent and therefore, only one independent mode shape corresponding to the frequency exists. The final solutions of $y_{2i}(s, t)$ and $z_{2i}(s, t)$ are given by

Downloaded 04 May 2010 to 171.66.16.34. Redistribution subject to ASME license or copyright; see http://www.asme.org/terms/Terms_Use.cfm

$$\begin{Bmatrix} y_{2i}(s,t) \\ z_{2i}(s,t) \end{Bmatrix} = \begin{Bmatrix} -Bf_i(s) \\ Af_i(s) \end{Bmatrix} q_1(t) = \mathbf{w_1(s)} q_1(t) \quad (24)$$

where i runs through 0 to n. A and B are described by Eq. (19) and function $f_i(s)$ is given by Eq. (21); and

$$q_1(t) = \begin{cases} S_{z0} e^{j\omega^{(1)}t} & \text{if} \quad A \neq 0, \\ S_{y0} e^{j\omega^{(1)}t} & \text{if} \quad A = 0 \quad \text{but} \quad B \neq 0. \end{cases} \quad (25)$$

Here, $\omega^{(1)} = \beta^{(1)}\sqrt{H/m}$ and $\beta^{(1)}$ is solved from equation $QD = 0$. The superscript (1) is used to distinct this frequency from the second independent frequency to be found next.

For case (b), a second independent frequency and it's associated mode shape must be found. They can be obtained by assuming $QD \neq 0$ that requires $\nu \neq 0$ and so $\tau \neq 0$, otherwise, $C_{y0} = C_{z0} = S_{y0} = S_{z0} = 0$ which yields only the zero (trivial) solution. Therefore, Eqs. (9), (10), (13), (14), and (15) produce

$$\nu = -(\beta^{(2)}H)^2\left(\frac{C_{y0}}{q_y}\right)$$

$$C_{z0} = q_z\left(\frac{C_{y0}}{q_y}\right)$$

$$S_{y0} = \left(\frac{QN_1}{QD}\right)\left(\frac{C_{y0}}{q_y}\right)$$

$$S_{z0} = \left(\frac{QN_2}{QD}\right)\left(\frac{C_{y0}}{q_y}\right) \quad (26)$$

and

$$\begin{Bmatrix} Y_i(s) \\ Z_i(s) \end{Bmatrix} = \begin{Bmatrix} f_{1i}(s) \\ f_{2i}(s) \end{Bmatrix}$$

$$= \begin{Bmatrix} C_{yi}\cos\beta^{(2)}(s-s_i) + S_{yi}\sin\beta^{(2)}(s-s_i) - C_{y0} \\ C_{zi}\cos\beta^{(2)}(s-s_i) + S_{zi}\sin\beta^{(2)}(s-s_i) - C_{z0} \end{Bmatrix}$$

$$\begin{Bmatrix} C_{yi} \\ S_{yi} \end{Bmatrix} = \left([D_0^i]\begin{Bmatrix} q_y \\ QN_1/QD \end{Bmatrix} + \boldsymbol{\gamma}_i\right)\left(\frac{C_{y0}}{q_y}\right)$$

$$\begin{Bmatrix} C_{zi} \\ S_{zi} \end{Bmatrix} = \left([D_0^i]\begin{Bmatrix} q_z \\ QN_2/QD \end{Bmatrix} + \boldsymbol{\zeta}_i\right)\left(\frac{C_{y0}}{q_y}\right) \quad (27)$$

where i runs through 0 to n. Next, substituting Eqs. (26) and (27) into Eq. (16) results in an equation of one variable $\beta^{(2)}$:

$$0 = (\beta^{(2)}L)\left[\frac{(\beta^{(2)}L)^2}{\lambda^2} - 1\right]QD + \left(\frac{\beta^{(2)}}{q^2}\right)$$

$$\times \sum_{i=0}^{n} P_i[(q_y - q_y D_0^i(1,1) - \gamma_{i1})QD - D_0^i(1,2)QN_1]$$

$$+ \sum_{i=0}^{n} SC(\beta^{(2)})\left([D_0^i]\begin{Bmatrix} QD \\ (q_yQN_1 + q_zQN_2)/q^2 \end{Bmatrix}\right.$$

$$\left. + \frac{1}{q^2}(q_y\boldsymbol{\gamma}_i + q_z\boldsymbol{\zeta}_i)QD\right) \quad (28)$$

which can be used to find the second independent frequency, $\beta^{(2)}$ $(=\omega^{(2)}\sqrt{m/H})$, by using a numerical iteration scheme. The corresponding mode shapes are given by Eq. (27).

Consider a special case: $n = 1$ and $q_z = 0$, that is, only one *vertical* concentrated load is considered and static loads are neglected, then Eq. (28) reduces to

$$0 = 2\sin\left(\frac{\beta L}{2}\right)\left\{\left[\frac{1}{\lambda^2}(\beta L)^3 - \beta L\right]\right.$$

$$\left.\times\cos\left(\frac{\beta L}{2}\right) + 2\sin\left(\frac{\beta L}{2}\right)\right\}$$

$$- \beta\left(\frac{F_1}{q_y}\right)\left[\frac{1}{\lambda^2}(\beta L)^3 - \beta L\right]\sin(\beta x_1)\sin(L_x - x_1)$$

$$+ \beta^2\left(\frac{F_1}{q_y}\right)^2\sin(\beta x_1) - \sin(L_x - x_1) \quad (29)$$

where the superscript (2) on β was dropped. If let $d = x_1/L$, $\Omega = \beta L$, $\Omega_1 = \Omega d$, $\Omega_2 = \Omega(1-d)$ and $m = F_1/q_yL$, then, Eq. (29) can be rewritten as

$$0 = 2\sin\left(\frac{\Omega}{2}\right)\left[\left(\frac{\Omega^3}{\lambda^2} - \Omega\right)\cos\left(\frac{\Omega}{2}\right) + 2\sin\left(\frac{\Omega}{2}\right)\right]$$

$$- m\Omega\left(\frac{\Omega^3}{\lambda^2} - \Omega\right)\sin\Omega_1\sin\Omega_2 + m^2\Omega^2\sin\Omega_1\sin\Omega_2 \quad (30)$$

which is identical to Eq. (38) given by Cheng and Perkins (1992a).

Now, back to Eq. (6), the second independent solution of $y_{2i}(s,t)$ and $z_{2i}(s,t)$ can be written as

$$\begin{Bmatrix} y_{2i}(s,t) \\ z_{2i}(s,t) \end{Bmatrix} = \mathbf{w_2(s)} q_2(t) \quad (31)$$

in which $i = 0, 1, 2, \cdots n$, and

$$\mathbf{w_2(s)} = \begin{Bmatrix} f_{1i}(s) \\ f_{2i}(s) \end{Bmatrix} \quad \text{and} \quad q_2(t) = \left(\frac{C_{y0}}{q_y}\right)e^{j\omega^{(2)}t} \quad (32)$$

where $f_{1i}(s)$ and $f_{2i}(s)$ are given in Eq. (27). Finally, combine Eqs. (24) and (31) to yield a complete solution of $y_{2i}(s,t)$ and $z_{2i}(s,t)$ for case (b):

$$\begin{Bmatrix} y_{2i}(s,t) \\ z_{2i}(s,t) \end{Bmatrix} = \begin{bmatrix} -Bf_i(s) & f_{1i}(s) \\ Af_i(s) & f_{2i}(s) \end{bmatrix}\begin{Bmatrix} q_1(t) \\ q_2(t) \end{Bmatrix}$$

$$= \langle \mathbf{w_1(s)}\mathbf{w_2(s)} \rangle \begin{Bmatrix} q_1(t) \\ q_2(t) \end{Bmatrix} \quad (33)$$

where i runs from 0 to n. This equation is similar to Eq. (22) of the antisymmetric case. This case associated with two independent frequencies may be, therefore, similarly called *symmetric* case.

From the above analysis, it has been found that there always exist two independent mode shapes associated with either one or two independent frequencies. To find a complete solution including all the three (longitudinal, vertical, and horizontal) direction motions, it is needed to find the approximation of mode shapes $U_i(s)$. They can be obtained by integrating Eq. (8) with the aid of boundary conditions as well as the continuity conditions at the locations of detuning pendulums, given by

$$u_0(0) = u_n(L) = 0, \quad u_{i-1}(s_i) = u_i(s_i) \quad (34)$$

where i runs through 1 to n. The derivations are straightforward and therefore, only the results are listed below.

Downloaded 04 May 2010 to 171.66.16.34. Redistribution subject to ASME license or copyright; see http://www.asme.org/terms/Terms_Use.cfm

(a) Antisymmetric case ($\tau = 0$, repeated frequencies):

$$U_{1i}(s) = \eta_i + E_{yi}Y_i(s) - \left(\frac{q_y}{\beta H}\right)[C_{yi}\sin\beta(s - s_i) - S_{yi}\cos\beta(s - s_i)]$$

$$\eta_0 = -\left(\frac{q_y}{\beta H}\right)S_{y0}$$

$$\eta_i = \eta_{i-1} - \left(\frac{q_y}{\beta H}\right)(S_{yi} + C_{yi-1}\sin\beta l_i - S_{yi-1}\cos\beta l_i) + \left(\frac{P_i}{H}\right)C_{y0}. \quad (35)$$

Replacing y by z and setting $P_i = 0$ in Eq. (35) results in $U_{2i}(s)$.

(b) Symmetric case ($\tau \neq 0$, different frequencies):

(i) $A = 0$, $B \neq 0$, $U_{1i}(s)$ is given by Eq. (35);
(ii) $A \neq 0$, $B = 0$, $U_{1i}(s)$ equals $U_{2i}(s)$ of Case (a);
(iii) $A \neq 0$, $B \neq 0$,

$$U_{1i}(s) = \eta_i + (AE_{yi} - BE_{zi})f_i(s) - \left(\frac{1}{\beta^{(1)}H}\right)(Aq_z - Bq_y) \times [C_{zi}\sin\beta^{(1)}(s - s_i) - S_{zi}\cos\beta^{(1)}(s - s_i)]$$

$$\eta_0 = -\left(\frac{1}{\beta^{(1)}H}\right)(Aq_z - Bq_y)S_{z0}$$

$$\eta_i = \eta_{i-1} + A\left(\frac{P_i}{H}\right)C_{yi} - \left(\frac{1}{\beta^{(1)}H}\right)(Aq_z - Bq_y) \times (S_{zi} + C_{zi-1}\sin\beta^{(1)}l_i - S_{zi-1}\cos\beta^{(1)}l_i) \quad (36)$$

and

$$U_{2i}(s) = \nu_i - \frac{(\beta^{(2)}H)^2}{AE}\left(\frac{C_{y0}}{q_y}\right)\left\{\left[1 + \left(\frac{q_z c_i}{qH}\right)^2\right]s + \frac{1}{3}\left(\frac{q}{H}\right)^2(s - \alpha_i)^3\right\} + E_{yi}f_{1i}(s) + E_{zi}f_{2i}(s) - \left(\frac{q_y}{\beta^{(2)}H}\right)[C_{yi}\sin\beta^{(2)}(s - s_i) - S_{yi}\cos\beta^{(2)}(s - s_i) - \beta^{(2)}C_{y0}s] - \left(\frac{q_z}{\beta^{(2)}H}\right)[C_{zi}\sin\beta^{(2)}(s - s_i) - S_{zi}\cos\beta^{(2)}(s - s_i) - \beta^{(2)}C_{z0}s]$$

$$\nu_0 = -\frac{(\beta^{(2)}q)^2}{3AE}\alpha_0^3 - \left(\frac{1}{\beta^{(2)}H}\right)(q_y S_{y0} + q_z S_{z0})$$

$$\nu_i = \nu_{i-1} + \left(\frac{P_i}{H}\right)(C_{yi} - C_{y0}) + \frac{(\beta^{(2)}H)^2}{AE}\left\{\left(\frac{q_z}{qH}\right)^2(c_i^2 - c_{i-1}^2)s_i + \frac{1}{3}\left(\frac{q}{H}\right)^2[(s_i - \alpha_i)^3 - (s_i - \alpha_{i-1})^3]\right\} - \left(\frac{q_y}{\beta^{(2)}H}\right)(S_{yi} + C_{yi-1}\sin\beta^{(2)}l_i - S_{yi-1}\cos\beta^{(2)}l_i) - \left(\frac{q_z}{\beta^{(2)}H}\right)(S_{zi} + C_{zi-1}\sin\beta^{(2)}l_i - S_{zi-1}\cos\beta^{(2)}l_i). \quad (37)$$

4 An Example

In this section, the methodology and explicit formulations described in the previous sections are applied to consider an example chosen from galloping analysis of transmission lines. Low degree-of-freedom models for galloping analysis are derived via the variational principle for given natural frequencies and vibration mode shapes. A three-degree-of-freedom model (Yu et al., 1993), described in the general form of

$$M\ddot{\mathbf{q}} + C\dot{\mathbf{q}} + K\mathbf{q} = \mathbf{F}, \quad (38)$$

has been successfully applied to transmission lines without control devices. Here, $\mathbf{q}$ represents the generalized coordinates corresponding to the vertical, horizontal and rotational movements of the transmission line. M, C, and K are mass, damping, and stiffness matrices, respectively. Solving the nonlinear algebraic equation $K\mathbf{q} = \mathbf{F}$ yields equilibrium solutions, and their stability conditions are determined from the linearized system of (38). If an equilibrium becomes unstable for certain system parameters, then *periodic, quasi-periodic,* or even more complicated dynamic motions may be initiated from the equilibrium. Then one needs to find the dynamical solutions and their stability conditions. A number of dynamic case studies can be found in Yu et al. (1993).

In order to study galloping control for transmission lines equipped with detuning pendulums (DP), a software package based on the method and formulations described in the previous sections has been developed. It has been successfully applied to study galloping control design using DP for transmission lines (Modelling, 1993) and subtransmission lines (Galloping, 1994). Some results of free vibration analysis will be presented here. The transmission line considered is the Pennsylvania Power and Light's single conductor line, S51. Galloping on this line was reported and the control device DPs was tested on this line by Ontario Hydro. Based on many years of field trials on this line and other lines, Ontario Hydro recommended a distribution for locating DPs along a span of a line for best controlling galloping. For example, if three DPs are used in one span of a line, then they should be located at $L_x/4$, $5L_x/12$, and $2L_x/3$. Accurate frequencies up to hundreds Hz and the associated mode shapes for such a span can be obtained virtually instantly through the software.

To demonstrate the free-vibration analysis, consider an important question which is often raised in galloping analysis. Since overhead transmission lines usually experience at least two types of vibrations: aeolian and galloping. Galloping is a low-frequency (0.1 to 3 Hz) large-amplitude oscillation, while aeolian vibration is a high-frequency (10 to 100 Hz) small-amplitude motion. Aeolian vibration may occur on a line almost everyday and cause the fatigue of conductors and suspensions. In practice, dampers are installed near suspensions (i.e., near the end supports) to reduce the aeolian vibration. It is interesting to note that an antigalloping control device reduces the vibrations near the midspans while an anti-aeolian vibration control device decreases the vibration amplitudes near the end of a span. So, is a galloping control device such as detuning pendulums also beneficial in controlling aeolian vibration? To help understand this question, let's consider the following *energy balance* equation for the analysis of aeolian vibration (Kraus and Hagedorn, 1990):

$$P_W = P_D + P_C \quad (39)$$

Downloaded 04 May 2010 to 171.66.16.34. Redistribution subject to ASME license or copyright; see http://www.asme.org/terms/Terms_Use.cfm

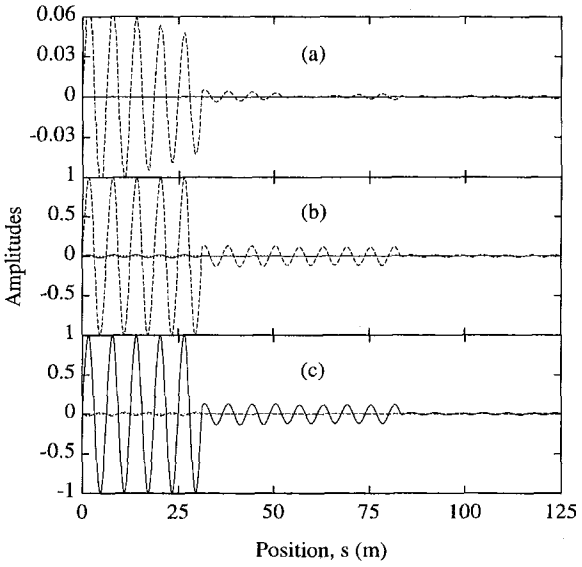


Fig. 4 The 41st mode shapes with DPs at Lx/4, 5 Lx/12 and 2 Lx/3: (*a*) U-mode shape; (*b*) Y-mode shape; and (c) Z-mode shape

where P_W is the power of the aerodynamic forces, P_D the power dissipated in the damper, and P_C the power dissipated in the conductor. Here, steady-state aeolian vibration solutions are assumed. The power imparted to the conductor by the aerodynamic forces is estimated on the basis of wind tunnel experiments. The power dissipation in conductor can be expressed as a function of the frequency and the amplitude of the vibration. Then the energy balance Eq. (39) can be used to predict approximately the maximum vibration amplitude or bending strain as a function of the vibration frequency. This shows the importance of finding accurate natural frequencies and vibration mode shapes for the study of aeolian vibration. Now consider again the line S51 with three DPs. The results shown in Figs. 4 and 5 give a comparison of 41st mode shapes (frequency 20.07 Hz) with the 42nd mode shapes (frequency 20.15 Hz). Each of these two figures shows the movement components along the longitudinal, vertical, and horizontal directions. Each direction consists of two independent mode shapes: one of them is the primary vertical (in-plane) mode and the other is the primary horizontal (out-plane) mode, denoted by dotted line and solid line, respectively.

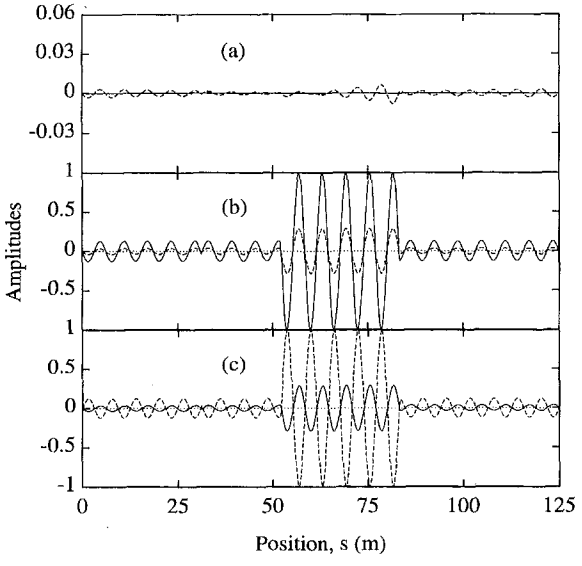


Fig. 5 The 42nd mode shapes with DPs at Lx/4, 5 Lx/12, and 2 Lx/3: (*a*) U-mode shape; (*b*) Y-mode shape; and (c) Z-mode shape

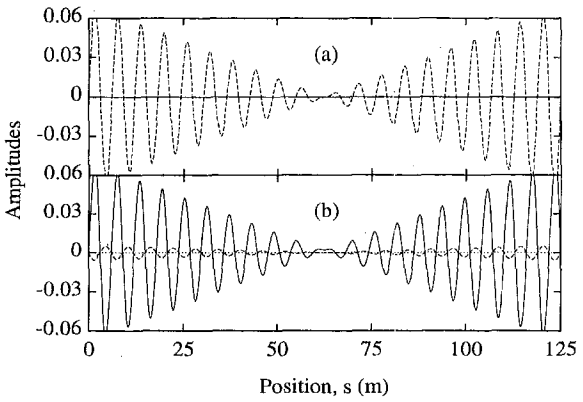


Fig. 6 U-mode shapes without detuning pendulums: (*a*) the 41st mode; (*b*) the 42nd mode

First, it has been noted that in both cases $A \neq 0$ and $B \neq 0$, indicating both cases being symmetric cases (see Eq. (18)). Secondly, it is noted from these two figures that variation of the positions of detuning pendulums greatly changes the mode shapes, implying that it is possible to achieve better control of galloping by adjusting the positions of detuning pendulums. However, it can be seen that the galloping motion is controlled better in some parts of the span than other parts. (In the case of no control devices, the Y-mode and Z-mode shapes are just normal sine waves.) For the 41st mode, the amplitude of the motion near the left end support is much large than that of other parts; while for the 42nd mode, the amplitudes of the motion are smaller near both end supports. In particular, the 41st mode changes its shapes sharply at the three positions of detuning pendulums while the 42nd mode changes its shapes significantly at the left and right locations of the detuning pendulums. For the U-mode shapes, the same trend becomes clear if one compares Fig. 4(*a*) and Fig. 5(*a*) with Fig. 6 which shows the 41st and 42nd U-mode shapes of the transmission line without detuning pendulums. It is seen from Fig. 6 that the 41st mode is antisymmetric and the 42nd mode is symmetric, but both the amplitudes increase towards the end supports. This explains why the U-mode shapes shown in Fig. 4(*a*) and Fig. 5(*a*) have a small portion of relatively large motion around the position of 75 m of the span. The same trend can be found in high-frequency motions: mode shapes change significantly from a frequency to an adjacent one.

The above observations seem to indicate that for this specific arrangements of DPs designed by Ontario Hydro, galloping control device (DP) is also beneficial for controlling the aeolian vibration for certain frequencies and mode shapes. How to find the "best" design for the distribution of DPs, which is not only good for controlling the galloping but also beneficial to controlling the aeolian vibration, needs further studies.

5 Concluding Remarks

An analytic methodology has been developed to find closed-form solutions of the natural frequencies and vibration mode shapes of an elastic cable under both distributed and concentrated loads. This method leads to solving for an equation of one unknown variable only, and therefore, avoids computing large dimensional matrix form of equations by using some other approaches such as finite element method. It has been shown that there always exist two sets of independent mode shapes associated with two sets of independent frequencies. This approach is particularly useful in dealing with high-frequency motions. However, for high-frequency modes, in order to obtain more accurate results, the local flexural boundary layers or the

Downloaded 04 May 2010 to 171.66.16.34. Redistribution subject to ASME license or copyright; see http://www.asme.org/terms/Terms_Use.cfm

longitudinal inertia should not be neglected. That is, Eq. (3) needs to be modified such that $\tilde{h}(t)$ is also function of s, $\tilde{h}(s, t)$. It is also possible to extend this method to consider multiple spans of cables as well as inclined cables under both distributed and concentrated loads.

Acknowledgments

This research has been partially supported by the Canadian Electrical Association (Project No. 321 T 672 A), Manitoba Hydro (Project No. T 085 C) and the Natural Science and Engineering Research Council of Canada (Grant No. S386A2). Comments from the anonymous reviewers are greatly appreciated.

References

Canadian Electrical Association, 1993 "Modelling of Conductor Galloping, Phase II," Technical Report, No. 321 T 672 A, Montreal, Quebec, Canada.

Cheng, S. P., and Perkins, N. C., 1992a, "Free vibration of a sagged cable supporting a discrete mass," *Journal of Acoustic Society of America,* Vol. 91, pp. 2654–2662.

Cheng, S. P., and Perkins, N. C., 1992b, "Closed-Form Vibration Analysis of Sagged Cable/Mass Suspensions," ASME JOURNAL OF APPLIED MECHANICS, Vol. 59, pp. 923–928.

Irvine, H. M., and Caughey, T. K., 1974, "The linear theory of free vibrations of a suspended cable," *Proceedings of Royal Society, London,* Vol. A341, pp. 299–315.

Irvine, H. M., 1981, *Cable Structures,* M.I.T. Press, Cambridge, MA.

Kraus, M., and Hagedorn, P., 1990, "Aeolian vibrations; wind energy input evaluated from measurements on an energized transmission line," IEEE PES Summer Meeting, Minneapolis, Minnesota, July 15–19.

Sergev, S. S., and Iwan, W. D., 1981, "The Natural Frequencies and Mode Shapes of Cables With Attached Masses," ASME *Journal of Energy Resources and Technology,* Vol. 103, pp. 237–242.

Triantafyllou, M. S., 1984, "The dynamics of taut inclined cables," *Quarterly of Journal of Mechanics and Applied Mathematics,* Vol. 37, pp. 421–440.

Triantafyllou, M. S., 1991, "Dynamics of cables, towing cables and mooring systems," *Shock and Vibration Digest,* Vol. 23, pp. 3–8.

Yu, P., Desai, Y. M., Shah, A. H., and Popplewell, N., 1993, "Three degree-of-freedom model for galloping, Part I: Formulation," *ASCE Journal of Engineering Mechanics,* Vol. 119, pp. 2404–2425.

Yu, P., Desai, Y. M., Popplewell, N., and Shah, A. H., 1993, "Three degree-of-freedom model for galloping, Part II: Solutions," *ASCE Journal of Engineering Mechanics,* Vol. 119, pp. 2426–2448.

Yu, P., Shah, A. H., and Popplewell, N., 1992, "Inertially Coupled Galloping of Iced Conductors," ASME JOURNAL OF APPLIED MECHANICS, Vol. 59, pp. 140–145.

Yu, P., Wong, P. S., and Kaempffer, F., 1995, "Tension of Conductor Under Concentrated Loads," ASME JOURNAL OF APPLIED MECHANICS, Vol. 62, pp. 802–809.

Downloaded 04 May 2010 to 171.66.16.34. Redistribution subject to ASME license or copyright; see http://www.asme.org/terms/Terms_Use.cfm

S. J. Cox
Department of Computational and Applied Mathematics,
Rice University,
P.O. Box 1892
Houston, TX 77251

J. Moro
Departamento de Mathematicas,
Universidad Carlos III,
Butarque 15,
Leganes (Madrid), Spain

A Lyapunov Function for Systems Whose Linear Part is Almost Classically Damped

We show that one may construct a Lyapunov function for any classically damped linear system. The explicit nature of the construction permits us to show that it remains a Lyapunov function under both perturbation of the linear part and introduction of a nonlinear term. We apply our findings to a stability analysis of the discrete, as well as continuous, damped mechanical transmission line.

1 Introduction

In this work we address the global stability of the zero solution of

$$u''(t) + Du'(t) + Ku(t) = f(u(t), u'(t)), \quad t > 0, \quad (1.1)$$

where $' \equiv (d/dt)$ and $u(t) \in \mathbf{R}^n$. One, now classical approach to such a problem is through the methods of A. M. Liapunov (1966). In particular, one constructs a positive definite functional whose time derivative along solutions of (1.1) is negative definite. Though the import of these ideas has been widely appreciated since their export to the west in the late 1950s, the Achilles' heel has remained the lack of a systematic procedure by which one may arrive at a Lyapunov function. Indeed, as evidenced by the text of Gajić and Qureshi (1995), contemporary work has rather focused on the numerical approximation of such functions.

In this paper we shall show that one may construct, by hand, a Lyapunov function for (1.1) when f is small and D and K almost commute. In Section 2 we shall specify our exact hypotheses and show that under these (1.1) indeed possesses global solutions. In Section 3 we proceed to construct the Lyapunov function. There we present inequalities which facilitate two distinct modes of application. In the first we imagine that one begins with a classically damped linear system and wishes to determine its robustness. That is, the extent to which the stiffness and damping may be perturbed and nonlinearity introduced without causing instability of the trivial solution. The second scenario deals with the situation in which one wishes to determine the amount of damping necessary to stabilize the trivial solution of a given nonlinear system. As an instance of this second scenario we consider, in Section 4, the stabilization of the mechanical transmission line. This line was first introduced as a discrete analog of a nonlinear Klein-Gordon equation. We close with an application of our method to this nonlinear partial differential equation.

2 Preliminaries

We ask that f vanish at the origin in order that zero be a steady solution of (1.1) and we ask the gradient of f at zero to vanish in order that it not interfere with the linear terms involving D and K. To be precise, we require

$$f(0, 0) = 0 \quad \text{and} \quad \nabla f(0, 0) = 0. \quad (2.1)$$

We shall also require f to be globally Lipschitz. More precisely, we assume the existence of a finite C for which

$$\|f(p_1, q_1) - f(p_2, q_2)\| \le C(\|p_1 - p_2\| + \|q_1 - q_2\|), \quad (2.2)$$

for all p_1, q_1, p_2, and q_2 in $\mathbf{R}^n$. This shall be enough to establish the global existence of a unique solution to (1.1). Such a result is most easily obtained with reference to the equivalent first-order system. To wit, we assign

$$V(t) \equiv \begin{pmatrix} u(t) \\ u'(t) \end{pmatrix}$$

and note that u satisfies (1.1) if and only if V satisfies

$$V'(t) = AV(t) + F(V(t)), \quad (2.3)$$

where

$$A = \begin{pmatrix} 0 & I \\ -K & -D \end{pmatrix} \quad \text{and} \quad F(V(t)) = \begin{pmatrix} 0 \\ f(V(t)) \end{pmatrix}.$$

Proposition 2.1 *If f satisfies (2.2) and (2.1) and $V_0 \in \mathbf{R}^{2n}$ then there exists a unique $V \in C^1(\mathbf{R}, \mathbf{R}^{2n})$ satisfying (2.3) for all t and $V(0) = V_0$.*

Proof: With our Lipschitz hypothesis on f we may invoke Miller and Michel (1982, Theorem 2.4.2) and conclude that (2.3), subject to $V(0) = V_0$, has a unique solution near $t = 0$. Also, it follows from (2.2) and (2.1) that

$$\|F(U)\| \le C\|U\| \quad \forall U \in \mathbf{R}^{2n}. \quad (2.4)$$

Now suppose $[0, \tau]$ to be the interval of existence. As such,

$$V(t) = V_0 + \int_0^t \{AV(s) + F(V(s))\} ds, \quad 0 \le t < \tau,$$

and so, recalling (2.4),

$$\|V(t)\| \le \|V_0\| + (\|A\| + C) \int_0^t \|V(s)\| ds, \quad 0 \le t < \tau.$$

It now follows from Gronwall's inequality (see Miller and Michel, 1982, Theorem 2.1.6) that

$$\|V(t)\| \le \|V_0\| e^{(\|A\| + C)t}, \quad 0 \le t < \tau,$$

and hence $V(t)$ is bounded on the closed interval $[0, \tau]$. From this we may conclude (see, e.g., Miller and Michel, 1982, Corollary 2.3.2) that V is in fact defined on the whole real line. ■

This result carried no restrictions on K and D. We shall see that in order to guarantee stability, both K and D will have to

Contributed by the Applied Mechanics Division of THE AMERICAN SOCIETY OF MECHANICAL ENGINEERS for publication in the ASME JOURNAL OF APPLIED MECHANICS.

Discussion on this paper should be addressed to the Technical Editor, Professor Lewis T. Wheeler, Department of Mechanical Engineering, University of Houston, Houston, TX 77204-4792, and will be accepted until four months after final publication of the paper itself in the ASME JOURNAL OF APPLIED MECHANICS.

Manuscript received by the ASME Applied Mechanics Division, Sept. 16, 1996; final revision, May 6, 1997. Associate Technical Editor: N. C. Perkins.

Copyright © 1997 by ASME

Downloaded 04 May 2010 to 171.66.16.34. Redistribution subject to ASME license or copyright; see http://www.asme.org/terms/Terms_Use.cfm

outweigh f. To state our precise conditions we follow Caughey and O'Kelly (1965) and recall that a system (whose mass matrix has been normalized to the identity) with symmetric and positive definite stiffness, K_0, and damping, D_0, matrices is said to be classically damped when

$$K_0 D_0 = D_0 K_0. \tag{2.5}$$

Such systems are also referred to as "normal mode" or "Caughey damped." With respect to (1.1) we suppose that K and D are both symmetric and positive definite and that there exists a classically damped pair, K_0 and D_0, for which

$$\|K - K_0\| \leq \delta \quad \text{and} \quad \|D - D_0\| \leq \delta. \tag{2.6}$$

Our main result states that if δ and C are sufficiently small, relative to K_0 and D_0, then the zero solution of (1.1) is globally asymptotically stable. The precise statement requires

$$\lambda \equiv \min_{v \in \mathbf{R}^n} \frac{\langle K_0 v, v\rangle}{\langle v, v\rangle} \quad \text{and} \quad \gamma \equiv \min_{v \in \mathbf{R}^n} \frac{\langle D_0 v, v\rangle}{\langle v, v\rangle}, \tag{2.7}$$

the least eigenvalues of K_0 and D_0, respectively.

3 The Lyapunov Function

Presence of a Lyapunov function shall lead to a proof of

Theorem 3.1 *If f satisfies (2.2) and K and D satisfy (2.6) and K_0 and D_0 commute and*

$$C + \delta < \frac{2\gamma\sqrt{(\gamma + 2\lambda)^2 + \lambda(2-\gamma)^2} - 2\gamma(\gamma + 2\lambda)}{(2-\gamma)^2}, \tag{3.1}$$

then the zero solution of (1.1) is globally asymptotically stable.

This inequality bounds the degree of the nonlinearity, C, and deviation from classically damped, δ, in terms of the known stiffness, λ, and damping, γ. For reference let us refer to the right side of this inequality as $\xi_+(\gamma, \lambda)$. This function clearly approaches zero as λ and/or γ tend to zero. Three other limits of interest are

$$\lim_{\gamma \to 2} \xi_+(\gamma, \lambda) = \frac{\lambda}{\lambda + 1}, \quad \lim_{\gamma \to \infty} \xi_+(\gamma, \lambda) = 2\sqrt{1 + \lambda} - 2$$

$$\text{and} \quad \lim_{\lambda \to \infty} \xi_+(\gamma, \lambda) = \gamma/2.$$

As mentioned in the Introduction we may also wish to know how large γ must be in order to stabilize a given nonlinear system. This is addressed by

Corollary 3.2 *Suppose that f satisfies (2.2) and K and D satisfy (2.6) and K_0 and D_0 commute. Let us call $\xi = C + \delta$. If*

$$\xi + \xi^2/4 < \lambda \quad \text{and}$$

$$\gamma > \frac{2\xi}{4\lambda - \xi^2 - 4\xi}\left(2\sqrt{\lambda^2 + \lambda(1-\xi) - \xi} + 2\lambda - \xi\right),$$

then the zero solution of (1.1) is globally asymptotically stable.

We build a Lyapunov function for the classically damped problem and then show that it is robust enough to serve as a Lyapunov function for the almost classically damped problem. To this end, let us first consider the linear classically damped system

$$U_0'(t) = A_0 U_0(t), \quad \text{where} \quad A_0 = \begin{pmatrix} 0 & I \\ -K_0 & -D_0 \end{pmatrix}. \tag{3.2}$$

As usual, we derive the Lyapunov function from energy considerations. We denote the instantaneous energy in U_0 by

$$E_0(t) = \langle S_0 U_0(t), U_0(t)\rangle \quad \text{where} \quad S_0 = \begin{pmatrix} K_0 & 0 \\ 0 & I \end{pmatrix},$$

and the total energy by

$$L_0 = \int_0^\infty E_0(t)dt.$$

As $U_0(t)$ is simply $e^{A_0 t}U_0(0)$ we recognize in L_0 the quadratic form

$$L_0(U_0(0)) = \langle \mathcal{E}_0 U_0(0), U_0(0)\rangle \text{ where } \mathcal{E}_0 = \int_0^\infty e^{A_0^T t} S_0 e^{A_0 t} dt.$$

It is not difficult to show that L_0 serves as a Lyapunov function for the full nonlinear system under the assumption that F is sufficiently small. However, as $\mathcal{E}_0$, and therefore L_0, is in general difficult to compute and/or estimate, one does not find sharp conditions in terms of bounds on f and K_0 and D_0 sufficient to guarantee the global stability of the zero solution of (1.1). Our contribution amounts to exploiting the fact, first noted by Cox (1997), that $\mathcal{E}_0$ may be computed in closed form when K_0 and D_0 commute.

This is most easily seen by recalling (see, e.g., Bellman, 1970, Section 13.5) that $\mathcal{E}_0$ is the solution of the Lyapunov equation

$$A_0^T \mathcal{E}_0 + \mathcal{E}_0 A_0 = -S_0. \tag{3.3}$$

Given this form, one easily checks that

$$\mathcal{E}_0 = \begin{pmatrix} \frac{1}{2}D_0 + K_0 D_0^{-1} & \frac{1}{2}I \\ \frac{1}{2}I & D_0^{-1} \end{pmatrix}$$

is the symmetric, positive definite solution. Now, in order to establish Theorem 3.1, we must show that

$$\frac{d}{dt} L_0(V(t)) < 0$$

for all t and for every nontrivial solution V of (2.3). Using only (2.3) and (3.3) we find

$$\begin{aligned}\frac{d}{dt} L_0(V(t)) &= \langle \mathcal{E}_0 V(t), V'(t)\rangle + \langle \mathcal{E}_0 V'(t), V(t)\rangle \\ &= \langle \mathcal{E}_0 V(t), AV(t) + F(V(t))\rangle \\ &\quad + \langle \mathcal{E}_0\{AV(t) + F(V(t))\}, V(t)\rangle \\ &= 2\langle \mathcal{E}_0 F(V(t)), V(t)\rangle \\ &\quad + \langle \{A^T\mathcal{E}_0 + \mathcal{E}_0 A\}V(t), V(t)\rangle.\end{aligned}$$

The strategy is now to show that as A is close to A_0, the second term is sufficiently negative to counteract the indefiniteness of the first term. In particular, given (2.6), we may write

$$K = K_0 + \delta\tilde{K} \quad \text{and} \quad D = D_0 + \delta\tilde{D}$$

$$\text{where} \quad \|\tilde{K}\| \leq 1 \quad \text{and} \quad \|\tilde{D}\| \leq 1.$$

This produces

$$A = A_0 + \delta\tilde{A}, \quad \text{where} \quad \tilde{A} = \begin{pmatrix} 0 & 0 \\ -\tilde{K} & -\tilde{D} \end{pmatrix},$$

and hence

$$\begin{aligned}\langle \{A^T\mathcal{E}_0 + \mathcal{E}_0 A\}V(t), V(t)\rangle &= \langle \{A_0^T\mathcal{E}_0 + \mathcal{E}_0 A_0\}V(t), V(t)\rangle \\ &\quad + \langle \{\tilde{A}^T\mathcal{E}_0 + \mathcal{E}_0\tilde{A}\}V(t), V(t)\rangle \\ &= -\langle S_0 V(t), V(t)\rangle - \langle \tilde{S}_0 V(t), V(t)\rangle,\end{aligned}$$

Downloaded 04 May 2010 to 171.66.16.34. Redistribution subject to ASME license or copyright; see http://www.asme.org/terms/Terms_Use.cfm

where

$$\tilde{S}_0 \equiv \tilde{A}^T\tilde{\mathcal{E}}_0 + \tilde{\mathcal{E}}_0\tilde{A} = \begin{pmatrix} \tilde{K} & \frac{1}{2}\tilde{D} + \tilde{K}D_0^{-1} \\ \frac{1}{2}\tilde{D} + D_0^{-1}\tilde{K} & D_0^{-1}D + \tilde{D}D_0^{-1} \end{pmatrix}.$$

We shall find it more convenient to now return to the original coordinates $V = [u\ u']$. In particular,

$$L_0(u, u') = L_0(V) = \langle \mathcal{E}_0 V, V\rangle$$
$$= \langle (K_0D_0^{-1} + D_0/2)u, u\rangle + \langle D_0^{-1}u', u'\rangle + \langle u, u'\rangle \quad (3.4)$$

and

$$\frac{d}{dt}L_0(u, u')$$
$$= \langle u, f\rangle + 2\langle u', D_0^{-1}f\rangle - \langle u, K_0u\rangle - \langle u', u'\rangle$$
$$- \delta\{\langle u, \tilde{K}u\rangle + \langle u, (\tilde{D} + 2\tilde{K}D_0^{-1})u'\rangle + 2\langle u', D_0^{-1}\tilde{D}u'\rangle\}.$$
$$\le C\|u\|(\|u\| + \|u'\|) + (2C/\gamma)\|u'\|(\|u\| + \|u'\|) - \lambda\|u\|^2$$
$$- \|u'\|^2 + \delta\{\|u\|^2 + (1 + (2/\gamma))\|u\|\|u'\| + (2/\gamma)\|u'\|^2\}$$
$$= (C + \delta - \lambda)\|u\|^2 + (C + \delta)(1 + (2/\gamma))\|u\|\,\|u'\|$$
$$+ ((C + \delta)(2/\gamma) - 1)\|u'\|^2$$

Assigning $\xi = C + \delta$ the above is negative so long as

$$\xi < \lambda \text{ and } \xi^2(1 + (2/\gamma))^2 < 4(\xi - \lambda)((2\xi/\gamma) - 1). \quad (3.5)$$

Collecting terms in the latter we find that

$$(2 - \gamma)^2\xi^2 + 4\gamma(2\lambda + \gamma)\xi - 4\lambda\gamma^2 < 0. \quad (3.6)$$

So long as $\gamma \neq 2$ this polynomial has the roots

$$\xi_\pm = (-2\lambda - \gamma \pm \sqrt{(2\lambda + \gamma)^2 + \lambda(2 - \gamma)^2})\frac{2\gamma}{(2 - \gamma)^2}.$$

The polynomial is clearly positive for ξ of large magnitude and so it can only be negative when ξ lies between ξ_- and ξ_+. We observe that $\xi_- < 0$ and that $\xi_+ > 0$ and that

$$\xi_- \to -\infty \quad \text{and} \quad \xi_+ \to \frac{\lambda}{\lambda + 1} \quad \text{as} \quad \gamma \to 2.$$

In addition, it is a simple matter to verify that $\xi_+ \le \lambda$. As such, the two conditions of (3.5) reduce to $\xi < \xi_+$, i.e.,

$$C + \delta < \frac{2\gamma\sqrt{(\gamma + 2\lambda)^2 + \lambda(2 - \gamma)^2} - 2\gamma(\gamma + 2\lambda)}{(2 - \gamma)^2}.$$

This completes our proof of Theorem 3.1. Regarding its Corollary we need only look on (3.6) as an inequality for a quadratic in γ. In particular, (3.6) brings

$$\gamma^2(\xi^2 + 4\xi - 4\lambda) + \gamma 4\xi(2\lambda - \xi) + 4\xi^2 < 0 \quad (3.7)$$

which, of course, as $2\lambda > \xi$, may only be satisfied when the coefficient of γ^2 is negative. As a result we must require

$$\xi + \xi^2/4 < \lambda. \quad (3.8)$$

With this, (3.7) is satisfied so long as γ exceeds the quadratic's greatest root, namely when

$$\gamma > \frac{2\xi}{4\lambda - \xi^2 - 4\xi}(2\sqrt{\lambda^2 + \lambda(1 - \xi) - \xi} + 2\lambda - \xi).$$

This inequality, together with (3.8), establishes Corollary 3.2.

4 The Mechanical Transmission Line

As an application of Corollary 3.2 we shall determine the amount of damping necessary to render stable the trivial solution of the mechanical transmission line depicted in Fig. 1. This line has been the subject of frequent study, (see, e.g., Remoissenet, 1994) since its introduction by Scott (1969). It consists of a series of n pendula connected by a spring and supported horizontally on a taut one meter length of wire.

With u denoting the angle of rotation of the pendula, the equation of motion of the ith pendulum takes the form

$$Ju_i'' = Q(u_{i+1} - 2u_i + u_{i-1}) - G\sin u_i - Ru_i', \quad i = 1, \ldots, n, \quad u_0 = u_{n+1} = 0. \quad (4.1)$$

Here J is the moment of inertia of a single pendulum (kg m^2), Q is the torque constant of that part of the spring separating two pendula (N m/rad), $G\sin u_i$ is the gravitational restoring torque (N m), and Ru_i' is the dissipative torque (N m) associated with the introduction of rotational damping. Casting this as in (1.1) we find

$$K = (Q/J)T + (G/J)I, \quad D = (R/J)I, \quad \text{and}$$
$$f = (G/J)(u - \sin(u)),$$

where T is the n by n symmetric tridiagonal matrix with 2 on the diagonal and -1 on the superdiagonal and I is the n by n identity matrix. Our interest is in stating simple conditions on J, Q, G, and R that guarantee the stability of the zero solution of (1.1) for such K, D, and f.

As D is simply a multiple of the identity our system is obviously classically damped. This produces $\delta = 0$ and one also finds

$$\lambda = (Q\mu + G)/J, \quad \gamma = R/J, \quad \text{and} \quad C = 2G/J$$

where

$$\mu = 4\sin^2\left(\frac{\pi}{2(n + 1)}\right)$$

is the least eigenvalue of T. A direct application of Corollary 3.2 now guarantees stability of the trivial solution when

$$G + G^2/J < Q\mu \quad \text{and} \quad R > \frac{2G}{Q\mu - G - G^2/J}$$
$$\times (Q\mu + \sqrt{(Q\mu + G)(Q\mu - G + J) - 2G}), \quad (4.2)$$

that is, when the stiffness dominates the inertial components of the pendulum and when the rotational damping is on the order of the reciprocal of their difference. However, as f is free of terms involving the velocity, u', one may suspect that sharper inequalities may be found. This is indeed the case though, rather than deriving them at this stage we shall find it instructive to first pass to the limit of a continuum of pendula. More precisely, we let the distance h between the pendula approach zero. We rewrite (4.1) as

$$(J/h)u_i'' = (Qh)\frac{[(u_{i+1} - u_i)/h] - [(u_i - u_{i-1})/h]}{h}$$
$$- (G/h)\sin u_i - (R/h)u_i'.$$

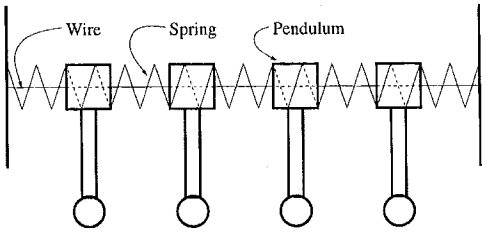


Fig. 1 The mechanical transmission line

Downloaded 04 May 2010 to 171.66.16.34. Redistribution subject to ASME license or copyright; see http://www.asme.org/terms/Terms_Use.cfm

As h tends to zero we find that J/h tends to J, the moment of inertia per meter of line (kg m^2/m), that Qh tends to $\mathcal{Q}$, the spring torque per meter of line (N m/rad m), that $(G/h)\sin u_l$ tends to $\mathcal{G}\sin u$, the gravitational torque per meter (N m/m), and that $(R/h)u_t'$ tends to $\mathcal{R}\partial u/\partial t$, the dissipative torque per meter (N m/m). The limiting differential equation is hence

$$Ju_{tt}(x,t) - \mathcal{Q}u_{xx}(x,t) + \mathcal{R}u_t(x,t) = -\mathcal{G}\sin u(x,t), \qquad 0 < x < 1, \quad 0 < t. \quad (4.3)$$

It is subject to the end conditions

$$u(0,t) = u(1,t) = 0, \quad 0 < t.$$

Freely adopting the Lyapunov function of (3.4) brings

$$\begin{aligned} L_0(u,u_t) &= \int_0^1 \{u[-(\mathcal{Q}/\mathcal{R})\partial_{xx} + (\mathcal{R}/2J)]u \\ &\quad + (J/\mathcal{R})u_t^2 + uu_t\}\,dx \\ &= \int_0^1 \{(1/\mathcal{R})(\mathcal{Q}u_x^2 + Ju_t^2) + (\mathcal{R}/2J)u^2 + uu_t\}\,dx. \end{aligned}$$

We note that the Euclidean inner product on $\mathbf{R}^n$ has given rise to the $L^2(0,1)$ inner product on $H_0^1(0,1)$, the class of square integrable functions that vanish at zero and one and possess square integrable derivatives. We first verify that L_0 is indeed positive definite. Invoking Hölder's inequality brings

$$\begin{aligned} L_0(u,u_t) &\geq (\mathcal{Q}/\mathcal{R})\|u_x\|^2 + (J/\mathcal{R})\|u_t\|^2 \\ &\quad - \|u\|\,\|u_t\| + (\mathcal{R}/2J)\|u\|^2 \\ &\geq (\mathcal{Q}/\mathcal{R})\|u_x\|^2 + \omega(\|u_t\|^2 + \|u\|^2) \end{aligned}$$

where

$$\omega = \frac{(J/\mathcal{R}) + (\mathcal{R}/2J) - \sqrt{(J/\mathcal{R})^2 + (\mathcal{R}/2J)^2}}{2} > 0.$$

Finally we demonstrate that the time derivative of L_0 is negative definite along solutions to (4.3). For this we make use of Rayleigh's Principle

$$\pi^2 \leq \frac{\int_0^1 w_x(x)^2\,dx}{\int_0^1 w(x)^2\,dx} \quad \forall w \in H_0^1(0,1).$$

Now

$$\begin{aligned} \frac{d}{dt}L_0(u,u_t) &= \int_0^1 \{(2/\mathcal{R})(\mathcal{Q}u_xu_{xt} + Ju_tu_{tt}) \\ &\quad + (\mathcal{R}/J)uu_t + uu_{tt} + u_t^2\}\,dx \\ &= \int_0^1 \{(2/\mathcal{R})(-\mathcal{Q}u_{xx} + Ju_{tt})u_t \\ &\quad + (1/J)(\mathcal{R}u_t + Ju_{tt})u + u_t^2\}\,dx \\ &= \int_0^1 \{(2/\mathcal{R})(-\mathcal{R}u_t - \mathcal{G}\sin u)u_t \\ &\quad + (1/J)(\mathcal{Q}u_{xx} - \mathcal{G}\sin u)u + u_t^2\}\,dx \\ &= \int_0^1 \{(2\mathcal{G}/\mathcal{R})u_t\sin u - u_t^2 \\ &\quad + (\mathcal{G}/J)u\sin u - (\mathcal{Q}/J)u_x^2\}\,dx \\ &\leq (2\mathcal{G}/\mathcal{R})\|u_t\|\,\|u\| - \|u_t\|^2 \\ &\quad + (\mathcal{G}/J)\|u\|^2 - (\mathcal{Q}/J)\|u_x\|^2 \\ &\leq \{(\mathcal{G} - \mathcal{Q}\pi^2)/(J\pi^2)\}\|u_x\|^2 \\ &\quad + (2\mathcal{G}/\mathcal{R}\pi)\|u_x\|\,\|u_t\| - \|u_t\|^2 \\ &\leq \zeta(\|u_x\|^2 + \|u_t\|^2) \end{aligned}$$

where

$$\zeta = \frac{\mathcal{G} - \mathcal{Q}\pi^2 - J\pi^2 + \sqrt{(\mathcal{G} - \mathcal{Q}\pi^2 - J\pi^2)^2 - 4(\mathcal{Q}\pi^2 - \mathcal{G} - \mathcal{G}^2J/\mathcal{R}^2)}}{2J\pi^2}.$$

Now ζ is negative only when

$$\mathcal{Q}\pi^2 > \mathcal{G} \quad \text{and} \quad \mathcal{R}^2 > \frac{J\mathcal{G}^2}{\mathcal{Q}\pi^2 - \mathcal{G}}. \quad (4.4)$$

In comparison to (4.2) we note that as $h \to 0$, $Qh \to \mathcal{Q}$ and $(\mu/h^2) \to \pi^2$, and so $Q\mu/h \to \pi^2$. These final bounds (4.4) are indeed sharper than (4.2). In particular, given prescribed inertial terms, $\mathcal{G}$ and J, (4.4) affords greater leeway in the choice of torque and damping values, $\mathcal{Q}$ and $\mathcal{R}$. Finally we remark that our application has focused on systems with classically damped linear part. A more extensive application of Corollary 3.2 to either the discrete or continuous line would incorporate variations in the system parameters. In such a case δ would signify the distance from the variable coefficient line to the classically damped line.

Acknowledgment

The work of the first author was supported by NSF Grant DMS-9258312.

References

Bellman, R., 1970, *Introduction to Matrix Analysis*, McGraw-Hill, New York.

Caughey, T. K., and O'Kelly, M. E., 1965, "Classical Normal Modes in Damped Linear Dynamic Systems," ASME JOURNAL OF APPLIED MECHANICS, Vol. 32, pp. 583–588.

Cox, S. J., 1997, "Designing for Optimal Energy Absorption, I: Lumped Parameter Systems," ASME *Journal of Vibration and Acoustics*, to appear.

Gajić, Z., and Qureshi, M. T. J., 1995, *Lyapunov Matrix Equation in System Stability and Control*, Academic Press, San Diego, CA.

Liapunov, A. M., 1966, *Stability of Motion*, Academic Press, San Diego, CA.

Miller, R. K., and Michel, A. N., 1982, *Ordinary Differential Equations*, Academic Press, San Diego, CA.

Remoissenet, M., 1994, *Waves Called Solitons*, Springer-Verlag, New York.

Scott, A. C., 1969, "A Nonlinear Klein-Gordon Equation," *American J. of Physics*, Vol. 37, No. 1, pp. 52–61.

Downloaded 04 May 2010 to 171.66.16.34. Redistribution subject to ASME license or copyright; see http://www.asme.org/terms/Terms_Use.cfm

On the Computation of Relative Rotations and Geometric Phases in the Motions of Rigid Bodies

O. M. O'Reilly
Assistant Professor,
Department of Mechanical Engineering,
University of California,
Berkeley, CA 94720-1740
Assoc. Mem. ASME.

In this paper, expressions are established for certain relative rotations which arise in motions of rigid bodies. A comparison of these results with existing relations for geometric phases in the motions of rigid bodies provides alternative expressions of, and computational methods for, the relative rotation. The computational aspects are illustrated using several examples from rigid-body dynamics: namely, the moment-free motion of a rigid body, rolling disks, and sliding disks.

1 Introduction

Consider the motion of a set of three mutually perpendicular material lines of a rigid body. If the orientation of one of these lines at time $t = t_0 + T$ is parallel to its orientation at $t = t_0$, then it is of interest of determine the overall rotation of the other lines relative to this one during the time interval T. From the work of Goodman and Robinson (1958), it is also known that part of this relative rotation is due to what is now known, using the terminology of Berry and Hannay (1988), as a geometric angle shift or phase. The purposes of the present paper are to obtain convenient relations for the relative rotation, to provide alternative methods for the calculation of the geometric phase, and to discuss some applications.

The results we use to establish the expressions for the relative rotation are adapted from differential geometry. Specifically, they provide us with a means of expressing Goodman and Robinson's result in a manner which allows the relative rotation to be easily computed. They also permit a further examination of the equivalence, which was noted by Marsden and Ratiu (1994), of their work to the results of Anandan (1988), Hannay (1985), Levi (1993), and Montgomery (1991) on this subject. Several additional results can be found in Zhuravlev (1996). The importance of relative rotation lies in its application to mechanical systems composed of rigid bodies. Examples of these applications may be found in the aforementioned references, Bloch et al. (1992) and Kelly and Murray (1995).

Our initial development of the relative rotation is based on Meusnier's theorem (on the geodesic curvature) and Bonnet's theorem (on the geodesic torsion) for a curve on a surface. Related results were used by Love (1893, Chapter 14) in the context of the kinematics of rods and Thomson (Lord Kelvin) and Tait (1867, 1912) in the context of rigid bodies. In Sections 123 and 126 of their treatise, Kelvin and Tait also discussed the kinematics of rods and established a result which shows that a certain relative rotation may be decomposed into the sum of a dynamic phase and a geometric phase. Their method of proof is similar to the later work of Goodman and Robinson (1958) on rigid bodies. It can be rederived by paralleling the developments of this paper using a constrained theory of a directed or Cosserat curve.[1] In a historical context, Kelvin and Tait's result from 1867 predates those which we found in the literature on geometric phases (cf. Berry, 1990). It is related, as is the work of this paper, to the discussions on geometric phases in space curves, Foucault's pendulum, light propagation in a twisted optical fiber, and magnetic chains which may be found in Balakrishnan et al. (1993a, b) and Kugler and Shtrikman (1988), among others.

Not withstanding the elegance and depth of Goodman and Robinson's work, the calculation of the relative rotation for a particular motion of a rigid body appears to be very difficult. In this paper, we show how their relative rotation can be obtained in an equivalent and (often) readily computed manner. These developments are discussed in Section 3 of this paper. Certain results pertaining to relative rotations and geometric phases are discussed in Section 4. In particular, three equivalent methods for calculating the relative rotation are discussed. We close the paper with several applications. In Section 5, the moment-free motion of a rigid body is discussed. This example serves to show how the results of the present paper compare with those of Levi (1993) and Montgomery (1991). In Section 6, relative rotations and geometric phases in the dynamics of rolling disks and sliding disks are examined. Parts of the preliminary developments for these two systems are based on O'Reilly (1996).[2] The applications we consider are by no means exhaustive. Indeed, we emphasize that the developments in this paper are valid for all mechanical systems comprised of a single rigid body.

2 Preliminaries on Rigid-Body Kinematics

We recall here some background on rigid-body kinematics as presented in Casey (1983, 1995). Consider a rigid body $\mathcal{B}$, and define a fixed reference configuration $\boldsymbol{\kappa}_0$ for $\mathcal{B}$. The current configuration at time t of $\mathcal{B}$ is denoted by $\boldsymbol{\kappa}$. A material point X of $\mathcal{B}$ in $\boldsymbol{\kappa}_0$ and $\boldsymbol{\kappa}$ is uniquely identified by the vectors $\mathbf{X}$ and $\mathbf{x}$, respectively. Each of these vectors is described with respect to a fixed origin (cf. Fig. 1). We recall the representations of the motion $\boldsymbol{\chi}$ of $\mathcal{B}$:

$$\mathbf{x} = \boldsymbol{\chi}(\mathbf{X}, t) = \mathbf{Q}\mathbf{X} + \mathbf{q} = \mathbf{Q}(\mathbf{X} - \bar{\mathbf{X}}) + \bar{\mathbf{x}}, \qquad (1)$$

where $\mathbf{Q} = \mathbf{Q}(t)$ is a proper-orthogonal (or rotation) tensor, $\mathbf{q} = \mathbf{q}(t)$ is a vector-valued function of time, and $\bar{\mathbf{X}}$ and $\bar{\mathbf{x}}$ are the

Contributed by the Applied Mechanics Division of THE AMERICAN SOCIETY OF MECHANICAL ENGINEERS for publication in the ASME JOURNAL OF APPLIED MECHANICS.

Discussion on the paper should be addressed to the Technical Editor, Professor Lewis T. Wheeler, Department of Mechanical Engineering, University of Houston, Houston, TX 77204-4792, and will be accepted until four months after final publication of the paper itself in the ASME JOURNAL OF APPLIED MECHANICS.

Manuscript received by the ASME Applied Mechanics Division, Oct. 24, 1996; final revision, Mar. 20, 1997. Associate Technical Editor: S. W. Shaw.

[1] This constrained theory is discussed by Antman (1995, Chapter VIII, Sections 15 and 16) and Naghdi and Rubin (1984, Section 4), among others. It is a particular constrained theory of the special Cosserat theory of rods discussed by Antman, where the rod is assumed to be unshearable.

[2] The interested reader is also referred to Cushman, Hermans, and Kemppianen (1996) for additional results on the dynamics of a rolling disk.

Copyright © 1997 by ASME

Downloaded 04 May 2010 to 171.66.16.34. Redistribution subject to ASME license or copyright; see http://www.asme.org/terms/Terms_Use.cfm

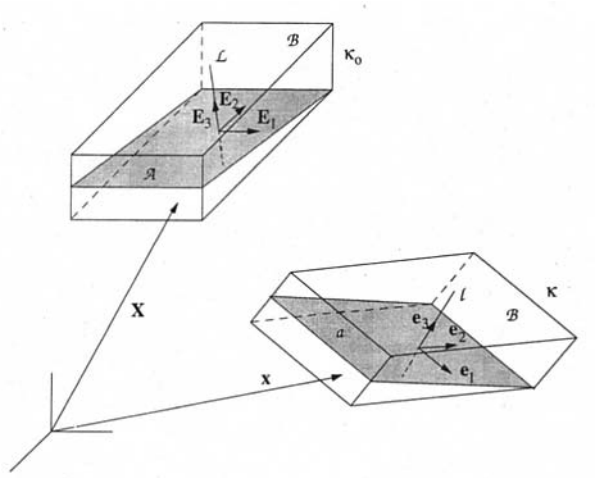


Fig. 1 A representative example of the reference κ_0 and current κ configurations of a rigid body $\mathcal{B}$. Examples of the material lines $\mathcal{L}$ and ℓ and the material planes $\mathcal{A}$ and $\mathscr{a}$ are also shown.

position vectors of the center of mass $\bar{X}$ of $\mathcal{B}$ in κ_0 and κ, respectively.

During a motion of $\mathcal{B}$, material lines in κ_0 are mapped onto material lines in κ under (1). We now consider a material line $\mathcal{L}$ defined by two material points in κ_0. The unit vector defined by these points is denoted by $\mathbf{E}_3$. It is convenient to use one of these material points and two others to define $\mathbf{E}_1$ and $\mathbf{E}_2$ such that $\{\mathbf{E}_1, \mathbf{E}_2, \mathbf{E}_3\}$ is a right-handed Cartesian basis for Euclidean three-space $\mathcal{E}^3$. Furthermore,[3]

$$\mathbf{e}_i = \mathbf{Q}\mathbf{E}_i, \tag{2}$$

form a corotational basis for $\mathcal{E}^3$, and $\mathbf{e}_3$ is along the image ℓ of $\mathcal{L}$ in κ. We denote the material planes in κ_0 whose normal is $\mathbf{E}_3$ by $\mathcal{A}$. Clearly, these material planes are mapped into the material planes $\mathscr{a}$ by χ, $\mathbf{e}_3$ is normal to $\mathscr{a}$, and $\mathscr{a}$ is spanned by $\{\mathbf{e}_1, \mathbf{e}_2\}$. Finally, we recall that the angular velocity vector of $\mathcal{B}$ is

$$\boldsymbol{\omega} = \sum_{i=1}^{3} \omega_i \mathbf{e}_i = -\tfrac{1}{2}\boldsymbol{\epsilon}[\dot{\mathbf{Q}}\mathbf{Q}^T], \tag{3}$$

where the third-order tensor $\boldsymbol{\epsilon}$ is known as the alternator. The superposed dot in (3) denotes the time derivative.

3 Relative Rotation in a Rigid Body

In this section, we will establish a decomposition of the tensor $\mathbf{Q}$ as the product of three rotation tensors: $\mathbf{Q} = \mathbf{Q}_3\mathbf{Q}_2\mathbf{Q}_1$. The tensors $\mathbf{Q}_2$ and $\mathbf{Q}_3$ will be defined in terms of the angular velocity vector of the rigid body. These two tensors are subsequently used to define the relative rotation tensor $\mathbf{R}$. As will be demonstrated in Section 4, the angle of rotation associated with this tensor is one of the principal concerns of Goodman and Robinson (1958), among others. The manner in which $\mathbf{Q}_2$ and $\mathbf{Q}_3$ are defined is based on classical results from differential geometry which may be found in Kreyszig (1959), McConnell (1947), and Spivak (1979).

To indicate how our developments are obtained from results in differential geometry, we first use the classical construction of a fixed space curve C in $\mathcal{E}^3$ which corresponds to a motion of $\mathcal{B}$: $\mathbf{p}(s) = \mathbf{p}(s_0) + \int_{s_0}^{s} \mathbf{e}_3(u)du$, where C is parameterized by $s = t$. Clearly, $\mathbf{e}_3$ is the unit tangent vector to C. The particular choice of the constant $\mathbf{p}(s_0 = t_0)$ is of no importance for the present purposes. The curve C may be considered to lie on a surface S. We assume the following: $\mathbf{p}(s) \in S$, $\mathbf{e}_3$ is the unit tangent vector to C on S, $\mathbf{e}_1$ is the unit normal vector to C on S, and $\{\mathbf{e}_3, \mathbf{e}_1, \mathbf{e}_2\}$ constitute the Darboux frame of C on S.[4] It follows from (3) that

$$\tau_g = \omega_3, \quad \kappa_g = \omega_1, \quad \kappa_n = \omega_2, \tag{4}$$

where τ_g, κ_g, and κ_n are the geodesic torsion, geodesic curvature, and normal curvature, respectively, of C on S.

If C is considered as a space curve, then, from (4) and Bonnet and Meusnier's theorems,[5] it follows that

$$\tau = \omega_3 - \dot{\phi}_3, \quad \kappa = \sqrt{\omega_1^2 + \omega_2^2}, \tag{5}$$

where τ and κ are the torsion and curvature, respectively, of C. The angle $\phi_3 = \phi_3(t)$ is uniquely defined either by

$$\cos(\phi_3) = \frac{\omega_2}{\sqrt{\omega_2^2 + \omega_1^2}}, \quad \sin(\phi_3) = \frac{\omega_1}{\sqrt{\omega_2^2 + \omega_1^2}}, \tag{6}$$

or in the degenerate case, where $\omega_1(t) = \omega_2(t) = 0$ for all $t \in (t_0, t_1)$, by

$$\phi_3(t) = \phi_3(t_0) + \int_{t_0}^{t} \omega_3(u)du. \tag{7}$$

The relations (6) are illustrated in Fig. 2. It is convenient to recall the Serret-Frenet relations for C:

$$\dot{\bar{\mathbf{e}}}_i = \boldsymbol{\omega}_I \times \bar{\mathbf{e}}_i, \quad \boldsymbol{\omega}_I = \tau\mathbf{e}_3 + \kappa\bar{\mathbf{e}}_2 \tag{8}$$

where $\mathbf{e}_3 = \bar{\mathbf{e}}_3$ is unit tangent vector to C, $\bar{\mathbf{e}}_1$ is the unit normal vector to C, $\bar{\mathbf{e}}_2$ is the unit binormal vector to C and $\boldsymbol{\omega}_1$ is the Darboux vector. The specification of ϕ_3 used here uniquely defines the Frenet triad $\{\mathbf{e}_3, \bar{\mathbf{e}}_1, \bar{\mathbf{e}}_2\}$. In the context of rods, related results were used by Love (1893, Section 233).

For a given $\boldsymbol{\omega}$, we define the rotation tensor $\mathbf{Q}_3$ using the above results:

$$\mathbf{Q}_3 = \cos(\phi_3)(\mathbf{e}_1 \otimes \mathbf{e}_1 + \mathbf{e}_2 \otimes \mathbf{e}_2) + \sin(\phi_3)(\mathbf{e}_2 \otimes \mathbf{e}_1 - \mathbf{e}_1 \otimes \mathbf{e}_2) + \mathbf{e}_3 \otimes \mathbf{e}_3. \tag{9}$$

Clearly, $\bar{\mathbf{e}}_i = \mathbf{Q}_3^T\mathbf{e}_i$, $\bar{\mathbf{e}}_3 = \mathbf{e}_3$. In words, $\mathbf{Q}_3$ transforms the Frenet triad into the Darboux triad. We next define a rotation tensor associated with the Frenet triad:

$$\bar{\mathbf{Q}} = \mathbf{Q}_3^T\mathbf{Q}. \tag{10}$$

It should be noted that $\bar{\mathbf{e}}_\alpha = \bar{\mathbf{Q}}\mathbf{E}_\alpha$ and $\mathbf{e}_3 = \bar{\mathbf{Q}}\mathbf{E}_3$. Furthermore, if $\omega_1(t) = \omega_2(t) = 0$ for all $t \in (t_0, t_1)$, then $\dot{\bar{\mathbf{Q}}} = \mathbf{0}$ and $\mathbf{Q}_3 = \mathbf{Q}$ during this time interval. This situation occurs in the case of a fixed axis rotation of $\mathcal{B}$ where $\mathbf{e}_3 = \mathbf{E}_3$ is the axis of rotation and the angle ϕ_3 suffices to determine the rotation of $\mathscr{a}$ relative to ℓ.

We now consider a fixed unit sphere which is embedded in $\mathcal{E}^3$, and define a set of Gaussian coordinates q^α for the sphere. Their coordinate surfaces are chosen such that the unit tangent vectors $\mathbf{a}_\alpha$ to the respective coordinate curves are orthonormal with $\{\mathbf{n}, \mathbf{a}_1, \mathbf{a}_2\}$ forming a right-handed basis, where $\mathbf{n}$ is the unit outward normal to the sphere. We next identify $\mathbf{e}_3$ with $\mathbf{n}$. The path traced by $\mathbf{e}_3$ on this sphere is known as the tangent

[3] In the sequel, the lower case Latin index i ranges over the values 1, 2, and 3, and the lower case Greek index α ranges over the values 1 and 2. The summation convention for repeated indices is not used in this paper.

[4] As pointed out by an anonymous reviewer, S can be considered as a ruled surface. The position vector of a point of S is $\mathbf{r}(s, u) = u\mathbf{e}_2(s) + \mathbf{p}(s)$, where u is the distance along the rule line $\mathbf{e}_2$ and $s = t$.

[5] We follow Darboux (1889, Section 505) in crediting of one of these theorems to Bonnet.

Downloaded 04 May 2010 to 171.66.16.34. Redistribution subject to ASME license or copyright; see http://www.asme.org/terms/Terms_Use.cfm

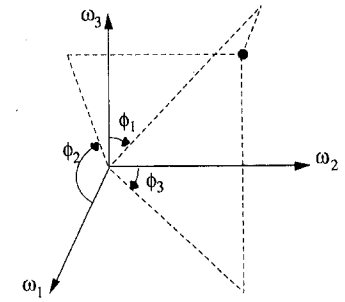


Fig. 2 The relative rotations ϕ_i (i = 1, 2, 3) and their definitions in terms of the components of the angular velocity vector $\boldsymbol{\omega} = \omega_1\mathbf{e}_1 + \omega_2\mathbf{e}_2 + \omega_3\mathbf{e}_3$. The nondegenerate case is shown here.

indicatrix $\mathcal{C}_t$ of C. We may define a rotation tensor $\mathbf{Q}_1$ and its associated angular velocity vector $\boldsymbol{\omega}_1$:

$$\mathbf{a}_\alpha = \mathbf{Q}_1\mathbf{E}_\alpha, \quad \mathbf{e}_3 = \mathbf{Q}_1\mathbf{E}_3,$$
$$\dot{\mathbf{a}}_\alpha = \boldsymbol{\omega}_1 \times \mathbf{a}_\alpha, \quad \dot{\mathbf{e}}_3 = \boldsymbol{\omega}_1 \times \mathbf{e}_3, \tag{11}$$

where

$$\boldsymbol{\omega}_1 = \omega_{11}\mathbf{a}_1 + \omega_{12}\mathbf{a}_2 + \omega_{13}\mathbf{e}_3 = -\tfrac{1}{2}\boldsymbol{\epsilon}[\dot{\mathbf{Q}}_1\mathbf{Q}_1^T]. \tag{12}$$

Because $\mathbf{Q}_1 = \mathbf{Q}_1(q^1(t), q^2(t))$, the three components of $\boldsymbol{\omega}_1$ are not independent. In addition, if $\dot{\mathbf{e}}_3(t) = \mathbf{0}$, then $\boldsymbol{\omega}_1 = \mathbf{0}$. Finally, we define $\mathbf{Q}_2$ such that $\bar{\mathbf{e}}_\alpha = \mathbf{Q}_2\mathbf{a}_\alpha$:

$$\mathbf{Q}_2 = \cos(\eta_3)(\mathbf{a}_1 \otimes \mathbf{a}_1 + \mathbf{a}_2 \otimes \mathbf{a}_2) + \sin(\eta_3)(\mathbf{a}_2 \otimes \mathbf{a}_1 - \mathbf{a}_1 \otimes \mathbf{a}_2) + \mathbf{e}_3 \otimes \mathbf{e}_3. \tag{13}$$

Clearly,

$$\bar{\mathbf{Q}} = \mathbf{Q}_2\mathbf{Q}_1. \tag{14}$$

For the case where $\dot{\mathbf{e}}_3(t) \neq \mathbf{0}$, the angle η_3 may be interpreted from the following identity:

$$\dot{\mathbf{e}}_3 = \boldsymbol{\omega}_1 \times \mathbf{e}_3 = \sqrt{\omega_1^2 + \omega_2^2}\,(\cos(\eta_3)\mathbf{a}_1 + \sin(\eta_3)\mathbf{a}_2) = \sqrt{\omega_1^2 + \omega_2^2}\,\bar{\mathbf{e}}_1. \tag{15}$$

In the degenerate case, where $\dot{\mathbf{e}}_3(t) = \mathbf{0}$, the angle η_3 is constant.

Using the methods of Casey and Lam (1986), (3), (5), and (8)–(13), the components of the angular velocity vectors of the various rotation tensors can be related:

$$\omega_3 = \dot{\phi}_3 + \dot{\eta}_3 + \omega_{13},$$
$$\omega_1 = \cos(\phi_3 + \eta_3)\omega_{11} + \sin(\phi_3 + \eta_3)\omega_{12},$$
$$\omega_2 = -\sin(\phi_3 + \eta_3)\omega_{11} + \cos(\phi_3 + \eta_3)\omega_{12}. \tag{16}$$

These equations are valid for all values of $\omega_i(t)$ and, consequently, all motions of $\mathcal{B}$. The relations between the various basis vectors and the angles are summarized in Fig. 3.

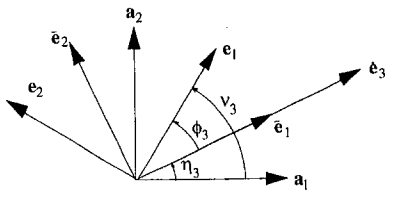


Fig. 3 A representative tangent plane of a point of the sphere illustrating the angles υ_3, ϕ_3, and η_3

We now suppose that during the motion of $\mathcal{B}$, ℓ coincides with itself after a time T:

$$\mathbf{e}_3(t_0 + T) = \mathbf{e}_3(t_0), \quad \mathbf{Q}_1(t_0 + T) = \mathbf{Q}_1(t_0). \tag{17}$$

It follows from (2) that the overall rotational motion of the body may be viewed as a rotation about $\mathbf{e}_3(t_0)$ through an angle $\Delta\upsilon_3$, which is the relative rotation of interest. The rotation tensor associated with this angle is

$$\mathbf{R} = \mathbf{Q}(t_0 + T)\mathbf{Q}^T(t_0) = \mathbf{Q}_3(t_0 + T)\mathbf{Q}_2(t_0 + T)\mathbf{Q}_2^T(t_0)\mathbf{Q}_3^T(t_0), \tag{18}$$

where

$$\mathbf{R} = \cos(\Delta\upsilon_3)(\mathbf{e}_1(t_0) \otimes \mathbf{e}_1(t_0) + \mathbf{e}_2(t_0) \otimes \mathbf{e}_2(t_0)) + \sin(\Delta\upsilon_3)(\mathbf{e}_2(t_0) \otimes \mathbf{e}_1(t_0) - \mathbf{e}_1(t_0) \otimes \mathbf{e}_2(t_0)) + \mathbf{e}_3(t_0) \otimes \mathbf{e}_3(t_0), \tag{19}$$

and

$$\Delta\upsilon_3 = \Delta\phi_3 + \Delta\eta_3, \; \Delta\phi_3 = \int_{t_0}^{t_0+T} \dot{\phi}_3\,dt, \quad \Delta\eta_3 = \int_{t_0}^{t_0+T} \dot{\eta}_3\,dt. \tag{20}$$

We emphasize that $\mathbf{e}_i(t_0 + T) = \mathbf{R}\mathbf{e}_i(t_0)$. The calculation of the relative rotation angle $\Delta\upsilon_3$ shall be elaborated upon shortly.

An alternative viewpoint of our decomposition of $\mathbf{Q}$ is to consider an intermediate motion $\mathbf{X}_I$ of $\mathcal{B}$: $\mathbf{x}_I = \mathbf{X}_I(\mathbf{X}, t) = \mathbf{Q}_1(\mathbf{X} - \bar{\mathbf{X}}) + \bar{\mathbf{x}}$. This motion defines an intermediate configuration $\boldsymbol{\kappa}_I$ of $\mathcal{B}$. The image of $\mathcal{L}$ in $\boldsymbol{\kappa}_I$ is identical to its image ℓ in $\boldsymbol{\kappa}$. By design, the images of the material planes $\mathcal{A}$ in $\boldsymbol{\kappa}_I$ and $\boldsymbol{\kappa}$ are coplanar and related by the tensor $\mathbf{Q}_3\mathbf{Q}_2$. It suffices to consider $\boldsymbol{\chi}_I$ to determine the location of ℓ in $\boldsymbol{\kappa}$.

Finally, two other angles of relative rotation, υ_1 and υ_2, can be defined by cyclically permuting the indices in (6), (7), and (13) in an obvious manner.

4 Some Results and Remarks on Relative Rotation

It is clear from the developments of the previous section that the relative rotation of interest is the additive decomposition of two angles. In this section, three methods of determining the relative rotation will be presented. Modulo additive multiples of 2π, they provide equivalent results.

In the first method, the angles $\Delta\phi_3$ and $\Delta\eta_3$ are determined. To do this it suffices to know $\omega_i(t)$, $\mathbf{e}_3(t)$, and $\dot{\mathbf{e}}_3(t)$. Moreover, if $\omega_i(t)$ are known for the motion of $\mathcal{B}$, then $\phi_i(t)$ can often be determined using the trajectory of $\omega_i(t)$ in the ω_1-ω_2-ω_3 space (see Fig. 2). It is noteworthy to record that

$$\dot{\phi}_3 = \frac{\dot{\omega}_1\omega_2 - \dot{\omega}_2\omega_1}{\omega_1^2 + \omega_2^2}, \text{ or } \dot{\phi}_3 = \omega_3. \tag{21}$$

These relations are often more convenient to use than (6) or (7) in certain calculations. Using the balance laws for $\mathcal{B}$, (21) may be expressed in a variety of manners which depend on the problem of interest and its associated conserved quantities. Concerning $(21)_1$, we note that it may be immediately integrated for certain cases. For example, if $\omega_1(t) = 0$ or $\omega_2(t) = 0$ for all t, then $\Delta\phi_3 = \phi_3(t_0 + T) - \phi_3(t_0) = 0$. Geometrically, $\Delta\phi_3$ is related to the rotation of $\mathbf{e}_\alpha$ relative to the $\bar{\mathbf{e}}_\alpha$. On the other hand, $\Delta\eta_3$ is related to the rotation of $\dot{\mathbf{e}}_3$ relative to $\mathbf{a}_\alpha$. If (17) holds and $\dot{\mathbf{e}}_3(t_0) = \dot{\mathbf{e}}_3(t_0 + T)$, then $\Delta\eta_3 = 0$, modulo additive multiples of 2π. The applications discussed in Sections 5 and 6 provide examples of situations where either $\Delta\phi_3$ or $\Delta\eta_3$ is 0, while the other is nontrivial.

The second method uses Euler angles $\{\varphi, \theta, \psi\}$ to parameterize $\mathbf{Q} = \mathbf{Q}(\psi)\mathbf{Q}(\theta)\mathbf{Q}(\varphi)$. In this case, $\mathbf{R}$ may be expressed in terms of these angles and their time derivatives using some

Downloaded 04 May 2010 to 171.66.16.34. Redistribution subject to ASME license or copyright; see http://www.asme.org/terms/Terms_Use.cfm

standard identities. In addition, the angles θ and φ can be considered as Gaussian coordinates for the sphere, i.e., $\mathbf{Q}_1 = \mathbf{Q}(\theta)\mathbf{Q}(\varphi)$. Specifically, for the Euler angles discussed in Synge and Griffith (1942) and Whittaker (1944),

$$\mathbf{e}_3 = \sin(\theta)(\cos(\varphi)\mathbf{E}_1 + \sin(\varphi)\mathbf{E}_2) + \cos(\theta)\mathbf{E}_3,$$

$$\boldsymbol{\omega}_1 = -\dot{\theta}\sin(\varphi)\mathbf{a}_1 + \dot{\varphi}\mathbf{a}_2 + \dot{\theta}\cos(\varphi)\mathbf{e}_3,$$

$$\dot{\psi} = \dot{\upsilon}_3 = \dot{\phi}_3 + \dot{\eta}_3 = \omega_3 - \omega_{13}. \tag{22}$$

We note that in specifying η_3 using a particular set of Euler angles, the specified ranges of these angles must be adhered to in order to avoid singularities. It should be clear from $(22)_3$, that the relative rotation angle υ_3 is none other than the Euler angle ψ: a result which was anticipated.

We now discuss the third method. In the process, we may compare the results of the previous section with those of Goodman and Robinson (1958), and also relate them to recent work in geometric phases. To proceed, we consider a motion of $\mathcal{B}$ where $\mathcal{C}_t$ closes after a time T but $\bar{\mathbf{e}}_1(t_0) \neq \bar{\mathbf{e}}_1(t_0 + T)$.[6] In other words, (17) holds but $\dot{\mathbf{e}}_3(t_0) \neq \dot{\mathbf{e}}_3(t_0 + T)$. It is necessary to use (15) and (18) to determine the relative rotation:

$$\Delta\upsilon_3 = \int_{t_0}^{t_0+T} \omega_3(u)du + \int_{t_0}^{t_0+T} -\omega_{13}(u)du. \tag{23}$$

Following Berry and Hannay (1988), the two integrals in (23) are known as the dynamic and geometric phases, respectively. In the event that $\mathcal{C}_t$ does not self-intersect during the interval $(t_0, t_0 + T)$, then a standard calculation in differential geometry using (11), the definition of Gaussian curvature and Stokes's theorem, the second integral in (23) may be shown to be equal to the solid angle enclosed by $\mathcal{C}_t$ on the unit sphere. Equivalently, (23) can be established as in Goodman and Robinson (1958) by using the Gauss-Bonnet theorem. The use of this theorem is based on the observations that $\bar{\mathbf{e}}_1$ is the tangent vector to $\mathcal{C}_t$, that the angle $\Delta\eta_3$ is related to the sum of the exterior angles $\chi_1 + \chi_2 + \ldots$ by $\Delta\eta_3 + \chi_1 + \chi_2 + \ldots = 0$ (modulo additive multiples of 2π), and that the geodesic curvature k_g of $\mathcal{C}_t$ on the sphere is the torsion τ of C: $k_g = \omega_3 - \dot{\phi}_3$.[7] Related results which describe the relative rotation in terms of a solid angle are presented in Kelvin and Tait (1867, 1912), Levi (1993), and Zhuravlev (1996), among others. We note that the interrelationships between geodesic curvature, anholonomy, Levi-Civita's parallel displacement and geometric phases in other systems are discussed by several authors (e.g., Balakrishnan et al., 1993a, b; Berry, 1990; Kugler and Shtrikman, 1988).

5 Application I: Moment-Free Motion of a Rigid Body

We recall, from the balance of angular momentum $\mathbf{H}$ of a rigid body $\mathcal{B}$ relative to its center of mass $\bar{X}$, that when the resultant external moment $\mathbf{M}$ acting on $\mathcal{B}$ is zero, then

$$\dot{\mathbf{H}} = \dot{\overline{\mathbf{J}\boldsymbol{\omega}}} = \mathbf{0}. \tag{24}$$

The moment of inertia tensor $\mathbf{J}$ of $\mathcal{B}$ relative to $\bar{X}$ in $\boldsymbol{\kappa}$ has the representation

$$\mathbf{J} = \lambda_1\mathbf{e}_1 \otimes \mathbf{e}_1 + \lambda_2\mathbf{e}_2 \otimes \mathbf{e}_2 + \lambda_3\mathbf{e}_3 \otimes \mathbf{e}_3. \tag{25}$$

It should be noted that we are choosing $\mathbf{e}_i$ to be the eigenvectors of $\mathbf{J}$. We recall that (24) has two integrals:

$$H = \|\mathbf{H}\|, \; E = \tfrac{1}{2}(\mathbf{J}\boldsymbol{\omega})\cdot\boldsymbol{\omega}. \tag{26}$$

Furthermore, the solutions $\omega_i(t)$ of (24) possess certain symmetries:

$$(t, \omega_1, \omega_2, \omega_3) \to (-t, -\omega_1, \omega_2, \omega_3),$$
$$(t, \omega_1, \omega_2, \omega_3) \to (-t, \omega_1, -\omega_2, \omega_3),$$
$$(t, \omega_1, \omega_2, \omega_3) \to (-t, \omega_1, \omega_2, -\omega_3). \tag{27}$$

As a consequence of (26), $\omega_i(t)$ lie on the intersection of the level sets of H and E.

We henceforth assume that $\lambda_1 > \lambda_2 > \lambda_3$ and presume that the reader has some familiarity with the qualitative nature of the trajectories of $\omega_i(t)$. The phase portraits for $\lambda_i\omega_i(t)$ can be found in Marsden and Ratiu (1994). The corresponding ones for $\omega_i(t)$, which are particularly relevant here, are easily seen to be qualitatively similar. Fixing E and varying H, the orbits $\omega_i(t)$ may be classified into three types: equilibria, periodic, and four (heteroclinic) orbits of infinite duration. For the periodic orbits, it is known that $\mathbf{Q}(t)$ is, in general, quasi-periodic (see, e.g., Whittaker, 1944, Section 69). This implies that it is unlikely that $\mathbf{e}_i(t)$ will return to its original orientation after a period T of the periodic orbit of $\omega_i(t)$.

Motivated by the work of Levi (1993) and Montgomery (1991), we consider the rotation of $\mathcal{B}$ relative to the material line which is periodically parallel to $\mathbf{H}$ during an orbit of $\omega_i(t)$ which has a finite period T. It is appropriate to elucidate the motivation for this calculation. From (24), it is clear that $\mathbf{H}$ is constant. Combined with the periodicity of $\omega_i(t)$, this implies that

$$\mathbf{H} = \sum_{i=1}^{3} \lambda_i\omega_i(t_0)\mathbf{e}_i(t_0) = \sum_{i=1}^{3} \lambda_i\omega_i(t_0 + T)\mathbf{e}_i(t_0 + T)$$
$$= \sum_{i=1}^{3} \lambda_i\omega_i(t_0)\mathbf{e}_i(t_0 + T). \tag{28}$$

It follows from (28) that there exists a material line in $\mathcal{B}$ which returns to its original orientation after a time period T. Furthermore, the orientation of this particular material line is parallel to $\mathbf{H}$ only when $t = t_0$ and $t = t_0 + T$.

To determine the relative rotation, we will use the first method discussed in Section 4. The previous discussion states that a particular material line will be parallel to $\mathbf{H}$ only when $t = t_0$ and $t = t_0 + T$. To calculate the relative rotation, we first need to define a particular corotational basis $\{\tilde{\mathbf{e}}_i\}$ such that $\tilde{\mathbf{e}}_3(t_0) = \tilde{\mathbf{e}}_3(T + t_0) = \mathbf{H}/H$. Without loss in generality, we choose t_0 such that $\omega_2(t_0) = 0$ and then define this corotational basis:

$$\tilde{\mathbf{e}}_1 = \frac{\lambda_3\omega_3(t_0)}{H}\mathbf{e}_1(t) - \frac{\lambda_1\omega_1(t_0)}{H}\mathbf{e}_3(t),$$

$$\tilde{\mathbf{e}}_2 = \mathbf{e}_2(t),$$

$$\tilde{\mathbf{e}}_3 = \frac{\lambda_1\omega_1(t_0)}{H}\mathbf{e}_1(t) + \frac{\lambda_3\omega_3(t_0)}{H}\mathbf{e}_3(t). \tag{29}$$

The relative rotation we seek is, from (16), (18), and (29), $\Delta\tilde{\upsilon}_3 = \Delta\tilde{\phi}_3 + \Delta\tilde{\eta}_3$. Recalling (23), this rotation is the sum of a geometric phase $\int_{t_0}^{t_0+T} -\tilde{\omega}_{13}(u)du$ and a dynamic phase $\int_{t_0}^{t_0+T} \tilde{\omega}_3(u)du$. To calculate this rotation, we will use a method which allows us to take advantage of existing analytical results for this system. In the interests of brevity, we will only outline the details of the calculations.

First, $\Delta\tilde{\phi}_3$ is calculated using $(21)_1$ and (29):

$$\Delta\tilde{\phi}_3 = \int_{t_0}^{T+t_0} \frac{\dot{\tilde{\omega}}_1(u)\omega_2(u) - \dot{\omega}_2(u)\tilde{\omega}_1(u)}{\tilde{\omega}_1^2(u) + \omega_2^2(u)}du, \tag{30}$$

where $\tilde{\omega}_i = \boldsymbol{\omega}\cdot\tilde{\mathbf{e}}_i$. This integral may be evaluated using analyti-

[6] This situation arises in the motion of the heavy axisymmetric rigid body with one point fixed (see, e.g., Goldstein, 1980, Fig. 5-9).

[7] A statement of the Gauss-Bonnet theorem can be found in McConnell (1947, p. 192, Ex. 12). Our notations for the exterior angle χ_1 and the geodesic curvature k_g correspond to ω_1 and σ, respectively, which are used by McConnell.

Downloaded 04 May 2010 to 171.66.16.34. Redistribution subject to ASME license or copyright; see http://www.asme.org/terms/Terms_Use.cfm

cal expressions for $\omega_i(t)$ which are readily available. Using them, it is easy to see that the projected trajectory of $\omega_i(t)$ onto the $\tilde{\omega}_1 - \omega_2$ plane is closed and hence $\Delta\tilde{\phi}_3 = 0$, modulo additive integer multiples of 2π. A representative selection of these trajectories is shown in Fig. 4, and confirms this result.[8] In conclusion, $\Delta\tilde{v}_3 = \Delta\tilde{\eta}_3$.

The second part of the calculation involves $\Delta\tilde{\eta}_3$. From (15) and (29), we recall that this angle is related to the orientational change of $\tilde{\mathbf{e}}_3(t)$ relative to $\mathbf{a}_1(t)$ during the time period of interest (cf. Fig. 3). Using the expressions for $\mathbf{e}_1(t)$ and $\mathbf{e}_3(t)$ in terms of the Euler angles $\{\varphi, \theta, \psi\}$ of Synge and Griffith (1942), one first calculates $\tilde{\mathbf{e}}_3(t)$ using $(29)_3$. Then, $\tilde{\mathbf{e}}_3(t)$ can be determined using their analytical results for $\omega_i(t)$, $\varphi(t)$, $\theta(t)$, and $\psi(t)$. Comparing the orientations of this vector after the period T with $\mathbf{a}_1(t_0) = \mathbf{a}_1(T + t_0)$, one finally concludes that

$$\Delta\tilde{v}_3 = \Delta\tilde{\eta}_3 = \varphi(t_0 + T) - \varphi(t_0). \tag{31}$$

In general, $\varphi(t)$ is quasi-periodic, and the relative rotation is nontrivial.

As noted by Montgomery (1991, Section IC), (31) is equivalent both to his Eq. (1) and Levi's (1993, Corollary 4). We remark, however, that they sought the equivalent relative rotation of $\mathcal{B}$ about $\mathbf{H}$ and they both used methods which were different from the one used here.

6 Application II: Rolling Disks and Sliding Disks

The second application of interest involves a thin disk of radius R and mass m which either rolls without slipping on a rough horizontal surface or slides on a smooth horizontal surface. A vertical gravitational force $-mg\mathbf{E}_3$ acts on the disk. These systems were recently discussed by the author (O'Reilly (1996)) who exploited classical integrability results by Appell (1900), Korteweg (1900), and Vierkandt (1892) to analyze the bifurcations of the steady motions of the disk.[9] For convenience, several of the results from this paper will be used here. Our aim is to determine the relative rotation of the disk about an axis which is perpindicular to the plane of the disk. Related work on other geometric phases in a controlled vertical disk were discussed by Bloch, Reyhanoglu and McClamroch (1992).

[8] Figure 4 was constructed using the symbolic manipulation package *Mathematica®*, the analytical expressions for $\omega_i(t)$ discussed in Synge and Griffith (1942) and the symmetries (27).

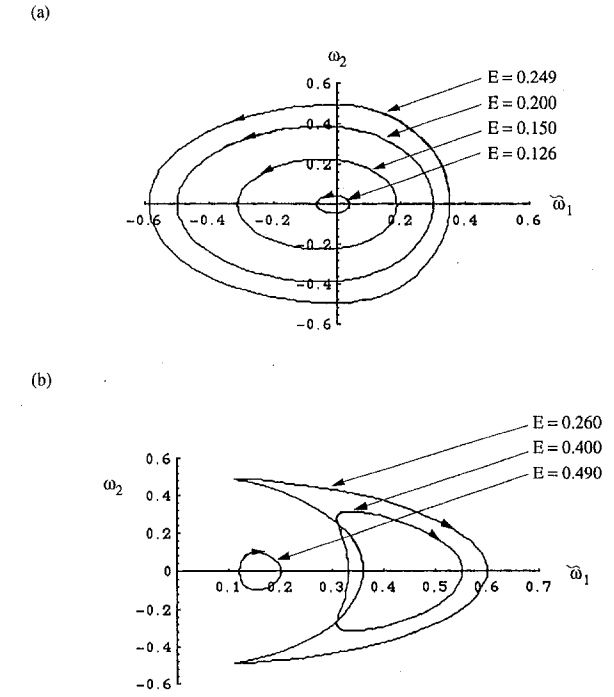


Fig. 4 The projections of $\omega_i(t)$ onto the $\tilde{\omega}_1 - \omega_2$ plane for the moment-free motion of a rigid body. Here, $\lambda_1 = 4$, $\lambda_2 = 2$, $\lambda_3 = 1$, $H = 1.0$, and E is varied: (a) $\lambda_1 > H^2/2E > \lambda_2$ and (b) $\lambda_2 > H^2/2E > \lambda_3$. The arrows on the projections indicate the directions of increasing t.

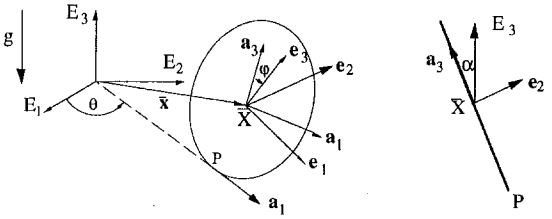


Fig. 5 A thin disk moving with one point P in contact with a horizontal surface. The basis $\{\mathbf{e}_1, \mathbf{e}_2, \mathbf{e}_3\}$ is corotational. The basis $\{\mathbf{a}_1, \mathbf{a}_2 = \mathbf{e}_2, \mathbf{a}_3\}$ is such that $\mathbf{a}_3$ is always parallel to the position vector of P relative to $\bar{X}$.

Referring to Fig. 5, three Euler angles $\{\varphi, \alpha, \theta\}$ are used to specify the rotation tensor $\mathbf{Q}$ of the disk. The angular velocity vector of the disk has the following representation:

$$\boldsymbol{\omega} = (\dot{\alpha}\cos(\varphi) - \dot{\theta}\cos(\alpha)\sin(\varphi))\mathbf{e}_1 + (\dot{\varphi} + \dot{\theta}\sin(\alpha))\mathbf{e}_2 + (\dot{\alpha}\sin(\varphi) + \dot{\theta}\cos(\alpha)\cos(\varphi))\mathbf{e}_3. \tag{32}$$

In addition,

$$\mathbf{e}_2 = \cos(\alpha)(-\sin(\theta)\mathbf{E}_1 + \cos(\theta)\mathbf{E}_2) - \sin(\alpha)\mathbf{E}_3. \tag{33}$$

The Euler angles α and θ are the Gaussian coordinates used to parameterize the sphere on which the tangent indicatrix lies. Furthermore, the angle α is the tilt angle of the disk. The disk is vertical when $\alpha = 0$ and collides with the horizontal surface when $\alpha = \pm\pi/2$.

Recalling some results from O'Reilly (1996), and using results which have the same form as (22), it may be shown for a rolling disk that

$$\dot{\theta} = f_3(\alpha, A, B)\sec(\alpha),$$
$$\dot{\varphi} = f_2(\alpha, A, B) - f_3(\alpha, A, B)\tan(\alpha), \tag{34}$$

where

$$\sqrt{\frac{4g}{(k^2+4)R}}\, f_2(\alpha, A, B) = AP_\mu(\sin(\alpha)) + BP_\mu(-\sin(\alpha)),$$
$$\sqrt{\frac{4g}{(k^2+4)R}}\, f_3(\alpha, A, B) = \frac{k^2+2}{2}\left[AP^1_\mu(\sin(\alpha)) - BP^1_\mu(-\sin(\alpha))\right]. \tag{35}$$

In (35), A and B are constants (integrals of the motion), k^2 is a parameter which is 1 for a disk and 2 for a hoop, $P_\mu(\cdot)$ and $P^1_\mu(\cdot)$ are associated Legendre functions, and

$$\mu = -\frac{1}{2} + \frac{1}{2}\sqrt{\frac{k^2-14}{k^2+2}}. \tag{36}$$

The tilt angle α is determined by a second-order differential equation of the form $d^2\alpha/dt^2 = -\partial U(\alpha, A, B)/\partial\alpha$ (O'Reilly, 1996).

To determine the relative rotation Δv_2 of the rolling disk, in general recourse must be made to numerical methods. The

[9] The reader is referred to Cushman, Hermans, and Kemppainen (1996) and O'Reilly (1996) where extensive lists of references to other works on the dynamics of disks can be found.

Downloaded 04 May 2010 to 171.66.16.34. Redistribution subject to ASME license or copyright; see http://www.asme.org/terms/Terms_Use.cfm

principal difficulty lies in determining T such that $\mathbf{e}_2(t_0) = \mathbf{e}_2(t_0 + T)$. We do not pursue this matter here and confine our attention to steady motions. A steady motion of the disk arises when the tilt angle α is a constant α_0. For a given A and B, α_0 is determined by the equation $\partial U(\alpha_0, A, B)/\partial\alpha = 0$. In this case, it follows from (33) and (34), that $\mathbf{e}_2(t)$ either describes a circle on the unit sphere or, in the event that $A = B \neq 0$ and $\alpha_0 = 0$, a fixed point. The latter case corresponds to a vertical disk moving in a straight line. In the former case, which is of interest here, the center of mass of the disk either describes a circle or it is stationary. A simple calculation using (33) and $(34)_1$, shows that $\mathbf{e}_2(t_0) = \mathbf{e}_2(t_0 + T)$ when

$$T = \frac{2\pi \cos(\alpha_0)}{f_3(\alpha_0, A, B)}. \tag{37}$$

As noted in Section 4, three equivalent methods may be used to determine $\Delta\upsilon_2$. The most direct method is to first notice that $\upsilon_2 = \varphi$, and to then use $(34)_2$ to conclude that

$$\Delta\upsilon_2 = \frac{2\pi f_2(\alpha_0, A, B)\cos(\alpha_0)}{f_3(\alpha_0, A, B)} - 2\pi \sin(\alpha_0). \tag{38}$$

The second method uses a decomposition of the form (20). As $\dot{\mathbf{e}}_2(t_0) = \dot{\mathbf{e}}_2(t_0 + T)$, $\Delta\eta_2 = 0$ and

$$\Delta\upsilon_2 = \Delta\phi_2 = \tan^{-1}\left(\frac{\omega_3(t_0+T)}{\omega_1(t_0+T)}\right) - \tan^{-1}\left(\frac{\omega_3(t_0)}{\omega_1(t_0)}\right). \tag{39}$$

Using (32) and some trigonometric identities, this method again yields (38). The third method uses a decomposition of the form (23). One calculates the dynamic ($\Delta\upsilon_{2d}$) and geometric ($\Delta\upsilon_{2g}$) phases by integrating $\omega_2(t)$ and determining the solid angle subtended by $\mathbf{e}_2$ on the unit sphere, respectively. After some calculations, we find that

$$\Delta\upsilon_{2d} = \frac{2\pi f_2(\alpha_0, A, B)\cos(\alpha_0)}{f_3(\alpha_0, A, B)},$$

$$\Delta\upsilon_{2g} = 2\pi - 2\pi \sin(\alpha_0). \tag{40}$$

Because $\Delta\upsilon_2 = \Delta\upsilon_{2d} + \Delta\upsilon_{2g}$, (40) is in expected agreement with (38) (modulo additive multiples of 2π).

The relative rotations in a sliding disk can be determined from the previous analysis by replacing f_2 by g_2 and f_3 by g_3:

$$\sqrt{\frac{4g}{(k^2+4)R}}\, g_2(\alpha, C, D) = C,$$

$$\sqrt{\frac{4g}{(k^2+4)R}}\, g_3(\alpha, C, D) = \sec(\alpha)(D - 2C\sin(\alpha)), \tag{41}$$

where C and D are integrals of the motion (cf. O'Reilly, 1996). A second-order differential equation, which may be found in this reference, governs $\alpha(t)$. Again, for a steady motion $\alpha = \alpha_0$ and $\mathbf{e}_2(t)$ either describes a circle on the unit sphere or, in the event that $D = 0$ and $\alpha_0 = 0$, a fixed point. For the former case, the relative rotation is

$$\Delta\upsilon_2 = \frac{2\pi C \cos^2(\alpha_0)}{D - 2C\sin(\alpha_0)} - 2\pi \sin(\alpha_0). \tag{42}$$

The latter case corresponds to a vertical disk moving in a straight line. It is of interest to note that a disk spinning steadily about the $\mathbf{E}_3$-axis arises when $\alpha_0 = 0$, $C = 0$, and $D \neq 0$. In this case, (42) provides the result $\Delta\upsilon_2 = 0$: which is expected because $\dot{\varphi} = 0$ for this motion.

Acknowledgment

The author is grateful to three anonymous reviewers for their constructive criticisms of an earlier draft of this paper.

References

Anandan, J., 1988, "Geometric Angles in Quantum and Classical Physics," *Physics Letters A,* Vol. 129, pp. 201–207.

Antman, S. S., 1995, *Nonlinear Problems of Elasticity,* Springer-Verlag, New York.

Appell, P., 1900, "Sur l'Intégration des Équations du Mouvement d'un Corps Pesant de Révolution Roulant par un Arête Circulaire sur un Plan Horizontal; Cas Particulier du Cerceau," *Rendiconti del Circolo Mathematico di Palermo* Vol. 14, pp. 1–6.

Balakrishnan, R., Bishop, A. R., and Dandoloff, R., 1993a, "Anholonomy of a Moving Space Curve and Applications to Classical Magnetic Chains," *Physical Review B,* Vol. 47, pp. 3108–3117.

Balakrishnan, R., Bishop, A. R., and Dandoloff, R., 1993b, "Gauge Freedom, Anholonomy, and Hopf Index of a Three-Dimensional Unit Vector Field," *Physical Review B,* Vol. 47, pp. 5438–5441.

Berry, M. V., 1990, "Anticipations of the Geometric Phase," *Physics Today,* Vol. 43, No. 12, pp. 34–40.

Berry, M. V., and Hannay, J. H., 1988, "Classical Non-Adiabatic Angles," *Journal of Physics A,* Vol. 21, pp. L325–L331.

Bloch, A. M., Krishnaprasad, P. S., Marsden, J. E., and Sánchez de Alvarez, G., 1992, "Stabilization of Rigid Body Dynamics by Internal and External Torques," *Automatica,* Vol. 28, pp. 745–756.

Bloch, A. M., Reyhanoglu, M., and McClamroch, N. H., 1992, "Control and Stabilization of Nonholonomic Dynamic Systems," *IEEE Transactions on Automatic Control,* Vol. 37, pp. 1746–1757.

Casey, J., 1983, "A Treatment of Rigid Body Dynamics," ASME JOURNAL OF APPLIED MECHANICS, Vol. 50, pp. 905–907. (Errata, Vol. 51, p. 227).

Casey, J., 1995, "On the Advantages of a Geometric Viewpoint in the Derivation of Lagrange's Equations for a Rigid Continuum," *Journal of Applied Mathematics and Physics (ZAMP),* Vol. 46, pp. S805–S847.

Casey, J., and Lam, V. C., 1986, "On the Relative Angular Velocity Tensor," ASME *Journal of Mechanisms, Transmission and Automation in Design,* Vol. 108, pp. 399–400.

Cushman, R., Hermans, J., and Kemppainen, D., 1996, "The Rolling Disc," *Nonlinear Dynamical Systems and Chaos,* H. W. Broer, S. A. van Gils, I. Hoveijn, and F. Takens, eds., *Progress in Nonlinear Differential Equations and their Applications,* Birkhäuser, Basel, Vol. 19, pp. 21–60.

Darboux, G., 1889, *Leçons sur la Théorie Générale des Surfaces,* Part II, Gauthier-Villars, Paris.

Goldstein, H., 1980, *Classical Mechanics,* 2nd ed., Addison-Wesley, Reading, MA.

Goodman, L. E., and Robinson, A. R., 1958, "Effect of Finite Rotations on Gyroscopic Sensing Devices," ASME JOURNAL OF APPLIED MECHANICS, Vol. 25, pp. 210–213.

Hannay, J. H., 1985, "Angle Variable Holonomy in Adiabatic Excursion of an Integrable Hamiltonian," *Journal of Physics A,* Vol. 18, pp. 221–230.

Kelly, S. D., and Murray, R. M., 1995, "Geometric Phases and Robot Locomotion," *Journal of Robotic Systems,* Vol. 12, pp. 417–431.

Kelvin, Lord, and Tait, P. G., 1912, *Treatise on Natural Philosophy,* Part I, Reprinted 6th ed., Cambridge University Press, Cambridge, UK.

Korteweg, D. J., 1900, "Extrait d'une Lettre à M. Appell," *Rendiconti del Circolo Mathematico di Palermo,* Vol. 14, pp. 7–8.

Kreyszig, E., 1959, *Differential Geometry,* University of Toronto Press, Toronto.

Kugler, M., and Shtrikman, S., 1988, "Berry's Phase, Locally Inertial Frames, and Classical Analogues," *Physical Review D,* Vol. 37, pp. 934–937.

Levi, M., 1993, "Geometric Phases in the Motion of Rigid Bodies," *Archive for Rational Mechanics and Analysis,* Vol. 122, pp. 213–229.

Love, A. E. H., 1893, *A Treatise on the Mathematical Theory of Elasticity,* Vol. II, Cambridge University Press, Cambridge, UK.

Marsden, J. E., and Ratiu, T. S., 1994, *Introduction to Mechanics and Symmetry,* Springer-Verlag, New York.

McConnell, A. J., 1947, *Applications of the Absolute Differential Calculus,* Corrected ed., Blackie and Son, London.

Montgomery, R., 1991, "How Much Does a Rigid Body Rotate? A Berry's Phase From the 18th Century," *American Journal of Physics,* Vol. 59, pp. 394–398.

Naghdi, P. M., and Rubin, M. B., 1984, "Constrained Theories of Rods," *Journal of Elasticity,* Vol. 14, pp. 343–361.

O'Reilly, O. M., 1996, "The Dynamics of Rolling Disks and Sliding Disks," *Nonlinear Dynamics,* Vol. 10, pp. 287–305.

Spivak, M., 1979, *A Comprehensive Introduction to Differential Geometry,* Vol. 3, 2nd ed., Publish or Perish, Berkeley, CA.

Synge, J. L., and Griffith, B. A., 1942, *Principles of Mechanics,* McGraw-Hill, New York.

Thomson, W., and Tait, P. G., 1867, *Treatise on Natural Philosophy,* Vol. 1, Clarendon Press, Oxford, UK.

Vierkandt, A., 1892, "Über gleitende und rollende Bewegung," *Monatshefte für Mathematik und Physik,* Vol. 3, pp. 31–54 and 97–134.

Whittaker, E. T., 1944, *A Treatise on the Analytical Dynamics of Particles and Rigid Bodies,* 4th ed., Dover Publications, New York.

Zhuravlev, V. F., 1996, "The Solid Angle Theorem in Rigid Body Dynamics," *Journal of Applied Mathematics and Mechanics (PMM),* Vol. 60, pp. 319–322.

Downloaded 04 May 2010 to 171.66.16.34. Redistribution subject to ASME license or copyright; see http://www.asme.org/terms/Terms_Use.cfm

Stochastic Averaging of Quasi-Integrable Hamiltonian Systems

W. Q. Zhu
Professor.

Z. L. Huang
Associate Professor.

Y. Q. Yang
Graduate Student.

Department of Mechanics,
Zhejiang University,
Hangzhou 310027, R. R. China

A stochastic averaging method is proposed to predict approximately the response of quasi-integrable Hamiltonian systems, i.e., multi-degree-of-freedom integrable Hamiltonian systems subject to lightly linear and (or) nonlinear dampings and weakly external and (or) parametric excitations of Gaussian white noises. According to the present method an n-dimensional averaged Fokker-Planck-Kolmogrov (FPK) equation governing the transition probability density of n action variables or n independent integrals of motion can be constructed in nonresonant case. In a resonant case with α resonant relations, an $(n + \alpha)$-dimensional averaged FPK equation governing the transition probability density of n action variables and α combinations of phase angles can be obtained. The procedures for obtaining the stationary solutions of the averaged FPK equations for both resonant and nonresonant cases are presented. It is pointed out that the Stratonovich stochastic averaging and the stochastic averaging of energy envelope are two special cases of the present stochastic averaging. Two examples are given to illustrate the application and validity of the proposed method.

1 Introduction

The stochastic averaging method is a powerful approximate technique for prediction of the response, decision of the stability, and estimation of the reliability of linear and nonlinear oscillators with lightly linear and (or) nonlinear dampings subject to weakly external (additive) and (or) parametric (multiplicative) excitations of wide-band random processes. It has been extensively used in theoretical investigation and engineering applications of nonlinear random vibration (Roberts and Spanos, 1986; Zhu, 1988, 1996). At present, there are basically two versions of the stochastic averaging method. One is often called Stratonovich stochastic averaging or standard stochastic averaging. It was initially developed by Stratonovich (1963) and later justified rigorously by Khasminskii (1966). This version of stochastic averaging method is applicable to multi-degree-of-freedom quasi-linear systems, i.e., multi-degree-of-freedom linear conservative systems subject to lightly linear and (or) nonlinear dampings and weakly external and (or) parametric excitations of wide-band random processes. The other version is usually called stochastic averaging of energy envelope or quasi-conservative averaging. It was initially proposed by Khasminskii (1964) and Landa and Stratonovich (1962). Later, the stochastic averaging equation of energy envelope was rederived by Zhu (1983) and Zhu and Lin (1991) based on a theorem due to Khasminskii (1968) and the possible change of the energy envelope due to Wong-Zakai correct terms was taken into account. This version of stochastic averaging method is applicable to single degree-of-freedom quasi-conservative systems, i.e., single degree-of-freedom linear or nonlinear conservative systems subject to lightly linear and (or) nonlinear dampings and weakly external and (or) parametric excitations of wide-band random processes.

There was no stochastic averaging method available for multi-degree-of-freedom quasi-nonlinear conservative systems until recently the present authors (1997) proposed a stochastic averaging method for multi-degree-of-freedom quasi-nonintegrable Hamiltonian systems, i.e., multi-degree-of-freedom nonintegrable Hamiltonian systems subject to lightly linear and (or) nonlinear dampings and weakly external and (or) parametric excitations of Gaussian white noises. Following this method, a one-dimensional averaged FPK equation governing the transition probibility density of the Hamiltonian can be constructed and, at least, the approximate stationary probability density of the response can be obtained readily. The results for an example show that the stochastic averaging method for quasi-nonintegrable Hamiltonian systems is feasible and valid, and consistent with the equivalent nonlinear system method for stochastically excited and dissipated nonintegrable Hamiltonian systems (Zhu, Soong, and Lei, 1994).

In the present paper, as a companion of the stochastic averaging for quasi-nonintegrable Hamiltonian systems (Zhu and Yang, 1997), a stochastic averaging method of quasi-integrable Hamiltonian systems is proposed. First, some concepts concerning integrable Hamiltonian systems are briefly reviewed. Then, the stochastic averaging equations for quasi-integrable Hamiltonian systems, including nonresonant and resonant systems, are derived based on a theorem due to Khasminskii (1968) and the procedures for obtaining the stationary solutions of the averaged FPK equations are proposed. Finally, two examples are given to illustrate the application and validity of the proposed method.

2 Integrable Hamiltonian Systems

Consider an n-degree-of-freedom Hamiltonian dynamical system governed by the following n pairs of Hamiltonian equations

$$\dot{q}_i = \frac{\partial H}{\partial p_i} \tag{1a}$$

$$\dot{p}_i = -\frac{\partial H}{\partial q_i}$$

$$i = 1, 2, \ldots, n \tag{1b}$$

where q_i and p_i are generalized displacements and generalized momenta, respectively; $H = H(\mathbf{q}, \mathbf{p})$ is a Hamiltonian with continuous first-order derivatives. A Hamiltonian system of n degree-of-freedom is said to be integrable or completely inte-

Contributed by the Applied Mechanics Division of THE AMERICAN SOCIETY OF MECHANICAL ENGINEERS for publication in the ASME JOURNAL OF APPLIED MECHANICS.

Discussion on this paper should be addressed to the Technical Editor, Professor Lewis T. Wheeler, Department of Mechanical Engineering, University of Houston, Houston, TX 77204-4792, and will be accepted until four months after final publication of the paper itself in the ASME JOURNAL OF APPLIED MECHANICS.

Manuscript received by the ASME Applied Mechanics Division, June 12, 1995; final revision, Apr. 9, 1997. Associate Technical Editor: M. Shinozuka.

 Copyright © 1997 by ASME

Downloaded 04 May 2010 to 171.66.16.34. Redistribution subject to ASME license or copyright; see http://www.asme.org/terms/Terms_Use.cfm

grable if there exist n independent integrals of the motion H_1, $H_2, \ldots, H_n$, which are in involution. This last term means that the H_i all commute with each other, i.e.,

$$[H_i, H_j] = 0$$
$$i, j = 1, 2, \ldots, n \tag{2}$$

where

$$[H_i, H_j] = \frac{\partial H_i}{\partial p_k}\frac{\partial H_j}{\partial q_k} - \frac{\partial H_i}{\partial q_k}\frac{\partial H_j}{\partial p_k}$$
$$k = 1, 2, \ldots, n \tag{3}$$

is the Poisson bracket of H_i and H_j.

The integrability of a Hamiltonian system can also be stated as follows. A Hamiltonian system of n degree-of-freedom governed by Eqs. (1a) and (1b) is said to be integrable or completely integrable if there exists a set of canonical transformations

$$I_i = I_i(\mathbf{q}, \mathbf{p}) \tag{4a}$$
$$\theta_i = \theta_i(\mathbf{q}, \mathbf{p})$$
$$i = 1, 2, \ldots, n \tag{4b}$$

such that the new Hamiltonian equations are of the following canonical form:

$$\dot{I}_i = -\frac{\partial}{\partial \theta_i} H(\mathbf{I}) = 0 \tag{5a}$$

$$\dot{\theta}_i = \frac{\partial}{\partial I_i} H(\mathbf{I}) = \omega_i(\mathbf{I}) \tag{5b}$$

where I_i and ω_i are action variables and frequencies associated with each degree-of-freedom, respectively; θ_i is the angle variable conjugated to I_i; and $H(\mathbf{I})$ is the transformed Hamiltonian independent of θ_i. Equations (5a) and (5b) are then trivially integrated to yield

$$I_i = \text{const.} \tag{6a}$$
$$\theta_i = \omega_i(\mathbf{I})t + \delta_i$$
$$i = 1, 2, \ldots, n \tag{6b}$$

where δ_i are arbitrary constants. Note that the set of I_i and δ_i constitute the set of $2n$ constants of integration. I_i are a set of such special constants that once they are known, the other set of constants δ_i can be obtained immediately. Thus, I_i can be regarded as n specially independent integrals of motion which satisfy Eq. (2), i.e.,

$$[I_i, I_j] = 0$$
$$i, j = 1, 2, \ldots, n. \tag{7}$$

One way to find the action-angle variables for a given Hamiltonian system is to solve the Hamilton-Jacobi equation associated with the system. However, this is generally a very difficult task except for a class of mechanical systems known as being separable. A rather simple subclass of the separable systems is one in which the Hamiltonian itself is the sum of n independent integrals of motion

$$H = \sum_{i=1}^{n} H_i(q_i, p_i). \tag{8}$$

The phase-space orbits of an n degree-of-freedom integrable Hamiltonian system will lie on an n-dimensional torus. The n-torus is a naturally periodic object and can be considered as the direct product of n independent 2π periodicities. The precise behavior of the orbits is determined by the values of frequencies ω_i. If ω_i are not rationally related, the orbits on the torus with that set of frequencies are almost periodic and the system is termed nonresonant. In this case, a single orbit will eventually cover the torus uniformly, that is, the flow is ergodic on the torus. The orbits on the torus are periodic or closed and the system is called completely resonant if ω_i are related by $n-1$ equations of the following form:

$$k_i^u \omega_i = 0$$
$$u = 1, 2, \ldots, n-1; \quad i = 1, 2, \ldots, n \tag{9}$$

where k_i^u are integers and not all zero for a fixed u. Obviously, ω_i may satisfy α $(1 \le \alpha < n-1)$ resonant relations of form (9). In this case, the orbits are periodic on some subtorus and almost periodic on the complemantary subtorus and the system is called partially resonant.

An integrable Hamiltonian system is termed nondegenerate if the condition

$$\det \left| \frac{\partial \omega_i(\mathbf{I})}{\partial I_j} \right| = \det \left| \frac{\partial^2 H(\mathbf{I})}{\partial I_i \partial I_j} \right| \neq 0 \tag{10}$$

is satisfied. This ensures that the frequencies vary from torus to torus and the system is nonlinear. On a given energy shell, some tori will be completely or partially covered by periodic orbits, whereas other tori will be covered by almost periodic orbits. For a nondegenerate system, the set of tori completely or partially covered with periodic orbits, although dense, will be infinitely outnumbered by the tori covered with almost periodic orbits. Thus, a nondegenerate system can be regarded as a nonresonant system.

For more information on the integrable Hamiltonian systems see Arnold (1989) and Tabor (1989).

3 Quasi-Integrable Hamiltonian Systems

Consider a quasi-integrable Hamiltonian system of n degree-of-freedom governed by the following equations of motion:

$$\dot{Q}_i = \frac{\partial H'}{\partial P_i} \tag{11a}$$

$$\dot{P}_i = -\frac{\partial H'}{\partial Q_i} - \epsilon c_{ij}\frac{\partial H'}{\partial P_j} + \epsilon^{1/2} f_{ik} W_k(t)$$
$$i, j = 1, 2, \ldots, n; \quad k = 1, 2, \ldots, m \tag{11b}$$

where Q_i and P_i are generalized displacements and momenta, respectively; $H' = H'(\mathbf{Q}, \mathbf{P})$ is twice differentiable Hamiltonian; $c_{ij} = c_{ij}(\mathbf{Q}, \mathbf{P})$ are differentiable functions; $f_{ik} = f_{ik}(\mathbf{Q}, \mathbf{P})$ are twice differentiable functions; ϵ is a small positive parameter; $W_k(t)$ are Gaussian white noises in the sense of Stratonovich with correlation functions

$$E[W_k(t)W_l(t+\tau)] = 2D_{kl}\delta(\tau)$$
$$k, l = 1, 2, \ldots, m. \tag{12}$$

The system governed by Eqs. (11a) and (11b) is generally nonlinear. The first summation terms on the right-hand side of Eq. (10b) may represent a set of lightly linear and (or) nonlinear damping forces while the second summation terms may include weakly external (additive) and (or) parametric (multiplicative) excitations of Gaussian white noises.

Equations (11a) and (11b) are equivalent to the following set of Itô equations:

$$dQ_i = \frac{\partial H'}{\partial P_i}\,dt \tag{13a}$$

$$dP_i = -\left(\frac{\partial H'}{\partial Q_i} + \epsilon c_{ij}\frac{\partial H'}{\partial P_j} - \epsilon D_{kl} f_{jl}\frac{\partial f_{ik}}{\partial P_j}\right)dt + \epsilon^{1/2} f_{ik}\,dB_k(t)$$
$$i, j = 1, 2, \ldots, n; \quad k, l = 1, 2, \ldots, m \tag{13b}$$

Downloaded 04 May 2010 to 171.66.16.34. Redistribution subject to ASME license or copyright; see http://www.asme.org/terms/Terms_Use.cfm

where $B_k(t)$ are the Wiener processes. The double summation terms on the right-hand side of Eq. (13b) are known as the Wong-Zakai correct terms (Wong and Zakai, 1965). These terms usually can be splitted into two parts: one has the effect of modifying the conservative forces and another modifying the damping forces. The first part can be combined with $-\partial H'/\partial Q_i$ to form an overall effective conservative forces $-\partial H/\partial Q_i$ with a new Hamiltonian $H = H(\mathbf{Q}, \mathbf{P})$ and with $\partial H/\partial P_i = \partial H'/\partial P_i$. The second part may be combined with $-\epsilon c_{ij}\partial H'/\partial P_j$ to constitute an effective damping forces $-\epsilon m_{ij}\partial H/\partial P_j$ with $m_{ij} = m_{ij}(\mathbf{Q}, \mathbf{P})$. With these accomplished, Eqs. (13a) and (13b) can be rewritten as

$$dQ_i = \frac{\partial H}{\partial P_i}\,dt \tag{14a}$$

$$dP_i = -\left(\frac{\partial H}{\partial Q_i} + \epsilon m_{ij}\frac{\partial H}{\partial P_j}\right)dt + \epsilon^{1/2} f_{ik}\,dB_k(t)$$

$$i, j = 1, 2, \ldots, n; \quad k = 1, 2, \ldots, m. \tag{14b}$$

In the following it is assumed that the Hamiltonian system governed by Eqs. (14a) and (14b) with $\epsilon = 0$ is integrable.

4 Stochastic Averaging Equations of Quasi-Integrable Hamiltonian Systems

The stochastic averaging equations of a quasi-integrable Hamiltonian system may be of one of the following three forms, depending upon whether the action-angle variables are obtainable or not and whether the Hamiltonian system is resonant or nonresonant.

4.1 Nonresonant Hamiltonian Systems With Known Action-Angle Variables. At first, consider the case where the Hamiltonian system governed by Eqs. (14a) and (14b) with $\epsilon = 0$ is nonresonant and the action-angle variables of the system are obtainable. Introduce the following canonical transformations:

$$I_r = I_r(\mathbf{Q}, \mathbf{P}) \tag{15a}$$

$$\Theta_r = \Theta_r(\mathbf{Q}, \mathbf{P})$$

$$r = 1, 2, \ldots, n \tag{15b}$$

where I_r and Θ_r are action-angle variables. The Itô equations for I_r and Θ_r can be obtained from Eqs. (14a) and (14b) by using Itô differential rule (Itô, 1951) as follows:

$$dI_r = \epsilon\left(-m_{ij}\frac{\partial H}{\partial P_j}\frac{\partial I_r}{\partial P_i} + D_{kl}f_{ik}f_{jl}\frac{\partial^2 I_r}{\partial P_i\partial P_j}\right)dt + \epsilon^{1/2}\frac{\partial I_r}{\partial P_i}f_{ik}\,dB_k(t) \tag{16a}$$

$$d\Theta_r = \left(\omega_r - \epsilon m_{ij}\frac{\partial H}{\partial P_j}\frac{\partial \Theta_r}{\partial P_i} + \epsilon D_{kl}f_{ik}f_{jl}\frac{\partial^2\Theta_r}{\partial P_i\partial P_j}\right)dt + \epsilon^{1/2}\frac{\partial\Theta_r}{\partial P_i}f_{ik}\,dB_k(t)$$

$$r, i, j = 1, 2, \ldots, n; \quad k = 1, 2, \ldots, m \tag{16b}$$

where Q_i and P_i on the right-hand sides of Eqs. (16a) and (16b) should be replaced by I_r and Θ_r in terms of Eqs. (15a) and (15b).

It is seen from Eqs. (16a) and (16b) that Θ_r are rapidly varying processes while I_r slowly varying ones. According to a theorem due to Khasminskii (1968), the I_r converge in probability to an n-dimensional diffusion process as $\epsilon \to 0$, in a time interval $0 \le t \le T$, where $T \sim 0(\epsilon^{-1})$. In other words, the I_r may be replaced in the first approximation by an n-dimensional diffusion process for small ϵ. For simplicity, the same symbol I_r will be used to denote the rth component of this diffusion process.

The Itô stochastic differential equations for this n-dimensional diffusion process are obtained by applying time averaging to Eq. (16a) under the condition that the I_r on the right-hand side of Eq. (16a) keep constant. Since the phase flow of an integrable Hamiltonian system in nonresonant case is ergodic on the n-dimensional torus, the time averaging can be replaced by phase space average. Thus, the averaged Itô differential equations for I_r are of the form

$$dI_r = \epsilon U_r(\mathbf{I})dt + \epsilon^{1/2}V_{rk}(\mathbf{I})dB_k(t)$$

$$r = 1, 2, \ldots, n, \quad k = 1, 2, \ldots, m \tag{17}$$

and the averaged FPK equation associated with Eq. (17) is

$$\frac{\partial p}{\partial t} = \epsilon\left\{-\frac{\partial}{\partial I_r}[a_r(I)p] + \frac{1}{2}\frac{\partial^2}{\partial I_r\partial I_s}[b_{rs}(I)p]\right\} \tag{18}$$

where

$$a_r(\mathbf{I}) = U_r(\mathbf{I}) = \frac{1}{(2\pi)^n}\int_0^{2\pi}\left(-m_{ij}\frac{\partial H}{\partial p_j}\frac{\partial I_r}{\partial p_i} + D_{kl}f_{ik}f_{jl}\frac{\partial^2 I_r}{\partial p_i\partial p_j}\right)d\theta \tag{19a}$$

$$b_{rs}(\mathbf{I}) = 2[\mathbf{V}\mathbf{D}\mathbf{V}^T]_{rs} = \frac{1}{(2\pi)^n}\int_0^{2\pi} 2D_{kl}f_{ik}f_{jl}\frac{\partial I_r}{\partial p_i}\frac{\partial I_s}{\partial p_j}\,d\theta$$

$$r, s, i, j = 1, 2, \ldots, n; \quad k, l = 1, 2, \ldots, m \tag{19b}$$

in which $\theta = [\theta_1, \theta_2, \ldots, \theta_n]^T$; $\mathbf{V} = [V_{rk}]$; $\mathbf{D} = [D_{kl}]$ and $\int_0^{2\pi}[\cdot]d\theta$ represents an n-fold integral. In Eq. (18), $p = p(\mathbf{I}, t|\mathbf{I}_0)$ with initial condition

$$p(\mathbf{I}, 0|\mathbf{I}_0) = \delta(\mathbf{I} - \mathbf{I}_0) \tag{20}$$

or $p = p(\mathbf{I}, t)$ with initial condition

$$p(\mathbf{I}, 0) = p(\mathbf{I}_0) \tag{21}$$

depending upon whether an initial state or an initial probability density is specified. The averaged FPK equation is also subjected to appropriate boundary conditions, i.e.,

$$-a_r(\mathbf{I})p + \frac{1}{2}\frac{\partial}{\partial I_s}[b_{rs}(\mathbf{I})p] = 0, \quad \mathbf{I} \in S$$

$$r, s = 1, 2, \ldots, n \tag{22}$$

which imply vanishing probability flows in n directions at the boundaries.

4.2 Resonant Hamiltonian Systems With Known Action-Angle Variables. Suppose that the integrable Hamiltonian system governed by Eqs. (14a) and (14b) with $\epsilon = 0$ is nearly resonant with the following α ($1 \le \alpha \le n - 1$) resonant relations

$$k_r^u\omega_r = 0(\epsilon)$$

$$u = 1, 2, \ldots, \alpha; \quad r = 1, 2, \ldots, n \tag{23}$$

and the action-angle variables are obtainable. Introduce α combinations Φ_u of angle variables

$$\Phi_u = k_r^u\Theta_r$$

$$u = 1, 2, \ldots, \alpha, \quad r = 1, 2, \ldots, n \tag{24}$$

The Itô equations for Φ_u can be obtained through appropriate combinations of Eq. (16b) as follows:

Downloaded 04 May 2010 to 171.66.16.34. Redistribution subject to ASME license or copyright; see http://www.asme.org/terms/Terms_Use.cfm

$$d\Phi_u = 0(\epsilon) + \epsilon\left(-m_{ij}\frac{\partial H}{\partial P_j}\frac{\partial \Phi_u}{\partial P_i} + D_{kl}f_{ik}f_{jl}\frac{\partial^2 \Phi_u}{\partial P_i \partial P_j}\right)dt + \epsilon^{1/2}\frac{\partial \Phi_u}{\partial P_i}f_{ik}dB_k(t)$$

$$u = 1, 2, \ldots, \alpha; \quad i, j = 1, 2, \ldots, n; \quad k, l = 1, 2, \ldots, m. \tag{25}$$

In this case the stochastic system is governed by n equations in Eq. (16a), α equations in Eq. (25) and $n - \alpha$ equations in Eq. (16b), say the first $n - \alpha$ equations of Eq. (16b). It is seen from these equations that $I_1, \ldots, I_n, \Phi_1, \ldots, \Phi_\alpha$, are slowly varying processes while $\Theta_1, \ldots, \Theta_{n-\alpha}$ are rapidly varying processes. Based on the Khasminskii's theorem (Khasmiuskii, 1968), the I_r, Φ_u converge in probability to an $(n + \alpha)$-dimensional diffusion process as $\epsilon \to 0$, in a time interval $0 \leq t \leq T$, where $T \sim 0\ (\epsilon^{-1})$. For simplicity, the same symbols $I_1, \ldots, I_n, \Phi_1, \ldots, \Phi_\alpha$ will be used to denote the $n + \alpha$ components of this diffusion process.

The Itô equations for this $(n + \alpha)$-dimensional diffusion process are obtained by applying time averaging to Eqs. (16a) and (25) under the condition that I_r, Φ_u on the right-hand sides of Eqs. (16a) and (25) keep constant. Due to the similar reason as that in nonresonant case, this time averaging can be replaced by phase space averaging with respect to $\Theta_1, \ldots, \Theta_{n-\alpha}$. Thus, we obtain the following averaged FPK equation:

$$\frac{\partial p}{\partial t} = \epsilon\left[-\frac{\partial}{\partial I_r}(a_r p) - \frac{\partial}{\partial \varphi_u}(a_u p) + \frac{1}{2}\frac{\partial^2}{\partial I_r \partial I_s}(b_{rs}p) + \frac{\partial^2}{\partial I_r \partial \varphi_u}(b_{ru}p) + \frac{1}{2}\frac{\partial^2}{\partial \varphi_u \partial \varphi_v}(b_{uv}p)\right] \tag{26}$$

where

$$a_r = a_r(\mathbf{I}, \boldsymbol{\varphi}) = \frac{1}{(2\pi)^{n-\alpha}}\int_0^{2\pi}\left(-m_{ij}\frac{\partial H}{\partial p_j}\frac{\partial I_r}{\partial p_i} + D_{kl}f_{ik}f_{jl}\frac{\partial^2 I_r}{\partial p_i \partial p_j}\right)d\theta_1 \tag{27a}$$

$$a_u = a_u(\mathbf{I}, \boldsymbol{\varphi}) = \frac{1}{(2\pi)^{n-\alpha}}\int_0^{2\pi}\left(\frac{0(\epsilon)}{\epsilon} - m_{ij}\frac{\partial H}{\partial p_j}\frac{\partial \varphi_u}{\partial p_i} + D_{kl}f_{ik}f_{jl}\frac{\partial^2 \varphi_u}{\partial p_i \partial p_j}\right)d\theta_1 \tag{27b}$$

$$b_{rs} = b_{rs}(\mathbf{I}, \boldsymbol{\varphi}) = \frac{1}{(2\pi)^{n-\alpha}}\int_0^{2\pi} 2D_{kl}f_{ik}f_{jl}\frac{\partial I_r}{\partial p_i}\frac{\partial I_s}{\partial p_j}d\theta_1 \tag{27c}$$

$$b_{ru} = b_{ru}(\mathbf{I}, \boldsymbol{\varphi}) = \frac{1}{(2\pi)^{n-\alpha}}\int_0^{2\pi} 2D_{kl}f_{ik}f_{jl}\frac{\partial I_r}{\partial p_i}\frac{\partial \varphi_u}{\partial p_j}d\theta_1 \tag{27d}$$

$$b_{uv} = b_{uv}(\mathbf{I}, \boldsymbol{\varphi}) = \frac{1}{(2\pi)^{n-\alpha}}\int_0^{2\pi} 2D_{kl}f_{ik}f_{jl}\frac{\partial \varphi_u}{\partial p_i}\frac{\partial \varphi_v}{\partial p_j}d\theta_1$$

$$r, s, i, j = 1, 2, \ldots, n; \quad u, v = 1, 2, \ldots, \alpha; \quad k, l = 1, 2, \ldots, m. \tag{27e}$$

in which $\boldsymbol{\varphi} = [\varphi_1, \varphi_2, \ldots, \varphi_\alpha]^T$ and $\theta_1 = [\theta_1, \theta_2, \ldots, \theta_{n-\alpha}]^T$. In Eq. (26), $p = p(\mathbf{I}, \boldsymbol{\varphi}, t|\mathbf{I}_0, \boldsymbol{\varphi}_0)$ with initial conditions

$$p(\mathbf{I}, \boldsymbol{\varphi}, 0|\mathbf{I}_0, \boldsymbol{\varphi}_0) = \delta(\mathbf{I} - \mathbf{I}_0)\delta(\boldsymbol{\varphi} - \boldsymbol{\varphi}_0) \tag{28}$$

or $p = p(\mathbf{I}, \boldsymbol{\varphi}, t)$ with initial condition

$$p(\mathbf{I}, \boldsymbol{\varphi}, 0) = p(\mathbf{I}_0, \boldsymbol{\varphi}_0). \tag{29}$$

Averaged FPK Eq. (26) is also subjected to appropriate boundary conditions. For examples, the conditions at the boundary $\mathbf{I} \in S$ are similar to those in Eq. (22) while p is a periodic function of φ_u with period 2π.

4.3 Nondegenerate Systems With Known N Independent Integrals Of Motion. Now suppose that the Hamiltonian system governed by Eqs. (14a) and (14b) with $\epsilon = 0$ is nondegenerate and n independent of integrals motion H_r are known. In this case the action-angle variables are often difficult to obtain and the system can be treated as nonresonant. Introduce transformations

$$H_r = H_r(\mathbf{Q}, \mathbf{P}) \tag{30}$$

and take $Q_1, \ldots, Q_n, H_1, \ldots, H_n$ as new variables. The Itô equations for H_r are obtained from Eqs. (14a) and (14b) by using Itô differential rule as follows:

$$dH_r = \epsilon\left(-m_{ij}\frac{\partial H}{\partial P_j}\frac{\partial H_r}{\partial P_i} + D_{kl}f_{ik}f_{jl}\frac{\partial^2 H_r}{\partial P_i \partial P_j}\right)dt + \epsilon^{1/2}\frac{\partial H_r}{\partial P_i}f_{ik}dB_k(t)$$

$$r, i, j = 1, 2, \ldots, n; \quad k, l = 1, 2, \ldots, m \tag{31}$$

while the Itô equations for Q_r are still those in Eq. (14a), provided P_i on the right-hand side of Eqs. (14a) and (31) are replaced by H_r in terms of Eq. (30). It is seen from Eqs. (14a) and (31) that Q_r are rapidly varying processes while H_r are slowly varying processes. According to the Khasminskii's theorem (Khasminskii, 1968), the H_r converge in probability to an n-dimensional diffusion process as $\epsilon \to 0$, in a time interval $0 \leq t \leq T$, where $T \sim 0(\epsilon^{-1})$. For simplicity, the same symbol H_r will be used to denote the rth component of this diffusion process.

The Itô equations for this n-dimensional diffusion process are obtained by applying time averaging to Eq. (31). The associated averaged FPK equation is of the form

$$\frac{\partial p}{\partial t} = \epsilon\left[-\frac{\partial}{\partial H_r}(a_r p) + \frac{1}{2}\frac{\partial^2}{\partial H_r \partial H_s}(b_{rs}p)\right] \tag{32}$$

where

$$a_r = a_r(\mathbf{H}) = \left\langle -m_{ij}\frac{\partial H}{\partial p_j}\frac{\partial H_r}{\partial p_i} + D_{kl}f_{ik}f_{jl}\frac{\partial^2 H_r}{\partial p_i \partial p_j}\right\rangle_t \tag{33a}$$

$$b_{rs} = b_{rs}(\mathbf{H}) = \left\langle 2D_{kl}f_{ik}f_{jl}\frac{\partial H_r}{\partial p_i}\frac{\partial H_s}{\partial p_j}\right\rangle_t \tag{33b}$$

in which $\mathbf{H} = [H_1, H_2, \ldots, H_n]^T$ and the symbol $\langle[\cdot]\rangle_t$ represents the following time-averaging operation:

$$\langle[\cdot]\rangle_t = \lim_{T\to\infty}\frac{1}{T}\int_{t_0}^{t_0+T}[\cdot]dt. \tag{34}$$

In performing the time-averaging operation, H_r are kept constant while q_r are treated as functions of time t.

The time averaging in Eqs. (33a) and (33b) may be replaced by phase-space averaging with respect to q_r depending upon the structures of n independent integrals of motion. For example, if the Hamiltonian H is the sum of n independent integrals H_i of motion, Eq. (8), and for each H_i there is a periodic orbit with period T_i, then the time averaging can be replaced by the averaging along these n periodic orbits sequently. Thus, the averaged drift and diffusion coefficients, instead of those in Eqs. (33a) and (33b), are

Downloaded 04 May 2010 to 171.66.16.34. Redistribution subject to ASME license or copyright; see http://www.asme.org/terms/Terms_Use.cfm

$$a_r = a_r(\mathbf{H}) = \frac{1}{T}\oint\left(-m_{rj}\frac{\partial H_j}{\partial p_j}\frac{\partial H_r}{\partial p_r} + D_{kl}f_{rk}f_{rl}\frac{\partial^2 H_r}{\partial p_r^2}\right) \times \prod_{\mu=1}^{n}\left(1\Big/\frac{\partial H_\mu}{\partial p_\mu}\right)dq_\mu \quad (35a)$$

$$b_{rs} = b_{rs}(\mathbf{H}) = \frac{1}{T}\oint\left(2D_{kl}f_{rk}f_{sl}\frac{\partial H_r}{\partial p_r}\frac{\partial H_s}{\partial p_s}\right) \times \prod_{\mu=1}^{n}\left(1\Big/\frac{\partial H_\mu}{\partial p_\mu}\right)dq_\mu \quad (35b)$$

where $\oint[\cdot]\prod_{\mu=1}^{n}dq_\mu$ represents an n-fold loop integral and

$$T = T(\mathbf{H}) = \prod_{\mu=1}^{n}T_\mu = \oint\prod_{\mu=1}^{n}\left(1\Big/\frac{\partial H_\mu}{\partial p_\mu}\right)dq_\mu. \quad (36)$$

In Eq. (32), $p = p(\mathbf{H}, t|\mathbf{H}_0)$ with initial condition

$$p(\mathbf{H}, 0|\mathbf{H}_0) = \delta(\mathbf{H} - \mathbf{H}_0) \quad (37)$$

or $p = p(\mathbf{H}, t)$ with initial condition

$$p(\mathbf{H}, 0) = p(\mathbf{H}_0) \quad (38)$$

depending upon whether an initial state or an initial probability density is specified. The averaged FPK equation is also subjected to appropriate boundary conditions, i.e.,

$$-a_r p + \frac{1}{2}\frac{\partial}{\partial H_s}(b_{rs}p) = 0, \quad \mathbf{H} \in S$$
$$r, s = 1, 2, \ldots, n, \quad (40)$$

which imply vanishing probability flows in n directions at the boundaries.

Before ending this section, two remarks concerning the relations between the present stochastic averaging and the Stratonovich stochastic averaging and the stochastic averaging of energy envelope are relevant. Obviously, for single degree-of-freedom quasi-Hamiltonian systems, the present stochastic averaging is reduced to the stochastic averaging of energy envelope. If the Hamiltonian system governed by Eqs. (14a) and (14b) with $\epsilon = 0$ is linear, then the quasi-Hamiltonian system governed by Eqs. (14a) and (14b) is a quasi-linear one. In this case, the action-angle variables are readily obtainable, the action variables can be replaced by the amplitudes and the present stochastic averaging in both nonresonant and resonant cases is reduced to the Stratonovich stochastic averaging. Therefore, the Stratonovich stochastic averaging and stochastic averaging of energy envelope are two special cases of the present stochastic averaging for multi-degree-of-freedom quasilinear systems and for single degree-of-freedom quasi-Hamiltonian systems, respectively.

5 Stationary Solutions of Averaged FPK Equations

The main advantage of the stochastic averaging of quasi-integrable Hamiltonian systems presented in the last section is to reduce the dimension of equations from $2n$ to n in nonresonant case, or to $n + \alpha$ in resonant case with α resonant relations. Another advantage of the stochastic averaging is to simplify the equations such that in the averaged FPK equations there is only potential probability flow and no circulatory probability flow. Under the conditions of vanishing probability flow at the boundaries, the probability flow may vanish everywhere inside the boundaries, that is, the averaged systems may belong to the class of stationary potential (Stratonovich, 1963), and the exact stationary solution of averaged FPK equation may be obtained.

The reduced FPK equation associated with averaged FPK Eq. (18) and boundary conditions (22) can be further reduced to the following n equations for vanishing probability flow in n directions

$$-a_r(\mathbf{I})p + \frac{1}{2}\frac{\partial}{\partial I_s}[b_{rs}(\mathbf{I})p] = 0$$
$$r, s = 1, 2, \ldots, n. \quad (40)$$

The solution of Eq. (40) may be assumed of the form

$$p(\mathbf{I}) = C\exp[-\lambda(\mathbf{I})] \quad (41)$$

where $\lambda(\mathbf{I})$ is the so-called probability potential and C is a normalization constant. Substituting Eq. (41) into Eq. (40), we obtain

$$b_{rs}\frac{\partial\lambda}{\partial I_s} = \frac{\partial b_{rs}}{\partial I_s} - 2a_r$$
$$r, s = 1, 2, \ldots, n. \quad (42)$$

These are n first-order linear partial differential equations for λ as function of I_r. If matrix $B = [b_{rs}]$ is nonsingular, so that its inverse $B^{-1} = G = [g_{rs}]$ exists, then Eq. (42) may be simplified to

$$\frac{\partial\lambda}{\partial I_i} = g_{ir}\left(\frac{\partial b_{rs}}{\partial I_s} - 2a_r\right). \quad (43)$$

If the following compatibility conditions are satisfied,

$$\frac{\partial}{\partial I_j}g_{ir}\left(\frac{\partial b_{rs}}{\partial I_s} - 2a_r\right) = \frac{\partial}{\partial I_i}g_{jr}\left(\frac{\partial b_{rs}}{\partial I_s} - 2a_r\right), \quad (44)$$

then a consistent λ function can be obtained as follows:

$$\lambda(\mathbf{I}) = \lambda_0 + \int_0^{(I_1, I_2, \ldots, I_n)}\frac{\partial\lambda}{\partial I_s}dI_s, \quad (45)$$

where the second summation terms on the right-hand side are a line integral and $\lambda_0 = \lambda(0)$. The exact stationary solution $p(\mathbf{I})$ of averaged FPK equation (18) is then obtained by substituting Eq. (45) into Eq. (41). The stationary probability density of generalized displacements and momenta can be derived from Eq. (41) as follows:

$$p(\mathbf{q}, \mathbf{p}) = p(\mathbf{I}, \boldsymbol{\theta})\left|\frac{\partial(\mathbf{I}, \boldsymbol{\theta})}{\partial(\mathbf{q}, \mathbf{p})}\right| = p(\boldsymbol{\theta}|\mathbf{I})p(\mathbf{I})\left|\frac{\partial(\mathbf{I}, \boldsymbol{\theta})}{\partial(\mathbf{q}, \mathbf{p})}\right| = \frac{1}{(2\pi)^n}p(\mathbf{I}) \quad (46)$$

where $|\partial(\mathbf{I}, \boldsymbol{\theta})/\partial(\mathbf{q}, \mathbf{p})|$ is the absolute value of the Jacobian determinant of the canonical transformations in Eqs. (15a) and (15b) and always equal to unity.

The exact stationary solution $p(\mathbf{H})$ of averaged FPK Eq. (32) can be obtained in a similar way and the stationary probability density in terms of $\mathbf{q}$ and $\mathbf{p}$ can be obtained as follows:

$$p(\mathbf{q}, \mathbf{p}) = p(\mathbf{q}, \mathbf{H})\left|\frac{\partial\mathbf{H}}{\partial\mathbf{p}}\right| = p(\mathbf{q}|\mathbf{H})p(\mathbf{H})\left|\frac{\partial\mathbf{H}}{\partial\mathbf{p}}\right| \quad (47)$$

where $|\partial(\mathbf{H})/\partial\mathbf{p}|$ is the absolute value of the Jacobian determi-

Downloaded 04 May 2010 to 171.66.16.34. Redistribution subject to ASME license or copyright; see http://www.asme.org/terms/Terms_Use.cfm

nant of the transformations in Eq. (30); $p(\mathbf{q}|\mathbf{H})$ is the probability density of $\mathbf{q}$ under the condition that $\mathbf{H}$ is constant. For the systems with separable Hamiltonian of form (8), a reasoning similar to that for single degree-of-freedom quasi-Hamiltonian systems (Stratonovich, 1963; Zhu, 1983) leads to

$$p(\mathbf{q}, \mathbf{p}) = p(\mathbf{H})/T(\mathbf{H}) \tag{48}$$

where T is defined by Eq. (36).

The exact stationary solution of averaged FPK Eq. (26) is more difficult to obtain. One way to obtain it is as follows. Assume that the solution is of the exponential form

$$p(\mathbf{I}, \boldsymbol{\phi}) = C \exp[-\lambda(\mathbf{I}, \boldsymbol{\phi})]. \tag{49}$$

Expand $\lambda(\mathbf{I}, \boldsymbol{\phi})$ and the drift and diffusion coefficients in Eqs. (27*a*) to (27*e*) into α-fold (finite or infinite) Fourier series with respect to $\boldsymbol{\phi}$. Substituting these expansions into Eq. (26) with $\partial p/\partial t = 0$, one obtains (finite or infinite) sets of equations of the form of Eq. (42) which must be satisfied by the Fouier coefficients of $\lambda(\mathbf{I}, \boldsymbol{\phi})$. The solution for $\lambda(\mathbf{I}, \boldsymbol{\phi})$ may be obtained under certain conditions. This procedure will be illustrated in example 1.

The stationary solution of averaged FPK Eq. (26) in terms of $\mathbf{q}$ and $\mathbf{p}$ is then

$$\begin{aligned} p(\mathbf{q}, \mathbf{p}) &= p(\mathbf{I}, \boldsymbol{\phi}, \boldsymbol{\theta}_1)\left|\frac{\partial(\mathbf{I}, \boldsymbol{\phi}, \boldsymbol{\theta}_1)}{\partial(\mathbf{q}, \mathbf{p})}\right| \\ &= p(\boldsymbol{\theta}_1|\mathbf{I}, \boldsymbol{\phi})p(\mathbf{I}, \boldsymbol{\phi})\left|\frac{\partial(\mathbf{I}, \boldsymbol{\phi}, \boldsymbol{\theta}_1)}{\partial(\mathbf{q}, \mathbf{p})}\right| \\ &= \frac{1}{(2\pi)^{(n-\alpha)}} p(\mathbf{I}, \boldsymbol{\phi})\left|\frac{\partial(\mathbf{I}, \boldsymbol{\phi}, \boldsymbol{\theta}_1)}{\partial(\mathbf{q}, \mathbf{p})}\right| \end{aligned} \tag{50}$$

where $|\partial(\mathbf{I}, \boldsymbol{\phi}, \boldsymbol{\theta}_1)/\partial(\mathbf{q}, \mathbf{p})|$ is the absolute value of the Jacobian determinant defined by the transformations in Eqs. (15*a*), (15*b*), and (24).

6 Extension

The stochastic averaging method developed for the systems governed by Eqs. (14*a*) and (14*b*) can be further extended to a more general class of systems, which include the quasi-integrable Hamiltonian systems as special cases. Consider a system governed by the following Itô equations:

$$dQ_i = D(\mathbf{Q})\frac{\partial H}{\partial P_i}\,dt \tag{51a}$$

$$dP_i = -\left[D(\mathbf{Q})\frac{\partial H}{\partial Q_i} + \epsilon m_{ij}\frac{\partial H}{\partial P_j}\right]dt + \epsilon^{1/2} f_{ik}\,dB_k(t) \tag{51b}$$

where $D(\mathbf{Q})$ is an arbitrary function of $\mathbf{Q}$. The system governed by Eqs. (14*a*) and (14*b*) is a special case with $D(\mathbf{Q}) = 1$. It is interesting to note that, in each case, i.e., whether the Hamiltonian system governed by Eqs. (51*a*) and (51*b*) with $D(\mathbf{Q}) = 1$ and $\epsilon = 0$ is integrable or nonintegrable, and resonant or nonresonant, the stochastically averaged FPK equation for Eqs. (51*a*) and (51*b*) is the same as that for Eqs. (14*a*) and (14*b*). Thus, the solution of the averaged FPK equation associated with Eqs. (51*a*) and (51*b*) in each case is also the same as that for Eqs. (14*a*) and (14*b*). The stationary probability density $p^*(\mathbf{q}, \mathbf{p})$ of generalized displacements and momenta of the system governed by Eqs. (51*a*) and (51*b*), based on the argument in a paper by Zhu and Yang (1996), is

$$p^*(\mathbf{q}, \mathbf{p}) = \frac{1}{D(\mathbf{q})}\,p(\mathbf{q}, \mathbf{p}) \tag{52}$$

where $p(\mathbf{q}, \mathbf{p})$ is the stationary probability density of the system governed by Eqs. (14*a*) and (14*b*).

7 Examples

Example 1. As a simple example, consider a two-degree-of-freedom system with uncoupled linear stiffness and coupled linear and polynomial-type nonlinear dampings subject to external excitations of two uncorrelated Gaussian white noises. The equations of motion of the system are of the form

$$\begin{aligned} &\ddot{X}_1 + \alpha_{11}\dot{X}_1 + \alpha_{12}\dot{X}_2 + \beta_1\dot{X}_1(X_1^2 + X_2^2) + \omega_1^2 X_1 = W_1(t) \\ &\ddot{X}_2 + \alpha_{21}\dot{X}_1 + \alpha_{22}\dot{X}_2 + \beta_2\dot{X}_2(X_1^2 + X_2^2) \\ &\qquad + \omega_2^2 X_2 = W_2(t) \end{aligned} \tag{1-1}$$

where $\omega_i\,(i = 1, 2)$ are constants; α_{ij}, $\beta_i\,(i, j = 1, 2)$ are small constants; $W_i(t)\,(i = 1, 2)$ are uncorrelated Gaussian white noises with small intensities $2D_{ii}$.

The Hamiltonian system associated with Eq. (1-1) is linear and the Hamiltonian can be expressed in terms of action variables as

$$H = \sum_{i=1}^{2} \omega_i I_i \tag{1-2}$$

where

$$I_i = \frac{1}{2\omega_i}(\dot{X}_i^2 + \omega_i^2 X_i^2), \quad i = 1, 2 \tag{1-3}$$

with the transformations in Eq. (1-3) and

$$\theta_i = -tg^{-1}\left(\frac{\dot{X}_i}{\omega_i X_i}\right), \quad i = 1, 2. \tag{1-4}$$

Equation (1-1) can be rewritten as the following Itô stochastic differential equations:

$$\begin{aligned} dI_i = &\left[-(\alpha_{i1}\dot{X}_1 + \alpha_{i2}\dot{X}_2 + \beta_i\dot{X}_i(X_1^2 + X_2^2))\frac{\dot{X}_i}{\omega_i} + \frac{D_{ii}}{\omega_i}\right]dt \\ &+ \frac{\dot{X}_i}{\omega_i}\,dB_i(t) \\ d\theta_i = &\left[\omega_i + [\alpha_{i1}\dot{X}_1 + \alpha_{i2}\dot{X}_2 + \beta_i\dot{X}_i(X_1^2 + X_2^2)]\right. \\ &\left.\times\frac{\omega_i X_i}{\omega_1^2 X_i^2 + \dot{X}_i^2} + D_{ii}\frac{2\omega_i X_i\dot{X}_i}{(\omega_i^2 X_i^2 + \dot{X}_i^2)^2}\right]dt \\ &- \frac{\omega_i X_i}{\omega_i^2 X_i^2 + \dot{X}_i^2}\,dB_i(t) \quad (i = 1, 2). \end{aligned} \tag{1-5}$$

Note that the repeated subscripts in Eq. (1-5) does not denote summation. Two cases are considered in the following.

I Nonresonant Case, i.e., $r\omega_1 + s\omega_2 \neq 0$, r, s-Integers. In this case the averaged FPK equation is of the form of Eq. (18) with the drift and diffusion coefficients

$$\begin{aligned} a_1 &= -a_{11}I_1 - \frac{\beta_1}{2\omega_1}I_1^2 - \frac{\beta_1}{\omega_2}I_1 I_2 + \frac{D_{11}}{\omega_1} \\ a_2 &= -a_{22}I_2 - \frac{\beta_2}{2\omega_2}I_2^2 - \frac{\beta_2}{\omega_1}I_1 I_2 + \frac{D_{22}}{\omega_2} \\ b_{11} &= \frac{2}{\omega_1}D_{11}I_1, \quad b_{22} = \frac{2}{\omega_2}D_{22}I_2, \quad b_{12} = b_{21} = 0. \end{aligned} \tag{1-6}$$

The stationary solution of the averaged FPK equation is of the form of Eq. (41) with $\partial\lambda/\partial I_s$ satisfying the following equations:

Downloaded 04 May 2010 to 171.66.16.34. Redistribution subject to ASME license or copyright; see http://www.asme.org/terms/Terms_Use.cfm

$$\frac{2D_{11}I_1}{\omega_1}\frac{\partial\lambda}{\partial I_1} = \frac{2D_{11}}{\omega_1} - 2\left(-\alpha_{11}I_1 - \frac{\beta_1}{2\omega_1}I_1^2 - \frac{\beta_1}{\omega_2}I_1I_2 + \frac{D_{11}}{\omega_1}\right)$$

$$\frac{2D_{22}I_2}{\omega_2}\frac{\partial\lambda}{\partial I_2} = \frac{2D_{22}}{\omega_2} - 2\left(-\alpha_{22}I_2 - \frac{\beta_2}{2\omega_2}I_2^2 - \frac{\beta_2}{\omega_1}I_1I_2 + \frac{D_{22}}{\omega_2}\right) \tag{1-7}$$

when $(\beta_1/D_{11})(\omega_1/\omega_2) = (\beta_2/D_{22})(\omega_2/\omega_1) = \gamma$, the averaged FPK equation has an exact stationary solution

$$p(I_1, I_2) = C\exp[\lambda(I_1, I_2)] \tag{1-8}$$

where

$$\lambda(I_1, I_2) = \frac{1}{D_{11}}\left(\alpha_{11}\omega_1 I_1 + \frac{\beta_1}{4}I_1^2\right) + \frac{1}{D_{22}}\left(\alpha_{22}\omega_2 I_2 + \frac{\beta_2}{4}I_2^2\right) + \gamma I_1 I_2. \tag{1-9}$$

The approximate stationary probability density of the displacements and velocities of original system Eq. (1-1) is then

$$p(x_1, \dot{x}_1; x_2, \dot{x}_2) = \frac{1}{4\pi^2}p(I_1, I_2)|_{I_i=(x_i^2+\omega_i^2\dot{x}_i^2)/2\omega_i}. \tag{1-10}$$

II Primary Resonant Case, i.e., $\omega_1 = \omega_2 = \omega$. Let $\theta_1 - \theta_2 = \varphi$. The averaged FPK equation in this case is of the form of Eq. (26) with the drift and diffusion coefficients

$$a_1 = -\alpha_{11}I_1 - \alpha_{12}\sqrt{I_1I_2}\cos\varphi - \frac{\beta_1}{2\omega}I_1^2 - \frac{\beta_1}{\omega}I_1I_2(1 - \tfrac{1}{2}\cos 2\varphi) + \frac{D_{11}}{\omega}$$

$$a_2 = -\alpha_{22}I_2 - \alpha_{21}\sqrt{I_1I_2}\cos\varphi - \frac{\beta_2}{2\omega}I_2^2 - \frac{\beta_2}{\omega}I_1I_2(1 - \tfrac{1}{2}\cos 2\varphi) + \frac{D_{22}}{\omega}$$

$$a_3 = \frac{1}{2}\left(\alpha_{12}\sqrt{\frac{I_2}{I_1}} + \alpha_{21}\sqrt{\frac{I_1}{I_2}}\right)\sin\varphi - \frac{1}{4\omega}(\beta_1I_2 + \beta_2I_1)\sin 2\varphi$$

$$b_{11} = \frac{2}{\omega}D_{11}I_1, \quad b_{22} = \frac{2}{\omega}D_{22}I_2, \quad b_{33} = \frac{1}{2\omega}\left(\frac{D_{11}}{I_1} + \frac{D_{22}}{I_2}\right)$$

$$b_{12} = b_{21} = b_{13} = b_{31} = b_{23} = b_{32} = 0. \tag{1-11}$$

The stationary solution of the averaged FPK equation is of the form of Eq. (49), i.e.,

$$p(I_1, I_2, \varphi) = C\exp[-\lambda(I_1, I_2, \varphi)] \tag{1-12}$$

where $\lambda(I_1, I_2, \varphi)$ satisfies the following partial differential equations:

$$\frac{2D_{11}I_1}{\omega}\frac{\partial\lambda}{\partial I_1} = \frac{2D_{11}}{\omega} - 2\left[-\alpha_{11}I_1 - \alpha_{12}\sqrt{I_1I_2}\cos\varphi - \frac{\beta_1}{2\omega}I_1^2 - \frac{\beta_1}{\omega}I_1I_2\left(1 - \frac{1}{2}\cos 2\varphi\right) + \frac{D_{11}}{\omega}\right]$$

$$\frac{2D_{22}I_2}{\omega}\frac{\partial\lambda}{\partial I_2} = \frac{2D_{22}}{\omega} - 2\left[-\alpha_{22}I_2 - \alpha_{21}\sqrt{I_1I_2}\cos\varphi - \frac{\beta_2}{2\omega}I_2^2 - \frac{\beta_2}{\omega}I_1I_2\left(1 - \frac{1}{2}\cos 2\varphi\right) + \frac{D_{22}}{\omega}\right]$$

$$\left(\frac{D_{11}}{2\omega I_1} + \frac{D_{22}}{2\omega I_2}\right)\frac{\partial\lambda}{\partial\varphi} = -\left(\alpha_{12}\sqrt{\frac{I_2}{I_1}} + \alpha_{21}\sqrt{\frac{I_1}{I_2}}\right)\sin\varphi + \frac{1}{2\omega}(\beta_1I_2 + \beta_2I_1)\sin 2\varphi. \tag{1-13}$$

Let

$$\lambda(I_1, I_2, \varphi) = \lambda_0(I_1, I_2) + \lambda_1(I_1, I_2)\cos\varphi + \lambda_2(I_1, I_2)\cos 2\varphi. \tag{1-14}$$

Substituting Eq. (1-14) into Eq. (1-13), we obtain three sets of partial differential equations for λ_0, λ_1, and λ_2. In the case that $\beta_1/D_{11} = \beta_2/D_{22} = \gamma_1$, $\alpha_{12}/D_{11} = \alpha_{21}/D_{22} = \gamma_2$, we obtain the exact stationary solution Eq. (1-12) with

$$\lambda(I_1, I_2, \varphi) = \frac{\alpha_{11}\omega}{D_{11}}I_1 + \frac{\alpha_{22}\omega}{D_{22}}I_2 + \frac{\beta_1}{4D_{11}}I_1^2 + \frac{\beta_2}{4D_{22}}I_2^2 + \gamma_1I_1I_2 - \frac{\gamma_1}{2}I_1I_2\cos 2\varphi + 2\gamma_2\omega\sqrt{I_1I_2}\cos\varphi. \tag{1-15}$$

The approximate stationary probability density of the displacements and velocities of original system Eq. (1-1) is of the form

$$p(x_1, \dot{x}_1; x_2, \dot{x}_2) = \frac{1}{2\pi}p(I_1, I_2, \varphi) \tag{1-16}$$

where $\varphi = \theta_1 - \theta_2$; I_i and θ_i are functions of x_i and $\dot{x}_i$ defined by Eqs. (1-3) and (1-4). Note that the Jacobian determinant $\partial(I_1, I_2, \theta_1, \varphi)/\partial(x_1, \dot{x}_1, x_2, \dot{x}_2) = 1$.

Some numerical results for marginal probability density $p(x_1, \dot{x}_1)$ obtained by using the proposed stochastic averaging method and from digital simulation are shown in Fig. 1, for a nonresonant case, and Fig. 2 for a primary resonant case. Similar result for $p(\varphi)$ in a primary resonant case is shown in Fig. 3. The system Eq. (1-1) with the parameters in Fig. 1 represents a van der Pol oscillator linearly and nonlinearly coupled with a linear oscillator with linear and nonlinear dampings, while that with the parameters in Fig. 2 and 3 two linearly and nonlinearly coupled van der Pol oscillators. It is seen from the comparison of theoretical results with simulation that the proposed method yields very good prediction.

Example 2. Consider a van der Pol oscillator nonlinearly coupled with a Duffing oscillator subject to external excitations of Gaussian white noises. The equation of motion of the system is of the form

$$\ddot{X}_1 + (\alpha_1X_2^4 + \alpha_2X_1^2 + \alpha_3\dot{X}_2^2 - \beta_1)\dot{X}_1 + \omega_1^2X_1 = W_1(t)$$
$$\ddot{X}_2 + (\alpha_4X_1^2 + \beta_2)\dot{X}_2 + kX_2^3 = W_2(t) \tag{2-1}$$

where ω_1 and k are constants; α_1, α_2, α_3, α_4, β_1 and β_2 are small constants; and W_i are uncorrelated Gaussian white noises with small intensities $2D_i$.

The Hamiltonian system associated with Eq. (2-1) is nonlinear and nonresonant, and has a separable Hamiltonian

$$H = H_1 + H_2 \tag{2-2}$$

where

$$H_1 = \tfrac{1}{2}\dot{X}_1^2 + \tfrac{1}{2}\omega_1^2X_1^2$$

$$H_2 = \frac{1}{2}\dot{X}_2^2 + \frac{k}{4}\dot{X}_2^4. \tag{2-3}$$

Downloaded 04 May 2010 to 171.66.16.34. Redistribution subject to ASME license or copyright; see http://www.asme.org/terms/Terms_Use.cfm

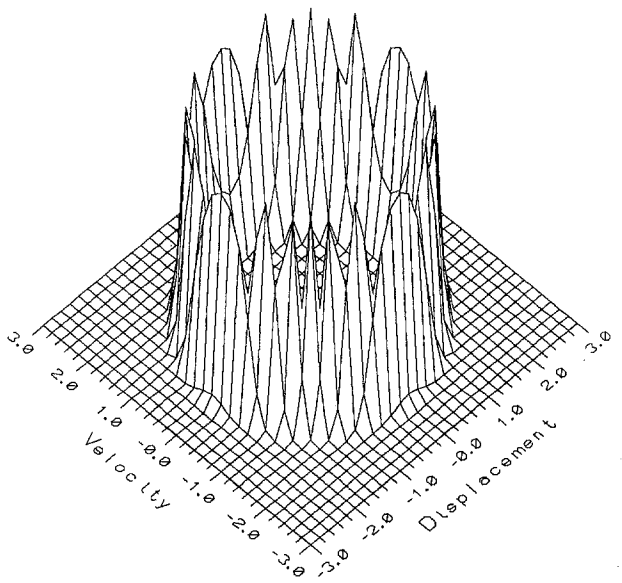


Fig. 1(*a*)

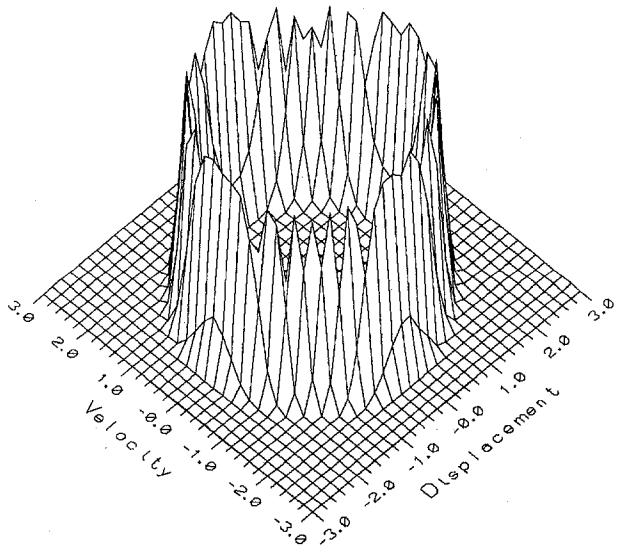


Fig. 1(*b*)

Fig. 1 Marginal probability density $p(x_1, \dot{x}_1)$ of stationary response of system (1-1) in nonresonant case. $\alpha_{11} = -0.05$, $\alpha_{22} = \alpha_{12} = \alpha_{21} = \beta_1 = \beta_2 = 0.05$, $\omega_1 = 1.0$, $\omega_2 = 1.414$, $D_{11} = D_{22} = 0.001$. (*a*) Using the present stochastic averaging method; (*b*) from digital simulation.

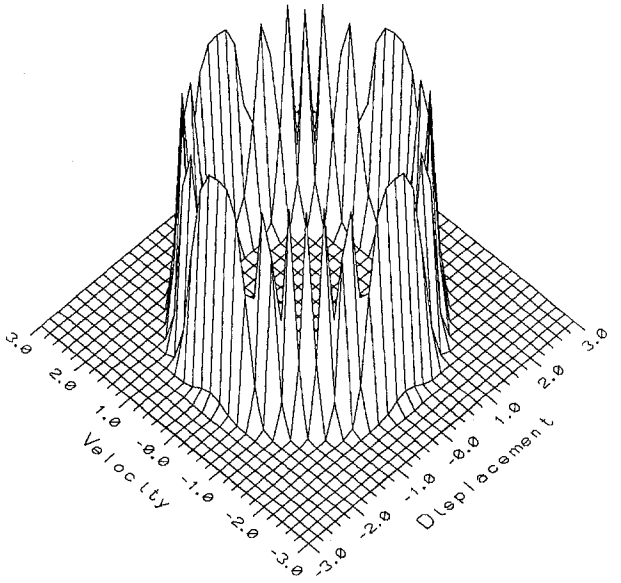


Fig. 2(*a*)

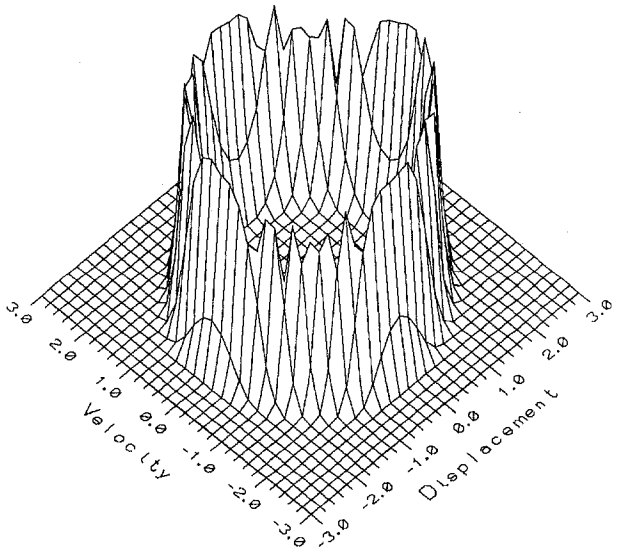


Fig. 2(*b*)

Fig. 2 Marginal probability density $p(x_1, \dot{x}_1)$ of stationary response of system (1-1) in primary resonant case. $\alpha_{11} = \alpha_{22} = -0.05$, $\alpha_{12} = \alpha_{21} = \beta_1 = \beta_2 = 0.05$, $\omega_1 = \omega_2 = 1.0$, $D_{11} = D_{22} = 0.001$. (*a*) Using the present stochastic averaging method; (*b*) from digital simulation.

Equation (2-1) is first converted into Itô equations from which the Itô equations for H_1 and H_2 are then obtained by using Itô differential rule as follows:

$$dH_1 = \left\{ -\left[\alpha_1 X_2^4 + \alpha_2 X_1^2 + \alpha_3 \left(2H_2 - \frac{k}{2} X_2^4 \right) - \beta_1 \right] \times (2H_1 - \omega_1^2 X_1^2) + D_1 \right\} dt \pm (2H_1 - \omega_1^2 X_1^2)^{1/2} dB_1(t)$$

$$dH_2 = \left\{ -\left[\alpha_4 X_1^2 + \beta_2 \right] \left(2H_2 - \frac{k}{2} X_2^4 \right) + D_2 \right\} dt \pm \left(2H_2 - \frac{k}{2} X_2^4 \right)^{1/2} dB_2(t). \quad (2\text{-}4)$$

The averaged FPK equations are of the form (32) with $r, s = 1, 2$. The drift and diffusion coefficients of the averaged FPK equation, according to Eqs. (35*a*), (35*b*), and (36) are

$$a_1 = -2\alpha_3 H_1 H_2 - \frac{\alpha_2 H_1^2}{2\omega_1^2} + \beta_1 H_1 + D_1$$

$$a_2 = -\left(\frac{\alpha_4 H_1}{\omega_1} + \beta_2 \right) G(H_2) + D_2$$

$$b_{11} = 2D_1 H_1$$

$$b_{12} = b_{21} = 0$$

$$b_{22} = 2D_2 G(H_2) \quad (2\text{-}5)$$

where $2\alpha_1 = k\alpha_3$ is assumed and

Downloaded 04 May 2010 to 171.66.16.34. Redistribution subject to ASME license or copyright; see http://www.asme.org/terms/Terms_Use.cfm

$$G(H_2) = \int_0^{A_2} \left(2H_2 - \frac{k}{2}x_2^4\right)^{1/2} dx_2 \Big/ \int_0^{A_2} \frac{dx_2}{\left(2H_2 - \frac{k}{2}x_2^4\right)^{1/2}} \tag{2-6}$$

in which $A_2 = (4H_2/k)^{1/4}$. Note that the assumption of $2\alpha_1 = k\alpha_3$ is not necessary and it is introduced here just for simplicity.

The exact stationary solution of the averaged FPK equation, if it exists, is of the form

$$p(H_1, H_2) = C \exp[-\lambda(H_1, H_2)] \tag{2-7}$$

where probability potential $\lambda(H_1, H_2)$ is the solution of the following two linear partial differential equations:

$$\frac{\partial \lambda}{\partial H_1} = \frac{1}{D_1}\left(2\alpha_3 H_2 - \frac{\alpha_2 H_1}{2\omega_1^2} - \beta_1\right)$$

$$\frac{\partial \lambda}{\partial H_2} = \frac{1}{D_2}\left(\frac{\alpha_4 H_1}{\omega_1} + \beta_3\right) - \frac{1}{4H_2}. \tag{2-8}$$

If $\alpha_4 D_1 = 2\alpha_3\omega_1 D_2$, then the compatibility condition is satisfied, i.e., $\partial^2\lambda/\partial H_1\partial H_2 = \partial^2\lambda/\partial H_2\partial H_1$, and the solution is

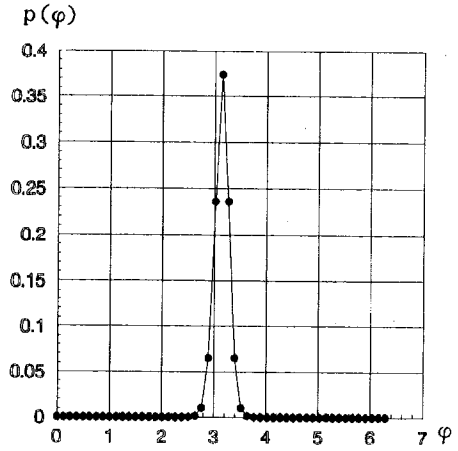


Fig. 3(a)

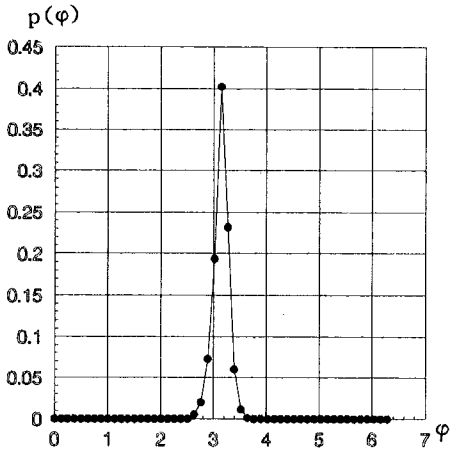


Fig. 3(b)

Fig. 3 Marginal probability density $p(\varphi) = p(\theta_1 - \theta_2)$ of stationary response of system (1-1) in primary resonant case. The parameters are the same as in Fig. 2 except $D_{11} = D_{22} = 0.01$. (a) Using the present stochastic averaging method; (b) from digital simulation.

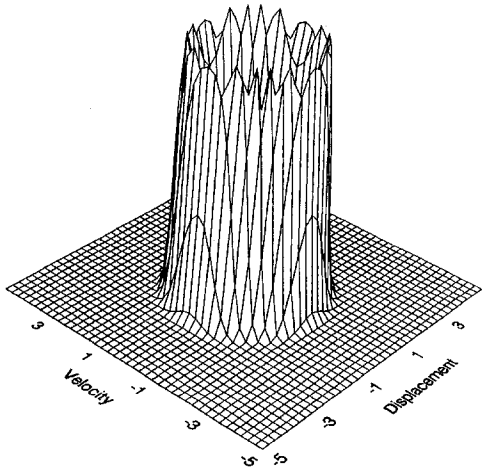


Fig. 4(a)

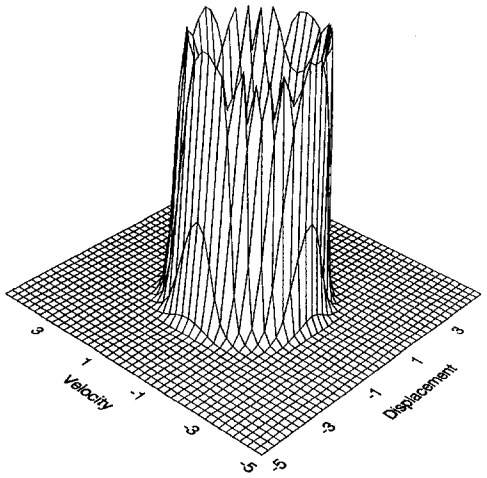


Fig. 4(b)

Fig. 4 Marginal probability density $p(x_1, \dot{x}_1)$ of stationary response of system (2-1). $\omega_1 = 1.0$, $k = 2.0$, $\alpha_1 = \beta_2 = 0.01$, $\alpha_2 = \alpha_4 = \beta_1 = 0.02$, $2D_1 = 2D_2 = 0.01$. (a) Using the present stochastic averaging method; (b) from digital simulation.

$$\lambda = \int_0^{(H_1,H_2)} \left(\frac{\partial \lambda}{\partial H_1} dH_1 + \frac{\partial \lambda}{\partial H_2} dH_2\right)$$

$$= \frac{1}{D_1}\left(\frac{\alpha_2 H_1^2}{4\omega_1^2} + \alpha_3 H_1 H_2 - \beta_1 H_1\right)$$

$$+ \frac{1}{D_2}\beta_2 H_2 - \frac{1}{4}\ln H_2. \tag{2-9}$$

The stationary probability density $p(H_1, H_2)$ is obtained by substituting Eq. (2-9) into Eq. (2-7) and the stationary probability density of displacements and velocities, according to Eq. (48), is

$$p(x_1, \dot{x}_1; x_2, \dot{x}_2) = C\frac{1}{T}\exp[-\lambda(H_1, H_2)]|_{H_i = H_i(x_i, \dot{x}_i)} \tag{2-10}$$

where C is a normalization constant and

$$T = 16\int_0^{A_1} \frac{dx_1}{(2H_1 - \omega_1^2 x_1^2)^{1/2}} \cdot \int_0^{A_2} \frac{dx_2}{\left(2H_2 - \frac{k}{2}x_2^4\right)^{1/2}}$$

$$= 4\pi F\left(\frac{\pi}{2}, \frac{1}{\sqrt{2}}\right) \Big/ \omega_1\left(\frac{H_2}{k}\right)^{1/4} \tag{2-11}$$

Downloaded 04 May 2010 to 171.66.16.34. Redistribution subject to ASME license or copyright; see http://www.asme.org/terms/Terms_Use.cfm

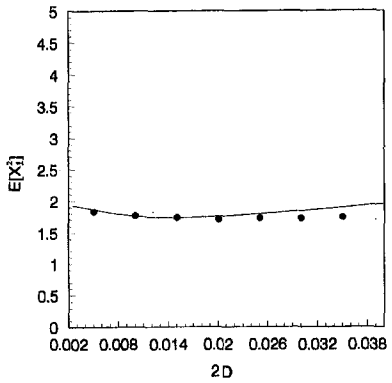


Fig. 5 Variance $E[X_1^2]$ of stationary response of system (2-1). The parameters are the same as in Fig. 4 except $2D_1 = 2D_2 = 2D$. (*a*) Using the present stochastic averaging method; (*b*) from digital simulation.

in which $F(\cdot,\cdot)$ is the generalized hypergeometric function and $A_1 = (2H_1/\omega_1^2)^{1/2}$.

The statistics of stationary displacement and velocity can be obtained by appropriate integration, e.g.,

$$E[X_1^2] = \int_{-\infty}^{\infty}\int\int\int x_1^2 p(x_1, \dot{x}_1; x_2, \dot{x}_2)\,dx_1\,d\dot{x}_1\,dx_2\,d\dot{x}_2$$

$$= C\int_0^{\infty}\int_0^{H} \exp[-\lambda(H_1, H - H_1)]H_1\,dH_1\,dH. \quad (2\text{-}12)$$

Some numerical results for $p(x_1, \dot{x}_1)$ and $E[X_1^2]$ obtained by using the proposed method and from digital simulation are shown in Figs. 4 and 5. It is seen that the theoretical results and those from digital simulation are in very good agreement.

8 Conclusions

In the present paper a stochastic averaging method for quasi-integrable Hamiltonian systems has been presented. The method includes the Stratonovich stochastic averaging and the stochastic averaging of an energy envelope as two special cases. This method and that for quasi-nonintegrable Hamiltonian systems (Zhu and Yang, 1997) constitute a complete set of stochastic averaging procedures for multi-degree-of-freedom quasi-Hamiltonian systems and provide powerful techniques for prediction of response of many nonlinear stochastic engineering systems.

Acknowledgment

The financial support from National Natural Science Foundation of China is acknowledged.

References

Arnold, V. I., 1989, *Mathematical Methods of Classical Mechanics,* 2nd ed., Springer-Verlag, New York.

Itô, K., 1951, "On stochastic Differential Equations," *Mem. Amer. Math. Soc.,* Vol. 4, pp. 289–302.

Khasminskii, R. Z., 1964, "On the Behavior of a Conservative System With Friction and Small Random Noise," *Prikladnaya Matematika i Mechanica* (Applied Mathamatics and Mechanics), Vol. 28, pp. 931–935 (in Russian).

Khasminskii, R. Z., 1966, "A Limit Theorem for Solutions of Differential Equations With Random Right Hand Sides," *Theory of Probability and Applications,* Vol. 11, pp. 390–405.

Khasminskii, R. Z., 1968, "On the Averaging Principle for Stochastic Differential Itô Equation," *Kibernetika,* Vol. 4, pp. 260–299 (in Russian).

Landa, P. S., and Stratonovich, R. L., 1962, "Theory of Stochastic Transitions of Various Systems Between Different States," *Vestnik MGU* (Proc. Moscow University), Series III, No. 1, pp. 33–45 (in Russian).

Roberts, J. B., and Spanos, P. D., 1986, "Stochastic Averaging: An Approximate Method of Solving Random Vibration Problems," *Int. J. Non-Linear Mech.,* Vol. 21, pp. 111–134.

Stratonovich, R. L., 1963, *Topics in the Theory of Random Noise,* Vol. 1, Gordon and Breach, New York.

Tabor, M., 1989, *Chaos and Integrability in Nonlinear Dynamics,* John Wiley and Sons, New York.

Zhu, W. Q., 1983, "Stochastic Averaging of the Energy Envelope of Nearly Lyapunov Systems," *Random Vibrations and Reliability,* Proc. IU-TAM Symposium, K. Hennig ed., Akademie, Berlin, pp. 347–357.

Zhu, W. Q., 1988, "Stochastic Averaging Methods in Random Vibration," ASME *Applied Mechanics Reviews,* Vol. 41, No. 5, pp. 189–199.

Zhu, W. Q., 1996, "Recent Developments and Applications of Stochastic Averaging Method in Random Vibration," ASME *Applied Mechanics Reviews,* Vol. 49, No. 10, Part 2, pp. 572–580.

Zhu, W. Q., and Lin, Y. K., 1991, "Stochastic Averaging of Energy Envelope," *ASCE Journal of Engineering Mechanics,* Vol. 117, pp. 1890–1905.

Zhu, W. Q., Soong, T. T., and Lei, Y., 1994, "Equivalent Nonlinear System Method for Stochastically Excited Hamiltonian Systems," ASME JOURNAL OF APPLIED MECHANICS, Vol. 61, pp. 618–623.

Zhu, W. Q., and Yang, Y. Q., 1996, "Exact Stationary Solutions of Stochastically Excited and Dissipated Integrable Hamiltonian Systems," ASME JOURNAL OF APPLIED MECHANICS, Vol. 63, pp. 493–500.

Zhu, W. Q., and Yang, Y. Q., 1997, "Stochastic Averaging of Quasi-Nonintegrable Hamiltonian Systems," ASME JOURNAL OF APPLIED MECHANICS, Vol. 64, pp. 157–164.

Downloaded 04 May 2010 to 171.66.16.34. Redistribution subject to ASME license or copyright; see http://www.asme.org/terms/Terms_Use.cfm

Time-Integral Variational Principles for Nonlinear Nonholonomic Systems

J. G. Papastavridis
Associate Professor of Mechanics,
School of Mechanical Engineering,
Georgia Institute of Technology,
Atlanta, GA 30332-0405

This is a comprehensive treatment of the time-integral variational "principles" of mechanics for systems subject to general nonlinear and possibly nonholonomic velocity constraints (i.e., equations of the form $f(t, q, \dot{q}) = 0$, where t = time and $q/\dot{q}$ = Lagrangean coordinates/velocities), in general nonlinear nonholonomic coordinates. The discussion is based on the Maurer-Appell-Chetaev-Hamel definition of virtual displacements and subsequent formulation of the corresponding nonlinear transitivity (or transpositional) equations. Also, a detailed analysis of the latter supplies a hitherto missing clear geometrical interpretation of the well-known discrepancies between the equations of motion obtained by formal application of the calculus of variations (mathematics) and those obtained from the principle of d'Alembert-Lagrange (mechanics); i.e., admissible adjacent paths (mathematics) are locally nonvirtual; and adjacent paths built from locally virtual displacements (mechanics) are not admissible. (These discrepancies, although revealed about a century ago, for systems under Pfaffian constraints (Hertz (1894), Hölder (1896), Hamel (1904), Maurer (1905), and others) seem to be relatively unknown and/or misunderstood among today's engineers.) The discussion includes all relevant nonlinear nonholonomic variational principles, in both unconstrained and constrained forms of their integrands, and the corresponding nonlinear nonholonomic equations of motion. Such time-integral formulations are useful both conceptually and computationally (e.g., multibody dynamics).

1 Introduction and Background

We consider a mechanical system S whose configurations of interest are determined completely and uniquely by the n holonomic *positional system parameters,* or Lagrangean coordinates, $q \equiv (q_1, \ldots, q_n) \equiv (q_k)$: In addition, S is subject to the following general (but as well behaved as needed) nonlinear and possibly nonholonomic velocity constraints:

$$f_D(t, q, \dot{q}) = 0 \ [\text{where rank } (\partial f_D/\partial \dot{q}_k) = m],$$

t = time, $\dot{q} \equiv (\dot{q}_1, \ldots, \dot{q}_n) \equiv (\dot{q}_k)$:
Lagrangean (holonomic) velocities. (1)

Throughout this paper, we shall assume the well-known summation convention over pairs of Latin indices, with the following index ranges:

Lower case Latin indices: $k, l, \ldots = 1, \ldots, n$

Upper case Latin indices:

$$D, D', D'', \ldots = 1, \ldots, m \ (D \text{ for Dependent})$$

$$I, I', I'', \ldots = m + 1, \ldots, n \ (I \text{ for Independent}).$$

In the linear velocity (and for simplicity, but no loss of generality, *scleronomic*) case, Eq. (1) assumes the (homogeneous in the $\dot{q}$s) Pfaffian form

$$f_D = a_{Dk}\dot{q}_k = 0 \quad [a_{Dk} = a_{Dk}(q), \text{ rank } (a_{Dk}) = m]. \quad (1a)$$

Next, as shown by Hamel (1949) and others, Eq. (1) amounts to the following Maurer-Appell-Chetaev-Hamel restrictions for the virtual displacements $\delta q \equiv (\delta q_k)$

$$(\partial f_D/\partial \dot{q}_k)\delta q_k = 0. \quad (2)$$

This condition results by requiring compatibility between the fundamental (differential) principles of mechanics: that of Lagrange with those of Jourdain and Gauss; and is fundamentally different from

$$\delta f_D = \left(\frac{\partial f_D}{\partial q_k}\right)\delta q_k + \left(\frac{\partial f_D}{\partial \dot{q}_k}\right)\delta \dot{q}_k, \quad (3)$$

which is obtained by formal application of variational mathematics. In the Pfaffian case, (2) reduces to the familiar

$$a_{Dk}\delta q_k = 0, \quad (4)$$

whereas (3) would have produced the incorrect form

$$\delta f_D = \left(\frac{\partial a_{Dk}}{\partial q_l}\right)\dot{q}_k\delta q_l + (a_{Dk})\delta \dot{q}_k = 0. \quad (5)$$

The above show that in the nonlinear case the operation $\delta(\ldots)$, where $(\ldots)$ is a general function of t, q, $\dot{q}$, cannot be calculated formally, but has to be specially tailored in order to produce the correct equations of motion.

2 The Variational Problem

2.1 Mechanics (Principle of d'Alembert-Lagrange). Let us assume for concreteness, but no loss in generality, a potential system described by the Lagrangean $L = T - V = L(t, q, \dot{q})$, where T and V are, respectively, its kinetic and potential energies. Its equations of motion are obtained by combining the fundamental

Contributed by the Applied Mechanics Division of THE AMERICAN SOCIETY OF MECHANICAL ENGINEERS for publication in the ASME JOURNAL OF APPLIED MECHANICS.
Discussion on this paper should be addressed to the Technical Editor, Professor Lewis T. Wheeler, Department of Mechanical Engineering, University of Houston, Houston, TX 77204-4792, and will be accepted until four months after final publication of the paper itself in the ASME JOURNAL OF APPLIED MECHANICS.
Manuscript received by the ASME Applied Mechanics Division, Oct. 22, 1996; final revision, Mar. 7, 1997. Associate Technical Editor: N. C. Perkins.

Copyright © 1997 by ASME

Downloaded 04 May 2010 to 171.66.16.34. Redistribution subject to ASME license or copyright; see http://www.asme.org/terms/Terms_Use.cfm

differential variational principle of Lagrange (LP), in holonomic variables,

$$E_k(L)\delta q_k = 0, \tag{6}$$

where $E_k(\ldots) \equiv (d/dt)(\partial \ldots/\partial \dot{q}_k) - (\partial \ldots/\partial q_k)$: Euler-Lagrange operator (in holonomic variables), with the virtual form of the constraints, Eq (2). Under the key assumption $\delta \dot{q}_k = (\delta q_k)^{\cdot}$, [where $(\ldots)^{\cdot} \equiv (d/dt)(\ldots)$] Eq. (6) leads readily to the *central equation*:

$$\delta L = \frac{d}{dt}(p_k \delta q_k), \tag{7}$$

where

$$\delta L = \left(\frac{\partial L}{\partial q_k}\right)\delta q_k + \left(\frac{\partial L}{\partial \dot{q}_k}\right)\delta \dot{q}_k, \tag{7a}$$

$p_k \equiv \partial L/\partial \dot{q}_k$: holonomic components of system (or "generalized") momentum; (7*b*).

And integrating (7) between the arbitrary time limits t_1, t_2 we obtain (with some easily understood notations)

$$\int_1^2 \delta L dt = \{p_k \delta q_k\}_1^2, \text{ under (2)}. \tag{8}$$

Finally, attaching or adjoining (2) to (8) via the m Lagrangean multipliers λ_D, we obtain the following *unconstrained* integral equation:

$$\int_1^2 \left[\delta L + \lambda_D\left(\frac{\partial f_D}{\partial \dot{q}_k}\right)\delta q_k\right] dt = \{p_k \delta q_k\}_1^2, \tag{9}$$

from which, by simple (and hopefully familiar) transformations, the well-known Routh-Voss equations follow:

$$E_k(L) = \lambda_D(\partial f_D/\partial \dot{q}_k) \quad [= \lambda_D a_{Dk}, \text{ in the Pfaffian case}]. \tag{10}$$

2.2 Mathematics (Lagrange's Problem). Here the mathematical problem, for the same system, is

$$\int_1^2 L dt = \text{stationary, under (1)}; \tag{11}$$

or, equivalently,

$$\delta \int_1^2 L dt = 0, \text{ under (1)} \rightarrow \delta f_D = 0. \tag{11a}$$

Using again the multiplier rule but with Lagrangean multipliers μ_D, we transform the above to the unconstrained equation:

$$\int_1^2 \delta(L + \mu_D f_D) dt = 0 \rightarrow \int_1^2 (\delta L + \mu_D \delta f_D) dt = 0, \tag{12}$$

from which, assuming that $\{p_k \delta q_k\}_1^2 = 0$ (something that does not affect the equations of motion, but does affect the approximate calculation of the motion via the so called direct variational methods) we readily obtain the Euler-Lagrange equations

$$E_k(L + \mu_D f_D) = E_k(L) + E_k(\mu_D f_D) = 0$$

or in extenso

$$E_k(L) = -\dot{\mu}_D\left(\frac{\partial f_D}{\partial \dot{q}_k}\right) - \mu_D \underbrace{\left[\frac{d}{dt}\left(\frac{\partial f_D}{\partial \dot{q}_k}\right) - \frac{\partial f_D}{\partial q_k}\right]}_{\equiv E_k(f_D) \neq 0, \text{ in general}} \tag{13}$$

$$\left\{= -\dot{\mu}_D a_{Dk} - \mu_D\left[\left(\frac{\partial a_{Dk}}{\partial q_l} - \frac{\partial a_{Dl}}{\partial q_k}\right)\dot{q}_l\right], \right.$$

$$\left. \text{in the Pfaffian case} \right\}. \tag{13a}$$

Comparing Eqs. (10) and (13) we immediately see that even if we identify λ_D with $-\dot{\mu}_D$, still these two sets of equations are, in general, different; i.e., *Eqs. (13) are mechanically incorrect.* This should not come as a surprise: the basic principle of mechanics is not the integral variational principle of Hamilton, i.e., Eqs. (11), (11*a*), but the differential variational principle of Lagrange, Eqs. (6), (2).

3 Geometric Interpretation

Let us try to understand the discrepancy between the mathematical Eqs. (13) and the mechanical Eqs. (10); what Hertz calls, respectively, the equations for the geodesic and straightest paths.

3.1 Quasi-Variables. To this end, we introduce the following quasi-(or nonholonomic) velocities:

$$\omega_D \equiv f_D(t, q, \dot{q}) = 0, \quad \omega_I \equiv f_I(t, q, \dot{q}) \neq 0, \tag{14a, b}$$

where the $n - m$ $f_I(\ldots)$ are arbitrary except that when the system (14*a*, *b*) is solved for the $n\dot{q}_k$: $\dot{q}_k = \dot{q}_k(t, q, \omega_D, \omega_I)$, and these expressions are inserted back into (14*a*) they satisfy them identically. The virtual forms of (14*a*, *b*) are, respectively,

$$\delta\theta_D \equiv (\partial f_D/\partial \dot{q}_k)\delta q_k \equiv (\partial \omega_D/\partial \dot{q}_k)\delta q_k = 0, \tag{15a}$$

$$\delta\theta_I \equiv (\partial f_I/\partial \dot{q}_k)\delta q_k \equiv (\partial \omega_I/\partial \dot{q}_k)\delta q_k \neq 0, \tag{15b}$$

where the corresponding nonlinear nonholonomic coordinates, or quasi-coordinates, θ_k are defined by $d\theta_k/dt \equiv \omega_k$, or $d\theta_k \equiv \omega_k dt$; but $\delta\theta_k \neq f_k(t, q, \delta q)$.

Inverting the above we readily obtain

$$\delta q_k = (\partial \dot{q}_k/\partial \omega_l)\delta\theta_l = (\partial \dot{q}_k/\partial \omega_I)\delta\theta_I \neq 0. \tag{16}$$

In the Pfaffian case, Eqs. (14*a*) – (16) reduce, respectively, to

$$\omega_D \equiv a_{Dk}\dot{q}_k = 0, \quad \omega_I \equiv a_{Ik}\dot{q}_k \neq 0; \tag{17a, b}$$

$$\delta\theta_D \equiv a_{Dk}\delta q_k = 0, \quad \delta\theta_I \equiv a_{Ik}\delta q_k \neq 0; \tag{18a, b}$$

$$\delta q_k = A_{kl}\delta\theta_l = A_{kI}\delta\theta_I \neq 0; \tag{19}$$

($(a_{kl})(A_{kl})$ are mutually inverse matrices).

3.2 The Transitivity Equations. $(\ldots)^{\cdot}$—differentiating (15*a*, *b*) and $\delta(\ldots)$—varying (14*a*, *b*) and then subtracting side by side, while invoking (16), we obtain the following transitivity equations (or bilinear covariants of Frobenius; see e.g., Hamel (1949), Novoselov (1966), and Mei (1985)):

$$(\delta\theta_k)^{\cdot} - \delta\omega_k$$

$$= \left(\frac{\partial \omega_k}{\partial \dot{q}_l}\right)[(\delta q_l)^{\cdot} - \delta\dot{q}_l] + \underbrace{\left[\left(\frac{\partial \omega_k}{\partial \dot{q}_l}\right)^{\cdot} - \frac{\partial \omega_k}{\partial q_l}\right]}_{\equiv E_l(\omega_k)} \delta q_l$$

$$= (") + H_{rk}\delta\theta_r$$

$$= (") - V_{rl}\left(\frac{\partial \omega_k}{\partial \dot{q}_l}\right)\delta\theta_r, \tag{20}$$

where

$$H_{rk} \equiv \left(\frac{\partial \dot{q}_l}{\partial \omega_r}\right)\left[\frac{d}{dt}\left(\frac{\partial \omega_k}{\partial \dot{q}_l}\right) - \frac{\partial \omega_k}{\partial q_l}\right] \equiv \left(\frac{\partial \dot{q}_l}{\partial \omega_r}\right)E_l(\omega_k)$$

(nonlinear Hamel coefficients), (20*a*)

Downloaded 04 May 2010 to 171.66.16.34. Redistribution subject to ASME license or copyright; see http://www.asme.org/terms/Terms_Use.cfm

$$V_{rl} \equiv \frac{d}{dt}\left(\frac{\partial \dot{q}_l}{\partial \omega_r}\right) - \frac{\partial \dot{q}_l}{\partial \theta_r} \equiv E_r^*(\dot{q}_l) = -\left(\frac{\partial \dot{q}_l}{\partial \omega_k}\right) H_{rk}$$

(nonlinear generalized Voronets coefficients), (20*b*)

and

$$\frac{\partial \ldots}{\partial \theta_r} \equiv \left(\frac{\partial \ldots}{\partial q_k}\right)\left(\frac{\partial \dot{q}_k}{\partial \omega_r}\right):$$

symbolic "quasi-chain rule." (20*c*)

Since the constraints are simply $\omega_D = 0$ (velocity form), or $d\theta_D = 0$ (kinematically admissible form), or $\delta\theta_D = 0$ (virtual form), Eqs. (20) yield

$$(\delta\theta_D)^{\cdot} - \delta\omega_D = \left(\frac{\partial \omega_D}{\partial \dot{q}_l}\right)[(\delta\dot{q}_l)^{\cdot} - \delta\dot{q}_l] + H_{lD}\delta\theta_l \quad (21a)$$

$$= (") - V_{ll}\left(\frac{\partial \omega_D}{\partial \dot{q}_l}\right)\delta\theta_l. \quad (21b)$$

In the Pfaffian case Eqs. (20), (21) reduce, respectively, to

$$(\delta\theta_k)^{\cdot} - \delta\omega_k = a_{kl}[(\delta q_l)^{\cdot} - \delta\dot{q}_l] + \gamma^k_{rs}\omega_s\delta\theta_r, \quad (22a)$$

$$(\delta\theta_D)^{\cdot} - \delta\omega_D = a_{Dl}[(\delta q_l)^{\cdot} - \delta\dot{q}_l] + \gamma^D_{ll'}\omega_{l'}\delta\theta_l; \quad (22b)$$

where the γ^k_{rs} are the famous (Ricci-Boltzmann-) Hamel coefficients; i.e., the H_{rk} are the nonlinear generalization of $\gamma^k_{rs}\omega_s$ (see e.g., Dobronravov (1970, pp. 166 ff.) and Hamel (1949, pp. 473 ff.)). From the above we draw the following important conclusions:

(i) if we assume that $(\delta q_k)^{\cdot} = \delta\dot{q}_k$

[or, equivalently, $d(\delta q_k) = \delta(dq_k)$], (23)

whether the $\dot{q}_k/dq_k/\delta q_k$ are constrained or not (which is the viewpoint of Hölder (1896), Hamel (1904), and Voronets (1901) et al., as well as that adopted in the calculus of variations) then

$$(\delta\theta_D)^{\cdot} - \delta\omega_D = H_{lD}\delta\theta_l \neq 0; \quad (24a)$$

and also

$$(\delta\theta_{l'})^{\cdot} - \delta\omega_{l'} = H_{ll'}\delta\theta_l \neq 0, \quad (24b)$$

and, conversely,

(ii) if we assume that $(\delta q_k)^{\cdot} \neq \delta\dot{q}_k$, for some or all values of k (which is the viewpoint of Suslov (1901) et al., and is in clear disagreement with the calculus of variations), then we may take

$$(\delta\theta_D)^{\cdot} = \delta\omega_D. \quad (25a)$$

and also

$$(\delta\theta_l)^{\cdot} = \delta\omega_l. \quad (25b)$$

Now, let us try to interpret the variations of mechanics and mathematics geometrically.

3.3 Mechanics. The constraints (14*a*) or (15*a*) hold for a generic time instant t as well as for its adjacent $t + dt$; i.e.,

$$\omega_D(t) = 0 \quad \text{and} \quad \omega_D(t + dt) = 0, \quad (26a)$$

or

$$\delta\theta_D(t) = 0 \quad \text{and} \quad \delta\theta_D(t + dt) = 0. \quad (26b)$$

Expanding the above *à* la Taylor, and invoking $(26a)_1$ and $(26b)_1$, we obtain, to the first order,

$$\omega_D + d\omega_D = 0 \Rightarrow d\omega_D = 0, \quad (27a)$$

or

$$\delta\theta_D + d(\delta\theta_D) = 0 \Rightarrow d(\delta\theta_D) = 0 \ [\text{or } (\delta\theta_D)^{\cdot} = 0]. \quad (27b)$$

Then the transitivity equations (21*a*), (22*a*) yield

$$-\delta\omega_D = \left(\frac{\partial \omega_D}{\partial \dot{q}_l}\right)[(\delta q_l)^{\cdot} - \delta(\dot{q}_l)] + H_{lD}\delta\theta_l \quad (28a)$$

$$\{= a_{Dl}[(\delta q_l)^{\cdot} - \delta(\dot{q}_l)] + (\gamma^D_{ll'}\omega_{l'})\delta\theta_l,$$

in the Pfaffian case}; (28*b*)

and therefore

- we cannot assume that both $(\delta q_l)^{\cdot} = \delta(\dot{q}_l)$ and $\delta(d\theta_D) = 0$ (or $\delta\omega_D = 0$) hold, it is either the one or the other;
- if we assume that $(\delta q_l)^{\cdot} = \delta(\dot{q}_l)$, Eqs. (23), then $\delta(d\theta_D) \neq 0$ or $\delta\omega_D \neq 0$; unless $H_{lD} = 0$ (in the Pfaffian case this reduces to the Frobenius integrability conditions $\gamma^D_{ll'} = 0$; and so, by analogy, $H_{lD} = 0$ become the necessary and sufficient conditions for the holonomicity of the nonlinear constraints (1).

These results, under (23), are depicted in Fig. 1.

3.4 Mathematics (i.e., Calculus of Variations). Here the constraints (14*a*) hold for both the fundamental arc I as well as for its adjacent $II = I + \delta I$, as a whole; i.e.,

$$\omega_D(I) = 0 \quad \text{and} \quad \omega_D(I + \delta I) = 0, \quad (29a)$$

or

$$d\theta_D(I) = 0 \quad \text{and} \quad d\theta_D(I + \delta I) = 0, \quad (29b)$$

from which, expanding as before, etc., we obtain

$$\omega_D + \delta\omega_D = 0 \Rightarrow \delta\omega_D = 0, \quad (30a)$$

or

$$d\theta_D + \delta(d\theta_D) = 0 \Rightarrow \delta(d\theta_D) = 0. \quad (30b)$$

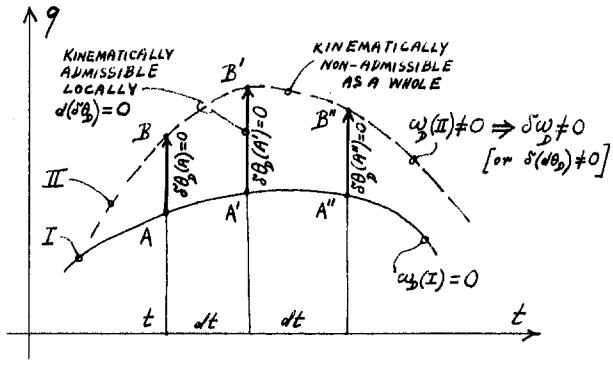


Fig. 1 The arc *I*: *AA'A"* . . . is kinematically (and eventually kinetically) admissible (KA); i.e., $\omega_D(I) = 0$. We have $\delta\theta_D(A) = 0$, $\delta\theta_D(A') = 0$, $\delta\theta_D(A") = 0$, . . . ; i.e., $d(\delta\theta_D) = 0$ or $(\delta\theta_D)^{\cdot} = 0$. But, by the transitivity equations, $\omega_D(II) = \omega_D(I) + \delta\omega_D \neq 0 \Rightarrow \delta\omega_D \neq 0$, or $\delta(d\theta_D) \neq 0$. Hence, the adjacent arc *II*: *BB'B"* . . . , built from locally KA (virtual) displacements, is not KA as a whole.

Downloaded 04 May 2010 to 171.66.16.34. Redistribution subject to ASME license or copyright; see http://www.asme.org/terms/Terms_Use.cfm

Then the transitivity Eqs. (21a), (22a), under (23), yield

$$(\delta\theta_D)^{\cdot} = H_{ID}\delta\theta_I \neq 0 \tag{31a}$$

$$[=(\gamma^D_{II'}\omega_{I'})\delta\theta_I \neq 0, \text{ in the Pfaffian case}]. \tag{31b}$$

These results, again under (23), are depicted in Fig. 2.

In sum, even assuming that $d(\delta q_k) = \delta(dq_k)$, due to the transitivity equations,

- we cannot assume that both

$$\delta(d\theta_D) = 0 \text{ (or } \delta\omega_D = 0), \quad \text{and}$$

$$d(\delta\theta_D) = 0 \text{ [or } (\delta\theta_D)^{\cdot} = 0];$$

- in mechanics ($\rightarrow$) we have

$$d(\delta\theta_D) = 0, \quad \text{or } (\delta\theta_D)^{\cdot} = 0 \text{ (and } d\omega_D = 0),$$

but $\delta(d\theta_D) \neq 0$, (or $\delta\omega_D \neq 0$), even though $d\theta_D = 0$, (or $\omega_D = 0$);

- in mathematics ($\uparrow$) we have

$$\delta(d\theta_D) = 0, \text{ or } \delta\omega_D = 0,$$

but $d(\delta\theta_D) \neq 0$ (or $(\delta\theta_D)^{\cdot} \neq 0$) and $d\omega_D \neq 0$, even though $\delta\theta_D = 0$, or $\omega_D = 0$.

These considerations explain the discrepancy between the equations of mechanics and mathematics, and show clearly that for nonholonomic systems (even conservative ones) the time integral of LP does not lead to a conventional mathematical variational problem; compactly and symbolically we can write

$$\underbrace{\int \delta L dt}_{\text{Mechanics}} \neq \underbrace{\delta \int L dt}_{\text{Mathematics}}.$$

For these reasons, certain authors have modified the integrand of the mechanical variational principle so as to produce a mathematical variational principle that yields the correct equations of motion, e.g., Borri (1994).

In the case of mechanics, and under (23), the transitivity equations yield for the dependent quasi-variables

$$\delta\omega_D = -H_{ID}\delta\theta_I = V_{Ik}\left(\frac{\partial\omega_D}{\partial\dot{q}_k}\right)\delta\theta_I \tag{32a}$$

$$[=\gamma^D_{II'}\omega_{I'}\delta\theta_I, \text{ in the Pfaffian case}], \tag{32b}$$

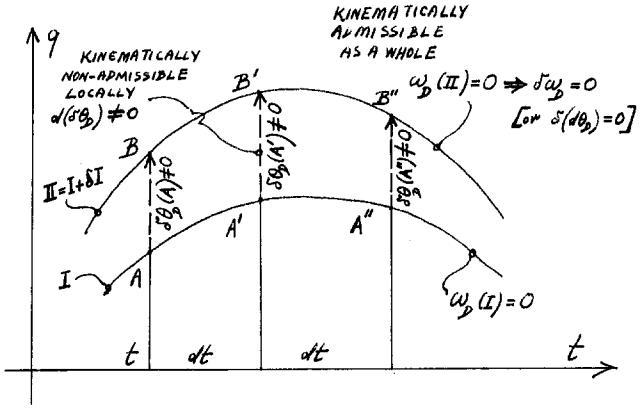


Fig. 2 The arc *I*: $AA'A''\ldots$ is KA; i.e., $\omega_D(I) = 0$. The adjacent arc *II* is KA as a whole; i.e., $\omega_D(II) = 0 \Rightarrow \delta\omega_D = 0$, or $\delta(d\theta_D) = 0$. But by the transitivity equations, $d(\delta\theta_D) \neq 0$ or $(\delta\theta_D)^{\cdot} \neq 0$, and therefore the first-order arrows $AB, A'B', A''B'', \ldots$ are nonvirtual, i.e., $\delta\theta_D(A) \neq 0$, $\delta\theta_D(A') \neq 0$, $\delta\theta_D(A'') \neq 0$. Hence *II* cannot be achieved from *I* by locally KA displacements.

and for the independent ones

$$\delta\omega_I = (\delta\theta_I)^{\cdot} - H_{I'I}\delta\theta_{I'} = (\delta\theta_I)^{\cdot} + V_{I'k}\left(\frac{\partial\omega_I}{\partial\dot{q}_k}\right)\delta\theta_{I'} \tag{33a}$$

$$[=(\delta\theta_I)^{\cdot} + \gamma^I_{I'I''}\omega_{I''}\delta\theta_{I'}, \text{ in the Pfaffian case}]. \tag{33b}$$

4 Integral Variational "Principles"

Let us now formulate the various integral variational formulae of mechanics. Applying chain rule to the general (i.e., nonpotential) form of LP,

$$\underbrace{\left[\frac{d}{dt}\left(\frac{\partial T}{\partial\dot{q}_k}\right) - \frac{\partial T}{\partial q_k}\right]}_{\equiv E_k(T)} - Q_k\Bigg]\delta q_k = 0, \tag{34}$$

where

$\delta' W = Q_k\delta q_k$: first-order virtual work of all *impressed* (i.e., physical, nonconstraint) forces, (34a)

and integrating it between the earlier instants t_1 and t_2 we obtain

$$\int_1^2 \Bigg[\underbrace{\left(\frac{\partial T}{\partial q_k}\right)\delta q_k + \left(\frac{\partial T}{\partial\dot{q}_k}\right)(\delta q_k)^{\cdot}}_{\neq \delta T, \text{ in general}} + Q_k\delta q_k\Bigg]dt = \{(p_k\delta q_k\}_1^2, \tag{35}$$

or, adding and subtracting $(\partial T/\partial\dot{q}_k)\delta\dot{q}_k$ to its integrand,

$$\int_1^2 \Bigg[\left(\frac{\partial T}{\partial q_k}\right)\delta q_k + \left(\frac{\partial T}{\partial\dot{q}_k}\right)(\delta q_k)^{\cdot} + \left(\frac{\partial T}{\partial\dot{q}_k}\right)(\delta\dot{q}_k - \delta\dot{q}_k) + Q_k\delta q_k\Bigg]dt = \{p_k\delta q_k\}, \tag{35a}$$

or, combining the first and third integral sums,

$$\int_1^2 \left\{\delta T + \left(\frac{\partial T}{\partial\dot{q}_k}\right)[(\delta q_k)^{\cdot} - \delta\dot{q}_k] + Q_k\delta q_k\right\}dt = \{p_k\delta q_k\}_1^2, \tag{36}$$

a general form which shows clearly the need for transitivity equations/assumptions. Next, with the helpful notations

$$T = T(t, q, \dot{q}) = T[t, q, \dot{q}(t, q, \omega)] = \underbrace{T^*(t, q, \omega) = T^*}_{\text{unconstrained,}} \tag{37a}$$

$$T^*(t, q, \omega_D = 0, \omega_I \neq 0) = \underbrace{T^*_o(t, q, \omega_I) = T^*_o}_{\text{constrained}}, \tag{37b}$$

noting the vector transformation equations between the system momenta

$$\frac{\partial T}{\partial\dot{q}_k} = \left(\frac{\partial T^*}{\partial\omega_I}\right)\left(\frac{\partial\omega_I}{\partial\dot{q}_k}\right), \tag{38}$$

$$\text{or} \quad \underbrace{p_k}_{\text{holonomic}} = \left(\frac{\partial\omega_I}{\partial\dot{q}_k}\right)\underbrace{P_I}_{\text{nonholonomic}},$$

$$\Rightarrow p_k\delta q_k = P_k\delta\theta_k, \tag{38a}$$

Downloaded 04 May 2010 to 171.66.16.34. Redistribution subject to ASME license or copyright; see http://www.asme.org/terms/Terms_Use.cfm

and invoking the transitivity Eqs. (20) (no constraint enforcement yet) we can rewrite (36) as

$$\int_1^2 \{\delta T + \delta' W + P_k[(\delta\theta_k)^\cdot - \delta\omega_k] - H_{rk}P_k\delta\theta_r\}\,dt = \{P_k\delta\theta_k\}_1^2, \quad (39a)$$

$$\int_1^2 \{\delta T + \delta' W + P_k[(\delta\theta_k)^\cdot - \delta\omega_k] + V_{rk}p_k\delta\theta_r\}\,dt = \{P_k\delta\theta_k\}_1^2, \quad (39b)$$

or, since

$$\delta T = \delta T^* = \left(\frac{\partial T^*}{\partial q_k}\right)\delta q_k + \left(\frac{\partial T^*}{\partial \omega_k}\right)\delta\omega_k = \left(\frac{\partial T^*}{\partial \theta_k}\right)\delta\theta_k + \left(\frac{\partial T^*}{\partial \omega_k}\right)\delta\omega_k, \quad (39c)$$

from which

$$\int_1^2 \{\delta T^* + P_k[(\delta\theta_k)^\cdot - \delta\omega_k]\}\,dt = \ldots = \int_1^2 \left[\left(\frac{\partial T^*}{\partial \theta_k}\right)\delta\theta_k + \left(\frac{\partial T^*}{\partial \omega_k}\right)(\delta\theta_k)^\cdot\right]dt = -\int_1^2 \left[\frac{d}{dt}\left(\frac{\partial T^*}{\partial \omega_k}\right) - \frac{\partial T^*}{\partial \theta_k}\right]\delta\theta_k\,dt + \{P_k\delta\theta_k\}_1^2, \quad (39d)$$

and with

$$\delta' W = Q_k\delta q_k = \Theta_k\delta\theta_k \equiv \delta' W^*$$

(definition of nonholonomic components of system impressed force Θ_k) (39e)

we obtain finally the integral variational equations

$$-\int_1^2 \left[\frac{d}{dt}\left(\frac{\partial T^*}{\partial \omega_k}\right) - \frac{\partial T^*}{\partial \theta_k} + \left(\frac{\partial T^*}{\partial \omega_r}\right)H_{kr} - \Theta_k\right]\delta\theta_k\,dt = 0, \quad (40a)$$

$$-\int_1^2 \left[\frac{d}{dt}\left(\frac{\partial T^*}{\partial \omega_k}\right) - \frac{\partial T^*}{\partial \theta_k} - \left(\frac{\partial T}{\partial \dot{q}_r}\right)^* V_{kr} - \Theta_k\right]\delta\theta_k\,dt = 0, \quad (40b)$$

from which the equations of motion follow: the first m with the constraint reactions as multipliers Λ_D, (since $\delta\theta_D = 0$ or $1\cdot\delta\theta_D = 0$), the remaining $n - m$ without them (i.e., $\Lambda_I = 0$, since $\delta\theta_I \neq 0 \Rightarrow 0\cdot\delta\theta_I = 0$):

$D = 1, \ldots m$:

$$\frac{d}{dt}\left(\frac{\partial T^*}{\partial \omega_D}\right) - \frac{\partial T^*}{\partial \theta_D} + \left(\frac{\partial T^*}{\partial \omega_r}\right)H_{Dr} = \Theta_D + \Lambda_D, \quad (41a)$$

$I = m + 1, \ldots, n$:

$$\frac{d}{dt}\left(\frac{\partial T^*}{\partial \omega_I}\right) - \frac{\partial T^*}{\partial \theta_I} + \left(\frac{\partial T^*}{\partial \omega_r}\right)H_{Ir} = \Theta_I; \quad (41b)$$

and similarly in terms of the V_{kr}.

Remark. Had we assumed $(\delta q_k)^\cdot = \delta(\dot{q}_k)$, then (36) would have led us to

$$\int_1^2 (\delta T + \delta' W)\,dt = \int_1^2 (\delta T^* + \delta' W^*)\,dt = \{P_k\delta\theta_k\}_1^2, \quad (42a)$$

where

$$\delta T^* = \left(\frac{\partial T^*}{\partial \theta_k}\right)\delta\theta_k + \left(\frac{\partial T^*}{\partial \omega_k}\right)\underbrace{[(\delta\theta_k)^\cdot - H_{rk}\delta\theta_r]}_{\delta\omega_k} = \left(\frac{\partial T^*}{\partial \theta_k}\right)\delta\theta_k + \frac{d}{dt}\left[\left(\frac{\partial T^*}{\partial \omega_k}\right)\delta\theta_k\right] - \left(\frac{\partial T^*}{\partial \omega_k}\right)^\cdot\delta\theta_k - H_{rk}\left(\frac{\partial T^*}{\partial \omega_k}\right)\delta\theta_r, \quad (42b)$$

so that

$$\int_1^2 \delta T^*\,dt = -\int_1^2 \left[\frac{d}{dt}\left(\frac{\partial T^*}{\partial \omega_k}\right) - \frac{\partial T^*}{\partial \theta_k} + H_{kr}\left(\frac{\partial T^*}{\partial \omega_r}\right)\right]\delta\theta_k\,dt + \{P_k\delta\theta_k\}_1^2, \quad (42c)$$

and similarly in terms of the V_{kr}, and that would have, obviously, led us to the earlier integral equations (40a, b); i.e., whether we assume that $(\delta q_k)^\cdot = \delta(\dot{q}_k)$ or not, if we are internally consistent we shall end up with the same equations of motion (just like in the case of the derivation of the equations of motion from the central equation of Heun-Hamel).

5 Constrained Forms of the "Principles"

Let us express the integrands of the preceding integral equations in terms of the constrained kinetic energy T_o^*, Eq. (37b), and its variations. We have successively

$$\delta T^* = \left(\frac{\partial T^*}{\partial q_k}\right)\delta q_k + \left(\frac{\partial T^*}{\partial \omega_D}\right)\delta\omega_D + \left(\frac{\partial T^*}{\partial \omega_I}\right)\delta\omega_I = \underbrace{\left(\frac{\partial T_o^*}{\partial q_k}\right)\delta q_k + \left(\frac{\partial T_o^*}{\partial \omega_I}\right)\delta\omega_I}_{\delta T_o^*} + \left(\frac{\partial T^*}{\partial \omega_D}\right)_o\delta\omega_D$$

$$= \delta T_o^* + \left(\frac{\partial T^*}{\partial \omega_D}\right)\delta\omega_D \quad [(\ldots)_o \equiv (\ldots)_{\omega_D=0}] \quad (43a)$$

$$= \delta T_o^* - \left(\frac{\partial T^*}{\partial \omega_D}\right)_o H_{ID}\delta\theta_I \quad (43b)$$

$$= \delta T_o^* + \left(\frac{\partial T}{\partial \dot{q}_k}\right)_o^* V_{IK}\delta\theta_I \quad (43c)$$

$$\left[= \delta T_o^* + \left(\frac{\partial T^*}{\partial \omega_D}\right)_o(-\gamma_{II'}^D\omega_I)\delta\theta_{I'}, \text{ in the Pfaffian case}\right] \quad (43d)$$

and so, for example (42a), assumes the following *constrained* forms

Downloaded 04 May 2010 to 171.66.16.34. Redistribution subject to ASME license or copyright; see http://www.asme.org/terms/Terms_Use.cfm

$$\int_1^2 \left[\delta T_o^* - H_{ID}\left(\frac{\partial T^*}{\partial \omega_D}\right)_o \delta\theta_I + \Theta_I \delta\theta_I \right] dt = \{P_I \delta\theta_I\}_1^2, \quad (44a)$$

$$\int_1^2 \left[\delta T_o^* + V_{Ik}\left(\frac{\partial T}{\partial \dot{q}_k}\right)^*_o \delta\theta_I + \Theta_I \delta\theta_I \right] dt = \{P_I \delta\theta_I\}_1^2, \quad (44b)$$

$$\left\{ \int_1^2 \left[\delta T_o^* - \gamma^D_{II'}\left(\frac{\partial T^*}{\partial \omega_D}\right)_o \omega_I \delta\theta_{I'} + \Theta_I \delta\theta_I \right] dt \right.$$
$$\left. = \{P_I \delta\theta_I\}_1^2, \text{ in the Pfaffian case} \right\}. \quad (44c)$$

Substituting into the above the expressions

$$\delta T_o^* = \left(\frac{\partial T_o^*}{\partial \theta_I}\right)\delta\theta_I + \left(\frac{\partial T_o^*}{\partial \omega_I}\right)\delta\omega_I$$
$$= \left(\frac{\partial T_o^*}{\partial \theta_I}\right)\delta\theta_I + \left(\frac{\partial T_o^*}{\partial \omega_I}\right)[(\delta\theta_I)^\cdot - H_{I'I}\delta\theta_{I'}] \quad (45a)$$
$$= (") + \left(\frac{\partial T_o^*}{\partial \omega_I}\right)\left[(\delta\theta_I)^\cdot + V_{I'k}\left(\frac{\partial \omega_I}{\partial \dot{q}_k}\right)\delta\theta_{I'}\right] \quad (45b)$$
$$\left[= (") + \left(\frac{\partial T_o^*}{\partial \omega_I}\right)[(\delta\theta_I)^\cdot - \gamma^I_{I'I''}\omega_{I'}\delta\theta_{I''}], \right.$$
$$\left. \text{in the Pfaffian case} \right], \quad (45c)$$

leads directly to the n-m reactionless (i.e., multiplierless), or *kinetic*, equations of motion (originally obtained by different methods by Johnsen and Hamel (late 1930s)):

$$\frac{d}{dt}\left(\frac{\partial T_o^*}{\partial \omega_I}\right) - \frac{\partial T_o^*}{\partial \theta_I} + H_{Ik}\left(\frac{\partial T^*}{\partial \omega_k}\right)_o = \Theta_I, \quad (46a)$$

$$\frac{d}{dt}\left(\frac{\partial T_o^*}{\partial \omega_I}\right) - \frac{\partial T_o^*}{\partial \theta_I} - V_{Ik}\left(\frac{\partial T}{\partial \dot{q}_k}\right)^*_o = \Theta_I, \quad (46b)$$

$$\left[\frac{d}{dt}\left(\frac{\partial T_o^*}{\partial \omega_I}\right) - \frac{\partial T_o^*}{\partial \theta_I} + \gamma^k_{II'}\left(\frac{\partial T^*}{\partial \omega_k}\right)_o \omega_{I'} = \Theta_I, \right.$$
$$\left. \text{in the Pfaffian case} \right]. \quad (46c)$$

6 Principle of Suslov et al.

Occasionally, the constraints (1) are given in the form

$$\dot{q}_D = \phi_D(t, q, \dot{q}_I). \quad (47)$$

This can be viewed as the following special case of (14a, b) and (15a, b):

$$\omega_D \equiv \dot{q}_D - \phi_D(t, q, \dot{q}_I) = 0, \quad \omega_I = \dot{q}_I \neq 0; \quad (47a, b)$$
$$\delta\theta_D = (\partial\omega_D/\partial\dot{q}_{D'})\delta q_{D'} + (\partial\omega_D/\partial\dot{q}_I)\delta q_I$$
$$= \delta q_D - \left(\frac{\partial \phi_D}{\partial \dot{q}_I}\right)\delta q_I = 0, \quad (47c)$$

$$\delta\theta_I = (\partial\omega_I/\partial\dot{q}_D)\delta q_D + (\partial\omega_I/\partial\dot{q}_{I'})\delta q_{I'}$$
$$= 0 + (1)\delta q_I \neq 0. \quad (47d)$$

For such a form, a number of authors, such as Suslov (1901) and Rumiantsev (1978, 1979), have utilized the following transitivity assumptions:

$$(\delta q_I)^\cdot = \delta\dot{q}_I, \quad (\delta q_D)^\cdot \neq \delta\dot{q}_D, \quad (48a, b)$$

but

$$\delta\omega_D = \delta\dot{q}_D - \delta\phi_D = 0 \Rightarrow \delta\dot{q}_D = \delta\phi_D. \quad (48c)$$

With the help of the above we successively obtain

$$(\delta q_D)^\cdot - \delta\dot{q}_D = \left[\left(\frac{\partial \phi_D}{\partial \dot{q}_k}\right)\delta q_k\right]^\cdot - \delta\phi_D$$
$$= \ldots = W_{ID}\delta q_I, \quad (49)$$

where

$$W_{ID} \equiv \underbrace{\left[\frac{d}{dt}\left(\frac{\partial \phi_D}{\partial \dot{q}_I}\right) - \frac{\partial \phi_D}{\partial q_I}\right]}_{E_I(\phi_D)} - \left(\frac{\partial \phi_D}{\partial q_{D'}}\right)\left(\frac{\partial \phi_{D'}}{\partial \dot{q}_I}\right);$$

(special nonlinear Voronets coefficients,

a specialization of the V_{ID} for (47a, b)), (49a)

i.e.,

$$(\delta q_D)^\cdot = \delta\dot{q}_D + W_{ID}\delta q_I = \delta\phi_D + W_{ID}\delta q_I. \quad (49b)$$

Remark. The special transitivity Eqs. (49) can also be obtained as follows:

Inverting (20) we readily obtain

$$(\delta q_I)^\cdot - \delta\dot{q}_I = \left(\frac{\partial \dot{q}_I}{\partial \omega_k}\right)[(\delta\theta_k)^\cdot - \delta\omega_k] - H_{rk}\left(\frac{\partial \dot{q}_I}{\partial \omega_k}\right)\delta\theta_r, \quad (49c)$$

and therefore, enforcing the constraints (15a),

$$(\delta q_D)^\cdot - \delta\dot{q}_D = \left(\frac{\partial \dot{q}_D}{\partial \omega_k}\right)\underbrace{[(\delta\theta_k)^\cdot - \delta\omega_k]}_{=0, \text{ by (25}a, b\text{)}} - \underbrace{H_{Ik}\left(\frac{\partial \dot{q}_D}{\partial \omega_k}\right)}_{=V_{ID}, \text{ by (20}b\text{)}}\delta\theta_I,$$

and finally invoking (47d), we obtain

$$(\delta q_D)^\cdot - \delta\dot{q}_D = V_{ID}\delta\theta_I \rightarrow W_{ID}\delta q_I, \text{ i.e., (49).} \quad (49d)$$

(Hence, in view of (25a) and (48c), the Suslov and Rumiantsev viewpoint amounts to assuming that both $\delta\omega_D = 0$ (mathematics) and $(\delta\theta_D)^\cdot = 0$ (mechanics). This in no way contradicts the preceding conclusions and Figs. 1, 2, because the latter assume that $(\delta q_D)^\cdot = \delta(\dot{q}_D)$.)

Next by applying chain rule to

$$T = \underbrace{T(t, q, \dot{q})}_{\text{unconstrained}} = T[t, q, \dot{q}_I, \dot{q}_D = \phi_D(t, q, \dot{q}_I)]$$
$$\equiv \underbrace{T_o(t, q, \dot{q}_I) = T_o}_{\text{specially constrained}} \quad (50a)$$

we readily obtain

$$\frac{\partial T_o}{\partial q_k} = \frac{\partial T}{\partial q_k} + \left(\frac{\partial T}{\partial \dot{q}_D}\right)\left(\frac{\partial \phi_D}{\partial q_k}\right), \quad (50b)$$

$$\frac{\partial T_o}{\partial \dot{q}_I} = \frac{\partial T}{\partial \dot{q}_I} + \left(\frac{\partial T}{\partial \dot{q}_D}\right)\left(\frac{\partial \phi_D}{\partial \dot{q}_I}\right), \quad (50c)$$

Downloaded 04 May 2010 to 171.66.16.34. Redistribution subject to ASME license or copyright; see http://www.asme.org/terms/Terms_Use.cfm

and therefore we find successively

$$\delta T = \left(\frac{\partial T}{\partial q_k}\right)\delta q_k + \left(\frac{\partial T}{\partial \dot{q}_k}\right)\delta \dot{q}_k$$

$$= \underbrace{\left[\frac{\partial T_o}{\partial q_k} - \left(\frac{\partial T}{\partial \dot{q}_D}\right)\left(\frac{\partial \phi_D}{\partial q_k}\right)\right]}_{\partial T/\partial q_k}\delta q_k$$

$$+ \underbrace{\left[\frac{\partial T_o}{\partial \dot{q}_I} - \frac{\partial T}{\partial \dot{q}_D}\left(\frac{\partial \phi_D}{\partial \dot{q}_I}\right)\right]}_{\partial T/\partial \dot{q}_I}\delta \dot{q}_I + \left(\frac{\partial T}{\partial \dot{q}_D}\right)\delta \dot{q}_D$$

$$= \underbrace{\left(\frac{\partial T_o}{\partial q_k}\right)\delta q_k + \left(\frac{\partial T_o}{\partial \dot{q}_I}\right)\delta \dot{q}_I}_{\delta T_o}$$

$$+ \left(\frac{\partial T}{\partial \dot{q}_D}\right)\left\{\delta \dot{q}_D - \underbrace{\left[\left(\frac{\partial \phi_D}{\partial q_k}\right)\delta q_k + \left(\frac{\partial \phi_D}{\partial \dot{q}_I}\right)\delta \dot{q}_I\right]}_{\delta \phi_D}\right\}$$

$$= \delta T_o + \left(\frac{\partial T}{\partial \dot{q}_D}\right)\underbrace{\delta(\dot{q}_D - \phi_D)}_{\delta \omega_D = 0} \qquad (50d)$$

i.e.,

$$\delta T = \delta T_o, \qquad (50e)$$

and therefore, with (48a)–(49), the integral Eq. (36) yields the nonlinear Suslov form:

$$\int_1^2 \left[\delta T_o + \left(\frac{\partial T}{\partial \dot{q}_D}\right)_o W_{ID}\delta q_I + \delta' W\right] dt = \{p_k \delta q_k\}_1^2, \qquad (51)$$

a generalization of the Pfaffian form of (36), originally given by Suslov (1901) (also in Suslov (1946)).

It is not hard to show that (51), with (50e), leads to the n-m special nonlinear Voronets equations:

$$\underbrace{\frac{d}{dt}\left(\frac{\partial T_o}{\partial \dot{q}_I}\right) - \frac{\partial T_o}{\partial q_I}}_{E_I(T_o)} - \left(\frac{\partial T_o}{\partial q_D}\right)\left(\frac{\partial \phi_D}{\partial \dot{q}_I}\right) -$$

$$- \left(\frac{\partial T}{\partial \dot{q}_D}\right)_o W_{ID} = Q_{I,o}, \qquad (52)$$

where

$$\underbrace{\delta' W}_{\text{unconstrained}} \equiv Q_k \delta q_k = \ldots = Q_{I,o}\delta q_I \equiv \underbrace{\delta' W_o}_{\text{constrained}} \qquad (52a)$$

Remark. Here too, had we assumed $(\delta q_k)^{\cdot} = \delta \dot{q}_k$, instead of (48$a$, b), we would still have obtained (51), but by a different route. Instead, then we would have had successively

$$0 \neq \delta \omega_D = \delta(\dot{q}_D - \phi_D)$$

$$= \delta \dot{q}_D - \delta \phi_D$$

$$= (\delta q_D)^{\cdot} - \delta \phi_D \quad \text{(by (23))}$$

$$= \left[\left(\frac{\partial \phi_D}{\partial \dot{q}_I}\right)\delta q_I\right]^{\cdot} - \delta \phi_D$$

$$= \ldots = W_{ID}\delta q_I, \qquad (53a)$$

$$\text{i.e.,} \quad (\delta q_D)^{\cdot} = \delta \dot{q}_D = \delta \phi_D + W_{ID}\delta q_I, \qquad (53b)$$

while (50d) would have yielded

$$\delta T = \delta T_o + \left(\frac{\partial T}{\partial \dot{q}_D}\right)\underbrace{\delta(\dot{q}_D - \phi_D)}_{\delta \omega_D \neq 0}$$

$$= \delta T_o + \left(\frac{\partial T}{\partial \dot{q}_D}\right)_o W_{ID}\delta q_I, \qquad (53c)$$

so that (36) → (42a) would have again produced (51).

Acknowledgments

The author is grateful to the lucid monograph of Novoselov (1966) for providing the initial inspiration for the writing of this paper; and hopes that the latter complements and extends that pioneering work. Also, he would like to thank the unknown reviewers for their helpful and constructive comments on the original manuscript.

References

Borri, M., 1994, "Numerical Approximations in Analytical Dynamics" *Applied Mathematics in Aerospace Science and Engineering,* A. Miele and A. Salvetti, eds., pp. 323–361.

Dobronravov, V. V., 1970, *Fundamentals of Nonholonomic System Mechanics,* Vischaya Shkola, Moscow (in Russian).

Hamel, G., 1904, "Über die virtuellen Verschiebungen in der Mechanik," *Mathematische Annalen,* Vol. 59, pp. 416–434.

Hamel, G., 1924, "Über nichtholonome Systeme," *Mathematische Annalen,* Vol. 92, pp. 33–41.

Hamel, G., 1949, *Theoretische Mechanik,* Springer, Berlin, pp. 492–499.

Maurer, L., 1905, "Über die Differentialgleichungen der Mechanik," *Kgl. Ges. d. Wiss. Göttingen, Nachrichten, Math.-Phys. Klasse,* Heft 2, pp. 91–116.

Mei, F.-X., 1985, *Foundations of Mechanics of Nonholonomic Systems,* Beijing Institute of Technology Press, Beijing (in Chinese).

Neimark, J. I., and Fufaev, N. A., 1972 *Dynamics of Nonholonomic Systems,* American Mathematical Society, Providence, RI (originally in Russian, 1967).

Novoselov, V. S., 1966, *Variational Methods in Mechanics,* Leningrad University Press, Leningrad (in Russian).

Rumiantsev, V. V., 1978, "On Hamilton's Principle for Nonholonomic Systems," *J. Applied Math. Mech.* (PMM), Vol. 42, pp. 407–419.

Rumiantsev, V. V., 1979, "On the Lagrange and Jacobi Principles for Nonholonomic Systems," *J. Appl. Math. Mech.* (PMM), Vol. 43, pp. 625–632.

Suslov, G. K., 1901–2, "On a particular variant of d'Alembert's Principle," *Matematisheskii Svornik,* Vol. 22, pp. 687–691 (in Russian).

Suslov, G. K., 1946, *Theoretical Mechanics,* Technical/Theoretical Literature (Gostehizdat), Moscow and Leningrad (in Russian).

Voronets, P., 1901–2, "On the Equations of Motion for Nonholonomic Systems," *Matematisheskii Svornik,* Vol. 22, pp. 659–686 (in Russian).

Downloaded 04 May 2010 to 171.66.16.34. Redistribution subject to ASME license or copyright; see http://www.asme.org/terms/Terms_Use.cfm

R. Chao
Department of Naval Architecture
and Marine Engineering,
National Cheng Kung University,
Tainan, Taiwan

N. Laws
Department of Mechanical Engineering,
University of Pittsburgh,
Pittsburgh, PA 15261
Mem. ASME

The Fiber-Matrix Interface Crack

The problem of an interface crack between a circular fiber and the surrounding matrix is considered. The problem is formulated and solved with the help of complex variable methods. It is essential to take into account the existence of contact zones at the crack tips. The solution procedure relies on the use of crack opening displacements as the primary variables. Ultimately the governing equations are shown to consist of two coupled singular integral equations together with contact and single valuedness conditions. In general these equations must be solved by numerical methods. Attention is focused on the lengths of the contact zones. It is shown that the lengths of these contact zones are essentially independent of one of the Dundurs parameters.

1 Introduction

There is a substantial literature on interface cracks at the junction of two elastic half-spaces. The apparent existence of the oscillating singularity was first given by Williams (1959). Significant contributions were then given by Erdogan (1963, 1965), Rice and Sih (1965), and England (1965). The dilemma posed by the cited papers is due to the fact that the so-called solution gives rise to overlapping of the materials in a "small" zone near the crack tips. It follows that the "solution" is not a solution to the stated problem. In the context of a penny-shaped crack at an interface, Willis (1972) employed similar ideas to show that overlapping was predicted over a large part of the crack surface.

This unsatisfactory situation was resolved by Comninou (1977, 1978a, b) who gave a correct solution to the problem and which showed that there was a contact zone at each crack tip.

Other authors, for example Atkinson (1982a, b), Sinclair (1980), Mak et al. (1980) have given alternative models to obviate the unacceptable feature of the "classical" solution. More recently Rice (1988) and Suo and Hutchinson (1989) have argued that the classical solution is acceptable for what is termed "small-scale contact." Of course, one can easily argue that if the early "solutions" of the 1960s had been correct there would have been no disagreement and no attempts to present the incorrect solution in a favorable light. However, from a practical perspective, the difficulties inherent in the Comninou-type solutions are extensive: The integral equations are not easy to solve, nor does the associated stress field fit conveniently into standard linear elastic fracture mechanics (Atkinson, 1982a, b).

More recently Gautesen and Dundurs (1987, 1988) have given analytical solutions of the Comninou equations and this certainly helps to elucidate the essential mechanics associated with the crack tips.

The present study is a contribution to the analogous problem of a crack at the interface between a circular fiber and the surrounding matrix. Previous investigations of this problem include those of England (1966), Perlman and Sih (1967), Toya (1974), and Piva (1982). In all the cited contributions, the authors obtain "solutions" which involve overlapping surfaces. The homogeneous counterpart of this problem was, of course, studied by Muskhelishvili (1954). The Muskhelishvili solution has been used by many authors. But, as noted by Toya (1974) and by Chao and Laws (1992), the Muskhelishvili solution fails when the crack surfaces come into contact because of the orientation of the applied loading. This observation prompted the present authors to investigate, inter alia, the proper solution of problems associated with an arc crack in a homogeneous material. Obviously a crucial prediction was the range of loads for which the crack remained open over its entire length.

In the context of an interface crack at a fiber-matrix interface, it appears that we can get crack closure from two sources: one due to the applied loads, the other due to the fact that the crack lies between dissimilar materials. But it is clear that we always have contact zones at the crack tips (and perhaps elsewhere), so there is no choice but to find a proper solution in all cases. This is attempted in the sequel.

As might be expected, our analysis is an extension of the analysis used in our earlier work (Chao and Laws, 1992). More precisely we use complex variable methods to solve the problem. We use a modified version of the Muskhelishvili (1954) potentials which enables us concisely to specify the interface conditions. The problem is then formulated in terms of crack-opening displacements. This leads to two coupled integral equations together with contact conditions and conditions which guarantee single valued displacements. These equations must be solved in order to predict the contact lengths, stress fields, etc. In this paper we restrict attention to the determination of the contact lengths. When the crack surfaces are frictionless our analysis confirms the existence of inverse square-root singularities for the shear stress ahead of the crack tips and the normal stress behind the crack tips (Park and Earmme, 1986). Indeed these observations are a necessary prelude to the numerical work.

The final discretization of the governing equations is obtained with the help of a technique due to Erdogan and Gupta (1972). Some of the numerical results are not unexpected—especially in relation to the relative lengths of the respective contact zones. An interesting conclusion is that the contact lengths are essentially independent of one of the Dundurs parameters.

2 Preliminaries

Consider an interfacial debond crack at the fiber matrix interface as shown in Fig. 1.

We consider the two-dimensional problem in which the infinite solid is loaded by uniform stresses at infinity. In addition we allow for arbitrary loading of the crack surfaces. The formulation, and solution, proposed here is an extension of the analysis developed by the present authors, Chao and Laws (1992), in their study of the problems attendant upon closure of an arc crack in a homogeneous material.

The problem is conveniently formulated in terms of the Muskhelishvili complex potentials. In standard notation

Contributed by the Applied Mechanics Division of THE AMERICAN SOCIETY OF MECHANICAL ENGINEERS for publication in the ASME JOURNAL OF APPLIED MECHANICS.

Discussion on this paper should be addressed to the Technical Editor, Professor Lewis T. Wheeler, Department of Mechancial Engineering, University of Houston, Houston, TX 77204-4792, and will be accepted until four months after final publication of the paper itself in the ASME JOURNAL OF APPLIED MECHANICS.

Manuscript received by the ASME Applied Mechanics Division, Oct. 15, 1996; final revision, Apr. 25, 1997. Associate Technical Editor: I. M. Daniel.

Copyright © 1997 by ASME

Downloaded 04 May 2010 to 171.66.16.34. Redistribution subject to ASME license or copyright; see http://www.asme.org/terms/Terms_Use.cfm

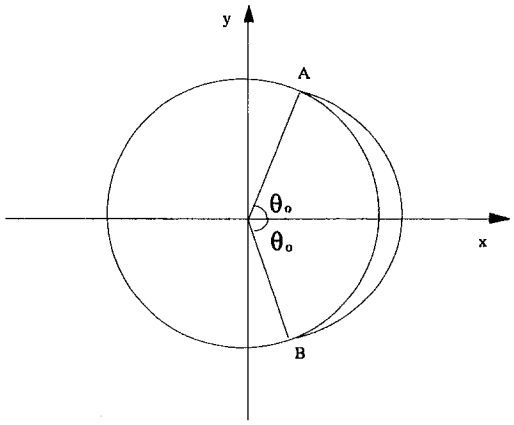


Fig. 1 Geometrical configuration of interface crack AB of half-angle θ_0

$$\sigma_{rr}^k + \sigma_{\theta\theta}^k = 2\{\phi_k'(z) + \overline{\phi}_k'(\overline{z})\}, \quad (1)$$

$$\sigma_{rr}^k + i\sigma_{r\theta}^k = \phi_k'(z) + \overline{\phi}_k'(\overline{z}) - z\overline{\phi}_k''(\overline{z}) - \frac{\overline{z}}{z}\overline{\psi}_k'(\overline{z}), \quad (2)$$

and

$$2\mu_k(u_k + iv_k) = \kappa_k\phi_k(z) - z\overline{\phi}_k'(\overline{z}) - \overline{\psi}_k(\overline{z}), \quad (3)$$

where σ_{rr}, $\sigma_{\theta\theta}$, $\sigma_{r\theta}$ are the stresses in polar coordinates. On the other hand u and v are the displacements in Cartesian coordinates. We follow England (1966) and use the label $k = 1$ to refer to the infinite matrix ($|z| > a$: denoted by S_+) and the label $k = 2$ to refer to the circular fiber ($|z| < a$: denoted by S_-), where a is the radius of the fiber. Also μ_k ($k = 1, 2$) are the respective shear moduli,

$$\kappa_k = 3 - 4\nu_k \quad \text{plane strain},$$

$$\kappa_k = \frac{3 - \nu_k}{1 + \nu_k} \quad \text{generalized plane stress},$$

with $\nu_k (k = 1, 2)$ denoting Poisson's ratio. Following Chao and Laws (1992), it is expedient to introduce the complex potentials

$$\chi_k(z) = z\overline{\phi}_k'\left(\frac{a^2}{z}\right) + \overline{\psi}_k\left(\frac{a^2}{z}\right). \quad (4)$$

The use of the complex potentials ϕ_k and χ_k greatly simplifies the analysis of the conditions at the crack.

At this juncture it is appropriate to observe that

$$\phi_1: S_+ \to \mathbf{C}, \quad \chi_1: S_- \to \mathbf{C},$$

$$\phi_2: S_- \to \mathbf{C}, \quad \chi_2: S_+ \to \mathbf{C},$$

where $\mathbf{C}$ is the set of all complex numbers. After some routine algebra we can show that

$$\sigma_{rr}^k + i\sigma_{r\theta}^k = \Phi_k(z) + \left\{1 - \frac{a^2}{z\overline{z}}\right\}\overline{\Phi}_k(\overline{z}) - \overline{z}\left\{1 - \frac{a^2}{z\overline{z}}\right\}\overline{\Phi}_k'(\overline{z}) + \frac{a^2}{z\overline{z}}\Xi_k\left(\frac{a^2}{\overline{z}}\right). \quad (5)$$

Here, as usual, $\phi_k'(z) = \Phi_k(z)$, $\chi_k'(z) = \Xi_k(z)$. Also, along any circle center O

$$2\mu_k\frac{d}{d\theta}(u_k + iv_k) = iz\left\{\kappa_k\Phi_k(z) - \left(1 - \frac{a^2}{z\overline{z}}\right)\overline{\Phi}_k(\overline{z}) + \overline{z}\left(1 - \frac{a^2}{z\overline{z}}\right)\overline{\Phi}_k'(\overline{z}) - \frac{a^2}{z\overline{z}}\Xi_k\left(\frac{a^2}{\overline{z}}\right)\right\}. \quad (6)$$

When the circle lies entirely within the matrix the label $k = 1$, and when the circle lies entirely within the fiber we have $k = 2$.

In the general formulation of the problem we allow for applied tractions on the inner and outer surfaces of the crack which are equal and opposite:

on outer surface:

$$(\sigma_{rr}^1 + i\sigma_{r\theta}^1)_+ = N(\theta) + iS(\theta) \quad |\theta| < \theta_0 \quad (7)$$

on inner surface:

$$(\sigma_{rr}^2 + i\sigma_{r\theta}^2)_- = N(\theta) + iS(\theta) \quad |\theta| < \theta_0. \quad (8)$$

Here the subscript + obviously refers to the limit as we approach the crack surface with $z \in S_+$. Similar remarks apply to the subscript $-$. We allow for arbitrary *uniform* stress but demand that there is no rigid rotation at infinity. In view of the fact that the applied tractions specified over the crack surfaces in Eqs. (7) and (8) are self-equilibrated, we can read off the behavior of the complex potentials at the origin and at infinity from Muskhelishvili (1954) in the form

$$\Phi_1(z) = \Gamma + O\left(\frac{1}{z^2}\right), \quad |z| \to \infty, \quad (9)$$

$$\Xi_1(z) = -\frac{\overline{\Gamma}'a^2}{z^2} + D_0 + O(z), \quad |z| \to 0, \quad (10)$$

$$\Phi_2(z) = A_0 + O(z), \quad |z| \to 0, \quad (11)$$

$$\Xi_2(z) = B_0 + O\left(\frac{1}{z^2}\right), \quad |z| \to \infty. \quad (12)$$

where A_0, B_0, and D_0 are complex constants. We also have the consistency condition, (Muskhelishvili, 1954),

$$B_0 = \overline{A}_0. \quad (13)$$

Since there is no rigid rotation at infinity, the constants Γ and Γ' are given by the standard formulae

$$\Gamma = \tfrac{1}{4}(\sigma_{xx}^\infty + \sigma_{yy}^\infty), \quad (14)$$

$$\Gamma' = -\tfrac{1}{2}(\sigma_{xx}^\infty - \sigma_{yy}^\infty - 2i\sigma_{xy}^\infty). \quad (15)$$

3 Interface Conditions

We first discuss the conditions which must be satisfied over the interface. From Eqs. (7) and (8) we see that over the crack itself we have

$$(\sigma_{rr}^1 + i\sigma_{r\theta}^1)_+ = (\sigma_{rr}^2 + i\sigma_{r\theta}^2)_- \quad |\theta| < \theta_0. \quad (16)$$

But clearly the condition (16) also applies over the uncracked part of the interface. With the help of Eq. (5) we can now show that over the entire circle $t = ae^{i\theta}$

$$\Phi_1(t)_+ + \Xi_1(t)_- = \Phi_2(t)_- + \Xi_2(t)_+. \quad (17)$$

Thus we define the function $F(z)$:

$$z \in S_+, \quad F(z) = \Phi_1(z) - \Xi_2(z), \quad (18)$$

$$z \in S_-, \quad F(z) = \Phi_2(z) - \Xi_1(z), \quad (19)$$

and it follows that $F(z)$ is continuous across the circle $|z| =$

Downloaded 04 May 2010 to 171.66.16.34. Redistribution subject to ASME license or copyright; see http://www.asme.org/terms/Terms_Use.cfm

a and analytic in the entire plane except possibly at the origin and at infinity. Indeed, $F(z)$ is analytic in the entire plane except possibly at the origin and at infinity.

Next, consider the displacements at the interface, or more precisely, the angular gradient of the displacements. Over the *uncracked* part of the interface we must have

$$\frac{d}{d\theta}(u_1 + iv_1)_+ = \frac{d}{d\theta}(u_2 + iv_2)_- \tag{20}$$

and with the help of Eq. (6) we find that over the *uncracked* part of the interface

$$\frac{\kappa_1}{\mu_1}\Phi_1(t)_+ - \frac{1}{\mu_1}\Xi_1(t)_- = \frac{\kappa_2}{\mu_2}\Phi_2(t)_- - \frac{1}{\mu_2}\Xi_2(t)_+. \tag{21}$$

Accordingly we define the function $G(z)$ through

$$z \in S_+: G(z) = \frac{\kappa_1}{\mu_1}\Phi_1(z) + \frac{1}{\mu_2}\Xi_2(z), \tag{22}$$

$$z \in S_-: G(z) = \frac{\kappa_2}{\mu_2}\Phi_2(z) + \frac{1}{\mu_1}\Xi_1(z). \tag{23}$$

It now follows that $G(z)$ is continuous over the *uncracked* interface and analytic elsewhere, except perhaps at zero and infinity. Thus $G(z)$ is analytic everywhere except over the crack and perhaps at zero and infinity.

The subsequent algebra is much simplified when we work with $F(z)$ and $G(z)$. It is easy to show that

$$\Phi_1(z) = \frac{\mu_1}{\mu_1 + \kappa_1\mu_2}\{F(z) + \mu_2 G(z)\},$$

$$\Xi_1(z) = \frac{\mu_1}{\mu_2 + \kappa_2\mu_1}\{-\kappa_2 F(z) + \mu_2 G(z)\},$$

$$\Phi_2(z) = \frac{\mu_2}{\mu_2 + \kappa_2\mu_1}\{F(z) + \mu_2 G(z)\},$$

$$\Xi_2(z) = \frac{\mu_2}{\mu_1 + \kappa_1\mu_2}\{-\kappa_1 F(z) + \mu_1 G(z)\}. \tag{24}$$

It is a simple matter to deduce the required behavior of $F(z)$ and $G(z)$ at zero and infinity from Eqs. (9)–(12). The asymptotic behavior at infinity is given by

$$F(z) = \Gamma - B_0 + O\left(\frac{1}{z^2}\right), \quad |z| \to \infty, \tag{25}$$

$$G(z) = \frac{\kappa_1}{\mu_1}\Gamma + \frac{1}{\mu_2}B_0 + O\left(\frac{1}{z^2}\right), \quad |z| \to \infty. \tag{26}$$

In addition the behavior at the origin is given by

$$F(z) = A_0 - D_0 + \frac{\bar{\Gamma}' a^2}{z^2} + O(z), \quad |z| \to 0, \tag{27}$$

$$G(z) = -\frac{1}{\mu_1}\frac{\bar{\Gamma}' a^2}{z^2} + \frac{\kappa_2}{\mu_2}A_0 + \frac{1}{\mu_1}D_0 + O(z), \quad |z| \to 0. \tag{28}$$

Of course we still need to make use of the consistency condition given in Eq. (13).

We have already seen that $F(z)$ is analytic in the entire plane except at the origin and infinity. But Eqs. (25) and (27) indicate that $F(z)$ has at most a second-order pole at the origin and is bounded at infinity. It follows that

$$F(z) = f_0 + \frac{f_2}{z^2} \quad \text{all } z \tag{29}$$

where f_0 and f_2 are constants. Also

$$f_0 = \Gamma - B_0 = A_0 - D_0, \tag{30}$$

$$f_2 = \bar{\Gamma}' a^2. \tag{31}$$

At this stage in the analysis we return to the traction conditions (7) and (8) which apply at the crack surfaces and recall that Eq. (16) was obtained by subtraction. Thus we now add (7) and (8) and make use of Eq. (5) to give

$$\Phi_1(t)_+ + \Xi_1(t)_- + \Phi_2(t)_- + \Xi_2(t)_+ = 2(N + iS) \quad |\theta| < \theta_0.$$

With the help of Eqs. (24) we can rewrite the interface condition (32) in terms of F and G:

$$G(t)_+ + \rho G(t)_- + \frac{1 - \kappa_1\kappa_2}{\mu_2 + \kappa_2\mu_1}F(t) = \frac{\mu_1 + \kappa_1\mu_2}{\mu_1\mu_2}(N + iS)$$
$$t = ae^{i\theta}, \quad |\theta| < \theta_0, \tag{33}$$

where

$$\rho = \frac{\mu_1 + \kappa_1\mu_2}{\mu_2 + \kappa_2\mu_1}. \tag{34}$$

In the standard problem of an interface crack loaded only by tractions at infinity, the temptation is to set $N = S = 0$ in Eq. (33) and then solve the resulting Hilbert problem for $G(z)$ (England, 1966). And this is precisely where the standard "solution" procedure goes wrong. As is now well known, the standard procedure goes wrong because the crack surfaces come into contact (except in certain pathological situations) and thus the normal and shear stresses on the crack surfaces are *not* zero over the contact region. It follows that we can not solve the problem merely by regarding Eq. (33) as a standard Hilbert problem for the determination of $G(z)$. Indeed we must provide an extended analysis of the problem in which N and S must be determined as part of the solution. The obvious suggestion is to regard the crack-opening displacements as the primary variables. In this event Eq. (33) will ultimately provide us with the singular integral equations for the determination of the crack-opening displacement gradients, together with the expressions for the evaluation of the contact stresses.

4 Reduction to Singular Integral Equations

We follow the pattern set in our earlier study (Chao and Laws, 1992), of the circular arc crack in a homogeneous solid in which we showed how to reduce the problem to a pair of coupled integral equations. In the present problem there are, however, significant additional difficulties.

With rare exceptions, the interfacial crack surfaces will come into contact. It is therefore *essential* to allow for contact stresses over the entire crack surface at the outset. Accordingly we must derive the general governing equations from which special cases may easily be obtained.

The key to the analysis is to work with the unknown crack opening displacements[1]:

$$D(t) = d(\theta) = (u_1 + iv_1)_+ - (u_2 + iv_2)_-,$$
$$t = ae^{i\theta}, \quad |\theta| < \theta_0. \tag{35}$$

More precisely, we use the *crack-opening displacement gradients* given by

$$d'(\theta) = b_x(\theta) + ib_y(\theta) = e^{i\theta}\{b_r(\theta) + ib_\theta(\theta)\},$$
$$|\theta| < \theta_0. \tag{36}$$

It may help if we state here that the aim of this section is to formulate the problem in terms of the crack-opening displacement gradient fields b_r and b_θ. Obviously

[1] The symbol D used here does not have the same interpretation as that used by Muskhelishvili (1954), England (1966), or many others.

Downloaded 04 May 2010 to 171.66.16.34. Redistribution subject to ASME license or copyright; see http://www.asme.org/terms/Terms_Use.cfm

$$d'(\theta) = itD'(t) \quad |\theta| < \theta_0. \tag{37}$$

It is easy to show that the requirement of single valued displacements leads to

$$\int_{-\theta_0}^{\theta_0} d'(\theta)d\theta = \int_{-\theta_0}^{\theta_0} D'(t)dt = 0. \tag{38}$$

The next step is to determine $d'(\theta)$ in terms of $G(t)$. This is accomplished by returning to Eq. (6) from which we may show that

$$2\mu_1 \frac{d}{d\theta}(u_1 + iv_1)_+ = it\{\kappa_1\Phi_1(t)_+ - \Xi_1(t)_-\}, \tag{39}$$

$$2\mu_2 \frac{d}{d\theta}(u_2 + iv_2)_- = it\{\kappa_2\Phi_2(t)_- - \Xi_2(t)_+\}. \tag{40}$$

When use is made of the definitions (22) and (23), we can show from (35), (39), and (40) that

$$2D'(t) = G(t)_+ - G(t)_- \quad |\theta| < \theta_0. \tag{41}$$

We have already seen that $G(z)$ is analytic in the whole complex plane except over the crack surface and at zero and infinity. But the behavior at zero and infinity is specified in Eqs. (28) and (26), respectively. It then follows from Eq. (41) that

$$G(z) = -\frac{1}{\pi i}\int_{-\theta_0}^{\theta_0} \frac{D'(t)}{t - z}dt + E_0 + \frac{E_2}{z^2}, \tag{42}$$

where E_0 and E_2 are (complex) constants. Furthermore the behavior of $G(z)$ at the origin, specified in Eq. (26), leads to

$$E_2 = -\frac{1}{\mu_1}\bar{\Gamma}'a^2, \tag{43}$$

and

$$E_0 - \frac{1}{\pi i}\int_{-\theta_0}^{\theta_0} \frac{D'(t)}{t}dt = \frac{\kappa_2}{\mu_2}A_0 + \frac{1}{\mu_1}D_0. \tag{44}$$

On the other hand, the behavior of $G(z)$ at infinity indicated in (26) leads to the result that

$$E_0 = \frac{\kappa_1}{\mu_1}\Gamma + \frac{1}{\mu_2}B_0. \tag{45}$$

We may now use Eqs. (30), (44), and (45) together with the single valued condition (13) to determine the constants A_0, B_0, E_0, and D_0. The results are

$$A_0 = \bar{B}_0 = \frac{(\kappa_1 + 1)\mu_2}{2\mu_2 + (\kappa_2 - 1)\mu_1}\Gamma - \frac{\mu_1\mu_2}{\pi a\{2\mu_2 + (\kappa_2 - 1)\mu_1\}} \times \int_{-\theta_0}^{\theta_0} b_\theta(\theta)d\theta + \frac{i\mu_2}{(\kappa_2 + 1)\pi a}\int_{-\theta_0}^{\theta_0} b_r(\theta)d\theta \tag{46}$$

$$D_0 = \frac{2\kappa_1\mu_2 - (\kappa_2 - 1)\mu_1}{2\mu_2 + (\kappa_2 - 1)\mu_1} - \frac{2\mu_1\mu_2}{\pi a\{2\mu_2 + (\kappa_2 - 1)\mu_1\}}\int_{-\theta_0}^{\theta_0} b_\theta(\theta)d\theta, \tag{47}$$

$$E_0 = \frac{2\kappa_1\mu_2 + \kappa_1\kappa_2\mu_1 + \mu_1}{\mu_1\{2\mu_2 + (\kappa_2 - 1)\mu_2\}}\Gamma - \frac{\mu_1}{\pi a\{2\mu_2 + (\kappa_2 - 1)\mu_1\}} \times \int_{-\theta_0}^{\theta_0} b_\theta(\theta)d\theta - \frac{i}{(\kappa_2 + 1)\pi a}\int_{-\theta_0}^{\theta_0} b_r(\theta)d\theta. \tag{48}$$

With the help of (30), (46), and (47) we can now evaluate the remaining unknown constant f_0 as

$$f_0 = \frac{(\mu_2 + \kappa_2\mu_1)(1 - \rho)}{2\mu_2 + (\kappa_2 - 1)\mu_1}\Gamma + \frac{\mu_1\mu_2}{\pi a\{2\mu_2 + (\kappa_2 - 1)\mu_1\}} \times \int_{-\theta_0}^{\theta_0} b_\theta(\theta)d\theta - \frac{i\mu_2}{(\kappa_2 + 1)\pi a}\int_{-\theta_0}^{\theta_0} b_r(\theta)d\theta. \tag{49}$$

Next, we may apply the Plemelj formulae to the expression for $G(z)$ given in Eq. (42) to show that

$$G(t)_+ + \rho G(t)_- = (1 - \rho)D'(t) - \frac{1 + \rho}{\pi i}\int_{-\theta_0}^{\theta_0} \frac{D'(\xi)}{\xi - t}d\xi + (1 + \rho)\left\{E_0 + \frac{E_2}{t^2}\right\}, \quad |\theta| < \theta_0. \tag{50}$$

Finally we may substitute (50) into (33) and make use of the formulae (46) to (49).

After some long algebraic manipulations, we obtain the complex singular integral equation:

$$\frac{C}{2\pi a}\int_{-\theta_0}^{\theta_0}\left\{\cot\left(\frac{\phi - \theta}{2}\right) + i\right\}\{b_r(\phi) + ib_\theta(\phi)\}d\phi - \frac{C\beta}{a}\{b_\theta(\theta) - ib_r(\theta)\} = N(\theta) + iS(\theta) - \frac{2(1 + \alpha)}{1 + \alpha - 2\beta}\Gamma + \frac{1 + \alpha}{1 + \beta}\bar{\Gamma}'e^{-2i\theta} + \frac{C(1 - \alpha)(1 + \beta)}{2\pi a(1 + \alpha - 2\beta)}\int_{-\theta_0}^{\theta_0} b_\theta(\phi)d\phi + \frac{iC(1 + \beta)}{2\pi a}\int_{-\theta_0}^{\theta_0} b_r(\phi)d\phi \tag{51}$$

where we have introduced the Dundurs parameters α, β, C defined through

$$\alpha = \frac{\mu_2(\kappa_1 + 1) - \mu_1(\kappa_2 + 1)}{\mu_2(\kappa_1 + 1) + \mu_1(\kappa_2 + 1)} \tag{52}$$

$$\beta = \frac{\mu_2(\kappa_1 - 1) - \mu_1(\kappa_2 - 1)}{\mu_2(\kappa_1 + 1) + \mu_1(\kappa_2 + 1)} \tag{53}$$

$$C = \frac{2\mu_1(1 + \alpha)}{(\kappa_1 + 1)(1 - \beta^2)} = \frac{2\mu_2(1 - \alpha)}{(\kappa_2 + 1)(1 - \beta^2)}. \tag{54}$$

The complete specification of the problem demands that we arrive at a suitable version of the contact conditions. In the first place, it is evident that we must ensure that

$$\sigma_{rr} \leq 0 \tag{55}$$

over the entire contact region. Second, we must derive an appropriate form of the geometrical contact condition. Following Chao and Laws (1992), who in turn rely on a technique due to Kalandiya (1975), we can show that

$$\left[\frac{d^2u_r^1}{d\theta^2} + u_r^1\right]_+ - \left[\frac{d^2u_r^2}{d\theta^2} + u_r^2\right]_- = b_\theta + \frac{db_r}{d\theta}.$$

Thus we can express the geometrical contact condition in the form

$$b_\theta(\theta) + \frac{db_r(\theta)}{d\theta} = 0. \tag{56}$$

Finally we need to express the requirement (38) for single-valued displacements in terms of b_r and b_θ. An elementary calculation yields

$$\int_{-\theta_0}^{\theta_0} e^{i\theta}(b_r + ib_\theta)d\theta = 0.$$

Separating this into real and imaginary parts gives

Downloaded 04 May 2010 to 171.66.16.34. Redistribution subject to ASME license or copyright; see http://www.asme.org/terms/Terms_Use.cfm

$$\int_{-\theta_0}^{\theta_0} \{b_r(\theta) \cos\theta - b_\theta(\theta) \sin\theta\} d\theta = 0, \quad (57)$$

$$\int_{-\theta_0}^{\theta_0} \{b_r(\theta) \sin\theta + b_\theta(\theta) \cos\theta\} d\theta = 0. \quad (58)$$

We conclude this section by noting that when the applied load at infinity is simple tension, T, at angle ω to the x-axis, without rigid rotation,

$$\Gamma = \tfrac{1}{4} T, \Gamma' = -\tfrac{1}{2} Te^{-2i\omega},$$

in which case Eq. (51) reduces to the pair of integral equations

$$\frac{C}{2\pi a}\int_{-\theta_0}^{\theta_0} \cot\frac{\phi-\theta}{2} b_r(\phi)d\phi - \frac{C\beta}{a} b_\theta(\theta)$$
$$= N(\theta) - \frac{1+\alpha}{2(1+\alpha-2\beta)} T$$
$$- \frac{1+\alpha}{2(1+\beta)} T\cos 2(\omega-\theta)$$
$$+ \frac{C(2-\beta-\alpha\beta)}{2\pi a(1+\alpha-2\beta)}\int_{-\theta_0}^{\theta_0} b_\theta(\phi)d\phi \quad |\theta| < \theta_0 \quad (59)$$

$$\frac{C}{2\pi a}\int_{-\theta_0}^{\theta_0} \cot\frac{\phi-\theta}{2} b_\theta(\phi)d\phi + \frac{C\beta}{a} b_r(\theta)$$
$$= S(\theta) - \frac{1+\alpha}{2(1+\beta)} T\sin 2(\omega-\theta)$$
$$+ \frac{C\beta}{2\pi a}\int_{-\theta_0}^{\theta_0} b_r(\phi)d\phi, \quad |\theta| < \theta_0. \quad (60)$$

For smooth contact $S = 0$. In this context we must solve Eqs. (59) and (60) subject to the pressure constraint (55) and the geometric compatibility condition (56) in the contact region, together with the single valued requirements (57) and (58). Of course, we must bear in mind that the contact lengths are to be determined as part of the solution.

There are some rather special situations in which the governing equations of this section experience some significant simplifications. One example is when the fiber and matrix have the same elastic moduli, so that $\alpha = \beta = 0$, in which case Eqs. (59) and (60) reduce to those given earlier by Chao and Laws (1992). A second example occurs in the plane-strain problem of a smooth interface crack opened by uniform pressure when both fiber and matrix are incompressible. In this case the parameter $\beta = 0$ and the integral equation (51) is solvable analytically. But this case is of no interest here since this solution can be read off directly from England's (1966) paper.

For the most part the authors are neither aware of, nor able to find, analytical solutions of the governing equations. We must, therefore, resort to numerical methods. At the time of writing, the only general procedure available to the authors consists of a numerical scheme based on the work of Erdogan and Gupta (1972), Comninou (1977), and Chao and Laws (1992). Details are given by Chao (1991).

5 Smooth Interface Crack Opened by Uniform Pressure

Perhaps the simplest problem to solve and to interpret relates to a smooth interface crack opened by uniform pressure with zero stress at infinity. Of course, we must keep in mind that the existence of contact zones at the ends of the crack means that the statement of the problem is more accurately described as the opening by uniform pressure over the *open* part of the crack.

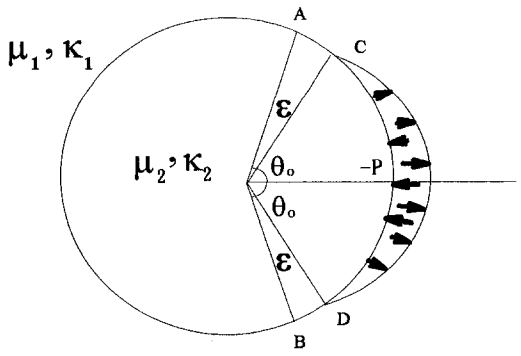


Fig. 2 Configuration of the smooth interface crack AB opened by normal pressure. AC and BD are the contact zones.

The numerical solution of this problem is not easy—especially since the extent of the contact zones must be determined as part of the solution. It is not appropriate here to go into details of the numerical scheme, since Chao (1991) has already given an extended discussion of various alternatives. It is useful to introduce the normalized angular coordinate

$$\xi = \frac{\tan\frac{\theta}{2}}{\tan\frac{\theta_0}{2}}.$$

The five governing equations may then be rewritten using the linear coordinate ξ which has the range $[-1, +1]$. Since we are looking for solutions for b_r and b_θ which have integrable singularities, a careful examination of the (complicated) singular integral equations provides two fundamental conclusions: The field b_θ has inverse square root singularities at the crack tips, whereas the field b_r vanishes at both crack tips—as might be expected from the study of the straight interface crack problem by Comninou and Schmueser (1979). These observations help to decide upon an efficient discretization procedure.

From a physical perspective, it is particularly useful to have some appreciation of the contact length. As indicated schematically in Fig. 2, when the original crack AB is loaded, we find two contact zones AC and BD. For convenience we use a normalized contact length, δ, defined by

$$\delta = \frac{\tan\frac{\epsilon}{2}}{\tan\frac{\theta_0}{2}}.$$

There are many physical parameters in this problem and this

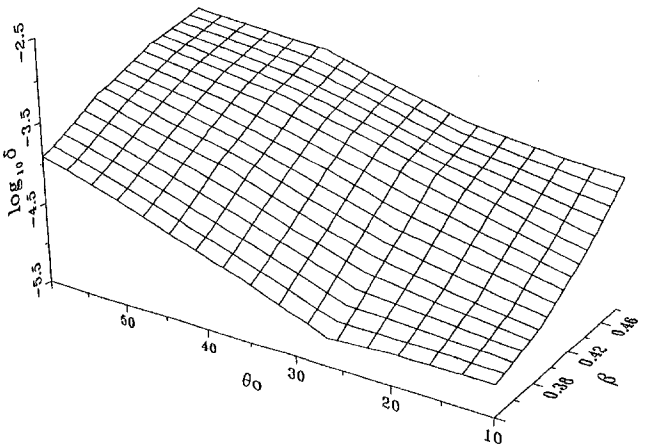


Fig. 3 Contact length at each crack tip for an interface crack opened by uniform internal pressure

Downloaded 04 May 2010 to 171.66.16.34. Redistribution subject to ASME license or copyright; see http://www.asme.org/terms/Terms_Use.cfm

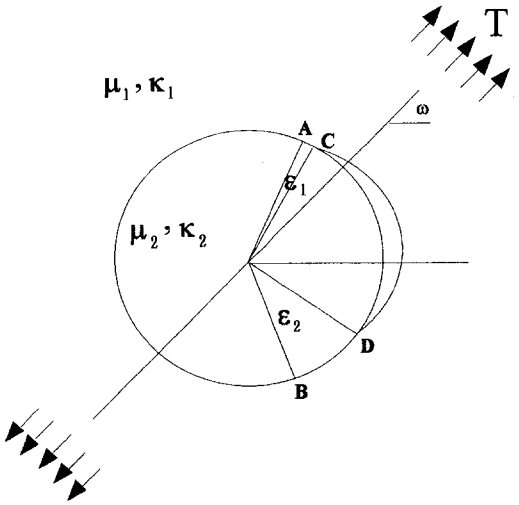


Fig. 4 Schematic diagram showing the different contact lengths for a crack, AB, under uniaxial loading, T, at infinity inclined at angle ω to the x-axis. Note that the contact zones AC and BD, which subtend angles ϵ_1, ϵ_2, respectively, at the origin are of different lengths.

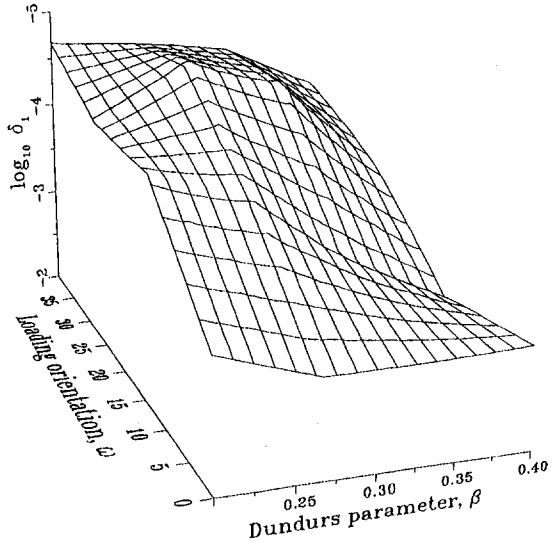


Fig. 6 Contact length at the upper crack tip A of a crack of half-angle $\theta_0 = 60$ deg, with Dundurs parameter $\alpha = 0.75$ for uniaxial loading of the matrix at infinity inclined at orientation ω to the x-axis. The variation of the contact length with ω and Dundurs parameter β is shown.

prevents us from offering a categorical set of conclusions. However, we have sufficient numerical results to assert, with confidence, that the normalized contact length, δ, and hence the actual contact length, is essentially independent of the Dundurs parameter α. Thus we need only plot the variation of δ versus the crack half-angle, θ_0, and the Dundurs parameter β—as shown in Fig. 3. As expected, the contact zones are quite small compared with crack size. For example, when $\theta_0 = 45$ deg and $\beta = 0.4$, each contact zone extends to about 0.1 percent of the total crack length. We also note the satisfying conclusion that for small values of θ_0, there is good agreement with the numerical results of Comninou (1997, 1978, 1979) and the analytical results of Gautesen and Dundurs (1987, 1988).

Clearly, we can also use our results to discuss the stresses everywhere—in particular, in the neighborhood of the crack tips. In fact we can show that the shear stress ahead of the crack tip has an inverse square root singularity, whereas the normal stress of the crack tip is finite—but large. In addition the normal stress over the closed part of the crack surface experiences the usual inverse square root singularity. The implications for stress intensity factors and energy release rates are thus expected to mirror the results for straight interfacial cracks. For the most part, this anticipated conclusion is confirmed by the numerical results. A full discussion will be given elsewhere.

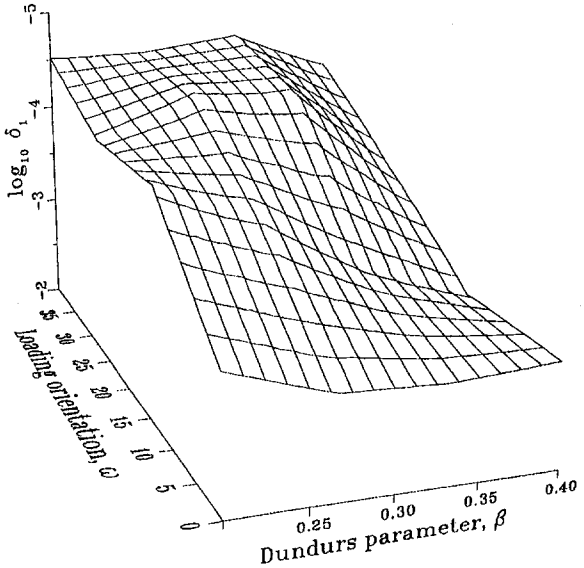


Fig. 5 Contact length at the upper crack tip A of a crack of half-angle $\theta_0 = 60$ deg, with Dundurs parameter $\alpha = 0.5$, for uniaxial loading of the matrix at infinity inclined at orientation ω to the x-axis. The variation of the contact length with ω and Dundurs parameter β is shown.

6 Uniaxial Loading

Perhaps the problem of greatest physical interest is uniaxial loading (see Fig. 4).

It is pertinent to remark that the subsequent analysis is an extension of our earlier study of the homogeneous arc crack problem, Chao and Laws (1992). A point of concern in that study was the extent to which the crack remained open for various orientations (ω) of the applied load. This issue was addressed by Toya (1974) on the basis of the Muskhelishvili (1954) solution. And it is reassuring that there is agreement on the range of crack angles (θ_0) and load orientations (ω) for which the crack in an infinite homogeneous material remains open (see Fig. 2 of Chao and Laws (1992) and Fig. 2 of Toya (1974).

In the case of interfacial cracks, the issue of open versus closed cracks is irrelevant. There is always[2] a contact zone at each end of the crack. Of course, one could argue that cracks whose contact zones were less than 0.1 percent (say) of the length of the crack, were essentially open. But it is not easy to give an unambiguous interpretation to such assertions. For definiteness, we here restrict our attention to a strict quantification of the lengths of the contact zones in various loading environments.

When the fiber-matrix system is subjected to uniaxial tension at infinity, it is obvious that the contact lengths at the ends of the crack are, in general different. With the help of Fig. 4 we define the two normalized contact lengths δ_1 and δ_2:

$$\delta_1 = \frac{\tan\frac{\epsilon_1}{2}}{\tan\frac{\theta_0}{2}}, \quad \delta_2 = \frac{\tan\frac{\epsilon_2}{2}}{\tan\frac{\theta_0}{2}}.$$

The difficulties which we experienced in the numerical work

[2] Apart from one or two pathological cases.

Downloaded 04 May 2010 to 171.66.16.34. Redistribution subject to ASME license or copyright; see http://www.asme.org/terms/Terms_Use.cfm

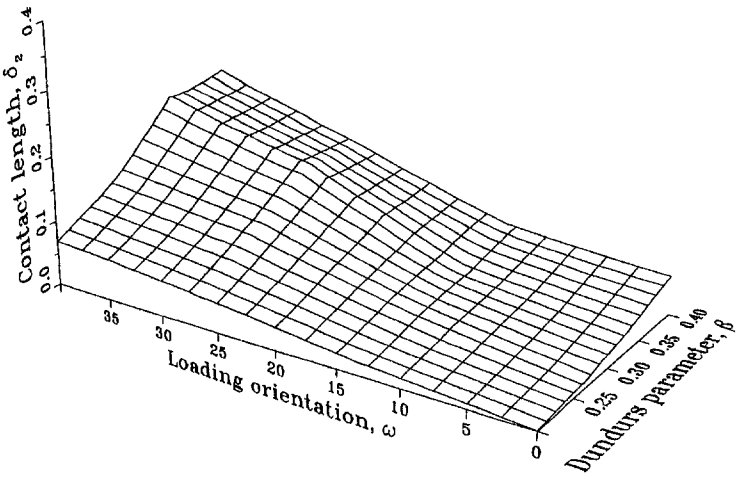


Fig. 7 Contact length at the lower crack tip B of a crack of half-angle θ_0 = 60 deg, with Dundurs parameter α = 0.5, for uniaxial loading of the matrix at infinity inclined at orientation ω to the x-axis. The variation of the contact length with ω and Dundurs parameter β is shown.

are many. A significant problem lies in the determination of the contact lengths, especially since the contact angle, ϵ_1, and thus δ_1, is extremely small—typically of the order of 10^{-5}. Thus the total number of collocation points in the Chebychev discretization of Erdogan and Gupta (1972) must be large. Nevertheless the number of collocation points in the contact zones will be small. Inevitably we have investigated the sensitivity of the results to the relatively small number of collocation points near A. Mercifully the essential results appear to be insensitive to the number of collocation points near A. But we emphasize that if the detailed stress distribution near the upper crack tip is important, then this assertion must be treated with caution.

A secondary issue is that for certain orientations of the applied load, the crack surfaces may come into contact in the central portions of the crack. But we do not consider this problem here.

The critical conclusions of the present study are contained in Figs. 5, 6, 7, and 8. The normalized length δ_1, of the contact zone at the upper end A is shown in Figs. 5 and 6. Each figure refers to a crack of half-angle θ_0 = 60 deg. Figure 5 shows the variation of δ_1 with load orientation ω and Dundurs parameter β for a fixed value α = 0.5. Figure 6 also shows the variation of δ_1 with ω and β but this time α = 0.75. As expected, the results show that δ_1 is extremely small. But perhaps of more interest is that the predicted contact lengths are almost identical. Furthermore we can report that this conclusion is valid for all values of α and for a wide range of crack half-angles θ_0. We therefore assert that the predicted contact zone at the upper crack tip, A, is essentially independent of the Dundurs parameter α.

Figures 7 and 8 show the variation of the normalized contact length, δ_2, at the lower end, B, of the crack. Experience with the homogeneous problem suggests that δ_2 may be quite large and certainly much larger than δ_1. The numerical results validate this expectation. In parallel with our remarks in the preceding paragraph we note that the predicted contact length at the lower tip, B, is also essentially independent of the Dundurs parameter α.

Finally we are able to offer the tentative conclusion that, for practical purposes, the contact length at both crack tips can be regarded as independent of the Dundurs parameter α.

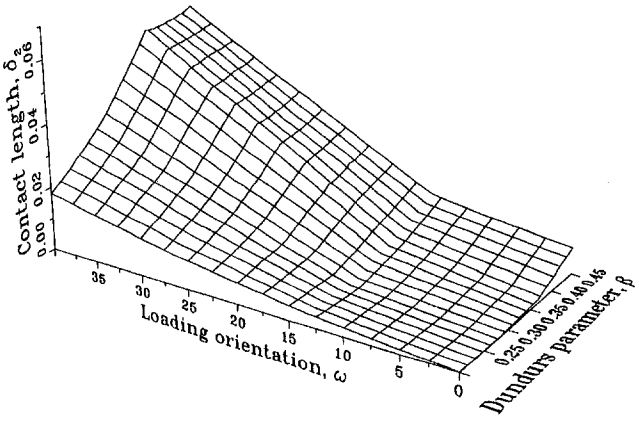


Fig. 8 Contact length at the lower crack tip B of a crack of half-angle θ_0 = 45 deg, with Dundurs parameter α = 0.5, for uniaxial loading of the matrix at infinity inclined at orientation ω to the x-axis. The variation of the contact length with ω and Dundurs parameter β is shown.

Acknowledgments

This work was supported in part by the US Air Force Office of Scientific Research under grant AFOSR-88-0104. The work of R. C. was also partially supported by the National Science Council under project NSC-86-2611-E-006-007.

References

Atkinson, C., 1982a, "The Interface Crack with a Contact Zone (an Analytical Treatment)," *International Journal of Fracture,* Vol. 18, pp. 161–177.

Atkinson, C., 1982b, "The Interface Crack with a Contact Zone (The Crack of Finite Length), *International Journal of Fracture,*" Vol. 19, pp. 131–138.

Chao, R., 1991, "Some Effects of Fiber-Matrix Debonding on the Response of Unidirectional Ceramic Matrix Composite Materials," Ph.D. thesis, University of Pittsburgh, Pittsburgh, PA.

Chao, R., and Laws, N., 1992, "Closure of an Arc Crack in an Isotropic Homogeneous Material Due to Uniaxial Loading," *Q. Jl. Mech. appl. Math.,* Vol. 45, pp. 629–640.

Comninou, M., 1977, "The Interface Crack," ASME JOURNAL OF APPLIED MECHANICS, Vol. 44, pp. 631–636.

Comninou, M., 1978, "The Interface Crack in a Shear Field," ASME JOURNAL OF APPLIED MECHANICS, Vol. 45, pp. 287–290.

Comninou, M., and Schmueser, D., 1979, "The Interface Crack in a Combined Tension-Compression and Shear Field," ASME JOURNAL OF APPLIED MECHANICS, Vol. 46, pp. 345–358.

England, A. H., 1965, "A Crack Between Dissimilar Media," ASME JOURNAL OF APPLIED MECHANICS, Vol. 32, pp. 400–402.

England, A. H., 1966, "An Arc Crack Around a Circular Elastic Inclusion," ASME JOURNAL OF APPLIED MECHANICS, Vol. 33, pp. 637–640.

Erdogan, F., 1963, "Stress Distribution in a Nonhomogeneous Elastic Plate With Cracks," ASME JOURNAL OF APPLIED MECHANICS, Vol. 30, pp. 232–237.

Erdogan, F., 1965, "Stress Distribution in Bonded Dissimilar Materials with Cracks," ASME JOURNAL OF APPLIED MECHANICS, Vol. 32, pp. 403–410.

Downloaded 04 May 2010 to 171.66.16.34. Redistribution subject to ASME license or copyright; see http://www.asme.org/terms/Terms_Use.cfm

Erdogan, F., and Gupta, G., 1972, "On the Numerical Solution of Singular Integral Equations," *Quarterly of Applied Mathematics,* Vol. 29, pp. 525–539.

Gautesen, A. K., and Dundurs, J., 1987, "The Interface Crack in a Tension Field," ASME JOURNAL OF APPLIED MECHANICS, Vol. 54, pp. 93–98.

Gautesen, A. K., and Dundurs, J., 1988, "The Interface Crack Under Combined Loading," ASME JOURNAL OF APPLIED MECHANICS, Vol. 55, pp. 580–586.

Kalandiya, A. I., 1975, *Mathematical Methods of Two-Dimensional Elasticity,* MIR Publishers, Moscow.

Mak, A. F., Keer, L. M., Chen, S. H., and Klewis, J. L., 1980, "A No-Slip Interface Crack," ASME JOURNAL OF APPLIED MECHANICS, Vol. 47, pp. 347–350.

Muskhelishvili, N. I., 1954, *Some Basic Problems of the Mathematical Theory of Elasticity,* Noordhoff, Groningen, (translated by J. R. M. Radok).

Park, J. H., and Earmme, Y. Y., 1986, "Application of Conservation Integrals to Interfacial Crack Problems," *Mechanics of Materials,* Vol. 5, pp. 261–276.

Perlman, A. B., and Sih, G. C., 1967, "Elastostatic Problems of Curvilinear Cracks in Bonded Dissimilar Materials," *Int. J. Engng. Sci.,* Vol. 5, pp. 856–867.

Piva, A., 1982, "A Crack Along a Circular Interface Between Dissimilar Media," *Meccanica,* Vol. 17, pp. 85–90.

Rice, J. R., 1988, "Elastic Fracture Mechanics Concepts for Interfacial Cracks," ASME JOURNAL OF APPLIED MECHANICS, Vol. 55, pp. 98–103.

Rice, J. R., and Sih, G. C., 1965, "Plane Problems of Cracks in Dissimilar Media," ASME JOURNAL OF APPLIED MECHANICS, Vol. 32, pp. 418–423.

Sinclair, G. B., 1980, "On the Stress Singularity at an Interface Crack," *International Journal of Fracture,* Vol. 16, pp. 111–119.

Shield, R. T., 1982, "Uniqueness for Elastic Crack and Punch Problems," ASME JOURNAL OF APPLIED MECHANICS, Vol. 49, pp. 516–518.

Suo, Z., and Hutchinson, J. W., 1989, "Sandwich Test Specimens for Measuring Interface Crack Toughness," *Materials Science and Engineering,* Vol. A107, pp. 135–143.

Toya, M., 1974, "A Crack Along the Interface of a Circular Inclusion Embedded in an Infinite Solid," *J. Mech. Phys. Solids,* Vol. 22, pp. 325–348.

Williams, M. L., 1959, "The Stresses Around a Fault or Crack in Dissimilar Media," *Bulletin of the Seismological Society of America,* Vol. 49, pp. 199–204.

Willis, J. R., 1972, "The Penny-Shaped Crack on an Interface," *Q. Jl. Mech. Appl. Math.,* Vol. 25, pp. 367–385.

Downloaded 04 May 2010 to 171.66.16.34. Redistribution subject to ASME license or copyright; see http://www.asme.org/terms/Terms_Use.cfm

Journal of Applied Mechanics

Brief Notes

A Brief Note is a short paper that presents a specific solution of technical interest in mechanics but which does not necessarily contain new general methods or results. A Brief Note should not exceed 1500 words *or equivalent* (a typical one-column figure or table is equivalent to 250 words; a one line equation to 30 words). Brief Notes will be subject to the usual review procedures prior to publication. After approval such Notes will be published as soon as possible. The Notes should be submitted to the Technical Editor of the JOURNAL OF APPLIED MECHANICS. Discussions on the Brief Notes should be addressed to the Editorial Department, ASME, United Engineering Center, 345 East 47th Street, New York, N. Y. 10017, or to the Technical Editor of the JOURNAL OF APPLIED MECHANICS. Discussions on Brief Notes appearing in this issue will be accepted until two months after publication. Readers who need more time to prepare a Discussion should request an extension of the deadline from the Editorial Department.

On Bonded Circular Inclusions in Plane Thermoelasticity

C. K. Chao[1] and M. H. Shen[2]

A general solution to the thermoelastic problem of a circular inhomogeneity in an infinite matrix is provided. The thermal loadings considered in this note include a point heat source located either in the matrix or in the inclusion and a uniform heat flow applied at infinity. The proposed analysis is based upon the use of Laurent series expansion of the corresponding complex potentials and the method of analytical continuation. The general expressions of the temperature and stress functions are derived explicitly in both the inclusion and the surrounding matrix. Comparison is made with some special cases such as a circular hole under remote uniform heat flow and a circular disk under a point heat source, which shows that the results presented here are exact and general.

1 Introduction

The thermal stresses induced by an insulated hole in an isotropic medium was studied by Florence and Goodier (1959, 1960). The same problem was solved by Chen (1967) for an orthotropic medium containing a circular or elliptic hole. Hwu (1990) studied the thermal stresses in an anisotropic body under uniform heat flow disturbed by an insulated elliptic hole using the Stroh formalism (Stroh, 1958). Following the Lekhnitskii complex potential approach, Tarn and Wang (1993) found the thermal stresses in anisotropic bodies with a hole or a rigid inclusion. Recently, Kattis and Meguid (1995) gave a solution of thermoelastic problems of an elastic curvilinear inclusion embedded in an elastic matrix where all singularities are located in the matrix. In this note, we aim to provide a general solution to the elastic inclusion problem subjected to a point heat source or a uniform heat flow. A point heat source considered in this note resides either outside or inside the circular inclusion. The analysis is based upon the complex variable theory and the method of analytical continuation which allows us to express the general solutions of the temperature and stress functions in a compact form. Some special examples are solved in closed form and are compared with existing analytical solutions, such as a point heat source in the circular disk and an infinite matrix with a circular elastic inclusion under a remote uniform heat flow.

2 Problem Formulation

Consider a circular elastic inclusion perfectly bonded to an infinite matrix subjected to a point heat source located either in the matrix (including infinity) or in the inclusion and a uniform heat flow applied at infinity. The regions occupied by the elastic matrix ($|z| > a$) and the inclusion ($|z| < a$) will be referred to as regions S_1 and S_2, respectively, and the quantities associated with these regions will be denoted by the corresponding subscripts (see Fig. 1). A point heat source in the system or a uniform heat flow at infinity causes a thermal stress distribution as a result of the different thermoelastic properties of the two phases. For a two-dimensional heat conduction problem, the resultant heat flow Q_j and the temperature T_j can be expressed in terms of a single complex potential $g_j'(z)$ as

$$Q_j = \int (q_{xj}dy - q_{yj}dx) = -k_j \,\mathrm{Im}[g_j'(z)] \tag{1}$$

$$T_j = \mathrm{Re}[g_j'(z)] \tag{2}$$

where Re and Im denote the real part and imaginary part of the bracketed expression, respectively. The quantities q_{xj}, q_{yj} in (1) are the components of heat flux in the x and y-direction, respectively, and k_j stands for the heat conductivity with $j = 1$ for S_1 and $j = 2$ for S_2. Once the heat conduction problem is solved, the temperature function $g_j'(z)$ is determined. For a two-dimensional theory of thermoelasticity, the components of the displacement and traction force can be expressed in terms of two stress functions $\phi_j(z)$, $\psi_j(z)$ and a temperature function $g_j'(z)$ as (Bogdanoff, 1954)

$$2G_j(u_j + iv_j) = \kappa_j\phi_j(z) - z\overline{\phi_j'(z)} - \overline{\psi_j(z)} + 2G_j\beta_j \int g_j'(z)dz \tag{3}$$

$$-Y_j + iX_j = \phi_j(z) + z\overline{\phi_j'(z)} + \overline{\psi_j(z)} \tag{4}$$

where G_j is the shear modulus, and $\kappa_j = (3 - \nu_j)/(1 + \nu_j)$, β_j

[1] Department of Mechanical Engineering, National Taiwan Institute of Technology, Taipei, Taiwan 106, Republic of China.
[2] Department of Mechanical Engineering, Nankai Jr. College of Technology, Nantou, Taiwan, Republic of China.

Contributed by the Applied Mechanics Division of THE AMERICAN SOCIETY OF MECHANICAL ENGINEERS for publication in the ASME JOURNAL OF APPLIED MECHANICS. Manuscript received by the ASME Applied Mechanics Division, Aug. 19, 1996; final revision, Sept. 19, 1996. Associate Technical Editor: X. Markenscoff.

Copyright © 1997 by ASME
Downloaded 04 May 2010 to 171.66.16.34. Redistribution subject to ASME license or copyright; see http://www.asme.org/terms/Terms_Use.cfm

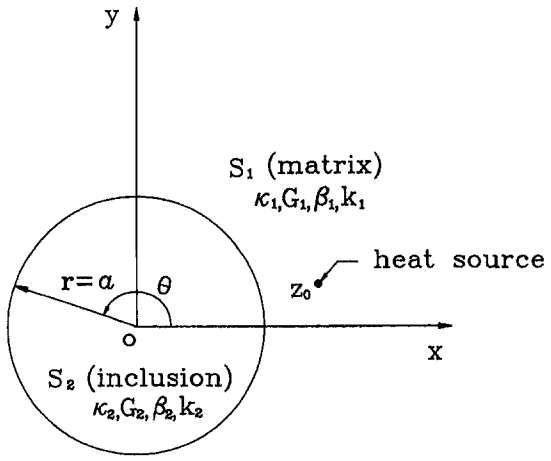


Fig. 1 A bonded circular inclusion subjected to a point heat source outside the inclusion

$= \alpha_j$ for plane stress and $\kappa_j = 3 - 4\nu_j$, $\beta_j = (1 + \nu_j)\alpha_j$ for plane strain with ν_j being the Poisson's ratio and α_j the thermal expansion coefficients. Primes denote differentiation with respect to z and a superimposed bar denotes the complex conjugate. For the condition that both the stresses and displacements are single-valued either in the matrix or in the inclusion, the stress functions $\phi_j(z)$, $\psi_j(z)$ must take the form

$$\phi_j(z) = A_j z \ln z + B_j \ln z + \phi_j^*(z) \tag{5}$$

$$\psi_j(z) = C_j \ln z + \psi_j^*(z) \tag{6}$$

where A_j is a real constant and B_j, C_j are complex constants which are related by the following equations

$$(\kappa_j + 1)A_j z + \kappa_j B_j + \bar{C}_j = \frac{-2G_j\beta_j}{2\pi i} \oint_{c_j} g_j'(t)dt \tag{7}$$

$$B_j - \bar{C}_j = 0 \tag{8}$$

where c_j is any surrounding contour within the region S_j (j = 1, 2). Note that the singularity of the term $z \ln z$ appeared in the stress functions, Eq. (5), results from the logarithmic singularity of the temperature function induced by a point heat source. The two holomorphic functions $\phi_j^*(z)$ and $\psi_j^*(z)$ in (5) and (6), respectively, can be expressed in a series form as

$$\phi_1^* = \sum_{m=1}^{\infty} L_m z^{-m}, \quad \psi_1^* = \sum_{m=1}^{\infty} M_m z^{-m} \tag{9}$$

$$\phi_2^* = \sum_{m=1}^{\infty} N_m z^m, \quad \psi_2^* = \sum_{m=1}^{\infty} P_m z^m \tag{10}$$

where the constant coefficients L_m, M_m, N_m, and P_m may be determined from the interface continuity conditions.

3 Temperature Field

3.1 A Point Heat Source in the Matrix. Consider a point heat source is located outside the inclusion (see Fig. 1), the temperature functions in the matrix and in the inclusion, respectively, can be written as

$$g_1'(z) = g_0'(z) + \mathbf{g}_1'(z) \tag{11}$$

$$g_2'(z) = \mathbf{g}_2'(z) \tag{12}$$

where $g_0'(z)$ represents the function associated with the unperturbed field which is related to the solutions of homogeneous media and is holomorphic in the entire domain except a singular point under a point heat source, and the points at zero or infinity. $\mathbf{g}_1'(z)$ (or $\mathbf{g}_2'(z)$) is the function corresponding to the perturbed field of matrix (or inclusion) and is holomorphic in region S_1 (or S_2) except some singular points. In the present study, the temperature function $g_0'(z)$ is given as (Ozisik, 1980)

$$g_0'(z) = -\frac{q}{2\pi k_1} \ln (z - z_0) \tag{13}$$

for a point heat source with the strength q located at the point $z = z_0$ in the matrix, and

$$g_0'(z) = \tau e^{-i\lambda} z \tag{14}$$

for a remote uniform heat flow with the constant temperature gradient τ directed at an angle λ with respect to the positive x-axis (see Fig. 2). $\mathbf{g}_1'(z)$ and $\mathbf{g}_2'(z)$ in (11) and (12), respectively, will be determined from the interface continuity conditions, i.e., $T_1 = T_2$ and $Q_1 = Q_2$ along the interface $z = \sigma = ae^{i\theta}$. Using the above boundary conditions and applying the method of analytical continuation (Chao and Lee, 1996), we obtain the final results as

$$g_1'(z) = g_0'(z) + \frac{k_1 - k_2}{k_1 + k_2} \bar{g}_0'\left(\frac{a^2}{z}\right) \tag{15}$$

$$g_2'(z) = \frac{2k_1}{k_1 + k_2} g_0'(z) \tag{16}$$

3.2 A Point Heat Source in the Inclusion. If a point heat source is located inside the inclusion (see Fig. 3), the temperature functions can be written as

$$g_1'(z) = \frac{-q}{2\pi k_1} \ln \frac{z}{a} + \mathbf{g}_1'(z) \tag{17}$$

$$g_2'(z) = \frac{-q}{2\pi k_2} \ln \frac{z}{a} + g_0'(z) + \mathbf{g}_2'(z) \tag{18}$$

where $g_0'(z)$ is given by

$$g_0'(z) = \frac{-q}{2\pi k_2} \ln \left(a - \frac{az_0}{z}\right). \tag{19}$$

Using the interface continuity conditions as mentioned above and the method of analytical continuation (Chao and Lee, 1996), the final expression for the temperature functions becomes

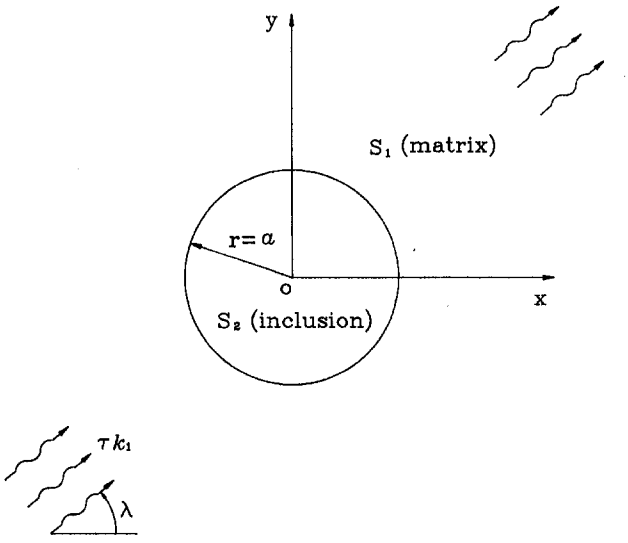


Fig. 2 A bonded circular inclusion subjected to a remote uniform heat flow

Downloaded 04 May 2010 to 171.66.16.34. Redistribution subject to ASME license or copyright; see http://www.asme.org/terms/Terms_Use.cfm

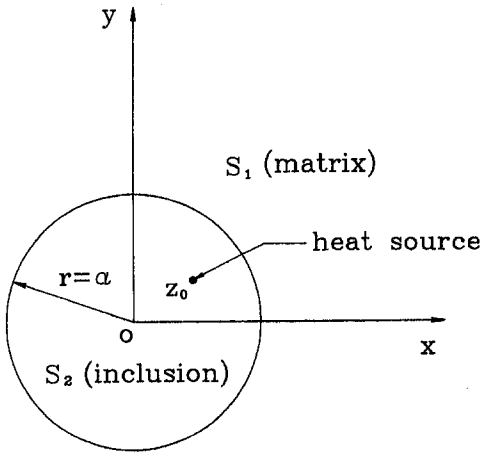


Fig. 3 A bonded circular inclusion subjected to a point heat source inside the inclusion

$$g_1'(z) = \frac{-q}{2\pi k_1} \ln \frac{z}{a} - \frac{q}{\pi(k_1 + k_2)} \ln \left(a - \frac{az_0}{z}\right) \quad (20)$$

$$g_2'(z) = \frac{-q}{2\pi k_2} \ln (z - z_0) - \frac{(k_2 - k_1)q}{2\pi(k_1 + k_2)k_2} \ln \left(a - \frac{z\bar{z}_0}{a}\right). \quad (21)$$

4 Thermal Stress Field

Having the temperature functions as derived previously, the general solutions for the stress and displacement fields can be obtained in terms of the complex potentials given in Eqs. (5) and (6) in which the constant coefficients A_j, B_j, and C_j may be determined from (7) and (8) while the two holomorphic functions $\phi_j^*(z)$ and $\psi_j^*(z)$ will be obtained from the interface continuity conditions.

4.1 A Point Heat Source in the Matrix. We now consider a heat source located in the matrix for which the temperature functions $g_1'(z)$, $g_2'(z)$ have been given in (15) and (16), respectively. Substituting (15) and (16) into (7) and using (8), one obtains

$$A_1 = \frac{G_1\beta_1 q}{\pi k_1(1 + \kappa_1)}, \quad B_1 = \frac{-G_1\beta_1 q z_0}{\pi k_1(1 + \kappa_1)}, \quad \text{for} \quad |z| > |z_0| \quad (22)$$

$$A_1 = B_1 = 0, \quad \text{for} \quad a < |z| < |z_0| \quad (23)$$

and

$$A_2 = B_2 = 0, \quad \text{for} \quad |z| < a. \quad (24)$$

Since the inclusion and the matrix are assumed to be perfectly bonded along the interface, the displacements and surface tractions at the interface must be continuous, i.e., $u_1 + iv_1 = u_2 + iv_2$ and $-Y_1 + iX_1 = -Y_2 + iX_2$ along the interface $z = \sigma = ae^{i\theta}$. Using the above boundary conditions and applying the method of analytical continuations (Chao and Lee, 1996), the constant coefficients appeared in (9) and (10) are obtained as

$$L_m = -\frac{2G_1G_2\beta_1}{G_1 + G_2\kappa_1} b_m \quad (25)$$

$$N_1 = \frac{-2G_1G_2(\beta_2 c_1 - \beta_1 a_1)}{(\kappa_2 G_1 + 2G_2 - G_1)} \quad (26)$$

$$N_m = -\frac{2G_1G_2}{G_2 + G_1\kappa_2}(\beta_2 c_m - \beta_1 a_m), \quad \text{for} \quad m \geq 2 \quad (27)$$

$$M_1 = [2N_1 - A_1(1 + \ln a^2)]a^2 \quad (28)$$

$$M_2 = \bar{N}_2 a^4 - B_1 a^2 \quad (29)$$

$$M_m = (m - 2)a^2 L_{m-2} + a^{2m}\bar{N}_m, \quad \text{for} \quad m \geq 3 \quad (30)$$

$$P_m = a^{-2m}\bar{L}_m - (m + 2)a^2 N_{m+2}. \quad (31)$$

Having the solutions in (25)–(31), the final expression of the stress functions can then be determined by substituting (9)–(10) and (22)–(24) into (5) and (6).

4.2 A Point Heat Source in the Inclusion. If a heat source is located in the inclusion, the constant coefficients in (5) and (6) can be determined by substituting (20) and (21) into (7) and (8) as

$$A_1 = \frac{G_1\beta_1 q}{\pi k_1(1 + \kappa_1)}, \quad B_1 = \frac{-G_1\beta_1 q z_0}{\pi(k_1 + k_2)(1 + \kappa_1)}, \quad \text{for} \quad |z| > a \quad (32)$$

$$A_2 = \frac{G_2\beta_2 q}{\pi k_2(1 + \kappa_2)}, \quad B_2 = \frac{-G_2\beta_2 q z_0}{\pi k_2(1 + \kappa_2)}, \quad \text{for} \quad |z_0| < |z| < a \quad (33)$$

and

$$A_2 = B_2 = 0, \quad \text{for} \quad |z| < |z_0|. \quad (34)$$

By using the interface continuity conditions and the method of analytical continuation (Chao and Lee, 1996), we finally obtain

$$L_m = -\frac{2G_1G_2}{G_1 + G_2\kappa_1}(\beta_1 e_m - \beta_2 h_m) \quad (35)$$

$$N_1 = \frac{-(G_2A_2 - G_1A_2)(1 + \ln a^2) - 2G_1G_2(\beta_2 f_1 - \beta_1 d_1)}{(\kappa_2 G_1 + 2G_2 - G_1)} \quad (36)$$

$$N_2 = -\frac{2G_1G_2}{G_2 + G_1\kappa_2}\beta_2 f_2 - \frac{G_2\bar{B}_2 - G_1\bar{B}_2}{(G_2 + G_1\kappa_2)a^2} \quad (37)$$

$$N_m = -\frac{2G_1G_2}{G_2 + G_1\kappa_2}\beta_2 f_m, \quad \text{for} \quad m \geq 3 \quad (38)$$

$$M_1 = [2N_1 + (A_2 - A_1)(1 + \ln a^2)]a^2 \quad (39)$$

$$M_2 = \bar{N}_2 a^4 + (B_2 - B_1)a^2 \quad (40)$$

$$M_m = (m - 2)a^2 L_{m-2} + a^{2m}\bar{N}_m, \quad \text{for} \quad m \geq 3 \quad (41)$$

$$P_m = a^{-2m}\bar{L}_m - (m + 2)a^2 N_{m+2}. \quad (42)$$

With the results in (35)–(42) the general solutions for the stress functions can then be obtained by substituting (32)–(34) and (9)–(10) into (5) and (6).

5 Examples

5.1 Elastic Circular Inclusion under Remote Heat Flow. As our first example, we consider a circular elastic inclusion perfectly bonded to a matrix which is subjected to a uniform heat flux with the temperature gradient τ directed at an angle λ with respect to the positive x-axis (see Fig. 2). The solution of temperature functions can be easily obtained by substituting (14) into (15) and (16) as

Downloaded 04 May 2010 to 171.66.16.34. Redistribution subject to ASME license or copyright; see http://www.asme.org/terms/Terms_Use.cfm

$$g_1'(z) = \tau e^{-i\lambda} z + \frac{\tau(k_1 - k_2)}{(k_1 + k_2)} e^{i\lambda} \frac{a^2}{z} \tag{43}$$

$$g_2'(z) = \frac{2k_1\tau}{(k_1 + k_2)} e^{-i\lambda} z. \tag{44}$$

Applying the formulae given in Section 4.1, the final solutions for the stress field can be given by

$$\phi_1(z) = \frac{-2G_1\beta_1\tau}{(1 + \kappa_1)} \frac{(k_1 - k_2)}{(k_1 + k_2)} a^2 e^{i\lambda} \ln z \tag{45}$$

$$\psi_1(z) = \frac{-2G_1\beta_1\tau}{(1 + \kappa_1)} \frac{(k_1 - k_2)}{(k_1 + k_2)} a^2 e^{-i\lambda} \ln z - \frac{G_1G_2\tau}{(G_1\kappa_2 + G_2)} \left(\frac{2k_1\beta_2}{(k_1 + k_2)} - \beta_1 \right) a^4 e^{i\lambda} \frac{1}{z^2} + \frac{2G_1\beta_1\tau}{(1 + \kappa_1)} \frac{(k_1 - k_2)}{(k_1 + k_2)} a^4 e^{i\lambda} \frac{1}{z^2} \tag{46}$$

$$\phi_2(z) = -\frac{2G_1G_2\tau}{G_1\kappa_2 + G_2} \left(\frac{2k_1\beta_2}{(k_1 + k_2)} - \beta_1 \right) e^{-i\lambda} z^2 \tag{47}$$

$$\psi_2(z) = 0. \tag{48}$$

The interfacial stresses along the inclusion boundary can be performed by using field solutions of the matrix or inclusion as

$$\sigma_{rr} = -\frac{G_1G_2\tau}{(G_1\kappa_2 + G_2)} \left(\frac{2k_1\beta_2}{(k_1 + k_2)} - \beta_1 \right) a \cos(\theta - \lambda)$$

$$\sigma_{r\theta} = -\frac{G_1G_2\tau}{(G_1\kappa_2 + G_2)} \left(\frac{2k_1\beta_2}{(k_1 + k_2)} - \beta_1 \right) a \sin(\theta - \lambda)$$

$$(\sigma_{\theta\theta})_1 = \left[\frac{-8G_1\beta_1\tau(k_1 - k_2)}{(1 + \kappa_1)(k_1 + k_2)} + \frac{2G_1G_2\tau}{(G_1\kappa_2 + G_2)} \times \left(\frac{2k_1\beta_2}{(k_1 + k_2)} - \beta_1 \right) \right] a \cos(\theta - \lambda)$$

$$(\sigma_{\theta\theta})_2 = -\frac{12G_1G_2\tau}{(G_1\kappa_2 + G_2)} \left(\frac{2k_1\beta_2}{(k_1 + k_2)} - \beta_1 \right) a \cos(\theta - \lambda).$$

When the inclusion is assumed to be an insulated and traction-free hole, the hoop stress along the hole boundary can be obtained by letting $k_2 = 0$ and $G_2 = 0$ as

$$\sigma_{\theta\theta} = -\frac{8G\beta\tau}{(1 + \kappa)} a \cos(\theta - \lambda)$$

which is in agreement with the result of Florence and Goodier (1959). For a special case of $k_1 = k_2$, $G_1 = G_2$ and $\beta_1 = \beta_2$, the solutions of the corresponding homogeneous problem is trivially given as

$$\phi(z) = \psi(z) = 0. \tag{49}$$

This is expected that there is no thermal stresses induced by a homogeneous body under the condition of free expansion.

5.2 A Point Heat Source at the Center of the Inclusion. As a second example we consider the inclusion subjected to a point heat source acting at the origin. The temperature functions can be obtained by putting $z_0 = 0$ into (20) and (21) as

$$g_1'(z) = -\frac{q}{2\pi k_1} \ln \frac{z}{a} - \frac{q}{\pi(k_1 + k_2)} \ln a \tag{50}$$

$$g_2'(z) = -\frac{q}{2\pi k_2} \ln z - \frac{(k_2 - k_1)q}{2\pi(k_1 + k_2)k_2} \ln a. \tag{51}$$

A direct application of the formulae given in Section 4.2, the stress functions can be obtained as

$$\phi_1(z) = \frac{G_1\beta_1 q}{\pi k_1(1 + \kappa_1)} z \ln z \tag{52}$$

$$\psi_1(z) = M_1/z \tag{53}$$

$$\phi_2(z) = \frac{G_2\beta_2 q}{\pi k_2(1 + \kappa_2)} z \ln z + N_1 z \tag{54}$$

$$\psi_2(z) = 0 \tag{55}$$

where N_1 and M_1 are

$$N_1 = \frac{q}{\kappa_2 G_1 + 2G_2 - G_1} \left\{ \frac{G_2\beta_2(G_1 - G_2)(1 + \ln a^2)}{\pi k_2(1 + \kappa_2)} - \frac{G_1G_2}{\pi} \left[\frac{\beta_2}{k_2} + \frac{(k_1 - k_2)\beta_2 \ln a}{(k_1 + k_2)k_2} - \frac{\beta_1}{k_1}(1 + \ln a) + \frac{2\beta_1 \ln a}{(k_1 + k_2)} \right] \right\}$$

$$M_1 = 2N_1a^2 + \frac{q}{\pi} \left[\frac{G_2\beta_2}{k_2(1 + \kappa_2)} - \frac{G_1\beta_1}{k_1(1 + \kappa_1)} \right] (1 + \ln a^2)a^2.$$

Note that, the stresses would not be bounded either at zero or at infinity due to the presence of the singular term $z \ln z$ appeared in the stress functions induced by a point heat source. Nevertheless, the solutions are useful as the outer boundary of a body remains finite.

5.2.1. Circular Disk. Consider a circular disk where the boundary surface is assumed to be free of traction and remain zero temperature. The corresponding temperature function and stress functions, respectively, can be obtained by letting $k_1 = \infty$ in (51) and $G_1 = 0$ in (54) as

$$g'(z) = -\frac{q}{2\pi k} \ln \frac{z}{a} \tag{56}$$

$$\phi(z) = \frac{G\beta q}{\pi k(1 + \kappa)} z \ln \frac{z}{a} - \frac{G\beta q}{2\pi k(1 + \kappa)} z \tag{57}$$

$$\psi(z) = 0. \tag{58}$$

Accordingly, the stress components are given by

$$\sigma_{rr} = \frac{2G\beta q}{\pi k(1 + \kappa)} \ln \frac{r}{a}$$

$$\sigma_{\theta\theta} = \frac{2G\beta q}{\pi k(1 + \kappa)} \ln \frac{r}{a} + \frac{2G\beta q}{\pi k(1 + \kappa)}$$

$$\sigma_{r\theta} = 0$$

which is the same as the results obtained by Parkus (1968) essentially by guessing.

Acknowledgment

The authors would like to thank the support by the National Science Council, Republic of China, through grant no. NSC. 84-2212-E011-022.

References

Bogdanoff, J. L., 1954, "Note on Thermal Stress," ASME JOURNAL OF APPLIED MECHANICS, Vol. 21, p. 88.

Downloaded 04 May 2010 to 171.66.16.34. Redistribution subject to ASME license or copyright; see http://www.asme.org/terms/Terms_Use.cfm

Chao, C. K., and Lee, J. Y., 1996, "Interaction Between a Crack and a Circular Elastic Inclusion Under Remote Uniform Heat Flow," *Int. J. Solids Structures*, Vol. 33, pp. 3865–3880.

Chen, W. T., 1967, "Plane Thermal Stress at an Insulated Hole Under Uniform Heat Flow in an Orthotropic Medium," ASME JOURNAL OF APPLIED MECHANICS, Vol. 34, pp. 133–136.

Florence, A. L., and Goodier, J. N., 1959, "Thermal Stress at Spherical Cavities and Circular Holes in Uniform Heat Flow," ASME JOURNAL OF APPLIED MECHANICS, Vol. 26, pp. 293–294.

Florence, A. L., and Goodier, J. N., 1960, "Thermal Stress Due to Disturbance of Uniform Heat Flow by an Insulated Ovaloid Hole," ASME JOURNAL OF APPLIED MECHANICS, Vol. 27, pp. 635–639.

Hwu, C., 1990, "Thermal Stresses in an Anisotropic Plate Disturbed by an Insulated Elliptic Hole or Crack," ASME JOURNAL OF APPLIED MECHANICS, Vol. 57, pp. 916–922.

Kattis, M. A., and Meguid, S. A., 1995, "Two-Phase Potentials for the Treatment of an Elastic Inclusion in Plane Thermoelasticity," ASME JOURNAL OF APPLIED MECHANICS, Vol. 62, pp. 7–12.

Ozisik, M. N., 1980, *Heat Conduction*, John Wiley and Sons, New York.

Parkus, H., 1968, *Thermoelasticity*, Blaisdell, Waltham, MA.

Stroh, A. N., 1958, "Dislocations and Cracks in Anisotropic Elasticity," *Phil. Mag.*, Vol. 7, pp. 625–646.

Tarn, J. Q., and Wang, Y. M., 1993, "Thermal Stresses in Anisotropic Bodies with a Hole or a Rigid Inclusion," *J. Thermal Stresses*, Vol. 16, pp. 455–471.

Influence of the Interface Periodic Array of Coplanar Cracks on the Free-Surface Oscillations

M. Ciarletta[3] and M. A. Sumbatyan[4]

The works of Angel and Achenbach (1985a, b) and Mikata and Achenbach (1988) are devoted to a scattering by the periodic array of cracks in an infinite homogeneous elastic plane for coplanar/inclined cracks with a normal/oblique incidence of a longitudinal/transverse wave. The method developed in the recent work of Mikata (1993) has considerable merits since it permits for the coplanar cracks derivation of integral equations with the kernels where there is no need for numerical integrations.

England (1965), Erdogan (1965), Comninou (1977), and some other authors aimed at development of analytical techniques in the static problems when there is a single finite-length interface crack on a boundary between two different elastic half-planes. This problem can be reduced to a system of two integral equations of the second kind with the singular kernels of Cauchy type, which can be explicitly solved.

We study here the problem that is contiguous to that considered by Yang and Bogy (1985).

Let on the boundary surface between two elastic media be a periodic array of coplanar cracks. The distance between two neighbour cracks is $2b$, the step of the array is $2a$. The thickness of the upper medium is d the lower medium is a half-space.

For both the media we apply the Lame representation for displacements and the wave potentials satisfy the wave equations:

$$\Delta\varphi + k_p^2\varphi = 0, \quad \Delta\psi + k_s^2\psi = 0, \tag{1}$$

with the velocity components in this two-dimensional problem being

$$u_x = \partial\varphi/\partial x + \partial\psi/\partial y, \; u_y = \partial\varphi/\partial y - \partial\psi/\partial x, \; u_z = 0. \tag{2}$$

At last, the boundary conditions must be taken into consideration:

$$\sigma_{xx} = \sigma_{xy} = 0, \quad x = \pm 0, \quad y \in \text{cracks}, \tag{3a}$$

$$\sigma_{xx} = \sigma_{xy} = 0, \quad x = d, \quad -\infty < y < \infty. \tag{3b}$$

Let φ_0 be an amplitude of the incident longitudinal wave. Then due to a symmetry of the problem with respect to the axis y, we have the following representation for the lower and the upper medium, respectively:

$$\begin{cases} \varphi_1 = \varphi_0 e^{ik_{p_1}x} + \mathrm{Re}^{-ik_{p_1}x} + \displaystyle\sum_{n=1}^{\infty} A_n \cos\left(\frac{\pi n}{a}y\right) e^{q_{1n}x} & (4a) \\ \qquad\qquad -\infty < x \le 0 & \\ \psi_1 = \displaystyle\sum_{n=1}^{\infty} B_n \sin\left(\frac{\pi n}{a}y\right) e^{r_{1n}x} & (4b) \end{cases}$$

$$\begin{cases} \varphi_2 = W \sin k_{p_2}(x-d) + \displaystyle\sum_{n=1}^{\infty}\left[C_n \,\mathrm{ch}\, q_{2n}(x-d) - \frac{r_{2n}^2 + \left(\frac{\pi n}{a}\right)^2}{2\frac{\pi n}{a} q_{2n}} \times D_n \,\mathrm{sh}\, q_{2n}(x-d)\right]\cos\left(\frac{\pi n}{a}y\right) & (5a) \\ \qquad\qquad 0 \le x \le d & \\ \psi_2 = \displaystyle\sum_{n=1}^{\infty}\left[D_n \,\mathrm{ch}\, r_{2n}(x-d) - \frac{2\left(\frac{\pi n}{a}\right)^2 - k_{s_2}^2}{2\frac{\pi n}{a} r_{2n}} \times C_n \,\mathrm{sh}\, r_{2n}(x-d)\right]\sin\left(\frac{\pi n}{a}y\right) & (5b) \end{cases}$$

(sh and ch = hyperbolic sine and cosine).

Here

$$q_{1n} = \left[\left(\frac{\pi n}{a}\right)^2 - k_{p_1}^2\right]^{1/2}, \quad r_{1n} = \left[\left(\frac{\pi n}{a}\right)^2 - k_{s_1}^2\right]^{1/2}, \tag{6a}$$

$$q_{2n} = \left[\left(\frac{\pi n}{a}\right)^2 - k_{p_2}^2\right]^{1/2}, \quad r_{2n} = \left[\left(\frac{\pi n}{a}\right)^2 - k_{s_2}^2\right]^{1/2}, \tag{6b}$$

k_{p_1}, k_{s_1} are the wave numbers for the first (lower) medium and k_{p_2}, k_{s_2} for the second (upper) one.

[3] Professor, DIMMA, University of Salerno, 84084 Fisciano (SA), Italy.

[4] Head, Laboratory of Diffraction Theory, Research Institute of Diffraction Theory, Research Institute of Mechanics and Applied Mathematics, 200/1 Stachki Prospect, Rostov-on-Don 344090, Russia.

Contributed by the Applied Mechanics Division of THE AMERICAN SOCIETY OF MECHANICAL ENGINEERS for publication in the ASME JOURNAL OF APPLIED MECHANICS. Manuscript received by the ASME Applied Mechanics Division, Dec. 5, 1996; final revision, May 7, 1997. Associate Technical Editor: X. Markenscoff.

Downloaded 04 May 2010 to 171.66.16.34. Redistribution subject to ASME license or copyright; see http://www.asme.org/terms/Terms_Use.cfm

Chao, C. K., and Lee, J. Y., 1996, "Interaction Between a Crack and a Circular Elastic Inclusion Under Remote Uniform Heat Flow," *Int. J. Solids Structures*, Vol. 33, pp. 3865–3880.

Chen, W. T., 1967, "Plane Thermal Stress at an Insulated Hole Under Uniform Heat Flow in an Orthotropic Medium," ASME JOURNAL OF APPLIED MECHANICS, Vol. 34, pp. 133–136.

Florence, A. L., and Goodier, J. N., 1959, "Thermal Stress at Spherical Cavities and Circular Holes in Uniform Heat Flow," ASME JOURNAL OF APPLIED MECHANICS, Vol. 26, pp. 293–294.

Florence, A. L., and Goodier, J. N., 1960, "Thermal Stress Due to Disturbance of Uniform Heat Flow by an Insulated Ovaloid Hole," ASME JOURNAL OF APPLIED MECHANICS, Vol. 27, pp. 635–639.

Hwu, C., 1990, "Thermal Stresses in an Anisotropic Plate Disturbed by an Insulated Elliptic Hole or Crack," ASME JOURNAL OF APPLIED MECHANICS, Vol. 57, pp. 916–922.

Kattis, M. A., and Meguid, S. A., 1995, "Two-Phase Potentials for the Treatment of an Elastic Inclusion in Plane Thermoelasticity," ASME JOURNAL OF APPLIED MECHANICS, Vol. 62, pp. 7–12.

Ozisik, M. N., 1980, *Heat Conduction*, John Wiley and Sons, New York.

Parkus, H., 1968, *Thermoelasticity*, Blaisdell, Waltham, MA.

Stroh, A. N., 1958, "Dislocations and Cracks in Anisotropic Elasticity," *Phil. Mag.*, Vol. 7, pp. 625–646.

Tarn, J. Q., and Wang, Y. M., 1993, "Thermal Stresses in Anisotropic Bodies with a Hole or a Rigid Inclusion," *J. Thermal Stresses*, Vol. 16, pp. 455–471.

Influence of the Interface Periodic Array of Coplanar Cracks on the Free-Surface Oscillations

M. Ciarletta[3] and M. A. Sumbatyan[4]

The works of Angel and Achenbach (1985a, b) and Mikata and Achenbach (1988) are devoted to a scattering by the periodic array of cracks in an infinite homogeneous elastic plane for coplanar/inclined cracks with a normal/oblique incidence of a longitudinal/transverse wave. The method developed in the recent work of Mikata (1993) has considerable merits since it permits for the coplanar cracks derivation of integral equations with the kernels where there is no need for numerical integrations.

England (1965), Erdogan (1965), Comninou (1977), and some other authors aimed at development of analytical techniques in the static problems when there is a single finite-length interface crack on a boundary between two different elastic half-planes. This problem can be reduced to a system of two integral equations of the second kind with the singular kernels of Cauchy type, which can be explicitly solved.

We study here the problem that is contiguous to that considered by Yang and Bogy (1985).

Let on the boundary surface between two elastic media be a periodic array of coplanar cracks. The distance between two neighbour cracks is $2b$, the step of the array is $2a$. The thickness of the upper medium is d the lower medium is a half-space.

For both the media we apply the Lame representation for displacements and the wave potentials satisfy the wave equations:

$$\Delta\varphi + k_p^2\varphi = 0, \quad \Delta\psi + k_s^2\psi = 0, \tag{1}$$

with the velocity components in this two-dimensional problem being

$$u_x = \partial\varphi/\partial x + \partial\psi/\partial y, \; u_y = \partial\varphi/\partial y - \partial\psi/\partial x, \; u_z = 0. \tag{2}$$

At last, the boundary conditions must be taken into consideration:

$$\sigma_{xx} = \sigma_{xy} = 0, \quad x = \pm 0, \quad y \in \text{cracks}, \tag{3a}$$

$$\sigma_{xx} = \sigma_{xy} = 0, \quad x = d, \quad -\infty < y < \infty. \tag{3b}$$

Let φ_0 be an amplitude of the incident longitudinal wave. Then due to a symmetry of the problem with respect to the axis y, we have the following representation for the lower and the upper medium, respectively:

$$\begin{cases} \varphi_1 = \varphi_0 e^{ik_{p_1}x} + \mathrm{Re}^{-ik_{p_1}x} + \displaystyle\sum_{n=1}^{\infty} A_n \cos\left(\frac{\pi n}{a}y\right) e^{q_{1n}x} & (4a) \\ \qquad\qquad -\infty < x \le 0 & \\ \psi_1 = \displaystyle\sum_{n=1}^{\infty} B_n \sin\left(\frac{\pi n}{a}y\right) e^{r_{1n}x} & (4b) \end{cases}$$

$$\begin{cases} \varphi_2 = W \sin k_{p_2}(x-d) + \displaystyle\sum_{n=1}^{\infty}\left[C_n \,\mathrm{ch}\, q_{2n}(x-d) - \frac{r_{2n}^2 + \left(\frac{\pi n}{a}\right)^2}{2\frac{\pi n}{a} q_{2n}} \times D_n \,\mathrm{sh}\, q_{2n}(x-d)\right]\cos\left(\frac{\pi n}{a}y\right) & (5a) \\ \qquad\qquad 0 \le x \le d & \\ \psi_2 = \displaystyle\sum_{n=1}^{\infty}\left[D_n \,\mathrm{ch}\, r_{2n}(x-d) - \frac{2\left(\frac{\pi n}{a}\right)^2 - k_{s_2}^2}{2\frac{\pi n}{a} r_{2n}} \times C_n \,\mathrm{sh}\, r_{2n}(x-d)\right]\sin\left(\frac{\pi n}{a}y\right) & (5b) \end{cases}$$

(sh and ch = hyperbolic sine and cosine).

Here

$$q_{1n} = \left[\left(\frac{\pi n}{a}\right)^2 - k_{p_1}^2\right]^{1/2}, \quad r_{1n} = \left[\left(\frac{\pi n}{a}\right)^2 - k_{s_1}^2\right]^{1/2}, \tag{6a}$$

$$q_{2n} = \left[\left(\frac{\pi n}{a}\right)^2 - k_{p_2}^2\right]^{1/2}, \quad r_{2n} = \left[\left(\frac{\pi n}{a}\right)^2 - k_{s_2}^2\right]^{1/2}, \tag{6b}$$

k_{p_1}, k_{s_1} are the wave numbers for the first (lower) medium and k_{p_2}, k_{s_2} for the second (upper) one.

[3] Professor, DIMMA, University of Salerno, 84084 Fisciano (SA), Italy.

[4] Head, Laboratory of Diffraction Theory, Research Institute of Diffraction Theory, Research Institute of Mechanics and Applied Mathematics, 200/1 Stachki Prospect, Rostov-on-Don 344090, Russia.

Contributed by the Applied Mechanics Division of THE AMERICAN SOCIETY OF MECHANICAL ENGINEERS for publication in the ASME JOURNAL OF APPLIED MECHANICS. Manuscript received by the ASME Applied Mechanics Division, Dec. 5, 1996; final revision, May 7, 1997. Associate Technical Editor: X. Markenscoff.

Copyright © 1997 by ASME

Downloaded 04 May 2010 to 171.66.16.34. Redistribution subject to ASME license or copyright; see http://www.asme.org/terms/Terms_Use.cfm

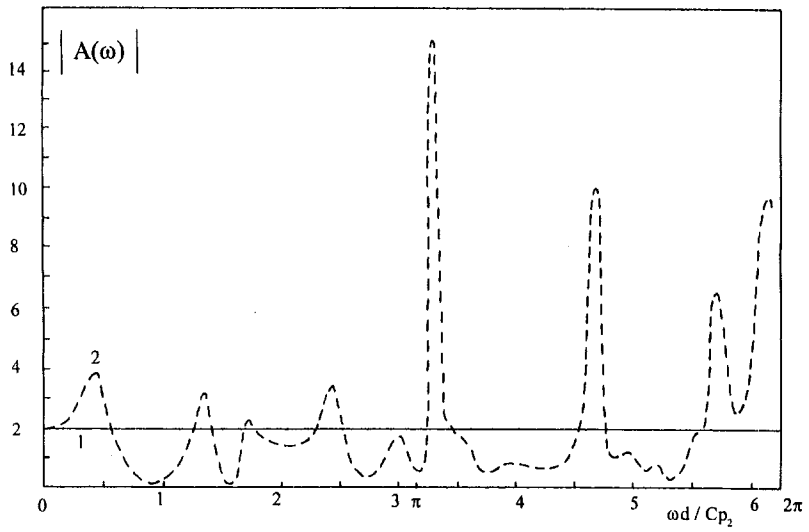


Fig. 1 Comparison of the transfer function for the case of absence (1) and presence (2) of the cracks ($y = 0$):

$C_{p_1} = 5.1$ km/s, $C_{s_1} = 2.7$ km/s, $\rho_1 = 2.7$ g/cm^3,

$C_{p_2} = 5.1$ km/s, $C_{s_2} = 2.7$ km/s, $\rho_2 = 2.7$ g/cm^3,

$d/a = 1$, $b/a = 0.2$.

Representations (4), (5) automatically satisfy the boundary conditions on the free surface $x = d$ (3b) and the main differential Eqs. (1). In addition, they possess the necessary periodicity and symmetry along the axis y. The only rest conditions are the boundary conditions on $x = 0$. They serve for determination of the unknown constants R, W, A_n, B_n, C_n, D_n.

Let us introduce the new unknown functions $g^\sigma(y)$ and $g^\tau(y)$ defined over the clearance: $\sigma_{xx} = g^\sigma(y)$, $x = 0$, $|y| < b$; $\sigma_{xy} = g^\tau(y)$, $x = 0$, $|y| < b$.

After that the continuity conditions $u_{x_1} = u_{x_2}$, $u_{y_1} = u_{y_2}$ ($x = 0$, $|y| < b$) lead to the following system of two integral equations (ctg = cotan):

$$\begin{cases} \displaystyle\int_{-b}^{b} g^\sigma(\eta)K_{11}(y-\eta)d\eta + \int_{-b}^{b} g^\tau(\eta)K_{12}(y-\eta)d\eta = -2ik_{p_1}\varphi_0 & (7a) \\ \displaystyle\int_{b}^{b} g^\sigma(\eta)K_{21}(y-\eta)d\eta + \int_{-b}^{b} g^\tau(\eta)K_{22}(y-\eta)d\eta = 0 & (7b) \end{cases} \quad |y| < b$$

where

$$K_{11}(y) = \frac{i}{2a\omega C_{p_1}\rho_1} - \frac{\operatorname{ctg}(k_{p_2}d)}{2a\omega C_{p_2}\rho_2} + \frac{1}{a}\sum_{n=1}^{\infty}\left(-\frac{k_{s_1}^2 q_{1n}}{\rho_1 C_{s_1}^2 \Delta_{1n}} + \alpha_n \frac{\beta_n\delta_n\gamma_n\epsilon_n + \zeta_n\eta_n}{\rho_2 C_{s_2}^2\Delta_{2n}}\right) \times \cos\left(\frac{\pi n}{a}y\right), \quad (8a)$$

$$K_{12}(y) = -\frac{1}{a}\sum_{n=1}^{\infty}\left[\frac{2q_{1n}r_{1n} - 2(\pi n/a)^2 + k_{s_1}^2}{\rho_1 C_{s_1}^2\Delta_{1n}}\frac{\pi n}{a} + \beta_n\frac{\alpha_n\zeta_n\gamma_n\epsilon_n - \delta_n\xi_n}{\rho_2 C_{s_2}^2\Delta_{2n}}\right] \times \sin\left(\frac{\pi n}{a}y\right), \quad (8b)$$

$$K_{21}(y) = \frac{1}{a}\sum_{n=1}^{\infty}\left[\frac{2q_{1n}r_{1n} - 2(\pi n/a)^2 + k_{s_1}^2}{\rho_1 C_{s_1}^2\Delta_{1n}}\frac{\pi n}{a} - \alpha_n\frac{\beta_n\zeta_n\gamma_n\epsilon_n + \mu_n\eta_n}{\rho_2 C_{s_2}^2\Delta_{2n}}\right] \times \sin\left(\frac{\pi n}{a}y\right), \quad (8c)$$

$$K_{22}(y) = \frac{1}{a}\sum_{n=1}^{\infty}\left[\frac{-k_{s_1}^2 r_{1n}}{\rho_1 C_{s_1}^2\Delta_{1n}} + \beta_n\frac{\alpha_n\mu_n\gamma_n\epsilon_n - \xi_n\nu_n}{\rho_2 C_{s_2}^2\Delta_{2n}}\right]\cos\left(\frac{\pi n}{a}y\right), \quad (8d)$$

and

$$\alpha_n = 2\frac{\pi n}{a}q_{2n}, \quad \beta_n = 2\frac{\pi n}{a}r_{2n}, \quad \gamma_n = 2\left(\frac{\pi n}{a}\right)^2 - k_{s_2}^2, \quad (9)$$

$$\delta_n = q_{2n}\operatorname{sh} q_{2n}d - \gamma_n \operatorname{sh} r_{2n}d/2r_{2n}, \quad (10)$$

$$\epsilon_n = \operatorname{ch} q_{2n}d - \operatorname{ch} r_{2n}d,$$

$$\zeta_n = \frac{\gamma_n}{2\pi n/a}\operatorname{ch} q_{2n}d - \frac{\pi n}{a}\operatorname{ch} r_{2n}d, \quad (11)$$

$$\eta_n = \gamma_n^2 \operatorname{sh} r_{2n}d - \alpha_n\beta_n \operatorname{sh} q_{2n}d,$$

$$\xi_n = \gamma_n^2 \operatorname{sh} q_{2n}d - \alpha_n\beta_n \operatorname{sh} r_{2n}d, \quad (12)$$

$$\mu_n = r_{2n}\operatorname{sh} r_{2n}d - \gamma_n \operatorname{sh} q_{2n}d/2q_{2n},$$

$$\nu_n = \frac{\gamma_n}{2\pi n/a}\operatorname{ch} r_{2n}d - \frac{\pi n}{a}\operatorname{ch} q_{2n}d. \quad (13)$$

Downloaded 04 May 2010 to 171.66.16.34. Redistribution subject to ASME license or copyright; see http://www.asme.org/terms/Terms_Use.cfm

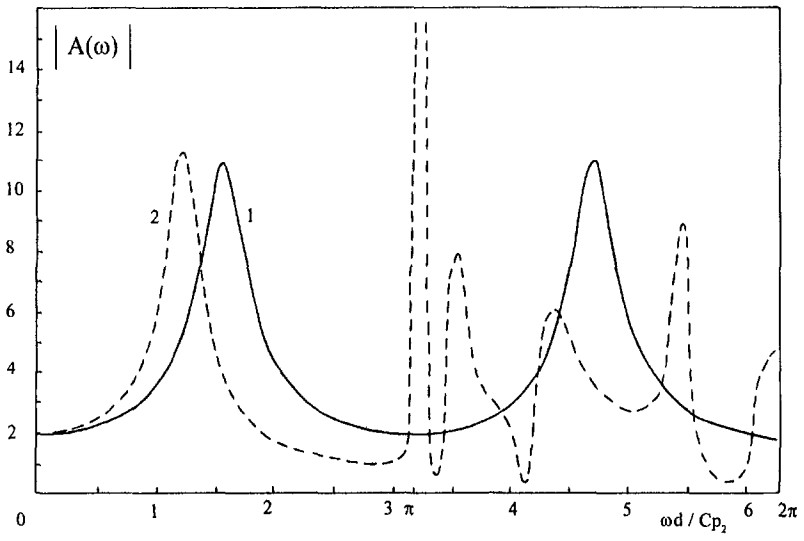


Fig. 2 Comparison of the transfer function for the case of absence (1) and presence (2) of the cracks ($y = 0$):

$C_{p_1} = 1.8$ km/s, $C_{s_1} = 1.1$ km/s, $\rho_1 = 2.2$ g/cm^3,

$C_{p_2} = 0.36$ km/s, $C_{s_2} = 0.21$ km/s, $\rho_2 = 2.0$ g/cm^3,

$d/a = 2$, $b/a = 0.5$.

Note that numerical treatment of the system (7), (8) does not need integration in the kernels, like in the method developed by Mikata (1993). The last system has been solved by using boundary element methods.

Some results of precise numerical calculations are shown in Figs. 1–2.

The main physical conclusions which may be drawn are the following:

1 The protective property of the array of cracks is not uniform and strongly depends upon the values of various physical parameters, especially upon the value of the frequency ω.

2 Oscillation of the free surface for small ω is always intensified with the cracks presence.

3 The general conclusion is that presence of a fault zone under the building construction is very dangerous.

Acknowledgments

The authors gratefully acknowledge the financial support provided under grant 60 percent M.U.R.S.T. (ITALY) and of G.N.F.M. of the Italian Research Council (C.N.R.).

References

Angel, Y. C., and Achenbach, J. D., 1985a, "Reflection and Trasmission of Elastic Waves by a Periodic Array of Cracks," ASME JOURNAL OF APPLIED MECHANICS, Vol. 52, pp. 33–41.

Angel, Y. C., and Achenbach, J. D., 1985b, "Reflection and Trasmission of Elastic Waves by a Periodic Array of Cracks: Oblique Incidence," *Wave Motion*, Vol. 7, pp. 375–397.

Comninou, M., 1977, "The Interface Crack," ASME JOURNAL OF APPLIED MECHANICS, Vol. 44, pp. 631–636.

England, A. H., 1965, "A Crack Between Dissimilar Media," ASME JOURNAL OF APPLIED MECHANICS, Vol. 32, pp. 400–402.

Erdogan, F., 1965, "Stress Distribution in Bonded Dissimilar Materials With Cracks," ASME JOURNAL OF APPLIED MECHANICS, Vol. 32, pp. 403–410.

Mikata, Y., 1993, "Reflection and Trasmission by a Periodic Array of Coplanar Cracks: Normal and Oblique Incidence," ASME JOURNAL OF APPLIED MECHANICS, Vol. 60, pp. 911–919.

Yang, H. J., and Bogy D. B., 1985, "Elastic Wave Scattering From an Interface Crack in a Layered Half Space," ASME JOURNAL OF APPLIED MECHANICS, Vol. 52, pp. 42–50.

On the Use of Deflection Components in Timoshenko Beam Theory

K. H. Lee[5,7] and C. M. Wang[6,7]

Introduction

In the displacement field of the Timoshenko beam, some researchers prefer to separate the total transverse deflection w^t into two components, namely, the bending deflection w^b and the shear deflection w^s, and do away with the rotation ψ as a variable. This decomposition into the two components can be performed easily by letting $\psi = -dw^b/dx$ and $w^t = w^b + w^s$ in the governing equations and boundary conditions. Here, x is the coordinate along the beam. Anderson (1953) and Miklowitz (1953) pointed out that the advantage of doing this in the study of flexural vibration of Timoshenko beams lay in the resulting simplification of the boundary conditions and of the expressions for the bending moment and the shear force. The use of deflection components was extended by Plantema (1966) to the bending and buckling of sandwich structures. These authors understood that the appropriate boundary condition for the deflection components should be in terms of the sum $w^t = w^b + w^s$. An important consequence of this is that an arbitrary constant can be added to one of the components and subtracted from the other without changing the physical problem. This is due to the

[5] Department of Mechanical and Production Engineering.

[6] Department of Civil Engineering.

[7] National University of Singapore, 10 Kent Ridge Crescent, Singapore 119260.

Contributed by the Applied Mechanics Division of THE AMERICAN SOCIETY OF MECHANICAL ENGINEERS for publication in the ASME JOURNAL OF APPLIED MECHANICS. Manuscript received by the ASME Applied Mechanics Division, Mar. 19, 1996; final revision, Sept. 5, 1996. Associate Technical Editor: J. N. Reddy.

Downloaded 04 May 2010 to 171.66.16.34. Redistribution subject to ASME license or copyright; see http://www.asme.org/terms/Terms_Use.cfm

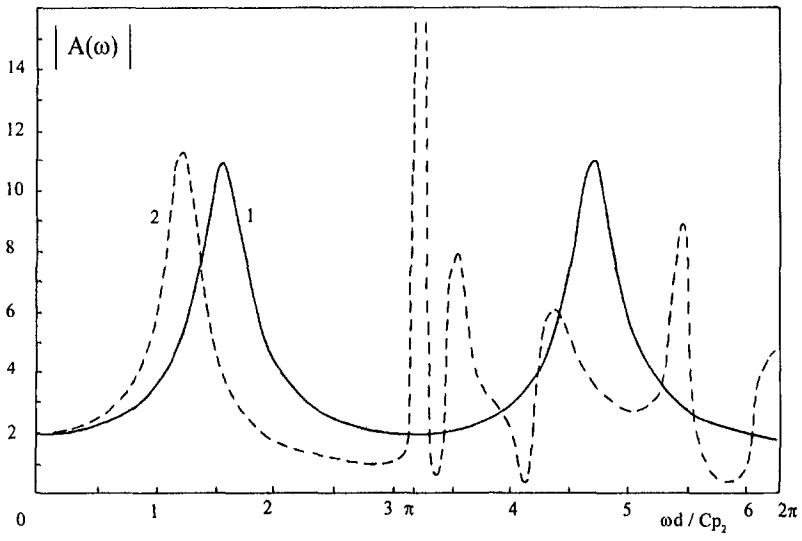


Fig. 2 Comparison of the transfer function for the case of absence (1) and presence (2) of the cracks ($y = 0$):

$C_{p_1} = 1.8$ km/s, $C_{s_1} = 1.1$ km/s, $\rho_1 = 2.2$ g/cm^3,

$C_{p_2} = 0.36$ km/s, $C_{s_2} = 0.21$ km/s, $\rho_2 = 2.0$ g/cm^3,

$d/a = 2$, $b/a = 0.5$.

Note that numerical treatment of the system (7), (8) does not need integration in the kernels, like in the method developed by Mikata (1993). The last system has been solved by using boundary element methods.

Some results of precise numerical calculations are shown in Figs. 1–2.

The main physical conclusions which may be drawn are the following:

1 The protective property of the array of cracks is not uniform and strongly depends upon the values of various physical parameters, especially upon the value of the frequency ω.

2 Oscillation of the free surface for small ω is always intensified with the cracks presence.

3 The general conclusion is that presence of a fault zone under the building construction is very dangerous.

Acknowledgments

The authors gratefully acknowledge the financial support provided under grant 60 percent M.U.R.S.T. (ITALY) and of G.N.F.M. of the Italian Research Council (C.N.R.).

References

Angel, Y. C., and Achenbach, J. D., 1985a, "Reflection and Trasmission of Elastic Waves by a Periodic Array of Cracks," ASME JOURNAL OF APPLIED MECHANICS, Vol. 52, pp. 33–41.

Angel, Y. C., and Achenbach, J. D., 1985b, "Reflection and Trasmission of Elastic Waves by a Periodic Array of Cracks: Oblique Incidence," *Wave Motion*, Vol. 7, pp. 375–397.

Comninou, M., 1977, "The Interface Crack," ASME JOURNAL OF APPLIED MECHANICS, Vol. 44, pp. 631–636.

England, A. H., 1965, "A Crack Between Dissimilar Media," ASME JOURNAL OF APPLIED MECHANICS, Vol. 32, pp. 400–402.

Erdogan, F., 1965, "Stress Distribution in Bonded Dissimilar Materials With Cracks," ASME JOURNAL OF APPLIED MECHANICS, Vol. 32, pp. 403–410.

Mikata, Y., 1993, "Reflection and Trasmission by a Periodic Array of Coplanar Cracks: Normal and Oblique Incidence," ASME JOURNAL OF APPLIED MECHANICS, Vol. 60, pp. 911–919.

Yang, H. J., and Bogy D. B., 1985, "Elastic Wave Scattering From an Interface Crack in a Layered Half Space," ASME JOURNAL OF APPLIED MECHANICS, Vol. 52, pp. 42–50.

On the Use of Deflection Components in Timoshenko Beam Theory

K. H. Lee[5,7] and C. M. Wang[6,7]

Introduction

In the displacement field of the Timoshenko beam, some researchers prefer to separate the total transverse deflection w^t into two components, namely, the bending deflection w^b and the shear deflection w^s, and do away with the rotation ψ as a variable. This decomposition into the two components can be performed easily by letting $\psi = -dw^b/dx$ and $w^t = w^b + w^s$ in the governing equations and boundary conditions. Here, x is the coordinate along the beam. Anderson (1953) and Miklowitz (1953) pointed out that the advantage of doing this in the study of flexural vibration of Timoshenko beams lay in the resulting simplification of the boundary conditions and of the expressions for the bending moment and the shear force. The use of deflection components was extended by Plantema (1966) to the bending and buckling of sandwich structures. These authors understood that the appropriate boundary condition for the deflection components should be in terms of the sum $w^t = w^b + w^s$. An important consequence of this is that an arbitrary constant can be added to one of the components and subtracted from the other without changing the physical problem. This is due to the

[5] Department of Mechanical and Production Engineering.

[6] Department of Civil Engineering.

[7] National University of Singapore, 10 Kent Ridge Crescent, Singapore 119260.

Contributed by the Applied Mechanics Division of THE AMERICAN SOCIETY OF MECHANICAL ENGINEERS for publication in the ASME JOURNAL OF APPLIED MECHANICS. Manuscript received by the ASME Applied Mechanics Division, Mar. 19, 1996; final revision, Sept. 5, 1996. Associate Technical Editor: J. N. Reddy.

Copyright © 1997 by ASME

Downloaded 04 May 2010 to 171.66.16.34. Redistribution subject to ASME license or copyright; see http://www.asme.org/terms/Terms_Use.cfm

Table 1 Comparison of quantities in Euler-Bernoulli and Timoshenko theories with those using deflection components in variational formulation

Theory	Euler-Bernoulli	Timoshenko	Deflection Components
Variables	w^e	w^t, ψ	w^b, w^s
Displacement Field	$u = -z\dfrac{dw^e}{dx}$	$u = z\psi$	$u = -z\dfrac{dw^b}{dx}$
	$w = w^e$	$w = w^t$	$w = w^b + w^s$
Governing Equations	$\dfrac{d^2M^e}{dx^2} = -q$	$\dfrac{dM^t}{dx} = V^t$	$\dfrac{d^2M^t}{dx^2} = -q$
		$\dfrac{dV^t}{dx} = -q$	$\dfrac{dV^t}{dx} = -q$
Boundary Conditions: Specify	$\left\{\begin{matrix} w^e \text{ or } \dfrac{dM^e}{dx} \\ \dfrac{dw^e}{dx} \text{ or } M^e \end{matrix}\right\}$	$\left\{\begin{matrix} w^t \text{ or } V^t \\ \psi \text{ or } M^t \end{matrix}\right\}$	$\left\{\begin{matrix} w^b \text{ or } \dfrac{dM^t}{dx} \\ w^s \text{ or } V^t \\ \dfrac{dw^b}{dx} \text{ or } M^t \end{matrix}\right\}$
Constitutive Equations	$M^e = -EI\dfrac{d^2w^e}{dx^2}$	$M^t = EI\dfrac{d\psi}{dx}$	$M^t = -EI\dfrac{d^2w^b}{dx^2}$
	$V^e = -EI\dfrac{d^3w^e}{dx^3}$	$V^t = kGA\left(\psi + \dfrac{dW^t}{dx}\right)$	$V^t = kGA\dfrac{dw^s}{dx}$

fact that only four end conditions are available for solving a pair of differential equations, one of which is third order and the other second order.

The growing use of variational principles encouraged researchers to obtain the governing equations and boundary conditions directly in terms of the bending deflection w^b and the shear deflection w^s instead of making the substitutions for the total deflection w^t and the rotation ψ. This can be seen, for example, in the work of Krishna Murty (1970a, 1970b, 1984), Senthilnathan et al. (1987), and Senthilnathan and Lee (1992) on refined higher-order beam and plate theories. One significant difference in taking this route is that the deflection components w^b and w^s need to be specified individually as boundary conditions instead of as a sum. Therefore, at clamped and simply supported ends and edges, both w^b and w^s are normally set to zero.

Given the tendency of researchers to prescribe both w^b and w^s to be zero at clamped and simply supported ends, this note aims to demonstrate, through an example, that such a specification can lead to incorrect solutions for statically indeterminate problems. It is then deduced that the bending deflection w^b is, in general, not the same as the Euler-Bernoulli deflection w^e.

Governing Equations and Boundary Conditions

Table 1 summarizes the governing equations and boundary conditions for the Euler-Bernoulli and Timoshenko beam theories together with those derived variationally for the deflection components w^b and w^s. The displacement fields and constitutive equations are also given in the table.

In Table 1, u is the axial displacement, w the transverse deflection, ψ the rotation of the normal to the axis of the beam, z the coordinate in the thickness direction, and the superscripts e and t denote quantities belonging to the Euler-Bernoulli and Timoshenko beams. Also, M is the bending moment, V the shear force, EI the flexural rigidity of the beam, GA the shear rigidity of the beam, and k the shear correction factor.

It can be deduced from the table that while the original governing differential equations for the Timoshenko beam consist of two coupled second-order equations in w^t and ψ, the governing equations obtained variationally for w^b and w^s actually comprise two uncoupled differential equations, one of which is fourth order and the other second order. Thus, as indicated in the table, the latter pair of equations require six instead of four end conditions for the complete solution of w^b and w^s. For clamped and simply supported ends, this implies the need to prescribe w^b and w^s individually despite the absence of physical conditions for these quantities.

One approach used to overcome this difficulty, though not necessarily correct, is to identify the bending deflection w^b with the Euler-Bernoulli deflection w^e. If this is true, the boundary conditions for w^b and w^s at clamped and simply supported ends are $w^b = w^s = 0$. The apparent rationale here is that since w^b is the component due to bending and w^e is the deflection in the absence of transverse shear deformation, then w^b is the same as w^e. As Table 1 shows, the identical forms of the governing equations, boundary conditions and constitutive equations for w^e, M^e and w^b, M^t also seem to lend support to this idea. However, strictly speaking, there is no logical basis for assuming in general that $w^b = w^s = w^e = 0$ at clamped and simply supported ends, and any perception that $w^b = w^e$ along the whole beam is certainly false. The example in the next section confirms these observations by showing that the assumptions lead to an incorrect solution.

Example

Consider a beam of length L clamped at one end ($x = 0$) and simply supported at the other end ($x = L$) subjected to an arbitrary transverse load. Using the boundary conditions $w^e = w^t = M^e = M^t = 0$ for the simply supported end and $w^e = w^t = (dw^e/dx) = (dw^b/dx) = 0$ for the clamped end, the correct solution for the deflection components w^b and w^s and the slope (dw^b/dx) in terms of the Euler-Bernoulli solution can be determined in the manner shown in Lee and Wang (1996), and is given by

$$w^b = w^e - \frac{(M_0^e + C_0)\Omega L^2}{EI} + \frac{3M_0^e\Omega x^2}{2(1 + 3\Omega)EI}\left(1 - \frac{x}{3L}\right) \quad (1)$$

$$w^s = \frac{(M^e + C_0)\Omega L^2}{EI} + \frac{3M_0^e\Omega^2 xL}{(1 + 3\Omega)EI} \quad (2)$$

Downloaded 04 May 2010 to 171.66.16.34. Redistribution subject to ASME license or copyright; see http://www.asme.org/terms/Terms_Use.cfm

$$w^t = w^e + \frac{(M^e - M_0^e)\Omega L^2}{EI} + \frac{3M_0^e \Omega x L}{(1 + 3\Omega)EI}\left(\Omega + \frac{x}{2L} - \frac{x^2}{6L^2}\right) \quad (3)$$

$$\frac{dw^b}{dx} = \frac{dw^e}{dx} + \frac{3M_0^e \Omega x}{(1 + 3\Omega)EI}\left(1 - \frac{x}{2L}\right). \quad (4)$$

In the above expressions, M_0^e is the bending moment in the Euler-Bernoulli beam at the clamped end, and Ω is the nondimensionalized shear parameter $EI/(kGAL^2)$. It is observed that the expressions for both w^b and w^s contain an undetermined constant C_0. This is a natural consequence of substituting $-(dw^b/dx)$ for ψ without increasing the number of end conditions. As expected, this constant does not appear in the expression for the sum $w^t = w^b + w^s$ which remains well defined.

Next, the same statically indeterminate problem is solved for the deflection component w^s in terms of the Euler-Bernoulli solution by assuming $w^b = w^e$ and $w^s = 0$ at $x = 0, L$. The following equations are recalled from Table 1:

$$\frac{d^2M^e}{dx^2} = -q, \quad \frac{dV^t}{dx} = -q, \quad V^t = kGA\frac{dw^s}{dx}. \quad (5, 6, 7)$$

Combining Eqs. (5) to (7) gives

$$kGA\frac{d^2w^s}{dx^2} = \frac{d^2M^e}{dx^2} \quad (8)$$

which yields the solution

$$w^s = \frac{M^e - M_0^e}{kGA} + \frac{M_0^e}{kGA}\left(\frac{x}{L}\right) = \frac{(M^e - M_0^e)\Omega L^2}{EI} + \frac{M_0^e \Omega x L}{EI} \quad (9)$$

on using the boundary conditions $w^s = 0$ at $x = 0, L$. The total deflection and slope are thus given, respectively, by

$$w^t = w^e + \frac{(M^e - M_0^e)\Omega L^2}{EI} + \frac{M_0^e \Omega x L}{EI} \quad (10)$$

$$\frac{dw^b}{dx} = \frac{dw^e}{dx}. \quad (11)$$

Clearly, the expressions given in Eqs. (9) to (11) are different from the correct ones shown in Eqs. (2) to (4). There is no way to adjust C_0 in Eq. (1) in order to make w^b equal to w^e along the whole beam. If they are made equal at the clamped end ($x = 0$), then $C_0 = -M_0^e$, and the deflection components w^b and w^s at the simply supported end ($x = L$) take on the values

$$w^b = \frac{M_0^e \Omega L^2}{(1 + 3\Omega)EI} \neq 0, \quad w^b \neq w^e \quad (12)$$

$$w^s = -\frac{M_0^e \Omega L^2}{(1 + 3\Omega)EI} \neq 0. \quad (13)$$

A similar result is obtained by setting w^b equal to w^e at the simply supported end ($x = L$). The obvious conclusion here is that it is not possible for w^b to be equal to w^e at more than one point on the beam. From this illustrative example, it is therefore deduced that the bending deflection w^b is, in general, not the same as the Euler-Bernoulli deflection w^e. A detailed treatment of general single-span beams of uniform cross section in Lee and Wang (1996) shows further that it is possible to assume w^b and w^e to be identical only for statically determinate beam problems but it is incorrect to do the same for statically indeterminate problems unless the latter problems are symmetric.

Conclusions

By decomposing the total transverse deflection w^t of the Timoshenko beam into its bending and shear components w^b and w^s and obtaining the governing equations variationally, it was shown that six (instead of four) end conditions were needed in order to determine the solution for w^b and w^s from the resulting pair of uncoupled differential equations. Due to the identical forms of the governing equations, boundary conditions and constitutive equations for the bending deflection w^b and the Euler-Bernoulli deflection w^e, the misleading assumption that $w^b = w^e$ along the beam is often made. Consequently, at clamped and simply supported ends, the usual practice is to prescribe $w^b = w^s = w^e = 0$ in order to provide the two additional end conditions. The present note demonstrated clearly through an example that this practice produced erroneous solutions for statically indeterminate problems. The perception that the Timoshenko bending deflection w^b and the Euler-Bernoulli deflection w^e are the same along the whole beam is therefore not justified.

References

Anderson, R. A., 1953, "Flexural Vibrations in Uniform Beams According to the Timoshenko Theory," ASME JOURNAL OF APPLIED MECHANICS, Vol. 20, pp. 504–510.

Krishna Murty, A. V., 1970a, "Vibrations of Short Beams," *AIAA Journal*, Vol. 8, pp. 34–38.

Krishna Murty, A. V., 1970b, "Analysis of Short Beams," *AIAA Journal*, Vol. 8, pp. 2098–2100.

Krishna Murty, A. V., 1984, "Toward a Consistent Beam Theory," *AIAA Journal*, Vol. 22, pp. 811–816.

Lee, K. H., and Wang, C. M., 1996, "The Deflection Components Method for Timoshenko Beam Theory," submitted for publication.

Miklowitz, J., 1953, "Flexural Wave Solutions of Coupled Equations Representing the More Exact Theory of Bending," ASME JOURNAL OF APPLIED MECHANICS, Vol. 20, pp. 511–514.

Plantema, F. J., 1966, *Sandwich Construction: The Bending and Buckling of Sandwich Beams, Plates, and Shells*, John Wiley and Sons, New York.

Senthilnathan, N. R., Lim, S. P., Lee, K. H., and Chow, S. T., 1987, "Buckling of Shear-Deformable Plates," *AIAA Journal*, Vol. 25, pp. 1268–1271.

Senthilnathan, N. R., and Lee, K. H., 1992, "Some Remarks on Timoshenko Beam Theory," ASME *Journal of Vibration and Acoustics*, Vol. 114, pp. 495–497.

The Occurrence of Painleve's Paradox in the Motion of a Rotating Shaft

E. V. Wilms[8,10] and H. Cohen[9,10]

The importance of Coulomb friction in modern work in frictional systems has been discussed by (Armstrong-Helouvry, Dupont, and Canudas de Wit, 1994). In the present work, we consider an unbalanced shaft rotating in bearings where there is Coulomb friction acting. We show that for certain values of the moments and products of inertia, motion becomes impossi-

[8] Associate Professor, Department of Civil and Geological Engineering.

[9] Distinguished Professor, Department of Applied Mathematics.

[10] University of Manitoba, Winnipeg, MB R3T 2N2, Canada.

Contributed by the Applied Mechanics Division of THE AMERICAN SOCIETY OF MECHANICAL ENGINEERS for publication in the ASME JOURNAL OF APPLIED MECHANICS. Manuscript received by the ASME Applied Mechanics Division, Apr. 29, 1996; final revision, Feb. 5, 1997. Associate Technical Editor: N. C. Perkins.

Downloaded 04 May 2010 to 171.66.16.34. Redistribution subject to ASME license or copyright; see http://www.asme.org/terms/Terms_Use.cfm

$$w^t = w^e + \frac{(M^e - M_0^e)\Omega L^2}{EI} + \frac{3M_0^e \Omega x L}{(1 + 3\Omega)EI}\left(\Omega + \frac{x}{2L} - \frac{x^2}{6L^2}\right) \quad (3)$$

$$\frac{dw^b}{dx} = \frac{dw^e}{dx} + \frac{3M_0^e \Omega x}{(1 + 3\Omega)EI}\left(1 - \frac{x}{2L}\right). \quad (4)$$

In the above expressions, M_0^e is the bending moment in the Euler-Bernoulli beam at the clamped end, and Ω is the nondimensionalized shear parameter $EI/(kGAL^2)$. It is observed that the expressions for both w^b and w^s contain an undetermined constant C_0. This is a natural consequence of substituting $-(dw^b/dx)$ for ψ without increasing the number of end conditions. As expected, this constant does not appear in the expression for the sum $w^t = w^b + w^s$ which remains well defined.

Next, the same statically indeterminate problem is solved for the deflection component w^s in terms of the Euler-Bernoulli solution by assuming $w^b = w^e$ and $w^s = 0$ at $x = 0, L$. The following equations are recalled from Table 1:

$$\frac{d^2M^e}{dx^2} = -q, \quad \frac{dV^t}{dx} = -q, \quad V^t = kGA\frac{dw^s}{dx}. \quad (5, 6, 7)$$

Combining Eqs. (5) to (7) gives

$$kGA\frac{d^2w^s}{dx^2} = \frac{d^2M^e}{dx^2} \quad (8)$$

which yields the solution

$$w^s = \frac{M^e - M_0^e}{kGA} + \frac{M_0^e}{kGA}\left(\frac{x}{L}\right) = \frac{(M^e - M_0^e)\Omega L^2}{EI} + \frac{M_0^e \Omega x L}{EI} \quad (9)$$

on using the boundary conditions $w^s = 0$ at $x = 0, L$. The total deflection and slope are thus given, respectively, by

$$w^t = w^e + \frac{(M^e - M_0^e)\Omega L^2}{EI} + \frac{M_0^e \Omega x L}{EI} \quad (10)$$

$$\frac{dw^b}{dx} = \frac{dw^e}{dx}. \quad (11)$$

Clearly, the expressions given in Eqs. (9) to (11) are different from the correct ones shown in Eqs. (2) to (4). There is no way to adjust C_0 in Eq. (1) in order to make w^b equal to w^e along the whole beam. If they are made equal at the clamped end ($x = 0$), then $C_0 = -M_0^e$, and the deflection components w^b and w^s at the simply supported end ($x = L$) take on the values

$$w^b = \frac{M_0^e \Omega L^2}{(1 + 3\Omega)EI} \neq 0, \quad w^b \neq w^e \quad (12)$$

$$w^s = -\frac{M_0^e \Omega L^2}{(1 + 3\Omega)EI} \neq 0. \quad (13)$$

A similar result is obtained by setting w^b equal to w^e at the simply supported end ($x = L$). The obvious conclusion here is that it is not possible for w^b to be equal to w^e at more than one point on the beam. From this illustrative example, it is therefore deduced that the bending deflection w^b is, in general, not the same as the Euler-Bernoulli deflection w^e. A detailed treatment of general single-span beams of uniform cross section in Lee and Wang (1996) shows further that it is possible to assume w^b and w^e to be identical only for statically determinate beam problems but it is incorrect to do the same for statically indeterminate problems unless the latter problems are symmetric.

Conclusions

By decomposing the total transverse deflection w^t of the Timoshenko beam into its bending and shear components w^b and w^s and obtaining the governing equations variationally, it was shown that six (instead of four) end conditions were needed in order to determine the solution for w^b and w^s from the resulting pair of uncoupled differential equations. Due to the identical forms of the governing equations, boundary conditions and constitutive equations for the bending deflection w^b and the Euler-Bernoulli deflection w^e, the misleading assumption that $w^b = w^e$ along the beam is often made. Consequently, at clamped and simply supported ends, the usual practice is to prescribe $w^b = w^s = w^e = 0$ in order to provide the two additional end conditions. The present note demonstrated clearly through an example that this practice produced erroneous solutions for statically indeterminate problems. The perception that the Timoshenko bending deflection w^b and the Euler-Bernoulli deflection w^e are the same along the whole beam is therefore not justified.

References

Anderson, R. A., 1953, "Flexural Vibrations in Uniform Beams According to the Timoshenko Theory," ASME JOURNAL OF APPLIED MECHANICS, Vol. 20, pp. 504–510.

Krishna Murty, A. V., 1970a, "Vibrations of Short Beams," *AIAA Journal*, Vol. 8, pp. 34–38.

Krishna Murty, A. V., 1970b, "Analysis of Short Beams," *AIAA Journal*, Vol. 8, pp. 2098–2100.

Krishna Murty, A. V., 1984, "Toward a Consistent Beam Theory," *AIAA Journal*, Vol. 22, pp. 811–816.

Lee, K. H., and Wang, C. M., 1996, "The Deflection Components Method for Timoshenko Beam Theory," submitted for publication.

Miklowitz, J., 1953, "Flexural Wave Solutions of Coupled Equations Representing the More Exact Theory of Bending," ASME JOURNAL OF APPLIED MECHANICS, Vol. 20, pp. 511–514.

Plantema, F. J., 1966, *Sandwich Construction: The Bending and Buckling of Sandwich Beams, Plates, and Shells*, John Wiley and Sons, New York.

Senthilnathan, N. R., Lim, S. P., Lee, K. H., and Chow, S. T., 1987, "Buckling of Shear-Deformable Plates," *AIAA Journal*, Vol. 25, pp. 1268–1271.

Senthilnathan, N. R., and Lee, K. H., 1992, "Some Remarks on Timoshenko Beam Theory," ASME *Journal of Vibration and Acoustics*, Vol. 114, pp. 495–497.

The Occurrence of Painleve's Paradox in the Motion of a Rotating Shaft

E. V. Wilms[8,10] and H. Cohen[9,10]

The importance of Coulomb friction in modern work in frictional systems has been discussed by (Armstrong-Helouvry, Dupont, and Canudas de Wit, 1994). In the present work, we consider an unbalanced shaft rotating in bearings where there is Coulomb friction acting. We show that for certain values of the moments and products of inertia, motion becomes impossi-

[8] Associate Professor, Department of Civil and Geological Engineering.

[9] Distinguished Professor, Department of Applied Mathematics.

[10] University of Manitoba, Winnipeg, MB R3T 2N2, Canada.

Contributed by the Applied Mechanics Division of THE AMERICAN SOCIETY OF MECHANICAL ENGINEERS for publication in the ASME JOURNAL OF APPLIED MECHANICS. Manuscript received by the ASME Applied Mechanics Division, Apr. 29, 1996; final revision, Feb. 5, 1997. Associate Technical Editor: N. C. Perkins.

Copyright © 1997 by ASME

Downloaded 04 May 2010 to 171.66.16.34. Redistribution subject to ASME license or copyright; see http://www.asme.org/terms/Terms_Use.cfm

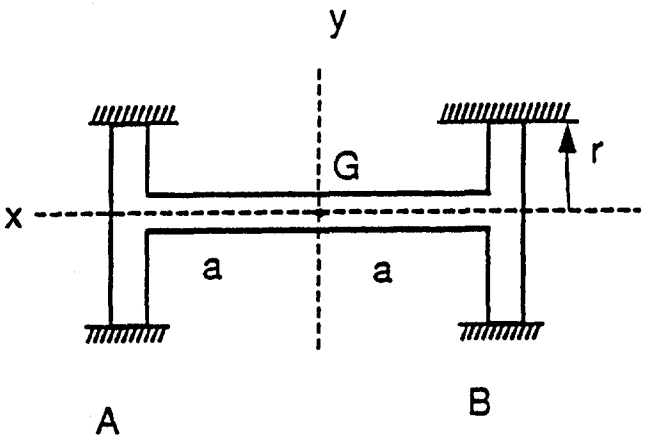


Fig. 1(*a*) The *x*-*y* plane

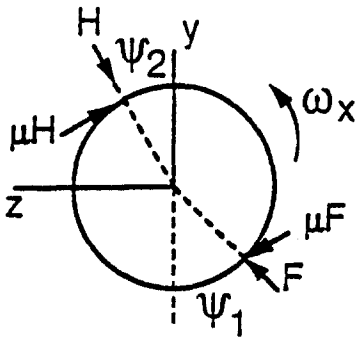


Fig. 1(*b*) The *y*-*z* plane

ble. The behavior is an example of Painleve's paradox, some of the earliest examples of which were considered by Lecornu (1905) and by Klein (1909). Some two-dimensional examples of the paradox were considered by (Wilms and Cohen, 1981, 1983). In the present study we consider a three-dimensional example.

The angular momentum of a rigid body is given by (Greenwood, 1965)

$$\tilde{H} = H_x\tilde{i} + H_y\tilde{j} + H_z\tilde{k} \tag{1}$$

where

$$H_x = I_{xx}\omega_x + I_{xy}\omega_y + I_{xz}\omega_z \tag{2a}$$

$$H_y = I_{yx}\omega_x + I_{yy}\omega_y + I_{yz}\omega_z \tag{2b}$$

$$H_z = I_{zx}\omega_x + I_{zy}\omega_y + I_{zz}\omega_z. \tag{2c}$$

In Eq. (1), $\tilde{i}$, $\tilde{j}$, and $\tilde{k}$ are unit vectors. In Eqs. (2) I_{xx}, I_{yy}, and I_{zz} are moments of inertia, I_{xy}, I_{xz}, and I_{yz} are products of inertia, and ω_x, ω_y, and ω_z are angular velocities.

The shaft is shown in Fig. 1(*a*) and Fig. 1(*b*). There is no gravity and the center of mass lies on the axis of rotation at point G.

The disks at A and B (as indicated in Fig. 1(*a*), are attached to the shaft, are a distance $2a$ apart, and run in bearings which are infinitesimally larger than the disks. We will follow Wilms and Cohen (1981, 1983), and consider point contact at the circumference. The forces on disk A are F, a normal force, and μF, a tangential friction force. The forces exerted on disk B are H and μH. Here μ is the coefficient of friction.

Since the center of mass is fixed in position, the sum of the forces must equal zero. We have then

$$H(\cos\psi_2 - \mu\sin\psi_2) + F(-\cos\psi_1 + \mu\sin\psi_1) = 0, \tag{3a}$$

$$H(\sin\psi_2 + \mu\cos\psi_2) + F(-\sin\psi_1 - \mu\cos\psi_1) = 0. \tag{3b}$$

A nonzero solution for F and H requires the vanishing of the determinant of the coefficients of H and F. After some simplification this condition yields $(1 + \mu^2)\sin(\psi_1 - \psi_2) = 0$. Hence, $\psi_1 = \psi_2 = \psi$, and $H = F$.

The other solution, $\psi_2 = \psi_1 + \pi$, yields $H = -F$, which is unphysical and may be ignored.

The moment of the forces about the x-axis is $M_x = 2_\mu rF$, where r is the radius of the disks.

The moment about the y-axis is

$$M_y = -2aF(\sin\psi + \mu\cos\psi), \tag{4a}$$

and about the z-axis,

$$M_z = 2aF(\cos\psi - \mu\sin\psi). \tag{4b}$$

We have then

$$M_x^2 = 4\mu^2r^2F^2, \tag{5}$$

and

$$M_y^2 + M_z^2 = 4a^2F^2(1 + \mu^2). \tag{6}$$

Since ω_x is the only component of angular velocity, Eqs. (1) and (2) yield

$$\tilde{H} = (\tilde{i}I_{xx} + \tilde{j}I_{xy} + \tilde{k}I_{xz})\omega_x. \tag{7}$$

The moment equation

$$\bar{M} = \dot{\tilde{H}} = (\dot{\tilde{H}})_r + \tilde{\omega}\times\tilde{H}, \tag{8}$$

then yields

$$M_x = I_{xx}\dot{\omega}_x, \tag{9a}$$

$$M_y = I_{xy}\dot{\omega}_x - I_{xz}\omega_x^2, \tag{9b}$$

$$M_z = I_{xz}\dot{\omega}_x + I_{xy}\omega_x^2. \tag{9c}$$

Equations (9) yield

$$M_x^2 = I_{xx}^2\dot{\omega}_x^2, \tag{10a}$$

$$M_y^2 + M_z^2 = (I_{xy}^2 + I_{xz}^2)(\dot{\omega}_x^2 + \omega_x^4). \tag{10b}$$

Equations (5), (6), and (10) yield

$$\dot{\omega}_x^2\left\{I_{xx}^2 - \frac{\mu^2r^2}{a^2(1+\mu^2)}(I_{xy}^2 + I_{xz}^2)\right\} = \frac{\mu^2r^2}{a^2(1+\mu^2)}(I_{xy}^2 + I_{xz}^2)\omega_x^4. \tag{11}$$

Equation (11) yields

$$\dot{\omega}_x = -\alpha\omega_x^2, \tag{12}$$

where

$$\alpha^2 = \frac{\mu^2r^2}{a^2(1+\mu^2)}(I_{xy}^2 + I_{xz}^2)\Big/\left\{I_{xx}^2 - \frac{\mu^2r^2}{a^2(1+\mu^2)}(I_{xy}^2 + I_{xz}^2)\right\}. \tag{13}$$

Since $M_x = I_{xx}\dot{\omega}_x = -2\mu rF$, $\dot{\omega}_x$ is negative, and hence the negative sign in Eq. (12).

Equation (12) may be solved to yield

$$\omega_x = \frac{\omega_{xo}}{1 + \alpha\omega_{xo}t}.$$

Here ω_{xo} is the initial value of ω_x. Equation (13) indicates that we obtain real solutions for ω_x only as long as α^2 is positive.

Downloaded 04 May 2010 to 171.66.16.34. Redistribution subject to ASME license or copyright; see http://www.asme.org/terms/Terms_Use.cfm

Physically it is always possible to construct a system so that α^2 is negative, (by making (r/a) sufficiently large, for example). The difficulty arises because the Coulomb friction law is not always compatible with the equations of rigid-body dynamics.

Everything will be resolved if either the bearings or the rotating body are made elastic. When no rigid-body solution exists, the shaft seizes up, and no motion occurs. We note that the phenomenon does not occur in the case of a balanced rotor as it results in $F = 0$. It may be shown that the paradox also occurs when the c.g. is off the axis of rotation.

References

Armstrong-Helouvry, B., Dupont, P., and Canudas de Wit, C., 1994, "A Survey of Models, Analysis Tools and Compensation Methods for the Control of Machines with Friction," *Automatica,* Vol. 30, No. 7, pp. 1083–1138.

Lecornu, L., 1905, "Sur le frottement de glissement," *Comptes Rendu,* Vol. 140, pp. 635–637.

Klein, F., 1909, "Zu Painleve's Kritic der Coulombschen Reibungsgesetze," *Zeitschrift für Mathematic und Physik,* Vol. 58, pp. 186–191.

Wilms, E. V., and Cohen, H., 1981, "Planar Motion of a Rigid Body with a Friction Rotor," ASME JOURNAL OF APPLIED MECHANICS, Vol. 48, pp. 205–206.

Wilms, E. V., and Cohen, H., 1983, "Limitations of the Coulomb Friction Model for Two Elementary Dynamical Systems," *International Journal of Mechanical Engineering Education,* Vol. 11, pp. 107–112.

Greenwood, D. T., 1965, *Principles of Dynamics,* Prentice-Hall, Englewood Cliffs, NJ.

Saddle-Point Principles for General Nonlinear Material Continua

A. Carini[11]

1 Introduction

A lot of techniques have been proposed for the theoretical and numerical treatment of inelastic (linear or nonlinear) boundary value problems, in particular for the elastic-plastic one. Some of these techniques rest on Colonnetti's idea (Colonnetti, 1918, 1950, 1955) of considering the material nonlinearities as imposed distortions in a supposedly linear elastic continuum. Colonnetti's approach to inelastic problems had numerous developments and applications in literature, particularly in elastoplasticity, by, among others, Ceradini (1966), Maier (1969), De Donato and Maier (1972), and Carter and Martin (1977). See also Koiter (1964) for some historical remarks on this topic.

Colonnetti's approach exploits the typical additive decomposition of the constitutive equations of many inelastic problems, into elastic and inelastic parts and, somehow, it is a precursor of the more recent *operator split* approach which is used in many fields, for instance in plasticity (Ortiz et al., 1983), in shakedown analysis (Zarka and Casier, 1979), and in micromechanics (Mura, 1987).

In previous works (Carini, 1996; Carini and De Donato, 1997) several *minimum principles* for the continuum problem with general nonlinear materials were shown. These principles rest on Colonnetti's idea and are based on the use of the solution of an *elastic auxiliary problem,* i.e., of the same problem in the elastic range with homogeneous boundary conditions in the presence of suitable distorsions.

The main characterizations of these minimum principles are (i) the energy meaning of the related functionals; (ii) their ability to specialize into well-known classical principles in case of linear elasticity and incremental elastoplasticity; (iii) their validity in all cases even in the lack of existence or uniqueness of the solution.

However, from a practical point of view, the main drawback which arises in the use of the above-mentioned functionals lies in the need to find the solution of the elastic auxiliary problem as already pointed out in Carini et al. (1995).

In this paper the above drawback is overcomed by the reformulation of the *minimum principles* as *saddle-point principles.*

After a brief preliminary description (in Section 2) of the continuum problem and a recall of the above-mentioned *minimum principles,* in Section 3 they are transformed reducing all terms of the functionals relevant to the auxiliary elastic problem to one term only. This allows us to recognize, in this term, the deformation energy of the elastic auxiliary problem and then to use classical extremum principles of elasticity for its evaluation. In this way, two new general *min-max* variational principles for the original problem are derived and later, in Section 4, an application is presented with reference to elastic-plastic material behavior.

2 Problem Formulation and Previous Variational Principles

A solid is considered to occupy a region Ω with a smooth external surface Γ in a triaxial orthogonal Cartesian reference system. Γ_u and Γ_p are the parts of surface Γ where displacements and surface tractions are imposed, respectively, while $\mathbf{x} = (x_1, x_2, x_3)$ denotes the position vector of a material point in Ω.

The external actions on the solid, i.e., the volume forces $F_i(\mathbf{x}; t)$ on Ω, the imposed displacements $v_i(\mathbf{x}; t)$ on Γ_u and the tractions $p_i(\mathbf{x}; t)$ on Γ_p, are given for any instant $t_0 \le t \le t_1$ of a known time interval $T = [t_0, t_1]$, through known time functions. We assume small strains and displacements, thus we consider the usual linear equilibrium and compatibility equations. Let's assume that the constitutive law is of the additive type, that is, the sum of two behaviors, the first one linear elastic and the second one inelastic, conceived as a deviation with respect to the linear elastic part.

The general inelastic problem is then here described by the following equations and it will be referred to as *problem P*:

Problem P:

$$\sigma_{ij,j} + F_i = 0 \quad \text{in} \quad \Omega \times T \tag{2.1}$$

$$\sigma_{ij} n_j = p_i \quad \text{on} \quad \Gamma_p \times T \tag{2.2}$$

$$\epsilon_{ij} = \tfrac{1}{2}(u_{i,j} + u_{j,i}) \quad \text{in} \quad \Omega \times T \tag{2.3}$$

$$u_i = v_i \quad \text{on} \quad \Gamma_u \times T \tag{2.4}$$

$$\sigma_{ij}(\mathbf{x}; t) = D_{ijhk}(\mathbf{x}; t)\epsilon_{hk}(\mathbf{x}; t) + \Psi^n_{ij}(\boldsymbol{\epsilon}(\mathbf{x}; t)) \tag{2.5}$$

$$\epsilon_{ij}(\mathbf{x}; t) = B_{ijhk}(\mathbf{x}; t)\sigma_{hk}(\mathbf{x}; t) + \Phi^n_{ij}(\boldsymbol{\sigma}(\mathbf{x}; t)) \tag{2.6}$$

$$u_i = \epsilon_{ij} = \sigma_{ij} = 0 \quad \text{on} \quad \bar{\Omega} \times (-\infty, t_0) \tag{2.7}$$

where $\bar{\Omega} = \Omega \cup \Gamma$. Relations (2.1) and (2.2) represent the indefinite and boundary equilibrium equations, respectively, while relations (2.3) and (2.4) represent the indefinite and boundary compatibility equations, respectively. Here, σ_{ij}, ϵ_{ij}, and u_i are the components of the stress tensor $\boldsymbol{\sigma}$, the strain tensor $\boldsymbol{\epsilon}$, and the displacement vector $\mathbf{u}$, respectively. Relations (2.5) and (2.6) represent the constitutive law in direct and invers form, respectively, where $D_{ijhk} = B^{-1}_{ijhk}$ is the time-dependent elastic moduli tensor with the usual simmetry and positive

[11] Department of Civil Engineering, University of Brescia, via Branze 38, 25123 Brescia, Italy.

Contributed by the Applied Mechanics Division of THE AMERICAN SOCIETY OF MECHANICAL ENGINEERS for publication in the ASME JOURNAL OF APPLIED MECHANICS. Manuscript received by the ASME Applied Mechanics Division, July 15, 1996; final revision, May 21, 1997. Associate Technical Editor: W. K. Liu.

Downloaded 04 May 2010 to 171.66.16.34. Redistribution subject to ASME license or copyright; see http://www.asme.org/terms/Terms_Use.cfm

Physically it is always possible to construct a system so that α^2 is negative, (by making (r/a) sufficiently large, for example). The difficulty arises because the Coulomb friction law is not always compatible with the equations of rigid-body dynamics.

Everything will be resolved if either the bearings or the rotating body are made elastic. When no rigid-body solution exists, the shaft seizes up, and no motion occurs. We note that the phenomenon does not occur in the case of a balanced rotor as it results in $F = 0$. It may be shown that the paradox also occurs when the c.g. is off the axis of rotation.

References

Armstrong-Helouvry, B., Dupont, P., and Canudas de Wit, C., 1994, "A Survey of Models, Analysis Tools and Compensation Methods for the Control of Machines with Friction," *Automatica,* Vol. 30, No. 7, pp. 1083–1138.

Lecornu, L., 1905, "Sur le frottement de glissement," *Comptes Rendu,* Vol. 140, pp. 635–637.

Klein, F., 1909, "Zu Painleve's Kritic der Coulombschen Reibungsgesetze," *Zeitschrift für Mathematic und Physik,* Vol. 58, pp. 186–191.

Wilms, E. V., and Cohen, H., 1981, "Planar Motion of a Rigid Body with a Friction Rotor," ASME JOURNAL OF APPLIED MECHANICS, Vol. 48, pp. 205–206.

Wilms, E. V., and Cohen, H., 1983, "Limitations of the Coulomb Friction Model for Two Elementary Dynamical Systems," *International Journal of Mechanical Engineering Education,* Vol. 11, pp. 107–112.

Greenwood, D. T., 1965, *Principles of Dynamics,* Prentice-Hall, Englewood Cliffs, NJ.

Saddle-Point Principles for General Nonlinear Material Continua

A. Carini[11]

1 Introduction

A lot of techniques have been proposed for the theoretical and numerical treatment of inelastic (linear or nonlinear) boundary value problems, in particular for the elastic-plastic one. Some of these techniques rest on Colonnetti's idea (Colonnetti, 1918, 1950, 1955) of considering the material nonlinearities as imposed distortions in a supposedly linear elastic continuum. Colonnetti's approach to inelastic problems had numerous developments and applications in literature, particularly in elastoplasticity, by, among others, Ceradini (1966), Maier (1969), De Donato and Maier (1972), and Carter and Martin (1977). See also Koiter (1964) for some historical remarks on this topic.

Colonnetti's approach exploits the typical additive decomposition of the constitutive equations of many inelastic problems, into elastic and inelastic parts and, somehow, it is a precursor of the more recent *operator split* approach which is used in many fields, for instance in plasticity (Ortiz et al., 1983), in shakedown analysis (Zarka and Casier, 1979), and in micromechanics (Mura, 1987).

In previous works (Carini, 1996; Carini and De Donato, 1997) several *minimum principles* for the continuum problem with general nonlinear materials were shown. These principles rest on Colonnetti's idea and are based on the use of the solution of an *elastic auxiliary problem,* i.e., of the same problem in the elastic range with homogeneous boundary conditions in the presence of suitable distorsions.

The main characterizations of these minimum principles are (i) the energy meaning of the related functionals; (ii) their ability to specialize into well-known classical principles in case of linear elasticity and incremental elastoplasticity; (iii) their validity in all cases even in the lack of existence or uniqueness of the solution.

However, from a practical point of view, the main drawback which arises in the use of the above-mentioned functionals lies in the need to find the solution of the elastic auxiliary problem as already pointed out in Carini et al. (1995).

In this paper the above drawback is overcomed by the reformulation of the *minimum principles* as *saddle-point principles.*

After a brief preliminary description (in Section 2) of the continuum problem and a recall of the above-mentioned *minimum principles,* in Section 3 they are transformed reducing all terms of the functionals relevant to the auxiliary elastic problem to one term only. This allows us to recognize, in this term, the deformation energy of the elastic auxiliary problem and then to use classical extremum principles of elasticity for its evaluation. In this way, two new general *min-max* variational principles for the original problem are derived and later, in Section 4, an application is presented with reference to elastic-plastic material behavior.

2 Problem Formulation and Previous Variational Principles

A solid is considered to occupy a region Ω with a smooth external surface Γ in a triaxial orthogonal Cartesian reference system. Γ_u and Γ_p are the parts of surface Γ where displacements and surface tractions are imposed, respectively, while $\mathbf{x} = (x_1, x_2, x_3)$ denotes the position vector of a material point in Ω.

The external actions on the solid, i.e., the volume forces $F_i(\mathbf{x}; t)$ on Ω, the imposed displacements $v_i(\mathbf{x}; t)$ on Γ_u and the tractions $p_i(\mathbf{x}; t)$ on Γ_p, are given for any instant $t_0 \le t \le t_1$ of a known time interval $T = [t_0, t_1]$, through known time functions. We assume small strains and displacements, thus we consider the usual linear equilibrium and compatibility equations. Let's assume that the constitutive law is of the additive type, that is, the sum of two behaviors, the first one linear elastic and the second one inelastic, conceived as a deviation with respect to the linear elastic part.

The general inelastic problem is then here described by the following equations and it will be referred to as *problem P*:

Problem P:

$$\sigma_{ij,j} + F_i = 0 \quad \text{in} \quad \Omega \times T \tag{2.1}$$

$$\sigma_{ij} n_j = p_i \quad \text{on} \quad \Gamma_p \times T \tag{2.2}$$

$$\epsilon_{ij} = \tfrac{1}{2}(u_{i,j} + u_{j,i}) \quad \text{in} \quad \Omega \times T \tag{2.3}$$

$$u_i = v_i \quad \text{on} \quad \Gamma_u \times T \tag{2.4}$$

$$\sigma_{ij}(\mathbf{x}; t) = D_{ijhk}(\mathbf{x}; t)\epsilon_{hk}(\mathbf{x}; t) + \Psi^n_{ij}(\boldsymbol{\epsilon}(\mathbf{x}; t)) \tag{2.5}$$

$$\epsilon_{ij}(\mathbf{x}; t) = B_{ijhk}(\mathbf{x}; t)\sigma_{hk}(\mathbf{x}; t) + \Phi^n_{ij}(\boldsymbol{\sigma}(\mathbf{x}; t)) \tag{2.6}$$

$$u_i = \epsilon_{ij} = \sigma_{ij} = 0 \quad \text{on} \quad \bar{\Omega} \times (-\infty, t_0) \tag{2.7}$$

where $\bar{\Omega} = \Omega \cup \Gamma$. Relations (2.1) and (2.2) represent the indefinite and boundary equilibrium equations, respectively, while relations (2.3) and (2.4) represent the indefinite and boundary compatibility equations, respectively. Here, σ_{ij}, ϵ_{ij}, and u_i are the components of the stress tensor $\boldsymbol{\sigma}$, the strain tensor $\boldsymbol{\epsilon}$, and the displacement vector $\mathbf{u}$, respectively. Relations (2.5) and (2.6) represent the constitutive law in direct and invers form, respectively, where $D_{ijhk} = B^{-1}_{ijhk}$ is the time-dependent elastic moduli tensor with the usual simmetry and positive

[11] Department of Civil Engineering, University of Brescia, via Branze 38, 25123 Brescia, Italy.

Contributed by the Applied Mechanics Division of THE AMERICAN SOCIETY OF MECHANICAL ENGINEERS for publication in the ASME JOURNAL OF APPLIED MECHANICS. Manuscript received by the ASME Applied Mechanics Division, July 15, 1996; final revision, May 21, 1997. Associate Technical Editor: W. K. Liu.

Copyright © 1997 by ASME

Downloaded 04 May 2010 to 171.66.16.34. Redistribution subject to ASME license or copyright; see http://www.asme.org/terms/Terms_Use.cfm

definiteness properties at any time t, while Ψ_{ij}^n and Φ_{ij}^n represent the "remaining" inelastic part operator of the constitutive law. Relations (2.7) represent the *initial conditions,* which are assumed as being homogeneous, for simplicity.

A stress distribution field $\sigma_{ij}^*(\mathbf{x}, t)$ is defined as *statically admissible* when it satisfies the following equilibrium equations:

$$\sigma_{ij,j}^* + F_i = 0 \quad \text{in} \quad \Omega \times T \tag{2.8}$$

$$\sigma_{ij}^* n_j = p_i \quad \text{on} \quad \Gamma_p \times T \tag{2.9}$$

while a stress distribution $\sigma_{ij}^{**}(\mathbf{x}, t)$ is defined as *self-equilibrated* when it satisfies the following *homogeneous* equilibrium equations:

$$\sigma_{ij,j}^{**} = 0 \quad \text{in} \quad \Omega \times T \tag{2.10}$$

$$\sigma_{ij}^{**} n_j = 0 \quad \text{on} \quad \Gamma_p \times T. \tag{2.11}$$

Analogously a strain field $\epsilon_{ij}^0(\mathbf{x}, t)$ is defined as *kinematically admissible* if it can be derived by means of the equation

$$\epsilon_{ij}^0 = \tfrac{1}{2}(u_{i,j}^0 + u_{j,i}^0) \quad \text{in} \quad \Omega \times T \tag{2.12}$$

from a displacement field $u_i^0(\mathbf{x}, t)$ satisfying the boundary conditions

$$u_i^0 = v_i \quad \text{on} \quad \Gamma_u \times T \tag{2.13}$$

while a strain field $\epsilon_{ij}^{00}(\mathbf{x}, t)$ is here defined as *self-compatible* if it can be derived by means of the equation

$$\epsilon_{ij}^{00} = \tfrac{1}{2}(u_{i,j}^{00} + u_{j,i}^{00}) \quad \text{in} \quad \Omega \times T \tag{2.14}$$

from a displacement field $u_i^{00}(\mathbf{x}, t)$ vanishing on Γ_u, i.e., that satisfies the *homogeneous* boundary conditions

$$u_i^{00} = 0 \quad \text{on} \quad \Gamma_u \times T. \tag{2.15}$$

In the following the symbols ϵ_{ij}^{ef} and σ_{ij}^{ef} represent, respectively, the strains and the stresses in the solid under the external actions F_i, p_i, v_i and under the hypothesis of a linear elastic behavior with material properties corresponding to B_{ijhk}.

In a previous paper (Carini, 1996) two minimum principles were shown. In particular the following two propositions were proved:

Proposition 1: *A statically admissible stress field σ_{ij}^* is a (or the) solution of problem P if and only if both the following conditions are satisfied:*

(i) *It minimizes (absolute minimum) the functional F_{ce}^I, where*

$$F_{ce}^I[\sigma_{ij}^*] = \int_T \left\{ \tfrac{1}{2} \int_\Omega \sigma_{ij}^* B_{ijhk} \sigma_{hk}^* d\Omega - \int_{\Gamma_u} v_i n_j \sigma_{ij}^* d\Gamma + \int_\Omega \Phi_{ij}^n(\boldsymbol{\sigma}^*)(\sigma_{ij}^* - \sigma_{ij}^{ef}) d\Omega + \tfrac{1}{2} \int_\Omega \sigma_{ij}^d(\boldsymbol{\sigma}^*) B_{ijhk} \sigma_{hk}^d(\boldsymbol{\sigma}^*) d\Omega \right\} dt. \tag{2.16}$$

(ii) *The minimum is equal to F_{ce}^0, where*

$$F_{ce}^0 = \int_T \left\{ \tfrac{1}{2} \int_\Omega \sigma_{ij}^{ef} \epsilon_{ij}^{ef} d\Omega - \int_{\Gamma_u} v_i n_j \sigma_{ij}^{ef} d\Gamma \right\} dt. \tag{2.17}$$

Proposition 2: *A kinematically admissible displacement field u_i^0 is a (or the) solution of problem P if and only if both the following conditions are satisfied:*

(i) *It minimizes (absolute minimum) the functional F_{tpe}^I, where*

$$F_{tpe}^I[u_i^0] = \int_T \left\{ \tfrac{1}{2} \int_\Omega \epsilon_{ij}^0 D_{ijhk} \epsilon_{hk}^0 d\Omega - \int_\Omega F_i u_i^0 d\Omega - \int_{\Gamma_p} p_i u_i^0 d\Gamma + \int_\Omega \Psi_{ij}^n(\boldsymbol{\epsilon}^0)(\epsilon_{ij}^0 - \epsilon_{ij}^{ef}) d\Omega + \tfrac{1}{2} \int_\Omega \epsilon_{ij}^s(\boldsymbol{\epsilon}^0) D_{ijhk} \epsilon_{hk}^s(\boldsymbol{\epsilon}^0) d\Omega \right\} dt. \tag{2.18}$$

(ii) *The minimum is equal to F_{tpe}^0, where*

$$F_{tpe}^0 = \int_T \left\{ \tfrac{1}{2} \int_\Omega \sigma_{ij}^{ef} \epsilon_{ij}^{ef} d\Omega - \int_\Omega F_i u_i^{ef} d\Omega - \int_{\Gamma_p} p_i u_i^{ef} d\Gamma \right\} dt. \tag{2.19}$$

It is worth noting that, in the functional (2.18), $\epsilon_{ij}^0 = \epsilon_{ij}^0(\mathbf{u}^0) = \tfrac{1}{2}(u_{i,j}^0 + u_{j,i}^0)$. In (2.16) σ_{ij}^d is the solution of the following *imposed strain elastic auxiliary problem P^d*:

Problem P^d:

$$\sigma_{ij,j}^d = 0 \quad \text{in} \quad \Omega \times T \tag{2.20}$$

$$\sigma_{ij}^d n_j = 0 \quad \text{on} \quad \Gamma_p \times T \tag{2.21}$$

$$\epsilon_{ij}^d = \tfrac{1}{2}(u_{i,j}^d + u_{j,i}^d) \quad \text{in} \quad \Omega \times T \tag{2.22}$$

$$u_i^d = 0 \quad \text{on} \quad \Gamma_u \times T \tag{2.23}$$

$$\epsilon_{ij}^d = B_{ijhk} \sigma_{hk}^d + d_{ij}, \tag{2.24}$$

where d_{ij} is interpreted as the *imposed distorsions* given by $d_{ij} = -\Phi_{ij}^n(\boldsymbol{\sigma}^*)$ being $\boldsymbol{\sigma}^*$ any statically admissible stress field.

Conversely in (2.18) ϵ_{ij}^s is the solution of the following *imposed stress* elastic auxiliary problem P^s:

Problem P^s:

$$\sigma_{ij,j}^s = 0 \quad \text{in} \quad \Omega \times T \tag{2.25}$$

$$\sigma_{ij}^s n_j = 0 \quad \text{on} \quad \Gamma_p \times T \tag{2.26}$$

$$\epsilon_{ij}^s = \tfrac{1}{2}(u_{i,j}^s + u_{j,i}^s) \quad \text{in} \quad \Omega \times T \tag{2.27}$$

$$u_i^s = 0 \quad \text{on} \quad \Gamma_u \times T \tag{2.28}$$

$$\sigma_{ij}^s = D_{ijhk} \epsilon_{hk}^s + s_{ij}, \tag{2.29}$$

where s_{ij} is interpreted as the *imposed stresses* given by $s_{ij} = -\Psi_{ij}^n(\boldsymbol{\epsilon}^0)$ being $\boldsymbol{\epsilon}^0$ any kinematically admissible strain field. It is worth noting that both propositions 1 and 2 have been proved assuming B_{ijhk} and D_{ijhk} as time independent; however, it is easy to verify their validity also when B_{ijhk} and D_{ijhk} are time dependent.

3 New Variational Principles

A main computational drawback of the above principles (proposition 1 and 2) lies in the need to evaluate the last term of (2.16) and (2.18) through the solution of the elastic auxiliary problem for every admissible stress field $\boldsymbol{\sigma}^*$ (for *proposition 1*) or for every compatible strain field $\boldsymbol{\epsilon}^0$ (for *proposition 2*) or, in other words, in the need to find Green functions of the elastic problem. However, the last two mentioned terms are representative of elastic energies which can be evaluated, using classical elasticity principles, by maximization of suitable functionals in additional new variables.

3.1 A Min-Max Extended Complementary Energy Principle. Following this path of reasoning and making reference to *proposition 1* it is possible to find functional F_{ce}^d to be maximized, in order to obtain the last term of (2.16), simply by

Downloaded 04 May 2010 to 171.66.16.34. Redistribution subject to ASME license or copyright; see http://www.asme.org/terms/Terms_Use.cfm

using the principle of virtual work as follows (at any instant t):

$$\frac{1}{2}\int_\Omega \sigma^d_{ij}(\boldsymbol{\sigma}^*)B_{ijhk}\sigma^d_{hk}(\boldsymbol{\sigma}^*)d\Omega = -\frac{1}{2}\int_\Omega \sigma^d_{ij}(\boldsymbol{\sigma}^*)B_{ijhk}\sigma^d_{hk}(\boldsymbol{\sigma}^*)d\Omega + \int_\Omega \Phi^n_{ij}(\boldsymbol{\sigma}^*)\sigma^d_{ij}d\Omega. \quad (3.1)$$

It is easy to recognize the right-end side of (3.1) as the (changed in sign) complementary energy value at the solution of the elastic problem (at instant t) with imposed distorsions $d_{ij} = -\Phi^n_{ij}(\boldsymbol{\sigma}^*)$. This means that, by virtue of the minimum principle of complementary energy, we can write

$$\frac{1}{2}\int_\Omega \sigma^d_{ij}(\boldsymbol{\sigma}^*)B_{ijhk}\sigma^d_{hk}(\boldsymbol{\sigma}^*)d\Omega = \max_{\sigma^{d**}_{ij}} \{F^d_{ce}[\sigma^{d}_{ij}{}^{**}, \sigma^*_{ij}]\} \quad (3.2)$$

where

$$F^d_{ce}[\sigma^{d}_{ij}{}^{**}, \sigma^*_{ij}] = \int_T \left\{ -\frac{1}{2}\int_\Omega \sigma^{d}_{ij}{}^{**}B_{ijhk}\sigma^{d}_{hk}{}^{**}d\Omega + \int_\Omega \Phi^n_{ij}(\boldsymbol{\sigma}^*)\sigma^{d}_{ij}{}^{**}d\Omega \right\} dt, \quad (3.3)$$

$\sigma^{d}_{ij}{}^{**}$ being any *self-equilibrated* stress field. Then, by substitution of Eq. (3.2), the functional (2.16) is transformed into the following new functional:

$$\mathcal{F}_{ce}[\sigma^*_{ij}, \sigma^{d}_{ij}{}^{**}] = \int_T \left\{ \frac{1}{2}\int_\Omega \sigma^*_{ij}B_{ijhk}\sigma^*_{hk}d\Omega - \int_{\Gamma_u} v_i n_j \sigma^*_{ij}d\Gamma + \int_\Omega \Phi^n_{ij}(\boldsymbol{\sigma}^*)(\sigma^*_{ij} - \sigma^{ef}_{ij})d\Omega - \frac{1}{2}\int_\Omega \sigma^{d}_{ij}{}^{**}B_{ijhk}\sigma^{d}_{hk}{}^{**}d\Omega + \int_\Omega \Phi^n_{ij}(\sigma^*_{ij})\sigma^{d}_{ij}{}^{**}d\Omega \right\} dt \quad (3.4)$$

and the following statement can be asserted:

Proposition 3: *A statically admissible stress field σ^*_{ij} and a self-equilibrated stress field $\sigma^{d}_{ij}{}^{**}$ are a (or the) solution of problem P and problem P^d, respectively, if and only if both the following conditions are satisfied:*

(i) *They make stationary (minimum respect to σ^*_{ij} and maximum respect to $\sigma^{d}_{ij}{}^{**}$) the functional (3.4);*
(ii) *The saddle-point value of the functional (3.4) is equal to F^0_{ce} Eq. (2.17).*

It is worth noting that whereas on the one hand the new functional does not require the preliminar solution of the elastic auxiliary problem or the evaluation of the stress Green function due to distorsions, on the other hand the new formulation is larger in terms of the number (double) of unknown fields required to solve the problem.

3.2 A Min-Max Extended Total Potential Energy Principle. In an analogous way it is possible to derive, from proposition 2, a new min-max principle through the determination of functional F^s_{tpe} to be maximized in order to obtain the last term of (2.18). This may be made simply by using the principle of virtual work as follows (at any instant t):

$$\frac{1}{2}\int_\Omega \epsilon^s_{ij}(\boldsymbol{\epsilon}^0)D_{ijhk}\epsilon^s_{hk}(\boldsymbol{\epsilon}^0)d\Omega = -\frac{1}{2}\int_\Omega \epsilon^s_{ij}(\boldsymbol{\epsilon}^0)D_{ijhk}\epsilon^s_{hk}(\boldsymbol{\epsilon}^0)d\Omega + \int_\Omega \Psi^n_{ij}(\boldsymbol{\epsilon}^0)\epsilon^s_{ij}d\Omega. \quad (3.5)$$

It is easy to recognize the right-end side of (3.5) as the (changed in sign) total potential energy value at the solution of the elastic problem (at instant t) with imposed stresses $s_{ij} = -\Psi^n_{ij}(\boldsymbol{\epsilon}^0)$. This means that, by virtue of the minimum principle of total potential energy, we can write

$$\frac{1}{2}\int_\Omega \epsilon^s_{ij}(\boldsymbol{\epsilon}^0)D_{ijhk}\epsilon^s_{hk}(\boldsymbol{\epsilon}^0)d\Omega = \max_{u^{s00}_i} \{F^s_{tpe}[u^{s00}_i, u^0_i]\} \quad (3.6)$$

where

$$F^s_{tpe}[u^{s00}_i, u^0_i] = \int_T \left\{ -\frac{1}{2}\int_\Omega \epsilon^{s00}_{ij}D_{ijhk}\epsilon^{s00}_{hk}d\Omega + \int_\Omega \Psi^n_{ij}(\boldsymbol{\epsilon}^0)\epsilon^{s00}_{ij}d\Omega \right\} dt, \quad (3.7)$$

ϵ^{s00}_{ij} being any *self-compatible* strain field (that is any strain field which can be derived from a displacement field u^{s00}_i satisfying the homogeneous boundary conditions $u^{s00}_i = 0$ on Γ_u). Then, by substitution of Eq. (3.6), the functional (2.18) can be transformed into the following new functional:

$$\mathcal{J}_{tpe}[u^0_i, u^{s00}_i] = \int_T \left\{ \frac{1}{2}\int_\Omega \epsilon^0_{ij}D_{ijhk}\epsilon^0_{hk}d\Omega - \int_\Omega F_i u^0_i d\Omega - \int_{\Gamma_p} p_i u^0_i d\Gamma + \int_\Omega \Psi^n_{ij}(\boldsymbol{\epsilon}^0)(\epsilon^0_{ij} - \epsilon^{ef}_{ij})d\Omega - \frac{1}{2}\int_\Omega \epsilon^{s00}_{ij}D_{ijhk}\epsilon^{s00}_{hk}d\Omega + \int_\Omega \Psi^n_{ij}(\boldsymbol{\epsilon}^0)\epsilon^{s00}_{ij}d\Omega \right\} dt \quad (3.8)$$

and the following statement can be asserted:

Proposition 4: *A kinematically admissible displacement field u^0_i and a displacement field u^{s00}_i vanishing on Γ_u are a (or the) solution of problem P and problem P^s, respectively, if and only if both the following conditions are satisfied:*

(i) *they make stationary (minimum respect to u^0_i and maximum respect to u^{s00}_i) the functional (3.8);*
(ii) *The saddle-point value of the functional (3.8) is equal to F^0_{tpe} Eq. (2.19).*

It is worth noting that, in the functional (3.8), $\epsilon^0_{ij} = \epsilon^0_{ij}(\mathbf{u}^0) = \frac{1}{2}(u^0_{i,j} + u^0_{j,i})$ and that $\epsilon^{s00}_{ij} = \epsilon^{s00}_{ij}(\mathbf{u}^{s00}) = \frac{1}{2}(u^{s00}_{i,j} + u^{s00}_{j,i})$.

In this case too, the same remark pointed out at the end of proposition 3 applies with reference to the fact that whereas, on the one hand, the new functional does not require the preliminar solution of the elastic auxiliary problem or the evaluation of the strain Green function due to imposed stresses, on the other hand, the new formulation is larger in terms of the number (double) of unknown fields required to solve the problem.

Remarks. In order to make a comparison with existing variational principles for the nonlinear continuum problem, let's summarize the main properties of the above two min-max principles:

(a) Each functional has a physical meaning amenable to an energy (which is useful for its construction).
(b) All the variables involved have a physical meaning (stress, strain, etc.).
(c) The specialization of the constitutive law (2.5) or (2.6) to the elastic case ($\Psi^n_{ij} = \Phi^n_{ij} = 0$) leads the functionals to the classical ones of the theory of elasticity.

When a comparison of the above properties is made with those of other existing variational principles for the nonlinear continuum problem, it so happens that some or all of the above-mentioned properties (a) to (c) do not apply or, rather, some drawbacks arise. In particular the following can be said.

Downloaded 04 May 2010 to 171.66.16.34. Redistribution subject to ASME license or copyright; see http://www.asme.org/terms/Terms_Use.cfm

1 With reference to the variational formulations derived using the linear or nonlinear method of adding the adjoint operator (see Morse and Feshbach, 1953), the following drawbacks occur: (a) the additional variables required by the method usually have no physical meaning; (b) in the case of the linear constitutive law the nonlinear (quadratic) part of the functional is not defined in sign, which means that the solution corresponds to a *non-oriented* saddle-point of the functional, that is, the solution does not correspond to the minimum of the functional with respect to a subset of the variables nor does it correspond to the maximum with respect to the remaining variables.

2 With reference to the variational formulations derived using the least square method, the following drawbacks occur: (a) the functionals lack physical meaning, (b) the functionals lead (when a discretized solution procedure is adopted) to equation systems with worse (i.e., larger) values of the conditioning index than those of the corresponding discretized equation systems derived from the above saddle-point principles (proposition 3 and 4) (see Carini et al., 1995); in fact, the present formulation (propositions 3 and 4) could be regarded as a *preconditioned* least-square formulation, interpreting the inverse of the elastic operator as a *preconditioning* operator (see Carini et al., 1995).

3 When using Tonti's general method for the variational formulation of any nonlinear problem (see Tonti, 1984) the above properties (a), (b), (c) cannot in general be guaranteed while, on the contrary, they are satisfied by the functionals of propositions 3 and 4. This derived by the use (see Carini and De Donato, 1997), as integrating operator, of the inverse of the linear elastic operator in deriving propositions 1 and 2 (from which proposition 3 and 4 are obtained). This emphasizes the peculiar role of the choice of a particular integrating operator in deriving, from Tonti's general method, variational formulations satisfying properties (a), (b), and (c).

4 For time-dependent problems and with reference to variational formulations which use convolutive bilinear forms (see, for instance, Gurtin, 1964; Tonti, 1973; Rafalski, 1969a, 1969b; Reiss and Haug, 1978), the following can be pointed out: (a) these variational formulations are valid only for linear problems with constant physical properties; (b) in contrast to these formulations, the present one applies to generally nonlinear time dependent problems; (c) the original formulation by Gurtin and Tonti is not an extremal formulation. In fact the solution corresponds to a *non-oriented* saddle-point of the functional. The subsequent formulation by Rafalski (1969a, b) and Reiss and Haug (1978), need integrations over unbounded intervals.

5 Finally, it is worth noting that, for the elastic-plastic problem formulated in terms of variational formulations based on nonlinear programming techniques (see, for instance, Comi et al., 1991; Romano et al., 1993), the existence of a potential (generally nonsmooth) is always required. In the author's opinion it is possible to overcome this drawback using the present formulation, as partially showed in Carini (1996) and in the following Section 4.

4 An Application to Incremental Elastoplasticity

As an application of the total potential energy principle (proposition 4) to elastoplasticity, in the following we consider the elastoplastic continuum problem in the presence of an incremental constitutive law with hardening and/or softening and non associated flow rule. The set of relations describing the above behavior is the following:

$$\dot{\sigma}_{ij} = D_{ijhk}\dot{\epsilon}^e_{hk} \tag{4.1}$$

$$\dot{\epsilon}_{ij} = \dot{\epsilon}^e_{ij} + \dot{\epsilon}^p_{ij} \tag{4.2}$$

$$\dot{\epsilon}^p_{ij} = \frac{\partial \psi(\sigma_{ij}, \alpha_\rho)}{\partial \sigma_{ij}}\dot{\lambda} \tag{4.3}$$

$$\dot{\alpha}_\rho = l_\rho(\sigma_{ij}, \alpha_\rho)\dot{\lambda} \tag{4.4}$$

$$\phi = \phi(\sigma_{ij}, \alpha_\rho) \le 0 \tag{4.5}$$

$$\dot{\lambda} = 0 \quad \text{in} \quad \Omega_e (\text{i.e., if } \phi < 0) \tag{4.6}$$

$$\dot{\phi} \le 0, \quad \dot{\lambda} \ge 0, \quad \dot{\phi}\dot{\lambda} = 0 \quad \text{in} \quad \Omega_p (\text{i.e., if } \phi = 0) \tag{4.7}$$

where Eq. (4.1) establishes the relation between the incremental stress $\dot{\sigma}_{ij}$ and the elastic incremental strains $\dot{\epsilon}^e_{ij}$; Eq. (4.2) states the additivity of the elastic and plastic strains; Eqs. (4.3) and (4.4) state the evolution of the inelastic kinematic variables $\dot{\epsilon}^p_{ij}$ and $\dot{\alpha}_\rho$ as a function of the plastic multipliers $\dot{\lambda}$ and of the plastic potential ψ being l_ρ a given nonlinear function of σ_{ij} and α_ρ. Equation (4.5) defines the elastic domain while the set of Eqs. (4.6)–(4.7) expresses the loading-unloading criterion. In a more compact form, all the Eqs. (4.1)–(4.7) may be written as follows:

$$\dot{\sigma}_{ij} = \bar{D}_{ijhk}\dot{\epsilon}_{hk} \tag{4.8}$$

where

$$\bar{D}_{ijhk} = D_{ijhk} - \frac{D_{ijmn}\dfrac{\partial \psi}{\partial \sigma_{mn}}\dfrac{\partial \phi}{\partial \sigma_{pq}}D_{pqhk}}{\dfrac{\partial \phi}{\partial \sigma_{mn}}D_{mnrs}\dfrac{\partial \psi}{\partial \sigma_{rs}} - \dfrac{\partial \phi}{\partial \alpha_\rho}l_\rho} \quad \text{if} \quad \phi = 0 \quad \text{and} \quad \dot{\phi} = 0 \tag{4.9}$$

while $\bar{D}_{ijhk} = D_{ijhk}$,

$$\text{if} \quad \phi < 0 \quad \text{or} \quad \phi = 0 \quad \text{and} \quad \dot{\phi} < 0 \tag{4.10}$$

being $\bar{D}_{ijhk} \neq \bar{D}_{hkij}$ as a consequence of the non-associated character of the constitutive law.

In order to write Eq. (4.8) in the split form (2.5), the following position can be adopted:

$$\bar{D}_{ijhk} = D_{ijhk} - cD^n_{ijhk} \tag{4.11}$$

with

$$D^n_{ijhk} \neq D^n_{hkij} \tag{4.12}$$

$$\begin{cases} c = 1 & \text{if} \quad \phi = 0 \quad \text{and} \quad \dot{\phi} = 0 \\ c = 0 & \text{if} \quad \phi < 0 \quad \text{or} \quad \phi = 0 \quad \text{and} \quad \dot{\phi} < 0 \end{cases} \tag{4.13}$$

leading finally to the following expression of the inelastic part of the constitutive law:

$$\Psi^n_{ij}(\dot{\epsilon}_{hk}) = -cD^n_{ijhk}\dot{\epsilon}_{hk}. \tag{4.14}$$

The application of the extended total potential energy principle (proposition 4) to the above elastic-plastic behavior finally leads to the following extended functional:

$$\begin{aligned} \mathcal{J}_{tpe}[\dot{u}^0_i, \dot{u}^{s00}_i] = {} & \tfrac{1}{2}\int_\Omega \dot{\epsilon}^0_{ij}D_{ijhk}\dot{\epsilon}^0_{hk}d\Omega - \int_\Omega \dot{F}_i\dot{u}^0_i d\Omega \\ & - \int_{\Gamma_p} \dot{p}_i\dot{u}^0_i d\Gamma - \int_{\Omega_p} c\dot{\epsilon}^0_{ij}D^n_{ijhk}(\dot{\epsilon}^0_{hk} - \dot{\epsilon}^{ef}_{hk})d\Omega \\ & - \tfrac{1}{2}\int_\Omega \dot{\epsilon}^{s00}_{ij}D_{ijhk}\dot{\epsilon}^{s00}_{hk}d\Omega - \int_{\Omega_p} c\dot{\epsilon}^0_{ij}D^n_{ijhk}\dot{\epsilon}^{s00}_{hk}d\Omega. \end{aligned} \tag{4.15}$$

An analogous functional was stated by Telega (1980), using the *nonlinear method of adding the adjoint operator*. However, it is worth noting that while both the present and Telega's approaches have the doubling of the unknown variables in common, the main differences between the two approaches may be summarized in the following two points:

(a) In the present approach the solution corresponds to the min-max of the functional (4.15) while with Telega's approach, the solution corresponds only to the stationarity of its analogous functional.

Downloaded 04 May 2010 to 171.66.16.34. Redistribution subject to ASME license or copyright; see http://www.asme.org/terms/Terms_Use.cfm

(b) As already said, in the present approach all variables of the functional (4.15) have a physical meaning; this is not true for all the variables of Telega's functional (in particular for the variables of the adjoint operator).

References

Carini, A., 1996, "Colonnetti's minimum principle extension to generally nonlinear materials," *Int. J. Solids Structures,* Vol. 33, pp. 121–144.

Carini, A., and De Donato, O., 1997, "A Comprehensive Energy Formulation for General Nonlinear Material Continua," ASME JOURNAL OF APPLIED MECHANICS, Vol. 64, pp. 353–360.

Carini, A., Gelfi, P., and Marchina, E., 1995, "An energetic formulation for the linear viscoelastic problem. Part I: Theoretical results and first calculations," *Int. J. Numer. Methods Eng.,* Vol. 38, pp. 37–62.

Carter, P., and Martin, J. B., 1977, "A note on the derivation of the kinematic rate theorem of plasticity from the free energy minimum principle," *Journal de Mécanique,* Vol. 16, pp. 791–802.

Ceradini, G., 1966, "A maximum principle for the analysis of elastic-plastic systems," *Meccanica,* Vol. 1, pp. 77–82.

Colonnetti, G., 1918, "Sul problema delle coazioni elastiche," *Rend. Accad. Lincei,* Vol. 27, Serie 5a, 2. sem.

Colonnetti, G., 1950, "Elastic equilibrium in the presence of permanent set," *Quart. Appl. Math.,* Vol. 7, pp. 353–362.

Colonnetti, G., 1955, *L'equilibre des corps déformables,* Dunod, Paris.

Comi, C., Corigliano, A., and Maier, G., 1991, "Extremum properties of finite-step solutions in elastoplasticity with non-linear mixed hardening," *Int. J. Solids Structures,* Vol. 27, pp. 965–981.

De Donato, O., and Maier, G., 1972, "Mathematical programming method for the inelastic analysis of reinforced concrete frames allowing for limited rotation capacity," *Int. J. Numer. Methods Eng.,* Vol. 4, pp. 307–329.

Gurtin, M. E., 1964, "Variational principles for linear initial-value problems," *Quart. Appl. Math.,* Vol. 22, pp. 252–256.

Koiter, W. T., 1964, "General theorems for elastic-plastic solids," *Progress in Solid Mechanics,* I. N. Sneddon and R. Hill, eds., Vol. 1, Chapter IV, pp. 167–221.

Maier, G., 1969, "Some theorems for plastic strain rates and plastic strains," *Journal de Mécanique,* Vol. 8, pp. 5–19.

Morse, P. M., and Feshbach, H., 1953, *Methods of theoretical physics,* Vol. I, McGraw-Hill, New York.

Mura, T., 1987, *Micromechanics of defects in solids,* Martinus Nijhoff, Dordrecht, The Netherlands.

Ortiz, M., Pinsky, P. M. and Taylor, L., 1983, "Operator split methods for the numerical solution of the elastoplastic dynamic problem," *Comput. Meths. Appl. Mech. Engrg.,* Vol. 39, pp. 137–157.

Rafalski, P., 1969, "Orthogonal projection method. I. Heat conduction boundary problem," *Bull. Acad. Polon. Sci., Sér. Sci. Techn.,* Vol. 17, pp. 63–67.

Rafalski, P., 1969, "Orthogonal projection method. II. Thermoelastic problem," *Bull. Acad. Polon. Sci., Sér. Sci. Techn.,* Vol. 17, pp. 69–74.

Reiss, R., and Haug, E. J., 1978, "Extremum principles for linear initial-value problems of mathematical physics," *Int. J. Engng. Sci.,* Vol. 16, pp. 231–251.

Romano, G., Rosati, L., and Marotti de Sciarra, F., 1993, "A variational theory for finite-step elastoplastic problems," *Int. J. Solids Structures,* Vol. 30, pp. 2317–2334.

Telega, J. J., 1980, "Variational principles for rate boundary-value problems in nonassociated plasticity," *ZAMM,* Vol. 60, pp. 71–82.

Tonti, E., 1973, "On the variational formulation for linear initial value problems," *Annali di Matematica Pura ed Applicata,* Vol. 45, pp. 331–359.

Tonti, E., 1984, "Variational formulation for every nonlinear problem," *Int. J. Engng. Sci.,* Vol. 22, pp. 1343–1371.

Zarka, J., and Casier, J., 1979, "Elastic-plastic response of a structure to cyclic loading: practical rules," *Mechanics Today,* Vol. 6, Nemat-Nasser, ed., Pergamon Press, New York, pp. 93–198.

Impact Coefficients and Tangential Impacts

R. M. Brach[12]

Introduction

The last decade has seen a flurry of papers on the topic of rigid-body impact theory. Despite the apparent simplicity of the topic, some challenging problems exist and there have been some interesting and, at times, controversial developments. For example, some dispute has arisen on how best to define and use coefficients, particularly coefficients associated with the process of restitution normal to the contact surface in the presence of Coulomb friction. At least five coefficients, e, have been proposed and discussed, one is a kinematic coefficient (defined as the ratio of normal velocity components) attributed to Newton. Another is a kinetic coefficient (ratio of normal contact impulses) attributed to Poisson. A third is an energetic coefficient (ratio of work done by normal contact impulses) defined by Stronge (1990). A fourth coefficient is by Ivanov (1992), (defined as a ratio of kinetic energy losses). Batlle and Cordona (1997) analyze three-dimensional tangential impacts and define another suitable for that problem. Coefficients associated with directions other than normal and processes other than compression have been defined and used (see Brach, 1991), but most of the controversy, so far, is with the normal coefficients.

Newton's coefficient has been used for collinear impacts and frictionless oblique impacts for nearly 300 years. Its use has been generalized and extended to three-dimensional collisions by Brach (1991, 1997). This approach has been extended to pseudo-rigid bodies by Cohen and Mac Sithigh (1996). Whereas the coefficient has an upper bound of unity for certain special conditions, it is now recognized that this is not true in general since a value of 1 sometimes can lead to a solution that violates energy conservation. Poisson's coefficient has likewise been known for many years; some, such as Wang and Mason (1992), claim that its use guarantees energy conservation but Newton's law does not. Poisson's coefficient also is bounded by 0 and 1 only for certain types of collisions and body orientations. The lack of unit bounds has prompted questions of "energetic consistency." In discussing the process of normal deformation, Stronge says that in a consistent theory the part of the energy dissipation during restitution cannot be larger than the corresponding part during compression. He then defines a coefficient using a work constraint such that $W_n^R \leq e^2 W_n^A$, where each W_n is the work done by the normal impulse during rebound and approach, respectively. Stronge also demands an energetically consistent (normal) coefficient of restitution to be one that is independent of the tangential contact process (friction). It remains to be determined under what conditions Stronge's coefficient has a unit upper bound.

Another question is sometimes raised concerning a dependence of coefficients on initial conditions. Some hold the notion that "impact coefficients" should be similar to material constants and should not depend on initial conditions. In the case of impact coefficients, dependence on initial conditions is not a drawback but a necessity. Newton's and other coefficients are quantities that represent nonlinear dynamic material behavior. If impact coefficients did *not* depend on initial conditions, they would have no utility. A requirement that impact coefficients be independent of each other is a lofty but impractical goal. When complicated, nonlinear three-dimensional contact processes are considered in the presence of inertial coupling, arbitrary initial conditions and perhaps nonpoint contact, the expectation of coefficient independence is unrealistic.

Newton's coefficient is said to lack energetical consistency; but other deficiencies are also claimed. The existence of a tangential impact, or Impact Without Collision (IW/OC), associated with Painlevé's Paradox (see Brogliato, 1996) has been given attention recently. Wang and Mason (1992) and Batlle (1993) use a tangential impact as an example of where the use of Newton's coefficient not only is said to be energetically inconsistent but is impossible to apply. The basis of this claim appears not to be that tangential impacts do not require normal deformation but rather that the definition of $e = -V_{cn}/v_{cn}$ is undefined for $v_{cn} = 0$. It is the purpose of this paper to address these issues and to determine whether or not the use of Newton's

[12] Department of Aerospace and Mechanical Engineering, University of Notre Dame, Notre Dame, IN 46556.

Contributed by the Applied Mechanics Division of THE AMERICAN SOCIETY OF MECHANICAL ENGINEERS for publication in the ASME JOURNAL OF APPLIED MECHANICS. Manuscript received by the ASME Applied Mechanics Division, Aug. 30, 1996; final revision, May 30, 1997. Associate Technical Editor: S. W. Shaw.

Downloaded 04 May 2010 to 171.66.16.34. Redistribution subject to ASME license or copyright; see http://www.asme.org/terms/Terms_Use.cfm

(b) As already said, in the present approach all variables of the functional (4.15) have a physical meaning; this is not true for all the variables of Telega's functional (in particular for the variables of the adjoint operator).

References

Carini, A., 1996, "Colonnetti's minimum principle extension to generally nonlinear materials," *Int. J. Solids Structures,* Vol. 33, pp. 121–144.

Carini, A., and De Donato, O., 1997, "A Comprehensive Energy Formulation for General Nonlinear Material Continua," ASME JOURNAL OF APPLIED MECHANICS, Vol. 64, pp. 353–360.

Carini, A., Gelfi, P., and Marchina, E., 1995, "An energetic formulation for the linear viscoelastic problem. Part I: Theoretical results and first calculations," *Int. J. Numer. Methods Eng.,* Vol. 38, pp. 37–62.

Carter, P., and Martin, J. B., 1977, "A note on the derivation of the kinematic rate theorem of plasticity from the free energy minimum principle," *Journal de Mécanique,* Vol. 16, pp. 791–802.

Ceradini, G., 1966, "A maximum principle for the analysis of elastic-plastic systems," *Meccanica,* Vol. 1, pp. 77–82.

Colonnetti, G., 1918, "Sul problema delle coazioni elastiche," *Rend. Accad. Lincei,* Vol. 27, Serie 5a, 2. sem.

Colonnetti, G., 1950, "Elastic equilibrium in the presence of permanent set," *Quart. Appl. Math.,* Vol. 7, pp. 353–362.

Colonnetti, G., 1955, *L'equilibre des corps déformables,* Dunod, Paris.

Comi, C., Corigliano, A., and Maier, G., 1991, "Extremum properties of finite-step solutions in elastoplasticity with non-linear mixed hardening," *Int. J. Solids Structures,* Vol. 27, pp. 965–981.

De Donato, O., and Maier, G., 1972, "Mathematical programming method for the inelastic analysis of reinforced concrete frames allowing for limited rotation capacity," *Int. J. Numer. Methods Eng.,* Vol. 4, pp. 307–329.

Gurtin, M. E., 1964, "Variational principles for linear initial-value problems," *Quart. Appl. Math.,* Vol. 22, pp. 252–256.

Koiter, W. T., 1964, "General theorems for elastic-plastic solids," *Progress in Solid Mechanics,* I. N. Sneddon and R. Hill, eds., Vol. 1, Chapter IV, pp. 167–221.

Maier, G., 1969, "Some theorems for plastic strain rates and plastic strains," *Journal de Mécanique,* Vol. 8, pp. 5–19.

Morse, P. M., and Feshbach, H., 1953, *Methods of theoretical physics,* Vol. I, McGraw-Hill, New York.

Mura, T., 1987, *Micromechanics of defects in solids,* Martinus Nijhoff, Dordrecht, The Netherlands.

Ortiz, M., Pinsky, P. M. and Taylor, L., 1983, "Operator split methods for the numerical solution of the elastoplastic dynamic problem," *Comput. Meths. Appl. Mech. Engrg.,* Vol. 39, pp. 137–157.

Rafalski, P., 1969, "Orthogonal projection method. I. Heat conduction boundary problem," *Bull. Acad. Polon. Sci., Sér. Sci. Techn.,* Vol. 17, pp. 63–67.

Rafalski, P., 1969, "Orthogonal projection method. II. Thermoelastic problem," *Bull. Acad. Polon. Sci., Sér. Sci. Techn.,* Vol. 17, pp. 69–74.

Reiss, R., and Haug, E. J., 1978, "Extremum principles for linear initial-value problems of mathematical physics," *Int. J. Engng. Sci.,* Vol. 16, pp. 231–251.

Romano, G., Rosati, L., and Marotti de Sciarra, F., 1993, "A variational theory for finite-step elastoplastic problems," *Int. J. Solids Structures,* Vol. 30, pp. 2317–2334.

Telega, J. J., 1980, "Variational principles for rate boundary-value problems in nonassociated plasticity," *ZAMM,* Vol. 60, pp. 71–82.

Tonti, E., 1973, "On the variational formulation for linear initial value problems," *Annali di Matematica Pura ed Applicata,* Vol. 45, pp. 331–359.

Tonti, E., 1984, "Variational formulation for every nonlinear problem," *Int. J. Engng. Sci.,* Vol. 22, pp. 1343–1371.

Zarka, J., and Casier, J., 1979, "Elastic-plastic response of a structure to cyclic loading: practical rules," *Mechanics Today,* Vol. 6, Nemat-Nasser, ed., Pergamon Press, New York, pp. 93–198.

Impact Coefficients and Tangential Impacts

R. M. Brach[12]

Introduction

The last decade has seen a flurry of papers on the topic of rigid-body impact theory. Despite the apparent simplicity of the topic, some challenging problems exist and there have been some interesting and, at times, controversial developments. For example, some dispute has arisen on how best to define and use coefficients, particularly coefficients associated with the process of restitution normal to the contact surface in the presence of Coulomb friction. At least five coefficients, e, have been proposed and discussed, one is a kinematic coefficient (defined as the ratio of normal velocity components) attributed to Newton. Another is a kinetic coefficient (ratio of normal contact impulses) attributed to Poisson. A third is an energetic coefficient (ratio of work done by normal contact impulses) defined by Stronge (1990). A fourth coefficient is by Ivanov (1992), (defined as a ratio of kinetic energy losses). Batlle and Cordona (1997) analyze three-dimensional tangential impacts and define another suitable for that problem. Coefficients associated with directions other than normal and processes other than compression have been defined and used (see Brach, 1991), but most of the controversy, so far, is with the normal coefficients.

Newton's coefficient has been used for collinear impacts and frictionless oblique impacts for nearly 300 years. Its use has been generalized and extended to three-dimensional collisions by Brach (1991, 1997). This approach has been extended to pseudo-rigid bodies by Cohen and Mac Sithigh (1996). Whereas the coefficient has an upper bound of unity for certain special conditions, it is now recognized that this is not true in general since a value of 1 sometimes can lead to a solution that violates energy conservation. Poisson's coefficient has likewise been known for many years; some, such as Wang and Mason (1992), claim that its use guarantees energy conservation but Newton's law does not. Poisson's coefficient also is bounded by 0 and 1 only for certain types of collisions and body orientations. The lack of unit bounds has prompted questions of "energetic consistency." In discussing the process of normal deformation, Stronge says that in a consistent theory the part of the energy dissipation during restitution cannot be larger than the corresponding part during compression. He then defines a coefficient using a work constraint such that $W_n^R \leq e^2 W_n^A$, where each W_n is the work done by the normal impulse during rebound and approach, respectively. Stronge also demands an energetically consistent (normal) coefficient of restitution to be one that is independent of the tangential contact process (friction). It remains to be determined under what conditions Stronge's coefficient has a unit upper bound.

Another question is sometimes raised concerning a dependence of coefficients on initial conditions. Some hold the notion that "impact coefficients" should be similar to material constants and should not depend on initial conditions. In the case of impact coefficients, dependence on initial conditions is not a drawback but a necessity. Newton's and other coefficients are quantities that represent nonlinear dynamic material behavior. If impact coefficients did *not* depend on initial conditions, they would have no utility. A requirement that impact coefficients be independent of each other is a lofty but impractical goal. When complicated, nonlinear three-dimensional contact processes are considered in the presence of inertial coupling, arbitrary initial conditions and perhaps nonpoint contact, the expectation of coefficient independence is unrealistic.

Newton's coefficient is said to lack energetical consistency; but other deficiencies are also claimed. The existence of a tangential impact, or Impact Without Collision (IW/OC), associated with Painlevé's Paradox (see Brogliato, 1996) has been given attention recently. Wang and Mason (1992) and Batlle (1993) use a tangential impact as an example of where the use of Newton's coefficient not only is said to be energetically inconsistent but is impossible to apply. The basis of this claim appears not to be that tangential impacts do not require normal deformation but rather that the definition of $e = -V_{cn}/v_{cn}$ is undefined for $v_{cn} = 0$. It is the purpose of this paper to address these issues and to determine whether or not the use of Newton's

[12] Department of Aerospace and Mechanical Engineering, University of Notre Dame, Notre Dame, IN 46556.

Contributed by the Applied Mechanics Division of THE AMERICAN SOCIETY OF MECHANICAL ENGINEERS for publication in the ASME JOURNAL OF APPLIED MECHANICS. Manuscript received by the ASME Applied Mechanics Division, Aug. 30, 1996; final revision, May 30, 1997. Associate Technical Editor: S. W. Shaw.

Copyright © 1997 by ASME

Downloaded 04 May 2010 to 171.66.16.34. Redistribution subject to ASME license or copyright; see http://www.asme.org/terms/Terms_Use.cfm

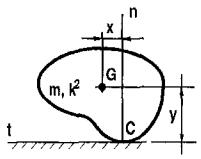


Fig. 1 Coordinates and dimensions

coefficient precludes analysis of tangential impacts. It will be seen that not only can tangential impacts be analyzed with this approach but that it indicates interesting system dynamics. For certain initial conditions, as a frictional parameter (the impulse ratio) is continuously changed, the dynamical response of the body instantaneously changes from no impact to an impact.

In the following a tangential impact is when a lamina has a rapid change in velocities due to contact with a fixed massive object and where the contact occurs in the plane of the lamina with a negligibly small initial relative normal velocity. This can be described as an *impact* (large forces, short duration) *without a collision* (without rapid or severe normal initial contact). Such impacts are examined using Newton's coefficient.

Tangential Impact

In this section the problem of a tangential collision is analyzed by an approach using Newton's coefficient of restitution and shows that not only can it be used but that it provides useful information on the nature of this type of collision. Consider the rigid body lamina, shown in Fig. 1, with mass m and centroidal inertia $I_G = mk^2$ as it makes contact at point C with a flat massive surface. The body makes no contact with anything other than at C and no significant external forces act other than the contact forces. The normal and tangential components of the initial velocities of m at the contact point are $v_{cn} = v_n + x\omega$ and $v_{ct} = v_t - y\omega$ where v_n and v_t are initial mass center velocities and ω is the initial angular velocity[13]. It is assumed that any tangential force that exists during contact can only be developed in the presence of a normal force. It is further assumed that a nonzero initial normal component of velocity is necessary to develop a normal force.

Consequently a tangential impact as defined here is one such that $v_{cn} = -\epsilon$, where $\epsilon > 0$ and $\epsilon \approx 0$, and $v_{ct} \gg v_{cn}$. Newton's coefficient is defined as $e = -V_{cn}/v_{cn}$. Note that the assumption that $\epsilon > 0$ differs from others who define a tangential impact as one with $v_{cn} \equiv 0$. However, it will be seen later that in most important equations, the limit of $\epsilon \to 0$ can be taken with no difficulty. It could be claimed that since the impact is a frictional one, then tangential restitution should be considered. It can be (see Brach, 1991) and in some applications likely should be. This is a separate problem and is not pursued here.

When using Newton's coefficient only two times are considered explicitly, the time contact is initiated and the time contact is lost. Other than it being compressive no restrictions are placed on the normal force, its net work or its impulse within this time period. Derivation of the system equations, definition of coefficients, and the method of obtaining solution equations is well covered elsewhere (see Brach, 1991). In this paper when considering Coulomb friction, f is the symbol used for the coefficient of friction; $\mu = P_t/P_n$ is the ratio of the tangential to normal *impulses* generated at the contact point. Certain intermediate variables appear in the expressions and are defined here. The tangent of the angle of approach, α, of the contact point relative to the n-axis is given by $r = \tan\alpha = v_{ct}/v_{cn}$. A function that appears in several solution equations is

$$M = [\mu(k^2 + y^2) - xy]/k_C^2 \tag{1}$$

where $k_C^2 = k^2 + x^2 + y^2$ is the radius of gyration of the mass m about the contact point. The value of the tangential impulse ratio that causes the relative tangential contact velocity to end at or before separation is designated by μ_0, where

$$\mu_0 = \frac{(k^2 + x^2) - (1 + e)xy/r}{(1 + e)(k^2 + y^2)/r + xy}. \tag{2}$$

A like value of limiting friction (for tangential collisions, $1/r = 0$) has been found by Stronge (1990) and Batlle (1993). The value of M for $\mu = \mu_0$ is designated as M_0. The expressions for the final contact velocities are

$$V_{cn} = -ev_{cn} \tag{3}$$

and

$$V_{ct} = v_{ct}(1 - M/M_0). \tag{4}$$

Note that for $x = 0$, $y = 0$, or both, $M/M_0 = \mu/\mu_0$ and for these values of x and y, $V_{ct} = v_{ct}(1 - \mu/\mu_0)$. The tangential impulse can never exceed the value needed to end sliding, so $|\mu| \leq |\mu_0|$. For Coulomb friction the value of μ depends on the friction coefficient and the sign of μ takes on the sign of μ_0.

Based on what appears in the literature, tangential impacts can occur when the mass center trails the contact point in the initial tangential motion (the moment of the frictional impulse tends to push the contact point toward the surface). On the other hand, contact point tangential velocity reversals occur when the mass center leads the contact point. So although reversal of the sliding direction is possible for planar collisions, this topic is not discussed here. In general, the kinetic energy loss, T_L, during the collision is given by:

$$2T_L/m = (1 + e)v_{cn}^2 \frac{k^2}{k^2 + x^2 - \mu xy}[(1 - e) + \mu r(2 - M/M_0)]. \tag{5}$$

Several important values of $T_L(e, \mu)$ are noted. If the tangential process is smooth or frictionless then $\mu = 0$ and $2T_{Lm}/m = (1 - e^2)v_{cn}^2[k^2/(k^2 + x^2)]$ where $e = 1$ corresponds to a perfectly elastic collision. For any impact there is a maximum energy loss, say T_{Lm}, which always is less than or equal to the initial energy. For central impacts, $T_L = T_{Lm}$ for $e = 0$ and $\mu = \mu_0$.

Example

The example of a long slender rod with tip contact is commonly used to illustrate collisions, including tangential ones[14] and is used here as well. All information for the following example is given in Table 1.

Case 1, Sliding Ends: Batlle (1993) states that for a tangential collision (which he also calls "dynamic wedging" and others call "jamb"), sliding stops before the normal contact velocity reaches its final value, V_{cn}. This condition is used here but relaxed for Case 2. When no sliding exists at separation, $\mu = \mu_0$, which for this example is $\mu_0 = -\frac{5}{3} = -1.667$. The final velocities for $e = 1$ are given in Table 1. The energy loss for $\mu = \mu_0$ comes from Eq. (5):

$$2T_L/m = (1 - e^2)v_{cn}^2 \frac{k^2 + y^2}{k_C^2} + 2(1 + e)v_{cn}v_{ct}\frac{xy}{k_C^2} + v_{ct}^2 \frac{k^2 + x^2}{k_C^2}. \tag{6}$$

[13] All time-dependent variables such as velocities and impulses with small or lower case symbols indicate initial values and capital or upper case ones are final values.

[14] Mason and Wang (1988), for example, use it to argue that such a rod in established sliding along a flat level rigid surface under the action of gravity undergoes a tangential impact and bounces away from the surface with varying amounts of energy. They do not determine the initial conditions that are necessary for such an event to occur or the time and position at which such an event will occur.

Downloaded 04 May 2010 to 171.66.16.34. Redistribution subject to ASME license or copyright; see http://www.asme.org/terms/Terms_Use.cfm

Table 1 Tangential impact example

(all units are S.I.)
$m = 1,\ x^2 + y^2 = 1,\ k^2 = 1/3,\ x = -1/\sqrt{2}$
$\mu = \mu_0 = -5/3,\ e = 1,\ r = -1 \times 10^5$
$v_{ct} = 10,\ v_{cn} = -1 \times 10^{-4},\ \omega = 0$
$V_n = 3.750,\ V_t = 3.750,\ \Omega = 5.303$
$V_{ct}/v_{ct} = 0,\ V_{cn}/v_{cn} = -1,\ 2T_L/m = 62.5$

Because $0 \leq T_L(e, \mu) \leq T_{Lm}$, V_{cn} and all final velocities are bounded. The products $e^2 v_{cn}^2$ and ev_{cn} are bounded because they must remain of the order of magnitude of $V_{cn} = -\epsilon e$.

Consequently, for $\epsilon \approx 0$, the first two terms of Eq. (6) are negligible, resulting in an expression for T_L that is independent of e. The independence of e indicates that if the tangential impulse necessary to stop sliding, $P_t = \mu_0 P_n$, can be developed by the contact process, it makes no difference if the normal impulse is perfectly elastic, inelastic, or perfectly plastic.

Case 2, Sliding Continues: Consider an impact under conditions identical to above except where the tangential resistance (such as Coulomb friction) can be varied from zero to produce any degree of roughness. For a smooth (frictionless) contact surface a tangential impulse cannot develop, $\mu = 0$. In this case conservation of energy shows that $0 \leq e \leq 1$, so that $|V_{cn}| \leq |v_{cn}|$. When the roughness is increased to produce retardation less than that necessary to end sliding ($|\mu| < |\mu_0|$), the final tangential contact velocity is given by Eq. (4). The quantity M/M_0 determines V_{ct}/v_{ct} and possesses some interesting properties. Figure 2 shows that M/M_0 approaches 1 as the magnitude of μ increases and approaches μ_0, and $(1 - M/M_0)$ correspondingly decreases. As ϵ grows smaller and r becomes large in magnitude, growth of M/M_0 is sudden. So for $r = -1 \times 10^5$, the analysis indicates that if the tangential process does not have a great enough roughness to cause the rod tip to stop sliding ($\mu = \mu_0 = -\frac{5}{3}$), then V_{ct} does not measurably decrease at all. For Coulomb friction, this implies that if $f < |\mu_0| = \frac{5}{3}$, the rod will simply continue to slide with virtually no reduction in tangential velocity and there is no impact. If $f \geq \frac{5}{3}$, then sliding will stop suddenly but with almost no normal rebound, a tangential impact, and the final motion of the rod consists of rotation about the contact point. The above condition for a tangential impact at a critical friction value μ_0 is the same condition found for a rigid rod sliding over a rigid surface under Coulomb friction with $v_{ct} = 0$ that corresponds to a singularity of the differential equations of motion (Genot, et al., 1997).

Discussion

The above analysis speaks for itself in showing that Newton's coefficient of restitution can be useful in analyzing collisions, even tangential ones. It also confirms that additional coefficients such as the tangential impulse ratio, μ, and its kinematically defined critical value, μ_0, can also be quite useful. What is quite amazing is that the above results apply to *any* contact processes meeting the usual conditions of rigid-body impact theory. Once particular contact processes are chosen, such as Coulomb friction or viscous friction (such as when a stone skips over the surface of a pond) for the tangential force system, additional analyses, including integration, may be necessary to acquire additional information. By example it is seen that the use of energy bounds, such as T_{Lm}, and kinematic constraints (used to determine μ_0) to provide bounds on the coefficients shows them to have a unique utility.

Stronge's energetic coefficient has been found not always to be independent of the coefficient of friction (see Stronge, 1995). With suitable bounds, both Newton's and Poisson's coefficients can be made to satisfy conservation of energy (such as through Stronge's impulse-work inequality), qualifying them to be energetically consistent. Consequently, it appears that some of the controversy over the different types of coefficients is a result of individual approaches and preferences. It has prompted Brogliato (1996) to observe that "*A constant fact in the 'modern' literature on this topic is that almost every author claims he betters and corrects the preceding works.*" Perhaps it eventually will be recognized that each type of impact coefficient and corresponding approach to impact have their own set of advantages and disadvantages. A prudent analyst will use whichever and all that provide the needed information.

Finally, it should be noted that so far, the practicality of tangential impacts (dynamic wedging, jamb or IW/OC), particularly with $v_{cn} \equiv 0$, is unexplored. Even theoretical analyses show that they may not occur (see Genot et al., 1997). There seems to be no experimental evidence that the conditions can exist for one to occur. Not only are the initial conditions intricate but the frictional level must be higher than most usual materials and surfaces can develop. Thus verification provides an experimental challenge.

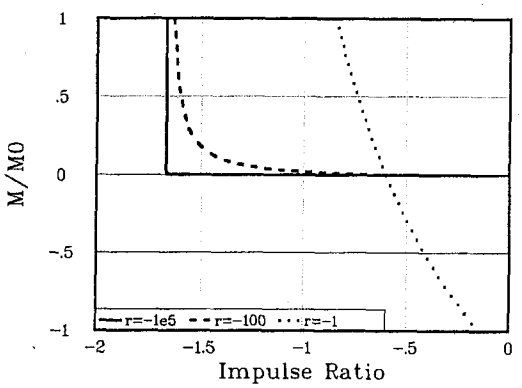


Fig. 2 Tangential control function, M/M_0, for the conditions in Table 1, $r = -1 \times 10^5$ ($\mu_0 = -5/3$), as well as for additional initial normal velocity values giving $r = -100$ ($\mu_0 = -1.632$) $r = -1$ ($\mu_0 = -0.846$)

Acknowledgment

The author would like to thank the reviewers for their helpful and valuable comments.

References

Batlle, J. A., 1993, "On Newton's and Poisson's Rules of Percussive Dynamics," ASME JOURNAL OF APPLIED MECHANICS, Vol. 60, pp. 376–381.

Batlle, J. A., and Cardona, S., 1997, "The Jamb Process in 3D Rough Collisions," submitted for publication.

Brach, R. M., 1991, *Mechanical Impact Dynamics,* John Wiley and Sons, New York.

Brach, R. M., 1997, "Formulation of Rigid Body Impact Problems using Generalized Coefficients," Int J Eng Sci., to appear.

Brogliato, B., 1996, *Nonsmooth Impact Mechanics, Models, Dynamics and Control,* Springer, London.

Cohen, H., and Mac Sithigh, G. P., 1996, "Collisions of pseudo-rigid bodies: A Brach-type treatment," *Int J Eng Sci,* Vol. 34, No. 3, pp. 249–256.

Genot, F., Brogliato, B., Brach, R., and Thuilot, B., 1997, "On LCP's and Tangential Impacts in Rigid Body Mechanics with Unilateral Constraints and Dry Friction," SYROCO '97, IFAC, Sept.

Ivanov, A. P., 1992, "Energetics of a Collision with Friction," *J Appl Math Mech,* Vol. 56, No. 4, pp. 527–534.

Mason, M. T., and Wang, Y., 1988, "On the inconsistency of rigid-body frictional planar mechanics," *IEEE International Conference on Robotics & Automation,* Philadelphia, PA, pp. 524–528.

Stronge, W. J., 1990, "Rigid Body Collisions with Friction," *Proc. Royal Soc., London,* Vol. A431, pp. 169–181.

Stronge, W. J., 1995, "Coupling of Friction and Internal Dissipation in Planar Collisions of Compliant Bodies," *Contact Mechanics,* M. Raous, M. Jean and J. J. Moreau, eds. Plenum, Press, New York.

Wang, Y., and Mason, M. T., 1992, "Two-Dimensional Rigid-Body Collisions With Friction," ASME JOURNAL OF APPLIED MECHANICS, Vol. 59, pp. 635–642.

Downloaded 04 May 2010 to 171.66.16.34. Redistribution subject to ASME license or copyright; see http://www.asme.org/terms/Terms_Use.cfm

On the Transient Response of a Spinning Disk Under a Space-Fixed Load

Jen-San Chen[15,17], **C.-M. Hsu**[16,17]

The titled problem is studied analytically by an eigenfunction expansion method. In the early stage following the excitation, symmetric deformation is observed when the rotation speed is around the first critical speed. At a rotation speed ten times higher than the first critical speed, at which the convective velocity of the media is comparable to the wave propagation speed, asymmetric deformation becomes apparent.

Introduction

The spinning disk is at the heart of hard disk, floppy disk, and optical recording devices. Excessive disk vibrations degrade the signal from the read/write head and may destroy the disk by a "head crash." The proper design of reliable disk drives requires a thorough understanding of the mechanical characteristics of the spinning disk. Among many other research topics, the response of a spinning disk under point loads is particularly of interest because it is a decisive factor in the performance of high-density disk drives. Mote (1970) investigated the stability of a stationary annular plates subjected to circumferentially moving loads with harmonically varying amplitude. Weisensel and Schlack (1993) extended Mote's work to include radially moving load. Benson and Bogy (1978) investigated the steady-state response of a spinning disk under a space-fixed point force. Cole and Benson (1988) later used an eigenfunction approach to extend the analysis to a spinning disk with mild bending rigidity. Ono and Maeno (1987) calculated the response of a spinning floppy disk under space-fixed harmonic excitation. While these extensive studies on the steady-state response and the response under harmonic excitation provide valuable physical insight into the behavior of disk deflection, very little information is obtained on the vibrant transient response immediately following the excitation. In view of the ever-increasing operating speed in the current disk drive industry, the transient response may be crucial to the performance of the disk drives. This note presents a closed-form solution to the transient response of a spinning disk under a space-fixed step load. Effects of rotation speed on the displacement history and the wave propagation phenomenon following the excitation are of special interest.

Equation of Motion

Consider an elastic circular disk clamped on the inner radius $r = a$ and free on the outer radius $r = b$. The disk is spinning with constant speed Ω. The spinning disk is initially undeformed laterally until the application of a space-fixed concentrated step force $FH(t)$ at position $r = \xi$, $\theta = 0$ at time $t = 0$. $H(t)$ represents the Heaviside step function. The equation of motion of the spinning disk, in terms of transverse displacement w, and with respect to the stationary coordinate system (r, θ), can be written as

$$w_{,tt} + 2\Omega w_{,\theta t} + \frac{D}{\rho h}\nabla^4 + \left(\Omega^2 - \frac{\sigma_\theta}{\rho r^2}\right)w_{,\theta\theta} - \frac{1}{\rho r}(\sigma_r r w_{,r})_{,r} = \frac{FH(t)}{r\rho h}\delta(r-\xi)\delta(\theta). \quad (1)$$

The parameters ρ, h, and D are the mass density, thickness, and flexural rigidity of the disk, respectively. $\delta(:)$ is the Dirac delta function. The axisymmetric in-plane stresses σ_r and σ_θ are due to the centrifugal effect.

Eigenfunction Expansion Method

The solution $w(r, \theta, t)$ of Eq. (1) can be expressed in terms of eigenfunctions $w_{mn} = R_{mn}(r)e^{in\theta}$ of the freely spinning disk as

$$w(r, \theta, t) = \sum_{m=0}^{\infty}\sum_{n=-\infty}^{\infty}[c_{mn}(t)w_{mn}(r, \theta)] \quad (2)$$

$c_{mn}(t)$ is a complex function of time. The radial function $R_{mn}(r)$ can be approximated by the nodal values obtained through a finite element procedure (Ono and Maeno, 1987). w_{mn} can be normalized such that $2\pi\int_a^b R_{mn}^2\, rdr = 1$. It is noted that the number of nodal diameters n is considered as negative for a forward mode. After substituting Eq. (2) into Eq. (1), multiplying both sides of Eq. (1) by $\bar{w}_{pq}$, integrating over the annular region, we can discretize Eq. (1) into a system of decoupled equations for $c_{mn}(t)$,

$$\ddot{c}_{mn} + 2in\Omega\dot{c}_{mn} + \omega_{mn}(\omega_{mn} + 2n\Omega)c_{mn} = F_{mn}H(t) \quad (3)$$

where $F_{mn} = (FR_{mn}(\xi))/\rho h$. The initial conditions for c_{mn} are $c_{mn}(0) = 0$ and $\dot{c}_{mn}(0) = 0$. The natural frequency ω_{mn} of a reflected wave in the super-critical speed range is considered as negative.

Equation (3) can be solved for c_{mn} as

$$\frac{c_{mn}(t)}{F_{mn}} = \frac{1}{\omega_{mn}(\omega_{mn} + 2n\Omega)} - \frac{1}{2(\omega_{mn} + n\Omega)}\left[\frac{e^{i\omega_{mn}t}}{\omega_{mn}} + \frac{e^{-i(\omega_{mn}+2n\Omega)t}}{\omega_{mn} + 2n\Omega}\right]. \quad (4)$$

After substituting Eq. (4) into Eq. (2) and rearranging the series we obtain the expression for the displacement of the spinning disk under a space-fixed concentrated step force as

$$w(r, \theta, t) = \sum_{m=0}^{\infty}\sum_{n=0}^{\infty}\alpha_{mn}R_{mn}(r)\left\{\frac{\cos n\theta}{\omega_{mn}(\omega_{mn} + 2n\Omega)} - \frac{1}{2(\omega_{mn} + n\Omega)}\left[\frac{\cos(n\theta + \omega_{mn}t)}{\omega_{mn}} + \frac{\cos(n\theta - \omega_{mn}t - 2n\Omega t)}{\omega_{mn} + 2n\Omega}\right]\right\} \quad (5)$$

where $\alpha_{m0} = F_{m0}$, and $\alpha_{mn} = 2F_{mn}$ when $n \neq 0$. The terms independent of time correspond to the steady-state deformation when appropriate damping mechanism is introduced. Furthermore, the signs of these terms depend on the product $\omega_{mn}(\omega_{mn} + 2n\Omega)$, which is positive in the subcritical speed range, and is negative in the super-critical speed range.

[15] Associate Professor.
[16] Graduate Student.
[17] Department of Mechanical Engineering, National Taiwan University, Taipei, Taiwan 107, Republic of China.

Contributed by the Applied Mechanics Division of THE AMERICAN SOCIETY OF MECHANICAL ENGINEERS for publication in the ASME JOURNAL OF APPLIED MECHANICS. Manuscript received by the ASME Applied Mechanics Division, Jan. 21, 1997; final revision, May 22, 1997. Associate Technical Editor: N. C. Perkins.

Copyright © 1997 by ASME

Downloaded 04 May 2010 to 171.66.16.34. Redistribution subject to ASME license or copyright; see http://www.asme.org/terms/Terms_Use.cfm

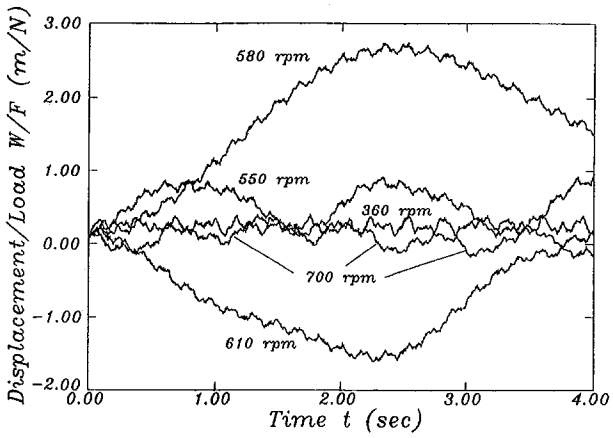


Fig. 1 Displacement-load ratio history at the load point under step force. The critical speed is 589 rpm

Examples and Discussions

Figure 1 shows the displacement-load ratio history at the load point as the flexible disk is under unit step load and rotates at several different speeds. The parameters used in the calculations are chosen to be representative of properties of a commercially available floppy disk; they are $\rho = 1.3 \times 10^3$ kg/m^3, $D = 2.1 \times 10^{-4}$ Nm, $h = 0.078$ mm, $a = 17.5$ mm, and $b = 65$ mm. The number of modes used in expansion (5) is restricted to $m < 5$ and $n < 30$. The loading position ξ/b is chosen to be 0.54. $\Omega = 360$ rpm is the operating speed of most floppy disk drives. It is observed that the mean displacement and the amplitude of the displacement variation increase as the rotation speed increases from 360 to 580 rpm. In particular, the response becomes unbounded as the rotation speed approaches the first critical speed, 589 rpm. It is also noted that the displacement at the load point is always in the same direction as the point force when the rotation speed is in the subcritical speed range. As the rotation speed continues to increase beyond the critical speed, say, 610 and 700 rpm, the displacement is primarily opposite to the direction of the point force, as expected in Eq. (5). The irregular zigzags in the load-point displacement curve

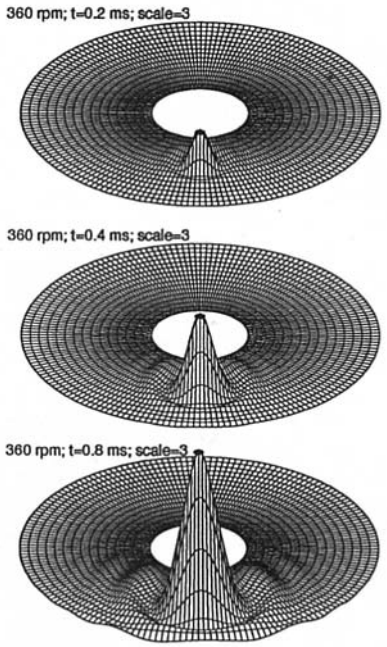


Fig. 2 The first 0.8 ms response of a disk spinning at 360 rpm

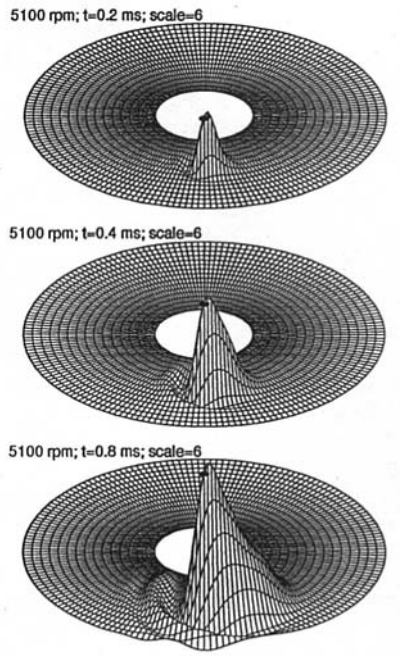


Fig. 3 The first 0.8 ms response of a disk spinning at 5100 rpm

may be considered as the result of complex continuous superposition of the waves reflecting from the free outer rim and the clamped inner rim, and the waves traveling in both directions circumferentially. It is noteworthy that similar phenomenon can also be observed in the transient response of a transporting tape under a space-fixed point load (Müftü and Benson, 1994).

Figure 2 shows the deformed shape at various time steps before 0.8 ms with a scale factor 3 for a disk spinning at 360 rpm. A black dot denotes the position of the space-fixed step force. It is noted that the deformation pattern is almost symmetric with respect to the loading point while the disk is rotating in the counterclockwise sense. Calculations at 0 and 610 rpm also show similar symmetric deformation pattern with different amplitudes at the early stage of the loading. In other words, rotation does not cause significant asymmetry in the deformation pattern at the very early stage of the excitation as the rotation speed is up to the range of the first critical speed.

It is expected that deformation pattern would appear asymmetric when the convective velocity of the rotating media is comparable to the phase speed of the propagating wave. We estimate roughly the rotation speed at which the convective velocity $b\Omega$ of the disk is comparable to the phase velocity of a wave with wave length equal to $\frac{1}{15}$ of the outer circumference of the disk as $\Omega = (15/b^2)\sqrt{D/\rho h}$, which is about 9950 rpm in the current case. Therefore, the convective velocity of the media for the disk rotating at 360 rpm is about $\frac{1}{36}$ of the phase velocity of the plate. In Fig. 3 we raise the rotation speed up to 5100 rpm and record the deformation evolution before 0.8 ms with a scale factor 6. Obvious asymmetry can be observed in the deformation pattern. In particular, waves tend to accumulate in the upstream region.

References

Benson, R. C., and Bogy, D. B., 1978, "Deflection of a Very Flexible Spinning Disk Due to a Stationary Transverse Load," ASME JOURNAL OF APPLIED MECHANICS, Vol. 45, pp. 636–642.

Cole, K. A., and Benson, R. C., 1988, "A Fast Eigenfunction Approach for Computing Spinning Disk Deflections," ASME JOURNAL OF APPLIED MECHANICS, Vol. 55, pp. 453–457.

Mote, C. D., 1970, "Stability of Circular Plates Subjected to Moving Loads," *Journal of the Franklin Institute,* Vol. 290, pp. 329–344.

Downloaded 04 May 2010 to 171.66.16.34. Redistribution subject to ASME license or copyright; see http://www.asme.org/terms/Terms_Use.cfm

Müftü, S., and Benson, R. C., 1994, "A Numerical Solution for the Transient Displacement of a Circumferentially Moving Cylindrical Shell," ASME *Journal of Vibration and Acoustics*, Vol. 116, pp. 567–572.

Ono, K., and Maeno, T., 1987, "Theoretical and Experimental Investigation on Dynamic Characteristics of a 3.5-Inch Flexible Disk Due to a Point Contact Head," *Tribology and Mechanics of Magnetic Storage Systems*, Vol. 3, SP.21, (STLE), pp. 144–151.

Weisensel, G. N., and Schlack, A. L., 1993, "Response of Annular Plates to Circumferentially and Radially Moving Loads," ASME JOURNAL OF APPLIED MECHANICS, Vol. 60, pp. 649–661.

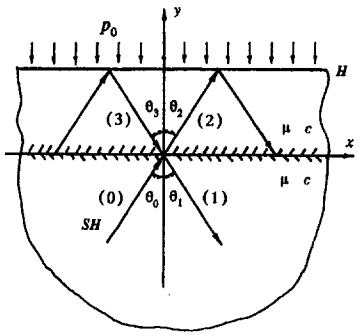


Fig. 1 A layer forced on a substrate with frictional contact

Slip With Friction Between a Layer and a Substrate Caused by SH Waves

Yu Guilan[18], Wang Yuesheng[19], and Gai Bingzheng[20]

Introduction

The propagation of elastic waves with a frictional contacting interface (termed unilateral interface by Comninou and Dundurs (1977)) has many new aspects such as the frictional energy dissipation, the distortion of reflected and refracted waves, etc. Such a problem was attacked by Miller (1978) and Miller and Tran (1979, 1981) using an approximate method—the method of equivalent linearization—and by Comninou and Dundurs (1977, 1979), Chez, Dundurs, and Comninou (1978), and Comninou, Dundurs, and Chez (1979) using the Fourier series technique and singular integral equation method. All of these works are limited to the case of an infinite medium. That is, the problem involves no characteristic length. Indeed, one may find that the mathematical procedure of the problem becomes very difficult when one of the dissimilar media is finite. Only Miller (1979) investigated the attenuation and dispersion of Love-type surface waves in an elastic layer bonded by Coulomb friction to an elastic half-space. He used an approximate method and obtained the results when the attenuation in the system is very small. In the present article, we consider the interaction of SH waves with a frictional contacting interface between a layer and a substrate. The layer and substrate are assumed to be made of the same material so that the problem is tractable. The Coulomb friction model is adopted by neglecting the kinematic locking for simplicity. The method used here is similar to that of Comninou's. However, the resulting equation is not a singular integral equation but a recurrence relation, and the results are drastically different from those for two semi-infinite dissimilar media.

[18] Department of Civil Engineering, Northern Jiaotong University, Beijing 100044, P. R. China.

[19] Institute of Engineering Mechanics, Northern Jiaotong University, Beijing 100044, P. R. China.

[20] Department of Astronautics and Mechanics, Harbin Institute of Technology, P. O. Box 344, Harbin 150001, P. R. China.

Contributed by the Applied Mechanics Division of THE AMERICAN SOCIETY OF MECHANICAL ENGINEERS for publication in the ASME JOURNAL OF APPLIED MECHANICS. Manuscript received and accepted by the ASME Applied Mechanics Division, May 5, 1995. Associate Technical Editor: D. M. Barnett.

Problem Formulation and Solution

The problem treated here is indicated in Fig. 1. An elastic layer of thickness H is forced on an elastic substrate by the applied pressure p_0. The layer and substrate are made of the same material with shear modulus μ and transverse wave speed $c = (\mu/\rho)^{1/2}$. An incident SH wave strikes the frictional contacting interface from the substrate under the angle θ_0. The only nonzero displacement component is along the z-direction. The displacement for the incident wave is taken as the real part of the typical form

$$u_z^{(0)} = C_0 \exp(i\zeta_0) \tag{1}$$

where $\zeta_0 = k(x \sin\theta_0 + y \cos\theta_0 - ct)$ with $k = \omega/c$. The coefficient C_0 is generally complex but is taken to be positive and real in the following analysis for simplicity. The associated reflected waves in the substrate and the transmitted waves in the layer may be written as

$$u_z^{(1)} = C_1 \exp(i\zeta_1) \tag{2}$$

and

$$u_z^{(2)} + u_z^{(3)} = C_2 \exp(i\zeta_2) + C_3 \exp(i\zeta_3) \tag{3}$$

where $\zeta_j = k(x \sin\theta_j - y \cos\theta_j - ct)$ for $j = 1, 3$ or $\zeta_j = k(x \sin\theta_j + y \cos\theta_j - ct)$ for $j = 0, 2$. It was demonstrated that Snell's law still holds for the unilateral interface (Comninou and Dundurs, 1977) and thus we have $\theta_0 = \theta_1 = \theta_2 = \theta_3$.

As Comninou and Dundurs (1977) did, we formulate the problem by constructing a corrective solution which modifies the results for the perfectly bonded interface (bilateral interface). Denoting the displacement and stress components in the bilateral problem by $u_z^{(n)}$ and $\tau_{yz}^{(n)}$ and those in the corrective solution by $\bar{u}_z^{(n)}$ and $\bar{\tau}_{yz}^{(n)}$, the results in the unilateral problem may be expressed as $u_z^{(n)} + \bar{u}_z^{(n)}$ and $\tau_{yz}^{(n)} + \bar{\tau}_{yz}^{(n)}$. The slip velocity at the interface is then defined as

$$V(\eta) = [\dot{\bar{u}}_z^{(2)} + \dot{\bar{u}}_z^{(3)} - \dot{\bar{u}}_z^{(1)}]_{y=0}, \tag{4}$$

where $\eta = \zeta_n|_{y=0}$. And the total shearing traction along the interface may be written as

$$\begin{aligned} S(\eta) &= [\tau_{yz}^{(0)} + \tau_{yz}^{(1)} + \bar{\tau}_{yz}^{(1)}]_{y=0} \\ &= [\tau_{yz}^{(2)} + \tau_{yz}^{(3)} + \bar{\tau}_{yz}^{(2)} + \bar{\tau}_{yz}^{(3)}]_{y=0}. \end{aligned} \tag{5}$$

The shearing traction transmitted by the perfectly bonded interface is (Achenbach, 1973)

$$\begin{aligned} [\tau_{yz}]_{y=0} &= [\tau_{yz}^{(0)} + \tau_{yz}^{(1)}]_{y=0} = [\tau_{yz}^{(2)} + \tau_{yz}^{(3)}]_{y=0} \\ &= \mathrm{Re}\{A_0 \exp[i(\eta + \gamma)]\} \end{aligned} \tag{6}$$

where $A_0 = 2\mu C_0 k \cos\theta_0 \sin\gamma$ and $\gamma = kH \cos\theta_0$. Adopting the Coulomb law for the dry friction at the interface, it is readily seen that the unilateral solution must satisfy the following boundary conditions at $y = 0$: In the stick zones,

Downloaded 04 May 2010 to 171.66.16.34. Redistribution subject to ASME license or copyright; see http://www.asme.org/terms/Terms_Use.cfm

Müftü, S., and Benson, R. C., 1994, "A Numerical Solution for the Transient Displacement of a Circumferentially Moving Cylindrical Shell," ASME *Journal of Vibration and Acoustics*, Vol. 116, pp. 567–572.

Ono, K., and Maeno, T., 1987, "Theoretical and Experimental Investigation on Dynamic Characteristics of a 3.5-Inch Flexible Disk Due to a Point Contact Head," *Tribology and Mechanics of Magnetic Storage Systems*, Vol. 3, SP.21, (STLE), pp. 144–151.

Weisensel, G. N., and Schlack, A. L., 1993, "Response of Annular Plates to Circumferentially and Radially Moving Loads," ASME JOURNAL OF APPLIED MECHANICS, Vol. 60, pp. 649–661.

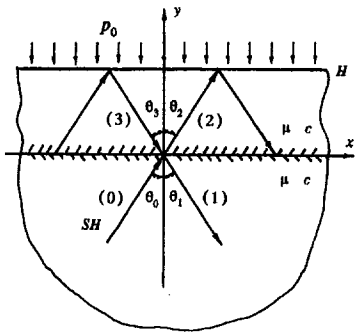


Fig. 1 A layer forced on a substrate with frictional contact

Slip With Friction Between a Layer and a Substrate Caused by SH Waves

Yu Guilan[18], Wang Yuesheng[19], and Gai Bingzheng[20]

Introduction

The propagation of elastic waves with a frictional contacting interface (termed unilateral interface by Comninou and Dundurs (1977)) has many new aspects such as the frictional energy dissipation, the distortion of reflected and refracted waves, etc. Such a problem was attacked by Miller (1978) and Miller and Tran (1979, 1981) using an approximate method—the method of equivalent linearization—and by Comninou and Dundurs (1977, 1979), Chez, Dundurs, and Comninou (1978), and Comninou, Dundurs, and Chez (1979) using the Fourier series technique and singular integral equation method. All of these works are limited to the case of an infinite medium. That is, the problem involves no characteristic length. Indeed, one may find that the mathematical procedure of the problem becomes very difficult when one of the dissimilar media is finite. Only Miller (1979) investigated the attenuation and dispersion of Love-type surface waves in an elastic layer bonded by Coulomb friction to an elastic half-space. He used an approximate method and obtained the results when the attenuation in the system is very small. In the present article, we consider the interaction of SH waves with a frictional contacting interface between a layer and a substrate. The layer and substrate are assumed to be made of the same material so that the problem is tractable. The Coulomb friction model is adopted by neglecting the kinematic locking for simplicity. The method used here is similar to that of Comninou's. However, the resulting equation is not a singular integral equation but a recurrence relation, and the results are drastically different from those for two semi-infinite dissimilar media.

[18] Department of Civil Engineering, Northern Jiaotong University, Beijing 100044, P. R. China.

[19] Institute of Engineering Mechanics, Northern Jiaotong University, Beijing 100044, P. R. China.

[20] Department of Astronautics and Mechanics, Harbin Institute of Technology, P. O. Box 344, Harbin 150001, P. R. China.

Contributed by the Applied Mechanics Division of THE AMERICAN SOCIETY OF MECHANICAL ENGINEERS for publication in the ASME JOURNAL OF APPLIED MECHANICS. Manuscript received and accepted by the ASME Applied Mechanics Division, May 5, 1995. Associate Technical Editor: D. M. Barnett.

Problem Formulation and Solution

The problem treated here is indicated in Fig. 1. An elastic layer of thickness H is forced on an elastic substrate by the applied pressure p_0. The layer and substrate are made of the same material with shear modulus μ and transverse wave speed $c = (\mu/\rho)^{1/2}$. An incident SH wave strikes the frictional contacting interface from the substrate under the angle θ_0. The only nonzero displacement component is along the z-direction. The displacement for the incident wave is taken as the real part of the typical form

$$u_z^{(0)} = C_0 \exp(i\zeta_0) \tag{1}$$

where $\zeta_0 = k(x \sin\theta_0 + y \cos\theta_0 - ct)$ with $k = \omega/c$. The coefficient C_0 is generally complex but is taken to be positive and real in the following analysis for simplicity. The associated reflected waves in the substrate and the transmitted waves in the layer may be written as

$$u_z^{(1)} = C_1 \exp(i\zeta_1) \tag{2}$$

and

$$u_z^{(2)} + u_z^{(3)} = C_2 \exp(i\zeta_2) + C_3 \exp(i\zeta_3) \tag{3}$$

where $\zeta_j = k(x \sin\theta_j - y \cos\theta_j - ct)$ for $j = 1, 3$ or $\zeta_j = k(x \sin\theta_j + y \cos\theta_j - ct)$ for $j = 0, 2$. It was demonstrated that Snell's law still holds for the unilateral interface (Comninou and Dundurs, 1977) and thus we have $\theta_0 = \theta_1 = \theta_2 = \theta_3$.

As Comninou and Dundurs (1977) did, we formulate the problem by constructing a corrective solution which modifies the results for the perfectly bonded interface (bilateral interface). Denoting the displacement and stress components in the bilateral problem by $u_z^{(n)}$ and $\tau_{yz}^{(n)}$ and those in the corrective solution by $\bar{u}_z^{(n)}$ and $\bar{\tau}_{yz}^{(n)}$, the results in the unilateral problem may be expressed as $u_z^{(n)} + \bar{u}_z^{(n)}$ and $\tau_{yz}^{(n)} + \bar{\tau}_{yz}^{(n)}$. The slip velocity at the interface is then defined as

$$V(\eta) = [\dot{\bar{u}}_z^{(2)} + \dot{\bar{u}}_z^{(3)} - \dot{\bar{u}}_z^{(1)}]_{y=0}, \tag{4}$$

where $\eta = \zeta_n|_{y=0}$. And the total shearing traction along the interface may be written as

$$\begin{aligned} S(\eta) &= [\tau_{yz}^{(0)} + \tau_{yz}^{(1)} + \bar{\tau}_{yz}^{(1)}]_{y=0} \\ &= [\tau_{yz}^{(2)} + \tau_{yz}^{(3)} + \bar{\tau}_{yz}^{(2)} + \bar{\tau}_{yz}^{(3)}]_{y=0}. \end{aligned} \tag{5}$$

The shearing traction transmitted by the perfectly bonded interface is (Achenbach, 1973)

$$\begin{aligned} [\tau_{yz}]_{y=0} &= [\tau_{yz}^{(0)} + \tau_{yz}^{(1)}]_{y=0} = [\tau_{yz}^{(2)} + \tau_{yz}^{(3)}]_{y=0} \\ &= \mathrm{Re}\{A_0 \exp[i(\eta + \gamma)]\} \end{aligned} \tag{6}$$

where $A_0 = 2\mu C_0 k \cos\theta_0 \sin\gamma$ and $\gamma = kH \cos\theta_0$. Adopting the Coulomb law for the dry friction at the interface, it is readily seen that the unilateral solution must satisfy the following boundary conditions at $y = 0$: In the stick zones,

Copyright © 1997 by ASME

Downloaded 04 May 2010 to 171.66.16.34. Redistribution subject to ASME license or copyright; see http://www.asme.org/terms/Terms_Use.cfm

$$V(\eta) = 0, \quad |S(\eta)| < f_s p_0 \tag{7}$$

and in the slip zones,

$$|S(\eta)| = f_k p_0, \quad \text{sgn } S(\eta) = \text{sgn } V(\eta) \tag{8}$$

where f_s and f_k denote the static and kinetic friction factors, respectively. Generally $f_k \leq f_s$. However, we assume $f_k = f_s$ in the present article for simplicity.

Because of the periodicity of the problem, the displacement components in the corrective solution may be written as the Fourier series

$$\bar{u}_z^{(n)} = \text{Re}\left\{\sum_{m=1}^{\infty} F_m^{(n)} \exp(im\zeta_n)\right\}, \quad n = 1, 2, 3 \tag{9}$$

with unknown complex coefficients $F_m^{(n)} = D_m^{(n)} + iE_m^{(n)}$.

The requirement that the shearing tractions be continuous across the interface and that the shear stresses vanish at the free surface $y = H$ leads to the following relations between the coefficients in (9):

$$F_m^{(1)} = 2iF_m^{(2)} \sin m\gamma \exp(im\gamma),$$
$$F_m^{(3)} = F_m^{(2)} \exp(2im\gamma). \tag{10}$$

Substituting (9) into (4) and (5), and taking the real parts, we have

$$V(\eta) = -kc \sum_{m=1}^{\infty} m(M_m \sin m\eta + N_m \cos m\eta) \tag{11}$$

and

$$S(\eta) = A_0 \cos(\eta + \gamma) + \mu k \cos\theta_0 \sum_{m=1}^{\infty} m(D_m^{(1)} \sin m\eta + E_m^{(1)} \cos m\eta) \tag{12}$$

where

$$D_m^{(1)} = M_m \sin^2 m\gamma + N_m \sin m\gamma \cos m\gamma,$$
$$E_m^{(1)} = -M_m \sin m\gamma \cos m\gamma + N_m \sin^2 m\gamma. \tag{13}$$

We set $\phi(\eta) = -(kc)^{-1}V(\eta)$. Then it follows from (11) that

$$\int_{-\pi}^{\pi} \phi(\xi)d\xi = 0 \tag{14}$$

$$M_m = \frac{1}{\pi m}\int_{-\pi}^{\pi} \phi(\xi) \sin m\xi d\xi,$$

$$N_m = \frac{1}{\pi m}\int_{-\pi}^{\pi} \phi(\xi) \cos m\xi d\xi. \tag{15}$$

Substituting (15) into (12) and making the use of the relation

$$\sum_{m=1}^{\infty} \cos mx = -\tfrac{1}{2} + \pi \sum_{m=-\infty}^{\infty} \delta(x - 2\pi m) \tag{16}$$

we obtain

$$S(\eta) = A_0 \cos(\eta + \gamma) + \tfrac{1}{2}\mu k \cos\theta_0[\phi(\eta) - \phi(\eta + 2\gamma)] \tag{17}$$

where we have considered the periodicity of $\phi(\eta)$, that is, $\phi(\eta \pm 2n\pi) = \phi(\eta)$.

Because of the periodicity of the field quantities in η and γ, only one representative interval, for instance $-\pi < \eta < \pi$ with $0 < \gamma < 2\pi$, has to be considered. We anticipate that generally there are two slip zones in one representative interval, and that the interface tractions are positive in the left slip zone $\alpha_1 < \eta < \beta_1$ and negative in the right slip zone $\alpha_2 < \eta < \beta_2$ (Comninou, Dundurs and Chez, 1979). Then the boundary condition (8) leads to

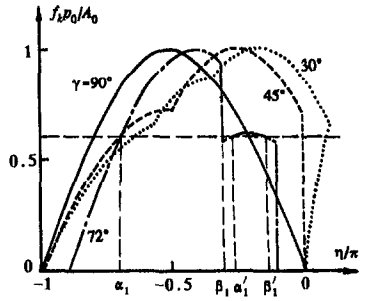


Fig. 2 Extent and location of left slip zone for given $f_k p_0/A_0$

$$A_0 \cos(\eta + \gamma) + \tfrac{1}{2}\mu k \cos\theta_0[\phi(\eta) - \phi(\eta + 2\gamma)] = f_k p_0, \quad \alpha_1 < \eta < \beta_1 \tag{18}$$

and

$$A_0 \cos(\eta + \gamma) + \tfrac{1}{2}\mu k \cos\theta_0[\phi(\eta) - \phi(\eta + 2\gamma)] = -f_k p_0, \quad \alpha_2 < \eta < \beta_2. \tag{19}$$

It is not difficult to conceive that the following relations must be true (Comninou, Dundurs, and Chez, 1979):

$$\alpha_2 = \alpha_1 + \pi, \quad \beta_2 = \beta_1 + \pi; \quad \phi(\eta \pm \pi) = -\phi(\eta). \tag{20}$$

Therefore, only one equation, say (18), has to be solved. The unknown parameters α_j and β_j are determined from

$$\phi(\alpha_j) = \phi(\beta_j) = 0. \tag{21}$$

In the next section we will demonstrate that in some situations there are four slip zones in one representative interval. These special cases must be treated individually.

Numerical Results and Discussion

In this section we will present some examples of the solution of (18) for $0 < \gamma \leq \pi/2$. The case for $\pi/2 < \gamma < 2\pi$ may be analyzed analogously. Rewrite (18) as

$$(4C_0 \sin\gamma)^{-1}[\phi(\eta) - \phi(\eta + 2\gamma)] = -\cos(\eta + \gamma) + f_k p_0/A_0, \quad \alpha_1 < \eta < \beta_1 \tag{22}$$

where $\phi(\eta) = 0$ for $\eta \notin (\alpha_1, \beta_1) \cup (\alpha_2, \beta_2)$, and it should also satisfy (20). It is seen from (22) that the solution depends strongly on the parameters γ and $f_k p_0/A_0$. In order to obtain the solution of $\phi(\eta)$ for given γ and $f_k p_0/A_0$, we first investigate the dependance of the interval (α_1, β_1) on the parameter $f_k p_0/A_0$ for a given γ. Clearly the local slip takes place only when $f_k p_0/A_0 \leq 1$ (we have assumed that $0 < \gamma \leq \pi/2$). For the special case of $f_k p_0/A_0 = 1$ the slip takes place at a point: $\alpha_1 = \beta_1 = -\gamma$. The location of slip zone for $f_k p_0/A_0 < 1$ is determined by the following steps: (i) decrease $f_k p_0/A_0$ by a small value from 1. Then make a guess for (α_1, β_1) using the bilateral solution as guidance; (ii) derive the exact $\phi(\eta)$ from (22) by recurrence and determine the "real" (α_1, β_1) by using (21); (iii) check whether the solution satisfies the boundary conditions (7) and (8); (iv) again decrease $f_k p_0/A_0$ by a small value and make a guess of (α_1, β_1) based on the solution of the bilateral problem and the solution obtained in the pervious steps; (v) repeat steps (ii)–(iv). Step (iii) is very important although the solution is generally correct. Indeed we have found that the solution obtained in step (ii) does not satisfy the boundary conditions when there are four slip zones. In this case the problem must be treated individually. But fortunately no much trouble arises. Equation (22) still holds if the interval (α_1, β_1) is divided into two parts.

Figure 2 shows curves determining the extent and location of the left slip zone for given $f_k p_0/A_0$ and some selected values

Downloaded 04 May 2010 to 171.66.16.34. Redistribution subject to ASME license or copyright; see http://www.asme.org/terms/Terms_Use.cfm

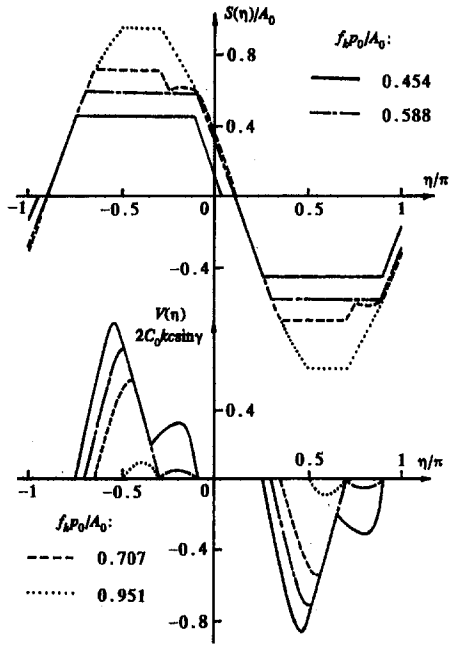


Fig. 3 Distributions of shearing tractions and slip velocity for $\gamma = 72$ deg

of parameter γ. It is seen from the curve for $\gamma = 72$ deg that an additional small slip zone denoted by (α_1', β_1') occurs besides the original one when $f_k p_0/A_0$ varies from 0.617 to 0.588 (or α_1 from -123.9 deg to -126 deg). Further calculation shows that only when $\gamma > 60$ deg can such a phenomenon take place. This feature is due to the effect of the characteristic length of H and was not found in the case of infinite media (Chez, Dundurs, and Comninou, 1978; Comninou, Dundurs, and Chez, 1979). The distributions of the shearing traction and the slip velocity are depicted in Fig. 3 for $\gamma = 72$ deg with different values of $f_k p_0/A_0$.

Acknowledgments

The work was supported by the China National Science Foundation under Grant No. 19472026.

References

Achenbach, J. D., 1973, *Wave Propagation in Elastic Solids,* North Holland, Amsterdam.

Chez, E. L., Dundurs, J., and Comninou, M., 1978, "Reflection and Refraction of SH Waves in Presence of Slip and Friction," *Bulletin of the Seismological Society of America,* Vol. 68, pp. 999–1011.

Comninou, M., and Dundurs, J., 1977, "Reflexion and Refraction of Elastic Waves in Presence of Separation," *Proceedings of the Royal Society, London,* Vol. A356, pp. 509–528.

Comninou, M., and Dundurs, J., 1979, "Interaction of Elastic Waves with a Unilateral Interface," *Proceedings of the Royal Society, London,* Vol. A368, pp. 141–154.

Comninou, M., Dundurs, J., and Chez, E. L., 1979, "Total Reflection of SH Waves in Presence of Slip and Friction," *Journal of the Acoustical Society of America,* Vol. 66, pp. 789–793.

Miller, R. K., 1978, "The Effects of Boundary Friction on the Propagation of Elastic Waves," *Bulletin of the Seismological Society of America,* Vol. 68, pp. 987–998.

Miller, R. K., 1979, "An Estimate of the Properties of Love-Type Surface Waves in a Frictionally Bonded Layer," *Bulletin of the Seismological Society of America,* Vol. 69, pp. 305–317.

Miller, R. K., and Tran, H. T., 1979, "Reflection, Refraction, and Absorption of Elastic Waves at a Frictional Interface: SH Motion," ASME JOURNAL OF APPLIED MECHANICS, Vol. 46, pp. 625–630.

Miller, R. K., and Tran, H. T., 1981, "Reflection, Refraction, and Absorption of Elastic Waves at a Frictional Interface: P and SV Motion," ASME JOURNAL OF APPLIED MECHANICS, Vol. 48, pp. 155–160.

Downloaded 04 May 2010 to 171.66.16.34. Redistribution subject to ASME license or copyright; see http://www.asme.org/terms/Terms_Use.cfm

Journal of Applied Mechanics

Discussion

Contact Between Elastic Bodies With an Elliptic Contact Interface in Torsion[1]

J. Jäger[2]. The authors present an excellent finite element study for torsional contact of elliptic contact areas and found the important parameters by comparison of FEM solutions for different parameters. They presented an analytic relationship between the torque and the rotation angle, which was obtained by a curve fit of FEM results for several values for b/a, where b and a denote the major and minor semi-axis of the contact ellipse, respectively. In a paper by Todd and Johnson (1987), hysteresis loops for rolling with spin have been analysed and compared with experiments. They approximated the torque M_z as a function of the angle of rotation β by $M_z = (a + b\beta)/(c + d\beta)$, with appropriate parameters a, b, c, d. Another approximation was proposed by Jäger (Eq. (7.65) in Jäger 1992), which can directly be compared with Cuttino and Dow's theory:

$$\frac{M_z}{M_S} = 1 - \exp\left(\frac{-M'_A}{M_S}\beta\right), \tag{1a}$$

$$M_S = \lim_{\beta\to\infty} M_z = \tfrac{3}{8} f F_z b E(k), \tag{1b}$$

$$M'_A = \lim_{\beta\to 0}\left(\frac{dM_z}{d\beta}\right) = \tfrac{3}{8} G b^3 E(k)\delta_T, \tag{1c}$$

$$\delta_T = \frac{16\pi(E(k) - 4\nu C(k)(1-k^2))}{9E(k)(B(k)D(k) - \nu C(k)E(k))}, \tag{1d}$$

$$k = \sqrt{1 - a^2/b^2}, \tag{1e}$$

where M_s is the torque for full sliding, M'_A the slope of the torque-rotation curve for $\beta \to 0$, F_z the normal force, f the coefficient of friction, G the shear modulus, ν Poisson's ratio, δ_T a geometric parameter, and $B(k)$, $C(k)$, $D(k)$, and $E(k)$ elliptic integrals as defined by Cuttino and Dow (1997). The stiffness M'_A is the reciprocal value of Mindlin's compliance for complete adhesion.

The moment (1a) has the two limits of M_S for full sliding and $M'_A\beta$ for complete adhesion. An exponential function was selected, because Lubkin's rotation β for torsion of spheres is proportional to the complete elliptic function $D(\sqrt{1 - a^{*2}/a^2})$, with the stick radius a^*. For small stick areas ($a^* \to 0$), the function has a logarithmic singularity. Thence, (1a) was so selected that β is a logarithmic function of M_z/M_S. In the case of two different bodies in contact, the combined rotation β and the stiffness M'_A for $\beta \to 0$ are

$$\beta = \beta_I + \beta_{II}, \quad \frac{1}{M'_A} = \frac{1}{M'_{AI}} + \frac{1}{M'_{AII}}, \tag{2}$$

where the indices I and II characterize body I and II, respectively. The reciprocals of the stiffnesses must be added, because the bodies act as two springs in series.

The approximation by Cuttino and Dow (1997) has the form

$$M_z = 0.62\,\frac{a+b}{2} f F_z\left(1 - \exp\left[-10\,\frac{\sqrt{JG}}{fF_z}\beta\right]\right),$$

$$J = \tfrac{1}{2} ab(a^2 + b^2). \tag{3}$$

We can rewrite Eqs. (1), with the result

$$M_z = \frac{3}{8} bE(k) f F_z\left(1 - \exp\left[-\frac{Gb^2}{fF_z}\delta_T\beta\right]\right). \tag{4}$$

Comparison of the corresponding values of Eqs. (3) and (4), before the parenthesis and in the square brackets, shows that the maximum difference is smaller than five percent for $a/b = \frac{1}{3}$.

The comparisons in Figs. 1 and 2 show that the approximation by Cuttino and Dow is very good in the whole range of a/b. Only for very small values, $\sqrt{J}$ approaches the origin as a square root, while δ_T has a logarithmic asymptote: $1/\ln(a/b)$. Also, the dependence on Poisson's ratio ν was not considered in their model. The authors did not mention Poisson's ratio, which must be about $\nu = 0.3$. There seems to be an error in Table 1 of Cuttino and Dow for the test cases of "Rnd Low G" and "Low Mod", where the shear modulus should be about 2.88E+4.

The solution by Cuttino and Dow is one of the very few quantitative FEM solutions in contact mechanics. Their results show that it is possible to obtain good approximations and to perform reliable parameter studies with FEM programs. Their FEM model consists of 7168 elements in total for a potential contact area of 128 points. In Jäger (1992), a BEM method has been used to solve contact problems numerically. With that program, it is possible to calculate 1000 contact points with an 80386/33MHz processor. It is available as shareware program from the author. If the dimension of Cuttino and Dow's FEM model would be enlarged by a factor three in each dimension, a potential contact area of 1.152 points would require 193.536 elements in total. The advantage of BEM calculations is that only the contact area must be discretized. There are other contact problems, however, such as contact of shells and conforming bodies, etc., which can not be solved with half-space theory. The approach by Cuttino and Dow seems to be a good example

[1] Cuttino, J. F., and Dow, T. A., "Contact Between Elastic Bodies With an Elliptic Contact Interface in Torsion," ASME JOURNAL OF APPLIED MECHANICS, Vol. 64, pp. 144–148.

[2] Jürgen Jäger, Blattwiesenstr 7, D-76227 Karlsruhe, Germany. j_jaeger@t-online.de.

Copyright © 1997 by ASME

Downloaded 04 May 2010 to 171.66.16.34. Redistribution subject to ASME license or copyright; see http://www.asme.org/terms/Terms_Use.cfm

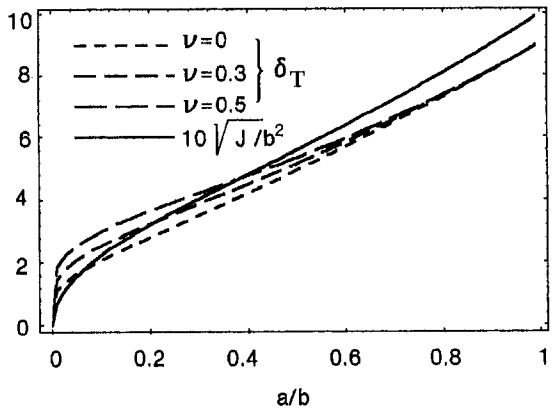


Fig. 1 δ_T compared with $10\sqrt{J}/b^2$

for such problems. Their study shows also that analytic solutions are very helpful for parameter identification with FEM programs.

The hysteresis curve for constant normal forces was also published in Jäger (1992):

$$\left.\begin{aligned}\frac{M_1 - M_z}{2M_S} &= 1 - \exp\left[\frac{-M_A'}{2M_S}(\beta_1 - \beta)\right], \text{ lower branch,}\\ \frac{M_z - M_1}{2M_S} &= 1 - \exp\left[\frac{-M_A'}{2M_S}(\beta - \beta_1)\right], \text{ upper branch,}\end{aligned}\right\} \quad -M_1 \le M_z \le M_1, \quad -\beta_1 \le \beta \le \beta_1 \quad (5)$$

and agrees completely with Cuttino and Dow's result (Their curve is shifted along the x-axis, so that $\beta_1 = 0$). It may be interesting in this context that an approximation for the torque of circular contact areas as a function of the stick radius a^* has been published (Eq. (24a) in Jäger, 1996).

$$M_z = fF_z a k^2(1 - k^2 + 3\pi k^2/16), \quad k^2 = 1 - a^{*2}/a^2,$$
$$\delta_T = 16^2/(9\pi), \quad E(1) = \pi/2, \quad \text{for spheres.} \qquad (6)$$

This approximation was obtained by adapting the fourth-order term of Deresiewicz's solution, so that the full sliding moment is reached for $k = 1$. The maximum error is smaller than two percent. For general load histories, increments of the type (6) can be superposed, and results for torsional impact of spheres

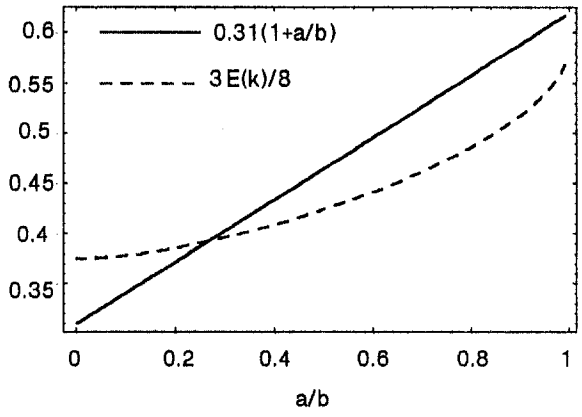


Fig. 2 Comparison of the factors in Eqs. (3) and (4) before the round parentheses

Table 1 Comparison of Eqs. (3) and (4)

ν	a/b	$0.31(1 + a/b)$	$3E(k)/8$	$10\sqrt{J}/b^2$	δ_T
0.3	1/3	0.4133	0.4003	4.3033	4.0899

have been compared with experiments in Jäger (1994). An extension of Lubkin's solution for axisymmetric bodies has been presented in Jäger (1995). These publications show that new analytic results are still possible.

The superposition technique in Jäger (1996) for arbitrary load histories distinguishes three basic contact regimes, depending on the size of the old and new slip area before and after application of a new load increment: no overlapping, partial overlapping, or complete overlapping of both areas. For torsion of elliptic contact areas, the stick area is geometrically different from the contact area, in that the major axes decreases much more than the minor axes, so that the the stick area becomes rounder (Jäger, 1992). Thence a fourth contact regime arises, where the contact areas can intersect each other, and this superposition technique can not be used for torsion of elliptic contact areas.

In the case of dissimilar materials in contact, the normal and tangential stress states are coupled. Normal compression induces tangential stresses and vice versa and the form and size of the stick area are almost unpredictable. Although these effects cannot be considered in the simple models above, Eq. (1a) is a good approximation for dissimilar materials. As example, a contact area with $a/b = 1/10$, $\nu_I = 0$, $\nu_{II} = 0.5$, $f = 0.1$ has been compared with Eq. (1a) in Jäger (1992) and good agreement has been found. This result is surprising, because problems with dissimilar material in contact have received considerable attention in contact mechanics and few simplifications have been found. It would also be interesting to see if problems with dissimilar material in contact can be solved by FEM methods.

One of the shortcomings of modern Contact Mechanics is the restriction of the half-space theory and the FEM method could provide new solutions. Open problems for Cuttino and Dow's model are, e.g., conforming contact, where the radius difference between ball and race is very small, or races in form of a shell, which cannot be regarded as half-spaces.

References

Cuttino, J. F., and Dow, T. A., 1997, "Contact Between Elastic Bodies With an Elliptic Contact Interface in Torsion," ASME Journal of Applied Mechanics, Vol. 64, pp. 144–148.

Jäger, J., 1992, "Elastic Impact With Friction," thesis, Inst. Inf. and Maths., TU Delft, The Netherlands.

Jäger, J., 1994, "Torsional Impact of Elastic Spheres," *Arch. Appl. Mech.*, Vol. 64, pp. 235–248.

Jäger, J., 1995, "Contact With Friction of Elastically Similar Bodies," *Impact, Waves and Fracture*, R. C. Batra, A. K. Mal, and G. P. MacSithigh, eds., ASME, New York, pp. 129–152.

Jäger, J., 1996, "Stepwise Loading of Half-Spaces in Elliptical Contact," ASME Journal of Applied Mechanics, Vol. 63, pp. 766–773.

Todd, M. J., and Johnson, K. L., 1987, "A Model for Colomb Torque Hysteresis in Ball Bearings," *Intl. J. Mech. Sci.*, Vol. 29, pp. 339–354.

Downloaded 04 May 2010 to 171.66.16.34. Redistribution subject to ASME license or copyright; see http://www.asme.org/terms/Terms_Use.cfm

Author's Closure[3]

The typographical errors in Table 1 of the paper by Cuttino and Dow have been corrected in the following table.

Table 1 Parameter variations for FEA test cases

	Rball (mm)	Rrace (mm)	N (N)	μ	G (N/mm^2)	a (mm)	b (mm)	a/b	ρ (mm)	J (mm^4)
Rnd CP	1.588	∞	14.14	0.1270	7.96E+4	0.0524	0.0526	1.00	0.0525	7.60E-6
Rnd Low G	1.588	∞	2.40	0.1270	2.88E+4	0.0407	0.0409	1.00	0.0408	2.76E-6
Mid CP	1.588	1.925	14.14	0.1270	7.96E+4	0.1210	0.0381	3.17	0.0795	3.71E-5
Low Fric	1.588	1.925	14.14	0.0625	7.96E+4	0.1210	0.0381	3.17	0.0795	3.71E-5
Hi Fric	1.588	1.925	14.14	0.2500	7.96E+4	0.1210	0.0381	3.17	0.0795	3.71E-5
Hi Norm	1.588	1.925	41.10	0.1270	7.96E+4	0.1727	0.0544	3.17	0.1136	1.54E-4
Low Mod	1.588	1.925	13.42	0.1270	2.88E+4	0.1668	0.0525	3.17	0.1097	1.34E-4
Lg Geom	3.176	3.850	14.14	0.1270	7.96E+4	0.1524	0.0480	3.17	0.1002	9.35E-5
Thin CP	1.588	1.734	14.14	0.1270	7.96E+4	0.1664	0.0333	5.00	0.0998	7.97E-5

[3] J. F. Cuttino, Department of Mechanical Engineering, The University of Alabama, 290 Hardaway Hall, Box 870276, Tuscaloosa, AL 35487-0276.

Investigation of a New Formulation of the Lagrange Method for Constrained Dynamic Systems[4]

P. Hagedorn[5]. The authors discuss a formulation of Lagrange's equations for constrained dynamical systems in which a stabilization of the constraints is obtained within the framework of variational methods. They present their new formulation both for holonomic as well as for nonholonomic constraints. The generalization from the case of holonomic to nonholonomic constraints, which sounds extremely plausible at a first glance, is however not correct. It is a known fact in the dynamics of nonholonomic systems that the action integral $\int_{t_0}^{t_1} L'dt$ for the augmented Lagrangian $L' = T - V - \mu f = L - \mu f$ is not stationary in the class of paths satisfying the equations of constraint (geometrically possible paths). Here T is the kinetic energy, V the potential energy, μ stands for the Lagrange multipliers and f for the constraints. This fact, which has been overseen by many authors during the last 100 years and as many times corrected afterwards, is explained, for example, in Pars (1968), Neimark and Fufaev (1972), and in Whittaker (1937). These authors show that the equations of motion of a dynamical system with nonholonomic constraints cannot be obtained via calculus of variations by applying the multiplier rule in the usual way. This caused the search for more general variational principles as well as for new formalisms for obtaining the correct equations of motion for nonholonomic systems.

Since this fact falls into oblivion with regularity, it might be useful to illustrate it with an example borrowed from Pars (1968) (see pages 529 and 530). Consider a particle P with position characterized by the cartesian coordinates (x, y, z) in inertial space and subjected to the single nonholonomic constraint

$$A_x\dot{x} + A_y\dot{y} + A_z\dot{z} + A = 0, \tag{1}$$

where A_x, A_y, A_z, and A may be functions of x, y, z, and t. The equations of motion are then given by

$$m\ddot{x} = X + \lambda A_x, \tag{2a}$$

$$m\ddot{y} = Y + \lambda A_y, \tag{2b}$$

$$m\ddot{z} = Z + \lambda A_z, \tag{2c}$$

both for (1) holonomic or nonholonomic, where X, Y, and Z are the given forces and λ is a Lagrange parameter representing the constraint forces. Consider the particular constraint

$$z\dot{x} - \dot{y} = 0 \tag{3}$$

with $X = Y = Z = 0$, $V \equiv 0$. We assume that all the coordinates have been normalized, so that they are nondimensional and the particle has unitary mass. The correct equations of motion obtained from (2) are given by

$$\ddot{x} = \lambda z, \tag{4a}$$

$$\ddot{y} = -\lambda, \tag{4b}$$

$$\ddot{z} = 0 \tag{4c}$$

to which the equation of constraint (3) has to be added. The parameter λ stands for the Lagrange parameter characterizing the force of constraint corresponding to (3). The solution of this system of differential equations is simple and for the initial conditions

$$x(0) = 0, \quad y(0) = 0, \quad z(0) = 0, \tag{5a}$$

$$\dot{x}(0) = u, \quad \dot{y}(0) = 0, \quad \dot{z}(0) = w, \tag{5b}$$

with $w \neq 0$ and with the abbreviation

$$\sinh \theta(t) = wt \tag{6}$$

yields

$$x(t) = \frac{u}{w}\theta(t), \tag{7a}$$

$$y(t) = \frac{u}{w}(\cosh \theta(t) - 1), \tag{7b}$$

$$z(t) = \sinh \theta(t). \tag{7c}$$

Let us now compare the correct equations of motion (4) as well as the solution (7) with equations obtained from the calculus of variations via the stationarity of the action integral with the augmented Lagrangian

[4] Rosen, A., and Edelstein, E., 1997, "Investigation of a New Formulation of the Lagrange Method for Constrained Dynamic Systems," ASME JOURNAL OF APPLIED MECHANICS, Vol. 64, pp. 116–122.

[5] Professor, Institut f. Mechanik, Technische Hochschule, D-64289, Darmstadt, Germany.

Copyright © 1997 by ASME

Downloaded 04 May 2010 to 171.66.16.34. Redistribution subject to ASME license or copyright; see http://www.asme.org/terms/Terms_Use.cfm

$$L' = \tfrac{1}{2}(\dot{x}^2 + \dot{y}^2 + \dot{z}^2) - \mu(z\dot{x} - \dot{y}). \quad (8)$$

The augmented Lagrangian L' leads to the differential equations,

$$\frac{d}{dt}(\dot{x} - \mu z) = 0, \quad (9a)$$

$$\frac{d}{dt}(\dot{y} - \mu) = 0, \quad (9b)$$

$$\frac{d}{dt}\dot{z} + \mu\dot{x} = 0, \quad (9c)$$

to which again the equation of constraint (3) must be adjoined. The motion given by (7) does not satisfy (9) for any choice of $\mu(t)$! In fact, from (6), (7c) follows $\ddot{z} \equiv 0$, so that (9c) leads to

$$\mu\dot{x} = 0. \quad (10)$$

Since $\dot{x}(t)$ does not vanish, one has

$$\mu(t) \equiv 0 \quad (11)$$

and (9a), (9b) assume the form

$$\ddot{x} = 0, \quad (12a)$$

$$\ddot{y} = 0. \quad (12b)$$

These differential equations are clearly not fulfilled by (7)! The motion (7) obtained by solving the correct differential Eqs. (4) is therefore not the solution to Euler-Lagrange's equations corresponding to (8).

For a system described by the Lagrangian L in generalized coordinates $\mathbf{q} = (q_1, q_2, \ldots, q_n)$ and by the additional constraints

$$f_r = \sum_{i=j}^{h} A_{ri}\dot{q}_i + A_r = 0, \quad r = 1, 2, \ldots, s, \quad (13)$$

the correct equations of motion are given by

$$\frac{d}{dt}\frac{\partial L}{\partial \dot{q}_i} - \frac{\partial L}{\partial q_i} = \sum_{r=1}^{s} \lambda_r A_{ri}, \quad i = 1, 2, \ldots, n \quad (14)$$

together with (13). They are **not** given by

$$\frac{d}{dt}\frac{\partial L'}{\partial \dot{q}_i} - \frac{\partial L'}{\partial q_i} = 0, \quad L' = L - \sum_{r=1}^{s} \mu_r f_r, \quad (15)$$

unless the constraints are holonomic.

In their paper the authors use an augmented Lagrangian with the constraint equations included in a form differentiated with respect to the time t. Although this seems to be useful for stabilizing the constraint equations in the case of holonomic systems, it clearly will yield differential equations which are not the correct equations of motion in the case of nonholonomic systems. The correct equations of motion can always be obtained from the principle of virtual velocities or any equivalent formalism. We nevertheless congratulate the authors for formulating a method including stabilization of the constraints which seems to work efficiently for holonomic systems.

References

Neimark, J. F., and Fufaev, N. A., 1972, *Dynamics of Nonholonomic Systems,* American Mathematical Society, Providence Rhode Island.

Pars, B. A., 1968, *Analytical Dynamics,* Heinemann, London.

Whittaker, E. T., 1937, *A Treatise on the Analytical Dynamics of Particles and Rigid Bodies,* Cambridge University Press, London.

Author's Closure

1 Introduction

The authors are very pleased with the interest of Professor Hagedorn in their paper and they appreciate his sympathetic remarks at the end of his discussion. Since the submission of Rosen and Edelstein (1997a), the new formulation was applied very successfully to the solution of various problems.

The authors are aware of the problematic nature of nonholonomic constraints that was continuously discussed in the literature during the years. Yet, it seems that part of the problems are the result of an incorrect approach. In many cases, researchers try to treat nonholonomic problems without properly addressing the various physical aspects associated with those problems. For instance, it is not clear what kind of physical problem is presented in the example discussed by Professor Hagedorn. Any lack of sound physical definition may be the root of the problem.

In order to present the importance of dealing with a well-defined physical problem, a relatively simple example will be discussed in what follows.

2 Description of the Example

A plane problem is considered. A particle moves along a straight path that forms a constant angle, α, with the x-axis (see Fig. 1). The path is allowed to move as a rigid body without any rotation. This motion depends on the velocity component $\dot{x}$ of the particle. The mathematical equation that describes this motion (constraint equation) is

$$y - tg\alpha \cdot x - \varepsilon \cdot \dot{x} = 0. \quad (1)$$

ε is a certain positive constant.

It is assumed that the path is perfectly smooth, such that the reaction force, N, that is applied by the path on the particle, is always normal to the path.

There are not any external forces that act on the particle.

It should be noted that since the straight path itself moves in the plane, in general the particle trajectory is not a straight line.

Based on the above description and using the Newton approach, the equations of motion are (for the sake of simplicity it is assumed that the mass is equal to unit, $m = 1$):

$$\ddot{y} = N \cdot \cos\alpha \quad (2a)$$

$$\ddot{x} = -N \cdot \sin\alpha. \quad (2b)$$

Differentiation of Eq. (1) twice with respect to time, results in

[6] Professor Aviv Rosen, Dean, Faculty of Aerospace Engineering, Technion–Israel Institute of Technology, Technion City, Haifa 32000, Israel.

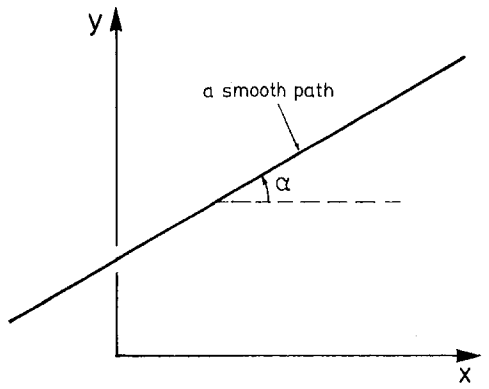


Fig. 1 Description of the example

Copyright © 1997 by ASME

Downloaded 04 May 2010 to 171.66.16.34. Redistribution subject to ASME license or copyright; see http://www.asme.org/terms/Terms_Use.cfm

$$\ddot{y} = tg\alpha \cdot \ddot{x} + \varepsilon \cdot \ddot{x}. \quad (3)$$

Substitution of the last equation into Eq. (2*a*) gives the following expression for N:

$$N = (tg\alpha \cdot \ddot{x} + \varepsilon \cdot \ddot{x})/\cos\alpha. \quad (4)$$

Substitution of the last expression into Eq. (2*b*) leads to the following differential equation for x:

$$\varepsilon \cdot tg\alpha \cdot \ddot{x} + (1 + tg^2\alpha)\ddot{x} = 0. \quad (5)$$

The solution of the last equation is

$$x = C_1 e^{-\nu \cdot t} + C_2 t + C_3 \quad (6a)$$

$$\nu = \frac{1 + tg^2\alpha}{\varepsilon \cdot tg\alpha}. \quad (6b)$$

According to Eqs. (1) and (4)

$$y = -C_1 \cdot e^{-\nu t}/tg\alpha + C_2(tg\alpha \cdot t + \varepsilon) + C_3 \cdot tg\alpha \quad (7a)$$

$$N = -C_1 \cdot \nu^2 \cdot e^{-\nu \cdot t}/\sin\alpha. \quad (7b)$$

If the initial conditions are $(x_0, \dot{x}_0, y_0, \dot{y}_0)$, then

$$x_0 = C_1 + C_3 \quad (8a)$$

$$\dot{x}_0 = -C_1 \cdot \nu + C_2 \quad (8b)$$

$$y_0 = -C_1/tg\alpha + C_2 \cdot \varepsilon + C_3 \cdot tg\alpha \quad (8c)$$

$$\dot{y}_0 = C_1 \cdot \nu/tg\alpha + C_2 \cdot tg\alpha. \quad (8d)$$

The initial conditions, Eqs. (8*a–d*), always satisfy Eq. (1). As expected, they cannot be arbitrarily chosen, and they depend on three parameters (C_1, C_2, C_3).

When $\varepsilon = 0$, the classical case of motion along a straight line is considered. In this case one obtains the classical solution:

$$x = x_0 + \dot{x}_0 \cdot t \quad (9a)$$

$$y = y_0 + \dot{y}_0 \cdot t. \quad (9b)$$

3 The "Regular" Variational Approach

If one uses the variational approach that was presented by Professor Hagedorn, then based on Eq. (1), and using the notation of Professor Hagedorn (see his Eq. (1)),

$$A_x = -\varepsilon; \quad A_y = 0. \quad (10)$$

Then, according to his Eqs. (2*a–c*) (recall that the external forces are equal to zero and a unit mass is considered),

$$\ddot{x} + \lambda \cdot \varepsilon = 0 \quad (11a)$$

$$\ddot{y} = 0. \quad (11b)$$

The solution of Eq. (11*b*) is immediately obtained as

$$y = D_1 \cdot t + D_2. \quad (12)$$

Equations (1) and (11*a*) are now solved simultaneously for x and λ. Differentiation of Eq. (1) twice with respect to time and using Eq. (11*b*), result in

$$\varepsilon \cdot \ddot{x} + tg\alpha \cdot \ddot{x} = 0. \quad (13)$$

The solution of the last equation is

$$x = D_3 \cdot e^{-\rho t} + D_4 \cdot t + D5 \quad (14a)$$

$$\rho = tg\alpha/\varepsilon. \quad (14b)$$

Substitution of Eqs. (12) and (14*a*) into Eq. (1) results in the following conditions:

$$D_1 = tg\alpha \cdot D_4 \quad (15a)$$

$$D_2 = tg\alpha \cdot D_5 + \varepsilon D_4. \quad (15b)$$

The solution as presented by Eqs. (12), (14*a*), and (15*a*, *b*) is different from that of the previous section (Eqs. (6*a*) and (7*a*)).

It seems that something is wrong with the "regular" variational approach that was presented here, it will be further discussed in what follows.

4 Using the New Variational Formulation of Rosen and Edelstein (1997a)

One detail that is missing from the derivation of Section 3 is the introduction of the condition that the linear path is smooth. When holonomic constraints are considered, a smooth path means that zero work is done by the reaction forces, thus "automatically" the condition of a smooth path is included within the variational approach (that seeks the solution of "minimum work"). This is not true in the case of nonholonomic constraints. Therefore the condition of a smooth path should be added. This condition can be stated as a zero acceleration along the path, and in the present example it is written in the following manner:

$$\ddot{x} + tg\alpha \cdot \ddot{y} = 0. \quad (16)$$

According to the new formulation of Rosen and Edelstein (1997a), the modified Lagrangian includes the kinetic energy and the constraints (1) and (16):

$$L_d = \tfrac{1}{2}(\dot{x}^2 + \dot{y}^2) - \lambda_1(y - tg\alpha \cdot x - \varepsilon \cdot \dot{x}) - \lambda_2(\ddot{x} + tg\alpha \cdot \ddot{y}). \quad (17)$$

In fact the formulation of Rosen and Edelsen (1997a) includes also the first time derivative of the first constraint. Yet, since this constraint derivative does not change the variational approach, it has been omitted for the sake of simplicity.

The equations of motion are obtained by using Eq. (17) of Rosen and Edelstein (1997a) that is copied here again because of its importance and for the sake of completeness:

$$-\frac{d^2}{dt^2}\left(\frac{\partial L_d}{\partial \ddot{q}_i}\right) + \frac{d}{dt}\left(\frac{\partial L_d}{\partial \dot{q}_i}\right) - \frac{\partial L_d}{\partial q_i} = Q_i. \quad (18)$$

q_i are the generalized coordinates of the problem (x and y in the present case), while Q_i are the generalized forces that are equal to zero in the present example.

Substitution of Eq. (17) into Eq. (18) gives the equations of motion (see Eqs. (19*a*, *b*) below). The constraints, Eqs. (1) and (16), complete the system of four differential equations:

$$\ddot{x} + \varepsilon \cdot \dot{\lambda}_1 - tg\alpha \cdot \lambda_1 + \ddot{\lambda}_2 = 0 \quad (19a)$$

$$\ddot{y} + \lambda_1 + tg\alpha \cdot \ddot{\lambda}_2 = 0 \quad (19b)$$

$$-\varepsilon \cdot \dot{x} - tg\alpha \cdot x + y = 0 \quad (19c)$$

$$\ddot{x} + tg\alpha \cdot \ddot{y} = 0. \quad (19d)$$

Differentiation of Eq. (19*c*) twice with respect to time and substitution for $\ddot{y}$ into Eq. (19*d*), gives a differential equation for x that is identical to Eq. (5). After obtaining the solution for x, y is obtained using Eq. (19*c*). Equations (19*a*, *b*) are used to find λ_1 and λ_2, that are related to the reaction forces (see Rosen and Edelstein (1997a)).

It can be concluded that the solution based on the new formulation of Rosen and Edelstein gives identical results to the Newton approach, unlike the "regular" variational approach that gives wrong results.

5 Conclusions

The treatment of nonholonomic constraints is usually more problematic than holonomic constraints. During the solution of

Downloaded 04 May 2010 to 171.66.16.34. Redistribution subject to ASME license or copyright; see http://www.asme.org/terms/Terms_Use.cfm

problems with nonholonomic constraints it is very important to consider carefully the physical aspects of the problem. Otherwise, one may find oneself solving a mathematical problem that does not have a sound physical basis.

The new formulation of the Lagrange method that was recently presented by Rosen and Edelstein, seems to offer a unified variational approach to both holonomic and nonholonomic constraints. For a simple example that was present above the new formulation gave results that were identical to the results of a Newtonian approach, while the "regular" approach to nonholonomic constraints failed to do that. The authors obtained similar results in other examples (Rosen and Edelstein, 1997b). Yet, the authors by no means feel that the difficulty of solving nonholonomic problems is over. The new formulation seems to be promising, but many more careful examinations of it are necessary in order to gain more confidence in its capabilities, further improve its performance, and knowing its limitations. The authors invite other researchers to test, extend, and improve the new formulation. For example, Eq. (18) can be extended to deal with Lagrangians that include derivatives higher than the second. If there exist problems that include high derivatives, the results of such an extension may be interesting.

Before closing, the authors would like to again thank Professor Hagedorn for his interesting and stimulating discussion.

References

Rosen, A., and Edelstein, E., 1997a, "Investigation of a New Formulation of the Lagrange Method for Constrained Dynamic Systems," ASME JOURNAL OF APPLIED MECHANICS, Vol. 64, pp. 116–122.

Rosen, A., and Edelstein, E., 1997b, "A New Examination of the Problem of Constrained Dynamics," TAE Report No. 805, Faculty of Aerospace Engineering, Technion–Israel Institute of Technology, Haifa, Israel.

Modal Decoupling of Systems Described by Three Linear Operators[7]

W. Kliem[8]. The author describes an interesting modal approach for linearized forced dynamic systems not necessarily having symmetric system operators (e.g., matrices). In this way a series of well-known characteristics of conventional modal analysis for symmetric systems is preserved. A crucial assumption in the authors paper is that the system of eigenfunctions (eigenvectors) is *complete.* Nevertheless, a few changes in the modal matrices using generalized eigenvectors and more general normalization relations allow an extension of the theory to the case with an insufficient number of eigenvectors (see Kliem, 1980).

For the sake of simplicity we demonstrate this generalization by dealing with a two-dimensional matrix differential equation:

$$M\ddot{u} + C\dot{u} + Ku = F(t), \quad (M \text{ nonsingular}). \tag{1}$$

We assume a simple eigenvalue μ and an eigenvalue λ with algebraic multiplicity three and geometric multiplicity one. This means that there corresponds only one eigenvector x_0 to the multiple eigenvalue λ. Such a case is, e.g., represented by the system matrices

$$M = \begin{bmatrix} 1 & 0 \\ 0 & 1 \end{bmatrix}, \quad C = \begin{bmatrix} -1 & 0 \\ 1 & 3 \end{bmatrix},$$

$$K = \begin{bmatrix} 1 & 3 \\ 1 & 2 \end{bmatrix}, \quad F(t) = \begin{bmatrix} f_1(t) \\ f_2(t) \end{bmatrix}.$$

We introduce $L(\lambda) = \lambda^2 M + \lambda C + K$, $L^{(1)}(\lambda) = 2\lambda M + C$, and $L^{(2)}(\lambda) = M$ and define in the usual way a right eigenvector x_0 and generalized eigenvectors x_1, x_2 by

$$L(\lambda)x_0 = 0, \quad L^{(1)}(\lambda)x_0 + L(\lambda)x_1 = 0,$$
$$L^{(2)}(\lambda)x_0 + L^{(1)}(\lambda)x_1 + L(\lambda)x_2 = 0$$

and similar left eigenvectors by

$$y_0^T L(\lambda) = 0, \quad y_0^T L^{(1)}(\lambda) + y_1^T L(\lambda) = 0,$$
$$y_0^T L^{(2)}(\lambda) + y_1^T L^{(1)}(\lambda) + y_2^T L(\lambda) = 0.$$

For the eigenvalue μ there exists one right and one left eigenvector

$$L(\mu)v_1 = 0, \quad w_1^T L(\mu) = 0.$$

With these vectors we define

$$v = x_2 + x_1 t + x_0 \frac{t^2}{2!}, \quad \dot{v} = x_1 + x_0 t, \quad \ddot{v} = x_0,$$

$$w = y_2 - y_1 t + y_0 \frac{t^2}{2!}, \quad -\dot{w} = y_1 - y_0 t, \quad \ddot{w} = y_0$$

and right and left *modal matrices*

$$R_{2\times 4} = [v_1 \quad \ddot{v} \quad \dot{v} \quad v], \quad L_{4\times 2} = \begin{bmatrix} w_1^T \\ w^T \\ -\dot{w}^T \\ \ddot{w}^T \end{bmatrix}.$$

R contains four arbitrary constants and so does L. The complete solution of the homogeneous part of (1) ($F(t) = 0$) is given by $u = \mathrm{Re}^{\Lambda t}$ where $\Lambda = \mathrm{diag}\{\mu\ \lambda\ \lambda\ \lambda\}$, compare the author's Eq. (7). To receive a solution of the inhomogeneous system (1), we *normalize* the two modal matrices by

$$RL = 0 \quad \text{and} \quad R\Lambda L + \dot{R}L = M^{-1}. \tag{2}$$

These Eqs. (2) substitute the authors orthogonality relations (6), (7), and (8). System (1) now has a solution

$$u = RD, \quad D = [d_1(t) \ldots d_4(t)]^T,$$
$$\text{with the restriction } R\dot{D} = R\Lambda D, \tag{3}$$

which is equivalent to the authors Eqs. (12) and (13).

The matrix D can be found by solving the *decoupled* first-order system

$$\dot{D} - \Lambda D = LF(t)$$

which is analogous to the authors Eq. (14).

In the case of harmonic excitation $F(t) = \Phi e^{i\omega t}$, where Φ is a constant column, the steady-state solution (3) becomes

$$u = R\{(i\omega I - \Lambda)^{-1}L + (i\omega I - \Lambda)^{-2}(-\dot{L}) + (i\omega I - \Lambda)^{-3}\ddot{L}\}\Phi e^{i\omega t} \tag{4}$$

or explicitly

$$u = \left\{\frac{v_1 w_1^T}{i\omega - \mu} + \frac{\ddot{v}w^T + \dot{v}(-\dot{w}^T) + v\ddot{w}^T}{i\omega - \lambda} + \frac{\ddot{v}(-\dot{w}^T) + \dot{v}\dot{w}^T}{(i\omega - \lambda)^2} + \frac{\ddot{v}\ddot{w}^T}{(i\omega - \lambda)^3}\right\}\Phi e^{i\omega t},$$

which resembles the well-known solution received by modal analysis for conservative systems. In the case of a complete set of eigenvectors, e.g., if all eigenvalues are distinct, we have $\dot{L} = \ddot{L} = 0$ and (4) is equivalent to the result of Wahed and Bishop (1976).

[7] Renshaw, A. A., 1997, "Modal Decoupling of Systems Described by Three Linear Operators," ASME JOURNAL OF APPLIED MECHANICS, Vol. 64, pp. 238–240.

[8] Department of Mathematics, Technical University of Denmark, Building 303, DK-Lyngby, Denmark.

Downloaded 04 May 2010 to 171.66.16.34. Redistribution subject to ASME license or copyright; see http://www.asme.org/terms/Terms_Use.cfm

problems with nonholonomic constraints it is very important to consider carefully the physical aspects of the problem. Otherwise, one may find oneself solving a mathematical problem that does not have a sound physical basis.

The new formulation of the Lagrange method that was recently presented by Rosen and Edelstein, seems to offer a unified variational approach to both holonomic and nonholonomic constraints. For a simple example that was present above the new formulation gave results that were identical to the results of a Newtonian approach, while the "regular" approach to nonholonomic constraints failed to do that. The authors obtained similar results in other examples (Rosen and Edelstein, 1997b). Yet, the authors by no means feel that the difficulty of solving nonholonomic problems is over. The new formulation seems to be promising, but many more careful examinations of it are necessary in order to gain more confidence in its capabilities, further improve its performance, and knowing its limitations. The authors invite other researchers to test, extend, and improve the new formulation. For example, Eq. (18) can be extended to deal with Lagrangians that include derivatives higher than the second. If there exist problems that include high derivatives, the results of such an extension may be interesting.

Before closing, the authors would like to again thank Professor Hagedorn for his interesting and stimulating discussion.

References

Rosen, A., and Edelstein, E., 1997a, "Investigation of a New Formulation of the Lagrange Method for Constrained Dynamic Systems," ASME JOURNAL OF APPLIED MECHANICS, Vol. 64, pp. 116–122.

Rosen, A., and Edelstein, E., 1997b, "A New Examination of the Problem of Constrained Dynamics," TAE Report No. 805, Faculty of Aerospace Engineering, Technion–Israel Institute of Technology, Haifa, Israel.

Modal Decoupling of Systems Described by Three Linear Operators[7]

W. Kliem[8]. The author describes an interesting modal approach for linearized forced dynamic systems not necessarily having symmetric system operators (e.g., matrices). In this way a series of well-known characteristics of conventional modal analysis for symmetric systems is preserved. A crucial assumption in the authors paper is that the system of eigenfunctions (eigenvectors) is *complete.* Nevertheless, a few changes in the modal matrices using generalized eigenvectors and more general normalization relations allow an extension of the theory to the case with an insufficient number of eigenvectors (see Kliem, 1980).

For the sake of simplicity we demonstrate this generalization by dealing with a two-dimensional matrix differential equation:

$$M\ddot{u} + C\dot{u} + Ku = F(t), \quad (M \text{ nonsingular}). \tag{1}$$

We assume a simple eigenvalue μ and an eigenvalue λ with algebraic multiplicity three and geometric multiplicity one. This means that there corresponds only one eigenvector x_0 to the multiple eigenvalue λ. Such a case is, e.g., represented by the system matrices

$$M = \begin{bmatrix} 1 & 0 \\ 0 & 1 \end{bmatrix}, \quad C = \begin{bmatrix} -1 & 0 \\ 1 & 3 \end{bmatrix},$$

$$K = \begin{bmatrix} 1 & 3 \\ 1 & 2 \end{bmatrix}, \quad F(t) = \begin{bmatrix} f_1(t) \\ f_2(t) \end{bmatrix}.$$

We introduce $L(\lambda) = \lambda^2 M + \lambda C + K$, $L^{(1)}(\lambda) = 2\lambda M + C$, and $L^{(2)}(\lambda) = M$ and define in the usual way a right eigenvector x_0 and generalized eigenvectors x_1, x_2 by

$$L(\lambda)x_0 = 0, \quad L^{(1)}(\lambda)x_0 + L(\lambda)x_1 = 0,$$
$$L^{(2)}(\lambda)x_0 + L^{(1)}(\lambda)x_1 + L(\lambda)x_2 = 0$$

and similar left eigenvectors by

$$y_0^T L(\lambda) = 0, \quad y_0^T L^{(1)}(\lambda) + y_1^T L(\lambda) = 0,$$
$$y_0^T L^{(2)}(\lambda) + y_1^T L^{(1)}(\lambda) + y_2^T L(\lambda) = 0.$$

For the eigenvalue μ there exists one right and one left eigenvector

$$L(\mu)v_1 = 0, \quad w_1^T L(\mu) = 0.$$

With these vectors we define

$$v = x_2 + x_1 t + x_0 \frac{t^2}{2!}, \quad \dot{v} = x_1 + x_0 t, \quad \ddot{v} = x_0,$$

$$w = y_2 - y_1 t + y_0 \frac{t^2}{2!}, \quad -\dot{w} = y_1 - y_0 t, \quad \ddot{w} = y_0$$

and right and left *modal matrices*

$$R_{2\times 4} = [v_1 \quad \ddot{v} \quad \dot{v} \quad v], \quad L_{4\times 2} = \begin{bmatrix} w_1^T \\ w^T \\ -\dot{w}^T \\ \ddot{w}^T \end{bmatrix}.$$

R contains four arbitrary constants and so does L. The complete solution of the homogeneous part of (1) ($F(t) = 0$) is given by $u = \mathrm{Re}^{\Lambda t}$ where $\Lambda = \mathrm{diag}\{\mu\ \lambda\ \lambda\ \lambda\}$, compare the author's Eq. (7). To receive a solution of the inhomogeneous system (1), we *normalize* the two modal matrices by

$$RL = 0 \quad \text{and} \quad R\Lambda L + \dot{R}L = M^{-1}. \tag{2}$$

These Eqs. (2) substitute the authors orthogonality relations (6), (7), and (8). System (1) now has a solution

$$u = RD, \quad D = [d_1(t) \ldots d_4(t)]^T,$$
$$\text{with the restriction } R\dot{D} = R\Lambda D, \tag{3}$$

which is equivalent to the authors Eqs. (12) and (13).

The matrix D can be found by solving the *decoupled* first-order system

$$\dot{D} - \Lambda D = LF(t)$$

which is analogous to the authors Eq. (14).

In the case of harmonic excitation $F(t) = \Phi e^{i\omega t}$, where Φ is a constant column, the steady-state solution (3) becomes

$$u = R\{(i\omega I - \Lambda)^{-1}L + (i\omega I - \Lambda)^{-2}(-\dot{L}) + (i\omega I - \Lambda)^{-3}\ddot{L}\}\Phi e^{i\omega t} \tag{4}$$

or explicitly

$$u = \left\{\frac{v_1 w_1^T}{i\omega - \mu} + \frac{\ddot{v}w^T + \dot{v}(-\dot{w}^T) + v\ddot{w}^T}{i\omega - \lambda} + \frac{\ddot{v}(-\dot{w}^T) + \dot{v}\dot{w}^T}{(i\omega - \lambda)^2} + \frac{v\ddot{w}^T}{(i\omega - \lambda)^3}\right\}\Phi e^{i\omega t},$$

which resembles the well-known solution received by modal analysis for conservative systems. In the case of a complete set of eigenvectors, e.g., if all eigenvalues are distinct, we have $\dot{L} = \ddot{L} = 0$ and (4) is equivalent to the result of Wahed and Bishop (1976).

[7] Renshaw, A. A., 1997, "Modal Decoupling of Systems Described by Three Linear Operators," ASME JOURNAL OF APPLIED MECHANICS, Vol. 64, pp. 238–240.

[8] Department of Mathematics, Technical University of Denmark, Building 303, DK-Lyngby, Denmark.

 Copyright © 1997 by ASME

Downloaded 04 May 2010 to 171.66.16.34. Redistribution subject to ASME license or copyright; see http://www.asme.org/terms/Terms_Use.cfm

Another example with two double eigenvalues where each possesses only one eigenvector (modeling a double pendulum with a follower force and an external torque) can be found in Kliem (1980).

This generalization was carried out in the discrete system analysis of Wahed and Bishop (1976), but can also be formulated in the operator analysis of the author.

References

Kliem, W., 1980, "Free and Forced Vibrations of a Linear Non-Conservative System with Multiple Eigenvalues," *ZAMM*, Vol. 60, pp. 569–575.

Wahed, I. F. A., and Bishop, R. E. D., 1976, "On the Equations Governing the Free and Forced Vibrations of a general Non-Conservative System," *Journal of the Mechanical Engineering Sciences*, Vol. 18, No. 1, pp. 6–10.

Downloaded 04 May 2010 to 171.66.16.34. Redistribution subject to ASME license or copyright; see http://www.asme.org/terms/Terms_Use.cfm

Journal of Applied Mechanics

Book Review

Dislocation Based Fracture Mechanics, by Johannes Weertman. World Scientific, River Edge, NJ, 1996.

REVIEWED BY L. M. KEER[1]

This book, by one of the major contributors to dislocation theory, gives a highly detailed look, using planar examples, into the materials science aspects of many important physical processes associated with fracture. The compendium of references provided by this excellently researched book will be invaluable for the advanced or beginning reader. It should also be emphasized that this book is suitable for teaching and contains many homework problems at the end of each chapter.

The reader is introduced to the subject of fracture mechanics in the first chapter through the use of the Griffith-Inglis and the Zener-Stroh-Koehler cracks as examples. However, to lead the reader to understand better the physics of dislocations requires the material in Chapter 2, which is devoted solely to dislocation mechanics. The material brings the reader up to date on recent issues as well as providing a sound grounding on basic principles. Next, a requisite level of mathematics is required in order to solve many of the subsequent examples and is provided by the introduction of Hilbert transforms and the Muskhelishvili equations.

[1] Professor, Department of Mechanical Engineering, Northwestern University, Evanston, IL 60208. Fellow, ASME.

Chapter 5 discusses issues associated with crack-tip shielding and antishielding by dislocations. Induced crack plane dislocation distributions, impurity atom crack-tip shielding and antishielding, and microcrack shielding and antishielding are analyzed in this chapter, which concludes with models for crack tip blunting.

The next three chapters investigate cracking in an elastic-plastic solid where Mode III, Mode II, and Mode I crack problems are solved. Since Weertman has contributed greatly to these areas in his research, the chapters are rich with detail and would be of interest to many readers. The steady-moving Yoffe crack is illustrated in Chapter 9 through several examples. Dislocation stress fields are first investigated for a uniformly moving crack. Next, stress fields are given for Modes I, II, and III cracks and a discussion of Yoffe crack branching is presented. Dislocation density field equations are given for plane and antiplane strain.

Chapter 10 is devoted to additional applications and also reveal some of Weertman's interest in geophysics as well as materials science. The topics discussed here are wide-ranging and involve crevasses and dikes, unstable slippage, edge cracks, interface cracks, fatigue crack propagation, and redundant and nonredundant dislocations.

Weertman's book will be good reading for a researcher who is interested in mechanics and materials science and provides a useful introduction to the subject together with advanced topics. The material contained will be suitable for a course in dislocation mechanics or micromechanics.

Copyright © 1997 by ASME

Downloaded 04 May 2010 to 171.66.16.34. Redistribution subject to ASME license or copyright; see http://www.asme.org/terms/Terms_Use.cfm